

AD-A094 291

GENERAL ELECTRIC CO CINCINNATI OH AIRCRAFT ENGINE GROUP F/G 20/1
HIGH VELOCITY JET NOISE SOURCE LOCATION AND REDUCTION. TASK 2. --ETC(U)
MAY 78 T F Balsa, P R GLIEBE, R A KANTOLA DOT-05-30034
R78AE6323 FAA-RD-76-79-2 NL

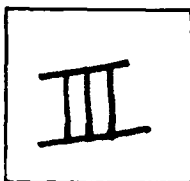
UNCLASSIFIED

9
م

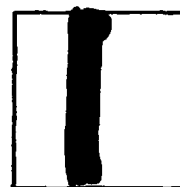
PHOTOGRAPH THIS SHEET

AD A091291

DTIC ACCESSION NUMBER



LEVEL



INVENTORY

GENERAL ELECTRIC CO. CINCINNATI OHIO
ENGINE GROUP
HIGH VELOCITY JET NOISE SOURCE LOCATION AND
REDUCTION. TASK 2. THEORETICAL DEVELOPMENTS AND BASIC
DOCUMENT IDENTIFICATION
EXPERIMENTS. FINAL REPT, May 78 REPT. NO. R78AEG323
Contract DOT-OS-30034 FAA-RD-76-79-2

DISTRIBUTION STATEMENT A

Approved for public release;
Distribution Unlimited

DISTRIBUTION STATEMENT

ACCESSION FOR	
NTIS	GRA&I
DTIC	TAB
UNANNOUNCED	
JUSTIFICATION	
BY	
DISTRIBUTION /	
AVAILABILITY CODES	
DIST	AVAIL AND/OR SPECIAL
A	

DISTRIBUTION STAMP

DTIC	
ELECTE	
JAN 28 1981	
S	D

DATE ACCESSIONED

See also TASK 1, AD-A041 848.

81 1 27 005

DATE RECEIVED IN DTIC

PHOTOGRAPH THIS SHEET AND RETURN TO DTIC-DDA-2

HIGH VELOCITY JET NOISE SOURCE LOCATION AND REDUCTION

TASK 2 - THEORETICAL DEVELOPMENTS AND BASIC EXPERIMENTS

TECHNICAL CONTRIBUTORS:

T.F. Balsa
P.R. Gliebe
R.A. Kantola

R. Mani
E.J. Stringas
J.C.F. Wang

GENERAL ELECTRIC COMPANY
AIRCRAFT ENGINE GROUP
CINCINNATI, OHIO 45215



FINAL REPORT

MAY 1978

Document is available to the public through the
National Technical Information Service,
Springfield, Virginia 22151

Prepared for

U.S. DEPARTMENT OF TRANSPORTATION
FEDERAL AVIATION ADMINISTRATION
Systems Research & Development Service
Washington, D.C. 20590

AD A094291

NOTICE

The contents of this report reflect the views of the General Electric Company which is responsible for the facts and the accuracy of the data presented herein. The contents do not necessarily reflect the official views or policy of the Department of Transportation. This report does not constitute a standard, specification or regulation.

1. Report No. FAA-RD-76-79, II		2. Government Accession No.		3. Recipient's Catalog No.	
4. Title and Subtitle High Velocity Jet Noise Source Location and Reduction Task 2 - Theoretical Developments and Basic Experiments				5. Report Date	
				6. Performing Organization Code	
7. Author(s) T.F. Balsa, P.R. Gliebe, R.A. Kantola, J.C.F. Wang R. Mani (Task 2 Technical Director) E.J. Stringas (Technical Project Manager)				8. Performing Organization Report No. R78AEG323	
9. Performing Organization Name and Address General Electric Company Advanced Engineering and Technology Programs Department Aircraft Engine Group Cincinnati, Ohio 45215				10. Work Unit No.	
				11. Contract or Grant No. DOT-OS-30034	
12. Sponsoring Agency Name and Address U.S. Department of Transportation Federal Aviation Administration Systems Research and Development Services Washington, D.C. 20590				13. Type of Report and Period Covered Task 2 Final Report Oct. 1973 - Aug. 1977	
				14. Sponsoring Agency Code ARD-550	
15. Supplementary Notes This report is in partial fulfillment of the subject program. Related documents to be issued in the course of the program include final reports of the following tasks: Task 1 - Activation of Facilities and Validation of Source Location Techniques; Task 1 Supplement - Certification of the General Electric Jet Noise Anechoic Test Facility; Task 3 - Experimental Investigation of Suppression Principles; Task 4 - Development/Evaluation of Techniques for Inflight Investigation; Task 5 - Investigation of "Inflight" Aero-Acoustic Effects; Task 6 - Noise Abatement Nozzle Design Guide. The FAA Program Manager for this effort was Mr. Robert S. Zuckerman.					
16. Abstract <p>This report presents the results of Task 2 conducted under the subject program over a period of 45 months. Task 2 was formulated as a fundamental theoretical and experimental study aimed at an understanding of the noise generation and suppression mechanisms of high velocity jets. The mechanisms investigated included changes in turbulence structure, fluid shielding, and alteration of convective amplification of jet noise sources. Several other areas such as a physical shielding, shock associated noise, lip noise, effect of fluid/particle additives on jet noise, orderly structure in jets, ejector aeroacoustics, and flight effects on jet noise were also investigated.</p> <p>The most significant achievements of Task 2 were as follows. A unified aeroacoustic theory composed of three ingredients was developed: (1) the prediction of mean properties of the jet plume, (2) deduction of turbulence properties relevant to jet noise by similarity arguments, and (3) the prediction of far-field noise including the effects of fluid shielding. A semiempirical shock noise prediction procedure was also developed. Exhaustive theory-data comparisons for a wide range of nozzle configurations and velocity/temperature combinations were conducted and have confirmed the essential validity of this model as a prediction tool. A comprehensive series of experiments with simple suppressor elements (such as a single rectangular tube, twin jets, linear arrays of jets, circular arrays of jets) was carried out and revealed the importance of acoustic shielding by adjacent jets. A fundamental series of experiments, specifically tailored to reveal fluid shielding as a jet noise suppression mechanism, was successfully conducted. Physical shielding was investigated both theoretically and experimentally. Lip noise was studied experimentally, and no evidence was found that it contributed significantly to jet noise at high velocities and with aerodynamically well-contoured nozzles (with or without external velocity). Surveys of previous work on particle/fluid injection showed this approach to be of little promise in suppression of high temperature jet noise. The orderly structure question was explored with the aid of simple experiments, but no conclusive demonstration of its relevance to jet noise (or its prediction) was achieved.</p> <p>Since the development of the unified aeroacoustic model was judged to be the most practically useful result of Task 2, a description of the computer program used to implement it is included in a supplemental volume to this final report, FAA-RD-76-79, IIA.</p>					
17. Key Words (Suggested by Author(s)) Jet Noise, Inflight Effects, Suppressor Nozzles, Acoustic Shielding, Jet Flows			18. Distribution Statement Document is available to the public through the National Technical Information Service, Springfield, Virginia, 22151		
19. Security Classif. (of this report) Unclassified		20. Security Classif. (of this page) Unclassified		21. No. of Pages 814	
				22. Price*	

* For sale by the National Technical Information Service, Springfield, Virginia 22151

METRIC CONVERSION FACTORS

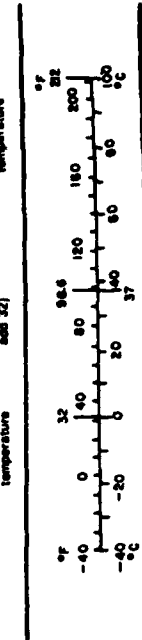
Approximate Conversions to Metric Measures

Symbol	When You Know	Multiply by	To Find	Symbol
LENGTH				
in	inches	2.5	centimeters	cm
ft	feet	30	meters	m
yd	yards	0.9	meters	m
mi	miles	1.6	kilometers	km
AREA				
sq in	square inches	6.5	square centimeters	cm ²
sq ft	square feet	0.09	square meters	m ²
sq yd	square yards	0.8	square meters	m ²
sq mi	square miles	2.6	square kilometers	km ²
acres	acres	0.4	hectares	ha
MASS (weight)				
oz	ounces	28	grams	g
lb	pounds	0.45	kilograms	kg
	short tons (2000 lb)	0.9	tonnes	t
VOLUME				
imp gal	imperial gallons	4	liters	l
U.S. gal	U.S. gallons	3.8	liters	l
qt	quarts	0.95	liters	l
pint	pints	0.47	liters	l
cup	cups	0.24	liters	l
fluid oz	fluid ounces	29.6	milliliters	ml
tblsp	tablespoons	15	milliliters	ml
teaspoon	teaspoons	5	milliliters	ml
fluid oz	fluid ounces	29.6	milliliters	ml
cup	cups	237	milliliters	ml
quart	quarts	946	milliliters	ml
gallon	gallons	3785	milliliters	ml
lit	liters	1	liters	l
cu ft	cubic feet	28.3	cubic meters	m ³
cu yd	cubic yards	0.76	cubic meters	m ³
TEMPERATURE (exact)				
°F	Fahrenheit temperature	5/9 (after subtracting 32)	Celsius temperature	°C

Approximate Conversions from Metric Measures

Symbol	When You Know	Multiply by	To Find	Symbol
LENGTH				
mm	millimeters	0.04	inches	in
cm	centimeters	0.4	inches	in
m	meters	3.3	feet	ft
m	meters	1.1	yards	yd
km	kilometers	0.6	miles	mi
AREA				
cm ²	square centimeters	0.16	square inches	in ²
m ²	square meters	1.2	square yards	yd ²
km ²	square kilometers	0.4	square miles	mi ²
ha	hectares (10,000 m ²)	2.5	acres	ac
MASS (weight)				
g	grams	0.035	ounces	oz
kg	kilograms	2.2	pounds	lb
t	tonnes (1000 kg)	1.1	short tons	st
VOLUME				
ml	milliliters	0.03	fluid ounces	fl oz
l	liters	2.1	pints	pt
l	liters	1.06	quarts	qt
l	liters	0.26	gallons	gal
m ³	cubic meters	35	cubic feet	ft ³
m ³	cubic meters	1.3	cubic yards	yd ³
TEMPERATURE (exact)				
°C	Celsius temperature	9/5 (then add 32)	Fahrenheit temperature	°F

*1 in = 2.54 exactly. For other exact conversions and more detailed tables, see NBS Misc. Publ. 286, Units of Length and Mass, NBS 62-76, 50 Centing No. C13.10.286.



PREFACE

This report describes the work performed under Task 2 of the DOT/FAA High Velocity Jet Noise Source Location and Reduction Program (Contract DOT-OS-30034). The objectives of the contract were:

- Investigation of the aerodynamic and acoustic mechanisms of various jet noise suppressors, including scaling effects.
- Analytical and experimental studies of the acoustic source distribution in such suppressors, including identification of source location, nature and strength, and noise reduction potential.
- Investigation of in-flight effects on the aerodynamic and acoustic performance of these suppressors.

The results of these investigations have led to the preparation of a design guide report for predicting the overall characteristics of suppressor concepts from models to full-scale static, to in-flight conditions, as well as a quantitative and qualitative prediction of the phenomena involved.

The work effort in this program was organized under the following major tasks, each of which is reported in a separate Final Report:

Task 1 -- Activation of Facilities and Validation of Source Location Techniques

Task 2 -- Theoretical Developments and Basic Experiments

Task 3 -- Experimental Investigation of Suppression Principles

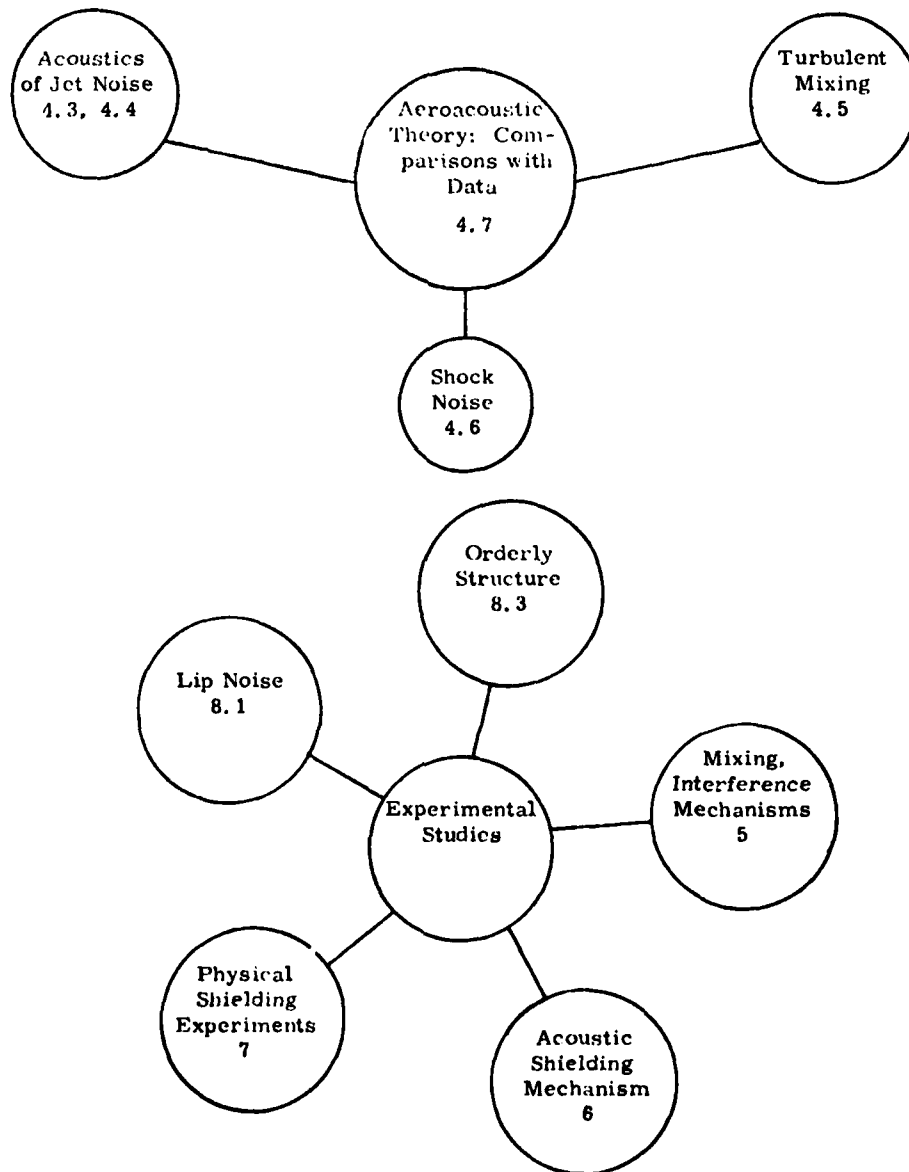
Task 4 -- Development and Evaluation of Techniques for "In-flight" Investigation

Task 5 -- Investigation of "In-flight" Aeroacoustic Effects on Suppressed Exhausts

Task 6 -- Preparation of Noise Abatement Nozzle Design Guide Report

Task 1 was an investigative and survey effort designed to identify acoustic facilities and test methods best suited to jet noise studies. Task 2 was a theoretical effort complemented by theory verification experiments which extended across the entire contract period of performance. Task 3 represented a substantial contract effort to gather various test data on a wide range of High Velocity Jet Nozzle suppressors. These data, intended to help identify several "optimum" nozzles for "in-flight" testing under Task 5, provide an extensive high quality data bank useful to preparation of the Task 6 design guide, as well as to future studies.

Task 2, the subject of the present report, was formulated as a fundamental theoretical and experimental study aimed at understanding of the noise generation and suppression mechanisms of high velocity jets. A gross overview of the most important results achieved in this study along with an indication of the relevant report sections is given in the following figure. The reader interested in the aero-acoustic theory which was used in the ultimate prediction procedure recommended herein need study only Sections 4.3 to 4.7. The reader interested in the experimental data acquired in the course of performing this task need study only Sections 5, 6, 7, and 8.1 and 8.3.



Overview of sections containing the most important results of this report.

ACKNOWLEDGEMENTS

The work from which Section 8.1, Lip Noise, was derived was performed by the University of British Columbia as subcontractor to the General Electric Company, under the direction of Professor T.E. Siddon. The work on Orderly Structure, reported in Section 8.3, was performed by the University of Southern California as subcontractor to the General Electric Company, under the direction of Professor John Laufer. Professor H.S. Ribner served as an overall consultant to Task 2 and to other phases of the program.

TABLE OF CONTENTS

<u>Section</u>	<u>Page</u>
1.0 SUMMARY	1
2.0 INTRODUCTION	4
3.0 FACILITIES DESCRIPTION	5
3.1 General Electric Corporate Research and Development (CRD) Outdoor Facility	5
3.1.1 Acoustic Arena	5
3.1.2 Jet Facility	6
3.1.3 Data Acquisition and Reduction System	6
3.2 Hole-in-the-Wall Source Location Measurements	9
3.3 Laser Velocimeter at CRD	11
4.0 THERORETICAL DEVELOPMENTS	17
4.1 Background and Overviews	17
4.2 Plug Flow Models	29
4.2.1 Low Frequency Model for Noncircular Jets	29
4.2.2 Convecting Sources in an Annular Jet	62
4.2.3 Conventional Bypass Coaxial Jet Noise	83
4.3 Generalized High Frequency Shielding Theory	98
4.3.1 Introduction	98
4.3.2 Formulation of the Problem	100
4.3.3 The Turning Points	104
4.3.4 No Turning Points - Problem 1	107
4.3.5 One Turning Point - Problem 2	112
4.3.6 Two Turning Points - Problem 3	118
4.3.7 Two Turning Points - Problem 4	119
4.3.8 One or Two Turning Points - Problems 5 and 6	123
4.3.9 Interpretive Remarks	123
4.3.10 Pressure Field of Convected Singularities	123
4.3.11 The Directivity of Noise	129
4.3.12 Conclusions	130
4.4 Acoustics of Flight Noise Prediction	131
4.4.1 Introduction	131
4.4.2 Formulation of the Problem	131
4.4.3 Solution of the Problem	132

TABLE OF CONTENTS (Continued)

<u>Section</u>	<u>Page</u>
4.4.4 Results for the Spectrum Using Moving Correlation	135
4.4.5 Spectrum of Noise in Flight	136
4.4.6 Discussion	138
4.4.7 Conclusions	138
4.5 Reichardt's Theory for Arbitrary Jet Flows	140
4.5.1 Introduction	140
4.5.2 Basic Equations and Assumptions	141
4.5.3 General Solution	147
4.5.4 Experimental Evaluation of Empirical Constants	149
4.5.5 Turbulent Structure Quantities	157
4.5.6 Base Pressure Efforts	158
4.5.7 Computational Procedures	160
4.5.8 Comparisons of Predictions with Experiment	170
4.5.9 Concluding Remarks	187
4.6 Shock-Cell Noise	190
4.6.1 Introduction	190
4.6.2 Review of a Theoretical Model for Conical Nozzles	190
4.6.3 Review of SNECMA Empirical Correlation	199
4.6.4 Experimental Correlations of Shock-Cell Noise for Conical Nozzles	199
4.6.5 Experimental Assessment of Relative Velocity Effects on Conical Nozzle Shock-Cell Noise	204
4.6.6 Experimental Evaluation of Noncircular Nozzle Shock-Cell Noise Characteristics	210
4.6.7 Experimental Evaluation of Annular Plug Nozzle Shock-Cell Noise Characteristics	217
4.6.8 Model Parametric Studies	223
4.6.9 Extension of Prediction Method to Non-circular Nozzles	228
4.6.10 Concluding Remarks	237
4.7 Unified Aeroacoustic Model for Jet Noise Prediction	241
4.7.1 Introduction	241
4.7.2 Outline of Method	242
4.7.3 Aerodynamic Calculation	244
4.7.4 Source Spectrum Prediction	250
4.7.5 Acoustic Prediction	254

TABLE OF CONTENTS (Continued)

<u>Section</u>	<u>Page</u>
4.7.6 Shock-Cell Noise Prediction	259
4.7.7 Aeroacoustic Model Integration	261
4.7.8 Data-Theory Comparisons	264
4.7.9 Diagnostic Evaluation of Jet Noise Suppression Mechanisms	322
4.7.10 In-Flight Jet Noise	362
4.7.11 Concluding Remarks	363
4.8 Physical Shielding	365
4.8.1 Shielding of Sound by a Semi-Infinite Barrier	365
4.8.2 Effect of Semi-Infinite Pipes on the Sound Field of Sources in Ducts	367
5.0 MIXING INTERFERENCE EXPERIMENTS	393
5.1 Single Round Jet Noise	393
5.1.1 Overall Power and Pressure Level	405
5.1.2 Power and Pressure Spectra	405
5.2 Single Rectangular Jet Noise	413
5.2.1 Experimental Apparatus	413
5.2.2 Experimental Results and Discussion	413
5.2.3 Effect of Velocity on Peak Frequency	429
5.2.4 Summary	434
5.3 Twin Round Jet Noise	435
5.3.1 Experimental Methods	435
5.3.2 Experimental Results and Discussion	435
5.3.3 Summary	466
5.4 Twin Rectangular Jet Noise	469
5.4.1 Experimental Results and Discussion	469
5.5 Linear Array Multitube Jet Noise	489
5.5.1 Overall Acoustic Power	489
5.5.2 Azimuthal and Polar Directivity	494
5.5.3 Power and Pressure Spectra	494
5.5.4 Summary	499
5.6 Circular Array Multitube Jet Noise	503
5.6.1 Overall Acoustic Power	503
5.6.2 Directivity	503
5.6.3 Power and Pressure Spectra	514
5.6.4 Summary	524

TABLE OF CONTENTS (Continued)

<u>Section</u>	<u>Page</u>
5.7 Laser Velocimeter Measurements	528
5.7.1 Calibration of the LV System	528
5.7.2 Experimental Results on Single Jets	528
5.7.3 Experimental Results on Twin Jets	548
5.7.4 Experimental Results on Seven-Jets Cluster Flows	552
5.8 Hole-in-the-Wall Source Location Measurements	579
5.8.1 Twin Round Jets	579
5.8.2 Twin Rectangular Jets	586
5.8.3 Concluding Remarks	595
6.0 ACOUSTIC SHIELDING EXPERIMENTS	596
6.1 Description of Test Program and Results	596
6.1.1 Test Results with a Stationary Source (Whistle)	596
6.1.2 Test Results with a Moving Source (A Small Jet Inside the Shielding Jet)	596
6.2 Theory-Data Comparisons	611
6.3 Conclusions	615
7.0 PHYSICAL SHIELDING EXPERIMENTS	616
7.1 Description of Test Program and Results	616
7.1.1 Results	616
7.2 Theory-Data Comparisons	628
7.2.1 Multitube Suppressor and Flat Plate Shield Experiments	628
8.0 OTHER TOPICS	638
8.1 Lip Noise	638
8.1.1 Fundamental Lip Noise Mechanisms	638
8.1.2 The Effect of External Flow	671
8.2 Particle/Fluid Injection	684
8.2.1 Physical Mechanisms of Damping	684
8.2.2 Practical Implications	685

TABLE OF CONTENTS (Concluded)

<u>Section</u>	<u>Page</u>
8.3 Orderly Structure	686
8.3.1 Facilities and Equipment	686
8.3.2 Experimental Procedure	696
8.3.3 Results and Discussion	704
8.3.4 Conclusions	731
8.4 Ejector Aeroacoustics	734
8.5 Physical Obstruction Noise	738
9.0 CONCLUDING REMARKS	740
10.0 RECOMMENDATIONS FOR FURTHER WORK	741
10.1 Aeroacoustic Model	741
10.2 Experimental Work	742
APPENDIX A - Jet Flow Field Calculation	745
B - Relation Between C_m and C_h	752
SYMBOLS AND ABBREVIATIONS	755
REFERENCES	772

LIST OF ILLUSTRATIONS

<u>Figure</u>	<u>Page</u>
3-1. CR&D Hot Jet Noise Facility.	7
3-2. Real Time Isometric Display of the Acoustic Spectra.	8
3-3. Acoustic Leakage and Nonclosure of Source Distribution.	10
3-4. "Hole-in-the-Wall" Experimental Apparatus.	12
3-5. Outdoor Hot Jet Facility at GE CRD.	13
3-6. Schematic of the LV Processor.	14
3-7. Block Diagram of the LV Data Acquisition System.	15
4-1. Idealized Geometry of an Arbitrary Jet.	30
4-2. Free Space Propagation Constant Versus Frequency (K_1^+ Versus κ).	35
4-3. Jet Propagation Constant Versus Frequency (K_2^+ Versus κ).	35
4-4. Geometry of Circular Jet.	47
4-5. Convective Amplification as Function of M and St.	50
4-6. Geometry of Elliptic Jet.	52
4-7. Theoretical Power Calculations for Elliptic Jet [$M = 0.7$, $c_1/c_2 = 1.0$, $\rho_1/\rho_2 = 1.0$, $\epsilon = k_0 \alpha$].	56
4-8. Theoretical Power Calculations for Elliptic Jet [$M = 0.9$, $c_1/c_2 = 1.0$, $\rho_1/\rho_2 = 1.0$, $\epsilon = k_0 \alpha$].	56
4-9. Δ SPL Between Quiet and Noisy Planes for Cold Jet [$\alpha/\beta = 9$, $M = 0.55$, ($M_c = 0.65M$), $St = 2fa (1 - M_c \cos \theta)/U$].	61
4-10. Δ SPL Between Quiet and Noisy Planes for Cold Jet.	61
4-11. Δ SPL Between Quiet and Noisy Planes for Hot Jet [$\alpha/\beta = 5$, $M = 0.7$ ($M_c = 0.65M$) $St = 2fa (1 - M_c \cos \theta)/U = 0.3$].	61
4-12. The Geometry of the Jet.	63
4-13. Total Radiated Power as a Function of Source Frequency, Planar Case and Cold Jet ($R = a/b$).	71

LIST OF ILLUSTRATIONS (Continued)

<u>Figure</u>		<u>Page</u>
4-14.	Radiated Power as a Function of Source Frequency ($R = a/b = 0.8$, $M = 0.9$, $\sigma = 0.5$).	75
4-15.	Total Radiated Power as a Function of Source Frequency, Circular Case and Cold Jet ($R = a/b$).	76
4-16.	Effective Number of Tubes as a Function of Inner to Total Number of Tubes.	78
4-17.	Geometry of Problem.	86
4-18.	Overall Sound Pressure Level at $\theta = 90^\circ$ as Function of Area and Velocity Ratios (Cold Jet, $U_{1j} = 980$ ft/sec).	93
4-19.	Sound Pressure Level at $\theta = 90^\circ$ as Function of Velocity Ratio ($AR = 3.9$, Cold Jet, $U_{1j} = 980$ ft/sec).	94
4-20.	Sound Pressure Level at $\theta = 90^\circ$ as Function of Velocity Ratio ($AR = 9.3$, Cold Jet, $U_{1j} = 980$ ft/sec).	94
4-21.	Sound Pressure Level as Function of Source Strouhal Number ($AR = 3.9$, $VR = 0.4$, Cold Jet, $U_{1j} = 980$ ft/sec).	96
4-22.	Sound Pressure Level as Function of Source Strouhal Number ($AR = 3.9$, $VR = 0.6$, Cold Jet, $U_{1j} = 980$ ft/sec).	96
4-23.	Sound Pressure Level as Function of Source Strouhal Number ($AR = 3.9$, $VR = 0.8$, Cold Jet, $U_{1j} = 980$ ft/sec).	96
4-24.	Sound Pressure Level as Function of Velocity Ratio ($AR = 2.1$, $St = 0.3$, Cold Jet, $U_{1j} = 980$ ft/sec).	96
4-25.	Sound Pressure Level at $\theta = 90^\circ$ as Function of Velocity Ratio ($AR = 4$, $TR = 2.1$, Hot Jet, $U_{1j} = 1000$ ft/sec, $T_{1j} = 1200^\circ R$).	97
4-26.	Geometry of the Problem.	101
4-27.	Turning Points of Shielding Function g^2 .	106
4-28.	Geometry of Acoustic Shielding in Modified Transverse Plane (ξ , θ).	115
4-29.	Geometry of Alternate Shielding Function $G^2 = g^2 - (v/r)^2$.	120

LIST OF ILLUSTRATIONS (Continued)

<u>Figure</u>		<u>Page</u>
4-30.	Geometry of the Problem.	133
4-31.	Nozzle in Forward Flight.	137
4-32.	Jet Nozzle Flow Coordinate System and Nomenclature.	142
4-33.	Relations Between Cartesian and Cylindrical Coordinates for Field Point (x,y,z) and Exit-Plane Point (O, η , ζ).	150
4-34.	Typical Centerline Mean Velocity Measurements for a Round Jet and Definition of Core Length L_c .	152
4-35.	Correlations of Core Length L_c for a Round Jet, Data from Harsha(66).	155
4-36.	Shear Stress at Point P Due to Contribution from Point Q; Cartesian and Cylindrical Coordinate Components.	162
4-37.	Example of Non-Circular Nozzle Contour Boundary.	164
4-38.	Examples of Multielement Nozzle Contour Boundaries.	166
4-39.	Coordinate System Transformation for Nozzles with a Plug/Centerbody.	169
4-40.	Non-coplanar Nozzle Configuration Examples.	171
4-41.	Comparison of Mean Centerline Velocity Decay 1.5 in. Diameter Conical Nozzle, $M_J = 0.98$.	171
4-42.	Comparison of Mean Velocity Profiles, 1.5 in. Diameter Conical Nozzle.	172
4-43.	Comparison of Turbulence Intensity Profiles, 1.5 in. Diameter Conical Nozzle.	172
4-44.	Comparison of Mean Velocity Profiles, 1.5 in. Diameter Conical Nozzle.	173
4-45.	Comparison of Turbulence Intensity Profiles, 1.5 in. Diameter Conical Nozzle.	173
4-46.	Comparison of Tube Centerline Mean Velocity Decay Twin Parallel Round Jets, $S/D = 1.33$, $M_J = 0.98$.	175

LIST OF ILLUSTRATIONS (Continued)

<u>Figure</u>		<u>Page</u>
4-47.	Comparison of Mean Velocity Profiles Twin Parallel Round Jets, $S/D = 1.333$.	176
4-48.	Comparison of Mean Velocity Profiles Twin Parallel Round Jets, $S/D = 1.333$.	176
4-49.	Comparison of Turbulence Intensity Profiles, Twin Parallel Round Jets.	177
4-50.	Comparison of Turbulence Intensity Profiles, Twin Parallel Round Jets.	177
4-51.	Comparison of Mean Velocity Profiles, Twin Parallel Round Jets.	178
4-52.	Comparison of Turbulence Intensity Profiles, Twin Parallel Round Jets.	178
4-53.	Comparison of Experimental and Predicted Mean Velocity Profiles for a 3.56 in. Conical Nozzle.	179
4-54.	Comparison of Experimental and Predicted Turbulence Intensity Profiles for a 3.56 in. Conical Nozzle.	180
4-55.	Comparison of Experimental and Predicted Mean Velocity Profiles for a 7.63 in. Effective Diameter C/D Plug Nozzle.	181
4-56.	Comparison of Experimental and Predicted Turbulence Intensity Profiles for a 7.63 in. Effective Diameter C/D Plug Nozzle.	182
4-57a.	Comparison of Experimental and Predicted Mean Velocity Profiles for a Coplanar Coannular Jet $AR = 0.647$; $V_{fan} =$ ft/sec; $V_{core} = 1200$ ft/sec; $T_{Tfan} = 1603^{\circ}$ R; $T_{Tcore} = 994^{\circ}$ R.	183
4-57b.	Comparison of Experimental and Predicted Mean Velocity Profiles for a Coplanar Coannular Jet $AR = 0.647$; $V_{fan} = 2400$ ft/sec; $V_{core} = 1200$ ft/sec; $T_{Tfan} = 1603^{\circ}$ R; $T_{Tcore} = 994^{\circ}$ R.	184
4-58a.	Comparison of Experimental and Predicted Turbulence Intensity Profiles for a Coplanar Coannular Jet $AR = 0.647$; $V_{fan} = 2400$ ft/sec; $V_{core} = 1200$ ft/sec, $T_{Tfan} = 1603^{\circ}$ R; $T_{Tcore} = 994^{\circ}$ R.	185

LIST OF ILLUSTRATIONS (Continued)

<u>Figure</u>		<u>Page</u>
4-58b.	Comparison of Experimental and Predicted Turbulence Intensity Profiles for a Coplanar Coannular Jet $AR = 0.647$; $V_{fan} = 2400$ ft/sec; $V_{core} = 1200$ ft/sec, $T_{Tfan} = 1603^\circ R$; $T_{Tcore} = 994^\circ R$.	186
4-59.	Comparison of Measured and Predicted Jet Centerline Turbulence Intensity.	188
4-60.	Schematic Representation of Shock Cell Formations in an Underexpanded Supersonic Jet.	191
4-61.	Illustration of Primary Components of a Conical Nozzle Shock Cell Noise Spectrum.	193
4-62.	Nomenclature for Geometric Relations Between a Given Shock Cell Source at x_n and Observer.	193
4-63.	SNECMA Model of Shock Cell Noise Component of Spectrum.	200
4-64.	OASPL Velocity Dependence, 3.56 in. Conical Nozzle, $V_o = 0$.	200
4-65.	Normalized OASPL Velocity Dependence, 3.56 in. Conical Nozzle, $V_o = 0$ (J85 Operating Line).	202
4-66.	Supersonic Point Velocity Dependence, 3.56 inch Conical Nozzle, $V_o = 0$.	202
4-67.	Supersonic Jet Normalized OASPL Correlation with Shock Strength, 3.56 in. Conical Nozzle, $V_o = 0$.	203
4-68.	Supersonic Jet OASPL Correlation with Shock Strength Parameter, 3.56 in. Conical Nozzle, $V_o = 0$, and $\theta_i = 30^\circ$.	203
4-69.	Supersonic Jet OASPL Correlation with Shock Strength Parameter β , 3.56 in. Conical Nozzle, $V_o = 0$, and $\theta_i = 60^\circ$.	205
4-70.	Supersonic Jet OASPL Correlation with Shock Strength Parameter β , 3.56 in. Conical Nozzle, $V_o = 0$, and $\theta_i = 90^\circ$.	205
4-71.	Shock-Associated Noise Spectrum, 3.56 in. Conical Nozzle, $V_o = 0$.	206

LIST OF ILLUSTRATIONS (Continued)

<u>Figure</u>		<u>Page</u>
4-72.	Shock-Associated Noise Spectrum, 3.56 in. Conical Nozzle, $V_o = 0$.	206
4-73.	Comparison of Peak Noise Frequency Predictions with Experimental Values, 3.56 in. Diameter Conical Nozzle, $V_o = 0$.	207
4-74.	Comparison of Peak Noise Predictions with Experimental Values, 3.56 in. Conical Nozzle, $V_o = 0$.	207
4-75.	Effect of Relative Velocity on Supersonic Jet Noise OASPL, 3.56 in. Conical Nozzle, $\theta_i = 30^\circ$.	208
4-76.	Effect of Relative Velocity on Supersonic Jet Noise OASPL, 3.56 in. Diameter Conical Nozzle, $\theta_i = 60^\circ$.	209
4-77.	Effect of Relative Velocity on Supersonic Jet Noise OASPL, 3.56 in. Diameter Conical Nozzle, $\theta_i = 90^\circ$.	209
4-78.	Effect of Relative Velocity on SPL Spectrum at $\theta_i = 30^\circ$, 3.56 in. Diameter Conical Nozzle.	211
4-79.	Effect of Relative Velocity on SPL Spectrum at $\theta_i = 60^\circ$, 3.56 in. Diameter Conical Nozzle.	211
4-80.	Supersonic Jet OASPL Correlation with Shock Strength Parameter 8, 2.0 in. Diameter STA Conical Nozzle, 100 ft Arc.	212
4-81.	Supersonic Jet OASPL Correlation with Shock Strength Parameter 8; Scale Model 8-Lobe Daisy Suppressor.	212
4-82.	Shock-Associated Noise Spectra, Scale-Model 8-Lobe Daisy Suppressor, Effect of Jet Temperature.	213
4-83.	Effect of Relative Velocity on Supersonic Jet Noise OASPL, Scale Model, 8-Lobe Daisy Suppressor.	215
4-84.	Shock-Associated Noise Spectra, Scale-Model 8-Lobe Daisy Suppressor; Effect of Forward Velocity.	216
4-85.	Shock-Associated Noise Spectra, Scale-Model 8-Lobe Daisy Suppressor; Effect of Forward Velocity.	216

LIST OF ILLUSTRATIONS (Continued)

<u>Figure</u>		<u>Page</u>
4-86.	Shock-Associated Noise Spectrum, 1.5 in. Diameter Conical Nozzle.	218
4-87.	Shock-Associated Noise Spectrum, 6:1 Aspect Ratio Rectangular Jet.	219
4-88.	Shock-Associated Noise Spectrum, 6:1 Aspect Ratio Rectangular Jet.	219
4-89.	Model Hardware for Parametric Nozzle Radius Ratio Study.	221
4-90.	Supersonic Jet OASPL Correlation with Shock Strength Parameter β , Annular Plug Nozzle.	222
4-91.	Normalized Shock Cell Noise OASPL Correlation N_{sh} vs. β , Annular Plug Nozzle.	222
4-92.	Shock-Associated Noise Spectra; Annular Plug Nozzle, $\theta_i = 50^\circ$.	224
4-93.	Shock-Associated Noise Spectra; Annular Plug Nozzle, $\theta_i = 50^\circ$.	224
4-94.	Shock-Associated Noise Spectra; Annular Plug Nozzle, $\theta_i = 50^\circ$.	224
4-95.	Predicted Effect of Number of Shock Cells N on Shock-Cell Noise Spectrum, HBF(69) Theory.	226
4-96.	Predicted Effect of N on Shock-Cell Noise Spectrum; HBF(69) Theory, Modified by Factor $N/8$.	227
4-97.	Predicted Effect of Shock Spacing Parameter $\epsilon = \Delta L/L_1$ on Shock-Cell Noise Spectrum, HBF(69) Theory.	227
4-98.	Predicted Effect of Eddy Convection Speed U_c on Shock-Cell Noise Spectrum, HBF(69) Theory.	229
4-99.	Shock-Cell Noise Group Source Spectrum and Cross-Correlation Spectrum Developed by Harper-Bourne and Fisher(69).	231

LIST OF ILLUSTRATIONS (Continued)

<u>Figure</u>		<u>Page</u>
4-100.	Predicted Interference Spectrum for a Two-Shock ($N = 2$) System.	232
4-101.	Predicted Shock-Cell Noise Spectrum Showing Superposition of Group Spectrum and Interference Spectrum.	232
4-102.	Comparison of Predicted and Measured Shock-Associated Noise Spectrum, 6:1 Aspect Ratio Rectangular Jet.	236
4-103.	Comparison of Measured and Predicted Shock-Associated Noise Spectra; Scale Model 8-Lobe Daisy Suppressor, Effect of Jet Temperature.	238
4-104.	Comparison of Measured vs. Predicted Shock-Associated Noise Spectra; Annular Plug Nozzle, $\theta_i = 50^\circ$.	238
4-105.	Reduction in Shock Noise OASPL Due to Nozzle Shape.	239
4-106.	Block Diagram of Jet Noise Aeroacoustic Prediction Model.	243
4-107.	Typical Jet Plume Flow Field Subdivision (Not to Scale), into Eddy Volume Elements.	245
4-108.	Typical Jet Plume Exhausting from a Nozzle of Arbitrary (Non-circular) Planform Shape.	246
4-109.	Typical Suppressor Nozzle Exit Plane Planform Shape.	248
4-110.	Quadrupole - Source/Observer Coordinate System Nomenclature.	251
4-111.	Possible Solution Types for a Maximum of Two Turning Points. Shaded Areas Denote Shielding of Source.	256
4-112.	Empirical Model of Shock Cell Noise Component of Spectrum: (a) Shock Cell Component Approximated by Straight Lines; (b) Model Representation of Shock Cell Spectrum and Correlation Parameters.	258
4-113.	Data/Theory Comparison Cases 1, 2, and 3: 4.64 inch Diameter Conical Nozzle.	269
4-114.	Data/Theory Comparison Case 4: 4.64 in. Conical Nozzle Operating at Supersonic Pressure Ratio.	273

LIST OF ILLUSTRATIONS (Continued)

<u>Figure</u>		<u>Page</u>
4-115.	Data/Theory Comparison Case 5: 0.79 Radius Ratio Plug Nozzle.	276
4-116.	Data/Theory Comparison Case 6: 0.79 Radius Ratio Plug Nozzle, $V_j = 1800$ fps.	279
4-117.	Data/Theory Comparison Case 7: 0.79 Radius Ratio Plug Nozzle, $V_j = 2340$ fps.	282
4-118.	Data/Theory Comparison Case 8: $AR = 2.0$ Coplanar Coaxial Jet, $VR = 0$.	285
4-119.	Data/Theory Comparison Case 9: $AR = 2.0$ Coplanar Coaxial Jet, $VR = 0.19$.	288
4-120.	Data/Theory Comparison Case 10: $AR = 2.0$ Coplanar Coaxial Jet, $VR = 0.4$.	291
4-121.	Data/Theory Comparison Case 11: $AR = 2.0$ Coplanar Coaxial Jet, $VR = 0.6$.	295
4-122.	Data/Theory Comparison Case 12: $AR = 2.0$ Coplanar Coaxial Jet, $VR = 0.8$.	297
4-123.	Data/Theory Comparison Case 13: $AR = 2.0$ Coplanar Coaxial Jet, $VR = 1.25$.	300
4-124.	Data/Theory Comparison Case 14: $AR = 2.0$ Coplanar Coaxial Heated Jet, $VR = 0.51$.	303
4-125.	Data/Theory Comparison Case 15: Inverted Flow Coplanar Jet, $AR = 0.4$, $VR = 1.5$.	306
4-126.	Data/Theory Comparison Case 16: Inverted Flow Coplanar Coannular Jet, $AR = 0.4$.	307
4-127.	Data/Theory Comparison Case 17: Inverted Flow Coplanar Coannular Jet, $AR = 0.65$, $VR = 1.5$.	308
4-128.	Data/Theory Comparison Case 18: Inverted Flow Coplanar Coannular Jet, $AR = 0.65$, $VR = 1.5$.	309
4-129.	Data/Theory Comparison Case 19: Inverted Flow Coplanar Coannular Jet, $AR = 0.65$, $VR = 2.0$.	312
4-130.	Data/Theory Comparison Case 20: Inverted Flow Coplanar Coannular Jet, $AR = 2.0$, $VR = 1.5$.	315

LIST OF ILLUSTRATIONS (Continued)

<u>Figure</u>		<u>Page</u>
4-131.	Data/Theory Comparison Case 21: Inverted Flow Coplanar Coannular Jet, AR = 2.0, VR = 2.0.	318
4-132.	Data/Theory Comparison Case 22: Inverted Flow Coplanar Coannular Plug Nozzle, AR = 0.65, VR = 1.5.	323
4-133.	Data/Theory Comparison Case 23: Inverted Flow Coannular Plug Nozzle, AR = 0.65, VR = 2.0.	327
4-134.	Data/Theory Comparison Cases 24-26: 7-Tube Nozzle, D/d = 3.0.	331
4-135.	Data/Theory Comparison Case 27: 32-Chute ($A_{ann}/A_j = 2.1$) Nozzle.	334
4-136.	Data/Theory Comparison Cases 28-36: 36-Chute Nozzle SPL Spectra.	338
4-137.	Data/Theory Comparison Cases 28-36: 36-Chute Nozzle OASPL Directivity.	344
4-138.	Data/Theory Comparison Cases 28-36: 36-Chute Nozzle PNL Directivity.	345
4-139.	Data/Theory Comparison Case 37: 8-Lobe Daisy Nozzle, $V_j = 1377$ fps.	346
4-140.	Data/Theory Comparison Case 38: 8-Lobe Daisy Nozzle, $V_j = 1800$ fps.	348
4-141.	Data/Theory Comparison Case 39: 8-Lobe Daisy Nozzle, $V_j = 2186$ fps.	350
4-142.	Comparison of Inverted Vs. Conventional Bypass Flow Mean Velocity Profiles; AR = 1.0, VR = 0.7.	353
4-143.	Comparison of Inverted Vs. Conventional Bypass Flow Mixing on Peak Axial Velocity Decay Rate; AR = 1.0, VR = 0.7.	354
4-144.	Comparison of Inverted Vs. Conventional Bypass Flow Mixing on Turbulence Velocity Profile Development; AR = 1.0, VR = 0.7.	355
4-145.	Effect of Inverted Vs. Conventional Flow Mixing on Far Field Acoustic Spectra; AR = 1.0, VR = 0.7.	356

LIST OF ILLUSTRATIONS (Continued)

<u>Figure</u>		<u>Page</u>
4-146.	Comparison of Inverted Vs. Conventional Bypass Flow Mixing on OASPL Directivity.	357
4-147.	Effect of Fluid Shielding on SPL Spectrum at $\theta_I = 150^\circ$, Conventional Bypass and Inverted Flow; $AR = 1.0$, $VR = 0.7$.	358
4-148.	Comparison of Predicted and Measured Flight Effect for J85/Aerotraine Conical Nozzle, 400 ft Sideline.	360
4-149.	Comparison of Predicted and Measured Flight Velocity Exponent m for J85/Aerotraine Conical Nozzle.	362
4-150.	Comparison of Measured and Predicted Flight Noise Spectra for J85/Aerotraine Conical Nozzle, $V_j = 2200$ fps, 400 ft Sideline.	363
4-151.	Sound Source Located in Vicinity of Semi-Infinite Plane Barrier.	366
4-152.	Variation of Attenuation with θ for $kr_o = 190$ and $\phi_o = 90^\circ$.	368
4-153.	Two-Dimensional Semi-Infinite Parallel Plate Wave Guide Model.	369
4-154.	Branch Cuts for $\gamma = (\alpha^2 - k^2)^{1/2}$.	370
4-155.	Simple Source in a Doubly Infinite Rigid Walled Duct.	378
4-156.	Rigid Walls: Effect of Frequency.	381
4-157.	Rigid Walls: Effect of X/B : P_{free}/P_{emb} , dB.	383
4-158.	Effect of Singularity Type.	384
4-159.	Effect of Singularity Type.	385
4-160.	Directivity, Rigid Walls (Including Free Singularities).	387
4-161.	Effect of Absorbent Walls.	391
5-1.	Test Matrix, Single Round Jet.	404
5-2.	Single Round Convergent Jet Noise, Overall Power.	406

LIST OF ILLUSTRATIONS (Continued)

<u>Figure</u>		<u>Page</u>
5-3.	Overall Power, Corrected for Density Ratio, Single Round Jet.	407
5-4.	Overall Sound Pressure Level at $\theta_j = 90^\circ$, Single Round Jet.	408
5-5.	Temperature Effect on Power Spectra, $d = 7/8$ in.	409
5-6.	Temperature Effect on Power Spectra, $d = 1-1/2$ in.	410
5-7.	Temperature Effect on SPL at $\theta_j = 90^\circ$, $d = 7/8$ in.	411
5-8.	Effect of Temperature on SPL at $\theta_j = 90^\circ$, $d = 1-1/2$ in.	412
5-9.	Rectangular Jet Nozzle.	414
5-10.	Total Power Comparison, Round Versus Rectangular.	415
5-11.	Effect of Velocity on Density Exponent, ω .	417
5-12.	Unheated SPL Spectra, Round Versus Rectangular.	418
5-13.	Power Spectra Comparison, Round Versus Rectangular.	420
5-14.	Directivity Comparison, Round Versus Rectangular.	421
5-15.	SPL Versus Convected Strouhal No., Rectangular.	422
5-16.	ΔSPL_ψ Versus θ , Theory and Experiments.	423
5-17.	Propagation Paths at Shallow Angles.	424
5-18.	PWL Spectra, Effect of Temperature, $V_j \approx 1000$ fps.	426
5-19.	Effect of Temperature on $\Delta OAPWL_\psi$.	427
5-20.	SPL Spectra, $\theta = 30^\circ$.	428
5-21.	SPL Spectra, $\theta = 90^\circ$.	430
5-22.	Effect of Density Ratio, ρ_0/ρ_j , on ΔSPL_ψ .	431
5-23.	ΔSPL_ψ Versus Convected Strouhal No., S_c .	432
5-24.	Peak Frequency Versus Jet Velocity.	433

LIST OF ILLUSTRATIONS (Continued)

<u>Figure</u>		<u>Page</u>
5-25.	Twin Round Jet Nozzles.	436
5-26.	Effect of Nozzle Spacing on Acoustic Power of Twin Round Jet at $M_j \approx 1$.	437
5-27.	Effect of Nozzle Spacing on Acoustic Power of Twin Round Jets, $M > 1$.	438
5-28.	Peak Polar Δ OASPL with Twin Round Nozzle Spacing.	440
5-29.	Change in Acoustic Power with Azimuthal Angle, Twin Round Jets.	441
5-30.	Directivity Comparison, Twin Round Vs. Single.	442
5-31.	Power Spectra Comparison, Twin Round Vs. Single.	444
5-32.	SPL Comparison, Twin Round Vs. Single.	445
5-33.	Azimuthal Difference Power Level, Twin Round.	446
5-34.	Twin Round Power Spectra.	447
5-35.	Twin Round Power Spectra.	448
5-36.	Twin Round Power Spectra, $T_j \approx 1700^\circ$ R, $S/d = 1.33$.	449
5-37.	Twin Round Power Spectra, $T_j \approx 1700^\circ$ R, $S/d = 2.67$.	450
5-38.	Twin Round Spectra, $T_j \approx 1700^\circ$ R, $S/d = 5$.	451
5-39.	Twin Round Power Spectra, $T_j \approx 1900^\circ$ R, $S/d = 5$.	452
5-40.	Azimuthal Difference Power Spectra, Twin Round for Various Spacings.	455
5-41.	Azimuthal Difference Pressure Spectra, Twin-Round.	456
5-42.	Frequency of Onset Shielding, f_m Versus Nozzle Spacing, Twin-Round.	457
5-43.	Shielded Angles Versus Frequency, Twin-Round.	458
5-44.	Twin-Jet Shielding Definition.	460

LIST OF ILLUSTRATIONS (Continued)

<u>Figure</u>		<u>Page</u>
5-45.	Sound Transmission Through a Layered Medium.	461
5-46.	Transmission Properties of a Heated High Velocity Layer at Frequencies of Minimum Transmission.	464
5-47.	Far Jet Shielded Angle, θ_n , Versus Shielding Distance of Near Jet, X_n , Twin-Round. ⁿ	465
5-48.	Acoustically Merged Distance Versus Twin-Round Nozzle Spacing.	467
5-49.	Twin Rectangular Jets.	470
5-50.	Effect of Nozzle Spacing on Acoustic Power of Twin-Rectangular Jets at $M_j < 1$.	471
5-51.	Effect of Nozzle Spacing on Acoustic Power of Twin-Rectangular Jets at $M_j \approx 1$.	472
5-52.	Change in Acoustic Power with Azimuthal Angle, Twin-Rectangular Jets.	474
5-53.	Directivity Comparison, Twin-Rectangular Versus Single.	475
5-54.	Power Spectra Comparison, Twin-Rectangular Versus Single.	476
5-55.	SPL Comparison, Twin-Rectangular Versus Single.	477
5-56.	Azimuthal Difference Power Level, Twin-Rectangular.	479
5-57.	Power Difference at $\psi = 0^\circ$, Single Plus 3 dB Less Twin Rectangular.	480
5-58.	Twin Rectangular Power Spectra, $V_j = 1000$ fps.	482
5-59.	Twin Rectangular Power Spectra, $T_j \approx 1200^\circ$ R, $S/t = 4.86$.	483
5-60.	Twin Rectangular Power Spectra.	484
5-61.	Twin Rectangular Power Spectra.	485
5-62.	Azimuthal Difference Power Spectra, Twin Rectangular for Various Spacings.	486

LIST OF ILLUSTRATIONS (Continued)

<u>Figure</u>		<u>Page</u>
5-63.	Azimuthal Difference Pressure Spectra, Twin Rectangular.	488
5-64.	Five-Jet Linear Array, Overall Power.	490
5-65.	Effect of Nozzle Spacing on Acoustic Power.	491
5-66.	Effect of Velocity on Azimuthal Power Difference.	492
5-67.	Effect of Velocity on Shielded Power Difference.	493
5-68.	Five-Jet Linear Array, Azimuthal Directivity, re $\psi = 0^\circ$.	495
5-69.	Five-Jet Linear Array, Polar Directivity.	496
5-70.	Linear Array, Power Spectra and Directivity.	497
5-71.	Linear Array, SPL Spectra.	498
5-72.	Power Spectra.	500
5-73.	Power Spectra, Effect of Spacing.	501
5-74.	Power Spectra.	502
5-75.	Overall Power Versus Velocity, $D/d = 3$.	504
5-76.	Overall Power Versus Velocity, $D/d = 4$.	505
5-77.	Overall Power Versus Velocity, $D/d = 6$.	506
5-78.	Density Exponent for OAPWL Vs. Velocity.	507
5-79.	Velocity Exponent for OAPWL Versus Temperature.	508
5-80.	Effect of Spacing on Overall Power, $T_j \approx 1250^\circ \text{ R.}$	509
5-81.	Effect of Spacing on Overall Power, $T_j \approx 1600^\circ \text{ R.}$	510
5-82.	Effect of Spacing on Overall Power, $T_j \approx 1900^\circ \text{ R.}$	511
5-83.	Azimuthal Variation of Overall Power, Subsonic.	512
5-84.	Azimuthal Variation of Overall Power, Supersonic.	513

LIST OF ILLUSTRATIONS (Continued)

<u>Figure</u>		<u>Page</u>
5-85.	Effect of Spacing on Azimuthal Power Difference.	515
5-86.	Polar Directivity, $D/d = 4$, 7-Tube Cluster.	516
5-87.	SPL Spectra, 7-Tube Cluster, $D/d = 4$.	517
5-88.	PWL Spectra, Effect of Spacing, 6-Tube Subsonic.	518
5-89.	PWL Spectra, Effect of Spacing, 7-Tube Subsonic.	519
5-90.	PWL Spectra, Effect of Spacing, 6-Tube Supersonic.	520
5-91.	PWL Spectra, Effect of Spacing, 7-Tube Supersonic.	521
5-92.	SPL Spectra, Effect of Spacing, 6-Tube.	522
5-93.	SPL Spectra, Effect of Spacing, 7-Tube.	523
5-94.	SPL Spectra, 6-Tube, $D/d = 3$, Cold, Subsonic.	525
5-95.	SPL Spectra, 6-Tube, $D/d = 3$.	526
5-96.	SPL Spectra, 6-Tube, $D/d = 3$.	527
5-97.	Radial Velocity and Turbulence Profiles of LV Calibration Jet Test Results ($D = 19.05$ mm).	529
5-98.	Axial Velocity and Turbulence Profiles of LV Calibration Jet Results ($D = 10.05$ mm).	530
5-99.	Axial Velocity Profiles of a Round Jet ($M = 0.967$, $D = 38.1$ mm).	531
5-100.	Radial Velocity Profiles of a Round Jet at $Y/D = 2$ ($M = 0.967$, $D = 38.1$ mm).	532
5-101.	Radial Velocity Profiles of a Round Jet at $Y/D = 6$ ($M = 0.967$, $D = 38.1$ mm).	533
5-102.	Radial Velocity Profiles of a Round Jet at $Y/D = 10$ ($M = 0.967$, $D = 38.1$ mm).	534
5-103.	Radial Velocity Profiles of a Round and a Rectangular Jet at $Y/D = 14$ ($M = 0.967$, $D = 38.1$ mm).	535

LIST OF ILLUSTRATIONS (Continued)

<u>Figure</u>		<u>Page</u>
5-104.	Single Rectangular Jet Configuration.	536
5-105.	Axial Velocity Profile of a Rectangular Jet ($M = 0.967$, $D = 38.1$ mm).	537
5-106.	Transverse Velocity Profiles of a Rectangular Jet at $Y/D = 2$ ($T_o = 294$ K, $\bar{U}_o = 303$ m/s, $D = 38.1$ mm).	538
5-107.	Transverse Velocity Profiles of a Rectangular Jet at $Y/D = 6$ ($T_o = 294$ K, $\bar{U}_o = 303$ m/s, $D = 38.1$ mm).	540
5-108.	Transverse Velocity Profiles of a Rectangular Jet at $Y/D = 10$ ($T_o = 294$ K, $\bar{U}_o = 303$ m/s, $D = 38.1$ mm).	541
5-109.	Transverse Velocity Profiles of a Rectangular Jet at $Y/D = 14$ ($T_o = 294$ K, $\bar{U}_o = 303$ m/s, $D = 38.1$ mm).	542
5-110.	Transverse Velocity Profiles of a Rectangular Jet at $Y/D = 6$ ($T_o = 644$ K, $\bar{U}_o = 448$ m/s, $D = 38.1$ mm).	543
5-111.	Transverse Velocity Profiles of a Rectangular Jet at $Y/D = 10$ ($T_o = 644$ K, $\bar{U}_o = 448$ m/s, $D = 38.1$ mm).	544
5-112.	Twin-Jet Configurations and Coordinates.	545
5-113.	Axial Velocity Profiles Along the Centerline of One of the Twin-Round Jets ($T_o = 644$ K, $\bar{U}_o = 448$ m/s, $D = 38.1$ mm).	546
5-114.	Radial Velocity Profiles of the Twin Round Jets at $Y/D = 2$ ($T_o = 644$ K, $\bar{U}_o = 448$ m/s, $D = 38.1$ mm).	547
5-115.	Radial Velocity Profiles of the Twin Round Jets at $Y/D = 6$ ($T_o = 644$ K, $\bar{U}_o = 448$ m/s, $D = 38.1$ mm).	549
5-116.	Radial Velocity Profiles of the Twin Round Jets at $Y/D = 10$ ($T_o = 644$ K, $\bar{U}_o = 448$ m/s, $D = 38.1$ mm).	550
5-117.	Radial Velocity Profiles of the Twin Round Jets at $Y/D = 14$ ($T_o = 644$ K, $\bar{U}_o = 448$ m/s, $D = 38.1$ mm).	551
5-118.	Radial Velocity Profiles of the Twin Round Jets at $Y/D = 2$ ($T_o = 294$ K, $\bar{U}_o = 303$ m/s, $D = 38.1$ mm).	553
5-119.	Axial Velocity Profiles Along the Centerline of One of the Twin Rectangular Jets ($T_o = 644$ K, $\bar{U}_o = 448$ m/s).	554

LIST OF ILLUSTRATIONS (Continued)

<u>Figure</u>		<u>Page</u>
5-120.	X-Transverse Velocity Profiles of the Twin Rectangular Jets at $Y/D = 2$ ($T_o = 644$ K, $\bar{U}_o = 448$ m/s).	555
5-121.	X-Transverse Velocity Profiles of the Twin Rectangular Jets at $Y/D = 6$ ($T_o = 644$ K, $\bar{U}_o = 448$ m/s).	556
5-122.	X-Transverse Velocity Profiles of the Twin Rectangular Jets at $Y/D = 10$ ($T_o = 644$ K, $\bar{U}_o = 448$ m/s).	557
5-123.	X-Transverse Velocity Profiles of the Twin Rectangular Jets at $Y/D = 14$ ($T_o = 644$ K, $\bar{U}_o = 448$ m/s).	558
5-124.	Z-Transverse Velocity Profiles of the Twin Rectangular Jets at $Y/D = 2$ ($T_o = 644$ K, $\bar{U}_o = 448$ m/s).	559
5-125.	Z-Transverse Velocity Profiles of the Twin Rectangular Jets at $Y/D = 6$ ($T_o = 644$ K, $\bar{U}_o = 448$ m/s).	560
5-126.	Z-Transverse Velocity Profiles of the Twin Rectangular Jets at $Y/D = 10$ ($T_o = 644$ K, $\bar{U}_o = 448$ m/s).	561
5-127.	Z-Transverse Velocity Profiles of the Twin Rectangular Jets at $Y/D = 14$ ($T_o = 644$ K, $\bar{U}_o = 448$ m/s).	562
5-128.	Schematic of the 7-Jet Duster Configuration and Coordinates.	564
5-129.	Axial Velocity Profile of the 7-Jet Cluster Flow Along One Jet Centerline ($\Delta Z = 6.67$ cm).	565
5-130.	Radial Velocity Profile of the 7-Jet Cluster Flow Around the Center Jet at $Y/D = 4$ ($\Delta Z = 6.67$ cm).	566
5-131.	Radial Velocity Profile of the 7-Jet Cluster Flow at $Y/D = 10$ ($\Delta Z = 6.67$ cm).	567
5-132.	Radial Velocity Profile of the 7-Jet Cluster Flow at $Y/D = 14$ ($\Delta Z = 6.67$ cm).	568
5-133.	Radial Velocity Profile of the 7-Jet Cluster Flow at $Y/D = 20$ ($\Delta Z = 6.67$ cm).	569
5-134.	Radial Velocity Profile of the 7-Jet Cluster Flow at $Y/D = 26$ ($\Delta Z = 6.67$ cm).	570

LIST OF ILLUSTRATIONS (Continued)

<u>Figure</u>		<u>Page</u>
5-135.	Axial Velocity Profile of the 7-Jet Cluster Flow Along the Centerline of the Center Jet ($\Delta Z = 3.81$ cm, $Z/D = 1.7$).	571
5-136.	Radial Velocity Profile of the 7-Jet Cluster Flows at $Y/D = 4$ ($\Delta Z = 3.81$ cm, $X/D = 0$).	573
5-137.	Radial Velocity Profiles of the 7-Jet Cluster Flows at $Y/D = 10$ ($\Delta Z = 3.81$ cm, $X/D = 0$).	574
5-138.	Radial Velocity Profile of the 7-Jet Cluster Flows at $Y/D = 14$ ($\Delta Z = 3.81$ cm, $X/D = 0$).	575
5-139.	Radial Velocity Profile of the 7-Jet Cluster Flows at $Y/D = 20$ ($\Delta Z = 3.81$ cm, $X/D = 0$).	576
5-140.	Radial Velocity Profiles of the 7-Jet Cluster Flows at $Y/D = 26$ ($\Delta Z = 3.81$ cm, $X/D = 0$).	577
5-141a.	"Hole-in-the-Wall" Test Matrix, Twin-Round.	580
5-141b.	"Hole-in-the-Wall" Experiment.	580
5-142.	Twin Round, Overall Power Decay.	581
5-143.	Twin Round, High Frequency Decay.	582
5-144.	Twin Round, Effect of Velocity and Temperature.	583
5-145.	Twin Round, Power Spectra ($S/d = 1.33$).	584
5-146.	Twin Round, Power Spectra, $S/d = 1.33$.	585
5-147.	Twin Round, $\Delta OAPWL$ Versus Axial Location.	587
5-148.	Twin Round, ΔPWL Versus Axial Location.	588
5-149.	Hole-in-the-Wall Test Matrix, Twin Rectangular.	589
5-150.	Twin Rectangular Overall Power Decay.	590
5-151.	Twin Rectangular High Frequency Power Decay.	591
5-152.	Twin Rectangular, Power Spectra, $S/t = 2.08$.	592

LIST OF ILLUSTRATIONS (Continued)

<u>Figure</u>		<u>Page</u>
5-153.	Twin Rectangular, Power Spectra, $S/t = 7.64$.	593
5-154.	Twin Rectangular, $\Delta OAPWL$ Versus Axial Location.	594
6-1.	Acoustic Shielding Experimental Test Facility.	597
6-2.	Schematic of the Coannular Jet Experiment Setup.	598
6-3.	SPL Spectrum of Whistle Alone.	599
6-4.	SPL Spectrum of Whistle with a Mach 0.6 Annular Shielding Jet Flow.	600
6-5.	SPL Spectra of Whistle with a Mach 0.8 Shielding Jet Flow.	601
6-6.	Directivity Patterns of Whistle with Shielding Jet Flows at Mach 0.6 and 0.8 ($f_c = 5$ kHz).	602
6-7.	Directivity Patterns of Whistle Alone ($f_c = 5$ kHz).	603
6-8.	Reduction in SPL Due to Shielding Jet Flow on a Stationary Source.	604
6-9.	Velocity Profile of the Annular Shielding Jet.	606
6-10.	Typical OASPL Directivity Patterns from Jet Shielding Experiments.	608
6-11.	Typical SPL Spectra at $T_j = 480^\circ$ R, $V_j = 850$ fps.	609
6-12.	Sound Power Level Spectrum at $a/b = 0.85$, $V_j = 850$ fps.	610
6-13.	SPL Shielding at $a/b = 0.85$, $T_j = 480^\circ$ R, $V_j = 840$ fps and $A = 8.4$.	612
6-14.	Reduction in SPL Due to Shielding Vs. the Temperature of the Shielding Jet Flow.	613
6-15.	Reduction in SPL Due to Shielding Vs. the Velocity of the Jet Flows.	614
7-1a.	Test Matrix.	617
7-1b.	Geometry of Experiment.	617

LIST OF ILLUSTRATIONS (Continued)

<u>Figure</u>		<u>Page</u>
7-2.	Shielding at $\theta_j = 30^\circ$.	618
7-3.	Shielding at $\theta_j = 60^\circ$.	619
7-4.	Shielding at $\theta_j = 90^\circ$.	620
7-5.	Effect of Shield Length and Emission Angle.	621
7-6.	Effect of Length, L, on Shielded Power.	622
7-7.	Effect of Jet Velocity on Shielding.	623
7-8.	Effect of Jet Temperature on Shielding.	624
7-9.	Power Spectra, Medium Offset High Subsonic.	625
7-10.	Power Spectra, Medium Offset Subsonic.	626
7-11.	Power Spectra, Medium Offset Supersonic.	627
7-12.	Power Spectra, Large Offset.	629
7-13.	Linear Radiator Model of Shielded Cluster.	630
7-14.	Comparison of Predicted and Measured Shielding Attenuation for 6-Tube Cluster, $V_j = 1500$ fps.	632
7-15.	Comparison of Predicted and Measured Shielding Attenuation for 6-Tube Cluster, $V_j = 1650$ fps.	634
8-1.	Normalized 90° Spectra as a Function of M_j .	639
8-2.	Postulated Contributions for Pure Jet Noise and Excess Jet Noise.	641
8-3a.	Control Surface Selected.	643
8-3b.	Coordinate System Used.	643
8-4.	Transition Outside Nozzle.	645
8-5.	Exit Plane Instability.	646
8-6.	Transition at Exit Plane.	649

LIST OF ILLUSTRATIONS (Continued)

<u>Figure</u>		<u>Page</u>
8-7.	Turbulent Boundary Layer at Sharp Edge.	650
8-8.	Internal Separation.	652
8-9.	Nozzle Screech Mechanism.	654
8-10.	Nozzle Configurations Tested.	656
8-11.	Basic Shielded and Unshielded Nozzle Spectra.	658
8-12.	Schematic of Nozzle Tip Shroud.	659
8-13.	Various Tip Nozzles on Fiberglass Cone.	661
8-14.	Various Tip Nozzles on Aluminum Cone.	661
8-15.	Effect of Trip Rings of Various Heights.	661
8-16.	Multivane Vortex Generator Effect.	663
8-17.	Contraction Cone Tip Nozzle Extender Tube Effect.	663
8-18.	Causality Correlations, $\phi = 0^\circ$, $\theta_j = 90^\circ$, $r = 1$ m.	664
8-19.	Z-Wise Variation of Lip Source Strength.	665
8-20.	Variation of $\overline{P_s P}(\tau)$ with ϕ .	666
8-21.	Source Strength Variation with ϕ .	667
8-22.	Estimates of Lip Noise Fractions.	669
8-23.	Vortex Shedding from Trailing Edge.	671
8-24.	Nozzle Transducer and Far-Field Microphone Locations.	673
8-25.	Far-Field 1/3 Octave Spectra at Each Test Point.	675
8-26.	OASPL at 90° Field Microphone Versus Velocity Ratio.	676
8-27.	Nozzle Correlation Functions on Outside Surface.	678
8-28.	Nozzle Correlation Functions, Inside Surface.	679
8-29.	Tangential Correlation - Inside Surface.	681

LIST OF ILLUSTRATIONS (Continued)

<u>Figure</u>		<u>Page</u>
8-30.	Tangential Correlation - Outside Surface.	682
8-31.	Typical Causality Correlations.	683
8-32.	Jet Noise Research Facility at USC.	687
8-33.	Schematic Diagram Showing Settling Chamber and a Subsonic Nozzle.	688
8-34.	Water Jet Stilling Chamber and Nozzle.	689
8-35.	Schematic of Water Jet Apparatus.	691
8-36.	Schematic Drawing of Elliptical Nozzle.	692
8-37.	Schematic Diagram Showing Contraction Section and Contour of 1/2-inch Diameter Nozzle.	693
8-38.	Schematic Diagram of 1/2-inch Diameter 2-foot Long Pipe Arrangement.	694
8-39.	Various Nozzle Configurations Used in the Water Jet.	695
8-40.	Interior of USC Anechoic Chamber.	697
8-41.	Schematic Diagram Showing Arrangement of Microphones for Far-Field Measurements at USC.	698
8-42.	Block Diagram of Experimental Setup for Axial Source Strength Measurement.	699
8-43.	Frequency Response of Filter Amplifier.	701
8-44.	Sketch of Arrangement for Hydrogen Bubble Photography.	703
8-45.	Peak-to-Peak Velocity Fluctuations Produced Near the Jet Exit Plane as a Result of a Periodic, Fixed-Amplitude Forcing.	705
8-46.	Dye Visualization of 5:1 Elliptic Nozzle (The Major Axis is in View). Dye is Introduced into the Nozzle Boundary Layer at a Jet Reynolds Number of 1325 (Based Upon Minor Diameter).	706

LIST OF ILLUSTRATIONS (Continued)

<u>Figure</u>		<u>Page</u>
8-47.	Dye Visualization of 5:1 Elliptic Jet at Reynolds Number 5300.	708
8-48.	Comparison of Directivities of Jet Noise Between Elliptical Nozzle and Conical Nozzle.	709
8-49.	Comparison of 1/3-Octave Sound Pressure Levels at $\theta_I = 90^\circ$.	710
8-50.	Comparison of 1/3-Octave Sound Pressure Levels at $\theta_I = 125^\circ$.	711
8-51.	Comparison of 1/3-Octave Sound Pressure Levels at $\theta_I = 150^\circ$.	712
8-52.	Comparison of Directivities of Jet Noise Between Nozzle, Smooth Pipe and Rough Pipe.	718
8-53.	Comparison of Directivities of Jet Noise Between Nozzle, Smooth Pipe, and Rough Pipe: Data have been Corrected for Equal Thrust.	719
8-54.	Comparison of Normalized 1/3-Octave Sound Pressure Levels at $\theta_I = 160^\circ$ Between Nozzle, Smooth Pipe, and Rough Pipe.	720
8-55.	Comparison of Normalized 1/3-Octave Sound Pressure Levels at $\theta_I = 90^\circ$ Between Nozzle, Smooth Pipe, and Rough Pipe.	721
8-56.	Contour Plot of Source Strength Distribution; 1/2-in. Nozzle, $U_j = 888$ fps.	722
8-57.	Contour Plot of Source Strength Distribution; 1/2-in. Diameter, 2-ft Long Smooth Pipe, $U_j = 867$ fps.	723
8-58.	Contour Plot of Source Strength Distribution; 1/2-in. Diameter, 2-ft Long Rough Pipe, $U_j = 378$ fps.	724
8-59.	Hydrogen Bubble Visualization of Axisymmetric Jet Flow at $Re = 5000$, Jet Diameter = 1.5 inch, Time Interval Between Lines - 35 m/s.	726
8-60.	Visually Determined Axisymmetric Jet Spreading Rate with Periodic Forcing.	728

LIST OF ILLUSTRATIONS (Concluded)

<u>Figure</u>		<u>Page</u>
8-61	Spreading of Jet with Inclined Exit Plane, $Re = 15,000$.	729
8-62.	Hydrogen Bubble Visualization of Jet with Inclined Exit Plane, $Re = 5,000$, $St_f = 0.45$.	730
8-63.	Visually Determined Spreading Rate for Hexagonal Array of Jets with Periodic Forcing at $Re_D = 15,000$.	732
8-64.	Attenuation Versus Nondimensionalized Ejector Length, Conical Primary Nozzle (Middleton, Ref. 128).	735
8-65.	Example of Ejector Nozzle Flow Field (Program Generated).	737

1.0 SUMMARY

The DOT High Velocity Jet Noise Source Location and Reduction Program, Contract DOT-OS-30034, was conceived to bring analytical and experimental tools to bear on understanding the fundamentals of jet noise for simple and complex suppressor nozzles.

Task 2 in particular is the most basic of this six-task program and was formulated as a fundamental theoretical and experimental study aimed at an understanding of the noise generating and suppression mechanisms of high velocity jets.

The physical view of jet noise adopted in this study is fairly conventional. The inherent instability of jet flows leads to jet turbulence with the energy of the turbulent eddies being extracted from the mean flow, this energy of the eddies being ultimately dissipated by viscosity. Jet noise is ascribed to this continuous process of the birth and decay of the eddies with the eddies being convected at velocities of the order of the jet velocity during their lifetime. When the nozzle operates supercritically and is not contoured to permit proper supersonic expansion, the flow aft of the nozzle exit plane is embedded with shocks and the passage of the turbulent eddies through the shocks generates "shock" noise. From a source point of view, only turbulent mixing and shock noise sources are considered in the ultimate prediction scheme developed in this report.

In the modeling of the sources of jet noise, this report leans heavily on the works of Lighthill, Ribner, and Ffowcs-Williams for turbulent mixing noise and on the work of Harper-Bourne/Fisher for shock noise. The first step in the analytic modeling is the prediction of the properties of the mean jet plume. A simplified eddy viscosity type approach based on Reichardt's inductive theory of turbulence is employed to achieve this. An independent check on the correctness of the plume mapping is obtained by extensive measurements with Laser Velocimeters (LV) of the velocity field in jet plumes. Similarity arguments and data from the rather sparse set of available time-dependent turbulence measurements carried out in jet flows are next used to establish a general procedure of deducing the turbulent source properties relevant to jet noise from the prediction of the mean plume properties. A feature of the present study is that the link to the far-field SPL (sound pressure level) spectra from the turbulent sources is carried out by fully accounting for acoustic/mean-flow interactions, via the so-called Lilley equation which may alternatively be also described as an inhomogeneous Orr-Sommerfield equation. The above steps have been integrated together to produce a unified aeroacoustic model which can, in principle, predict far-field SPL spectra given only the nozzle exit geometry, upstream stagnation pressures, and temperature. Multiple flow systems such as dual-flow exhaust systems can be readily accommodated in this prediction scheme. The prediction scheme includes a semiempirical method of prediction of shock noise adopted from the work of Harper-Bourne and Fisher. This unified prediction scheme is extensively applied to a great variety of jet noise

data from round nozzles, conventional bypass systems, inverted flow systems, and multielement nozzle exhaust systems over a wide range of velocities and temperatures of interest in jet noise. Generally, very satisfactory agreement is obtained in all these theory - data comparisons, including the trends of parametric variations. The procedure is general enough to handle both flight and static cases. While the bulk of theory - data comparisons were carried out for the static case, some comparisons with fair success have also been carried out for flight cases. The development of this unified universal aeroacoustic prediction based largely on first principles (empiricism is chiefly introduced in the eddy viscosity method used in the plume prediction and also in the similarity arguments used to infer time-dependent turbulence quantities needed to predict jet noise) is believed to be the most significant technical achievement of this task. Hence, full details of the pertinent equations, computer program, etc., needed to implement this method are described in a supplement to this report, FAA-RD-76-79, IIa.

Physical shielding offers a possibility of reducing the jet noise reaching the observer on the ground. Pertinent solutions relevant to shielding by plane barriers and by pipe-like enclosures are given. Comparisons with an experiment on physical shielding were conducted and reveal fair agreement, except that at shallow angles to the jet axis, the measured attenuation at high frequencies exceeds the predicted attenuation. The pipe enclosure study shows that low frequency jet noise may be actually enhanced by use of ejectors, and, in general, physical shielding benefits are confined to the inlet arc. Thus, beneficial effects for ejectors can accrue only from aerodynamic considerations rather than physical shielding considerations, unless treated ejectors are employed.

Several single-element and multielement experiments with round and rectangular tubes were carried out with mapping of the far-field sound over an entire hemisphere to assess acoustic shielding effects. Very pronounced shielding of jet noise by jet flows is demonstrated at suitable high velocity and temperature conditions. LV measurements carried out in several of these configurations revealed that jet turbulence structure is not significantly altered by jet temperature or jet Mach number.

A series of basic experiments to verify fluid shielding and the importance of acoustic/mean-flow interactions was also carried out, and results obtained for the dependence of the shielding on jet velocity, jet temperature, shield thickness, source frequency, and angle of observation are in accord to a high degree with the corresponding theoretical analysis.

Lip noise was investigated experimentally, both with and without external velocity, by cross-correlation techniques, and it appears that lip noise is not a significant noise source for practical jet velocities and with reasonably contoured nozzles upstream of the nozzle exit plane. A literature survey was carried out of the possibilities of jet noise suppression by the use of particle/fluid additives, and it appears unlikely that any significant benefit can be derived by any of these schemes, especially for heated jet flows.

The role of large-scale structures in jet noise was explored in a sub-contract effort by the University of Southern California and was not conclusive in establishing their direct relevance to jet noise. Nor was it

possible to derive any new insight into any novel concept of jet noise suppression associated with large-scale structures. It was also not clear what amendment, if any, was needed to the unified aeroacoustic model described earlier to reflect the role of large-scale structures.

In conclusion, it appears that for practical purposes jet noise phenomena at high velocities and temperatures can be largely explained as a combination of mixing noise and shock noise. It was necessary in this study to evolve a comprehensive aeroacoustic model devoted equally to all aspects of jet noise known to be important, such as turbulent mixing, convective amplification, acoustic/mean-flow interaction, and shock noise. But once such a unified scheme was evolved, the success of the present task suggests that rational preliminary design decisions can be arrived at with high confidence before committing to a test program, with the aid of the prediction tools developed herein. It is reiterated that these prediction tools have been embodied in a computer program available in a supplement to this report, FAA-RD-76-79, IIa.

2.0 INTRODUCTION

Jet noise has been studied extensively over the past 25 years dating back to the early 1950's when the first papers of Lighthill laid a basis for theoretical analysis of jet noise. Lighthill's theory provided some powerful scaling laws on the basis of which the variation of jet noise with jet velocity, jet temperature, and angle of observation could be correlated for a given nozzle exhaust geometry. The quality of experimental jet noise data acquired in the late 1960's and early 1970's improved markedly over that used earlier to test Lighthill's predictions. The improvements included careful suppression of upstream noise sources, extensive use of spectral analysis, and the acquisition of data over very wide parametric ranges of velocity and temperature.

The more recent experiments have revealed systematic discrepancies between the data and the predictions of Lighthill's theory. Moreover, from a practical point of view, the single-flow, round convergent nozzle is itself too noisy in terms of its jet noise output so that a more comprehensive aeroacoustic jet noise prediction scheme encompassing complex exhaust nozzle configurations was clearly called for. In the early 1970's, a major improvement over Lighthill's theory occurred with the acceptance of the fact that the influence of the mean jet flow environment on the elementary turbulent noise sources (the so-called "eddies") was not accounted for in Lighthill's theory, and that accounting for this "acoustic/mean-flow interaction" does help to resolve almost all the theory - data discrepancies observed with Lighthill's theory for single-flow, round nozzle noise.

Many of these improvements for single-flow, round nozzle noise were achieved in the course of a fundamental study sponsored by the USAF-DOT (Contract F33615-73-C-2031). It seemed logical, therefore, to pursue the structure developed in that study and inquire whether the same methodology could be extended to predict the noise from complex suppressor nozzles. A main objective of the present study (Section 4) was to demonstrate that such an exercise is feasible.

Based on the desirability of separating various mechanisms of jet noise suppression, such as alteration of turbulence levels, acoustic/mean-flow interaction, physical shielding, etc., Sections 5, 6, and 7 describe a wide variety of experiments carried out during the program designed to elucidate the relative importance of the various mechanisms. In Sections 6 and 7, relevant theoretical results from Section 4 are used to analyze the experimental results.

Section 8 is devoted to several topics such as lip noise, the role of large-scale structures in jet noise, etc., that have often been mentioned in recent years as influencing suppression phenomena but whose precise importance has not been clarified.

The remaining sections summarize the conclusions and recommendations for further work.

3.0 FACILITIES DESCRIPTION

This section summarizes the salient features of the facilities and associated diagnostic instrumentation utilized in the experimental portions of this program. Since the General Electric Corporate Research and Development (CRD) outdoor jet noise facility was the primary site for Task 2 jet noise experiments, a summary description of its capabilities is given in Section 3.1. Further details of its capabilities and validation checkout tests can be found in the Task 1 final report of this program.

Other facilities were briefly utilized for specialized investigations, but descriptions of these facilities are included in the sections where these investigations are reported. These include (1) the University of British Columbia Anechoic Jet Noise facility, used for lip noise experimental investigations (see Section 8.1); (2) the General Electric Evendale Outdoor Jet Noise facility (JENOTS), used for lip noise relative velocity experiments (see again Section 8.1); and (3) the University of Southern California Anechoic Jet Noise facility, utilized for experimental studies of orderly structure and its relevance to jet noise (see Section 8.3). All of these facilities are also described in detail in the Task 1 final report.

Summary descriptions of the "hole-in-the-wall" technique for source location diagnosis (Section 3.2) and the Laser Velocimeter for jet plume flow measurements (Section 3.3) are included herein, since these were the primary "unconventional" experimental measurement tools utilized in Task 2. Again, further details of these devices may be found in the Task 1 final report.

3.1 GENERAL ELECTRIC CORPORATE RESEARCH AND DEVELOPMENT (CRD) OUTDOOR FACILITY

The experimental noise investigations of Task 2 required the construction of a new facility at the General Electric Corporate Research and Development (CRD) Center. An outdoor facility was constructed which offers a unique combination of capabilities, including hemispherical microphone coverage, permanently installed microphones, acoustically treated ground plane, and real-time data processing. This facility is intended primarily for high-temperature jet noise research and, as such, has a silenced burner capable of operation to 2000° R.

3.1.1 Acoustic Arena

Acoustic suppression between combinations of elemental jet flows can be quite small on a total power basis and requires detailed azimuthal far-field measurements to allow the investigator to determine the relative importance between different proposed suppression mechanisms. A hemispherically swept array of microphones is provided in the CRD facility to survey the far-field directivity patterns of nonaxisymmetric nozzles or suppressor configurations

as shown in Figure 3-1. Twelve 1/2-inch B&K model 4133 microphones are attached to a traversing boom that pivots about the jet axis. These microphones are positioned every 10°, starting at $\theta = 20^\circ$ to the jet axis and ending at $\theta = 130^\circ$. To avoid an obstruction in the jet plume, a large hoop is used to provide a centerless pivot on the downstream end of the microphone boom. The boom can be moved to any azimuthal angle by the two overhead cables. Since the paths traversed by the microphones are circular arcs centered on the jet axis, any deviation of the radiation patterns from axisymmetry can be detected easily. A microphone arc of nine feet is used with the distance in terms of nozzle diameters ranging from 72 to 123.

Outdoor acoustic facilities are extremely dependent on weather conditions, and in areas where the weather is very changeable, as in the Northeastern United States, the ability to respond quickly to favorable weather conditions is crucial to the utilization rate of the facility. To avoid long startup and shutdown times, a hermetically sealed microphone holder was designed to allow permanent installation. An additional benefit of this approach is that the electronic noise floor is measured easily when the microphones are covered. An acoustically treated surface resulted in free field data above 500Hz. By using large sheets of acoustical foam, a reasonable reduction of the ground reflection problem can be obtained with minimal time required to lay down and take up the coverings. To allow testing during the winter months, the 30 x 28 foot concrete pad is heated electrically to remove ice and snow.

3.1.2 Jet Facility

To provide the heated air for the high temperature tests, two heaters are used. A large natural-gas-fired heat exchanger pre-heats the air to about 400° F, and this warm air is fed into the burner end of the combustor muffler through a 4-inch pipe, as can be seen on Figure 3-1. Two small JP4 combustors are used to provide the remainder of the heat addition. To prevent combustion noise from contaminating the jet noise downstream of the burners, the wall of the plenum is lined with 2 inches of Kaowool and faced with a 1/8-inch-thick perforated sheet (45% porosity) of Hastelloy X. No significant burner or other upstream noise contamination was noted in any of the data presented in this report.

3.1.3 Data Acquisition and Reduction System

Data acquisition is controlled by an HP 2100 series mini-computer that obtains the acoustic signals from a GR 1921 real-time one-third-octave band analyzer and samples the temperatures and pressure signals. By the use of a scanning multichannel amplifier, GR 1566, each microphone signal is analyzed sequentially, and the signal level of each one-third-octave band (100 Hz to 80 KHz) is stored on magnetic tape. The effective frequency range depends on the microphones used. For operational monitoring, a three-dimensional plot of the one-third-octave band analysis of the sound pressure level, SPL, of each microphone is displayed on an oscilloscope as the microphone array is sampled. A typical oscilloscope display is shown in Figure 3-2. For backup and when longer averaging times are necessary, the acoustic signals can be recorded simultaneously on a Sangamo Sabre IV tape recorder. After all of



Figure 3-1. CR&D Hot Jet Noise Facility.

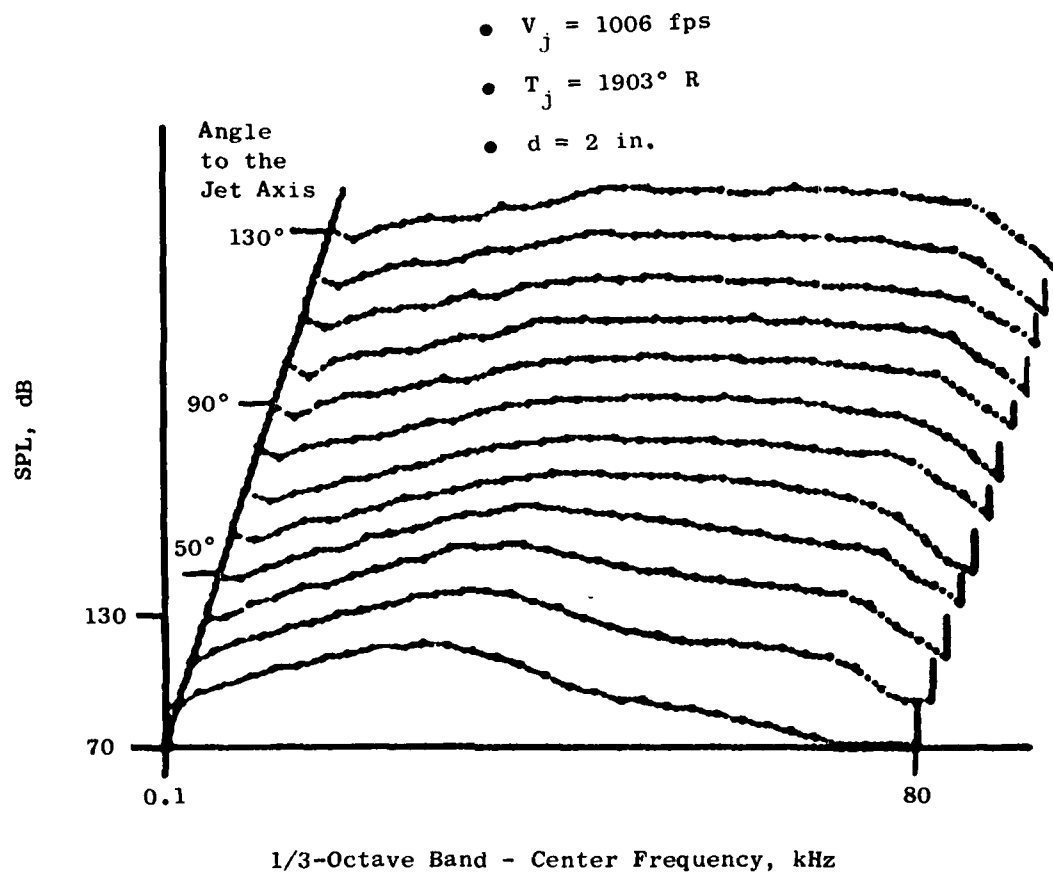


Figure 3-2. Real Time Isometric Display of the Acoustic Spectra.

the signals have been accumulated, the computer corrects the data for non-uniform response of the microphones and can correct for any known non-free-field effects of the arena. Using these corrected values of the sound pressure level, the computer then calculates the overall average sound pressure levels for each microphone, the one-third-octave band acoustic power levels, and the overall acoustic power level. The raw and calculated data are then stored on magnetic tape.

While the computer is processing the acoustic data, simultaneous measurement and calculation of all pertinent parameters for determination of the nozzle exit conditions and ambient conditions also are carried out and recorded on magnetic tape. Since all the pertinent data exists on one magnetic tape, the acoustic information is normalized by the computer immediately following the test.

3.2 HOLE-IN-THE-WALL SOURCE LOCATION MEASUREMENTS

The "hole-in-the-wall" experiment is a means of determining the axial distribution of noise sources in a jet plume. There are several versions of this method, but their common feature is that the jet is caused to flow through an aperture that is made as small as possible without affecting the jet or producing additional noise through buffeting or toroidal edge - tones. The idea is to separate the jet noise into two parts: upstream of the aperture and downstream of the aperture.

Of course, the aperture cannot completely separate the noise, as there is noise leakage through the aperture in both directions, with preference for contributions from upstream sources to appear downstream of the hole in the wall. Potter and Jones^{(1)*}, in the original version of this method, used a reverberant chamber and a movable jet nozzle. They claim to be able to establish closure on the noise distribution by first determining the distribution by upstream measurements and then by reversing the experiment and determining the distribution by downstream measurements. This contention must be examined in more detail. A schematic representation of a hole-in-the-wall experiment is shown in Figure 3-3, using two back-to-back reverberant or anechoic chambers (A and B) with an aperture between them. In this experiment, the acoustic power in both A and B will be simultaneously measured. The sum of the acoustic power must be a constant, P_t , if there is no interaction noise. Suppose that the aperture could completely separate the noise, then as the jet was withdrawn into Chamber A, the power measured in Chamber B, P_B , would decrease. Due to leakage, however, the measured value of P_B will be larger than the true value. The acoustic power measured in A will likewise be decreased by an identical amount so that "reversing" the experiment (as done by Potter and Jones) does not establish closure as it reproduces the same cumulative power distribution in both cases.

In a more recent study, McGregor and Simcox⁽²⁾ have used a movable jet and a fixed absorbent chamber to absorb the upstream noise, and measured the downstream noise with an outdoor microphone array. This method is more attractive in that it does not require that the reverberant characteristics of the chamber be calibrated, and the jet itself is not as subject to possible

* Superscript numbers in parentheses refer to the references contained in the Reference List.

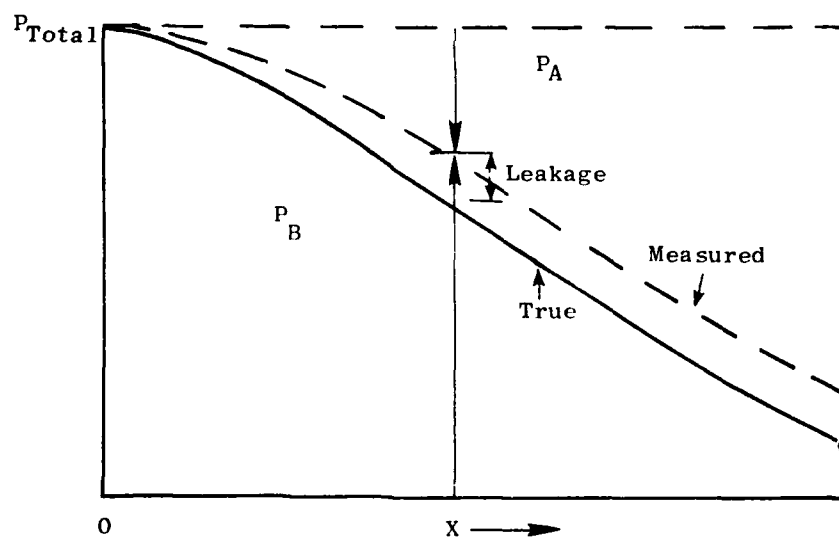
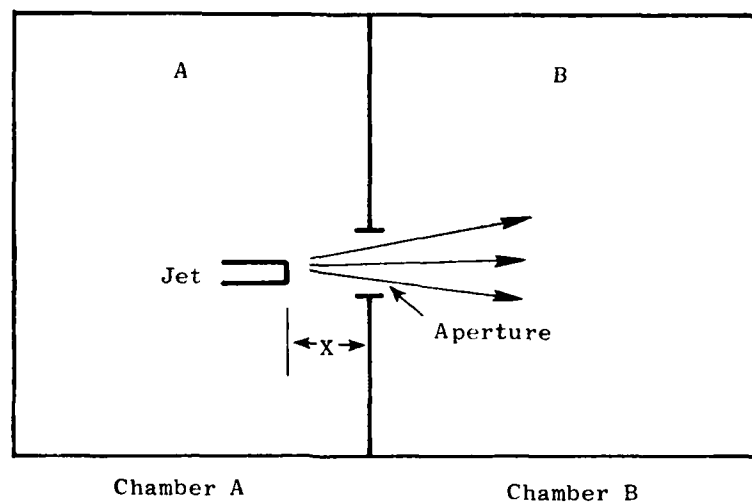


Figure 3-3. Acoustic Leakage and Nonclosure of Source Distribution.

46

excitation due to high acoustic level inside the chamber. In this method, it is necessary, however, to calibrate the aperture diameter versus axial distance to maintain closure on the total jet power.

A third, slightly different, version of the "hole-in-the-wall" is used in this study, with a translating absorbent chamber and a fixed jet nozzle and microphone array. Figure 3-4 shows the absorbent chamber mounted on a cart that can traverse axially on a set of rails. The chamber is constructed of 1/2-inch transite and lined with 2 inches of high temperature Kaowool acoustic material. Two industrial mufflers are used to silence the entrainment air inlets. A series of orifice plates are used to provide the aperture.

3.3 LASER VELOCIMETER AT CRD

The LV system developed at GE CRD consists of (1) laser, (2) optics, (3) processor, and (4) data acquisition and analysis system. The laser used during this experiment was an argon ion laser with maximum power of 4 watts at 5145 Å wavelength. The optics consisted of a single-color, dual-scatter off-axis back scattering arrangement. The transmitting optics had a focal length of 563 mm. The receiving optics assembly, located at 6° relative to laser beam axis, contained an f/5 receiving lens. A photomultiplier was used as the photodetector. The laser interference fringes at the scattering volume were oriented for the axial velocity and its turbulence measurement. The entire laser and LV optics were mounted rigidly on an X-Z table for obtaining transverse velocity distributions, where the Y axis is along the jet centerline. The X-Z table was driven by two independent stepping motors along X and Z directions, respectively, to an accuracy of 0.02 mm per move. The motion of the table was controlled remotely by a numerical indexer via a teletypewriter. The X-Z table was mounted on two tracks on the ground, parallel to the jet centerline (Y axis), in order to obtain various jet downstream station measurements (Figure 3-5).

The electrical signal from the photomultiplier was amplified via a wide-band preamplifier mounted on the X-Z table, and transmitted to the LV processor located inside a data control trailer 15 m away from the jet facility. The LV principle and the digital-counter-type LV processor are described in detail by Asher(3). A schematic of the LV signal processing technique is shown in Figure 3-6. A 500 MHz digital clock was used in the processor for particle transit time measurement.

The LV data acquisition system block diagram is shown in Figure 3-7. The analog LV signal, proportional to the flow velocity, was input to the Northern Scientific pulse height analyzer. A velocity histogram (probability density function) was constructed after a large amount of LV data were collected in the pulse height analyzer. The histogram was then recorded on a digital cassette recorder. The recorded LV histogram data were transmitted to a computer at 1200 baud at the end of each test for off-line analysis.



Figure 3-4. "Hole-in-the Wall" Experimental Apparatus.

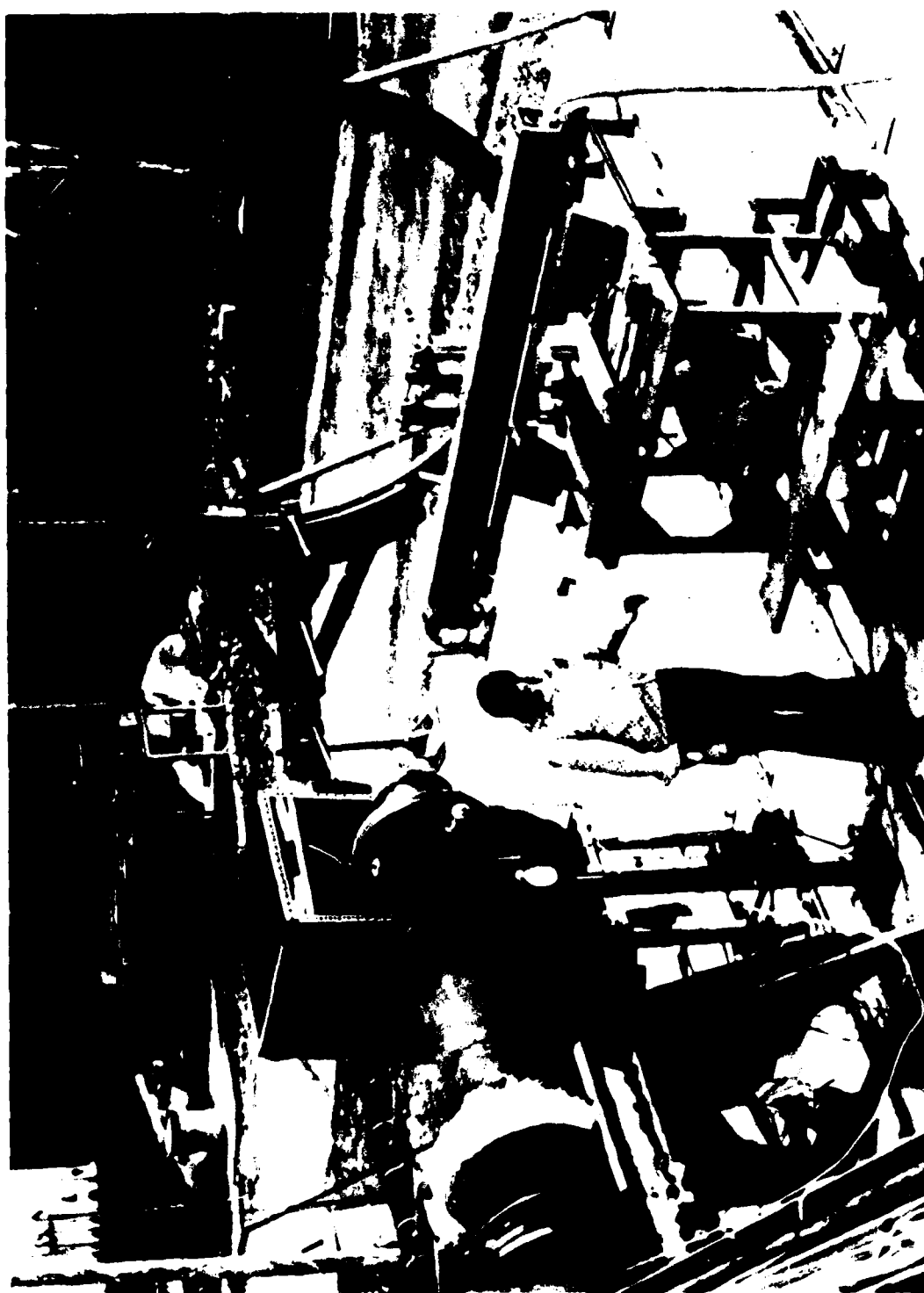


Figure 3-5. Outdoor Hot Jet Facility at GE CRD.

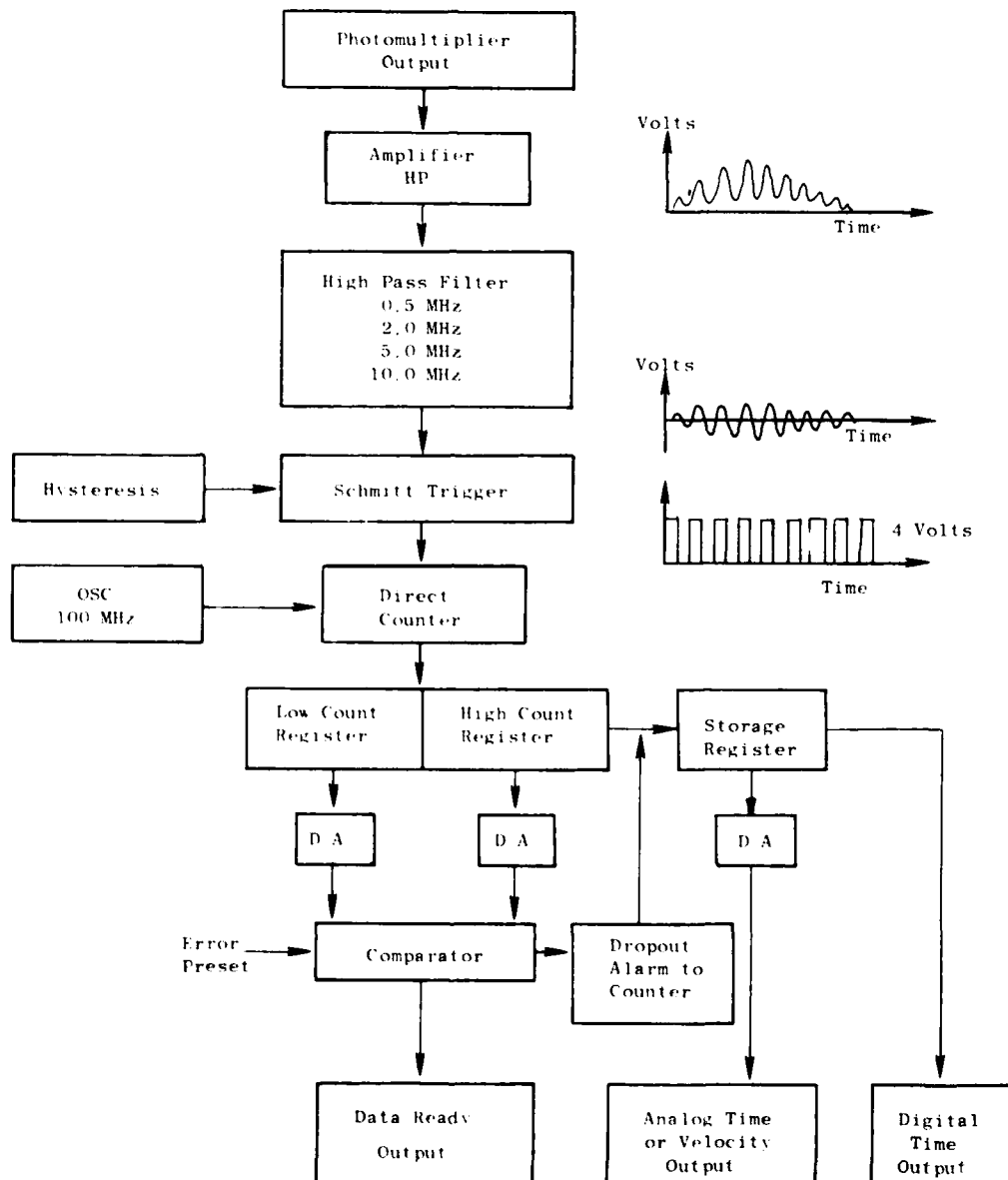


Figure 3-6. Schematic of the LV Processor.

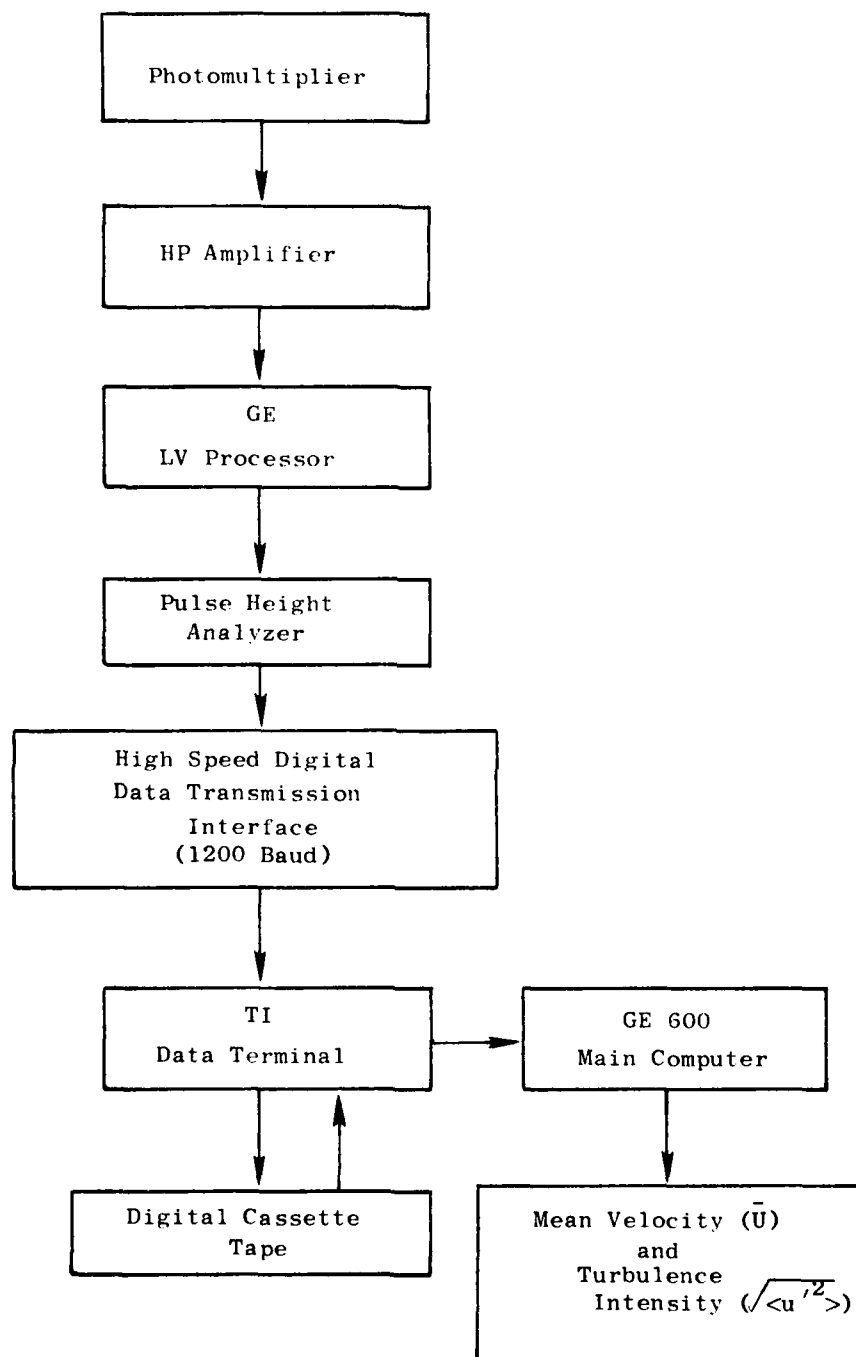


Figure 3-7. Block Diagram of the LV Data Acquisition System.

The seeding material used for the light scattering particles was 1 μm diameter alumina powder. The alumina powder was fluidized in a fluidized bed before it was fed into the plenum chamber of the jet flow. Special care had to be taken in positioning the seeding probe inside the plenum chamber to obtain the best seeding distribution for each jet configuration.

4.0 THEORETICAL DEVELOPMENTS

4.1 BACKGROUND AND OVERVIEW

The problem of jet noise in gas turbine exhaust systems arises from mixing of the jet exhaust stream with the ambient atmosphere. The mixing process is extremely unsteady at high Reynolds numbers characteristic of gas turbine engines, so that one is inevitably dealing with a noisy flow. From a fundamental point of view, one may say that noise is a consequence of a flow being both unsteady and compressible. Jet flows are unsteady because the mixing of two streams at different velocities is inherently unstable* and hence a continuous source of turbulence.

The basis for the understanding of jet noise was laid in the early 1950's in two papers of Lighthill^(4,5). Lighthill introduced his theory of jet noise as follows. The exact equations of continuity and motion can be written as:

$$\frac{\partial \rho}{\partial t} + \frac{\partial}{\partial x_j} (\rho v_j) = 0 \quad (1)$$

$$\frac{\partial}{\partial t} (\rho v_i) + \frac{\partial}{\partial x_j} (\rho v_i v_j + p_{ij}) = 0 \quad (2)$$

$$p_{ij} = p \delta_{ij} - \tau_{ij} \quad (3)$$

In equations (1), (2), and (3), ρ denotes density, v_i denotes the i^{th} component of velocity (Cartesian components), x_i the corresponding space coordinate, p_{ij} the compressive stress tensor consisting of a pressure term $p \delta_{ij}$ (δ_{ij} is the Kronecker delta function), and τ_{ij} the viscous stress tensor. It is characteristic of Lighthill's development of the jet noise problem that he used the momentum equation in Reynolds form and that he made no use of the energy equation (which for an inviscid, nonheat-conducting gas of specific heat ratio γ would be

$$\frac{Dp}{Dt} = \frac{\gamma p}{\rho} \frac{D\rho}{Dt}$$

with D/Dt denoting a differentiation following the fluid). It should be noted that equations (1) and (2) assume the absence of any explicit mass or force sources in the fluid, and are thus tailored to reveal noise sources in the absence of any obvious sources such as unsteady combustion, struts (which may induce fluctuating forces), etc. This development is certainly pertinent to

* The word "unstable" is only intended to convey that it is the instability of a jet exhaust flow that causes the generation of the intensely turbulent free shear layers. It is not intended to imply the presence of resonant or ordered structure phenomena.

jet noise since it is hoped that the burning, etc., is complete by the time the flow leaves the nozzle, and struts, etc., are usually absent in the exhaust plume.

By taking $\partial/\partial t$ of equation (1) and $\partial/\partial x_i$ of equation (2) and subtracting the latter from the former, one arrives at the Lighthill equation (which is an exact equation), namely

$$\frac{\partial^2 \rho}{\partial t^2} - a_0^2 \nabla^2 \rho = \frac{\partial^2}{\partial x_i \partial x_j} (T_{ij}) \quad (4)$$

where $T_{ij} = \rho v_i v_j + (p - a_0^2 \rho) \delta_{ij} - \tau_{ij}$. The term a_0 is (so far) any constant velocity, but for low Mach number, unheated flows at least, it will be convenient to take a_0 as the undisturbed speed of sound, thus eliminating (approximately) the term $(p - a_0^2 \rho) \delta_{ij}$ in T_{ij} . In equation (4), the usual convention that repeated indices imply summation over the repeated index from 1 to 3 is followed.

The ingenuity of Lighthill's manipulating equations (1) and (2) to lead to (4) notwithstanding, it is important to note that a somewhat deeper idea than mere manipulation is involved in the development of equation (4). Source-free linear acoustics of a uniform, homogeneous medium is governed by the equation

$$L_0 \rho = \frac{\partial^2 \rho}{\partial t^2} - a_0^2 \nabla^2 \rho = 0 \quad (5)$$

On the other hand, if sources, say $s(\bar{x}, t)$, are present, equation (5) would be modified to

$$L_0 \rho = s(\bar{x}, t) \quad (6)$$

Based on equations (5) and (6), one may say that, in attempting to cast the jet noise problem in the framework of classical, linear acoustics of a stationary, uniform, homogeneous medium, Lighthill saw that noise sources arise in this analogy to the extent that in a fluid flow $\partial^2 \rho / \partial t^2$ is not balanced by $a_0^2 \nabla^2 \rho$. In other words, if one wishes to draw an analogy to the linear acoustics of a stationary, uniform, homogeneous medium, the sources are precisely the extent to which the pertinent wave equation for such a flow ($L_0 \rho = 0$) is not satisfied. The ingenuity of Lighthill's formulation is, of course, in showing that this residual or imbalance was exactly $\partial^2 / \partial x_i \partial x_j (T_{ij})$.

Retarded time solutions to equation (4) can be written down formally, but they show immediately that no further progress can be made unless intuitive assessments are made of the "source" term T_{ij} . Lighthill argued that with a_0 taken as the speed of sound in the undisturbed medium and neglecting viscous stresses the dominant part of T_{ij} would be $\rho v_i v_j$. To make further

progress, he assumed that $(\rho v_i v_j)$ could be approximated by $\rho_j v_{ti} v_{tj}$, where ρ_j is the mean jet density and v_{ti} the nonacoustic portion of the fluid velocities. If these arguments are accepted, the source terms can then be estimated, at least on a similarity basis.

The second key idea that Lighthill advanced relates to the consequences of the source term appearing in equation (4) as a double divergence. The physical result that he deduced was that jet noise was due to a large number of small, statistically independent volumes (called eddies) with each of these eddies contributing noise of a quadrupole character. To understand this, one must first note that if the spatial extent over which the $\rho v_i v_j$ term of T_{ij} is correlated as small compared to the wavelength of the emitted sound, the source region is what is termed "compact" in acoustic terminology, and can be treated essentially as a point source*. Mathematically, at a given frequency, one would approximate $\rho_j v_{ti} v_{tj}$ by a three-dimensional delta function representation as $\rho_j Q \delta(\vec{x}) \exp(j\omega t)$. To decide when the source regions are indeed compact, a dimensional argument must be resorted to, as follows.

If ℓ denotes a length scale of the eddies and u the value of the velocity, Lighthill points out that the associated frequency will be proportional to (u/ℓ) , so that the ratio (ℓ/λ) (λ being the wavelength of the emitted sound) will be proportional to (u/a_0) . Based on this, one may say that, if the flow Mach numbers are small, the eddies are likely to be compact. The condition of low Mach number flows by itself is too restrictive and not very interesting because jet flows are not noisy at low Mach numbers.

To cope with the high Mach number jet noise problem, Lighthill points out that the eddies that create jet noise are convected with the flow, and in their own frame of reference are actually decaying rather slowly (hot film measurements of jet flows with two spatially separated probes confirm this). The reader is referred to Lighthill's papers^(4,5) for a fuller exposition of these ideas. The end result is that when eddy convection is accounted for, the resulting source compactness condition is that the turbulent (fluctuating velocity) Mach number (M_t) must be small. The reasons for this modified condition are that a frozen, subsonically convecting pattern generates no sound and hence only the time variations (frequencies) in the eddy's own (convected) frame of reference create sound. These frequencies (in the eddy's own frame of reference) are proportional to (u'/ℓ) where u' is the fluctuating velocity. The condition that M_t be small is likely to be met even for high speed jets, since turbulence levels (referenced to the jet exit velocity) rarely exceed 15% or so. Thus, even for a Mach 2.0 jet, M_t will not exceed 0.3.

There is a small price to be paid for this ability to cope with high jet Mach numbers; the linear acoustic theory has to be developed to handle the problem of radiation from convected quadrupoles, and the usual Doppler effects on frequency, pressure amplitudes, directivity, etc., have to be considered. The development of the consequences of convection of the quadrupoles was a major contribution of Lighthill's analysis.

* As will be pointed out shortly, it is neither physically desirable (especially in dealing with high jet velocities) nor mathematically necessary to assume source compactness in jet noise theory. Source noncompactness effects were first treated by Ffowes-Williams⁽⁶⁾ and Ribner⁽⁷⁾ and are fully accounted for in this report though the Lighthill notion of ascribing jet noise to a large number of statistically independent volumes is retained while accounting for source noncompactness effects within these volumes.

Analytical details of how to solve the problem of radiation from convected quadrupoles (within the framework of classical, linear acoustics of a uniform, stationary, homogeneous medium) are given in Lighthill's papers, and the details of the procedure are not repeated herein. The purpose here is to summarize broadly the predicted results.

The results can be classified into: (1) those associated with nonconvective aspects, and (2) those associated with the convection of the eddies. The principal type (1) result is that the acoustic power radiated by a point quadrupole of strength Q and frequency ω is proportional to $\omega^4 Q^2$. Since the frequency itself scales as (u/l) and since, for a given nozzle geometry, l is expected to be insensitive to jet velocity and jet temperature (at least as a first approximation), Lighthill's formulation predicts that jet noise power at low jet Mach numbers (and the mean square pressure at any given far-field angle) would scale as $\rho_j^2 U^8$ when jet velocity U and jet density are varied (note that the quadrupole strength Q itself would vary as $\rho_j U^2$). It is worth repeating that the eighth power velocity law is crucially related to the point quadrupole nature of the jet noise radiation. The point quadrupole nature of the sources in turn exist not only because equations (1) and (2) can be manipulated to yield equation (4), but also because the most important part of T_{ij} is estimated to be $\rho v_i v_j$ and because it is further assumed (confirmed by experimental observations) that the Reynolds stresses $(v_i v_j)$ are correlated over lengths small compared to the acoustic wavelength corresponding to the frequency at which the eddies radiate.

The convective aspects of Lighthill's results will now be stated. The result for the acoustic pressure of a convected point quadrupole is that its pressure is modified from that of a stationary point quadrupole as

$$p_M = \frac{p_S}{(1 - M_c \cos \theta)^3} \quad (7)$$

where p_M is the pressure of the moving quadrupole, M_c is its convection Mach number (referenced to the speed of sound of the uniform, homogeneous, stationary medium through which it moves). The angle θ is the angle made between the source-observer direction and the line of source motion, with the source position taken at the instant where the source was when it emitted the radiation reaching the observer at current time. The pressure p_S is that which a stationary source (located at the retarded position) would produce at the same far-field location. Equation (7) has the restriction that it is valid only for point quadrupoles convecting at a uniform velocity.

In applying equation (7) to the jet noise problem, Lighthill suggested that the mean square pressure would vary as

$$\langle p_M^2 \rangle = \frac{\langle p_S^2 \rangle}{(1 - M_c \cos \theta)^6} \quad (8)$$

Ffowcs-Williams⁽⁶⁾ and Ribner⁽⁷⁾ showed, however, that two changes need to be made to equation (8) before it can be applied to the jet noise problem. First they showed that when the integration over a finite jet volume of a large number of statistically independent eddies is carried out, the proper factor in the denominator of equation (8) ought to be $(1 - M_c \cos\theta)^5$ rather than $(1 - M_c \cos\theta)^6$. The eddy convection velocity by measurement for round nozzle flows is found to be roughly 65% of the ideal jet exit velocity.

The second modification introduced by Ffowcs-Williams and Ribner is of considerable importance. Note first, that if the frequency of the eddy in its own frame of reference is ω_0 , the frequency of the emitted sound in the far field is given by the Doppler shift formula $\omega_0/(1 - M_c \cos\theta)$. This means that however small ω_0 might be, for supersonic eddy convection ($M_c > 1$), the observed frequency along the direction $\theta_c = \cos^{-1}(1/M_c)$ is infinite and the associated wavelength is zero. This means that however small the correlated source region, it cannot be regarded as compact along the direction θ_c . This difficulty with the original Lighthill result (a foretaste of which is that equation (8) "blows up" or is singular at $M_c \cos = 1$) led Ffowcs-Williams and Ribner to independently develop a more generally valid result,

$$\langle p^2 \rangle = \frac{\rho_j^2 U^8}{[(1 - M_c \cos\theta)^2 + \alpha^2 M_c^2]^{5/2}} \quad (9)$$

where α^2 is a semiempirical constant (noncompactness parameter) allowing for finite eddy correlation volumes.

Essentially, the picture of jet noise prediction that emerged in the early 1960's or so was as follows. The total acoustic power was predicted and measured to vary as U^8 at low jet velocities transitioning, to a U^3 - law at high jet velocities. The directionality was predicted to be basically as $[(1 - M_c \cos\theta)^2 + \alpha^2 M_c^2]^{-5/2}$ with Ribner's⁽⁷⁾ development predicting an additional $\cos^2\theta$ type dependence at low frequencies. The spectral distribution for geometrically similar nozzles was predicted to scale such that $f\ell/V_j$ was constant. This last result was not so much an insight from the Lighthill equation as simply based on dimensional reasoning. When jet temperature was changed (keeping jet velocity constant), by virtue of the fact that jets are essentially constant-pressure flows, jet density will also be changed and the theory suggests that noise power and mean squared pressure would vary as ρ_j^2 . In subsequent work, Lighthill suggests that because jet noise arises from the mixing of the jet with the ambient, the strength of the quadrupoles ought to be taken as proportional to $(\rho_j + \rho_0)/2$ where ρ_0 is the density of the ambient fluid rather than just to ρ_j . Hence, he suggested that the variation with jet density might be expressible as a power law ρ_j^ω , where ω lies between 1 and 2.

Apart from the source aspects (such as low frequency shear noise), the predictions of the Lighthill theory, whether for the U^8 -law, the ρ_j to the power 1 to 2 dependence, or the $[(1 - M_c \cos\theta) + \alpha^2 M_c^2]^{-5/2}$ directivity, are not noticeably frequency dependent.

The Lighthill theory led to at least two notable ideas for jet noise suppression. Since the thrust of a jet varies as $A_j V_j^2$ (where A_j is the jet exhaust area) and its acoustic power as $A_j V_j^8$, it is easily demonstrable that jet noise could be reduced at constant thrust by raising exhaust area and lowering jet velocity. The high bypass ratio fan engine is an embodiment of this concept, and indeed by and large, the noise of these engines (especially the ones that power the wide bodied transports averaging bypass ratios of 5:1) is not dominated by jet mixing noise at all. For straight turbojet cycles, ideas due to Greatrex⁽⁸⁾ and others led to the notions of "mixer" nozzles such as the daisy nozzles. The exact basis by which such nozzles serve to reduce noise was not completely understood, but it seemed clear that at least one ingredient in the reduction was the tendency for these nozzles to produce enhanced jet mixing by allowing for greater entrainment (as compared to a circular nozzle), and thus reducing the integrated value of the Lighthill stress tensor ($\rho v_i v_j$).

The experimental data in the early 1960's tended to confirm several of the Lighthill predictions in the gross aggregate. Peak overall sound pressure levels, overall power levels (abbreviated as OAPWL), etc., showed the $U^8 - U^3$ behavior. The directivity of the overall sound pressure levels tended to follow roughly a $(1 - M_c \cos \theta)^{-5}$ type variation with M_c taken as $0.65 M_j$. The predicted density dependence was, however, never checked out carefully. When nozzle size was varied (other things being kept equal), frequencies do scale inversely as the length ratio but when jet velocity is varied (other things being held fixed), the measured far-field frequencies do not appear to scale linearly with velocity as would be expected from the notion that $(f \ell / V)$ stays constant.

One of the first measured discrepancies from the Lighthill theory was the fact that the directivity of the high frequency noise in jets with subsonic eddy convection velocities often did not follow the predicted $(1 - M_c \cos \theta)^{-5}$ directivity, but exhibited a heart-shaped dip near the jet axis. Another significant discrepancy was what has been picturesquely termed by Ribner as the "reverse" Doppler shift. If one measured jet noise from $\theta = 0$ to $\theta = 90^\circ$ (again for convenience restricting oneself to jets with subsonic eddy convection velocities), one would expect from the Lighthill theory that the sound field at shallow angles would be dominated by higher frequencies while that at the more broadside angles would be dominated by lower frequencies. This is because, by the Doppler shift formula, the emitted frequency is related to the source frequency ω_0 by the expression $\omega_0 / (1 - M_c \cos \theta)$. Actual measurements exhibit the reverse tendency, with the sound pressure level at 90° to the jet axis often being peaked at a frequency three times higher than that at $\theta = 30^\circ$. Ribner⁽⁹⁾ has explained this "reverse" Doppler shift as due to two features. First, Ribner's self noise - shear noise decomposition itself shows that the low-frequency noise will be biased towards the jet axis, whereas the high-frequency noise is omnidirectional. Second, Ribner points out that the mean-flow velocity and temperature profiles would refract away the high-frequency sound from the jet axis. Indeed, Ribner and his students performed several experiments in the mid-1960's with artificial sound sources (discrete frequency point sources) in jet flows which exhibit heart-shaped dips close to the jet axis in the far field quite similar to jet noise data itself.

A series of experiments conducted by Lush⁽¹⁰⁾ were notable for the fact that for subsonic unheated jets, over a range of velocities [91.4-304.8 m/sec (300-1000 ft/sec)], an attempt was made to make a fairly detailed theory - data comparison with the Lighthill theory.

Lush begins (in terms of theory - data comparison) by noting that, from the Lighthill theory, one would expect the far-field acoustic pressure on a given arc (for a given nozzle exhausting into a given ambient) to vary as

$$\langle p^2 \rangle (\theta, \omega) \sim \frac{\rho_j^2 V_j^8 F_I(\theta, \omega_0) G(\omega_0)}{(1 - M_c \cos \theta)^5} \quad (10)$$

where $\omega = \omega_0 / (1 - M_c \cos \theta)$.

In equation (10), $F_I(\theta, \omega_0)$ would be the intrinsic directionality of the sound at a source frequency ω_0 and $G(\omega_0)$ the intrinsic source spectrum [not predicted at all by the Lighthill theory but determined in principle by knowledge of the turbulent dynamics of the eddy in its own frame of reference]. Lush assumes that $F_I(\theta, \omega_0)$ is essentially unity (i.e., he takes the intrinsic directionality to be omnidirectional) and also neglects the $(\alpha^2 M_c^2)$ type correction in the denominator of equation (10). His experiments, being with subsonic jets, involved $M_c < 0.65$, so that the $(\alpha^2 M_c^2)$ term was always small compared to $(1 - M_c \cos \theta)^2$. To avoid the need to know $G(\omega_0)$, Lush examined the variation of $\langle p^2 \rangle (\theta, \omega)$ with fixed ω_0 and varying θ . Finally, in seeking to collapse data from different nozzle sizes, and at different velocities from a given nozzle size, Lush examined the directivity at fixed values of $[\omega_0 d / 2\pi U]$, where U is the jet velocity. This procedure involves determining the directivity at fixed-source Strouhal numbers and entails examining the far-field acoustic pressures at a frequency dependent on the angle, i.e., at $[\omega_0 / (1 - M_c \cos \theta)]$. Also, a suitable value of M_c must be assumed, and Lush chose the traditional estimate of $M_c = 0.65 M_j$. Since Lush was working with room temperature air jets operated at subcritical pressure ratios, the variation of ρ_j^2 in his experiments was quite small and therefore negligible. Consistent with his assumption of an omnidirectional $F_I(\theta, \omega_0)$, Lush expected (from Lighthill's theory) that the variation of $\langle p^2 \rangle (\theta, \omega)$ at fixed (ω_0, U) would vary with θ as $(1 - M_c \cos \theta)^{-5}$. At fixed (θ, ω) the variation with U would be as $U^8 / (1 - M_c \cos \theta)^5$. Data for $\omega(1 - M_c \cos \theta)d / 2\pi U$ from 0.03 to 1.00 (which brackets the range of frequencies occurring in jet noise quite well) was examined by Lush. With regard to the directivity at fixed-source Strouhal numbers, he found that an expression of type $(1 - M_c \cos \theta)^{-5}$ overestimates the variation with angle of the measured data at high source Strouhal numbers, and conversely, at low Strouhal numbers the variation is underestimated. Similarly, at shallow angles to the jet axis and at high frequencies, $U^8 / (1 - M_c \cos \theta)^5$ overestimates the measured variation with U , and conversely, at shallow angles and low frequencies the measured variation with U is underestimated by this expression. At large angles to the jet axis, Lighthill's theory and ideas work fairly well. For example, at $\theta = 90^\circ$, the pressures scale very well as U^8 and the peak frequency scales extremely well at U/d . Correspondingly at shallow angles, e.g., at $\theta = 30^\circ$, the peak frequency appears almost insensitive to jet velocity.

It is appropriate to note the rather significant discrepancies from the Lighthill theory found by Hoch, et al⁽¹¹⁾ in the area of heated jet noise. As mentioned earlier, the Lighthill theory leads one to expect that the mean square pressures (as well as the acoustic power) will vary as ρ_j^ω where ω lies between 1 and 2 when jet density alone is varied. Measurements by Hoch and his colleagues of this "jet density exponent" ω showed it to be a strong function of $\log_{10} (V_j/C_0)$ where V_j is the jet velocity and C_0 the ambient speed of sound. Often, ω is negative for $V_j < C_0$ being as small as -0.5, while ω approaches 2 for V_j/C_0 approaching and exceeding 1.6. Heating the jet flow (at constant V_j) also tends to bias the relative power spectrum towards lower and lower frequencies.

The estimation by Lighthill that $(\rho_j v_j)$ is the most important part of T_{ij} , and his subsequent approximation of it by $(\rho_j v_{ti} v_{tj})$, has proved most valuable in providing key insights into the jet noise problem as evidenced by the previous discussion. It is also true, however, that this approximation essentially suppresses all effects associated with the influence of the mean-flow velocity and temperature environment of the jet, i.e., convection, refraction, and shielding of the radiation from the moving eddies.

This neglect of mean-flow effects in the Lighthill development was pointed out by several writers in the 1960's, notably Ribner⁽⁷⁾, Powell⁽¹²⁾, Phillips⁽¹³⁾, and Csanady⁽¹⁴⁾. The refraction effect alluded to earlier is, of course, one example of this. Powell⁽¹²⁾ pointed this out by stressing that convection of the elementary quadrupole generators leads to a difficulty with the theory. Since the mean square pressure of a conglomerate of moving quadrupoles is different from that of a stationary one by the factor $(1 - M_c \cos \theta)^{-5}$, by integrating this factor weighted by $\sin \theta$ (to account for the solid angle) from $\theta = 0^\circ$ to $\theta = \pi$, one can show that the acoustic power of the moving quadrupole ought to be greater than that for a stationary one by a factor $(1 + M_c^2)/(1 - M_c^2)^2$. This means that from the Lighthill theory, one would expect the overall power level to vary as $U^8 (1 + M_c^2)/(1 - M_c^2)^2$. As Powell points out, based on this, one can expect not just an eighth power law but a power law with a velocity exponent ranging from 9 to 16. Experiments, of course, show a faithful adherence to an eighth power law. Lighthill himself was aware of this difficulty, but felt that the turbulence intensity of jet flows (as a fraction of the jet velocity) diminished with increasing jet Mach number in a manner sufficient to restore the eighth power law. The faithful adherence to an eighth power law of the overall sound pressure level (OASPL) at 90° to the jet axis, however, fails to support this contention. Ribner, Powell, and Csanady have suggested a much more reasonable resolution. Consider an eddy moving in a jet flow. The reason that the eddy moves is, of course, that the jet fluid moves. Relative to its immediate environment, the eddy is actually not moving at all. At high frequencies in particular, one would expect the power radiation of the eddy to be governed by its immediate environment, and since the eddy has no velocity relative to this environment, one would not expect "convective amplification" at high frequencies. (The enhancement of power in the Lighthill theory by the factor $(1 + M_c^2)/(1 - M_c^2)^2$ is often referred to as "convective amplification.")

The idea of systematically accounting for the effect of the jet flow on the radiation by the quadrupoles was pursued intensively first by Phillips⁽¹³⁾ and subsequently somewhat more completely by Lilley⁽¹⁵⁾. To explain this idea, Lighthill's notion that jet noise sources arise to the extent to which some "standard" source-free wave equation is not satisfied is employed. In Lilley's development, the standard equation chosen is not the equation governing wave propagation in a stationary, uniform, homogeneous medium. Lilley notes that to a rough, first approximation, the jet flow may be treated as a constant pressure, parallel sheared flow. The equation governing wave propagation in this type of flow is the Orr-Sommerfeld equation often used to study the stability of such flows. Symbolically denoting this by $L_{OS}(p') = 0$, Lilley attempts to determine by using the full equations of motion the extent to which $L_{OS}(p') \neq 0$. This exercise may be symbolically summarized by saying that

$$L_{OS}(p') = S_{Lilley}(\bar{x}, t) \quad (11)$$

The problem with equation (11), however, is that it is not so easy to estimate S_{Lilley} from the full equations of motion. Lilley assumes the following: (1) the mean-flow is at constant static pressure, (2) the gas is inviscid, nonheat conducting, and of constant specific heat ratio γ without any externally imposed heat, mass, or momentum sources, (3) all field variables decompose into a steady and fluctuating part, e.g., $u_i = \bar{u}_i + u'_i$, where an overbar denotes a time average or steady part (also let r denote $\log(p/p_0)$ where p_0 is a reference pressure and c the local speed of sound), (4) the mean-flow is unidirectional and depends only on one transverse coordinate x_2 , i.e., $\bar{u}_1 = V(x_2)\delta_{11}$, (5) whenever second order products of fluctuating quantities such as $r'u'_i$, r'^2 , $(c^2)'u'_i$, $(c^2)'r'$ appear, they are neglected (however, second order velocity products such as $u'_i u'_j$ are retained), (6) \bar{c}^2 is only a function of x_2 . By subtracting the time averaged portions of the equations of motion from the full equations of motion (using the six assumptions previously listed), and defining $\bar{D}/\bar{D}t$ as

$$\frac{\bar{D}}{\bar{D}t} = \left\{ \frac{\partial}{\partial t} + V(x_2) \frac{\partial}{\partial x_1} \right\},$$

Lilley shows that one can develop an equation of type (11) as follows:

$$\begin{aligned} & \frac{\bar{D}^3(r')}{\bar{D}t^3} + 2 \frac{dV}{dx_2} \frac{\partial}{\partial x_1} \left(\bar{c}^2 \frac{\partial r'}{\partial x_2} \right) \\ & - \frac{\bar{D}}{\bar{D}t} \frac{\partial}{\partial x_1} \left(\bar{c}^2 \frac{\partial r'}{\partial x_1} \right) = - 2\gamma \frac{dV}{dx_2} \frac{\partial^2 (u'_2 u'_k)}{\partial x_1 \partial x_k} \\ & + \gamma \frac{\bar{D}}{\bar{D}t} \frac{\partial^2 (u'_i u'_j)}{\partial x_1 \partial x_j} \end{aligned} \quad (12)$$

From this point on, Lilley's equation (12) is followed through in terms of application to jet noise in a manner similar to Lighthill's equation. The quantity r' for small values of p' relative to p_0 may be shown to be equal to (p'/p_0) . Taking u'_i on the righthand side of equation (12) to be the known, solenoidal, turbulent velocity fluctuations, (12) provides an inhomogeneous Orr-Sommerfeld equation for (p'/p_0) much as Lighthill's theory provides an inhomogeneous uniform, homogeneous, stationary medium wave equation.

Several assumptions have to be made in arriving at equation (12), but granting the validity of these assumptions, a source term is obtained in equation (12) which is purely quadratic in the fluctuating velocities, unlike Lighthill's equation (or Phillip's⁽¹³⁾ equation which was a predecessor to Lilley's equation). While there is no doubt that Lighthill's equation is exact and thus contains, in principle, all the physics of jet noise (but then so do the full equations of motion), it also seems that precisely because intuitive estimates of source terms are ultimately involved, Lilley's development is better tailored to the high speed, high temperature jet noise problem. It is, however, only proper to note the limitations of Lilley's equation. It neglects jet spread by assuming a parallel, sheared flow. It assumes the jet flow to be at constant static pressure. With multielement suppressors under static conditions, significant variations of "base" pressure occur, thus, making the constant static pressure assumption questionable. Despite the fact that the neglect of terms is carried out systematically [assumption (5)], it is true that Lilley's development assumes fundamentally that jet mixing and jet noise is a process that can be regarded as a small perturbation about a parallel, sheared flow. Since fluctuating velocities as high as 40% of the local mean velocity are common, and even local flow reversals can occur in jet flows, a "small perturbation" assumption can clearly be questioned. It is not as easy to solve Lilley's equation as it is to solve Lighthill's equation. In particular it is noted that it is almost impossible to solve Lilley's equation when the jet cross section is not axially symmetric (e.g., for a rectangular jet or a daisy nozzle, etc.).

A final objection to Lilley's equation arises from the fact that it is an inhomogeneous Orr-Sommerfeld equation. Since there are unstable solutions to the homogeneous Orr-Sommerfeld equation, it is clear that even without any "sources" equation (11) can yield solutions that yield acoustic radiation in the far field. The only solution to the homogeneous form of Lighthill's equation $\partial^2 \rho / \partial t^2 - a_0^2 \nabla^2 \rho = 0$ satisfying the outgoing wave radiation condition in the far field is the trivial solution $\rho \equiv 0$.

While this difficulty with Lilley's equation is still a matter of controversy, it is felt that since Lilley's approach could be regarded as a passive analogy approach similar to Lighthill's, there is no need to avoid using it on the basis of the possibility of unstable solutions to the homogeneous Orr-Sommerfeld equation. The motivation to use an equation of the Lilley type is that practically all the previously cited discrepancies between the Lighthill theory and experimental data can be resolved if we systematically account for acoustic/mean-flow interactions on the basis of an equation of Lilley's type. Acoustic mean flow interactions affect jet noise radiation in several ways. First, the mean temperature and velocity fields of the jet flow cause the radiated sound to be refracted generally leading to a diminution of sound pressure levels close to the jet exhaust axis, especially at high frequencies. Second, as recently recognized, the mean flow structure around the radiating eddies provides an acoustic impedance

environment that fundamentally alters the radiation efficiency with which the eddies radiate from what it would be if the eddies radiated into a stationary, homogeneous medium (as assumed by Lighthill). The latter aspect is a feature that has long been recognized in the nonaeronautical acoustic disciplines, e.g., in architectural acoustics, where it is well known that the radiation efficiency of a source is a function of the impedance environment that it is exposed to. The acoustic-mean flow interaction is strongly frequency dependent.

It should be reiterated that the developments to follow in this report have in fact retained several key ideas of the Lighthill theory. The two most important of these ideas are (1) the idea of identifying the "residual" from a standard wave equation as the source term for jet noise, and (2) the recognition of the convected, compact, quadrupole nature of the eddies. A mixing analysis is used to derive the evolution of the mean velocity and temperature of the jet plume downstream of the nozzle exit plane. The analysis is based on Reichardt's inductive theory of free turbulence. Reichardt's theory is undoubtedly considered simplistic by many workers in the turbulence modeling area, but because the governing equations in Reichardt's theory are linear (for the axial momentum and enthalpy fluxes), it is the only technique that allows construction of quite complex jet flow fields with relatively simple mathematics. This capability is rather important since it is necessary to have a capability to handle flow fields from complex nozzle shapes such as dual-flow systems, lobed nozzles, etc.

Having mapped the jet plume in terms of the mean velocity and mean temperature, the jet is broken up into a large number of elemental volumes. Similarity arguments essentially derived by Davies et al⁽¹⁶⁾ are next used to associate a quadrupole strength, quadrupole convection velocity, quadrupole self-oscillation frequency ω_0 , and a source spectrum (peaked at ω_0) with each volume. As an example, Davies, et al show by measurement that ω_0 is proportional to dV/dr for round jets (where r is a radial coordinate). The local mean velocity and mean temperature profile at the axial station where the elemental volume is located are used in the acoustic theory [based on Lilley's equation (12)] to obtain the far-field SPL spectrum generated by each elemental volume. Summing up all the elemental volume contributions in a mean square sense (i.e., treating the jet, as suggested by Lighthill, as a large assemblage of uncorrelated elemental generators), the total far-field SPL spectrum is obtained. Note that the method considers analytically all aspects of the jet noise problem known to be important, namely evolution of the mean properties of the plume, relevant quadrupole parameters such as convection velocities, source frequencies, etc., and the influence of the jet flow and temperature profiles on the radiation by the eddies. Some empirical constants are involved, especially in the mixing analysis and relation of quadrupole parameters to the mean flow properties, but the end result is a prediction of absolute sound pressure levels in various one-third-octave bands at any angle and radius in the far field, given the nozzle exhaust geometry and distribution of temperature and velocity at the nozzle exit plane.

Shock-associated noise arises with supercritical operation and associated underexpansion of the flow (unless carefully contoured nozzles are used to avoid underexpansion) leading to shock waves in the flow field aft of the nozzle plane. Shock screech involves a feedback mechanism and can result in pure tones of very high intensity, but, fortunately, a very high degree of nozzle symmetry and upstream smoothness seems necessary to produce screech. Practical jet configurations, especially heated engine flows, seem to be free from any significant screech phenomena.

The mechanism by which shocks can produce broadband noise has been known for several years. In a uniformly flowing, homogeneous medium, three linearized unsteady modes of motion can be identified, namely, sound waves, shear waves, and entropy waves. To first order of smallness, such modes propagate independently of each other but if the flow has very steep gradients in localized areas, even to first order, mode scattering or mode conversion can occur whereby, for example, a shear wave produces sound and entropy waves, etc. Shocks in the flow obviously create such localized steep gradients in the flow, and since turbulence in a flow can be thought of as a superposition of shear waves, it is easy to see that there is a situation of shear wave - shock interaction leading to sound production.

A semiempirical model for shock-associated broadband noise based on shock-turbulence interaction has been developed by Harper-Bourne and Fisher for round convergent nozzles and has been found to be extremely useful in predicting this component of jet noise. The physical picture employed by Harper-Bourne and Fisher is that as the turbulent eddies convect through the shocks, they generate broad band noise at each encounter. In addition, however, to the extent that the eddy is coherent between two encounters, an "interference" spectrum also will be produced. The adaptation of the Harper-Bourne and Fisher method used herein considers both these sources.

The prediction procedure outlined previously can then be modified to add on (in a mean square sense) a shock-noise component (as discussed above) to the previously discussed "turbulent mixing" noise. Extensive theory and data comparisons for conical nozzles, dual flow systems of both the conventional type and the inverted flow type, and multielement nozzles (and for certain cases with flight) are presented.

Several additional analytical items not directly relevant to the unified aeroacoustic method were also developed during this program. While the final method used treats the jet flow as a parallel, axisymmetric sheared flow, several approximations of the jet flow as a plug flow were also developed during the first phase of the study. One of these is tailored to reveal acoustic shielding phenomena in a noncircular jet. The motivation here is that such noncircular jets are known to display the phenomena of "quiet" and "noisy" planes. Expressions for the power and directivity of convecting sources shielded by an annular plug flow jet were also developed to provide a basis for examining the test results of Section 6.2. A plug flow model relevant to the prediction of conventional bypass coaxial jet noise was also developed. In both Sections 4.2.1 and 4.2.3, theory - data comparisons are presented. In Section 4.8, physical shielding theory relevant to shielding by wing-like surfaces and by semi-infinite pipe like enclosures (relevant to possible physical shielding benefits of ejectors) is developed.

The above overview has attempted to give a perspective of how the basic ideas of jet noise have evolved since Lighthill's work and how the proposed aeroacoustic prediction method is founded on the latest advances in jet noise theory.

4.2 PLUG FLOW MODELS

4.2.1 Low Frequency Model for Noncircular Jets

A low frequency asymptotic theory for the shielding of noise by jets of arbitrary cross section is discussed in this section. The results of the theory provide an explanation for the appearance of the quiet and noisy planes of a slot jet. The arguments in favor of this explanation are derived from a model problem in which a pulsating mass source is convecting along the axis of an infinitely long column of fluid of arbitrary cross section. The method of matched asymptotic expansions is applied to derive expressions for the radiative power and the acoustic pressure of the source.

The solution for the elliptic jet indicates that the radiative power in the horizontal plane (containing the major axis) is less than that for the vertical plane (containing the minor axis). This difference in power varies with source Strouhal and jet Mach numbers. The effects of jet temperature are also included in the analysis. The theoretical results for the sound pressure level are in reasonable agreement with experimental findings for slot nozzles. The theory indicates that acoustic shielding offered by jets is most important at high frequencies and at high Mach numbers.

4.2.1.1 The Radiated Power

4.2.1.1.1 Introduction

The work of Mani⁽¹⁷⁾ concentrates on shielding offered by circular jets. It is natural to extend his results to jets of arbitrary cross section. The purpose of this section is to show how such extension can be carried out at low frequencies and to assess the effect of noncircularity on acoustic shielding. It should be borne in mind, however, that shielding is most effective at high frequencies so that a low frequency theory can, at most, indicate trends as the frequency is increased. (By comparing the present approximate results to Mani's exact results for a circular jet, an upper limit for the validity of this low frequency theory can be established. This upper limit is reasonably high so that a low frequency theory can provide useful information even for moderately high frequencies.)

Considerable experimental evidence (Olsen⁽¹⁸⁾) indicates that the noise characteristics of noncircular jets at high frequency are a strong function of the specific plane of measurement. Not only are the spatial distributions of the pressure level different, but also the power radiated per unit polar angle varies with the angle itself (Figure 4-1).

In this section, it is shown that a plausible explanation for the appearance of the quiet and noisy planes is acoustic shielding. The arguments in favor of this explanation are drawn from the results of a model problem.

The formulation of the problem parallels that of Mani⁽¹⁷⁾ quite closely. It is assumed that the jet velocity profile can be sufficiently represented by a constant velocity profile (i.e., by a plug flow jet). Certainly, at low frequencies, the precise form of the radial gradients could be handled by an extension of this asymptotic theory. The basic idea is to divide the flow regime, in the sense of matched asymptotic expansions, into two regions, one in the vicinity, the other distant from the jet. In the inner region the axial gradients can be neglected since the appropriate length scale is the diameter of the jet. On the other hand, the pressure in the outer region obeys the classical wave equation so that the velocity (or its gradient) does not enter in the outer solution. The basic approach used in this section is also applicable to slow axial variations in the mean flow.

4.2.1.1.2 Formulation of the Model Problem

It is assumed that the acoustic field obeys a linear wave equation of the form

$$\left(\frac{\partial}{\partial t} + \tilde{U} \frac{\partial}{\partial x}\right)^2 \phi - \tilde{c}^2 \phi_{xx} - \tilde{c}^2 \Delta \phi = D \quad (13)$$

where ϕ is the velocity potential, D is the disturbance that generates the acoustic field, t is time, x is an axial coordinate along which the fluid velocity is $(\tilde{U} + \phi_x)$ where $\tilde{U} = \text{const}^*$. The undisturbed speed of sound is represented by the constant \tilde{c} and $\Delta = \nabla^2$ is the Laplacian in the transverse coordinates. Physically, equation (13) represents the propagation of an acoustic disturbance, whose fluid velocity is $(\phi_x, \nabla \phi)$ in a uniform stream of speed \tilde{U} .

As with all partial differential equations, equation (13) is solved in a specific space domain. This domain is illustrated in Figure 4-1 together with the appropriate values of \tilde{U} , \tilde{c} , and the undisturbed density $\tilde{\rho}$. Thus, for $r < r_j$, $\tilde{U} = U$, $\tilde{c} = c_2$, $\tilde{\rho} = \rho_2$; for $r > r_j$, $\tilde{U} = 0$, $\tilde{c} = c_1$, $\tilde{\rho} = \rho_1$, where

$$r = r_j(\theta) \quad 0 \leq \theta < 2\pi \quad (14)$$

is the equation of a doubly infinite cylinder.

* Note that \tilde{U} , \tilde{c} , ..., etc., are assumed to be sectionally constant.

Guided by the desire to maintain simplicity, to model the source term D , it is assumed that

$$D = e^{-i\omega_0 t} \delta(x - Ut) f(r, \theta) / a^2 \quad i = \sqrt{-1} \quad (15)^*$$

where ω_0 is a given constant and $f(r, \theta)$ is a given function such that $f = 0$ for $r > r_j$. Physically, the source term represented by equation (15) is a harmonically oscillating disturbance of frequency ω_0 , concentrated at a point on the centerline given by $x = Ut$. In other words the source is convecting at speed U in the positive x direction. The assumption that the source convection speed is the same as the jet speed is made for simplicity and will be relaxed in the next section.

Across the jet-quiescent region interface, the continuity of the perturbation pressure, p , and the particle displacement are required. The assumption of particle displacement continuity implies negligible mixing between the jet and the surrounding medium. The expression for the perturbation pressure is most easily derivable from the linearized x -momentum equation, and is given by

$$p = -\tilde{\rho}(\phi_t + U\phi_x) \quad (16a)$$

where $\tilde{\rho}$ is the undisturbed density in the appropriate region. The particle displacement, η , obeys

$$\frac{\partial \phi}{\partial n} = \eta_t + U\eta_x \quad (16b)$$

where $\partial \phi / \partial n$ is the velocity normal to the mean location of the jet-quiescent region interface.

The undisturbed static pressure is also continuous across the jet boundary. This implies that for a given ambient condition, the jet density or speed of sound (i.e., temperature) determines uniquely the undisturbed thermodynamic state of the jet.

The governing equation is hyperbolic, and it requires initial conditions for uniqueness. These can easily be provided (for example, $\phi = \partial \phi / \partial t = 0$ at $t = 0$). In the present context, however, the interest is in the long time solution and the initial conditions have negligible effect on this.

With the above preliminary remarks in mind, the time and x dependence in equation (13) are extracted through Fourier transforms. Define

* " a " is a linear dimension characteristic of the nozzle size

$$\phi^* = \frac{1}{\sqrt{2\pi}} \int_{-\infty}^{\infty} e^{i\omega t} \phi \, dt \quad (17a)$$

$$\phi = \frac{1}{\sqrt{2\pi}} \int_{-\infty}^{\infty} e^{-i\omega t} \phi^* \, d\omega \quad (17b)$$

and*

$$\phi^* = \overline{\phi^*} e^{i(\omega - \omega_0)x/U} \quad (17c)$$

After these transforms, the resultant equation for $\overline{\phi^*}$ is given in the still-air region by

$$\Delta \overline{\phi^*} + k_0^2 (K_1^+)^2 \overline{\phi^*} = 0 \quad (18a)$$

and in the jet region by

$$\Delta \overline{\phi^*} + k_0^2 (K_2^+)^2 \overline{\phi^*} = \frac{-1}{(2\pi)^{\frac{1}{2}} c_2^2 U} f(r, \theta)/a^2 \quad (18b)$$

or

$$\Delta \overline{\phi^*} - k_0^2 (K_2^-)^2 \overline{\phi^*} = \frac{-1}{(2\pi)^{\frac{1}{2}} c_2^2 U} f(r, \theta)/a^2 \quad (18c)$$

where $k_0 = \omega_0/c_1$.

The propagation constants K_1^+ , K_2^+ and K_2^- are given by

$$(K_1^+)^2 = \kappa^2 - (\kappa - 1)^2/M^2 \quad (19a)$$

* After performing the Fourier transform in time, it is clear that the x dependence of the solution must be of the form given by equation (17c). Note that a Fourier transform in x also leads to (17c) after inversion.

$$(K_2^+)^2 = \Gamma_{12} \rho_{21} - (\kappa - 1)^2/M^2 \quad (19b)$$

$$(K_2^-)^2 = (\kappa - 1)^2/M^2 - \Gamma_{12} \rho_{21} \quad (19c)$$

where $\kappa = \omega/\omega_0$, $M = U/c_1 < 1$, $\rho_{21} = \rho_2/\rho_1$, and $\Gamma_{12} = \Gamma_1/\Gamma_2$ where

$$\Gamma = (1 - R/c_p)^{-1} \quad (19d)$$

The gas constant is denoted by R , and c_p is the constant pressure specific heat. An additional assumption in deriving equations (19b and c) is that the gas is thermally perfect (but not calorically perfect).

The case $(K_1^+)^2 \geq 0$ is relevant here (otherwise the far-field solution dies off exponentially in the transverse variable), that is, $1/(1+M) \leq \kappa \leq 1/(1-M)$. When $(K_1^+)^2 > 0$, that is $1/(1+M) \leq \kappa \leq 1+M\sqrt{\Gamma_{12}\rho_{21}}$ equation (18b) holds; otherwise (18c) holds.

The behavior of K_1^+ , K_2^+ is shown in Figures 4-2 and 4-3 for parametric values of M . In these figures, it is assumed that $\Gamma_{12}\rho_{21} = 1$.

To complete the present framework for the formulation of the problem, the t and x dependence of the matching conditions for the interface are extracted. In the still-air region, one finds that the transforms of equations (16a and b) are

$$\overline{p^*} = i \rho_1 \omega \overline{\phi^*} \quad (20a)$$

$$\overline{\eta^*} = \frac{i}{\omega} \frac{\partial \overline{\phi^*}}{\partial n} \quad (20b)$$

and in the jet region

$$\overline{p^*} = i \rho_2 \omega_0 \overline{\phi^*} \quad (20c)$$

$$\overline{\eta^*} = \frac{i}{\omega_0} \frac{\partial \overline{\phi^*}}{\partial n} \quad (20d)$$

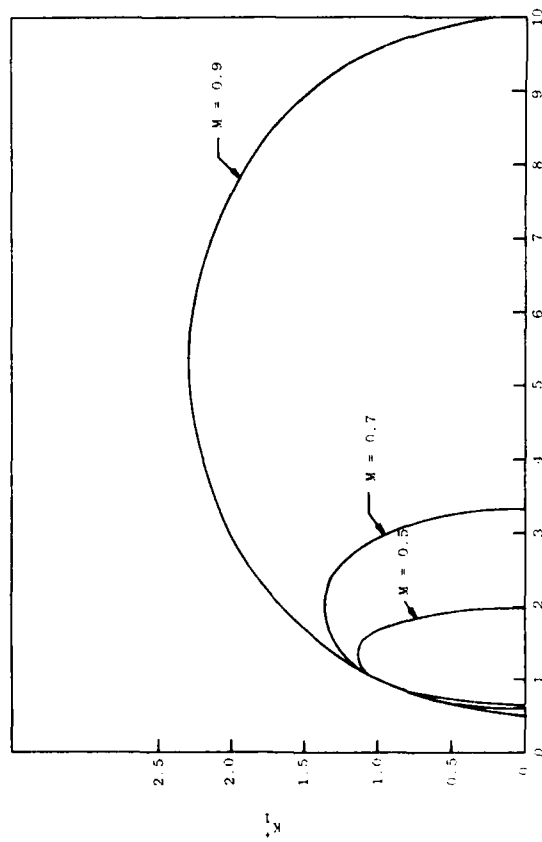


Figure 4-2. Free Space Propagation Constant Versus Frequency (K_1^+ Versus κ).

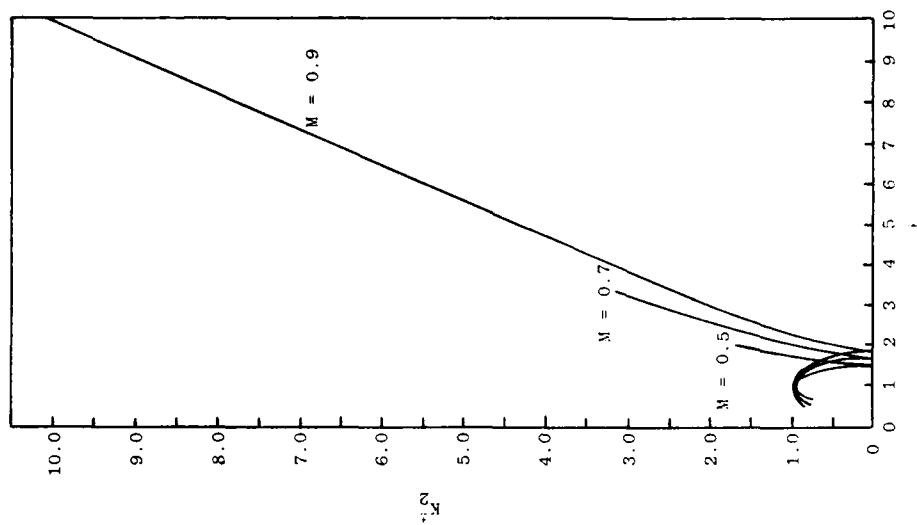


Figure 4-3. Jet Propagation Constant Versus Frequency (K_2^+ Versus κ).

Thus the canonical problem to be solved is

$$\Delta\phi \pm k_0^2 K^2 \phi = f(r, \theta)/a^2 \quad (21a)$$

with boundary conditions across the jet interface

$$\left. \begin{aligned} \kappa \phi_1 &= \rho_{21} \phi_2 \\ \left(\frac{\partial \phi}{\partial n}\right)_1 &= \kappa \left(\frac{\partial \phi}{\partial n}\right)_2 \end{aligned} \right\} \text{ on } r = r_j \quad (21b)$$

$$\left. \begin{aligned} \kappa \phi_1 &= \rho_{21} \phi_2 \\ \left(\frac{\partial \phi}{\partial n}\right)_1 &= \kappa \left(\frac{\partial \phi}{\partial n}\right)_2 \end{aligned} \right\} \text{ on } r = r_j \quad (21c)$$

where K^2 stands for $(K_1^+)^2$, $(K_2^+)^2$ or $(K_2^-)^2$. Note that $\phi = - (2\pi)^{1/2} c_2^2 \bar{U} \phi^*$ and ϕ_2 denotes the solution in the jet with ϕ_1 in the ambient medium.

It can be shown that, after taking the convective derivative, $(\partial/\partial t + \bar{U} \partial/\partial x)$, of equations (13) and (15), the following equations result:

$$\left(\frac{\partial}{\partial t} + \bar{U} \frac{\partial}{\partial x}\right)^2 p - c_2^2 p_{xx} - c_2^2 \Delta p = i \rho_2 \omega_0 e^{-i\omega_0 t} \delta(x - Ut) f(r, \theta)/a^2 \quad (22a)$$

and

$$p_{tt} - c_1^2 p_{xx} - c_1^2 \Delta p = 0 \quad (22b)$$

in the jet and quiescent regions respectively. Therefore, the convective derivative of the solution to equation (21a) provides the solution of equation (22). The left side of equation (22) is essentially that of Lilley's equation with \bar{U} and \bar{c} sectionally constant. Also note that differentiating the solution of equation (22) with respect to x once (twice) yields the solution for a generalized axial pressure dipole (quadrupole). Furthermore, by specializing $f(r, \theta)$ to suitable singular distributions, the solution to any point dipole or quadrupole field can be readily obtained. As an example, let $f(r, \theta) = \delta(r - r_0)\delta(\theta - \theta_0)/r$ where r_0 and θ_0 are parameters. Differentiating this solution of equation (22) with respect to r_0 and θ_0 yields the solution for an $(r - \theta)$ quadrupole.

The above remarks imply that if the source solution (i.e., the Green's function) to equation (21a) is known, the solution for an arbitrary forcing function $f(r, \theta)$ can be written down by superposition. Since the jet has a completely arbitrary cross section, the origin of the coordinate system can

be placed at the source location. Thus the canonical problem can be replaced by

$$\Delta \phi \pm k_0^2 K^2 \phi = \delta(r)/r \quad (23)$$

without any loss of generality. Boundary conditions [(21b) and (21c)] are, of course retained.

4.2.1.1.3 Expansion of the Inner and Outer Solutions

It is convenient to introduce an inner variable $\tilde{r} = r/a$ and rewrite equation (23) as

$$\frac{\partial^2 \phi}{\partial \tilde{r}^2} + \frac{1}{\tilde{r}} \frac{\partial \phi}{\partial \tilde{r}} + \frac{1}{\tilde{r}^2} \frac{\partial^2 \phi}{\partial \theta^2} + \epsilon^2 K^2 \phi = \tilde{\Delta} \phi + \epsilon^2 K^2 \phi = \frac{\delta(\tilde{r})}{\tilde{r}} \quad (24)$$

where a denotes the characteristic size of the jet and $\epsilon = k_0 a$. It is desired to find an asymptotic solution of (24) as $\epsilon \rightarrow 0$. For the time being, it is assumed that K^2 is about unity, and it is later shown how to improve the asymptotic solution where K^2 is considerably larger.

The asymptotic limit $\epsilon \rightarrow 0$ clearly corresponds to a low frequency solution of equation (22).

Consider inner gauge functions $\delta_{\nu\mu}^{(i)}(\epsilon) = (\epsilon/2)^{2\nu} \log^\mu(\epsilon/2)$ and expand the inner solution, outside the jet, $\phi^{(i)}$ as

$$\phi^{(i)} = \sum_{\nu, \mu} \delta_{\nu\mu}^{(i)}(\epsilon) \phi_{\nu\mu}^{(i)} \quad \begin{array}{l} \nu = 0, 1, \dots \\ \mu = 0, 1, \dots, \nu + 1 \end{array} \quad (25)$$

The form of the inner gauge functions is suggested by the results of classical slender body theory (Germain⁽²⁰⁾). The supersonic flow over a slender body is formally equivalent to the low frequency theory of a pulsating body, [Miles⁽²¹⁾, Landau and Lifshitz⁽²²⁾]. Thus, it is not surprising that the same gauge functions arise in the present problem that did in classical slender body theory. After substituting equation (25) into (24) and collecting like gauge functions of ϵ , there results

$$1: \tilde{\Delta} \phi_{00}^{(i)} = 0 \quad (\text{"lowest" order solution}) \quad (26a)$$

$$\log \frac{\epsilon}{2}: \tilde{\Delta} \phi_{01}^{(i)} = 0 \quad (26b)$$

$$\left(\frac{\epsilon}{2}\right)^2 \log^2 \left(\frac{\epsilon}{2}\right): \tilde{\Delta}\phi_{12}^{(i)} = 0 \quad (26c)$$

$$\left(\frac{\epsilon}{2}\right)^2 \log \left(\frac{\epsilon}{2}\right): \tilde{\Delta}\phi_{11}^{(i)} + 4K^2 \phi_{01}^{(i)} = 0 \quad (26d)$$

$$\left(\frac{\epsilon}{2}\right)^2: \tilde{\Delta}\phi_{10}^{(i)} + 4K^2 \phi_{00}^{(i)} = 0 \quad \text{etc.} \quad (26e)$$

Thus, the sequence of inner solutions satisfies Poisson's (or Laplace's) equation. The inhomogeneous terms are either given or are known from the lower order solutions.

Next an outer variable $R = k_0 r = \epsilon \tilde{r}$ is introduced, along with a sequence of outer gage functions $\delta_{\nu\mu}^{(o)}(\epsilon)$ (to be determined by matching asymptotically the outer solution to the inner solution). Equation (23) can then be rewritten as

$$\frac{\partial^2 \phi}{\partial R^2} + \frac{1}{R} \frac{\partial \phi}{\partial R} + \frac{1}{R^2} \frac{\partial^2 \phi}{\partial \theta^2} + K^2 \phi = \square \phi = 0 \quad R > 0 \quad (27)$$

If the outer solution is represented by

$$\phi^{(o)} = \sum_{\nu, \mu} \delta_{\nu\mu}^{(o)}(\epsilon) \phi_{\nu\mu}^{(o)} \quad (28a)$$

then each term in the expansion obeys

$$\square \phi_{\nu\mu}^{(o)} = 0 \quad (28b)$$

Clearly the sequence of outer solutions obeys the homogeneous Helmholtz equation.

4.2.1.1.4 Inner and Outer Solutions and Results of Asymptotic Matching

The inner and outer gage functions $\delta_{\nu\mu}^{(i)}$ and $\delta_{\nu\mu}^{(o)}$ are regrouped to form a three-term asymptotic sequence to the required order of accuracy. Then the first three terms of this new gage sequence are:

$$\delta_1(\epsilon) = 1, \log(\epsilon/2), \log^2(\epsilon/2) \quad (29a)$$

$$\delta_2(\epsilon) = (\epsilon/2), (\epsilon/2) \log(\epsilon/2), (\epsilon/2) \log^2(\epsilon/2) \quad (29b)$$

$$\delta_3(\epsilon) = (\epsilon/2)^2, (\epsilon/2)^2 \log(\epsilon/2), (\epsilon/2)^2 \log^2(\epsilon/2) \quad (29c)$$

The matching is done, term by term, for the coefficient of each δ_n ($n = 1, 2, 3$). Such regrouping is absolutely essential for the success of the asymptotic matching principle as given by Van Dyke⁽²³⁾. The reasons for regrouping are thoroughly discussed in a series of papers by Fraenkel⁽²⁴⁾. The point here is that a given function can be expanded in several different sequences of gage functions $\delta_{\mu\nu}^{(1)}$ and $\delta_{\mu\nu}^{(0)}$. Since the function is given, there can be no question on the validity of any of these expansions. However, not all of these expansions satisfy the asymptotic matching principle of Van Dyke⁽²³⁾. In other words, it is possible to have a situation in which the expansion is correct, but the inner and outer solutions cannot be matched. Such is the case in the present analysis if term by term matching is required for the gage sequences $\delta_{\mu\nu}^{(1)}$ and $\delta_{\mu\nu}^{(0)}$. If the regrouping is done according to equation (29), however, the inner and outer solutions can be matched. After a step-by-step application of the asymptotic matching principle, it is found that in the inner region (but outside the jet):

$$\phi_{00}^{(i)} = A_0^{(1)} + B_0^{(1)} \log \tilde{r} + \sum_{n=1}^{\infty} \tilde{r}^{-n} (C_n^{(1)} \cos n\theta + D_n^{(1)} \sin n\theta) \quad (30a)$$

$$\phi_{01}^{(i)} = A_0^{(2)} \quad (30b)$$

$$\phi_{12}^{(i)} = A_0^{(3)} \quad (30c)$$

$$\phi_{11}^{(i)} = A_0^{(4)} + B_0^{(4)} \log \tilde{r} + \sum_{n=1}^{\infty} \tilde{r}^{-n} (C_n^{(4)} \cos n\theta + D_n^{(4)} \sin n\theta) \quad (30d)$$

$$- 2K^2 \tilde{r} (C_1^{(1)} \cos \theta + D_1^{(1)} \sin \theta) - K^2 \tilde{r}^2 A_0^{(2)}$$

$$\begin{aligned}
\phi_{10}^{(i)} = & A_0^{(5)} + B_0^{(5)} \log \tilde{r} + \sum_{n=1}^{\infty} \tilde{r}^{-n} (C_n^{(5)} \cos n\theta + D_n^{(5)} \sin n\theta) \\
& - 2K^2 \tilde{r} (\log K + \tilde{\gamma} - \frac{1}{2} - \frac{\pi i}{2}) (C_1^{(1)} \cos \theta + D_1^{(1)} \sin \theta) \\
& - K^2 A_0^{(1)} \tilde{r}^2 - K^2 B_0^{(1)} \tilde{r}^2 (\log \tilde{r} - 1) \\
& - 2K^2 \tilde{r} \log \tilde{r} (C_1^{(1)} \cos \theta + D_1^{(1)} \sin \theta) \\
& + K^2 \sum_{n=2}^{\infty} \frac{1}{(n-1)} \frac{1}{\tilde{r}^{n-2}} (C_n^{(1)} \cos n\theta + D_n^{(1)} \sin n\theta)
\end{aligned} \tag{30e}$$

where $A_0^{(m)}$, $B_0^{(m)}$, $C_n^{(m)}$, $D_n^{(m)}$ ($m = 1, 2, \dots$, $n = 1, 2, \dots$) are constants, $\tilde{\gamma} = 0.57721$ (Euler's constant) and $i = \sqrt{-1}$. It is observed that the lowest order solution behaves as $\log \tilde{r}$ as $\tilde{r} \rightarrow \infty$, and that both $\phi_{01}^{(1)}$ and $\phi_{12}^{(1)}$ are constants (actually the latter result comes from matching inner and outer solutions to all orders). Thus the lowest order solution is a "classical" solution to Laplace's equation in the sense that $(\partial \phi_{00}^{(1)} / \partial \tilde{r})$ vanishes at infinity.

Similarly, the matched outer solution is given by

$$\begin{aligned}
\phi^{(o)} = & \left[A_{01} + A_{02} \left(\frac{\epsilon}{2}\right)^2 \log\left(\frac{\epsilon}{2}\right) + A_{03} \left(\frac{\epsilon}{2}\right)^2 \right] H_0^{(1)}(KR) \\
& + \left(\frac{\epsilon}{2}\right) H_1^{(1)}(KR) (A_{11} \cos \theta + B_{11} \sin \theta) \\
& + \left(\frac{\epsilon}{2}\right)^2 H_2^{(1)}(KR) (A_{21} \cos 2\theta + B_{21} \sin 2\theta) + \dots
\end{aligned} \tag{31}$$

where A_{01} , A_{02} , A_{03} , A_{11} , B_{11} , A_{21} , and B_{21} are constants and $H_n^{(1)}$ ($n = 0, 1, 2, \dots$) are Hankel functions. The outer solution coefficients are given in terms of the inner solution coefficients by

$$A_{01} = \frac{\pi}{2i} B_0^{(1)} \quad (32a)$$

$$A_{02} = \frac{\pi}{2i} B_0^{(4)} \quad (32b)$$

$$A_{03} = \frac{\pi}{2i} B_0^{(5)} \quad (32c)$$

and

$$A_{11} = \pi i K C_1^{(1)} \quad (33a)$$

$$B_{11} = \pi i K D_1^{(1)} \quad (33b)$$

$$A_{21} = \pi i K^2 C_2^{(1)} \quad (33c)$$

$$B_{21} = \pi i K^2 D_2^{(1)} \quad (33d)$$

Similarly, the inner solution constants are obtained from

$$A_0^{(1)} = A_{01} \left[1 + \frac{2i}{\pi} (\log K + \tilde{\gamma}) \right] \quad (34a)$$

$$A_0^{(2)} = \frac{2i}{\pi} A_{01} \quad (34b)$$

$$A_0^{(3)} = \frac{2i}{\pi} A_{02} \quad (34c)$$

$$A_0^{(4)} = A_{02} \left[1 + \frac{2i}{\pi} (\log K + \tilde{\gamma}) \right] + \frac{2i}{\pi} A_{03} \quad (34d)$$

$$A_0^{(5)} = A_{03} \left[1 + \frac{2i}{\pi} (\log K + \tilde{\gamma}) \right] \quad (34e)$$

It is observed that the outer solution is matched to the inner solution outside the jet (i.e., both of these regions are in the quiescent region) so that in this section K^2 is to be replaced by $(K_1^+)^2$ and $\phi_{\nu\mu}^{(i)}$ is the inner solution outside the jet.

The above results are obtained by a systematic application of the "strict" rules of singular perturbations. In this particular example, it is also possible to circumvent many of the algebraic steps that lead to the final results, by observing that the outer solution can be written down to any order of accuracy. Rewriting this solution in terms of the inner variable and expanding in terms of ε , there results

$$\phi^{(0)} = \sum_{n=0}^{\infty} H_n^{(1)}(KR) \left(\frac{\varepsilon}{2}\right)^n \left[A_{n1} \cos n\theta + B_{n1} \sin n\theta + \dots \right] \quad (35a)$$

or

$$\begin{aligned} \phi^{(0)} = & A_{01} \left[1 + \frac{2i}{\pi} (\log \tilde{r} + \log K + \tilde{\gamma}) \right] \\ & - \frac{i}{\pi} \sum_{n=1}^{\infty} \frac{(n-1)!}{K^n \tilde{r}^n} (A_{n1} \cos n\theta + B_{n1} \sin n\theta) \\ & + \frac{2i}{\pi} A_{01} \log \frac{\varepsilon}{2} + \dots \end{aligned} \quad (35b)$$

$$= \phi_{00}^{(i)} + \log\left(\frac{\varepsilon}{2}\right) \phi_{01}^{(i)} + \dots \quad (35c)$$

From equation (35), it is possible to deduce the form of $\phi_{00}^{(i)}$ and the relationship between the near-field coefficients $A_0(1)$, $B_0(1)$, $C_n(1)$, $D_n(1)$ and the far-field coefficients A_{01} , A_{n1} , and B_{n1} . This relationship is given by the asymptotic matching principle for $n = 1, 2$. Furthermore, it also appears that $\phi_{01}^{(i)} = \text{constant}$, and that A_{n1} and B_{n1} are proportional to $C_n(1)$ and $D_n(1)$. Thus part of the nonsymmetric outer solution is matched to the nonsymmetric part of the lowest order inner solution.

4.2.1.1.5 Inner and Jet Solutions and Results of Matching Pressure and Particle Displacement Across Jet Boundary

The sequence of inner equations (26) for the velocity potential is also satisfied by the potential inside the jet, $\phi_{\nu\mu}^{(J)}$. Thus the lowest order solution inside the jet satisfies

$$\tilde{\Delta} \phi_{00}^{(J)} = \frac{\delta(\tilde{r})}{\tilde{r}} \quad (36a)$$

and an application of Gauss' theorem shows that

$$\iint_a \tilde{\Delta}\phi_{00}^{(j)} \tilde{r} d\tilde{r} d\theta = 2\pi = \int_{\partial a} \frac{\partial\phi_{00}^{(j)}}{\partial n} ds \quad (36b)$$

where a is the jet cross sectional area, ∂a denotes the jet boundary and ds is the arc length along the boundary. Similarly, from equation (26a)

$$\iint_{\bar{a}} \tilde{\Delta}\phi_{00}^{(i)} \tilde{r} d\tilde{r} d\theta = 0 = \int_{\partial\bar{a}} \frac{\partial\phi_{00}^{(i)}}{\partial n} ds \quad (36c)$$

where \bar{a} is the annular area between the jet and a large circle of radius \tilde{r} . The boundary $\partial\bar{a}$ consists of two parts, namely, the jet boundary and the circle. Combining equations (36b and 36c) and matching condition (21c) yields

$$2\pi \kappa = \int_{\text{circle}} \frac{\partial\phi_{00}^{(i)}}{\partial n} ds \quad (37)$$

Finally, the contour integral in equation (37) is evaluated explicitly using equation (30a). The result is

$$B_0^{(1)} = \kappa \quad (38a)$$

By a completely analogous argument, it is found

$$B_0^{(4)} = \frac{2}{\pi} \kappa a \left[(K_1^+)^2 + \kappa^2 \rho_{12} (K_2^+)^2 \right] \quad (38b)$$

and

$$B_0^{(5)} = \frac{2}{\pi} \left[(K_1^+)^2 \iint_a \phi_{00}^{(i)} \tilde{r} d\tilde{r} d\theta + \kappa (K_2^+)^2 \iint_a \phi_{00}^{(j)} \tilde{r} d\tilde{r} d\theta \right] \quad (38c)$$

Note that the interface matching conditions [equation (21)] were applied for each coefficient of the gage functions. In particular, $\phi_{01}^{(i)} = \text{constant}$ outside the jet implies that $\phi_{01}^{(j)} = \text{constant}$ inside the jet.

The remarkable outcome of this asymptotic expansion is that the outer field, to the required order, depends only on the lowest order inner and jet solutions. Both of these solutions satisfy Laplace's equation.

4.2.1.1.6 Calculation of the Acoustic Power of the Source

The acoustic power of the source is calculated by integrating the product of the pressure and normal component of the velocity over a large cylinder enclosing the jet. The mathematical technique is fully described by Morse and Ingard⁽²⁵⁾.

Expressing the velocity potential in the far field as

$$\phi^{(0)} = \sum_n H_n^{(1)}(k_0 K_1^+ r) (A_n \cos n\theta + B_n \sin n\theta) \quad (39a)$$

a comparison of equations (39a) and (31) shows that

$$A_0 = A_{01} + A_{02} \left(\frac{\epsilon}{2}\right)^2 \log\left(\frac{\epsilon}{2}\right) + A_{03} \left(\frac{\epsilon}{2}\right)^2 \quad (39b)$$

$$A_1 = \left(\frac{\epsilon}{2}\right) A_{11} \quad (39c)$$

$$B_1 = \left(\frac{\epsilon}{2}\right) B_{11} \quad (39d)$$

$$A_2 = \left(\frac{\epsilon}{2}\right)^2 A_{21} \quad (39e)$$

$$B_2 = \left(\frac{\epsilon}{2}\right)^2 B_{21} \quad (39f)$$

where coefficients A_n, B_n ($n = 0, 1, 2, \dots$) are, in general, complex.

The expressions for the perturbation pressure and radial component of the velocity are given by the x-t Fourier inverse of equation (39a),

$$p = -\rho_1 \frac{\partial \phi}{\partial t} = \frac{i \rho_1}{4\pi^2 c_2^2 U} \int_{\frac{\omega_0}{1+M}}^{\frac{\omega_0}{1-M}} \exp[i(\omega - \omega_0)x/U - i\omega t] \omega \sum_n H_n^{(1)}(A_n \cos n\theta + B_n \sin n\theta) d\omega \quad (40a)$$

$$\phi_r = \frac{k_0}{4\pi^2 c_2^2 U} \int_{\frac{\omega_0}{1+M}}^{\frac{\omega_0}{1-M}} \exp[i(\omega - \omega_0)x/U - i\omega t] K_1^+ \sum_n H_n^{(1)*} (A_n \cos n\theta + B_n \sin n\theta) d\omega \quad (40b)$$

and the radiative power of the source is

$$P = \frac{\rho_1}{4\pi^2 U c_2^2} \int_0^{2\pi} P_\theta d\theta \quad (41a)$$

where

$$P_\theta = \int_{\frac{\omega_0}{1+M}}^{\frac{\omega_0}{1-M}} \omega d\omega \left| \sum_n e^{-in\frac{\pi}{2}} (A_n \cos n\theta + B_n \sin n\theta) \right|^2 \quad (41b)$$

P is the total power and P_θ is the "power in a plane*" whose orientation is determined by the polar angle θ . Observe that the integral for P_θ is evaluated over a frequency range defined by the Doppler limits.

Consider now a very brief discussion of the Kelvin-Helmholtz instability. This classic problem has been examined by a number of authors including Miles(26), Batchelor and Gill(27), and more recently by Jones and Morgan(28). The conclusion of Jones and Morgan, although only qualitatively relevant to the present problem, is that the long time solution of a harmonically pulsating source (switched on at $t = 0$) is a harmonically varying (in time) acoustic field which contains an additive element that grows exponentially with distance downstream but decays exponentially from the jet interface. In fact, the complete solution to the present problem can be written in the form $\psi = \phi + \phi_1$ where ϕ is obtained from the above analysis and ϕ_1 is the unstable solution. The approach at this point is to ignore the unstable contribution to the acoustic field. Of course, this approach cannot be justified mathematically. On the other hand, the physical justification is clear, since the actual jet is reasonably stable with a bounded acoustic field. It should be noted, however, that there are Mach number limitations on this physical justification [Ffowcs-Williams(29)].

* P_θ is also proportional to the power per unit polar (or azimuthal) angle θ .

This concludes the formal analysis of this section. These results are now applied to two specific jet configurations.

4.2.1.1.7 Circular Jet - Radiation from Off Axis Sources

Mani⁽¹⁷⁾ has examined theoretically the radiation from sources convecting along the centerline of a circular jet. The present asymptotic theory is used to extend his results to the off-axis case in the low frequency limit.

The geometry of the jet is shown in Figure 4-4. The jet boundary is given by $R = 1$, and the source is located at $R = R_0 < 1$ and $\theta = \theta_0$.

The lowest order inner and jet solutions obey Laplace's equation [(26a and (36a)]. These solutions are denoted by $\phi^{(1)} = \phi_{00}^{(i)}$ and $\phi^{(2)} = \phi_{00}^{(j)}$ respectively. Thus

$$\phi^{(1)} = A_0 + B_0 \log R + \sum_{n=1}^{\infty} R^{-n} (C_n \cos n\theta + D_n \sin n\theta) \quad (42a)$$

$$\phi^{(2)} = \alpha_0 + \log r + \sum_{n=1}^{\infty} R^n (\alpha_n \cos n\theta + \beta_n \sin n\theta) \quad (42b)$$

where $A_0, B_0, \alpha_0, C_n, D_n, \alpha_n$ and β_n ($n = 1, 2, \dots$) are constants. The jet solution may be rewritten by using a well-known Fourier expansion of $\log r$ for $R > R_0$

$$\begin{aligned} \phi^{(2)} = \alpha_0 + \log R + \sum_{n=1}^{\infty} \left[\alpha_n R^n - \frac{1}{n} \left(\frac{R_0}{R} \right)^n \cos n\theta_0 \right] \cos n\theta \\ + \sum_{n=1}^{\infty} \left[\beta_n R^n - \frac{1}{n} \left(\frac{R_0}{R} \right)^n \sin n\theta_0 \right] \sin n\theta \end{aligned} \quad (42c)$$

The constants A_0, B_0, \dots , etc., are determined by matching the pressure and particle displacement across the jet boundary, $R = 1$. The results of this matching are

$$B_0 = \kappa \quad (43a)$$

$$C_n = -\frac{2}{n} \kappa \frac{R_0^n \cos n\theta_0}{1 + \rho_{12}^2 \kappa^2} \quad n = 1, 2, \dots \quad (43b)$$

$$D_n = -\frac{2}{n} \kappa \frac{R_0^n \sin n\theta_0}{1 + \rho_{12}^2 \kappa^2} \quad n = 1, 2, \dots \quad (43c)$$

where $\kappa = \omega/\omega_0$ and $\rho_{12} = \rho_1/\rho_2$.

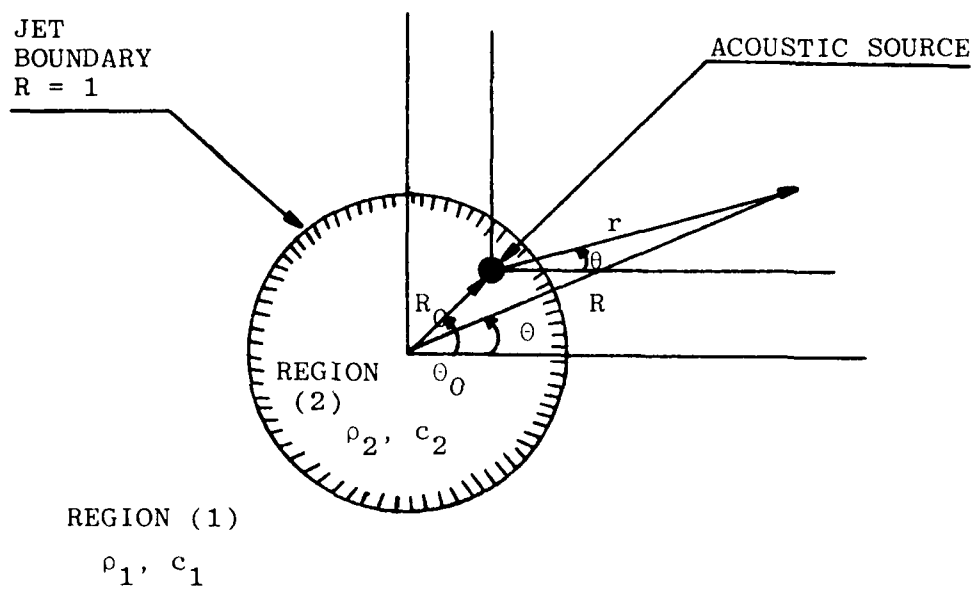


Figure 4-4. Geometry of Circular Jet.

It is observed that as $r \rightarrow \infty$, coordinate systems (R, θ) and (r, θ) are related by

$$r = R[1 - \frac{R_0}{R} \cos(\theta - \theta_0) + \dots] \quad (44a)$$

$$\theta = \theta + \frac{R_0}{R} \sin(\theta - \theta_0) + \dots \quad (44b)$$

and

$$R = r[1 - \frac{r_0}{r} \cos(\theta - \theta_0) + \dots] \quad (44c)$$

$$\theta = \theta + \frac{r_0}{r} \sin(\theta - \theta_0) + \dots \quad (44d)$$

where $r_0 = R_0$ and $\theta_0 = \theta_0 + \pi$. The point (r_0, θ_0) denotes the coordinates of the jet axis relative to the coordinate system attached to the source. After using coordinate transformation (44) in equation (42a), it is found that, as $r \rightarrow \infty$,

$$\begin{aligned} \phi^{(1)} = & A_0 + B_0 \log r - B_0 \left[\frac{r_0}{r} \cos(\theta - \theta_0) + \frac{1}{2} \left(\frac{r_0}{r} \right)^2 \cos 2(\theta - \theta_0) + \dots \right] \\ & + C_1 \frac{\cos \theta}{r} + D_1 \frac{\sin \theta}{r} \\ & + \frac{\cos 2\theta}{r^2} (C_2 + C_1 r_0 \cos \theta_0 - D_1 r_0 \sin \theta_0) \\ & + \frac{\sin 2\theta}{r^2} (D_2 + C_1 r_0 \sin \theta_0 + D_1 r_0 \cos \theta_0) + \dots \end{aligned} \quad (45)$$

Thus the far-field coefficients (32) and (33) are given by equations (38) and 45) as

$$A_{01} = \frac{\pi}{2i} \kappa \quad (46a)$$

$$A_{02} = -i\pi \kappa [(K_1^+)^2 + \kappa^2 \rho_{12} (K_2^+)^2] \quad (46b)$$

$$\begin{aligned} A_{03} = & \pm \frac{\pi i}{2} \kappa (K_2^+)^2 r_0' + \frac{\pi i}{2} \kappa [(K_1^+)^2 + (K_2^+)^2] \\ & - \frac{\pi^2}{2} \kappa [1 + \frac{2i}{\pi} (\log K_1^+ + \gamma)] [(K_1^+)^2 + \kappa^2 \rho_{12} (K_2^+)^2] \end{aligned} \quad (46c)$$

$$A_{11} = \pi i K_1^+ \kappa r_0 \cos \theta_0 (2/\Omega^+ - 1) \quad (46d)$$

$$B_{11} = \pi i K_1^+ \kappa r_0 \sin \theta_0 (2/\Omega^+ - 1) \quad (46e)$$

$$A_{21} = \frac{\pi i}{2} (K_1^+)^2 \kappa r_0^2 \cos 2\theta_0 \Omega^-/\Omega^+ \quad (46f)$$

$$B_{21} = \frac{\pi i}{2} (K_1^+)^2 \kappa r_0^2 \sin 2\theta_0 \Omega^-/\Omega^+ \quad (46g)$$

where $\Omega^\pm = 1 \pm \rho_{12} \kappa^2$.

Before the numerical results for the total power P are presented, some possible nonuniformities in the asymptotic expansion are briefly discussed. It is seen from Figure 4-2 that K_1^+ is of order unity; therefore, the harmonic terms $A_{11} \dots B_{21}$ exhibit no nonuniformities. On the other hand, it is seen from Figure 4-3 that terms proportional to K_2^+ may become much larger than unity. In this case the asymptotic expansion has a small range of validity restricted to very small values of ϵ . To extend this range, observe that the nonuniformity comes from the axially-symmetric terms. An examination of the structure of the complete axially-symmetric solution, reveals that the nonuniformity arises from a binomial expansion. To eliminate this difficulty, the constant A_0 given by (39b) is replaced by

$$A_0' = \frac{A_{01}^2}{A_{01} - A_{02}(\frac{\epsilon}{2})^2 \log \frac{\epsilon}{2} - A_{03}(\frac{\epsilon}{2})^2} \quad (47)$$

In the limit as $\epsilon \rightarrow 0$ equations (47) and (39b) are clearly equivalent. However, for finite values of ϵ , (47) has a much wider range of validity than equation (39b) in this particular example.

In Figure 4-5, a comparison between the exact calculations by Mani and the results of the present asymptotic theory for the total radiative power (41a) is shown. The power is shown to be a function of the convective Mach number and the source Strouhal number. It is seen that the agreement between the two results is excellent over the entire Mach number range (up to 0.9) and a wide range of Strouhal numbers.

By differentiating the expression for the velocity potential (45) with respect to the source coordinates, it is a simple matter to derive the pressure and velocity field of an off axis quadrupole shielded by a circular jet. For example, $\partial^2 \phi^{(1)} / \partial r_0 \partial \theta_0$ is the velocity potential of an $(r - \theta)$ quadrupole whose radiated power can be readily obtained.

A complete physical interpretation of these results is given by Mani⁽¹⁷⁾. To reemphasize, however, the above calculations show the frequency dependence of convective amplification. It is known from experiments [Lush⁽³⁰⁾] that the data for the sound pressure level as a function of directivity angle (at

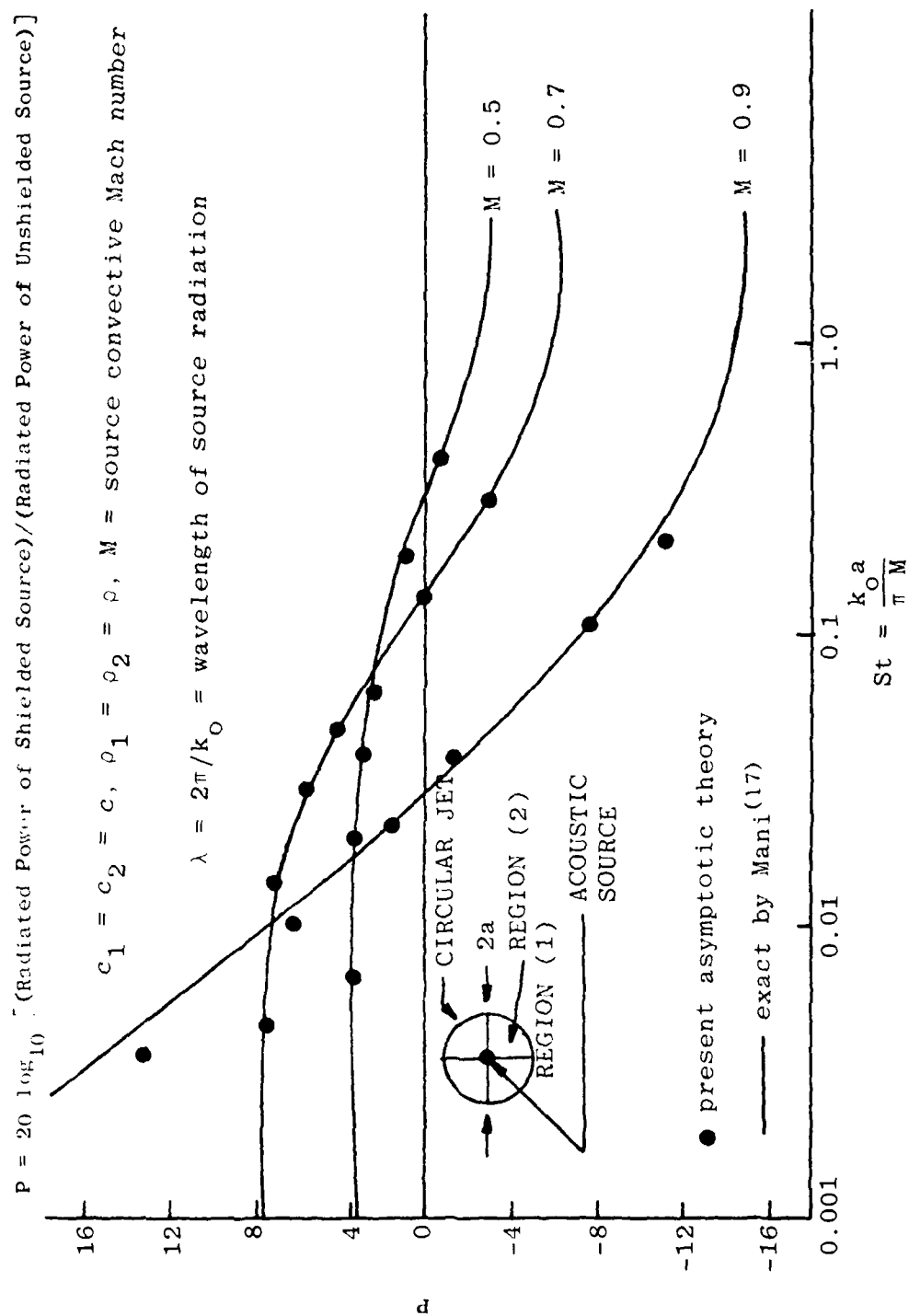


Figure 4-5. Convective Amplification as Function of M and St .

constant source frequency) is under estimated at low frequencies by the Lighthill theory. Also, the Lighthill theory over estimates the sound pressure level at high frequencies. This is interpreted to mean that convective amplification is frequency dependent. Furthermore, the results in Figure 4-5 show such dependence for the total power. Of course, the connection between the results of Lush and that in Figure 4-5 is qualitative in nature; this will be further discussed in Section 4.2.1.2.

An extremely important point is that acoustic shielding is confined to the refractive zone of silence, but shielding is more than refraction since it affects the radiated power. In other words, measurements outside of the zone of silence would show negligible shielding. Such measurements are insufficient, however, for the computation of total power. Thus, to look at the effects of fluid shrouding or shielding, the sound pressure level must be obtained in the zone of silence.

4.2.1.1.8 Elliptic Jet - Radiation from Axial Source

Consider an elliptic jet whose semi-axes are given by $\alpha, \beta \geq 0$ where $\alpha \geq \beta$. The source is located at the center of the ellipse. Introduce elliptic coordinates (μ, ν) ($0 \leq \mu < \infty, 0 \leq \nu < 2\pi$) by the transformation

$$r = \frac{a}{2} \sqrt{\cosh^2 \mu - \sin^2 \nu} \quad 0 \leq r \quad (48a)$$

$$\theta = \tan^{-1}(\tanh \mu \tan \nu) \quad 0 \leq \theta < 2\pi \quad (48b)$$

where $a = 2\sqrt{\alpha^2 - \beta^2}$ is the focal length and (r, θ) is a polar coordinate system (Figure 4-6). The equation of the ellipse is given by

$$\mu = \mu_1 = \log[(\alpha + \beta)/\sqrt{\alpha^2 - \beta^2}].$$

The lowest order inner and jet solutions obey Laplace's equation (26a) and (36a). These solutions are denoted by $\phi^{(1)} = \phi_{00}^{(1)}$ and $\phi^{(2)} = \phi_{00}^{(J)}$ respectively. Thus

$$\phi^{(1)} = A_0 + B_0 \mu + \sum_{n=1}^{\infty} C_n e^{-n\mu} \cos n\nu \quad (49a)$$

$$\begin{aligned} \phi^{(2)} = & \alpha_0 + \left(\mu + \log \frac{a}{4}\right) - 2 \sum_{n=1}^{\infty} \frac{1}{n} e^{-n\mu} \cos n\nu \cos \frac{n\pi}{2} \\ & + \sum_{n=1}^{\infty} \alpha_n \sinh n\mu \cos n\nu \end{aligned} \quad (49b)$$

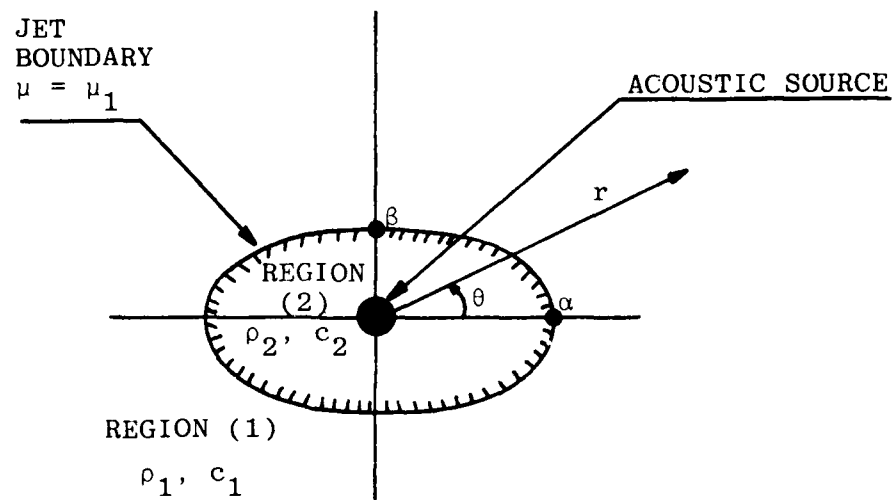


Figure 4-6. Geometry of Elliptic Jet.

where $A_0, B_0, \alpha_0, C_n, \alpha_n$ ($n = 1, 2, \dots$) are constants, again to be determined by matching pressure and particle displacement across the jet boundary. Observe that the terms in equation (49b) that do not involve any of these unknown constants represent $\log r$ in elliptic coordinates.

The matching across the jet boundary yields

$$B_0 = \kappa \quad (50a)$$

$$C_n = -\frac{4}{n} \kappa \frac{\cos \frac{n\pi}{2}}{\Omega^+ - \Omega^- e^{-2n\mu_1}} \quad n = 1, 2, \dots \quad (50b)$$

and

$$\alpha_1 = 0 \quad (50c)$$

$$\alpha_2 = -\frac{2}{\frac{\Omega^+}{\Omega^-} - e^{-4\mu_1}} e^{-4\mu_1} \quad (50d)$$

where, as before, $\kappa = \omega/\omega_0$, $\rho_{12} = \rho_1/\rho_2$ and $\Omega^\pm = 1 \pm \rho_{12} \kappa^2$.

The transformation to elliptic coordinates (48) simplifies to

$$\mu = \log \frac{4r}{a} - \left(\frac{a}{4}\right)^2 \frac{\cos 2\theta}{r^2} + \dots \quad (51a)$$

$$v = \theta + \left(\frac{a}{4}\right)^2 \frac{\sin 2\theta}{r^2} + \dots \quad (51b)$$

as $r \rightarrow \infty$ and, in the same limit, it is found that

$$e^{-n\mu} \cos n\nu = \left(\frac{a}{4r}\right)^2 \cos n\theta + n\left(\frac{a}{4r}\right)^{n+2} \cos(n+2)\theta + \dots \quad (51c)$$

$$n = 1, 2, \dots$$

Using equation (51) in (49b) and the general results of the asymptotic theory, it is found that the far-field coefficients are given by

$$A_{01} = \frac{\pi}{2i} \kappa \quad (52a)$$

$$A_{02} = -i\pi \alpha \beta \kappa [(K_1^+)^2 + \rho_{12} \kappa^2 (K_2^+)^2] \quad (52b)$$

$$A_{03} = -i[(K_1^+)^2 t_1 + \kappa (K_2^+)^2 t_2] \quad (52c)$$

where

$$t_1 = \pi \alpha \beta \kappa \left\{ \log \frac{\alpha + \beta}{2} - \frac{1}{2} \frac{\beta}{\alpha} - \frac{\pi i}{2} \left[1 + \frac{2i}{\pi} (\log K_1^+ + \tilde{\gamma}) \right] \right. \\ \left. - (1 - \beta/\alpha) \frac{1}{\Omega^+ - \left(\frac{\alpha - \beta}{\alpha + \beta} \right)^2 \Omega^-} \right\} \quad (52d)$$

and

$$t_2 = \pi \alpha \beta \left\{ \rho_{12} \kappa^2 \log \frac{\alpha + \beta}{2} - \frac{1}{2} \frac{\beta}{\alpha} \right. \\ \left. - \frac{\pi i}{2} \kappa^2 \rho_{12} \left[1 + \frac{2i}{\pi} (\log K_1^+ + \tilde{\gamma}) \right] \right. \\ \left. - \frac{1}{2} \left(1 - \frac{\beta}{\alpha} \right) \frac{\frac{\Omega^+}{\Omega^-} - \frac{\alpha - \beta}{\alpha + \beta}}{\frac{\Omega^+}{\Omega^-} - \left(\frac{\alpha - \beta}{\alpha + \beta} \right)^2} \right\} \quad (52e)$$

$$A_{11} = B_{11} = 0 \quad (52f)$$

$$A_{21} = \frac{\pi i}{4} (K_1^+)^2 \kappa (\alpha^2 - \beta^2) \frac{1 + \left(\frac{\alpha - \beta}{\alpha + \beta} \right)^2}{\frac{\Omega^+}{\Omega^-} - \left(\frac{\alpha - \beta}{\alpha + \beta} \right)^2} \quad (52g)$$

$$B_{21} = 0 \quad (52h)$$

The asymptotic expansion appears to be uniformly valid for all values of $\beta \leq \alpha$. Thus, this low frequency theory is not restricted to configurations with "low departure from axial symmetry."

The power, P_θ , (41b) in a plane inclined at an angle θ relative to the major axis is calculated as a function of θ for parametric values of $\epsilon = k_0\alpha$ ($\alpha = 1$) and β . The results are shown in Figures 4-7 and 4-8 for two different source Mach numbers. At given values of θ , β , and M , e.g., $\theta = 0^\circ$, $\beta = 0.5$ and $M = 0.7$, the source radiative power decreases with increasing source frequency. The power of a given geometry at a fixed value of θ and for moderate values of ϵ decreases with increasing Mach number. These observations are consistent with the results in Figure 4-5 for a circular jet.

The difference in acoustic power between the quiet plane ($\theta = 0$) and the noisy plane ($\theta = 90^\circ$) increases with the source Strouhal and Mach numbers. According to these calculations, the difference in power between the two planes is completely negligible at low frequencies and is on the order of a few dB at higher frequencies.

The total radiative power of the source (41a) varies inversely with the jet cross-sectional area at given Strouhal and Mach numbers. This observation is easily deducible from the results of Figures 4-6 and 4-7 and agrees with the fluid shielding hypothesis of Mani. In simple terms, the radiative efficiency of the source varies inversely with the amount of moving fluid surrounding it.

4.2.1.2 The Directivity of Sound

4.2.1.2.1 Introduction

In Section 4.2.1.1, the results for the radiative power of a source surrounded by an arbitrary jet were derived. These results showed that acoustic shielding had a significant effect on the power; the purpose of this section is to investigate the effects of shielding on the directivity of the sound.

The present analysis is similar to the one presented for the power, therefore, only the basic framework without details will be developed. A comparison between theory and data will be presented also.

4.2.1.2.2 Formulation of the Problem

It is again assumed that the acoustic field is generated by a moving point source translating with velocity U_c along the axis of a slug flow jet of arbitrary cross section (Figure 4-1). The source is pulsating with radian frequency ω_0 in its own reference frame. The velocity potential, ϕ , of the acoustic field obeys

$$\begin{aligned} & \left(\frac{\partial}{\partial t} + U \frac{\partial}{\partial x} \right)^2 \phi - \tilde{c}^2 \phi_{xx} - \tilde{c}^2 \Delta \phi \\ & = \exp(-i\omega_0 t) \delta(x - U_c t) \delta(y) \delta(z) \end{aligned} \quad (53)$$

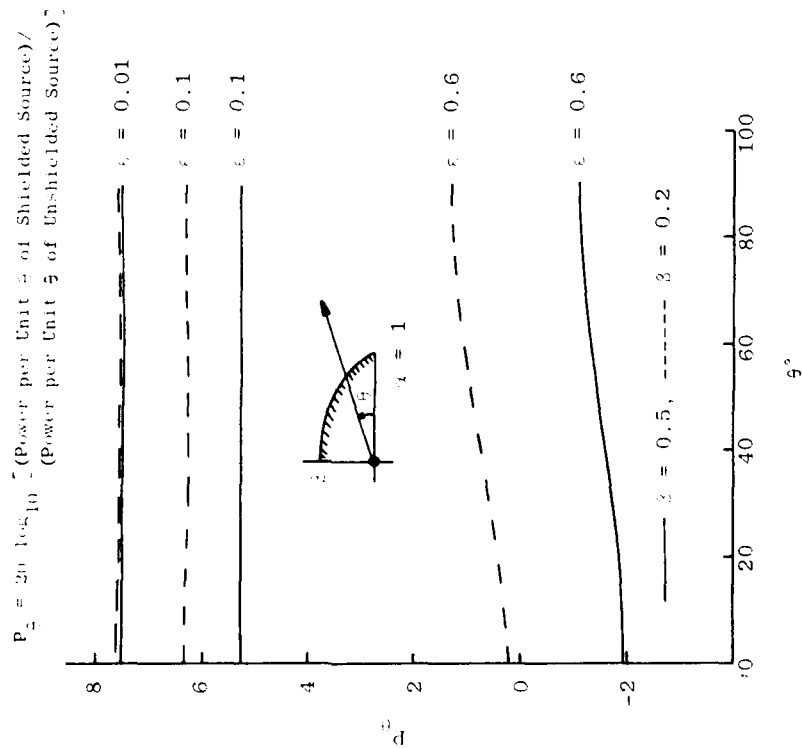


Figure 4-7. Theoretical Power Calculations for
Elliptic Jet [$M = 0.7$, $c_1/c_2 = 1.0$,
 $c_1/c_2 = 1.0$, $\epsilon = k_0$].

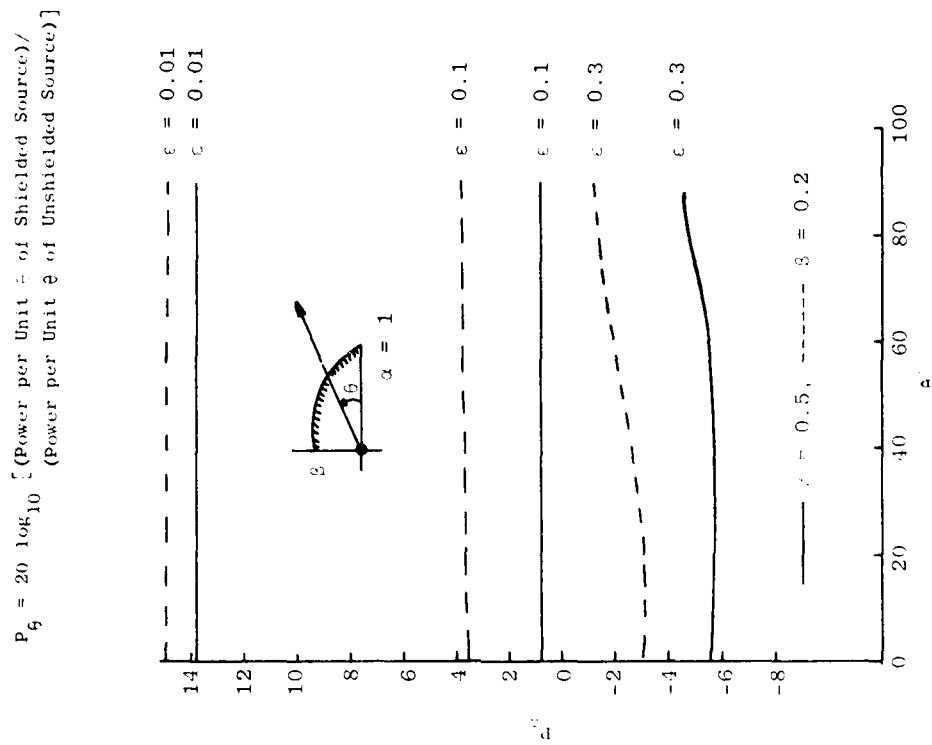


Figure 4-8. Theoretical Power Calculations for
Elliptic Jet [$M = 0.9$, $c_1/c_2 = 1.0$,
 $c_1/c_2 = 1.0$, $\epsilon = k_0$].

where, as before, \bar{U} and \bar{c} are sectionally constant representing the mean jet velocity and acoustic speed. Note that here the convection speed U_c need not be the same as the jet velocity U . Also, Δ denotes the Laplacian in the transverse variables.

It turns out that the most convenient representation for the directivity is obtained by taking Fourier transforms with respect to x , rather than t as in the previous section. Thus define

$$\bar{\phi} = \left(1/\sqrt{2\pi}\right) \int_{-\infty}^{\infty} e^{-isx} \phi dx \quad (54a)$$

whose inverse is

$$\phi = \left(1/\sqrt{2\pi}\right) \int_{-\infty}^{\infty} e^{isx} \bar{\phi} ds \quad (54b)$$

where s is the transform variable. After applying the above transformation (54a) to (53) and introducing a new dependent variable,

$$\phi = -(2\pi)^{3/2} c_2^2 \bar{\phi} \exp [it(\omega_0 + U_c s)] \quad (55)$$

it is found that the velocity potential ϕ obeys, in the jet and quiescent regions, respectively,

$$\text{Jet: } \Delta \phi + k_0^2 K_2^2 \phi = \delta(r)/r \quad (56a)$$

$$\text{Ambient: } \Delta \phi + k_0^2 K_1^2 \phi = 0 \quad (56b)$$

$$\text{where } K_2^2 = (c_1/c_2)^2 [1 + (M_c - M)\sigma]^2 - \sigma^2 \quad (56c)$$

$$\text{and } K_1^2 = (1 + M_c \sigma)^2 - \sigma^2 \quad (56d)$$

Here $k_0 = \omega_0/c_1$, $M_c = U_c/c_1$, $M = U/c_1$ and $\sigma = s/k_0$.

Thus, the convective Mach number and the jet acoustic speed are denoted by M_c and M respectively. The Fourier transform variable, $s = k_0 \sigma$, can be interpreted as an axial wave number.

Without going into details, it may be shown by applying Fourier transformation (54a) to the matching of the pressure and particle displacement (16) across the jet interface, that

$$\left. \begin{aligned} \kappa \phi_1 &= \rho_{21} \phi_2 \\ \left(\frac{\partial \phi}{\partial n} \right)_1 &= \kappa \left(\frac{\partial \phi}{\partial n} \right)_2 \end{aligned} \right\} \text{ on } r = r_j \quad (57a)$$

(57b)

This time the meaning of κ is slightly different, namely

$$\kappa = \frac{1 + M_c^2}{1 + (M_c^2 - M)^2} \quad (57c)$$

$\rho_{21} = \rho_2/\rho_1$ and ϕ_2 denotes the solution in the jet while ϕ_1 in the ambient medium. Of course, $\partial/\partial n$ stands for differentiation in the normal direction to the jet-ambient region interface.

4.2.1.2.3 A Solution of the Problem

Again the problem to be solved is Helmholtz's equation (56) with suitable matching conditions across the jet boundary (57). In fact equations (56) and (57) are exactly the same as (23) and (21) so that the low frequency solution of Section 4.2.1.1 is directly usable for the directivity provided that the following change of variables occurs:

Correspondence Principle

Power	→	Directivity
$(K_1^+)^2$		K_1^2
$(K_2^+)^2$		K_2^2
κ		κ

Thus the details of the asymptotic expansion will not be reproduced in this section.

4.2.1.2.4 Calculation of the Directivity of the Source

While the details of the asymptotic matching are identical for the and directivity calculations, the calculation for the acoustic pressure proceeds somewhat differently. The objective now is to obtain the representation for the pressure.

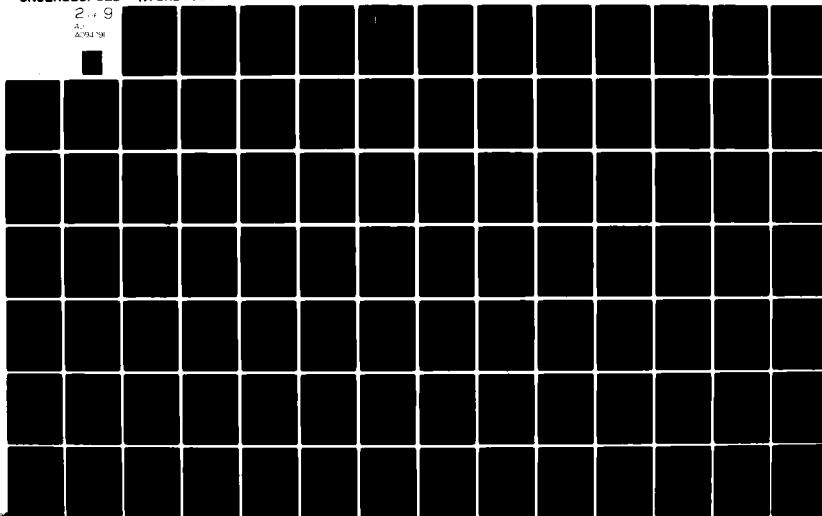
AD-A094 291

GENERAL ELECTRIC CO CINCINNATI OH AIRCRAFT ENGINE GROUP F/G 20/1
HIGH VELOCITY JET NOISE SOURCE LOCATION AND REDUCTION. TASK 2. --ETC(U)
MAY 78 T F Balsa, P R GLIEBE, R A KANTOLA DOT-05-30034
R78AE6323 FAA-RD-76-79-2 NL

UNCLASSIFIED

2-49

AD-A094 291



In the outer field, from equation (39a), the velocity potential is expressible as

$$\phi^{(o)} = \sum_{n=0}^{\infty} (A_n \cos n\theta + B_n \sin n\theta) H_n^{(1)}(k_o K_1 r) \quad (58)$$

where the A_n 's and B_n 's are defined by equation (39). The pressure in the acoustic far field is simply proportional to the time derivative of the velocity potential so that using equation (55) the following expression results:

$$p = \frac{-i\rho_1}{4\pi^2 c_2^2} \int_{-\infty}^{\infty} e^{isx} ds e^{-it(\omega_o + U_c s)} (\omega_o + U_c s) \times \sum_{n=0}^{\infty} (A_n \cos n\theta + B_n \sin n\theta) H_n^{(1)}(k_o K_1 r) \quad (59)$$

For the calculation of power, an integral of the type in equation (59) was evaluated numerically; for the directivity, this integral may be evaluated by the method of stationary phase. The entire procedure is given by Carrier, Krook, and Pearson⁽³¹⁾, with the final result:

$$p = - \frac{\rho_1 \omega_o}{2\pi^2 c_2^2} \frac{e^{-i\omega_o(t - R/c_1)}}{R(1 - M_c \cos\theta)^2} \times \sum_{n=0}^{\infty} (A_n \cos n\theta + B_n \sin n\theta) \Big|_{\sigma=\sigma_*} \quad (60a)$$

where σ_* is the point of stationary phase given by

$$\sigma_* = \frac{\cos\theta}{1 - M_c \cos\theta} \quad (60b)$$

Very loosely speaking, R is the distance from the jet and θ is the angle with respect to the jet axis. The final expression for the pressure is valid as $R \rightarrow \infty$.

One can make a number of observations with respect to equation (60a). First, the acoustic pressure decays as R^{-1} in the far field; the phase difference between the source and the observed signal is simply the travel time

R/c_1 , and a convecting mass source has an explicit convective amplification factor of $(1 - M_c \cos \theta)^{-2}$. Additional (implicit) convective amplification is present in coefficients A_n and B_n because of fluid shielding.

4.2.1.2.5 Directivity of a Slot Jet

First it should be emphasized that the directivity of a slot jet involves two angles; one is the familiar angle to the jet axis θ , the other is the azimuthal angle ϕ . To obtain the pressure field of a convecting source in an elliptic or slot jet, expressions (56) are used in the definitions of A_n and B_n along with the correspondence principle, of

A major difference between quadrupole and simple point sources is that quadrupoles have a higher explicit convective amplification factor. In the following discussion, the ratio (or the difference on a logarithmic scale) of the far-field pressures at two different values of azimuthal angles (ϕ) is shown as a function of the angle to the jet axis (θ). The effect of the explicit convective amplification cancels by taking this ratio so that it does not matter whether the pressure for sources or quadrupoles are used in the theory data comparisons. It is possible that quadrupoles themselves have an intrinsic azimuthal directivity; this is the case for an isolated quadrupole but is not likely the case for an "equivalent" quadrupole that represents the noise of an elliptic or slot jet.

The experimental data of Olsen, et al. (18) for the sound pressure level (SPL) of slot jets were reduced at constant source Strouhal number; the length scale used in the definition of the Strouhal number is the major diameter of the jet. The observed frequency is denoted by f . In Figure 4-9, the difference in sound pressure levels* between the noisy (vertical) and quiet (horizontal) planes is shown as a function of angle to jet axis at three values of source Strouhal number. The largest difference occurs at $\theta = 30^\circ$ to 50° ; this difference increases with frequency and is completely negligible at 90° to the jet axis.

The trend with velocity is shown in Figure 4-10. The maximum Δ SPL increases with jet velocity; however, at the lower jet velocity there is some disagreement between theory and experiment, at least with respect to the absolute levels. However, the insensitivity of the noise difference as a function of the angle to jet axis is reproduced well.

The effect of jet temperature at constant source Strouhal number and jet velocity is shown in Figure 4-11. The maximum value of Δ SPL increases with jet temperature, consistent with Mani's findings on acoustic shielding of round jets.

Two remarks are in order to explain why the agreement between theory and experiment cannot be more than qualitative. First, the data show considerable scatter; obviously this is because the differences in noise (on

* For the theoretical calculations, the sound pressure is defined as $10 \log_{10} |p|^2$ where p is given by equation (60a)

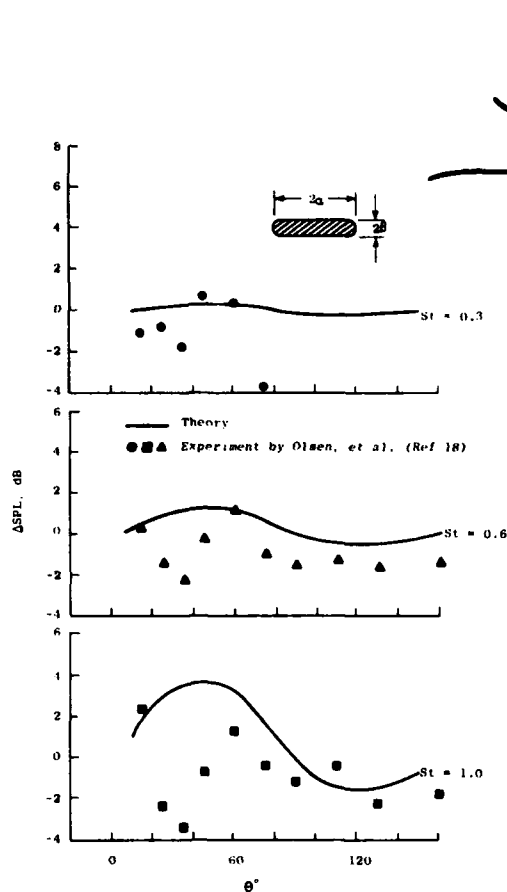


Figure 4-9. Δ SPL Between Quiet and Noisy Planes for Cold Jet [$\alpha/\beta = 9$, $M = 0.55$, ($M_c = 0.65M$), $St = 2fa(1 - M_c \cos \theta)/U$]. Peak St at $\theta = 90^\circ$ is 3.5.

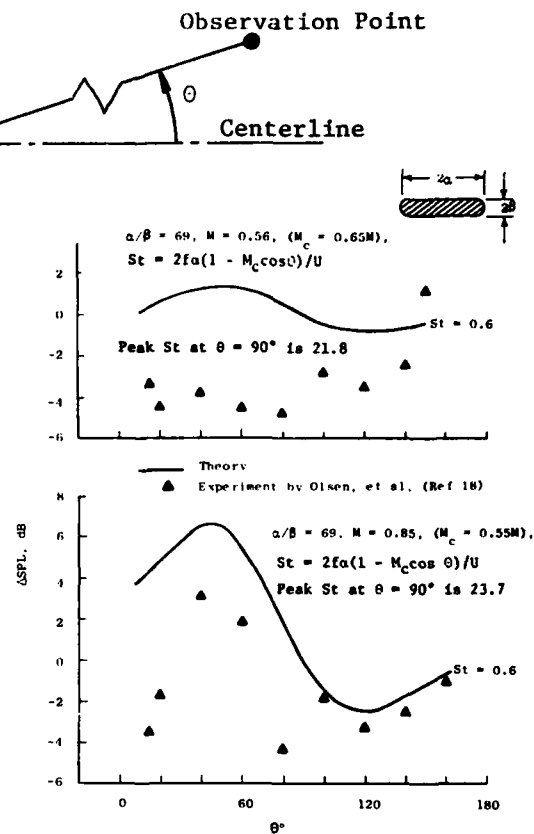


Figure 4-10. Δ SPL Between Quiet and Noisy Planes for Cold Jet.

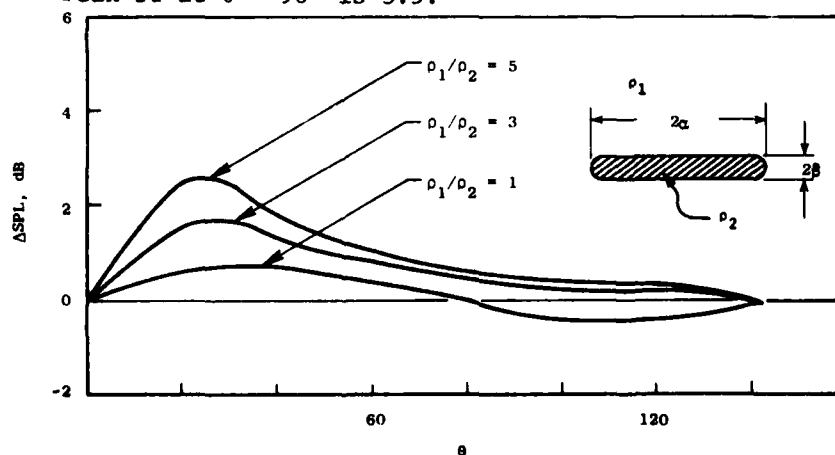


Figure 4-11. Δ SPL Between Quiet and Noisy Planes for Hot Jet [$\alpha/\beta = 5$, $M = 0.7$ ($M_c = 0.65M$) $St = 2fa(1 - M_c \cos \theta)/U = 0.3$].

the order of 2 to 4 dB) are comparable to the errors in the measurement (probably on the order of 1 dB). Second, the analysis is only approximate.

4.2.1.2.6 Conclusions

It is shown that, in the low frequency limit, the inner and outer solutions obey the Poisson and Helmholtz equations, respectively. The appropriate inner length scale is the jet diameter and the outer length scale is the wavelength. The outer solution, to order $(\epsilon/2)^2$ where $\epsilon = \omega_0 a/c_1$, depends only on the lowest order inner and jet solutions. The error in the outer field is of order $(\epsilon^3 \log \epsilon)$.

The asymptotic results for the circular jet indicate that the present theory is accurate to values of ϵ up to 0.7 or 0.8. The nonuniformity of the expansion associated with the limit $M \rightarrow 1$ (ϵ fixed) can be eliminated, for the most part, by expressing the coefficient of the axially symmetric part of the far field as a fraction. As $\epsilon \rightarrow 0$, the power of the jet becomes independent of jet shape. This conclusion appears plausible since in this limit all jets appear in the far field as "thin line." The results for the elliptic jet offer one qualitative explanation for the presence and location of certain experimentally observed quiet planes. This explanation is purely acoustic and centers around the shrouding effect of the mean flow.

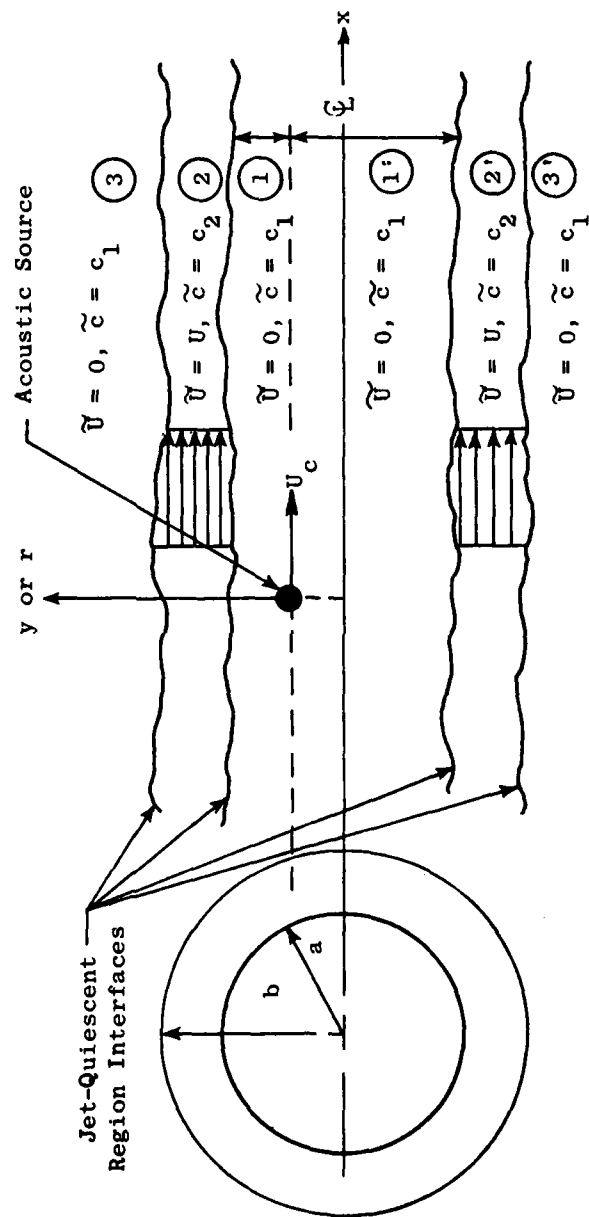
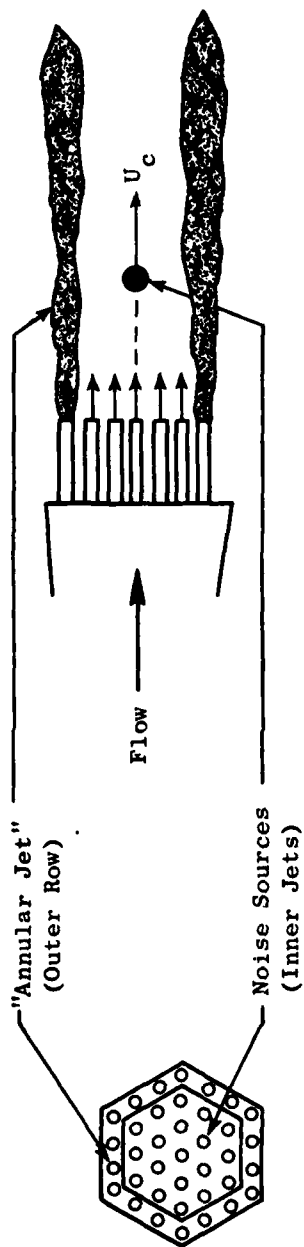
4.2.2 Convecting Sources in an Annular Jet

The radiation from a convecting monopole source shielded by an annular, doubly infinite jet of fluid is calculated in this section. The jet velocity is idealized by a constant profile (i.e., slug flow) and the source is of a single frequency in its own moving frame. The results of this model problem are used to throw some light on the jet shielding hypothesis for multitube suppressors and to rationalize one empirical expression for the effective number of radiating tubes. The theoretical predictions for the pressure are compared to experimental data under Acoustic Shielding Experiments (Section 6.0).

4.2.2.1 The Radiated Power

4.2.2.1.1 Introduction

A typical suppressor nozzle of the multitube type is shown in Figure 4-12. This suppressor is generally an array of "small" jets of diameter d separated by a distance L . This array is usually two-dimensional; the basic idea is to divide the exhaust of an engine into a number of smaller jets. Near the exit plane of these jets (assume coplanar exits), where the high frequency noise is generated, the aerodynamic interaction between adjacent jets is small if $L/d \gg 1$. Thus, the high frequency power radiated by the



$U = \text{Constant}, c_1 = \text{Constant}, c_2 = \text{Constant}$

$\bar{U} = \text{Jet Velocity}, \tilde{c} = \text{Speed of Sound}$

Figure 4-12. The Geometry of the Jet.

suppressor should be given by the product of the power of a single jet and the number of jets. It is found experimentally that the actual radiated power is considerably smaller than this product (Gray, et al)⁽³²⁾.

The physical model used here separates the array of jets into two classes: (1) the outer row (usually a circular row) of jets and (2) the inner jets. In the mathematical model, the outer row of jets is represented by an annular jet with a slug velocity and temperature profile (Figure 4-12). The inner jets are represented by convecting sources; these sources are simple mass sources. Generalization to higher order sources can be made. It is known that the "source" of jet noise is of the quadrupole type - the choice of a mass source is motivated by simplicity, with the expectation that the results of this theory will provide the qualitative features of the actual acoustic field.

The purpose is to derive the expression for the far-field radiated power of a convecting source surrounded by an annular jet and to show the dependence of this power on various parameters. Finally, a comparison is made between theoretical and experimental results. This comparison shows that the high frequency power reduction in multitube suppressors can be explained by acoustic - mean flow interaction.

4.2.2.1.2 Formulation of the Problem

It is assumed that the acoustic field obeys the linear wave equation

$$\left(\frac{\partial}{\partial t} + \tilde{U} \frac{\partial}{\partial x}\right)^2 \phi - \tilde{c}^2 \phi_{xx} - \tilde{c}^2 \Delta \phi = \mathcal{D} \quad (61)$$

where ϕ is the perturbation velocity potential, \mathcal{D} is the disturbance that generates the acoustic field, t is time, and x is an axial coordinate along which the fluid velocity is $(U + \phi_x)$.

The undisturbed speed of sound and the undisturbed fluid velocity in the x direction are given by \tilde{c} and \tilde{U} respectively. The geometry of the problem and the variation of \tilde{U} and \tilde{c} with respect to the transverse variable (y in the planar case or r in the axially symmetric case) are shown in Figure 4-12. The operator Δ represents the Laplacian in the transverse variable.

There remains to model the source term \mathcal{D} . Here guidance is provided by the simplicity and the success of the approach of Mani⁽¹⁷⁾, who assumed that

$$\mathcal{D} = e^{-i\omega_0 t} \delta(x - Ut) \delta(\tilde{P}) \quad i = \sqrt{-1} \quad (62)$$

where ω_0 is a given constant and $\delta(\tilde{P})$ is a symbolic representation of the δ -distribution whose support is the point \tilde{P} . It is also assumed that the source is in region ① or ①'.

The solution to equation (61) represents the acoustic field of a convecting point mass source whose strength oscillates at frequency ω_0 in the reference frame that moves with the source. The source is surrounded by an idealized jet system whose velocity and temperature (essentially c_2) are represented by constant (i.e., slug) profiles. The assumption that the source convection speed is the same as the jet speed is made for simplicity (i.e., $U_c = U$). This restriction will be relaxed later. The primary interest is in the power radiated in the far field, the dependence of this power on the jet velocity and thickness and on the location of the source.

Across the jet-quiet region interfaces the continuity of the perturbation pressure, p , and the particle displacement η are required. The expression for the perturbation pressure is easily derivable from the x-momentum equation, and is given by

$$p = -\bar{\rho} (\phi_t + \tilde{U} \phi_x) \quad (63)$$

where $\bar{\rho}$ is the undisturbed density. Under the additional assumption that the undisturbed static pressure is also continuous across the interface, $\bar{\rho}$ and \tilde{c} cannot be specified independently.

The particle displacement η is related to the transverse velocity component through the equation

$$\frac{\partial \eta}{\partial t} + \tilde{U} \frac{\partial \eta}{\partial x} = \frac{\partial \phi}{\partial y} \quad \text{or} \quad \frac{\partial \phi}{\partial r} \quad (64)$$

The interface conditions (63) and (64) are satisfied on the surfaces $y = \pm a$, $y = \pm b$ (or $r = a$, $r = b$), that is, on the mean location of the interface, consistent with the linearization assumption already invoked in implying that equation (61) holds. Equation (64) implies that there is negligible mixing between the jet and the surrounding medium, that is, the interface consists of particles of fixed identity.

The governing equation (61) is hyperbolic and it requires initial conditions for uniqueness. These can readily be provided (for example, $\phi = \partial \phi / \partial t = 0$ at $t = 0$). In the present context, however, the interest is in the long time solution as $t \rightarrow \infty$. That is, the "periodic" solution that results after all the transients associated with the starting of the source (at $t = 0$) have become negligibly small is desired. The time dependence in equation (61) is extracted through Fourier transforms, as follows:

Defining

$$\phi^* = \frac{1}{\sqrt{2\pi}} \int_{-\infty}^{\infty} e^{i\omega t} \phi \, dt \quad (65a)$$

and

$$\phi = \frac{1}{\sqrt{2\pi}} \int_{-\infty}^{\infty} e^{-i\omega t} \phi^* \, d\omega \quad (65b)$$

(101)

and
$$\phi^* = \overline{\phi^*} e^{i(\omega - \omega_0)x/U} \quad (65c)$$

so that $\overline{\phi^*} = \overline{\phi^*}(y \text{ or } r; \omega)$. The form of the x-dependence in (65c) can be obtained by a Fourier transform in x or by observing that (65c) is consistent with the time transform of equation (61) and all boundary conditions. The resultant equation for $\overline{\phi^*}$ is given in the still-air region ($\tilde{U} = 0$) by

$$\Delta \overline{\phi^*} + k_0^2 (K_1^+)^2 \overline{\phi^*} = - \frac{\delta(\tilde{P})}{c_1^2 \sqrt{2\pi} U} \quad (66a)$$

and in the jet region ($\tilde{U} = U$) by

$$\Delta \overline{\phi^*} + k_0^2 (K_2^+)^2 \overline{\phi^*} = 0 \quad (66b)$$

or

$$\Delta \overline{\phi^*} - k_0^2 (K_2^-)^2 \overline{\phi^*} = 0 \quad (66c)$$

where $k_0 = \omega_0/c_1$.

The propagation constants K_1^+ , K_2^+ and K_2^- are given by

$$(K_1^+)^2 = [\kappa^2 - (\kappa - 1)^2/M^2] \quad (67a)$$

$$(K_2^+)^2 = \Gamma_{12} \rho_{21} - (\kappa - 1)^2/M^2 \quad (67b)$$

$$(K_2^-)^2 = (\kappa - 1)^2/M^2 - \Gamma_{12} \rho_{21} \quad (67c)$$

where $\kappa = \omega/\omega_0$, $M = U/c_1$, $\rho_{21} = \rho_2/\rho_1$ and $\Gamma_{12} = \Gamma_1/\Gamma_2$ where

$$\Gamma = (1 - R/C_p)^{-1} \quad (67d)$$

The gas constant is denoted by R and C_p is the constant pressure specific heat. An additional assumption in deriving (67b and c) is that the gas is thermally perfect. The interest is only in the case when $(K_1^+)^2 \geq 0$ (otherwise the far-field solution dies off exponentially in the transverse variable), that is $1/(1+M) \leq \kappa \leq 1/(1-M)$. When $(K_2^+)^2 \geq 0$, that is

$1/(1 + M) \leq \kappa \leq 1 + M\sqrt{\Gamma_{12} \rho_{21}}$, equation (66b) is used; otherwise (66c) applies. Of course, (66b and 66c) are really identical - the distinction is artificial and is made only to enable one to take the positive square root of K_2^{\pm} in writing down the solution explicitly.

To complete the formulation of the problem, a Fourier transform of the matching conditions for the interface is performed. In the still-air region, the transforms of equation (63) and (64) are

$$\overline{p^*} = i \rho_1 \omega \overline{\phi^*} \quad (68a)$$

$$\overline{\eta^*} = \frac{i}{\omega} \frac{\partial \overline{\phi^*}}{\partial n} \quad (68b)$$

and in the jet regions,

$$\overline{p^*} = i \rho_2 \omega_0 \overline{\phi^*} \quad (68c)$$

$$\overline{\eta^*} = \frac{i}{\omega_0} \frac{\partial \overline{\phi^*}}{\partial n} \quad (68d)$$

where $\partial/\partial n$ denotes normal differentiation to the interface in the transverse plane.

Thus the canonical problem to be solved is equation (66) with matching conditions (68) across all interfaces.

4.2.2.1.3 The Planar Problem

Consider a convecting line source with instantaneous coordinates at (Ut, y_0) where $y_0 = \text{const} < a$. Let this source be surrounded by two plane jets whose boundaries are given by $y = \pm a$ and $y = \pm b$ ($b \geq a$) (see Figure 4-12). The objective is to determine the effect of the fluid jets on the power radiated by the source, and to examine the sensitivity of the power on the precise location of the source (i.e., on y_0).

In some applications, a source of noise (not necessarily a point mass source) is surrounded by a real jet. One such configuration was investigated experimentally by Cowan and Crouch⁽³³⁾ in connection with sound transmission through a two-dimensional shielding jet. Another application is encountered in jet noise suppressors where the outer row of jets surround the inner rows. In our idealized model, the inner rows are treated as noise sources and the outer row as the shielding jet. Of course, in a suppressor the "shielding jet" is not planar but circular. It is quite difficult to solve the problem for the circular geometry when the noise sources are off the axis, since the flow field is axially nonsymmetric. To shed some light on the power radiated by off axis sources, the easier planar problem is considered. Note that at very high frequencies the difference between the circular and planar solutions is small.

In this section, y is used to denote the transverse variable and $\delta(P) = \delta(y - y_0)$ with $y_0 = a\sigma$, $0 \leq \sigma \leq 1$. It is assumed that $\Gamma_{12} = 1$ and $\rho_{21} = 1$, that is the jet is cold ($c_1 = c_2 = c$) and has the same isentropic index as the ambient medium. The solutions to equations (66) are written down as a linear combination of exponentials with unknown coefficients. These coefficients are determined by enforcing matching conditions (68) across all the interfaces. For example, outside the jet,

$$\overline{\phi^*} = E \exp(ik_0 K_1^+ y) \quad y > b \quad (69a)$$

$$\overline{\phi^*} = \tilde{E} \exp(-ik_0 K_1^+ y) \quad y < -b \quad (69b)$$

where E and \tilde{E} are independent of y and (69a and 69b) satisfy the radiation condition as $|y| \rightarrow \infty$. The final results for E and \tilde{E} are

$$\begin{bmatrix} E \\ \tilde{E} \end{bmatrix} = \begin{bmatrix} \alpha_2 \\ \alpha_1 \end{bmatrix} \times \frac{1}{c^2 \sqrt{2\pi} k_0 K_1^+ \Delta^*} \quad (70a)$$

where $c = c_1 = c_2$ and

$$\Delta^* = -2 \left[-\beta \sin(ak_0 K_1^+) + \alpha \cos(ak_0 K_1^+) \right] \left[\beta \cos(ak_0 K_1^+) + \alpha \sin(ak_0 K_1^+) \right] \quad (70b)$$

$$\begin{bmatrix} \alpha_1 \\ \alpha_2 \end{bmatrix} = \begin{bmatrix} -\beta \sin[ak_0 K_1^+(1 + \sigma)] + \alpha \cos[ak_0 K_1^+(1 + \sigma)] \\ -\beta \sin[ak_0 K_1^+(1 - \sigma)] + \alpha \cos[ak_0 K_1^+(1 - \sigma)] \end{bmatrix} \quad (70c)$$

with

$$\alpha = e^{ik_0 b K_1^+} \left[\cos[k_0 K_2^+(b - a)] - i \frac{1}{\kappa^2} \frac{K_1^+}{K_2^+} \sin[k_0 K_2^+(b - a)] \right] \quad (71a)$$

and

$$\beta = i e^{ik_0 b K_1^+} \left[\cos[k_0 K_2^+(b - a)] - i \kappa^2 \frac{K_2^+}{K_1^+} \sin[k_0 K_2^+(b - a)] \right] \quad (71b)$$

Equations (71) are valid when $1/(1+M) \leq \kappa \leq (1+M)$, that is when the disturbance propagates through the jets with little "attenuation." However, when $(1+M) \leq \kappa \leq 1/(1-M)$, K_2^+ is replaced by $-i K_2^-$. In the latter case, the disturbance is "attenuated" considerably [since $(\cos, \sin) \rightarrow (\cosh, \sinh)$]. This region of attenuation corresponds to the classical zone of silence; see, for example, Morse and Ingard⁽²⁵⁾. The perturbation pressure and transverse velocity in the far field are obtained by inverting the Fourier time transform (65b) and adjoining the exponential x behavior (65c).

The total power, P , radiated by the source, as computed by integrating $(p \phi_y)$ around a surface $|y| = \text{const} \rightarrow \infty$, is given by

$$P = P' + \tilde{P}' \quad (72a)$$

where

$$\left. \begin{array}{l} P' \\ \tilde{P}' \end{array} \right\} = \int_{1/(1+M)}^{1/(1-M)} \frac{\rho k_0^3}{2\pi c^2 U} \frac{|E'|^2}{|\tilde{E}'|^2} \frac{K_1^+}{K_1^-} \kappa d\kappa \quad (72b)$$

and

$$\left. \begin{array}{l} E' \\ \tilde{E}' \end{array} \right\} = c^2 \sqrt{2\pi} U \left. \begin{array}{l} E \\ \tilde{E} \end{array} \right\}$$

with $\rho_1 = \rho_2 = \rho$. Physically, P' represents the radiated power in the upper region ($y > 0$) and \tilde{P}' in the lower ($y < 0$). When $y_0 \neq 0$, that is when the flow field is not symmetric with respect to y , $P' \neq \tilde{P}'$. The mathematical details entering in the derivation of equation (72b) are discussed by Morse and Ingard⁽²⁵⁾.

The following limiting cases of the general solution can be observed:

As $b \rightarrow a$

$$|E'|^2 = |\tilde{E}'|^2 = |\tilde{E}_0'|^2 = \frac{1}{4k_0^2 (K_1^+)^2} \quad (73a)$$

and

$$P = P_0 = \frac{\rho k_0}{4\pi c^2 U} \int_{1/(1+M)}^{1/(1-M)} \frac{\kappa d\kappa}{K_1^+} \quad (73b)$$

or

$$P_0 = \frac{\rho k_0}{4c^3} \frac{1}{(1-M^2)^{3/2}} \quad (73c)$$

Equation (73c) gives the power radiated by a moving source in the absence of the shielding jets.

The limit $M \rightarrow 0$ ($U \rightarrow 0$, c fixed) is considerably more difficult to obtain because the solution becomes unbounded [see equation (66a)]. To circumvent this difficulty, a variable ξ is introduced,

$$\xi = \frac{\kappa - 1}{M} \quad (74a)$$

and K_1^+ and K_2^+ are rewritten in terms of ξ . The result is

$$K_1^+ = \sqrt{(1 + M\xi)^2 - \xi^2} \quad , \quad -\frac{1}{1+M} \leq \xi \leq \frac{1}{1-M} \quad (74b)$$

and

$$K_2^+ = \sqrt{1 - \xi^2} \quad (74c)$$

As $M \rightarrow 0$, $-1 \leq \xi \leq 1$ and

$$K_1^+ \approx \sqrt{1 - \xi^2} = K_2^+ \quad (74d)$$

The range of κ for which K_2^- applies has shrunk to zero.

Also, $\kappa = 1 + M\xi \approx 1$. Thus

$$|E'|^2 = |\tilde{E}'|^2 = \frac{1}{4 k_0^2 (1 - \xi^2)} \quad (75a)$$

$$p^* = \frac{\rho k_0}{4c^3} \quad (75b)$$

so that equation (75b) represents the power radiated by a stationary source in the absence of jet shielding. Both equations (73c) and (75b) can be obtained by other methods.

4.2.2.1.4 The Axially Symmetric Problem

As stated previously, the purpose here is to provide some theoretical information on the noise radiated by jet noise suppressors. In the model, the inner jets of the suppressor are represented by convecting acoustic sources and the outer most row of jets by an annular plug flow jet. The results of the analysis for the planar geometry showed that the total radiated power is not very sensitive to the precise location of the source (see Figure 4-13). This is interpreted to mean that, even for the circular geometry, the

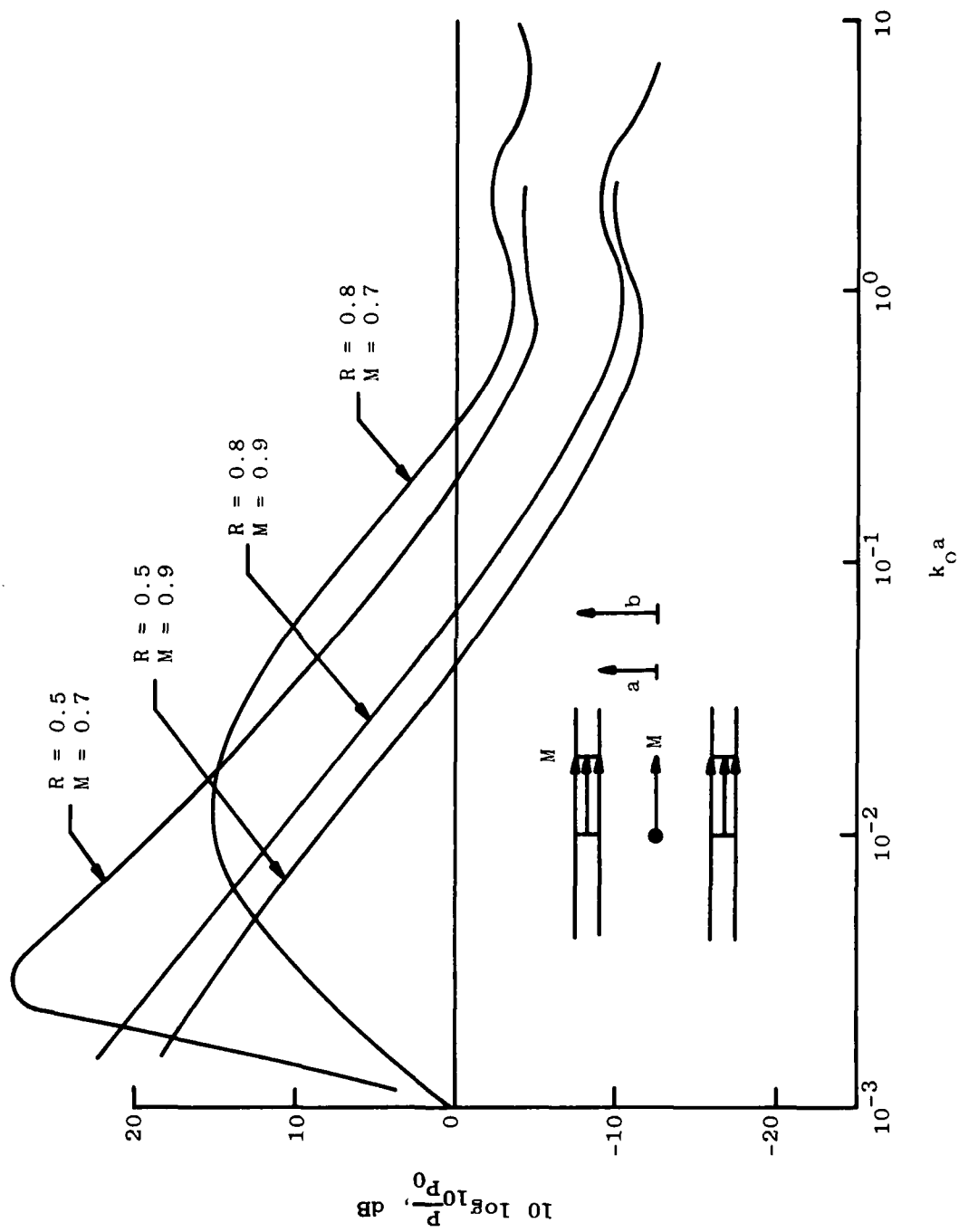


Figure 4-13. Total Radiated Power as a Function of Source Frequency, Planar Case and Cold Jet ($R = a/b$).

individual noise sources (i.e., the inner jets) may be lumped into an effective source and placed on the axis of the annular jet.

Thus, the idealized problem that is solved is shown again in Figure 4-12. A convecting acoustic source (on the axis) is surrounded by an annular jet, and it is desired to examine the effect of the annular jet on the radiated power.

Let r denote the transverse variable, and let $\delta(\vec{P}) = \delta(r)/(2\pi r)$. Since the flow field is axially symmetric, consider regions ①, ②, and ③ only. The solution to equations (66) in region ③ is

$$\overline{\varphi} = D H_0^{(1)}(k_0 K_1^+ r) \quad r > b \quad (76)$$

where D is a constant and $H_0^{(1)}$ is a Hankel function. The analysis parallels quite closely that of the previous section except that trigonometric and exponential functions (of real arguments) are replaced by corresponding Bessel functions. The details are omitted herein, but the final results are

$$D = \frac{1}{4\sqrt{2\pi} U c_1^2} D' \quad (77a)$$

where

$$D' = \frac{W(k_0 a K_1^+)}{\beta J_0(k_0 a K_1^+) - \alpha J_0'(k_0 a K_1^+)} \quad (77b)$$

and

$$\alpha = H_0^{(1)}(k_0 b K_1^+) \frac{W(k_0 a K_2^+, k_0 b K_2^+)}{W(k_0 b K_2^+)} - \frac{\rho_{21}}{\kappa^2} \frac{K_1^+}{K_2^+} H_0^{(1)'}(k_0 b K_1^+) \frac{L(k_0 a K_2^+, k_0 b K_2^+)}{W(k_0 b K_2^+)} \quad (77c)$$

$$\beta = H_0^{(1)'}(k_0 b k_1^+) \frac{W(k_0 b k_2^+, k_0 a k_2^+)}{W(k_0 b k_2^+)} + \frac{\kappa^2}{\rho_{21}} \frac{k_2^+}{k_1^+} H_0^{(1)}(k_0 b k_1^+) \frac{L'(k_0 a k_2^+, k_0 b k_2^+)}{W(k_0 b k_2^+)} \quad (77d)$$

The various cross products of the Bessel functions are defined by

$$W(Z, \zeta) = J_0(Z)Y_0'(\zeta) - J_0'(\zeta)Y_0(Z) \quad (78a)$$

$$I(Z, \zeta) = J_0(Z)Y_0(\zeta) - J_0(\zeta)Y_0(Z) \quad (78b)$$

$$L'(Z, \zeta) = J_0'(Z)Y_0'(\zeta) - J_0'(\zeta)Y_0'(Z) \quad (78c)$$

and

$$W(Z) = W(Z, Z) \quad (78d)$$

Note that equations (77) and (78) hold when the disturbance is propagating through the jet with little attenuation, that is, when $1/(1+M) \leq \kappa \leq 1+M\sqrt{\Gamma_{12}\rho_{21}}$. When κ is outside this range, J_0 and Y_0 are replaced by I_0 and K_0 respectively, and K_2^+ by K_2^- . Note that J_0 , Y_0 , I_0 and K_0 are Bessel functions [Abramowitz and Stegun⁽³⁴⁾].

The total power radiated across a very large cylinder $r = \text{const} \rightarrow \infty$ is given by

$$P = \int_{1/(1+M)}^{1/(1-M)} \frac{\rho k_0^2}{8\pi c_1^2 U} |D'|^2 \kappa d\kappa \quad (79)$$

P is obtained by integrating $(p \phi_r)$ around a large cylinder surrounding the jet. The mathematical details are very similar to the planar case.

4.2.2.1.5 Discussion of Results

The theoretical results for the plane and circular geometries are shown in Figures 4-13, 4-14, and 4-15.

The total radiated power as a function of source frequency is shown in Figures 4-13 and 4-15. For small values of $(k_0 a)$, the jet-source configuration radiates more power than the corresponding freely moving source. This observation is consistent with the findings of Mani⁽¹⁷⁾ for a single round jet. On the other hand, for larger values of $k_0 a$, the jets provide considerable shielding in the sense that the total radiated power is reduced. It is observed that the power reduction varies directly with the jet Mach number and thickness.

Figure 4-14 shows that the location of the source has little effect on the total radiated power. One interprets this result to mean that the precise location of the source is irrelevant; what matters are the jet Mach number and thickness. Clearly, at low frequencies the radiated power is independent of the details of the jet as shown by Balsa⁽³⁵⁾. Thus, at low frequencies the location of the source is not important. This conclusion is borne out by the results of Figure 4-14. What is surprising is that even at higher frequencies the radiated power is relatively independent of source location. Similar results were also obtained by Mani⁽¹⁷⁾ for a plane (or slot) jet. Since the model has a highly-idealized shear layer built into it, one may state that even in (real) sheared flows the precise location of the source is not too important.

Although the presented results were obtained for cold annular jets (i.e., $\rho_1/\rho_2 = 1$, $c_1/c_2 = 1$), the general theory is applicable to hot jets as well. The limiting case of $\rho_1/\rho_2 \rightarrow \infty$ is easy to obtain analytically. The result is that the far-field radiated power is zero; thus the jets act as a vacuum shield around the disturbance. The power radiated by the source, which now is channeled down the inner cylinder $r = a$, is given by the waveguide solution for which $p = 0$ on $r = a$.

Using the above results, a possible explanation for some of the experimental results observed from suppressors is now proposed.

Consider an idealized model in which the radiated noise from a jet engine suppressor may be divided into two distinct spectra, one centered about a very high frequency, the other about a very low frequency. From dimensional reasoning, it is plausible that the high frequency noise is generated near the outlet of the suppressor tubes, whereas the low frequency noise comes from the region where the individual jets from the tubes have merged into a single large jet. In the usual engineering analysis on noise suppression, it is assumed that the high frequency power may be computed by multiplying the power of a single jet by a certain number, say, N_{eff} , called the effective number of tubes. It turns out that in all experimental configurations $N_{eff} < N_{total}$, where N_{total} is the total number of tubes in the suppressor bundle.

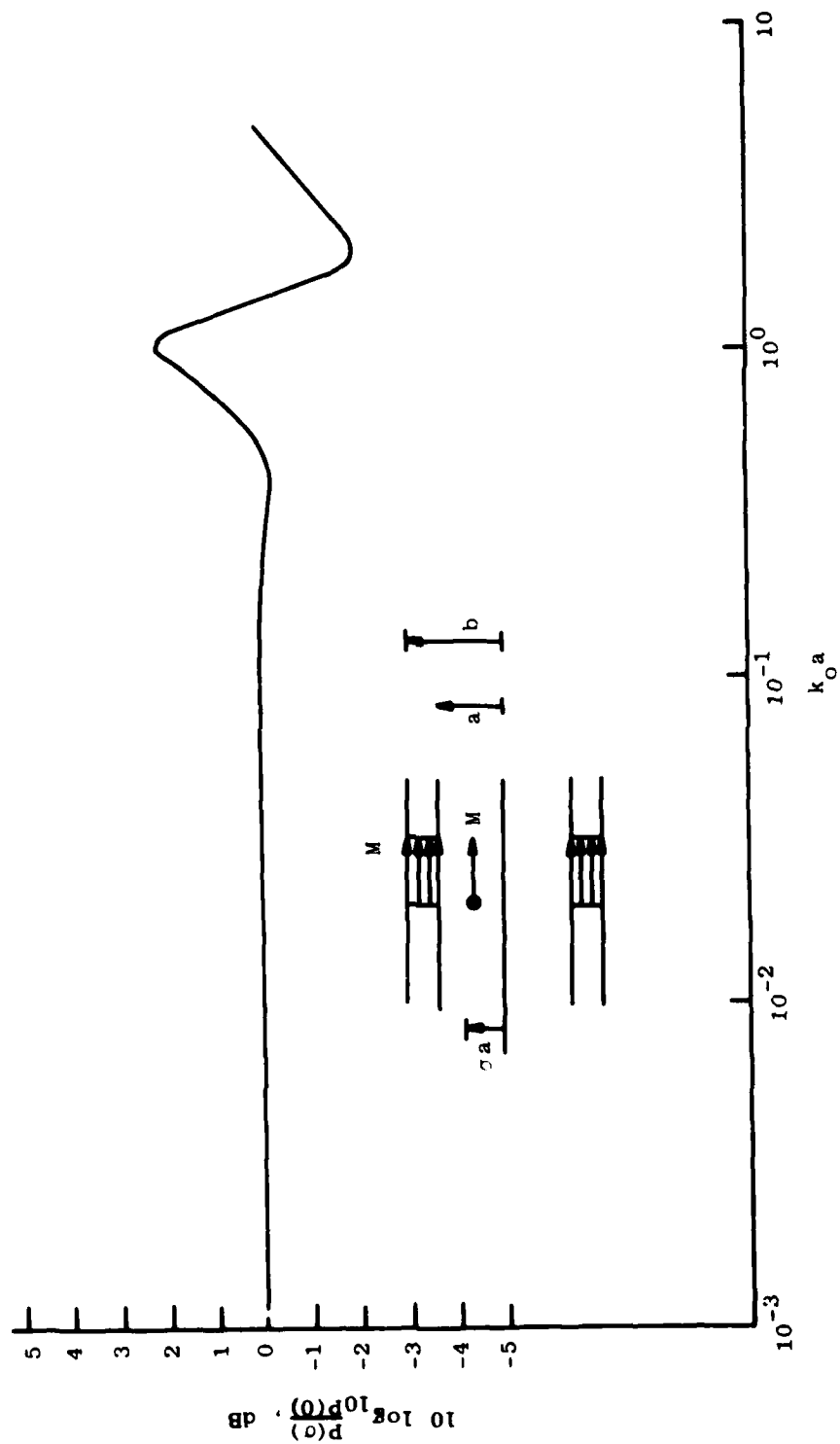


Figure 4-14. Radiated Power as a Function of Source Frequency
($R = a/b = 0.8$, $M = 0.9$, $\sigma = 0.5$).

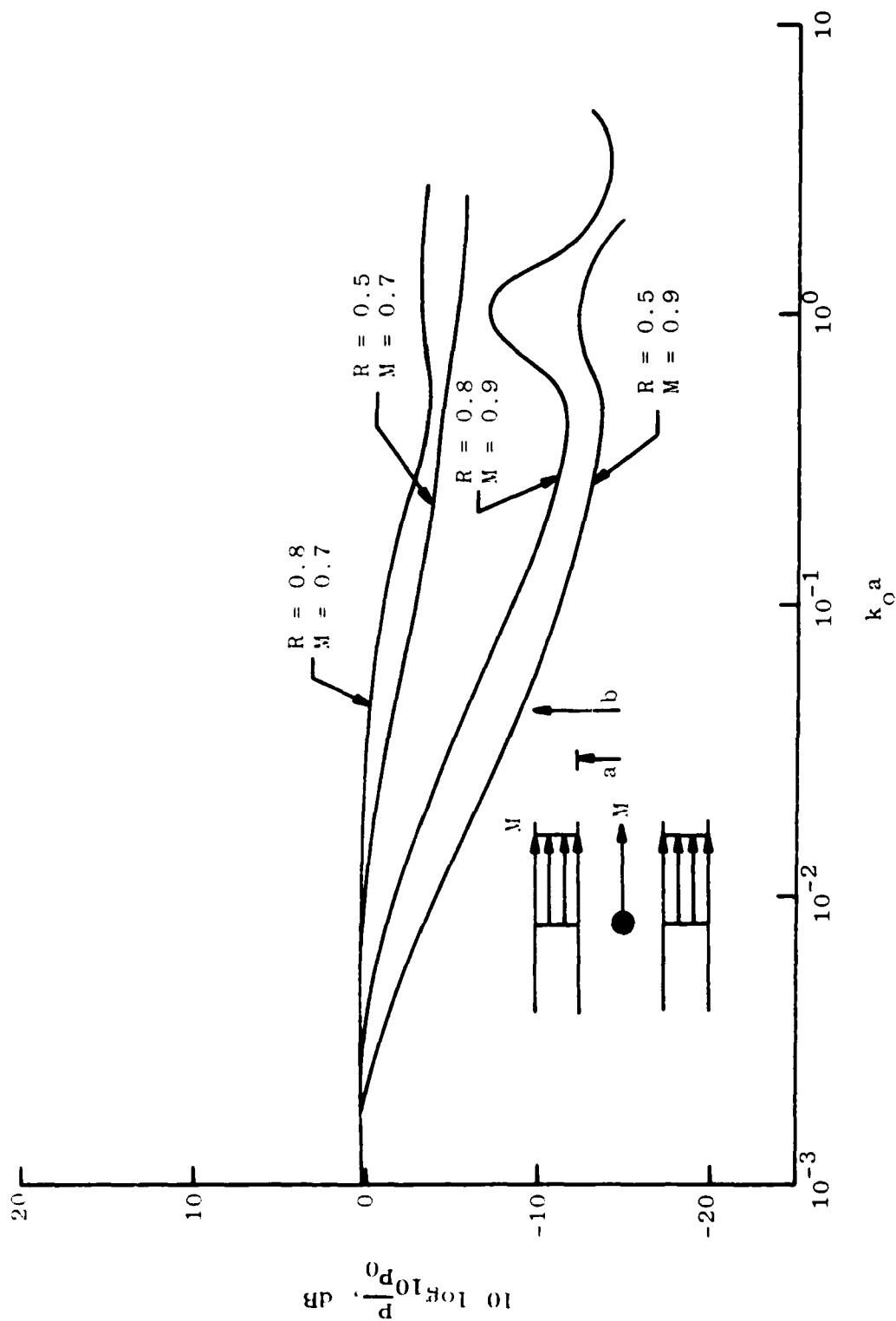


Figure 4-15. Total Radiated Power as a Function of Source Frequency, Circular Case and Cold Jet ($R = a/b$).

Several empirical expressions for N_{eff} have been proposed. One such expression, adapted by Motsinger(36) but originally due to Eldred, is plotted in Figure 4-16. This curve applies to "all" the high velocity multitube suppressor configurations that were studied by Motsinger. It is a very approximate correlation of existing multitube suppressor data.

Motsinger examined eighteen different suppressor configurations with the number of tubes varying from 37 to 253 and jet exhaust velocities in the range of 1800 fps and upwards. N_{eff} is the ratio of the acoustic power radiated by the suppressor to that radiated by a single contributing jet. The number of effective tubes, N_{eff} , was found to correlate quite well with the ratio of the inner to the total number of tubes, N_{inner}/N_{total} . Also N_{eff} was quite insensitive to the temperature and velocity of the exhaust.

Based on the theoretical calculations for the model problem, a simple explanation for N_{eff} is now proposed, assuming that the number of tubes in a given region is proportional to the area of the region. Thus, the quantity $\sqrt{N_{inner}/N_{total}}$ is interpreted as $R = a/b$. This assumption is valid only when the number of tubes in the tube bundle is very large. In this limit, by superposition, one finds that

$$\frac{N_{eff}}{N_{total}} = \frac{1}{2} \frac{N_{outer}}{N_{total}} + \eta \frac{N_{inner}}{N_{total}} \quad (81)$$

where η is the "radiation efficiency" of the inner tubes. Each outer tube is assumed to radiate 50% of the power of a single isolated jet. Here N_{outer} denotes the number of outer tubes.

The radiation efficiency of the inner tubes may be obtained from Figure 4-15. As an approximation, assume that the jet exhaust velocity is 1800 fps; the average merged jet velocity is about 1000 fps -- this average velocity is to be used in the present calculations because they are based on slug flow profiles. Thus $10 \log_{10} \eta$ is essentially the ordinate in Figure 4-15, $M \approx 0.9$ and $(N_{inner}/N_{total})^{1/2} = a/b = R$. The acoustic efficiency is to be obtained at large frequencies ($k_0 a \rightarrow \infty$) by averaging out the oscillations. The two theoretical points for $R = 0.5$ and 0.8 , calculated from equation (81) are also shown in Figure 4-16.

The point to be made is that the high frequency noise reduction for multitube suppressors does not come from aerodynamic interference (i.e., aerodynamic interaction between adjacent jets), since there is little interference at the exit plane of the jets (especially if the jets are far apart), where most of the high frequency noise is generated. Rather, the power reduction is a consequence of acoustic-mean flow interactions, estimated through this crude model.

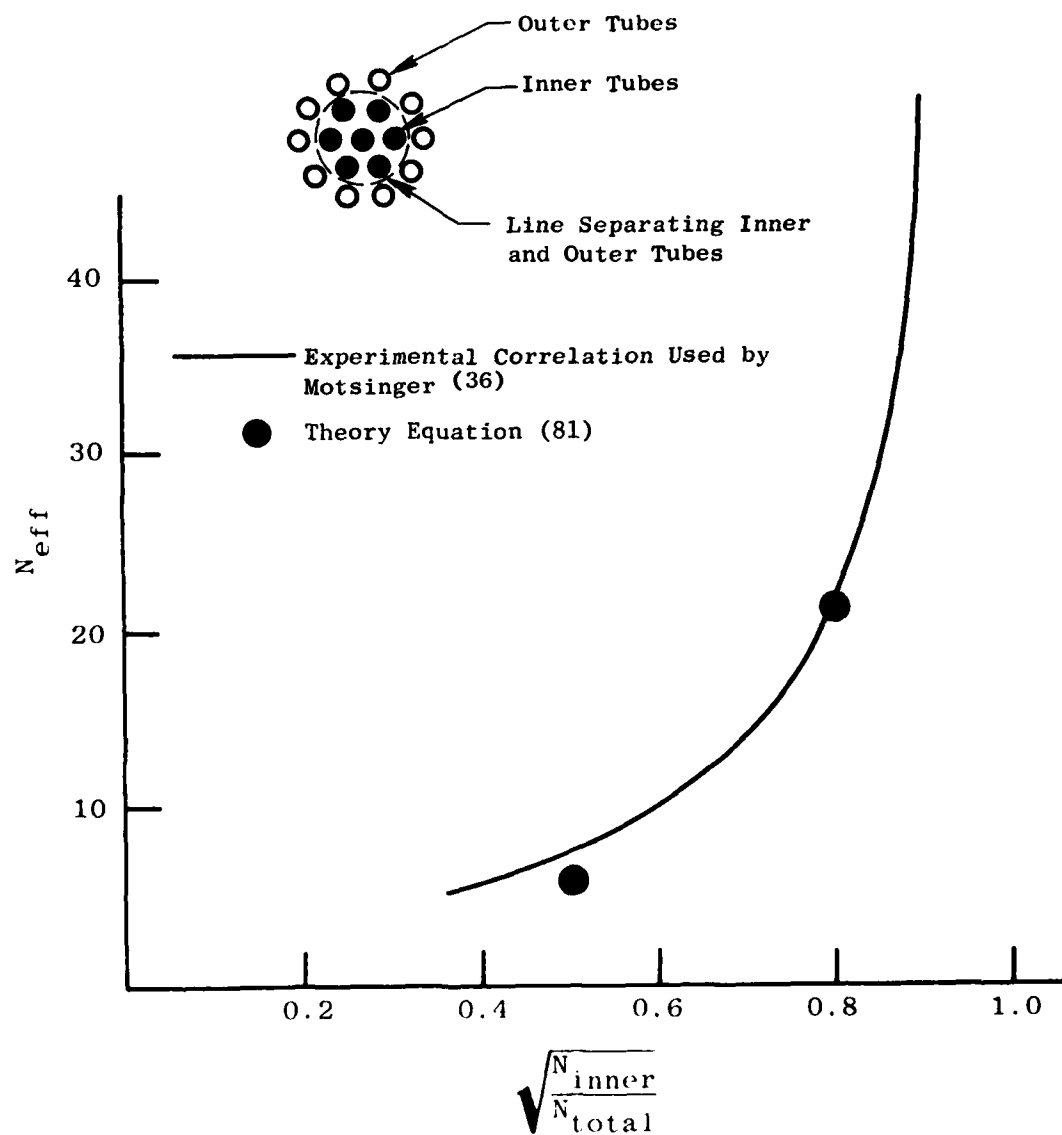


Figure 4-16. Effective Number of Tubes as a Function of Inner to Total Number of Tubes.

4.2.2.2 The Directivity of Sound

4.2.2.2.1 Introduction

The results for the power radiated by a convecting mass source surrounded by an annular jet were derived in the previous section. The purpose of this section is to sketch briefly how the expressions for the far-field pressure can be obtained for the same problem.

In jet noise measurements, one is usually interested in the spectra of the sound pressure level. In order to verify the properties of acoustic shielding in detail, an experiment was devised (see Section 6) which gave the dependence of "acoustic shielding" on jet velocity, jet temperature, annular jet thickness, frequency, and angle to the jet axis. The expressions to be derived in this section provide the same dependence; however, the actual theory-data comparisons are presented in Section 6.2.

It is emphasized that the solution of this problem, together with the experimental data, confirms the general effects of acoustic shielding derived by Mani(37,38) for circular jets. This confirmation establishes the importance of acoustic shielding in jet noise.

4.2.2.2.2 Formulation of the Problem

It is assumed that the velocity potential ϕ of the acoustic field obeys the linear equation

$$\begin{aligned} & \left(\frac{\partial}{\partial t} + \tilde{U} \frac{\partial}{\partial x} \right)^2 \phi - \tilde{c}^2 \phi_{xx} - \tilde{c}^2 \Delta \phi \\ & = \exp(-i\omega_0 t) \delta(x - U_c t) \delta(y) \delta(z) \end{aligned} \quad (82)$$

where \tilde{U} and \tilde{c} are sectionally constant. These denote the mean jet velocity and acoustic speed, respectively (see Figure 4-12). In this section, the geometry is restricted to that of an annular jet; (y, z) are coordinates in the transverse plane and the point mass source is convecting along the axis of the jet system with speed U_c . Note that in this part of the analysis the source convection speed may differ from the jet velocity. The source is oscillating at circular frequency ω_0 in its own reference frame. As before, Δ denotes the Laplacian in the transverse plane. The other variables are defined in the cited figure.

The simplest representation for the acoustic pressure is obtained by using Fourier transformation in the axial variable x . Defining

$$\bar{\phi} = \frac{1}{\sqrt{2\pi}} \int_{-\infty}^{\infty} e^{-isx} \phi \, dx \quad (83a)$$

whose inverse is

$$\phi = \frac{1}{\sqrt{2\pi}} \int_{-\infty}^{\infty} e^{isx} \bar{\phi} ds \quad (83b)$$

the transformation (83a) is applied to (82). The results are, after the introduction of a new dependent variable, Φ ,

$$\Phi = - (2\pi)^{3/2} c_1^2 \bar{\Phi} \exp [it(\omega_0 + U_c s)] \quad (84a)$$

$$\Delta \Phi + k_0^2 K_1^2 \Phi = \delta(r)/r \quad (84b)$$

and

$$\Delta \Phi + k_0^2 K_2^2 \Phi = 0 \quad (84c)$$

where $k_0 = \omega_0/c_1$. Note that s is a Fourier transform variable (essentially an axial wave number) and equation (84b) is valid in the quiescent regions ① and ③ whereas (84c) is valid in the annular jet, region ② (Figure 4-12). K_1 and K_2 are defined by

$$K_1^2 = (1 + M_c \sigma)^2 - \sigma^2 \quad (85a)$$

and

$$K_2^2 = \left(\frac{c_1}{c_2}\right)^2 [1 + (M_c - M)\sigma]^2 - \sigma^2 \quad (85b)$$

where $\sigma = s/k_0$, $M_c = U_c/c_1$ and $M = U/c_1$. The convective and jet acoustic Mach numbers are denoted by M_c and M , respectively. The variables K_1 and K_2 are the radial propagation constants in the quiescent and jet regions, respectively.

The Fourier x -transform of the interface conditions is straightforward. The matching conditions, to be satisfied on the mean location of the two interfaces, are

$$\kappa \phi_1 \text{ or } 3 = \frac{\rho_2}{\rho_1} \phi_2 \quad (86a)$$

$$\left(\frac{\partial \Phi}{\partial r}\right)_{1 \text{ or } 3} = \kappa \left(\frac{\partial \Phi}{\partial r}\right)_2 \quad (86b)$$

where

$$\kappa = \frac{1 + M_c \sigma}{1 + (M_c - M) \sigma} \quad (86c)$$

The subscripts 1 and 3 are to be used for the matching at $r = a$ and $r = b$, respectively, and refer to the solutions in the quiescent regions. Subscript 2 refers to the solution in the annular jet.

4.2.2.2.3 A Solution of the Problem

As for the elliptic jet [equation (14)], there is a complete correspondence between the equations for the directivity and those for the power provided that the following equivalence is made [equations (84), (86), and (66), (68)]:

Correspondence Principle

Power	→	Directivity
$(K_1^+)^2$		$K_1^2 = K_3^2$
$(K_2^+)^2$		K_2^2
κ		κ
$-c_1 (2\pi)^{3/2} U \phi^*$		ϕ

Thus the solution for the velocity potential is given by the results of Section 4.2.2.1.4, provided that the above correspondence principle is observed. More exactly,

$$\phi = \frac{\pi}{2} D' H_0^{(1)}(k_0 K_1 r) \quad (87)$$

where D' is given by equations (77b), and (87) is valid in region ③, and $H_0^{(1)}$ is the Hankel function. The pressure in the ambient region outside the jet is proportional to the time derivative of the velocity potential. Invoking the inverse Fourier transformation, the final result for the pressure p is

$$p = - \frac{i \rho_1}{8 \pi c_1^2} \int_{-\infty}^{\infty} D' H_0^{(1)}(k_0 K_1 r) (\omega_0 + U_c s) \times e^{-i \omega_0 t} e^{i s (x - U_c t)} ds \quad (88)$$

117

4.2.2.2.4 The Far-Field Directivity of the Source

In the far field, as $k_0 R \rightarrow \infty$, where R is the distance between the source and the observer, (88) can be evaluated by the method of stationary phase. This procedure is discussed by Carrier, Krook, and Pearson⁽³¹⁾. The Hankel function is expanded in its asymptotic form and then the stationary phase procedure is applied to obtain the final result for the pressure p :

$$p = - \frac{\omega_0 \sigma_1}{4\pi c_1^2} \frac{e^{-i\omega_0(t - R/c_1)}}{R(1 - M_c \cos\theta)^2} \quad (D')_\sigma = \sigma_* \quad (89a)$$

where

$$\sigma_* = \frac{\cos \theta}{1 - M_c \cos \theta} \quad (89b)$$

The point of stationary phase is denoted by σ_* and θ is the angle with respect to the jet axis. The coefficient D' is to be evaluated at the point of stationary phase.

4.2.2.2.5 Discussion

It can be observed that the far field decays as R^{-1} as $R \rightarrow \infty$, that the explicit convective amplification of a mass source is two powers of the Doppler factor $(1 - M_c \cos\theta)$, and that the phase difference between the source and observed signals is the travel time R/c_1 . The entire effect of acoustic shielding is contained in the coefficient D' . In the absence of annular jet, $D' = -i$ and p then agrees with the classical result for a convecting source in a quiescent medium. It should be observed from equation (77) that the coefficient D' depends on the thickness of the shielding jet (through $k_0 a$ and $k_0 b$), the density ratio $\rho_{21} = \rho_2/\rho_1$, the convective Mach number M_c , jet acoustic Mach number M , and the angle to the jet axis θ . This dependence will be shown explicitly under the theory-data comparisons of Section 6.2.

The most significant effect of shielding is at shallow angles to the jet axis, typically $\theta \leq 50^\circ$. This effect shows up as a greatly reduced sound pressure level in the far field. Note that convective amplification increases the pressure at shallow angles whereas acoustic shielding reduces it. However, convective amplification is frequency independent, whereas acoustic shielding is strongly frequency dependent. This feature of the model enables one to predict different directivities at different frequencies. In the presence of a shielding jet, the total convective amplification of the source is considerably different from the classical result. This is because propagation constants K_1 and K_2 also depend on $M_c \cos \theta$.

4.2.2.2.6 Conclusions

It has been shown that the power radiated by a convecting mass source depends on the environment in which the radiation takes place. For the specific geometry considered, the radiated power varies inversely with jet Mach number, jet thickness and source frequency. These results are consistent with Mani's⁽¹⁷⁾ findings for a different geometry. The radiated power of a given mass source is not a constant, and this points to the nonconservation of the Rayleigh acoustic energy density in sheared flows. This also holds for higher order singularities such as dipoles and quadrupoles, since these can be obtained from suitable superposition of simple sources.

It is believed that the exceptionally good agreement shown in Figure 4-16 is rather fortuitous. A two point theory data comparison is hardly an adequate basis for drawing substantial conclusions. It can be concluded though that this preliminary result lends credence to the idea that the noise power reduction observed at high frequencies in multitube suppressors is probably caused by acoustic mean flow interaction and is not due to interference effects.

4.2.3 Conventional Bypass Coaxial Jet Noise

In the previous two sections, the power and directivity of elliptic and annular jets were examined. The next step in complexity is to introduce an "inner" or "core" flow in the annular jet. This configuration simulates the jet plume of conventional bypass engines. The annular and round jet results will be limiting cases of this section for suitable outer-to-inner jet velocity ratios.

Two additional steps will be taken in this section. First, the acoustic field of convecting pressure quadrupoles (rather than simple mass sources) will be derived, and second, the strength of these quadrupoles will be predicted by an aerodynamic theory. This leads to a rational scheme for the prediction of the absolute directivity of coaxial jet noise. A brief sketch of the aerodynamic mixing calculation is given in Appendix A; a more detailed description is found in Sections 4.5 and 4.7.

4.2.3.1 Introduction

Considerable progress was made in the early 1970's in understanding the noise produced by hot and cold round jets. This progress was a direct result of careful and accurate jet noise measurements and of new theoretical developments. The theoretical effort focused on the important acoustic/mean flow interaction phenomenon.

It was desirable to extend this understanding to other nozzle configurations. The primary motivation was to develop a tool to study the parametric dependence of noise on nozzle shape. Such a tool would be indispensable in the search for a "quiet" nozzle. A secondary objective was to check the generality of the concepts developed for describing round-nozzle jet noise.

In this section, a model of the aeroacoustic characteristics of coplanar, coaxial nozzles is developed. This is the simplest extension of the round jet work. Considerable acoustic data exist for this geometry and comparisons of predictions with experiment are presented for a wide range of inner-to-outer stream velocity ratios and exhaust area ratios. The measured features of coaxial jet noise are predicted quite well.

4.2.3.2 General Remarks

The development of the present prediction method rests on two primary assumptions: (1) the dominant jet noise generation mechanism is the random momentum fluctuations of the small-scale turbulent structure in the mixing regions of the jet plume; and (2) the propagation of this noise to the far-field observer is significantly altered by the surrounding jet flow in which the turbulent eddies are embedded and convecting. The jet produces an intrinsic noise intensity spectrum, directly relatable to the statistical aerodynamic properties of the jet (i.e., mean velocity and density distributions, and local turbulent structure properties such as length-scale, intensity), which is modified by acoustic/mean flow interactions.

The prediction method follows a sequence of three basic steps: (1) prediction of the aerodynamic characteristics (mean velocity, density and turbulent structure properties); (2) evaluation of the turbulent mixing noise at 90° to the jet axis utilizing the flow properties from (1) and the Lighthill-Ribner theory; and (3) construction of the far-field sound spectrum at various observer positions, utilizing the results of (1, 2) and accounting for the source convection and acoustic/mean flow interaction using Lilley's equation.

The acoustic aspects of the problem are described in some detail; the aerodynamic aspects are sketched out in Appendix A. Extensive theory - data comparisons are also presented.

4.2.3.3 Formulation of Problem

In this section, expressions for the pressure fields associated with convecting quadrupoles are developed. These quadrupoles are assumed to move along the axis of the jet; arbitrarily placed sources are discussed in Section 4.3.

It is assumed that the mean velocity and temperature fields in a coaxial jet (for the purposes of estimating the acoustic radiation) can be approximated by sectionally constant (i.e., plug) profiles. Lilley's equation for this special situation reduces to [see Mani⁽³⁷⁾]:

$$\left(\frac{\partial}{\partial t} + U \frac{\partial}{\partial x}\right)^2 p - \tilde{c}^2 p_{xx} - \tilde{c}^2 \Delta p = \frac{\delta(x - U_c t) \delta(r - r_0) \delta(\theta - \theta_0)}{r} e^{-i\omega_0 t} \quad (90)$$

where p is the acoustic pressure, \bar{U} , \bar{c} are the mean jet velocity and acoustic speeds, U_c is the source convection speed, and Δ is the Laplacian in the transverse variables. The instantaneous location of the source is (Ut, r_0, θ_0) and this source is oscillating at circular frequency ω_0 in its own (moving) reference frame. The geometry of the problem is shown in Figure 4-17; \bar{U} and \bar{c} take on values $U_1, U_2, U_3 = 0$ and c_1, c_2, c_3 in the core, fan and ambient regions, respectively. Coordinates (x, r, θ) comprise a cylindrical system with x along the jet axis. Also, time is denoted by t . Note that U_1 is some representative average value of inner stream velocity, not necessarily equal to nozzle exit value; the same remark holds for U_2 in the outer stream.

The right hand side of equation (90) is a convecting pressure source. From the solution for p , the pressure fields for all quadrupoles can be derived. Then these solutions for the quadrupoles are combined in a suitable way to deduce the solution to Lilley's equation with the actual self-noise source as the forcing term.

4.2.3.4 Solution of the Problem

The solution to equation (90), satisfying suitable jump conditions across the fluid interfaces at $r = a$ and $r = b$, and obeying the Sommerfeld radiation condition at $r = \infty$, is obtained by Fourier transforms. Define the multiple Fourier transform of p as

$$\bar{p} = \frac{1}{2\pi} \int_{-\infty}^{\infty} \int_{-\infty}^{\infty} \int_{-\pi}^{\pi} p e^{in\theta} e^{-i\Omega t} e^{-isx} d\theta dt dx \quad (91)$$

whose inverse is

$$p = \frac{1}{4\pi^2} \int_{-\infty}^{\infty} \int_{-\infty}^{\infty} \sum_{n=-\infty}^{\infty} \bar{p} e^{in\theta} e^{i\Omega t} e^{isx} d\Omega ds \quad (92)$$

and applying the transformation (91) to (90), after a number of integrations by parts (ignoring contributions from upper and lower limits), the following equation is obtained:

$$\frac{d^2 \bar{p}}{dr^2} + \frac{1}{r} \frac{d\bar{p}}{dr} + \left[\frac{(\Omega + \bar{U}s)^2}{\bar{c}^2} - s^2 - \frac{n^2}{r^2} \right] \bar{p} = F \frac{\delta(r - r_0)}{r} e^{in\theta_0} \quad (93)$$

$$\text{where } F = -\delta(\Omega + \Omega_1)/c_1^2, \quad \Omega_1 = \omega_0 + U_c s \quad (94)$$

Here, Ω , s and n are the Fourier transform variables. They can be interpreted as the frequency, axial, and circumferential wave numbers, respectively.

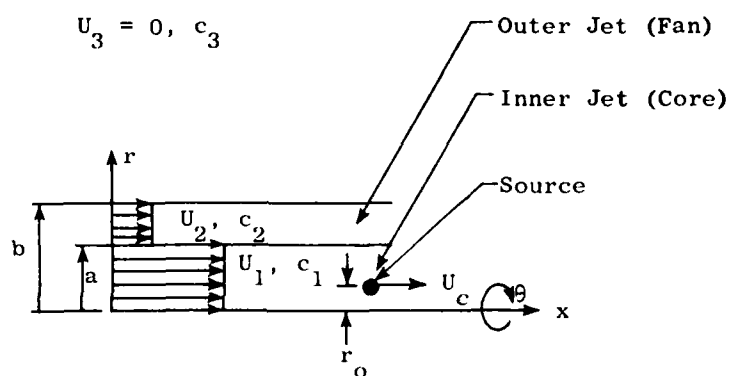


Figure 4-17. Geometry of Problem.

The solution of equation (93) is in terms of Bessel functions. The actual form of the solution (whether one uses regular or modified Bessel functions) is a strong function of the algebraic sign of

$$K^2 = \frac{(\Omega + \tilde{U} s)^2}{\tilde{c}^2} - s^2 \quad (95)$$

It is required that K^2 in the ambient region, K_3^2 , be positive, since otherwise no wave propagation takes place in the far field. This places a certain restriction on Ω and s . For these same values of Ω and s , the values of K^2 in regions one (K_1^2) and two (K_2^2) may be positive or negative. K^2 may be interpreted as a radial propagation constant in each of the regions.

Across the interfaces, continuity of pressure and particle displacement is enforced. This is because the interface must consist of particles of fixed identity. If $[f]$ denotes the jump in f across an interface, one then requires that

$$\left[\bar{p} \right] = 0 \quad (96)$$

$$\left[\frac{1}{\tilde{\rho}} \frac{1}{(\Omega + \tilde{U} s)^2} \frac{d\bar{p}}{dr} \right] = 0 \quad (97)$$

on $r = a, b$

where $\tilde{\rho}$ is the undisturbed fluid density in a given region. Since the undisturbed static pressure is assumed to be a constant throughout the jet, \bar{p} is directly calculable in terms of \tilde{c} . Note that, for the coaxial jet problem, there are two interfaces; one at $r = a$ and another at $r = b$ ($b > a$). Across the source location $r = r_0$, \bar{p} is continuous, and $d\bar{p}/dr$ changes by $F \exp(i n \theta_0)$.

The above jump conditions and the radiation condition at infinity render the solution to the problem unique. The required solution involves a tremendous amount of algebra involving very lengthy expressions, which need not be reproduced here. The final result for the acoustic pressure in the ambient region is given by

$$p = - \frac{1}{2\pi^2 c_1^2} e^{-i\omega_0 t} \sum_{n=0}^{\infty} \epsilon_n \cos n(\theta - \theta_0) \times \int_{-\infty}^{\infty} e^{i s(x - U_c t)} \left[A J_n(K_1 r_0) H_n^{(1)}(K_3 r) \right] ds \quad (98a)$$

$\Omega = -\Omega_1$

where ϵ_n is the Neumann factor ($\epsilon_0 = \frac{1}{2}$, $\epsilon_n = 1$, $n \geq 1$),

and A is given by

$$A = \frac{W(K_1 a)}{r_0 K_1 W(K_1 r_0)} \left[\frac{\rho_1}{\rho_2} \frac{K_2 \left(\frac{\Omega}{\Omega^2} + \frac{U_1 s}{U_2 s} \right)^2}{K_1} \beta J_n(K_1 a) - \alpha J_n'(K_1 a) \right]^{-1} \quad (98b)$$

The parameters α and β in the above expressions for A are given by

$$\alpha = H_n^{(1)}(K_3 b) \frac{W(K_2 a, K_2 b)}{W(K_2 b)} + \frac{\rho_2}{\rho_3} \frac{K_3}{K_2} \frac{(\Omega + U_2 s)^2}{\Omega^2} H_n^{(1)'}(K_3 b) \frac{L(K_2 b, K_2 a)}{W(K_2 b)} \quad (98c)$$

$$\beta = H_n^{(1)}(K_3 b) \frac{L'(K_2 a, K_2 b)}{W(K_2 b)} + \frac{\rho_2}{\rho_3} \frac{K_3}{K_2} \frac{(\Omega + U_2 s)^2}{\Omega^2} H_n^{(1)'}(K_3 b) \frac{W(K_2 b, K_2 a)}{W(K_2 b)} \quad (98d)$$

The auxiliary functions occurring in equation (98) are defined as follows:

$$W(z, \zeta) = J_n(z) Y_n'(\zeta) - J_n'(\zeta) Y_n(z) \quad (99a)$$

$$L(z, \zeta) = J_n(z) Y_n(\zeta) - J_n(\zeta) Y_n(z) \quad (99b)$$

$$L'(z, \zeta) = J_n'(z) Y_n'(\zeta) - J_n'(\zeta) Y_n'(z) \quad (99c)$$

$$W(z) = W(z, z) \quad (99d)$$

where J_n and Y_n are Bessel functions, and the primes denote differentiations. $W(z)$ is, of course, the Jacobian, and $H_n^{(1)}$ is the Hankel function of the first kind [Abramowitz and Stegun⁽³⁴⁾].

The above solution for the pressure in the ambient field is valid as long as $(K_1^2, K_2^2, \text{ and } K_3^2) > 0$. When K_1 is negative, equations (98) and (99) are still valid provided that all the Bessel functions whose argument involves K_1 are replaced by their modified counterparts. Similar remarks hold for K_2 . The solution given by p represents the acoustic pressure for a simple source convecting with velocity U_c , having a source strength of unity and frequency ω_0 . The source is at an arbitrary point in the core region (region ①) of the jet, $r = r_0$. Note that $K = |K_2|^{1/2}$.

It is seen that the expression for the pressure of a convecting source is a superposition of certain cylindrical (i.e., the sum over n) and axial (i.e., the integral over s) waves. The weighting factor, A , being an extremely complex function of the geometry (a, b), source convection velocity U_c , jet core and fan velocities U_1, U_2 , jet temperature and source frequency, is evaluated numerically.

4.2.3.5 The Far Field of Quadrupoles

In principle, it is possible to evaluate the integral in equation (98a) numerically and then differentiate the resultant expression with respect to the source coordinates (r_0, θ_0) in order to generate the dipole and quadrupole solutions to Lilley's equation. On the other hand, whenever the observation point is in the far field, it is possible to evaluate this s integral by the method of stationary phase. The technique is classical and therefore only the final result need be quoted. In the limit as $(r^2 + x^2)^{1/2} \rightarrow \infty$, equation (98a) can be reduced to the following:

$$p = \sum_{n=0}^{\infty} B_n \cos n (\theta - \theta_0) J_n (K_1 r_0) \quad (100a)$$

where

$$B_n = \frac{i \epsilon_n}{\pi^2 c_1^2} \frac{e^{-i\omega_0(t - R/c_3)}}{R(1 - M_c \cos \theta)} A e^{-in\pi/2} \quad (100b)$$

and R is the distance from the jet nozzle to the observer located at angle θ with respect to the x -axis, and M_c is the source convection Mach number U_c/c_3 . Also, A is to be evaluated at the point of stationary phase, given by

$$s = k_0 \frac{\cos \theta}{1 - M_c \cos \theta} \quad (100c)$$

where $k_0 = \omega_0/c_3$. Equations (100) contain the results of Lighthill for the limiting condition $c_1 = c_2 = c_3$, $U_1 = U_2 = 0$, as well as the round jet results of Mani for $a = b$. Thus (100) is a generalization of all previous acoustic theories.

Thus far, the location of the source, r_0 , has remained arbitrary. Physically, the most appropriate location for the source is along the nozzle lip line (i.e., at $r_0 = a$ and $r_0 = b$). However, in the case of a slug flow model of a round jet, Mani^(37,38) (see Section 4.2.2) has found that the precise location of the source is not too important, and that sources convecting on the jet centerline sufficiently explain most of the characteristics of both hot and cold round jet noise. Thus, in this analysis, $r_0 = 0$ is assumed.

Equation (100) is now expanded in a Taylor series about $r_0 = 0$, yielding the result

$$p = C_0 + y_0 C_1 \cos \theta + z_0 C_1 \sin \theta + (y_0^2 - z_0^2) C_2 \cos 2\theta + 2y_0 z_0 C_2 \sin 2\theta - \frac{1}{4} |K_1^2| (y_0^2 + z_0^2) C_0 + O(r_0^3) \quad (101a)$$

where

$$C_n = \frac{B_n |K_1^2|^{n/2}}{2^n \Gamma(n+1)} \quad (101b)$$

and (y_0, z_0) denote the transverse coordinates of the source. $\Gamma(n)$ is the Gamma function.

The transverse dipole and quadrupole solutions can be obtained from equation (101a) by differentiation with respect to y_0 and z_0 , and then setting $r_0 = 0$. Also, differentiations with respect to x generate longitudinal dipole and quadrupole solutions. This latter operation is equivalent to multiplication by s given by equation (100c); symbolically, $\partial/\partial x \rightarrow s$.

As an example, consider the on-axis y - y quadrupole $Q_{22} = Q_{yy}$. The solution in terms of the simple source solution is given by

$$Q_{22} = Q_{yy} = \left[\frac{\partial^2 p}{\partial y_0^2} \right]_{r_0=0} = 2 C_2 \cos 2\theta - \frac{1}{2} |K_1^2| C_0 \quad (102)$$

The square of the amplitude of this quadrupole is given by

$$|Q_{22}|^2 = Q_{22} Q_{22}^*$$

where Q^* is the complex conjugate of Q . If we define, for any quadrupole (i, j) ,

$$a_{ij} = \frac{1}{8\pi^2} \int_0^{2\pi} \int_0^{2\pi} |Q_{ij}|^2 d\theta d\theta_0 \quad (103)$$

we find that

$$a_{22} = C_2 C_2^* + \frac{1}{8} K_1^4 C_0 C_0^* \quad (104)$$

Physically, a_{22} is the aximuthal average of the amplitude of a ring of totally incoherent y-y quadrupoles.

The expression for acoustic pressure (101a) is valid for a "unit" convecting (and compact) velocity fluctuation. Both in the Lilley and Lighthill formulations, the strength of the noise source is proportional to the jet density. Mani⁽³⁸⁾ has shown that a compact velocity quadrupole in a heated jet generates dipole-like and simple source-like forcing functions. A detailed derivation of these terms is omitted herein for brevity, but the final expressions are quoted below:

$$a_{11} = \frac{1}{2} k_0^4 \rho^2 \frac{\cos^4 \theta}{(1 - M_c \cos \theta)^4} C_0 C_0^* \quad (105a)$$

$$a_{12} = \frac{1}{4} k_0^2 \frac{\cos^2 \theta}{(1 - M_c \cos \theta)^2} \left[\left(\frac{d\rho}{dr} \right)^2 C_0 C_0^* + \rho^2 C_1 C_1^* \right] \quad (105b)$$

$$a_{22} = \frac{3}{16} \left[\left(\frac{\partial^2 \rho}{\partial r^2} \right)^2 + \frac{1}{r^2} \left(\frac{\partial \rho}{\partial r} \right)^2 \right] C_0 C_0^* + \frac{1}{2} \left(\frac{\partial \rho}{\partial r} \right)^2 C_1 C_1^* + \rho^2 \left[C_2 C_2^* + \frac{1}{8} K_1^4 C_0 C_0^* \right] \quad (105c)$$

$$a_{23} = \frac{1}{16} \left[\left(\frac{\partial^2 \rho}{\partial r^2} \right)^2 + \frac{1}{r^2} \left(\frac{\partial \rho}{\partial r} \right)^2 \right] C_0 C_0^* + \frac{1}{4} \left(\frac{\partial \rho}{\partial r} \right)^2 C_1 C_1^* + \rho^2 C_2 C_2^* \quad (105d)$$

In these equations, $(\rho, \partial \rho / \partial r, \partial^2 \rho / \partial r^2)$ are some representative values of the density and its various gradients. The exact computation of these gradients follows the procedures proposed by Mani⁽³⁸⁾. Note that when $\rho = 1$ equation (105c) reduces to (104) as required.

Finally, these various quadrupole solutions are combined so that the noise source is effectively an eddy of isotropic turbulence, as suggested

by Ribner⁽³⁹⁾. In the present terminology, the approximate mean square pressure is given by

$$\overline{p^2} \sim (a_{11} + 4a_{12} + 2a_{22} + 2a_{23}) \quad (106)$$

The factor of proportionality in this equation is directly relatable to the turbulence properties in the jet supplied by the aerodynamic calculation. If $\overline{p^2}$ is known at one angle (say $\theta = 90^\circ$), this factor can be found and equation (106) can be used to find the mean square pressure at all other angles. Thus, the absolute level and directivity in each frequency band can be estimated.

4.2.3.6 Discussion of Results

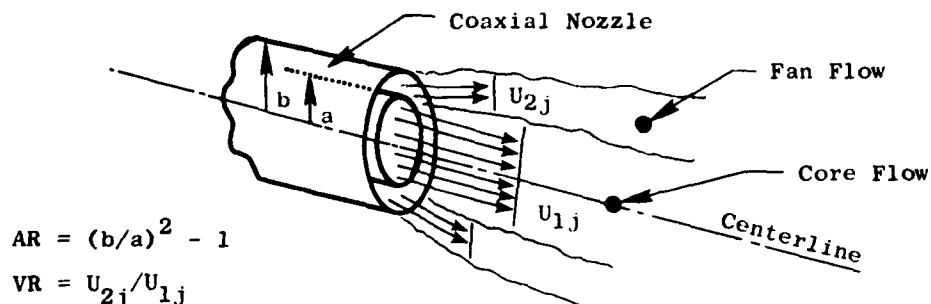
In applying the previously described model to coaxial jet noise predictions, three further assumptions had to be made. The first assumption concerns the selection of a diameter of characteristic length D to use in determining the typical frequency of each jet slice. A suitable expression for D which satisfies the limiting conditions when $U_2 = 0$ or $U_1 = U_2$ is

$$\frac{D}{2} = \frac{U_{1j}}{U_{\max}} a + \frac{U_{2j}}{U_{\max}} (b - a) \quad (107)$$

an assumption was also made that the "suitable average" values of U_1 and U_2 used in evaluation of the directivity expressions of the previous section are given by 65% of the corresponding nozzle exit values. Further, the source convection velocity was assumed to be 65% of U_1 evaluated at the nozzle exit.

Figure 4-18 shows overall sound pressure level (OASPL) variations with velocity ratio VR and area ratio AR , at an observer angle $\theta = 90^\circ$. These predictions essentially come from the aerodynamic portion of the prediction model and the Lighthill-Ribner theory of jet noise. The data (denoted by symbols) shown is from Olsen⁽⁴⁰⁾, and the theory is indicated by a solid line. There is remarkably good agreement at all area and velocity ratios. In particular, both the location and the magnitude of the noise minimum is predicted correctly. This noise minimum is a direct consequence of the reduction in turbulence intensity in the inner-to-outer stream mixing layer as the outer flow velocity is increased to about 40% of the inner flow velocity. * Further increases in outer flow velocity cause the outer-to-ambient stream mixing layer turbulence to produce the dominant noise. Figures 4-19 and 4-20 show corresponding SPL (sound pressure level) spectra at two area ratios and several velocity ratios. The agreement attained between theory and experiment was found to be quite good. The data are free field and lossless for pure mixing noise.

* For the precise relationship between the turbulent mixing parameter and velocity ratio, see equation (280).



$$AR = (b/a)^2 - 1$$

$$VR = U_{2j}/U_{1j}$$

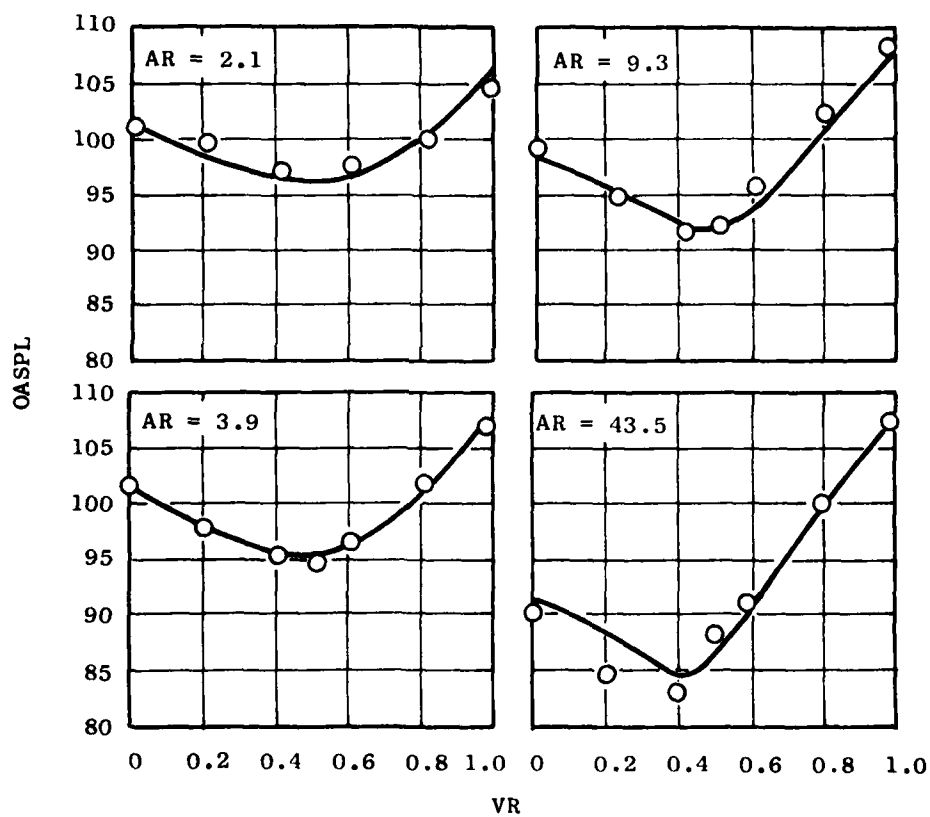


Figure 4-18. Overall Sound Pressure Level at $\theta = 90^\circ$ as Function of Area and Velocity Ratios (Cold Jet, $U_{1j} = 980$ ft/sec).

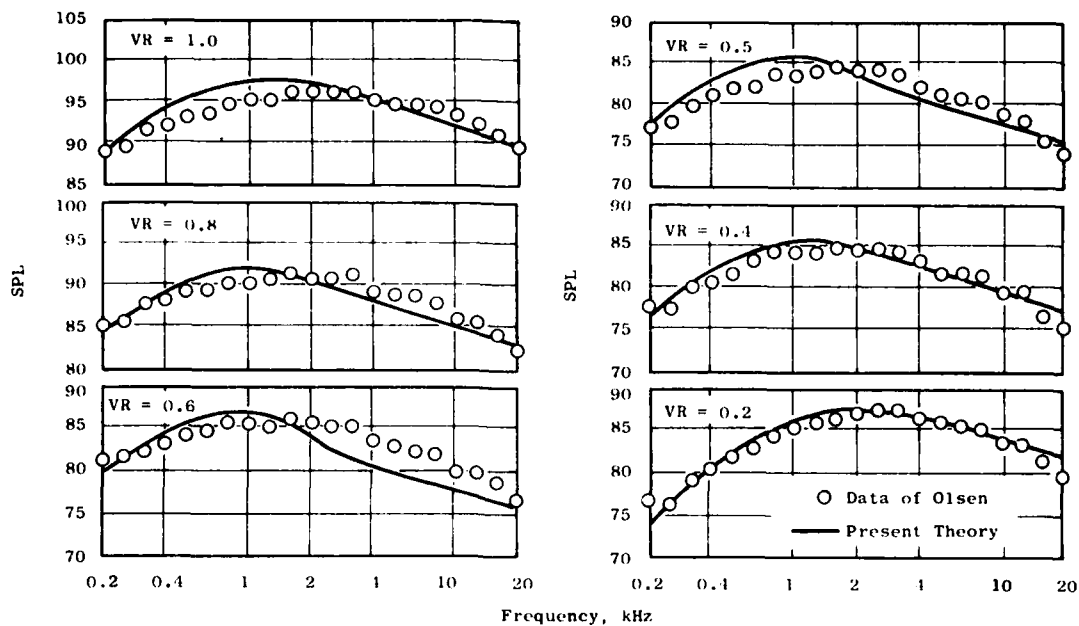


Figure 4-19. Sound Pressure Level at $\theta = 90^\circ$ as Function of Velocity Ratio ($AR = 3.9$, Cold Jet, $U_{lj} = 980$ ft/sec).

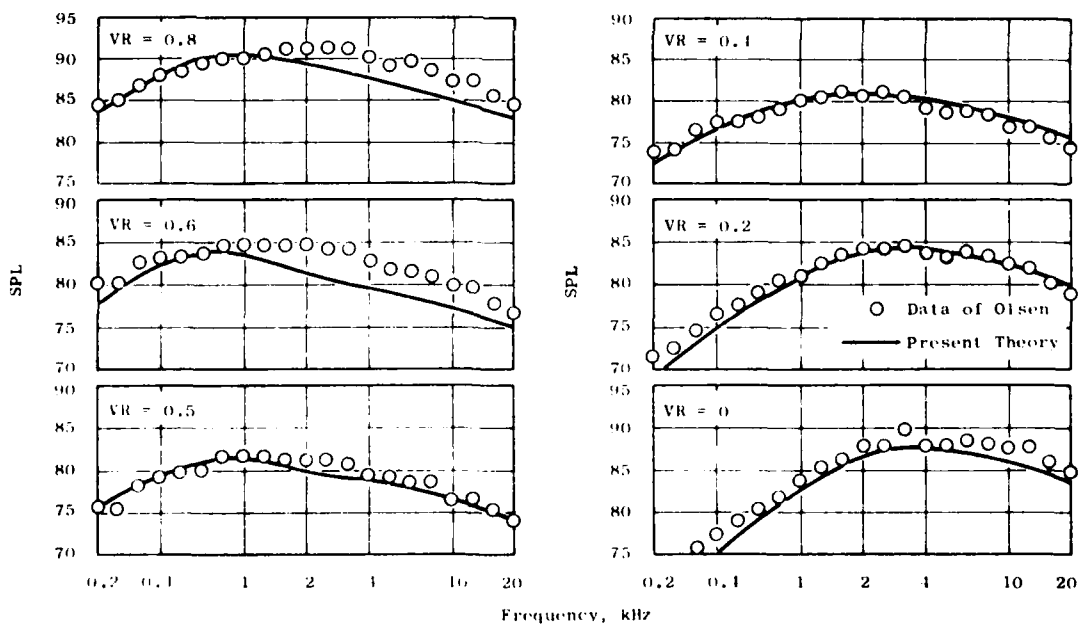


Figure 4-20. Sound Pressure Level at $\theta = 90^\circ$ as Function of Velocity Ratio ($AR = 9.3$, Cold Jet, $U_{lj} = 980$ ft/sec).

Figures 4-21 through 4-23 show the SPL as a function of observer angle θ , at constant values of source Strouhal number $St = f a(1 - M_c \cos\theta)/U_{1j}$. These results, for $AR = 3.9$, are shown at velocity ratios of 0.4, 0.6, and 0.8, respectively. It may be recalled that the SPL at $\theta = 90^\circ$ comes from the turbulence prediction and the Lighthill-Ribner theory. The acoustic theory, equations (100) - (106) extends the 90° prediction to all other angles. It is seen that the agreement between theory and experiments is good except at high frequencies and shallow angles, where refraction is generally overestimated. This is a limitation of the slug flow assumption, as Mani⁽³⁷⁾ also obtained similar results for round jets.

Figure 4-24 shows SPL versus VR trends at several angles and Strouhal numbers. Again, the acoustic theory is quite successful in predicting the directivity pattern, while the basic turbulence/intrinsic intensity models yield the correct absolute levels.

Finally, in Figure 4-25, the SPL spectra for a heated coaxial jet are shown at several velocity ratios. Again the agreement between theory and data [from Kazin, et al.⁽⁴¹⁾] is seen to be very good.

4.2.3.7 Conclusions

In summary, it appears that the present model is capable of predicting many of the observed characteristics, including absolute level, of coaxial jet noise. The noise reduction of coaxial jets, for $VR \leq 1$, was found to be primarily a result of reduction in turbulence intensity. A number of improvements in the theory will be described in the following sections. These include a better description of the turbulence spectrum (i.e., the slice-of-jet approach is replaced by a local eddy-volume discretization of the jet plume), and the slug flow is replaced by continuous sheared velocity and temperature profiles.

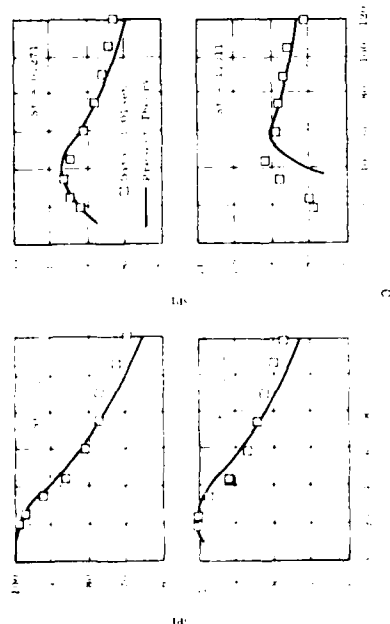


Figure 4-21. Sound Pressure Level as Function of Source Strouhal Number ($AR = 3.9$, $VR = 0.4$, Cold Jet, $U_{lj} = 980$ ft/sec).

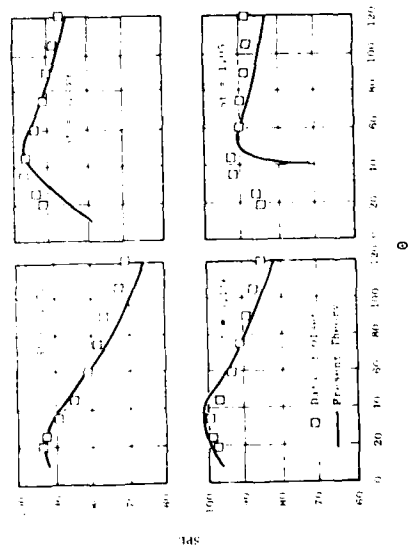


Figure 4-23. Sound Pressure Level as Function of Source Strouhal Number ($AR = 3.9$, $VR = 0.8$, Cold Jet, $U_{lj} = 980$ ft/sec).

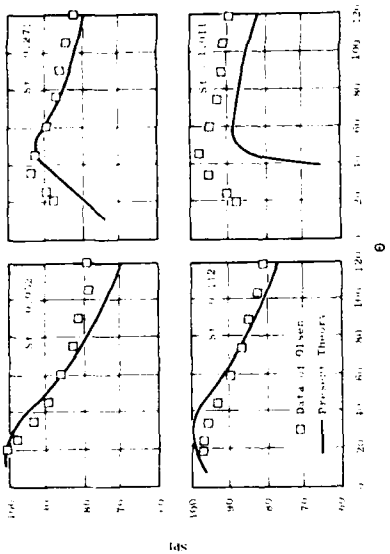


Figure 4-22. Sound Pressure Level as Function of Source Strouhal Number ($AR = 3.9$, $VR = 0.6$, Cold Jet, $U_{lj} = 980$ ft/sec).

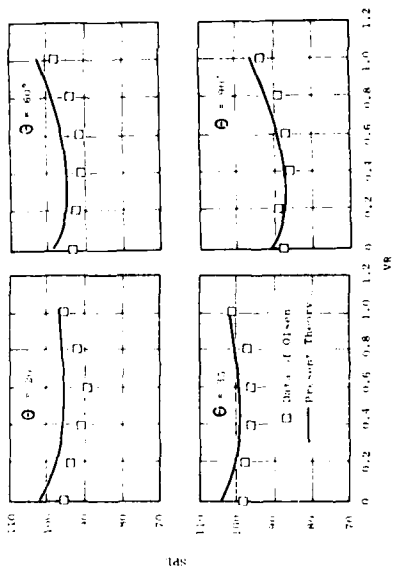


Figure 4-24. Sound Pressure Level as Function of Velocity Ratio ($AR = 2.1$, $St = 0.3$, Cold Jet, $U_{lj} = 980$ ft/sec).

132

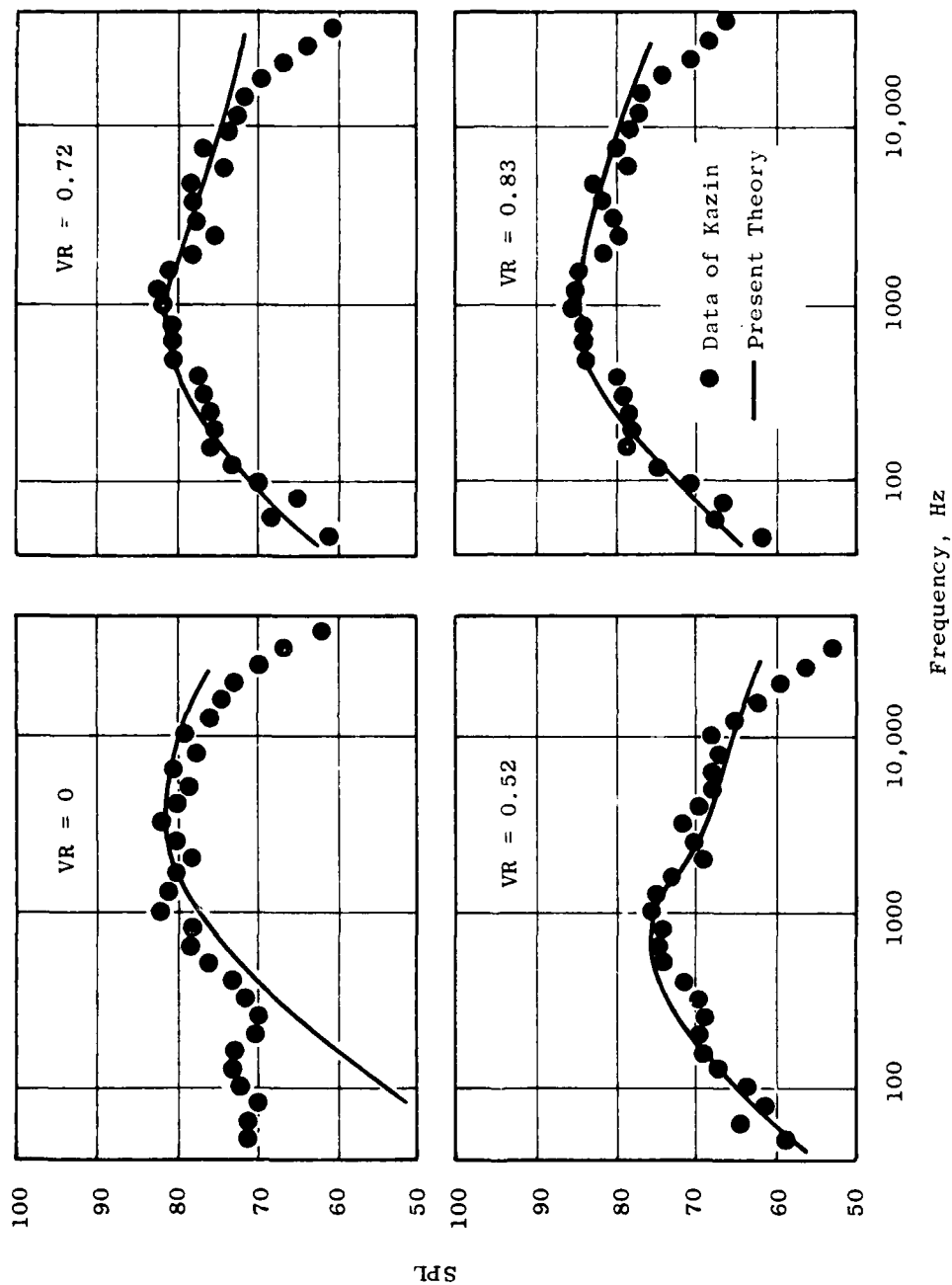


Figure 4-25. Sound Pressure Level at $\theta = 90^\circ$ as Function of Velocity Ratio
 (AR = 4, TR = 2.1, Hot Jet, $U_{1j} = 1000$ ft/sec, $T_{1j} = 1200^\circ$ R).

4.3 GENERALIZED HIGH FREQUENCY SHIELDING THEORY

The purpose of this section is to derive expressions for the pressure field of various high frequency convected singularities immersed in parallel jet-like sheared flows. These expressions include the simultaneous effects of fluid and source convection, refraction, and jet temperature. There is no restriction on the location of these singularities; they can be anywhere within the jet but the convection velocity is assumed to be parallel to the jet axis.

The theoretical results show the explicit form of the fluid shielding integral. This quantity depends rather strongly on the precise location of the source; the closer the source is to the jet boundary, the less is the effect of acoustic-mean flow interaction. It is also shown that convective amplification for the pressure of a quadrupole is increased by a factor of $(1 - M_j \cos \theta)^{-1}$ over the classical results, where M_j is the jet Mach number and θ is the angle from the jet axis. Thus acoustic mean flow interaction not only implies "refraction" but also additional convective amplification due, not to source convection, but to fluid motion. Interesting effects due to temperature are also evident.

Finally, the results of this section form the backbone of the acoustic portion of the unified aeroacoustic model described in Section 4.7.

4.3.1 Introduction

Lighthill⁽⁴²⁾, in his classic theory of jet noise, identified the most prominent source of noise as the double divergence of the tensor uu where u is the fluid velocity. He also showed that the acoustic pressure fluctuations that are driven by this source obey the classical wave equation. Since the source of noise is embedded in the jet, the pressure fluctuations propagate through a region of nonuniform velocity (and perhaps temperature) before they reach the observer. The Lighthill theory clearly fails to account for this physical effect, that is, it does not take acoustic mean flow interactions into account explicitly.

Recently it has been recognized, especially through the work of Mani^(17, 43, 37, 38), that these acoustic mean flow interactions are extremely important and explain quantitatively many of the observed characteristics of cold and hot jet noise. Perhaps the most significant finding of Mani is that "convection amplification" is frequency dependent, where, in the definition of convection amplification both source and fluid convection effects (i.e., a nonzero jet velocity) are now included. Several other authors, notably Ribner⁽⁷⁾, Csanady⁽¹⁴⁾, Schubert⁽⁴⁴⁾ and Pao⁽⁴⁵⁾ have qualitatively explained a number of phenomena by acoustic mean flow interactions.

Three points in connection with Mani's work are to be made. First, he treats round jets exclusively; second, for the purposes of estimating the acoustic field, he replaces the actual jet velocity and temperature profiles by uniform or slug flow profiles; and third, he assumes that the quadrupole noise sources are convecting along the centerline of the jet.

Various generalizations to Mani's work have been made. The slug flow theory was successfully extended by Gliebe and Balsa⁽⁴⁶⁾ to coaxial jets, the slug flow profiles were replaced by monotonic and continuously varying profiles for on-axis sources by Balsa⁽⁴⁷⁾ and Goldstein⁽⁴⁸⁾, and results for arbitrarily located sources in continuously varying monotonic profiles were derived by Balsa⁽⁴⁹⁾ and Goldstein^(50, 51).

It should be noted that the slug flow theories become quite inadequate at high jet velocities (~ 2000 fps) and at "small" angles to the jet axis ($\sim < 50^\circ$). This is especially true for nonmonotonic velocity or temperature profiles. These are encountered in inverted-flow nozzle exhaust systems. An indication for the systematic failure of the slug flow theories may be seen from the work of Mani^(37, 38) or Gliebe and Balsa⁽⁴⁶⁾; although the theory data comparisons in these references are restricted to jet velocities of less than 1000 fps.

In any case, it is now known that a satisfactory (i.e., rational and accurate) theory of jet noise can be developed based, to a large extent, on the radiation field of quadrupoles immersed in parallel sheared flows. For the purposes of the acoustic theory, the locations of these quadrupoles are arbitrary -- clearly these locations must be determined by independent means such as an aerodynamic mixing calculation. It is also sufficient, especially at high jet velocities, to consider only the high frequency radiation from these sources. Tester and Morfey⁽⁵²⁾ numerically find the high frequency asymptote is attained very rapidly. Similar sentiments were expressed by Pao⁽⁴⁵⁾.

The starting point for the present theory is Lilley's equation in which the jet velocity and temperature profiles are arbitrary functions of the radial variable r . The relevance of Lilley's equation to jet noise has been questioned by a number of authors for various mathematical and physical reasons. It is felt that if acoustic mean flow interactions are important, as they really are, the Lilley equation must be a first approximation of these effects. This conjecture is supported by the success of the work of Mani. The approach is to solve Lilley's equation for a convected point source of circular frequency ω . This solution is a Green's function. The approximate solution that is presented is valid to lowest order as $ka \rightarrow \infty$ ($k = \omega/c_\infty$) where a is the jet radius and c_∞ is the ambient speed of sound. It is next shown how to obtain the corresponding results for quadrupole singularities and how to combine these to describe the radiation pattern from convecting isotropic turbulence.

Thus the present work is similar to the high frequency work of Pao⁽⁴⁵⁾. There are a number of important differences, however, some of which are: the current use of Lilley's rather than Phillips'⁽¹³⁾ equation and the current treatment of a cylindrical rather than a planar shear layer. The present work is also quite closely related to the high frequency result of Goldstein⁽⁵¹⁾; however it is felt that the current results are much simpler, more explicit, and more general.

4.3.2 Formulation of the Problem

It is assumed that physical space is spanned by a stationary cylindrical coordinate system (r, θ, x') where x' is along the jet axis, as shown in Figure 4-26. Lilley's equation is given by

$$\begin{aligned}
 L(p; U, x') &= \frac{1}{c^2} D_U^3 p - D_U \Delta p - \frac{d}{dr} (\log c^2) D_U \frac{\partial p}{\partial r} \\
 &+ 2 \frac{dU}{dr} \frac{\partial^2 p}{\partial x' \partial r} = \rho D_U \nabla \cdot \nabla \cdot (\underline{u}' \underline{u}') - \overline{\underline{u}' \underline{u}'} \\
 &- 2\rho \frac{dU}{dr} \frac{\partial}{\partial x'} \nabla \cdot (\underline{u}' \underline{u}') - \overline{\underline{u}' \underline{u}'}
 \end{aligned} \tag{108a}$$

with

$$D_U = \frac{\partial}{\partial t} + U \frac{\partial}{\partial x'} \tag{108b}$$

and

$$\Delta = \frac{\partial^2}{\partial (x')^2} + \frac{\partial^2}{\partial r^2} + \frac{1}{r} \frac{\partial}{\partial r} + \frac{1}{r^2} \frac{\partial^2}{\partial \theta^2} \tag{108c}$$

where t denotes time, p is the acoustic pressure, $c = c(r)$ is the undisturbed speed of sound, $U = U(r)$ is the mean or time average jet velocity and $\rho = \rho(r)$ is the mean jet density. The turbulent velocity fluctuations are given by \underline{u}' and the overbar denotes an appropriate average (u'_r is the radial component). The solution to equation (108a) can be written down formally as $t \rightarrow \infty$ provided that the solution to

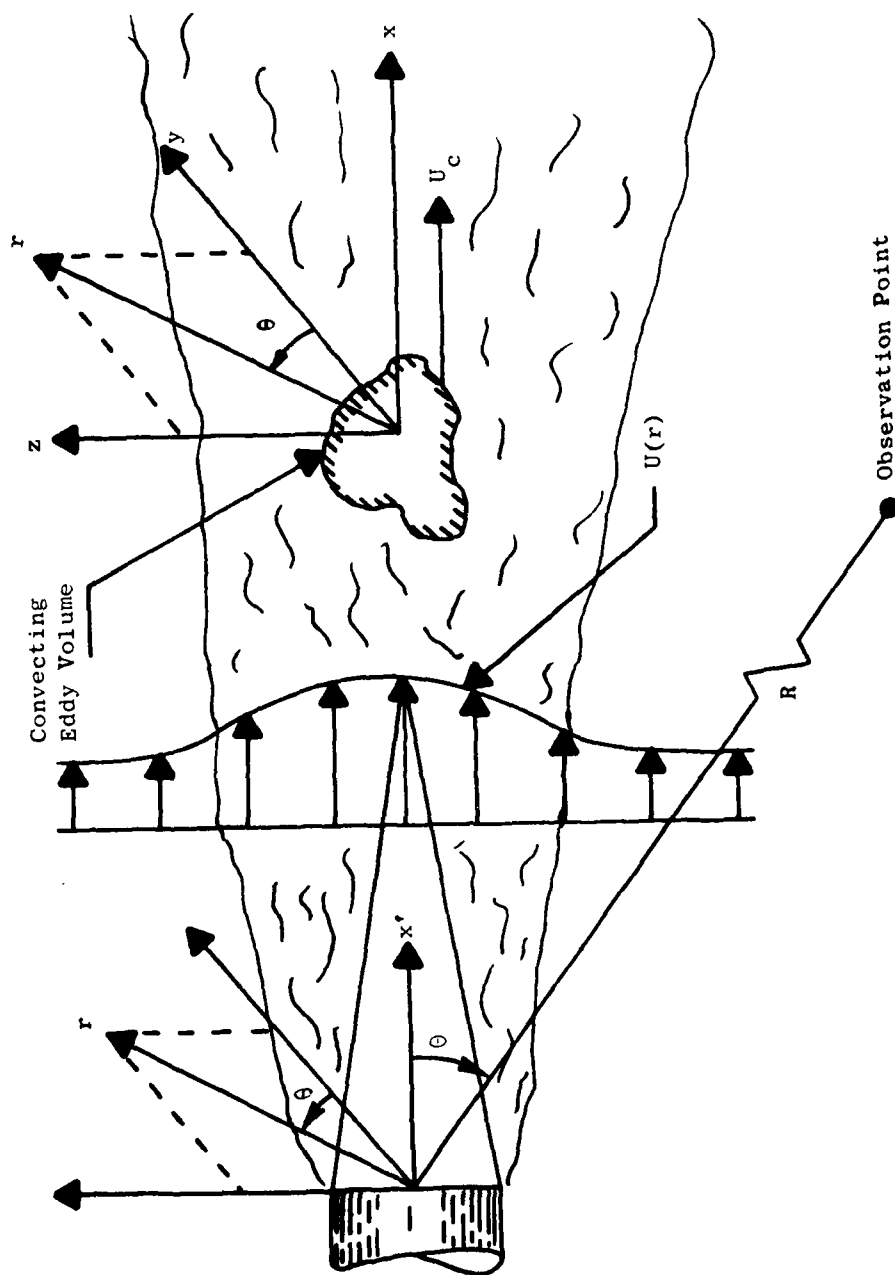


Figure 4-26. Geometry of the Problem.

$$L(g; U, x') = e^{-i\omega t} \frac{\delta(x' - U_c t) \delta(r - r_0) \delta(\theta - \theta_0)}{r} \quad (109a)$$

is known. In equation (109a), $i = \sqrt{-1}$, ω , $U_c > 0$, r_0 and θ_0 are given constants (i.e., independent t , r , θ and x'). Equation (109a) simply defines a Green's function. Actually, using the Galilean transformation $x = x' - U_c t$, it is possible to rewrite (109a) as

$$L(g; V, x) = e^{-i\omega t} \frac{\delta(x) \delta(r - r_0) \delta(\theta - \theta_0)}{r} \quad (109b)$$

where

$$V = U - U_c \quad (109c)$$

Thus the canonical problem to be solved is equation (109c) with suitable radiation condition as $\sqrt{r^2 + x^2} \rightarrow \infty$. The solution to equations (109a and b) represents the pressure field of a convected monopole source. This pressure field obeys Lilley's equation.

After using the sequence of Fourier transformations (110a), one finds that equation (109b) reduces to (110b) where

$$\bar{g} = \frac{e^{i\omega t}}{\sqrt{2\pi}} \int_{-\infty}^{\infty} e^{-isx} dx \int_{-\pi}^{\pi} e^{in\theta} g d\theta \quad (110a)$$

$$-\infty \leq s \leq \infty; n = 0, \pm 1, \dots$$

and

$$\begin{aligned} \frac{d^2 \bar{g}}{dr^2} + \left[\frac{1}{r} + \frac{d}{dr} \log\left(\frac{c}{c_\infty}\right)^2 + \frac{2s}{k - Ns} \frac{dN}{dr} \right] \frac{d\bar{g}}{dr} \\ + \left[\frac{(k - Ns)^2}{(c/c_\infty)^2} - s^2 - \frac{n^2}{r^2} \right] \bar{g} \\ = \frac{i}{\sqrt{2\pi}} \frac{1}{c_\infty} \frac{1}{(-k + Ns)} e^{in\theta_0} \frac{\delta(r - r_0)}{r} \end{aligned} \quad (110b)$$

with $N = V/c_\infty$, $k = \omega/c_\infty$, and c_∞ is the ambient speed of sound. Note that the inverse Fourier transformation of (110a) is given by

$$g = \frac{e^{-i\omega t}}{2\pi\sqrt{2\pi}} \sum_{n=-\infty}^{\infty} e^{-in\theta} \int_{-\infty}^{\infty} e^{isx} \bar{g} \, ds \quad (111)$$

The coefficient of $d\bar{g}/dr$ in (110b) can be eliminated by a standard transformation. Defining

$$p = \sqrt{r} \frac{c}{c_\infty} \frac{1}{-k + Ns} \bar{g} \quad (112a)$$

(110b) then reduces to

$$\begin{aligned} p_{rr} + \left\{ k^2 \left[\frac{(1 - N\sigma)^2}{(c/c_\infty)^2} - \sigma^2 \right] - \frac{n^2 - 1/4}{r^2} \right\} p \\ + \left[\frac{1}{r} \frac{\psi_r}{\psi} + \frac{\psi_{rr}}{\psi} - 2 \left(\frac{\psi_r}{\psi} \right)^2 \right] p \\ = \frac{i}{\sqrt{2\pi}} \frac{c}{c_\infty^2} \frac{1}{k^2} \frac{1}{(1 - N\sigma)^2} e^{in\theta_0} \frac{\delta(r - r_0)}{\sqrt{r}} \end{aligned} \quad (112b)$$

where $\sigma = s/k$ and

$$\psi = \frac{1 - N\sigma}{c/c_\infty} \quad (112c)$$

For small values of r , the term $(n^2 - 1/4) r^{-2}$ dominates the left hand side, (note that $r^{-1} \psi_r/\psi$ has a removable singularity at $r = 0$) whereas, for $kr \gg 1$ the term $k^2[\dots]$ dominates since terms involving ψ are of order (a^{-2}) by hypothesis, and $ka \gg 1$. Thus the terms involving ψ can be neglected for all values of r as long as $ka \gg 1$; therefore, (112b) simplifies to

$$P_{rr} + \left\{ k^2 q(r, 0) - \frac{n^2 - 1/4}{r^2} \right\} P \quad (113a)$$

$$= \frac{i}{\sqrt{2\pi}} \frac{c}{c_\infty} \frac{1}{k^2} \frac{1}{(1 - N\sigma)^2} e^{in\theta_0} \frac{\delta(r - r_0)}{\sqrt{r}}$$

where $k = \omega/c_\infty$, $\sigma = s/k$, $N = (U - U_c)/c_\infty$

$$g^2(r; \sigma) = \frac{(1 - N\sigma)^2}{(c/c_\infty)^2} - \sigma^2$$

and

(113b)

The qualitative behavior of P depends on the algebraic sign of g^2 -- P is "oscillatory" for $g^2 > 0$ and "exponential" for $g^2 < 0$. The turning points of g^2 , that is, the values of r for which $g = 0$, are next examined.

4.3.3 The Turning Points

The quantity g^2 is called the shielding function*. For given velocity and temperature profiles it is a function of the axial wave number $\sigma = s/k$ (s is the x -Fourier transform variable). It is possible to show, by using the method of stationary phase for evaluating the s -integral in equation (111) that, at each point in the far field, the pressure depends only on one value σ , for example σ_* , where

$$\sigma_* = \frac{\cos \theta}{1 - M_c \cos \theta} \quad (114)$$

The far-field observation point makes an angle θ with respect to the jet axis and $M_c = U_c/c_\infty$ is the convective Mach number. Physically, equation (114) means that most of the sound that is observed at a point (R, θ) in the far field travels along the line segment joining the emission and observation points. This line segment has length R and makes the angle θ with the jet axis. Thus (R, θ) are really retarded coordinates [Morse and Ingard⁽²⁵⁾];

* When g^2 is positive, it may be interpreted as a local "propagation constant".

in jet noise they are generally interpreted as the distance from the jet and the angle with respect to jet axis [Lighthill⁽⁴²⁾].

It is also convenient to introduce an alternate shielding† function

$$G^2 = g^2 - \frac{v^2}{r^2} \quad ; \quad v = n/k \quad (115)$$

so that G^2 is essentially the curly bracket in equation (113a) provided that $k \rightarrow \infty$ for (n/k) fixed. Both G^2 and g^2 will be used in the analysis.

It turns out that when the acoustic Mach number* $N = V/c_\infty = (U - U_c)/c_\infty$ exceeds unity or when the jet velocity or temperature profiles are nonmonotonic, the shielding function, g^2 , may have none, one, or two turning points or zeros, depending on the value of the angle to the jet axis. These possibilities are illustrated schematically in Figure 4-27; the zeros or turning points are denoted by r_0 . For certain mean profiles, one could encounter more than two turning points, however, for technologically relevant exhaust profiles, no more than two have ever been found.

The illustrations in Figure 4-27 show all the turning points as simple zeros. Clearly somewhere between $\theta = 90^\circ$ and 70° , a situation exists in which the shielding function is nonnegative and has a double zero. Similar pathological cases may exist for other values of the angle θ . Also, the axis $r = 0$ is a particularly rich source of mathematically interesting alternatives. These rather specific situations are not treated here; they are briefly discussed by Balsa⁽⁴⁹⁾.

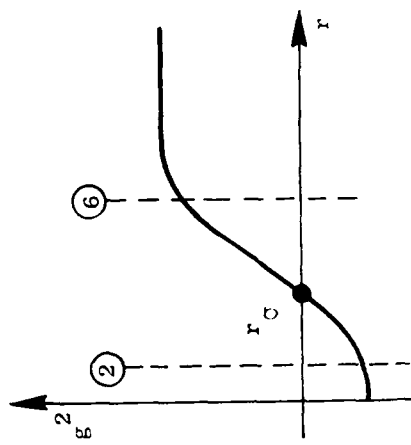
It is assumed that the turning points are simple and well separated. This means that the distance between the axis and a turning point or the distance between two consecutive turning points is at least one wavelength. In the strict asymptotic sense, as the frequency $\omega \rightarrow \infty$, one should have no difficulty in meeting these criteria, except perhaps in certain narrow regions of width of order $(\omega^{-1}) \rightarrow 0$.

As pointed out above, the radial location of the source, r_0 , is arbitrary. The specific form of the solution depends on the relationship between the turning points and the radial coordinate of the source. There are six equivalence classes of problems; these are designated as ①, ②... in Figure 4-27. The dashed vertical lines indicate the possible locations of the source. As long as $r_0 < r_0$, the solution will be qualitatively and physically similar to that of Problem ②. Similar remarks apply to the other situations. In the following, detailed solutions will be given for each of these possible alternatives.

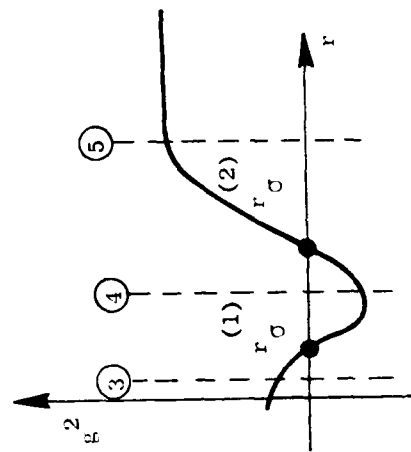
* For subsonic ($N < 1$) round jets one encounters at most one turning point.

† See footnote on page 104.

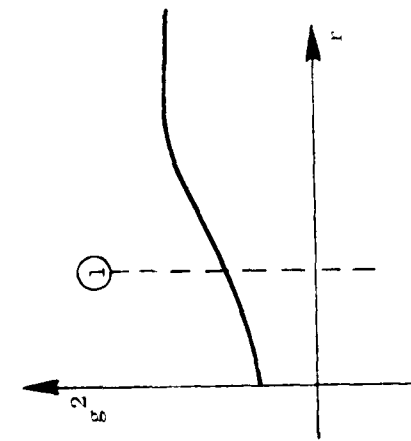
14/1



Typically
 $\theta \approx 40^\circ$
 One Turning Point



Typically
 $\theta \approx 70^\circ$
 Two Turning Points



Typically
 $\theta \approx 90^\circ$
 No Turning Point

Figure 4-27. Turning Points of Shielding Function g^2 .

4.3.4 No Turning Points - Problem ①

The treatment of the case for which g^2 has no turning points is the easiest because algebraic details are at a minimum and the solution resembles quite closely that of the classical wave equation.

The key point is to observe that the homogeneous version of equation (113a) has solutions of the form $(\xi/g)^{1/2} C_n(k\xi)$ where C_n is any Bessel function of order n and

$$\xi = \int_0^r g \, dr \quad (116)$$

Thus one writes, on either side of the source,

$$P = \begin{cases} B (\xi/g)^{1/2} J_n(k\xi) & r < r_0 \\ A (\xi/g)^{1/2} H_n^{(1)}(k\xi) & r > r_0 \end{cases} \quad (117)$$

where J_n is the Bessel function of first kind and $H_n^{(1)}$ is the Hankel function, so that P satisfies the finiteness and radiation conditions at $r = 0, \infty$ respectively, as required.

The constants A, B are determined by imposing that P is continuous across the source location, r_0 , and that dP/dr jumps by an amount \hat{e} where

$$\hat{e} = \frac{i}{\sqrt{2\pi} r_0} \frac{c_0}{c_\infty^2} \frac{1}{k^2} \frac{1}{(1 - N_0 \sigma)^2} e^{in\theta_0} \quad (118)$$

The last result can be obtained by integrating equation (113) across a narrow region that includes the point $r = r_0$. The subscript "o" denotes the value of a quantity evaluated at the location of the source; $c_0 = c(r_0)$, etc.

Solving for these constants and substituting them into equation (117), one finds for $r > r_0$

$$P = \frac{\pi}{2i} \hat{e} \left(\frac{\xi_0}{g_0} \right)^{1/2} \left(\frac{\xi}{g} \right)^{1/2} H_n^{(1)}(k\xi) J_n(k\xi_0) \quad (119)$$

It should be emphasized that all of these results are valid only at high frequencies ($k = \omega/c_\infty \rightarrow \infty$). At lower frequencies, additional terms are present; here, these are discarded because they are asymptotically small.

From here on, the calculation of the Green's function is extremely simple. First \bar{g} is obtained from equation (112) and then g is obtained from equation (111). An intermediate result is

$$g = -\frac{e^{-i\omega t}}{8\pi c_\infty} \int_{-\infty}^{\infty} e^{i\sigma kx} \left(\frac{c_0}{c} \right) \left(\frac{\xi_0}{g_0 r_0} \right)^{1/2} \left(\frac{\xi}{gr} \right)^{1/2} \frac{1 - N\sigma}{(1 - N_0\sigma)^2} d\sigma \quad (120)$$

$$\times \sum_{n=-\infty}^{\infty} e^{in(\theta_0 - \theta)} H_n^{(1)}(k\xi) J_n(k\xi_0)$$

The above infinite sum is evaluated by the addition theorems for Bessel functions [Magnus⁽⁵³⁾] and the σ - integral is evaluated by the method of stationary phase [Carrier⁽³¹⁾]. The final result is, as the observation point recedes to infinity,

$$g = \frac{i}{4\pi c_\infty kR} \frac{c_0/c_\infty}{(1 - M_0 \cos \theta)^2} \left(\frac{\xi_0}{r_0 g_0} \right)^{1/2} \quad (121)$$

$$\times e^{i\omega(R/c_\infty - t)} \exp \left\{ ik \left[\int_0^\infty (g - g_\infty) dr - \xi_0 \cos(\theta - \theta_0) \right] \right\}$$

where c_∞ is the speed of sound at infinity, $k = \omega/c_\infty$ and g_∞ is the value of g at infinity. Note that $M_0 = U(r_0)/c_\infty$ is the jet Mach number at the location of the source. It should be noted that functions of the axial wave number, σ , are to be evaluated at

$$\sigma = \sigma_* = \frac{\cos \theta}{1 - M_c \cos \theta} \quad (122)$$

where σ_* is the point of stationary phase. In particular,

$$g^2 = \frac{\left(\frac{c}{c_\infty}\right)^{-2} (1 - M \cos \theta)^2 - \cos^2 \theta}{(1 - M_c \cos \theta)^2} \quad (123a)$$

where $M = U(r)/c_\infty$, $c = c(r)$, $M_c = U_c/c_\infty$ and

$$\xi_0 = \int_0^{r_0} g \, dr \quad (123b)$$

Note that the far-field Green's function decays inversely with distance R ; it has a convective amplification factor of $(1 - M_0 \cos \theta)^{-2}$ where M_0 is proportional to the jet velocity (not to the source convective velocity); it depends explicitly on the square root of the absolute temperature at the source $c_0 \sim \sqrt{T_0}$, and it depends implicitly on jet temperature and velocity through functions g_0 and ξ_0 .

The phase delay R/c_∞ represents the travel time from the origin of the convecting coordinate system to the observation point, and the additional phase terms in equation (121) represent a correction to account for the fact that the signal comes from point $x = 0$, $r = r_0$ and $\theta = \theta_0$ and not from the origin ($x = r = 0$). To see this, consider the Lighthill theory ($M = 0$, $c/c_\infty = 1$), so that, from equation (123a)

$$g = g_\infty = \frac{\sin \theta}{1 - M_c \cos \theta} \quad (124a)$$

and

$$\xi_0 \cos(\theta - \theta_0) = \frac{\xi \cdot \xi_0}{R(1 - M_c \cos \theta)} \quad (124b)$$

where $\zeta \cdot \zeta_0$ are the transverse coordinates of the observation point and the source respectively. In this special case, the actual time delay is $[R - \zeta \cdot \zeta_0 / R (1 - M_c \cos \theta)] / c_\infty$; a classical result that is well known. In the presence of mean flow, the time delay is somewhat different from the classical results. This is because the signal propagates along curved rays rather than straight lines between the source and the observer.

The final expression for the Green's function (121) is certainly extremely simple. An alternate expression, although more complex, will now be derived because the approach developed below will be needed later on; it is also the method used by Goldstein⁽⁵¹⁾.

The key observation is that the governing radial equation for P

$$P_{rr} + k^2 G^2 P = \hat{e} \quad ; \quad G^2 = g^2 - (n/kr)^2 \quad (125)$$

can also be solved by the WKBJ technique [Carrier⁽³¹⁾]. When g^2 is positive for all values of r , G^2 may be positive or negative, depending on the magnitude of the "circumferential harmonic" $n/kr = v/r$. It is well known that, at high frequencies, the most important contribution to P comes from those values of (v/r) for which the shielding function G^2 is positive at the source (i.e., $G_0 > 0$); this contribution is

$$P = \frac{\hat{e}}{ik \sqrt{G G_0}} e^{-i\pi/4} \cos(k\chi_0 - \frac{\pi}{4}) \exp(ik\chi) \quad (126a)$$

where

$$\chi = \int_{r_{0v}}^r G dr \quad (126b)$$

and $r_{0v} = r_0$ is the unique zero of G^2 . Note that the subscript "o" again represents the value of a function at the location of the source (e.g.,

$$\chi_0 = \int_{r_{0v}}^{r_0} G dr \text{ and } e \text{ is given by equation (118).}$$

After substituting equation (126) into (112a) and (111) one obtains, as $r \rightarrow \infty$,

$$\begin{aligned}
 g = & - \frac{e^{-i\omega t}}{4\pi^2 c k} \int_{-\infty}^{\infty} e^{i\sigma kx} \frac{c_0}{c_{\infty}} \frac{1 - N_{\infty}^{\sigma}}{(1 - N_0^{\sigma})^2} \frac{d\sigma}{\sqrt{g_{\infty} r}} \\
 & \times e^{-i\pi/4} \sum_{n=-\infty}^{\infty} \frac{e^{in(\theta_0 - \theta)}}{\sqrt{G_0 r_0}} \cos(k\chi_0 - \frac{\pi}{4}) \\
 & \times \exp \left[ik \int_{r_{\sigma v}}^{\infty} (G - g_{\infty}) dr + ik g_{\infty} (r - r_{\sigma v}) \right]
 \end{aligned} \tag{127}$$

where $N_{\infty} = -M_c$ is the value of N at infinity. In the far field as $k(x^2 + r^2)^{1/2} \rightarrow \infty$ equation (127) becomes, by the method of stationary phase,

$$\begin{aligned}
 g = & \frac{i}{4\pi c_{\infty} kR} \frac{c_0/c_{\infty}}{(1 - M_0 \cos \theta)^2} e^{i\omega(R/c_{\infty} - t)} \frac{1}{\pi} \left(\frac{2\pi}{kr_0} \right)^{1/2} \\
 & \times \sum_{n=-\infty}^{\infty} \frac{e^{in(\theta_0 - \theta)}}{\sqrt{G_0}} \cos(k\chi_0 - \frac{\pi}{4}) \exp \left[ik \int_{r_{\sigma v}}^{\infty} (G - g_{\infty}) dr - ik g_{\infty} r_{\sigma v} \right]
 \end{aligned} \tag{128}$$

A comparison of equation (128) and (121) provides the value of the series in (128); this value will be needed in the following analysis. Actually, it is possible to evaluate the sum directly by replacing it by an integral and then evaluating the latter by the method of stationary phase. The analysis is quite simple and explicit for $g^2 = \text{constant} = g_{\infty}^2$, where it is found that

$$\sum = \frac{k}{2} \left(\frac{2\pi r_0}{k} \right)^{1/2} \exp \left[-ik g_\infty r_0 \cos(\theta - \epsilon_0) \right] \quad (129a)$$

as $k \rightarrow \infty$. The major contribution to the sum comes from the vicinity of

$$v = n/k = g_\infty r_0 \sin(\theta_0 - \theta) \quad (129b)$$

The solution given by Goldstein⁽⁵¹⁾ is in the form of an infinite series (128); but the series can also be evaluated to obtain the simple closed form result given by equation (121). Equation (126a) is related to the Debye expansion of Bessel functions [Abramowitz and Stegun⁽³⁴⁾].

4.3.5 One Turning Point - Problem ②

Consider next the problem in which the shielding function, g^2 , has a unique turning point at $r = r_\sigma$ so that $r_\sigma > r_0$. The solution for P can again be written down as linear combinations of Bessel functions for $r < r_\sigma$. The only point to note is that now the appropriate solutions of the homogeneous version of equation (113a) are modified Bessel functions $I_n(k\xi)$ and $K_n(k\xi)$, where

$$\xi = \int_0^r f dr \quad r < r_\sigma \quad (130)$$

and $g^2 = -f^2$. Thus f^2 is positive whenever g^2 is negative.

For definiteness, it is required that P have the form

$$P = \begin{cases} A (\xi/f)^{1/2} I_n(k\xi) & r < r_0 \\ (\xi/f)^{1/2} [BI_n(k\xi) + CK_n(k\xi)] & r_0 < r < r_\sigma \end{cases} \quad (131a)$$

$$(131b)$$

so that P is finite on the axis. Across the source location, r_0 , the continuity of P and the jump in dP/dr determine two of the three constants, A , B , and C . The modified Bessel functions in equation (131b) are then expanded in their Hankel asymptotic forms ($k\xi \rightarrow \infty$, n fixed) to obtain real exponential functions of positive and negative arguments.

These exponentials are matched to trigonometric functions (i.e., to exponentials of imaginary argument) across the turning point by use of the classical WKB turning point conditions [Carrier(31)]. For $r > r_\sigma$, only outgoing waves can be present; this additional constraint determines coefficients A, B, and C uniquely.

The solution for the transform of the Green's function is, as $k\xi_* \rightarrow \infty$,

$$P = \frac{\pi}{2i} \hat{\epsilon} \left(\frac{\xi_0}{f_0} \right)^{1/2} \left(\frac{\xi_*}{g} \right)^{1/2} \times \left(\frac{2}{\pi k \xi_*} \right)^{1/2} \exp i \left(k \xi_* - \frac{\pi}{4} \right) e^{-k \xi_\sigma} I_n(k \xi_0) \quad (132)$$

where

$$\xi_\sigma = \int_0^{r_\sigma} f dr, \quad \xi_* = \int_{r_\sigma}^r g dr$$

and $\hat{\epsilon}$ again given by equation (118). The mathematical resemblance between equations (132) and (119) is very close, especially if the Hankel function in the latter is expanded for large values of its argument. In fact, equation (132) could have been obtained from equation (119) by a suitable analytic continuation.

Nevertheless there are important physical differences. The phase factor in equation (119) (apart from some unimportant constants) is essentially

$$\xi = \int_0^r g dr = \int_0^{r_\sigma} g dr + \int_{r_\sigma}^r g dr \quad (133a)$$

On the other hand, the phase of equation (132) is essentially

$$\xi_* = \int_{r_\sigma}^r g dr \quad (133b)$$

and it appears that the first contribution to the integral in equation (133a)

has been converted into the real exponential $\exp(-k\xi_0) = \exp(-k \int_0^{r_0} f dr)$.

This point will be discussed further in the following paragraphs.

The Fourier inversion of P can be explicitly carried out by the method of stationary phase and the resultant infinite series in the circumferential harmonics can be evaluated by another addition theorem for Bessel functions. The final result for the Green's function is

$$g = \frac{i}{4\pi c_\infty kR} \frac{c_0/c_\infty}{(1 - M_0 \cos\theta)^2} \left(\frac{\xi_0}{r_0 f_0}\right)^{1/2} \quad (134)$$

$$\times e^{i\omega(R/c_\infty - t)} \exp\left[ik \int_{r_0}^{\infty} (g - g_\infty) dr - ik g_\infty r_0\right] e^{-k[\xi_0 - \xi_0 \cos(\theta - \theta_0)]}$$

where the above is to be evaluated at $\sigma = \sigma_*$ equation (122).

After comparing the expressions corresponding to the two cases treated so far (i.e., zero and one turning point) one sees that, when a turning point is present and the source lies in the negative region of the shielding function, the ratio of the amplitudes of the two Green's functions (i.e., the ratio of the far-field pressures generated by convecting point sources) is proportional to

$$\exp\left\{-k[\xi_0 - \xi_0 \cos(\theta - \theta_0)]\right\}$$

The geometric interpretation of the argument of the above exponential easily

follows in (ξ, θ) space ($\xi = \int_0^r f dr$).

Figure 4-28 shows that the exponential damping (or "attenuation") of the signal is proportional to $kd = \omega d/c_\infty$, where d is some effective distance of fluid surrounding the source. Thus, the deeper the source is embedded in the jet and the higher is its frequency, the smaller will be its pressure amplitude in the far field. Roughly speaking, this diminution of the far-field acoustic pressure is a direct consequence of acoustic shielding. It is also observed that shielding depends on jet velocity, temperature, and observer angle θ through the function f,

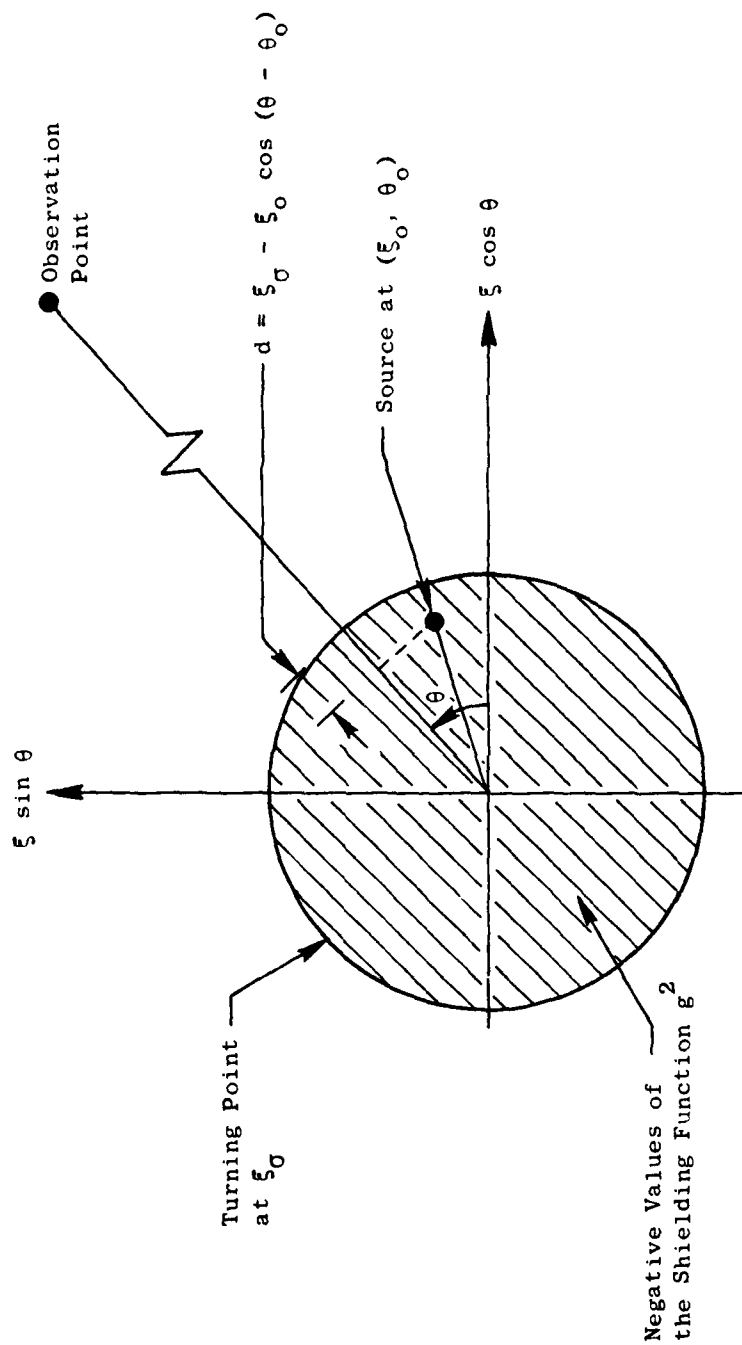


Figure 4-28. Geometry of Acoustic Shielding in Modified Transverse Plane (ξ, θ) .

$$f^2 = -g^2 = \frac{\cos^2 \theta - (1 - M \cos \theta)^2 (c/c_\infty)^{-2}}{(1 - M_c \cos \theta)^2}$$

It is also worthwhile to obtain a representation of the solution by the WKBJ technique directly applied to equation (113a). The function G^2 has a unique zero at $r = r_{\sigma v}$ where $r_{\sigma v} \geq r_\sigma$. At the location of the source $r = r_0$, $G^2 = G_0^2$ is, of course, negative. Writing $F^2 = -G^2$ for negative values of G^2 , one obtains following Goldstein⁽⁵¹⁾

$$P = \frac{\hat{e}}{2ik\sqrt{GF_0}} e^{-i\pi/4} \exp(-k \int_r^{r_{\sigma v}} F dr) \quad (135a)$$

$$\times \exp(ik\chi)$$

where

$$\chi = \int_{r_{\sigma v}}^r G dr \quad (135b)$$

The Green's function in the far field reduces to

$$g = \frac{i}{4\pi c_\infty kR} \frac{c_0/c_\infty}{(1 - M_0 \cos \theta)^2} e^{i\omega(R/c_\infty - t)} \frac{1}{2\pi} \left(\frac{2\pi}{kr_0}\right)^{1/2}$$

$$\times \sum_{n=-\infty}^{\infty} \frac{e^{in(\theta_0 - \theta)}}{\sqrt{F_0}} \exp(-k \int_{r_0}^{r_{\sigma v}} F dr) \quad (136)$$

$$\times \exp \left[ik \int_{r_{\sigma v}}^{\infty} (G - g_\infty) dr - ik g_\infty r_{\sigma v} \right]$$

The last result can be obtained from equation (128) by comparing (135a) and (126a). Again functions of σ in equation (136) are to be evaluated at the point of stationary phase.

Consider next the evaluation of the infinite sum in (136). It would first appear that most of the contribution to the sum comes from small values of (n/kr) , so that, with the exception of the $\exp [in (\theta_0 - \theta)]$ term, it is possible to set n to zero. This is because the larger and larger circumferential harmonics are attenuated more and more severely by the real exponential factor whose argument is proportional to the (large) frequency. This analysis says that

$$g \sim \exp(-k \int_{r_0}^{r_\sigma} f dr) \delta(\theta - \theta_0)$$

so that all the radiation takes place in the $\theta = \theta_0$ direction; the "amplitude" in that direction is reduced by a certain integral of the shielding function $f^2 = -g^2$. While this result is inadequate for the radiation from a point source because all the energy is channeled into a very narrow region about the point $\theta = \theta_0$ (hence the amplitude becomes infinite), it is reasonably adequate for a ring source in a jet. This is obtained by integrating the Green's function; from equation (136) one finds

$$\int_{-\pi}^{\pi} g d\theta_0 \sim \exp(-k \int_{r_0}^{r_\sigma} f dr) \left(\frac{2\pi}{k f_0 r_0} \right)^{1/2} \quad (137a)$$

whereas from equation (134)

$$\begin{aligned} \int_{-\pi}^{\pi} g d\theta_0 &\sim \left(\frac{\xi_0}{r_0 f_0} \right)^{1/2} e^{-k \xi_\sigma} \int_{-\pi}^{\pi} I_0(k \xi_0) d\theta_0 \\ &\sim \left(\frac{2\pi}{k r_0 f_0} \right)^{1/2} \exp\left(-\int_{r_0}^{r_\sigma} f dr\right) \end{aligned} \quad (137b)$$

as $k\xi_0 \rightarrow \infty$. The factors of proportionality in equation (137) are identical. Note that the last result is obtained by noting that $\exp [k\xi_0 \cos (\theta - \theta_0)]$ is the generating function of the modified Bessel function I_n . Thus the crude summation proposed above gives the correct result for a ring source; alternatively, it gives the correct value for the circumferentially averaged radiation field. A comparison of equation (136) and (134) also shows the more exact value of the infinite series in question.

4.3.6 Two Turning Points -- Problem ③

Consider now the case in which there are two turning points at $r_0^{(1)}$ and $r_0^{(2)}$, so that $r_0^{(1)} < r_0^{(2)}$ and $r_0^{(1)} > r_0$. In this situation, there are four distinct regions in which the solution for P must be considered. On either side of the source one has expressions similar to equation (131) except that the modified Bessel functions I_n and K_n are replaced by J_n and Y_n , respectively, and f is replaced by g in the definition of ξ . Across the source location, r_0 , the usual two conditions are imposed; two applications of the WKBJ turning point conditions and the Sommerfeld radiation condition render the solution unique.

The s or σ integral is again evaluated by the method of stationary phase, and the infinite sum is obtained from a suitable addition theorem for Bessel functions. The details follow the ideas developed in the previous section; the final result for the far-field Green's function is

$$g = \frac{i}{4\pi c_\infty kR} \frac{c_0/c_\infty}{(1 - M_0 \cos \Theta)} \left(\frac{\xi_0}{r_0 g_0} \right)^{1/2} \times e^{i\omega(R/c_\infty - t)} \exp \left[ik \int_{r_\sigma^{(2)}}^{\infty} (g - g_\infty) dr - ik g_\infty r_\sigma^{(2)} \right] e^{-k\xi_\sigma^{(1,2)}} \quad (138a)$$

$$\times \sin [k\xi_0 \cos (\theta - \theta_0) + k\xi_\sigma^{(1)}] / \sin (2k\xi_\sigma^{(1)})$$

where

$$\xi_0 = \int_0^{r_0} g dr \quad (138b)$$

$$\xi_{\sigma}^{(1)} = \int_0^{r_{\sigma}^{(1)}} g \, dr \quad (138c)$$

$$\xi_{\sigma}^{(1,2)} = \int_{r_{\sigma}^{(1)}}^{r_{\sigma}^{(2)}} f \, dr \quad (138d)$$

Several observations are in order. First the reduction in the amplitude of the far-field Green's function is proportional to $\exp [-k\xi_{\sigma}^{(1,2)}]$ where $\xi_{\sigma}^{(1,2)}$ is the integral of the square root of the negative of the shielding function between the two turning points. Because of this, the far-field pressure is relatively insensitive to the location of the source; similar results were found for a slug flow annular jet when the source was placed in the zero velocity region in the center of the jet. More interestingly, however, the solution shows the existence of resonances whenever

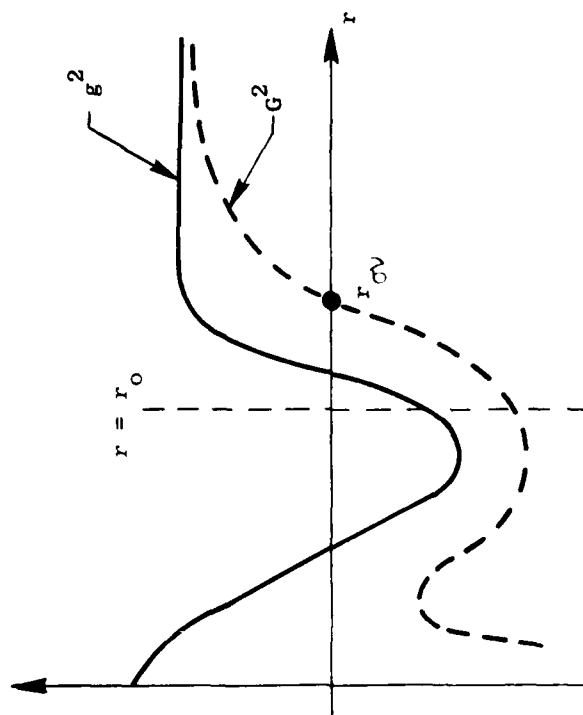
$$\frac{\xi_{\sigma}^{(1)}}{\lambda} = \frac{1}{4}, \frac{1}{2}, \frac{3}{4}, \dots$$

where $\lambda = 2\pi c_{\infty}/\omega$ is the wavelength of radiation. The first resonance occurs when the effective distance between the axis and the first turning point is one-quarter wavelength; this condition is analogous to the classical resonance condition for an open-closed tube. There is also a possibility for a perfect null in the far field whenever

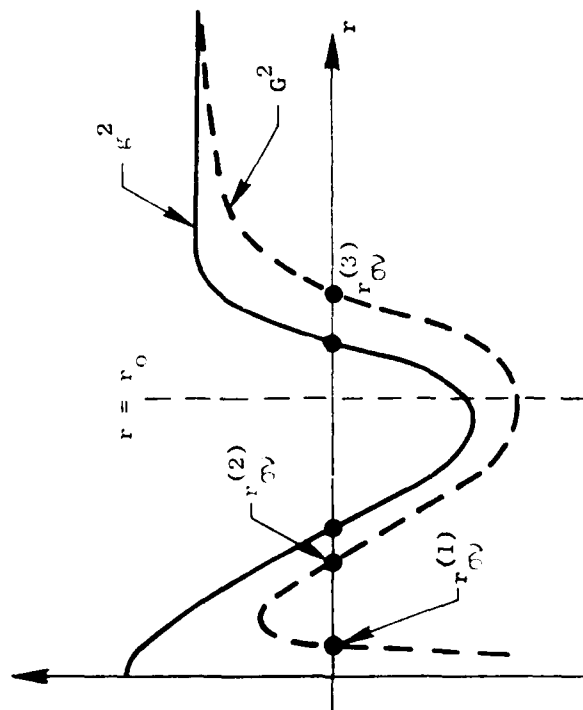
$$\frac{\xi_0 \cos(\theta - \theta_0) + \xi_{\sigma}^{(1)}}{\lambda} = \frac{1}{2}, 1, \frac{3}{2}, \dots$$

4.3.7 Two Turning Points -- Problem ④

Consider again the case in which the shielding function g^2 has two turning points, but this time the source is located in between them. This problem will be solved by an application of the classical WKBJ technique. Thus the alternate shielding functions G^2 and $F^2 = -G^2$ will be used. The geometry is elaborated in Figure 4-29.



Large Values of $(v/r)^2$



Small Value of $(v/r)^2$

Figure 4-29. Geometry of Alternate Shielding Function $G^2 = g^2 - (v/r)^2$.

Assume first that $(n/kr) = (v/r)$ is so small that $G^2 = g^2 - (v/r)^2$ has three turning points at $r_{\sigma v}^{(1)}$, $r_{\sigma v}^{(2)}$ and $r_{\sigma v}^{(3)}$. Clearly the source must lie between $r_{\sigma v}^{(2)}$ and $r_{\sigma v}^{(3)}$. There are altogether five regions in which the transform of the Green's function must be considered. These are $r < r_{\sigma v}^{(1)}$, $r_{\sigma v}^{(1)} < r < r_{\sigma v}^{(2)}$, $r_{\sigma v}^{(2)} < r < r_0$, $r_0 < r < r_{\sigma v}^{(3)}$ and $r_{\sigma v}^{(3)} < r$. In each of these regions, the solution is written as an exponential function (with real or imaginary argument) according to the WKB procedure [Carrier⁽³¹⁾]. The matching of these solutions across the turning points and the source, and the requirement of outgoing waves for large values of the radial variable, render the solution unique. This is given by, for $r < r_{\sigma v}^{(3)}$,

$$P = \frac{\hat{\epsilon}}{k\sqrt{GF_0}} e^{-i\pi/4} \exp\left(-k \int_{r_0}^{r_{\sigma v}^{(3)}} F dr\right) \quad (139a)$$

$$\times \frac{2 + \alpha\beta}{4i + \alpha\gamma} \exp\left(ik \int_{r_{\sigma v}^{(3)}}^r G dr\right)$$

where

$$\alpha = \tan\left(k \int_{r_{\sigma v}^{(1)}}^{r_{\sigma v}^{(2)}} G dr\right) \quad (139b)$$

$$\beta = \exp\left(-2k \int_{r_{\sigma v}^{(2)}}^{r_0} F dr\right) \quad (139c)$$

$$\gamma = \exp \left(-2k \int_{r_{\sigma v}^{(2)}}^{r_{\sigma v}^{(3)}} F dr \right) \quad (139d)$$

For larger values of (v/r) , there is only one turning point at $r = r_{\sigma v}$ (see Figure 4-29). In this case, the solution is considerably simpler for $r > r_{\sigma v}$

$$P = \frac{\hat{\epsilon}}{2ik\sqrt{GF_0}} e^{-i\pi/4} \exp \left(-k \int_{r_0}^{r_{\sigma v}} F dr \right) \exp \left(ik \int_{r_{\sigma v}}^r G dr \right) \quad (140)$$

because there are fewer regions to consider. The quantity $\hat{\epsilon}$ is given by equation (118).

Consider now equation (139a). At high frequencies, the exponential factors β and γ are vanishingly small. These factors are multiplied by $\alpha = \tan k(\cdot)$ which may become large, so that the factors $\alpha\beta$ and $\alpha\gamma$ may be of order unity in certain narrow regions. These regions could be classified as resonances; they are ignored in the present analysis. As discussed previously (see Section 4.3.3), the current analysis does not take into account the behavior of the pressure in certain singular or nonuniform regions. These regions exist in the present mathematical model but are thought to be unimportant for the physics of high velocity jets. Thus equation (139a) essentially reduces to (140). In an asymptotic sense there is only one solution [i.e., (140)] which is independent of the number of turning points or the value of (v/r) .

It is worthwhile to discuss the asymptotic equivalence of (139a) and (140) from another point of view. Physically, one would expect the solution to depend, at high frequencies, only on the conditions (i.e., jet velocity and temperature) between the source and the far-field observer. This is clearly shown by equation (140) in which the dependence on the shielding function enters only for $r > r_0$. Conversely, from equation (139a), it is seen that values of the shielding function for $r < r_0$ affect the solution exponentially weakly. In other words, the dominant part of the radiation arrives directly from the source (rather than from multiple reflections from the shear layer). In any case, the appropriate solution of this section, equation (140), is identical to (135a) of Section 4.3.5, so that the analysis here need not be carried any further.

4.3.8 One or Two Turning Points -- Problems ⑤ and ⑥

These two problems generate a number of possibilities which are all asymptotically equivalent. The dominant contribution to the solution comes from those values of (v/r) for which G^2 is positive at the source. The shielding function G^2 will have a number of turning points at $r < r_0$. From the preceding section it was noted that only the turning point nearest to the source affects the solution significantly; the effect of the other (if any) turning points is exponentially weak. The solution is

$$P = \frac{\hat{\epsilon}}{ik\sqrt{GG_0}} e^{-i\pi/4} \exp\left(ik \int_{r_{0v}}^r G dr\right) \cos\left(k \int_{r_{0v}}^{r_0} G dr - \frac{\pi}{4}\right) \quad (141)$$

where r_{0v} is the nearest zero of G^2 to r_0 ($r < r_0$). This representation of the solution agrees with equation (126a), and the results for the Green's function follow from (121).

4.3.9 Interpretive Remarks

This concludes the formal derivation of the expressions for the far-field Green's function under the assumed behavior of the shielding function. Although a priori, there were six classes of problems, three of these were found to be redundant in the sense that they reduced to one of the other classes. Thus, the solutions to problems ①, ②, and ③ generate all the required results.

The main point to be made is that, when the shielding function g^2 is negative in a region R between the source and the observer, the far-field pressure is exponentially small. The argument of this exponential is proportional to the source frequency and to the width of this region R . The presence of this (real) exponential is a direct consequence of acoustic shielding, i.e., the source does not communicate directly with the ambient, but radiates through a high velocity and high temperature jet.

It would be convenient, following this comprehensive discussion of the nature of the solutions to the fundamental acoustic shielding equation (as a function of the number of turning points of the shielding/propagation function g^2), to be able to provide simple formulae or criteria by which the number of these turning points can be generally determined. Unfortunately, due to the dependence of g^2 on the local jet velocity and temperature profiles and the far field radiation angle of interest, no simple substitute has been found for the need to actually compute $g^2(r)$ and hence determine the number of turning points. This procedure can be readily computerized, and indeed is a part of the computer program contained in the supplement to this report. For simple exhaust flows such as the conical nozzle flow, one can say that, within the zone of silence, one turning point will occur, and none will occur outside the zone of silence. For more complex exhaust flows, especially with inverted flows, no such simple result can be stated.

4.3.10 Pressure Field of Convected Singularities

The solution of

$$L(S; U, \mathbf{x}') = \rho D_U e^{-i\omega t} \frac{\delta(\mathbf{x}' - U_c t) \delta(\mathbf{r} - \mathbf{r}_0) \delta(\theta - \theta_0)}{r} \quad (142)$$

is required, where S may be thought of as a pressure source in analogy with the classical wave equation. After evaluating the derivatives on the right hand side, it is found that the forcing term in equation (142) reduces to

$$\rho \left[-i\omega e^{-i\omega t} \frac{\delta(\mathbf{x}' - U_c t) \delta(\mathbf{r} - \mathbf{r}_0) \delta(\theta - \theta_0)}{r} + (U - U_c) e^{-i\omega t} \frac{\delta'(\mathbf{x}' - U_c t) \delta(\mathbf{r} - \mathbf{r}_0) \delta(\theta - \theta_0)}{r} \right] \quad (143)$$

where δ' is the derivative of the δ -function. Thus, S is expressible in terms of g and $\partial g / \partial \mathbf{x}'$. In fact,

$$S = \rho_0 \left[-i\omega + (U_0 - U_c) ik \sigma_* \right] g \quad (144a)$$

or

$$S = -ik \rho_0 c_\infty \frac{1 - M_0 \cos \theta}{1 - M_c \cos \theta} g \quad (144b)$$

It is now observed that the coefficients of the Lilley operator are independent of \mathbf{x}' , \mathbf{r}_0 and θ_0 . Thus, any derivative (with respect to \mathbf{x}' , \mathbf{r}_0 or θ_0) of the left hand side of equation (142) is directly transferable to S . Similarly, these differentiations, when applied to the right hand side, yield higher order singularities. These singularities model the various dipole and quadrupole solutions of Lilley's equation. For example, a suitable linear combination of $\partial S / \partial \mathbf{r}_0$ and $\partial S / \partial \theta_0$ produces a transverse dipole, and $\partial S / \partial \mathbf{r}_0$ represents an r -dipole.

The objective now is to derive the expressions for the quadrupoles that will be used in the prediction of jet noise. The procedure is outlined below for the y -dipole, \mathcal{D}_y :

$$\mathcal{D}_y = \partial S / \partial y_0 = \cos \theta_0 \partial S / \partial \mathbf{r}_0 - \frac{\sin \theta_0}{r_0} \frac{\partial S}{\partial \theta_0} \quad (145a)$$

where y_0 is the y -component of the source coordinate. Next the magnitude of \mathcal{D}_y is calculated from equations (144b, 121); this is then averaged circumferentially with respect to θ_0 and θ . If

$$a_y = \frac{1}{4\pi^2} \int_{-\pi}^{\pi} d\theta_o \int_{-\pi}^{\pi} d\theta |D_y|^2 \quad (145b)$$

where $|\cdot|$ denotes the magnitude of a (complex) quantity, then it follows from equations (121) and (144b) that

$$a_y = \frac{\rho_{\infty}^2}{32\pi^2 R^2} \frac{k^2 g_o^2}{(c_o/c_{\infty})^2} (1 - M_o \cos\theta)^{-2} (1 - M_c \cos\theta)^{-2} \quad (146a)$$

$$\times \frac{1}{2} \left(\frac{\xi_o}{r_o g_o} \right) \left[1 + (\xi_o / r_o g_o)^2 \right]$$

where

$$\xi_o = \int_0^{r_o} g \, dr$$

The subscript "o" denotes the value of a quantity at the location of the singularity $r = r_o$.

A similar expression arises from Problem ② in which there is a turning point. In the latter case, however, there is at least one difficulty that immediately occurs in connection with the expression for the pressure field of a dipole and other singularities. When the singularity is near to the turning point, $f_o \rightarrow 0$ so that $a_y \rightarrow \infty$. This is physically unrealistic and is a direct failure of the present theory. The difficulty arises because the source is now too close to the turning point (i.e., the distance between source and turning point is less than a wavelength) so the parameter $k\delta$ is no longer small, where δ is the separation between the source and turning point. There is a rigorous mathematical procedure for circumventing this difficulty; however, it leads to great complexity. A much simpler, albeit approximate, physical approach for resolving the problem was taken. If a dipole is situated in the vicinity of the jet axis, or if g is a slowly varying function of r (i.e., approximately a constant), the last factor in equation (146a) reduces to unity. This suggests ignoring the last factor even in a more general case. This approximation is adopted in this section to obtain the simplest possible results.

An alternate way to look at this approximation is to note that the precise location of the source is important only for the calculation of the exponential (i.e., rapidly varying) shielding factor; the precise location of the source is unimportant for the calculation of certain other quantities. Thus, those latter quantities may be approximated by assuming that the source lies on the axis of the jet. In this case it is found that

$$a_y \cong \frac{\rho_\infty^2}{32 \pi^2 R^2} \frac{k^2 g_0^2}{(c_0/c_\infty)^2} (1 - M_0 \cos \theta)^{-2} (1 - M_c \cos \theta)^{-2} \quad (146b)$$

where it is emphasized that equation (146b) is valid for the case in which g^2 has no turning points (i.e., Problem ①).

The circumferentially averaged far-field pressure of a convecting ring of y-dipoles is proportional to the square of the frequency and is inversely proportional to the local temperature at the singularity. There is a convective amplification of $(1 - M_0 \cos \theta)^{-2}$ due to the jet velocity and a "classical" convective amplification of $(1 - M_c \cos \theta)^{-4}$ due to source convection. This is because the shielding function g_0^2 itself has a convective amplification of $(1 - M_c \cos \theta)^{-2}$.

The various quadrupole solutions are now summarized. Defining

$$\alpha = \frac{\rho_\infty^2}{16 \pi^2 R^2} \frac{1}{(c_0/c_\infty)^2} (1 - M_0 \cos \theta)^{-2} (1 - M_c \cos \theta)^{-2} \quad (147)$$

The following quadrupole solutions can be derived:

Problem ①

$$a_{yy} = 3 \alpha k^4 g_0^4 / 8 \quad (148a)$$

$$a_{yz} = a_{yy} / 3 \quad (148b)$$

$$a_{xx} = \frac{\alpha k^4 \cos^4 \theta}{(1 - M_c \cos \theta)^4} \quad (148c)$$

$$a_{xy} = \frac{\alpha k^4 g_0^2 \cos^2 \theta}{2 (1 - M_c \cos \theta)^2} \quad (148d)$$

Problem ②

Defining

$$\beta = \exp \left(-2k \int_{r_0}^{r_\sigma} f \, dr \right) \quad (149a)$$

$$\gamma = \left[1 + 4\pi k \int_0^{r_0} f \, dr \right]^{1/2} \quad (149b)$$

then

$$a_{yy} = 3 \alpha \beta \, k^4 f_0^4 / 8\gamma \quad (149c)$$

$$a_{yz} = a_{yy}/3 \quad (149d)$$

$$a_{xx} = \frac{\alpha \beta \, k^4 \cos^4 \theta}{\gamma (1 - M_c \cos \theta)^4} \quad (149e)$$

$$a_{xy} = \frac{\alpha \beta \, k^4 f_0^2 \cos^2 \theta}{2\gamma (1 - M_c \cos \theta)^2} \quad (149f)$$

To obtain equation (149) it has been assumed that the modified Bessel function $I_n(x)$ can be approximated by $(1 + 2\pi x)^{-1/2} \exp(x)$ for all values of x . The error in this approximation does not exceed 10%.

These results for Problem ② reveal an interesting effect. For quadrupoles situated in the vicinity of the jet axis, $\gamma \sim 1$, whereas for quadrupoles far from the axis, $\gamma \sim k^{1/2} \gg 1$. As the radius of the ring of quadrupoles increases, the exponential shielding factor (149a) generally

decreases. However, the above variation in γ tends to reduce the far-field pressure, or equivalently, increase the effective shielding.

Referring to Figure 4-28, as the individual members of the ring are moved towards the jet boundary, the shielding of those quadrupoles that lie in the vicinity of the angle θ decreases. On the other hand, the shielding of those quadrupoles that lie in the vicinity of $(\theta + \pi)$ will increase. The net result for shielding of a ring of quadrupoles is a decrease due to the exponential factor but an increase due to the factor γ . This variation in γ was found to be fairly important for jet velocities under 1000 fps but totally unimportant for higher velocities. In this report, γ will be set to unity.

Problem ③

These results are the same as those of Problem ① except the expressions are multiplied by the exponential shielding factor

$$\exp \left(-2k \int_{r_{\sigma}^{(1)}}^{r_{\sigma}^{(2)}} f dr \right)$$

Problem ④

The results are the same as those of Problem ② except

$$\beta = \exp \left(-2k \int_{r_0}^{r_{\sigma}^{(2)}} f dr \right)$$

Also γ is set to unity as discussed under Problem ②.

Problems ⑤ and ⑥

These results are identical to those of Problem ①.

This concludes the derivation of the circumferentially averaged pressure field of a ring of incoherent quadrupoles. It should be emphasized that this derivation is not perfectly rigorous; difficulties arise, for example, when the source is too close to the turning point. The present work suggests a reasonable approach to handle these difficulties. It is believed that the final expressions of this section are accurate enough for use in the prediction of jet noise.

4.3.11 The Directivity of Noise

To predict the directivity of noise, the pressure field of the various quadrupoles must be combined in a specific manner to represent the radiation pattern from convecting and isotropic turbulence. The work of Ribner⁽³⁹⁾ provides these weighting factors as

$$\overline{p^2} \sim (a_{xx} + 4a_{xy} + 2a_{yy} + 2a_{yz}) \quad (150)$$

where $\overline{p^2}$ is the mean square acoustic pressure in the far field. The factor of proportionality in equation (150) is related to the intensity of turbulence, as such, it comes from an aerodynamic mixing calculation. The detailed coupling of jet aerodynamics and acoustics is described in Section 4.7. Observe that equation (150) was also used very successfully by Mani^(37, 38) in his prediction of round jet noise.

Ribner derived (150) for Lighthill's equation. It turns out that for Lilley's equation (150) is essentially correct only for Problems ①, ③, ⑤, and ⑥; in other words, only when the shielding function g^2 is positive at the source. In this case, all the quadrupoles contribute to the noise.

When the shielding function is negative at the source (i.e., Problems ② and ④)

$$\overline{p^2} \sim a_{xx} \quad (151)$$

and the dominant contribution to the far-field pressure comes from an (x - x) quadrupole. The derivation of this result is quite lengthy and will not be reproduced here. Suffice to say that Pao⁽⁴⁵⁾ finds exactly the same result for Phillips' equation. Roughly speaking, the reason is that the time delay is associated only with the x-location of the source. There is no time delay due to the radial location of the source since equation (134) contains no phase factor depending on this quantity.

For example, for Problem ①, (150) becomes

$$\overline{p^2} \sim \frac{\alpha k^4}{(c_0/c_\infty)^4} \frac{(1 - M_0 \cos \theta)^4}{(1 - M_c \cos \theta)^4} \quad (152)$$

so that the unshielded far-field pressure is expected to be amplified by three powers of the Doppler factor. This is determined from (152) and the definition of α (147) and the correction of one Doppler factor as given by Ffowcs-Williams⁽⁶⁾. This fairly low convective amplification is generally observed

in jet noise outside the zone of relative silence Balsa(47, 49). Within the zone of silence the convective amplification becomes seven powers* of the Doppler factor (This is determined from (151), (123a), (148a) and (147)). At low frequencies, this large amplification remains, whereas, at high frequencies, acoustic shielding tends to reduce the far-field sound pressure level, consistent with the actual behavior of jet noise directivities at fixed source frequencies.

4.3.12 Conclusions

Expressions have been derived to predict the directivity of jet noise for arbitrary jet velocity and temperature profiles. The present theory combines the classical ideas of Lighthill, Ribner, and Ffowcs-Williams with those of Mani to provide simple results for the estimation of acoustic shielding.

It is found that due to fluid (rather than source) convection there is additional convective amplification that depends on the jet velocity at the source. The total convective amplification of an eddy can vary from three to seven powers of the Doppler factor depending on the angle to the jet axis. At high frequencies and shallow angles to the jet axis, the sound in the far field is greatly reduced. This is attributed to the shrouding effect of the mean flow.

Outside the zone of silence, jet noise varies as the third power of the average jet density [see equation (152)]. Within the zone of silence, the noise is explicitly proportional to the density. However, there is also an implicit dependence through the exponential shielding integral.

Finally, these acoustic results have been coupled with the calculation of the turbulent properties of jets to provide an absolute prediction of noise; this is presented in Section 4.7. In all of this development only the self-noise is considered, for reasons discussed by Mani(37, 38) and Goldskin⁽⁵¹⁾.

*These factors include the correction of one Doppler factor as given by Ffowcs-Williams(6).

4.4 ACOUSTICS OF FLIGHT NOISE PREDICTION

A detailed discussion of the effect of forward motion on the generation of noise is not the objective of this section. However, the effect of flight on the acoustics of jet noise will be discussed.

These acoustic flight effects are very similar for the Lighthill and Lilley equations; therefore, only a brief outline of the derivation will be given (the classical results for Lighthill's equation are well documented).

4.4.1 Introduction

The effect of aircraft forward motion on jet noise was studied by Ribner(7) and Ffowcs-Williams(6). They find that the acoustic intensity varies as

$$U_{rel}^7 U_J |1 - M_c^* \cos \theta|^{-5} |1 + M_\infty \cos \theta|^{-1}$$

where U_J is the jet velocity (relative to the nozzle), U_{rel} is the jet velocity relative to a stationary observer, M_c^* is the eddy convection Mach number relative to a stationary observer, M_∞ is the acoustic Mach number of the aircraft and θ is the angle to the jet axis.

The above result is based on a rigorous treatment of the acoustics consistent with the Lighthill theory, and on some crude assumptions with respect to the generation of noise (i.e., turbulence).

This result shows that noise should decrease in flight due to the reduction of the turbulent shear (essentially the relative velocity effect, U_{rel}^7) and that noise should increase in the forward quadrant ($90^\circ < \theta < 180^\circ$) due to aircraft motion. Experimental data do behave in this general fashion, although the above scaling principle is, by no means, very accurate.

The purpose of this section is to derive the corresponding results for Lilley's equation. Only the effect of flight on the acoustics is given since this effort is not concerned here with the behavior of turbulence in flight.

4.4.2 Formulation of the Problem

Assume that physical $\underline{x} = (x', y, z)$ space is spanned by a stationary cylindrical coordinate system (r, θ, x') , where x' is along the jet axis. Lilley's equation is given by

$$\begin{aligned}
L(p; U, \mathbf{x}') &= \frac{1}{c^2} D_U^3 p - D_U \Delta p - \frac{d}{dr} (\log c^2) D_U \frac{\partial p}{\partial r} \\
&+ 2 \frac{dU}{dr} \frac{\partial^2 p}{\partial \mathbf{x}' \partial r} = \rho D_U F(\mathbf{x}, t)
\end{aligned} \quad (153a)$$

with

$$D_U = \frac{\partial}{\partial t} + U \frac{\partial}{\partial \mathbf{x}'} \quad (153b)$$

and

$$F = \nabla \cdot \nabla \cdot (\underline{u}' \underline{u}' - \overline{\underline{u}' \underline{u}'}) \quad (153c)$$

The Laplacian is denoted by

$$\Delta = \frac{\partial^2}{\partial (\mathbf{x}')^2} + \frac{\partial^2}{\partial r^2} + \frac{1}{r} \frac{\partial}{\partial r} + \frac{1}{r^2} \frac{\partial^2}{\partial \theta^2} \quad (153d)$$

and t denotes time, p is the acoustic pressure, $c = c(r)$ is the undisturbed speed of sound, $U = U(r)$ is the mean or time average jet velocity and $\rho = \rho(r)$ is the mean jet density. The turbulent velocity fluctuations are given by \underline{u}' and the overbar denotes an appropriate average (u'_r is the radial component). The geometry is illustrated in Figure 4-30.

The quantity F is the source of noise; only the self-noise part is considered for the reasons discussed by Mani(37). At infinity, the jet velocity is assumed to have a nonzero value U_∞ , so that in the present section the acoustics of a jet placed in a large wind tunnel of free stream U_∞ will be considered. It is shown how these results can be used to obtain the sound pressure level in flight in section 4.4.5.

4.4.3 Solution of the Problem

The solution of the above problem is obtained by the techniques discussed in section 4.3. Again, there are six equivalence classes of problems, but only one of these will be considered in detail. This is the case in which the shielding function g^2 (123a) has no turning point.

The effect of a nonzero tunnel or jet velocity at infinity is extremely simple for the acoustics and results in referencing all velocities to the free stream U_∞ . Hence, the expressions derived in section 4.3 (for $U_\infty = 0$) are directly applicable provided that the following replacement of variables occurs:

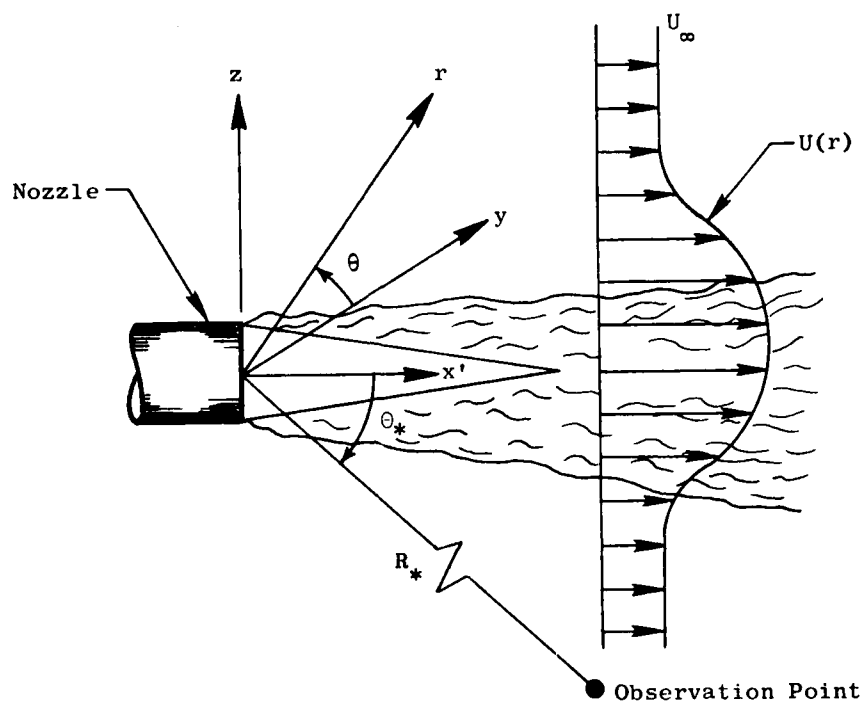


Figure 4-30. Geometry of the Problem.

$$M_c \rightarrow \tilde{M}_c = M_c - M_\infty \quad (154a)$$

$$M \rightarrow \tilde{M} = M - M_\infty \quad (154b)$$

where on the right hand sides of (154), M and M_c are the jet and source convection velocities (normalized by c_∞ = speed of sound at infinity) relative to the nozzle, and $M_\infty = U_\infty/c_\infty$ is the free stream Mach number. A derivation of this equivalence principle is given by Balsa⁽⁵⁴⁾.

It will now be convenient to treat a "stationary" source for which $M_c = 0$. The effects of source convection will be introduced at a later stage through a moving turbulence correlation.

From equations (121) and (144b) of the previous section and by the principle of superposition, it is possible to show that

$$p = \frac{\rho_\infty}{4\pi R (1 + M_\infty \cos \theta)} \int \frac{c_\infty}{c_o} \frac{dx_o}{1 - \tilde{M}_o \cos \theta} F[\underline{x}_o, t - R/c_\infty + \tau] \quad (155a)$$

where

$$\tau = - \int_0^\infty (g - g_\infty) \frac{dr}{c_\infty} + \frac{\underline{x}_o \cdot \underline{\zeta}_o}{c_\infty (1 + M_\infty \cos \theta)} \quad (155b)$$

$$\underline{\zeta} = (\zeta_1, \zeta_2, \zeta_3) = (\cos \theta, \Gamma \cos \theta, \Gamma \sin \theta) \quad (155c)$$

and

$$\Gamma = \left[\frac{(1 - \tilde{M} \cos \theta)^2}{(c/c_\infty)^2} - \cos^2 \theta \right]^{1/2} \quad (155d)$$

Here ρ_∞ , c_∞ , g_∞ are the values of the density, speed of sound and shielding function at infinity, $R \rightarrow \infty$ is the (retarded) distance from the jet and θ is the (retarded) angle to the jet axis. The subscript "o" denotes the value of a quantity at the source point \underline{x}_o .

$$g = \Gamma / (1 + M_\infty \cos \theta) \quad (156a)$$

and

$$\xi = \int_0^r g \, dr \quad (156b)$$

The integral in equation (155a) is evaluated over the jet volume. An approximation implied in the validity of (155a) is that $\xi_0 \approx g_0 r_0$.

The principal result (155a) expresses the far-field pressure as a suitable integral of the double divergence of the Lighthill stress tensor evaluated at the retarded time. The effects of the shrouding jet are shown in the factor $(c_\infty/c) (1 - \tilde{M} \cos \theta)^{-1}$ and in the coefficient Γ . If $(c/c_\infty) = 1$ and $\tilde{M} = 0$, $\Gamma = \sin \theta$. Note that the components of $\underline{\zeta}$ in (155c) are written in the order x' , y , and z .

The relationship between the retarded coordinates (R, θ) and actual (tunnel) coordinates (R_*, θ_*) is given by Morse and Ingard (55)

$$\frac{R}{R_*} = \frac{1}{(1 + M_\infty^2 - 2M_\infty \cos \theta)^{1/2}} \quad (157a)$$

$$\theta_* = \cos^{-1} \left\{ \frac{\cos \theta - M_\infty}{(1 + M_\infty^2 - 2M_\infty \cos \theta)^{1/2}} \right\} \quad (157b)$$

For a definition of tunnel coordinates, see Figure 4-30.

4.4.4 Results for the Spectrum Using Moving Correlation

The purpose here is to give the expression for the 1/3 octave band spectrum of the noise of a jet placed in a wind tunnel. The results can be written down by inspection from the derivation presented by Goldstein (51).

Define the autocorrelation of the acoustic pressure at a fixed point in the far field by

$$P(\tau) = \overline{p(t) p(t+\tau)} = \int_{-\infty}^{\infty} p(t) p(t+\tau) \, dt \quad (158)$$

where τ is an arbitrary time delay. The power spectrum of jet noise is defined as

$$I_\omega = \frac{1}{2\pi} \int_{-\infty}^{\infty} P(\tau) \exp(i\omega\tau) \, d\tau \quad (159)$$

so that from Goldstein(51)

$$\omega I_{\omega} = \frac{\pi}{2} \frac{\rho_{\infty}^2}{c_{\infty}^4 R^2} \left(\frac{\omega}{1 + M_{\infty} \cos \theta} \right)^5 \frac{\zeta_i \zeta_j \zeta_k \zeta_{\ell}}{(1 + M_{\infty} \cos \theta)} \int \left(\frac{c_{\infty}}{c_0} \right)^2 \frac{d\mathbf{x}_0}{(1 - \tilde{M}_0 \cos \theta)^2} \times H_{ijk\ell} \left\{ \frac{\mathbf{x}_0}{c_{\infty}(1 + M_{\infty} \cos \theta)}, \omega \frac{1 - \tilde{M}_c \cos \theta}{1 + M_{\infty} \cos \theta} \right\} \quad (160a)$$

The quantity ωI_{ω} is essentially the 1/3 octave band spectrum, repeated indices denote summation, and the integral without limit denotes integration over the jet volume. The observed radian frequency is denoted by ω .

The spectrum of the moving turbulence correlation is denoted by

$$H_{ijk\ell}(\underline{x}, \underline{k}, \omega) = \frac{1}{(2\pi)^4} \int_{-\infty}^{\infty} d\tau \int_{-\infty}^{\infty} d\underline{\xi} R_{ijk\ell}(\underline{x}, \underline{\xi}, \tau) \exp[i\omega(\tau - \underline{k} \cdot \underline{\xi})] \quad (160b)$$

Note that $R_{ijk\ell}(\underline{x}, \underline{\xi}, \tau)$ is the usual convecting two point correlation of the Lighthill stress tensor at points $(\underline{x} + \underline{\xi}/2)$ and $(\underline{x} - \underline{\xi}/2)$. As such \underline{x} is the mean coordinate of the points and $\underline{\xi}$ is the separation vector. The velocity fluctuations at these points are correlated with a time delay τ . The turbulence is assumed to convect at Mach number M_c relative to the nozzle and $\tilde{M}_c = M_c - M_{\infty}$.

The interpretation of equation (160a) is interesting. The noise that is observed at frequency ω in the tunnel is generated by turbulence at frequency $\omega(1 - M_c \cos \theta)/(1 + M_{\infty} \cos \theta)$. For $M_{\infty} = 0$ this reduces to the well known Doppler shifted frequency. The wave number of turbulence that contributes to this noise is simply $\omega c_0(1 + M_{\infty} \cos \theta)^{-1}/c_{\infty}$. The estimation of $R_{ijk\ell}$ or $H_{ijk\ell}$ comes from the aerodynamic mixing calculation.

4.4.5 Spectrum of Noise in Flight

Consider now a nozzle convecting to the left at Mach number $M_{\infty} = U_{\infty}/c_{\infty}$ (Figure 4-31). Imposing a uniform velocity of U_{∞} on this system renders the nozzle stationary and produces a uniform stream of speed U_{∞} at infinity. This corresponds to the previous wind tunnel situation except for the following modification: when the nozzle is in forward flight, the observer is generally stationary relative to the ambient so that there is motion between the

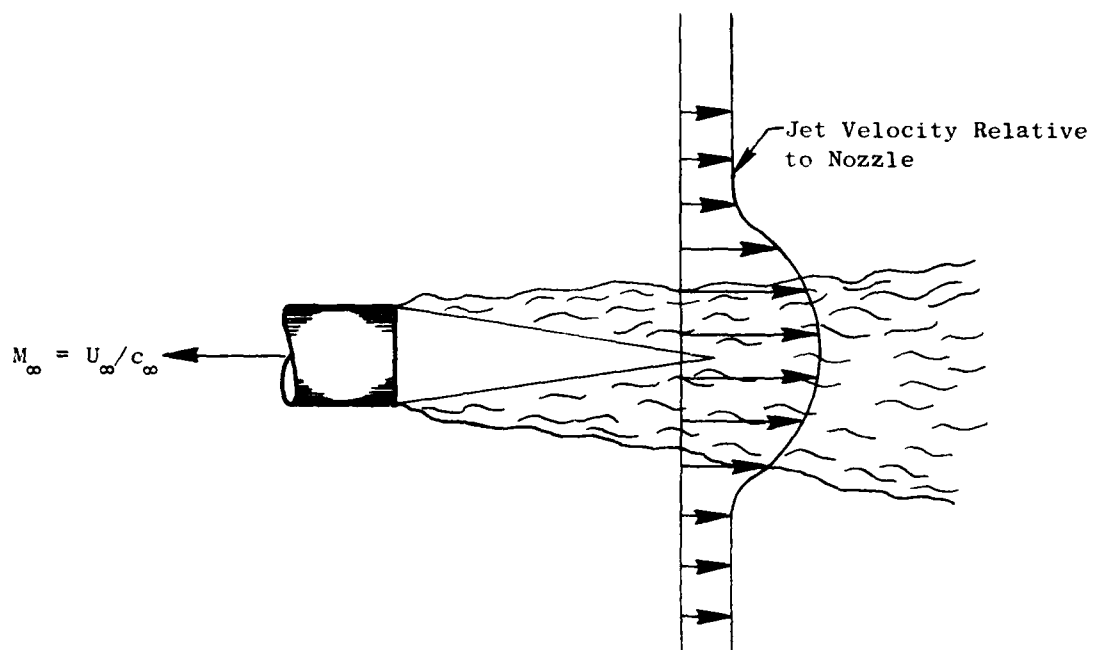


Figure 4-31. Nozzle in Forward Flight.

observer and the nozzle. On the other hand, in the wind tunnel there is no motion between the observer and the nozzle. To account for this difference, one must Doppler shift the tunnel results by the amount $\Omega = \omega / (1 + M_\infty \cos \theta)$.

Thus the spectrum of the sound pressure level in forward flight becomes

$$W = \frac{\pi}{2} \frac{\rho_\infty^2}{c_\infty^4 R^2} \Omega^5 \frac{\zeta_i \zeta_j \zeta_k \zeta_l}{(1 + M_\infty \cos \theta)} \int \left(\frac{c_\infty}{c_0} \right)^2 \frac{d\mathbf{x}_0}{(1 - \tilde{M}_0 \cos \theta)^2} H_{ijkl} \left\{ \frac{\mathbf{x}_0}{c_\infty}, \frac{\Omega \zeta_0}{c_\infty}, \Omega (1 - \tilde{M}_c \cos \theta) \right\} \quad (161)$$

where Ω is the observed frequency.

4.4.6 Discussion

First it is interesting to consider the limiting form of equation (161) as $M_\infty \rightarrow 0$. In this case

$$\tilde{M} \rightarrow M$$

$$\tilde{M}_c \rightarrow M_c$$

so that, apart from the dynamic factor of $(1 + M_\infty \cos \theta)^{-1}$, the spectrum of the noise from a stationary nozzle is functionally identical to that of a nozzle in forward flight provided that in the latter case all velocities are referenced to U_∞ .

Forward flight also produces an amplification factor of $(1 + M_\infty \cos \theta)^{-1}$ which will increase slightly the noise in the forward quadrant ($90^\circ < \theta < 180^\circ$).

Actually, forward flight will change the magnitude of the spectrum of turbulence somewhat because of reduced mixing. Therefore, in addition to the above relatively simple acoustic effects, there are more complex effects due to changes in the turbulence structure. These can be calculated from a computer model for the aerodynamic mixing but it is very difficult to give an accurate a priori estimate for them with any kind of generality.

4.4.7 Conclusions

To predict jet noise in flight, one can use the expressions derived in sections 4.3.10 and 4.3.11, provided that a convective amplification factor $(1 + M_\infty \cos \theta)^{-1}$ is adjoined to the mean square acoustic pressure and all

velocities (jet and convection) are referenced to the flight velocity. In other words, nozzle fixed jet and convection velocities are to be replaced by the corresponding observer fixed velocities. Apart from the Doppler shift of $\Omega = \omega / (1 + M_{\infty} \cos \theta)$, there is complete equivalence between the spectra in flight and in a wind tunnel. They both produce a dynamic "correction" of one Doppler factor.

4.5 REICHARDT'S THEORY FOR ARBITRARY JET FLOWS

4.5.1 Introduction

An essential ingredient to the study of jet noise is the description of the jet plume flow field. The turbulent mixing of the exhaust flow with the ambient surroundings constitutes a primary noise source mechanism. The spatial distributions of plume mean (time-averaged) properties such as velocity, density, etc., determine the degree to which the generated noise is amplified due to convection and/or shielded as it propagates through the plume to the ambient field. Possible approaches to reducing the noise emitted by a turbulent jet include: (1) alteration of the mixing process, (2) reduction of convection effects, and (3) reinforcement of the flow shielding effects. These concepts for reducing jet noise require a thorough grasp of the fluid mechanics of turbulent jets, and, therefore, a method for predicting turbulent jet flows is indispensable. Traditionally, jet noise reduction has been achieved by exhaust nozzle area shaping and flow division. Examples of area shaping include elliptic and rectangular nozzles, multiple-lobe nozzles, etc. Examples of flow division include multitube nozzles and multispoke/chute nozzles. A survey of experimental results pertinent to these types of jet nozzles was given by Stringas and Mani(56); a major conclusion of this survey was that a systematic approach to the understanding of jet flow structure for arbitrarily shaped nozzles was required to provide a technological basis for design optimization without resorting to expensive and time-consuming parametric testing.

The development of an accurate computational prediction method for the flow field of turbulent jets emanating from nozzles of arbitrary geometric shape was undertaken to fulfill the requirements described above. Several approaches to modeling free turbulent flows relevant to the jet plume problem have been established for simple round jets. An excellent review of the current state of the art on turbulent flow modeling has been published by Launder and Spalding(57). This review covers the range in modeling complexity from the simple 1925 Prandtl mixing length model to the more recent highly sophisticated multiequation closure models which require numerical finite-difference solution techniques.

Motivated by the desire to establish a prediction method for turbulent jets of arbitrary initial cross section, an assessment was made of the past and current modeling approaches, with a view toward selecting the approach which would require a minimal amount of development, and at the same time provide (potentially) the required accuracy for the intended application. Consideration was also given to ease of implementation as a practical computational procedure. The method finally selected for further development was that of Kendal(58), which is an extension of the work of Alexander et al.(59) to arbitrary nozzle shapes. The method is based on Reichardt's(60) inductive theory of free turbulence; a key feature of this theory was the establishment of a linear governing equation for momentum transport. This linearity feature permits invoking the superposition principle to construct quite complex flow fields utilizing elementary solution forms, considerably simplifying the mathematical and computational aspects of the problem. Although

more modern and rigorous methods were available for simple jet flows, there was no other technique available which offered the capability of modeling jet flows typical of aircraft engine suppressor nozzles (e.g., multi-lobes, multitubes, multispoke/chute nozzles).

Although the developments of Reichardt's(60) theory, as proposed by Alexander(59) and Kendall(58), have been approached from the viewpoint of superposition of elemental "point source" jet solutions to construct complex jet solutions, a more formal mathematical treatment is given herein which recognizes the analogy with transient heat conduction problems. Additionally, a formal extension to include the effects of prescribed pressure gradients on the plume is also given, in anticipation of recognizing the influence of variable base pressure effects on multielement nozzle flows. Considerable attention is also given to calculation of those turbulent structure properties relevant to noise generation. The formal mathematical treatment employed herein, utilizing Green's function methods, is shown to yield results identical to those obtained using the superposition approach.

During the course of the theoretical development, certain constants related to the mixing and entrainment properties of the flow arise. These constants must be evaluated experimentally, and methods for deriving these constants from experimental data are discussed. Comparisons of predicted and measured flow field quantities are presented for several nozzle geometries of interest, and the strengths and weaknesses of the prediction method are discussed. Finally, suggestions are made for extensions and improvements in the theoretical model.

4.5.2 Basic Equations and Assumptions

Consider a jet emanating from a nozzle of arbitrary cross section, as shown in Figure 4-32. The governing equations for axial momentum transport and conservation of mass, in absence of laminar viscous stresses, are as follows:

$$\frac{\partial u}{\partial t} + u \frac{\partial u}{\partial x} + v \frac{\partial u}{\partial y} + w \frac{\partial u}{\partial z} + \frac{1}{\rho} \frac{\partial p}{\partial x} = 0 \quad (162)$$

$$\frac{\partial \rho}{\partial t} + \frac{\partial}{\partial x} (\rho u) + \frac{\partial}{\partial y} (\rho v) + \frac{\partial}{\partial z} (\rho w) = 0 \quad (163)$$

where (u, v, w) are the (x, y, z) - components of instantaneous fluid velocity, respectively; and p is the static pressure and ρ is the density. Time is denoted by t. By multiplying equation (162) by ρ and combining with (163), the conservative form of the momentum equation is arrived at:

$$\frac{\partial}{\partial t} (\rho u) + \frac{\partial}{\partial x} (\rho u^2) + \frac{\partial}{\partial y} (\rho uv) + \frac{\partial}{\partial z} (\rho uw) + \frac{\partial p}{\partial x} = 0 \quad (162a)$$

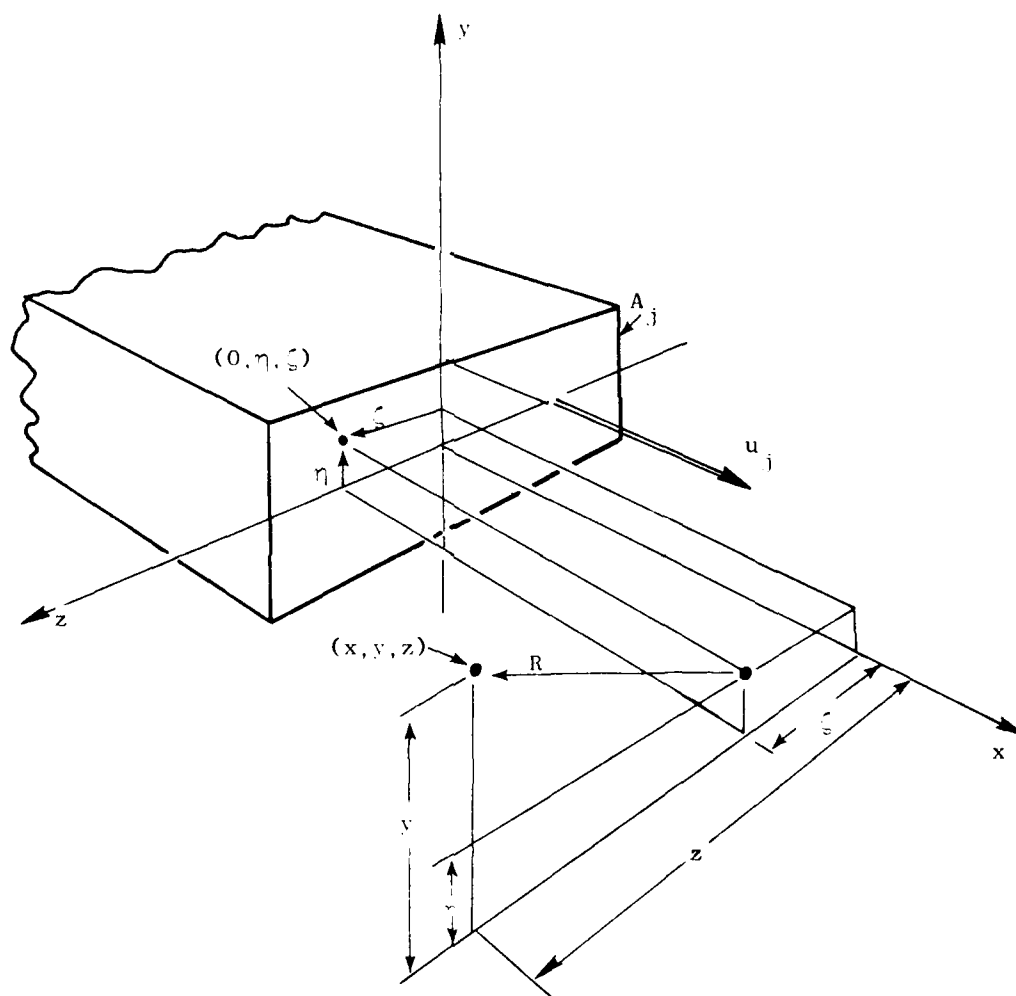


Figure 4-32. Jet Nozzle Flow Coordinate System and Nomenclature.

Consider next the instantaneous flow variables to be comprised of a mean value and an unsteady, fluctuating component; e.g., $u = \bar{u} + u'$, $v = \bar{v} + v'$, etc., where overbars denote time-average values and primes denote unsteady components. The unsteady (turbulent) component has the property that

$$\lim_{T \rightarrow \infty} \frac{1}{T} \int_t^{t+T} u' dt = 0$$

With these distinctions, it can be shown that equation (162), after time-averaging and assuming that density fluctuations are small ($\rho'/\bar{\rho} \ll 1$), has the well-known form

$$\begin{aligned} \bar{\rho} \left(\bar{u} \frac{\partial \bar{u}}{\partial x} + \bar{v} \frac{\partial \bar{u}}{\partial y} + \bar{w} \frac{\partial \bar{u}}{\partial z} \right) + \frac{\partial \bar{p}}{\partial x} = - \frac{\partial}{\partial x} (\bar{\rho} \overline{u'^2}) \\ - \frac{\partial}{\partial y} (\bar{\rho} \overline{u'v'}) - \frac{\partial}{\partial z} (\bar{\rho} \overline{u'w'}) \end{aligned} \quad (164)$$

The assumption that terms involving ρ' are negligible amounts to an assumption that the turbulence Mach number $|u'/c| \ll 1$. See, for example, Hinze⁽⁶¹⁾, p. 19.

Equation (162a) can also be time-averaged, and the mean quantities can be assumed invariant with time. The result is as follows:

$$\frac{\partial}{\partial x} (\overline{\rho u^2}) + \frac{\partial}{\partial y} (\overline{\rho uv}) + \frac{\partial}{\partial z} (\overline{\rho uw}) + \frac{\partial \bar{p}}{\partial x} = 0 \quad (164a)$$

Both equations (164 and 164a) contain the same simplifying assumptions. Equation (164) is the classical turbulent flow equation usually employed to analyze turbulent flow problems, and explicitly displays the turbulent stresses $(\bar{\rho} \overline{u'^2})$, $(\bar{\rho} \overline{u'v'})$, $(\bar{\rho} \overline{u'w'})$ on the right-hand side. Equation (164a), which is employed herein, contains these same quantities implicitly through the relations

$$\left. \begin{aligned} \overline{\rho u^2} &\approx \bar{\rho} \overline{u^2} + \bar{\rho} \overline{u'^2} \\ \overline{\rho uv} &\approx \bar{\rho} \overline{uv} + \bar{\rho} \overline{u'v'} \\ \overline{\rho uw} &\approx \bar{\rho} \overline{uw} + \bar{\rho} \overline{u'w'} \end{aligned} \right\} \quad (165)$$

The point to be made is that, in the Reichardt approach which follows, the starting point is the same as in the classical theories of turbulence, and that the departure arises in modeling the turbulent shear stresses, an area which by no means has a universally accepted method of approach.

The Reichardt⁽⁶⁰⁾ hypothesis that the transverse momentum fluxes are proportional to the corresponding traverse gradients of the axial momentum flux is now invoked. A discussion of the implications of this hypothesis is given by Hinze⁽⁶¹⁾, pp. 290-293. The following relationships are therefore assumed:

$$\overline{\rho uv} = -\lambda(x) \frac{\partial}{\partial y} (\overline{\rho u^2}); \quad \overline{\rho uw} = -\lambda(x) \frac{\partial}{\partial z} (\overline{\rho u^2}) \quad (166)$$

The proportionality factor λ is assumed to be at most a function of axial coordinate x . Substituting equation (166) into (164a) yields the following governing equation for $\overline{\rho u^2}$:

$$\frac{\partial}{\partial x} (\overline{\rho u^2}) - \lambda(x) \left[\frac{\partial^2}{\partial y^2} (\overline{\rho u^2}) + \frac{\partial^2}{\partial z^2} (\overline{\rho u^2}) \right] = -\frac{\partial p}{\partial x} \quad (167)$$

Reichardt's original theory presumed constant static pressure throughout the flow, as is usually the case for wakes, jets, etc. The pressure gradient term will be retained herein, however, in the hope of being able to assess reduced base pressure effects typically occurring in multielement nozzle flows, as discussed in the introduction. The assumption is made that the pressure distribution in the jet plume is known, either from experiment or from an independent auxiliary calculation. The pressure gradient term in equation (167) is therefore treated as a known "source" term. This approach was first suggested by Kantola⁽⁶²⁾.

Let $f = \overline{\rho u^2}$ and $Q = -\partial p / \partial x$. Equation (167) can therefore be rewritten as follows:

$$L(f) = Q(x, y, z) \quad (168)$$

where

$$L(f) = \left\{ \frac{\partial}{\partial x} - \lambda(x) \left[\frac{\partial^2}{\partial y^2} + \frac{\partial^2}{\partial z^2} \right] \right\} f \quad (169)$$

A solution of equation (168) is sought with the appropriate boundary conditions. As pointed out by Kantola⁽⁶²⁾, equation (168) is analogous to the diffusion equation for transient heat conduction, the momentum transport coefficient λ corresponding to a time-varying thermal conductivity. A list of analogous properties is presented below:

Reichardt Theory	Thermal Diffusion
$\overline{\rho u^2}$ axial momentum	T = temperature
x axial direction	t = time
$\lambda(x)$ = momentum transport coefficient	$\alpha(t)$ = thermal diffusivity

In the Reichardt theory, the total momentum at the nozzle exit plane $x = 0$ is conserved in the axial direction in the same manner as the total heat energy is conserved with time in the thermal diffusion problem. The analogous thermal problem which corresponds to the jet momentum problem is a time decay of an initial temperature distribution, with a time-varying thermal conductivity. From this analogy, it is apparent that the jet momentum must be specified over the entire exit plane $x = 0$.

It has been implicitly assumed that Reichardt's mixing hypothesis, equation (166), holds even in the presence of a pressure gradient. This assumption may be questioned on the grounds that pressure gradients may alter the transverse momentum independent of the mixing process itself. To examine this effect, consider the time-averaged transverse momentum (y, z) equations, as follows:

$$\frac{\partial}{\partial x} (\overline{\rho uv}) + \frac{\partial}{\partial y} (\overline{\rho v^2}) + \frac{\partial}{\partial z} (\overline{\rho vw}) = - \frac{\partial \bar{p}}{\partial y} \quad (170)$$

$$\frac{\partial}{\partial x} (\overline{\rho uw}) + \frac{\partial}{\partial y} (\overline{\rho vw}) + \frac{\partial}{\partial z} (\overline{\rho w^2}) = - \frac{\partial \bar{p}}{\partial z}$$

Assuming that the jet plume flow direction is primarily axial, such that $v/u \ll 1$ and $w/u \ll 1$, the terms $\overline{\rho v^2}$, $\overline{\rho vw}$ and $\overline{\rho w^2}$ are probably much smaller than the terms involving $\overline{\rho uv}$ and $\overline{\rho uw}$. Equations (170) can then be approximated by

$$\frac{\partial}{\partial x} (\overline{\rho uv}) \approx - \frac{\partial \bar{p}}{\partial y}; \quad \frac{\partial}{\partial x} (\overline{\rho uw}) \approx - \frac{\partial \bar{p}}{\partial z} \quad (171)$$

Thus, the additional contributions to the transverse momentum by the traverse pressure gradients are given by direct integration of equation (171):

$$\begin{aligned} \overline{\rho uw} &\approx (\overline{\rho uv})_0 - \int_0^x (\partial \bar{p} / \partial y) d\xi \\ \overline{\rho uv} &\approx (\overline{\rho uw})_0 - \int_0^x (\partial \bar{p} / \partial z) d\xi \end{aligned} \quad (172)$$

Assuming that the exit-plane distributions of $\overline{\rho uv}$ and $\overline{\rho uw}$ are known, Reichardt's mixing hypothesis is then modified by the additional contributions given by equation (172):

$$\begin{aligned}\overline{\rho uv} &= (\overline{\rho uv})_0 - \int_0^x (\partial \bar{p} / \partial y) d\xi - \lambda(x) \frac{\partial}{\partial y} (\overline{\rho u^2}) \\ \overline{\rho uw} &= (\overline{\rho uw})_0 - \int_0^x (\partial \bar{p} / \partial z) d\xi - \lambda(x) \frac{\partial}{\partial z} (\overline{\rho u^2})\end{aligned}\quad (173)$$

Substitution of relations (173) into (164a) yields the same equation form as (168, 169), but with $Q(x, y, z)$ now defined as follows:

$$\begin{aligned}Q(x, y, z) &= - \left[\frac{\partial}{\partial y} (\overline{\rho uv})_0 + \frac{\partial}{\partial z} (\overline{\rho uw})_0 \right] - \frac{\partial \bar{p}}{\partial x} \\ &+ \int_0^x \left[\frac{\partial^2 \bar{p}}{\partial y^2} + \frac{\partial^2 \bar{p}}{\partial z^2} \right] d\xi\end{aligned}\quad (174)$$

If the flow is axial at the exit plane, the first term in (174) vanishes. If the transverse pressure gradients are small and/or constant, the third term in (174) vanishes. Therefore, the approximation $Q \approx -\partial \bar{p} / \partial x$ is not very restrictive for practical applications. It will henceforth be assumed that $Q = -\partial \bar{p} / \partial x$, although the exact form for Q assumed does not affect the solution procedure. It will also be assumed that equation (166) is sufficient to model the Reichardt hypothesis.

For heated jets, the temperature distributions are also required. The stagnation enthalpy flux, in absence of viscous (molecular) dissipation and heat losses due to conduction and radiation, is a conserved property. Defining stagnation enthalpy H as

$$H = c_p T + \frac{1}{2} (u^2 + v^2 + w^2) \sim c_p T_e \quad (175)$$

where c_p is the specific heat at constant pressure and T_e is the ambient temperature, the governing equation for stagnation enthalpy transport is given by

$$\frac{\partial H}{\partial t} + u \frac{\partial H}{\partial x} + v \frac{\partial H}{\partial y} + w \frac{\partial H}{\partial z} = \frac{1}{\rho} \frac{\partial p}{\partial t} \quad (176)$$

Similar to the axial momentum transport equation development, equation (176) is combined with the continuity equation (177) and time-averaged to yield the following:

$$-\frac{\partial}{\partial x} (\overline{\rho u H}) + \frac{\partial}{\partial y} (\overline{\rho v H}) + \frac{\partial}{\partial z} (\overline{\rho w H}) = 0 \quad (177)$$

Analogous to the Reichardt hypothesis concerning momentum transport, it is assumed that the transverse momentum flux is proportional to the corresponding transverse gradient of axial enthalpy flux:

$$\overline{\rho v H} = -\lambda_h(x) \frac{\partial}{\partial y} (\overline{\rho u H}) ; \quad \overline{\rho w H} = -\lambda_h(x) \frac{\partial}{\partial z} (\overline{\rho u H}) \quad (178)$$

Substitution of relations (178) into (177) yields the following governing equation for $(\overline{\rho u H})$:

$$\frac{\partial}{\partial x} (\overline{\rho u H}) - \lambda_h(x) \left[\frac{\partial^2}{\partial y^2} (\overline{\rho u H}) + \frac{\partial^2}{\partial z^2} (\overline{\rho u H}) \right] = 0 \quad (179)$$

Hence the governing equation for enthalpy flux $(\overline{\rho u H})$ has the same form as equations (167) or (168) and (169) for momentum transport, except that the right-hand side $Q=0$. The solution of equations (168) and (169) applies equally to (179). A new variable, the enthalpy transport coefficient $\lambda_h(x)$, is introduced which is also permitted to vary with downstream distance x . As will be subsequently shown, these transport coefficients λ and λ_h must be evaluated from experimental measurements.

4.5.3 General Solution

A formal solution to equation (168) can be obtained utilizing the Green's function techniques discussed, e.g., by Greenberg⁽⁶³⁾. With the boundary condition that the transverse gradients of f , i.e., $\partial f/\partial y$ and $\partial f/\partial z$, vanish as $y \rightarrow \infty$ and $z \rightarrow \infty$, respectively, the following general solution has been obtained:

$$f(x, y, z) = \iiint_V G Q dV + \iint_S [fG]_{\xi=0} dS \quad (180)$$

where $G(\xi, \eta, \zeta; x, y, z)$ is the Green's function which satisfies the adjoint equation to (168) and (169),

$$-\frac{\partial G}{\partial \xi} - \lambda(\xi) \left[\frac{\partial^2 G}{\partial \eta^2} + \frac{\partial^2 G}{\partial \zeta^2} \right] = \delta(\xi-x) \delta(\eta-y) \delta(\zeta-z) \quad (181a)$$

subject to the boundary conditions

$$\left[\frac{\partial G}{\partial \eta} \right]_{\eta \rightarrow \pm \infty} = 0, \quad \left[\frac{\partial G}{\partial \zeta} \right]_{\zeta \rightarrow \pm \infty} = 0, \quad [G]_{\xi \rightarrow \infty} = 0 \quad (181b)$$

The volume integral V is over the domain of f , i.e., $V(0 \leq \xi \leq \infty, -\infty \leq \eta \leq \infty, -\infty \leq \zeta \leq \infty)$, where (ξ, η, ζ) are the variables of integration corresponding to the (x, y, z) coordinate directions, respectively. The surface integral S is over the nozzle exit plane at $x = 0$, i.e., $S(-\infty \leq \eta \leq \infty, -\infty \leq \zeta \leq \infty)$. The first term in equation (180) represents the effect of the pressure gradient source term Q on f , and the second term represents the initial datum plane diffusion as a function of axial distance x . The Green's function solution which satisfies (181) is given by the following:

$$G(\xi, \eta, \zeta; x, y, z) = \frac{H(x - \xi)}{4\pi a^2} e^{-(y-\eta)^2/4a^2} e^{-(z-\zeta)^2/4a^2} \quad (182)$$

where

$$a^2 = \int_{\xi}^x \lambda(x) dx, \quad a_0^2 = \int_0^x \lambda(x) dx \quad (183)$$

and H is the Heaviside step function. Substitution of (182) into equation (180) yields the final form of the general solution of equation (168), which applies to either $f = \overline{\rho u^2}$ or $f = \overline{\rho uH}$, as follows:

$$\begin{aligned} f(x, y, z) = & \int_0^x \frac{1}{4\pi a^2} \int_{-\infty}^{\infty} \int_{-\infty}^{\infty} Q e^{-(y-\eta)^2/4a^2} e^{-(z-\zeta)^2/4a^2} d\eta d\zeta d\xi \\ & + \int_{-\infty}^{\infty} \int_{-\infty}^{\infty} \frac{1}{4\pi a_0^2} f(0, \eta, \zeta) e^{-(y-\eta)^2/4a_0^2} e^{-(z-\zeta)^2/4a_0^2} d\eta d\zeta \end{aligned} \quad (184)$$

Thus, given the exit - plane ($\xi = 0$) distribution of f and the distribution of the source function Q throughout the field, the value of f at any point (x, y, z) can be computed by equation (184). For momentum transport, $f = \overline{\rho u^2}$ and $Q = -\partial \overline{p}/\partial x$. For heat transport, $f = \overline{\rho uH}$ and $Q = 0$. It may be noted that, in recent approaches to turbulent flow modeling, an analogy is usually drawn between transport of heat and the transport of any conservative scalar property of the flow, such as species concentration, turbulent kinetic energy, and even turbulent mixing length scale [see, e.g., Launder and Spalding (57)]. This analogy can also apply to Reichardt's theory as developed herein as well.

4.5.4 Experimental Evaluation of Empirical Constants

The general solution for the momentum and enthalpy flux given by equation (184) is characterized by a transport coefficient $\lambda(x)$ and a corresponding mixing layer thickness $a(\xi, x)$, the two quantities being related through equation (183). These quantities are permitted to vary with axial distance along the plume, but should be independent of cross-stream coordinates (y, z) . Ideally, these parameters should be independent of nozzle shape, type, and exhaust plane conditions.

Prior to performing a numerical evaluation of the empirical mixing parameters (λ, a) , it is convenient to recast equation (184) in cylindrical coordinates, since, in many cases of interest, the symmetry of the problem can be exploited in this coordinate system. In the cylindrical coordinate system, a point at (x, y, z) is defined by cylindrical coordinates (x, r, ϕ) , where $r = \sqrt{y^2 + z^2}$ and $\phi = \tan^{-1}(z/y)$. The integration variables (ξ, η, ζ) have corresponding cylindrical coordinates (ξ, v, α) , where $v = \sqrt{\eta^2 + \zeta^2}$ and $\alpha = \tan^{-1}(\zeta/\eta)$. Equation (184) can therefore be written in the following form:

$$f(x, r, \phi) = \int_0^x \frac{1}{\pi b^2} \int_0^{2\pi} \int_0^\infty Q e^{-R^2/b^2} v dv d\alpha d\xi \quad (185)$$

$$+ \int_0^{2\pi} \int_0^\infty \frac{1}{\pi b^2} f(0, v, \alpha) e^{-R^2/b^2} v dv d\alpha$$

$$\left. \begin{aligned} \text{where} \quad R^2 &= (z-\zeta)^2 + (y-\eta)^2 \\ \text{or} \quad R^2 &= r^2 + v^2 - 2rv \cos(\phi-\alpha) \end{aligned} \right\} \quad (186)$$

$$\text{and} \quad b = 2a \quad (187)$$

For the case of free turbulent mixing with no pressure gradients, ($Q=0$), equation (185) agrees exactly with the result of Grose and Kendall⁽⁵⁸⁾ obtained using the superposition technique. Note that henceforth the parameter $b=2a$ will be considered the characteristic mixing layer thickness instead of a , to be consistent with previous notation of prior authors. The coordinate notation in cylindrical coordinates is illustrated in Figure 4-33.

In order to evaluate the parameters b and λ , the special case of an axisymmetric round jet with no pressure gradients is considered. Also, it is assumed that there is uniform flow at the nozzle exit plane. For this case equation (185) reduces to

$$f(x, r, \phi) = \frac{f_j}{\pi b_o^2} \int_0^{2\pi} \int_0^{d/2} e^{-R^2/b_o^2} v dv d\alpha \quad (188)$$

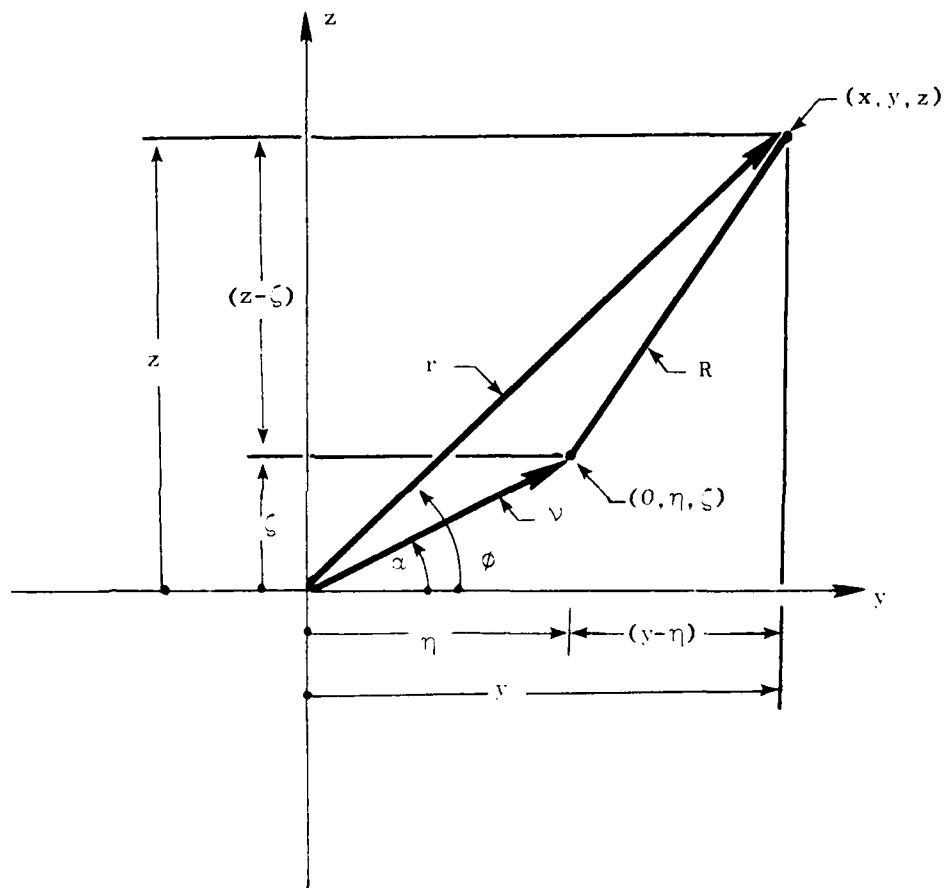


Figure 4-33. Relations Between Cartesian and Cylindrical Coordinates for Field Point (x, y, z) and Exit-Plane Point $(0, \eta, \zeta)$.

where d is the nozzle exit diameter. Along the jet centerline $r=0$, the argument R reduces to x , and the above expression can be integrated directly to give

$$f(x) = f(x,0,0) = f_j \left[1 - e^{-d^2/4b_0^2} \right] \quad (189)$$

Thus, if the variation of b_0 with x is known, the centerline distribution of f can be computed from equation (189). Conversely, if the centerline distribution of f is available from experiment, the function $b_0(x)$ can be inferred. In particular for the axisymmetric round jet, equation (189) yields

$$\frac{b_0(x)}{d} = \frac{1}{2} \left[-\ln \left[1 - f(x)/f_j \right] \right]^{-1} \quad (190)$$

If first the incompressible or isothermal jet with $f = \overline{u^2}$ is considered, then $f(x)/f_j = [u(x)/u_j]^2$, where u_j is the jet nozzle exit velocity. Unfortunately, within experimental accuracy, $u(x)=u_j$ for the first few diameters ($0 \leq x \leq 4d$), so that equation (190) cannot be used to evaluate $b(x)$ in that region. However, if we consider the region of the jet where centerline velocity decay is predominant, i.e., $x/d \gg 1$, so that $f(x)/f_j$ is appreciably less than unity, then equation (190) can be approximated by

$$\frac{b_0(x)}{d} = \frac{1}{2} \left[\sqrt{\frac{f_j}{f(x)}} \right]^{-1} = \frac{1}{2} \sqrt{\frac{f_j}{f(x)}} = \frac{1}{2} \frac{u_j}{u(x)} \quad (191)$$

where $u(x)$ is the jet centerline ($r=0$) mean velocity distribution. From measurements of $u(x)$, $b_0(x)$ can then be evaluated. It is a well-known result (see, e.g., VonGlahn et al, ref. 67) that the centerline velocity $u(x)$ decays as $1/x$ in the fully-developed similarity region. This is illustrated in Figure 4-34. This experimental observation implies that b_0 is proportional to x , i.e.,

$$b_0 = C_m x \quad (192)$$

where C_m is a constant, termed the momentum spreading parameter. If a straight-line curve is fitted to experimental measurements of $u(x)$, on a logarithmic scale as shown in Figure 4-34, having a slope of (-1) , the intercept at $u(x)/u_j = 1$ defines a potential core length L_c , also shown in Figure 4-34. By graphically determining L_c , the momentum spreading constant can be computed using equations (190) and (191) with $u(x) = u_j$ and $x = L_c$:

$$C_m = \frac{1}{2(L_c/d)} \quad (193)$$

$$\frac{u(x)}{u_j} = \frac{1}{2 C_m} \left(\frac{x}{d} \right)^{-1} \quad (194)$$

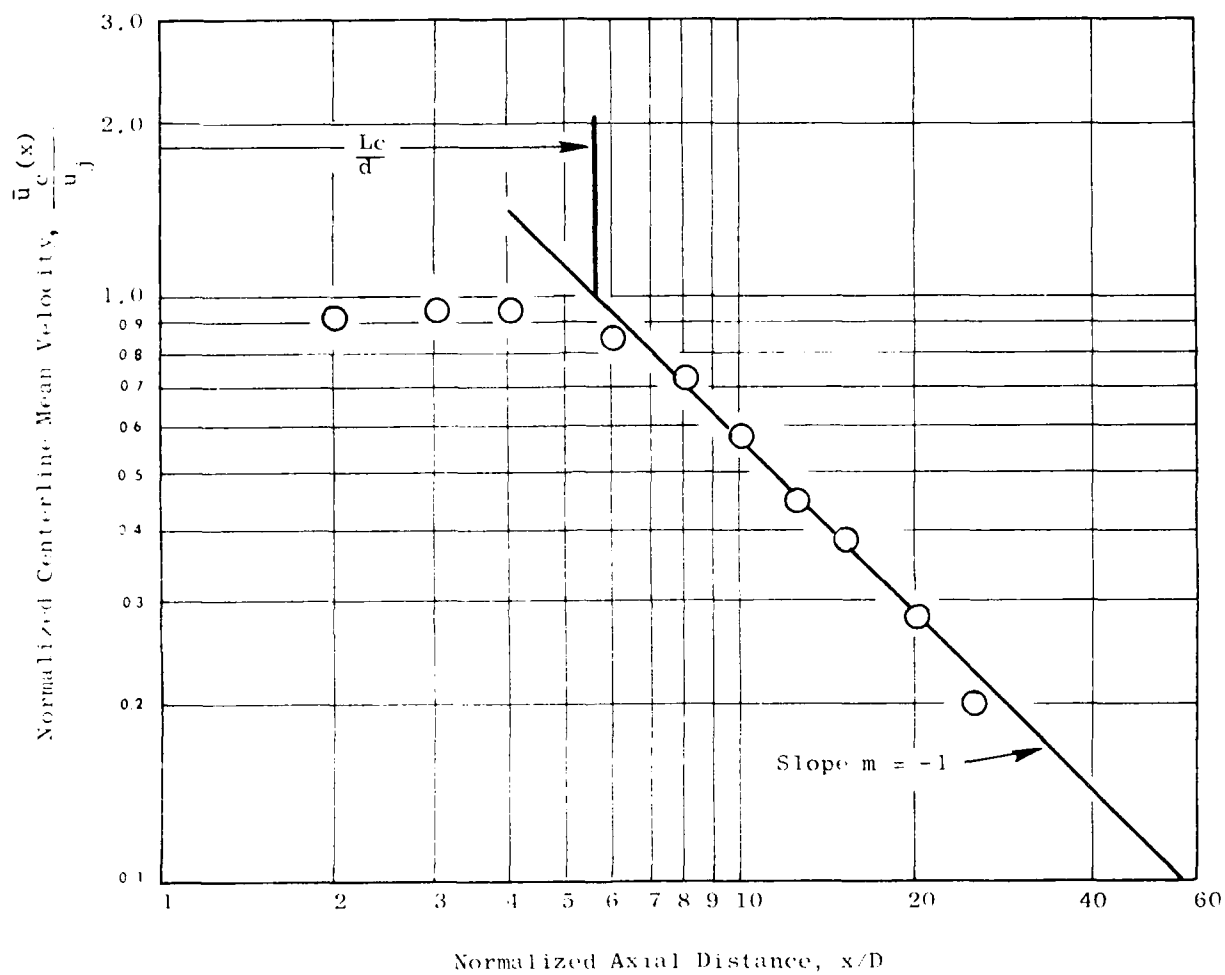


Figure 4-34. Typical Centerline Mean Velocity Measurements for a Round Jet and Definition of Core Length L_c .

Many investigators have developed correlations for the centerline velocity distributions of round jets as a function of jet exhaust Mach numbers M_j , free-stream to jet velocity ratio u_e/u_j , and nozzle shape. These empirical correlations have been employed to determine the functional dependence of C_m on the parameters M_j , u_e/u_j , and nozzle shape. A summary of the relevant correlations is given in the following paragraphs.

Forstall and Shapiro(64) correlated experimental round jet measurements of mean velocity with the ratio of external flow velocity u_e to nozzle exit velocity u_j , and proposed the following correlation:

$$\frac{u(x) - u_e}{u_j - u_e} = \frac{L_c}{x}, \quad x > L_c \quad (195)$$

$$L_c/d = 4 + 12 (u_e/u_j)$$

Bradbury(65) has proposed the following correlation of centerline velocity for round jets in a coflowing stream:

$$\frac{u(x) - u_e}{u_j - u_e} = 6.82 \sqrt{\frac{u_j}{u_j - u_e}} \left(\frac{x}{d} \right)^{-1} \quad (196)$$

Harsha(66) did a very thorough and extensive survey of published data on plane and axisymmetric jets and wakes, critically evaluating the experimental configurations and conditions for possible sources of erroneous or misleading measurements. Although Harsha encountered difficulty in obtaining agreement among the several data sources examined, he did identify two important parameters which affect the axial velocity decay rate: (1) nozzle Reynolds number $Re_d = \rho u_j d / \mu$, and (2) nozzle exit plane internal and external boundary layer thickness. For a jet issuing into still air, Harsha (1971) obtained a correlation with Reynolds number of the form

$$\frac{u(x)}{u_j} = 2.13 (Re_d)^{0.097} \left(\frac{x}{d} \right)^{-1} \quad (197)$$

Harsha(66) recommended Bradbury's(65) formula, equation (196), for correlating the influence of external flow velocity ratio, but cautioned that the nozzle exit plane conditions (turbulence levels and boundary layer thicknesses) have a strong influence on the velocity ratio effect. Although no quantitative method for estimating these influences was recommended, Harsha did present an example numerical calculation (using a Prandtl eddy viscosity model finite-difference prediction procedure) which showed a definite trend of increasing boundary layer thickness producing more rapid plume decay.

This trend opposes the tendency of velocity ratio to retard the velocity decay, as predicted by equations (195) and (196).

VonGlahn et al (67) proposed a correlation for jet centerline velocity decay which depends on jet exit Mach number M_j and nozzle flow coefficient C_n , as follows:

$$\frac{u(x)-u_c}{u_j-u_c} = \left[\frac{x}{C_n d \sqrt{1+M_j}} \right]^{-2} \quad (198)$$

where

$$x = 1 + \frac{1}{2} \left(\frac{u_c}{u_j-u_c} \right)$$

Comparing equation (198) with (195) suggests that $L_c \sim \sqrt{1+M_j}$. A compilation of data at various Mach numbers was presented by Harsha (66), and these data, in the form of centerline velocity as a function of axial distance, were used to evaluate the dependency of L_c on M_j . Shown in Figure 4-35 is a plot of $L_c/d\sqrt{1+M_j}$ as a function of M_j . It is seen from this plot that the functional dependence $L_c \sim \sqrt{1+M_j}$ holds quite well for $M_j < 1.5$. Also shown is the linear dependence $L_c \sim (1 + 0.5 M_j)$ suggested by Harsha, which also correlates quite well. The data used in Figure 4-35, however, represent ideally expanded jet behavior for $M_j > 1$. For convergent nozzles operating underexpanded, the correlation may not be applicable.

With the exception of VonGlahn's method for $u_c > 0$, all of the above correlations can be put into the form

$$\frac{u(x)-u_c}{u_j-u_c} = \frac{L_c}{x}$$

where

$$L_c = L_c(u_c/u_j, M_j, Re_d, \text{etc.})$$

This form is related to C_m , the Reichardt momentum spreading rate, through equation (193). Taking into account the variances among the various experimental results, the following equation for C_m was derived:

$$C_m = \frac{0.55(1+Re_d^{-0.09})}{(1+C_1 VR)(1+C_2 M_j)} \quad (199)$$

AD-A094 291

GENERAL ELECTRIC CO CINCINNATI OH AIRCRAFT ENGINE GROUP F/G 20/1
HIGH VELOCITY JET NOISE SOURCE LOCATION AND REDUCTION. TASK 2. --ETC(U)
MAY 78 T F Balsa, P R GLIEBE, R A KANTOLA DOT-05-30034
R78AE6323 FAA-RD-76-79-2 NL

UNCLASSIFIED

319

AD-A094 291

AD-A094 291

AD-A094 291

AD-A094 291

AD-A094 291

AD-A094 291

AD-A094 291

AD-A094 291

AD-A094 291

AD-A094 291

AD-A094 291

AD-A094 291

AD-A094 291

AD-A094 291

AD-A094 291

AD-A094 291

AD-A094 291

AD-A094 291

AD-A094 291

AD-A094 291

AD-A094 291

AD-A094 291

AD-A094 291

AD-A094 291

AD-A094 291

AD-A094 291

AD-A094 291

AD-A094 291

AD-A094 291

AD-A094 291

AD-A094 291

AD-A094 291

AD-A094 291

AD-A094 291

AD-A094 291

AD-A094 291

AD-A094 291

AD-A094 291

AD-A094 291

AD-A094 291

AD-A094 291

AD-A094 291

AD-A094 291

AD-A094 291

AD-A094 291

AD-A094 291

AD-A094 291

AD-A094 291

AD-A094 291

AD-A094 291

AD-A094 291

AD-A094 291

AD-A094 291

AD-A094 291

AD-A094 291

AD-A094 291

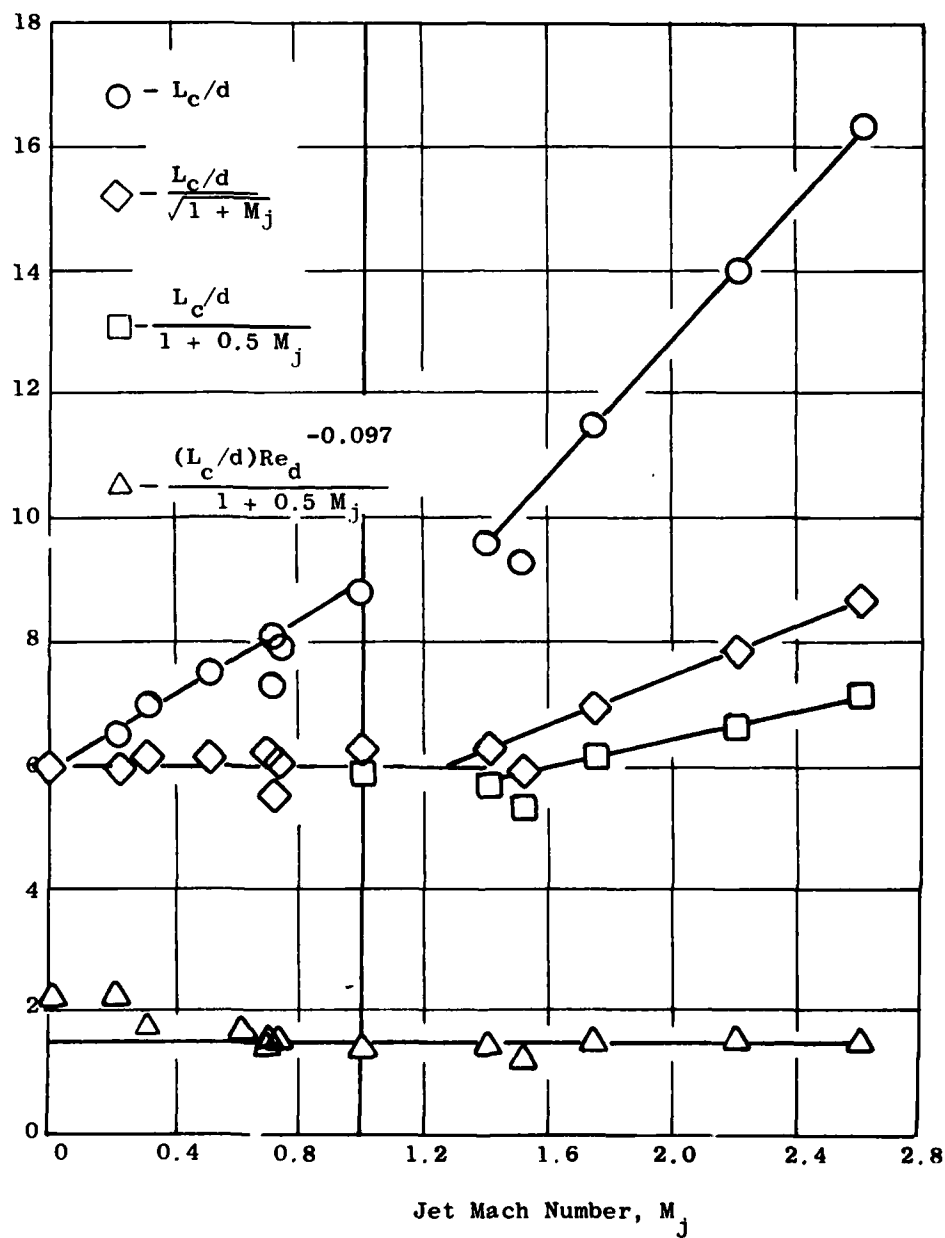


Figure 4-35. Correlations of Core Length L_c for a Round Jet, Data from Harsha (66).

171

where $VR = u_e/u_j$, and c_1 and c_2 are empirical constants, having tentative values of $c_1 = 1$ and $c_2 = 0.5$. The corresponding correlation of L_c , given by equations (193) and (199), is also shown for the same data set in Figure 4-35. It can be seen that this correlation works quite well even for the high Mach number data ($M_j > 1.5$), primarily because the effect of changing Reynolds number is now accounted for.

The formulation for C_m presented in equation (199) is only a preliminary guide; the presence of upstream turbulence, inner and outer boundary layers on the nozzle walls, the presence of shock-cells in the initial expansion region, all may have an effect on C_m which is not apparent from equation (199). In practice, it has been found that C_m varies much less with VR and M_j than would be anticipated from equation (199), based on flow measurements for several nozzles tested in the experimental portion of the present program. This is interpreted to be a characteristic of the particular facilities, nozzle designs and operating conditions employed, and some judgment is required in selecting a value of C_m for prediction purposes. Equation (199) is a good initial estimate, but small adjustments may be necessary to account for the aforementioned auxiliary effects.

From equation (183), the momentum transport coefficient $\lambda_m(x)$ can be obtained C_m , and is as follows:

$$\lambda_m(x) = \frac{C_m^2 x}{2} \quad (200)$$

For the heat transport equation, i.e., for $f = \overline{\rho u h}$, much less data exist from which one can extract the empirical heat transport coefficient $\lambda_h(x)$ and/or the enthalpy flux shear layer thickness $b_h(x)$. In general (see, e.g., Hinze(61), and Launder and Spalding(57)), temperature profiles diffuse more rapidly than velocity profiles in a free turbulent jet. Using some simplifying assumptions, it can be shown that a relation exists between C_m and the corresponding heat spreading rate C_h as a function of the turbulent Prandtl number, for a round jet:

$$\frac{C_h}{C_m} \approx \sqrt{\frac{2}{1 + Pr_t}} \quad (201)$$

The details of the derivation of equation (201) are given in Appendix B. Launder and Spalding(57) estimated that $Pr_t \approx 0.7$ for a round jet. This would, with equation (201), imply that $C_h \approx 1.1 C_m$. In practice, this has been found to yield satisfactory predictions for heated jets.

4.5.5 Turbulent Structure Quantities

The general solution given by equation (184) permits a numerical evaluation of the quantities $\overline{\rho u^2}$ and $\overline{\rho uH}$. From the generalized Reichardt hypothesis given by equation (166), the quantities $\overline{\rho uv}$ and $\overline{\rho uw}$ can also be evaluated. For the constant pressure mixing case $Q = 0$, equation (184) and equations (166) yield the following solution forms:

$$[\overline{\rho u^2}] (x, y, z) = \frac{1}{\pi b_m^2} \int_{-\infty}^{\infty} \int_{-\infty}^{\infty} [\overline{\rho u^2}]_j (\eta, \zeta) e^{-R^2/b_m^2} d\eta d\zeta \quad (202)$$

$$[\overline{\rho uH}] (x, y, z) = \frac{1}{\pi b_h^2} \int_{-\infty}^{\infty} \int_{-\infty}^{\infty} [\overline{\rho uH}]_j (\eta, \zeta) e^{-R^2/b_h^2} d\eta d\zeta \quad (203)$$

$$[\overline{\rho uv}] (x, y, z) = \frac{2\lambda_m}{\pi b_m^2} \int_{-\infty}^{\infty} \int_{-\infty}^{\infty} [\overline{\rho u^2}]_j (\eta, \zeta) \left(\frac{y-\eta}{b_m^2} \right) e^{-R^2/b_m^2} d\eta d\zeta \quad (204)$$

$$[\overline{\rho uw}] (x, y, z) = \frac{2\lambda_m}{\pi b_m^2} \int_{-\infty}^{\infty} \int_{-\infty}^{\infty} [\overline{\rho u^2}]_j (\eta, \zeta) \left(\frac{z-\zeta}{b_m^2} \right) e^{-R^2/b_m^2} d\eta d\zeta \quad (205)$$

where $R^2 = (z-\zeta)^2 + (y-\eta)^2$, as before. Subscripts j indicate evaluation at the jet exit plane $x=0$. The turbulent shear stresses τ_y and τ_z are given by

$$\tau_y = -\overline{\rho u'v'} \quad \tau_z = -\overline{\rho u'w'}$$

From equation (165), these can be expressed as follows:

$$\tau_y = \overline{\rho} \overline{u} \overline{v} - \overline{\rho uv}$$

$$\tau_z = \overline{\rho} \overline{u} \overline{w} - \overline{\rho uw}$$

Kendall(58) has attempted to derive a formulation for $(\bar{\rho} \bar{u} \bar{v})$ by manipulating the continuity equation (163) to solve for $\bar{\rho} \bar{v}$, assuming that $\bar{\rho} \bar{u} = (\bar{\rho} \bar{u}^2)/\bar{u}$ and $\bar{u} \approx \sqrt{(\bar{\rho} \bar{u}^2)/\bar{\rho}}$. Because of the approximations involved, the resulting expressions for τ_y are in practice less accurate than the simpler approach of neglecting $\bar{\rho} \bar{u} \bar{v}$ altogether. The simpler approach has been adopted herein, so that τ_y and τ_z are approximated by

$$\tau_y \approx - \overline{\rho u v} \quad \tau_z \approx - \overline{\rho u w} \quad (206)$$

In addition to τ_y and τ_z , an analogous axial component of shear stress τ_x can be defined, as follows:

$$\tau_x = \lambda \frac{\partial}{\partial x} (\bar{\rho} \bar{u}^2)$$

Substituting equation (202), the following expression for τ_x is obtained:

$$\tau_x = \frac{2\lambda_m}{\pi b_m^2} \left(\frac{1}{b_m} \frac{db_m}{dx} \right) \int_{-\infty}^{\infty} \int_{-\infty}^{\infty} [\bar{\rho} \bar{u}^2]_j (n, \zeta) \left(\frac{R^2}{b_m^2} - 1 \right) e^{-R^2/b_m^2} dnd\zeta \quad (207)$$

where $db_m/dx = C_m$ and $\lambda_m = 1/2 b_m db_m/dx$, as before.

For comparison with experiment, the axial turbulence velocity u' is required, since this is a turbulence parameter which is easily measured. A stronger motivation for being able to predict u' is that it is a primary ingredient in the computation of mixing noise. An expression was developed which relates u' to τ_x , τ_y , and τ_z as follows:

$$\bar{\rho} (u')^2 \approx \sqrt{\tau_y^2 + \tau_z^2 + (10 \tau_x)^2} \quad (208)$$

where the factor of 10 on τ_x was determined from comparisons with experimental measurements on simple round jets. On the axis of a simple round jet, τ_y and τ_z vanish [see equations (204) and (205)], so that $(u')^2$ is determined entirely by τ_x .

4.5.6 Base Pressure Effects

A qualitative estimate of the effects of reduced base pressure on the mixing characteristics of multi-element nozzles can be made by examining the general solution for momentum transport in cylindrical coordinates given by equation (185):

174

$$\begin{aligned}
 f(x, r, \phi) = & \int_0^x \frac{1}{\pi b^2} \int_0^{2\pi} \int_0^\infty Q e^{-R^2/b^2} v dv d\alpha d\zeta \\
 & + \int_0^{2\pi} \int_0^\infty \frac{1}{\pi b^2} f(0, v, \alpha) e^{-R^2/b_o^2} v dv d\alpha
 \end{aligned}
 \tag{185}$$

where $f = \overline{pu^2}$ and $Q = -\partial \overline{p}/\partial x$. The simple case where $\overline{p} = \overline{p}(x)$ is first considered. For this case, the first term in (185) can be integrated directly with respect to v and α to give the following:

$$f(x, r, \phi) = - \int_0^x (\partial \overline{p}/\partial x) dx + \int_0^{2\pi} \int_0^\infty \frac{f(0, v, \alpha)}{\pi b_m^2} e^{-R^2/b_m^2} v dv d\alpha$$

This expression can be rewritten in the form

$$f(x, r, \phi) + \overline{p}(x) = \frac{1}{\pi b_m^2} \int_0^{2\pi} \int_0^\infty [f(0, v, \alpha) + \overline{p}(0)] e^{-R^2/b_m^2} v dv d\alpha$$

Thus, for the simple case \overline{p} is a function of x (axial distance) only, the quantity $(\overline{pu^2} + \overline{p})$ represents the appropriate momentum transport parameter rather than just $\overline{pu^2}$. For a given distribution of $(\overline{p} + \overline{pu^2})$, increasing static pressure will decrease $\overline{pu^2}$ and vice versa. The qualitative statement can therefore be made that reduced base pressures at the nozzle exit plane of a multielement nozzle will cause the plume momentum to decay more rapidly, since the static pressure will increase in the downstream direction.

The more general case of radial, circumferential, and axial variations in static pressure requires numerical evaluation of known, specified pressure distributions. Although the formulations presented herein have included the effects of static pressure variations, the numerical calculation procedure and associated computer program have not been developed to include these effects. This is a possible area for further development of the theoretical prediction model.

4.5.7 Computational Procedure

The flow field solution described in the preceding sections has been reformulated for numerical computations in cylindrical coordinates. The pressure gradient terms have been omitted in the present version. The relevant equations in Cartesian coordinates are as follows:

Momentum Transport:

$$\overline{\rho u^2} - \rho_e u_e^2 = \frac{1}{\pi b_m^2} \iint (\rho_j u_j^2 - \rho_e u_e^2) e^{-R^2/b_m^2} d\eta d\zeta \quad (209)$$

Heat Transport:

$$\overline{\rho u H} = \frac{1}{\pi b_h^2} \iint (\rho_j u_j H_j) e^{-R^2/b_h^2} d\eta d\zeta \quad (210)$$

Shear Stresses:

$$\tau_x = \frac{2\lambda_m}{\pi b_m^2} \left(\frac{1}{b_m} \frac{db_m}{dx} \right) \iint (\rho_j u_j^2 - \rho_e u_e^2) \left(\frac{R^2}{b_m^2} - 1 \right) e^{-R^2/b_m^2} d\eta d\zeta \quad (211)$$

$$\tau_y = - \frac{2\lambda_m}{\pi b_m^2} \iint (\rho_j u_j^2 - \rho_e u_e^2) \frac{y-\eta}{b_m^2} e^{-R^2/b_m^2} d\eta d\zeta \quad (12)$$

$$\tau_z = - \frac{2\lambda_m}{\pi b_m^2} \iint (\rho_j u_j^2 - \rho_e u_e^2) \frac{z-\zeta}{b_m^2} e^{-R^2/b_m^2} d\eta d\zeta \quad (212)$$

where

$$R^2 = (y-\eta)^2 + (z-\zeta)^2 \quad (214)$$

$$\lambda_m = \frac{b_m}{2} \frac{db_m}{dx}, \quad \lambda_h = \frac{b_h}{2} \frac{db_h}{dx} \quad (215)$$

$$b_m = C_m x, \quad b_h = C_h x \quad (216)$$

$$C_m = \frac{0.3333 \text{ Re}_d^{-0.097}}{(1+c_1 \text{ VR}) (1+c_2 M_j)} \quad (217)$$

$$C_h = C_m \sqrt{\frac{2}{1 + \text{Pr}_t}} \quad (218)$$

and Re_d is the Reynolds number of the nozzle element ($\rho_j u_j d_j / \mu_j$), M_j is the element Mach number (u_j / c_j), Pr_t is the fluid turbulent Prandtl number ($\mu c_p / k$)_j, and c_1 and c_2 are empirical constants.

The above equations are first transformed to cylindrical coordinates to facilitate numerical computations. A field point $P(x, y, z)$ has corresponding cylindrical coordinates $P(x, r, \phi)$. A point in the nozzle exit plane $Q(\xi, \eta, \zeta)$ has corresponding cylindrical coordinates $Q(\xi, v, \alpha)$. The projection of the field point P onto the nozzle exit plane is separated from Q by distance R , as shown in Figure 4-36. The shear stresses τ_r and τ_ϕ are related to the Cartesian components τ_y and τ_z by the following expressions:

$$\left. \begin{aligned} \tau_r &= \tau_y \cos \phi + \tau_z \sin \phi \\ \tau_\phi &= \tau_z \cos \phi - \tau_y \sin \phi \end{aligned} \right\} \quad (219)$$

Utilizing the above expressions and the geometric relationships noted in Figure 4-36, the following set of equations, in cylindrical coordinates, is obtained:

Momentum Transport:

$$\left[\overline{\rho u^2} - \rho_e u_e^2 \right] = \frac{1}{\pi b_m^2} \iint (\rho_j u_j^2 - \rho_e u_e^2) e^{-R^2/b_m^2} v dv d\alpha \quad (220)$$

Heat Transport:

$$\overline{\rho u H} = \frac{1}{\pi b_h^2} \iint (\rho_j u_j H_j) e^{-R^2/b_h^2} v dv d\alpha \quad (221)$$

197

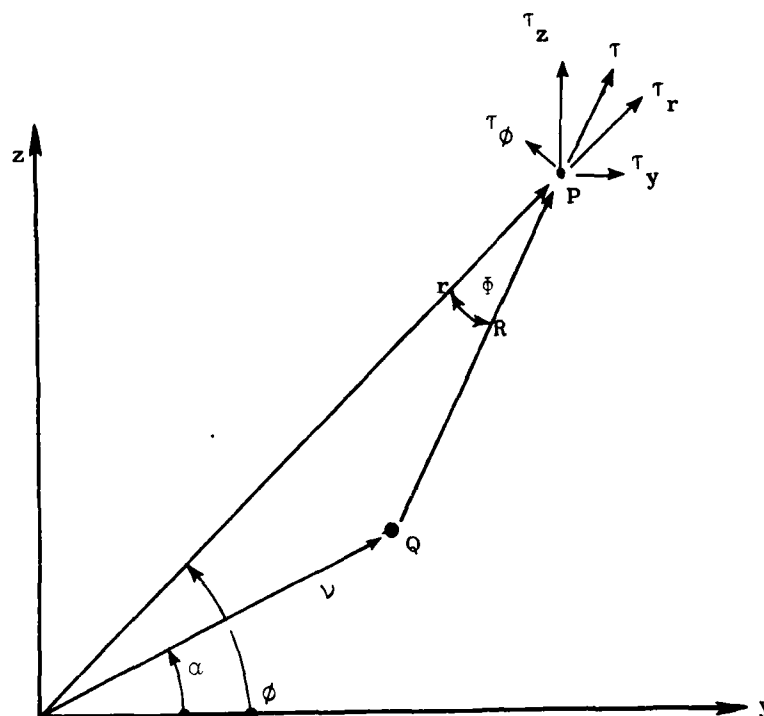


Figure 4-36. Shear Stress at Point P Due to Contribution from Point Q; Cartesian and Cylindrical Coordinate Components.

Shear Stresses:

$$\tau_x = \frac{C_m^2}{\pi b_m^2} \iint (\rho_j u_j^2 - \rho_e u_e^2) \left(\frac{R^2}{b_m^2} - 1 \right) e^{-R^2/b_m^2} v dv d\alpha \quad (222)$$

$$\tau_r = \frac{C_m^2}{\pi b_m^2} \iint (\rho_j u_j^2 - \rho_e u_e^2) \frac{R}{b_m} \cos \phi e^{-R^2/b_m^2} v dv d\alpha \quad (223)$$

$$\tau_\phi = - \frac{C_m}{\pi b_m^2} \iint (\rho_j u_j^2 - \rho_e u_e^2) \frac{R}{b_m} \sin \phi e^{-R^2/b_m^2} v dv d\alpha \quad (224)$$

where ϕ is the angle between vectors r , and R , and is given by the relation:

$$R \cos \phi = r - v \cos (\phi - \alpha) \quad (225)$$

The integrations indicated in the above expressions, over the exit-plane area, are carried out with r and ϕ held constant. This integration can be replaced by an equivalent integration with respect to the variables R and ϕ . Thus the quantity $v dv d\alpha$ in the above expressions is replaced by $R dR d\phi$.

Consider a nozzle of arbitrary planform shape as shown in Figure 4-37. The flow properties are assumed to be uniform over the nozzle exit plane, having values (ρ_j, u_j, H_j) inside the closed contour and (ρ_e, u_e, H_e) outside the closed contour. The area integrations over the nozzle exit plane possess non-zero contributions only within the nozzle contour boundary. The integration with respect to R can be evaluated analytically in equations (221) through (224), reducing these expressions to a contour integral around the boundary, where ϕ is the integration variable and $R = R_0(\phi)$ defines the contour shape. Integrating equations (221) through (224) with respect to R over the interval $0 < R < R_0$, the following expressions are obtained:

Momentum Transport:

$$\overline{\rho u^2} - \rho_e u_e^2 = \frac{1}{2\pi} \oint (\rho_j u_j^2 - \rho_e u_e^2) \left[1 - e^{-R_0^2/b_m^2} \right] d\phi \quad (226)$$

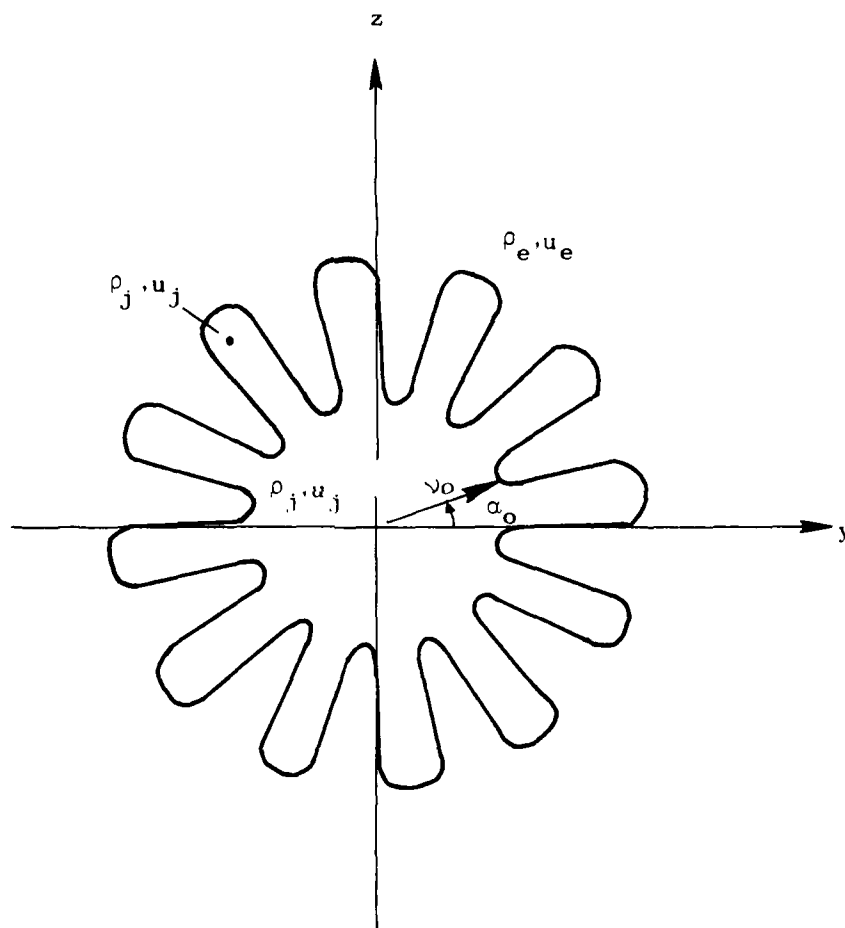


Figure 4-37. Example of Non-Circular Nozzle Contour Boundary.

Heat Transport:

$$\overline{\rho u H} = \frac{1}{2\pi} \oint \left(\rho_j u_j H_j \right) \left[1 - e^{-R_o^2/b_m^2} \right] d\phi \quad (227)$$

Shear Stresses:

$$\tau_x = -\frac{C_m^2}{2\pi} \oint \left(\rho_j u_j^2 - \rho_e u_e^2 \right) \left[\frac{R_o^2}{b_m^2} e^{-R_o^2/b_m^2} \right] d\phi \quad (228)$$

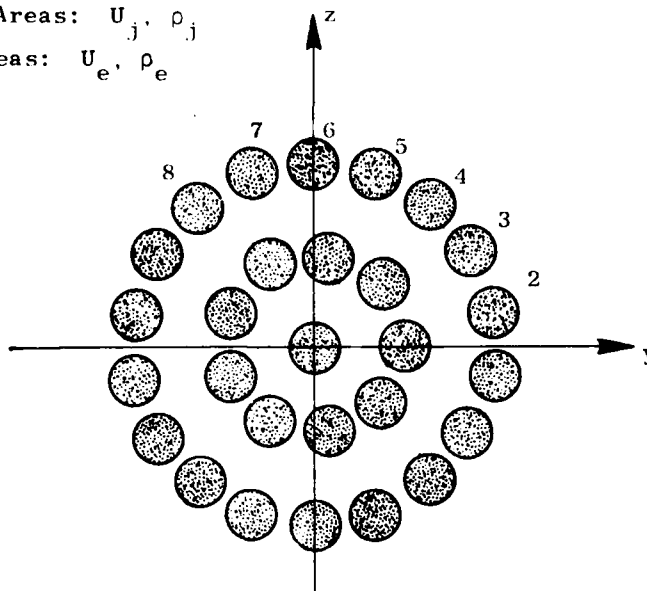
$$\tau_r = \frac{C_m}{2\pi} \oint \left(\rho_j u_j^2 - \rho_e u_e^2 \right) \left[\frac{\sqrt{\pi}}{2} \operatorname{erf} \left(\frac{R_o}{b_m} \right) - \frac{R_o}{b_m} e^{-R_o^2/b_m^2} \right] \cos \phi d\phi \quad (229)$$

$$\tau_\phi = \frac{C_m}{2\pi} \oint \left(\rho_j u_j^2 - \rho_e u_e^2 \right) \left[\frac{\sqrt{\pi}}{2} \operatorname{erf} \left(\frac{R_o}{b_m} \right) - \frac{R_o}{b_m} e^{-R_o^2/b_m^2} \right] \sin \phi d\phi \quad (230)$$

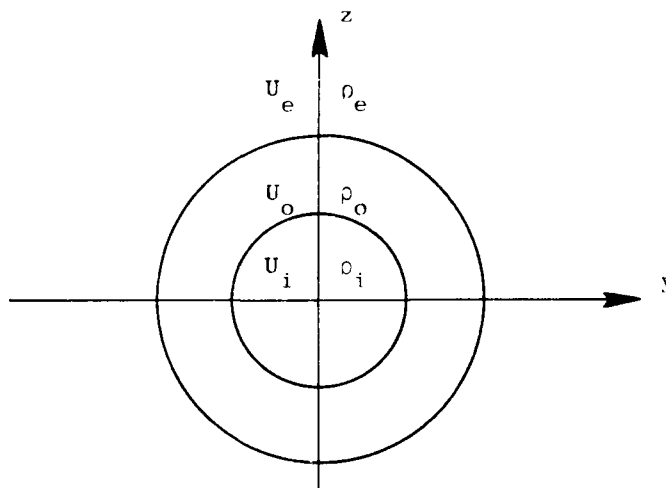
In the above expressions, the integration \oint is taken around the closed boundary. If there are several nozzle elements, as in the case of a multi-tube nozzle, illustrated in Figure 4-38a, the integration is performed over each of the boundary contours defining each element, summing the contributions of each element to arrive at the total contribution at a given field point P. If a given contour surrounds nozzle another contour, as in the case of a coannular nozzle (Figure 4-38b), the outer contour integration is carried out as before, with (ρ_j, u_j, H_j) set equal to (ρ_i, u_i, H_i) , respectively, i.e., the exhaust plane conditions inside the inner contour. However, for the inner contour integration, the values of (ρ_e, u_e, H_e) are replaced by (ρ_o, u_o, H_o) ; the idea is to compute the diffusion of momentum, heat, etc., between the fluids inside and outside of a given boundary contour. The contributions of the inner and outer boundary contour integrations are then summed as before, to give the total contribution at a given field point P.

301

Shaded Areas: U_j, ρ_j
 Open Areas: U_e, ρ_e



(a) Example Multitube Nozzle



(b) Example Coaxial Nozzle

Figure 4-38. Examples of Multielement Nozzle Contour Boundaries.

Given a nozzle planform geometry and exit plane flow conditions, the quantities $(\overline{\rho u^2}, \overline{\rho u H}, \tau_x, \tau_r, \text{ and } \tau_\phi)$ can be computed at all field points P of interest throughout the jet plume, utilizing equations (226) through (230) in the above-described procedure. To evaluate the corresponding variables $(\overline{\rho}, \overline{u}, \overline{T})$ at each point, consider the definition of $\overline{\rho u H}$:

$$\overline{\rho u H} = \langle \overline{\rho u} [C_p T - C_p T_e + u^2/2] \rangle \quad (231)$$

where $\langle . . . \rangle$ denotes a time average. From perfect gas relations, $\overline{\rho u C_p T} = \frac{\gamma}{\gamma-1} \overline{\rho u}$; defining the variable ψ as

$$\psi = \overline{\rho C_p T} + \frac{1}{2} \overline{\rho u^2} = \frac{\gamma}{\gamma-1} \overline{p} + \frac{1}{2} \overline{\rho u^2} \quad (232)$$

equation (231) can then be approximated by the following:

$$\overline{\rho u H} \approx \psi \overline{u} - C_p T_e \overline{\rho u}$$

Multiplying through by \overline{u} and making a further assumption that $\overline{\rho u} \cdot \overline{u} \approx \overline{\rho u^2}$, the following quadratic equation for \overline{u} , in terms of $\overline{\rho u H}$ and $\overline{\rho u^2}$ is obtained:

$$\psi \overline{u^2} - (\overline{\rho u H}) \overline{u} - C_p T_e (\overline{\rho u^2}) = 0 \quad (233)$$

Where ψ is given by equation (232). Solving the above for \overline{u} ,

$$\overline{u} = \frac{\overline{\rho u H}}{2\psi} + \sqrt{\frac{(\overline{\rho u H})^2}{4\psi^2} + \frac{C_p T_e (\overline{\rho u^2})}{\psi}} \quad (234)$$

Having computed \overline{u} from equation (234), the remaining mean flow parameters $\overline{\rho}$ and \overline{T} are evaluated from the relations

$$\overline{\rho} = \frac{\overline{\rho u^2}}{\overline{u^2}}, \quad \overline{T} = \frac{\overline{p}}{\overline{\rho} R} \quad (235)$$

where R is the universal gas constant. The turbulence intensity u' is then computed from a relation analogous to (208), as follows:

$$\overline{\rho} (u')^2 = \sqrt{\tau_r^2 + \tau_\phi^2 + (10 \tau_x)^2} \quad (236)$$

The factor of 10 (as mentioned previously) in the above expression was derived from matching this equation to experimental data for a round nozzle at low Mach number, along the jet centerline. To see this more clearly, consider a round jet of radius a , and evaluate equations (228) through (230) along the centerline $r=0$. Then $R_0 = a$, a constant, and the integrations result in the following:

$$\tau_x = C_m^2 \left(\rho_j u_j^2 - \rho_e u_e^2 \right) \frac{a^2}{b_m^2} e^{-a^2/b_m^2} \quad (237)$$

and $\tau_r = \tau_\phi = 0$. Substituting the above into equation (236) gives the following expression for the turbulence intensity along the centerline of a cold ($\rho \approx \rho_j \approx \rho_e$) round jet:

$$(u')^2 = 10 C_m^2 \left(u_j^2 - u_e^2 \right) \frac{a^2}{b_m^2} e^{-a^2/b_m^2} \quad (238)$$

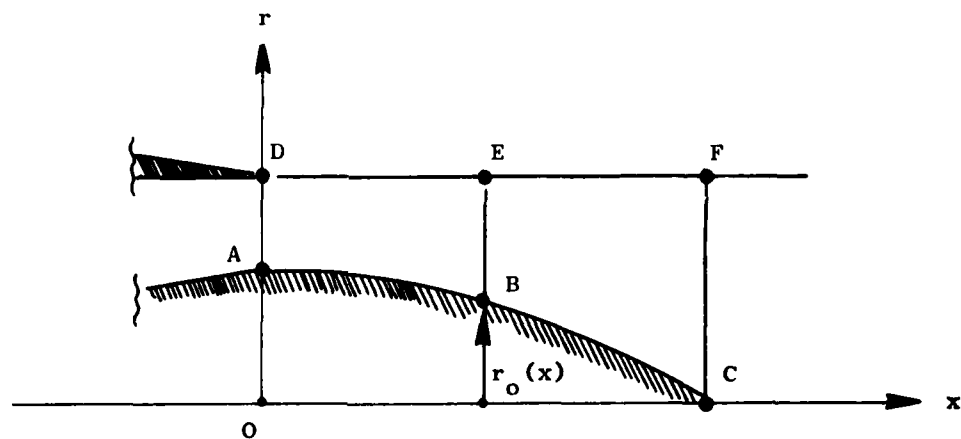
By virtue of the relation $b_m = C_m x$, this expression duplicates quite well the experimentally observed dependence of u' on axial distance along the centerline.

A modification to this computational procedure has been developed for nozzles with a centerbody or plug, as illustrated in Figure 4-39. The modification consists of a transformation and stretching of the radial coordinates r and v , such that the centerbody or plug surface is transformed to a "needle" lying along the x -axis. The stretching is incorporated to maintain constant annulus area between the circles $r = \text{constant}$ and $v = \text{constant}$, respectively. The transformation and stretching, illustrated in Figure 4-39, essentially forces the flow to follow the centerbody contour, with a vanishing normal gradient in flow properties on the plug surface. No boundary layer development is calculated on the centerbody surface, although an effective contour which includes surface boundary layer displacement thickness can be input to the calculation. Streamline curvature effects due to centerbody curvature are not accounted for. The centerbody geometry can be defined by the radial coordinate of the surface as a function of x , $r_0 = r_0(x)$. The nozzle contour boundary integrations required in evaluating equations (226) through (230) contain $R(\phi)$, which can be written in terms of r and v_0 through equation (186),

$$R^2 = r^2 + v_0^2 - 2rv_0 \cos(\phi - \alpha_0)$$

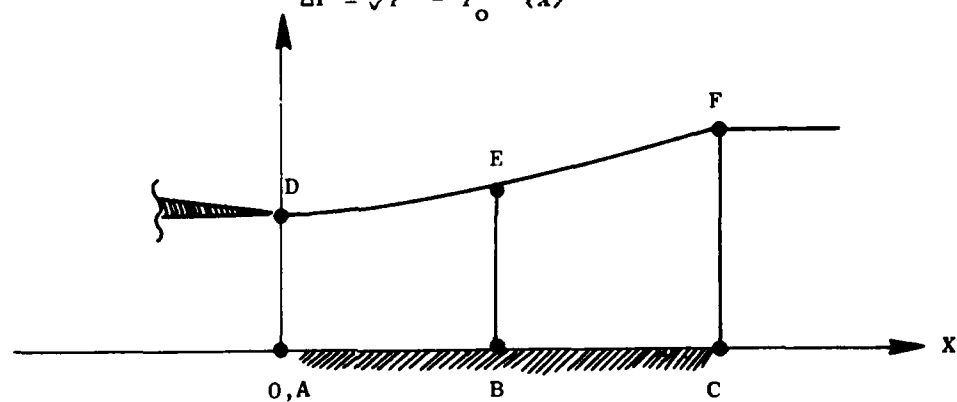
This can be rewritten in the form

$$R^2 = (r - v_0)^2 + 2rv_0 [1 - \cos(\phi - \alpha_0)]$$



(a) Actual Centerbody Geometry

$$\Delta r = \sqrt{r^2 - r_o^2(x)}$$



(b) Transformed Plane Geometry

Figure 4-39. Coordinate System Transformation for Nozzles with a Plug/Centerbody.

300

When a centerbody is present, r and v_o are replaced by Δr and Δv , defined as follows:

$$\left. \begin{aligned} \Delta r &= \sqrt{r^2 - r_o^2(x)} \\ \Delta v &= \sqrt{v_o^2 - r_o^2(0)} \end{aligned} \right\} \quad (239)$$

so that $R^2 = (\Delta r - \Delta v)^2 + 2 \Delta r \Delta v [1 - \cos(\phi - \alpha)]$.

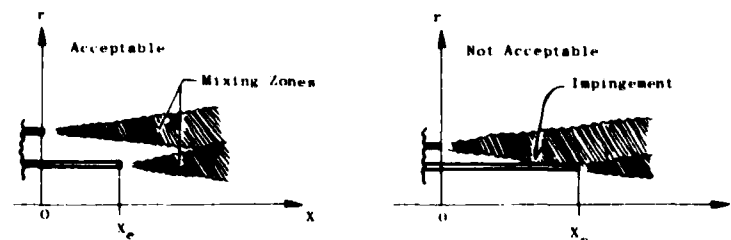
Note that v_o and α_o are the cylindrical coordinates of the nozzle contour which surrounds the centerbody. This transformation and stretching is similar to the von Mises transformation for laminar boundary layers (see Schlichting⁽⁶⁸⁾, p. 136), where the (x, r) - coordinates are transformed to (x, ψ) -coordinates; ψ being the stream function defined by $\rho u r = \partial \psi / \partial r$ and $\rho v r = -\partial \psi / \partial x$.

For cases where nozzle elements are not coplanar, an additional modification has been devised. This modification consists of replacing x by $(x - x_e)$, where x_e is the axial location of the exit plane of the particular nozzle element for which the boundary contour integration is being evaluated. Each nozzle element can have a different value of x_e (a coplanar nozzle would have all nozzle elements at the same x_e , e.g., $x_e = 0$), as long as the mixing zones of any one element do not impinge or "cross" the surface of any other element in the nozzle array. Figure 4-40 illustrates the possible types of non-coplanar nozzle configurations which can be analyzed, and also shows configurations which will result in an erroneous answer.

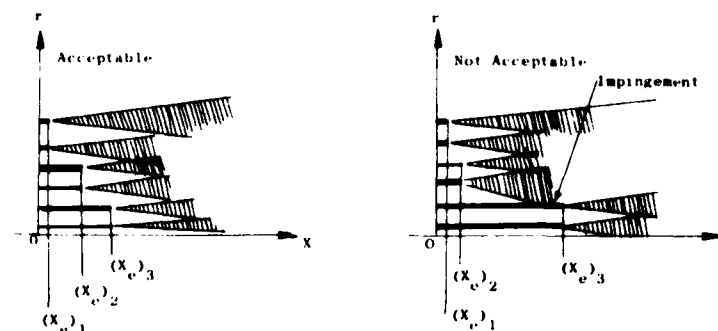
4.5.8 Comparisons of Predictions with Experiment

Several comparisons have been made of the distributions of mean velocity \bar{u} and turbulence intensity u' in turbulent jets. The experimental measurements were made on single round jets and twin round jets using a laser velocimeter (LV). These measurements are reported in Section 5.7. The prediction procedure described in the previous section was exercised and the results were compared with the measured distributions. Details of the computation procedure and associated FORTRAN computer program are given in Section 4.7 and in the supplementary volume of this report.

The first set of data/theory comparisons, for a 1.5-inch diameter convergent round nozzle, is shown in Figures 4-41 through 4-45. Figure 4-41 shows predicted and measured centerline distributions of mean velocity \bar{u}_c . Two cases are shown: (1) $T_{Tj} = 530^\circ \text{ R}$, and (2) $T_{Tj} = 1160^\circ \text{ R}$. Both cases have the same exit Mach number $M_j \approx 0.98$. Note that the hot jet decays more rapidly than the cold jet, and this is predicted by the theory. Shown in Figures 4-42 and 4-43 are radial distributions of mean velocity \bar{u} and turbulence intensity u' , respectively, at several axial stations, for case (1), the cold round jet. The corresponding radial distributions of \bar{u} and u' for case (2), the heated round jet, are shown in Figures 4-44 and 4-45, respectively. In general, the mean velocity profile predictions compare well with the experimental measurements. There is less satisfactory agreement for the



(a) Staggered Conical Nozzle



(b) Staggered Multi-Tube Nozzle

Figure 4-40. Non-Coplanar Nozzle Configuration Examples.

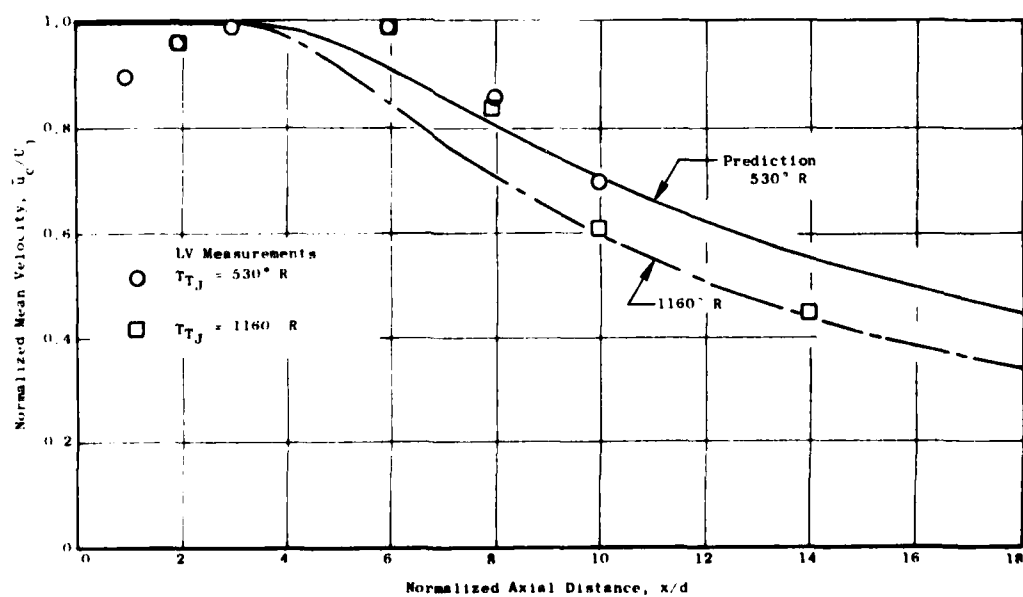


Figure 4-41. Comparison of Mean Centerline Velocity Decay 1.5 in. Diameter Conical Nozzle, $M_j \approx 0.98$.

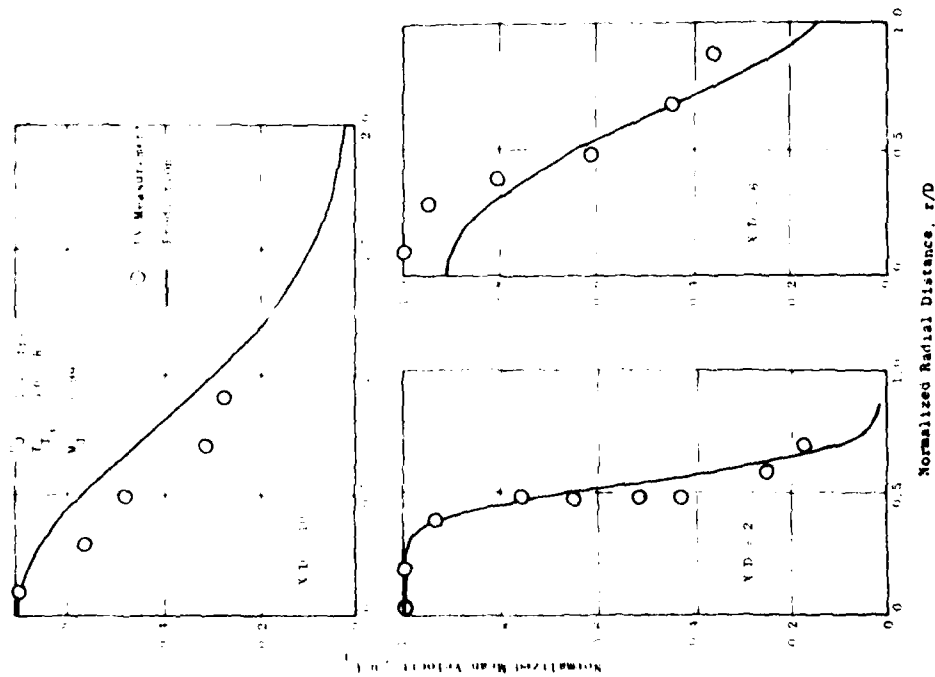


Figure 4-42. Comparison of Mean Velocity Profiles, 1.5 in. Diameter Conical Nozzle.

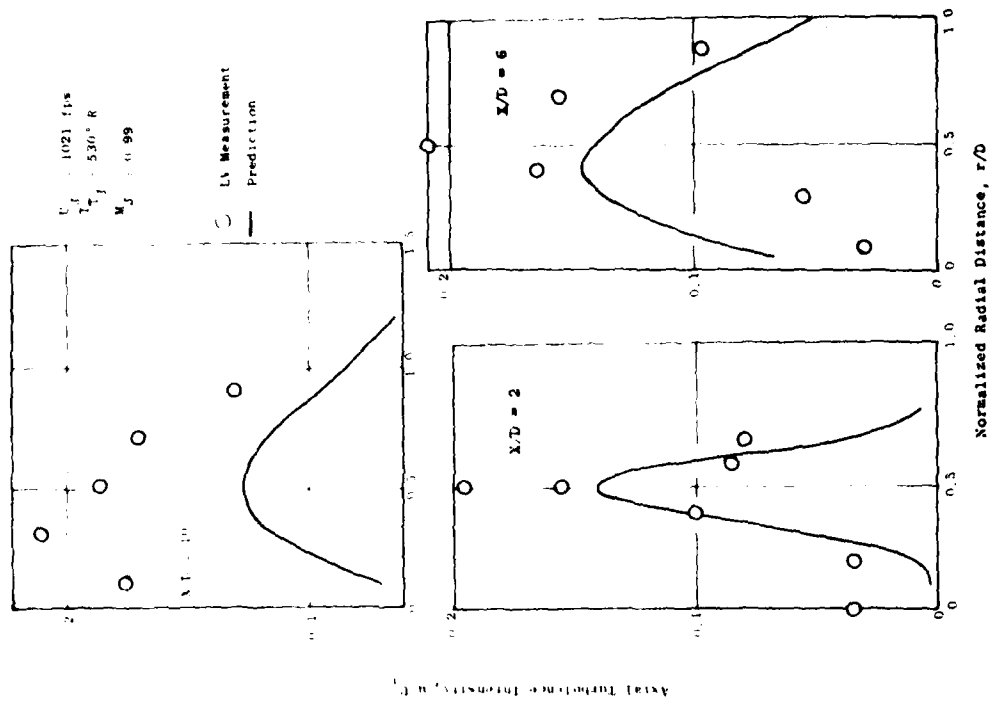


Figure 4-43. Comparison of Turbulence Intensity Profiles, 1.5 in. Diameter Conical Nozzle.

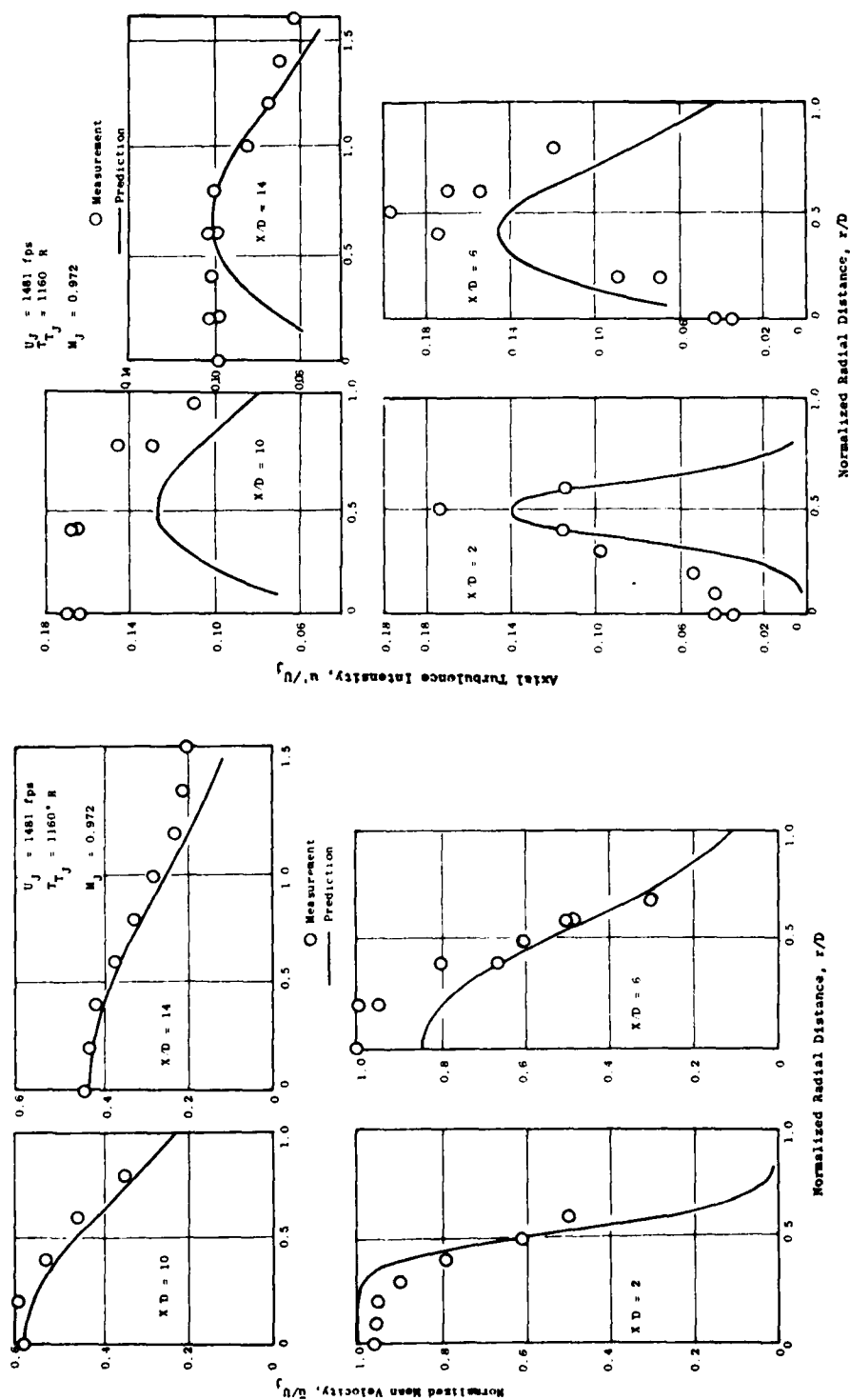


Figure 4-44. Comparison of Mean Velocity Profiles, 1.5 in. Diameter Conical Nozzle.

Figure 4-45. Comparison of Turbulence Intensity Profiles, 1.5 in. Diameter Conical Nozzle.

turbulence velocity profiles (Figures 4-43 and 4-45), although the predicted shapes and relative changes with axial distance appear to qualitatively exhibit the experimental trends.

Several data/theory comparisons were made on a twin parallel round jet; the configuration details and experimental measurements are described in Section 5.7. Some of these comparisons are shown in Figures 4-46 through 4-52. The jet element centerline mean velocity decay comparisons are shown in Figure 4-46 for a tube element spacing-to-diameter ratio of 1.33; exit plane Mach number is again $M_j \approx 0.98$, for (1) $T_{Tj} = 530^\circ \text{ R}$ (cold jet), and (2) $T_{Tj} = 1160^\circ \text{ R}$ (hot jet). Some sample mean velocity (\bar{u}) profiles for the (1) cold jet and (2) hot jet are shown in Figures 4-47 and 4-48, respectively. The corresponding turbulence intensity (u') profiles are shown in Figures 4-49 and 4-50. Finally, some mean and turbulence velocity profiles are shown in Figures 4-51 and 4-52, respectively, for a larger element spacing-to-diameter ratio of 3.333.

In general, the results of the data/theory comparisons shown in Figures 4-46 through 4-52 for the twin round jet configurations indicate that the diffusion and merging of the two jets is less rapid (with respect to axial variations) than predicted by the theory, i.e., the coalescence of the two jets into one is observed to occur further downstream than is predicted by the theory. The diffusive effects are over-emphasized in the Reichardt approach to turbulent flow modeling, a characteristic which had been recognized before.

Laser velocimeter measurements have also been carried out in Tasks 3 and 4 of this program, on several jet nozzle configurations. Comparisons of theoretical predictions with these sets of data are covered in depth in the Task 3 final report. However, it is appropriate to present some of these results herein, as they illustrate some of the key features of the theory. The first example, taken from Task 4 LV measurements, is for a conical nozzle. Mean velocity profiles and turbulence velocity profiles are shown in Figures 4-53 and 4-54, respectively. This example is shown because it shows comparisons at many more axial stations, and also represents data from a different facility and measurement system. These comparisons show much better agreement between theory and experiment than those shown in Figures 4-44 and 4-45. At least part of the improved agreement can be attributed to better data quality.

The second example, taken from Task 3 experiments, is a plug nozzle, i.e., a round nozzle with a tapered centerbody. Mean velocity profiles are shown in Figures 4-55 and 4-56, respectively. These comparisons show good agreement between theory and experiment, and lend confidence to the transformation/stretching technique used to modify the Reichardt theory for predicting jet flows with a centerbody.

The third example, selected from the Task 3 experiments, is a coplanar, coannular nozzle with an outer-to-inner area ratio of 0.65. The outer-to-inner velocity ratio at the nozzle exit plane is 2.0. Figure 4-57 shows mean velocity profile comparisons, while Figure 4-58 shows turbulence velocity

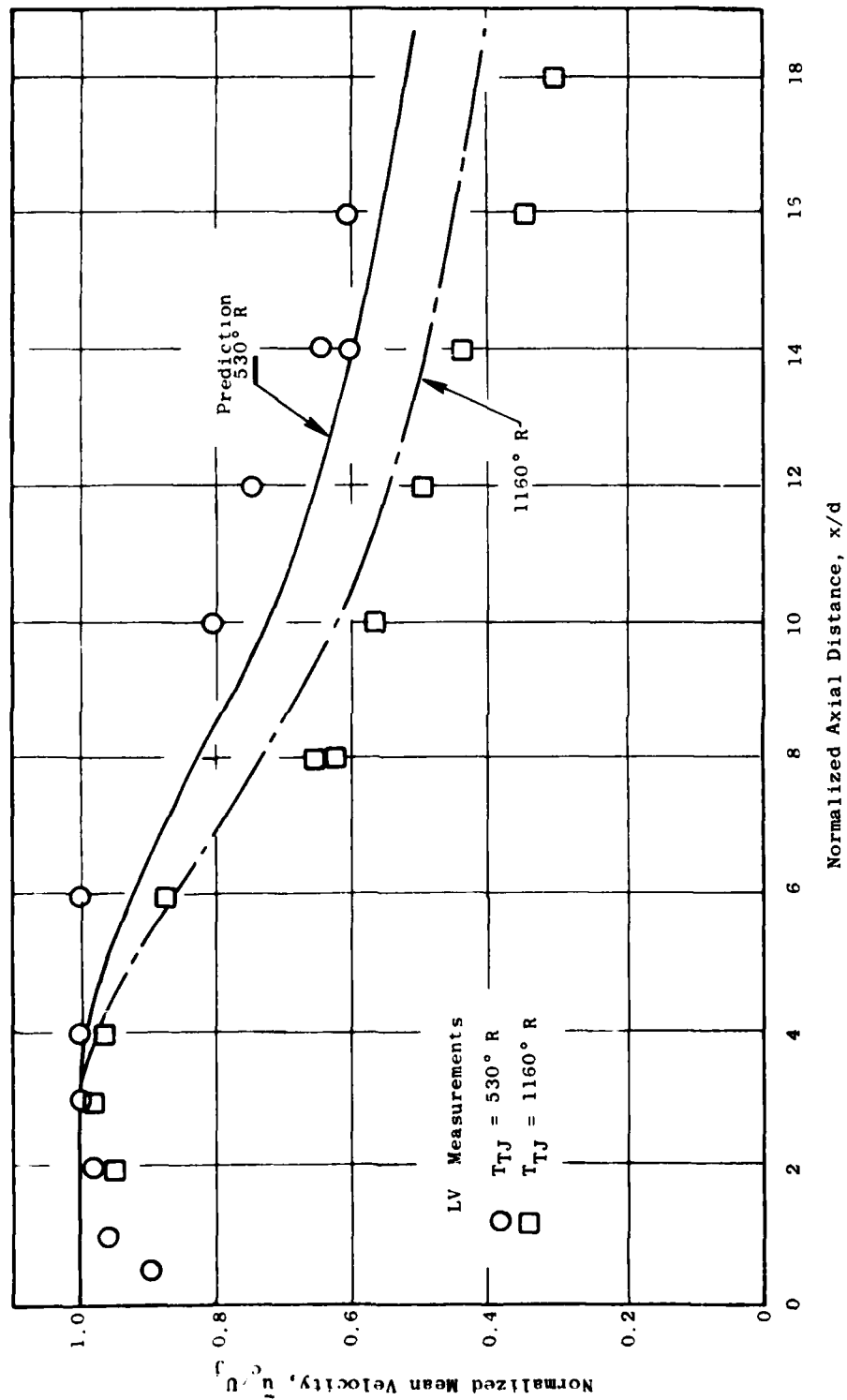


Figure 4-46. Comparison of Tube Centerline Mean Velocity Decay Twin Parallel Round Jets, $S/D = 1.33$, $M_J = 0.98$.

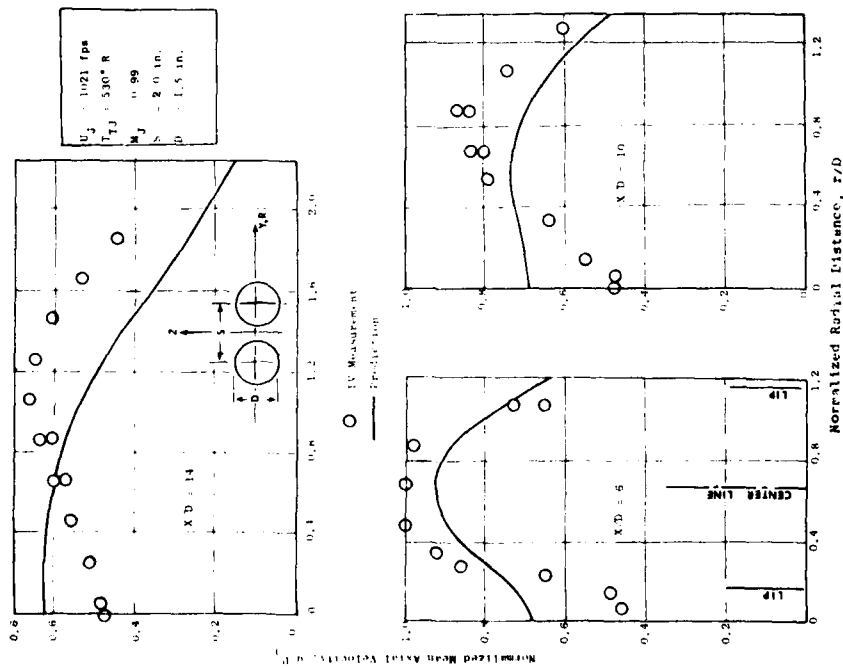


Figure 4-47. Comparison of Mean Velocity Profiles Twin Parallel Round Jets, $S/D = 1.333$.

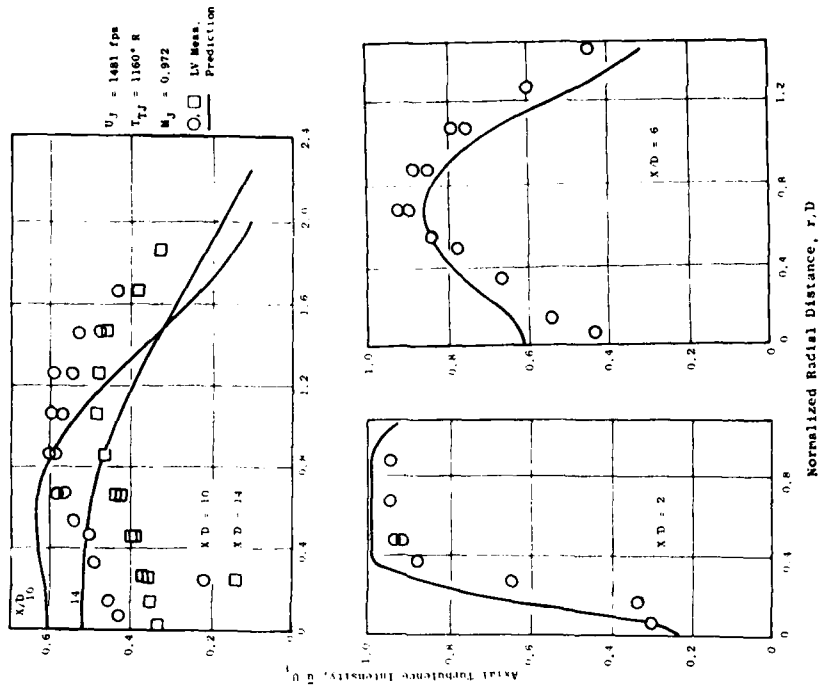


Figure 4-48. Comparison of Mean Velocity Profiles Twin Parallel Round Jets, $S/D = 1.333$.

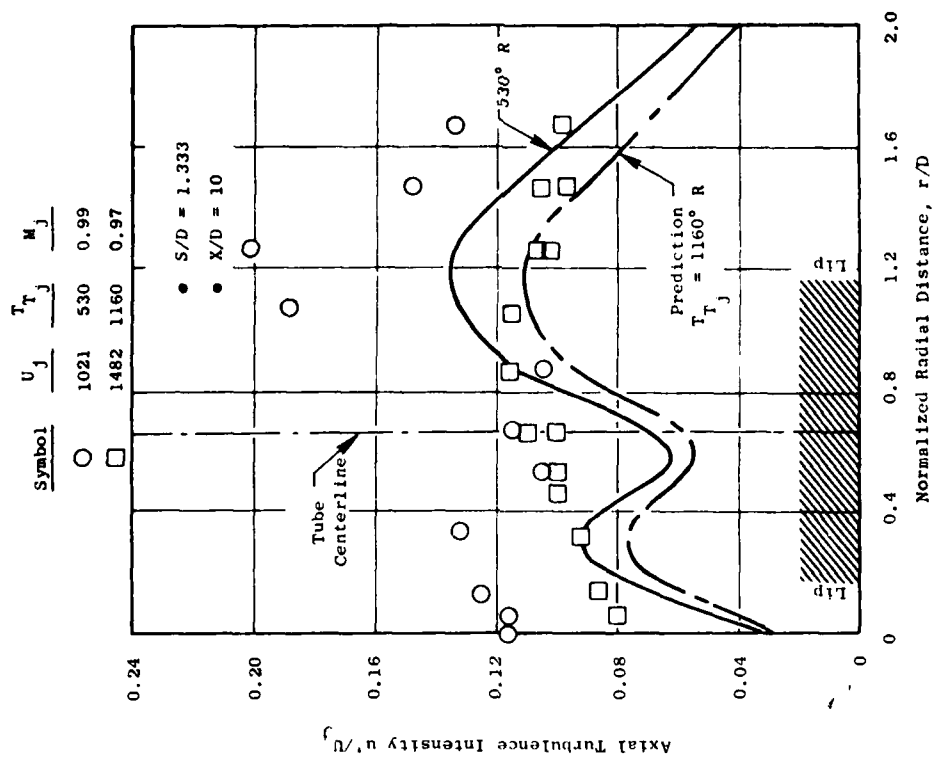


Figure 4-50. Comparison of Turbulence Intensity Profiles, Twin Parallel Round Jets.

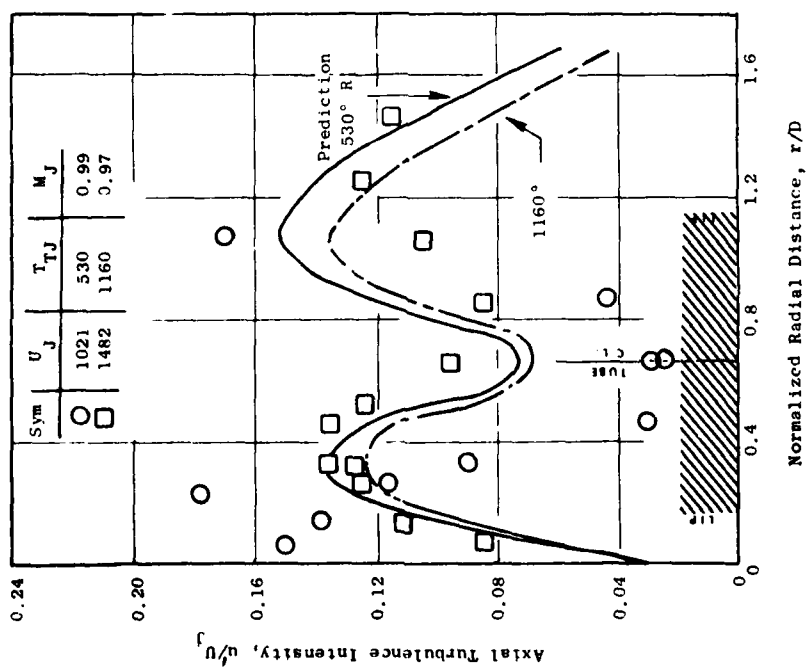


Figure 4-49. Comparison of Turbulence Intensity Profiles - Twin Parallel Round Jets.

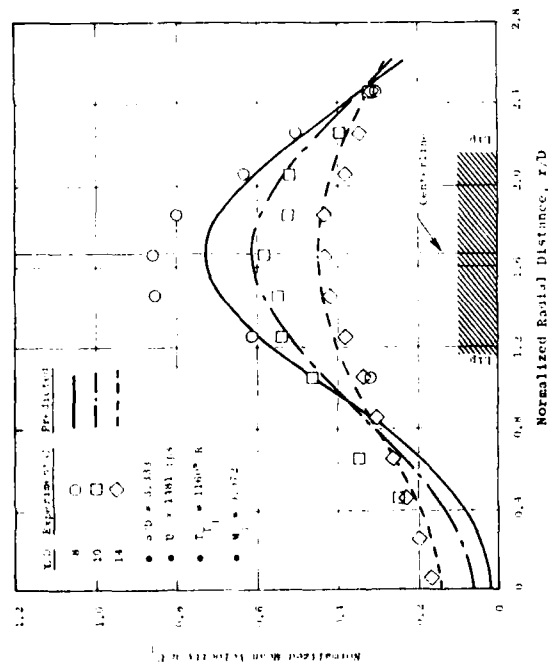


Figure 4-51. Comparison of Mean Velocity Profiles, Twin Parallel Round Jets.

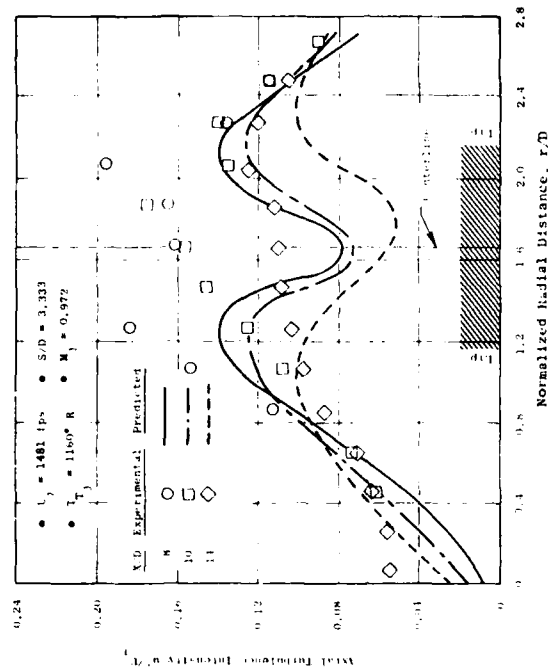


Figure 4-52. Comparison of Turbulence Intensity Profiles, Twin Parallel Round Jets.

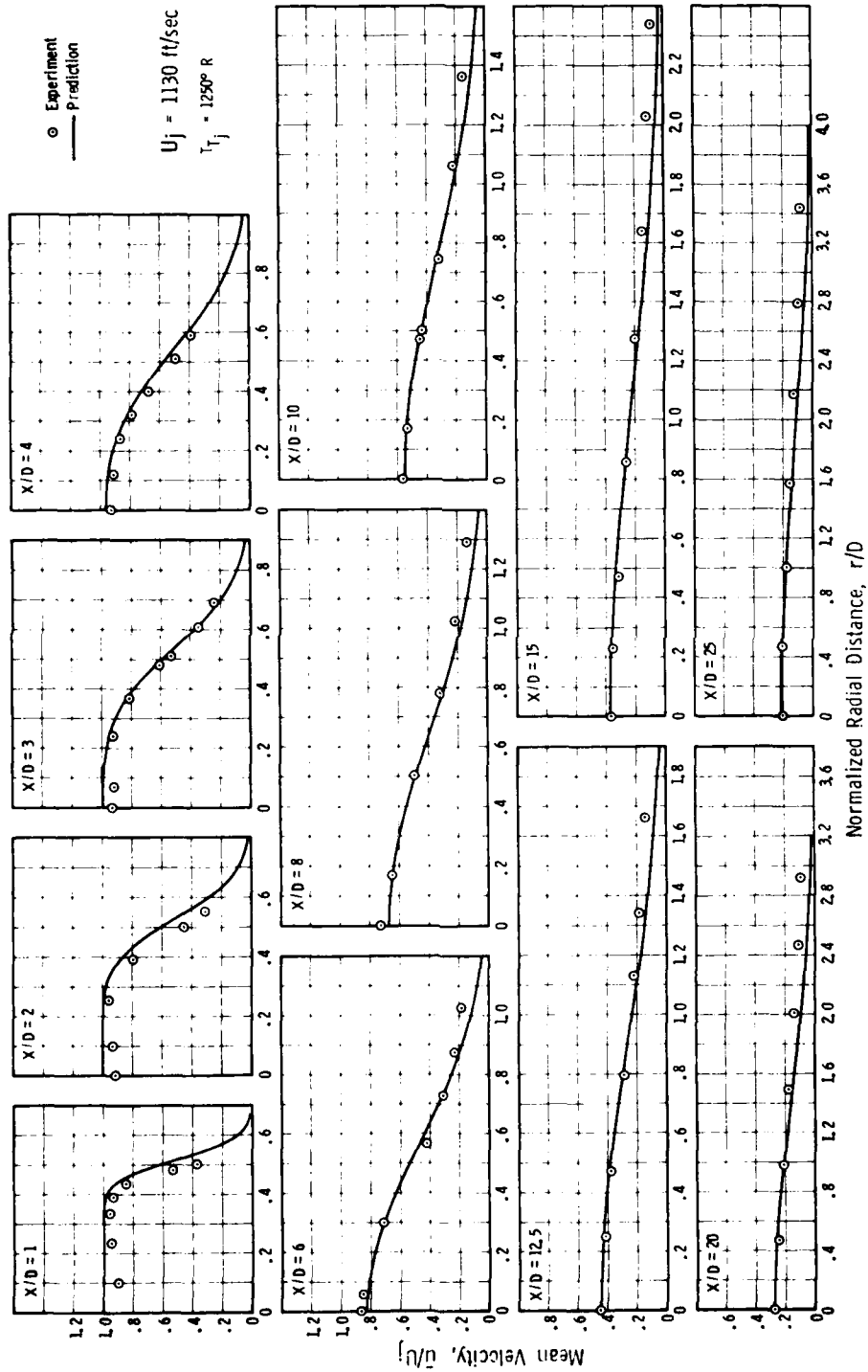


Figure 4-53. Comparison of Experimental and Predicted Mean Velocity Profiles for a 3.56 in. Conical Nozzle.

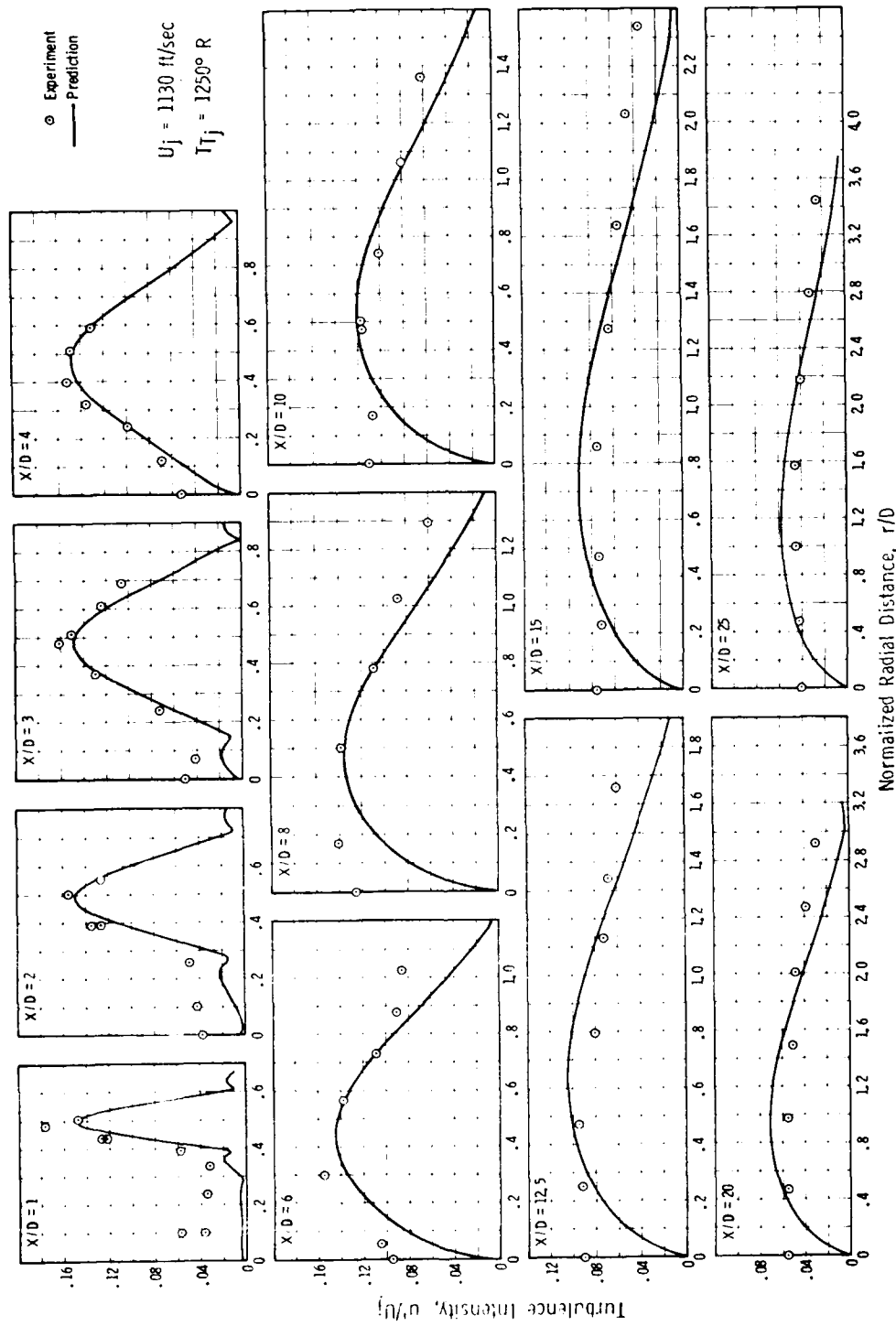


Figure 4-54. Comparison of Experimental and Predicted Turbulence Intensity Profiles for a 3.56 in. Conical Nozzle.

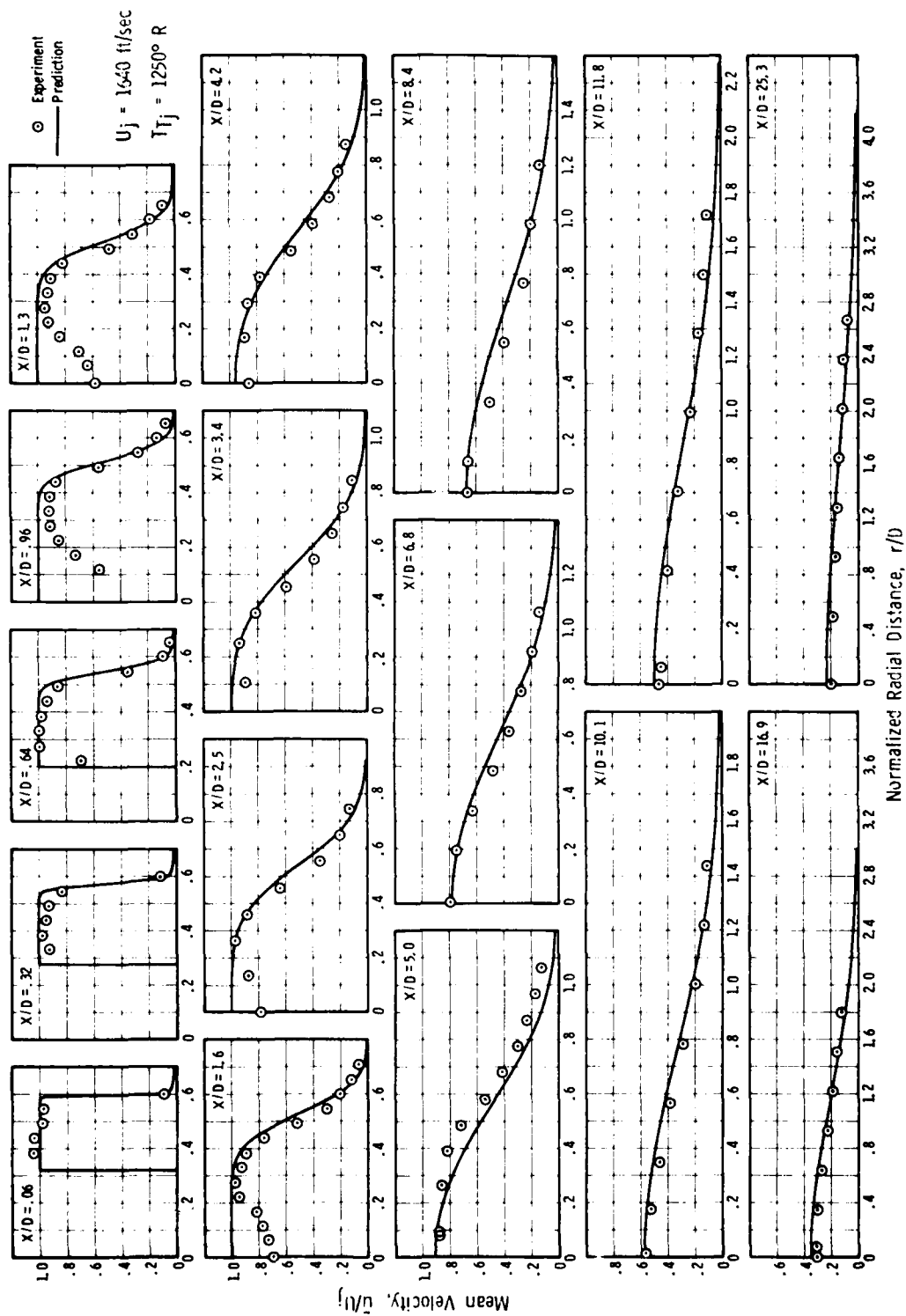


Figure 4-55. Comparison of Experimental and Predicted Mean Velocity Profiles for a 7.63 in. Effective Diameter C/D Plug Nozzle.

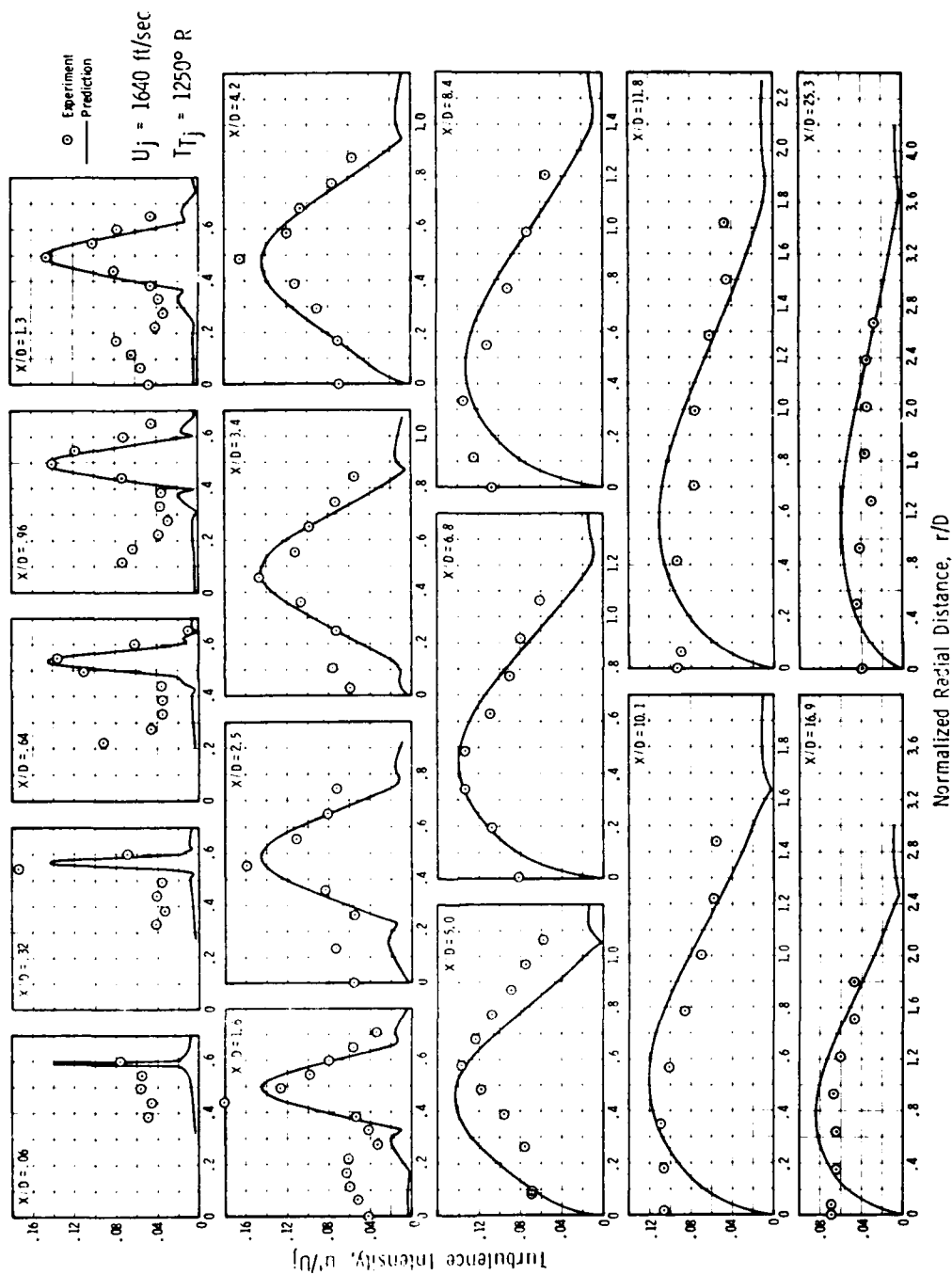


Figure 4-56. Comparison of Experimental and Predicted Turbulence Intensity Profiles for a 7.63 in. Effective Diameter C/D Plug Nozzle.

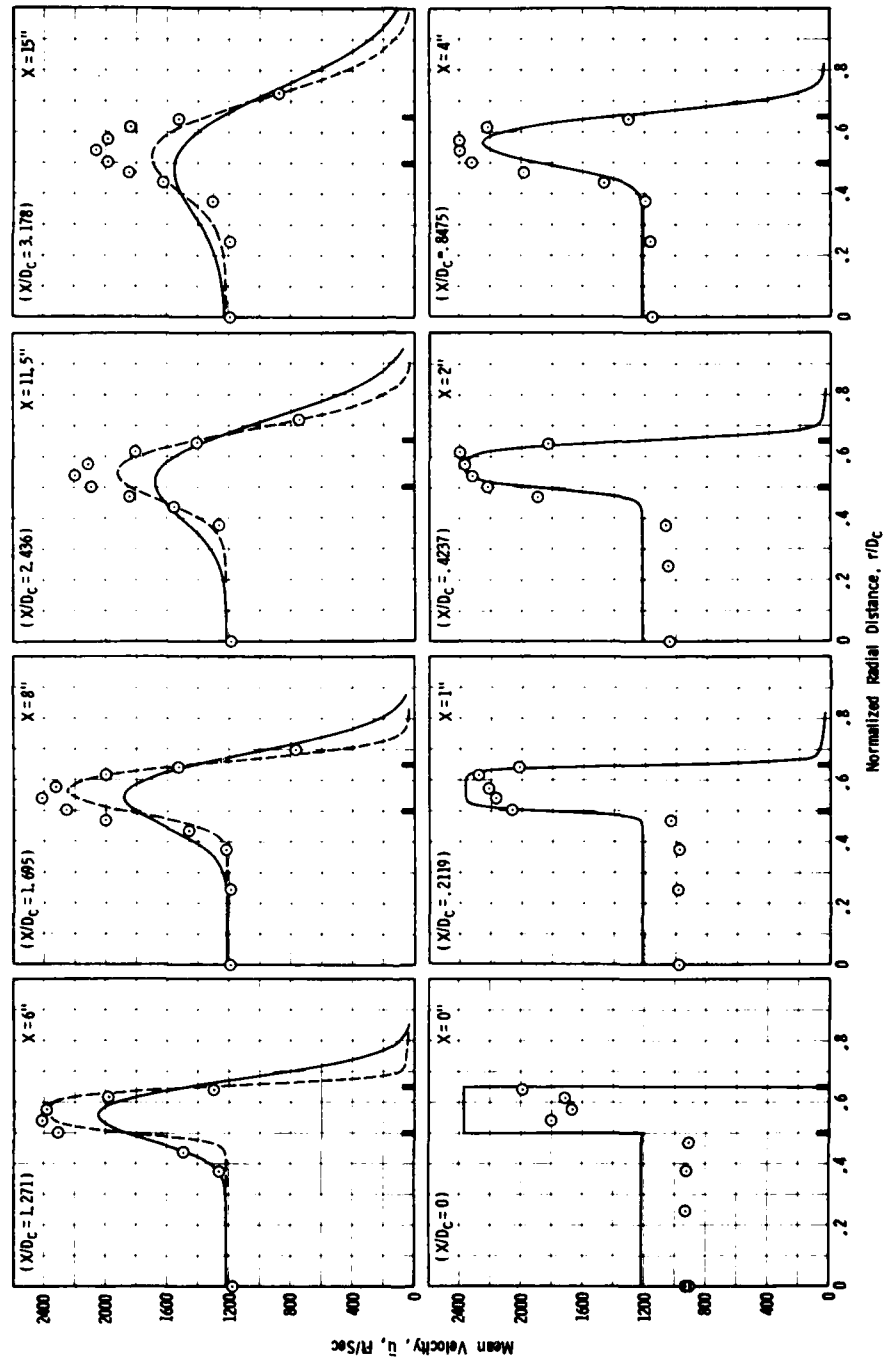


Figure 4-57a. Comparison of Experimental and Predicted Mean Velocity Profiles for a Coplanar Coannular Jet AR = 0.647; V_{fan} = 2400 ft/sec; V_{core} = 1200 ft/sec; T_{fan} = 1603° R; T_{core} = 994° R.

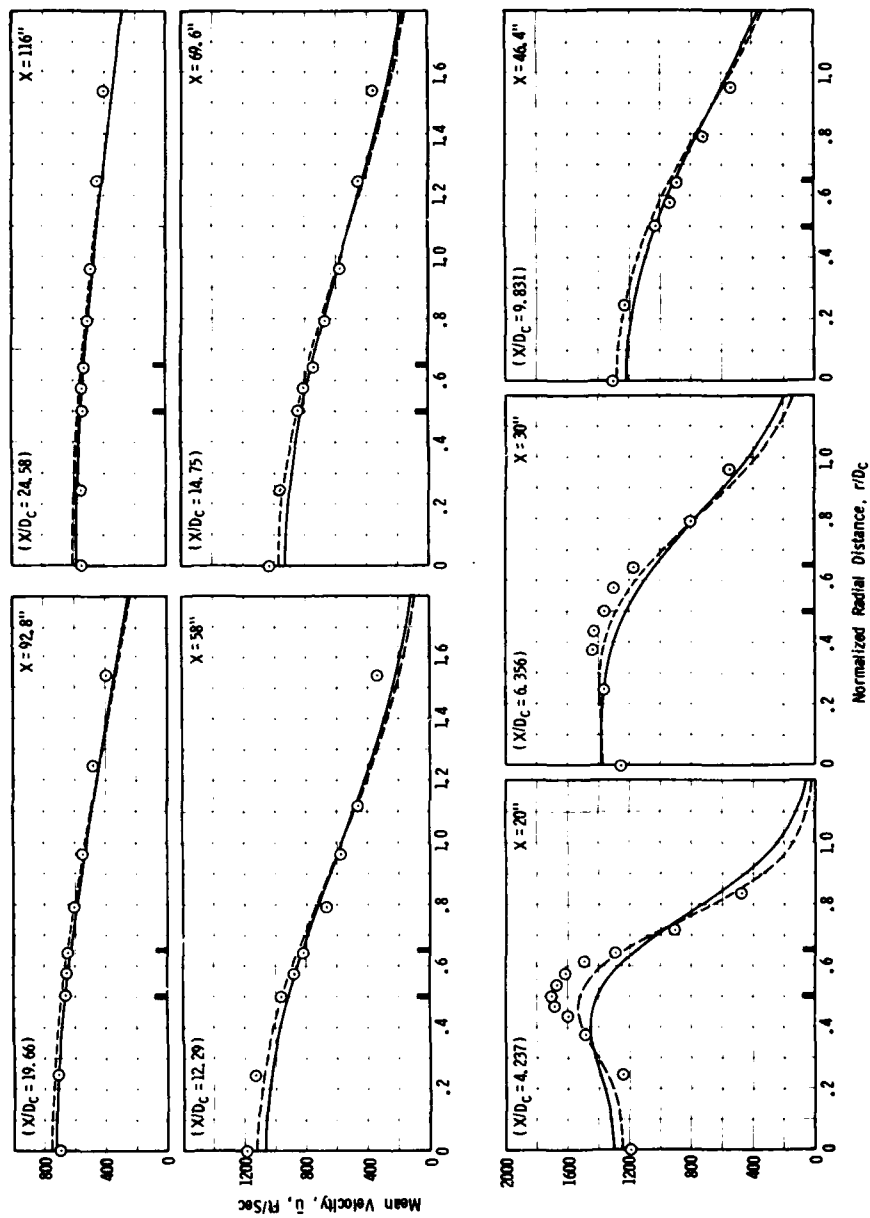


Figure 4-57b. Comparison of Experimental and Predicted Mean Velocity Profiles for a Coplanar Coannular Jet AR = 0.647; $V_{fan} = 2400$ ft/sec; $V_{core} = 1200$ ft/sec; $T_{Tfan} = 1603^\circ R$; $T_{Tcore} = 994^\circ R$.

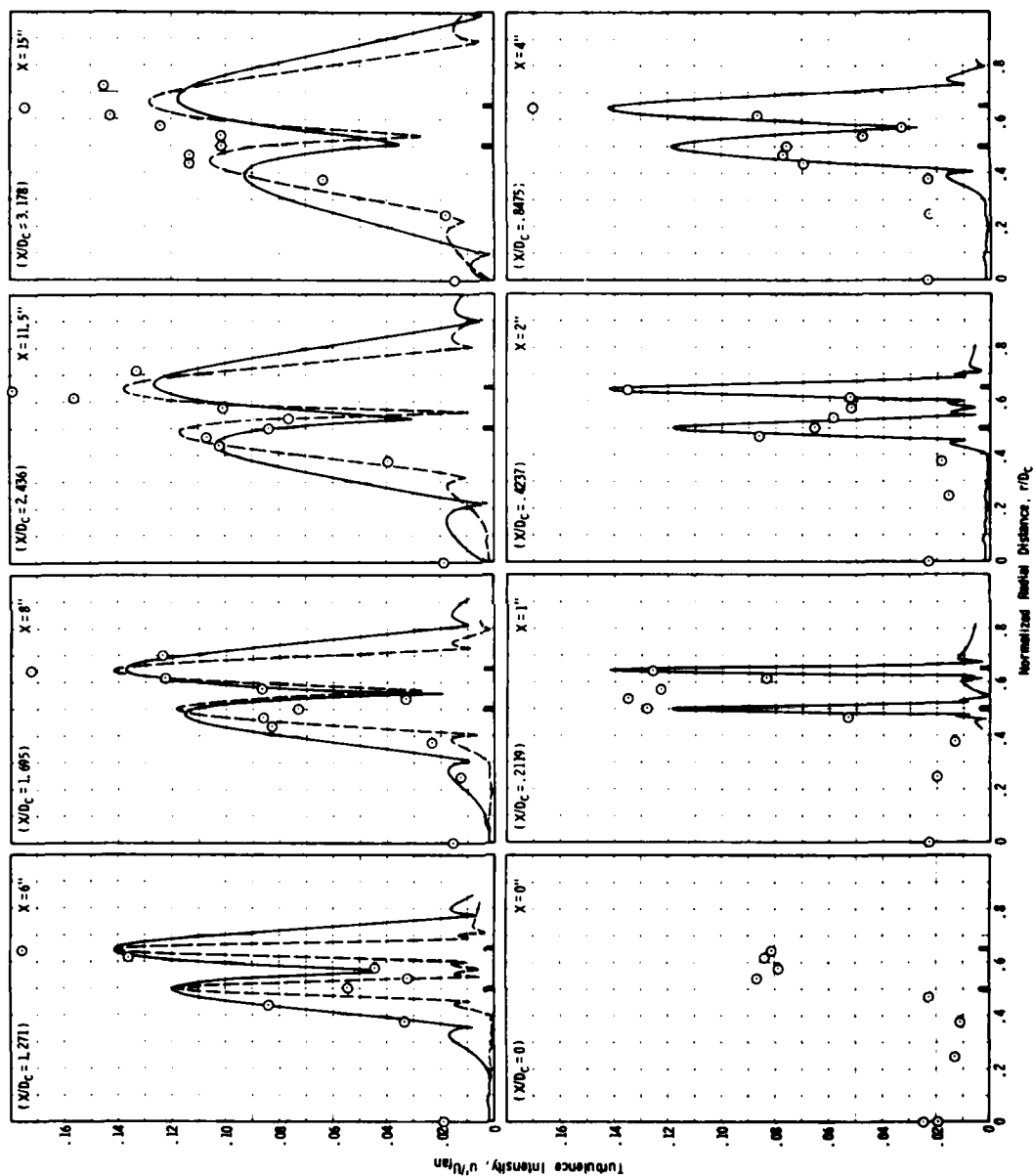


Figure 4-58a. Comparison of Experimental and Predicted Turbulence Intensity Profiles for a Coplanar Coannular Jet AR = 0.647; V_{fan} = 2400 ft/sec; V_{core} = 1200 ft/sec, T_{Tfan} = 1603° R; T_{Tcore} = 994° R.

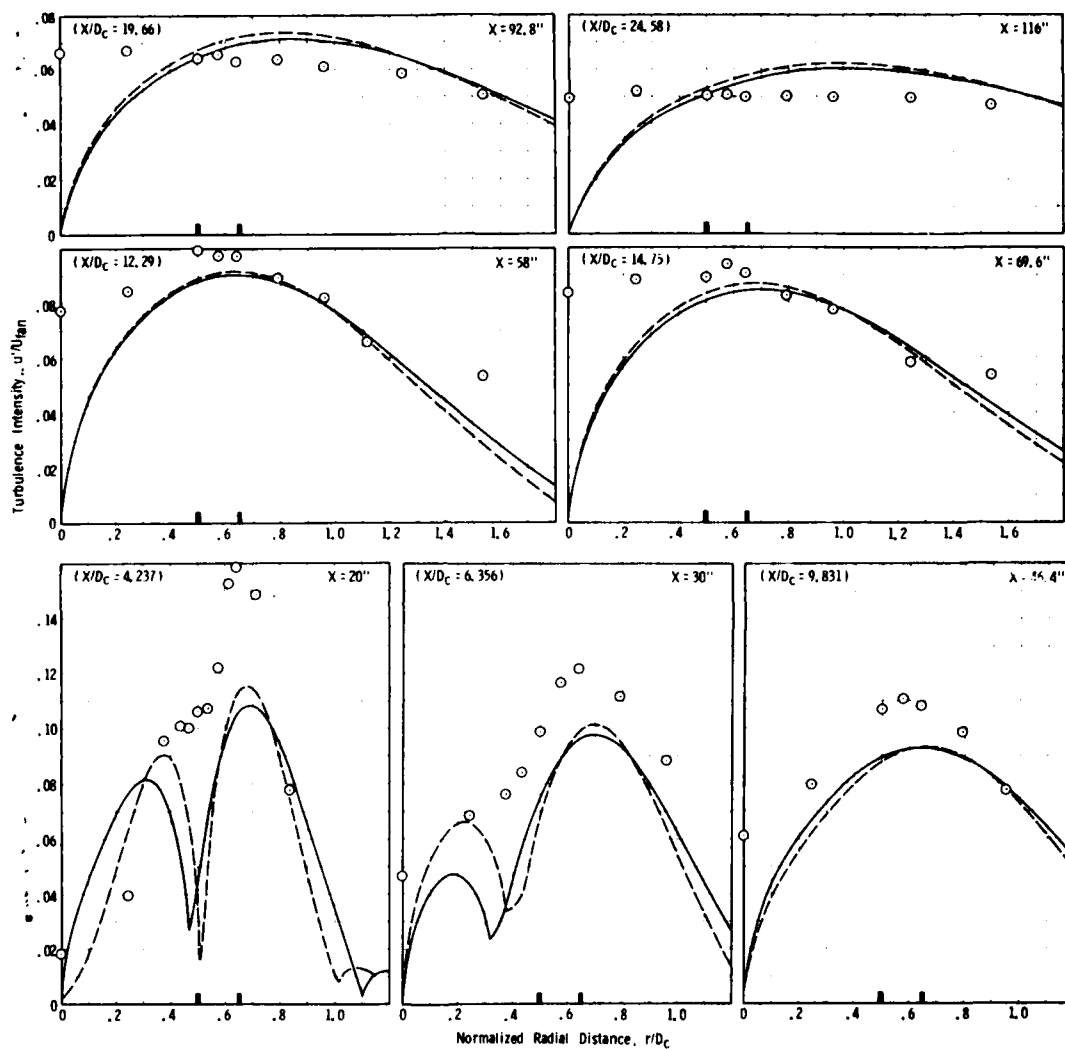


Figure 4-58b. Comparison of Experimental and Predicted Turbulence Intensity Profiles for a Coplanar Coannular Jet $AR = 0.647$;
 $V_{fan} = 2400$ ft/sec; $V_{core} = 1200$ ft/sec, $T_{Tfan} = 1603^\circ R$;
 $T_{Tcore} = 994^\circ R$.

comparisons. There are two predictions shown in these figures. The solid line represents predictions made with the origin $x = 0$ located at the nozzle exit plane, as is conventional practice. However, it may be noted from the experimental measurements in Figure 4-57 that full expansion to isentropic velocities does not occur until some distance downstream of the nozzle exit plane. This is because the outer stream pressure ratio is considerably higher than the choking value, causing external expansion downstream of the nozzle exit plane. Since the outer stream static pressure is transmitted to the inner stream, the inner stream pressure ratio is controlled by the outer stream static pressure variation and does not reach full expansion pressure ratio until the outer stream static pressure has reduced to the ambient value. From the mean velocity profile measurements shown in Figure 4-57, full expansion occurs at $x = 0.85 D_c$. A first approximation to modeling this effect is to merely shift the origin of the calculation to $x_e = 0.85 D_c$ for both inner and outer streams. This calculation is shown as the dashed line in Figures 4-57 and 4-58. It can be seen that this modification gives much better agreement with the measurements. This example was chosen to illustrate the possible consequence of supercritical pressure ratio jets and show how one can still utilize the present theory to model such flows.

The final data/theory comparison included in this section is shown in Figure 4-59. Here the centerline distribution of turbulence velocity for a conical subsonic jet as predicted by equation (236) is shown, along with the jet centerline measurements from Figure 4-54. The general shape is predicted quite well, lending confidence to the assumed model given by equation (236).

4.5.9 Concluding Remarks

The preceding sections have attempted to present a rather complete treatment of modeling complex jet flows by an adaptation and extension of Reichardt's method. The method is quite general in that it is capable of analyzing momentum and heat transport (as well as species concentration, as discussed by Alexander, et al.⁽⁵⁹⁾). The samples of data/theory comparisons shown herein have demonstrated that it is a reasonably accurate procedure.

It is conceivable that a much more refined turbulence model could be developed within the framework of Reichardt's method by employing the generalized transport equation approach of Launder and Spalding⁽⁵⁷⁾. Transport equations of the diffusion type for such turbulence properties as kinetic energy, mixing length, Kolmogorov frequency, etc., could be developed and incorporated into the general computational procedure, eliminating the need for some of the assumptions and approximations made in Section 4.5.5. This would be no easy task since the present state of the art in so-called two-equation models of turbulence is only now beginning to show promise of providing meaningful results. The benefit, aside from having a hopefully more accurate prediction of turbulence intensity, length-scale, characteristic frequency, etc., would be the ability to account for upstream history. The present method does not recognize the presence of turbulence generated upstream of the nozzle exit plane, and only predicts the turbulent stresses generated at a point, ignoring the contributions convected from upstream points in the flow.

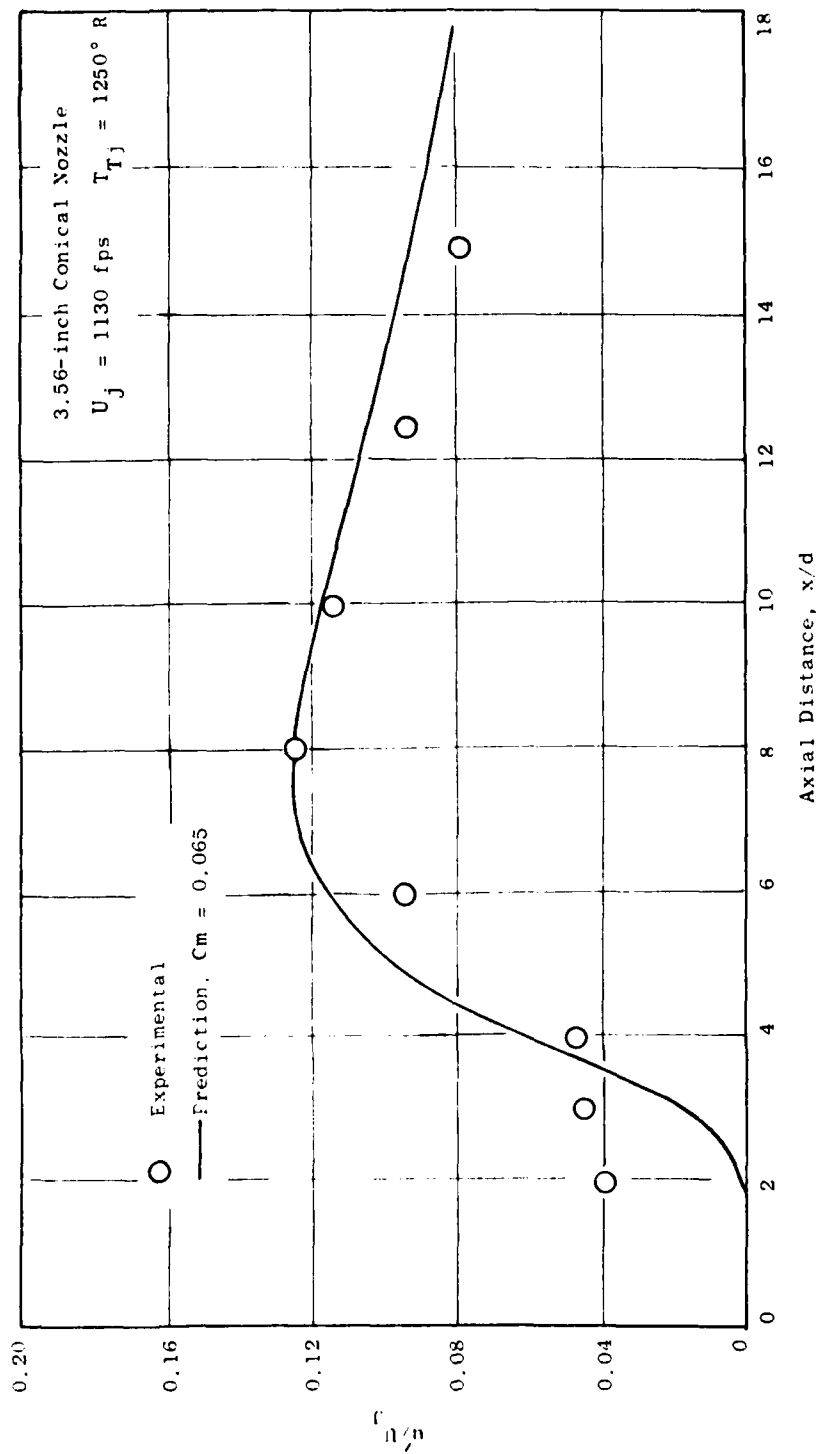


Figure 4-59. Comparison of Measured and Predicted Jet Centerline Turbulence Intensity.

The effects of solid surfaces (plugs, centerbodies, shrouds, etc.) in the jet plume can be more rigorously modeled if a finite-difference (downstream-marching) technique is employed. This would also relieve some of the restrictions on non-coplanar nozzle elements currently present in the model computation procedure. An additional advantage to the finite-difference solution method would be the capability for analyzing internal mixer nozzle flows. The abandonment of the closed-form solution method, however, would probably only be practical for axisymmetric nozzles; i.e., the fully three-dimensional jet finite-difference computation could be too ambitious and costly an undertaking for the benefits to be gained.

4.6 SHOCK-CELL NOISE

4.6.1 Introduction

Shock-cell broad-band noise is a dominant contributor to the acoustic far field of high velocity conical nozzle jets operating at highly supercritical pressure ratios. A theoretical model of the shock-cell noise mechanism has been proposed by Harper-Bourne and Fisher(69) and it is very successful in predicting the characteristic features of conical nozzle jet noise for supercritical pressure ratios, in the forward arc where jet mixing noise is low relative to the shock-cell noise contribution.

Recognizing the importance of this noise mechanism for high velocity jets, a study was undertaken to extend the basic principles developed for the conical nozzle jet to noncircular nozzles, i.e., coannular, multilobe, multi-tube, etc., applicable to mechanically suppressed exhaust systems. In addition, the influence of aircraft motion on shock-cell noise was studied and assessed. An extension to the Harper-Bourne/Fisher (HBF) model was formulated to predict noncircular nozzle shock-cell noise, based on examination of shock-cell noise characteristics of a wide variety of nozzle shapes.

The work summarized herein begins with a review of the conical nozzle shock-cell noise mechanisms as proposed by HBF; the shock-cell noise scaling principles arising from the theoretical model are tested using experimental data obtained as part of this program. A semiempirical prediction method is discussed which permits rapid computation of shock-cell noise spectra for conical nozzles. Utilizing experimental measurements from a free-jet facility, the effects of forward motion on shock-cell noise source alteration are assessed. Following the work on conical nozzles, the experimentally-observed characteristics of the shock-cell noise produced by noncircular nozzles are examined and correlated. Based on these studies, an extension of HBF theory to noncircular nozzles is formulated. Finally, a prediction procedure applicable to mechanically suppressed exhaust systems in flight is proposed, and suggestions for further work are made.

4.6.2 Review of a Theoretical Model for Conical Nozzles

The physical process by which shock-cell noise is generated, as proposed by HBF, is described as follows. In a convergent nozzle operating at supercritical pressure ratios, a pattern of regularly spaced shock formations exists. These shock patterns divide the plume into cells, as shown schematically in Figure 4-60. The spacing and strength of these shocks diminish in the downstream direction due to the mixing of the jet plume with the ambient air. The mixing process also produces turbulence in the form of statistically regular eddies which convect downstream with the flow. As these eddies pass through (or by) the shock fronts, they disturb the shocks, causing them to emit acoustic waves. The acoustic waves from the various shock cells can constructively or destructively interfere, depending on the shock spacing, the eddy convection velocity, and the life-time of a given eddy.

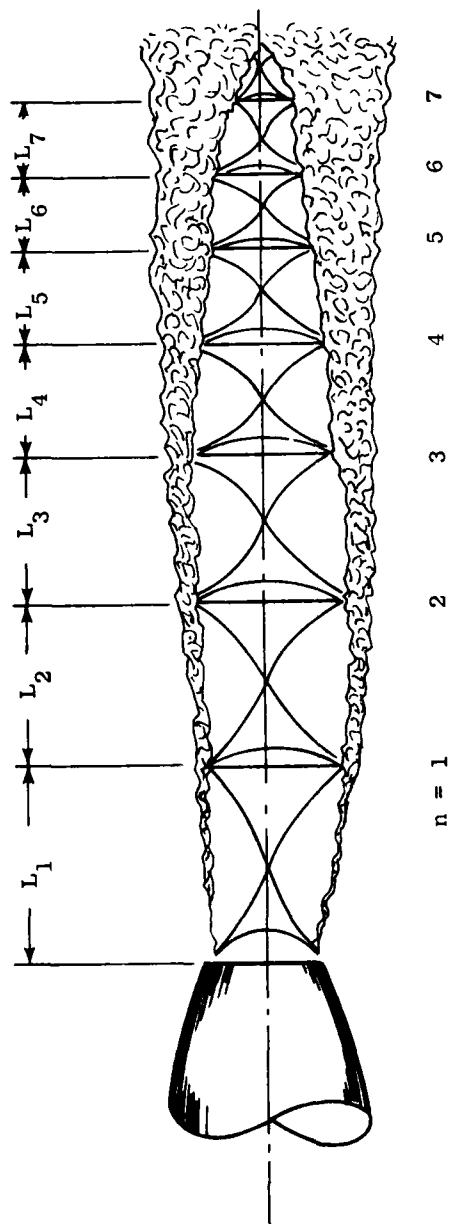


Figure 4-60. Schematic Representation of Shock Cell Formations in an Underexpanded Supersonic Jet.

As mentioned above, the primary physical mechanism for the production of broad-band noise by the presence of shock cells in the jet plume is the emission of acoustic waves by the shock fronts as they are "disturbed" by the passage of turbulent eddies through and/or by them. The eddies, produced in the mixing layers of the plume, are themselves unsteady fluctuating "blobs" of vorticity, so that the emitted acoustic waves from the shocks have characteristics which are related to the unsteadiness of the turbulent disturbances, i.e., their characteristic frequency and amplitude. The strength of the emitted wave must also be a function of the shock strength. The process is similar to the linear "transfer function" model of Ribner(70), where a vorticity wave of given amplitude and frequency is input to a shock, and the output is a transmitted vorticity wave, an internally generated entropy wave, and a pressure (acoustic) wave.

Each shock in the jet plume emits acoustic waves in a random or broad-band fashion, related to the randomness of the disturbing turbulence. The far-field time-average correlation of this emission, after summing the contributions from all the shocks, produces a spectrum made up of two basic components. First, the sum of the mean-square pressure signals from each shock produces a "group spectrum" which is rather broadband in character, similar to a jet mixing noise spectrum. The second component, referred to as the "interference spectrum", results from the selective reinforcement and cancellation which occurs between emitted waves from neighboring shocks. The superposition of these two components results in the rather "peaky" spectrum shape observed for shock-cell noise. This is illustrated in Figure 4-61.

Harper-Bourne and Fisher(69) (HBF) proposed a model based on the assumption that each shock cell is effectively a stationary (relative to the nozzle) emitter of pressure waves of the form

$$P_n(t) \sim A_n(\omega) \cos [\omega(t - x_n/U_c)] \quad (240)$$

where $P_n(t)$ is the unsteady pressure at time t generated by the n th cell (or source), as it is disturbed by a turbulent eddy passing through it (at a convection speed U_c , oscillating at frequency ω). Here x_n denotes the axial distance downstream from the nozzle exit of the n th cell, and $A_n(\omega)$ denotes the amplitude of the pressure wave. The pressure in the far field at a distance r_0 from the nozzle exit plane and distance r_n from the source is then expressed as

$$P_n(r_0, \theta_1, t) = \frac{A_n(\omega)}{r_0} \cos[\omega(t - x_n/U_c - r_n/a_0)] \quad (241)$$

where a_0 is the ambient speed of sound. Note that x_n/U_c is just the time taken for an eddy to travel from the nozzle lip to the n th cell, and r_n/a_0 is the time required for the generated pressure wave to reach the observer. Also, θ_1 is the observer angle with respect to the upstream axis of the nozzle, shown in Figure 4-62.

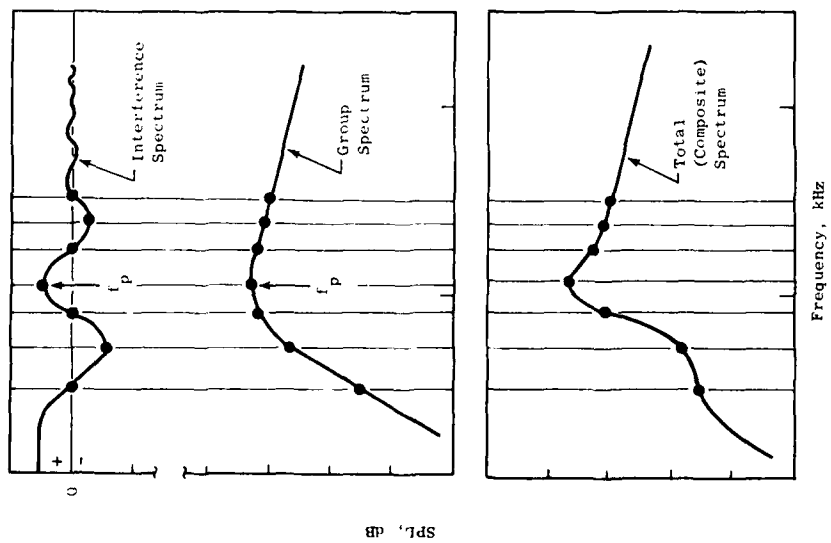


Figure 4-61. Illustration of Primary Components of a Conical Nozzle Shock Cell Noise Spectrum.

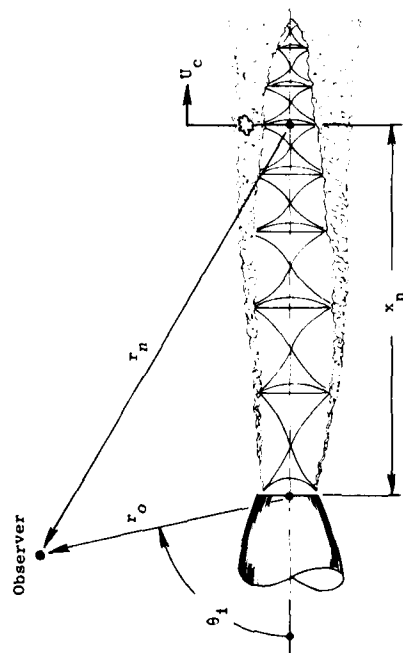


Figure 4-62. Nomenclature for Geometric Relations Between a Given Shock Cell Source at x_n and Observer.

By summing the contributions over all cells, squaring and forming a time-average, the mean-square pressure level in the far field was shown by HBF to have the form

$$\overline{p^2}(r_o, \theta_i, \omega) = \frac{1}{2r_o^2} \sum_n \sum_m A_n(\omega) A_m(\omega) \times \cos[(\omega/U_c)(x_n - x_m)(1 + M_c \cos \theta_i)] \quad (242)$$

where $M_c = U_c/a_o$. From equation (242) it can be inferred that the sound level will have a maximum when

$$\frac{\omega}{U_c} (x_n - x_m)(1 + M_c \cos \theta_i) = 2\pi$$

and multiples thereof. This implies that the spectrum will peak at a frequency f_p given by

$$f_p = \frac{\omega}{2\pi} = \frac{U_c}{L(1 + M_c \cos \theta_i)} \quad (243)$$

where $L = x_n - x_m$ is the shock-cell spacing between two adjacent cells. The peak frequency expression given by equation (243) agrees quite well with experimental shock noise spectrum peaks, as demonstrated by HBF. For round nozzles, it was found that the shock cell spacing (for the n th cell) was related to nozzle diameter and pressure ratio as follows:

$$\left. \begin{aligned} L_n &= L_1 - (n-1)\Delta L \\ \text{where } L_1 &= 1.31 \beta D \\ \text{and } \Delta L &= 0.06 L_1 \end{aligned} \right\} \quad (244)$$

The average spacing L_{avg} appropriate to estimating peak frequency in equation (243) is given by

$$L_{avg} = 1.1 \beta D \quad (245)$$

$$\text{where } \beta = \sqrt{M_j^2 - 1} \quad (246)$$

The nozzle diameter is D , and the ideally-expanded (Isentropic) Mach number M_j is given by

$$M_j^2 = \frac{2}{\gamma-1} \left[\left(\frac{P_{Tj}}{P_o} \right)^{\frac{\gamma-1}{\gamma}} - 1 \right] \quad (247)$$

where γ is the ratio of specific heats, P_{Tj} is the nozzle stagnation pressure, and P_o is the ambient static pressure.

In order to completely define the spectrum, HBF employed cross-correlation of fluctuations measured at various shock cell locations using Laser-Schlieren techniques. These measurements, along with certain similarity assumptions, defined the products $A_n(\omega) A_m(\omega)$ for all combinations of m and n , in terms of a normalized "group source spectrum" and a normalized cross-correlation "interference" spectrum. If we set $n = m$, equation (242) yields the simple form

$$\overline{p_o^2}(r_o, \theta_i, \omega) = \frac{1}{2r_o^2} \sum_{n=1}^N A_n^2(\omega) \quad (248)$$

This is the autocorrelation or group source spectrum which would result if there were no constructive or destructive interference effects. We now define

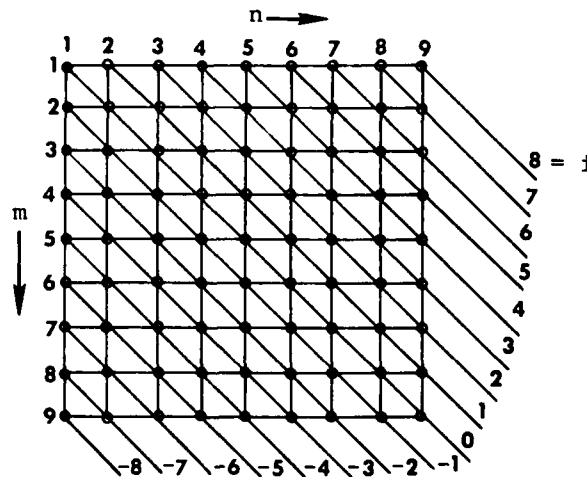
$$A_o(\omega) = \sum_{n=1}^N A_n^2(\omega) \quad (249)$$

$$\text{and } A_{mn}(\omega) = A_m(\omega) A_n(\omega) \quad (250)$$

The double summation over (m, n) can be replaced by a summation over (n, i) , where

$$i = n - m$$

The summation matrix is graphically illustrated in the sketch below:



Since $i = 0$ gives the $A_0(\omega)$ = component, and since $A_m(\omega)A_n(\omega) = A_n(\omega)A_m(\omega)$, and since $\cos(-\phi) = \cos(\phi)$, the summation in equation (242) can be written as follows:

$$\begin{aligned} \overline{p^2}(r_o, \theta_i, \omega) = & \frac{1}{2r_o^2} \left\{ A_0(\omega) + 2 \sum_{i=1}^{N-1} \sum_{n=1}^{N-i} A_{nm}(\omega) \right. \\ & \left. \times \cos \left[\frac{\omega}{U_c} (x_n - x_m) (1 + M_c \cos \theta_i) \right] \right\} \end{aligned} \quad (251)$$

Now from Figure 4-60 and equations (244) it can be seen that

$$\begin{aligned} x_n &= L_1 \left[n - \frac{\Delta L}{L_1} \sum_{j=0}^{n-1} j \right] \\ x_m &= L_1 \left[m - \frac{\Delta L}{L_1} \sum_{j=0}^{m-1} j \right] \end{aligned} \quad (252)$$

From the relationship $\sum_{j=1}^J j = \frac{1}{2} J(J+1)$ it can be shown that equation (252) yields the following expression for $x_n - x_m$:

$$x_n - x_m = i L_1 \left[1 - \frac{1}{2} \epsilon (2n+i-1) \right], \quad \epsilon = \Delta L / L_1 \quad (253)$$

Substituting equation (253) into (251) yields the following form for the far-field sound pressure spectrum:

$$\begin{aligned} \overline{p^2}(r_o, \theta_i, \omega) = & \frac{1}{2r_o^2} \left\{ A_0(\omega) + 2 \sum_{i=1}^{N-1} \sum_{n=1}^{N-i} A_{nm}(\omega) \right. \\ & \left. \times \cos \left[\frac{\omega i L_1}{U_c} (1 + M_c \cos \theta_i) \left(1 - \frac{1}{2} \epsilon [2n+i-1] \right) \right] \right\} \end{aligned} \quad (254)$$

The cross-correlation spectrum $A_{nm}(\omega)$ was assumed by HBF to be related to the average $A_0(\omega)$ per cell, i.e.,

$$A_{nm}(\omega) = \frac{1}{N} A_0(\omega) C_i(\omega) \quad (255)$$

where $C_i(\omega)$ is the cross-correlation spectrum between any two cells m and n , dependent only on the difference $i = n - m$. From the Laser-Schlieren measurements, HBF deduced that $C_i(\omega)$ should possess the form

$$C_i(\omega) = C_1^\alpha(\omega), \alpha = i^2 \quad (256)$$

and $C_1(\omega)$ is the correlation spectrum between any two adjacent cells ($i = 1$). The functions $A_0(\omega)$ and $C_1(\omega)$ were determined empirically. The overall sound pressure is given by

$$\overline{p^2}(r_o, \theta_i) = \int_0^\infty \overline{p^2}(r_o, \theta_i, \omega) d\omega$$

By assuming that the interference terms in equation (254) contribute negligibly to the integration, it is seen that [HBF⁽⁶⁹⁾],

$$\overline{p^2}(r_o, \theta_i) = \frac{1}{2r_o^2} \int_0^\infty A_o(\omega) d\omega$$

It was found empirically by HBF that

$$\text{OASPL} = 158.5 + 10 \log_{10} [(D/r_o)^2 \beta^4] \quad (257)$$

where $\beta = \sqrt{M_j^2 - 1}$. Hence

$$\overline{p^2}(r_o, \theta_i) \sim \frac{D^2}{r_o^2} \beta^4 \sim \frac{1}{2r_o^2} \int_0^\infty A_o(\omega) d\omega$$

HBF assumed a form for $A_o(\omega)$ as follows:

$$A_o(\omega) = f(P_{Tj}/P_o) H_o(\omega L_1/a_o) \quad (258)$$

where S_n is a Strouhal number defined by $S_n = \omega L_1/a_o$, and $H_o(S_n)$ is a "universal" spectrum shape function. Noting that $d\omega = (a_o/L_1) dS_n$, and combining the above two expressions, we find that

$$D^2 \beta^4 \sim \frac{a_o}{L_1} f(P_{Tj}/P_o) \int_0^\infty H_o(S_n) dS_n$$

Since the integral in the above is just a constant, it is found that

$$f(P_{Tj}/P_o) \sim L_1 D^2 \beta^4 / a_o \quad (259)$$

HBf further simplified equation (259) by substituting L_1 from (244) to give $f \sim D^3 \beta^5 / a_o$, but this is only correct for a conical nozzle, whereas, equation (259) is more general. It can further be shown that, by integrating equation (254) over a bandwidth $\Delta\omega$, the one-third octave spectrum can be obtained as follows:

$$\begin{aligned} \overline{p^2}(r_o, \theta_i, \omega) &= \frac{b\omega_M A_o(\omega_M)}{2r_o^2} \left\{ 1 + \frac{2}{N} \sum_{i=1}^{N-1} C_i(\omega_M) \right. \\ &\quad \left. \sum_{n=1}^{N-i} \frac{\cos(K\omega_M) \sin(Kb\omega_M/2)}{(Kb\omega_M/2)} \right\} \end{aligned} \quad (260)$$

where

$$K = \frac{iL_1}{U_c} (1 + M_c \cos \theta_i) \left[1 - \frac{1}{2} \epsilon (2n+i-1) \right] \quad (261)$$

and ω_M = one-third octave center frequency, and b is the percent bandwidth $b = \Delta\omega/\omega_M = 0.23155$.

From the HBF work, several important features of shock cell broad-band noise were revealed, and these are as follows:

- (1) The overall level (OASPL) is independent of jet temperature;
- (2) The overall level (OASPL) is omnidirectional, i.e., independent of observer angle θ_i ;
- (3) The overall level (OASPL) varies as the fourth power of the shock strength parameter β [see equation (257)].
- (4) The spectrum peak noise frequency is a function of jet velocity and shock spacing [see equation (243)].

4.6.3 Review of SNECMA Empirical Correlation

An empirical correlation method for predicting shock cell noise of conical nozzles is presented by SNECMA⁽⁷¹⁾. The method is based on an empirical observation that the shock-cell noise component of the far-field spectrum can be sufficiently represented by two straight lines, as illustrated in Figure 4-63. According to SNECMA, the low-frequency side of the spectrum has a slope of ~ 20 dB per octave. In contrast, the high-frequency side of the spectrum, α , was found to have a slope which varies with β and θ_i , and with jet stagnation temperature, T_{Tj} .

In this empirical approach, the spectrum peak frequency is determined from the HBF relation, equation (243). The peak level is then correlated as a function of β , θ_i and T_{Tj} . This correlation exhibits characteristics which differ from the HBF model in the following ways:

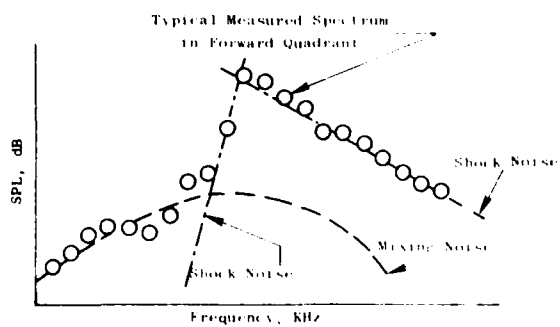
1. Shock-cell noise characteristics, both peak level and high-frequency spectrum slope, depend on jet temperature. To be noted is the fact that this correlation displays a significant temperature dependence only in the rear quadrant ($\theta_i > 90^\circ$), where separating of mixing noise and shock-cell noise contributions from the total noise is most difficult.
2. The overall noise level is not omni-directional, but the variation is small.
3. The variation of overall level with β is not a simple power dependence.

Upon examining the data base used for deriving the correlations presented by SNECMA⁽⁷¹⁾, it appears as though the case for a variable high-frequency spectrum slope α as a function of β , θ_i , and T_{Tj} may be overstated. In fact, a constant slope of $\alpha = 3$ dB per octave appears to "fit" most of the data quite well, and additionally agrees with the HBF model. Similarly, it is felt that the data base for the peak level correlation was insufficient, both in quantity and consistency in trends, to conclude that there was a significant dependence on jet temperature or angle.

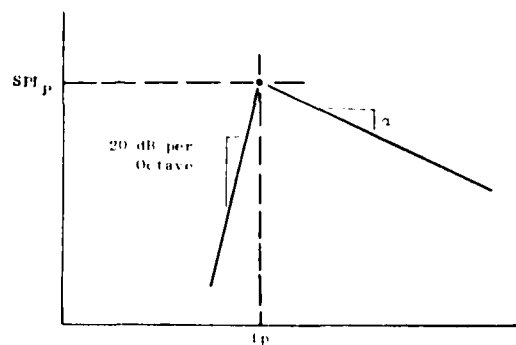
4.6.4 Experimental Correlations of Shock-Cell Noise for Conical Nozzle

To verify the basic physical concepts of shock cell noise emission proposed by Harper-Bourne and Fisher⁽⁶⁹⁾, a detailed study of experimental results obtained by Clapper, et al.⁽⁷²⁾ was undertaken to isolate the shock-cell noise contributions and test the observed characteristics against the HBF model. The acoustic results for a conical nozzle operating at turbojet cycle conditions were first examined.

Scale-model test results for a 3.56-inch (9.04 cm) nozzle are summarized in Figure 4-64. Shown are OASPL versus V_j/a_o data at observer angles of $\theta_i = 30^\circ, 90^\circ$, and 150° . Also shown are "best-fit" lines representing V_j^8 scaling, as would be predicted by the classical Lighthill⁽⁴⁾ result for jet



(a) Shock Cell Component Approximated by Straight Lines



(b) Model Representation of Shock Cell Spectrum and Correlation Parameters.

Figure 4-63. SNECMA Model of Shock Cell Noise Component of Spectrum.

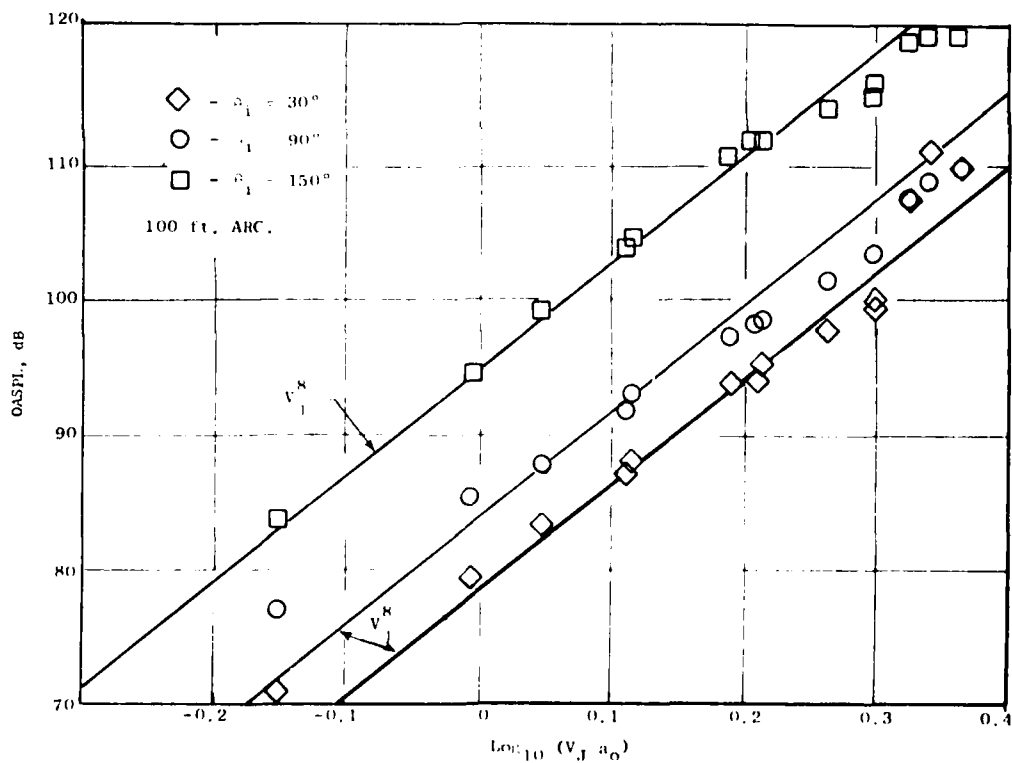


Figure 4-64. OASPL Velocity Dependence-3.56 in. Conical Nozzle, $V_0 = 0$.

mixing noise. It can be seen from this figure that overall sound pressure level (OASPL) obeys the V_j^8 - rule quite well for $V_j/a_0 < 1.6$. Above $V_j/a_0 = 1.6$, the OASPL falls below the V_j^8 - rule for $\theta_i = 90^\circ$ and 150° , while at $\theta_i = 30^\circ$, the data first drops below the "Lighthill" line, then rises above it for $V_j/a_0 > 2.0$. This is at first glance puzzling, since no "violent" departure from the classical result is apparent, even though the high velocity data correspond to supercritical pressure ratios where the HBF⁽⁶⁹⁾ theory would predict shock cell noise to be predominant. However, since this data corresponds to variations in P_{Tj} and T_{Tj} simultaneously (simulating a J85 engine operating line), jet temperature effects on mixing noise are actually confusing the picture.

To clarify this point, the results in Figure 4-64 were normalized for jet temperature effects via the density exponent method proposed by Cocking⁽⁷³⁾, as follows:

$$\text{OASPL}_n = \text{OASPL} - 10 \log_{10} \left[\left(\frac{\rho_j}{\rho_{isa}} \right)^\omega \frac{A_j}{r_o^2} \right] \quad (262)$$

where

$$\omega = 0.44 + 4.60 \log_{10} (V_j/a_0)$$

If the temperature effects are properly corrected for, this normalization should yield an adherence to the V_j^8 -rule, provided only mixing noise is contributing. These results are shown in Figure 4-65. It can be seen that in fact the noise levels are now higher than the V_j^8 -line at both $\theta_i = 90^\circ$ and 30° , for $V_j/a_0 > 1.6$ -2.0. A closer examination of supercritical pressure ratio data ($M_j > 1$) at $\theta_i = 30^\circ$ was carried out, using the points shown in Figure 4-64 plus additional test points taken where temperature T_{Tj} was held fixed and P_{Tj} was varied. These results are shown in Figure 4-66, in both uncorrected and normalized form [per equation (262)]. It can be seen from this figure that the temperature normalization fails to collapse the data onto a single line.

According to the HBF⁽⁶⁹⁾ theory, the OASPL should be only a function of the pressure ratio parameter β , given by equation (246). The data of Figure 4-66 was replotted versus β to test this hypothesis. The data at $\theta_i = 30^\circ$ should be shock-cell noise dominated, since jet mixing noise is relatively low at this angle. Figure 4-67 shows the normalized OASPL as a function of β , while Figure 4-68 shows the unnormalized OASPL versus β . These figures show that correcting for temperature effects when the noise is shock-cell dominated is the wrong thing to do. Figure 4-68 demonstrates that OASPL correlates quite well with β ; equation (257) derived by HBF is also shown in this figure, and the data for all temperatures collapse close to this line which varies as β^4 . Deviation from this line occurs at low values of β , as expected, because the mixing noise begins to again dominate the spectrum as the shock strength (as measured by β) diminishes. To complete the picture,

2-7

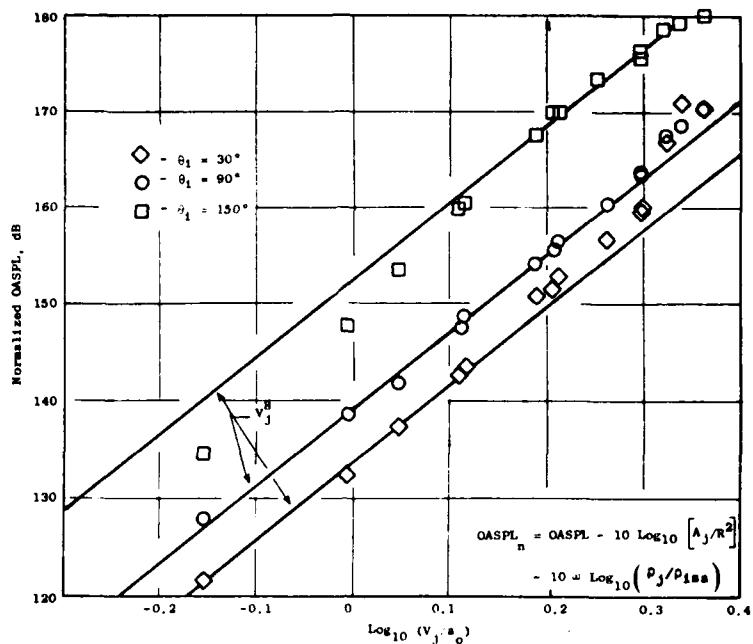


Figure 4-65. Normalized OASPL Velocity Dependence, 3.56 in. Conical Nozzle, $V_o = 0$ (J85 Operating Line).

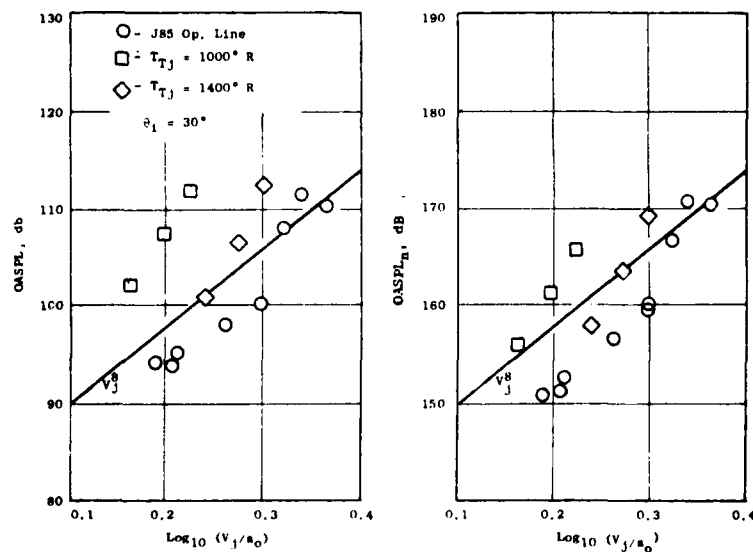


Figure 4-66. Supersonic Point Velocity Dependence, 3-56 inch Conical Nozzle, $V_o = 0$.

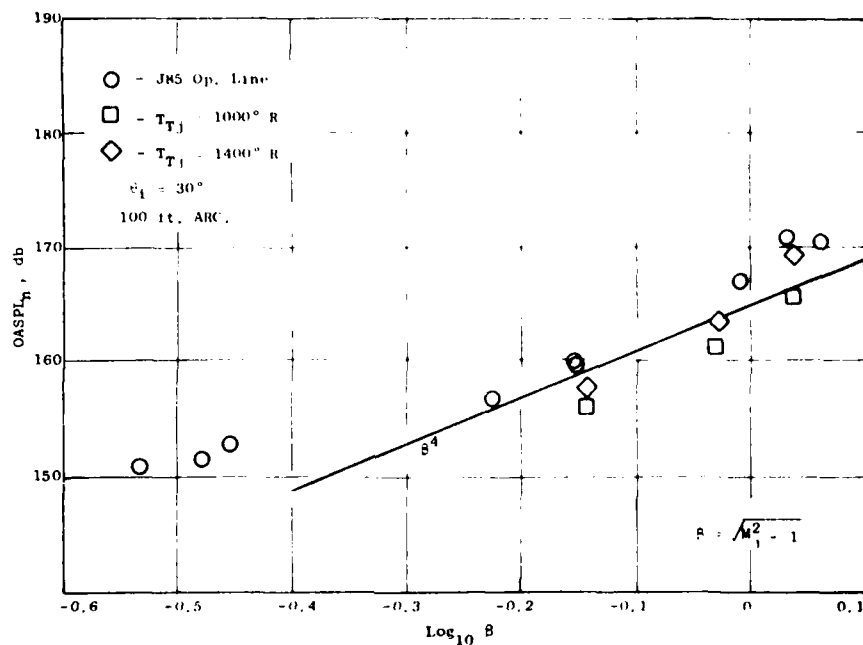


Figure 4-67. Supersonic Jet Normalized OASPL Correlation with Shock Strength, 3.56 in. Conical Nozzle, $V_o = 0$.

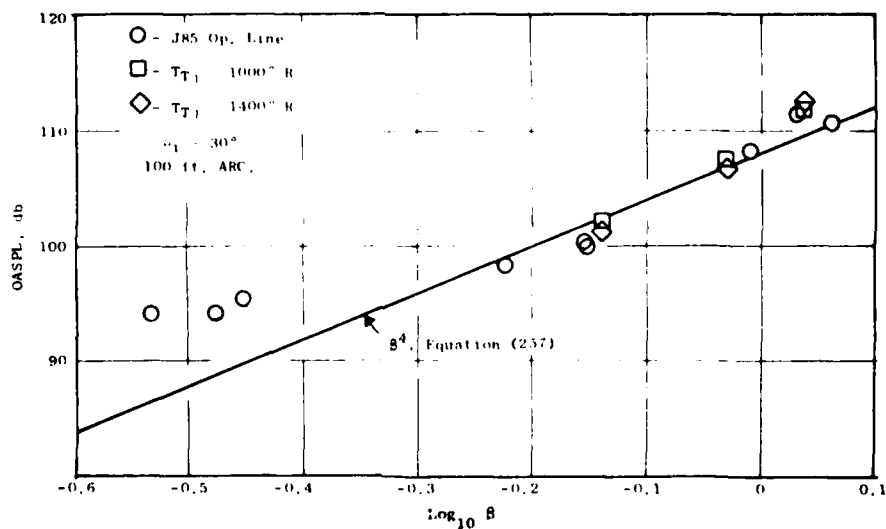


Figure 4-68. Supersonic Jet OASPL Correlation with Shock Strength Parameter, 3.56 in. Conical Nozzle, $V_o = 0$, and $\theta_1 = 30^\circ$.

the corresponding data for $\theta_i = 60^\circ$ and 90° are shown as a function of β in Figures 4-69 and 4-70, respectively. These figures also show very good correlation with equation (257) for $\beta > 0.6$. Thus, to summarize these results, the shock-cell component of OASPL derived from the measurements of Clapper, et al.(72) substantiate the HBF model with respect to dependence on β^4 and insensitivity to temperature.

If shock-cell noise is indeed dependent on r and not a function of temperature, then the sound pressure level (SPL) spectra for different values of T_{Tj} but the same P_{Tj}/P_o (and β) should be the same. Experimental SPL spectra at several values of T_{Tj} , all having $r = 1.08$, are shown in Figures 4-71 and 4-72 for $\theta_i = 30^\circ$ and 60° , respectively. It can be seen that, even though jet velocity varied from 1900 to 2500 fps for these data points, the spectra are virtually identical. Also shown on these figures is the spectrum predicted by the HBF theory, equation (260), for $V_j = 1896$ ft/sec. Calculations at $V_j = 2258$ and 2486 ft/sec gave virtually the same results (See page 228 and Figure 4-98). The agreement between theory and experiment is seen to be quite good.

As a final test of the HBF theory, the peak noise frequencies of the experimental shock-cell-dominated test points were compared with equation (243). Shown in Figure 4-73 are predicted and measured peak frequencies as a function of θ_i for one test point. The agreement is excellent for $\theta_i < 100^\circ$; beyond $\theta_i = 100^\circ$, mixing noise dominates the spectrum and the shock-cell noise peaks are too obscured to evaluate from the data. Additional comparisons are shown in Figure 4-74 for a lower jet temperature, at two values of β (0.725 and 1.08). This comparison illustrates how the peak noise frequency is predicted and observed to drop with increasing β . It should be pointed out that the predicted peak noise frequency given by equation (243) is a narrow-band frequency, whereas the experimental values are 1/3-octave values, so that some error is associated with discerning the exact 1/3-octave band in which the narrow-band peak is contained.

Based on the experimental data analysis presented above, it can be concluded that the HBF theory is sufficient to explain all of the significant characteristics of shock-cell noise emission from conical nozzle underexpanded jets.

4.6.5 Experimental Assessment of Relative Velocity Effects on Conical Nozzle Shock-Cell Noise

Having established confidence in the theory of Harper-Bourne and Fisher(69) for static conical nozzles, the effects of simulated flight external flow were explored. The as measured test data of Clapper, et al.(72) were utilized, which consisted of the same jet operating points as those in Figures 4-68 through 4-70 taken with several values of free-stream velocity V_o , in a free-jet wind tunnel facility. The OASPL data for the supercritical nozzle pressure ratio conditions were plotted versus β for $\theta_i = 30^\circ$, 60° , and 90° , as shown in Figures 4-75 through 4-77, respectively. The average of the static ($V_o = 0$) data from Figures 4-68 through 4-70 is also shown for comparison. These comparisons indicate that the basic shock cell noise source strength is unaltered by the presence of external flow.

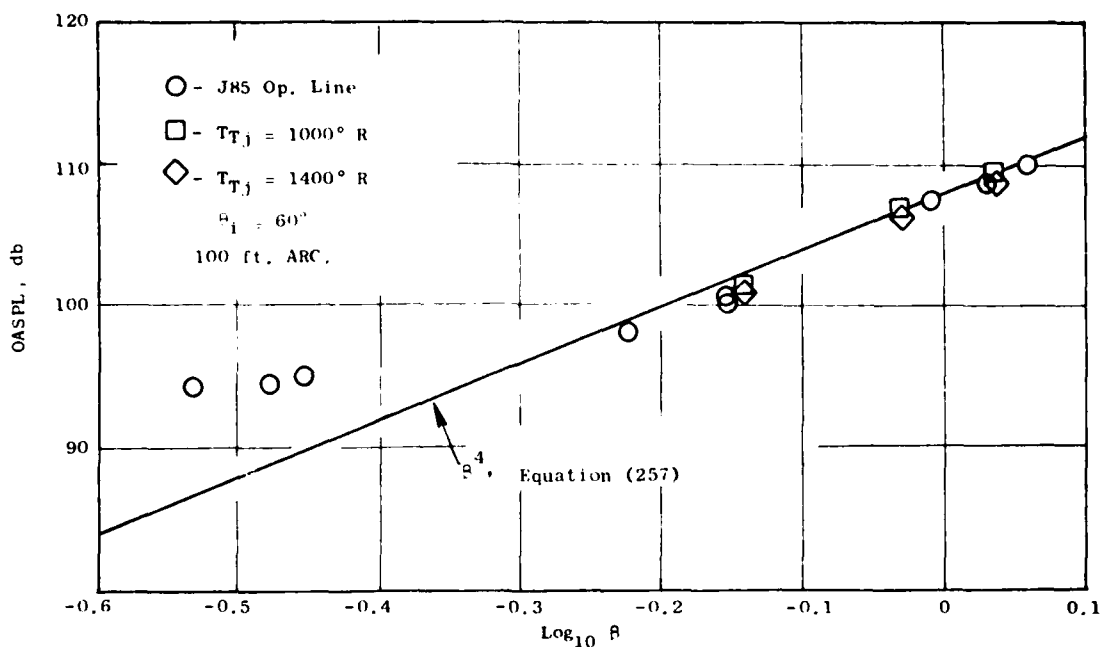


Figure 4-69. Supersonic Jet OASPL Correlation with Shock Strength Parameter β , 3.56 in. Conical Nozzle, $V_0 = 0$ and $\theta_i = 60^\circ$.

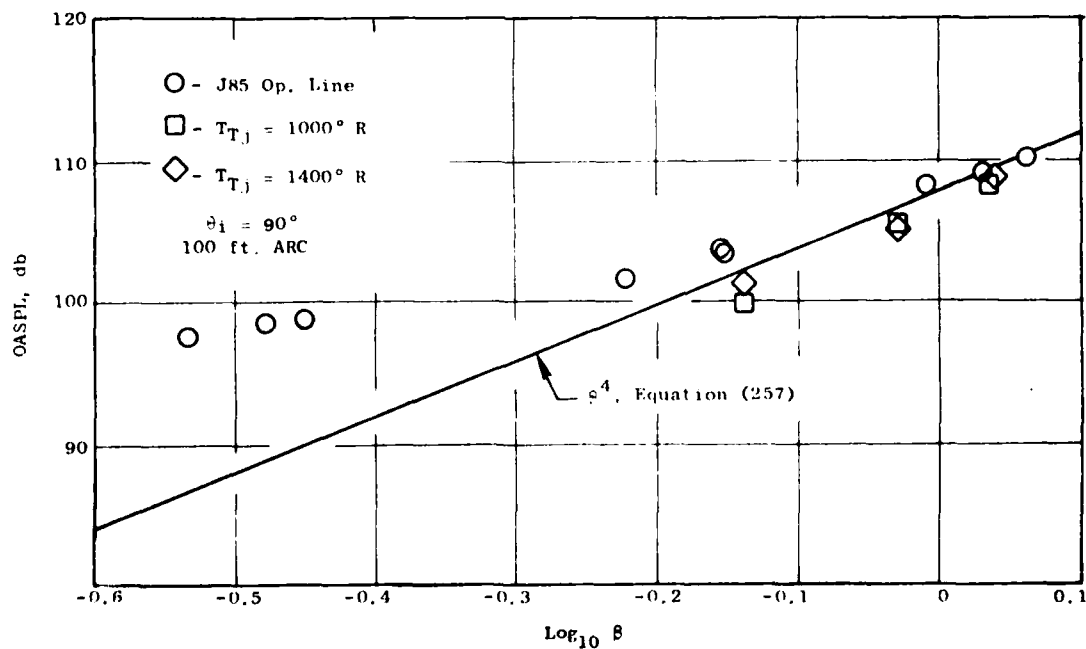


Figure 4-70. Supersonic Jet OASPL Correlation with Shock Strength Parameter β , 3.56 in. Conical Nozzle, $V_0 = 0$ and $\theta_i = 90^\circ$.

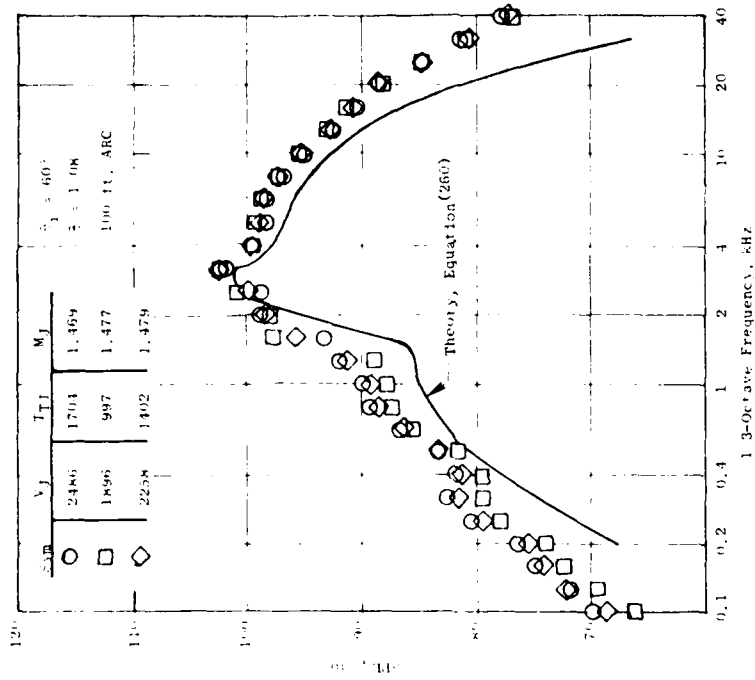


Figure 4-71. Shock-Associated Noise Spectrum, 3.56 in. Conical Nozzle, $V_o = 0$.

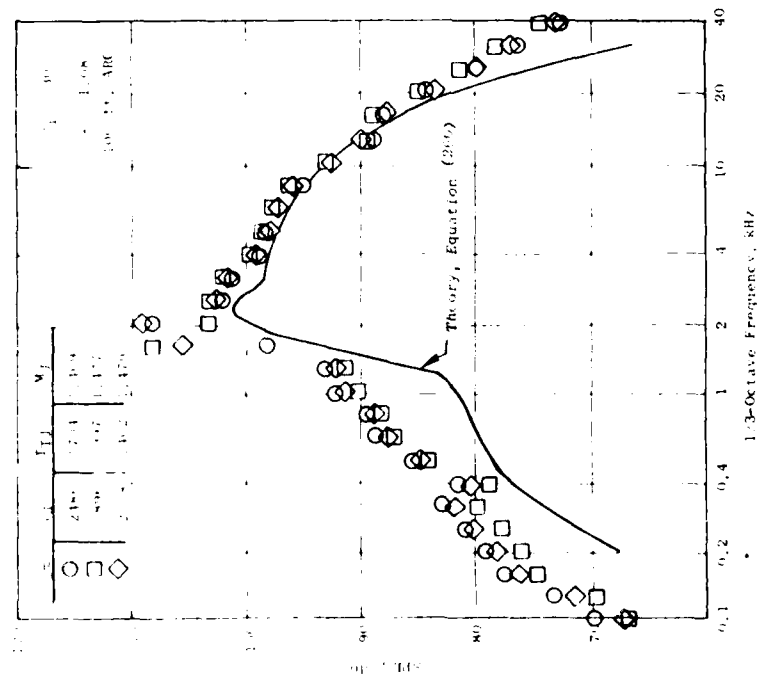


Figure 4-72. Shock-Associated Noise Spectrum, 3.56 in. Conical Nozzle, $V_o = 0$.

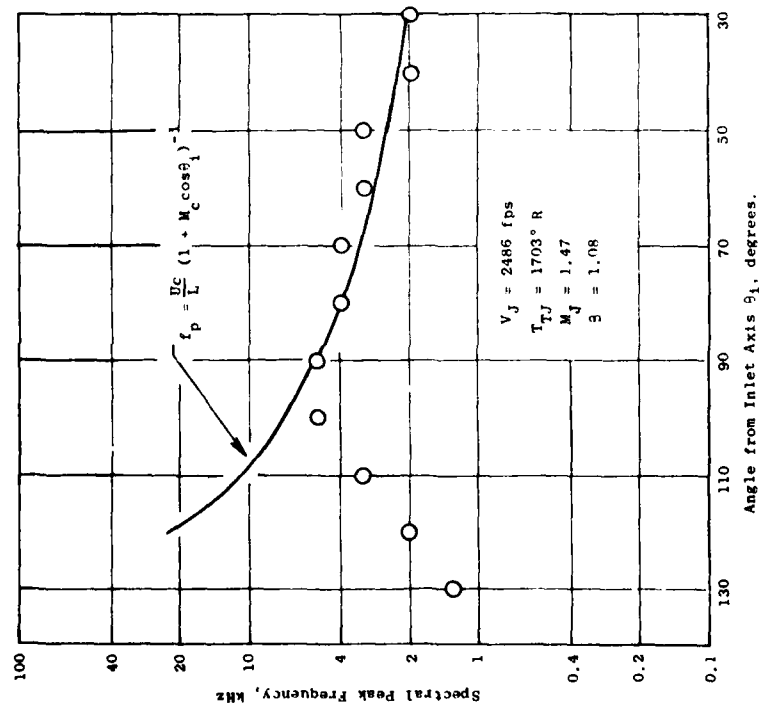


Figure 4-73. Comparison of Peak Noise Frequency Predictions with Experimental Values; 3.56 in. Diameter Nozzle, $V_0 = 0$.

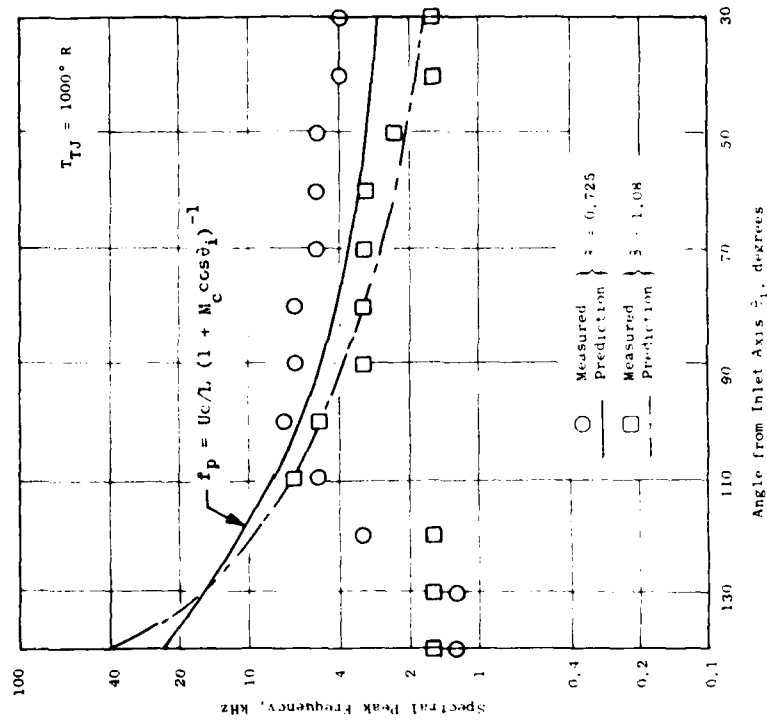


Figure 4-74. Comparison of Peak Noise Predictions with Experimental Values; 3.56 in. Conical Nozzle, $V_0 = 0$.

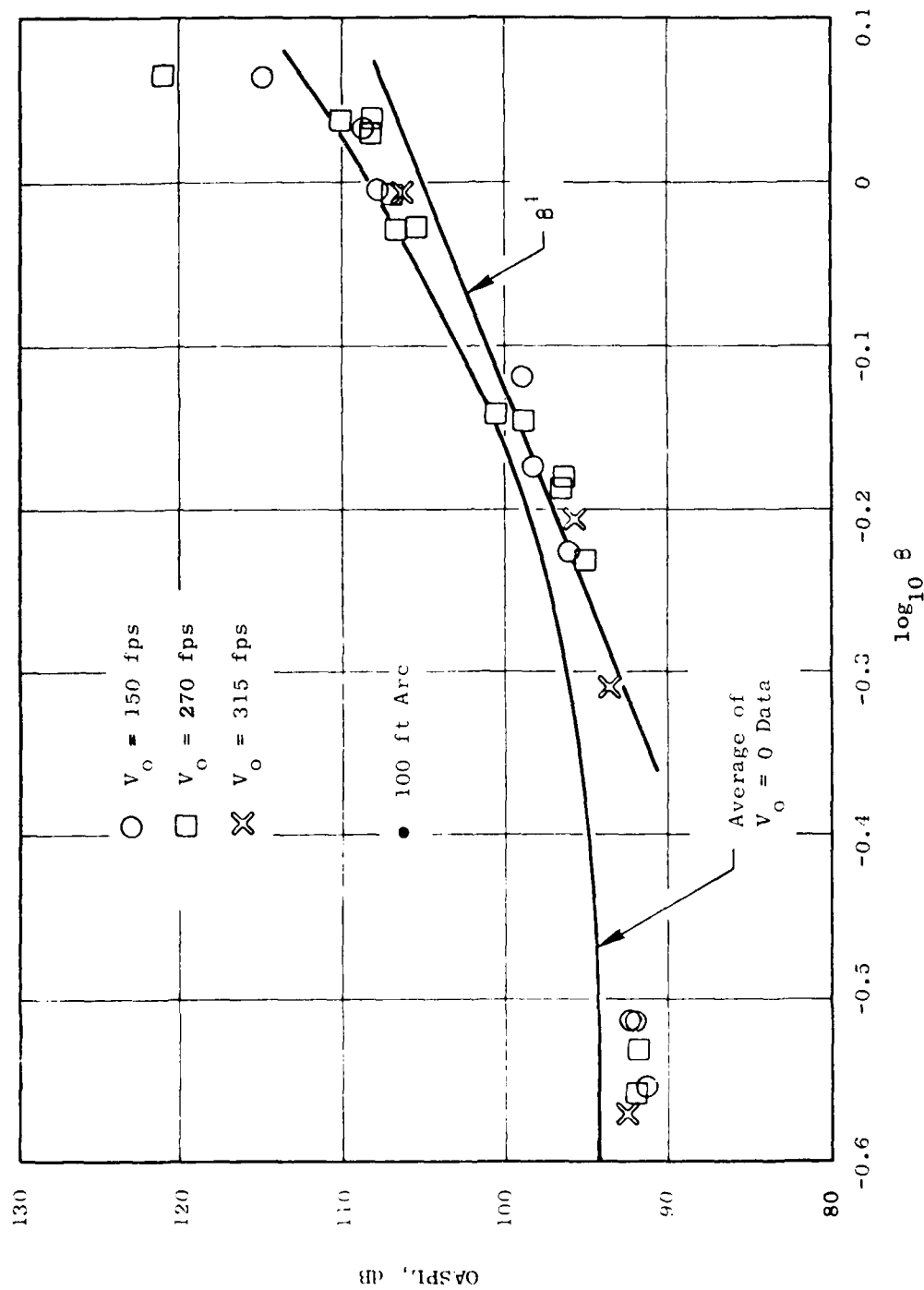


Figure 4-75. Effect of Relative Velocity on Supersonic Jet Noise OASPL, 3.56 in. Conical Nozzle, $\theta_i = 30^\circ$.

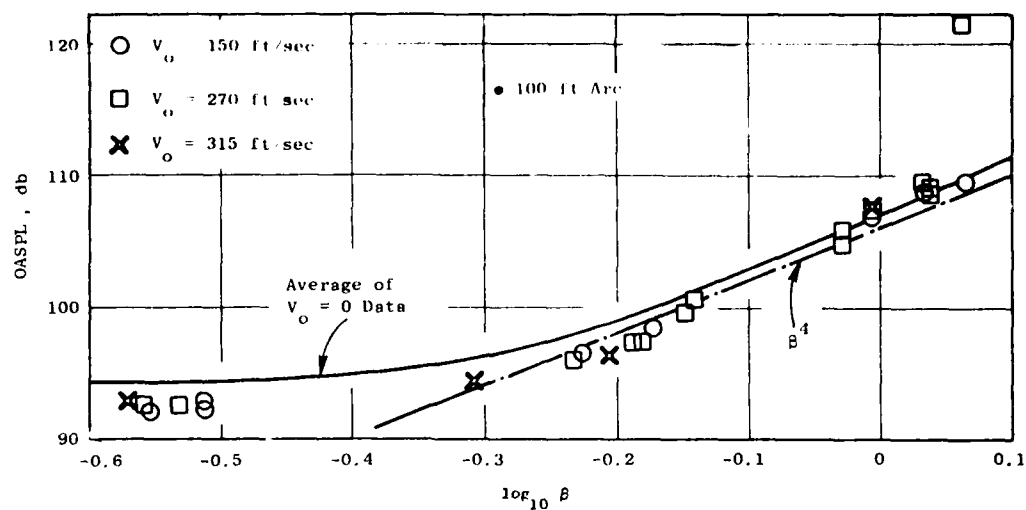


Figure 4-76. Effect of Relative Velocity on Supersonic Jet Noise OASPL
3.56 in. Diameter Conical Nozzle, $\theta_i = 60^\circ$.

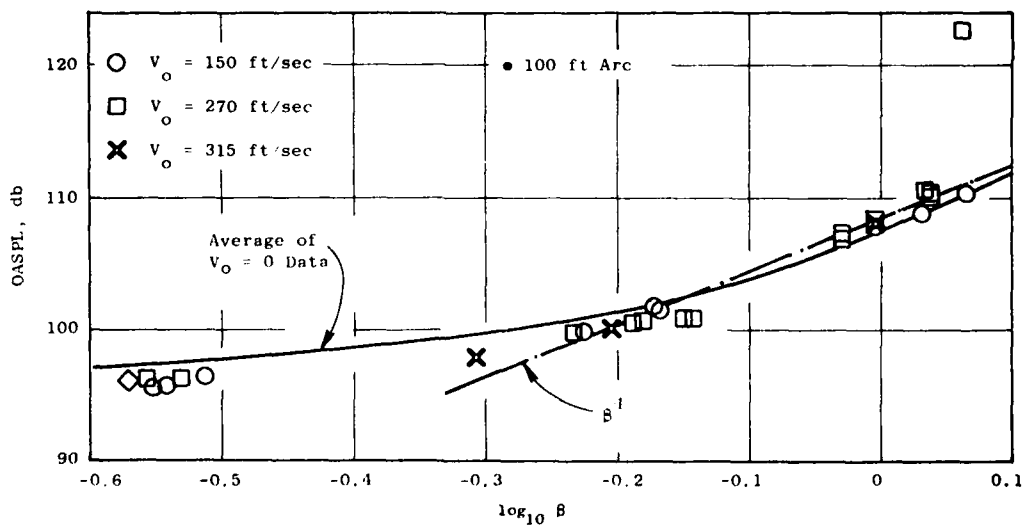


Figure 4-77. Effect of Relative Velocity on Supersonic Jet Noise OASPL,
3.56 in. Diameter Conical Nozzle, $\theta_i = 90^\circ$.

Comparisons of SPL spectra at $\beta = 1.08$ are shown for $\theta_i = 30^\circ$ and 60° in Figures 4-78 and 4-79, respectively. It can be seen that the spectrum is not appreciably affected by the external flow velocity. It can be speculated that the peak frequency f_p should shift as external flow velocity is increased; e.g.,

$$f_p \sim U_c \sim 0.7 (V_j + V_o)$$

For the test conditions shown in Figures 4-78 and 4-79, however, the change in peak frequency would only be about 10%, not large enough to detect with any certainty from 1/3-octave spectra.

Additional (but limited in scope) data on a 2.0-inch (5.08 cm) diameter conical nozzle was obtained by Clapper, et al.⁽⁷²⁾, and the data are summarized in Figure 4-80. These data, although containing a little more scatter, essentially substantiate the trends and conclusions derived from the 3.56-inch (9.04 cm) diameter nozzle data discussed above.

4.6.6 Experimental Evaluation of Noncircular Nozzle Shock-Cell Noise Characteristics

In the experimental program conducted by Clapper, et al. an eight-lobe daisy nozzle also was tested over the same range of operating conditions as the conical nozzles discussed in the previous section. The supercritical data ($M_j > 1$) for $V_o = 0$ are shown in Figure 4-81 as OASPL versus β , for several jet temperatures. It is seen that the β^4 dependency is again observed, but that the levels are approximately 4 dB lower than that predicted by equation (257) for an equivalent area conical nozzle. The noise is seen to be independent of jet temperature, as is for the conical nozzle. Corresponding SPL spectra at $\theta_i = 30^\circ$ and 60° are shown in Figure 4-82 for several jet temperatures. It can be seen that the high-frequency portion of the spectra ($f > 4\text{KHz}$) exhibit the characteristics of shock cell noise observed for conical nozzles; viz., invariance with jet temperature at constant value of β .

Based on the operating conditions of the data shown in Figure 4-82, the peak-noise frequencies predicted by equation (243), utilizing equation (245) to estimate shock spacing L , are tabulated below, for the following assumptions:

- (1) $D = D_{eq}$, equivalent total area diameter $\sqrt{4A_j/\pi}$
- (2) $D = D_h$, hydraulic diameter $\frac{4A_j}{P_w}$, P_w = wetted perimeter of nozzle
- (3) $D = D_{eq,n}$, equivalent lobe area diameter $\sqrt{4A_n/\pi}$

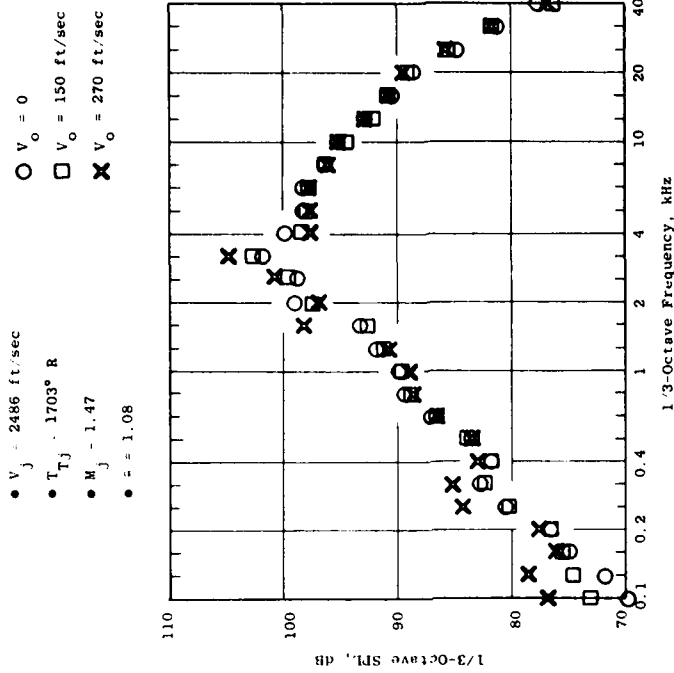


Figure 4-79. Effect of Relative Velocity on SPL Spectrum at $\theta_i = 60^\circ$, 3.56 in. Diameter Conical Nozzle.

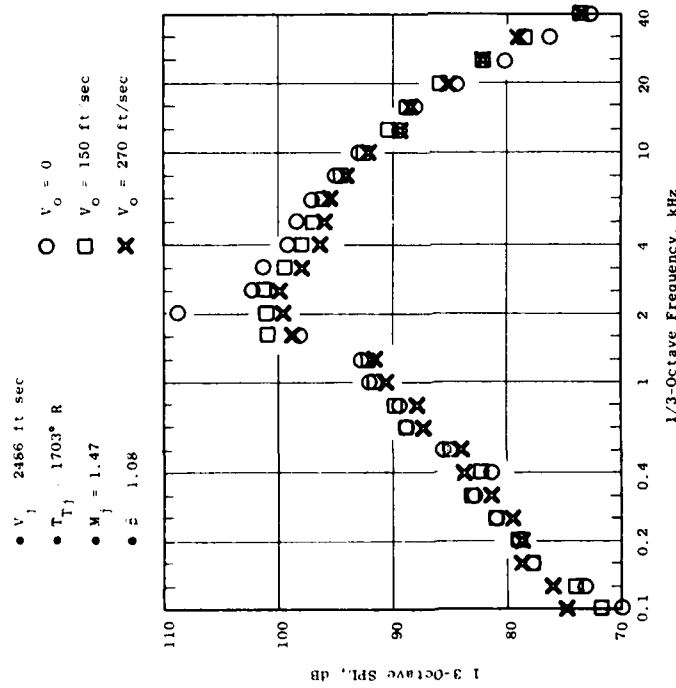


Figure 4-78. Effect of Relative Velocity on SPL Spectrum at $\theta_i = 30^\circ$, 3.56 in. Diameter Conical Nozzle.

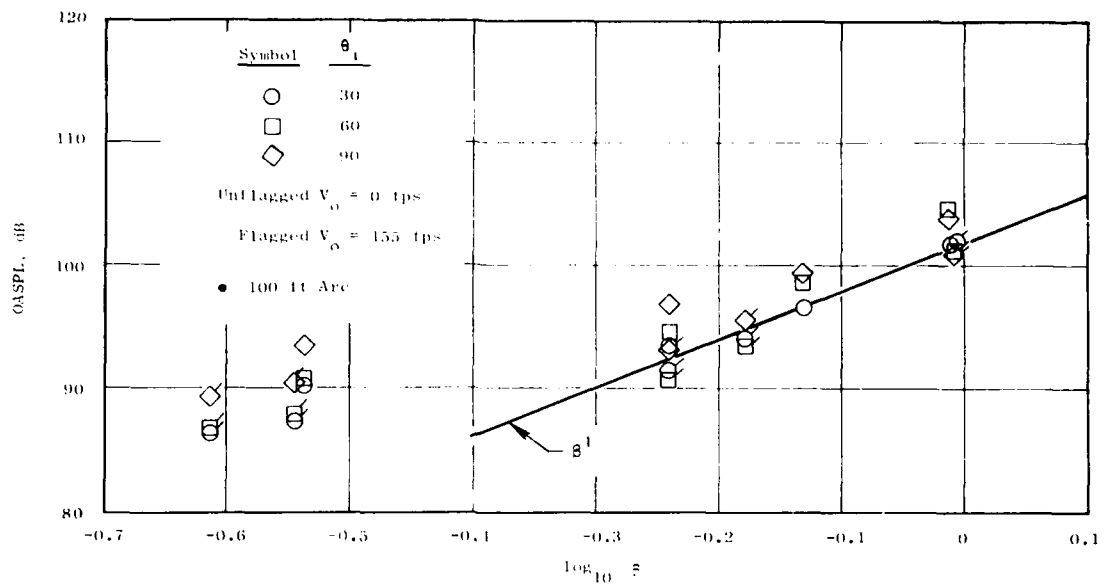


Figure 4-80. Supersonic Jet OASPL Correlation with Shock Strength Parameter β , 2.0 in. Diameter STA Conical Nozzle, 100 ft Arc.

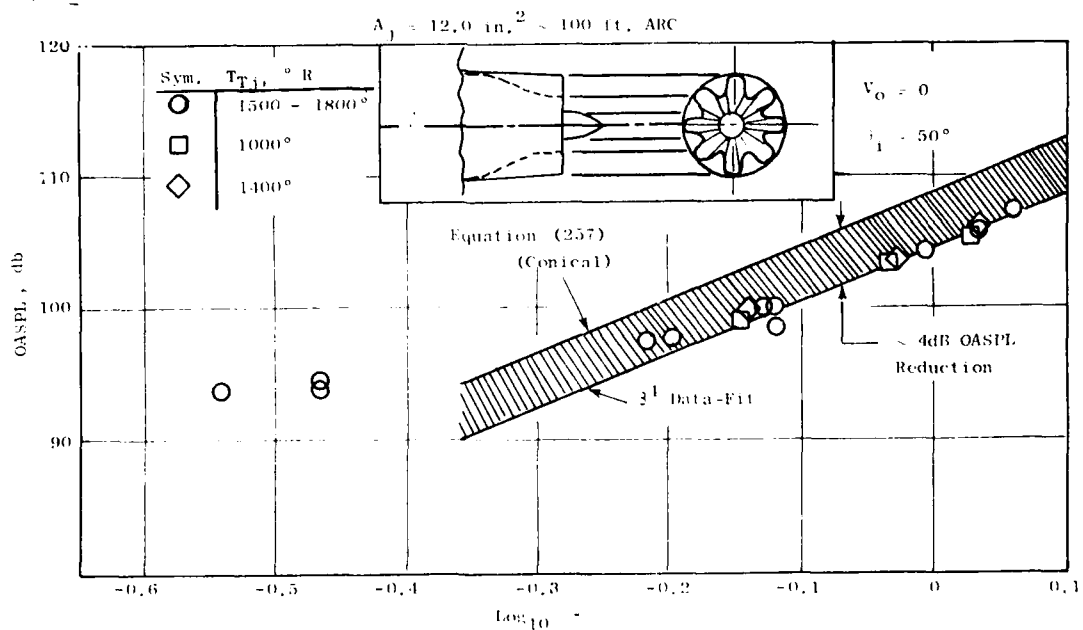


Figure 4-81. Supersonic Jet OASPL Correlation with Shock Strength Parameter β ; Scale Model 8-Lobe Daisy Suppressor.

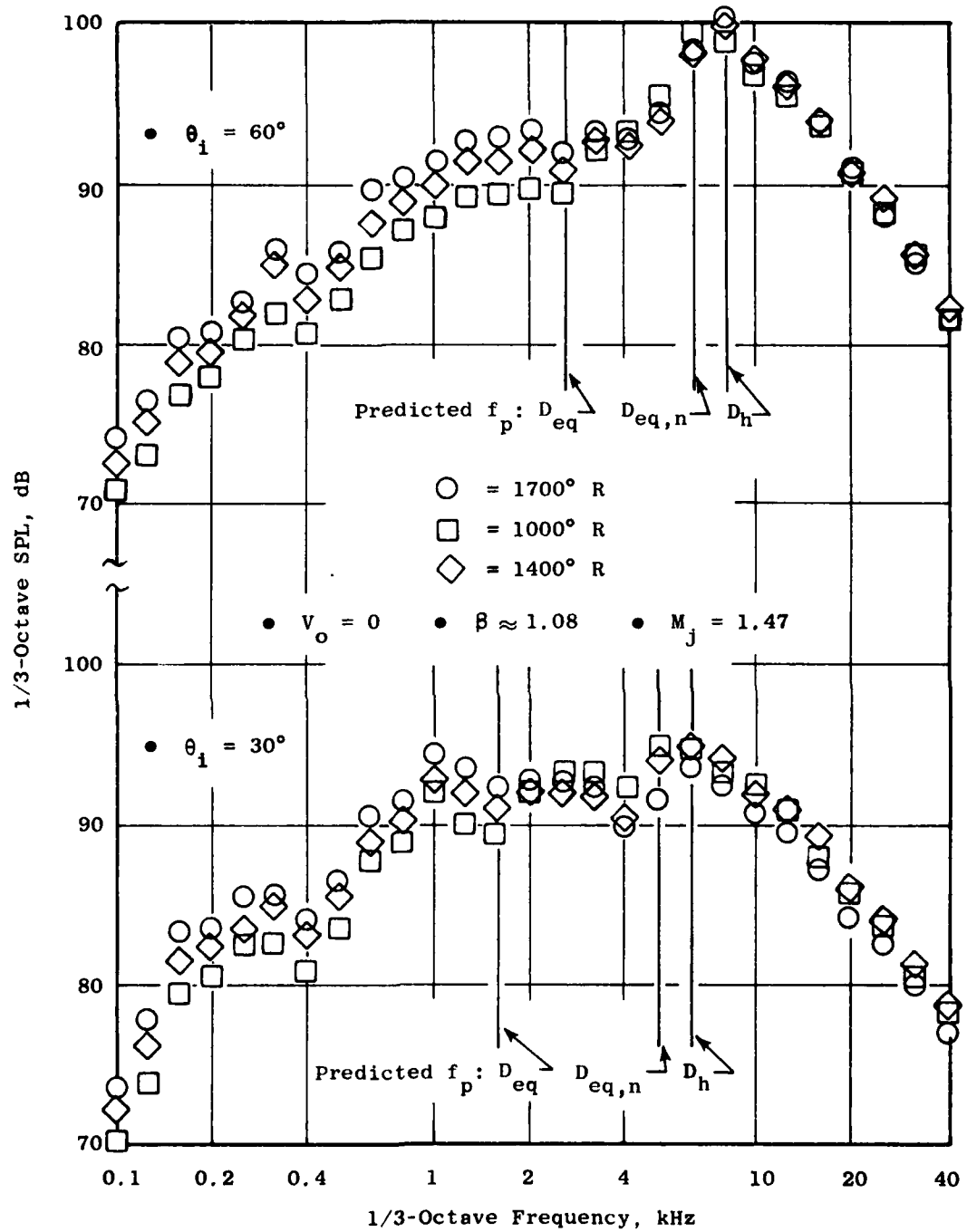


Figure 4-82. Shock-Associated Noise Spectra, Scale-Model, 8-Lobe Daisy Suppressor, Effect of Jet Temperature.

Predicted Peak-Noise Frequencies (Hz)

8-Lobe Daisy Nozzle

(Figure 4-82)

$$\beta = 1.08$$

$$M_j = 1.47$$

$$P_{Tj}/P_o = 3.48$$

Symb.	T_{Tj}	$\theta_i = 30^\circ$			$\theta_i = 60^\circ$		
		D_{eq}	D_h	$D_{eq,n}$	D_{eq}	D_h	$D_{eq,n}$
□	1000	1681	6202	4753	2138	7891	6047
◇	1400	1812	6687	5142	2360	8710	6675
○	1700	1895	6994	5360	2502	9234	7077

The predicted peak-noise frequencies for $T_{Tj} = 1400^\circ \text{ R}$ are indicated by arrows on Figure 4-82. It can be seen that the predictions for f_p based on $D = D_h$ agree best with the observed peak noise location, although $D = D_{eq, n}$ also gives close (within one 1/3-octave band) agreement. The predictions indicated in Figure 4-82 have been adjusted from those values listed in the above table to nearest 1/3-octave band center frequency. The 4 dB lower levels relative to a conical nozzle shown in Figure 4-81 do not, however, scale with either hydraulic diameter or lobe equivalent diameter. From equation (257), the OASPL should scale as $20 \log_{10} (D/D_{eq})$ relative to a conical nozzle, where D is the "effective" shock-cell diameter for the non-circular nozzle. The eight-lobe nozzle has characteristic dimensions $D_{eq} = 3.91$ inches, $D_h = 1.06$ inches, and $D_{eq,n} = 1.38$ inches. For $D = D_{eq,n}$, the reduction relative to a conical nozzle would then be 9.0 dB, while for $D = D_h$, it would be 11.3 dB. Both of these reductions are much larger than the 4 dB reduction observed, and it is therefore not correct to predict non-circular nozzle shock-cell noise levels by merely using element-related dimensions $D_{eq,n}$ or D_h in the conical nozzle prediction equations.

Clapper, et al.(72) have also run the scale-model, eight-lobe nozzle with external flow in the free-jet wind tunnel facility. The as measured supercritical pressure ratio data with various external flow velocities V_o are shown in Figure 4-83, at $\theta_i = 50^\circ$. The average of the static data ($V_o = 0$) from Figure 4-81 is also shown as a solid line. It is observed that the OASPL levels for $V_o > 0$ are all lower than the static line $V_o = 0$, by about 2 - 3 dB with no obvious dependency on the level of V_o itself. This is, at first glance, puzzling, because the conical nozzle data indicated no significant dependence of shock-cell noise on V_o , and these (eight-lobe) results suggest a significant reduction with the presence of V_o , but no trends with the level of V_o . To further study this anomalous behavior, spectra were compared at selected conditions where shock-cell noise was thought to be significant, Figures 4-84 and 4-85. From these spectral comparisons, several observations can be made. First, the actual peak SPL level changes are relatively small with changes in V_o ; in fact, Figure 4-85, which shows spectra at the lowest jet temperature and highest external flow velocity, indicates only 1 - 2 dB reduction in peak SPL due to $V_o (=300 \text{ fps})$. The mixing noise is expected to

Sym V_o , ft/sec

○ 150-160

□ 280-300

✕ 340

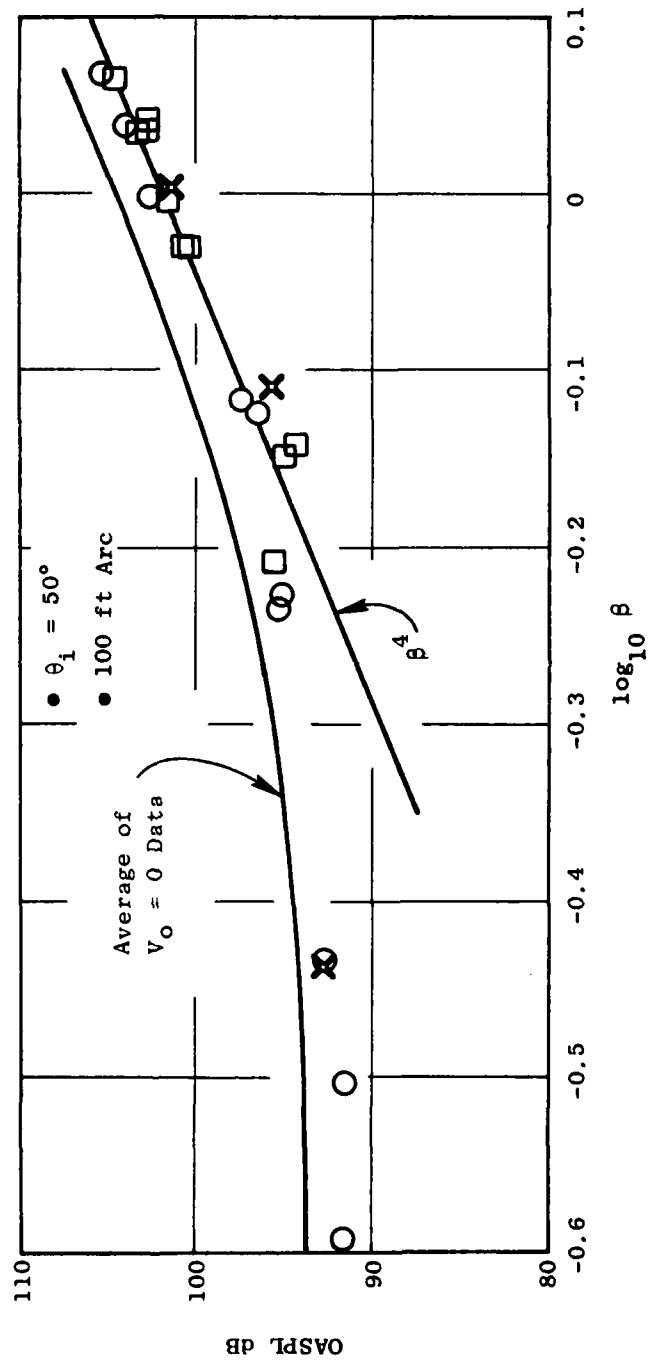


Figure 4-83. Effect of Relative Velocity on Supersonic Jet Noise OASPL, Scale-Model, 8-Lobe Daisy Suppressor.

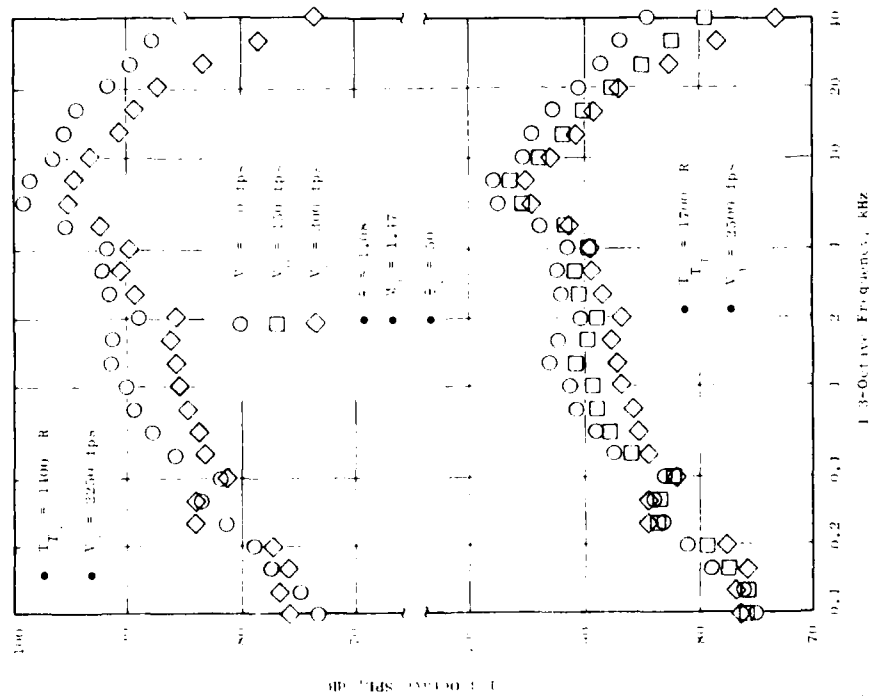


Figure 4-84. Shock-Associated Noise Spectra, Scale-Model 8-Lobe Daisy Suppressor; Effect of Forward Velocity.

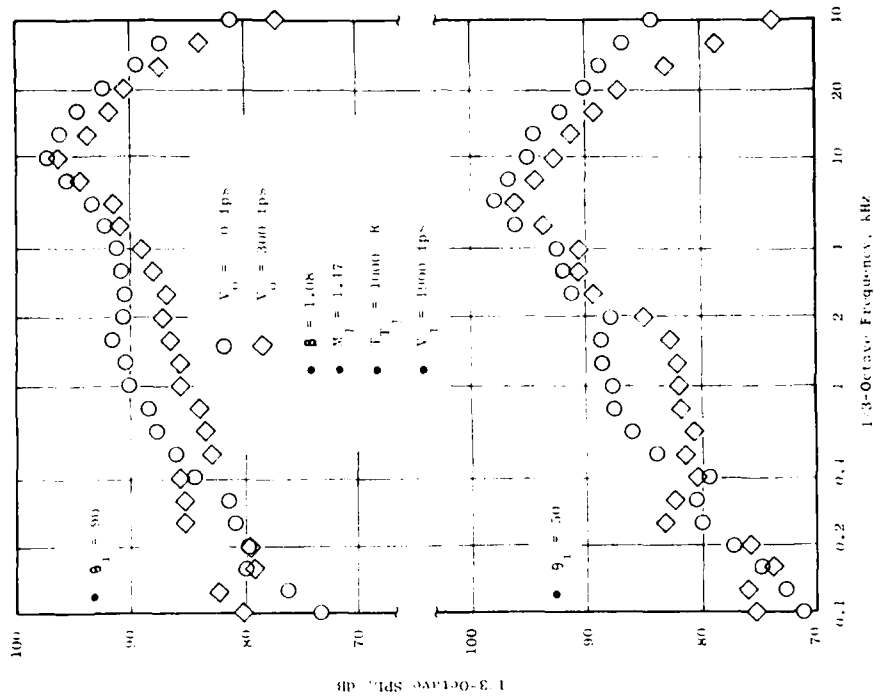


Figure 4-85. Shock-Associated Noise Spectra, Scale-Model 8-Lobe Daisy Suppressor; Effect of Forward Velocity.

be lowered appreciably with the addition of external flow, and it is seen that the low-frequency noise ($f < 2000$ Hz.) does drop appreciably, on the order of 5 dB. The second observation is that the slope of the high-frequency end of the spectrum becomes progressively steeper as V_0 is increased.*

The noise of a 6:1 aspect ratio rectangular jet was investigated experimentally by Kantola and is reported in Section 5.2. A baseline 1.5-inch diameter conical nozzle was also tested in the same facility, at the same operating conditions, to provide reference data for comparison purposes (see Section 5.1). Figure 4-86 shows the baseline conical nozzle SPL spectra at $\theta_1 = 60^\circ$ for several jet temperatures at approximately the same jet Mach number ($\beta \approx 0.80$). The spectral collapse at high frequencies (no temperature effect) is again observed; it is noted, however, that the peak SPL and OASPL are about 1 to 2 dB higher than would be predicted by the HBF(69) model. The corresponding spectra for a 6:1 aspect ratio nozzle with the same nozzle area are shown in Figures 4-87 and 4-88. The spectra are shown as measured at several azimuthal angles ψ , to assess the effects of asymmetry.

Comparing Figures 4-86 and 4-88, it is seen that, at approximately the same value of β , the rectangular nozzle peak SPL is about 2 dB lower than that of the conical nozzle. The peak-noise frequency appears to be about 1 to 2 1/3-octave bands higher for the rectangular nozzle. Figure 4-87, for $\beta = 0.726$, indicates a small change, 2 - 3 dB, with azimuthal angle, the "noisy plane" being $\psi = 0^\circ$. At the peak-noise frequency, however, the change is appreciably larger, on the order of 5 dB. Figure 4-88 shows spectra for $\beta = 0.78$, and no appreciable change with ψ is indicated for this case.

From experimental observations utilizing Schlieren photographs, Kurn(74) deduced that the shock cell geometry of rectangular nozzles scales with nozzle hydraulic diameter. Again utilizing equations (243) and (245) to predict the peak-noise frequency, it is found that the spectra in Figure 4-88 should peak at 8000 Hz for $D = D_{eq}$ and 13,500 Hz for $D = D_h$. It is seen that the actual peak occurs midway between these two predictions, leaving the identification of the "correct" scaling dimension inconclusive for this case. It may be noted that the assumption that $U_c = 0.7 V_j$ applied also for rectangular nozzles may be in error, contributing to the discrepancy between observed and predicted peak-noise frequency.

4.6.7 Experimental Evaluation of Annular Plug Nozzle Shock Cell Noise Characteristics

Current technology nozzles envisioned for high jet velocity applications (e.g., supersonic transport propulsion systems) contain a centerbody or plug to provide high supersonic cruise performance. The annular jet formed between the nozzle shroud and plug may produce significantly different shock cell

*These observations can be partially explained by consideration of the free-jet shear layer turbulence absorption effects as discussed by Clapper, et al.; correcting for shear layer absorption will tend to negate the relative velocity effect.

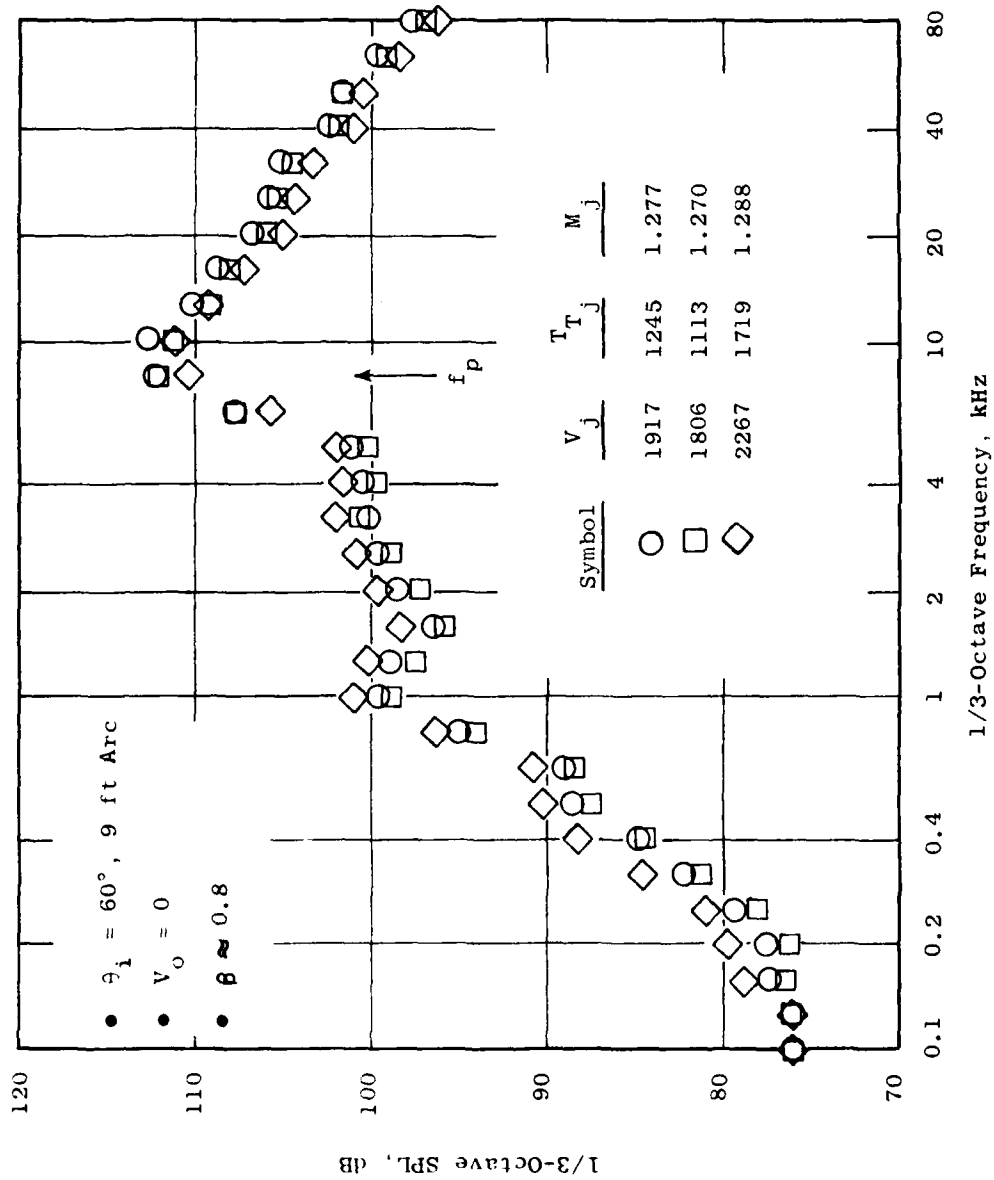


Figure 4-86. Shock-Associated Noise Spectrum, 1.5 in. Diameter Conical Nozzle.

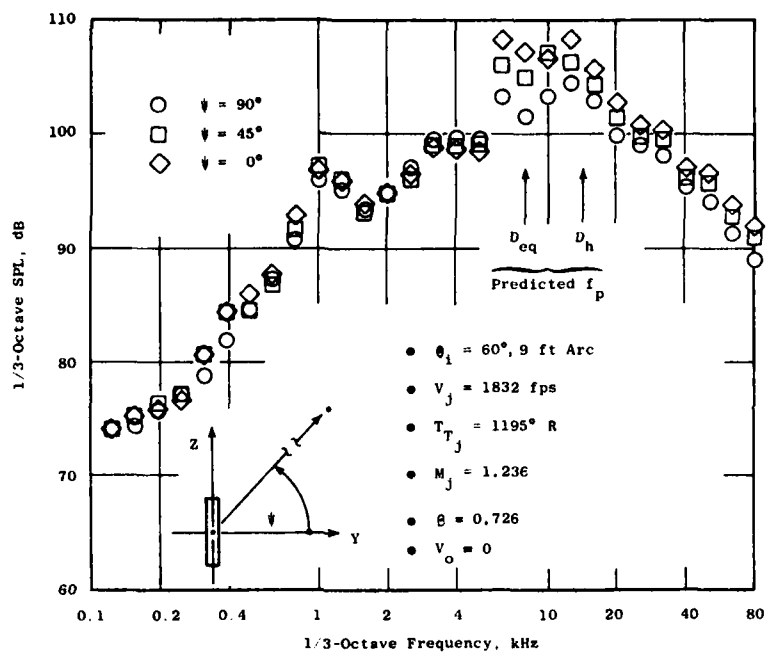


Figure 4-87. Shock-Associated Noise Spectrum, 6:1 Aspect Ratio Rectangular Jet.

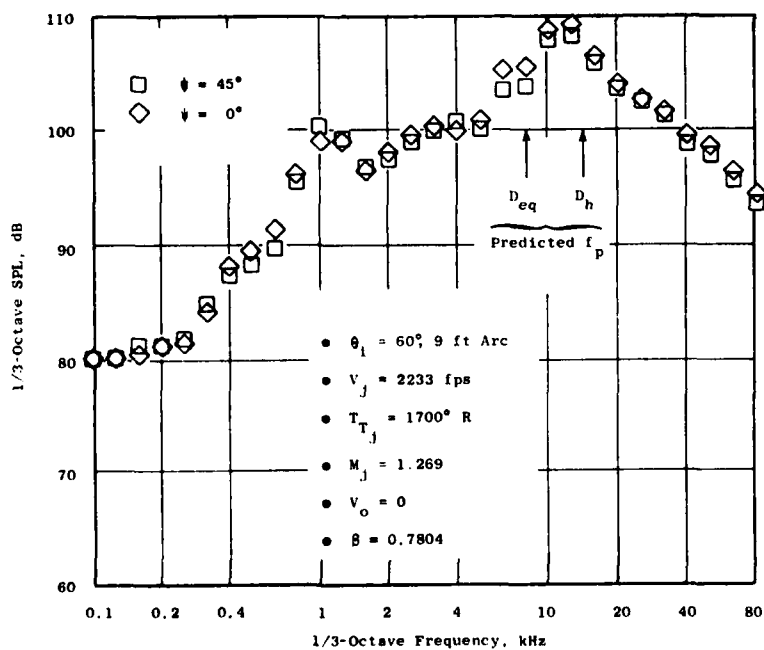


Figure 4-88. Shock-Associated Noise Spectrum, 6:1 Aspect Ratio Rectangular Jet.

patterns than an equivalent - area conical nozzle when operating at under-expanded pressure ratios. The presence of the plug or centerbody provides a guided-expansion surface for the supersonic expansion/compression process. Additionally, the turbulent boundary layer on the plug surface may interact with the impinging shocks, modifying their characteristics. It can therefore be expected that the shock-cell noise characteristics of an annular plug nozzle will be different from an equivalent-area conical nozzle. It is important to assess these differences, because the basic annular plug nozzle system is a much more relevant "baseline" configuration than a conical nozzle when measuring the improvements to be gained with suppressor nozzles.

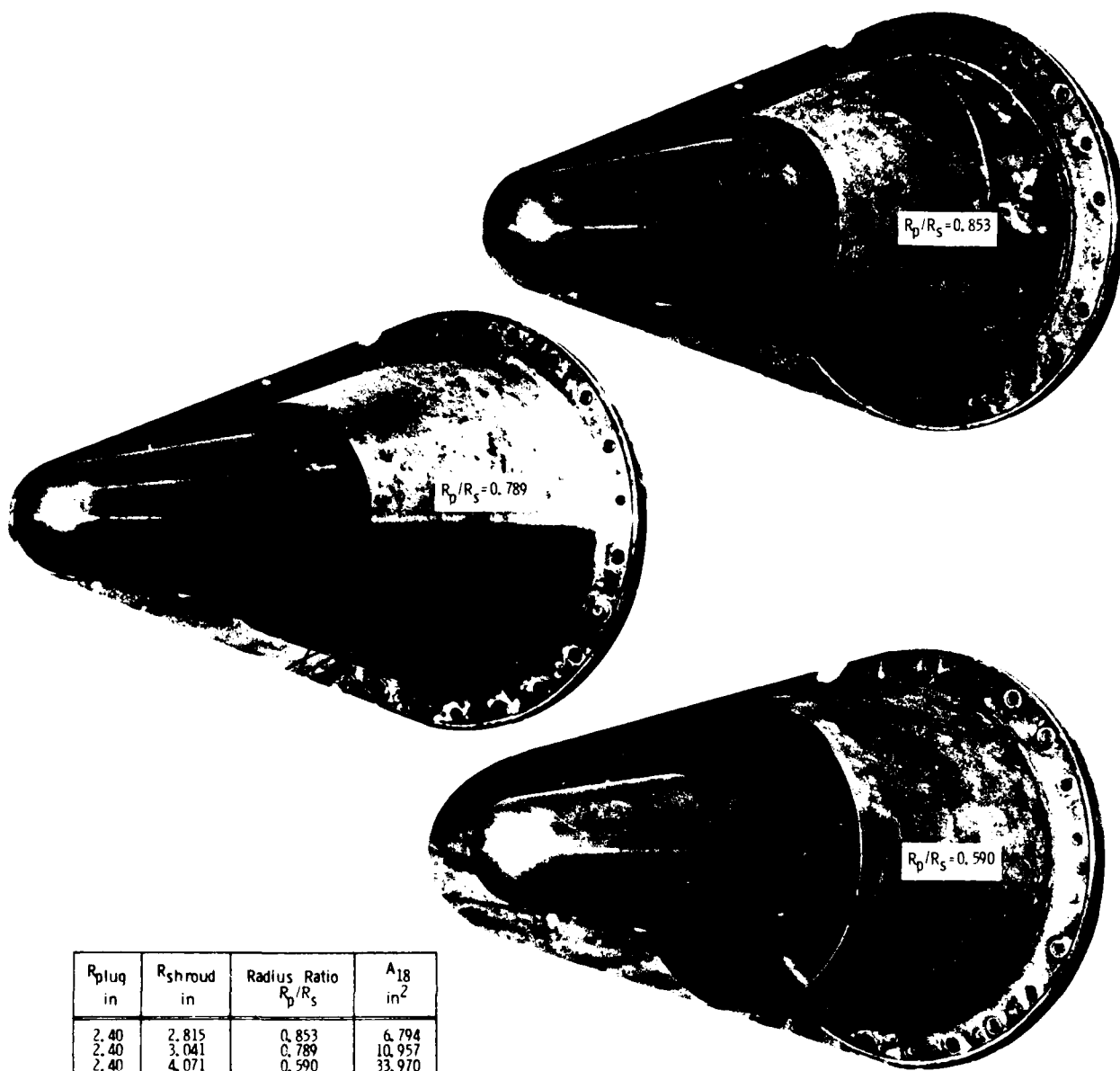
The far- field acoustic characteristics of three different annular plug nozzles were measured (in Task 3 of the present program) to provide baseline characteristics as a function of plug geometry. The three configurations tested are shown in Figure 4-89. A composite of measured OASPL values at forward-arc angles of $\theta_i = 30^\circ$ and 50° (where shock-cell noise is expected to dominate) is shown in Figure 4-90, for all test points taken at supercritical nozzle pressure ratios. The OASPL is plotted versus $\log_{10}\beta$, as was done in the previous sections. It can be observed that the OASPL in the forward arc, for the three annular plug nozzles tested, follows the β^4 - dependency quite well. These three nozzles all have different exit flow areas (the plug geometries are all the same but the shroud diameters are different, see Figure 4-89), so a normalization must be carried out to discern the deviation from conical nozzle behavior. Equation (257) yields the OASPL for a conical nozzle; if we define the normalized shock cell noise OASPL as

$$N_{sh} = \text{OASPL} - 40 \log_{10}(\beta) - 20 \log_{10}(D_{eq}/r_o) \quad (263)$$

we have $N_{sh} = 158.5$ dB for the conical nozzle. The results in Figure 4-90 have been normalized per equation (263) and plotted versus β , in Figure 4-91. The normalized data should be insensitive to β if the proper normalization has been applied, and it is seen from Figure 4-91, that this is indeed the case. A line representing the conical nozzle value $N_{sh} = 158.5$ is also shown for reference. The levels for all three plug nozzles are seen to be below the conical line, by about 3 to 5 dB, and there is a consistent trend with radius ratio, N_{sh} tending to be lower for higher radius ratios. The arithmetic average values of N_{sh} at $\theta_i = 30^\circ$, 50° , and 70° , as well as the average for all three angles, is tabulated below.

Annular Plug Nozzle Average Values
of Normalized OASPL - N_{sh}

R_p/R_s	$\theta_i = 30^\circ$	$\theta_i = 50^\circ$	$\theta_i = 70^\circ$	Avg.	No. of Points
0.853	152.9	153.8	153.9	153.6	9
0.789	154.8	155.1	155.5	155.1	14
0.590	154.9	155.4	155.8	155.4	4



R_{plug} in	R_{shroud} in	Radius Ratio R_p/R_s	A_{18} in ²
2.40	2.815	0.853	6.794
2.40	3.041	0.789	10.957
2.40	4.071	0.590	33.970

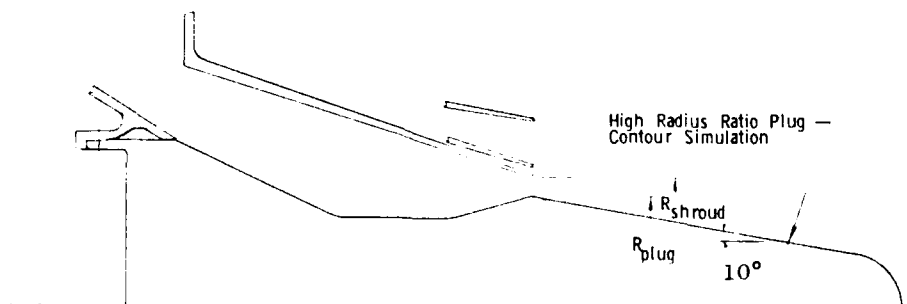


Figure 4-89. Model Hardware for Parametric Nozzle Radius Ratio Study.

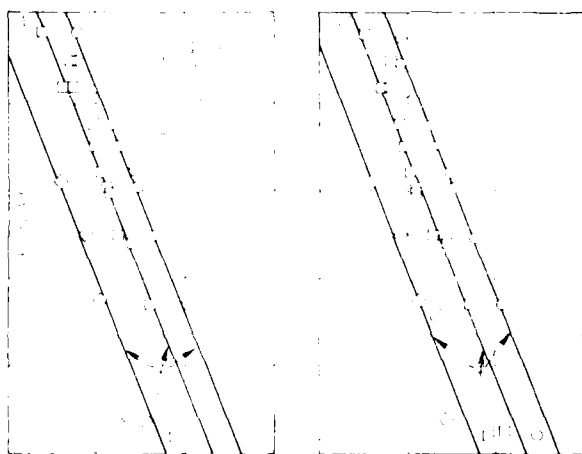


Figure 4-90. Supersonic Jet OASPL Correlation with Shock Strength Parameter β , Annular Plug Nozzle.

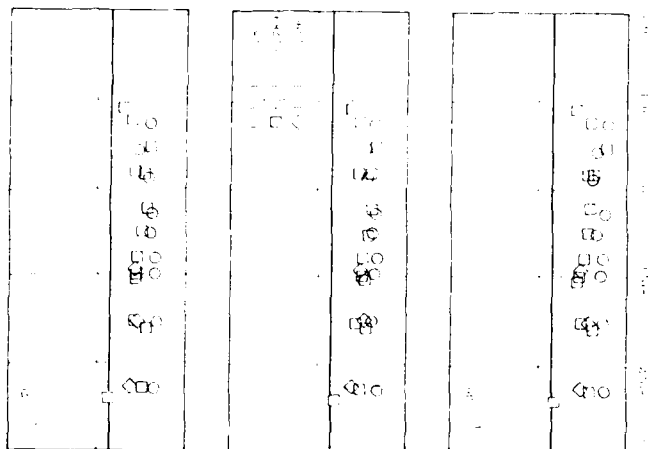


Figure 4-91. Normalized Shock Cell Noise OASPL Correlation N_{sh} vs. β , Annular Plug Nozzles.

Spectrum comparisons were made at $\theta_i = 50^\circ$, and these are shown in Figures 4-92 through 4-94. The test points chosen were those where shock-cell noise was expected to be dominant, and where the points were common to at least two of the three configurations. Figure 4-92 shows spectrum comparisons for all three configurations at a pressure ratio of $P_{Tj}/P_o = 2.65$. Figure 4-93 shows spectra at $\theta_i = 50^\circ$ for the two highest radius ratios tested, at a pressure ratio of $P_{Tj}/P_o = 3.28$. Finally, Figure 4-94 shows spectra for the two highest radius ratios, at a pressure ratio of 3.55. The lowest radius ratio nozzle ($R_p/R_s = 0.590$) was not tested at the higher pressure ratios due to the large mass flows required exceeding the facility capacity.

It is observed that these spectra do not possess the same shape as exhibited by a conical nozzle. In particular, there appears to be a tendency to form two peaks, their separation increasing with increasing radius ratio. The spectra also appear to be much more "broadband" in character. Further discussion of the observed characteristics of annular plug nozzle shock-cell noise is postponed to Section 4.6.9, where extensions of the basic HBF theory are proposed for explaining these characteristics.

4.6.8 Model Parametric Studies

In Section 4.6.2, the theoretical hypothesis of HBF⁽⁶⁹⁾ for the mechanisms of shock-cell noise was reviewed, and most all of the important features of shock-cell noise (produced by conical nozzles) resulting from the theory were verified in Section 4.6.4, through a critical examination of extensive parametric data. In Sections 4.6.5 - 4.6.7, an experimental assessment of the shock-cell noise of noncircular nozzles was attempted, with the emphasis being placed upon how the shock-cell noise characteristics departed from conical nozzle behavior. It was found that, in general, noncircular nozzle shock-cell noise OASPL does scale with β^4 for a given nozzle geometry, independent of the jet temperature. The absolute levels and spectrum shapes were, however, found to be different than that for an equivalent-area conical nozzle. In this section, a critical examination is made of the HBF model itself, to see if it contains any or all of the basic physical parameters required to predict noncircular nozzle shock noise behavior. By systematically varying the key physical parameters in the model, their effects on spectrum shape and level can be assessed, and these effects can be related to the experimentally-observed departures from conical-nozzle behavior exhibited by noncircular nozzles.

The Harper-Bourne/Fisher⁽⁶⁹⁾ model formulation, reviewed in Section 4.6.2, identifies several key parameters which characterize the shock-cell noise emission. These parameters can be categorized as follows:

1. General Operating Conditions:

- | | |
|--------------------------------|-----------------|
| (1) Shock strength parameter | β |
| (2) Convection velocity | U_c |
| (3) Observation point location | θ_i, r_o |

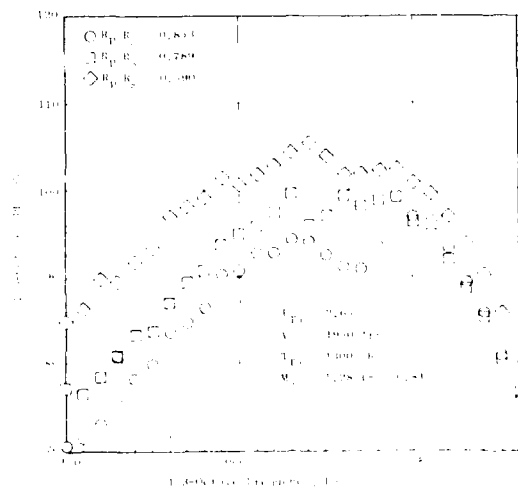


Figure 4-92. Shock-Associated Noise Spectra; Annular Plug Nozzle, $\theta_1 = 50^\circ$.

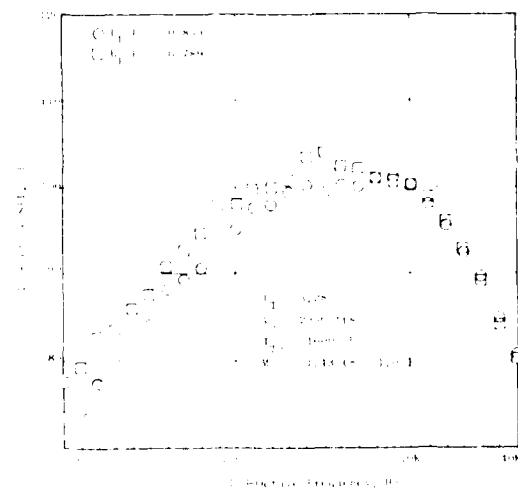


Figure 4-93. Shock-Associated Noise Spectra; Annular Plug Nozzle, $\theta_1 = 50^\circ$.

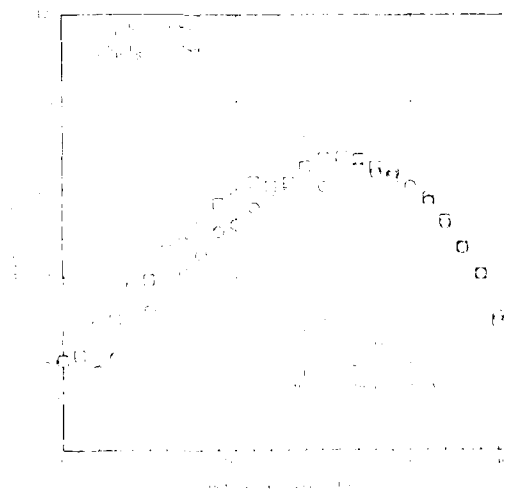


Figure 4-94. Shock-Associated Noise Spectra; Annular Plug Nozzle, $\theta_1 = 50^\circ$.

2. Shock cell geometry:

- (4) Number of shock cells N
- (5) Shock spacing parameters L_1, L_{avg}, ϵ

3. Turbulence/Shock Correlation Spectra:

- (6) Group source spectrum $H_o(S_n)$
- (7) Cross-correlation spectrum $C_1(S_n)$

The first parameter investigated was the number of shock cells N . Predictions were made for a typical operating condition of $P_{Tj}/P_o = 3.29$ and $V_j = 2370$ fps (722 m/s). The jet diameter and observer radius was selected to be 3.73 inches (9.5 cm) and 40 feet (12.2 m), respectively. The predictions [utilizing equation (260)] were made for $N = 2, 4, 6$, and 8 , and are shown in Figure 4-95. It is observed from these spectral predictions that the number of shock cells N has no influence on the high and low ends of the spectrum. In the region around the peak frequency, the effect of increasing N is to give a smoother spectrum. For small values of N , the spectrum exhibits a more oscillatory "sawtooth" behavior, but the basic shape remains unaltered. This uncovers one problem with the correlation function $H_o(S_n)$; namely, it is based on conical nozzle levels for 8 shock cells. If there are more or less than 8 cells, the level of $H_o(S_n)$ should be adjusted by the factor $(N/8)$. This correction was incorporated into the model and the calculations of Figure 4-95 were repeated. The results are shown in Figure 4-96. From this exercise, it is seen that reducing the number of shock cells will, according to the HBF theory, reduce the shock noise level without any appreciable alteration of the basic spectrum shape.

The second parameter studied was the shock spacing parameter $\epsilon = \Delta L/L_1$, which governs the rate where successive shocks come closer and closer together [see equation (244)]. For conical nozzles, HBF(69) found that $\epsilon = 0.06$. Parametric computations were made for $-0.06 \leq \epsilon \leq +0.12$, and these results are shown in Figure 4-97. The case where $\epsilon = 0$ corresponds to equal shock cell spacing. For $\epsilon < 0$, the spacing increases with downstream distance, while for $\epsilon > 0$, the spacing decreases with downstream distance. The effect of increasing ϵ is to smooth out the jump in the spectrum near $f = f_p$, and simultaneously lower the peak SPL. For $\epsilon = 0$, the spectrum becomes uncharacteristically oscillatory; evidently the actual unequal shock spacings mitigate the reinforcements and cancellations which occur at the higher harmonics of f_p . It is noted that $\epsilon = -0.06$ again smooths out the spectrum but lowers the peak-noise frequency. The major effect of increasing ϵ is that of reducing the steepness of the spectrum slope below the peak-noise frequency. Some of the noncircular nozzle data reviewed in previous sections tend to exhibit this trend, and, therefore, one characteristic of noncircular geometries may be that the shock spacings decrease more rapidly with downstream distance compared to a conical nozzle. However, this effect could also be the result of mixing noise level being higher relative to the shock noise level than for the conical nozzle case.

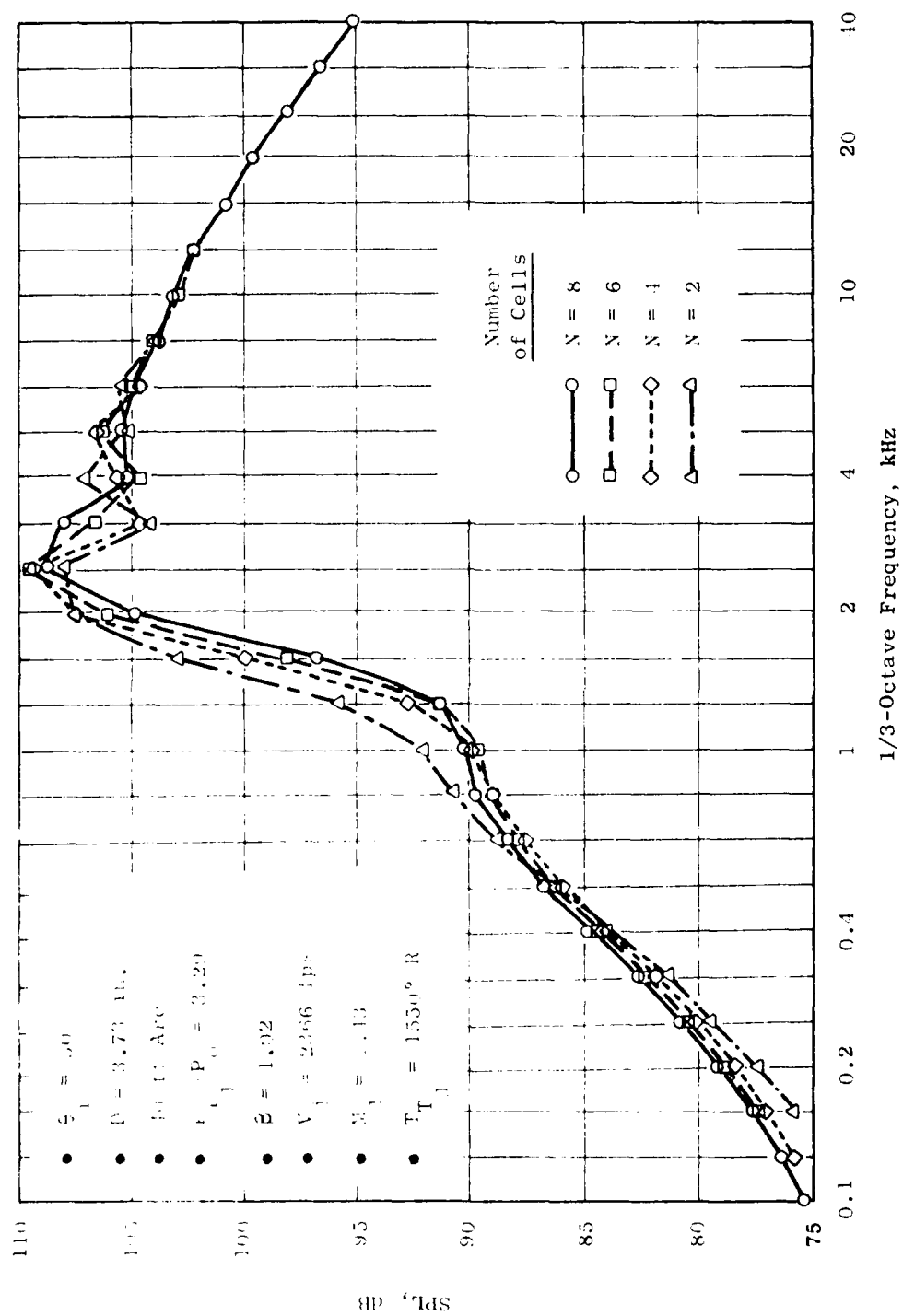


Figure 4-95. Predicted Effect of Number of Shock Cells N on Shock-Cell Noise Spectrum, HBF(69) Theory.

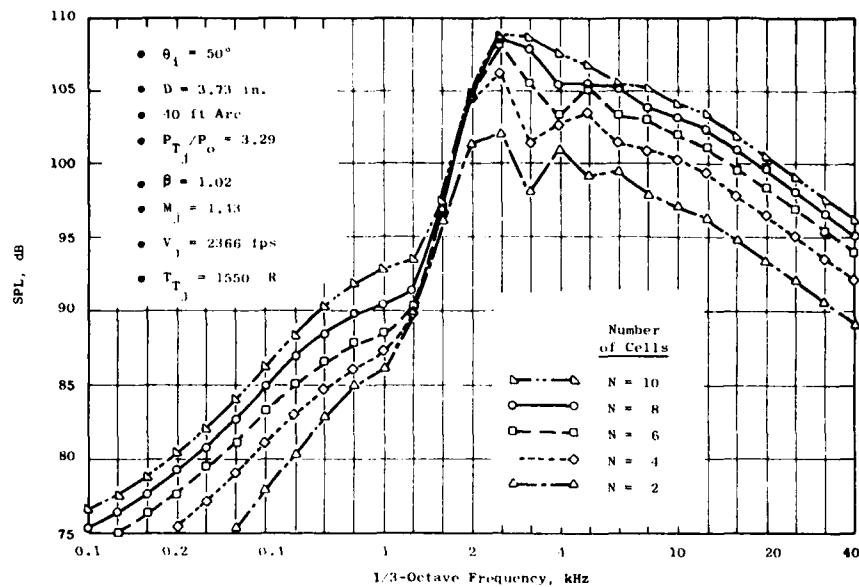


Figure 4-96. Predicted Effect of N on Shock-Cell Noise Spectrum; HBF (69) Theory, Modified by Factor $N/8$.

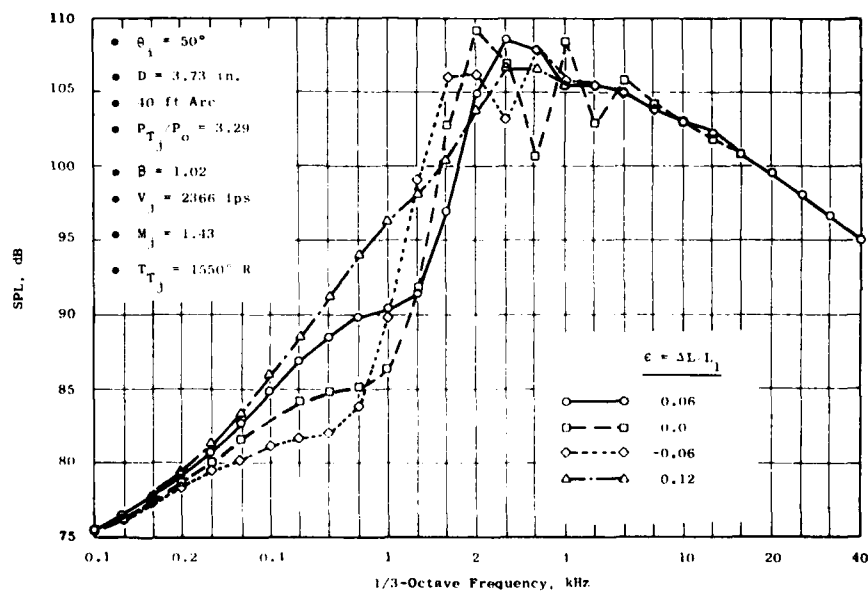


Figure 4-97. Predicted Effect of Shock Spacing Parameter $\epsilon = \Delta L/L_1$ on Shock-Cell Noise Spectrum, HBF (69) Theory.

The third parameter studied was convection velocity U_c . It is known that noncircular nozzles, especially suppressor types which exhibit substantially faster plume mixing, exhibit lower convection speeds than equivalent-area conical nozzles. To see what effect this might have on the shock cell noise, the ratio U_c/V_j was varied from 0.5 to 0.7. The computed spectrum changes are shown in Figure 4-98. Over the range of U_c/V_j examined, there seems to be very little effect of U_c on either spectrum shape or level.

It is possible to vary the shapes of the "universal" spectrum functions $H_0(S_n)$ and $C_1(S_n)$ and study their influence. However, it can be intuitively recognized, without numerical computations, that making the group source spectrum $H_0(S_n)$ broader or narrower than the empirically determined shape will just make the corresponding SPL spectrum broader or narrower, respectively. Also, there is no obvious way (which reflects physical insight or empirical observation) to vary $C_1(S_n)$ from its established shape, so no further parametric studies of these variables were carried out.

4.6.9 Extension of Prediction Method to Noncircular Nozzles

It was demonstrated in the previous section (see Figure 4-95) that the spectrum shape predicted by the HBF(69) theory does not significantly change if $N = 2$, relative to $N = 8$ shock cells. Consider, therefore, the case of a two-shock system, $N=2$; in this case, equation (260) reduces to the following:

$$\overline{p^2}(r_o, \theta_i, \omega_M) = \frac{b\omega_M A_0 (\omega_M)}{2r_o^2} \left\{ 1 + C_1(\omega_M) \frac{\cos(K\omega_M) \sin(Kb\omega_M/2)}{(Kb\omega_M/2)} \right\} \quad (264)$$

where

$$K = \frac{L_1}{U_c} (1 + M_c \cos \theta_i) (1 - \epsilon), \quad N=2 \quad (265)$$

for low frequencies, say $K\omega_M < 5$, the term

$$\frac{\cos(K\omega_M) \sin(Kb\omega_M/2)}{(Kb\omega_M/2)} \sim \cos(K\omega_M)$$

since $\sin x/x \sim 1$ for small x , and $b/2 \sim 0.1$.

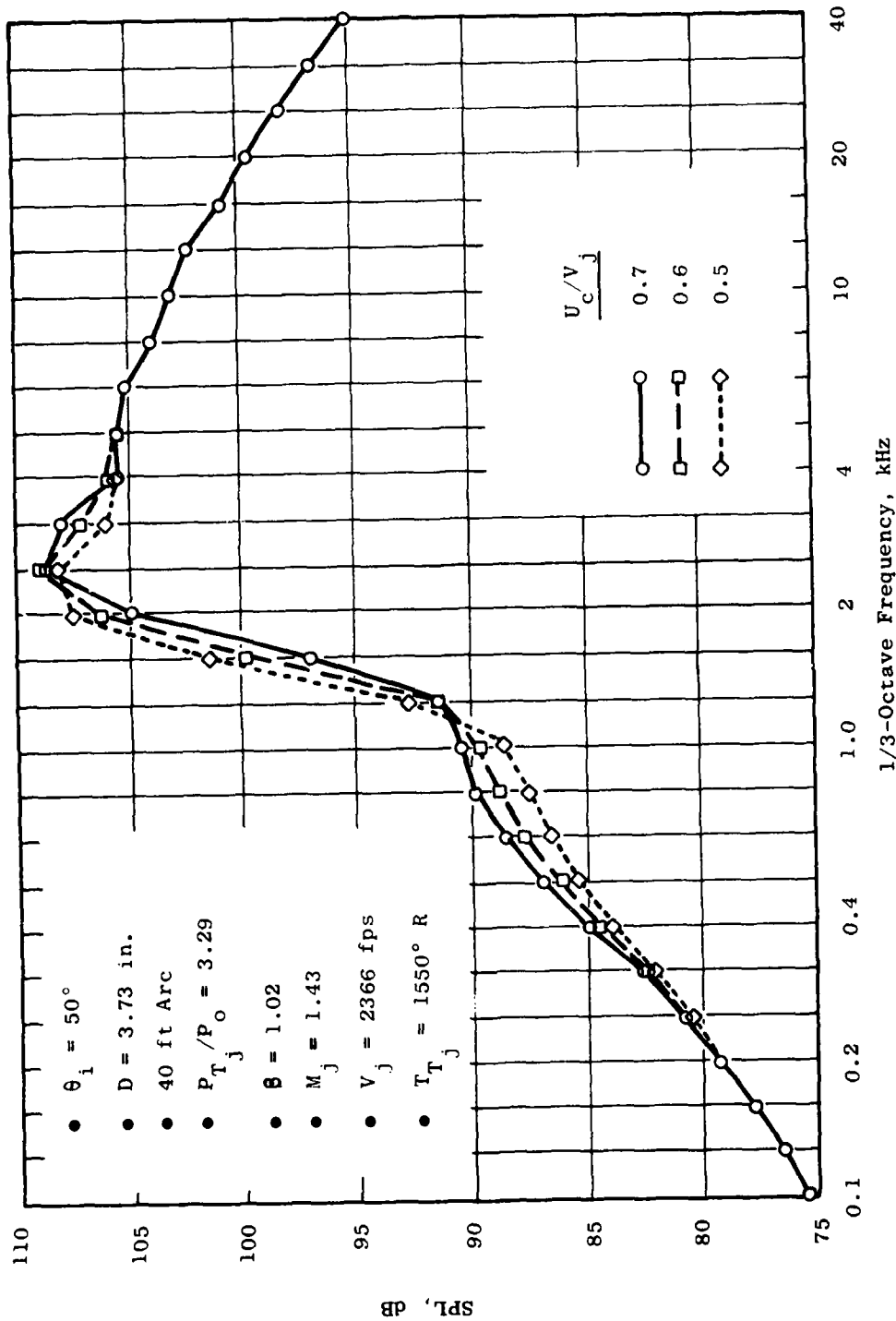


Figure 4-98. Predicted Effect of Eddy Convection Speed U_c on Shock-Cell Noise Spectrum, HBF(69) Theory.

Conversely, for high frequencies, say $K\omega_M > 25$, this same term approaches zero. Both $C_1(S_n)$ and the factor $[\sin(K\omega_M b/2)/(K\omega_M b/2)]$ act as damping terms to $\cos(K\omega_M)$. At low frequencies, as $\cos(K\omega_M) \rightarrow 1$, the spectrum approaches the limit

$$\frac{1}{p^2} (r_o, \theta_i, \omega_M) \rightarrow \frac{b\omega_M A_o(\omega_M)}{2r_o^2} [1 + C_1(\omega_M)]$$

Thus, at low frequencies, the spectrum asymptote is characterized by $A_o(\omega_M)[1 + C_1(\omega_M)]$, while at high frequencies the spectrum asymptote is characterized by $A_o(\omega_M)$.

The total spectrum is characterized by the basic group source spectrum $A_o(\omega_M)$, to which is added a damped cosine term. The characteristic jump and subsequent peak of the total spectrum occurs between the first negative extremum and second positive extremum, respectively, of $\cos(K\omega_M)$. Hence, the jump occurs at $K\omega_M = 3\pi/2$, and the peak occurs at $K\omega_M = 2\pi$. A good approximation to the interference term in equation (264) is given by

$$c_1(\omega_M) \frac{\cos(K\omega_M) \sin(Kb\omega_M/2)}{(Kb\omega_M/2)} \approx k_1 e^{-k_2(K\omega_M)^q} \cos(K\omega_M) \quad (266)$$

As $K\omega_M \rightarrow 0$, this term approaches $C_1(0) = 0.72$. It was found that $k_1 = 0.72$, $k_2 = 0.002$, and $q = 2$ gives a good fit to the left-hand side of the above expression. Since this term in equation (264) contributes only damped "wiggles" to the spectrum beyond the peak frequency, and since the effect of adding more terms in the series ($N = 3, 4, 5$, etc.) is to fill in these wiggles anyway, we can just cut off this term beyond the third zero of $\cos(K\omega_M)$.

Figure 4-99 shows the HBF group source spectrum $H_o(S_n)$ and Cross-correlation spectrum $C_1(S_n)$ as determined from computational studies using measured far-field spectra. It is seen that $H_o(S_n)$ has a shape typical of broadband jet mixing noise, probably characteristic of that portion of the mixing noise produced in the supersonic region close to the jet nozzle. The cross-correlation spectrum $C_1(S_n)$ is constant at low frequencies and falls off to zero at high frequencies, so that the interference terms become less important at high frequencies.

The interference spectrum was computed for the example case shown in Figure 4-95, using the approximation given by the left-hand side of equation (266). The computed spectrum is shown in Figure 4-100 with and without the cross-correlation factor $C_1(S_n)$. It is seen that the effect of $C_1(S_n)$ is to damp out the high frequency wiggles, as well as to reduce the peak and valley amplitudes at low frequencies. The addition of the interference spectrum (with the factor C_1) to the group spectrum is shown in Figure 4-101. The curve labeled SPL_o denotes the sound pressure spectrum produced by the group source spectrum alone; the curve labeled SPL_1 denotes the SPL spectrum produced by summing the SPL_o spectrum and the interference spectrum. This simple example for a two-shock system shows how the observed shock-cell noise spectrum shape evolves from the summation of the group (broadband) and interference (reinforcement and cancellation) spectra.

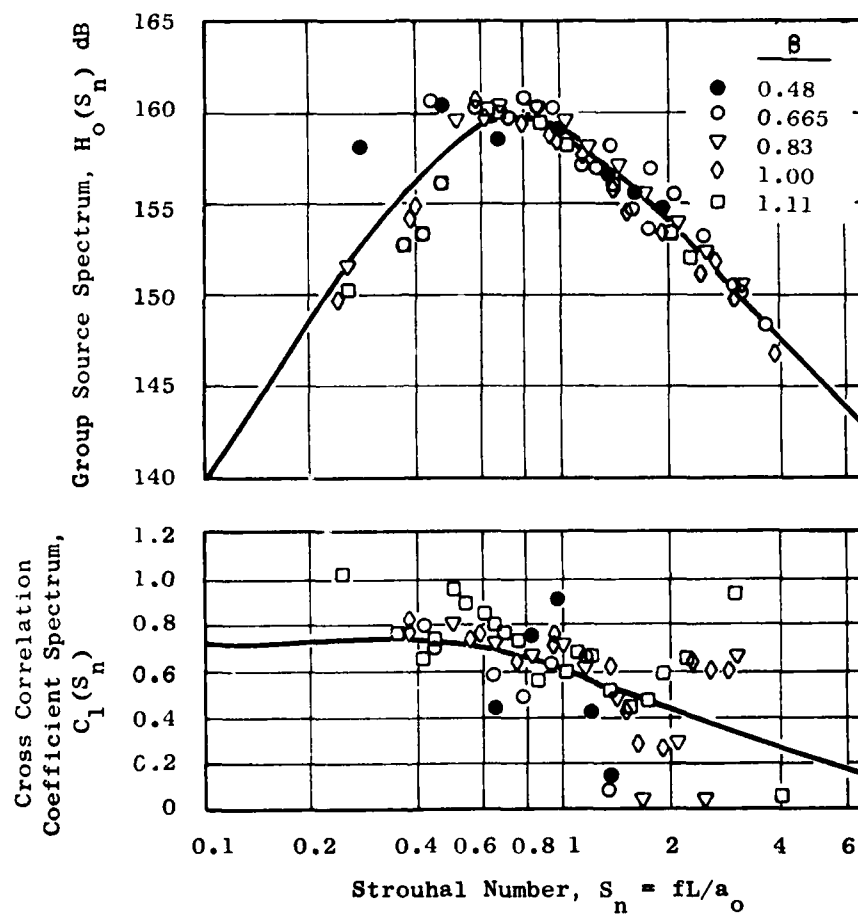


Figure 4-99. Shock-Cell Noise Group Source Spectrum and Cross-Correlation Spectrum Developed by Harper-Bourne and Fisher (69).

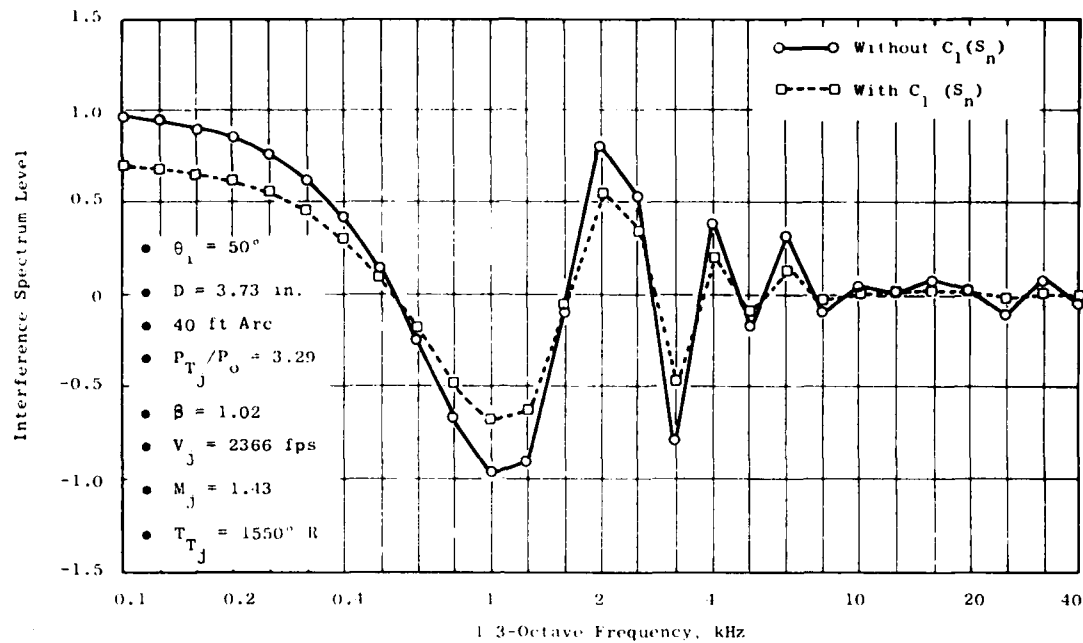


Figure 4-100. Predicted Interference Spectrum for a Two-Shock ($N = 2$) System.

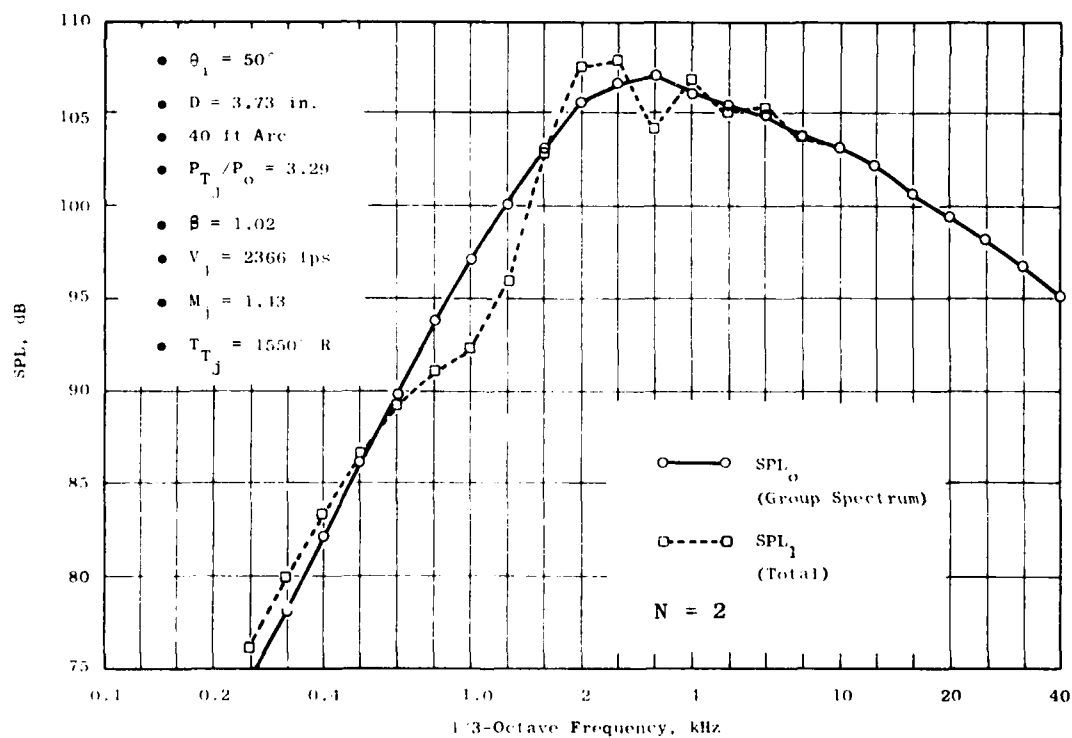


Figure 4-101. Predicted Shock-Cell Noise Spectrum Showing Superposition of Group Spectrum and Interference Spectrum.

The above example exercise serves as a guide to generalizing the HBF theory to noncircular nozzles. The following modifications to the basic HBF model are proposed to allow the prediction of noncircular nozzle shock-cell noise:

1. Shock-cell spacing should be maintained as a parameter independent of equivalent diameter, so that the shock cell spacing characteristic of noncircular nozzles can be accounted for. By assuming that L_1 (position of first shock) is proportional to hydraulic diameter, as suggested by the experimental evidence of Kurn(74), the peak noise frequency is predicted quite well for the eight-lobe nozzle, as shown in Figure 4-82, see Section 4.6.6. For nozzles with solid boundaries guiding the external expansion process, however, hydraulic diameter may not be the correct scaling length, and shock spacing should therefore be evaluated from flow field measurements (e.g., laser velocimeter, Schlieren photography) and/or computations (e.g., method-of-characteristics, finite-difference methods). This becomes important for plug nozzles.
2. The HBF model correlates the group source spectrum level (and hence OASPL) with diameter-to-distance ratio $(D/R_o)^2$. It is suggested that the dependence on D^2 is in reality a dependence on shock-front through-flow area, which may be quite different from total exit area for non-circular nozzles. This may provide an explanation for the lower apparent shock-cell noise OASPL for lobe nozzles (Figure 4-81), and annular plug nozzles (Figure 4-91).
3. The HBF model correlates group source spectrum level (and hence OASPL) with shock strength parameter β^4 . It is suggested that the correlation dependency on β^4 is strictly correct only for normal shocks. Although a β^4 -dependency for a given nozzle type may be observed, a geometry which has significantly different shock pattern obliquity may not yield the same correlation level. For example, the static pressure ratio across a two-dimensional oblique shock is given by

$$\frac{P_2}{P_1} = \frac{2\gamma}{\gamma+1} (M_1 \sin \phi)^2 - \frac{\gamma-1}{\gamma+1}$$

where M_1 is the upstream Mach number and ϕ is the oblique angle the shock front makes with the upstream flow direction. In terms of pressure rise across the shock, the expression can be rewritten as

$$\frac{\Delta P}{P_1} = \frac{P_2 - P_1}{P_1} = \frac{2\gamma}{\gamma+1} \beta^{*2}$$

where

$$\beta^{*2} = (M_1 \sin \phi)^2 - 1$$

For $\phi = 90^\circ$, i.e., the normal shock case, β^* reduces to the HBF parameter β . If the value of ϕ were known for a particular geometry, a more "universal" correlation might be achieved on the basis of β^{*4} rather than β^4 . Again, this requires additional experimental and/or analytical information on the shock structure.

4. Extrapolation of the static prediction of shock-cell noise to in-flight conditions can probably be done by simply applying the dynamic correction factor $(1 - M_a \cos \theta_i)^{-4}$, as suggested by the experimental results reported by Drevet, et al. (75). This is consistent with the notion that the shock cells are fixed relative to the nozzle. The influence of relative velocity itself is small, as shown by the free-jet results in Figures 4-75 through 4-80 and Figures 4-83 through 4-85. The small changes observed are most likely due to changes in shock spacing, which again requires experimental and/or analytical evaluation.
5. The number of shock cells may be different for noncircular nozzles. The HBF value of $N = 8$ is implicit in the group source spectrum shown in Figure 4-99. For $N \neq 8$, the group source spectrum levels should therefore be corrected by a factor $N/8$.

The above proposed extensions to the basic HBF shock noise theory for predicting noncircular nozzle noise (in flight) all require additional knowledge of the shock structure characteristics for the particular nozzle being considered. In many cases, e.g., multitube and multichute nozzles, the relevant shock structure parameters such as N , L_1 , ϵ , etc., are not presently known. For certain cases, however, the changes in these parameters relative to a conical nozzle can be obtained, and this information can be utilized to test the hypothesis that, if the correct shock-cell structure is incorporated into the model, the HBF theory will provide a reasonable prediction of the shock-cell noise.

For the case of simple rectangular nozzle, Kurn (74) has shown that the shock-cell structure scales with hydraulic diameter. Predictions were made of the shock cell noise for the 6:1 aspect ratio nozzle shown in Figure 4-88. The group source spectrum was assumed to scale on equivalent diameter for both level and frequency, while the interference spectrum was assumed to scale with hydraulic diameter. By combining equations (258) and (260), the following expression for the prediction of the mean-square sound pressure level is obtained:

$$\begin{aligned} \overline{P^2}(r_o, \theta_i, \omega_M) = & \frac{b}{2} \frac{\omega_M L_1}{a_o} \frac{D^2}{r_o^2} \beta^4 H_o(S_n) \left[1 + \right. \\ & \left. + \frac{2}{N} \sum_{i=1}^{N-1} C_i(S_n) \sum_{n=1}^{N-i} \frac{\cos(K\omega_M) \sin(Kb\omega_M/2)}{(Kb\omega_M/2)} \right] \end{aligned} \quad (267)$$

where

$$K = \frac{iL_1}{U_c} (1 + M_c \cos \theta_i) \left[1 - \frac{1}{2} \epsilon (2n+i-1) \right] \quad (268)$$

and

$$C_i(S_n) = C_1^\alpha(S_n), \quad \alpha = i^2 \quad (269)$$

It is assumed that $D = D_{eq}$ and that

$$L_{avg} = 1.1\beta D_{eq}; \quad L_1 = 1.31\beta D_h \quad (270)$$

The Strouhal number S_n then becomes

$$S_n = \frac{\omega_M L_{avg}}{a_o} = \frac{1.1\beta D_{eq} \omega_M}{a_o} \quad (271)$$

Defining the parameter $G(S_n)$ as

$$G(S_n) = \frac{N}{8} \frac{b}{2} \frac{\omega_M L_{avg}}{a_o} H_o(S_n) \quad (272)$$

equation (267) then becomes

$$\begin{aligned} \overline{P^2}(r_o, \theta_i, \omega_M) &= \frac{D_h}{D_{eq}} \frac{D_{eq}^2}{r_o^2} \beta^4 G(S_n) \left[1 + \right. \\ &\quad \left. + \frac{2}{N} \sum_{i=1}^{N-1} C_i(S_n) \sum_{n=1}^{N-i} \frac{\cos(K\omega_M) \sin(Kb\omega_M/2)}{(Kb\omega_M/2)} \right] \end{aligned} \quad (273)$$

Note that the 1/3-octave group source spectrum $G(S_n)$ is identical to the SAE version of the HBF narrow-band spectrum $H_o(S_n)$, except for the additional factor of $N/8$ which was proposed and discussed in previous paragraphs herein.

Utilizing equations (268) and (273), the shock cell noise of the aforementioned 6:1 aspect ratio nozzle was predicted and compared with experimental measurements. The comparison is shown in Figure 4-102, and the agreement

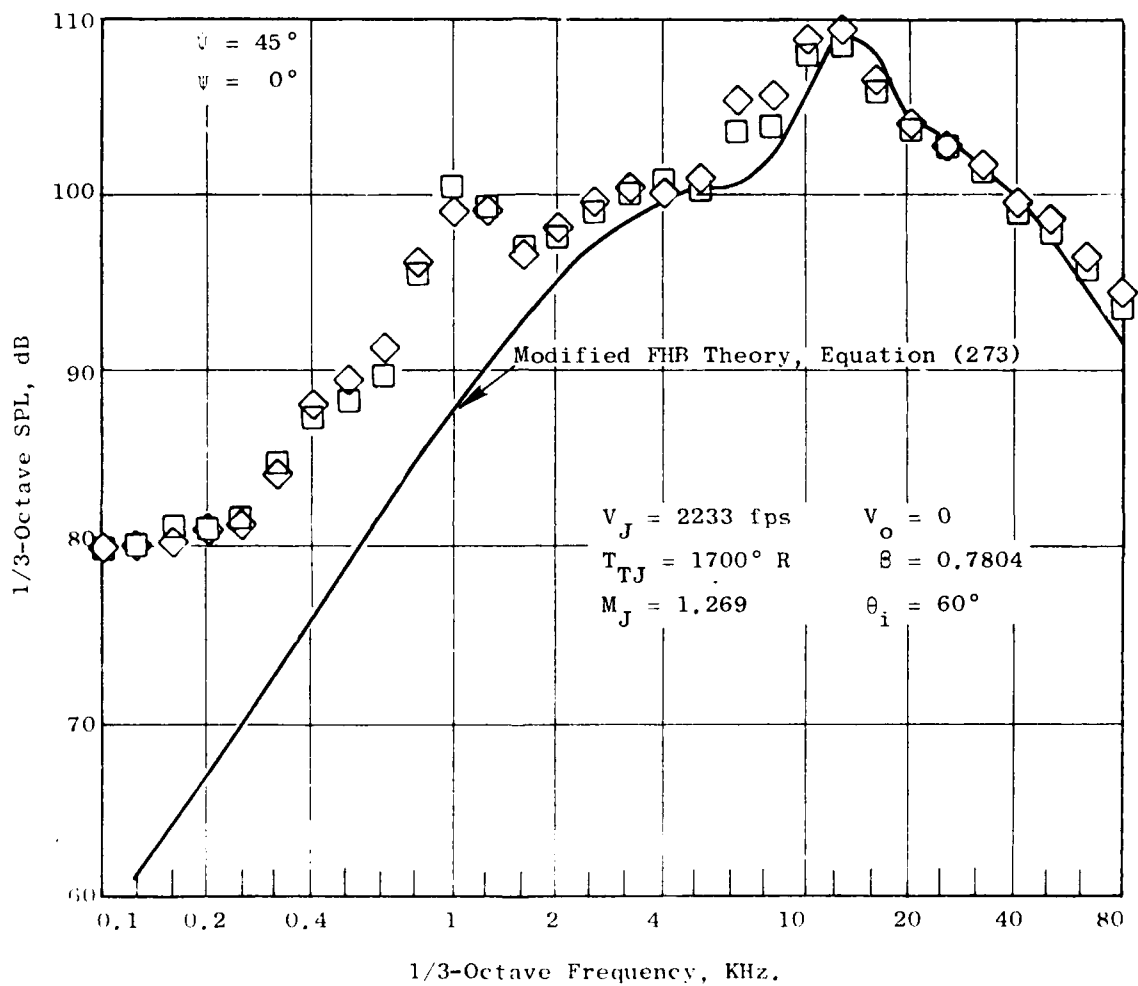


Figure 4-102. Comparison of Predicted and Measured Shock-Associated Noise Spectrum, 6:1 Aspect Ratio Rectangular Jet.

between prediction and experiment is seen to be quite good. Note that when the hydraulic diameter is substantially smaller than the equivalent diameter (in this case, $D_h/D_{eq} = 0.620$), the interference spectrum is shifted to higher frequencies relative to the group source spectrum, resulting in a change in spectrum shape relative to that of an equivalent conical nozzle. For this prediction, eight shock cells ($N = 8$) were assumed, for lack of any evidence to the contrary. The factor D_h/D_{eq} in equation (273) reduces the shock noise level by about 2.0 dB relative to the equivalent-area conical nozzle, and this agrees with the observed 2.5 dB reduction, discussed in Section 4.6.6.

Equation (273) was also used to predict the measured spectra shown in Figure 4-82 for the eight-lobe daisy nozzle. A comparison of the predicted and measured spectra are shown in Figure 4-103. Similarly, the measured annular nozzle spectra shown in Figure 4-92 were also predicted using equation (273), and the comparisons are shown in Figure 4-104. These comparisons show reasonable agreement between prediction and experiment. In viewing these results, it should be kept in mind that the predictions represent only the shock-cell component of the total noise spectrum, whereas the data represents the sum of both shock-cell noise and jet mixing noise (plus any other excess noise mechanisms which may be present). Also, the predicted spectra were computed assuming the conical nozzle values of $N = 8$ and $\epsilon = 0.06$; these may well not be the correct values for the eight-lobe and annular plug nozzles, but no experimental or analytical information was available to provide better values. Although not shown herein, it was found that the annular plug nozzle predicted spectrum shapes could be improved by using $\epsilon = 0.12$ instead of $\epsilon = 0.06$, based on numerical experiments. This may be related to the presence of the plug external expansion surface increasing the rate at which successive shock cell spacings decrease. Further flow field shock structure measurements are needed to verify this supposition.

The factor D_h/D_{eq} in equation (273) represents one effect of noncircular geometry on the shock-cell noise level. The reduction in shock cell noise relative to a conical nozzle due to this factor is shown in Figure 4-105. Also shown are the measured OASPL reductions relative to a conical nozzle for the various noncircular nozzles investigated herein. The range of D_h/D_{eq} covered by the data is rather limited, but the agreement between predicted and measured reductions is reasonably good.

4.6.10 Concluding Remarks

A detailed review of the Harper-Bourne/Fisher⁽⁶⁹⁾ theory for the broadband shock-cell noise of underexpanded supersonic jets has been carried out. The theory has been verified in all its important aspects for conical nozzles through a detailed examination of parametric acoustic data and comparisons with the theoretical predictions. Based on analysis of free-jet data, it was found that external flow relative velocity effects on the shock-cell noise characteristics are small. Examination of noncircular (e.g., rectangular, eight-lobe daisy, and annular plug) nozzle acoustic data showed that the HBF⁽⁶⁹⁾ theory dependencies on shock-strength parameter β and insensitivity to jet

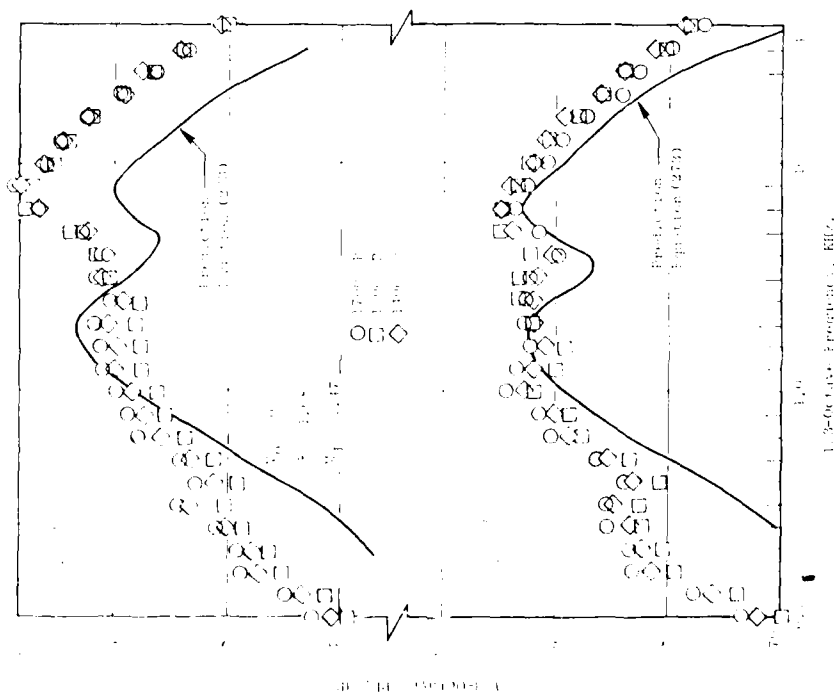


Figure 4-103. Comparison of Measured and Predicted Shock-Associated Noise Spectra; Scale Model 8-Lobe Daisy Suppressor, Effect of Jet Temperature.

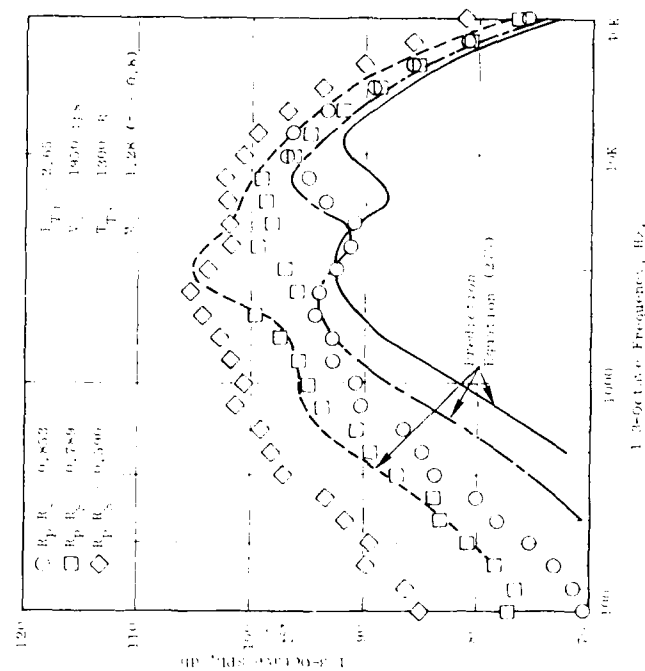


Figure 4-104. Comparison of Measured vs. Predicted Shock-Associated Noise Spectra; Annular Plug Nozzle, $\theta_i = 50^\circ$.

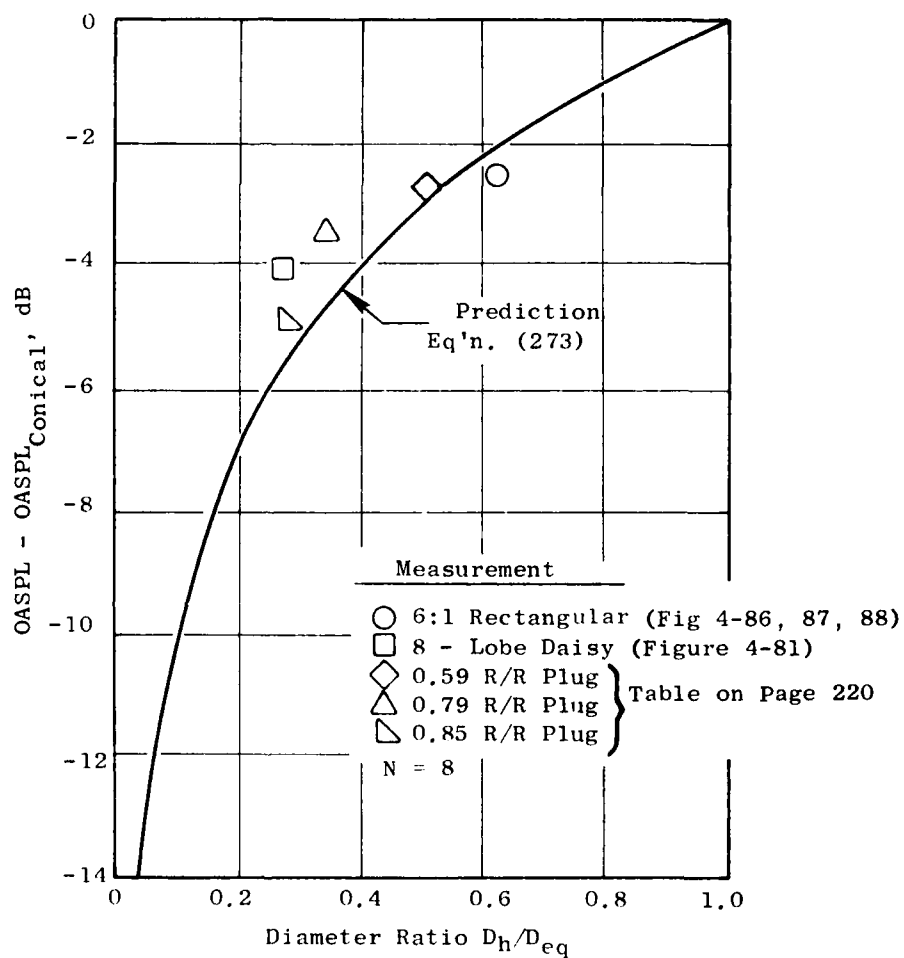


Figure 4-105. Reduction in Shock Noise OASPL Due to Nozzle Shape.

temperature applied to noncircular nozzles as well. However, noise levels relative to a conical nozzle are significantly lower, and this reduction depends on nozzle shape. The shock-cell noise spectrum shape also differs from that of a conical nozzle, and the difference also depends on nozzle shape. For the eight-lobe nozzle, a small dependency of shock-cell noise on relative velocity was observed.

Modifications to the basic HBF theory were identified for predicting noncircular nozzle shock-cell noise behavior. The assumption was made that the basic physical mechanisms contained in the HBF model are correct, and that inclusion of the correct shock structure parameters for the particular nozzle being considered would provide a correct prediction. This approach points to the need for further work on experimentally (and theoretically) defining the shock-cell behavior of noncircular nozzles, since little or no information on these important ingredients is available at the present time. Preliminary data/theory comparisons for simple rectangular and annular plug nozzles using a modification of the HBF theory to account for nozzle shape effects gave encouraging results, lending credence to the methodology adopted herein.

On a more fundamental basis, the "universal" group source spectrum and cross-correlation coefficient spectrum functions developed by HBF were assumed to be applicable to any nozzle type. These functions relate the input turbulence disturbance characteristics to the output acoustic emission characteristics of a given shock front. For noncircular nozzles, the input turbulence characteristics may well be different than that for a conical nozzle, and a comprehensive study of this element of the theory may be required to properly model the noncircular nozzle shock-cell noise behavior. A link with the turbulent mixing noise spectrum produced by the supersonic portion of the jet may be possible.

A final point to consider is that the available evidence suggests that shock-cell noise is not appreciably altered by the presence of external flow or relative velocity. In-flight, dynamic (doppler) effects tend to raise the noise levels in the forward quadrant where shock-cell noise is most important. The resulting directivity pattern or field shape (considering both shock-cell noise and turbulent mixing noise) becomes much flatter in flight. Considering that shock-cell noise has a higher peak frequency than mixing noise, the resulting perceived noise level corrected for flight duration effects (EPNL) may well be controlled by the shock-cell noise component in flight. It therefore becomes very important to be able to properly account for shock-cell noise in flight when evaluating potential noise abatement nozzles for high jet velocity propulsion systems.

4.7 UNIFIED AEROACOUSTIC MODEL FOR JET NOISE PREDICTION

4.7.1 Introduction

Many suppressor nozzles have been designed in the past utilizing intuitive notions of how to suppress jet noise which have demonstrated substantial noise reduction. Often, the noise reduction has been obtained at the expense of considerable thrust loss and increased engine weight, in addition to higher manufacturing cost and complexity. Seemingly minor changes to these suppressor nozzle designs, made for the purpose of improving thrust performance, often resulted in substantial loss of noise suppression. It is therefore desirable to have a quantitative prediction technique available for estimating the aerodynamic and acoustic characteristics of suppressor-type nozzle configurations. With such a technique, design and optimization studies can be conducted prior to construction and testing, thus minimizing the time and cost of development. A useful technique must be sensitive to the controllable nozzle design variables, and should be based on a minimum of empiricism. That empiricism which is necessary should be tied more or less to physical (flow and acoustic propagation) characteristics rather than geometric parameters in order to be "universal" in a normalized (but perhaps restricted) sense.

With the above objectives and guidelines in mind, a unified aerodynamic/acoustic prediction technique described in this section was developed for assessing the noise characteristics of suppressor nozzles. The technique utilizes an extension of Reichardt's method (Section 4.5) to provide predictions of the jet plume aerodynamic flow field (velocity, temperature, and turbulence intensity distributions). The small-scale turbulent fluctuations produced in the mixing regions of the jet are assumed to be the primary source of noise generation, as in the classical theories of jet noise. The alteration of the generated noise by the jet plume itself as it propagates through the jet to the far-field observer (sound/flow interaction or fluid shielding) is modeled utilizing the high-frequency shielding theory described in Section 4.3.

These basic modeling elements (flow field prediction, turbulent mixing noise generation, and sound/flow interaction) have been coupled together in a discrete volume-element formulation. The jet plume is divided into elemental volumes, each roughly the size of a representative turbulence correlation volume appropriate to that particular location in the plume. Each volume element is assigned its own characteristic frequency, spectrum, and acoustic intensity. The sound/flow interaction effects for each volume element are evaluated from the flow environment of the element, and the resultant contribution to the far field is determined. The individual volume elements are assumed to be uncorrelated with each other, so that the total contribution to the far field is simply the sum of the individual volume element contributions.

Previous work on modeling of jet aeroacoustic characteristics has been confined to simple round and coannular jets. One of the first attempts at developing a comprehensive aerodynamic/acoustic jet model was published by

Lee, Kendall, et al.⁽⁷⁶⁾ and Grose and Fendall⁽⁵⁸⁾. This approach utilized an extension of Reichardt's method for predicting the jet flow properties for round and lobe-type nozzles (this method is adopted herein). Only acoustic power spectra are predicted, based on a "slice-of-jet" model wherein the power per axial slice is computed and related to a certain frequency band by means of empirically-derived frequency vs. axial distance relationships. Successful predictions are confined to low Mach numbers. The volume-element summation or "lump-of-jet" approach was first developed by Benzakein, et al.⁽⁷⁸⁾ for round and coannular jets. A finite-difference turbulent-kinetic-energy model was developed to predict the jet flow field, while the classical Lighthill⁽⁴⁾ and Ffowcs-Williams⁽⁶⁾ formulations were employed, with suitable empirical modifications, to predict the noise from each volume element. Extensions of the method of Benzakein, et al. to distinguish between self-noise and shear-noise, proposed by Jones⁽⁷⁹⁾ and Ribner⁽³⁹⁾, were developed by Knott⁽⁸⁰⁾ and Moon⁽⁸¹⁾. Recently, Chen⁽⁸²⁾ has applied Kendall's⁽⁵⁸⁾ method to predicting power spectra of coannular jets.

The above methods either ignore the sound/flow interaction effects, or recognize only source convection in absence of a shrouding flow. This has been shown to give incorrect simulation [see Mani^(37,38)] for all but the lowest jet velocities, especially when predicting sound pressure level spectra at observer angles close to the jet axis. The aeroacoustic model discussed in this section is directed toward predicting high velocity jet noise [1500 - 3000 fps (457 - 914 m/s)], for arbitrary nozzle shapes, including sound pressure level spectra at any observer location.

4.7.2 Outline of Method

A block diagram of the computation sequence for the jet noise prediction to be described is shown in Figure 4-106. The jet plume is subdivided into elemental volumes which are approximately the size of a typical turbulent correlation volume or "eddy size". Figure 4-107 illustrates how a jet plume is typically subdivided into "eddy" volume elements. The subdivisions are very small close to the nozzle exit plane where the turbulence length-scales are small. The volume elements are made progressively larger in the downstream direction, simulating the increasing length-scale with downstream distance.

Figure 4-108 illustrates a jet plume exhausting from a nozzle of arbitrary shape. Utilizing the modified Reichardt theory described in Section 4.5, the mean velocity, temperature, density, and turbulent shear stress distributions can be computed throughout the jet plume. The required inputs are nozzle shape, nozzle exit plane total pressures and temperatures, and ambient total and static pressures and temperatures. The modified Reichardt theory can provide the aerodynamic properties at any arbitrary point in the plume because of the closed-form solution formulation (the calculation is not a finite-difference method whose grid points are established/dictated by the accuracy/stability requirements of the numerical procedure). The flow properties are therefore, computed at the geometric centers of these eddy volume elements.

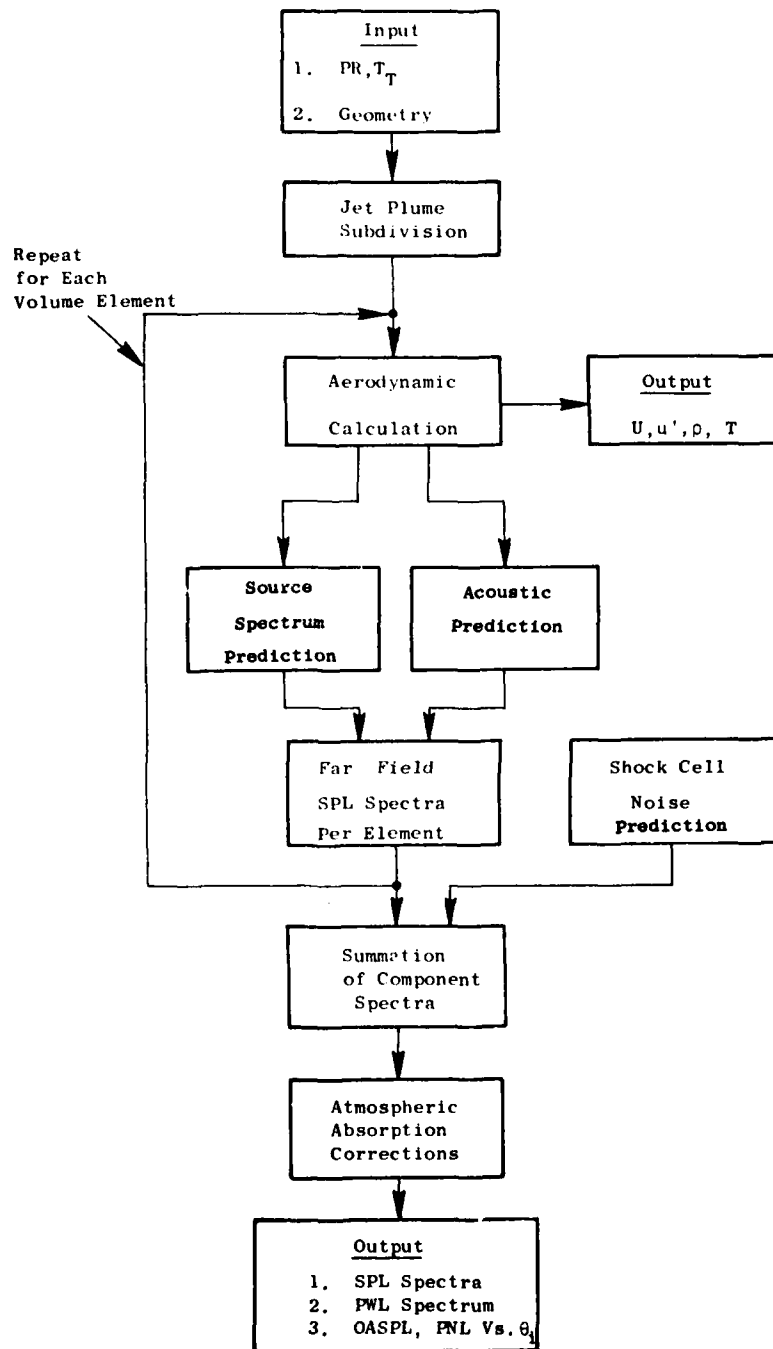


Figure 4-106. Block Diagram of Jet Noise Aeroacoustic Prediction Model.

The noise source spectrum generated by each of the volume elements is estimated from the classical Lighthill⁽⁴⁾ expressions for noise produced by free turbulence, assuming that the turbulence can be modeled as locally-isotropic, convecting quadrupole sources of sound [as proposed by Ribner⁽³⁹⁾]. The turbulent structure parameters (intensity, length-scale, characteristic frequency, spectrum) required for computing the generated noise are derived from the calculated mean-flow distributions using previously established empirical similarity relations, developed by Davies, et al.^(16, 83).

The effect of convection and fluid shielding on the emitted sound of each volume element is computed. The flow properties (mean velocity profiles and temperature profiles) in the vicinity of the element determine the amount of flow shrouding or fluid shielding seen by that element.

From the generated noise spectrum and the predicted modifications due to convection and fluid shielding, the net emitted noise level at each observer angle and 1/3-octave band frequency of interest is calculated. The contributions from each volume element in the jet are summed on a mean-square pressure basis, assuming that individual volume elements are uncorrelated with each other. This provides the total sound pressure predicted 1/3-octave band spectrum observed in the far field.

In addition to the calculation of turbulent mixing noise, the shock-cell broadband noise is also computed using a modification of the Harper-Bourne and Fisher⁽⁶⁹⁾ method as described in Section 4.6. The mixing noise spectra and the shock-cell noise spectra are summed on a mean-square pressure basis to yield the total jet noise spectra, at each far-field observer angle.

Atmospheric attenuation corrections, using the method of Bass, et al.⁽⁸⁴⁾, are made to the predicted spectra to account for air attenuation at the appropriate far-field distance. The overall sound pressure levels (OASPL), perceived noise levels (PNL) and sound power spectrum (PWL) are also evaluated from the far-field sound pressure spectra.

Each of the major elements shown in Figure 4-106 are described below; then a select number of data/theory comparisons are given, followed by a discussion of application of the model for identification of noise suppression mechanisms. A brief summary of the model limitations and capabilities is given, followed by suggestions for further work on extending the model.

4.7.3 Aerodynamic Calculation

The jet plume flow field is computed using the extension of Reichardt's method developed in Section 4.5. The method basically consists of predicting the diffusive transport of momentum flux and enthalpy flux from a specified exit plane distribution to various axial stations along the plume. In addition, the various components of turbulent shear stress are also calculated, being related to directional derivatives of the axial component of momentum flux. From these distributions, the mean axial velocity, density, and turbulence intensity distributions are estimated.

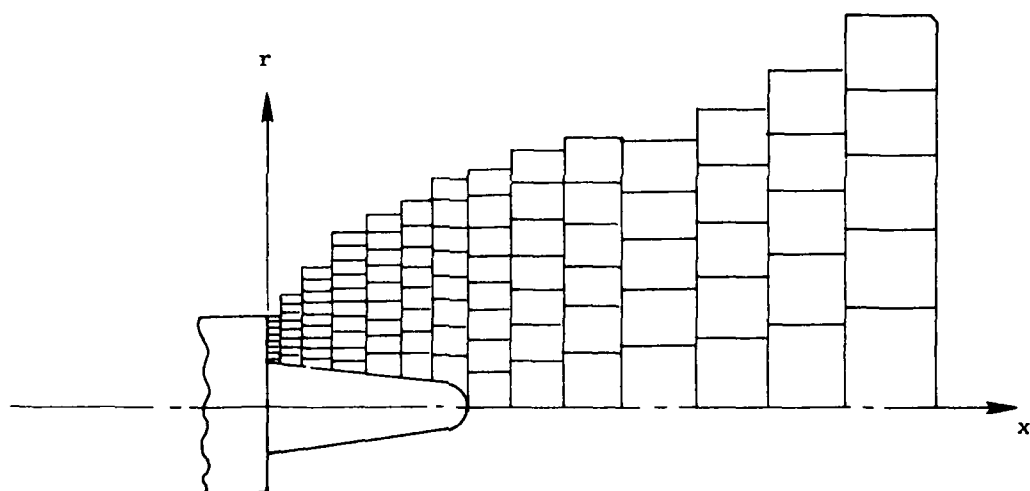


Figure 4-107. Typical Jet Plume Flow Field Subdivision (Not to Scale), into Eddy Volume Elements.

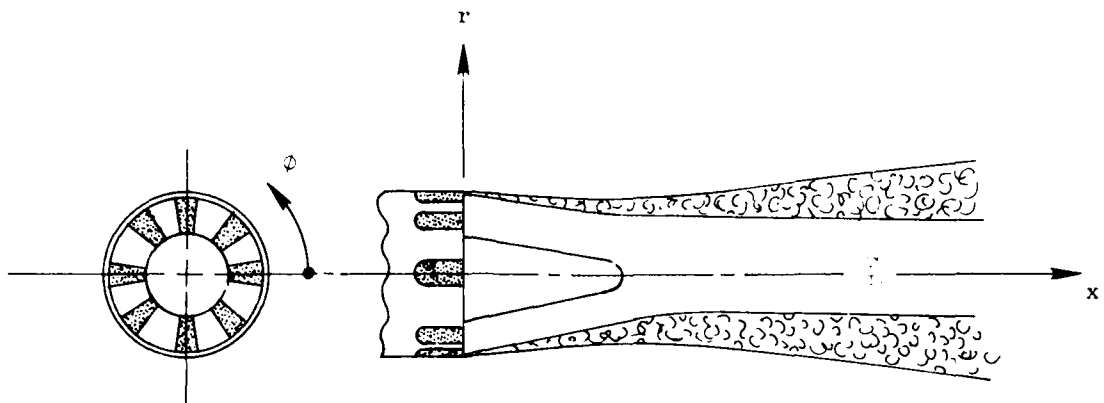


Figure 4-108. Typical Jet Plume Exhausting from a Nozzle of Arbitrary (Non-Circular) Planform Shape.

A typical suppressor nozzle planform shape at the nozzle exit plane is shown in Figure 4-109. The nozzle contour can be defined by coordinates (v_o, α) . The jet nozzle exit plane conditions are denoted by subscript "j", and the ambient field (external flow) conditions are denoted by subscript "a". The flow conditions at any flow field point (x, r, ϕ) are computed from the following equations, taken from Section 4.5.7:

Momentum Transport:

$$\rho U^2 - \rho_a U_a^2 = \frac{1}{2\pi} \oint (\rho_j U_j^2 - \rho_a U_a^2) \left[1 - e^{-R_o^2/b_m^2} \right] d\phi \quad (274)$$

Heat Transport:

$$\rho UH = \frac{1}{2\pi} \oint (\rho_j U_j H_j) \left[1 - e^{-R_o^2/b_h^2} \right] d\phi \quad (275)$$

Shear Stresses:

$$\frac{\tau_x}{\rho} = -\frac{C_m^2}{2\pi} \oint (U_j^2 - U_a^2) \left[\frac{R_o^2}{b_m^2} e^{-R_o^2/b_m^2} \right] d\phi \quad (276)$$

$$\frac{\tau_r}{\rho} = \frac{C_m}{2\pi} \oint (U_j^2 - U_a^2) \left[\frac{\sqrt{\pi}}{2} \operatorname{erf} \left(\frac{R_o}{b_m} \right) - \frac{R_o}{b_m} e^{-R_o^2/b_m^2} \right] \cos \phi d\phi \quad (277)$$

$$\frac{\tau_\phi}{\rho} = \frac{C_m}{2\pi} \oint (U_j^2 - U_a^2) \left[\frac{\sqrt{\pi}}{2} \operatorname{erf} \left(\frac{R_o}{b_m} \right) - \frac{R_o}{b_m} e^{-R_o^2/b_m^2} \right] \sin \phi d\phi \quad (278)$$

where \oint denotes a contour integral around the nozzle planform boundary.

In the above equations, U , ρ , and H are the mean velocity, density and enthalpy, respectively, and τ_x , τ_r , and τ_ϕ are the x , r , and ϕ - components of turbulent shear stress. The coordinates R_o and ϕ are defined by the relations

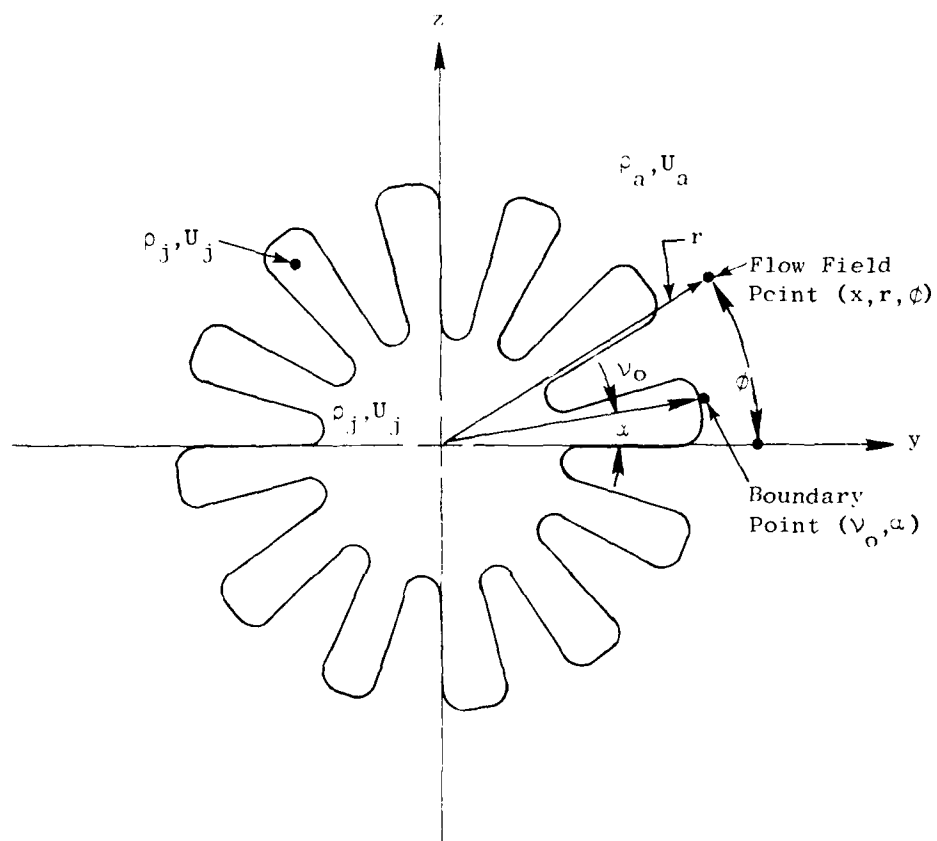


Figure 4-109. Typical Suppressor Nozzle Exit Plane Planform Shape.

$$\left. \begin{aligned} R_o^2 &= (r-v_o)^2 + 2rv_o[1 - \cos(\phi - \alpha)] \\ \text{and } R_o \cos \phi &= r - v_o \cos(\phi - \alpha) \end{aligned} \right\} \quad (279)$$

The turbulent mixing length parameters $b_m = C_m x$ and $b_h = C_h x$ are determined by the momentum spreading rate parameter C_m and enthalpy spreading parameter C_h . Empirical expressions for these have been developed in Section 4.5, and are as follows:

$$C_m = \frac{0.075}{(1+C_1 VR)(1+C_2 M_j)}, \quad C_h = 1.15 C_m \quad (280)$$

where $VR = U_a/U_j$ and $M_j = U_j/C_j$, the jet exit Mach number. The constants C_1 and C_2 were determined from calibrations with conical nozzle flow field velocity measurements, and values of $C_1 = 0.25$ and $C_2 = 0.08$ were found to give the best agreement with experiments. Equation (280) is actually a simplified version of the relations developed in Section 4.5, since the explicit dependence on Reynolds number and Prandtl number has been omitted.

The velocity and density are determined from the distributions of (ρU^2) and (ρUH) from the following expressions:

$$U = \frac{\rho UH}{2\psi} + \sqrt{\left(\frac{\rho UH}{2\psi}\right)^2 + \frac{C_p T_a (\rho U^2)}{\psi}} \quad (281)$$

$$\text{where } H = C_p T + \frac{1}{2}U^2 - C_p T_a \quad (282)$$

$$\text{and } \psi = \frac{\gamma}{\gamma-1} P_a + \frac{1}{2} (\rho U^2) \quad (283)$$

$$\text{and } \rho = \frac{(\rho U^2)}{U^2}; \quad T = \frac{P_a}{\rho R_g} \quad (284)$$

In the above expressions, C_p and R_g are the specific heat at constant pressure and universal gas constant, respectively [$R_g = \gamma C_p / (\gamma-1)$], γ is the ratio of specific heats, and p_a is the jet static pressure, assumed to be equal to the ambient static pressure. The local temperature is T , and T_a is the ambient static value.

The axial turbulence intensity u' is computed from the shear stress components utilizing the following expression:

$$(u')^2 = \sqrt{(\tau_r/\rho)^2 + (\tau_\phi/\rho)^2 + (10\tau_x/\rho)^2} \quad (285)$$

For nozzles with an axisymmetric centerbody or plug, modifications to the above computation procedure were developed in Section 4.5. This modification consists of a coordinate transformation of the variables (R_0, ϕ) as follows:

$$\left. \begin{aligned} R_0^2 &= (\Delta r - \Delta v)^2 + 2 \Delta r \Delta v [1 - \cos(\phi - \alpha)] \\ R_0 \cos \phi &= \Delta r - \Delta v \cos(\phi - \alpha) \end{aligned} \right\} \quad (286)$$

$$\text{where } \Delta r = \sqrt{r^2 - r_b^2(x)} \quad \text{and} \quad \Delta v = \sqrt{v_o^2 - r_b^2(0)}$$

and $r_b(x)$ is the centerbody/plug contour coordinate specification. For $r_b(x) = 0$, equations (286) reduce to equation (279).

Equations (274) through (286) completely define the flow field calculation procedure. As discussed in the previous section, the flow properties are evaluated at all field points corresponding to eddy volume element centers (x, r, ϕ) required for the subsequent noise prediction.

4.7.4 Source Spectrum Prediction

The noise spectrum generated by a given eddy volume element in absence of convection and fluid shielding effects is referred to herein as the source spectrum. As discussed in Section 4.3, each eddy volume element consists of quadrupole sources of various orientations. It is assumed herein that the turbulence is locally isotropic, so that the relative contributions of the various quadrupole types are specified in some consistent fashion.

In the absence of convection and refraction effects, the mean-square sound pressure in the far field due to a finite volume of turbulence is given by, e.g., Lighthill⁽⁴⁾ as

$$\overline{p^2}(R, \theta, \phi) = \frac{R_1 R_2 R_3 R_4}{16\pi^2 c_a^2 R^6} \int_{\vec{y}} \int_{\vec{z}} \frac{d\vec{y} d\vec{z}}{|\vec{y} - \vec{z}|^4} (\overline{(\rho v_i v_j)})(\overline{(\rho v_k v_l)}) d\vec{y} d\vec{z} \quad (287)$$

where \vec{y} denotes the position vector within the turbulence, \vec{z} denotes the separation vector for the cross-correlation between $(\rho v_i v_j)$ at $\vec{y} - 1/2 \vec{z}$, $(\rho v_k v_l)$ at $\vec{y} + 1/2 \vec{z}$, and τ denotes the time delay of the cross-correlation. A sketch of the coordinate system nomenclature is shown in Figure 4-11. The terms $(\rho v_i v_j)$ and $(\rho v_k v_l)$ are the fluctuating momentum stresses due by the turbulent motion relative to the moving fluid. Ribner⁽³⁰⁾ states that, by assuming that the sound field is axisymmetric and that the turbulence is locally isotropic, only a few of the 81 possible combinations of indices (i, j, k, l) in equation (287) are significant and the source strength is characterized by the term

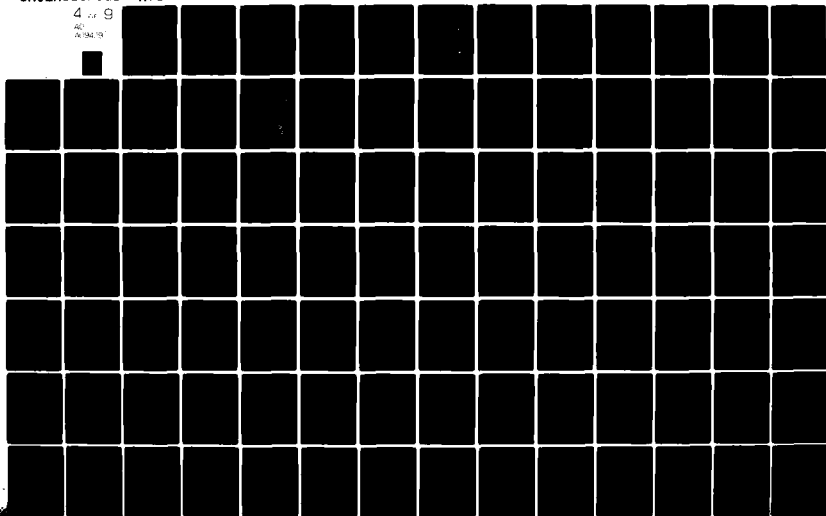
AD-A094 291

GENERAL ELECTRIC CO CINCINNATI OH AIRCRAFT ENGINE GROUP F/G 20/1
HIGH VELOCITY JET NOISE SOURCE LOCATION AND REDUCTION. TASK 2. --ETC(U)
MAY 78 T F Balsa, P R GLIEBE, R A KANTOLA DOT-05-30034
R78AE6323 FAA-RD-76-79-2 NL

UNCLASSIFIED

4 of 9

ALL INFORMATION CONTAINED HEREIN IS UNCLASSIFIED



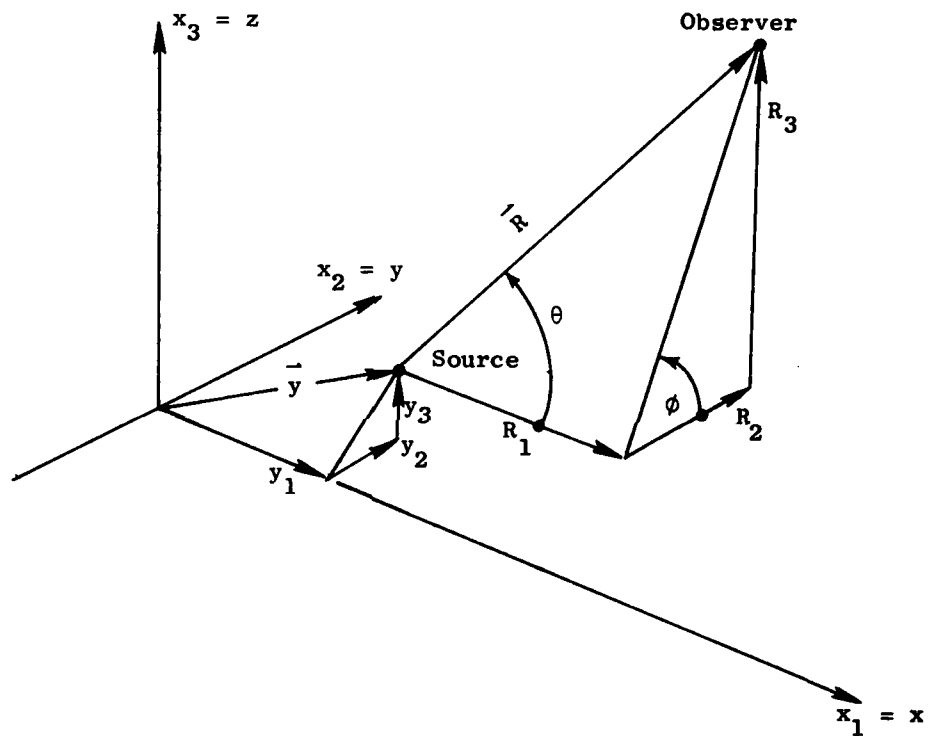


Figure 4-110. Quadrupole - Source/Observer Coordinate System Nomenclature.

$$I_{ijkl} = \int_{\bar{\xi}} \frac{\partial^4}{\partial \tau^4} (\rho v_i v_j) (\rho v_k v_l) d\bar{\xi} \quad (288)$$

It is assumed that the turbulence is quasi-incompressible, and the source strength can then be expressed in terms of the fourth-order velocity correlation tensor $S_{ijkl} = \overline{(v_i v_j v_k v_l)}$ as follows:

$$I_{ijkl} = \rho^2 \int_{\bar{\xi}} \frac{\partial^4}{\partial \tau^4} S_{ijkl} d\bar{\xi} \quad (289)$$

Ribner⁽³⁹⁾ assumes the tensor S_{ijkl} to be expressible in terms of linear combinations of second-order correlations [see e.g., Lin⁽⁸⁵⁾ Pg. 43] as follows:

$$S_{ijkl} = S_{ik} S_{jl} + S_{il} S_{jk} + S_{ij} S_{kl} \quad (290)$$

where $S_{ij} = \overline{v_i v_j}$, etc. The isotropic turbulence model of Batchelor⁽⁸⁶⁾ is then used to evaluate the various source terms I_{ijkl} . The second-order correlations are assumed to be separable functions of $\bar{\xi}$ and τ , i.e.,

$$S_{ij}(\bar{\xi}, \tau) = R_{ij}(\bar{\xi}) g(\tau) \quad (291)$$

$$\text{where } R_{ij}(\bar{\xi}) = (u')^2 \left[\left(f + \frac{1}{2} \bar{\xi} f' \right) \delta_{ij} - \frac{1}{2} f' \xi_i \xi_j / \bar{\xi} \right] \quad (292)$$

$$\text{and } f = f(\xi) = \exp(-\pi \xi^2 / L_x^2), \quad \xi^2 = \xi_1^2 + \xi_2^2 + \xi_3^2 \quad (293)$$

and L_x is the longitudinal macroscale of the turbulence. The function $g(\tau)$ is the time-delay factor. By direct substitution of expressions (290) through (293) into (289), Ribner⁽³⁹⁾ derives the following expressions for the various source strength components:

$$I_{1111} = \frac{\sqrt{2}}{4} L_x^3 \rho^2 (u')^4 [g^2(\tau)]^{iv} \quad (294)$$

444

$$I_{2222} = I_{3333} = I_{1111} \quad (a) \quad (295a)$$

$$I_{1122} = I_{1133} = I_{2233} = \frac{1}{8} I_{1111} \quad (b) \quad (295b)$$

$$I_{1212} = I_{1313} = I_{2323} = \frac{7}{16} I_{1111} \quad (c) \quad (295c)$$

The remaining components are either redundant (e.g., $I_{1212} = I_{2121}$) or do not contribute. The above expressions correspond to Ribner's "self noise" contributions, since v_i represents the fluctuating component of the total velocity vector. The so-called "shear noise" component identified by Ribner is not considered herein, for reasons discussed by Mani(37,38).

The spectrum of I_{1111} is obtained by a Fourier transformation of equation (294), which yields the following expression:

$$I_{1111}(\Omega) = \frac{1}{2\pi} \int_{-\infty}^{\infty} I_{1111}(\tau) e^{i\Omega\tau} d\tau$$

or

$$I_{1111}(\Omega) = \frac{\sqrt{2}}{8\pi} L_x^3 \rho^2(u')^4 \Omega^4 \int_{-\infty}^{\infty} g^2(\tau) e^{i\Omega\tau} d\tau \quad (296)$$

where Ω is the frequency in a reference frame moving with the turbulent eddy. Following Ribner's suggestion, the time delay factor $g(\tau)$ is assumed to have the form

$$g(\tau) = e^{-(\tau/\tau_0)^2} \quad (297)$$

Substituting equation (297) into (296) yields the following form for the source intensity spectrum, where the subscripts (1111) have been omitted for brevity:

$$I(\Omega) = \frac{\sqrt{2}}{4} L_x^3 \rho^2(u')^4 \Omega^4 H(\Omega\tau_0) \quad (298)$$

where

$$H(\Omega\tau_0) = \frac{1}{2\pi} \int_{-\infty}^{\infty} g^2(\tau/\tau_0) e^{i\Omega\tau_0(\tau/\tau_0)} d(\tau/\tau_0)$$

$$\text{or } H(\Omega\tau_0) = \frac{1}{2\pi} \sqrt{\frac{\pi}{2}} e^{-(\Omega\tau_0)^2/8} \quad (299)$$

The term τ_0 represents the characteristic time delay which determines the minimum "significant" correlation in a moving reference frame. For example, one criterion might be that τ_0 is the time delay for which the correlation falls to 1/e of its peak value, or 10% of its peak value, etc. Alternatively, it can be defined as $\tau_0 = \int_{-\infty}^{\infty} g(\tau) d\tau$. Davies, et al. (16) have made measurements of the cross correlation of $(v_1 v_1)$ in a subsonic round jet, in the initial mixing zones. Their results show that τ_0 (based on 1/e criterion) was proportional to the inverse of the mean shear, i.e.,

$$\tau_0 \sim \left(\frac{\partial U}{\partial r} \right)^{-1} \quad (300)$$

In addition, they found that L and τ_0 could be correlated with turbulence intensity u' by the relation

$$u' \tau_0 \sim L_x \quad (301)$$

combining (301) and (298), the final expression for source intensity spectrum is obtained:

$$I(\Omega) \sim \rho^2 (u')^7 (\Omega \tau_0)^4 \exp \left[-\frac{1}{8} (\Omega \tau_0)^2 \right] \quad (302)$$

The turbulence spectrum is essentially represented by equation (299), while the noise spectrum is represented by (302). The noise spectrum is essentially the turbulence spectrum multiplied by frequency to the fourth power.

The constant of proportionality in (302) must be determined empirically. Equation (302) represents the source intensity spectrum of an x-x quadrupole, with indices (1111). From equation (295b), the cross correlations between quadrupoles of different types are weak; for example, the correlation between a(11) or (x-x) quadrupole and a(33) or (z-z) quadrupole to give the contribution I_{1133} is only 1/8 of that for I_{1111} . It can therefore be assumed that the quadrupoles of a given type do not effectively correlate with quadrupoles of other types, correlating significantly only with themselves. Similarly, the factor 7/16 which relates (x-y), (x-z), and (y-z) quadrupole contributions to the (x-x) quadrupole contribution in equations (295c) can be replaced by 1/2 without significant loss of generality or accuracy.

4.7.5 Acoustic Prediction

In Section 4.3, expressions were developed for the far-field noise of convected quadrupoles imbedded in a parallel shear flow, utilizing high-frequency asymptotic solutions to Lilley's⁽¹⁵⁾ equation. These expressions, for a source of unit volume and unit strength, when applied to a collection of sources distributed throughout a parallel shear flow model of the jet plume, yield the following equation for the far-field noise spectrum:

$$\bar{p}^2(R, \theta, \Omega) = \int_y \alpha (a_{xx} + 4a_{xy} + 2a_{yy} + 2a_{yz}) d\vec{y} \quad (303)$$

where the integration is over the entire jet plume. The factors a_{xx} , a_{xy} , a_{yy} , and a_{yz} are the directivity factors for each of the contributing quadrupole types contained in each turbulent eddy volume element. The factor α is given by*

$$\alpha = \frac{I(\Omega)}{16\pi^2 R^2 C_a^4} \left(\frac{\rho_a}{\rho_o} \right)^2 \left(\frac{C_a}{C_o} \right)^2 (1 - M_o \cos \theta)^{-2} (1 - M_c \cos \theta)^{-1} \quad (304)$$

where $I(\Omega)$ is given by equation (302), and subscript "o" refers to the volume-element or eddy-center location conditions. The parameters M_o and M_c are defined as

$$M_o = U_o/C_a \quad M_c = U_c/C_a \quad (305)$$

where U_c is the effective convection velocity of the eddy.

The directivity factors a_{xx} , a_{xy} , a_{yy} and a_{yz} have different forms, depending on the location of the source and the velocity and temperature profiles in the vicinity of the source. As discussed in Section 4.3, these factors depend explicitly upon a shielding function g^2 , which has the form:

$$g^2(r) = \frac{(1 - M \cos \theta)^2 (C_a/C)^2 - \cos^2 \theta}{(1 - M_c \cos \theta)^2} \quad (306)$$

where $C = C(r)$ and $M = M(r) = U(r)/C_a$. Given a velocity $U(r)$ and temperature profile $C(r) \sim \sqrt{T(r)}$, the shielding function profile can be computed per equation (306). Depending on the observer angle θ and the profile shapes, the profile of $g^2(r)$ may have both positive and negative "zones", or may be positive for all values of r . If a negative region exists, the possibility of fluid shielding of the sound source exists, depending on the location of the sound source relative to the negative or shielding zone. The location $r = r_o$ where $g^2(r)$ crosses zero is termed a turning point. In practice, more than one turning point can occur, although more than two turning points is very rare.

A maximum of two turning points is considered herein. This allows six possible situations regarding the source location relative to a shielding zone. These are illustrated qualitatively in Figure 4-111. This figure shows $g^2(r)$ plotted versus radial distance in the jet plume for six cases. In case (a), $g^2(r)$ is positive for all values of r , and shielding of the source does not occur regardless of where it is located radially in the jet. In case (b), the source is located outboard of the region where $g^2(r)$ is negative, and still no shielding occurs. In case (c), however, the source is located inboard of the turning point, $r_o < r_{o1}$, and lies inside the shielding zone. The source will therefore be shielded to some extent.

*Note that α has one less doppler factor than that given by Section 4.3 to account for the reduced number of eddies which contribute at a given time for a fixed source region, as discussed by Ffowcs-Williams (6).

(241)

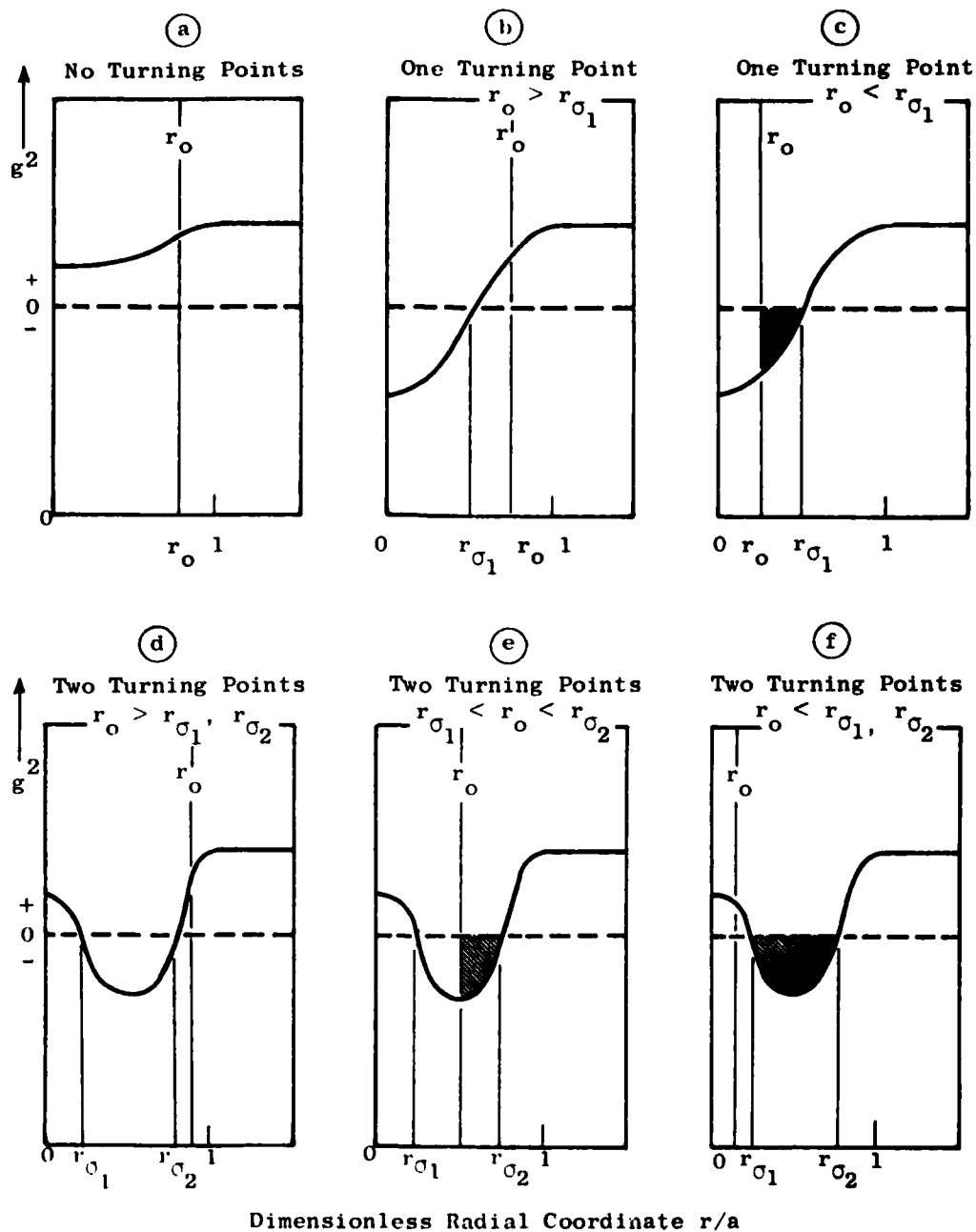


Figure 4-111. Possible Solution Types for a Maximum of Two Turning Points. Shaded Areas Denote Shielding of Source.

Cases (d,e,f) of Figure 4-111, show that there are two turning points, r_{01} and $r_{02} > r_{01}$. In case (d), the source lies outside of both turning points and, therefore, sees no shielding. In case (e), the source lies between the two turning points and thus is shielded by the fluid layer between $r = r_0$ and $r = r_{02}$. Finally, in case (f), the source lies inboard of both turning points and, therefore, is shielded by the entire fluid layer $r_{01} < r < r_{02}$.

The acoustic radiation solutions for all of the six cases illustrated in Figure 4-111 are worked out in detail in Section 4.3, and yield different forms for the directivity factors a_{xx} , a_{xy} , a_{yy} , and a_{yz} for each case. These directivity factors have the following forms:

$$a_{xx} = \frac{\cos^4 \theta}{(1-M_c \cos \theta)^4} \beta_{xx} \quad (307a)$$

$$a_{xy} = \frac{g_o^2 \cos^2 \theta}{2(1-M_c \cos \theta)^2} \beta_{xy} \quad (307b)$$

$$a_{yy} = \frac{3}{8} g_o^4 \beta_{yy} \quad (307c)$$

$$a_{yz} = \frac{1}{8} g_o^4 \beta_{yz} \quad (307d)$$

where g_o^2 is the value of $g^2(r)$ at the source radius $r = r_0$. The shielding coefficients β_{xx} , β_{xy} , β_{yy} , and β_{yz} depend upon the case encountered in Figure 4-112. If the parameters β_{01} , β_{02} , and β_{12} are defined as

$$\beta_{01} = \exp \left\{ -2k \int_{r_0}^{r_{01}} |g^2(r)|^{1/2} dr \right\} \quad (308a)$$

$$\beta_{02} = \exp \left\{ -2k \int_{r_0}^{r_{02}} |g^2(r)|^{1/2} dr \right\} \quad (308b)$$

$$\beta_{12} = \exp \left\{ -2k \int_{r_{01}}^{r_{02}} |g^2(r)|^{1/2} dr \right\} \quad (308c)$$

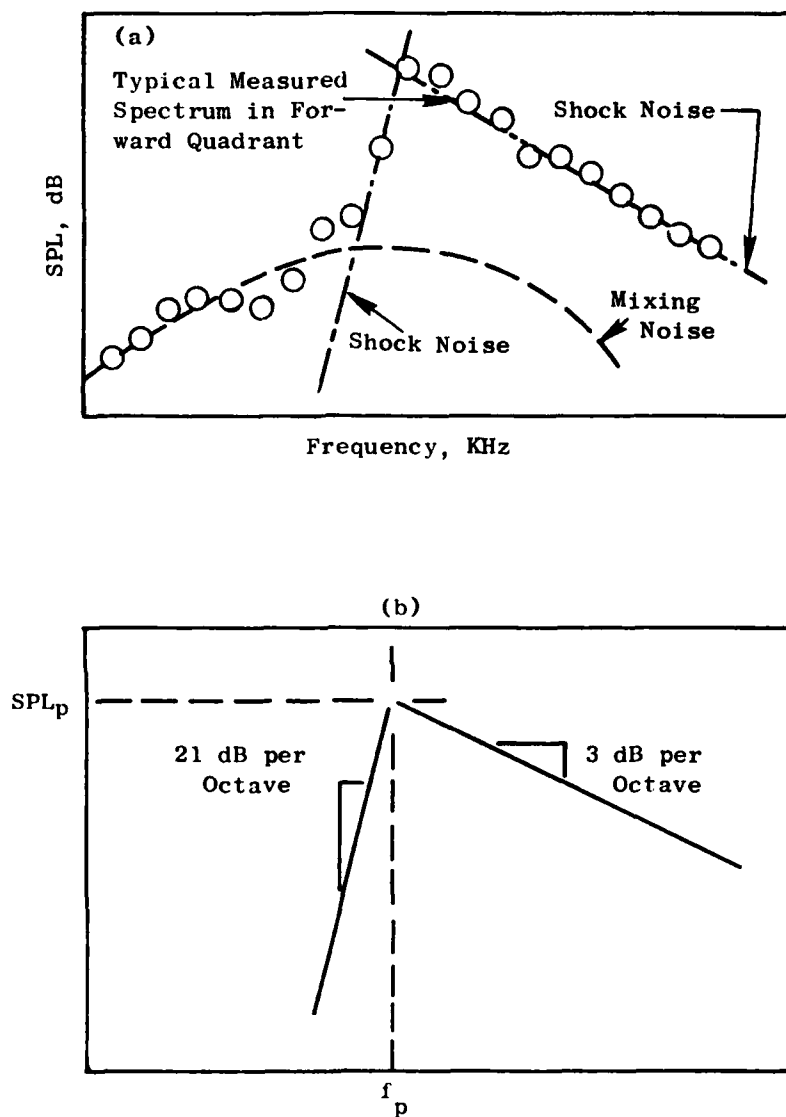


Figure 4-112. Empirical Model of Shock Cell Noise Component of Spectrum: (a) Shock Cell Component Approximated by Straight Lines; (b) Model Representation of Shock Cell Spectrum and Correlation Parameters.

where $k = \Omega/C_a$, the shielding coefficients are then determined from the following table:

Table 4.7.1. Shielding Coefficients β_{ij} .

Case	β_{xx}	β_{xy}	β_{yy}	β_{yz}
a	1	1	1	1
b	1	1	1	1
c	β_{01}	0	0	0
d	1	1	1	1
e	β_{02}	0	0	0
f	β_{12}	β_{12}	β_{12}	β_{12}

Note that a value for β_{xx} , etc., of unity [as in cases (a), (b), and (d)] indicates no fluid shielding. When the source is imbedded within the shielding zone, as in cases (c) and (e), only the x-x quadrupole contributes, for reasons explained in Section 4.3.

4.7.6 Shock-Cell Noise Prediction

As was discussed in Section 4.7.2, the shock-cell broadband noise prediction is based on a modification of the theory of Harper-Bourne and Fisher⁽⁶⁹⁾. A thorough discussion of this theory and its application to noncircular nozzles can be found in Section 4.6.

Although the analysis of Section 4.6 demonstrates that noncircular nozzle shock-cell noise exhibits the same scaling of noise level with operating conditions as that for a conical nozzle, the influence of nozzle shape on noise level and spectrum shape is not quantified to the extent that a verified prediction method can be established. A method of predicting the shock-cell structure (number of cells, spacing, etc.) is required for development of a general shock-cell noise prediction procedure. An interim shock-cell noise prediction method has therefore been adopted for incorporation into the unified aeroacoustic prediction model, with the expectation of replacement by a more general method at some future date.

The interim method is essentially that of Deneuille⁽⁸⁷⁾, with some modifications to simplify the calculation and incorporate some of the ideas developed in Section 4.6 for noncircular nozzles. The modifications for

simplifying the calculation procedure are discussed in detail by Gliebe(88). The method consists of modeling the shock-cell noise component of the spectrum by two straight lines, as illustrated in Figure 4-112. The primary variables required are peak sound pressure level, SPL_p , and the frequency, f_p , at which this occurs.

Given a nozzle operating at pressure ratio, PR , jet velocity U_j , having total flow area A_j , equivalent diameter $D_{eq} = \sqrt{4A_j/\pi}$, and hydraulic diameter $D_h = 4A_j/P_w$ (where P_w is the nozzle boundary wetted perimeter), the parameters SPL_p and f_p can be computed as a function of observer angle θ_I . The computation proceeds as follows:

- (1) compute shock strength parameter β from

$$\beta = \sqrt{M_j^2 - 1} \quad (309)$$

$$\text{where } M_j^2 = \frac{2}{\gamma - 1} \left[\frac{\gamma - 1}{PR^\gamma - 1} \right] \quad (310)$$

- (2) compute average shock-cell spacing L_{avg} from

$$L_{avg} = 1.1 \beta D_{eq} \quad (311)$$

- (3) compute peak noise frequency from

$$f_p = \frac{U_c}{L_{avg}} (1 + M_c \cos \theta_I)^{-1} \quad (312)$$

$$\text{where } U_c = 0.7 U_j \quad \text{and} \quad M_c = U_c / C_a.$$

- (4) compute peak SPL from

$$\begin{aligned} SPL_p(\theta_I) = & 152.6 + 40 \log_{10}(\beta) + 10 \log_{10}(A_j/R^2) \\ & + 10 \log_{10}(D_h/D_{eq}) - 40 \log_{10}(1 - M_a \cos \theta_I) \\ & + 10 \log_{10}(N/8) \end{aligned} \quad (313)$$

where $M_a = U_a/C_a$, the flight Mach number, and N is the number of shock cells. Use $N = 8$ for conical nozzles. Experimental measurements of cell number for other nozzles are required to provide input values of N . As a guide, use $N = 8$ unless available experimental data indicates otherwise. It is suspected that, for multicute/spoke nozzles, $N = 4$ is a more realistic value.

The spectrum shape is then calculated from the assumed two straight-line model shown in Figure 4-112. The equations are as follows:

$$\left. \begin{aligned} \text{SPL}(f, \theta_I) &= \text{SPL}_p(\theta_I) - 10 \log_{10}(f/f_p), \quad f > f_p \\ \text{SPL}(f, \theta_I) &= \text{SPL}_p(\theta_I) + 70 \log_{10}(f/f_p), \quad f < f_p \end{aligned} \right\} \quad (314)$$

Equations (309) through (314) completely describe the shock-cell noise prediction method for obtaining 1/3-octave spectra at any observer angle θ_I .

4.7.7 Aeroacoustic Model Integration

The preceding sections have outlined the basic structure of the prediction method and have presented the component building blocks in detail. This section describes how these building blocks are tied together. Additionally, some practical considerations are presented which resulted from experience in exercising the model, and which were found helpful in producing reasonably accurate predictions while maximizing computational efficiency.

The mixing noise spectrum is computed from equation (303), with the integration over the jet plume $\int(\cdot) d\vec{y}$ replaced (or approximated) by a summation over all eddy-volume elements. Since equation (303) represents the narrowband spectrum in terms of source frequency Ω (emitted frequency in a reference frame moving with the eddy), a conversion is made to 1/3-octave based on observed center frequency f . It is assumed that the 1/3-octave band level can be approximated by the narrow band level evaluated at the center frequency, multiplied by the band width, rather than integrating the narrowband level distribution over the band width. To convert to observed frequency, the standard 1/3-octave center frequencies are used. For each eddy-volume element, at each observer angle $\theta_I = 180^\circ - \theta$, the source frequency is calculated for each 1/3-octave center frequency from the relation

$$\Omega = 2\pi f (1 - M_c \cos\theta) \quad (315)$$

Having evaluated the characteristic time delay τ_0 from equation (300), the spectrum shape of a given eddy, equation (302), determines the amount contributed by a given eddy at that 1/3-octave frequency. Theoretically, all eddies contribute some amount at all 1/3-octave frequencies, but the rather "peaky" nature of $I(\Omega)$ given by equation (302) dictates that the major contribution of an eddy will be in the vicinity of $\Omega \sim 4/\tau_0$.

Computationally, the integrand of equation (303) can be expressed explicitly in terms of observed frequency, since the source frequency always occurs in the combination $\Omega/(1 - M_c \cos\theta)$. The one exception is in the exponent of the spectrum function $I(\Omega)$, equation (302). For example, the

product αa_{xx} can be rewritten as

$$\alpha a_{xx} \sim \frac{\rho_a^2 (u')^7 (2\pi f \tau_o)^2 \beta_{xx} \cos^4 \theta}{16\pi^2 R^2 C_a^2 (1-M_o \cos \theta)^2} \left(\frac{C_a}{C_o} \right)^2 \exp \left[-\frac{(\Omega \tau_o)^2}{8} \right]$$

Similar expressions can be derived for αa_{xy} , etc.

The eddy convection factor $(1 - M_c \cos \theta)$ has a singularity at $M_c \cos \theta = 1$. To circumvent this computational difficulty, it is replaced by a modified convection factor as suggested by Ffowcs-Williams⁽⁶⁾ and Ribner⁽³⁹⁾ as follows:

$$C = (1 - M_c \cos \theta) \rightarrow \sqrt{(1 - M_c \cos \theta)^2 + (\alpha_t u' / C_a)^2} \quad (316)$$

where, as Ffowcs-Williams and Ribner have shown, the term $(\alpha_t u' / C_a)$ accounts for the finite life-time of the eddy as it is convected downstream. The constant α_t was determined from comparison of prediction with experiments to be approximately 0.5, independent of source location, jet operating conditions, and nozzle geometry. The additional assumption was made that the flow convection factor $(1 - M_o \cos \theta)$ can be replaced by the modified eddy convection factor C given by equation (316).

It was also found that the eddy convection Mach number must be a function of the local flow Mach number of the eddy-volume being considered. Several expressions for M_c were tried, and the one which was found to give the best results over a wide range of nozzle operating conditions and geometries was as follows:

$$M_c = \frac{1}{2} (M_o + 0.65 M_j) \quad (317)$$

where $M_j = U_j / C_a$, the nozzle exit acoustic Mach number. Equation (317) represents a simple average of the classical assumption $M_c = 0.65 M_j$ and the local Mach number $M_o = M(r_o)$. For suppressor nozzles, equation (317) works best if M_j is replaced by the postmerged potential core Mach number $M_m = U_m / C_a$. This can be evaluated from the results of the flow field calculation described in Section 4.7.3.

The formulation for u' , the turbulence intensity, as given by equation (285), yields reasonable agreement with flow field measurements, at least for subsonic round jets. The noise levels at low frequencies, however, are underpredicted when this form for u' is employed. Diagnostic calculations reveal that this underprediction, which occurs even for subsonic jets, is associated with the eddy volume elements far downstream in the jet, in the fully-developed similarity region. In particular, the contribution due to τ_x along the center-line of the jet is underestimated. This has subsequently been

attributed to the assumption of isotropic turbulence which was adopted, and to the neglect of upstream history (turbulence convected from upstream stations) in the aerodynamic model.

To circumvent these difficulties, an amplification factor is introduced to enhance the contribution of τ_x to the calculation of u' used in the noise computation. Subsequent numerical experiments with multielement suppressor nozzles have revealed a similar problem with the contribution of τ_ϕ to u' . Equation (285) was therefore modified to calculate an equivalent u' representative of the noise-producing turbulence level existing in the flow, as follows:

$$(u')_{eq}^2 = \sqrt{(\tau_r/\rho)^2 + \delta_t (\tau_\phi/\rho)^2 + \beta_t (10\tau_x/\rho)^2} \quad (318)$$

where δ_t and β_t are empirically-determined constants. From numerical experiments, it was found that $\delta_t = 2.0$ and $\beta_t = 4.0$ gave the best results over the range of jet velocities, jet temperatures, and nozzle geometries examined. Two additional modifications are made for nonaxisymmetric nozzles (multilobe chute, tube, etc.). First, the acoustic theory, derived in Section 4.3 and summarized in Section 4.7.5, applies only to axisymmetric jets. The necessary assumption is made that a representative average radial profile at each axial station can be derived which, when inserted in the acoustic calculation, will adequately model the acoustic characteristics of the asymmetric jet. The mass-averaged values of U and ρ are calculated from the azimuthal average of the quantities ρU^2 and ρUH , utilizing equations (281) through (284). The resulting distributions of $U(x,r)$ and $\rho(x,r)$ are then employed in the acoustic calculation described in Section 4.7.5.

The second modification required for nonaxisymmetric jets is the revision of equation (300) for computing the characteristic time delay of each volume element. For a multichute or lobe nozzle, for example, there are volume elements close to the nozzle exit plane which have negligible radial gradients $\partial U/\partial r$ but large azimuthal gradients $\partial U/\partial \phi$. It is therefore assumed that τ_0 is a function of both $\partial U/\partial r$ and $\partial U/\partial \phi$. From Reichardt's hypothesis (see Section 4.5), the transverse shear stresses are related to $\partial U/\partial r$ and $\partial U/\partial \phi$ by the approximate formulae

$$\frac{\tau_r}{\rho} \approx \lambda \frac{\partial U^2}{\partial r} \quad \text{and} \quad \frac{\tau_\phi}{\rho} \approx \frac{\lambda}{r} \frac{\partial U^2}{\partial \phi}$$

where $\lambda = C_m^2 x/2$. Thus the transverse derivatives of U can be expressed in terms of τ_r and τ_ϕ as follows:

$$\frac{\partial U}{\partial r} \approx \frac{(\tau_r/\rho)}{UC_m^2 x} \quad \text{and} \quad \frac{1}{r} \frac{\partial U}{\partial \phi} \approx \frac{(\tau_\phi/\rho)}{UC_m^2 x}$$

A new transverse derivative $\partial U / \partial n$ is therefore defined in terms of the above r and ϕ derivatives as follows,

$$\frac{\partial U}{\partial n} = \frac{1}{UC_m^2 x} \sqrt{\left(\frac{\tau_r}{\rho}\right)^2 + \mu_t \left(\frac{\tau_\phi}{\rho}\right)^2} \quad (319)$$

such that $\tau_o \sim \left(\frac{\partial U}{\partial n}\right)^{-1} \quad (320)$

The parameter μ_t is an empirical constant which must be evaluated from comparison with experiments. Equations (319) and (320) replace equation (300), and reduce to equation (300) when the jet flow is axisymmetric, i.e., $\partial U / \partial \phi = 0$. It is found from numerical experiments that $\mu_t = 2.0$ gives best agreement with far-field acoustic measurements.

In the case of heated jets at low nozzle exit velocities ($V_j < 1400$ fps), additional dipole and simple source terms associated with the velocity fluctuations imbedded in transverse gradients of the mean flow density become important. This aspect of heated jet noise is discussed by Mani(38). These low velocity noise source contributions are not incorporated into the final aeroacoustic prediction model. This requires reformulation of Mani's(38) results in the framework of the high-frequency shielding theory described in Section 4.3. Such additional development is necessary to extend the model to low-velocity heated jet noise applications.

Section 4.4 shows that for prediction of jet noise in flight the mean square sound pressure level should be multiplied by the dynamic amplification factor $(1 + M_a \cos \theta)^{-1}$ (where $M_a = U_a / c_a$). In addition, the convection and flow Mach numbers should be replaced by $(M_c - M_a)$ and $(M_o - M_a)$, respectively (where M_c and M_o are evaluated in a reference frame fixed to the nozzle).

Finally, in all predictions of 1/3-octave spectra, the atmospheric attenuation corrections given by Bass, et al.(84) are applied, using standard-day corrections (70% relative humidity and 59° F dry-bulb temperature) evaluated at the center frequency.

4.7.8 Data-Theory Comparisons

Extensive data/theory comparisons have been carried out for a wide variety of nozzle configurations, using the aeroacoustic model described above. Comparisons are made between predicted and measured far-field acoustic spectra over a range of velocity and temperature conditions. A summary of the various cases examined is given in Table 4.7.2. Prior to carrying out these data - theory comparisons, extensive calibrations of the empirical constants contained in the model were carried out utilizing cold round jet experimental results (Olsen, et al.(18) and Tanna, et al.(89)).

Table 4.7.2. Data - Theory Comparison Case Summary.

Case	Fig.	Nozzle Type	D _{eq}	AR	PR	T _{Tj}	V _j	VR	TR	R
1	4-113	Conical	4.64	---	2.06	1739	1211	---	---	40
2	4-113		4.64	---	1.98	1203	1602	---	---	40
3	4-113		4.64	---	1.95	704	1985	---	---	40
4	4-114		4.64	---	3.67	1504	2380	---	---	40
5	4-115	0.79 R/R Plug	3.74	---	1.73	820	1200	---	---	40
6	4-116		3.74	---	2.45	1190	1800	---	---	40
7	4-117		3.74	---	3.29	1557	2340	---	---	40
8	4-118	Coplanar Coaxial	4.64	2.00	1.80	549	1009	0	0	40
9	4-119	(Conv. Bypass)	4.64	2.00	1.80	551	1012	0.19	0.982	40
10	4-120		4.64	2.00	1.80	549	1012	0.402	0.991	40
11	4-121		4.64	2.00	1.80	547	1009	0.597	0.996	40
12	4-122		4.64	2.00	1.80	546	1006	0.799	0.998	40
13	4-123		4.64	2.00	1.80	550	1007	1.255	0.998	40
14	4-124		4.64	2.00	1.80	1292	999	0.513	0.436	40
15	4-125	Coplanar Coaxial	2.94	0.40	2.45	1178	1792	1.50	1.189	40
16	4-126	(Inverted Flow)	2.94	0.40	3.26	1607	2366	1.99	1.622	40
17	4-127	Coplanar Coaxial	3.74	0.647	2.20	998	1481	1.53	1.919	40
18	4-128	(Inverted Flow)	3.74	0.647	2.42	1196	1797	1.49	1.201	40
19	4-129		3.74	0.647	3.27	1603	2366	1.94	1.613	40
20	4-130	Coplanar Coaxial	6.58	2.00	2.07	996	1500	1.47	1.775	40
21	4-131	(Inverted Flow)	6.58	2.00	2.74	1311	1991	1.92	2.256	40
22	4-132	Dual Flow Plug	3.75	0.647	2.46	1200	1811	1.47	1.200	40
23	4-133	(Inverted Flow)	3.75	0.647	3.27	1650	2402	1.97	1.650	40
24	4-134	7-Tube	2.32		1.56	1616	1525	---	---	9
25	4-134			---	1.84	1605	1750	---	---	9
26	4-134			---	2.71	1602	2200	---	---	9
27	4-135	32-Chute (2.1)		---	2.65	1685	2246	---	---	320
28	4-136	36-Chute (1.5)	21.12	---	1.74	820	1200	---	---	2400
29	4-136			---	1.99	1618	1871	---	---	(S/L)
30	4-136			---	3.06	1766	2428	---	---	
31	4-137	36-Chute (2.0)	21.12	---	1.74	820	1200	---	---	2400
32	4-137			---	2.00	1632	1892	---	---	(S/L)
33	4-137			---	2.95	1756	2387	---	---	
34	4-138	36-Chute (2.5)	21.12	---	1.74	820	1200	---	---	2400
35	4-138			---	2.02	1619	1890	---	---	(S/L)
36	4-138			---	3.00	1757	2400	---	---	
37	4-139	8-Lobe Daisy	11.50	---	1.58	1290	1377	---	---	400
38	4-140			---	1.99	1497	1800	---	---	(S/L)
39	4-141			---	2.53	1686	2186	---	---	

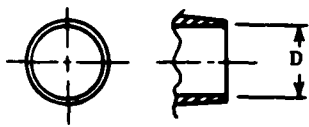
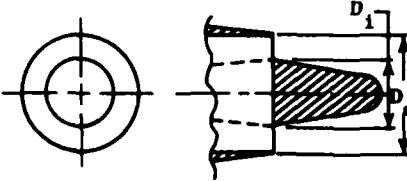
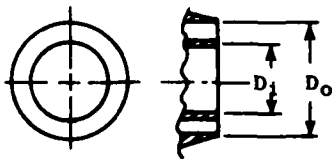
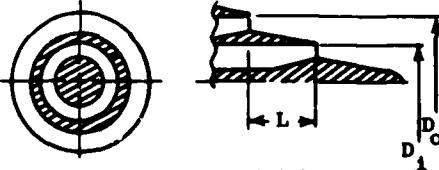
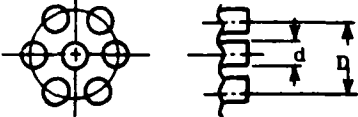
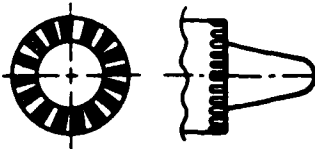
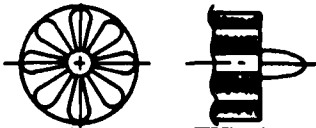
Cases 1 - 23 in Table 4.7.2 represent axisymmetric jet configurations, while cases 24 - 40 represent multielement nozzles of various shapes and element numbers. The experimental data for these comparisons were obtained from the experimental phases of tasks 2, 3, and 4 of the present program. The definitions of the parameters listed in Table 4.7.2 are given below.

- D_{eq} - Equivalent flow - area diameter $\sqrt{4A_j/\pi}$, inches; for dual-flow systems, D_{eq} is based on primary stream flow area. For conventional bypass nozzles, the inner stream is the primary stream; for inverted-flow nozzles, the outer stream is the primary stream.
- AR - Outer-to-inner stream area ratio
- PR - Primary stream stagnation-to-ambient pressure ratio
- T_{Tj} - Primary stream stagnation temperature, ° R
- V_j - Primary stream ideal jet velocity, fps
- VR - Outer-to-inner stream velocity ratio
- TR - Outer-to-inner stream stagnation temperature ratio
- R - Observer distance, ft. All cases are presented on a constant-radius arc except cases (28 - 39), which are on a sideline (S/L).

A summary of the basic geometric characteristics of each of the nozzle configurations listed in Table 4.7.2 is given in Table 4.7.3. Further details of the nozzle hardware are reported in the Task 3 results of this program. Details of the seven-tube nozzle, cases (24 - 26), are reported in Section 5.6 of this report.

At the time that many of the data - theory comparison studies were being conducted, the shock-cell noise component of the aeroacoustic model was not developed to the point that predictions for noncircular nozzles could be made with confidence. In these cases, data - theory comparisons were made with the shock-cell noise component omitted from the prediction, and forward-arc spectral comparisons were sometimes avoided because of the expected shock-cell noise contamination of the data. Those cases where shock-cell noise was included in the prediction were: case 4 (conical); case 26 (7-tube nozzle; and case 39 (8-lobe nozzle). In addition, for cases 6 and 7 (0.79 radius-ratio plug nozzle), the equivalent-area conical nozzle shock-noise OASPL is indicated on the appropriate figure. Omission of the shock-cell noise component in the prediction of multichute nozzle cases shows that forward-arc noise can still be predicted accurately, indicating that shock-cell noise is not a significant factor for these cases.

Table 4.7.3. Data/Theory Comparison Configurations.

Cases	Figures	Type
1-4	4-113 - 4-114	Conical Nozzle $D = 4.64$ in. 
5-7	4-115 - 4-117	Annular Plug Nozzle $A_j = 10.96$ in. ² $D_1/D_o = 0.79$ 
		Coplanar Coaxial
8-14	4-118 - 4-124	AR = 2.0 Conv. Bypass
15-16	4-125 - 4-126	AR = 0.4 Inverted Flow
17-19	4-127 - 4-129	AR = 0.65 Inverted Flow
20-21	4-130 - 4-131	AR = 2.0 Inverted Flow
		
22-23	4-132 - 4-133	Inverted-Flow Coannular Plug AR = 0.64 $D_o/D_i = 1.37$ $L/D_o = 0.73$ 
24-26	4-134	7-Tube $D/d = 3.0$ 
		Multi-Chute
27	4-135	32 Chutes, $A_{ann}/A_j = 2.1$
28-30	4-136	36 Chutes, $A_{ann}/A_j = 1.5$
31-33	4-137	36 Chutes, $A_{ann}/A_j = 2.0$
34-36	4-138	36 Chutes, $A_{ann}/A_j = 2.5$
		
37-39	4-139 - 4-144	8-Lobe $A_{ann}/A_j = 1.83$ $D_1/D_o = 0.23$ 

Some general observations can be made about the data - theory comparisons which apply to certain classes of nozzle geometries and/or to certain regimes of operation. Cases 1 - 3 represent operation of a conical nozzle at a fixed pressure ratio ($PR \approx 2.0$) and varying jet velocity by variation of jet temperature. The nozzle exit Mach number is approximately unity, and therefore shock-cell noise should not be present. The degree to which theory agrees with data for these cases is therefore a test of the turbulent mixing noise and flow shielding components of the prediction model. In considering all of the comparisons shown in Figure 4-113, there does not appear to be any obvious deficiency in the model.

Case 4 (shown in Figure 4-114) demonstrates the coupling of the shock-cell and mixing noise components of the model. This (conical nozzle) case contains substantial supersonic flow ($PR = 3.67$), and shock-cell noise dominates the forward-arc noise ($\theta_1 \leq 90^\circ$). The good agreement observed between data and theory indicates that the assumption that mixing noise and shock-cell noise are noninteractive and can be calculated independently is a reasonable one.

Cases 5 - 7 (Figures 4-115 through 4-117) show reasonably good agreement between data and theory, and demonstrate the ability of the model to simulate plug nozzle flow fields and associated noise characteristics. The shock-cell noise component was not included in these predictions, but the shock-cell noise OASPL levels for an equivalent - area conical nozzle are indicated on the directivity curves where applicable. These results confirm the observations made in Section 4.6 that annular plug nozzles exhibit lower shock-cell noise than a conical nozzle.

The conventional bypass coplanar coaxial jet data - theory comparisons, cases 8 - 14 (shown in Figures 4-118 through 4-124) generally show good agreement between data and theory for all cases. The model adequately duplicates the observed changes in spectral characteristics with outer-to-inner stream velocity ratio. One discrepancy noted is the tendency to predict a steeper fall-off of the high frequency side of the spectrum than is observed for $0.4 < VR < 0.6$. This tendency applies to cases 10 - 11, which are ambient temperature jets. For the heated inner stream condition with $VR = 0.5$, case 14, underprediction of the high-frequency noise does not appear to be as much of a problem.

Data - theory comparisons for the inverted-flow coplanar coaxial jets are shown in Figures 4-125 through 4-131. The area ratios vary from 0.4 to 2.0, and velocity ratios of 1.5 and 2.0 are examined for each area ratio. These cases are representative of dual-flow exhaust systems applicable to duct-burning turbofan and variable-cycle engine systems. In general, there is good agreement between data and theory with no apparent consistent failure of the model. When these predictions were first attempted, the model did not correctly predict the observed double-peak spectrum shape at angles close to the jet axis, $130^\circ \leq \theta_1 \leq 180^\circ$.

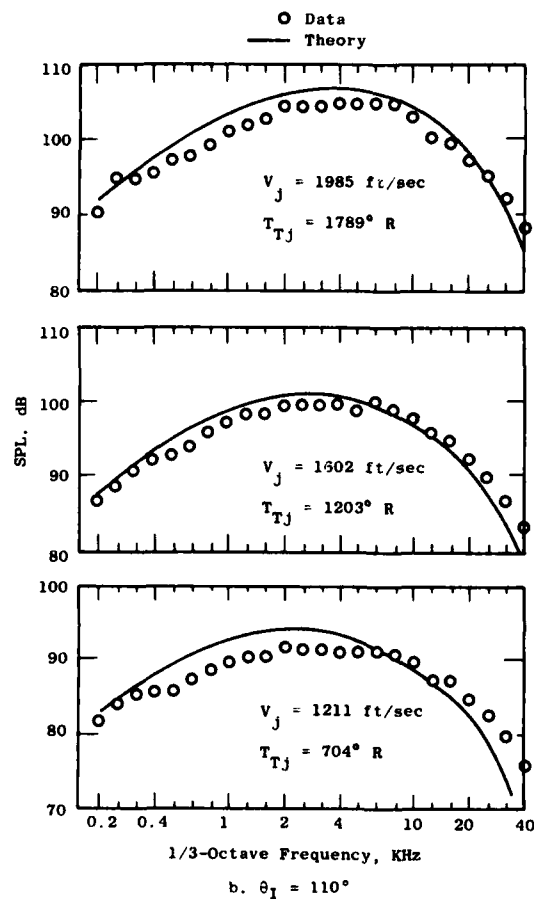
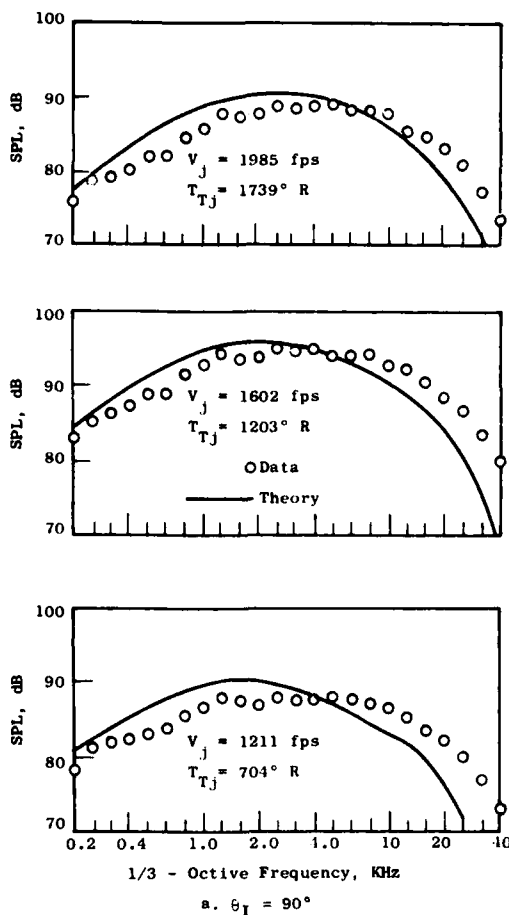


Figure 4-113. Data/Theory Comparison Cases 1, 2, and 3; 4.64 inch Diameter Conical Nozzle.

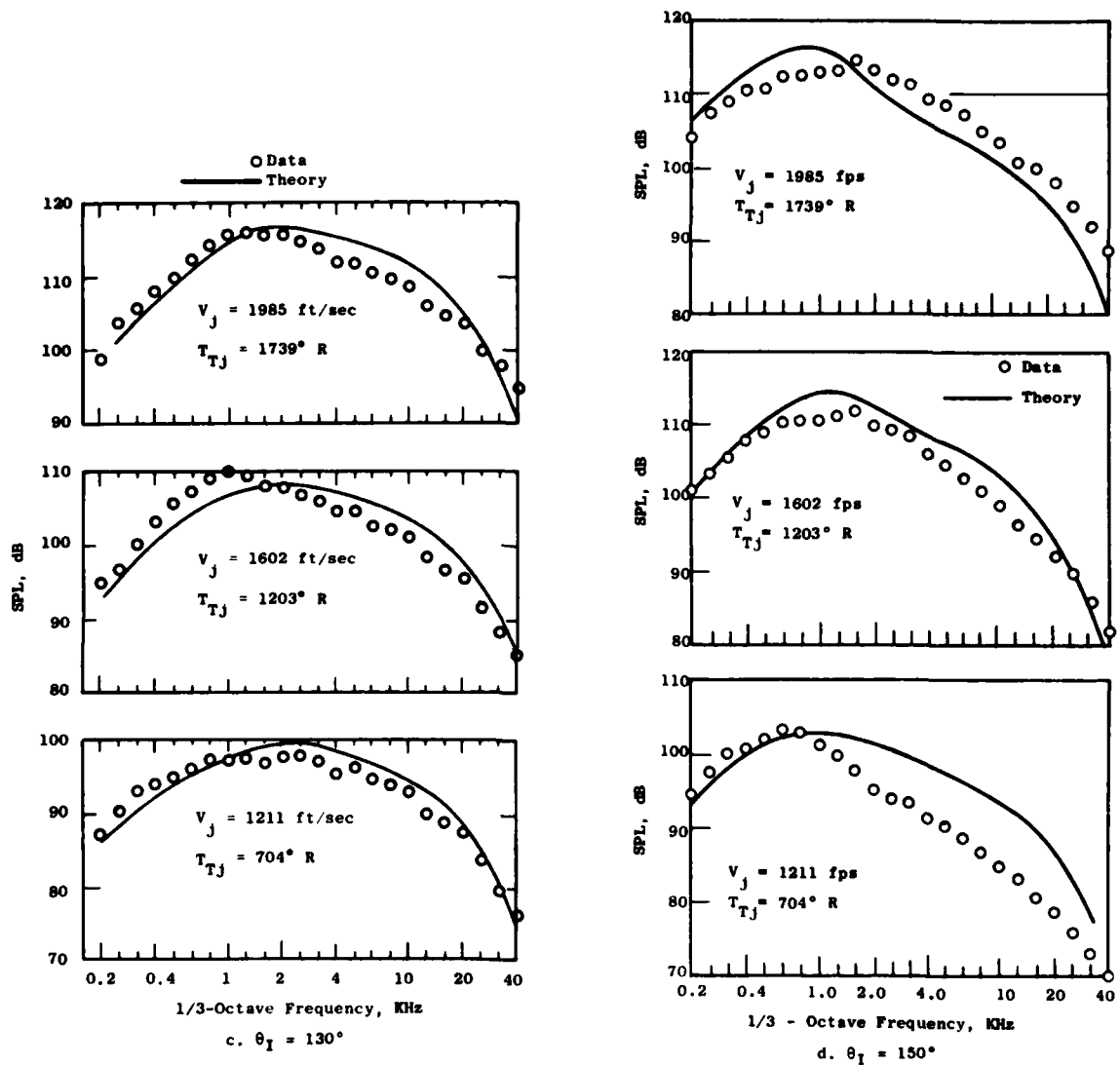


Figure 4-113. Data/Theory Comparison Cases 1, 2, and 3; 4.64 inch Diameter Conical Nozzle (Continued).

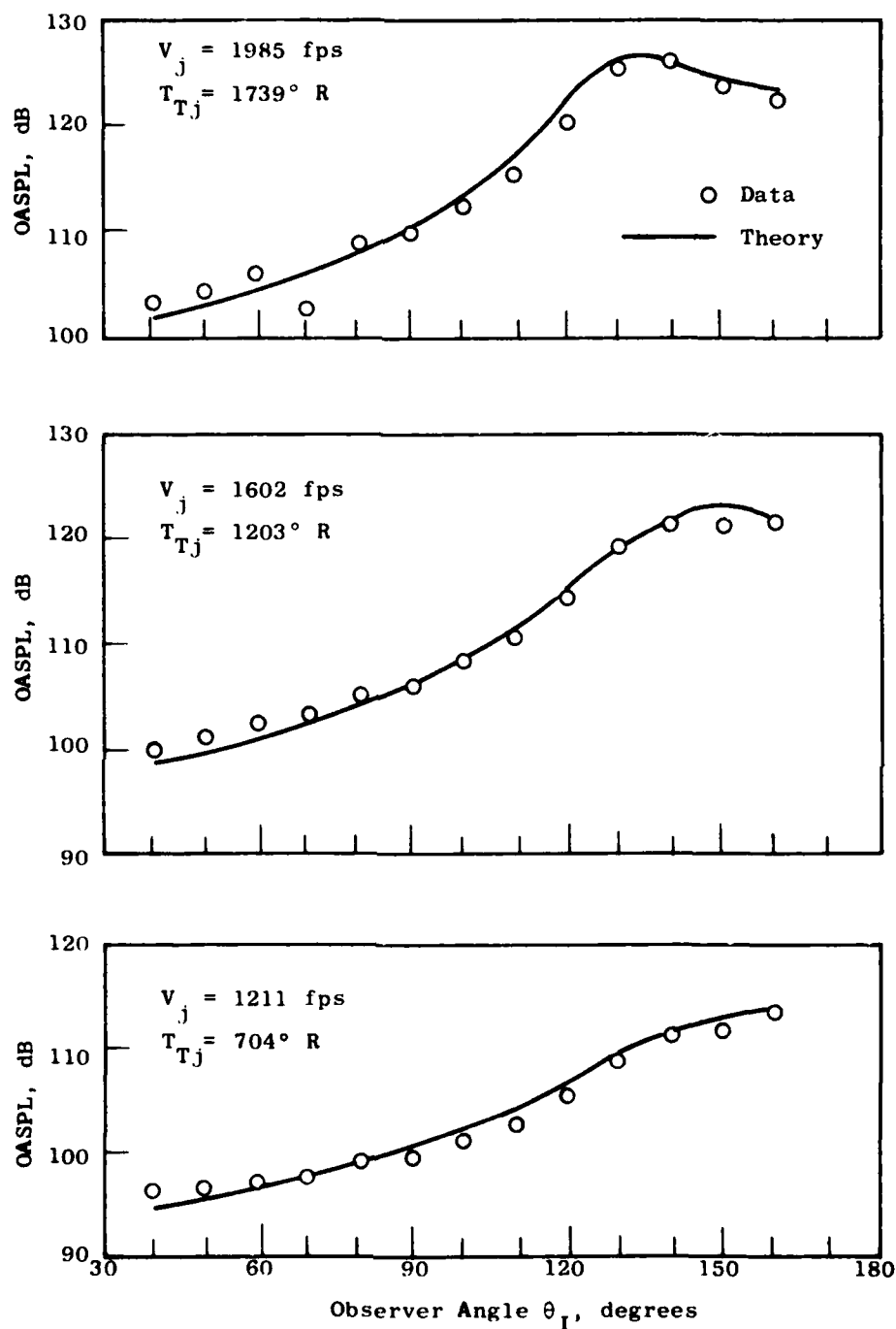


Figure 4-113. Data/Theory Comparison Cases 1, 2 and 3: 4.64 in. Diam. Conical Nozzle (Continued); (e) OASPL Directivity.

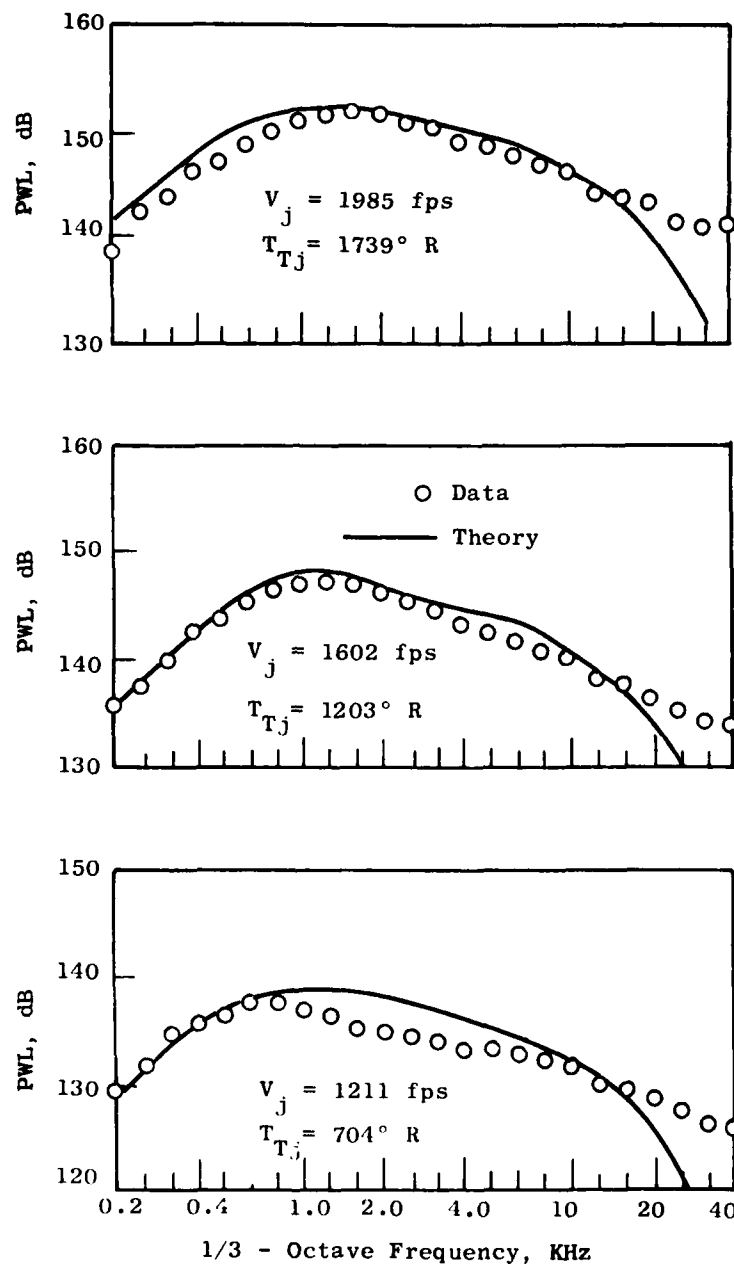


Figure 4-113. Data/Theory Comparison Cases 1, 2 and 3:
4.64 in. Diameter Conical Nozzle (Concluded);
(f) PWL Spectra.

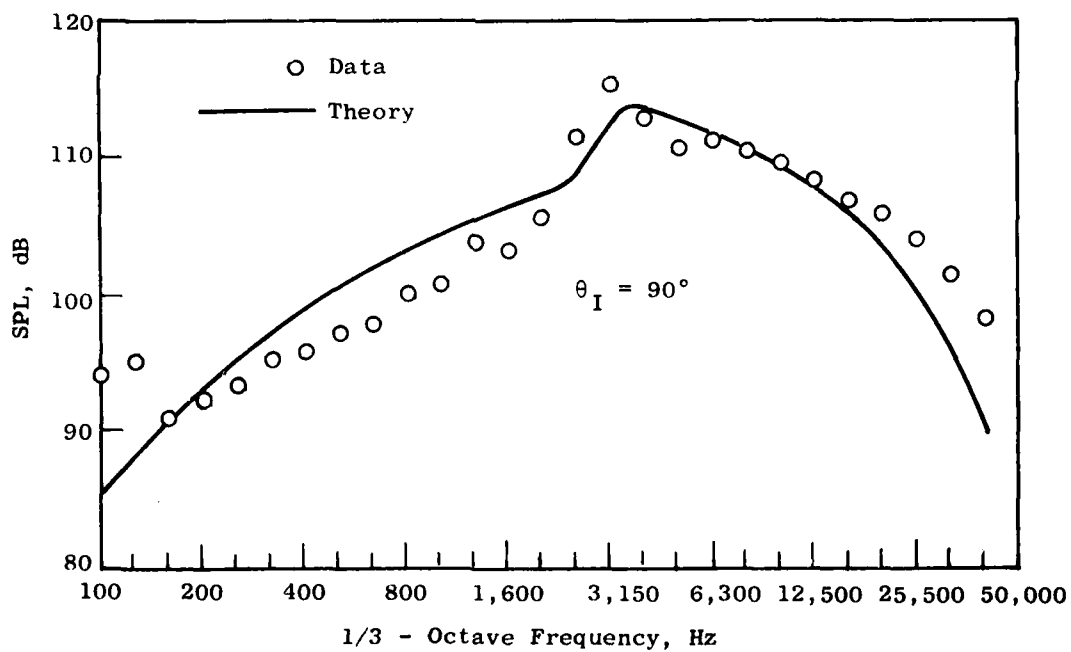
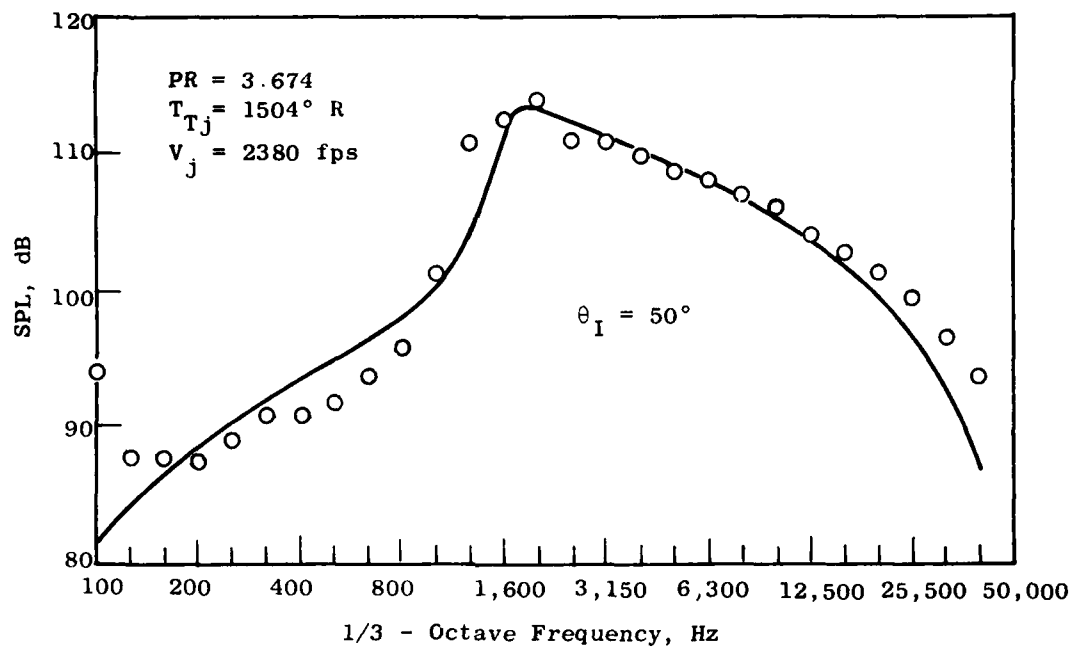


Figure 4-114. Data/Theory Comparison Case 4: 4.64 in. Conical Nozzle Operating at Supersonic Pressure Ratio; (a) SPL Spectra at $\theta_I = 50^\circ$ and 90° .

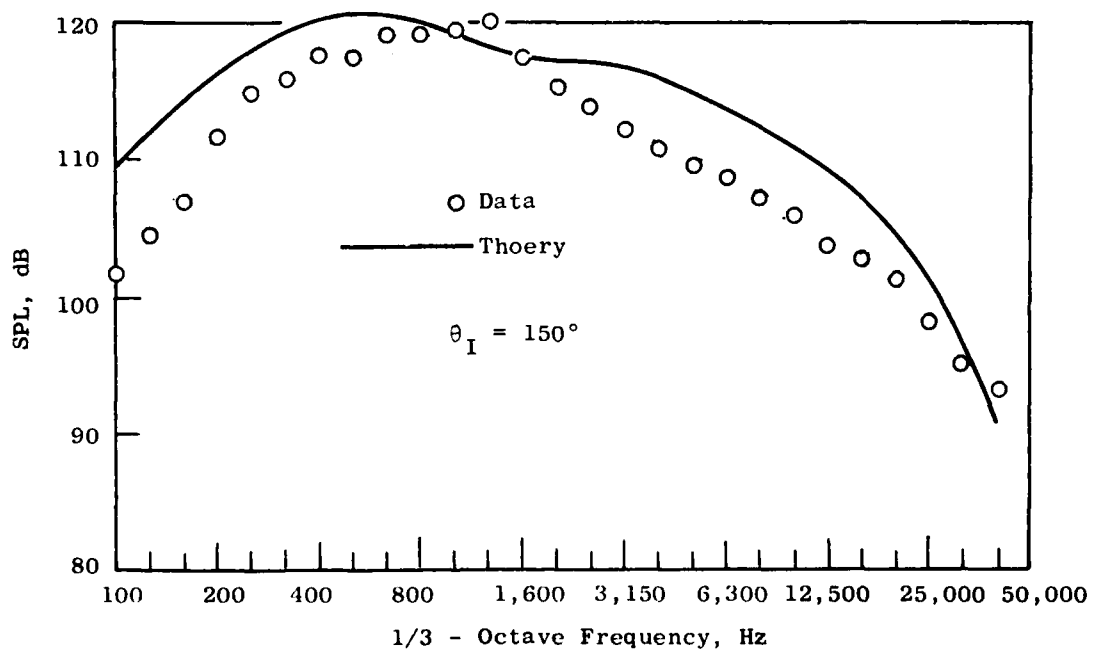
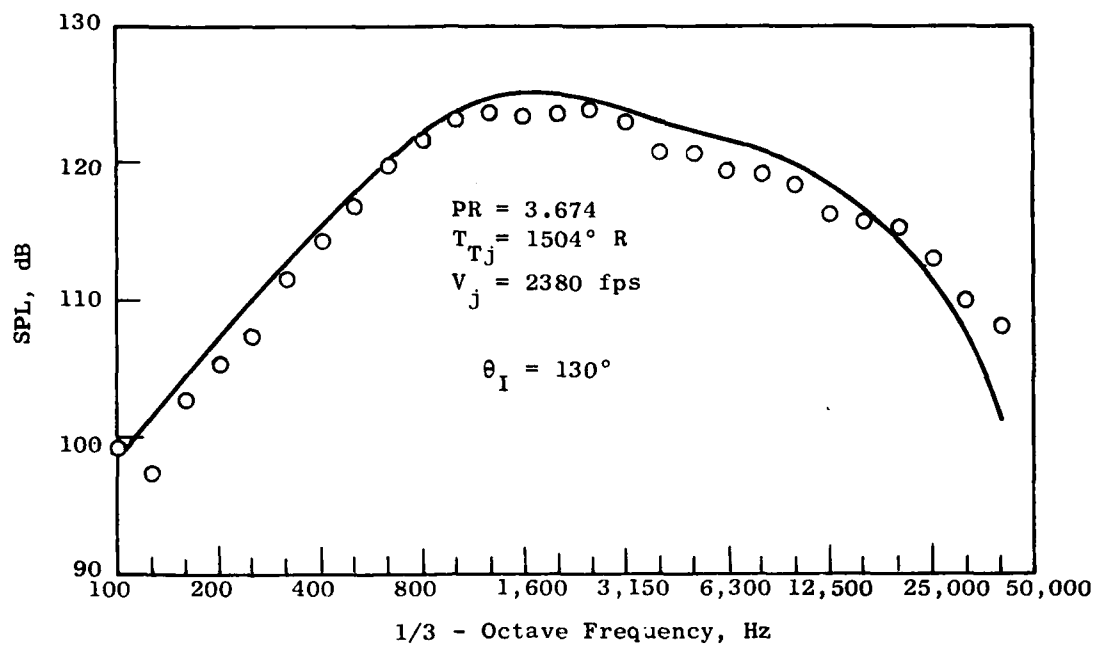


Figure 4-114. Data/Theory Comparison Case 4: 4.64 in. Diam. Conical Nozzle Operating at Supersonic Pressure Ratio (Continued); (b) SPL Spectra at $\theta_I = 130^\circ$ and 150° .

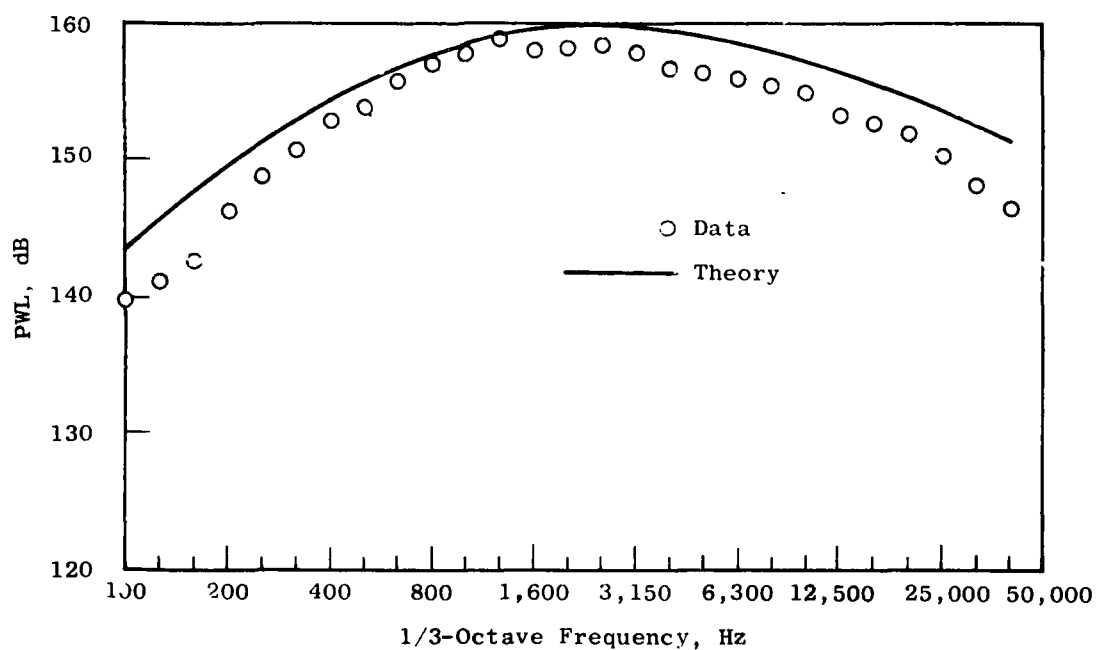
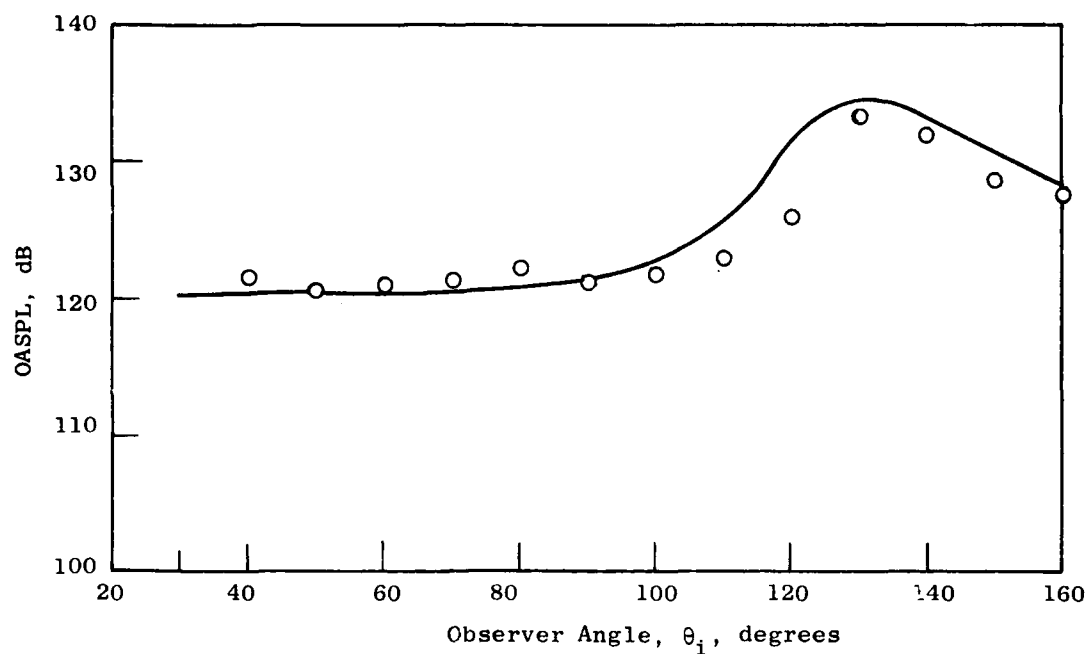


Figure 4-114. Data/Theory Comparison Case 4: 4.64-inch Conical Nozzle Operating at Supersonic Pressure Ratio (Concluded); (c) OASPL Directivity and PWL Spectrum.

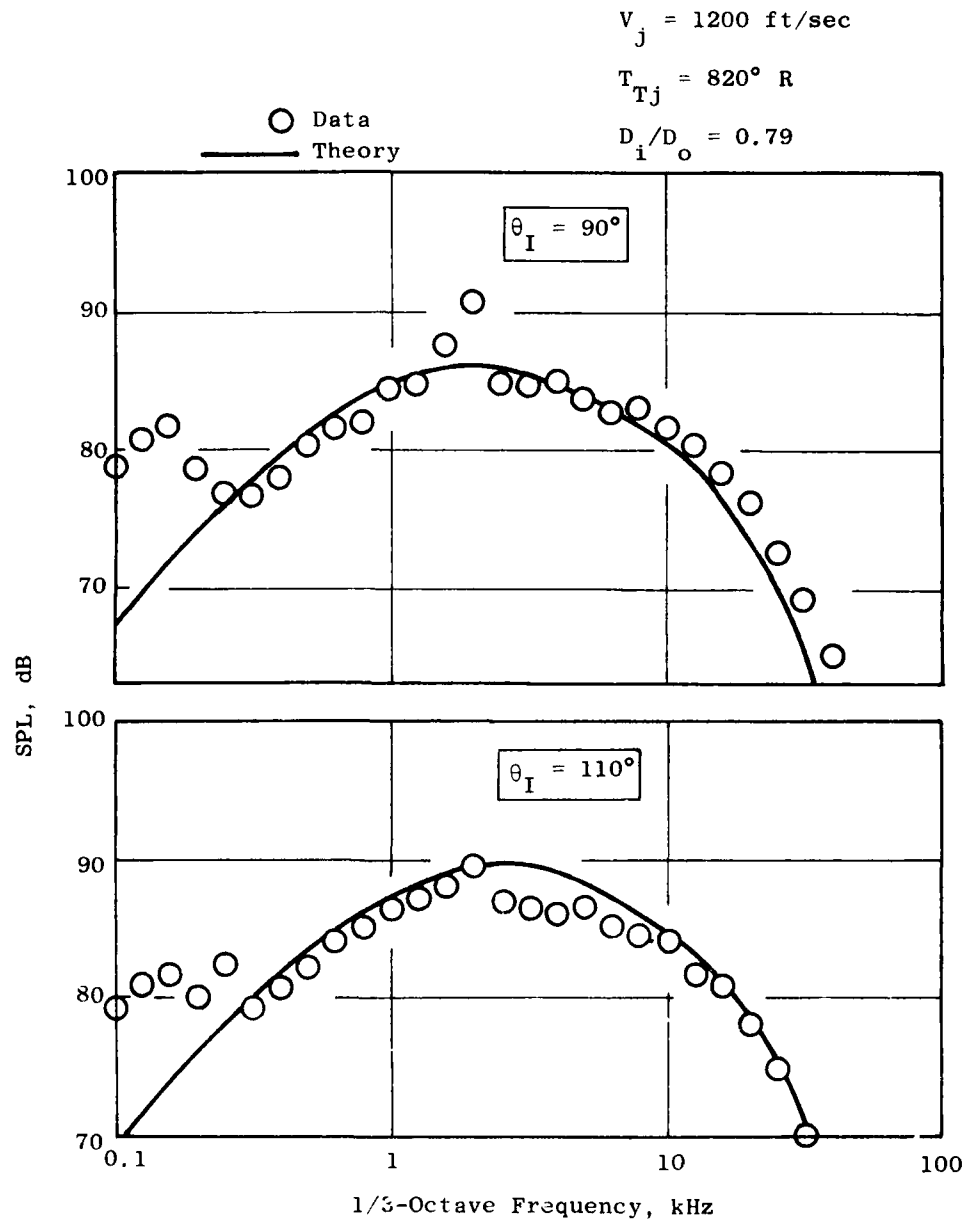


Figure 4-115. Data/Theory Comparison Case 5; 0.79 Radius Ratio Plug Nozzle; (a) SPL Spectra at $\theta_I = 90^\circ$ and 110° .

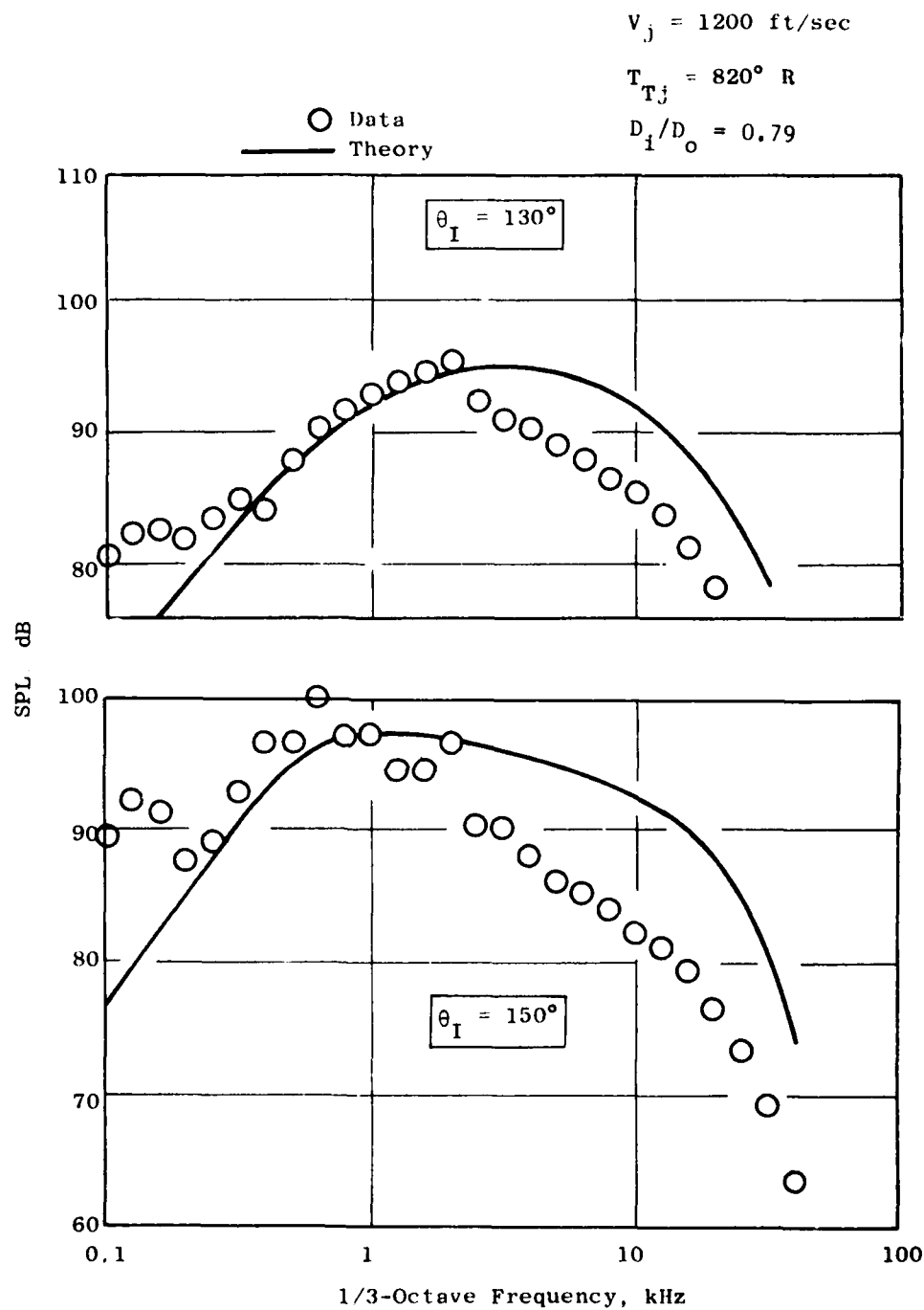


Figure 4-115. Data/Theory Comparison Case 5; 0.79 Radius Ratio Plug Nozzle (Continued); (b) SPL Spectra at $\theta_I = 130^\circ$ and 150° .

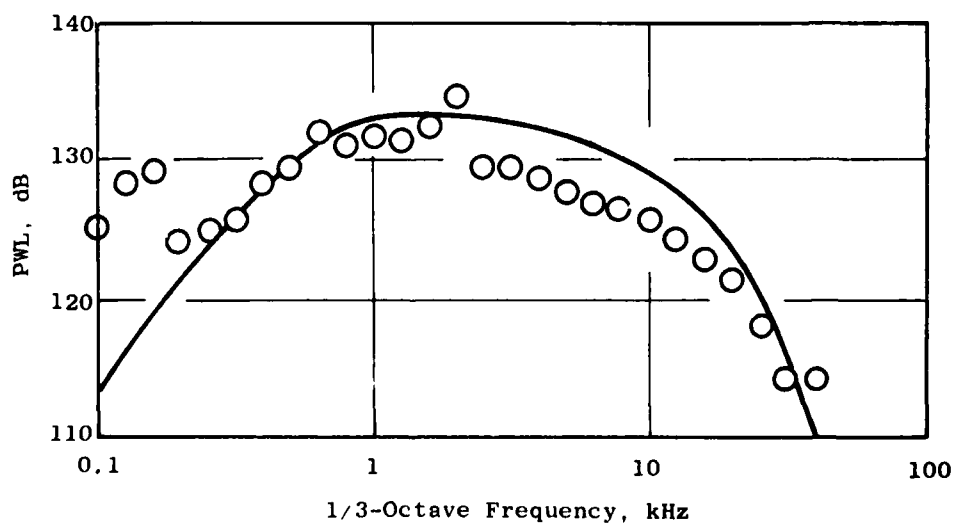
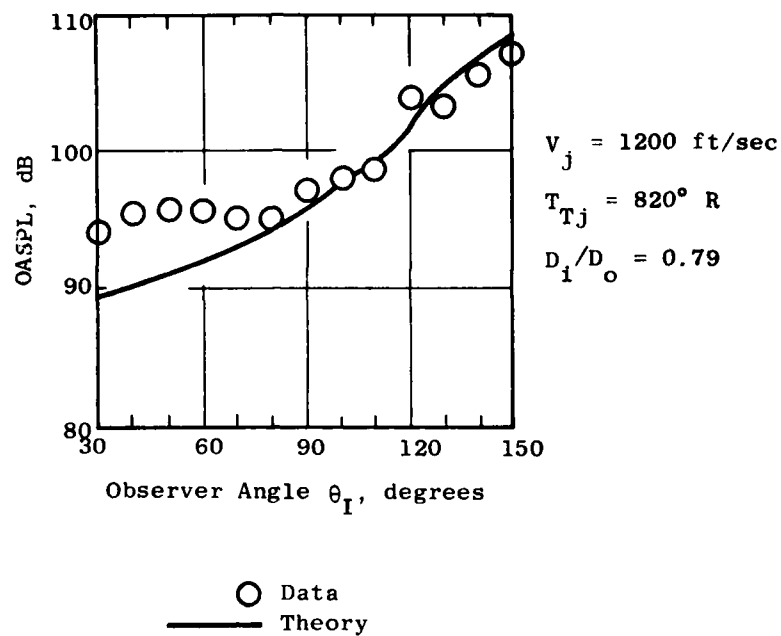


Figure 4-115. Data/Theory Comparison Case 5; 0.79 Radius Ratio Plug Nozzle (Concluded); (c) OASPL Directivity and PWL Spectrum.

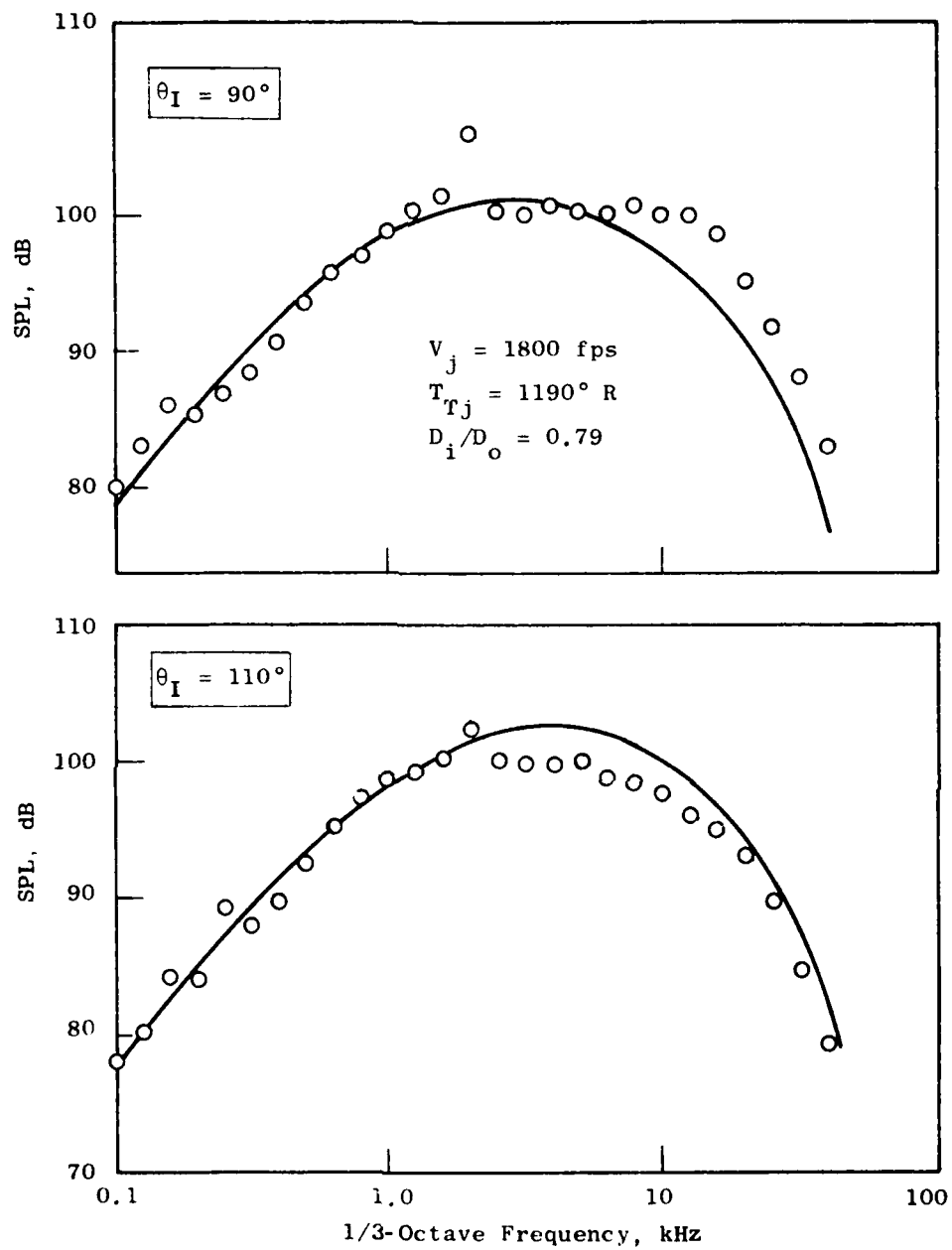


Figure 4-116. Data/Theory Comparison Case 6: 0.79 Radius Ratio Plug Nozzle, $V_j = 1800$ fps; (a) SPL Spectra at $\theta_I = 90^\circ$ and 110° .

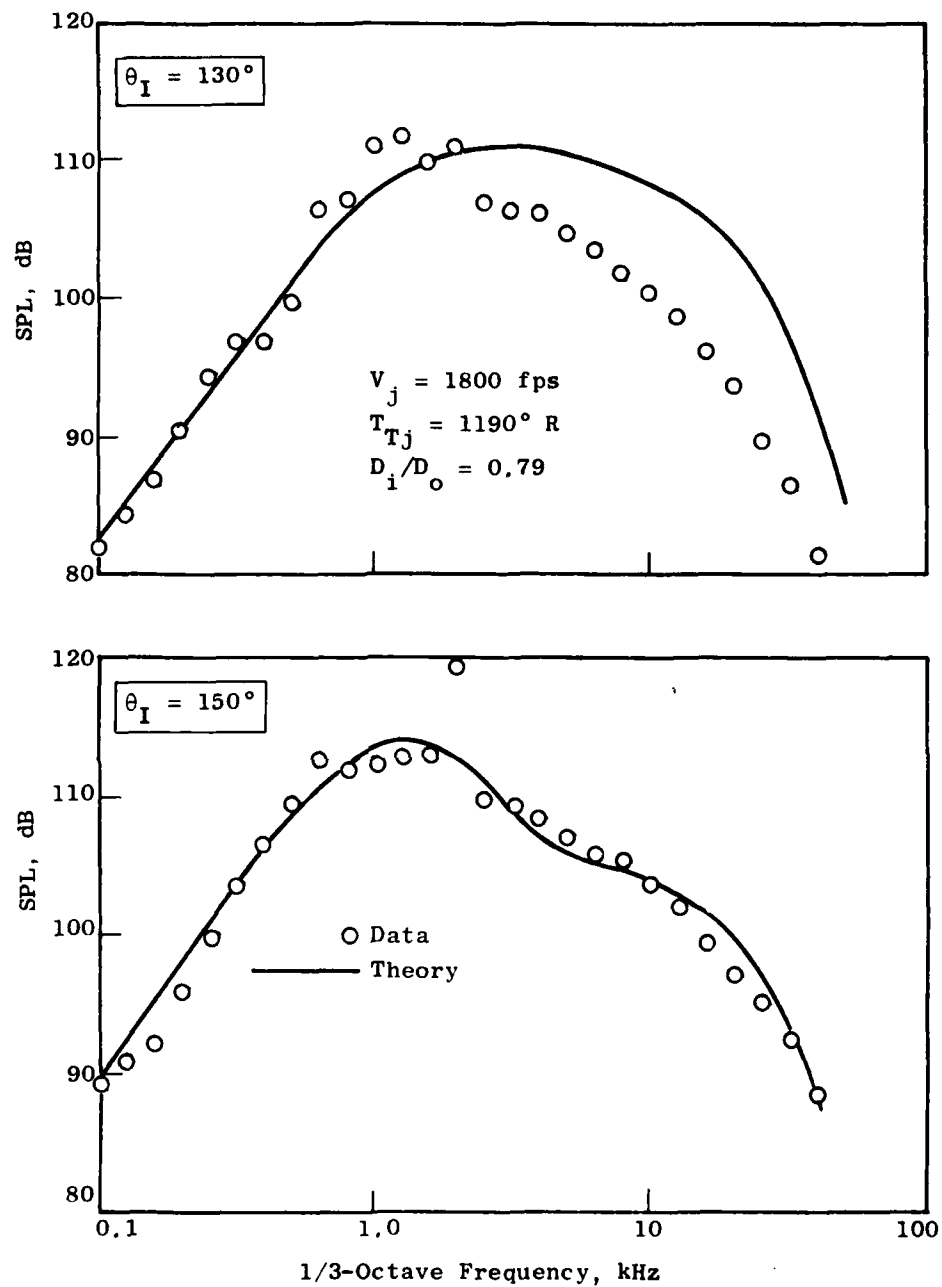


Figure 4-116. Data/Theory Comparison Case 6: 0.79 Radius Ratio Plug Nozzle, $V_j = 1800$ fps (Continued); (b) SPL Spectra at $\theta_I = 130^\circ$ and 150° .

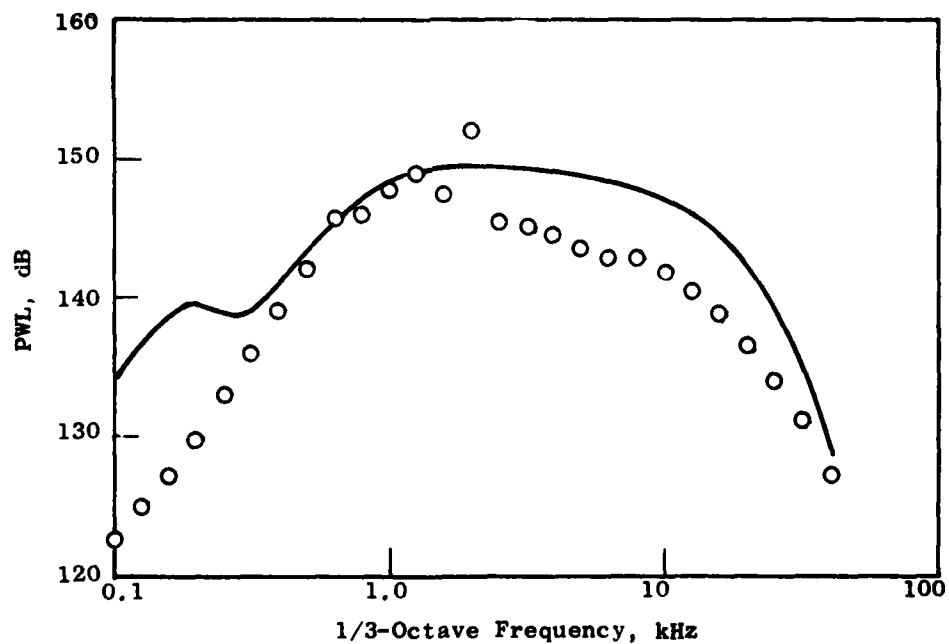
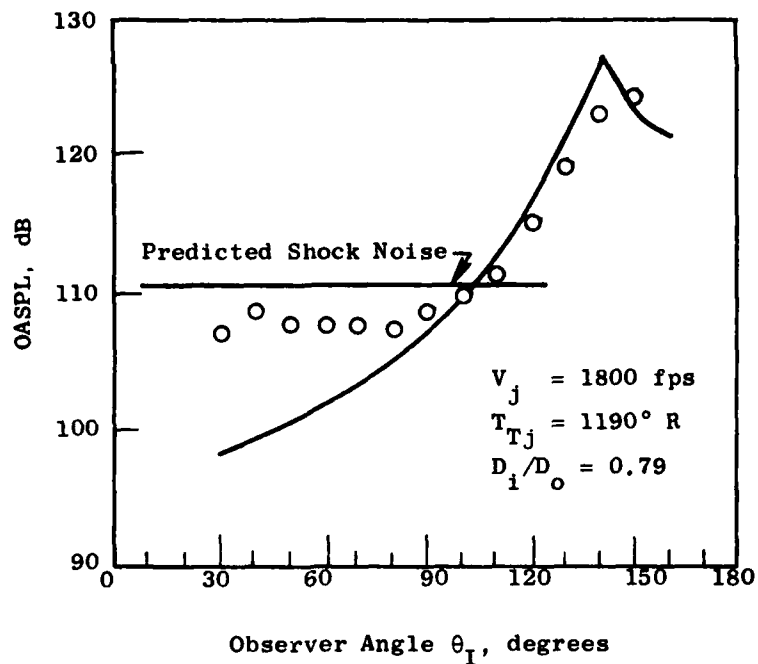


Figure 4-116. Data/Theory Comparison Case 6: 0.79 Radius Ratio Plug Nozzle, $V_j = 1800$ fps (Concluded); (c) OASPL Directivity and PWL Spectrum.

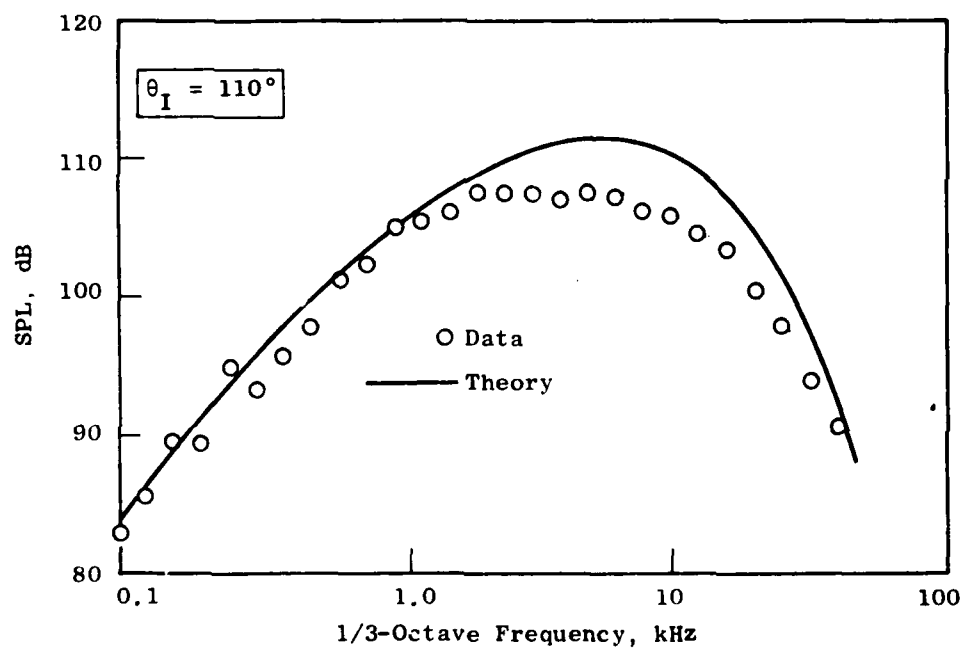
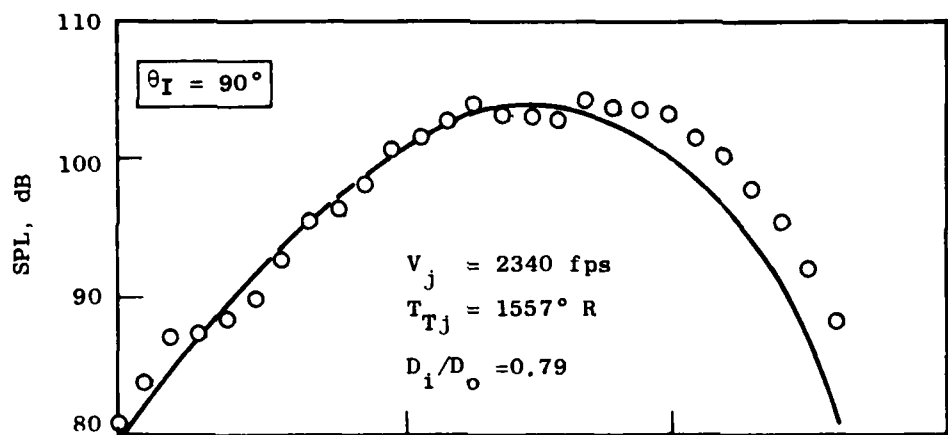


Figure 4-117. Data/Theory Comparison Case 7: 0.79 Radius Ratio Plug Nozzle, $V_j = 2340$ fps; (a) SPL Spectra at $\theta_I = 90^\circ$ and 110° .

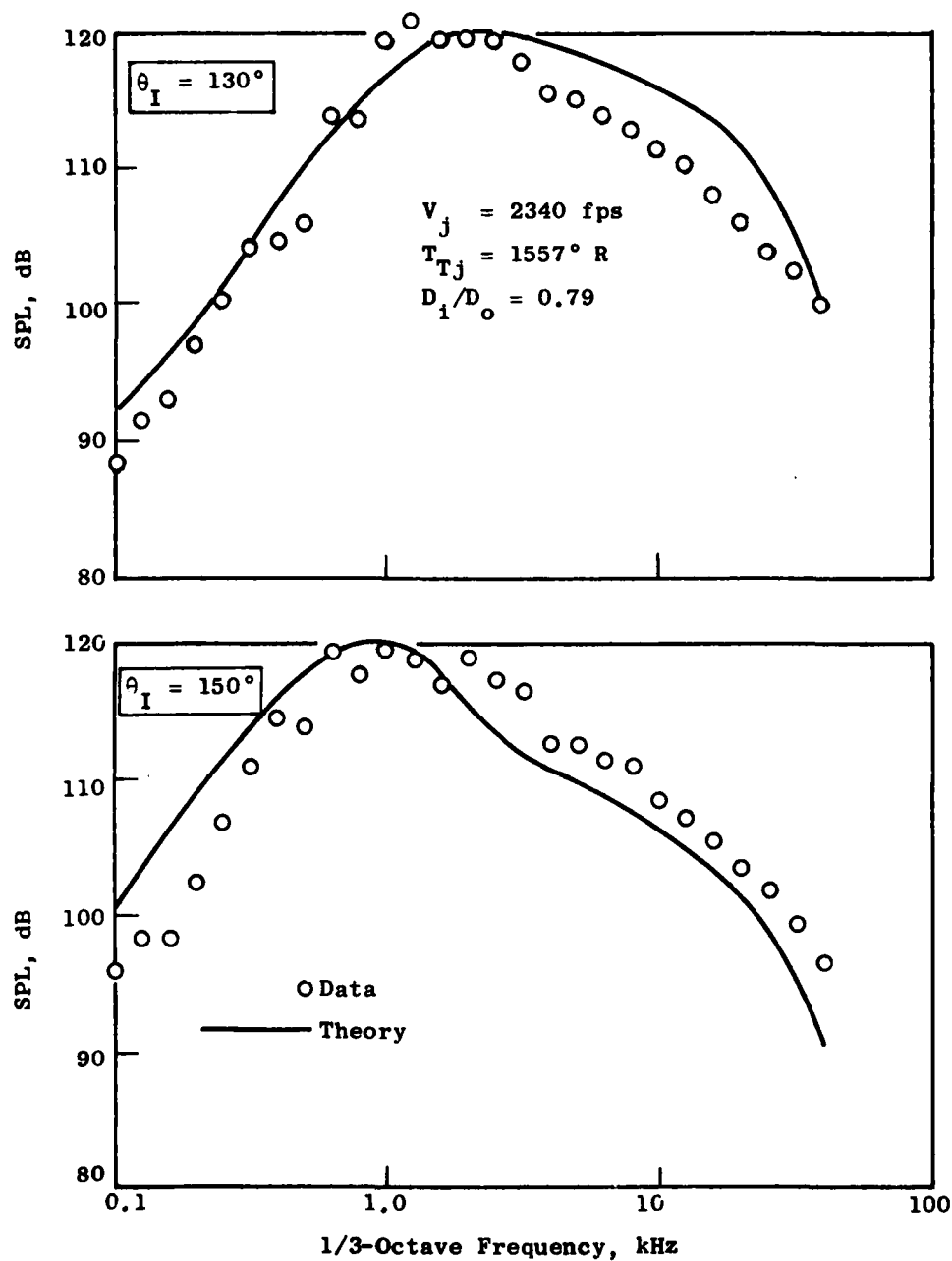


Figure 4-117. Data/Theory Comparison Case 7: 0.79 Radius Ratio Plug Nozzle, $V_j = 2340 \text{ fps}$ (Continued);
 (b) SPL Spectra at $\theta_I = 130^\circ$ and 150° .

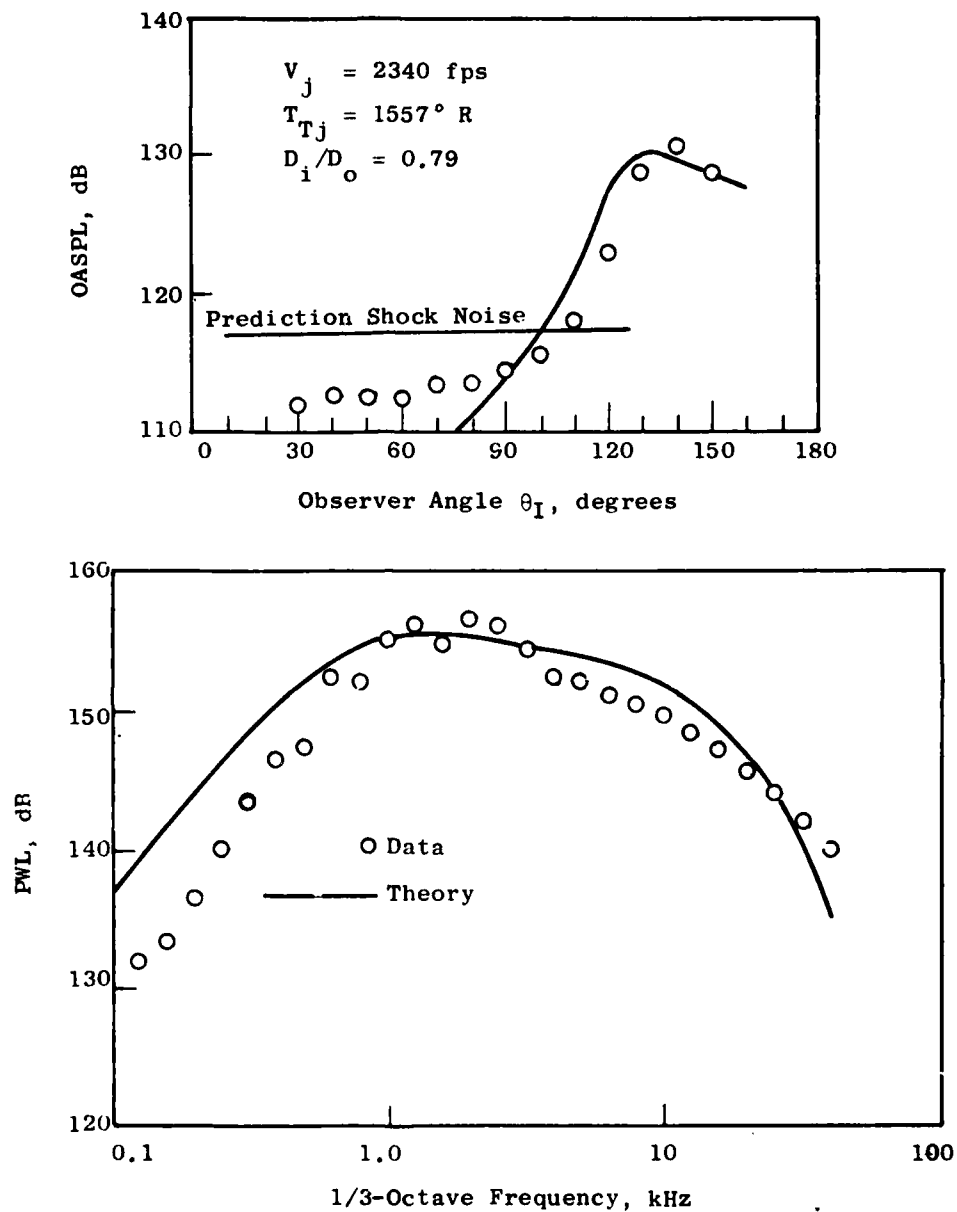


Figure 4-117. Data/Theory Comparison Case 7: 0.79 Radius Ratio Plug Nozzle, $V_j = 2340$ fps (Concluded); (c) OASPL Directivity and PWL Spectrum.

	Inner	Outer
PR	1.798	1.0
T_{TJ}	549	-
v_j	1009	0

○ Data
— Theory

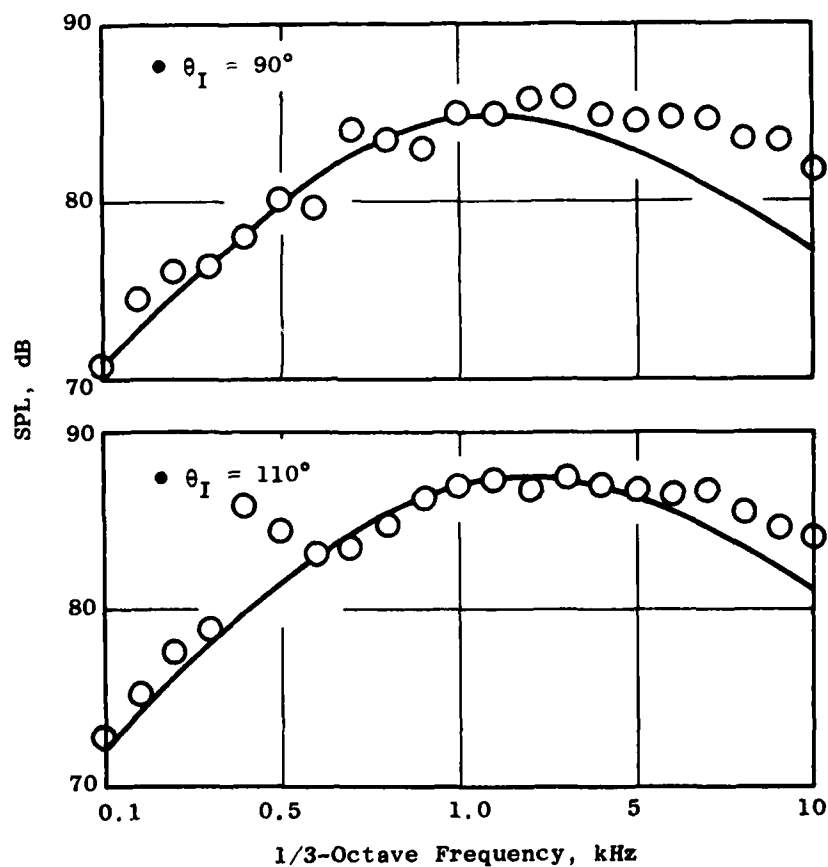


Figure 4-118. Data/Theory Comparison Case 8; AR = 2.0
Coplanar Coaxial Jet, VR = 0; (a) SPL
Spectra at $\theta_I = 90^\circ$ and 110° .

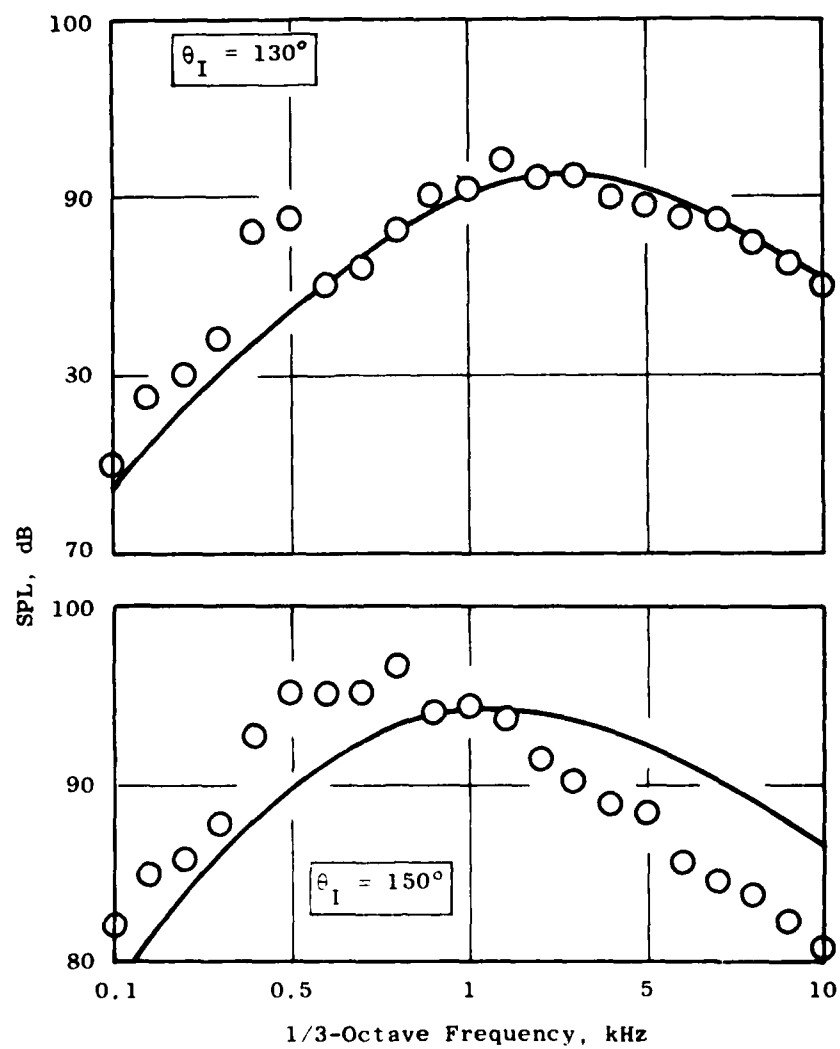


Figure 4-118. Data/Theory Comparison Case 8; AR = 2.0
Coplanar Coaxial Jet, VR = 0 (Continued); (b) SPL
Spectra at $\theta_I = 130^\circ$ and 150° .

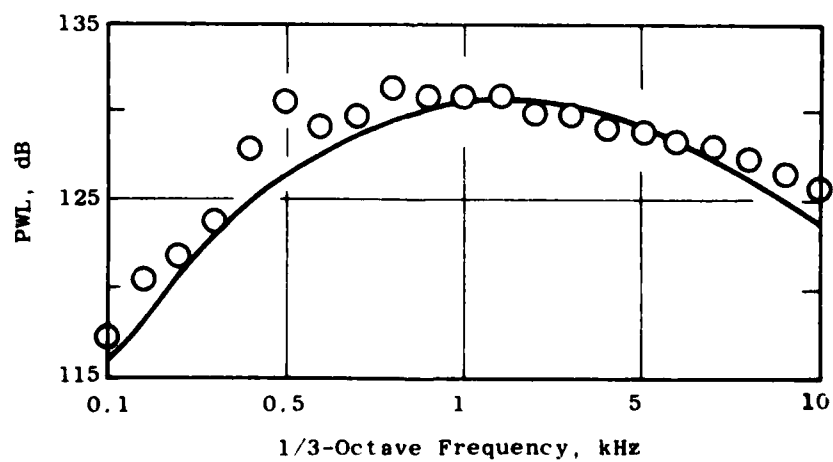
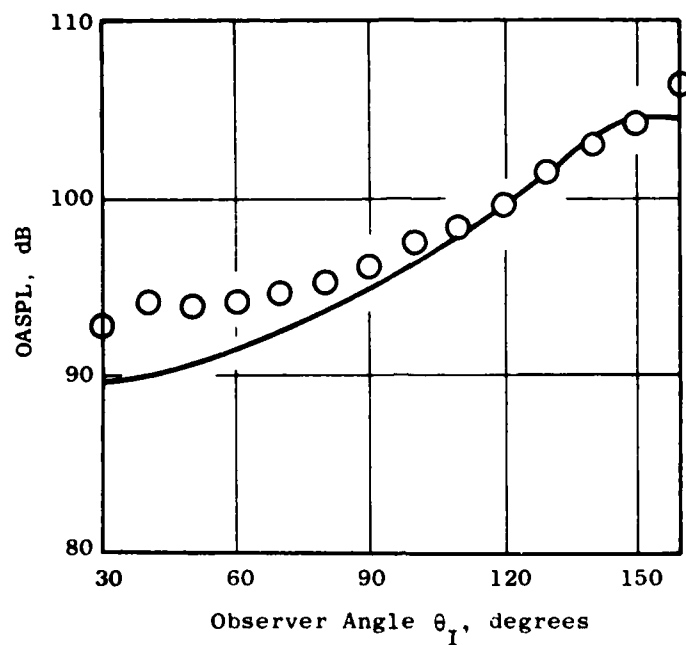
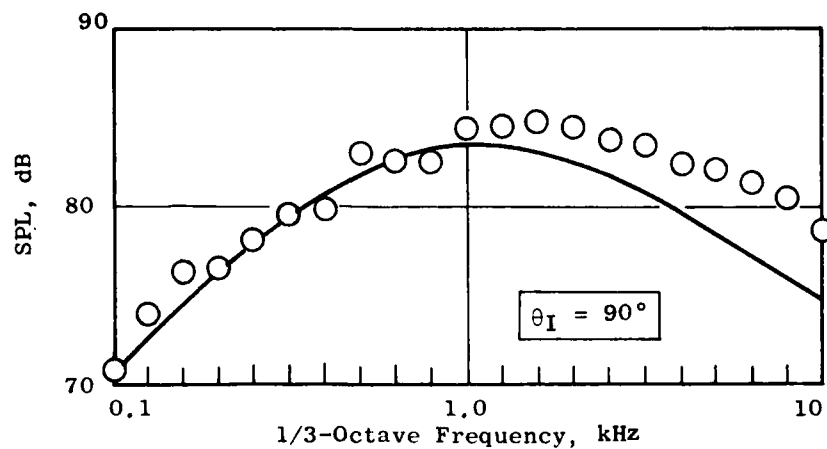


Figure 4-118. Data/Theory Comparison Case 8; AR = 2.0
 Coplanar Coaxial Jet, VR = 0 (Concluded);
 (c) OASPL Directivity and PWL Spectrum.



	Inner	Outer
PR	1.801	1.020
T_{Tj}	551	541
V_j	1012	191.6

○ Data
— Theory

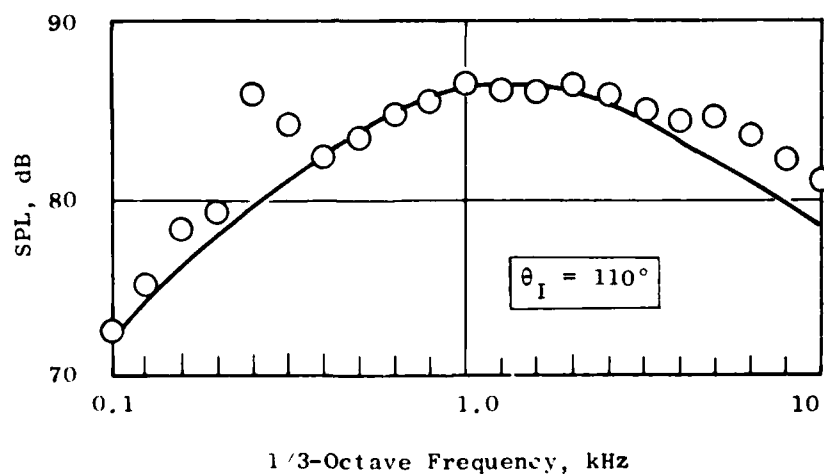


Figure 4-119. Data/Theory Comparison Case 9: AR = 2.0 Coplanar Coaxial Jet, VR = 0.19;
(a) SPL Spectra at $\theta_I = 90^\circ$ and 110° .

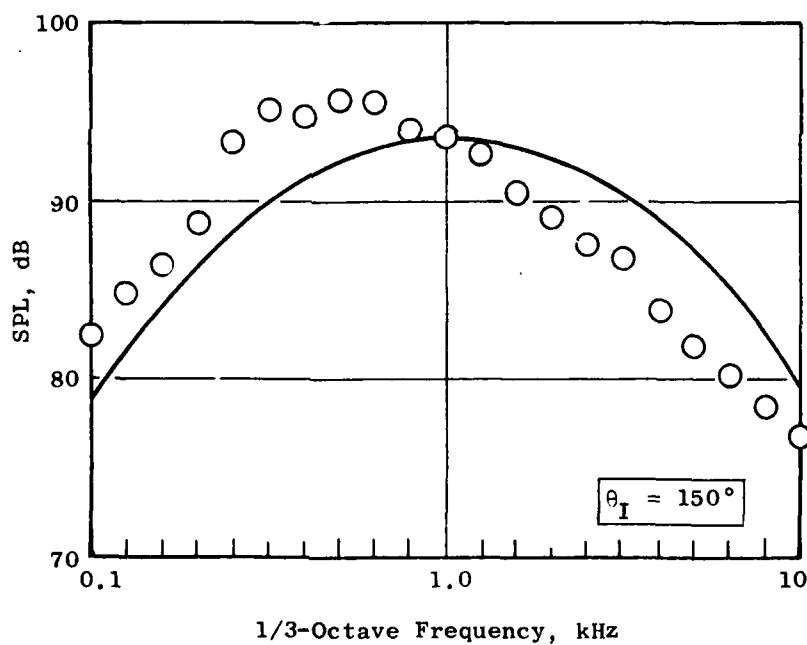
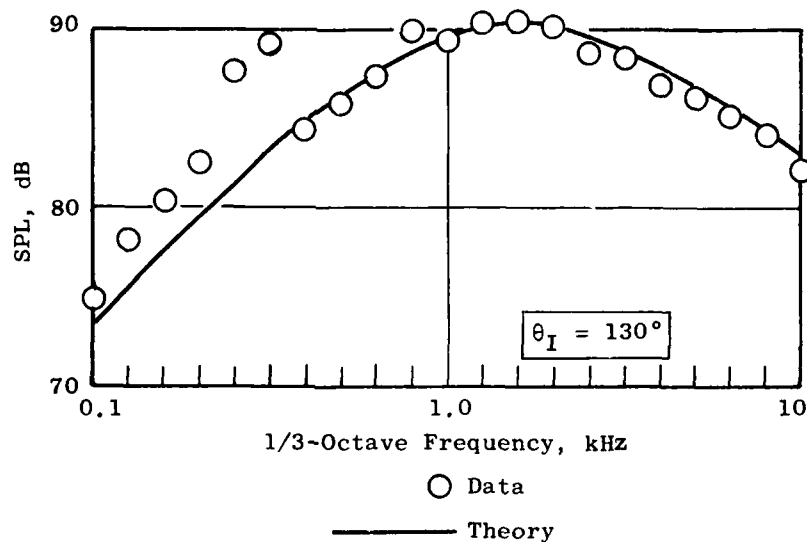
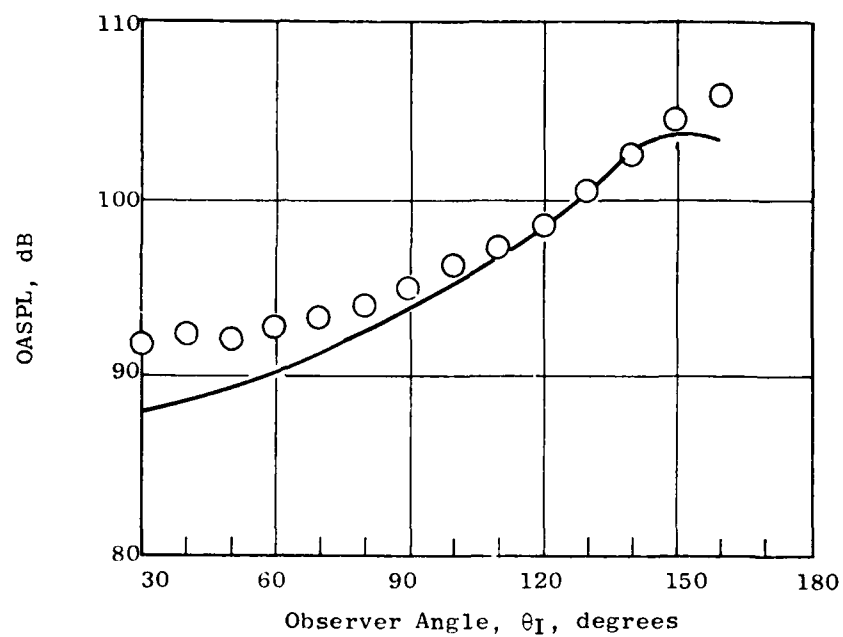


Figure 4-119. Data/Theory Comparison Case 9: AR = 2.0 Coplanar Coaxial Jet, VR = 0.19; (Continued); (b) SPL Spectra at $\theta_I = 130^\circ$ and 150° .



○ Data
— Theory

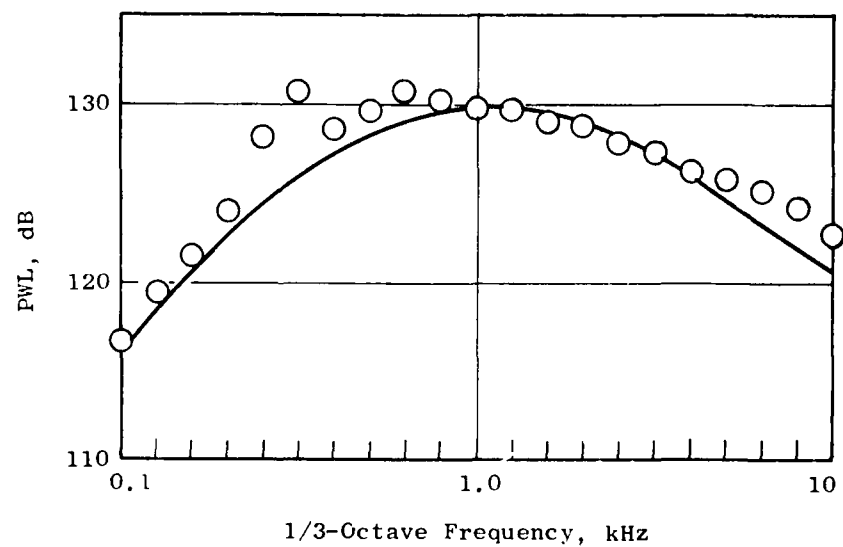
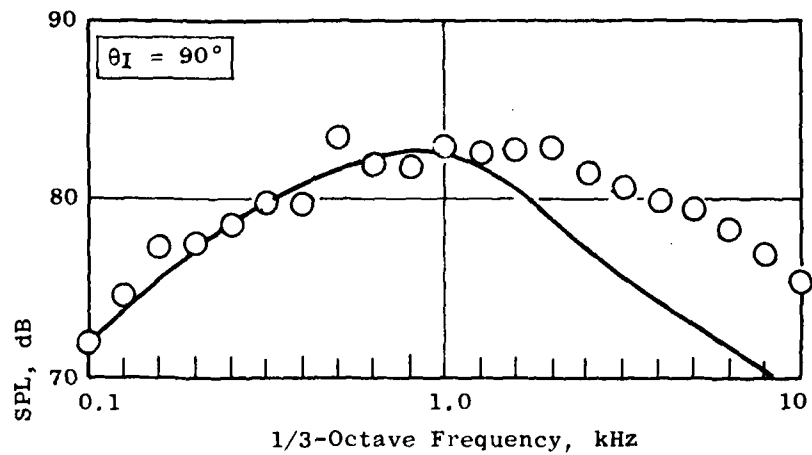


Figure 4-119. Data/Theory Comparison Case 9: AR = 2.0 Coplanar Coaxial Jet, VR = 0.19; (Concluded); (c) OASPL Directivity and Power Spectrum.



	Inner	Outer
PR	1.803	1.094
T_{Tj}	549	544
V_j	1012	407

○ Data
— Theory

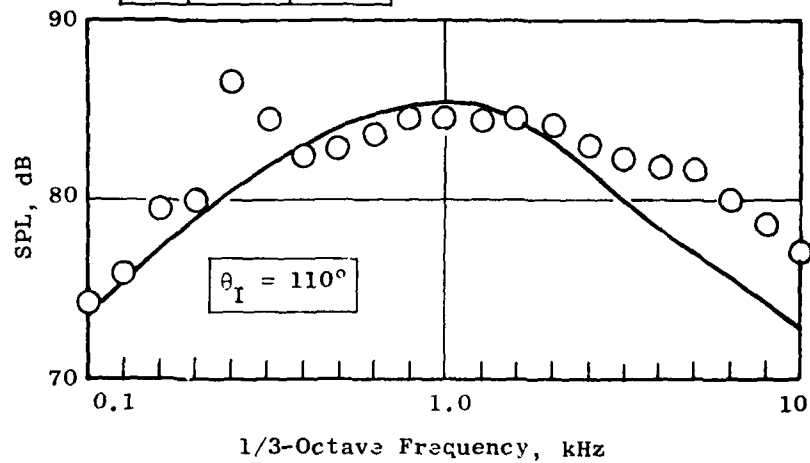


Figure 4-120. Data/Theory Comparison Case 10:
AR = 2.0 Coplanar Coaxial Jet; VR =
0.4; (a) SPL Spectra at $\theta_I = 90^\circ$
 110° .

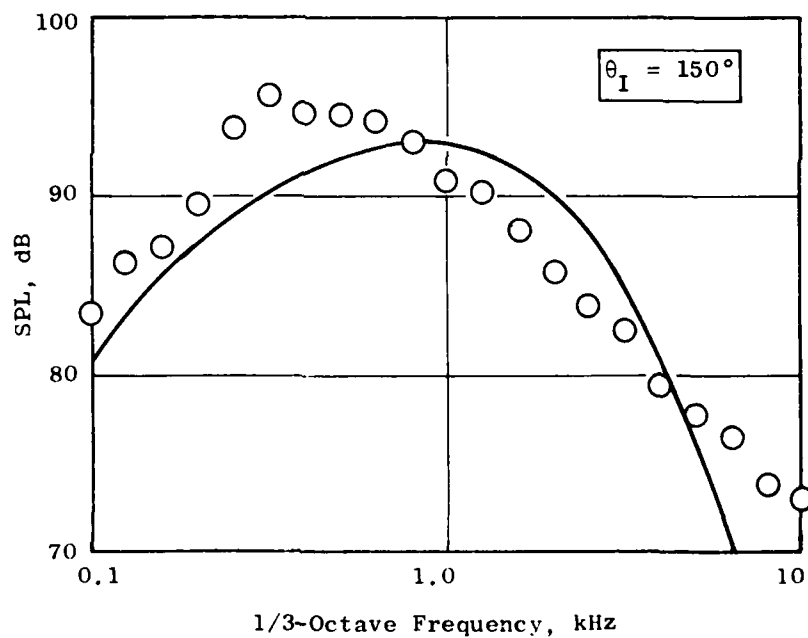
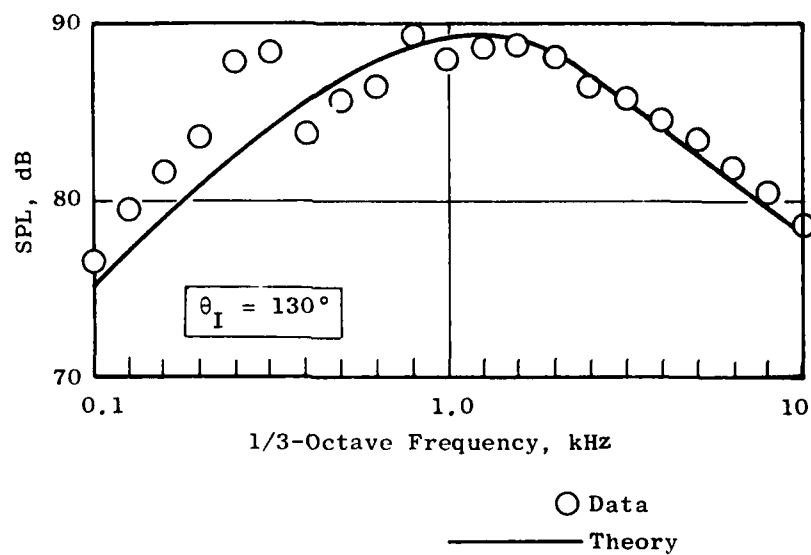


Figure 4-120. Data/Theory Comparison Case 10:
AR = 2.0 Coplanar Coaxial Jet, VR =
0.4 (Continued); (b) SPL Spectra at
 $\theta_I = 130^\circ$ and 150° .

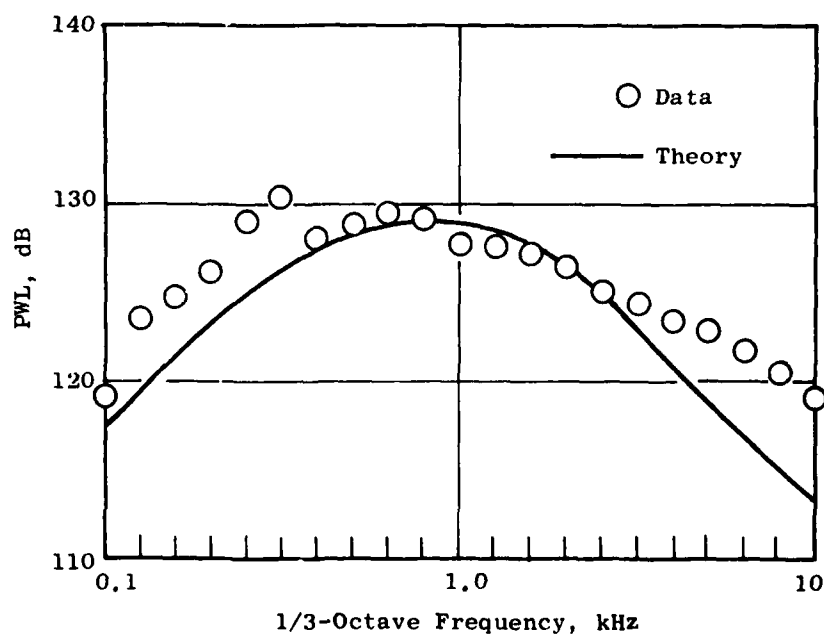
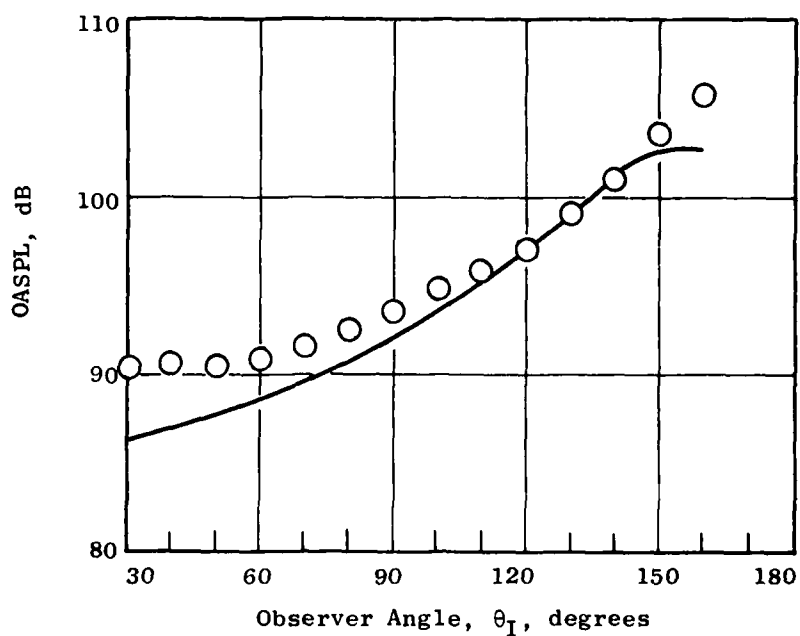
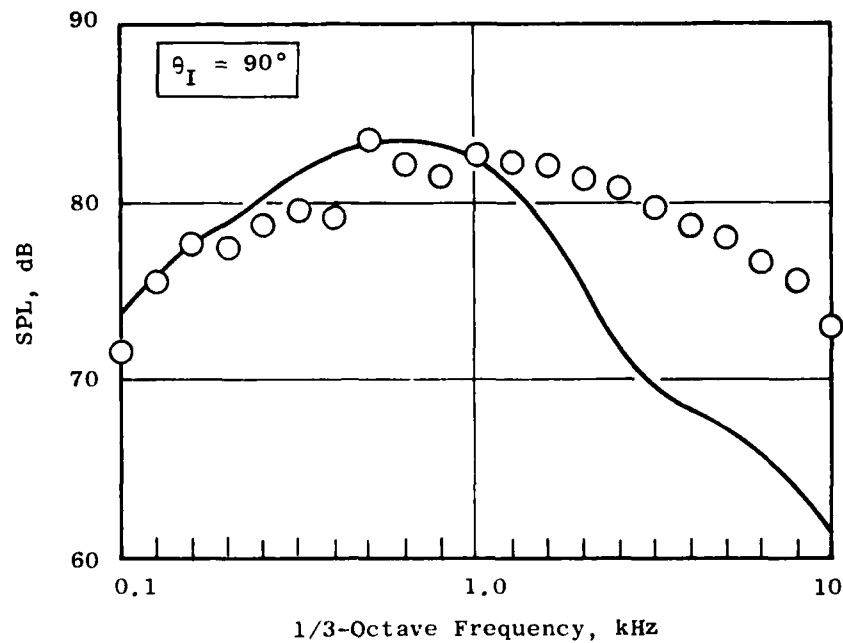


Figure 4-120. Data/Theory Comparison Case 10: AR = 2.0 Coplanar Coaxial Jet, VR = 0.4; (Concluded); (c) OASPL Directivity and Power Spectrum.



	Inner	Outer
PR	1.803	1.220
T_{Tj}	547	545
V_j	1009	602

○ Data
— Theory

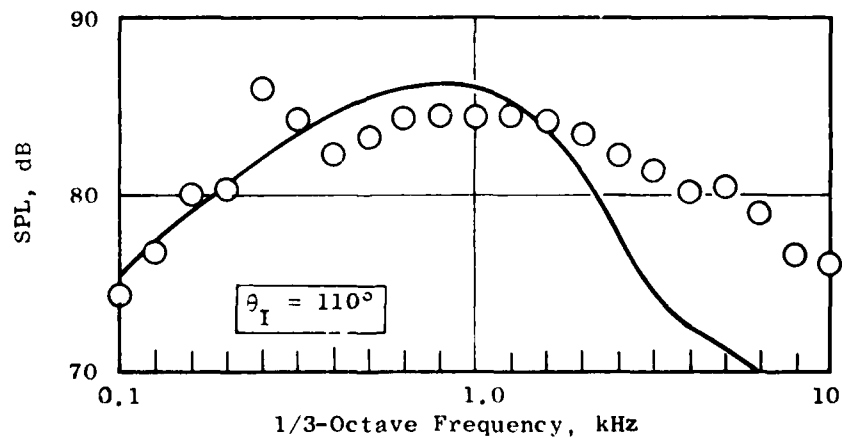


Figure 4-121. Data/Theory Comparison Case 11: AR = 2.0 Coplanar Coaxial Jet, VR = 0.6;
(a) SPL Spectra at $\theta_I = 90^\circ$ and 110° .

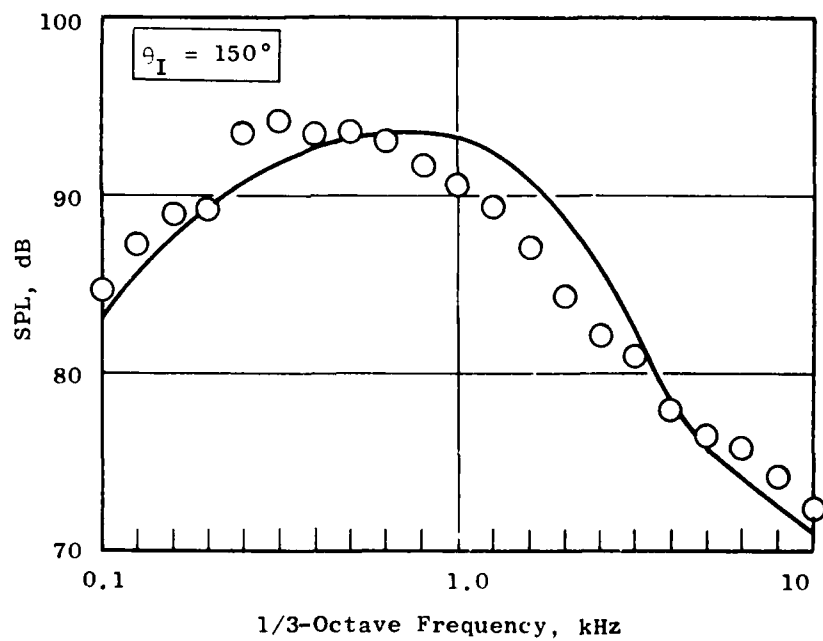
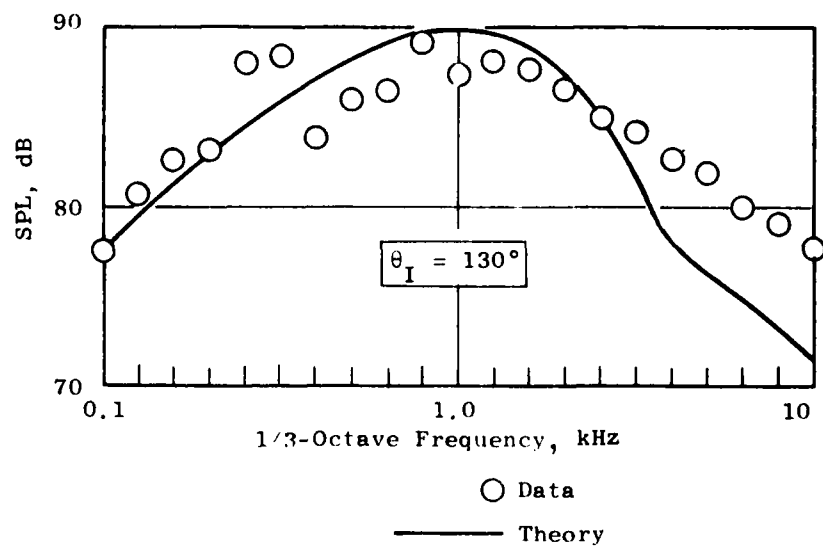
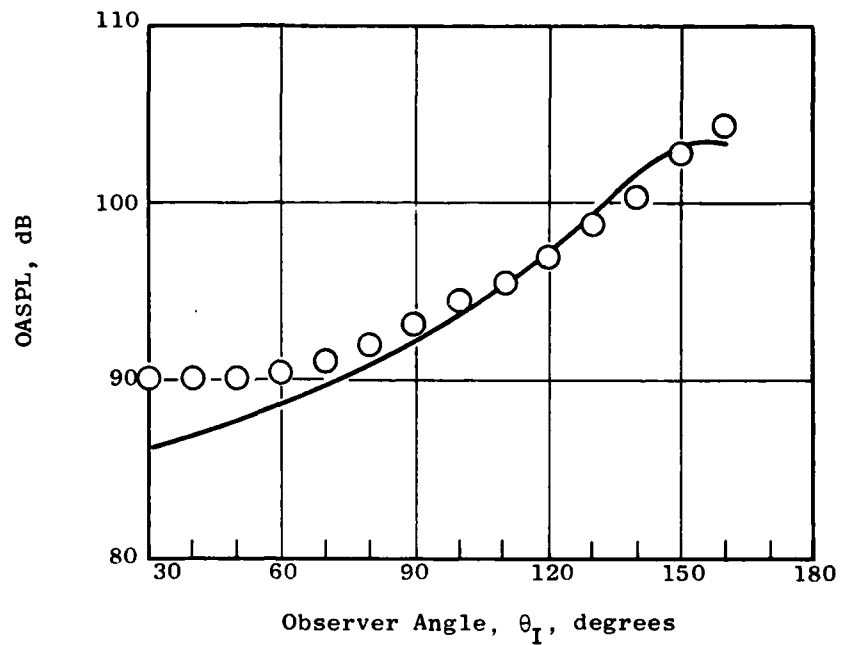


Figure 4-121. Data/Theory Comparison Case 11: AR = 2.0 Coplanar Coaxial Jet, VR = 0.6; (Continued); (b) SPL Spectra at $\theta_I = 130^\circ$ and 150° .



○ Data

— Theory

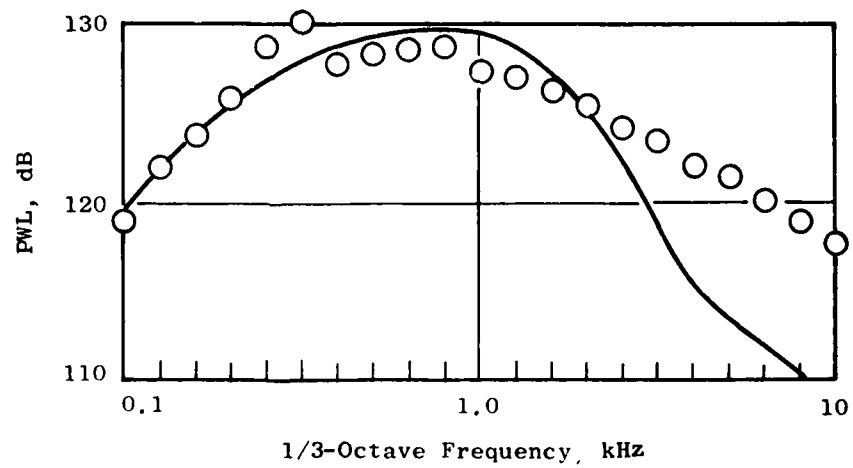
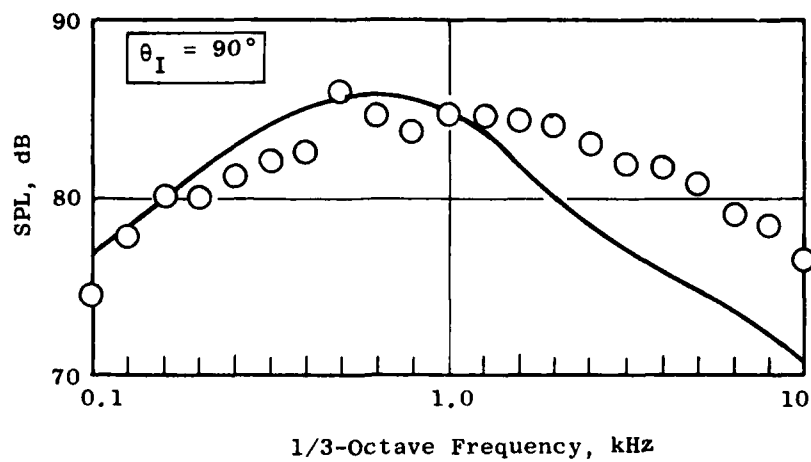


Figure 4-121. Data/Theory Comparison Case 11: AR = 2.0 Coplanar Coaxial Jet, VR = 0.6; (Concluded); (c) OASPL Directivity and Power Spectrum.



	Inner	Outer
PR	1.797	1.439
T_{Tj}	546	545
V_j	1006	804

○ Data
— Theory

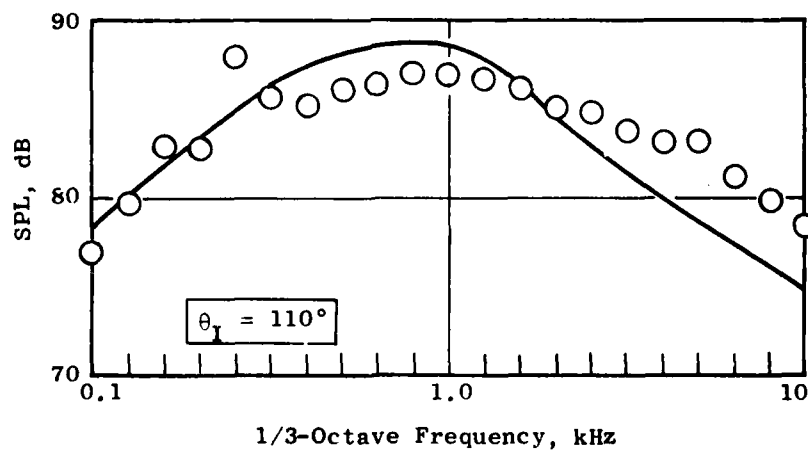


Figure 4-122. Data/Theory Comparison Case 12: AR = 2.0 Coplanar Coaxial Jet, VR = 0.8;
(a) SPL Spectra at $\theta_I = 90^\circ$ and 110° .

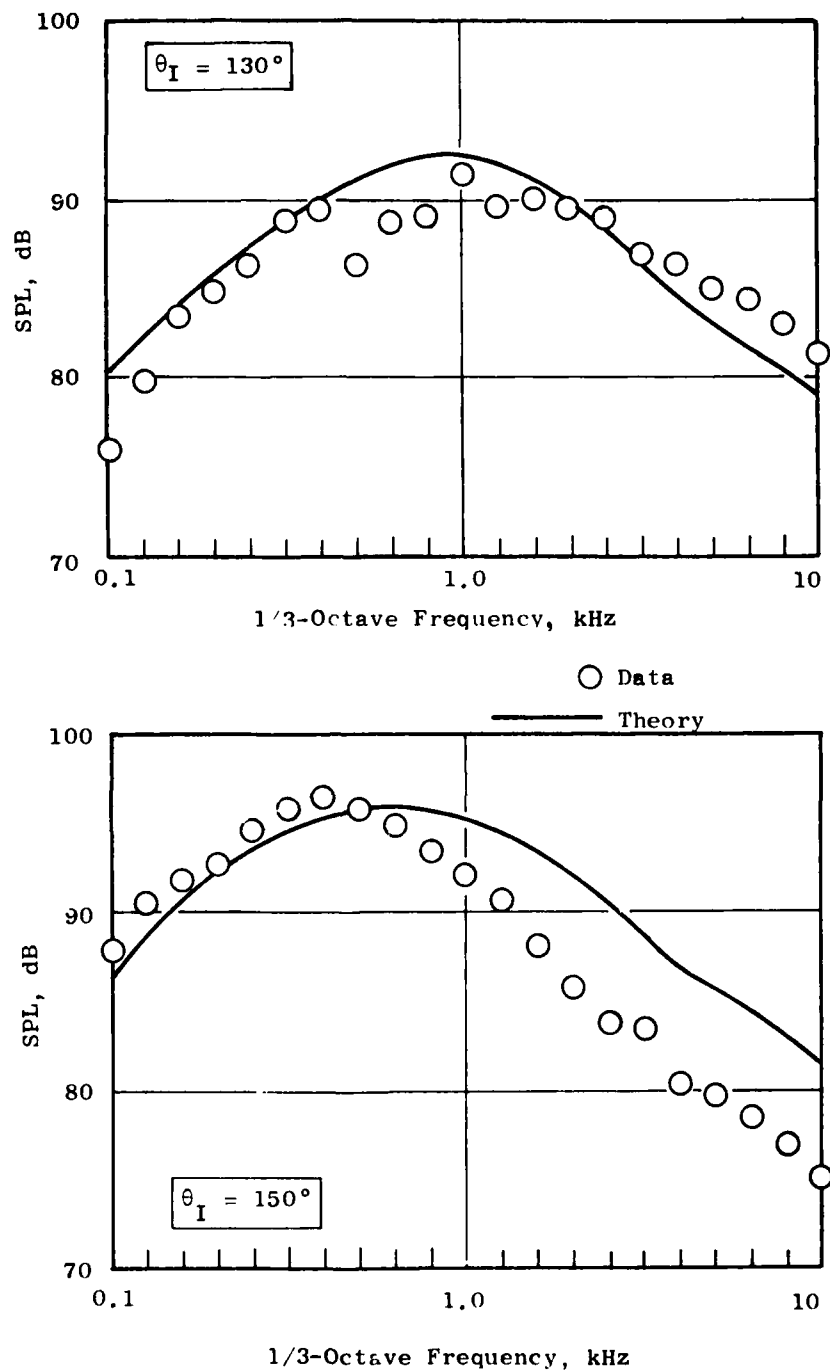


Figure 4-122. Data/Theory Comparison Case 12:
 AR = 2.0 Coplanar Coaxial Jet, VR =
 0.8 (Continued); (b) SPL Spectra at
 $\theta_I = 130^\circ$ and 150° .

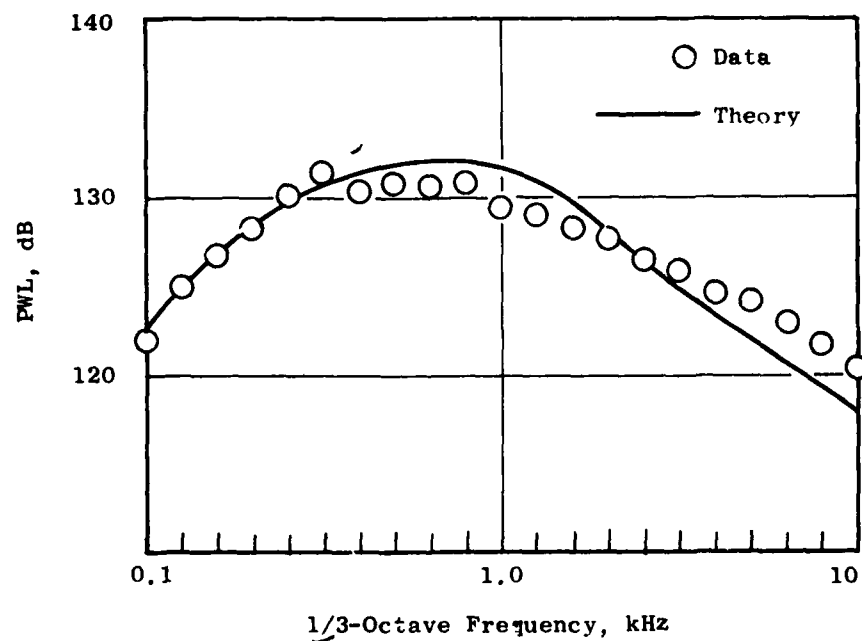
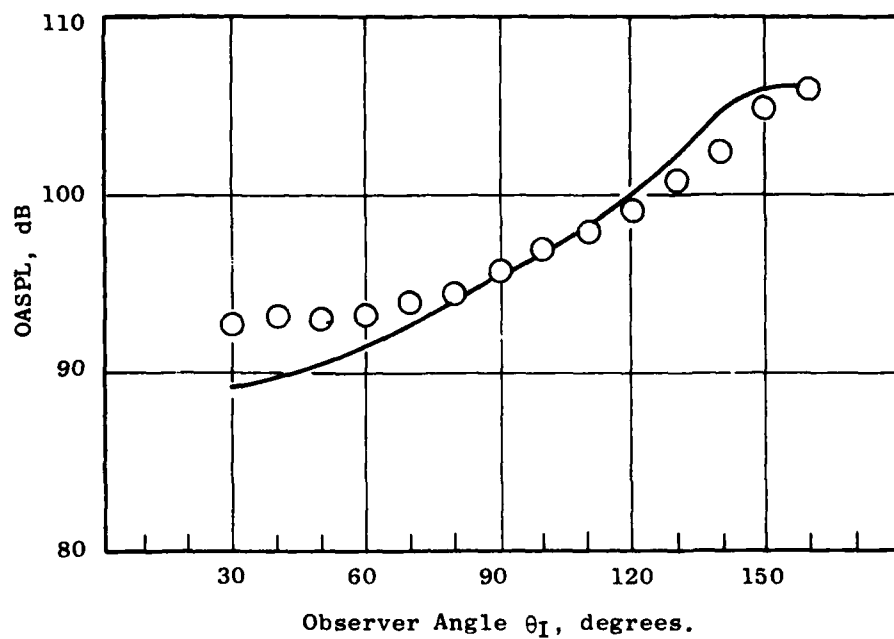
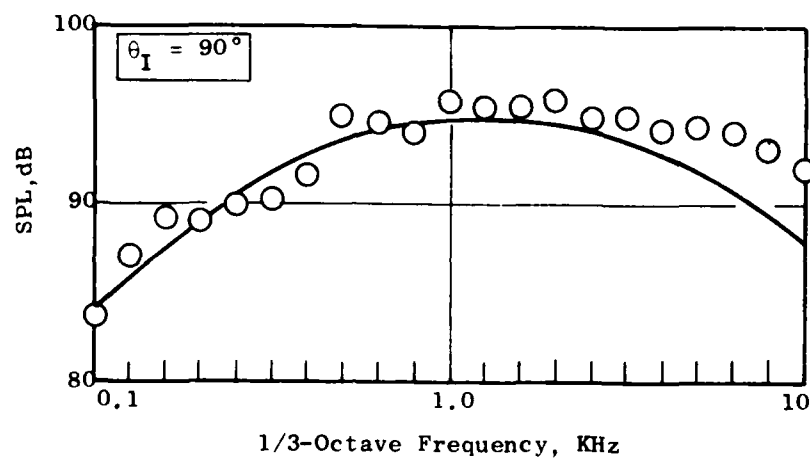


Figure 4-122. Data/Theory Comparison Case 12: AR = 2.0 Coplanar Coaxial Jet, VR = 0.8, (Concluded); (c) OASPL Directivity and Power Spectrum.



	Inner	Outer
PR	1.791	2.636
T_{Tj}	550	549
V_j	1007	1264

○ Data

— Theory

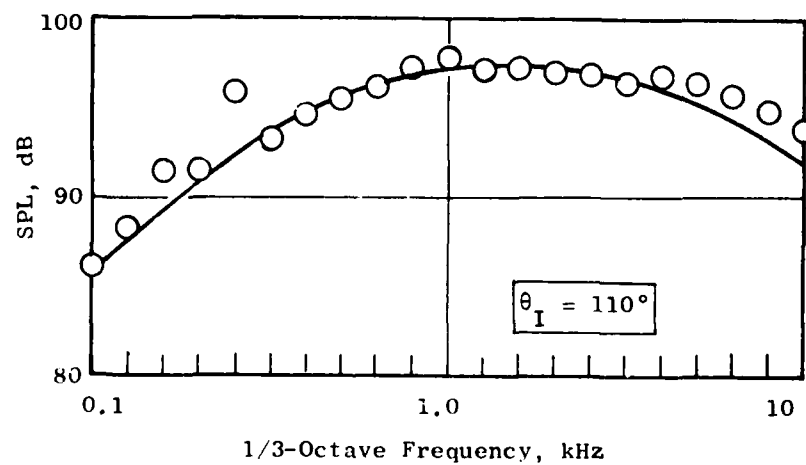


Figure 4-123. Data/Theory Comparison Case 13: AR = 2.0 Coplanar Coaxial Jet, VR = 1.25; (a) SPL Spectra at $\theta_I = 90^\circ$ and 110° .

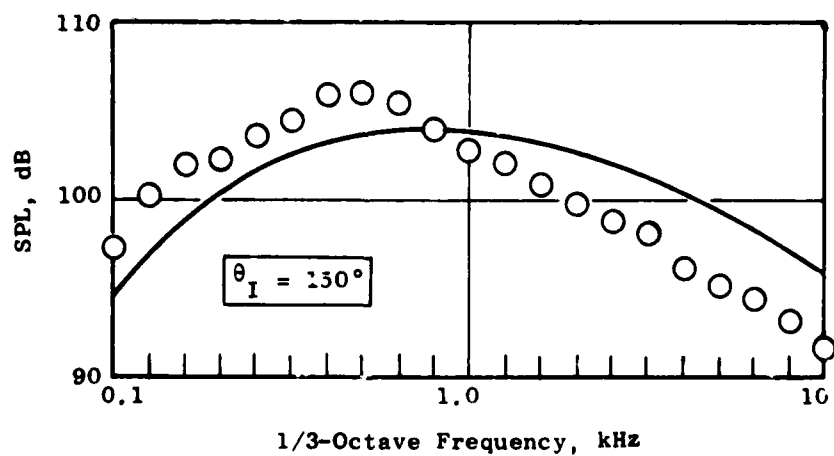
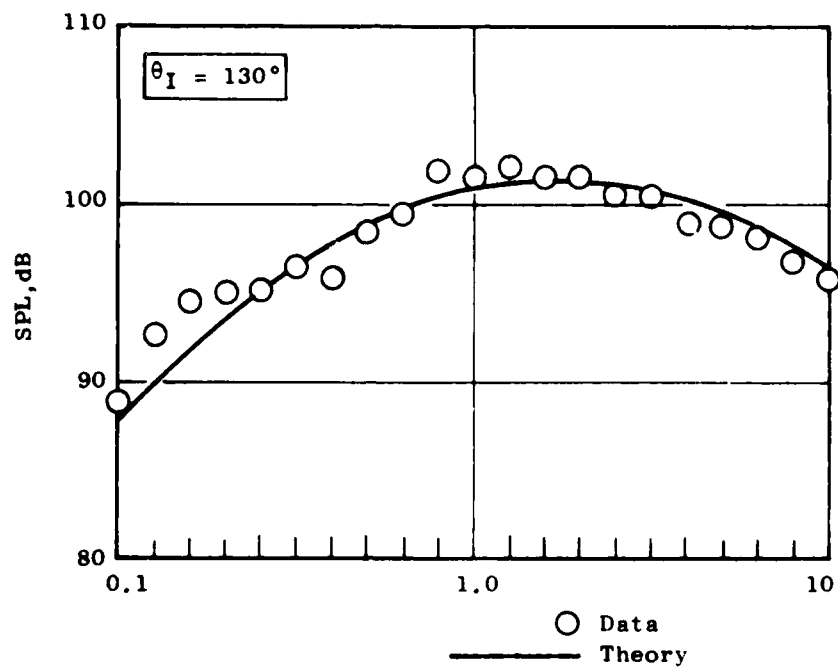


Figure 4-123. Data/Theory Comparison Case 13: AR = 2.0 Coplanar Coaxial Jet, VR = 1.25; (Continued); (b) SPL Spectra at $\theta_I = 130^\circ$ and 150° .

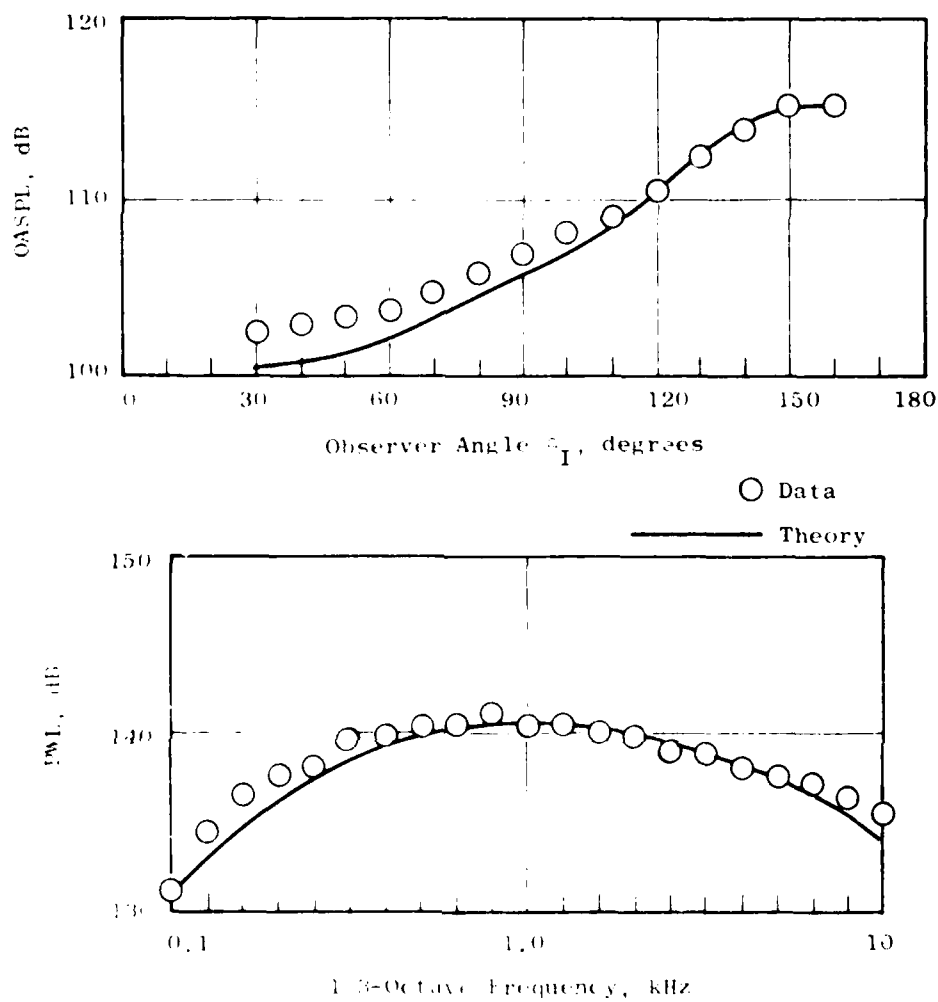


Figure 4-123. Data-Theory Comparison Case 13: AR = 2.0 Coplanar Coaxial Jet, VR = 1.25; (Concluded); (c) OASPL Directivity and Power Spectrum.

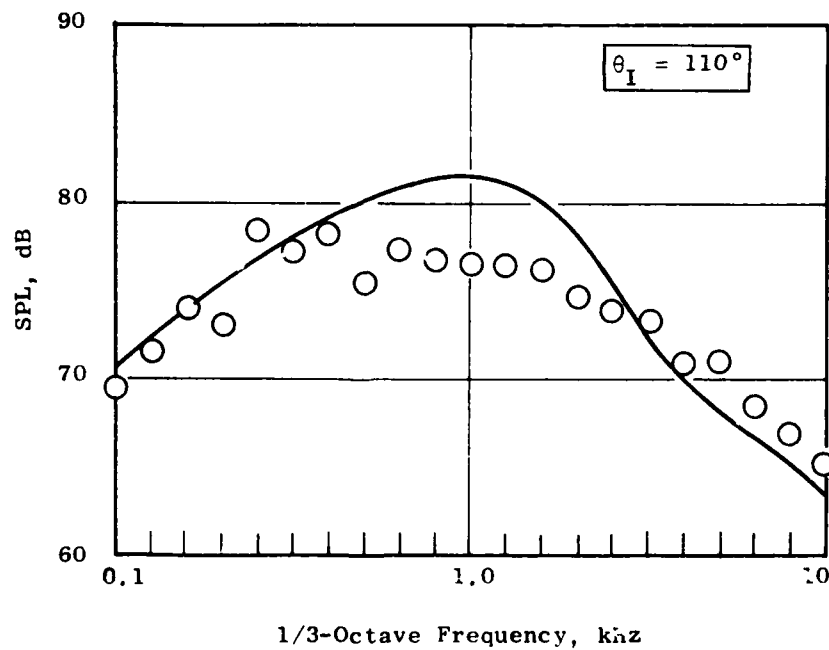
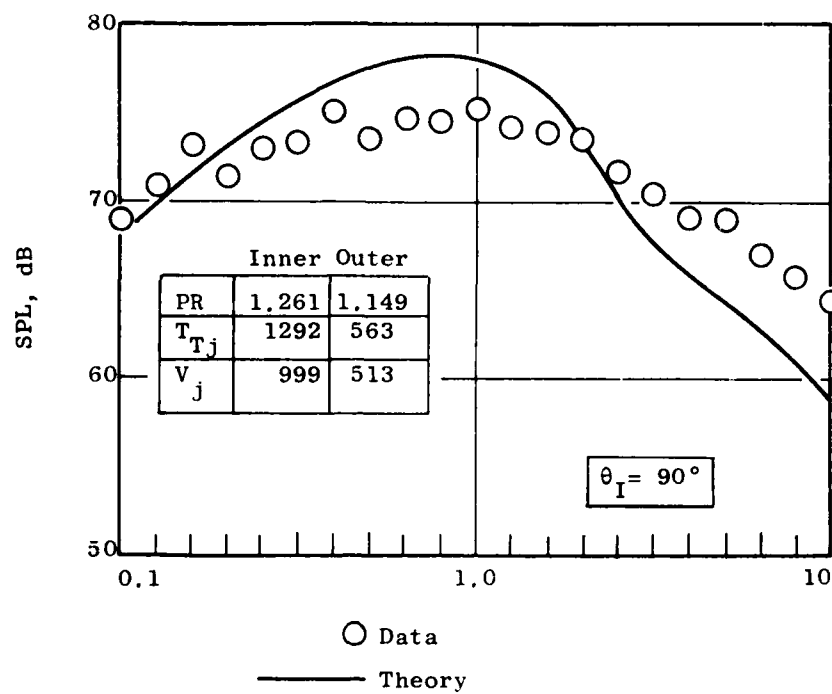


Figure 4-124. Data/Theory Comparison Case 14: $AR = 2.0$ Coplanar Coaxial Heated Jet, $VR = 0.51$; (a) SPL Spectra at $\theta_I = 90^\circ$ and 110° .

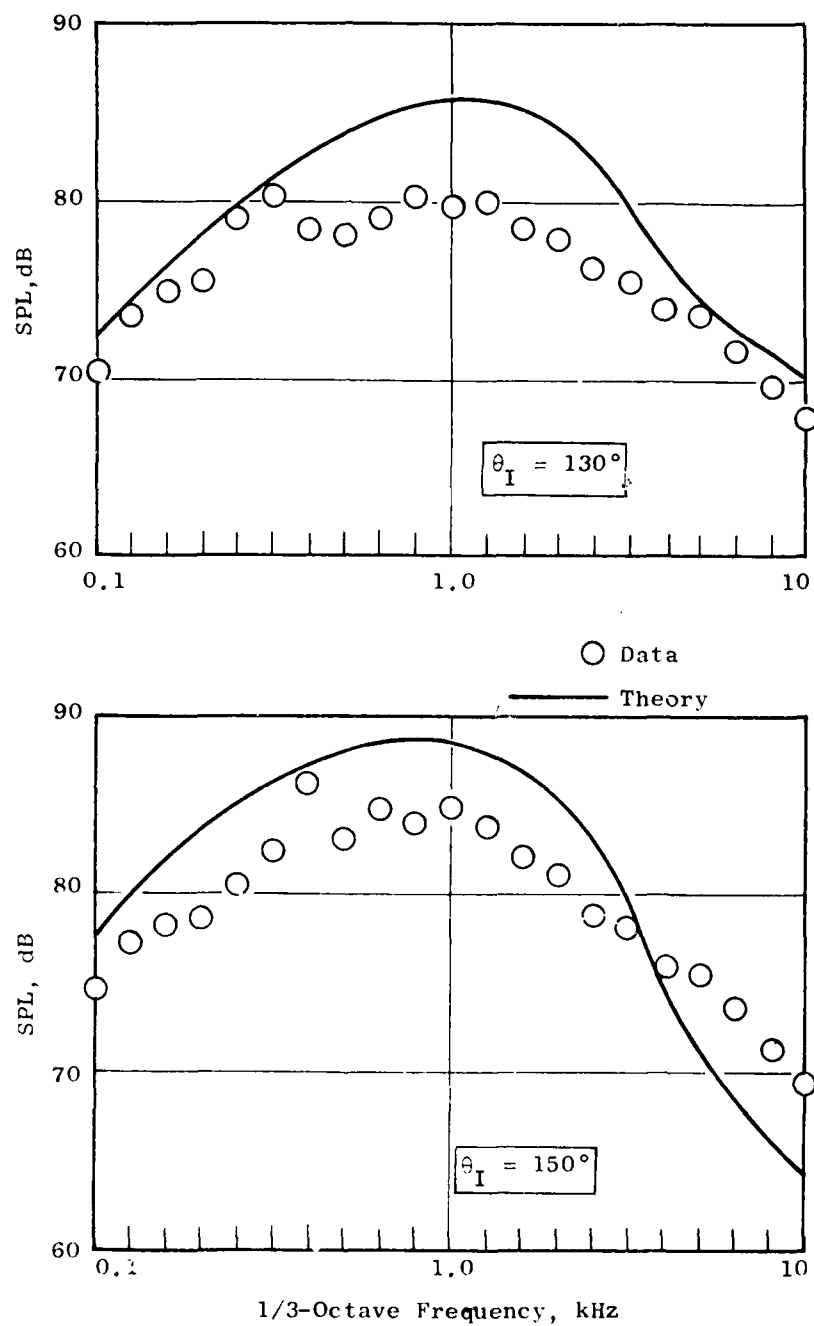


Figure 4-124. Data/Theory Comparison Case 14: AR = 2.0 Coplanar Coaxial Heated Jet, VR = 0.51 (Continued); (b) SPL Spectra at $\theta_I = 130^\circ$ and 150° .

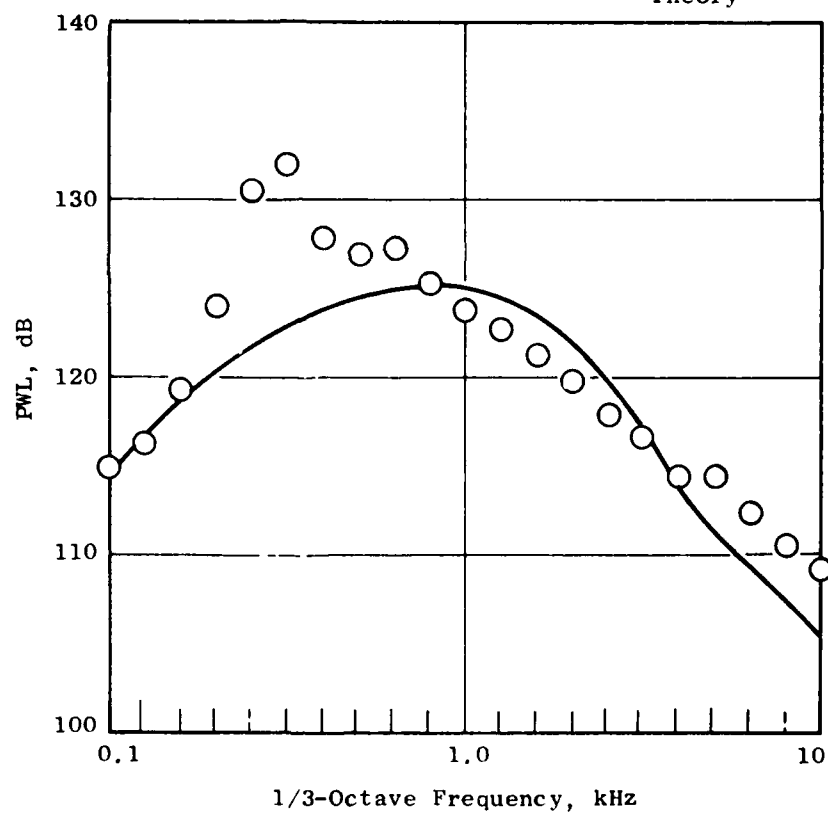
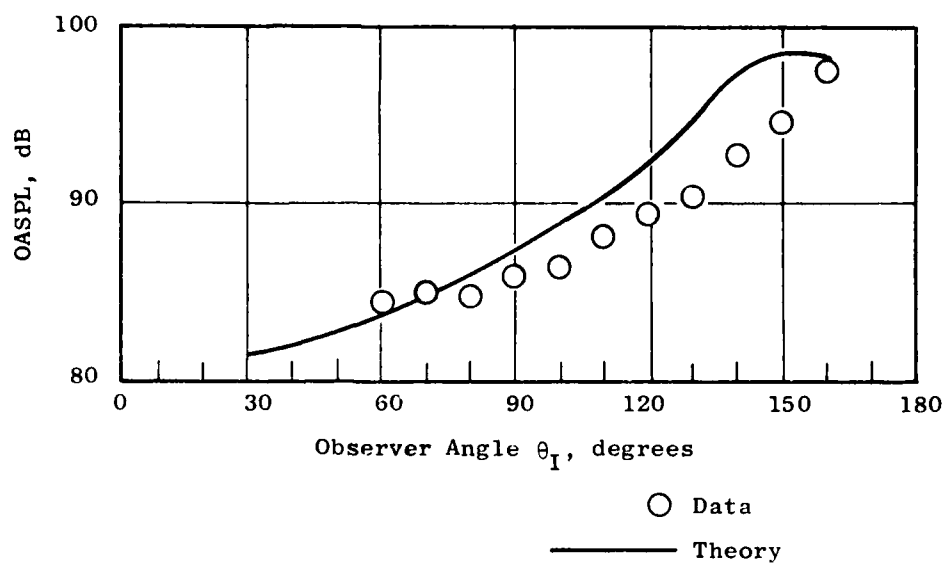


Figure 4-124. Data/Theory Comparison Case 14: AR = 2.0 Coplanar Coaxial Heated Jet, VR = 0.51 (Concluded); (c) OASPL Directivity and Power Spectrum.

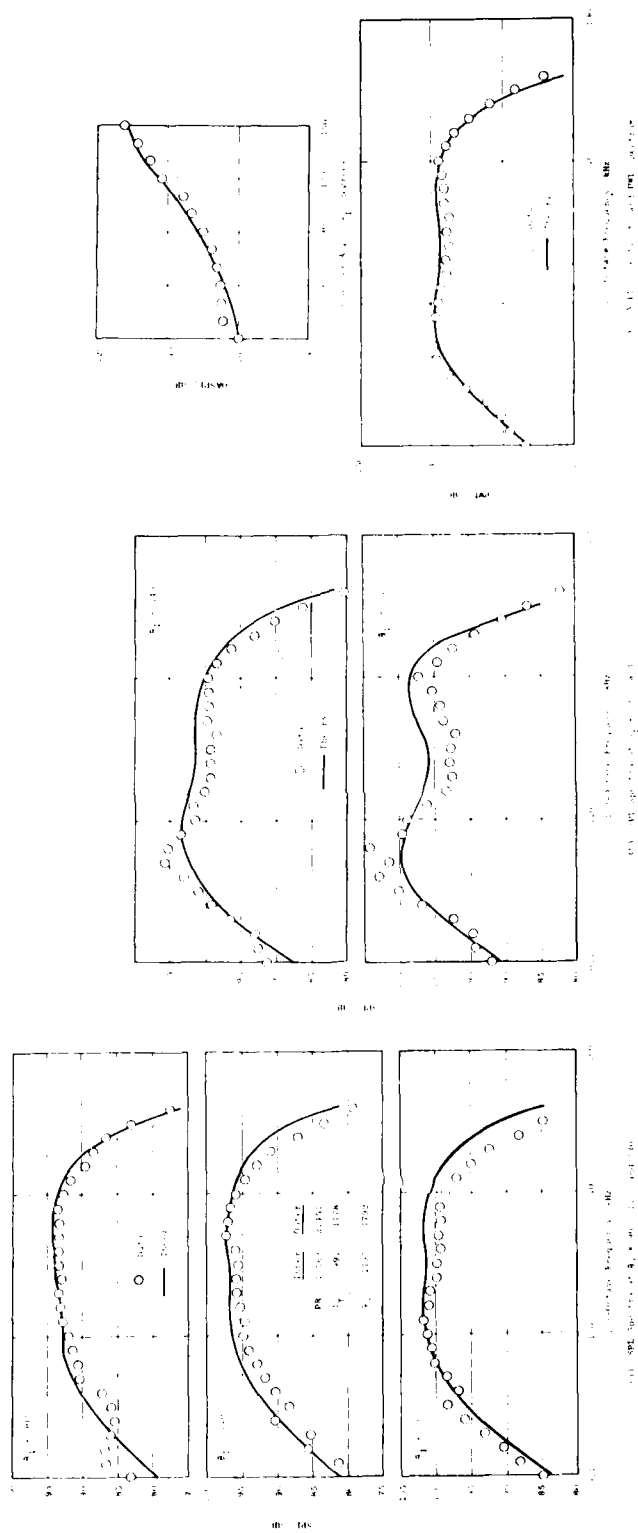
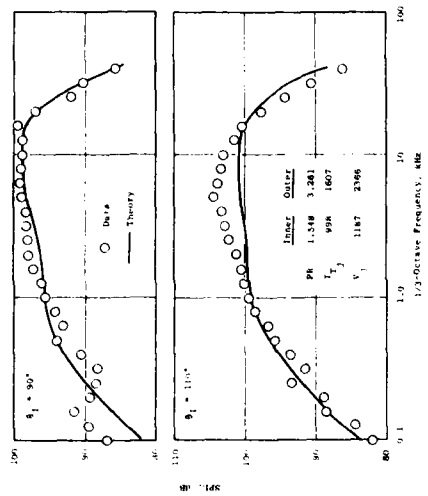
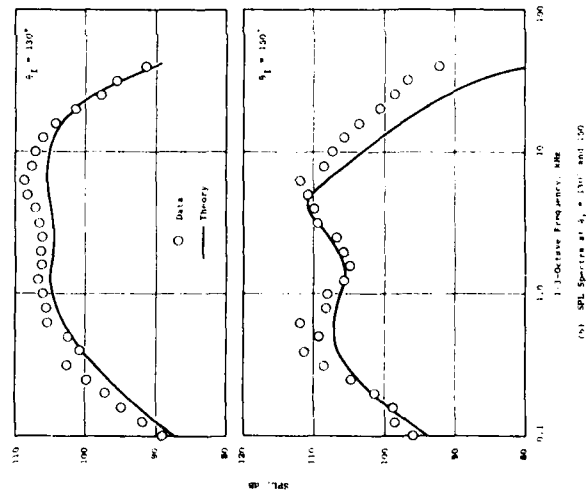


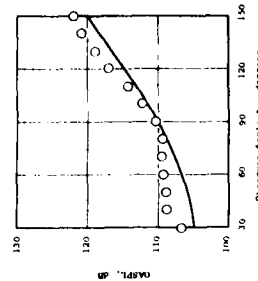
Figure 4-125. Data/Theory Comparison Case 15: Inverted Flow Coplanar Coannular Jet, $AR = 0.4$, $VR = 1.5$.



(a) SPL Spectra at $\theta_1 = 90$ and 110°



(b) SPL Spectra at $\theta_1 = 130$ and 150°



(c) OASPL Directivity and Power Spectra

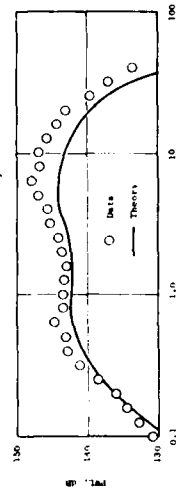


Figure 4-126. Data/Theory Comparison Case 16: Inverted Flow Coplanar Coannular Jet, $AR = 0.4$, $VR = 2.0$.

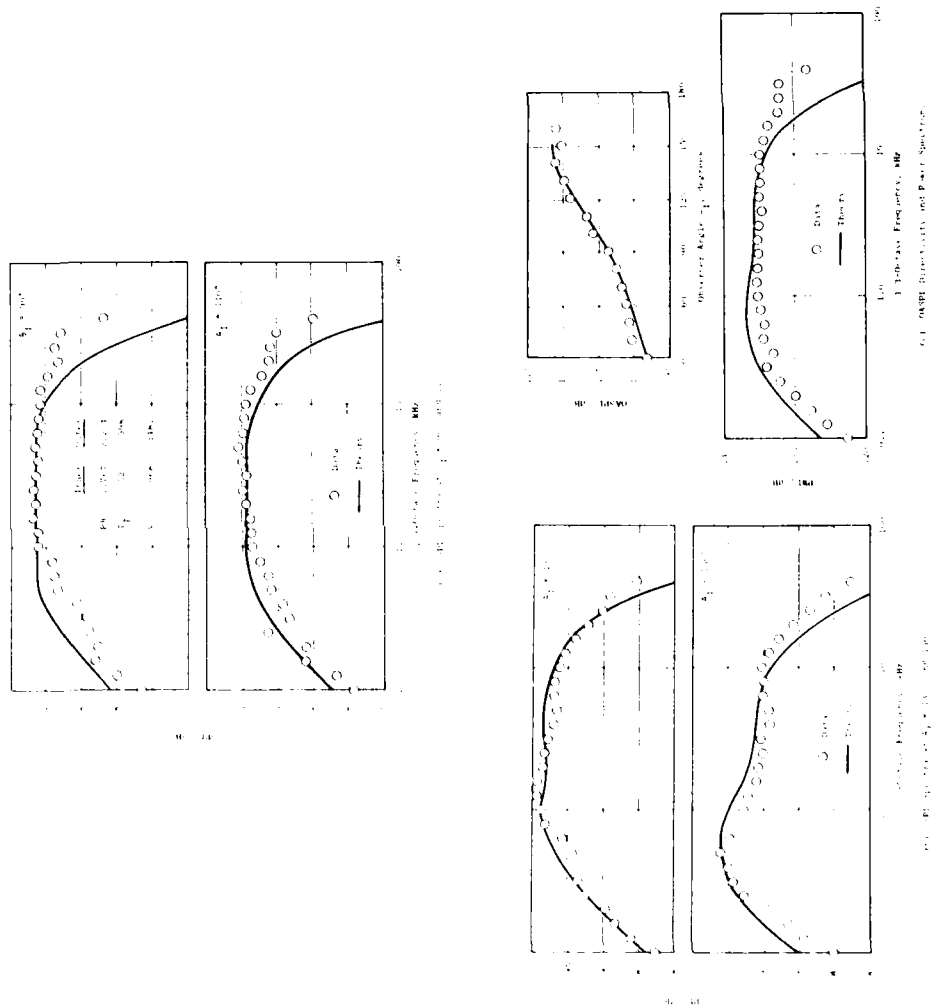


Figure 4-127. Data/Theory Comparison Case 17: Inverted Flow Coplanar Coannular Jet, $AR = 0.65$, $VR = 1.5$.

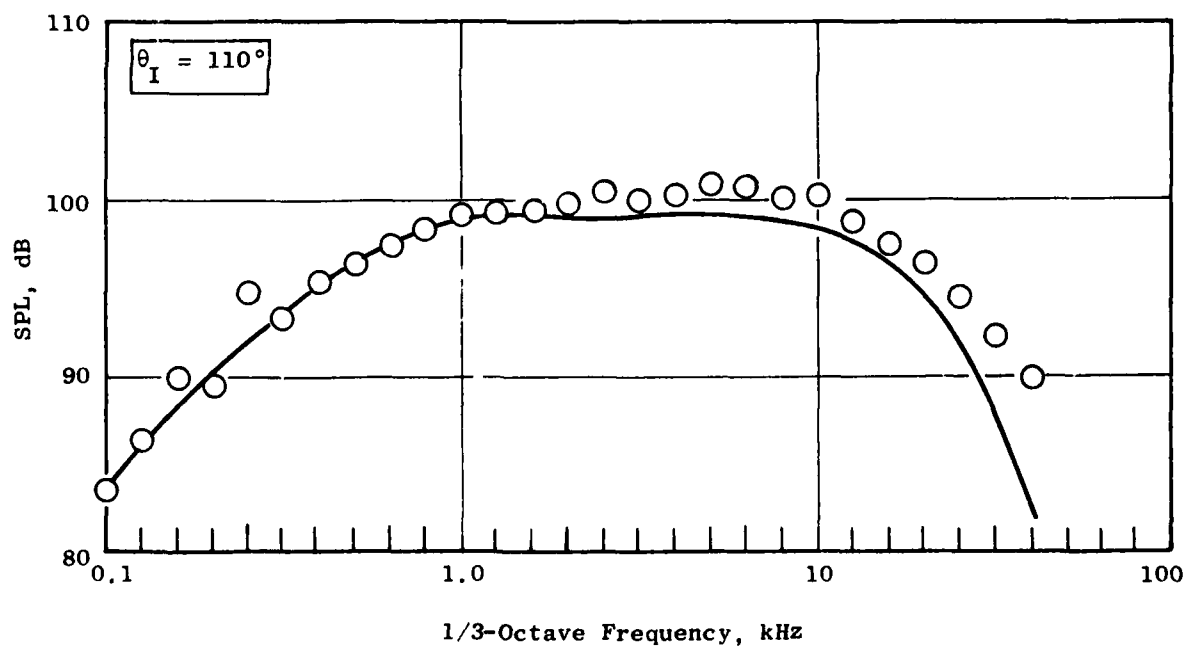
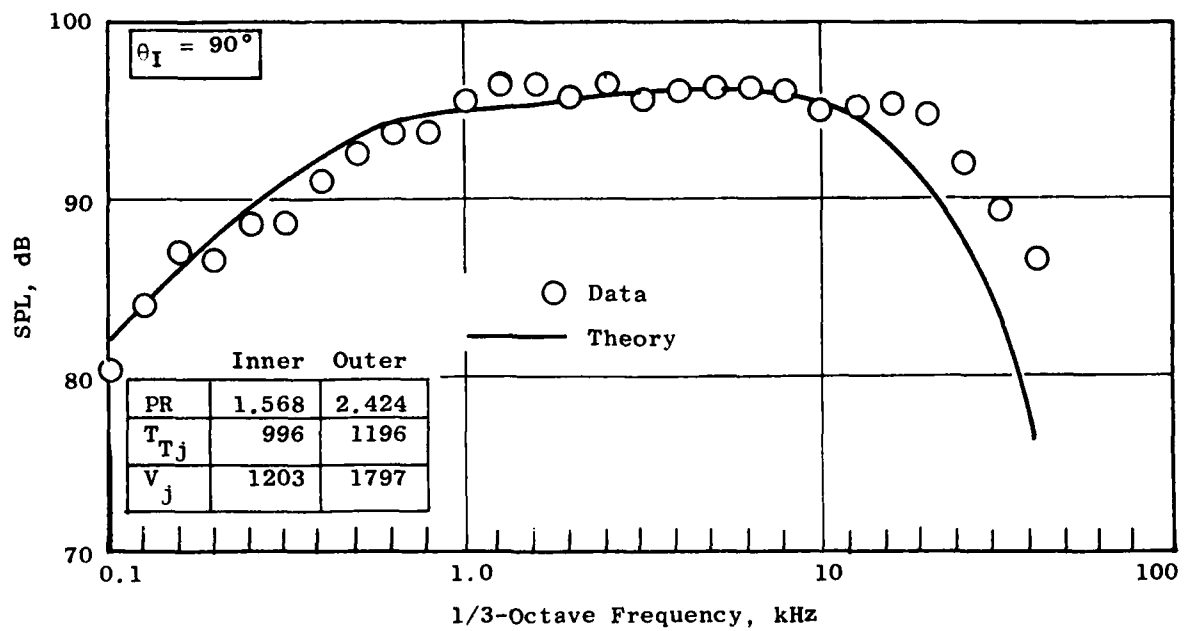


Figure 4-128. Data/Theory Comparison Case 18: Inverted Flow Coplanar Coannular Jet, $AR = 0.65$, $VR = 1.5$; (a) SPL Spectra at $\theta_I = 90^\circ$ and 110° .

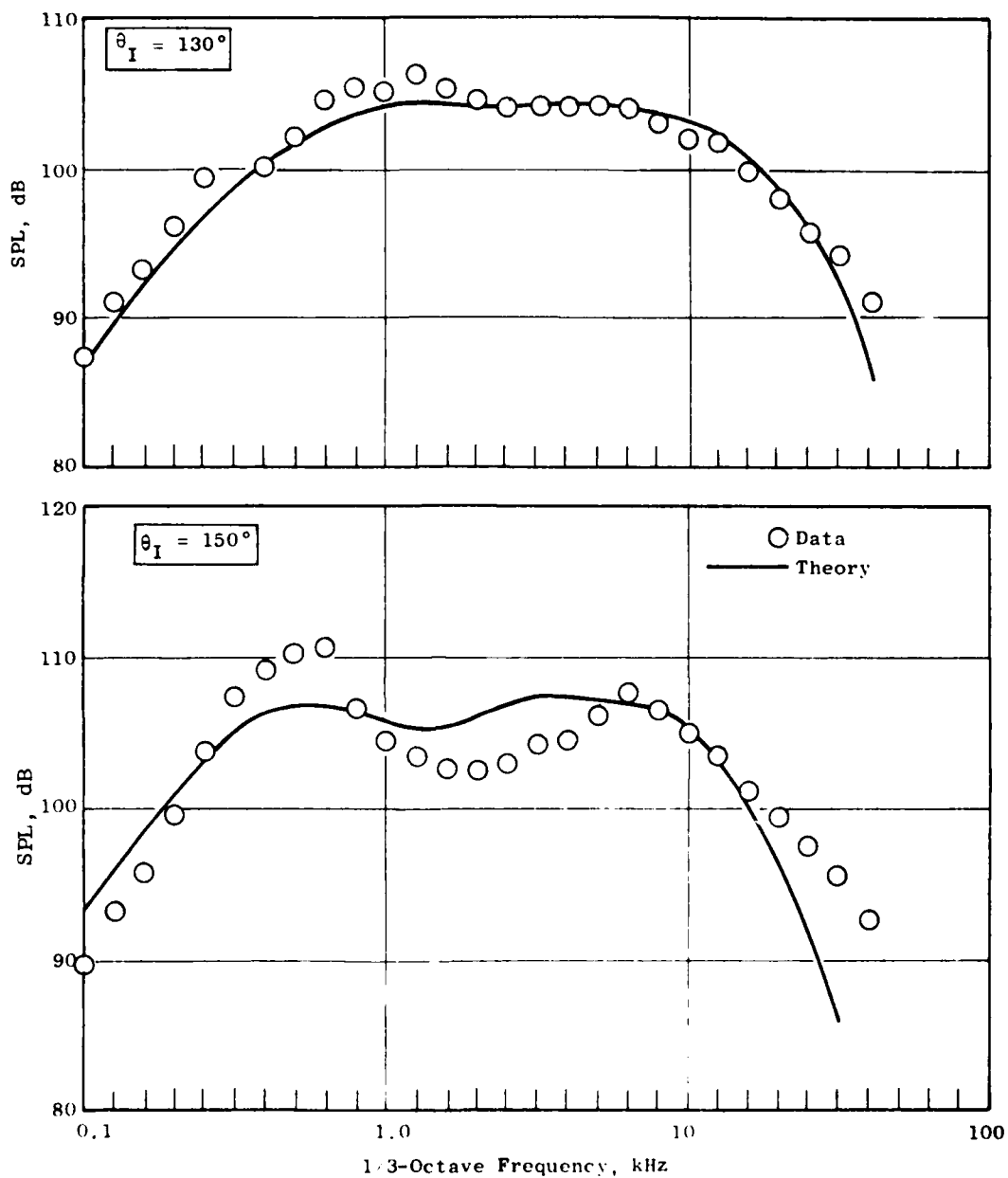


Figure 4-128. Data/Theory Comparison Case 18; Inverted Flow Coplanar Coannular Jet, AR = 0.65, VR = 1.5 (Continued); (b) SPL Spectra at $\theta_I = 130^\circ$ and 150° .

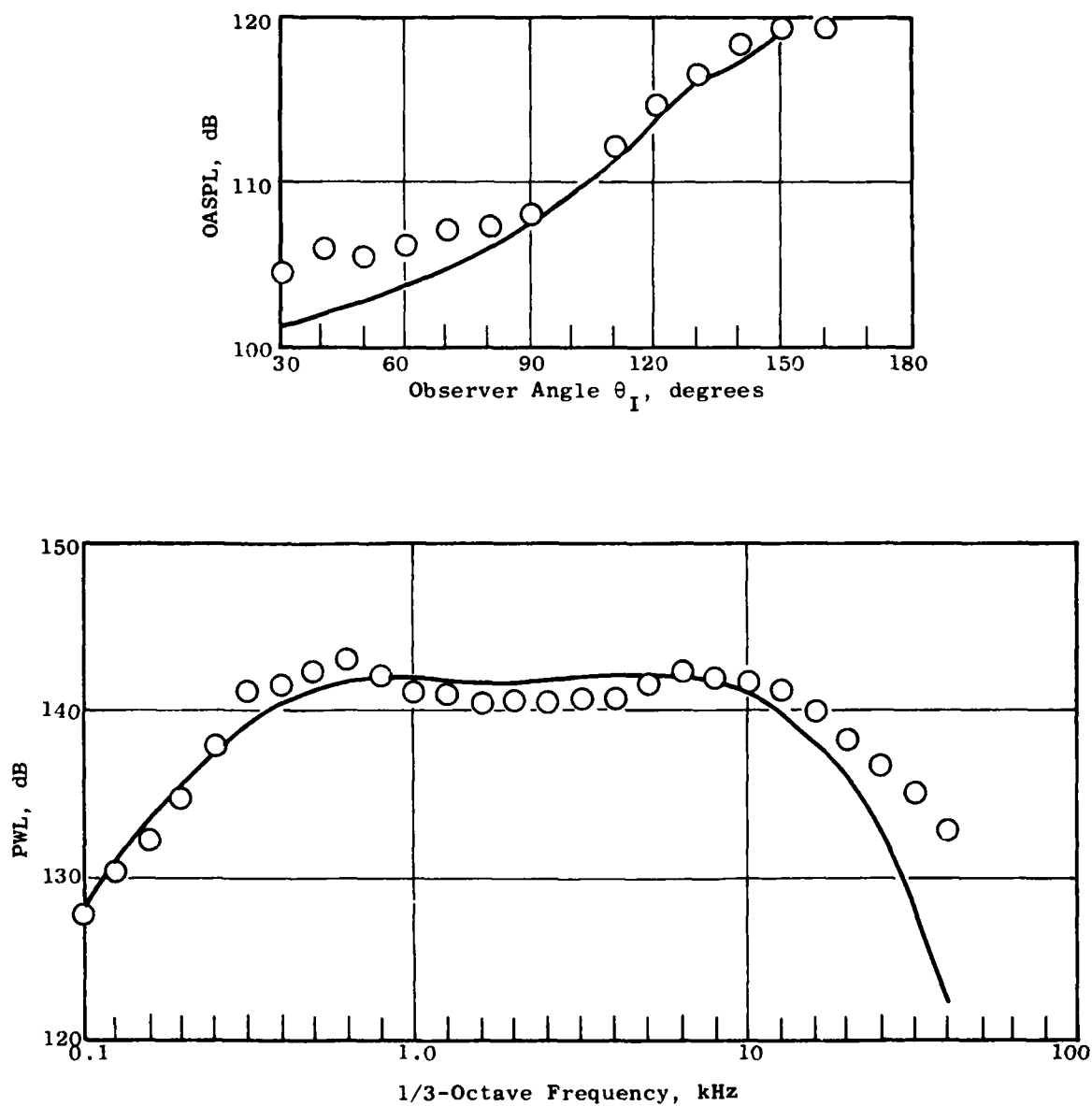


Figure 4-128. Data/Theory Comparison Case 18; Inverted Flow Coplanar Coannular Jet, AR = 0.65, VR = 1.5 (Concluded); (c) OASPL Directivity and Power Spectrum.

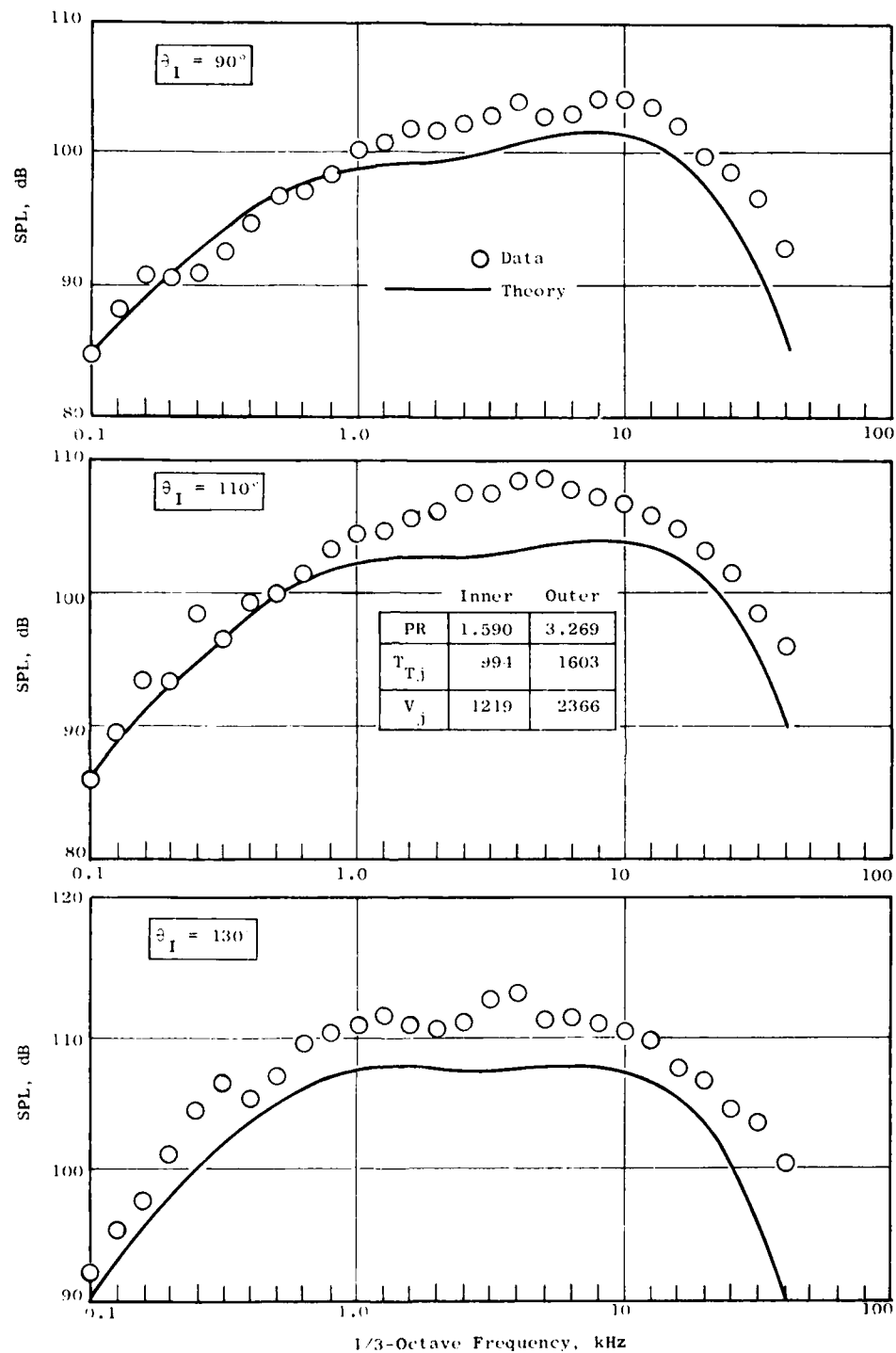


Figure 4-129. Data/Theory Comparison Case 19: Inverted Flow Coplanar Coannular Jet, $AR = 0.65$, $VR = 2.0$; (a) SPL Spectra at $\theta_I = 90^\circ$, 110° , and 130° .

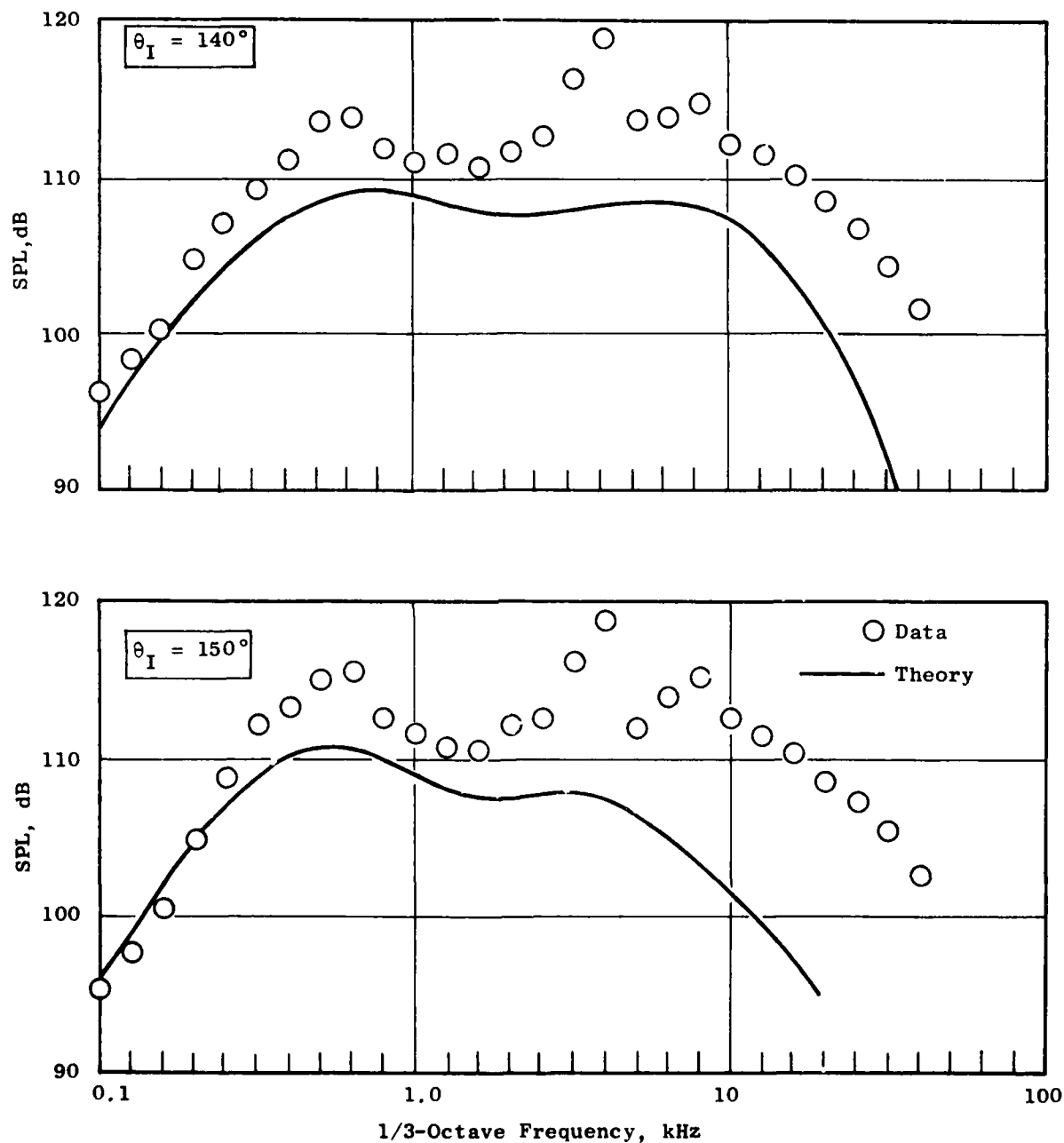


Figure 4-129. Data/Theory Comparison Case 19: Inverted Flow Coplanar Coannular Jet, AR = 0.65, VR = 2.0 (Continued); (b) SPL Spectra at $\theta_I = 140^\circ$ and 150° .

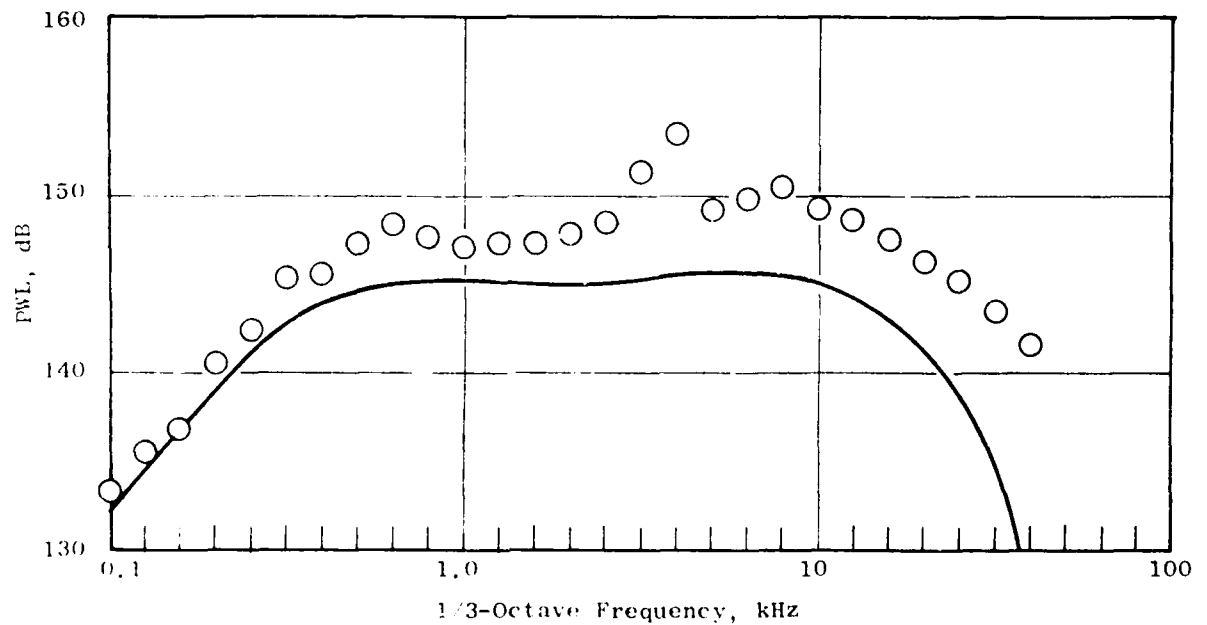
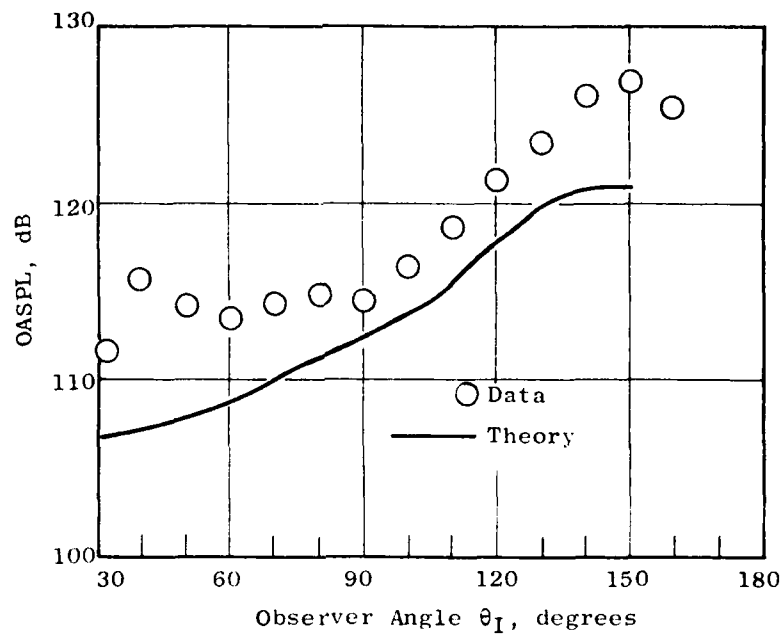
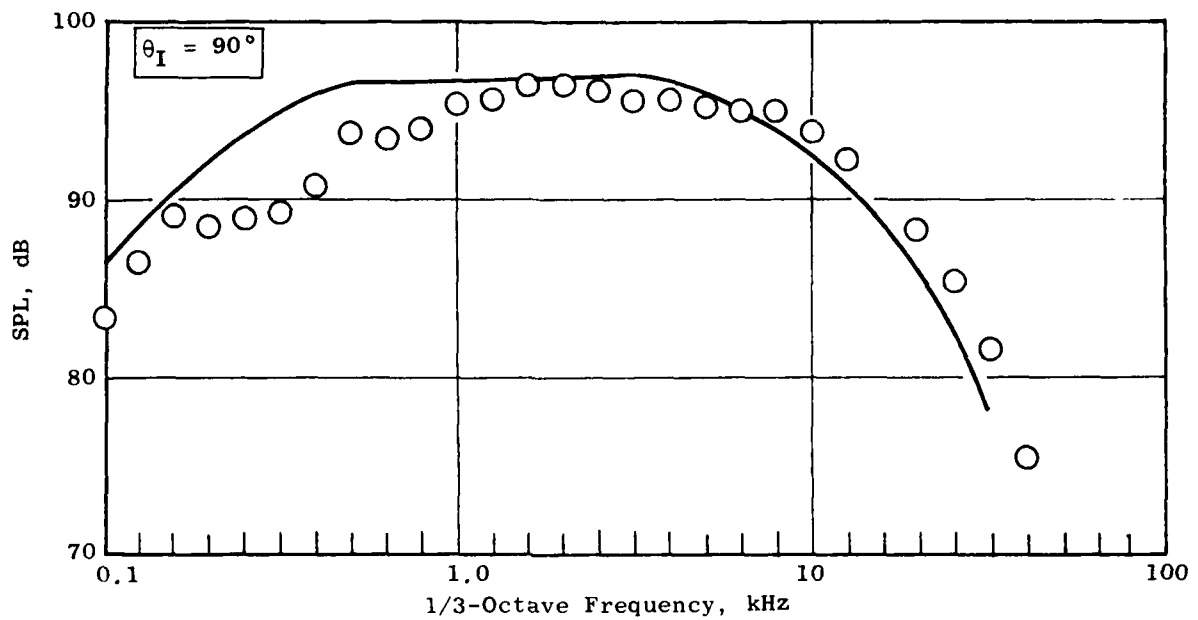


Figure 4-129. Data/Theory Comparison Case 19: Inverted Flow Coplanar Coannular Jet, AR = 0.65, VR = 2.0 (Concluded); (c) OASPL Directivity and PWL Spectrum.



	Inner	Outer
PR	1.801	2.071
T_{Tj}	561	996
V_j	1022	1500

○ Data
— Theory

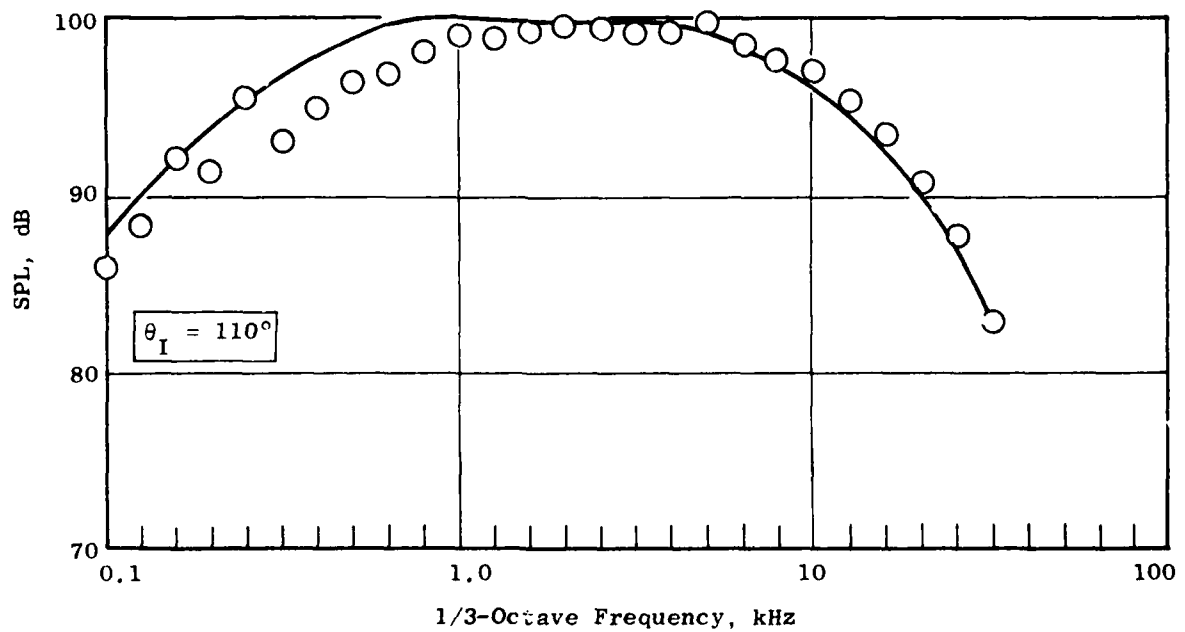


Figure 4-130. Data/Theory Comparison Case 20: Inverted Flow Coplanar Coannular Jet, AR = 2.0, VR = 1.5; (a) SPL Spectra at $\theta_I = 90^\circ$ and 110° .

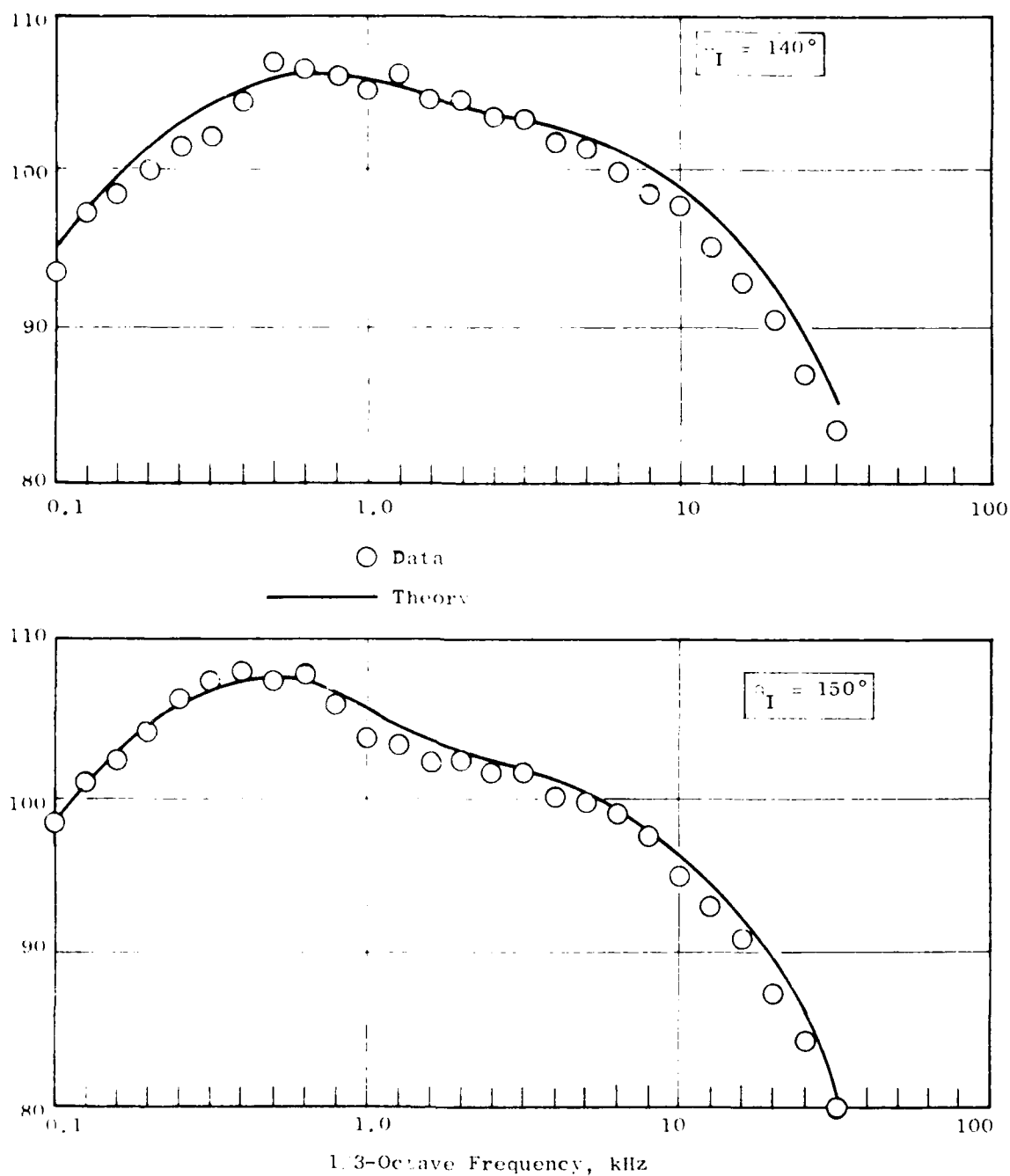
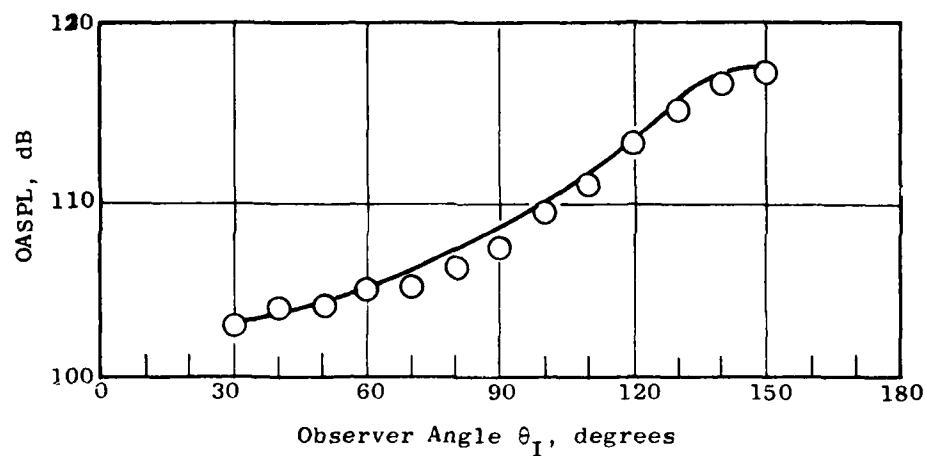


Figure 4-130. Data Theory Comparison Case 20: Inverted Flow Coplanar Coannular Jet, AR = 2.0, VR = 1.5 (Continued); (b) SPL Spectra $\theta_I = 140^\circ$ and 150° .



○ Data
 — Theory

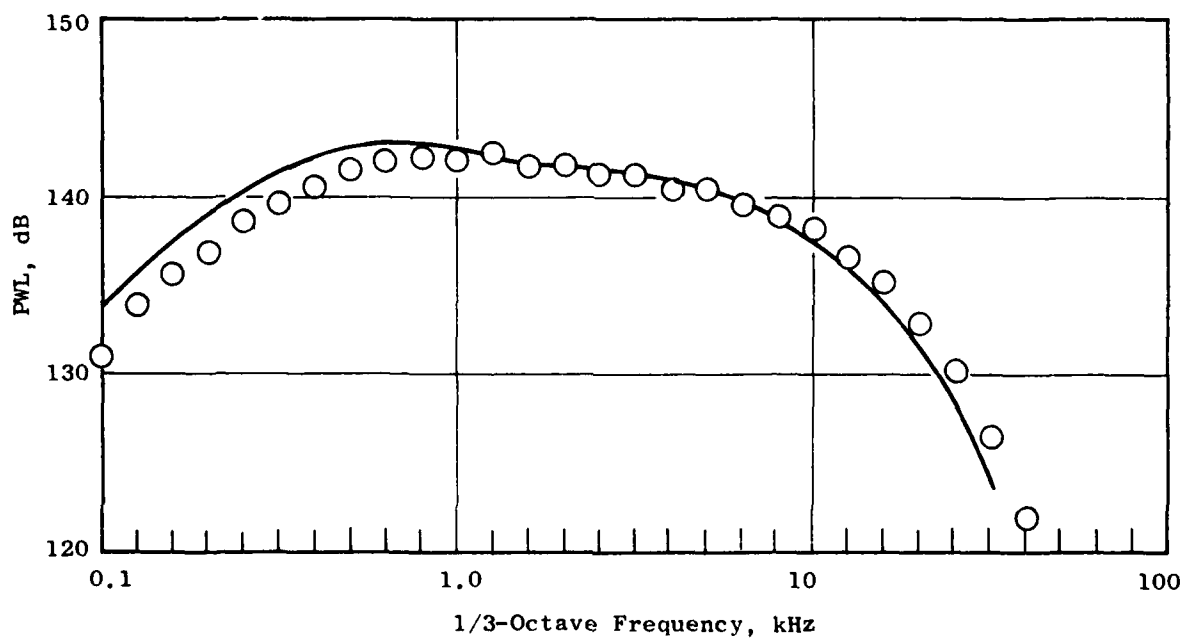


Figure 4-130. Data/Theory Comparison Case 20: Inverted Flow Coplanar Coannular Jet, AR = 2.0, VR = 1.5 (Concluded); (c) OASPL Directivity and PWL Spectrum.

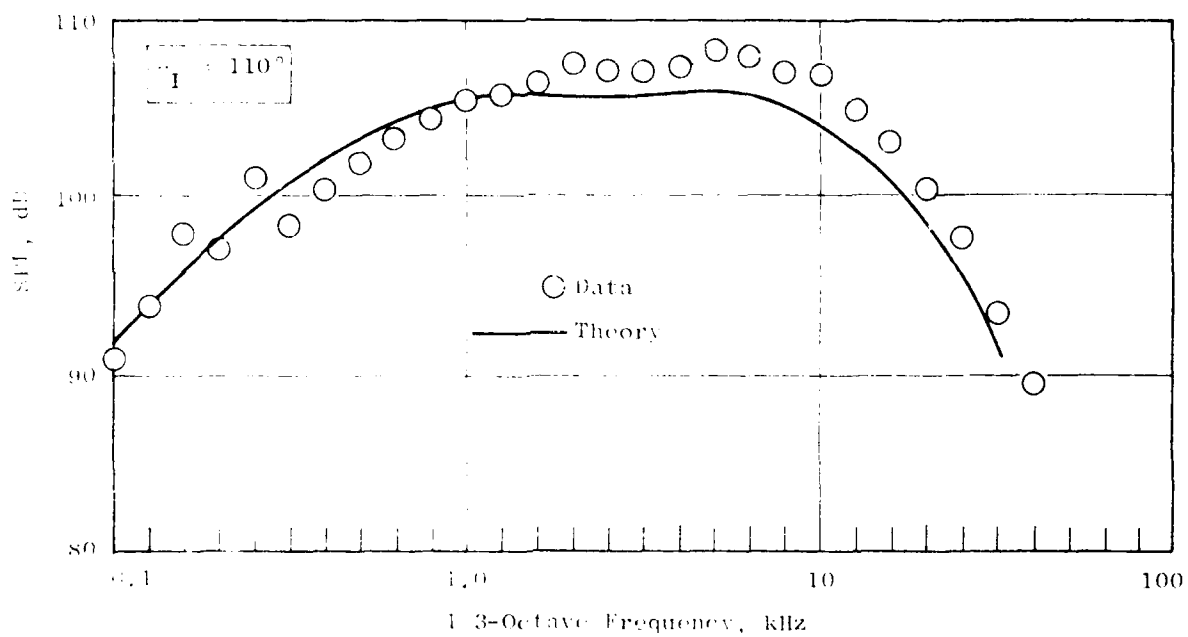
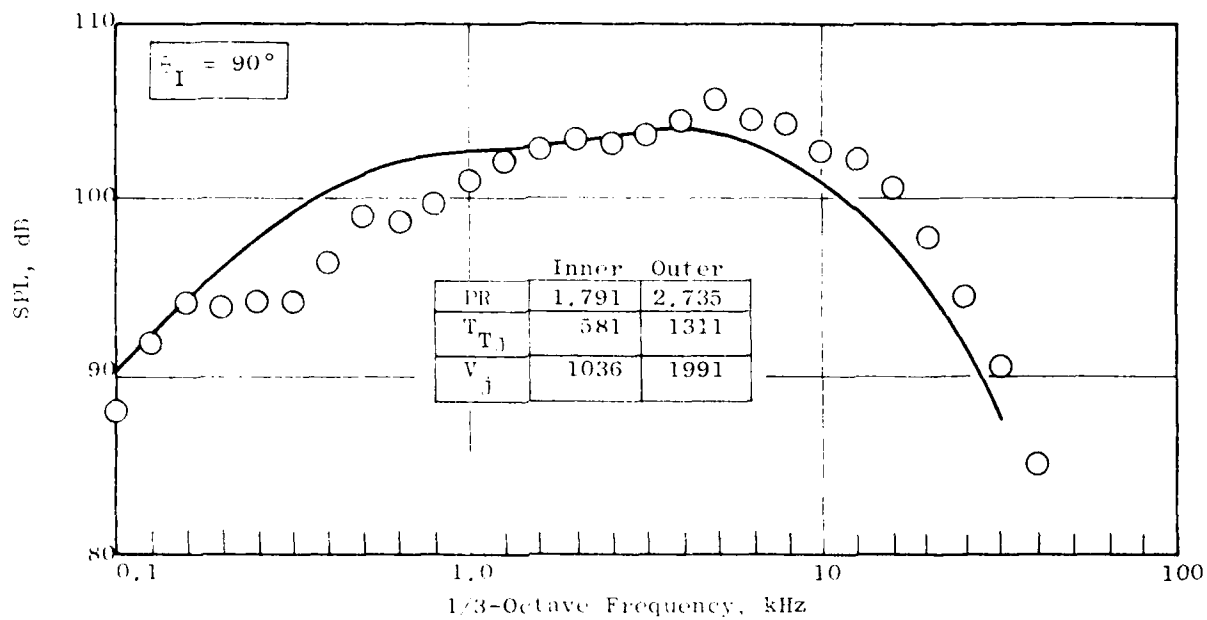


Figure 4-131. Data Theory Comparison Case 21: Inverted Flow Coplanar Coannular Jet, AR = 2.0, VR = 2.0; (a) SPL Spectra at $\theta_I = 90^\circ$ and 110°

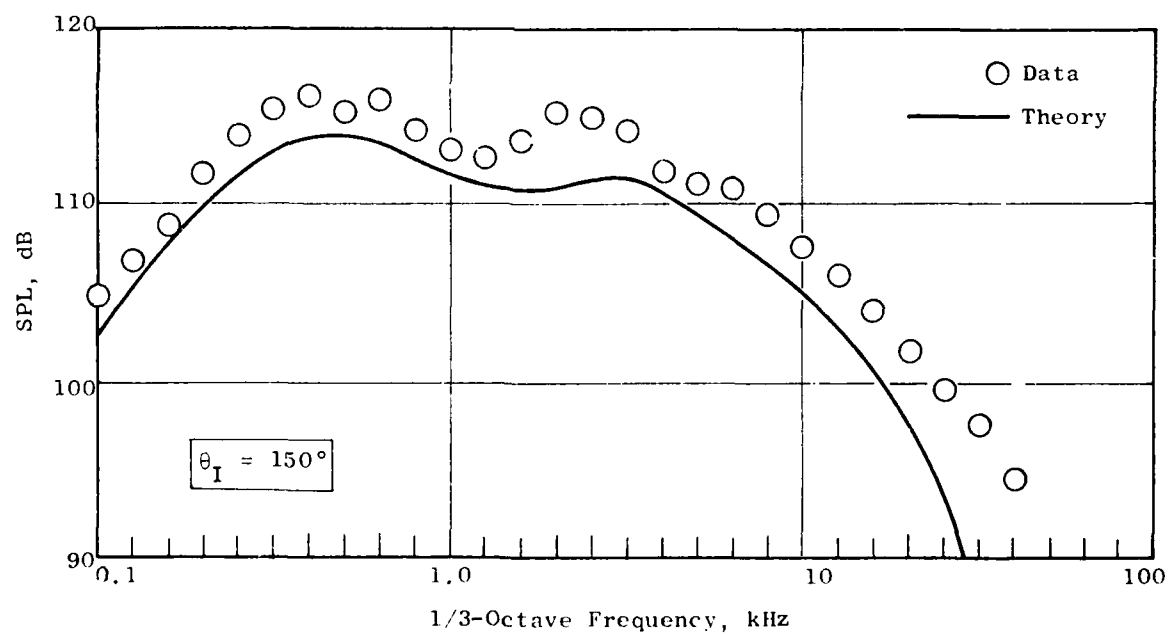
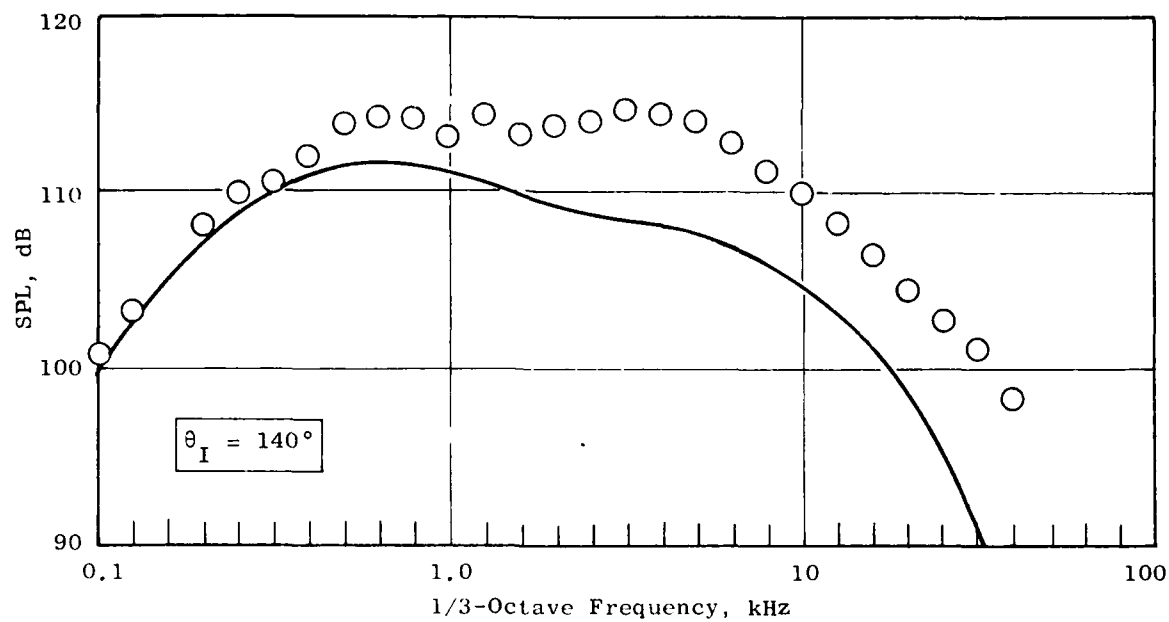


Figure 4-131. Data/Theory Comparison Case 21: Inverted Flow Coplanar Coannular Jet, AR = 2.0, VR = 2.0 (Continued); (b) SPL Spectra at $\theta_I = 140^\circ$ and 150° .

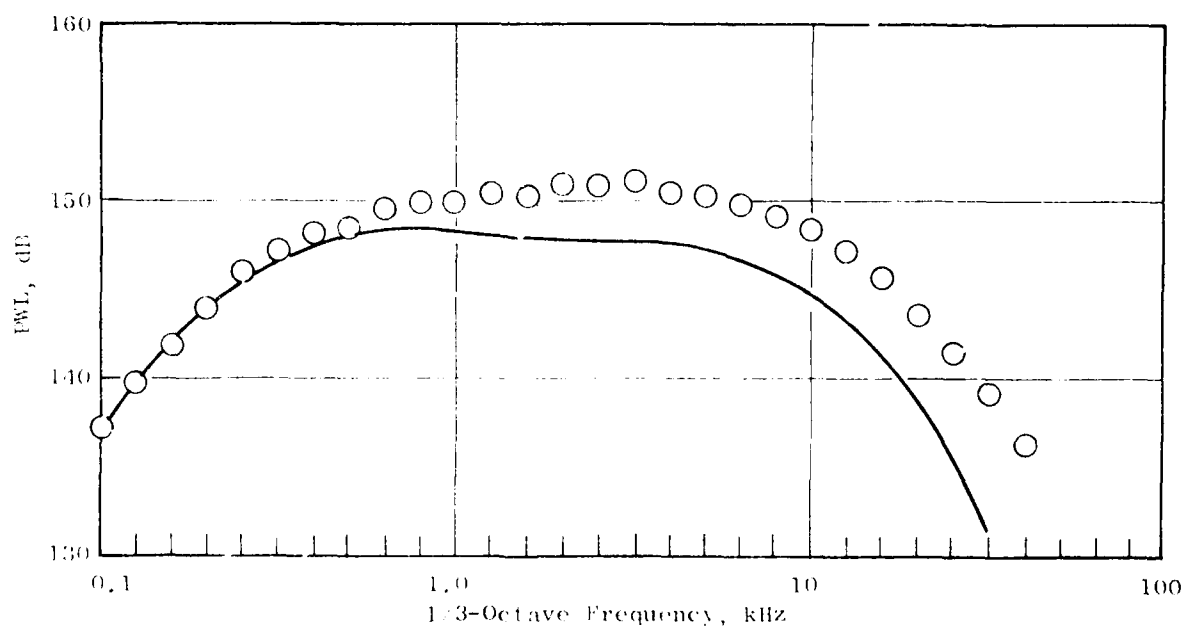
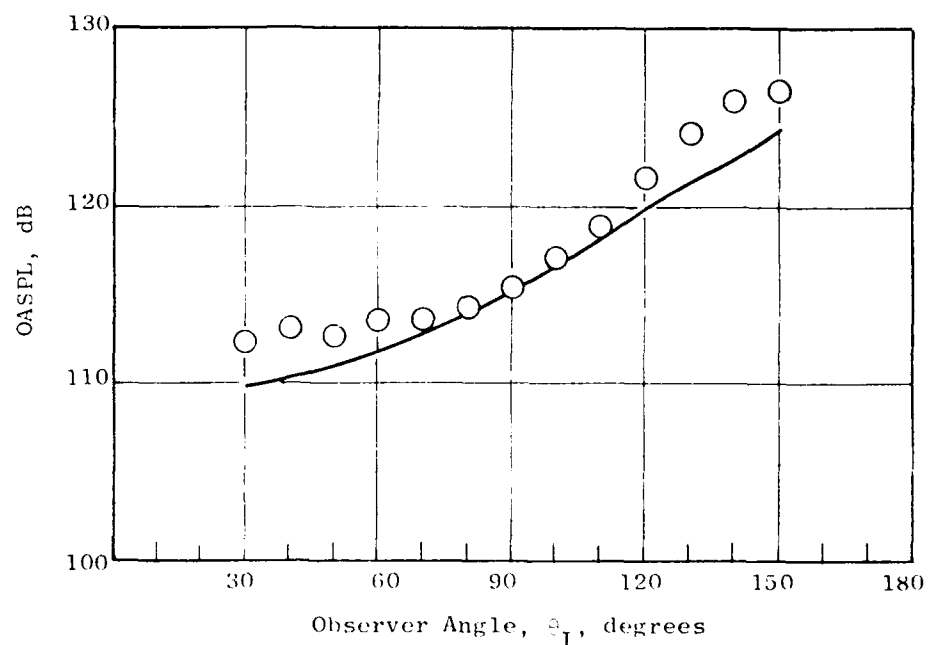


Figure 4-131. Data Theory Comparison Case 21: Inverted Flow Coplanar Coannular Jet, AR = 2.0, VR = 2.0 (Concluded); (c) OASPL Directivity and Power Spectrum.

In order to understand the reasons for the difficulties encountered in matching the data at angles close to the jet axis, detailed diagnostic studies and computations were undertaken. The noise contributed by each "slice-of-jet" to the total noise signature was determined for one test point, and further diagnostic computations, to break down the contributions of each radial volume element, were made for those axial slices found to be dominant. It was found that the noise at angles close to the jet axis is dominated by radiation from a small region around the fan stream potential core tip, approximately 1 to 2 diameters (based on fan equivalent area) downstream of the nozzle exit plane. The low frequency spectral peak apparently arises from the rapid axial diffusion along the centerline of the fan stream after the potential core. The high frequency peak results from the large convective effects produced in this region by eddies traveling at the Mach wave condition relative to the observer.

In order to achieve the correct balance between convection, shielding, and source strength for those volume elements in this region, it is necessary to set $\beta_t = 0$ for those axial stations upstream of $x = 10 D_{eq}$. This results in too low a level for the high-frequency end of the spectrum, and, therefore, the levels of u' are arbitrarily raised by 10% to offset this effect whenever $\beta_t = 0$.

The above interim modification is a somewhat crude way of deleting physically unrealistic noise sources from the model output. The problem arises with those eddy volumes which have rapid axial diffusion (i.e., large τ_x) but no significant radial shear stress (i.e., $\tau_r \sim 0$). Thus u' is large according to equation (318), and the characteristic time-delay τ_0 , is infinite according to equations (319) and (320). Since the characteristic frequency is proportional to the reciprocal of τ_0 this implies that the eddy radiates at high intensity and almost zero frequency. Due to the large doppler factor (Mach wave condition), this high intensity noise is shifted into the observed frequency range at even higher intensity.

Several alternative techniques for improving the aft-angle spectrum predictions have been explored. These included the following:

1. Skipping those eddies which are radiating at the Mach wave condition,
2. Smoothing of the convection factor radial distribution in the vicinity of the eddies at the Mach wave condition,
3. Adding an axial gradient component to the dominant frequency (time constant) calculation,
4. Modifying the doppler factor constant α_t .

All of these (except 2) have some beneficial effect, but sometimes produce undesirable side effects, and the effects of one modification sometimes depend on the presence or absence of the others. The technique of setting $\beta_t = 0$ and raising u' by 10% for $x < 10 D_{eq}$ works better than any of these

alternative methods, is simple to implement, and is equally effective for any of the combinations of AR and VR examined. The modification has virtually no effect on either conventional bypass coaxial jet or conical nozzle jet predictions, and has been found to be equally effective (and necessary) for multielement nozzle predictions. A more sophisticated analytical method for handling this problem is a worthwhile goal of future model development efforts.

The data - theory comparisons for a staggered exit, dual-flow plug nozzle (typical of advanced supersonic transport engine systems) are shown in Figures 4-132 and 4-133, corresponding to cases 27 and 28, respectively. Again, the agreement between prediction and experiment is satisfactory, demonstrating the capability of the model to handle dual-flow systems with inner shrouds and centerbodies.

The remaining cases (24 - 39) represent multielement suppressor configurations of various shapes, sizes, and degrees of complexity. In general, the data - theory comparisons presented in Figures 4-134 through 4-141 for these cases show reasonable agreement, with only a few isolated discrepancies of any consequence.

There is some difficulty with the model in predicting the correct spectrum shape at angles close to the jet axis ($\theta_j = 130^\circ$) for multielement configurations. The double-peak characteristic shape is not always predicted in the correct balance, i.e., the low frequency peak is too high and the high frequency peak is too low or vice-versa. This difficulty is thought to be a consequence of neglecting base-pressure effects in the aerodynamic calculation. There is also evidence that, for multielement nozzles, a vortex-shedding type of excess noise source exists which contaminates the measured jet noise spectrum, particularly at the lower jet velocities. The aero-acoustic prediction model does not account for these excess noise sources, and therefore underpredicts the observed noise levels at low jet velocities. Future model developments should require extensions to include both base-pressure effects and excess noise sources.

4.7.9 Diagnostic Evaluation of Jet Noise Suppression Mechanisms

Based on the successes achieved in predicting the aerodynamic and acoustic characteristics of single- and dual-flow nozzles discussed in Section 4.7.5, it is worthwhile to utilize the theory to analyze the noise suppression mechanisms of conical nozzles. The question of how flow inversion (ducting the high velocity hot stream to the outside) can provide noise benefits for dual-flow exhaust systems is of particular interest.

Theoretical predictions were made for both a conventional bypass and an inverted-flow conical nozzle where the nozzles were sized to give the same thrust, equal primary (high velocity) flow areas, and the same secondary (low velocity) flow areas. The two nozzles, therefore, have equivalent thrust, mass flow, primary and secondary stream velocities, and temperatures; the differences in noise should therefore be solely a function of jet plume

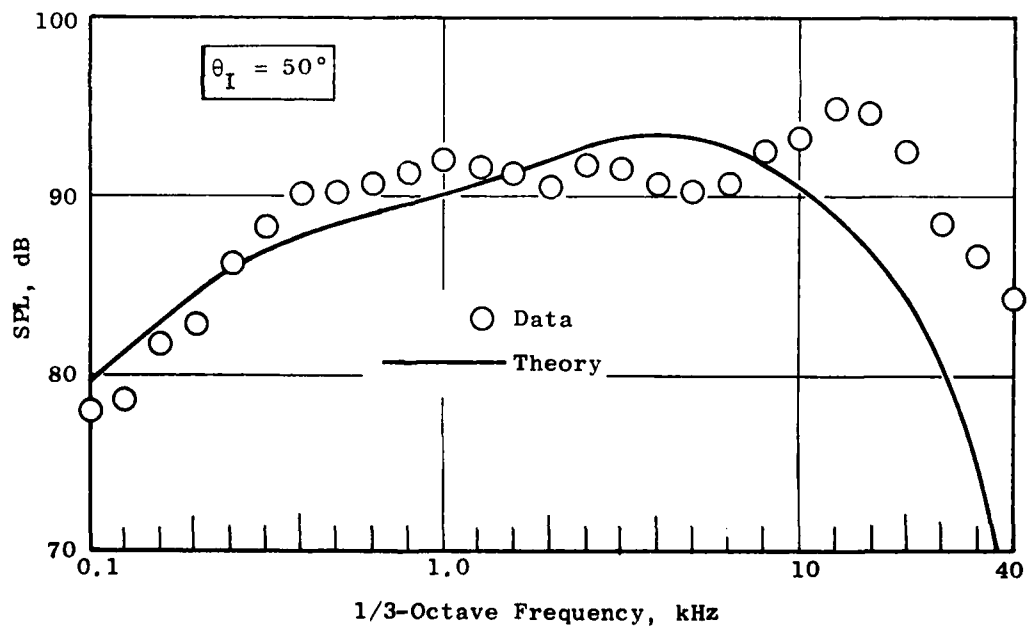
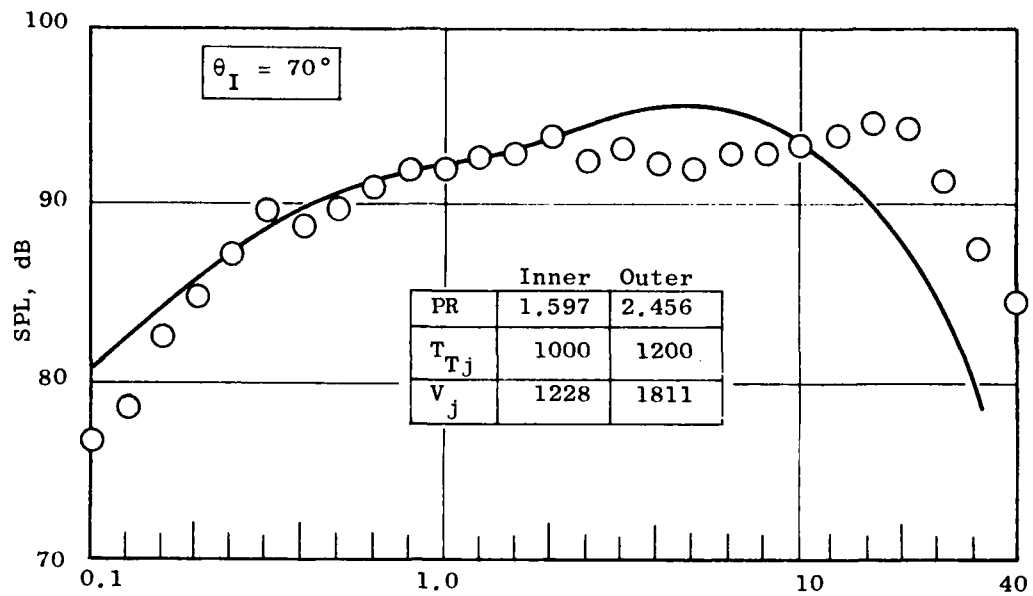


Figure 4-132. Data/Theory Comparison Case 22: Inverted Flow Coannular Plug Nozzle, AR = 0.65, VR = 1.5; (a) SPL Spectra at $\theta_I = 50^\circ$ and 70° .

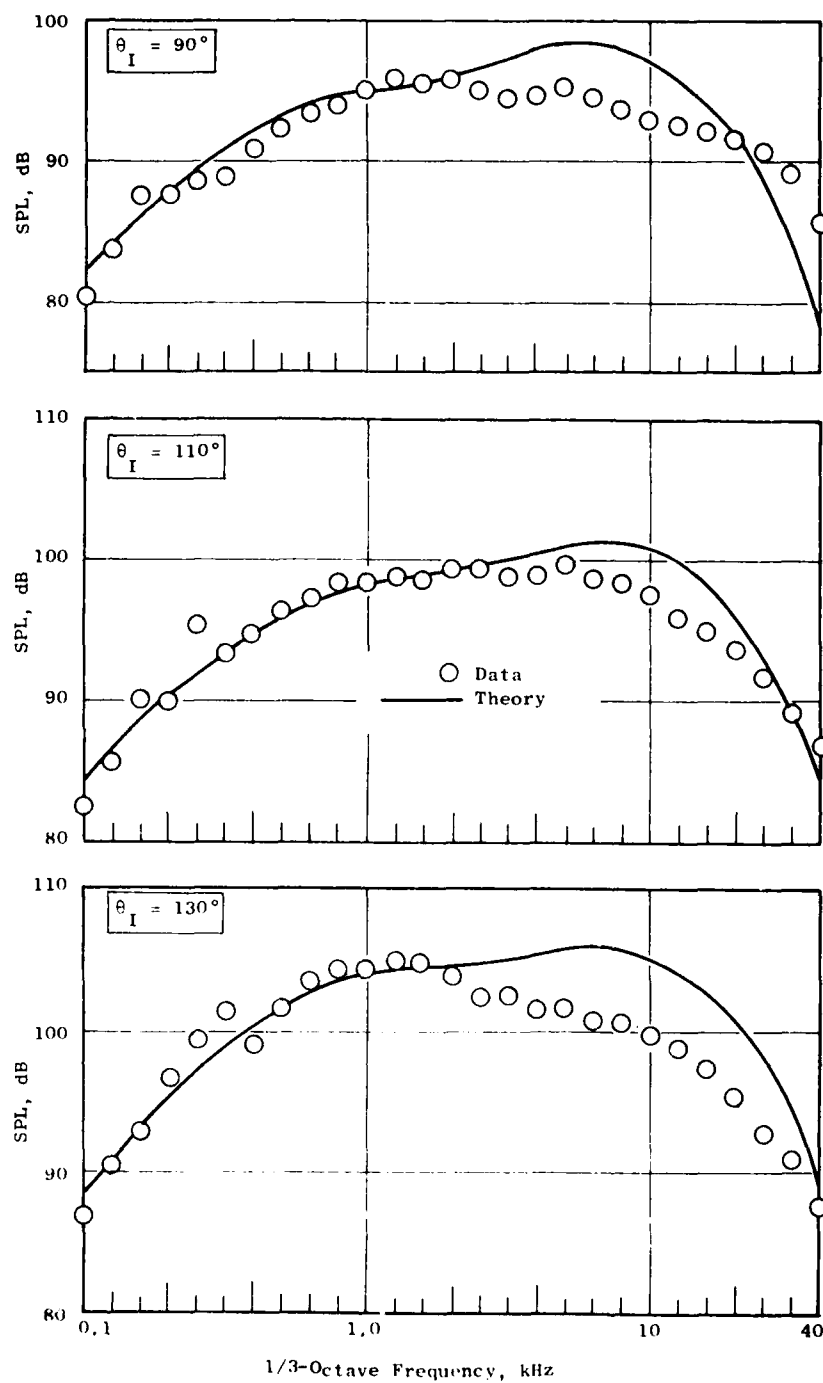


Figure 4-132. Data/Theory Comparison Case 22: Inverted-Flow Coannular Plug Nozzle, AR = 0.65, VR = 1.5 (Continued); (b) SPL Spectra at $\theta_I = 90^\circ$, 110° and 130° .

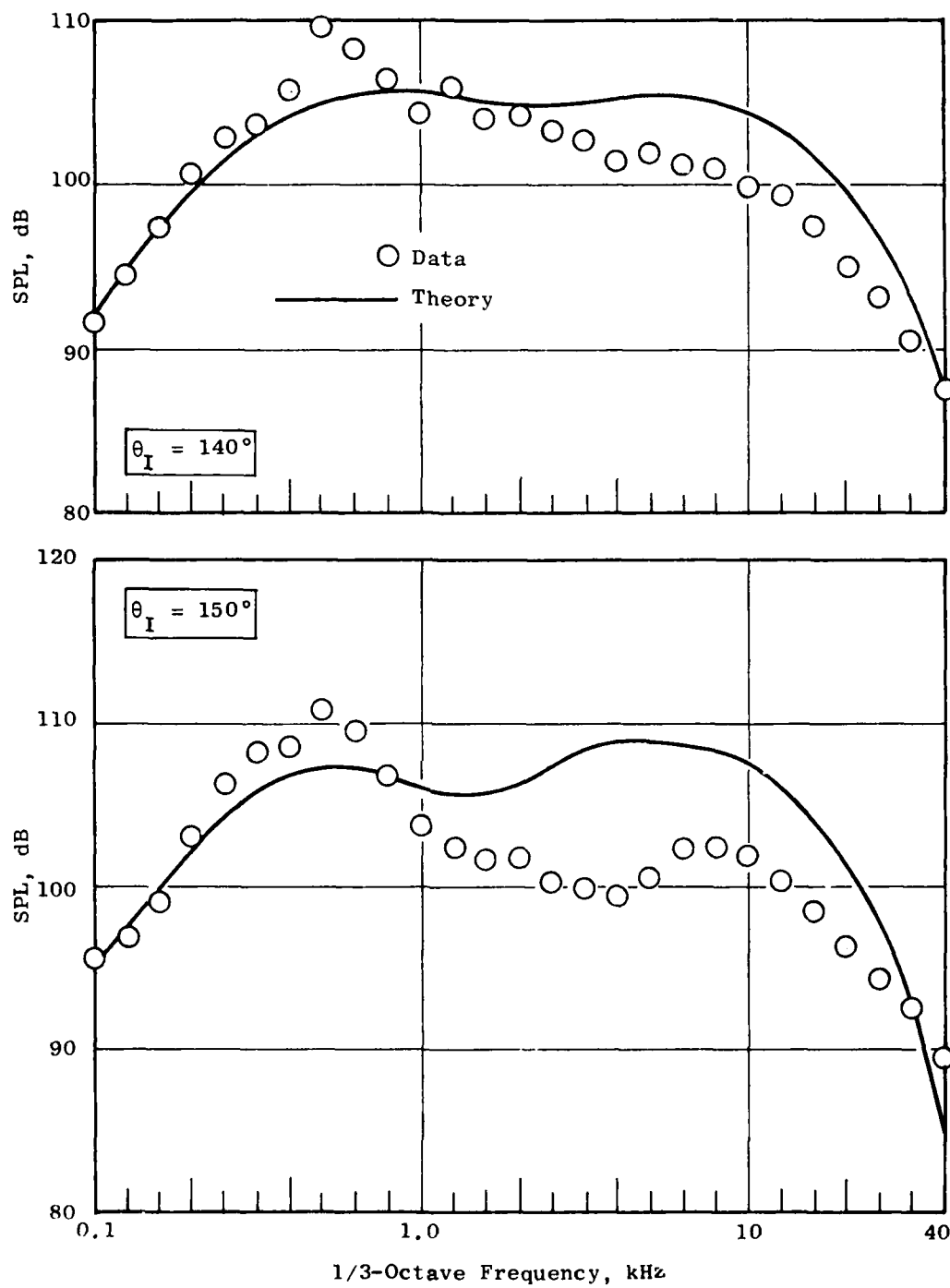


Figure 4-132. Data/Theory Comparison Case 22: Inverted-Flow Coannular Plug Nozzle, AR = 0.65, VR = 1.5 (Continued); (c) SPL Spectra at $\theta_I = 140^\circ$ and 150° .

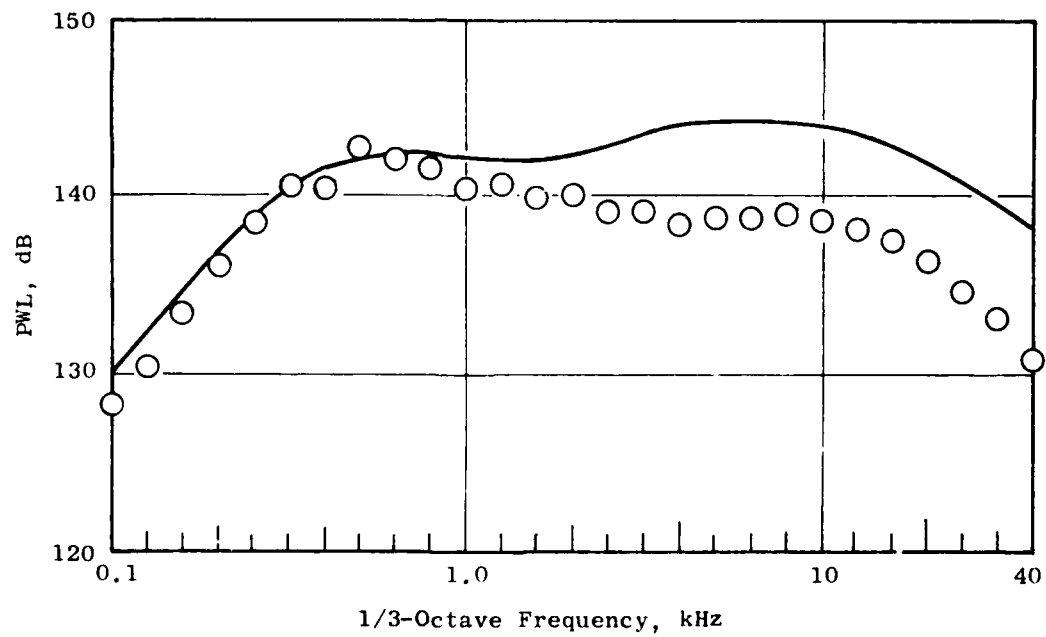
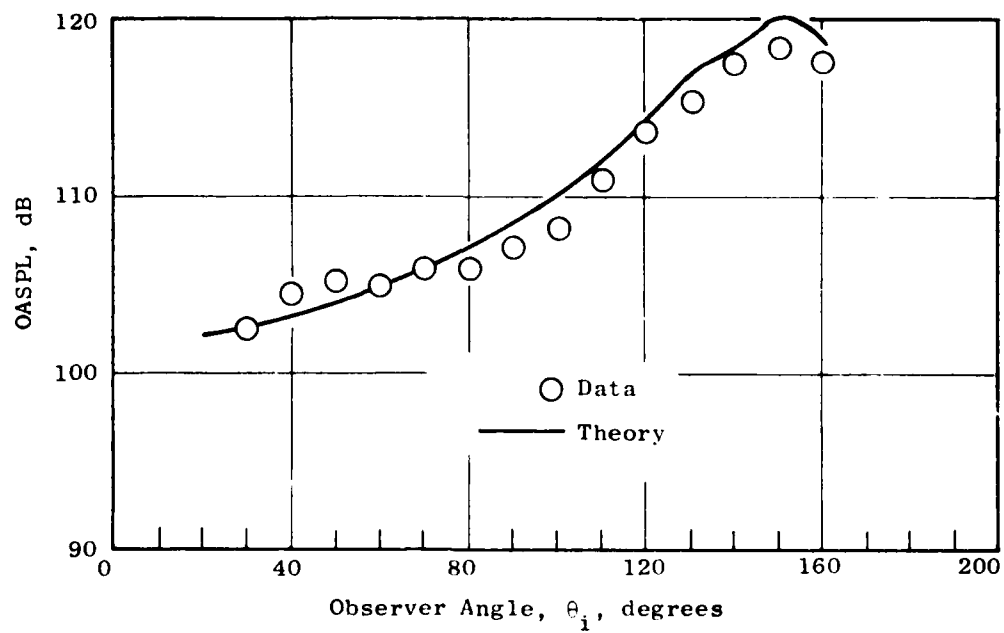


Figure 4-132. Data/Theory Comparison Case 22: Inverted-Flow Caonnular Plug Nozzle, AR = 0.65, VR = 1.5 (Concluded); (d) OASPL Directivity and Power Spectrum.

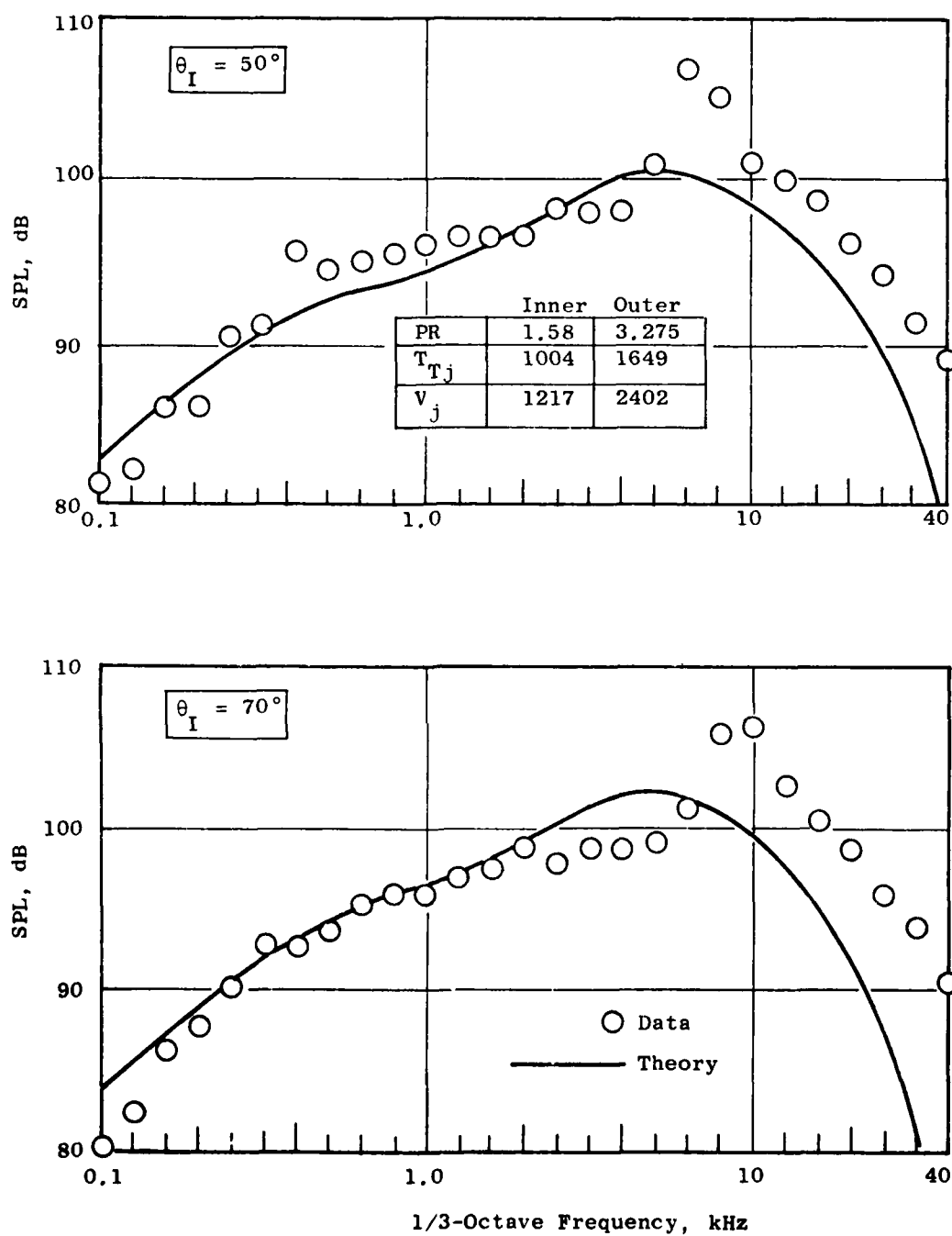


Figure 4-133. Data/Theory Comparison Case 23: Inverted-Flow Co-annular Plug Nozzle, AR = 0.65, VR = 2.0; (a) SPL Spectra at $\theta_I = 50^\circ$ and 70° .

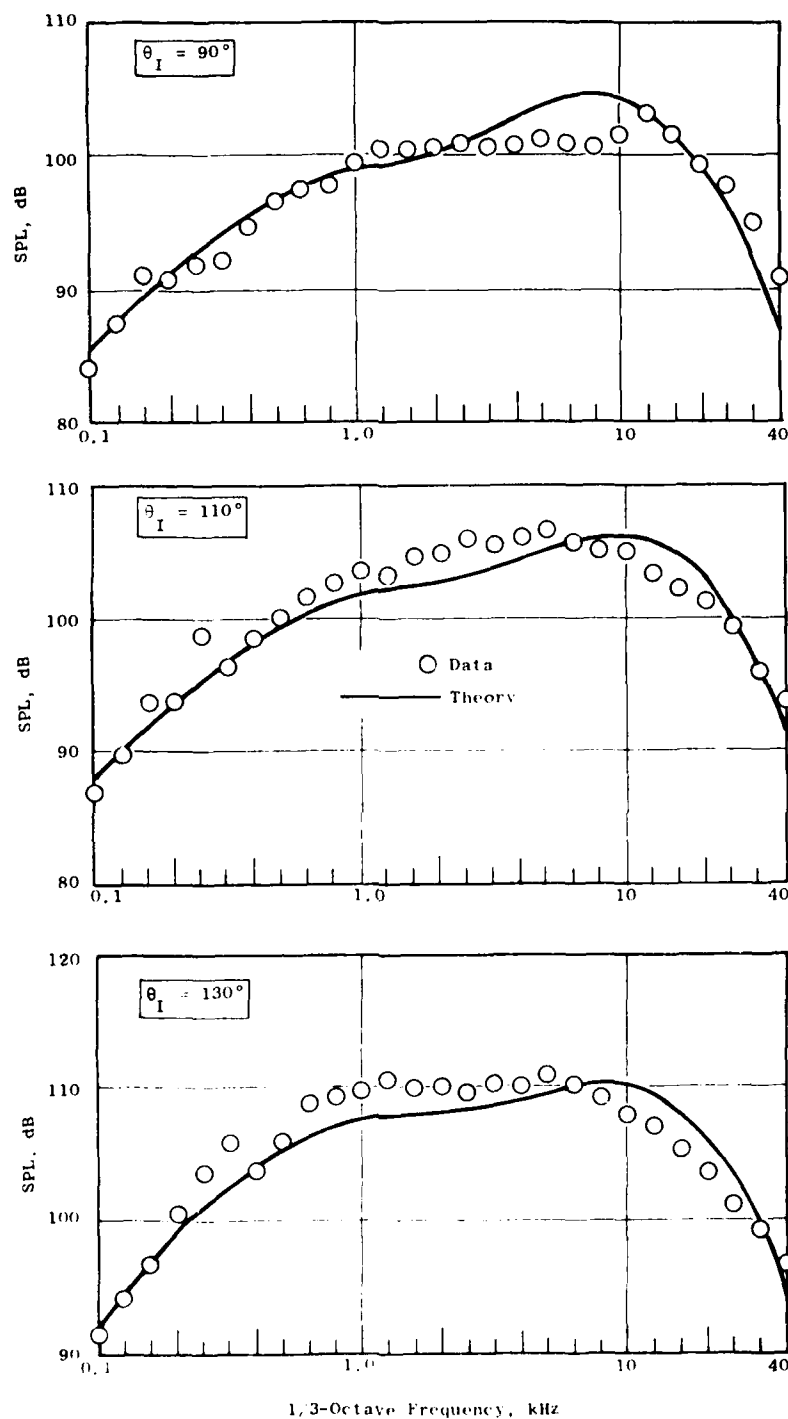


Figure 4-133. Data/Theory Comparison Case 23: Inverted-Flow Coannular Plug Nozzle, AR = 0.65, VR = 2.0 (Continued); (b) SPL Spectra at $\theta_I = 90^\circ$, 110° and 130° .

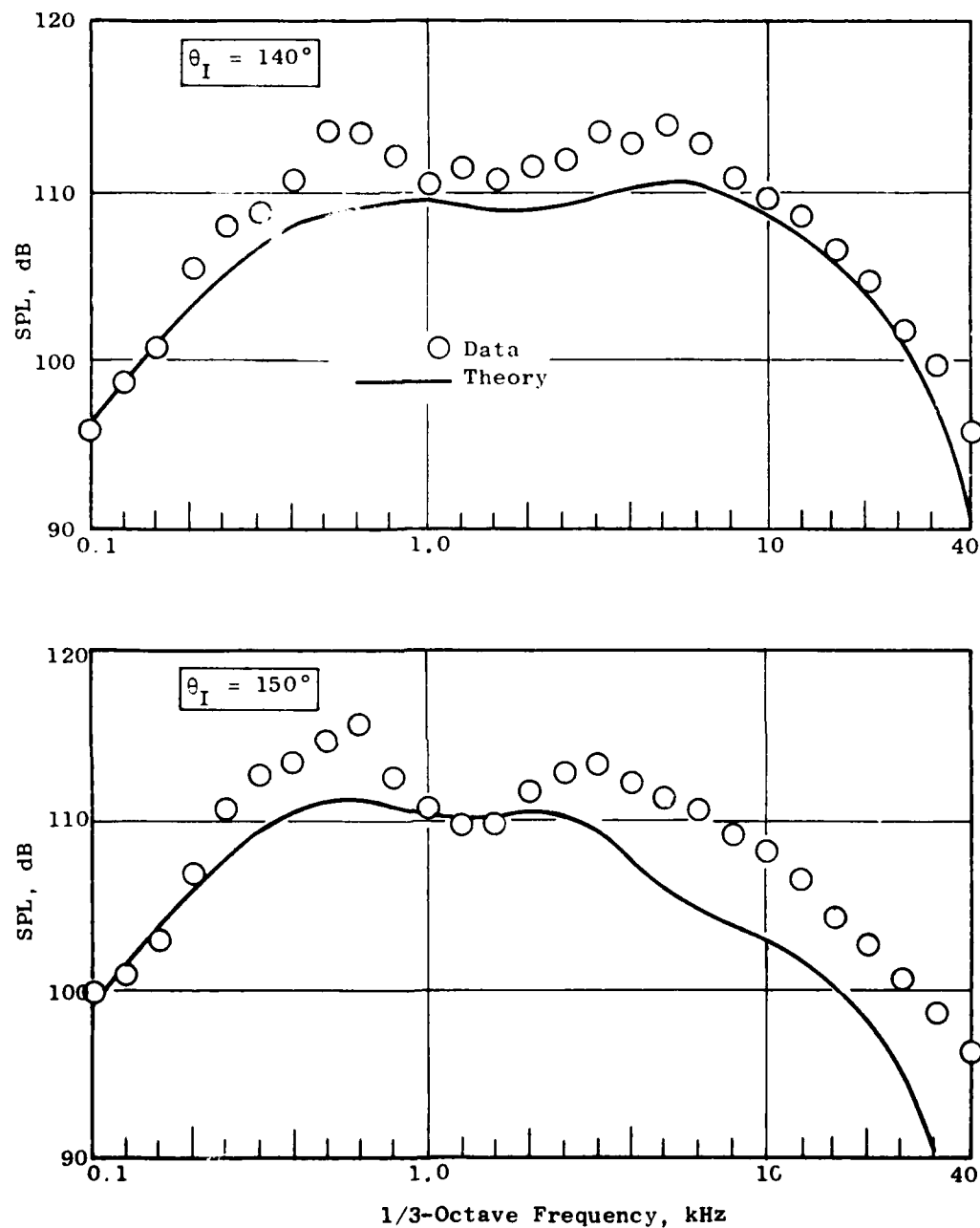


Figure 4-133. Data/Theory Comparison Case 23: Inverted Flow Coannular Plug Nozzle, AR = 0.65, VR = 2.0 (Continued); (c) SPL Spectra at $\theta_I = 140^\circ$ and 150° .

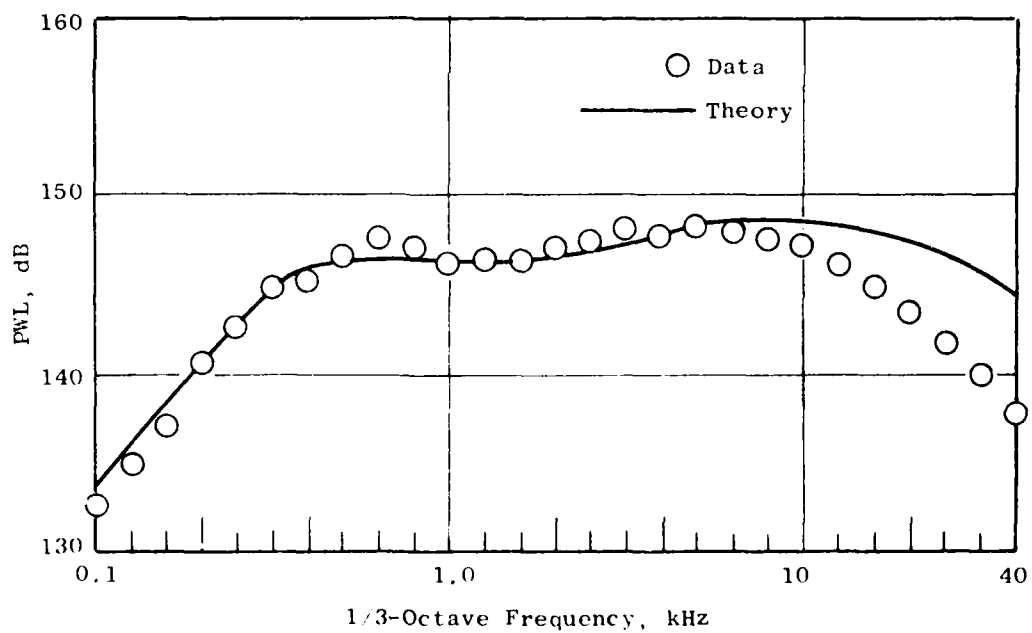
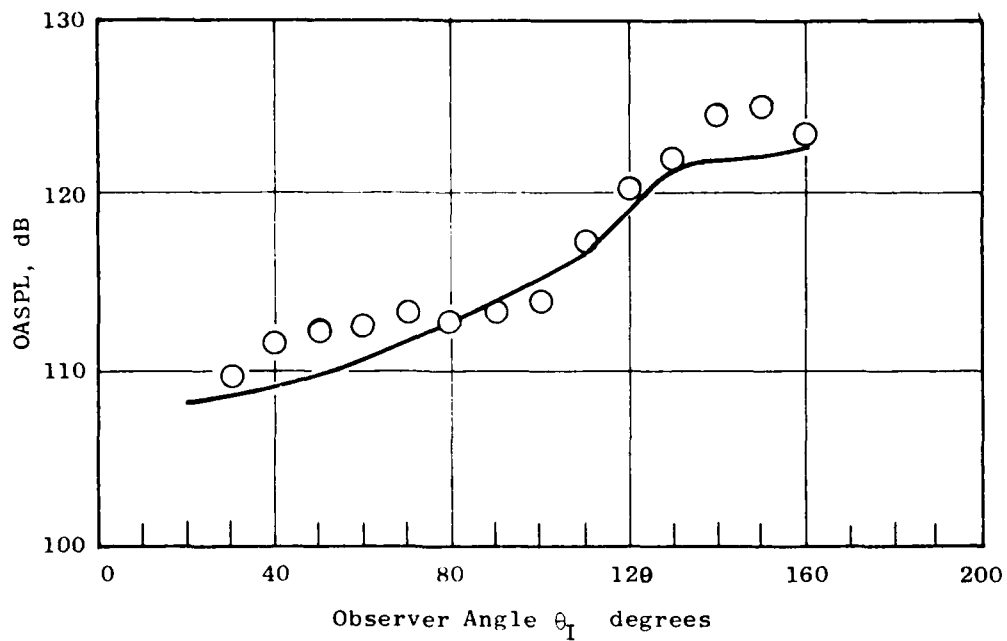
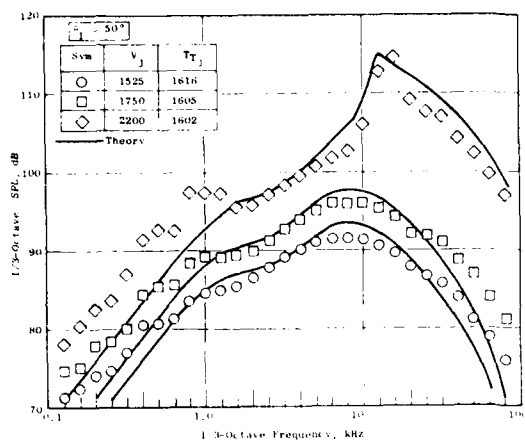
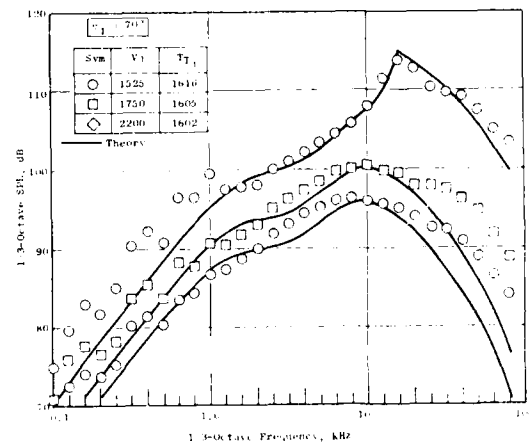


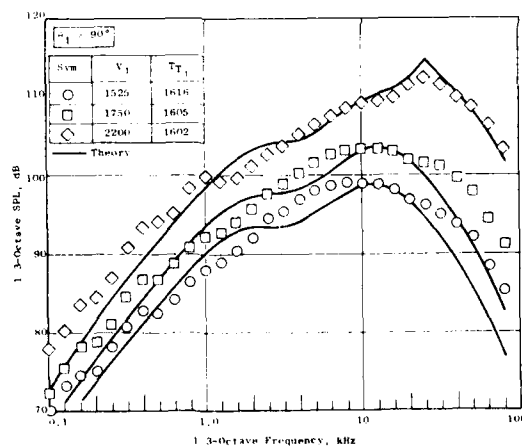
Figure 4-133. Data/Theory Comparison Case 23: Inverted Flow Coannular Plug Nozzle, AR = 0.65, VR = 2.0 (Concluded); (a) OASPL Directivity and Power Spectrum.



(a) SPL Spectra at $\theta_I = 50^\circ$

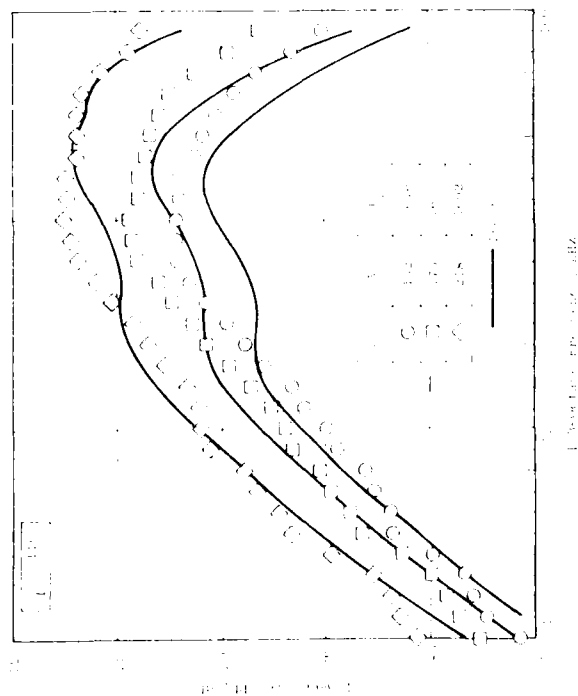


(b) SPL Spectra at $\theta_I = 70^\circ$

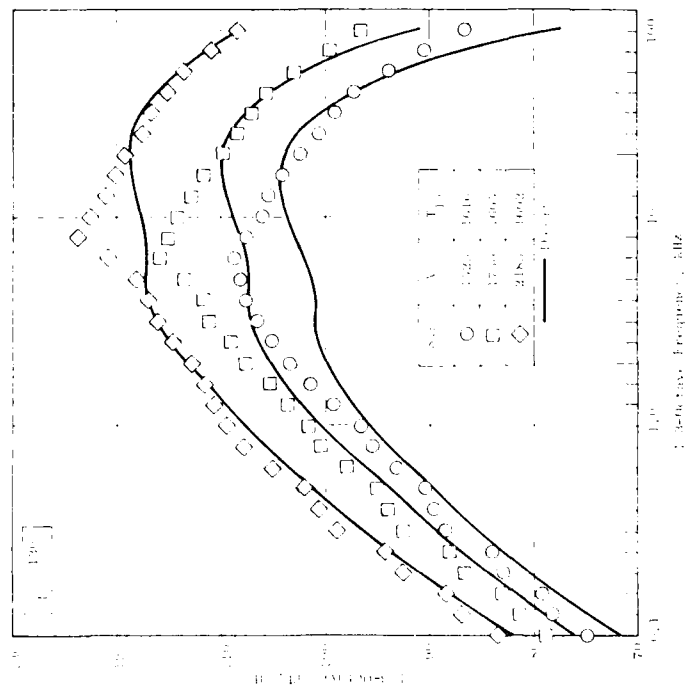


(c) SPL Spectra at $\theta_I = 90^\circ$

Figure 4-134. Data/Theory Comparison Cases 24-26:
7-Tube Nozzle, $D/d = 3.0$.

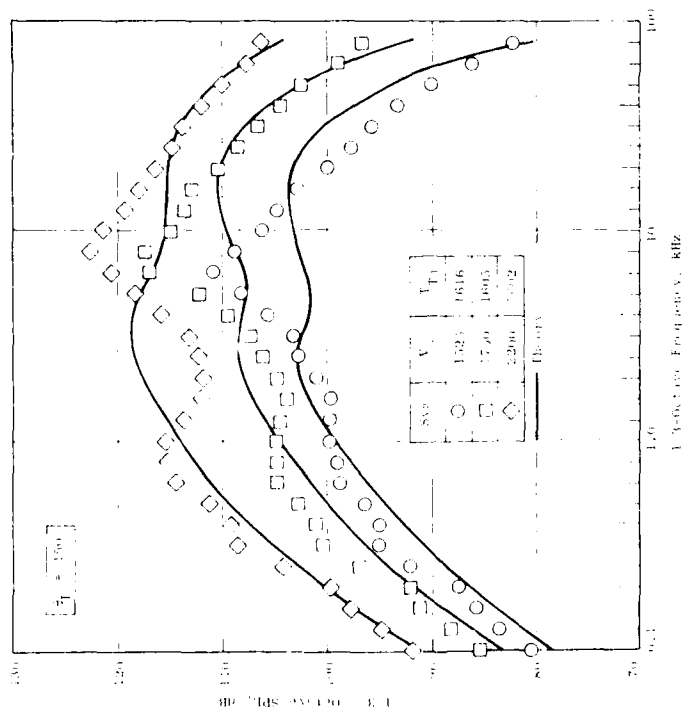


(d) SPL Spectra at $\theta_I = 110^\circ$

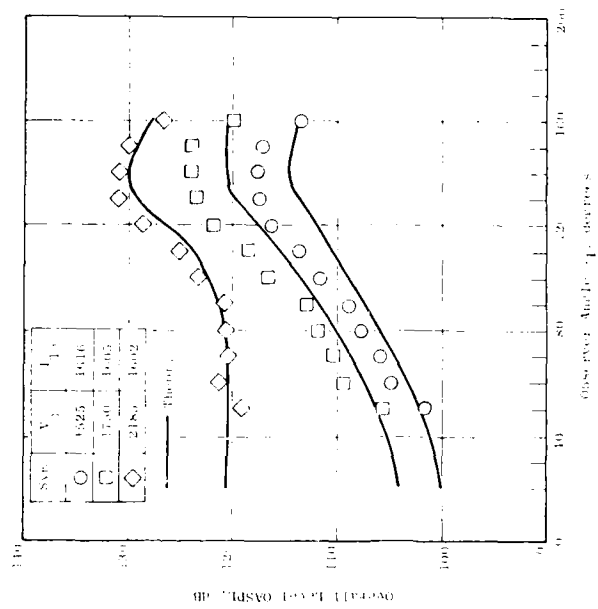


(e) SPL Spectra at $\theta_I = 130^\circ$

Figure 4-134. Data/Theory Comparison Cases 24-26:
7-Tube Nozzle, $D/d = 3.0$ (Continued).

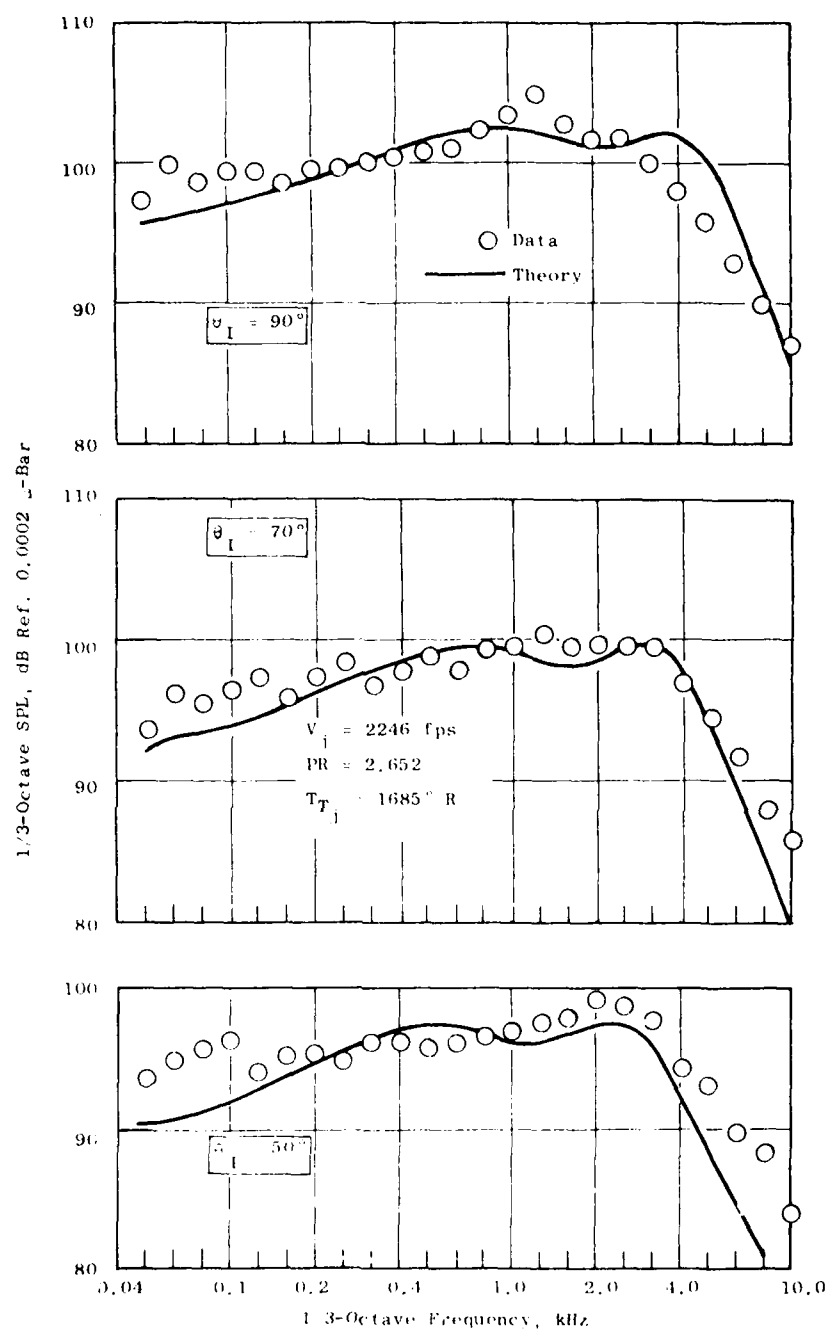


(f) SPL Spectra at $\theta_I = 150^\circ$



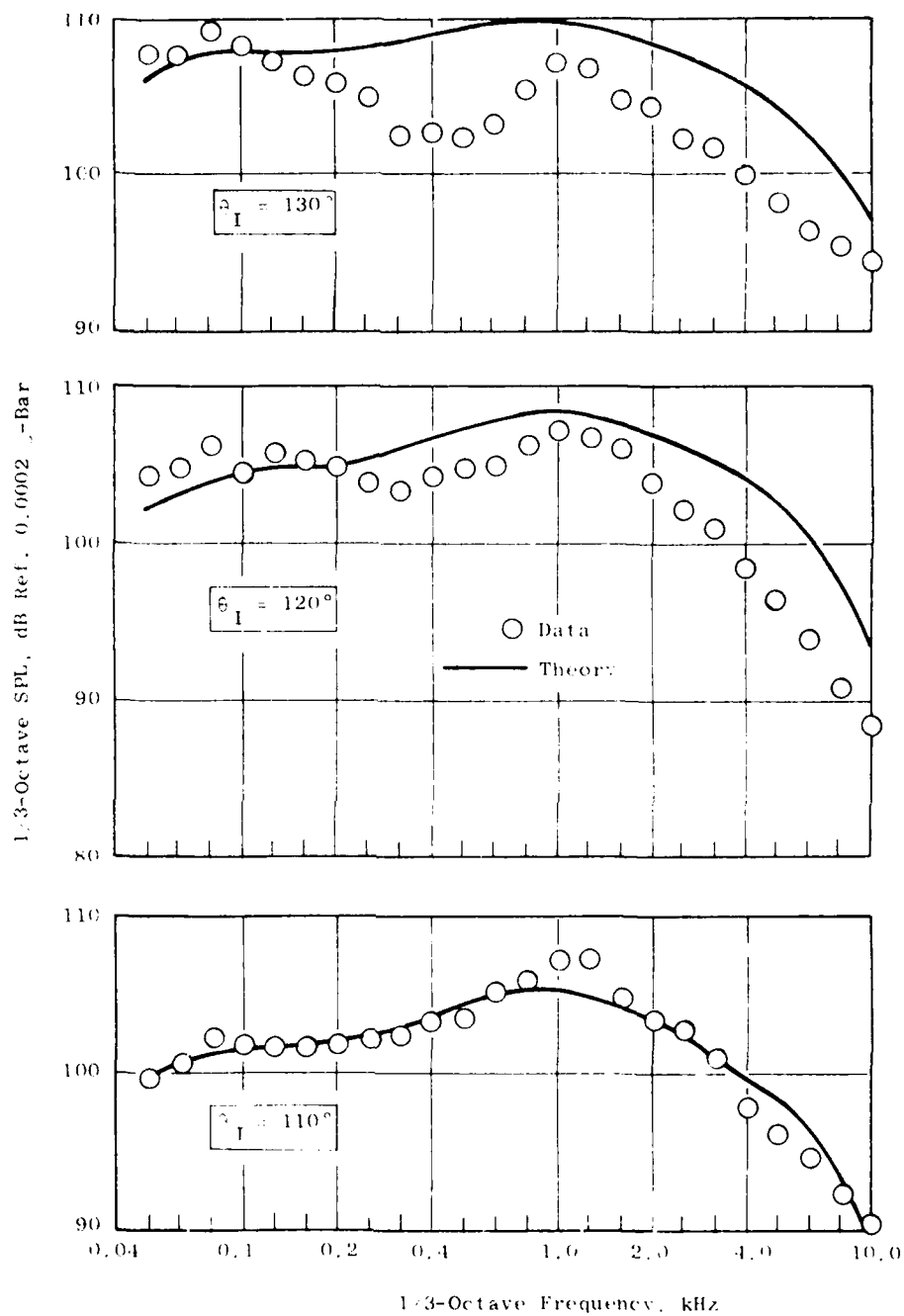
(g) OASPL Directivity

Figure 4-134. Data/Theory Comparison Cases 24-26:
7-Tube Nozzle, $D/d = 3.0$ (Concluded).



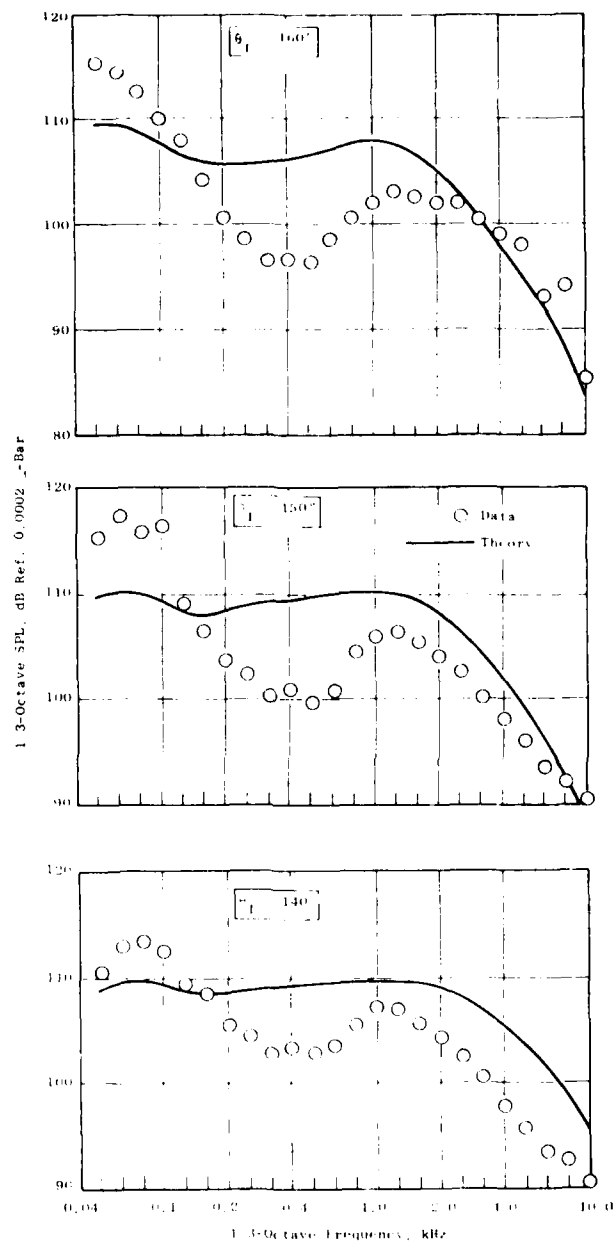
(a) SPL Spectra at $\theta_I = 50^\circ, 70^\circ$ and 90°

Figure 4-135. Data/Theory Comparison Case 27: 32-Chute
($A_{ann}/A_j = 2.1$) Nozzle.



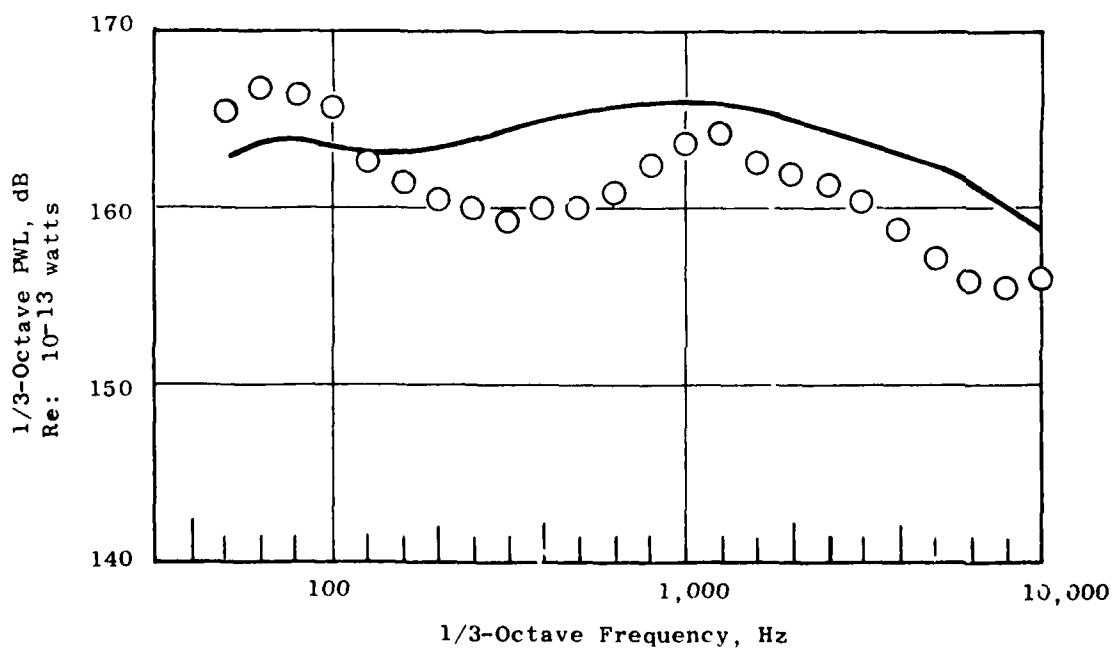
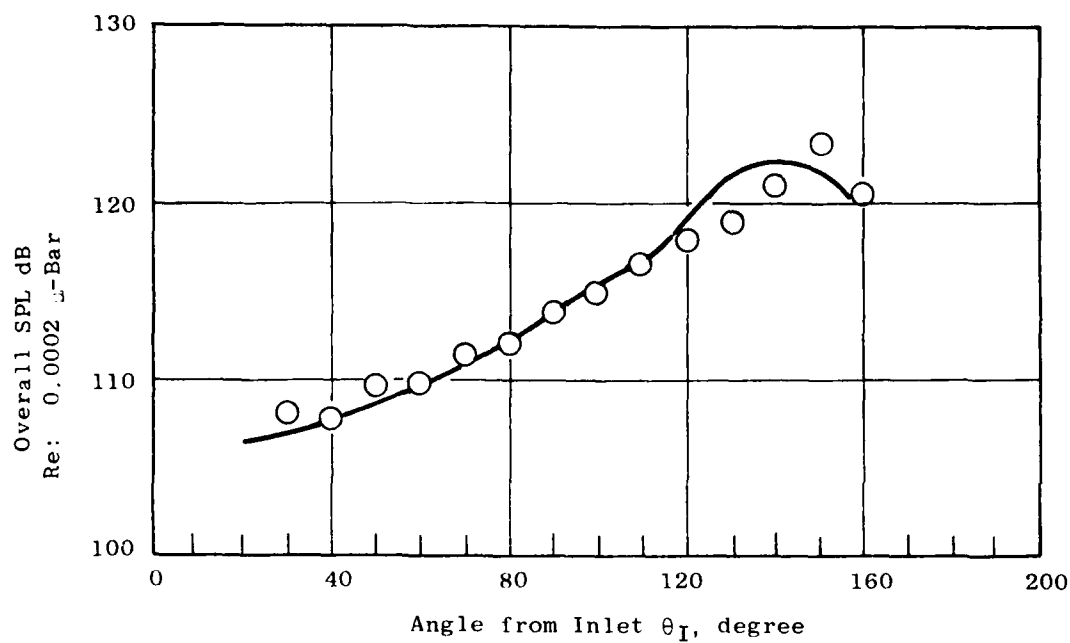
(b) SPL Spectra at $\theta_I = 110^\circ$, 120° and 130°

Figure 4-135. Data/Theory Comparison Case 27: 32-Chute ($A_{ann}/A_j = 2.1$) Nozzle (Continued).



(c) SPL Spectra at $\theta = 140^\circ, 150^\circ$ and 160°

Figure 4-135. Data/Theory Comparison Case 27: 32-Chute ($A_{ann}/A_j = 2.1$) Nozzle (Continued).



(d) OASPL Directivity and Power Spectrum

Figure 4-135. Data/Theory Comparison Case 27. 32-Chute ($A_{ann}/A_j = 2.1$) Nozzle (Concluded).

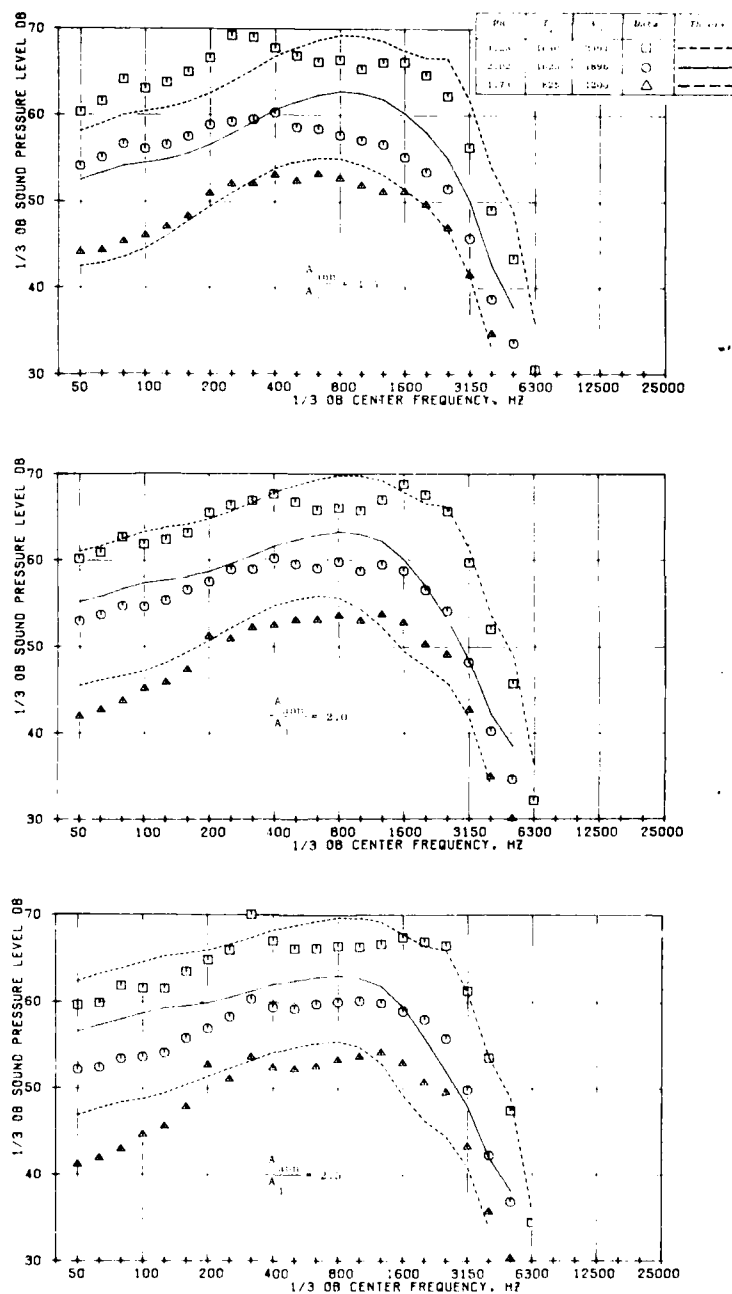


Figure 4-136. Data/Theory Comparison Cases 28-36:
36-Chute Nozzle SPL Spectra,
(a) at $\theta_I = 50^\circ$.

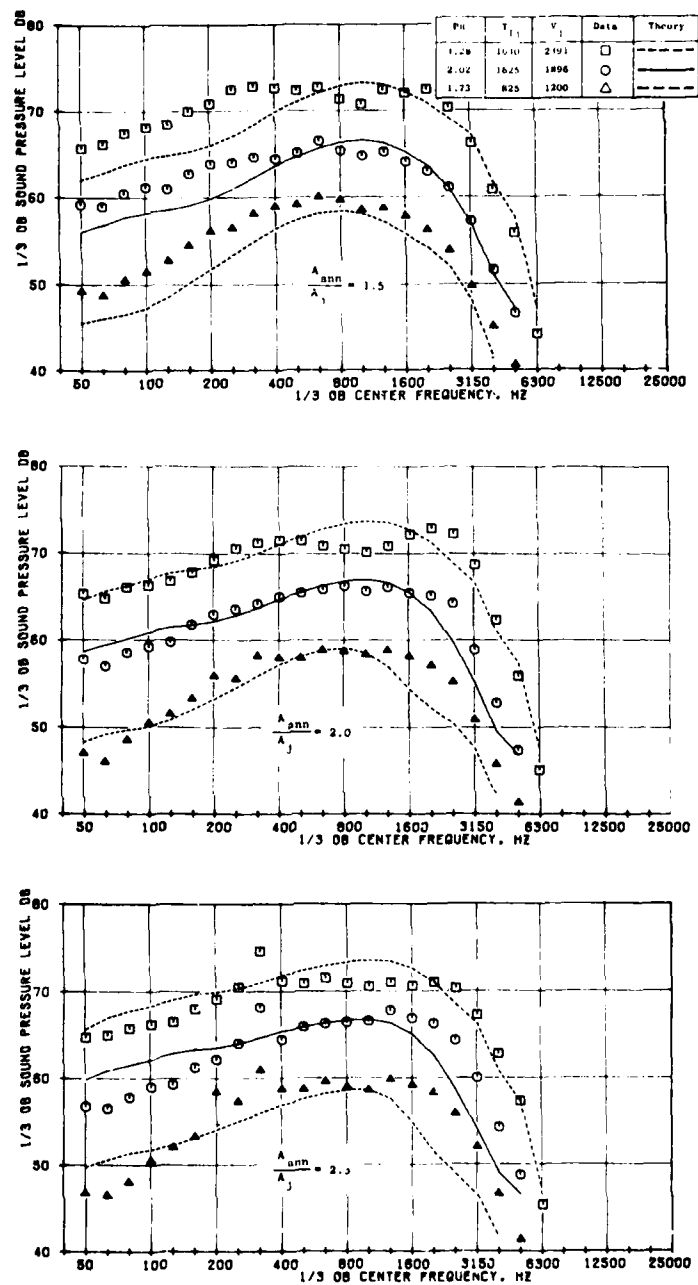


Figure 4-136 Data/Theory Comparison Cases 28-36:
36-Chute Nozzle SPL Spectra (Continued);
(b) $\theta_I = 70^\circ$.

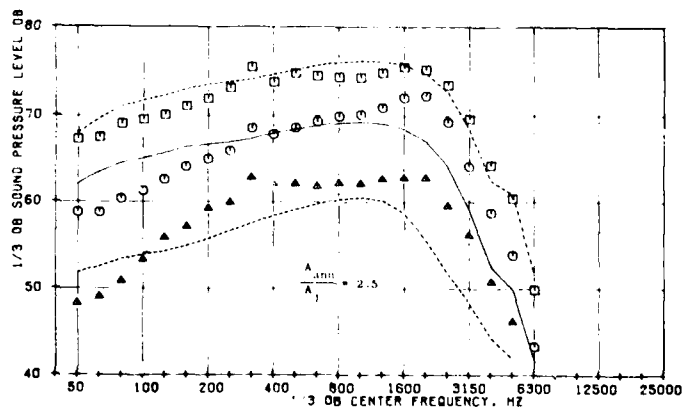
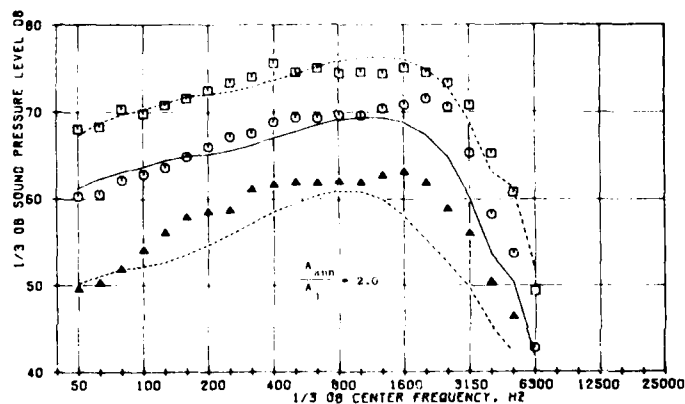
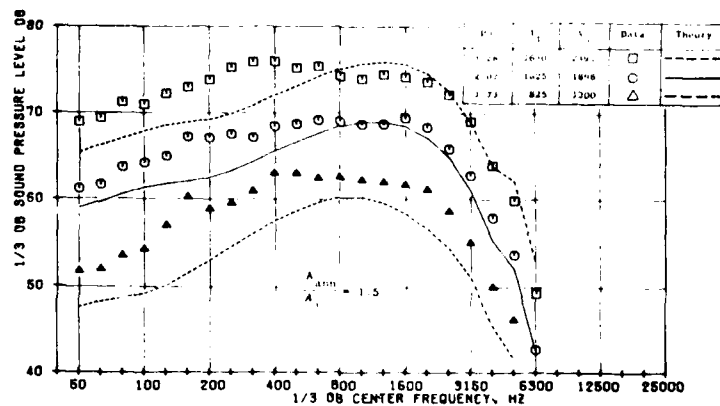


Figure 4-136. Data/Theory Comparison Cases 28-36:
36-Chute Nozzle SPL Spectra (Continued);
(c) $\theta_I = 90^\circ$.

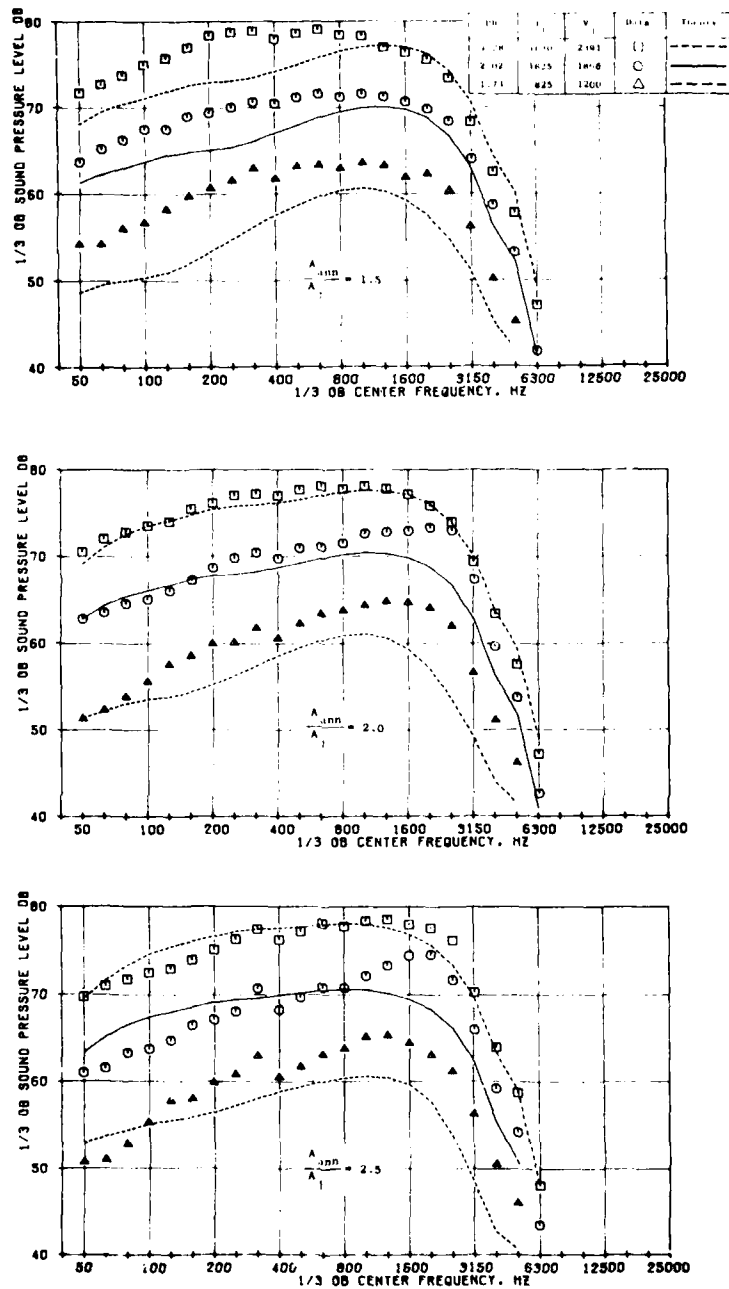


Figure 4-136. Data/Theory Comparison Cases 28-36:
36-Chute Nozzle SPL Spectra (Continued);
(d) $\theta_I = 110^\circ$.

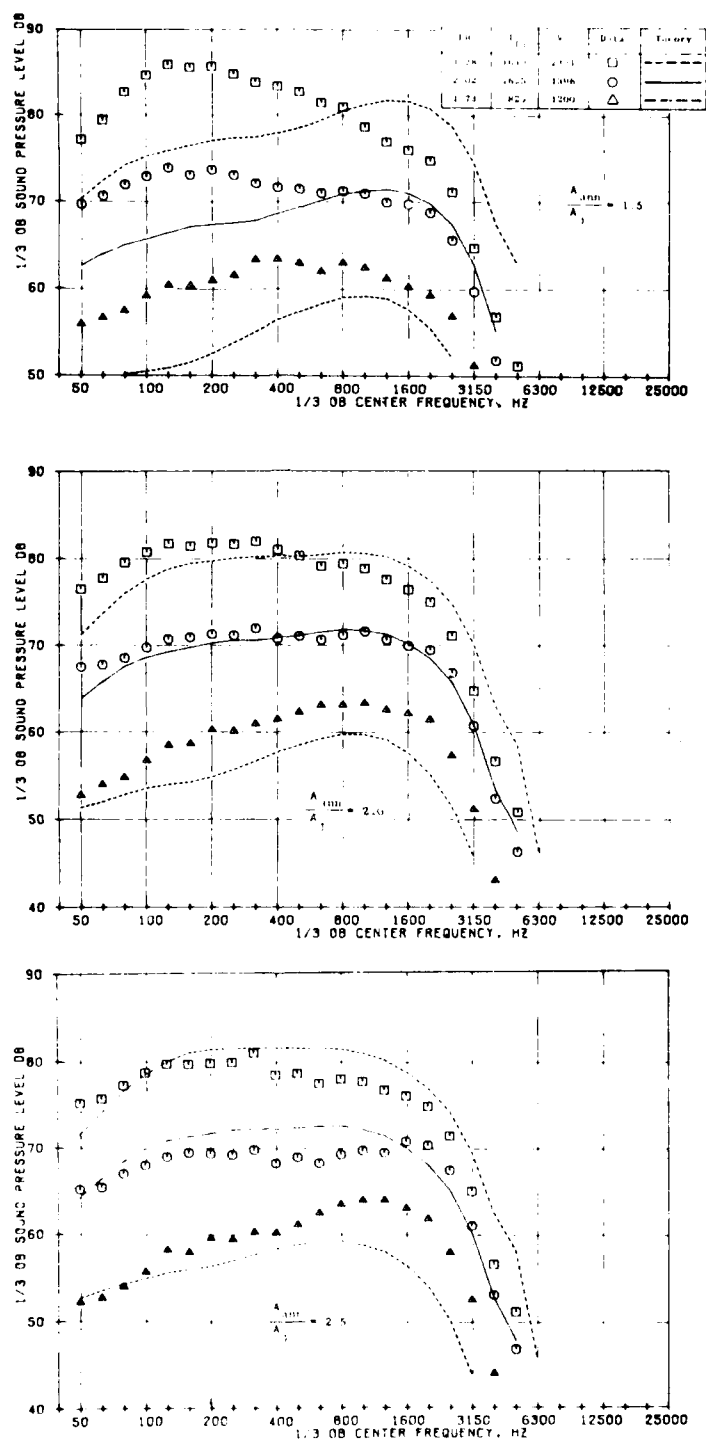


Figure 4-136. Data/Theory Comparison Cases 28-36:
36-Chute Nozzle SPL Spectra (Continued);
(c) $\theta_I = 130^\circ$.

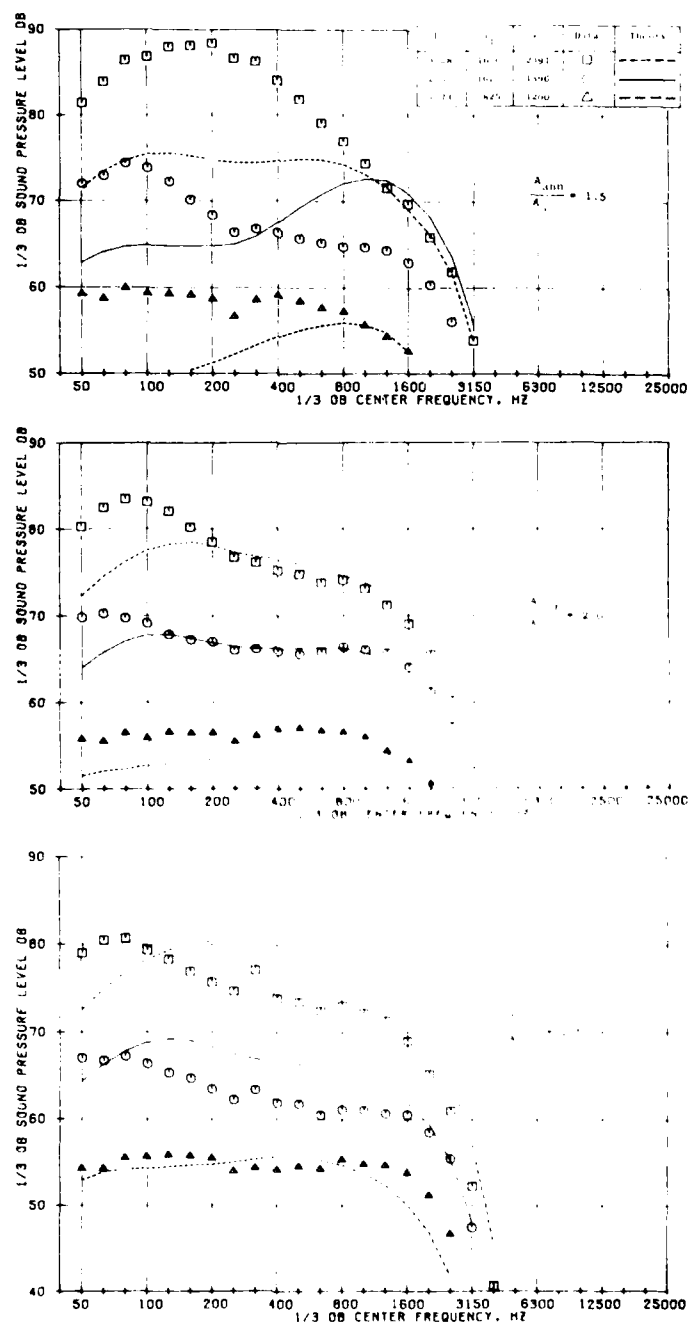


Figure 4-136. Data/Theory Comparison Cases 28-36:
36-Chute Nozzle SPL Spectra (Concluded);
(f) $\theta_I = 150^\circ$.

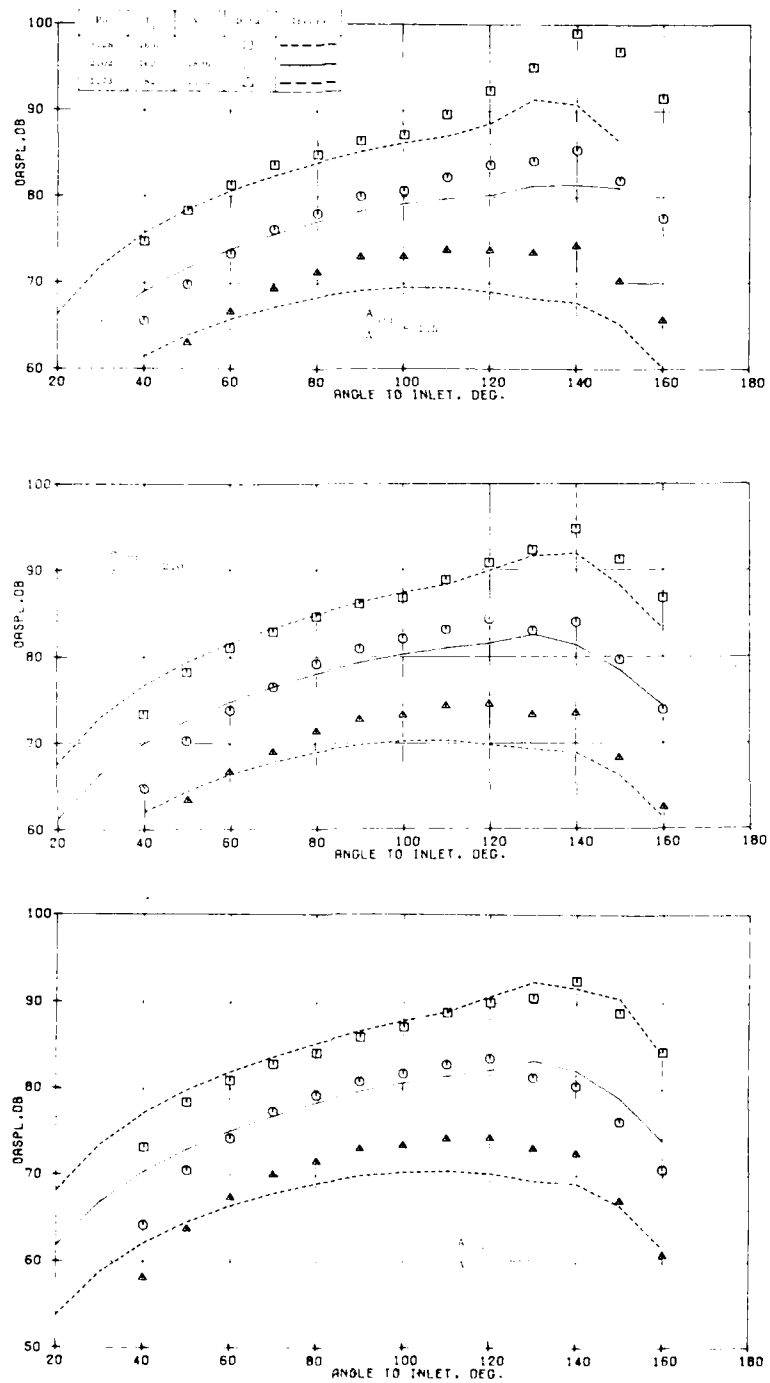


Figure 4-137. Data/Theory Comparison Cases 28-36:
36-Chute Nozzle OASPL Directivity.

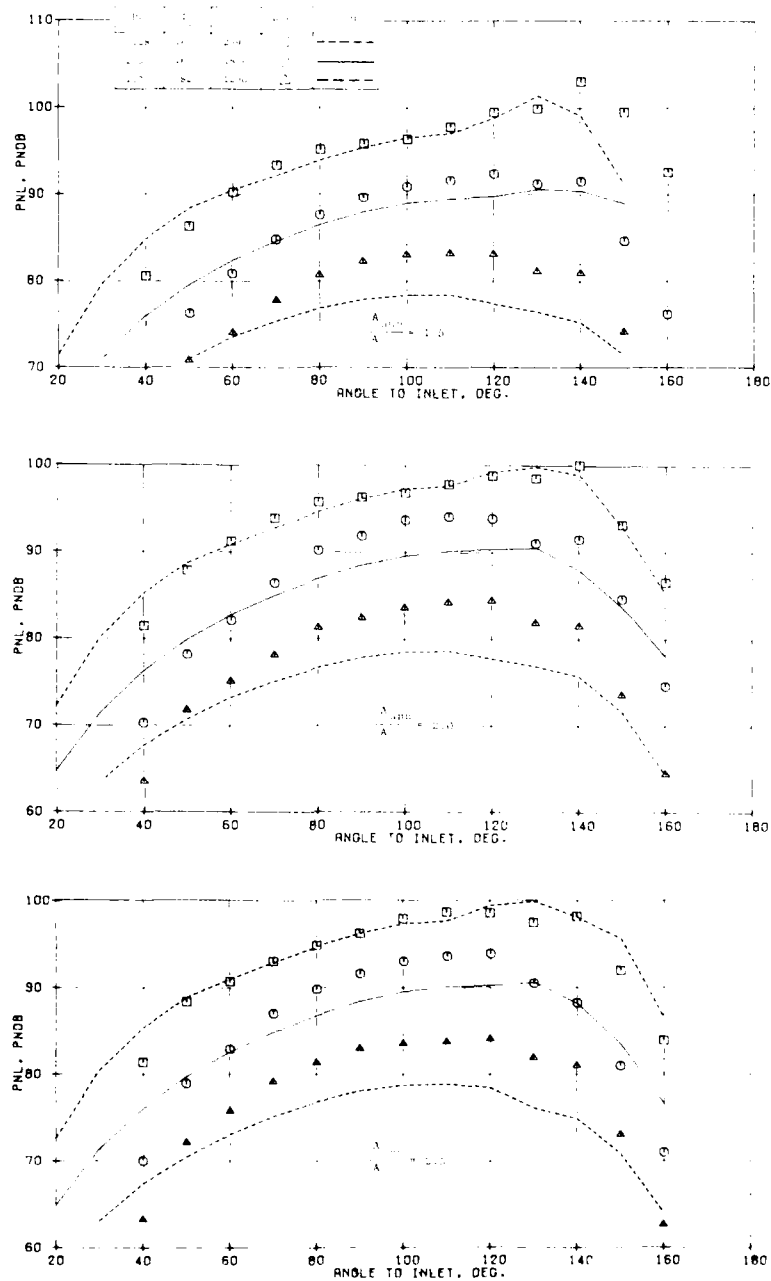
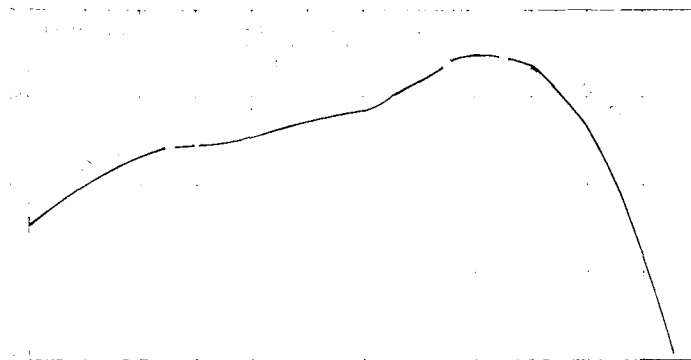
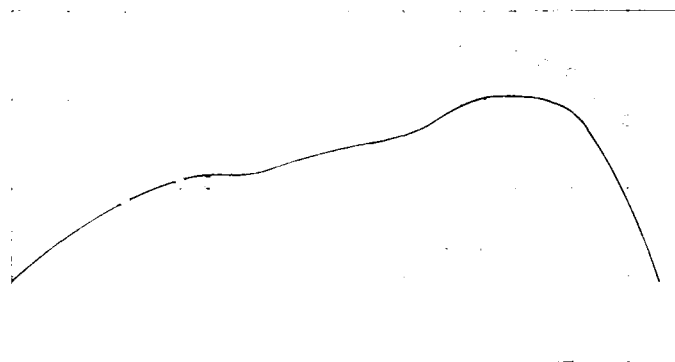


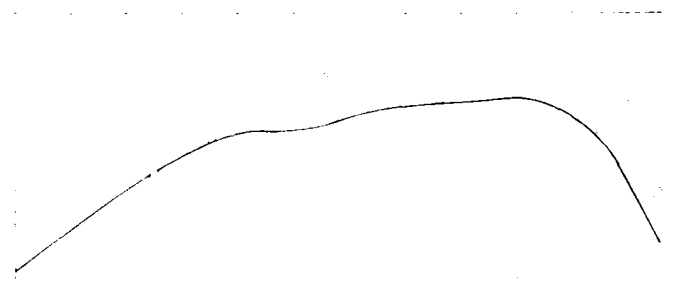
Figure 4-138. Data/Theory Comparison Cases 28-36;
36-Chute Nozzle PNL Directivity.



(a) SPL Spectrum at $\theta_I = 50^\circ$



(b) SPL Spectrum at $\theta_I = 90^\circ$



(c) SPL Spectrum at $\theta_I = 130^\circ$

Figure 4-139. Data Theory Comparison Case 37: 8 Lobe Daisy Nozzle, $V_J = 1377$ fps.

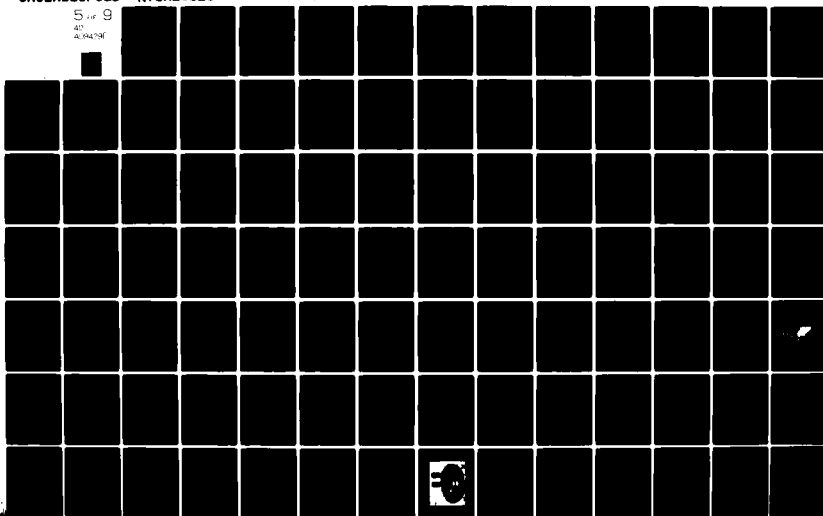
AD-A094 291

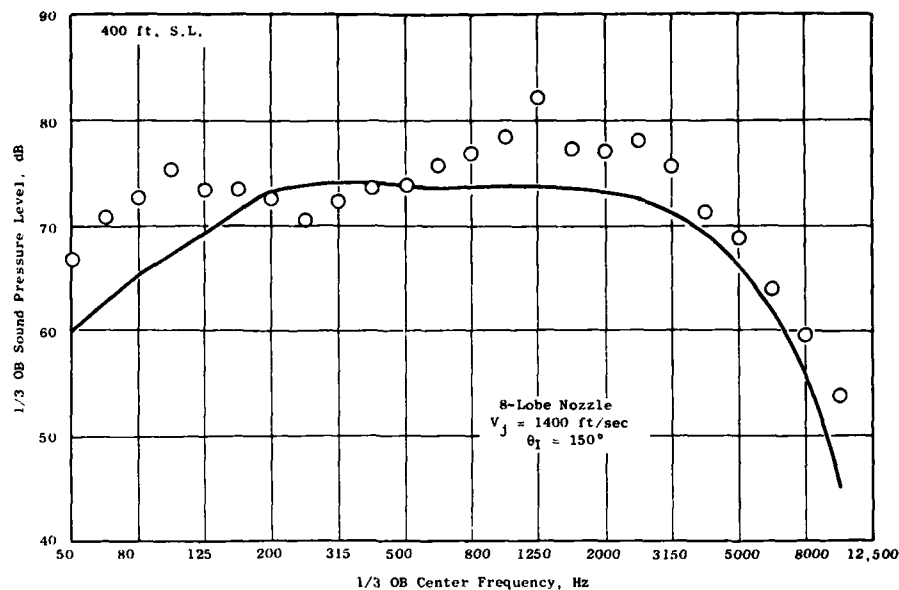
GENERAL ELECTRIC CO CINCINNATI OH AIRCRAFT ENGINE GROUP F/G 20/1
HIGH VELOCITY JET NOISE SOURCE LOCATION AND REDUCTION. TASK 2. --ETC(U)
MAY 78 T F Balsa, P R GLIEBE, R A KANTOLA DOT-05-30034
R78AE6323 FAA-RD-76-79-2 NL

UNCLASSIFIED

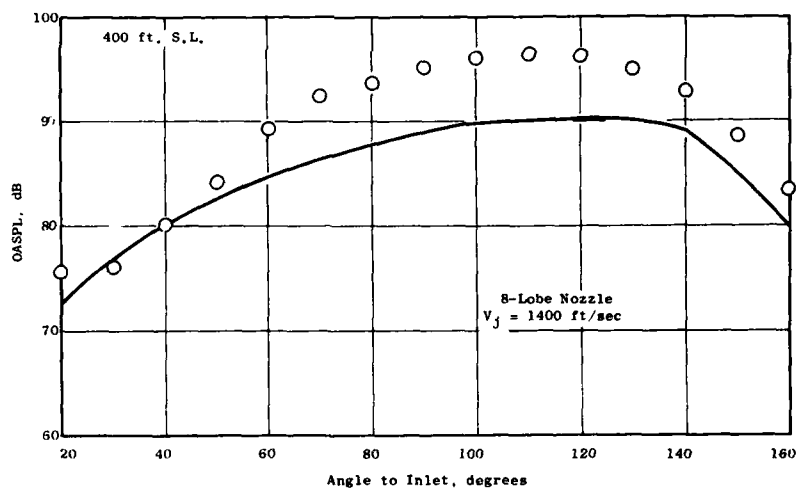
5 of 9

AD
AL344796



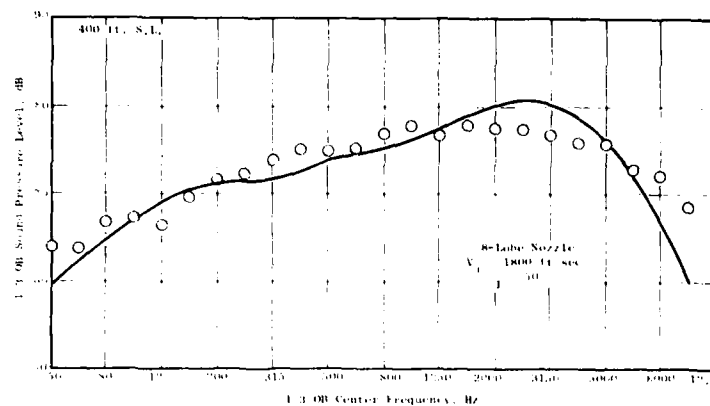


(d) SPL Spectrum at $\theta_I = 150^\circ$

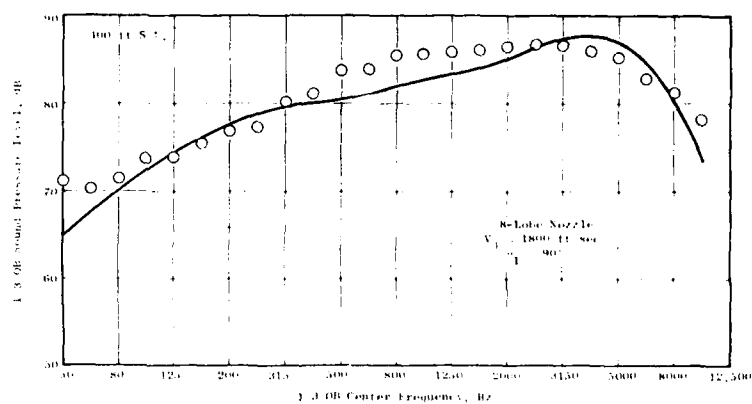


(e) OASPL Directivity.

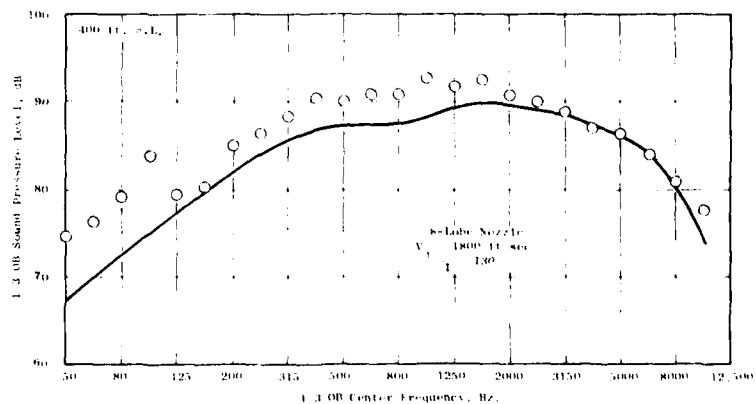
Figure 4-139. Data/Theory Comparison Case 37: 8-Lobe Daisy Nozzle, $V_j = 1377$ fps (Concluded).



(a) SPL Spectrum at $\theta_I = 50^\circ$

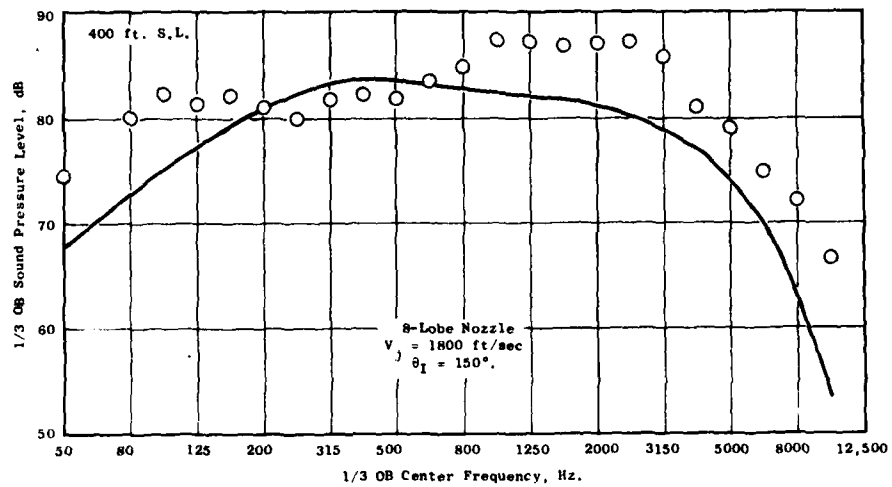


(b) SPL Spectrum at $\theta_I = 90^\circ$

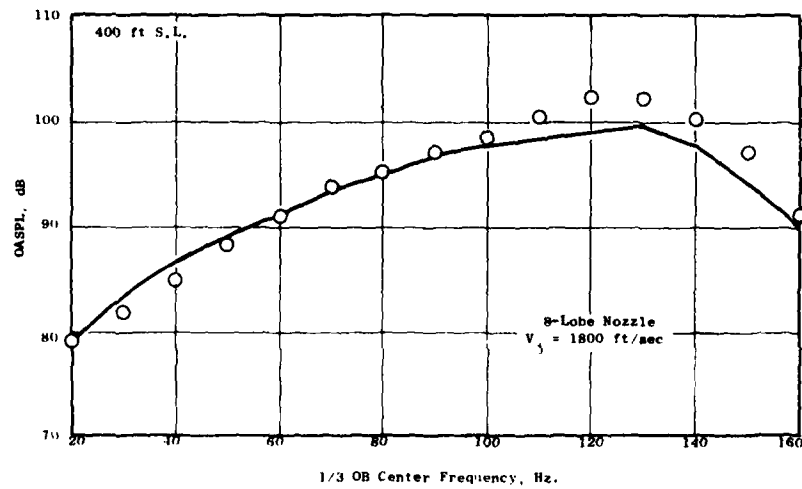


(c) SPL Spectrum at $\theta_I = 130^\circ$

Figure 4-140. Data/Theory Comparison Case 38: 8-Lobe Daisy Nozzle, $V_j = 1800$ fps.

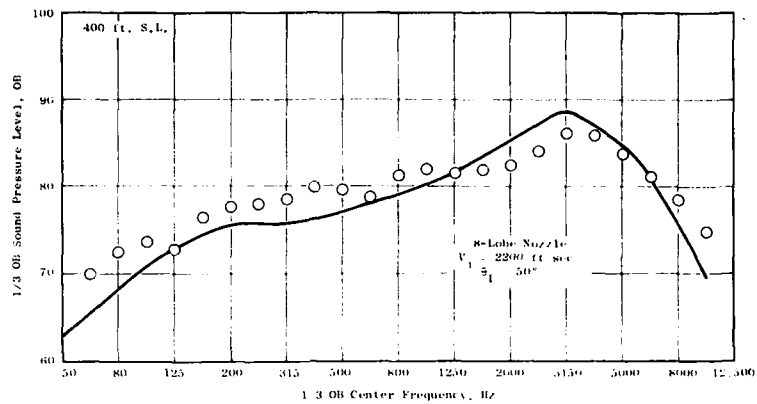


(d) SPL Spectrum at $\theta_I = 150^\circ$

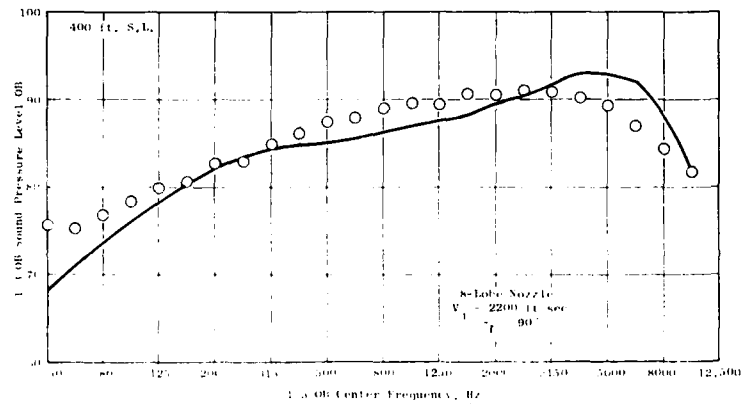


(e) OASPL Directivity

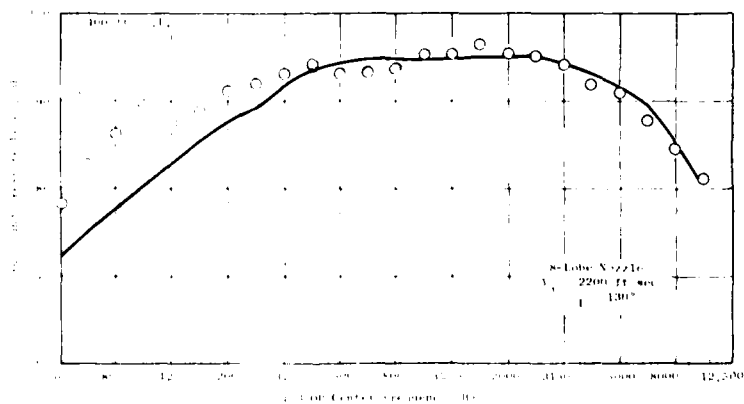
Figure 4-140. Data/Theory Comparison Case 38: 8-Lobe Daisy Nozzle, $V_j = 1800 \text{ fps}$ (Concluded).



(a) SPL Spectrum at $\theta_I = 50^\circ$

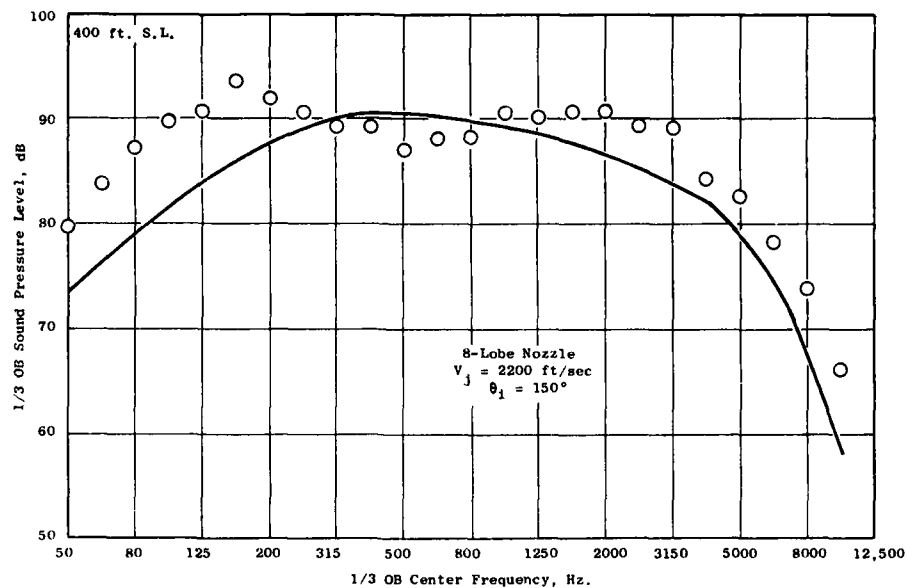


(b) SPL Spectrum at $\theta_I = 90^\circ$

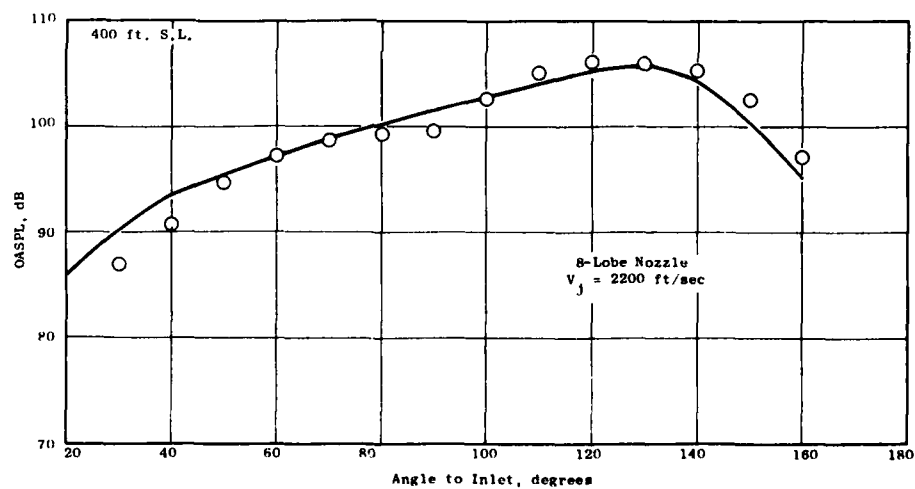


(c) SPL Spectrum at $\theta_I = 130^\circ$

Figure 4-141. Data/Theory Comparison Case 39: 8-Lobe Daisy Nozzle, $V_j = 2186$ fps.



(d) SPL Spectrum at $\theta_1 = 150^\circ$



(e) OASPL Directivity

Figure 4-141. Data/Theory Comparison Case 39: 8-Lobe Daisy Nozzle, $V_j = 2186$ fps (Concluded).

profile development and mixing. Redefining $VR = V_s/V_p$ and $AR = A_s/A_p$, where subscripts p and s refer to primary (high velocity) and secondary (low velocity) streams, respectively, back-to-back calculations of aerodynamic and acoustic characteristics were carried out for $AR = 1.0$ and $VR = 0.7$. Figure 4-142 shows comparisons of mean velocity profiles at several axial stations. The peak velocity axial decays are shown in Figure 4-143. Figures 4-142 and 4-143 show that flow inversion produces more rapid plume decay. Figure 4-144 shows comparisons of axial turbulence velocity (a key ingredient in mixing noise source strength) at several axial stations along the plume. These comparisons show the expected lower turbulence levels at small values of x/D_{eq} for the conventional bypass jet, and, correspondingly, the higher levels of turbulence at large x/D_{eq} .

The corresponding far-field acoustic spectrum comparisons are shown in Figure 4-145. At $\theta_I = 90^\circ$, the inverted-flow nozzle exhibits higher noise at high frequencies and lower noise at low frequencies. Since the high frequency noise generally comes from regions close to the nozzle exit, the higher high-frequency noise correlates with the higher turbulence levels at small values of x/D_{eq} shown in Figure 4-144. Similarly, low frequency noise is primarily from the fully developed regions far downstream, and the lower low frequency noise of the inverted-flow nozzle correlates with its lower turbulence levels for large x/D_{eq} (Figure 4-144).

The results at $\theta_I = 130^\circ$, however, show the inverted-flow jet noise to be lower throughout the spectrum. This is primarily a result of reduced convective amplification, i.e., lower eddy convection speeds. The eddy convection speed is proportional to the peak mean axial velocity, and the comparison of peak velocity curves shown in Figure 4-143 implies that the inverted-flow jet exhibits lower convection speeds and therefore reduced convective amplification. Figure 4-146 shows a comparison of overall sound pressure level (OASPL) versus θ_I for the two jets. The shallower slope of the directivity curve for the inverted-flow jet is a result of reduced convective amplification.

To demonstrate the influence of flow shielding as a sound emission mechanism, the back-to-back calculations were repeated with the shielding effects suppressed. These results are shown in Figure 4-147, along with the previous results, at $\theta_I = 150^\circ$. Flow shielding is observed to play a major role for both nozzles. The results shown in Figure 4-147 imply that the flow shielding is less for the inverted-flow jet, but that the reduced convective amplification more than compensates for this loss.

The noise suppression mechanisms for multielement nozzles appear to be similar to those deduced for inverted-flow, coannular nozzles. More extensive diagnostic analysis of noise suppression mechanisms utilizing the aeroacoustic model for several classes of suppressor nozzles are reported in the Task 3 final report of the present program.

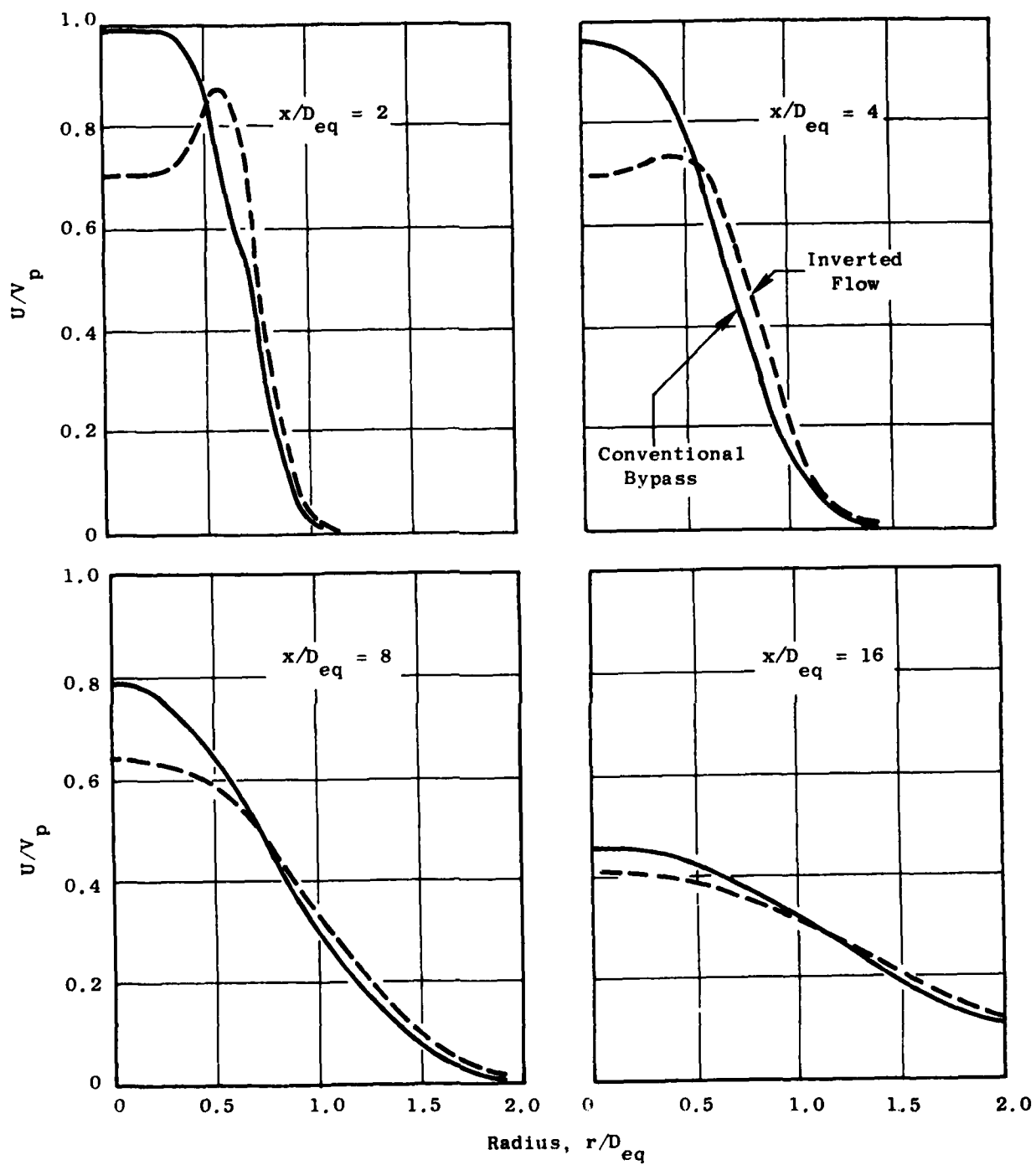


Figure 4-142. Comparison of Inverted Vs. Conventional Bypass Flow Mean Velocity Profiles; AR = 1.0, VR = 0.7.

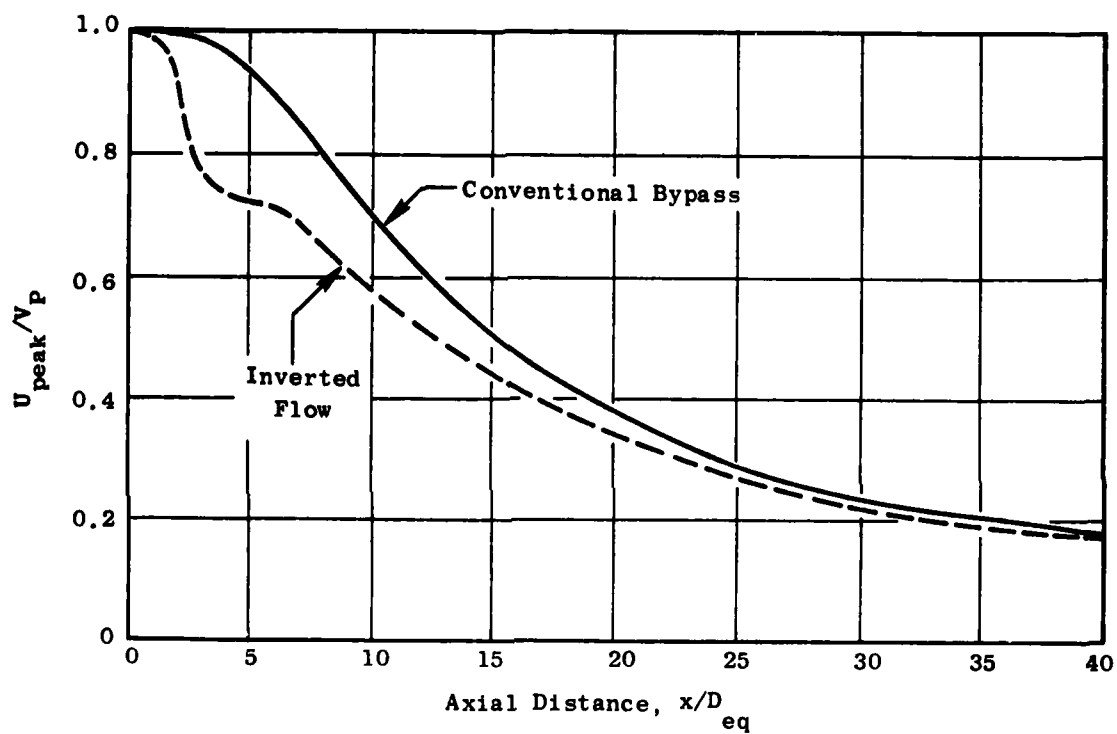


Figure 4-143. Comparison of Inverted Vs. Conventional Bypass Flow Mixing on Peak Axial Velocity Decay Rate; AR = 1.0, VR = 0.7.

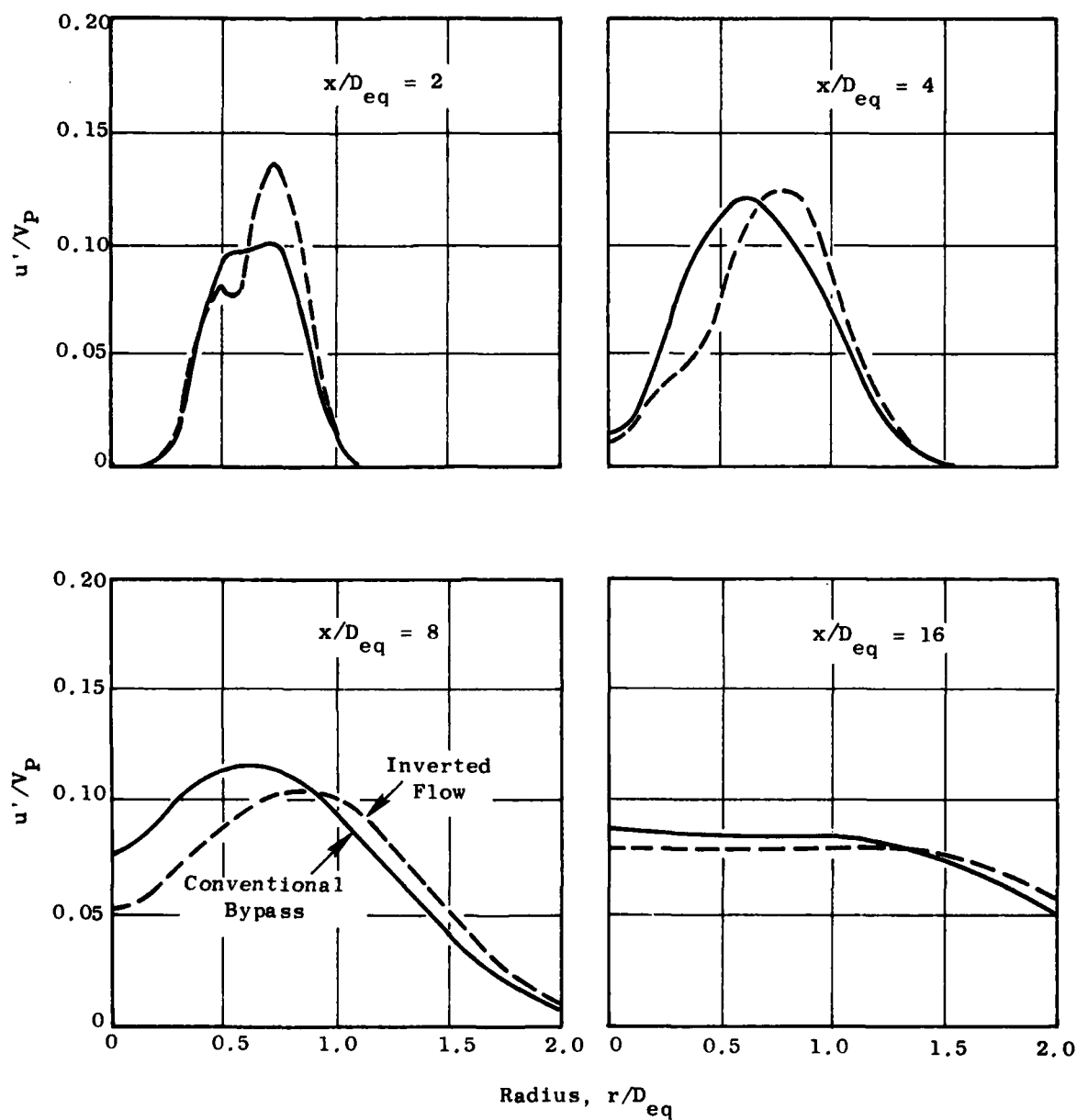


Figure 4-144. Comparison of Inverted Vs. Conventional Bypass Flow Mixing on Turbulence Velocity Profile Development; AR = 1.0, VR = 0.7.

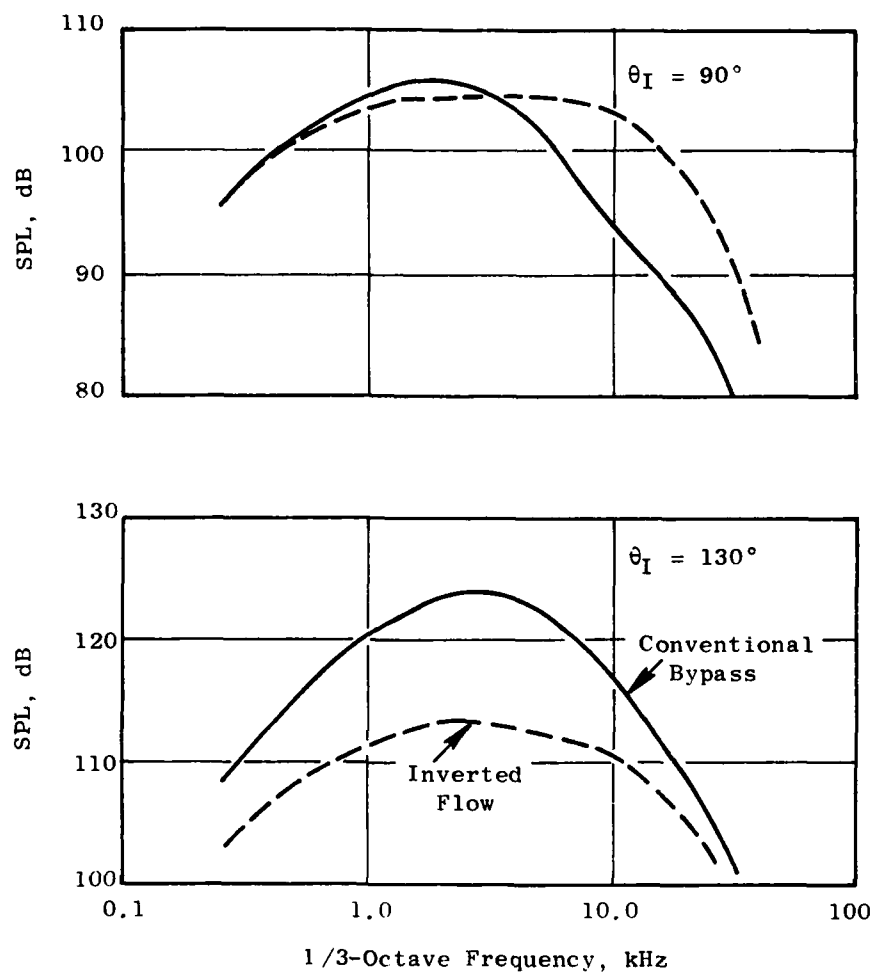


Figure 4-145. Effect of Inverted Vs. Conventional Flow Mixing on Far Field Acoustic Spectra; AR = 1.0, VR = 0.7.

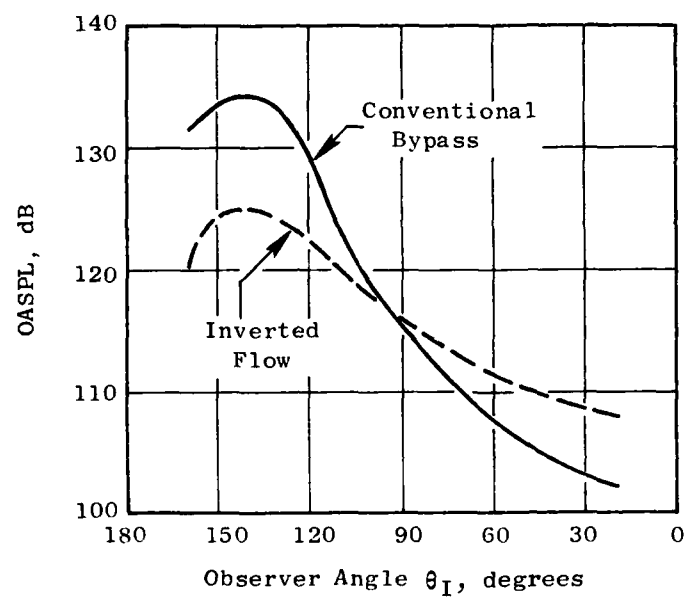


Figure 4-146. Comparison of Inverted Vs. Conventional Bypass Flow Mixing on OASPL Directivity.

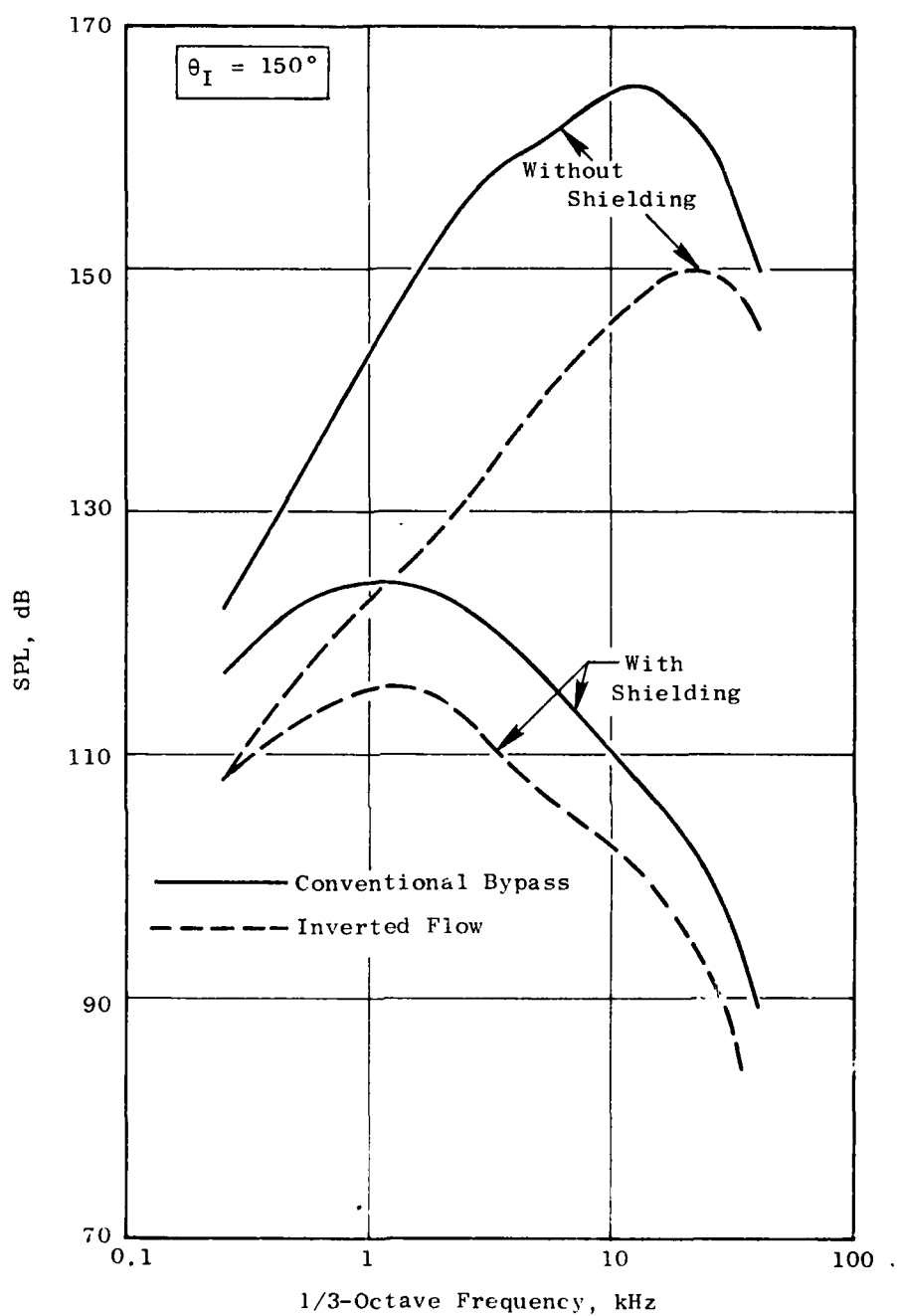


Figure 4-147. Effect of Fluid Shielding on SPL Spectrum at $\theta_I = 150^\circ$, Conventional Bypass and Inverted Flow; AR = 1.0, VR = 0.7.

4.7.10 In-flight Jet Noise

Section 4.7.8 presents extensive data - theory comparisons for a wide variety of nozzle operating conditions and nozzle geometries. All of these comparisons are for stationary nozzles. Although the primary emphasis in developing the unified aeroacoustic jet noise prediction model has been on static jet noise, some preliminary assessments of the model capability for in-flight jet noise prediction have been made.

As discussed in Section 4.4, the acoustic propagation aspects of the in-flight jet noise problem can be analyzed by reviewing the jet plume in a reference frame fixed to the nozzle, so that the plume is subjected to an external flow (wind tunnel mode). The computation of the acoustic propagation (convection and shielding) effects is performed as in the static case, with all Mach number profiles $M(r)$ and $M_c(r)$ [as computed from equation (318)] replaced by $M(r) - M_a$ and $M_c(r) - M_a$, respectively. The turbulent mixing calculation is also unaltered from the static case, but the momentum profiles have a non-zero external boundary (free-stream) value. The momentum and enthalpy spreading constants C_m and C_h are, of course, reduced when $M_a > 0$, as discussed in Section 4.5.4, and expressed by equation (280). The shock cell broadband noise calculation is the same as the static procedure except for the addition of a dynamic correction factor $(1 - M_a \cos \theta_I)^{-4}$ as proposed by Drevite et al (75), and given by equation (313).

It is recognized that the nozzle external cowl boundary layer profile and turbulence levels may have an important influence on the plume mixing process in flight. This effect is accounted for only insofar as the modeled variation of C_m with VR is representative of realistic aircraft engine installation conditions. The C_m versus VR dependence used in the computations described herein was derived from coaxial jet centerline decay measurements, as discussed in Section 4.5.4.

Predictions of the in-flight jet noise of a convergent conical nozzle have been compared with the Bertin Aerotrain simulated flight noise results which were obtained by Clapper, et al.⁽⁷²⁾ in Task 4 of this program. Figure 4-148 shows the resulting comparisons between predicted and measured in-flight results, in terms of OASPL versus θ_I directivity. The difference between static and flight levels, $(OASPL_{static} - OASPL_{flight})$ is shown rather than absolute levels. The predicted trends agree well with the data except for the lower jet velocities at angles close to the jet axis. In particular, the theory correctly predicts the observed amplification of jet noise in the forward quadrant ($\theta_I < 90^\circ$) due to flight.

One method proposed for predicting flight effects on jet noise is the velocity exponent method of Bushell⁽⁹⁰⁾. This method consists of predicting the flight effect from the following expression:

$$\begin{aligned} OASPL_{static} - OASPL_{flight} = \\ = 10 \log_{10} \left[\left(\frac{v_j}{v_{rel}} \right)^m (1 - M_a \cos \theta_I) \right] \end{aligned} \quad (321)$$

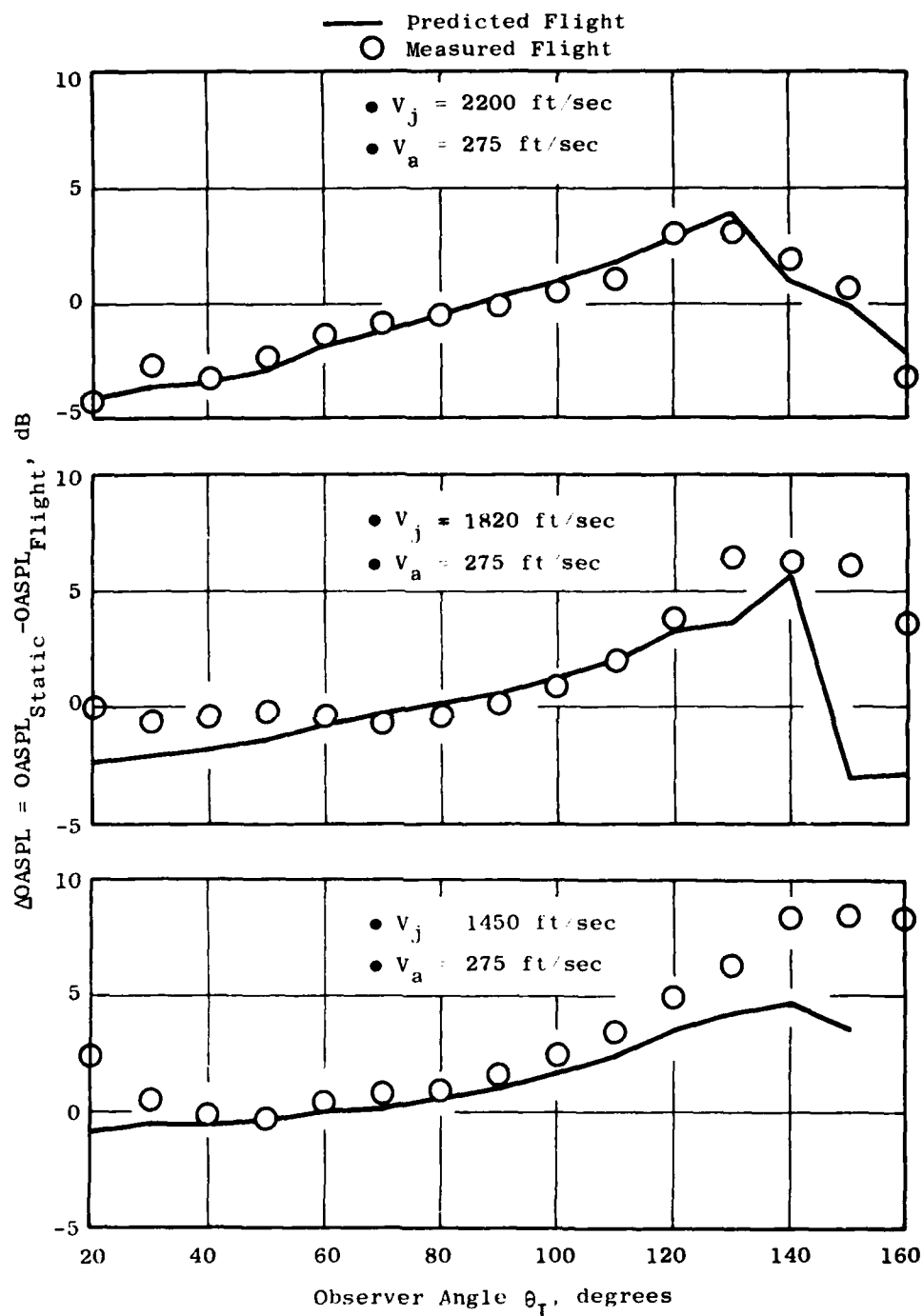


Figure 4-148 Comparison of Predicted and Measured Flight Effect for J85/Aerotraine Conical Nozzle, 400 ft Sideline.

where $V_{rel} = V_j - V_0$ and m is an empirically derived exponent which is specified as a function of θ_I . Alternatively, from measured static and flight noise levels, equation (321) can be inverted to solve for the flight velocity exponent m . This has been done for both the measured and predicted flight and static results, and a comparison of the measured and predicted flight exponents is shown in Figure 4-149. The theory again predicts the effect of θ_I (and V_j) on the flight exponent m quite well except for angles close to the jet axis. Note that the exponent is (and is predicted to be) a function of V_j .

Some example data - theory comparisons of SPL spectra are shown in Figure 4-150. The theory predicts the observed changes in spectrum shape due to flight quite well.

Although the flight effect aspects of the aeroacoustic model are not completely resolved, the results obtained thus far are encouraging, and suggest that no new, "mysterious" mechanisms are controlling the observed jet noise in flight. Further refinement of the model to correct the deficiencies at angles close to the jet axis for low jet velocities is required.

4.7.11 Concluding Remarks

Preliminary comparisons of predictions with experiment have shown that the present theoretical model is capable of predicting many of the observed aerodynamic and acoustic characteristics of single and dual flow nozzles. The inherently lower noise of a conventional bypass coaxial jet relative to a conical nozzle is a result of lower turbulence intensity. The lower noise levels of an inverted flow coannular nozzle, however, are a result of the competing influences of mixing noise, convective amplification and acoustic shielding alterations. These competing influences are in a delicate balance, and the type of calculation indicated herein, summing up all the contributions to determine the net effect in the far field, is required to properly predict the noise characteristics of complex nozzles.

The aero-acoustic jet noise prediction model in its present form is based on the following noise source generation/propagation mechanisms:

1. Turbulent mixing - major source of noise in turbulent jets;
2. Convective amplification - enhancement of noise generated by the turbulent eddies due to their motion (convection in the jet plume) relative to the observer;
3. Fluid shielding - shrouding or trapping of the sound waves generated in the plume by the jet plume itself.

Several modifications to the model were made during the course of development; these were modifications all in the modeling of the jet plume turbulent structure; e.g., prediction of turbulent eddy convection speeds, turbulent correlation decay times, etc. This portion of the modeling was the most difficult to carry out because of the scarcity of relevant experimental data; many simplifying assumptions concerning the nature of the turbulent structure were made because no better information is available.

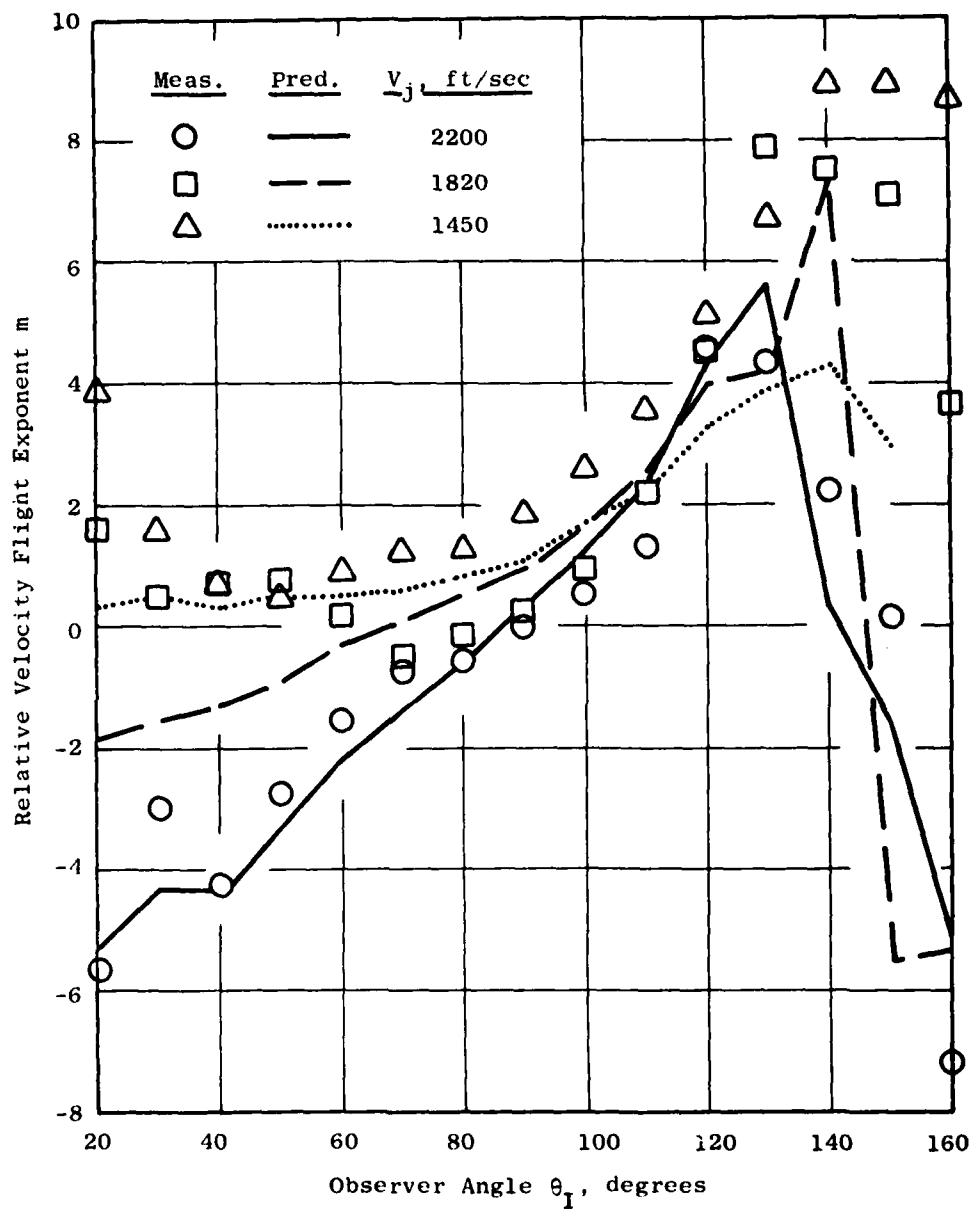


Figure 4-149. Comparison of Predicted and Measured Flight Velocity Exponent m for J85/AeroTrain Conical Nozzle.

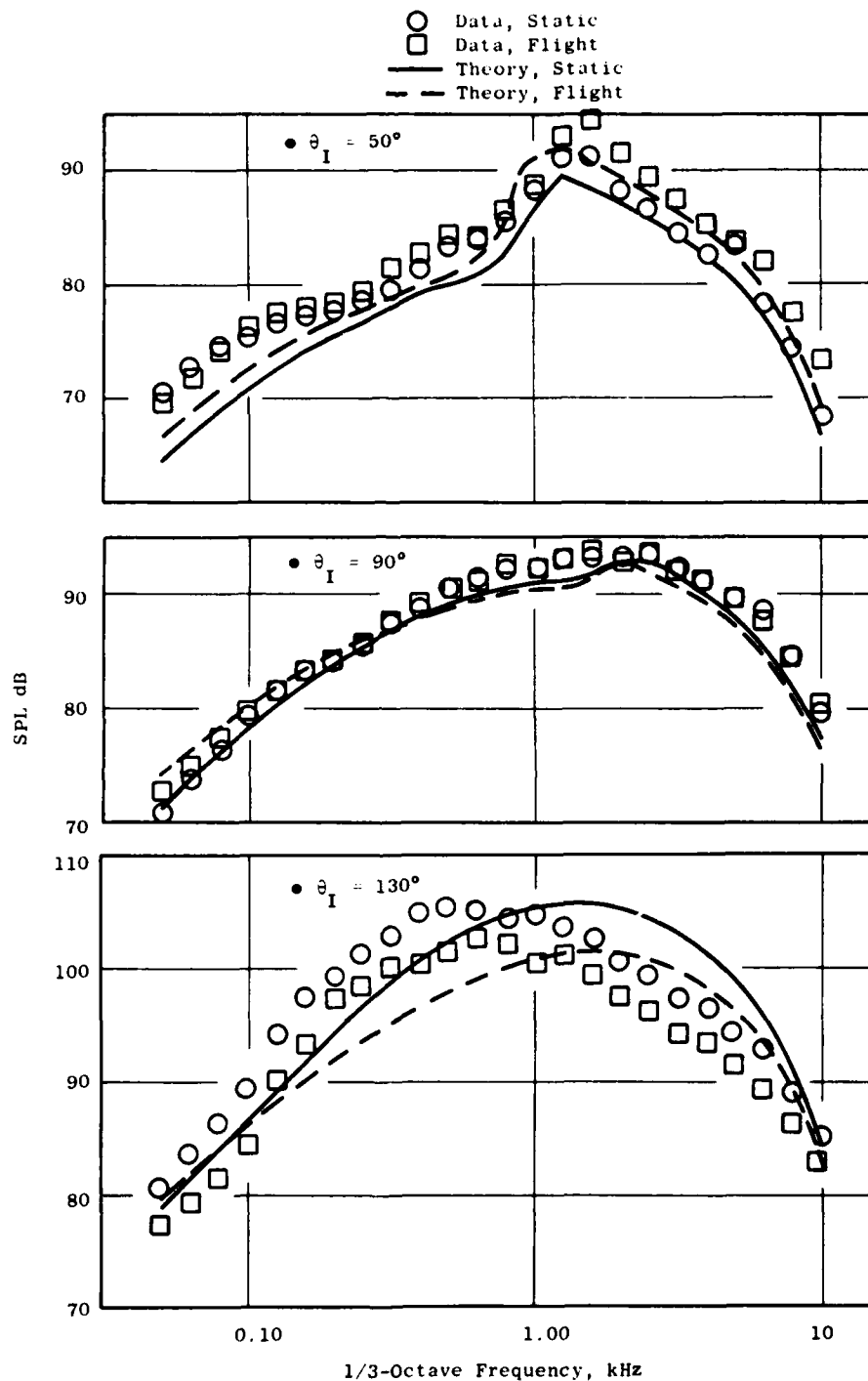


Figure 4-150. Comparison of Measured and Predicted Flight Noise Spectra for J85/Aerotraine Conical Nozzle, $V_j = 2200$ fps, 400 ft Sideline.

Nevertheless, the prediction method adequately duplicates the primary aero-acoustic characteristics of a wide variety of jet types and conditions with the idealized model that has been constructed, and a few empirical adjustments made to compensate for these idealizations.

In summary, from the successful results achieved to date, a useful (and powerful) prediction tool has been established for assessing the acoustic characteristics of various exhaust nozzle types. This tool can provide useful diagnostic and design optimization information and assist in the selection of low noise nozzles for future AST system applications.

Several areas of improvement in the model have been identified, including: (1) better definition of the turbulent structure parameters relevant to jet noise, (2) the addition of the dipole and monopole density gradient source terms to improve low velocity heated jet predictions, (3) further development of the shock-cell noise prediction for multielement nozzles, (4) extension of the aerodynamic model to include base-pressure effects, (5) inclusion of a chute shedding excess noise prediction component in the model, and, (6) further verification of and improvements in the prediction of in-flight jet noise.

4.8 PHYSICAL SHIELDING

This section discusses physical shielding by semi-infinite pipes. The case of semi-infinite barriers is discussed extensively in the literature, e.g., Bowman, et al.(91) and Butler(92), and hence is only summarized herein. Model problems relevant to the area of physical shielding by semi-infinite pipes, are posed and solved. In both cases, a simple approximate method of dealing with "absorbent" walls based on suggestions of Butler is also developed.

These calculations can be used to predict the alteration of sound fields due to the presence of ejector type enclosures or plane barriers if the distribution of the sources producing the sound field is known. Thus, as far as ejector aeroacoustics is concerned, the utility of the calculations reported in Section 4.8.2 is limited to qualitative insights because the aerodynamic jet analysis discussed in Section 4.5 has not been extended to encompass the effect of ejector shrouds for reasons discussed in Section 8.4. However, the results of Section 4.8.1 can be used whenever it is feasible to assume that the sound source distribution in the jet plume is not altered by the introduction of a plane barrier. An example of such an application to assess the effects of physical shielding will be given in Section 7.2.

4.8.1 Shielding of Sound by a Semi-Infinite Barrier

Figure 4-151 illustrates a sound source located in the vicinity of a semi-infinite plane barrier. The coordinates of the source location are (r_0, ϕ_0) , and the coordinates of the observer are given by (r, ϕ, z_0) . The source emits at frequency ω . This problem is discussed in detail by Butler(92). The resulting solution shows that, for $r \gg r_0$ and $kr_0 \gg 1$, there is negligible attenuation of the sound for $\phi < \pi + \phi_0$, corresponding to the case where the observer has a direct "line of sight" to the source. The parameter k is given by ω/c , where c is the ambient speed of sound. For $\phi = \pi + \phi_0$, the exact solution gives 6 dB attenuation. For $\phi > \pi + \phi_0$ (i.e., for the observer being in the shadow region of the source), Butler recommends an expression due to Bowman, et al.(91) for the attenuation. For a hard wall barrier with $R_1 = \sqrt{(r + r_0)^2 + z_0^2}$, the attenuation, in dB is $20 \log_{10} |(UkR)|$ where

$$U = \frac{[\sec [1/2(\phi - \phi_0)] + \sec [1/2(\phi + \phi_0)]]}{2\sqrt{2\pi k R_1} (kr)^{1/2} (kr_0)^{1/2}} \quad (322)$$

If also, $z_0 \ll r$, the attenuation expression simplifies to:

$$20 \log_{10} \left| \frac{\sec [1/2(\phi - \phi_0)] + \sec [1/2(\phi + \phi_0)]}{2\sqrt{2\pi k r_0}} \right| \quad (323)$$

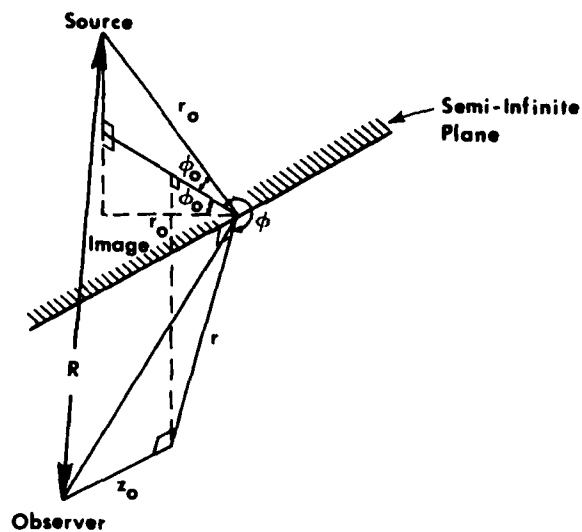


Figure 4-151. Sound Source Located in Vicinity of Semi-Infinite Plane Barrier.

For an "absorbent" wall, Butler suggests taking the arithmetic average of the solutions for a hard wall and a soft wall (with boundary conditions $\partial p / \partial n = 0$ and $p = 0$, respectively). The rationale here is that the solution of equation (322) can be identified as having two parts: one representing the contribution from the direct source and the other representing an image source (see Figure 4-151). The effect of an "absorbent" surface is to eliminate the image source. The expressions corresponding to (322) and (323) become:

$$U = \frac{\sec [1/2(\phi - \phi_0)]}{2\sqrt{2\pi k R_1} (kr)^{1/2} (kr_0)^{1/2}} \quad (324)$$

and

$$20 \log_{10} \left\{ \left| \frac{\sec [1/2(\phi - \phi_0)]}{2\sqrt{2\pi k r_0}} \right| \right\} \quad (325)$$

Some interesting conclusions can be drawn from equations (323) and (325) regarding the dependence of the attenuation on: (1) frequency, (2) angular penetration into the shadow zone, and (3) distance of source from the edge of the plate. The dependence of attenuation is basically $-10 \log_{10} (f)$ where f is the frequency. Thus, for example, by doubling the frequency the attenuation is expected to be enhanced by about 3 dB. The angular penetration into the shadow zone can be defined as $\theta = (\phi - \phi_0 - \pi)$. The variation of the attenuation with θ for $(kr_0) = 190$ and $\phi_0 = 90^\circ$ is shown in Figure 4-152. The cases, of both a rigid wall and an "absorbent" wall are shown. It should be noted that Butler's scheme of treating "absorbent" walls intrinsically limits the effectiveness of a treated wall over a hard wall to 6 dB. Finally, the dependence of the attenuation on r_0 is $-10 \log (r_0)$. This dependence should be used with caution, however, because if r_0 is changed either by altering the length of the plate or by moving the source, etc., the result may be to alter ϕ_0 also.

4.8.2 Effect of Semi-Infinite Pipes on the Sound Field of Sources in Ducts

The solution discussed in Section 4.8.1 is relevant to situations where the intent is to shield jet noise sources from the ground by wing shields. If, on the other hand, ejector shrouds (treated or untreated) are employed, a more relevant model problem is one in which the effects of confinement by a semi-infinite pipe on the power, directivity, etc., of acoustic sources are examined.

A model problem incorporating the above features, and yet retaining the ability to obtain an explicit solution, is illustrated in Figure 4-153.

The two-dimensional problem of a semi-infinite parallel plate waveguide irradiated by a line singularity is considered in Figure 4-153. Six singularity types are considered: a simple source, x-dipole, y-dipole, xx quadrupole, xy quadrupole, and yy quadrupole, of harmonic time dependence $\exp(-j\omega t)$. The waveguide is of width $2b$ and is embedded with the singularity to an extent x_0 within the duct on the duct centerline. Flow effects are not considered, and two types of wall boundary conditions (hard wall and pressure release) are considered. The approximate result for an "absorbent" wall is obtained by arithmetically averaging these two solutions as in Section 4.8.1.

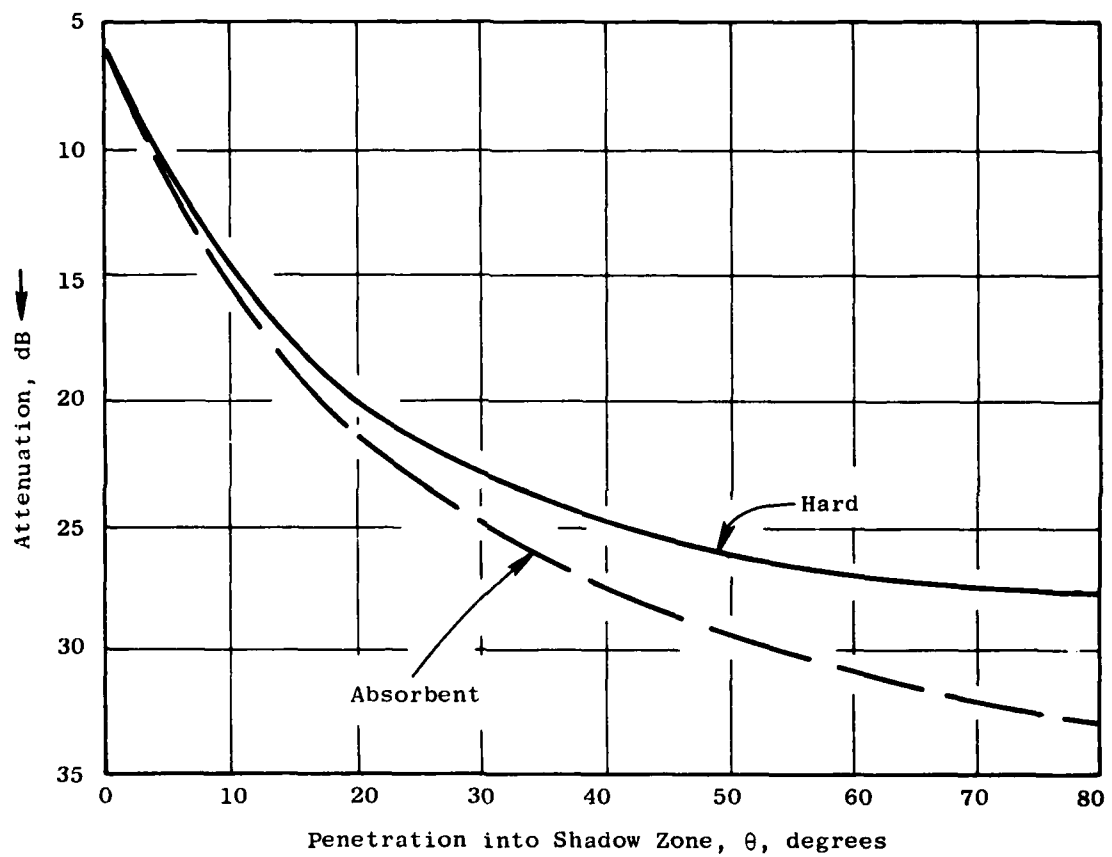


Figure 4-152. Variation of Attenuation with θ for $kr_0 = 190$ and $\phi_0 = 90^\circ$.

Both the directivity and the power of the sound field relative to the case where there is no semi-infinite pipe are desired (i.e., the case of free singularity). The relevant nondimensional parameters are (kb) , (x_0/b) , singularity type, and wall boundary condition (i.e., "absorbent" or rigid wall). The solution technique employed is the Wiener-Hopf method (see Noble(93)).

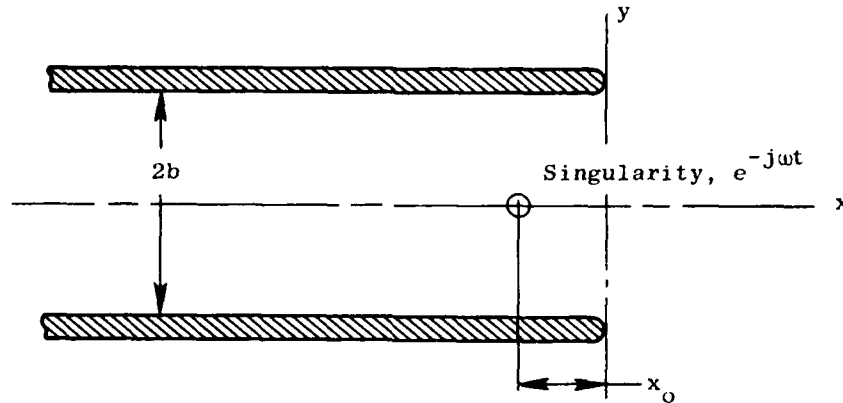


Figure 4-153. Two-Dimensional Semi-Infinite Parallel Plate Wave Guide Model.

The problem statement for a simple source with hard-wall boundary conditions is as follows. A velocity potential, $\phi(x, y)$ is sought such that ϕ satisfies:

$$\nabla^2 \phi + k^2 \phi = \delta(x + x_0) \delta(y) \quad (326)$$

subject to the boundary condition that $\partial \phi / \partial y = 0$ on $y = \pm b$ for $x < 0$, and that ϕ is continuous for $y = \pm b$ and $x > 0$. Introducing axial Fourier transforms $\phi(\alpha, y)$ defined by

$$\phi(\alpha, y) = \frac{1}{\sqrt{2\pi}} \int_{-\infty}^{\infty} \phi(x, y) e^{j\alpha x} dx \quad (327)$$

and

$$\phi(x, y) = \frac{1}{\sqrt{2\pi}} \int_{-\infty}^{\infty} \phi(\alpha, y) e^{-j\alpha x} d\alpha \quad (328)$$

It is found that ϕ satisfies the equation

$$\frac{d^2\phi}{dy^2} - \gamma^2\phi = \frac{1}{\sqrt{2\pi}} e^{-j\alpha x_0} \delta(y) \quad (329)$$

where $\gamma^2 = (\alpha^2 - k^2)$.

A particular solution for ϕ is

$$\phi_{inc} = \frac{-e^{-\gamma|y|} e^{-j\alpha x_0}}{2\sqrt{2\pi}\gamma}$$

Since γ has branch points at $\alpha = \pm k$, branch cuts can be defined as in Figure 4-154 such that γ tends to $\pm |\alpha|$ as $\alpha \rightarrow \pm \infty$ along the real axis.

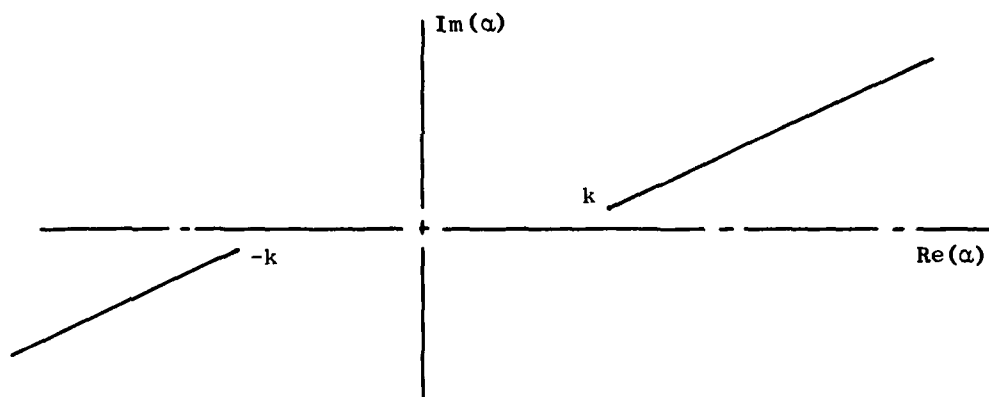


Figure 4-154. Branch Cuts for $\gamma = (\alpha^2 - k^2)^{1/2}$.

Adopting the usual convention of considering the lossless acoustic problem as the limit of a system with damping, k is assigned a small positive imaginary part which is ultimately set equal to zero. The inversion path in equation (328) has to pass below the branch point at k and above that at $-k$. The solution has the form:

$$\phi(\alpha, y) = B(\alpha) \cosh(\gamma y) - \frac{e^{-\gamma|y|} e^{-j\alpha x_0}}{2\sqrt{2\pi}\gamma} \quad (330)$$

for $0 \leq y < b$, and the form

$$\phi(\alpha, y) = A(\alpha) e^{-\gamma y} \text{ for } y > b \quad (331)$$

From the symmetry of the problem, it suffices to consider $y \geq 0$. From the continuity of $d\phi/dy$ for all x across $y = b$, it is deduced that

$$B(\alpha) \sinh(\gamma b) + A(\alpha) e^{-\gamma b} - \phi_{\text{inc}}(\alpha, b) = 0 \quad (332)$$

noting that $\phi'_{\text{inc}}(\alpha, b) = -\gamma \phi_{\text{inc}}(\alpha, b)$. From the boundary condition that

$$\frac{\partial \phi}{\partial y} = 0 \text{ for } y = b_+ \text{ and } x < 0, \text{ it is deduced that}$$

$$\gamma A(\alpha) e^{-\gamma b} = F_+(\alpha) \quad (333)$$

where $F_+(\alpha)$ is analytic in an upper half plane. Similarly, by continuity of ϕ at $y = b$ for $x > 0$, and using the above solution for $B(\alpha)$ in terms $A(\alpha)$ and $\phi_{\text{inc}}(\alpha, b)$ [equation (332)], the following expression is obtained:

$$A(\alpha) e^{-\gamma b} \left\{ 1 + \frac{\cosh(\gamma b)}{\sinh(\gamma b)} \right\} - \phi_{\text{inc}} \left[1 + \frac{\cosh(\gamma b)}{\sinh(\gamma b)} \right] = G_-(\alpha) \quad (334)$$

where $G_-(\alpha)$ is analytic in a lower half plane.

Using equation (333) in (334) one obtains

$$\frac{F_+(\alpha) (\gamma b)}{(\alpha + k) e^{-\gamma b} \sinh(\gamma b)} - \frac{(\alpha - k) \phi_{\text{inc}} b e^{\gamma b}}{\sinh(\gamma b)} = (\alpha - k) G_-(\alpha) b \quad (335)$$

Defining $\frac{e^{-\gamma b} \sinh(\gamma b)}{\gamma b}$ as $L(\alpha)$, the Wiener Hopf procedure says that if

$L(\alpha)$ can be decomposed as $L_+(\alpha) L_-(\alpha)$ (product decomposition) where $L_{\pm}(\alpha)$ are analytic in an upper/lower half plane, and if further denoting

$$\frac{(\alpha - k) \phi_{\text{inc}}(\alpha, b) b e^{\gamma b} L_-(\alpha)}{\sinh(\gamma b)} \quad (336)$$

by $S(\alpha)$, $S(\alpha)$ can be decomposed into $[S_+(\alpha) + S_-(\alpha)]$, where $S_{\pm}(\alpha)$ are analytic in an upper/lower half plane (additive decomposition), then

$$F_+(\alpha) = (\alpha + k) L_+(\alpha) S_+(\alpha)$$

and

$$A(\alpha) = \frac{(\alpha + k) L_+(\alpha) S_+(\alpha) e^{\gamma b}}{\gamma} \quad (337)$$

Now

$$S(\alpha) = \frac{-e^{-j\alpha x_0} (\gamma b) L_-(\alpha)}{2\sqrt{2\pi} \sinh(\gamma b) (\alpha + k)} \quad (338)$$

where

$$\Phi_{inc} = \frac{-e^{-j\alpha x_0} e^{-\gamma b}}{2\sqrt{2\pi} \gamma}$$

By a well known decomposition theorem [see Noble⁽⁹³⁾, p. 13],

$$S_+(\alpha) = \frac{1}{2\pi j} \int_{-\infty}^{\infty} \frac{S(\zeta) d\zeta}{(\zeta - \alpha)} \quad (339)$$

where $\text{Im}(\zeta) < \text{Im}(\alpha)$. Since $S(\zeta)$ has a term varying as $\exp(-j\zeta x_0)$ with $x_0 > 0$, the contour integral in equation (339) needs to be closed by a lower half plane semicircle, yielding for $S_+(\alpha)$

$$S_+(\alpha) = \frac{-e^{jkx_0} L_-(-k)}{2\sqrt{2\pi} (\alpha + k)} + \sum_{r=1}^{\infty} \frac{(-)^{r+1} e^{jx_0 k_r} L_-(-k_r) (1 + \frac{k}{k_r})}{2\sqrt{2\pi} (\alpha + k_r)} \quad (340)$$

where $k_r = \left\{ k^2 - \left(\frac{r\pi}{b} \right)^2 \right\}^{1/2}$ for $kb > r\pi$ and $k_r = j \left\{ \left(\frac{r\pi}{b} \right)^2 - k^2 \right\}^{1/2}$

for $kb < r\pi$

The product decomposition of $L(\alpha)$ is discussed on page 104 of Noble. Since, for large r , $k_r \rightarrow (j r \pi / b)$, the above series for $S_+(\alpha)$ will converge exponentially. However, the convergence will be slower the smaller the value of x_0 . Note that the above method does not apply at all for $x_0 < 0$, i.e., for singularities not embedded within the duct.

Thus $A(\alpha)$ is completely determined. Now $\phi(x, y)$ for $y > b$ is:

$$\phi(x, y) = \frac{1}{\sqrt{2\pi}} \int_{-\infty}^{\infty} A(\alpha) e^{-j\alpha x} d\alpha e^{-\gamma y} \quad (341)$$

Noble⁽⁹³⁾ shows that with $x = r \cos \theta$, $y = r \sin \theta$, as $r \rightarrow \infty$ (far field),

$$\phi(x, y) \rightarrow \frac{(2k\pi)^{1/2}}{\sqrt{2\pi}} e^{-j\pi/4} \sin(\theta) A(-k \cos \theta) r^{-1/2} \exp(jkr) \quad (342)$$

Consider now the case where the walls are of the pressure-release type, i.e., $\phi = 0$ on $y = \pm b$ for $x < 0$. The formal steps involved in equations (326) to (331) still apply. Now however, it is ϕ that is continuous across $y = b$ for all x . Hence:

$$A(\alpha) e^{-\gamma b} = B(\alpha) \cosh(\gamma b) - \frac{e^{-\gamma b} e^{-j\alpha x_0}}{2\sqrt{2\pi} \gamma} \quad (343)$$

Also, because $\phi = 0$ for $y \rightarrow b_+$ and $x < 0$, it is found that

$$A(\alpha) e^{-\gamma b} = F_+(\alpha) \quad (344)$$

Note that $F_+(\alpha)$ and $G_-(\alpha)$ merely denote analytic functions in the upper and lower half planes, and it is not intended that the $F_+(\alpha)$ appearing in equation (344) is the same as that appearing in (333).

Finally, because $\partial\phi/\partial y$ is continuous for $y = b$ and $x > 0$,

$$\gamma A(\alpha) e^{-\gamma b} + \gamma B(\alpha) \sinh(\gamma b) + e^{-\gamma b} e^{-j\alpha x_0} = G_-(\alpha) \quad (345)$$

Eliminating $B(\alpha)$ with the aid of equation (343) and using (344) one obtains:

$$\frac{F_+(\alpha) \gamma}{e^{-\gamma b} \cosh(\gamma b)} + \frac{e^{-j\alpha x_0}}{2\sqrt{2\pi} \cosh(\gamma b)} = G_-(\alpha) \quad (346)$$

Let $K(\alpha) = e^{-\gamma b} \cosh(\gamma b)$, and again let $K(\alpha)$ be factorable as $K_+(\alpha) K_-(\alpha)$ where $K_+(\alpha)$ and $K_-(\alpha)$ are analytic in upper and lower half planes. This factorization is discussed in detail on pages 102 - 104 of Noble⁽⁹³⁾. Since γ can be written as $\sqrt{(\alpha - k)(\alpha + k)}$, i.e., as a product of two factors, one analytic in an upper half plane and the other in a lower half plane, $S(\alpha)$ can be decomposed as follows:

$$\begin{aligned} S(\alpha) &= \frac{K_-(\alpha) e^{-j\alpha x_0}}{2\sqrt{2\pi} \cosh(\gamma b) \sqrt{(\alpha - k)}} \\ &= S_+(\alpha) + S_-(\alpha) \end{aligned} \quad (347)$$

It can be shown that:

$$A(\alpha) = e^{\gamma b} F_+(\alpha) = \frac{-K_+(\alpha) S_+(\alpha) e^{\gamma b}}{\sqrt{(\alpha + k)}} \quad (348)$$

As in the case of the rigid wall problem, the additive decomposition theorem of Noble can be applied to yield the following result for $S_+(\alpha)$,

$$S_+(\alpha) = \sum_{r=0}^{\infty} \frac{K_-(-k_{r+1/2}) e^{jx_0 k_{r+1/2}} (r+1/2) \pi (-)^{r+1}}{(\alpha + k_{r+1/2}) 2\sqrt{2\pi} b^2 k_{r+1/2} (-k_{r+1/2} - k)^{1/2}}$$

where

$$k_{r+1/2} = \left\{ k^2 - [(r+1/2) \pi / b]^2 \right\}^{1/2} \quad \text{if } kb > (r+1/2) \pi$$

and

$$k_{r+1/2} = j \left\{ [(r+1/2) \pi / b]^2 - k^2 \right\}^{1/2} \quad \text{if } kb < (r+1/2) \pi \quad (349)$$

As in equations (341) and (342), $\phi(x, y)$ can then be evaluated asymptotically for large r .

Complex as the above two solutions may seem, their physical interpretation is not. In both cases, the source first excites duct waveguide modes as if the duct were doubly-infinite, and then the waves produced to the right of the source radiate to the right of the source according to the "transfer function" linking far-field radiation to a given incident duct waveguide mode (as discussed e.g., in Noble⁽⁹³⁾, pages 105-110).

The above solutions can be immediately differentiated with respect to x_0 once to obtain the solutions for an x-dipole and twice to obtain the solutions for an xx quadrupole. This is because, for any function $f(x + x_0)$, $\partial^2/\partial x^2 [f(x + x_0)] = \partial^2/\partial x_0^2 [f(x + x_0)]$, and, hence, the solution for higher order axial singularities may be obtained by differentiating the solutions for the simple source with respect to axial source position. The resulting effect is to simply multiply each term in the series of equation (340) by $(jk_-)^n$ and that of (349) by $(jk_{r+1/2})^n$ where n is the relevant number of differentiations. Because of the exponential terms $\exp(j x_0 k_r)$ or $\exp(j x_0 k_{r+1/2})$, there is no problem with the convergence of either series, though the convergence does get poorer as x_0 becomes small.

Consider now the case of a transverse singularity; i.e., with the source term $\delta(x + x_0) \delta'(y)$ in equation (326) rather than $\delta(x + x_0) \delta(y)$. Since the source term is antisymmetric in y , all the solutions will also be antisymmetric. Since the basic procedure is similar to the previously-discussed problems, only the broad outlines will be indicated. ϕ_{inc} is now $\{\pm e^{-\gamma|y|} e^{-j\alpha x_0/2\sqrt{2\pi}}\}$, obtained by differentiating the previous expression for ϕ_{inc} with respect to y . A solution of type $[B \sinh(\gamma y) + \phi_{inc}]$ is assumed for ϕ for $-b < y < b$, and one of type $\pm A(\alpha) e^{-\gamma|y|}$ is assumed for $y > b$ and $y < -b$. For the case of rigid walls, continuity of $d\phi/dy$ for $y = b$ and all x yields one relation between $B(\alpha)$, ϕ_{inc} and $A(\alpha)$. Since $\partial\phi/\partial y = 0$ for $y = b$ and $x < 0$, $\gamma A(\alpha) e^{-\gamma b}$ is again analytic in an upper half plane. Finally, continuity of $\phi(x, y)$ for $y = b$ and $x > 0$ again yields a Wiener-Hopf equation whose solution is

$$A(\alpha) = \frac{K_+(\alpha) S_+(\alpha) e^{\gamma b}}{\sqrt{(\alpha - k)}} \quad (350)$$

where

$$S_+(\alpha) = \sum_{r=0}^{\infty} e^{j x_0 k_{r+1/2}} (-)^{r+1} K_-(-k_{r+1/2}) \sqrt{(-k_{r+1/2} - k)} (r+1/2)\pi / [(\alpha + k_{r+1/2}) 2\sqrt{2\pi} b^2 k_{r+1/2}] \quad (351)$$

The analogous result for the y-dipole in a pressure release duct is:

$$A(\alpha) = e^{\gamma b} L_+(\alpha) S_+(\alpha) \quad (352)$$

where

$$S_+(\alpha) = \sum_{r=1}^{\infty} \frac{L_-(-k_r) e^{jx_0 k_r} (-)^{r+1} (k_r^2 - k^2)}{k_r 2\sqrt{2\pi} (\alpha + k_r)} \quad (353)$$

Solutions (350) and (352) can be differentiated with respect to x_0 (effectively a multiplication of series (351) by $(jk_{r+1/2})$ and of series (353) by (jk_r) to derive the solutions for an xy quadrupole.

Finally, consider the case of a yy quadrupole in the semi-infinite waveguide. ϕ_{inc} is now

$$\left\{ \frac{\delta(y) e^{-j\alpha x_0}}{\sqrt{2\pi}} - \frac{\gamma e^{-\gamma|y|} e^{-j\alpha x_0}}{2\sqrt{2\pi}} \right\}$$

and is symmetric in y . Now (for rigid walls),

$$A(\alpha) = \frac{(\alpha + k) L_+(\alpha) S_+(\alpha) e^{\gamma b}}{\gamma}$$

where

$$S_+(\alpha) = \sum_{r=1}^{\infty} \frac{(-)^{r+1} L_-(-k_r) e^{jx_0 k_r} (k + k_r)^2 [1 - (k/k_r)]}{2\sqrt{2\pi} (\alpha + k_r)} \quad (354)$$

For pressure release walls,

$$A(\alpha) = \frac{-K_+(\alpha) S_+(\alpha) e^{\gamma b}}{\sqrt{\alpha + k}} \quad (355)$$

with

$$S_+(\alpha) = \sum_{r=0}^{\infty} (-)^r \pi (r+1/2) K_- (-k_{r+1/2}) e^{jx_0 k_{r+1/2}} (-k_{r+1/2} - k)^{1/2} \left(1 - \frac{k}{k_{r+1/2}}\right) / [(\alpha + k_{r+1/2}) 2\sqrt{2\pi} b^2] \quad (356)$$

This completes the formal derivation of the solutions for the various singularities embedded in the semi-infinite duct.

The solutions for the "free" singularities can be obtained by using equations (341) and (342) with ϕ_{inc} being substituted for $A(\alpha)$. For convenience, these "free" singularity far-field directivities are tabulated below.

Singularity Type	Far-Field Directivity of ϕ
Line Source	$-j/k$
Line Axial Dipole	$\cos \theta$
Line y Dipole	$\sin \theta$
Line xx Quadrupole	$jk \cos^2 \theta$
Line xy Quadrupole	$2jk \sin \theta \cos \theta$
Line yy Quadrupole	$jk \sin^2 \theta$

The result for the xy quadrupole in the above tabulation was multiplied by 2 to render its peak value (at $\theta = 45^\circ$) as jk .

The above results were programmed for computation as follows. The directivity of the embedded singularity is calculated every 5° from $\theta = 0^\circ$ to $\theta = 180^\circ$. It is compared to that of the "free" singularity over these same angles. Comparisons are made for the six singularity types for both hard wall ducts and for "absorbent" ducts (taking the arithmetic average of the solutions for a hard wall and pressure release waveguide). Detailed calculations were carried out for $kb = 0.2, 0.5, 1, 2, 3, 6, 10, \text{ and } 20$, and for $x/b = 0.25, 0.5, 1, 2, \text{ and } 5$. By integrating the expressions for the mean square pressure

from $\theta = 0^\circ$ to $\theta = 180^\circ$, total power changes were also inferred. To provide another reference limit (other than the "free" singularity limit) theory and calculations were also developed to compute the power changes if the singularities were embedded in doubly infinite pipes (both pressure release and rigid wall pipes were considered). This theory is much more straightforward than that for semi-infinite pipes and is briefly indicated below.

Consider a simple source in a doubly infinite rigid walled duct (Figure 4-155).

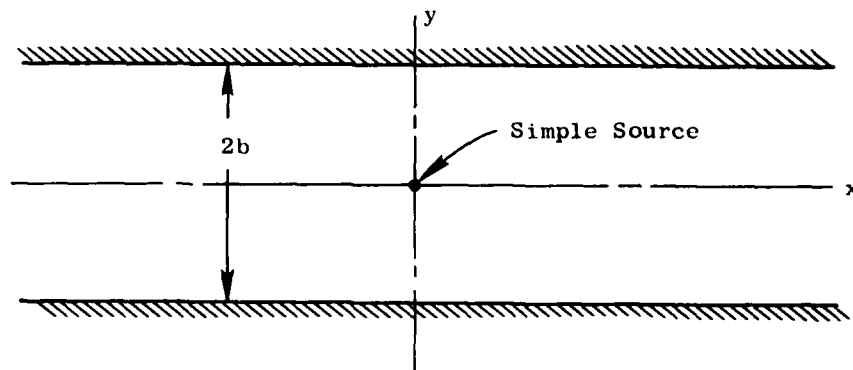


Figure 4-155. Simple Source in a Doubly Infinite Rigid Walled Duct.

The mathematical problem is to solve for

$$\nabla^2 \phi + k^2 \phi = \delta(x) \delta(y) \quad (357)$$

subject to $\partial \phi / \partial y = 0$ on $y = \pm b$ and outgoing waves as $x \rightarrow \pm \infty$.

Noting that the excitation is symmetric in y , the solution for $x > 0$ can be written as

$$\phi = \frac{e^{jkx}}{4 jkb} + \sum_{r=1}^{\infty} \frac{e^{jk_r x} \cos(r\pi y/b)}{2 jk_r b} \quad (358)$$

Again, differentiating these solutions with respect to x once will yield the solutions for the x -dipole and differentiating twice will yield the solutions for the xx quadrupole. For power calculations, only r values such that $kb > r\pi$ are of interest. The power transmitted down the pipe to each side will be

$$\int_{-b}^b |\phi|^2 \left(\frac{k_r}{k}\right) dy = \frac{2b}{16k^2 b^2} + \sum_1^R 1/(4bk k_r) \quad (359)$$

where R is the largest integer for which $kb > r\pi$. Since the solution to $[\nabla^2 \phi + k^2 \phi = \delta(x) \delta(y)]$ in free space can be shown to have a power on this basis of $(1/4k)$, the ratio of powers (i.e., that of the power of the embedded singularity to that of the free singularity) can be shown to be

$$\frac{1}{2kb} + \sum_1^R \frac{1}{bk_r} \quad (360)$$

Differentiating (358) twice with respect to y yields the solution for a yy quadrupole. Power ratios can again be derived analogously.

The solution for the y dipole in a rigid-wall duct can be derived by using the expansion formula

$$\delta'(y) = -\frac{\pi}{2} \sum_0^{\infty} (r + 1/2) \sin \left[(r + 1/2) \frac{\pi y}{b} \right] \quad (361)$$

Based on this, one can show that the solution to $\nabla^2 \phi + k^2 \phi = \delta'(y) \delta(x)$, subject to $\partial \phi / \partial y = 0$ on $y = \pm b$, and ϕ antisymmetric in y, is

$$\phi = \frac{j\pi}{2b^2} \sum_0^{\infty} \frac{e^{jk_{r+1/2}x} (r+1/2)}{(k_{r+1/2})} \sin \left[(r+1/2) \frac{\pi y}{b} \right] \quad (362)$$

A power ratio can be derived from equation (362) by computing

$$\int_{-b}^b |\phi|^2 \left(\frac{k_{r+1/2}}{k}\right) dy$$

and dividing by $(k/8)$ which is the power of a "free" dipole on this basis. The result is

$$\frac{2\pi^2}{k^2 b^2} \sum_0^{R'} (r+1/2)^2 / (bk_{r+1/2}) \quad (363)$$

The solution of equation (362) can be differentiated with respect to x to yield the result for an xy quadrupole in a rigid duct.

Consider now the simple source in a pressure release duct. The expansion formula,

$$\delta(y) = \frac{1}{b} \sum_0^{\infty} \cos [(r+1/2) \frac{\pi y}{b}],$$

is relevant, and the solution for ϕ is:

$$\phi = \frac{1}{2jb} \sum_0^{\infty} \frac{e^{jk_{r+1/2}x} \cos [(r+1/2) \pi y/b]}{k_{r+1/2}} \quad (364)$$

Differentiating (364) with respect to x once and twice gives the solution for an x dipole and an xx quadrupole, respectively, in a pressure-release duct. Interestingly enough, the solution of equation (349) when differentiated with respect to y will yield the solution for a y dipole in a pressure release duct. Differentiating this latter solution with respect to x will, in turn, yield the solution for an xy quadrupole in a pressure release duct. Finally, solution of (362) differentiated once with respect to y will yield the solution for a yy quadrupole in a pressure release duct.

The important results of the analytical parametric study carried out in this section shall be discussed, under the headings of: (1) effect of frequency (kb variation holding other parameters fixed), (2) effect of (x_0/b) or the depth of embedding, (3) effect of singularity type, (4) effects on directivity, (5) effects of "absorbent" walls, and (6) implications for ejector acoustics. Discussions of (1), (2), and (3) will be for the power changes (from "free" to embedded) with rigid wall pipes while those for (5) will be for the power change from rigid to "absorbent". Discussion of (6) will also be for rigid wall pipes.

Effect of Frequency - The power changes [$P_{free}/P_{emb.}$] in dB are shown in Figure 4-156 for various values of x/b , for a simple source and an $x-y$ quadrupole. The simple source never experiences any enhancement and is often diminished in a manner similar to the 3-7 dB type diminution experienced for the source in a doubly infinite pipe. For the xy quadrupole, significant

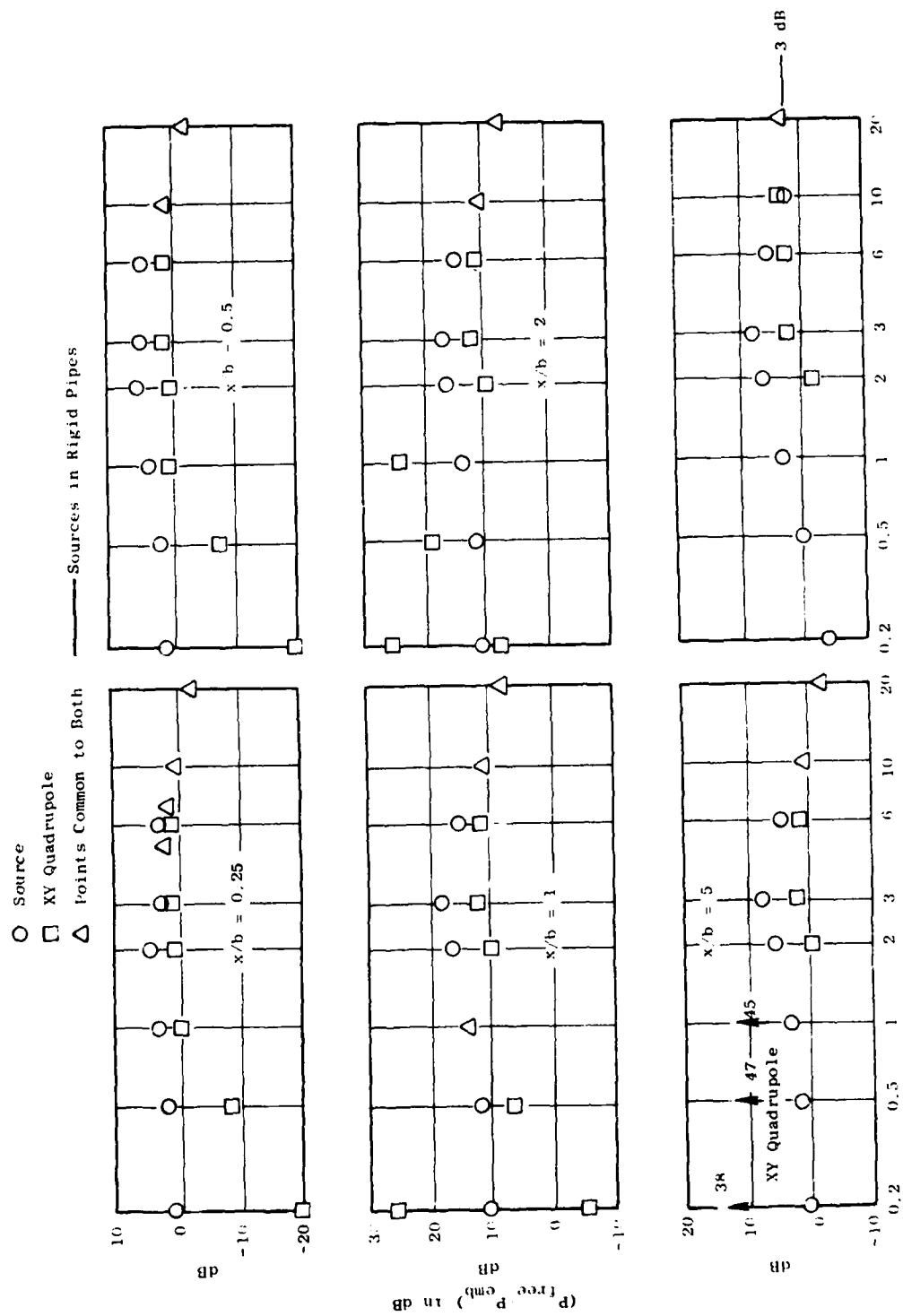


Figure 4-156. Rigid Walls; Effect of Frequency.

power enhancement can occur for $kb < 1$ and $x/b < 2$. That is, the embedded quadrupole can generate far more power than a "free" quadrupole (of the same strength) due to strong interaction with the duct edges. For $x/b < 2$, the enhancement increases as kb decreases, since low frequency waves can "sense the edges" substantially. For $x/b \geq 2$, there is no significant enhancement, and decreasing kb no longer has an adverse effect, due to the fact that for $kb < \pi/2$ the xy quadrupole excites only nonpropagating duct modes whose decay rate is greater the lower the value of kb .

Effect of (x_0/b) - These results are shown in Figure 4-157. As might be anticipated from Figure 4-156, simple source results are not very interesting. The xy quadrupole results for $kb = 0.2, 0.5$, and 1 show the dramatic alleviation of the edge interaction enhancement by deeper embedding. Once kb exceeds $\pi/2$ (the "cut on" frequency for the xy quadrupole), the behavior of the xy quadrupole solutions becomes very similar to those of the simple source. This is expected, since for a simple source, x dipole and xx quadrupole, the "cut on" value of kb equal 0 with rigid walls. In Figure 4-157, for kb greater than appropriate "cut on" frequency, the results for the source in a doubly infinite pipe are also shown.

Effect of Singularity Type - These results are shown in Figures 4-158 and 4-159. The "cut on" values of kb for a rigid walled duct are: (1) 0 for the simple source, x dipole, xx quadrupole; (2) $\pi/2$ for the y dipole, xy dipole; and (3) π for the yy quadrupole. Above these "cut on" values, the embedded semi-infinite pipe values generally lie between the doubly infinite pipe and free space value (0 dB) with a preference for the latter at low frequencies (except at very close spacings for quadrupole singularities), and for the former at high frequencies. Below these cut on values, the xy quadrupole alone generally shows the previously noted enhancement at low frequencies $kb \leq 1$ and for $(x/b < 2)$. The y dipole is not singular enough (inasmuch as edge interactions themselves are of dipole character) to exhibit any significant enhancement. The yy quadrupole does show 10 dB type enhancement at $kb = 0.2$ and $x/b = 0.25$, but with its "high" cut on frequency ($kb = \pi$), any significant embedding destroys such enhancement. Another minor point of Figure 4-159 is that, at high frequencies (especially for the smaller x/b), the transverse singularities (y dipole, xy quadrupole, and yy quadrupole) are closer to the free space values (0 dB) (as compared to the doubly infinite pipe values) than are the axial singularities. This is because the benefits of physical shielding really occur at large angles to the jet axis (θ_j tending to 180°) where these singularities are weak.

Effects on Directivity - The mechanism by which embedded singularities radiate to the far field is that they first excite duct wave guide modes as if the duct were doubly infinite, and these then radiate to the far field from the open end (in addition to producing reflected waves in the duct). At low frequencies, the characteristic directionality of axial singularities is more or less completely destroyed, and their radiation patterns become very similar to that of a source in a duct, being more or less omnidirectional in the "illuminated" portion of the exhaust arc and exhibiting a characteristic shielding effect in the inlet arc. The shielding increases (generally) with frequency, angle from jet axis and, to some extent, with depth of embedding.

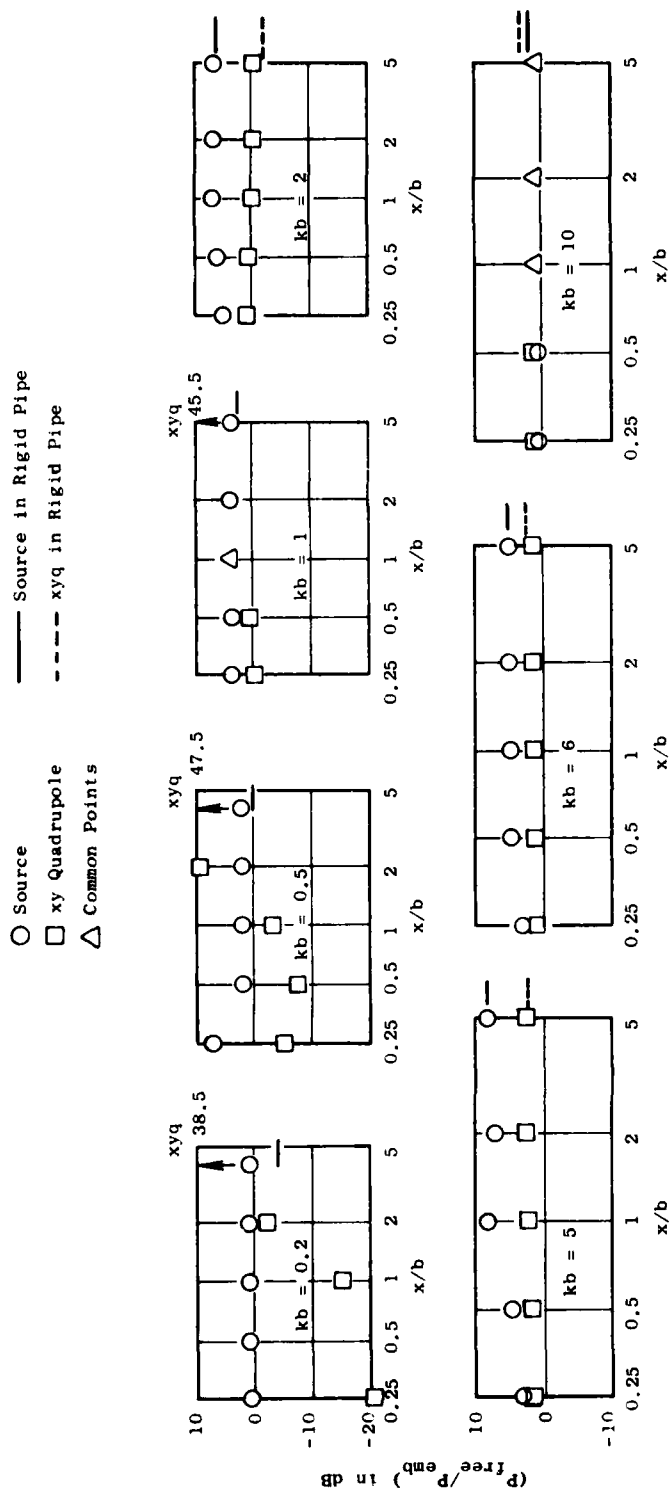


Figure 4-157. Rigid Walls: Effect of X/B : P_{free}/P_{emb} , dB.

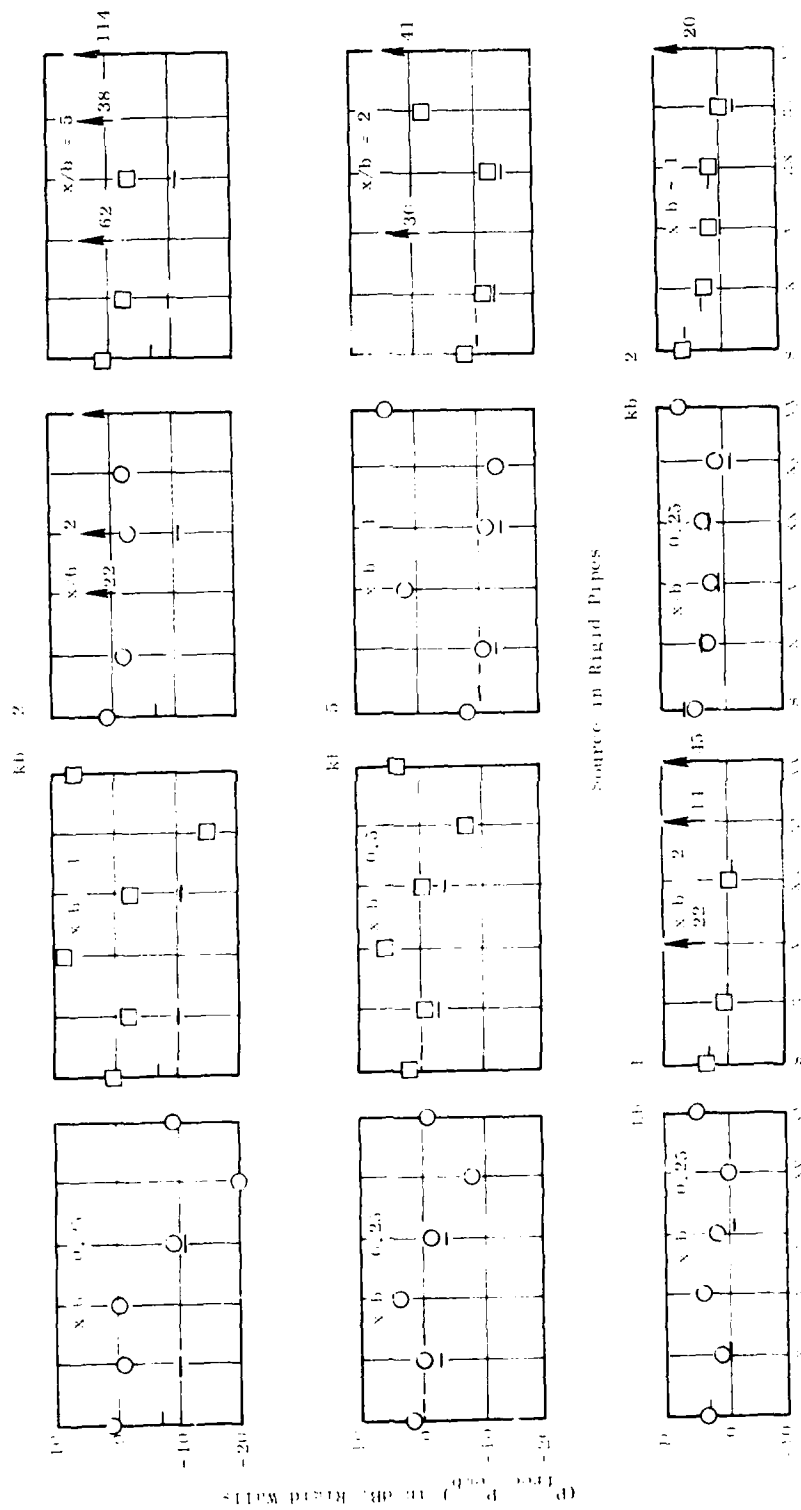


Figure 4-158. Effect of Singularity Type.

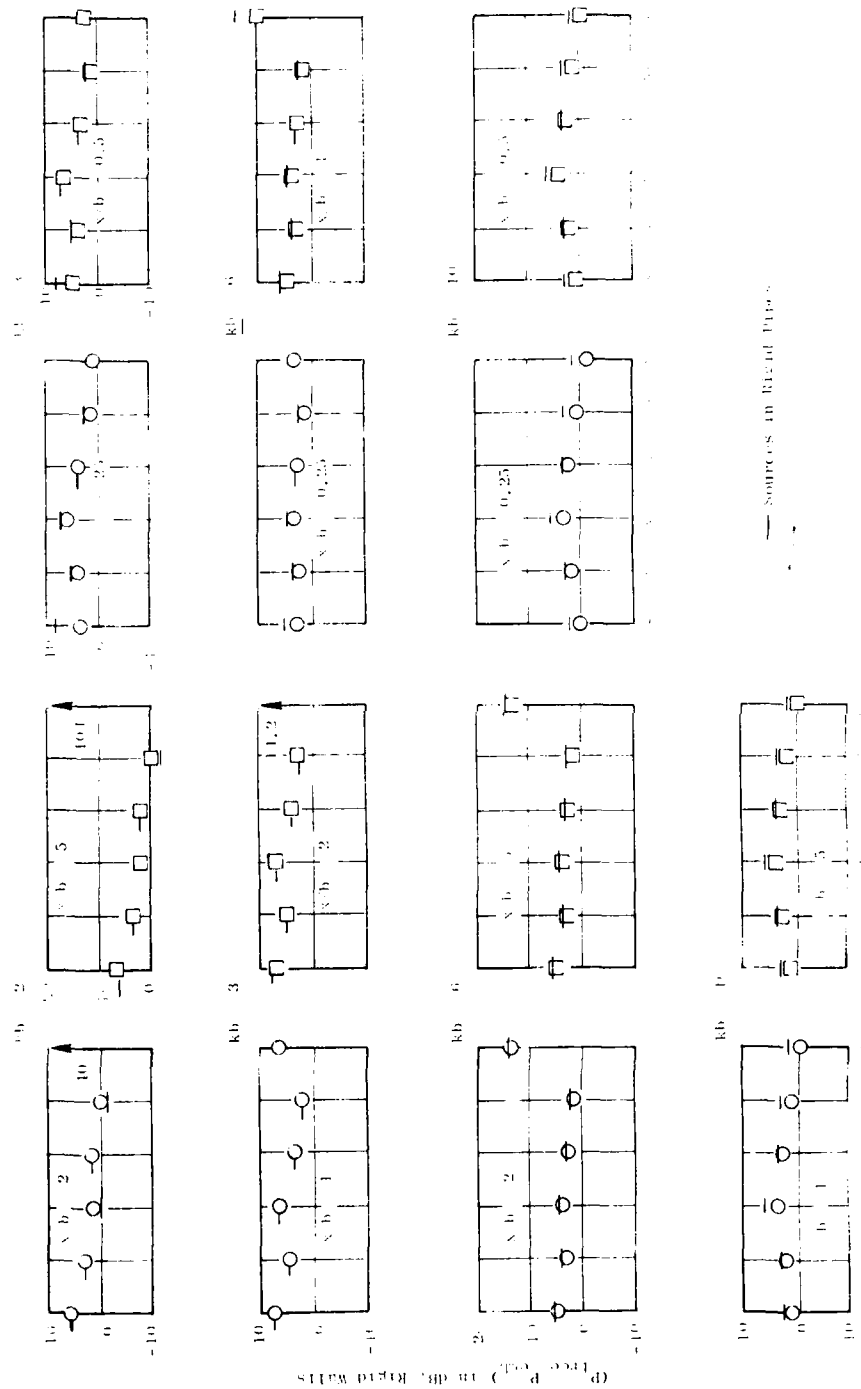


Figure 4-159. Effect of Singularity Type.

Figure 4-160 shows some of the directivity results, where the directivity of the "free" singularity is also shown. The directivity of the embedded singularity can be inferred from the formula $(p'_{emb})_{dB} = (p'_{free})_{dB} - (p'_{free}/p'_{emb})_{dB}$. At low frequencies, the transverse singularities generally exhibit a directivity pattern resembling that of a transverse dipole in a plate [i.e., varying as $\sin(\theta_j/2)$]. At high frequencies a remarkable, exact solution results. The type of duct waveguide modes excited by the various singularities can be tabulated as shown in Table 4.8-1.

Table 4.8-1. Waveguide Duct Mode Types.

$$n = 0, 1, 2, 3, \dots$$

Singularity	Rigid Walls		Pressure Release	
Source	$\cos(n\pi y/b)$	①	$\cos[(n + 1/2)\frac{\pi y}{b}]$	②
x dipole	$\cos(n\pi y/b)$	①	$\cos[(n + 1/2)\frac{\pi y}{b}]$	②
y dipole	$\sin[(n + 1/2)\frac{\pi y}{b}]$	②	$\sin(n\pi y/b)$	①
xx quadrupole	$\cos(n\pi y/b)$	①	$\cos[(n + 1/2)\frac{\pi y}{b}]$	②
xy quadrupole	$\sin[(n + 1/2)\frac{\pi y}{b}]$	②	$\sin(n\pi y/b)$	①
yy quadrupole	$\cos(n\pi y/b) (n \neq 0)$	①	$\cos[(n + 1/2)\frac{\pi y}{b}]$	②

Associated with the singularity-boundary conditions shown as ① in Table 4.8-1, one can associate angles $\theta_n = \sin^{-1}(n\pi/kb)$ and angles $\theta_{n-1/2} = \sin^{-1}[(n - 1/2)\pi/kb]$ with the combinations shown as ②. These angles are all less than $\pi/2$, and only a few of these will exist, depending on how large kb becomes (there will be more and more such angles as kb increases). The remarkable fact is that, for the combinations shown as ①, the far-field acoustic pressure is exactly the same as its free-field value except for a phase shift of $\exp(jk_n x_0)$ where $k_n = \{k^2 - (n\pi/b)^2\}^{1/2}$ at the angles θ_n . This result is independent of x_0 . Similarly, for the combinations shown as ②, the pressure is unchanged at $\theta_{n+1/2}$ except for a phase shift $\exp(jk_{n+1/2} x_0)$, where $k_{n+1/2} = \{k^2 - [(n+1/2)\pi/b]^2\}^{1/2}$. Based on this exact result, the result for high frequencies (with regard to directivity changes) can be explained as follows: In the exhaust arc (for $0 \leq \theta_j \leq 90^\circ$), at the above mentioned angles, the ratio p'_{emb}/p'_{free} is unity. Between these angles (which become increasingly close together as kb goes up) there are characteristic diffraction valleys and peaks which are more intense as kb becomes small

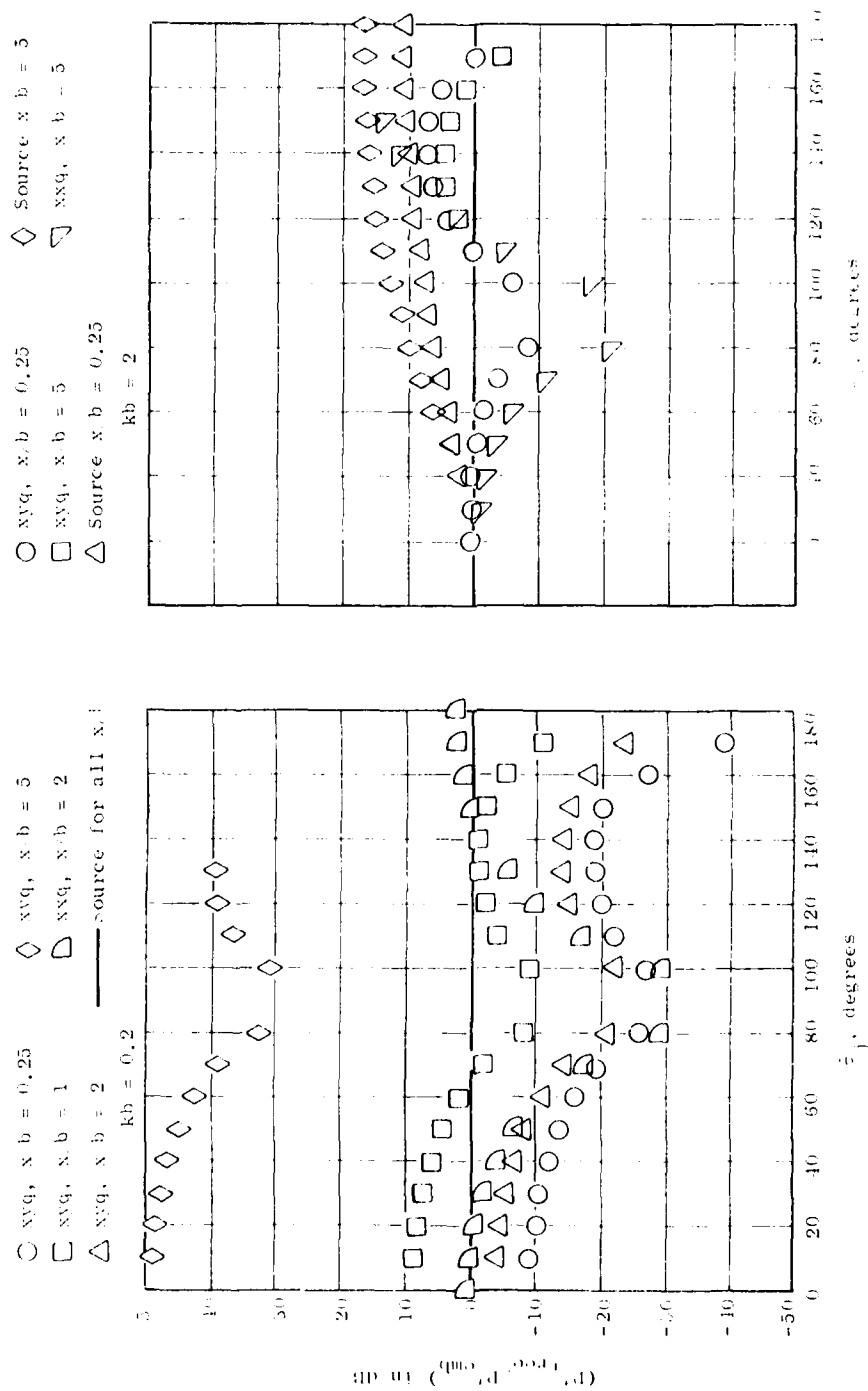


Figure 4-160. Directivity, Rigid Walls.

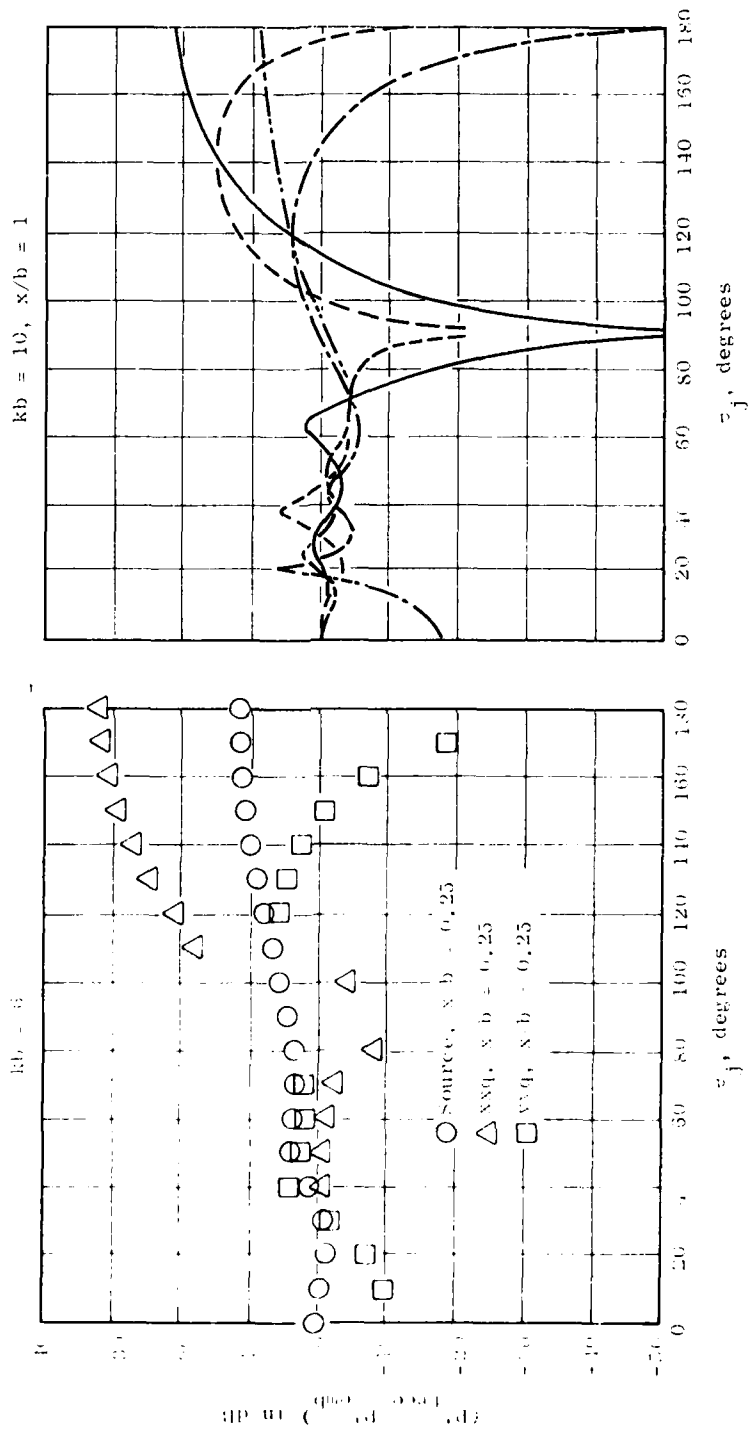


Figure 4-160. Directivity, Rigid Walls (Continued).

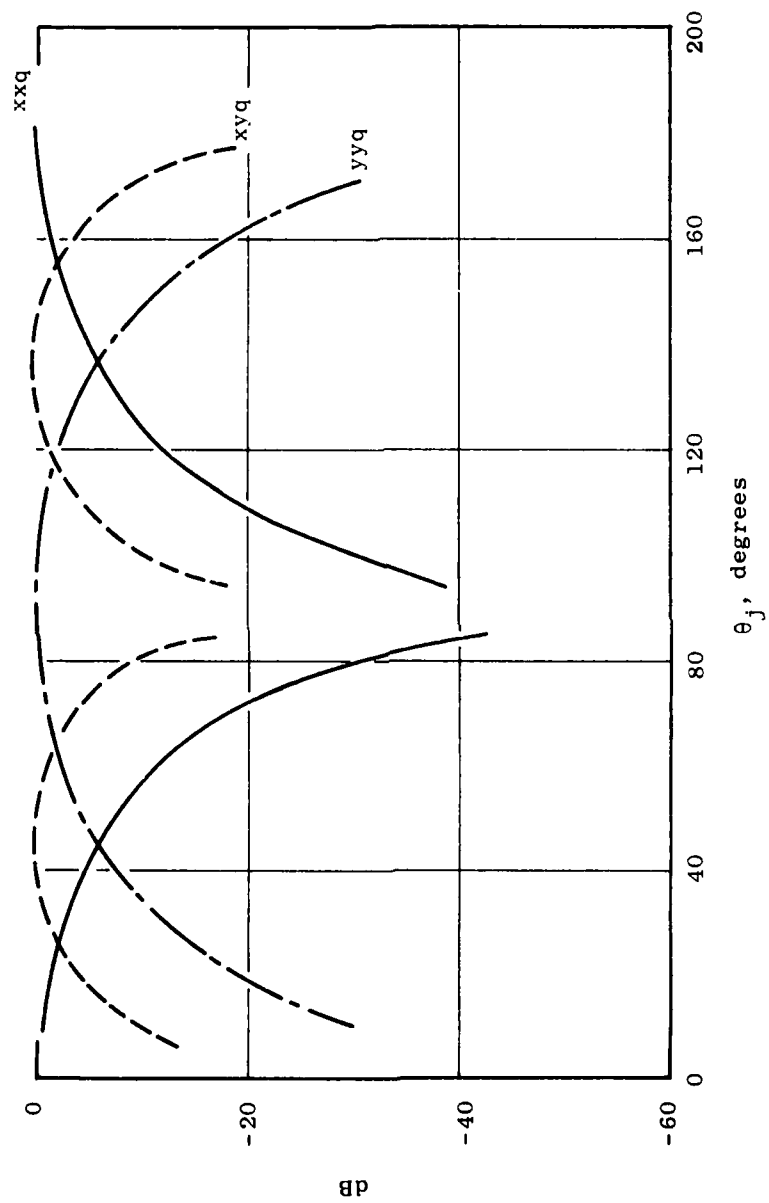


Figure 4-160. Directivity of Free Singularities (Concluded).

the more complex the singularity, the smaller x/b is, and the greater the value of θ_j . Beyond $\theta_j = 90^\circ$, there is strong physical shielding, which increases with kb , x/b , θ_j , and is most pronounced for the xx quadrupole, and least pronounced for the yy quadrupole (shielding being estimated from the ratio p'_{free}/p'_{emb}).

Effects of "Absorbent" Walls - It is reiterated that the modeling in the present analysis of the effect of absorbent walls is quite crude, being based on suggestions by Butler⁽⁹⁴⁾ that some estimate of this effect can be obtained by taking the arithmetic average of the solution for rigid and pressure-release walls. This approximation basically limits the predicted power change due to "absorbing" walls to about 6 dB (except for possible unusual phasing and duct cut-off effects). The results are shown in Figure 4-161. Two aspects of the results, while correct in the context of the present model, ought to perhaps be viewed with skepticism. First, for $kb < \pi$ and large embedding, absorbing walls are actually predicted to increase the acoustic power of a yy quadrupole over the case of rigid walls. This is because the cut-on frequency for a yy quadrupole with pressure release walls is actually less ($kb = \pi/2$) for pressure-release walls than for rigid walls ($kb = \pi$). Second, for large kb (for example, $kb = 20$ results), absorptive walls are predicted to have a very small effect. This is because, with centerline source placement, at high kb the walls are too distant from the source to significantly affect its radiation. High frequency jet noise sources may be located well off-axis, so that they are quite close to the "absorbent" walls. Hence the results of Figure 4-161 should not be misconstrued as implying that lined ejectors will be ineffective at high frequencies. Apart from these two reservations, the results of Figure 4-161 are quite reasonable. Absorbent walls are more effective on transverse singularities, especially with short depths of immersion. This is presumably because of the stronger concentration in the direction of the walls of the free fields of such singularities (as compared to axial singularities whose free fields are more focused parallel to the duct axis). With $x/b \geq 2$, at low frequencies such differences disappear, and treatment is rather uniformly effective on all singularities (except for the previously noted case of the yy quadrupoles). At high frequencies, differences (based on singularity type) persist even with deep embedding, and one continues to notice rather greater effectiveness for the transverse singularities. Deeper embedding helps in enhancing treatment effectiveness, but in the present model this is only true up to an x/b value of approximately 2.

Implications for Ejector Acoustics - It should be noted first of all that this effort addresses only the physical shielding or acoustics aspects of embedding jet noise sources in a containment such as an ejector. An ejector undoubtedly alters the aerodynamics of the jet plume in a major way (source alteration), and this issue is not addressed in the present study. Also, the present study only addresses the sources that lie inside the ejector, since these are the only ones that are expected to be subject to shielding/solid surface interaction effects. The implications of this study are as follows: Identifying "2b" in Figure 4-153 with the duct diameter and considering jets with exit Mach number from 1 to 2 and low Strouhal numbers of the order 0.25 to 0.5, the use of ejectors may actually have a negative effect unless they are quite long (L/D substantially greater than unity). This is because

substantial power enhancement occurs for the xy quadrupole, in this Strouhal number regime with ejectors of L/D of order unity, much of this enhancement occurring at right angles to the jet axis and in the inlet arc. With regard to directionality at such low Strouhal numbers, the patterns will be far less directional in the sideline and inlet arc portions than the "free" jet patterns. At high frequencies, ejectors can provide a real shielding benefit especially at large angles to the jet axis ($\theta_j \geq 90^\circ$). In the exhaust arc itself ($\theta_j \leq 90^\circ$), the ejector shielding effects (at high frequencies) are minimal being confined to minor diffraction effects. A treated ejector does help to mitigate some of the low frequency power enhancement effects since it is most effective along the sideline and inlet arc directions where much of the power enhancement occurs. As might be expected, treatment, to be effective, does require the sources to be close (in terms of wave lengths) to the treated surface. The enhancement of low frequency power previously referred to will be an adverse effect only to the extent that the flow inside the ejector is turbulent.

5.0 MIXING INTERFERENCE EXPERIMENTS

A series of experiments has been conducted to evaluate the acoustic and aerodynamic characteristics of various types of single- and multielement jets. The various configurations tested were comprised of simple shapes and arrays which could be used to examine and isolate various jet noise mechanisms. The following configurations were tested:

1. Single round Jet ($d = 7/8"$ diam. and 1.5" diam.)
2. Single rectangular jet, 6:1 aspect ratio
3. Twin round jets, $1.33 \leq s/d \leq 5.0^*$
4. Twin rectangular jets, $2.08 \leq s/t \leq 13.89^*$
5. Five-jet linear arrays
6. Six- and seven-tube clustered arrays

Tables 5-1 through 5-5 list the test point conditions for each of these configurations where acoustic data were taken. Table 5-6 summarizes the conditions and locations where laser velocimeter flow field measurements were taken for each configuration. Finally, source location measurements using the "hole-in-the-wall" technique were made for selected configurations, and these are summarized in Tables 5-7 and 5-8.

The following sections describe each of these experiments in detail, with an emphasis placed on evaluation of the various jet noise mechanisms identified in Section 4.

5.1 SINGLE ROUND JET NOISE

A series of experiments were conducted to provide data on the individual round jets used in twin-round linear array and circular array configurations. These experiments were performed with the same 7/8-in. and 1.5-in. diameter, which were used in the multijet tests. The test parameters were arranged to produce the same velocity and temperature as in the multijet tests. A map of the velocities and temperatures is shown in Figure 5-1. All of these tests were carried out at the CRD jet noise facility with the microphone boom in a horizontal position, $\psi = 0$, and with 8 inches of acoustical foam covering the concrete pad. A complete description of this facility is available in a paper by Kantola⁽⁹⁴⁾. To establish the validity of this data set, the experimental results obtained here are compared to well established prior information. It should be noted that corrections have not been applied to these data for ground reflection and atmospheric absorption due to the acoustical foam ground cover and to the short microphone radius of 9 ft.

* s denotes the minimum center-to-center distance between two nozzles and t the width of the rectangular nozzle.

Table 5-1. Test Point Conditions for Single Round Jet.⁽¹⁾

Velocity (fps)	Temperature (° R)					
	530	1250	1600	1700	1900	2000
1000	SR 7/8 ⁽²⁾ SR SRE	SR 7/8 SR SRE	SR 7/8	SR SRE	SR 7/8 SR SRE	SRE
1500		SR 7/8 SR SRE	SR 7/8	SR SRE	SR 7/8 SR SRE	SRE
175		SR 7/8	SR 7/8		SR 7/8	
1900		SR SRE		SR SRE	SR SRE	SRE
2175		SR 7/8	SR 7/8			
2300				SR	SR 7/8 SR SRE	
2450						SRE

(1) In all cases except the single round jet, measurements in at least three and as many as five azimuthal planes were made.

(2) Configuration; SR 7/8 = Single Round (d = 7/8 in.)
 SR = Single Round (d = 1.5 in.)
 SR = Single Rectangular = SRE

Table 5-2. Test Point Conditions for Twin Round Jets.
(Spacing will be shown in boxes, s/d)

Velocity (fps)	Temperature (° R)					
	530	1250	1600	1700	1900	2000
1000	1.33,2.0 2.67,1.67 5	1.33 2.67 5		1.33 2.67 5	1.33 2.67 5	
1500		1.33,5.0 1.67 2.00 2.67 3.67		1.33 2.67 5	1.33 2.67 5	
1750				1.33 2.67 3.67 5.0		
1900		1.33 2.67 5 2.0		1.33 2.67 5	1.33 2.67 5	
2175						
2250				1.33 2.67 5 1.67		
2400					1.33 2.67 5	

Table 5-3. Test Point Conditions for Twin Rectangular Jets.

Velocity (fps)	Temperature (° R)					
	530	1250	1600	1700	1900	2000
1000	2.08 3.47 4.86 6.48 13.89	4.96 13.89		4.96 13.89	4.86	4.86 13.89
1500		2.08 3.47 4.86 7.4		7.4 13.89 4.86	4.86	4.86 13.89
1750				3.47 7.4 13.89 4.86		
1900		2.08 4.96	2.08		4.86	4.86 13.89
2175						
2275			2.08 4.86 13.89			
2400						4.86 13.89

Table 5-4. Test Point Conditions for Five-Jet Linear Array.

Velocity (fps)	Temperature (° R)					
	530	1250	1600	1700	1900	2000
1000	(1) L M S	L M S	L M S		L M S	
1500		L M S	L M S		L M S	
1750		L M S	L M S		L M S	
1900						
2175			L M S			
2375		S			L M S	

(1)
L - Large
M - Medium
S - Small

Test 5-5. Test Point Conditions for Six- and
Seven-Tube Clustered Arrays.

Configuration: Clustered Arrays.

Velocity (fps)	Temperature (° R)					
	530	1250	1600	1700	1900	2000
1000	6L ⁽¹⁾ 6M 6S	6L 6M 6S	6L, 7L ⁽²⁾ 6M, 7M 6S, 7S		6L 6M 6S	
1500		6L, 7L 6M, 7M 6S, 7S	6L, 7L 6M, 7M 6S, 7S		6L, 7L 6M, 7M 6S, 7S	
1750		6L 6M 6S	6L, 7L 6M, 7M 6S, 7S		6L 6M 6S	
1900						
2175			6L, 7L 6M, 7M 6S, 7S			
2375		6L 6S			6L 6M 6S	

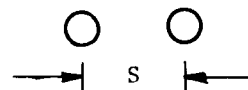
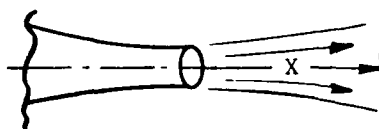
(1) 6L - Large 6 tube
6M - Medium 6 tube
6S - Small 6 tube

(2) 7S - Large 7 tube
7M - Medium 7 tube
7S - Small 7 tube

Table 5-6. LV Measurements.

Configuration	T_0 , °K	\bar{U}_0 , m/sec	M	Radial Traverse at Axial Station (Diameter Y/D) Corresponding to X/D
1. Single Round	294	100	0.3	2, 6, 9
2. Single Round	294	303	0.967	2, 6, 10
3. Single Round	644	448	0.967	2, 6, 10, 14
4. Single Rectangular	294	303	0.967	2, 6, 10, 14
5. Single Rectangular	644	448	0.967	2, 6, 10, 14
6. Twin Round at 2 in. Separations	294	303	0.967	6, 8, 10, 14
7. Twin Round at 2 in. Separations	644	448	0.967	2, 6, 8, 10, 14
8. Twin Round at 5 in. Separations	644	448	0.967	2, 6, 8, 10, 14
9. Twin Rectangular at 2 in. Separations	644	448	0.967	2, 6, 8, 10, 14
10. Twin Rectangular at 4.125 in. Separations	644	448	0.967	2, 6, 8, 10, 14

Table 5-7. Hole-In-The-Wall Measurements
for Twin-Round Nozzles.

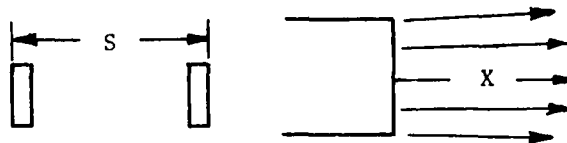


Temperature (° R)	Velocity (fps)	S Spacing (inches)	X Distance (inches)
560	1000	2.0	4.5
			15
			22
			23
		3.0	0
			21
1250	1500	2.0	0
			0.75
			1.0
			4.5
			5.0
			9.5
			15.0
			22.0
		3.0	0
			4.5
			9.0
			13.0
			14.0
			15.0
			21.0
		5.5	0
			4.0
			4.5
			8.0
			9.0
			15.0
			21.0

Table 5-7. Hole-In-The-Wall Measurements
for Twin-Round Nozzles (Concluded).

Temperature (° R)	Velocity (fps)	Spacing (inches)	Distance (inches)
1600	1750	2.0	5.0
			9.5
			15.0
			22.0
		3.0	0
			4.5
			9.0
			15.0
			21.0
		5.5	0
			4.5
			9.0
			15.0
			21.0

Table 5-8. Hole-In-The-Wall Measurements
for Twin-Rectangular Nozzles.



Temperature (° R)	Velocity (fps)	S Spacing (inches)	X Distance (inches)
1250	1500	4 1/8	0
			1.5
			2.75
			4.5
			5.5
			10.0
			11.5
			16.0
			17.5
			23.5
			25.5
1250	1500	1 1/8	0
			1.0
			1.5
			4.0
			4.5
			5.0
			10.5
			11.5
			15.5
			16.5
			17.5
			24.0
			25.5

Table 5-8. Hole-In-The-Wall Measurements for
Twin-Rectangular Nozzles (Concluded).

Temperature (° R)	Velocity (fps)	Spacing (inches)	Distance (inches)
1250	1500	1 7/8	0
			1.5
			1.75
			2.0
			4.0
			4.5
			10.5
			11.0
			11.5
			15.5
			16.5
			22.0
			24.0

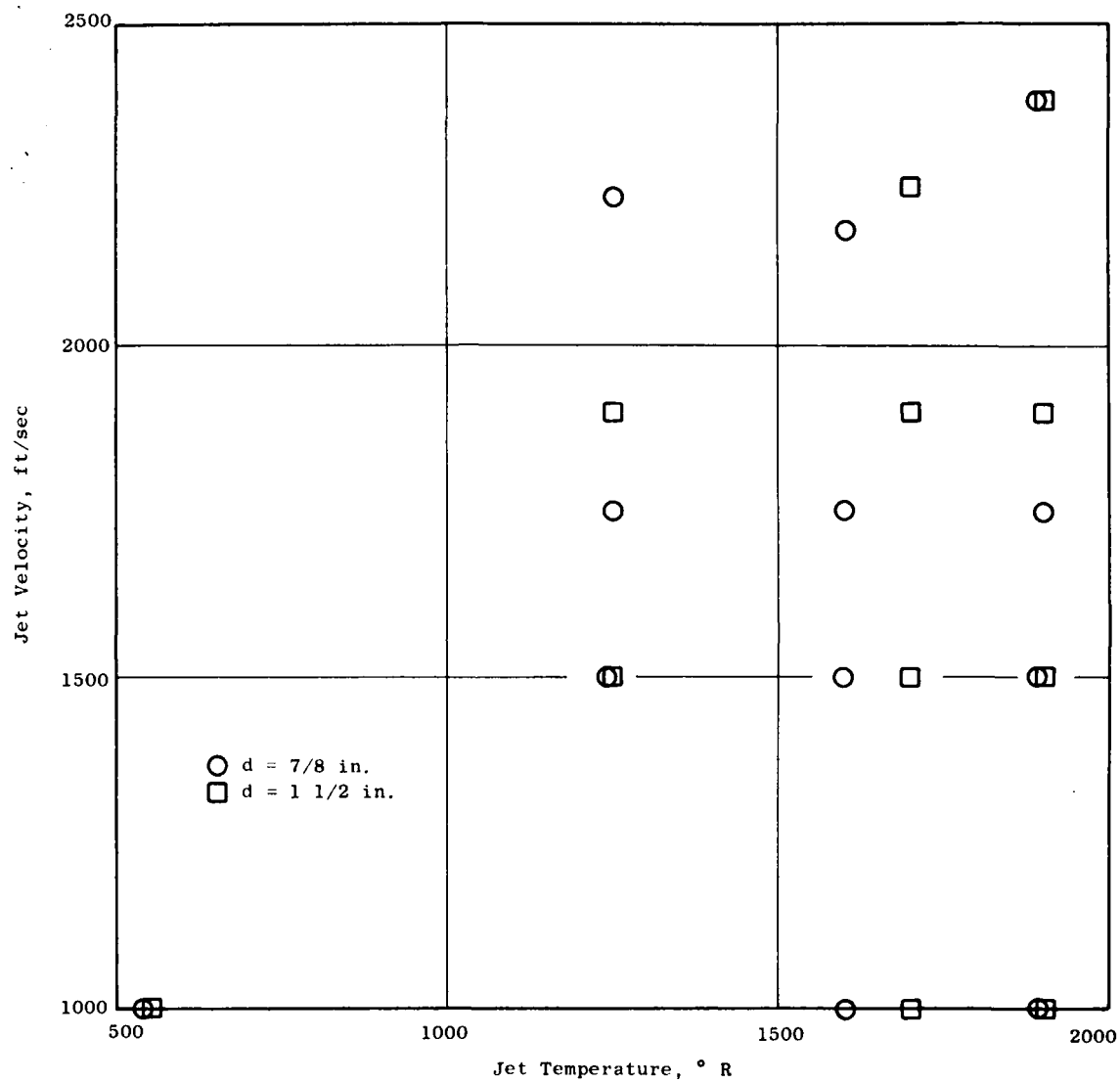


Figure 5-1. Test Matrix, Single Round Jet.

5.1.1 Overall Power and Pressure Level

When compared against Lighthill's predictions, as in Figure 5-2, the data from both nozzles show some variations in level at a given value of the Lighthill correlation parameter, $\rho_0 A_j V_j^8 / a_0^5$. This is expected because there is a large variation of jet density in the data, and the Lighthill prediction improperly accounts for the density ratio effect. There are no apparent systematic differences in level based on nozzle size.

The empirical method developed by Hoch, et al (11) properly accounts for the effect of density ratio. The result shown on Figure 5-3 indicates very good data collapse and suggests that on an overall power basis the data is representative of uncontaminated jet noise.

The overall sound pressure level data at right angles to the jet axis also collapses very well as seen on Figure 5-4.

5.1.2 Power and Pressure Spectra

As shown on Figure 5-3, the overall power can be readily normalized by using Hoch's variable-density exponent method. However, the temperature (hence density ratio) also affects the spectral shape. At a relatively low velocity of 1000 fps, increasing the temperature causes a shift of the peak of the power spectra to lower frequencies as seen in Figures 5-5 and 5-6. This spectral warping is independent of nozzle diameter as there is good agreement between the two nozzle sizes at both the hot and cold conditions. At a right angle to the jet axis, the main effect is a reduction of the high frequency pressure level with increased jet temperature, as seen on Figures 5-7 and 5-8.

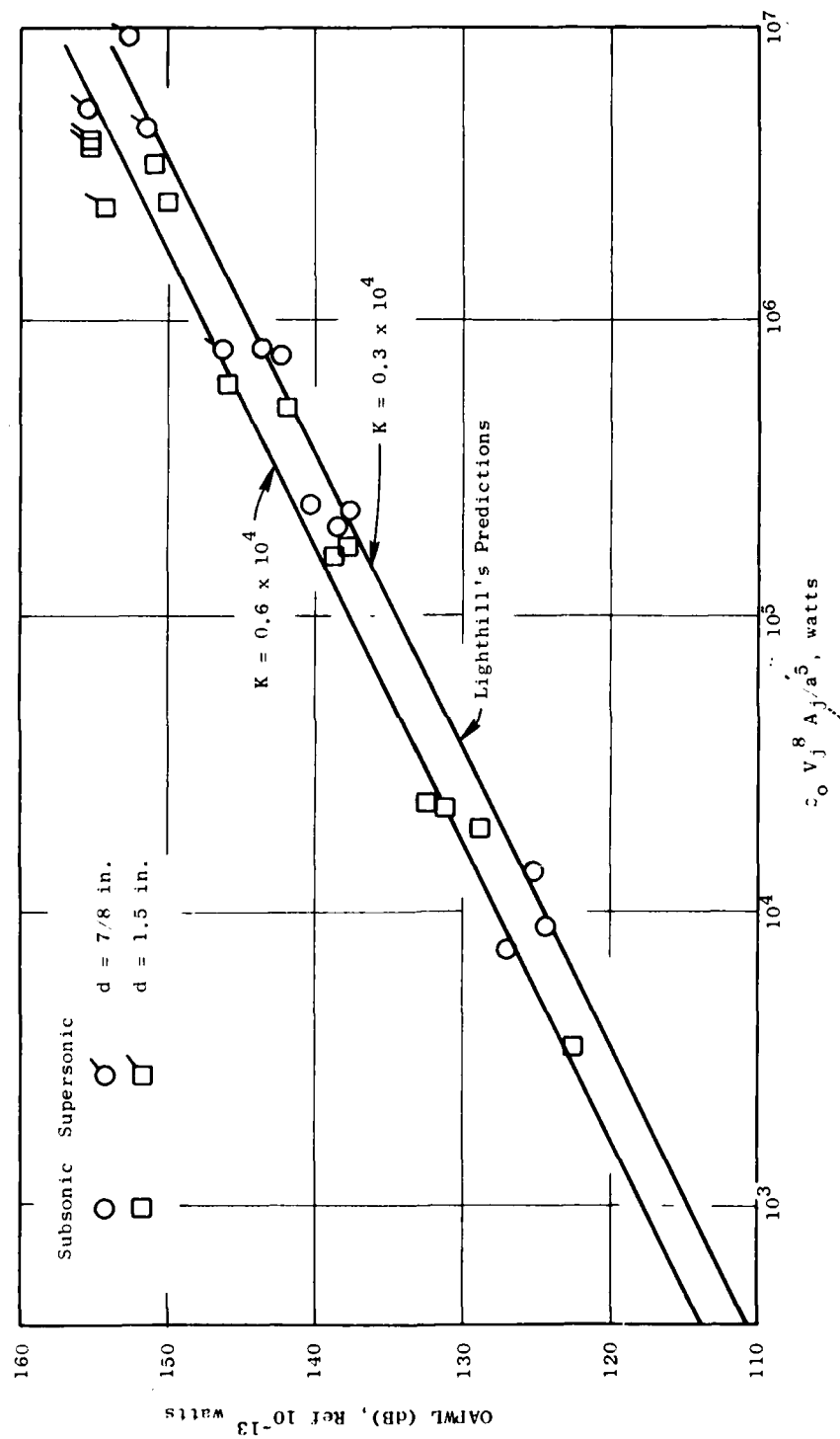


Figure 5-2. Single Round Convergent Jet Noise, Overall Power.

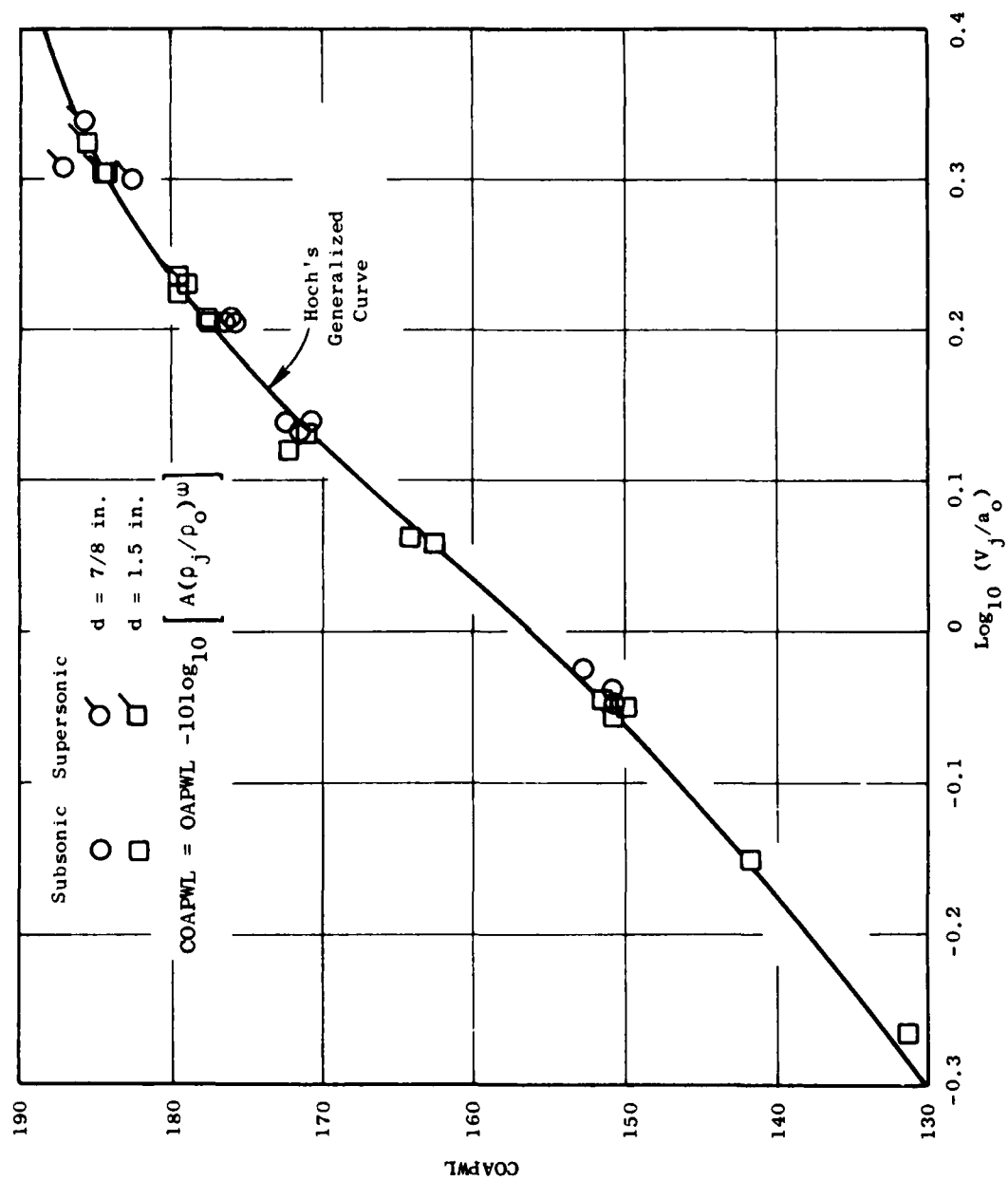


Figure 5-3. Overall Power, Corrected for Density Ratio, Single Round Jet.

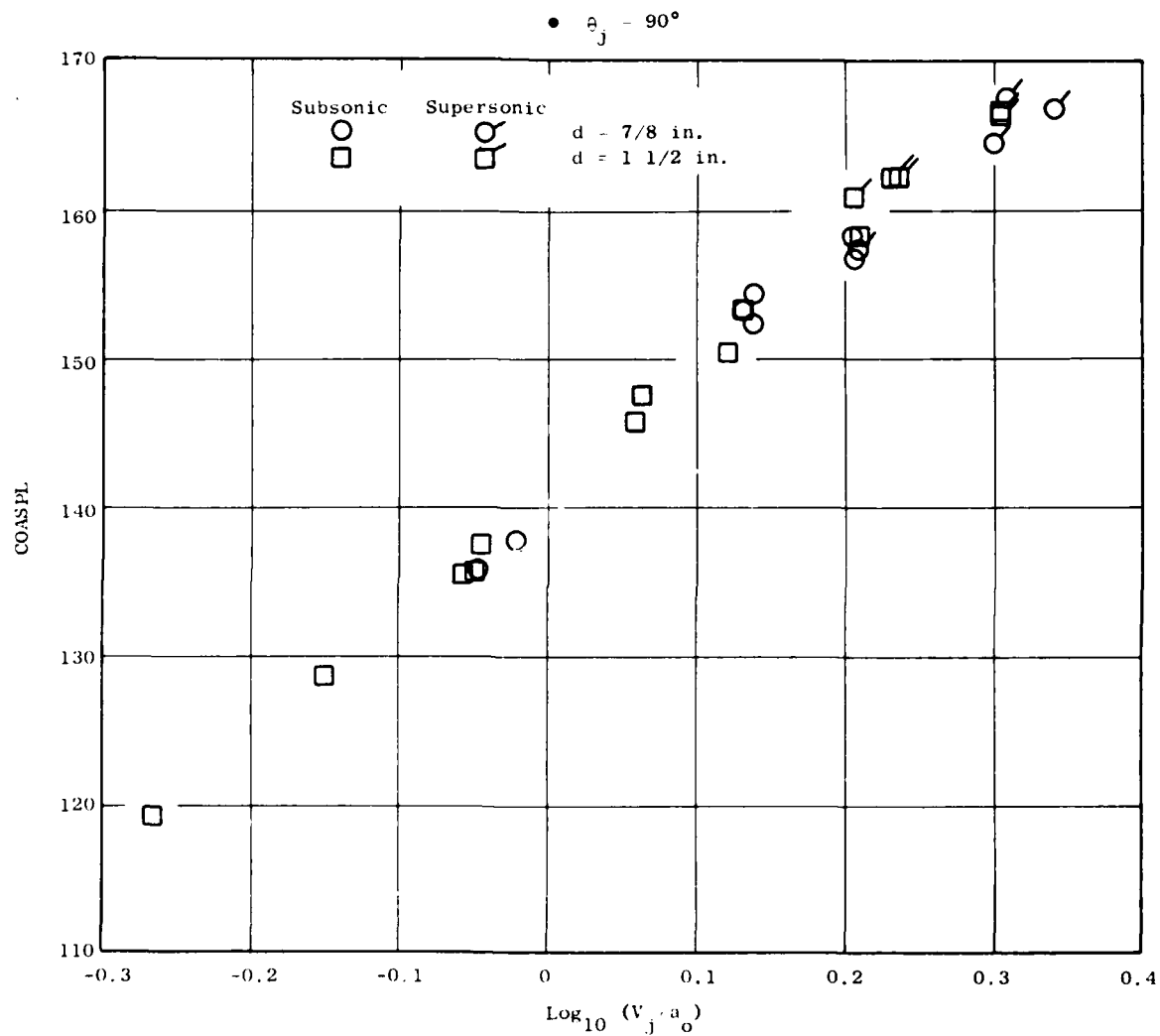


Figure 5-4. Overall Sound Pressure Level at $\theta_j = 90^\circ$, Single Round Jet.

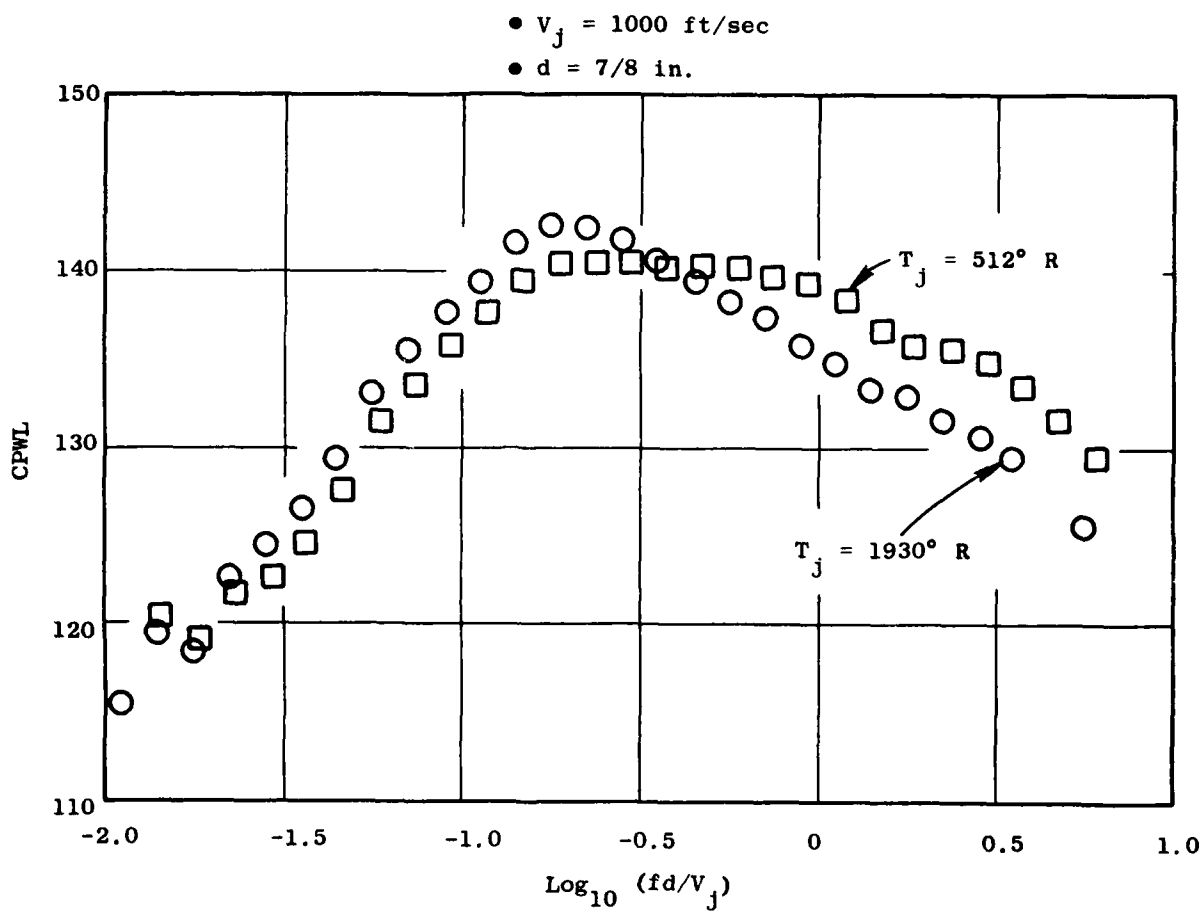


Figure 5-5. Temperature Effect on Power Spectra, $d = 7/8 \text{ in.}$

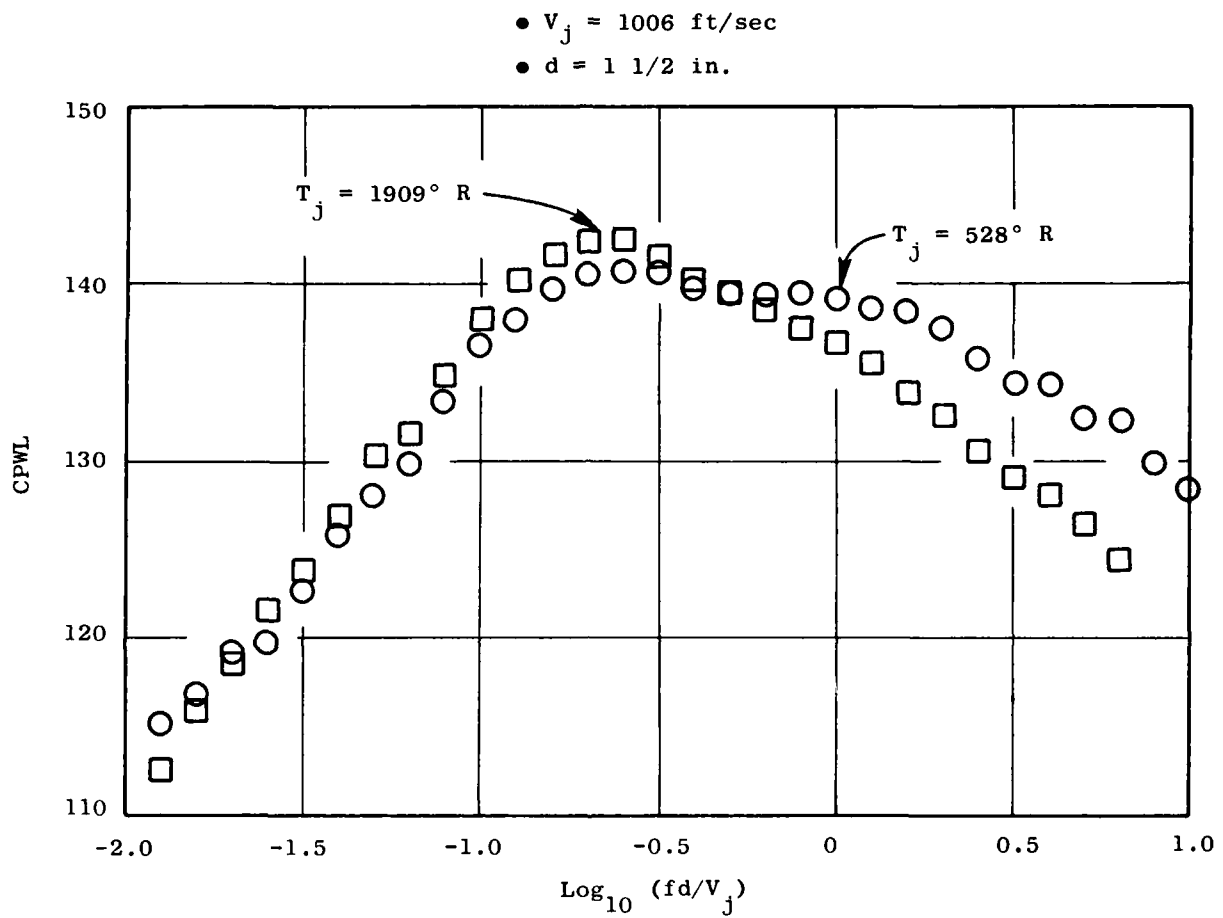


Figure 5-6. Temperature Effect on Power Spectra for $d = 1 \frac{1}{2} \text{ in.}$

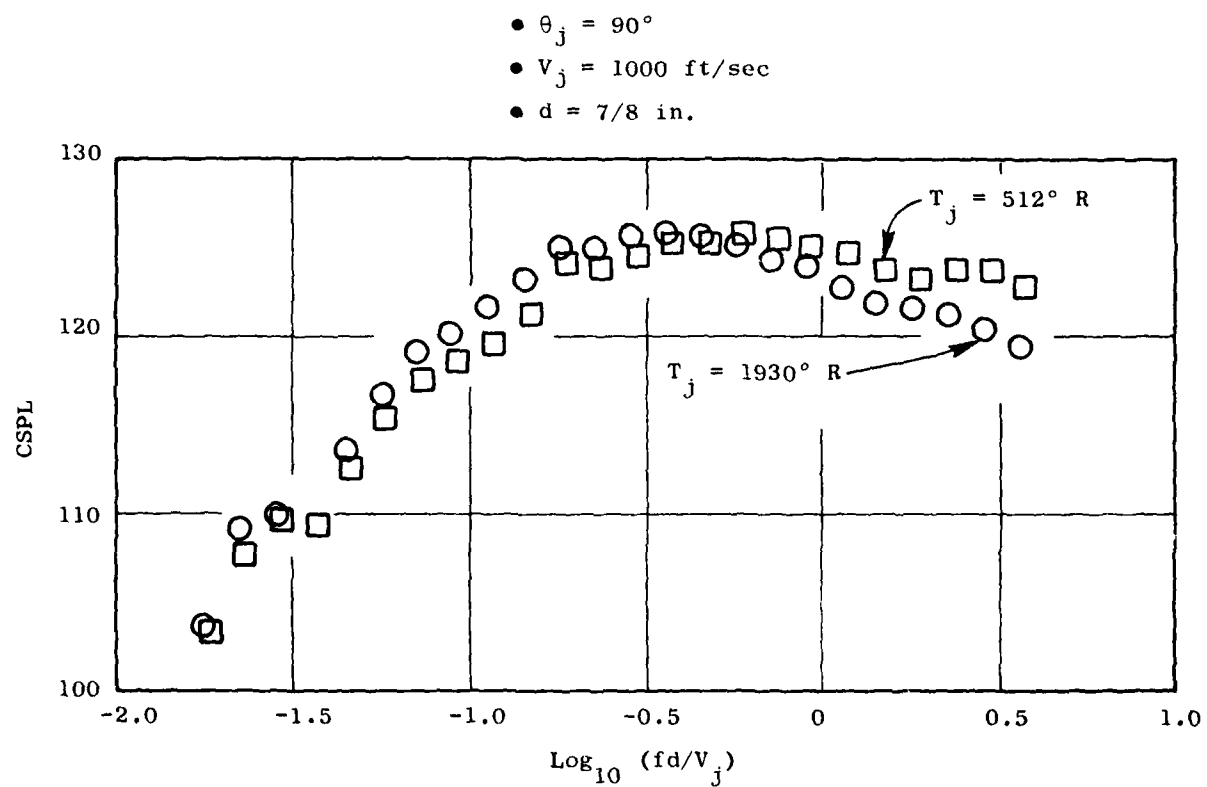


Figure 5-7. Temperature Effect on SPL at $\theta_j = 90^\circ$, $d = 7/8$.

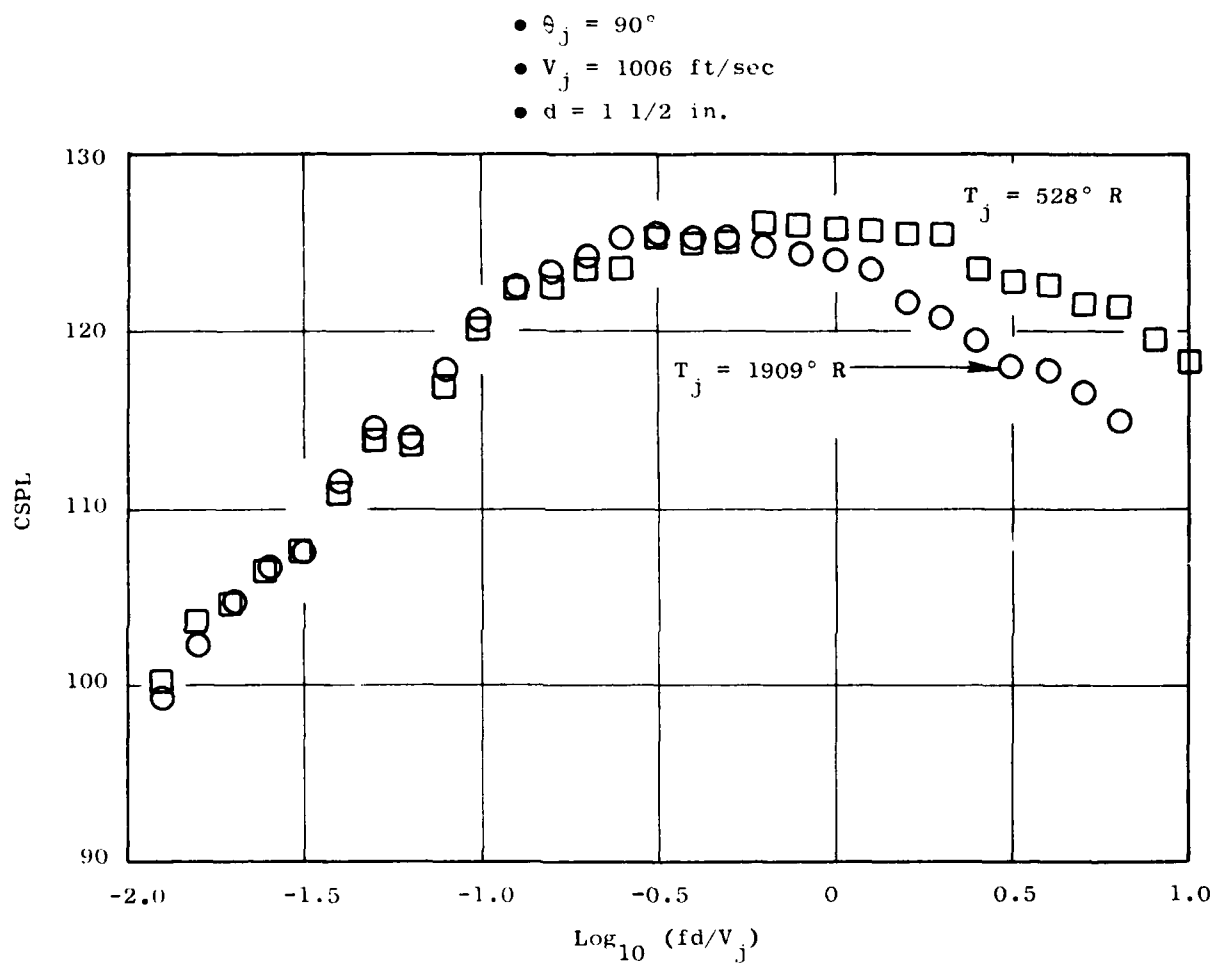


Figure 5-8. Effect of Temperature on SPL at $\theta_j = 90^\circ$, $d = 1 \frac{1}{2} \text{ in.}$

5.2 SINGLE RECTANGULAR JET NOISE

A study of the noise characteristics of rectangular jets was conducted to examine the significant noise mechanisms in both rectangular and round jets. By changing the exit plane geometry of a jet from circular to rectangular shape, there should be corresponding changes in the turbulent and/or "coherent, orderly structure," [see Crighton⁽¹⁹⁾] and acoustic shielding or sound/flow interaction, [see, Balsa⁽³⁵⁾]. No attempt is made herein to delineate between "coherent structure" and other turbulent mixing effects; these are considered to be noise source effects which depend on the unsteady properties of the jet plume, in contrast to "acoustic shielding" effects which depend on the mean properties of the jet plume. Prior experimental investigations, (18,95,96) of rectangular jet noise have not considered these aspects and have been limited to unheated low speed flow. A primary emphasis of the present work is to present the experimental information in such a way as to separately define the effects of turbulent mixing and acoustic shielding.

This study of rectangular jet noise is carried out for heated, high velocity jets typical of the thermodynamic conditions of interest in jet engines. A rectangular nozzle with an aspect ratio of 6:1 was tested over a velocity range from 800 to 2400 fps and a temperature range from ambient to 2000° R. For comparison purposes, round jet noise using an equal area round nozzle (diameter equal to 1.5 inches) was measured concurrently over the same velocity and temperature range.

5.2.1 Experimental Apparatus

The tests reported herein were carried out at the jet noise test facility of the General Electric Research and Development Center (see Section 3.1).

The rectangular nozzle is shown in Figure 5-9. Jet velocities quoted herein are based on the plenum pressure and temperature, assuming isentropic expansion to ambient pressure. All of the aerodynamic data (pressures and temperatures) were measured continuously, and the average of 6 to 7 data points during a typical acoustic reading was used to determine the jet velocity and temperature. A General Radio 1/3-Octave Band Analyzer (GR1921), using a 4-second integration time, was used to measure the acoustic levels. The microphones were sampled sequentially through the use of a General Radio Multichannel Amplifier (GR1566), with a total time to read the 12 microphones of slightly less than a minute. No corrections for ground reflections were used and corrections for atmospheric absorption were not applied to the data due to the relatively short microphone radius of 9 feet.

5.2.2 Experimental Results and Discussion

5.2.2.1 Overall Acoustic Power

The noise of the rectangular jet is compared with that of an equivalent-area round jet on an overall acoustic power basis in Figure 5-10. Three azimuthal measurement planes, $\psi = 0, 45^\circ$ and 90° , are used to obtain the

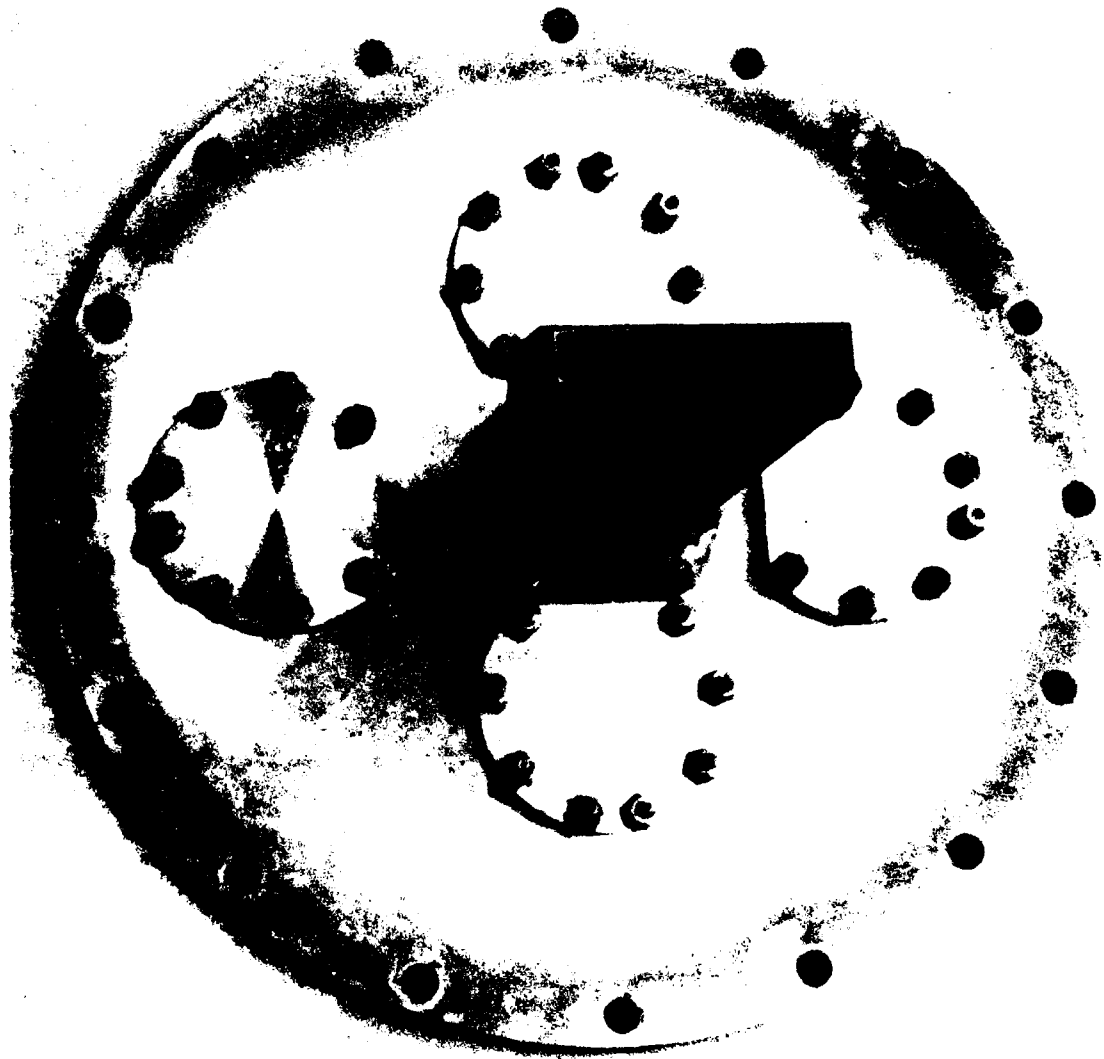


Figure 5-9. Rectangular Jet Nozzle.

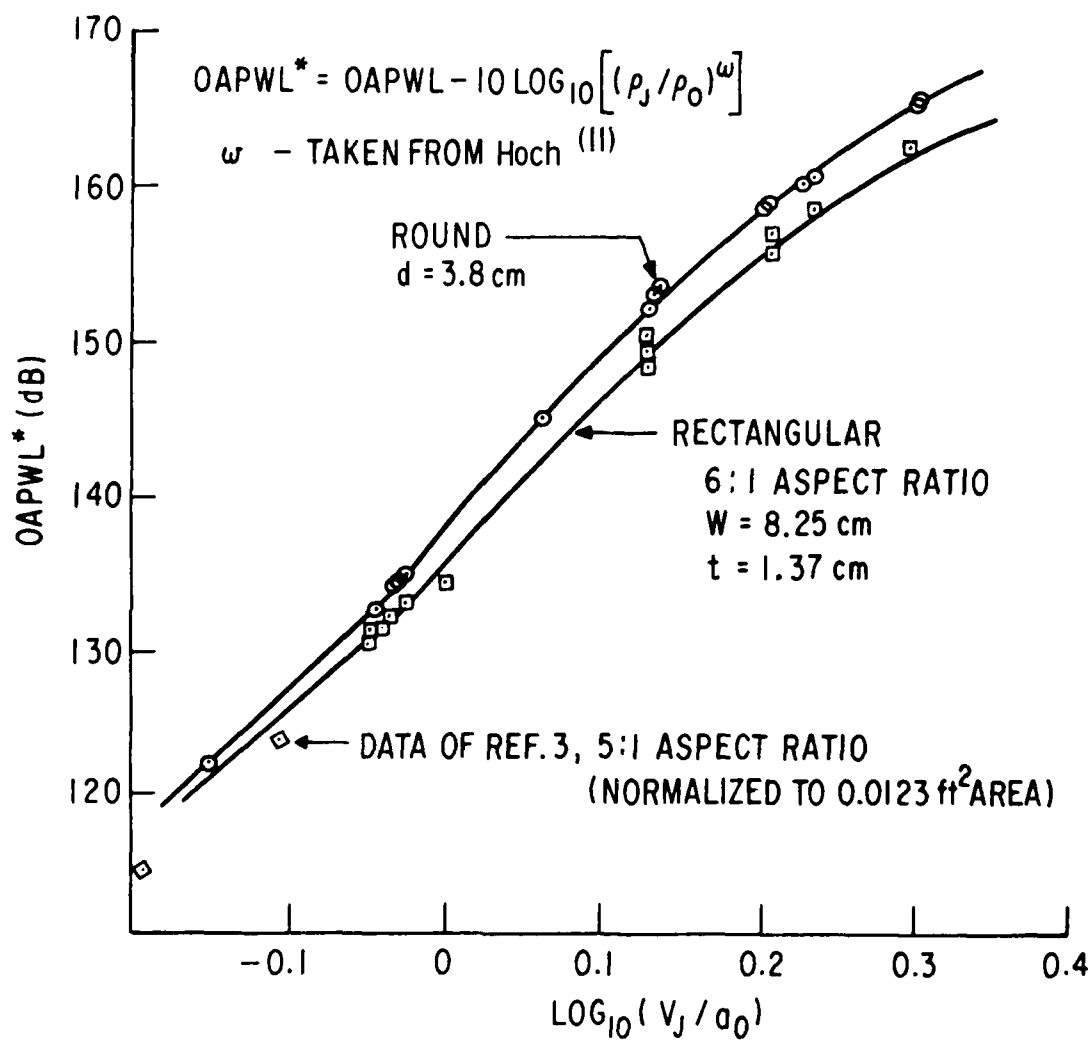


Figure 5-10. Total Power Comparison, Round Versus Rectangular.

acoustic power levels of the rectangular jets. The round jet noise is greater than the rectangular jet noise, the difference being small at low velocity, but increasing to almost 3 dB at high jet velocity. The data agree with the low velocity results of Mestrello and McDaid⁽⁹⁵⁾ which is also shown on Figure 5-10.

Hoch's⁽¹¹⁾ method of correcting for the effect of variable jet density was applied to the data presented on Figure 5-10. The dependence of the density exponent, ω , on the ratio of jet velocity to ambient speed of sound, V_j/a_0 , as used in Figure 5-10, is shown on Figure 5-11. Figure 5-10 is a good example of the type of data collapse possible with Hoch's method because data at many different temperatures have been reduced to the same curve. The jet density exponent for rectangular jets was also determined in the manner of Hoch, et al. A comparison between Hoch's results for round jets and the present results for rectangular jets are shown on Figure 5-11. The density exponent for the rectangular jet is qualitatively similar to that of a round jet. There is, however, a noticeable difference in level.

5.2.2.2 Spectral and Directivity Comparisons

A prominent feature of rectangular jet noise is the existence of distinct "quiet" and "loud" planes. Defining the azimuthal angle, ψ , as shown in Figure 5-12, the quiet plane contains the major axis of the jet while the loud plane contains the minor axis. Crighton⁽¹⁹⁾ used a stability analysis to predict that a elliptical jet would have more rapid growth of spatial disturbances (flapping modes) in the plane parallel to the minor axis and this would lead to enhanced noise emission in the loud plane. Balsa⁽³⁵⁾ also predicted differences between the loud plane and quiet plane based on acoustic shielding considerations. It is necessary to examine the data in a manner which separates the source alteration effects (such as Crighton's flapping mode instability) from acoustic shielding effects. It is known from previous theoretical work (see Section 4.2) that acoustic shielding effects are negligible at $\theta = 90^\circ$ for cold jets. (This is strictly true only for nonturbulent flow, because the instantaneous variation of the local velocity vector in turbulent flow, causes a loss of acoustic transmission even for acoustic waves that are normal to the mean flow direction. This effect of turbulence on the transmission of sound has been measured by Norum⁽⁹⁷⁾).

Unheated high subsonic jet noise from round and rectangular nozzles is compared on Figure 5-12. At an emission angle of 90° , the differences between the round and rectangular jet noise are minimal but significant. It is, therefore, concluded that the turbulent field of the rectangular jet differs slightly from that of the round jet. This difference in noise spectra would remain relatively constant with emission angle if source alteration was the dominant effect, but at angles of $\theta = 30^\circ$ and 60° there are somewhat larger differences in the round and rectangular jet noise spectra.

At $\theta = 90^\circ$, the rectangular jet noise SPL at $\psi = 90^\circ$ is larger than at $\psi = 0^\circ$. This reversal of the quiet and loud planes is not expected

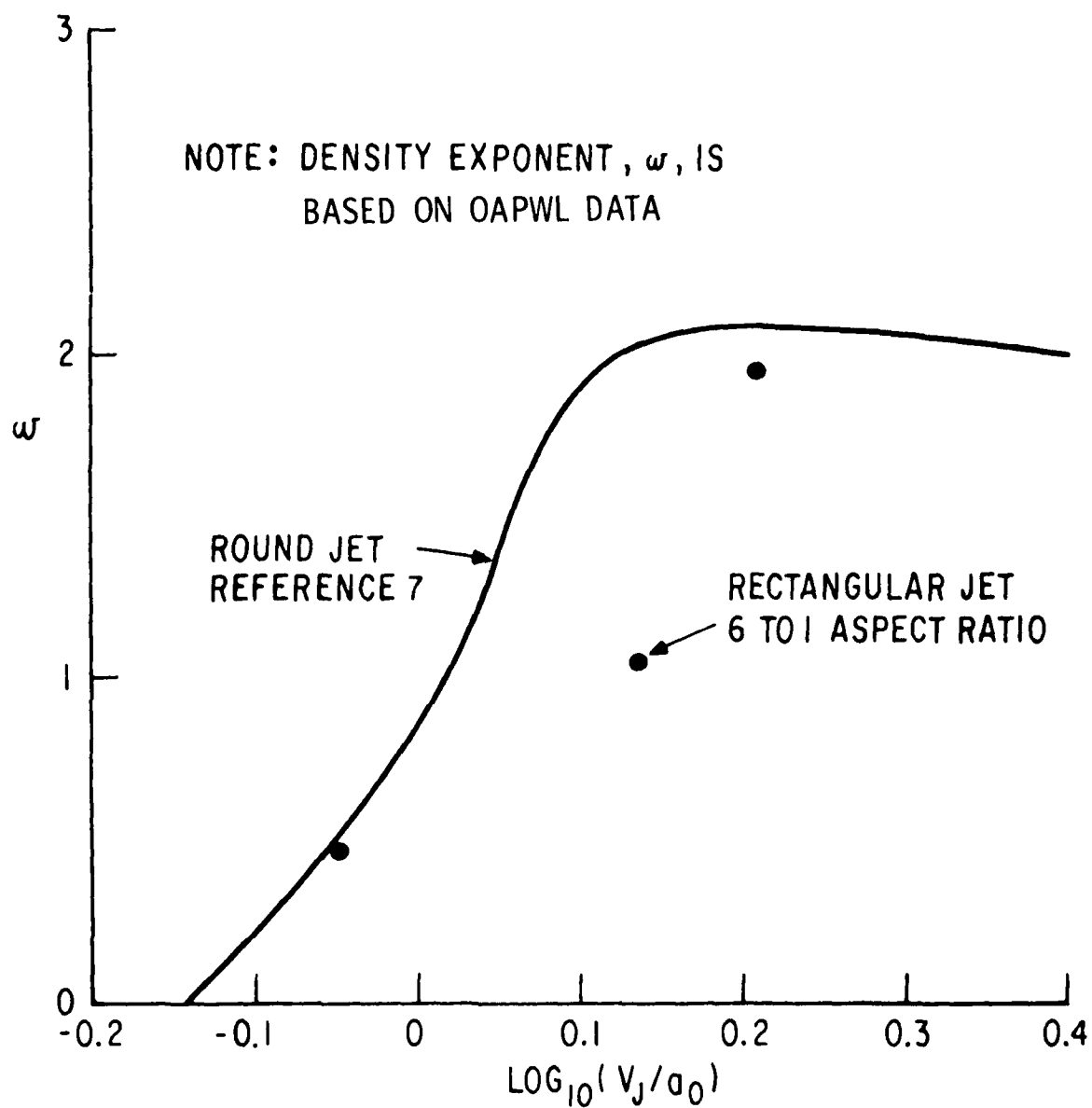


Figure 5-11. Effect of Velocity on Density Exponent, ω .

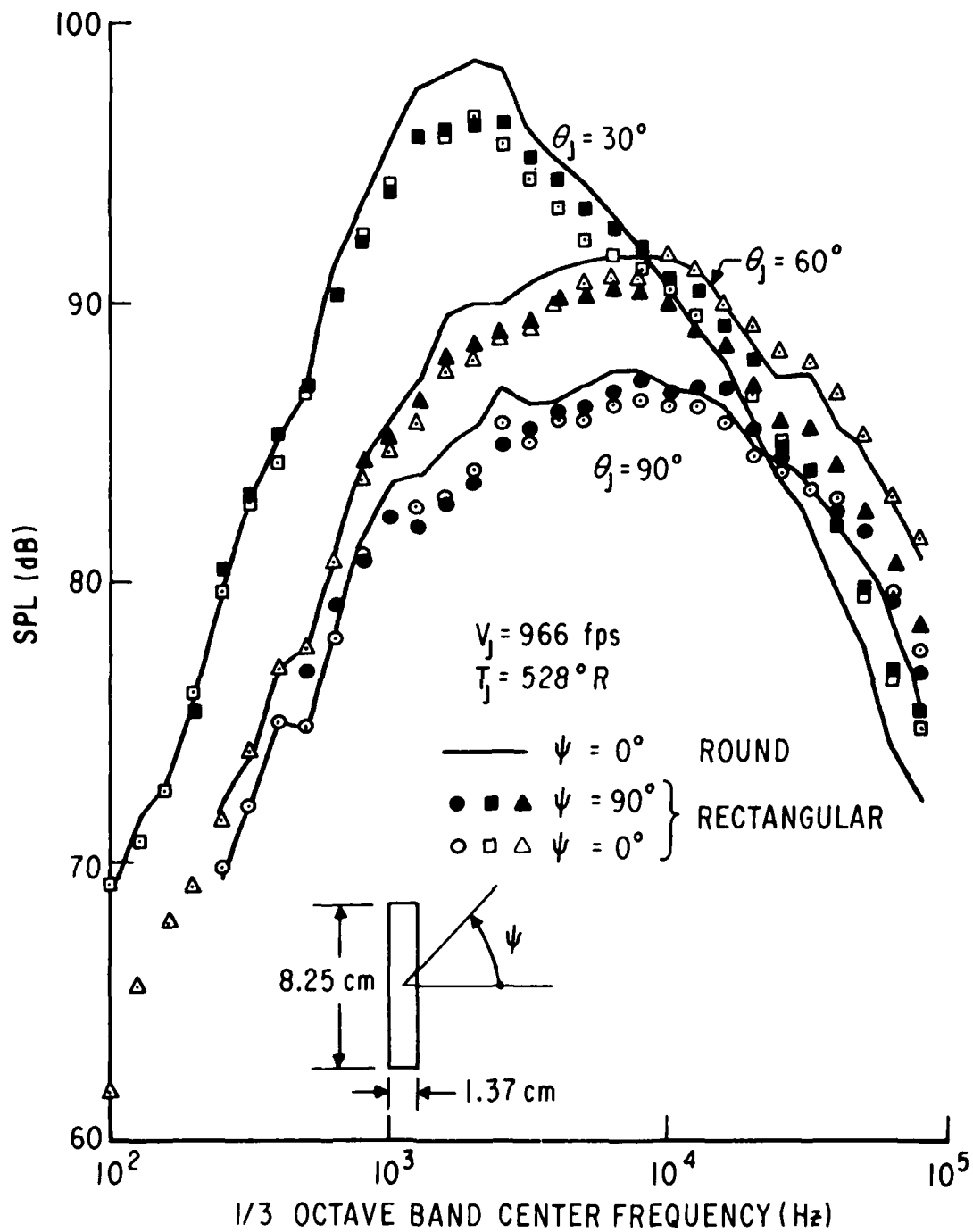


Figure 5-12. Unheated SPL Spectra, Round Versus Rectangular.

from Crighton's⁽¹⁹⁾ work and it cannot be explained by the acoustic shielding theory of Balsa⁽³⁵⁾ which would predict an axisymmetric sound field for these conditions. It is unlikely that the turbulent flow effects on the shielding mechanism could produce this reversal of the quiet and loud planes shown in Figure 5-12. This reversal is, therefore, judged to be due to an asymmetric source distribution.

As the angle between observer direction and the jet axis decreases, the SPL levels in the $\psi = 0^\circ$ plane become dominant. Figure 5-12 shows that at $\theta = 60^\circ$ the SPL levels in the $\psi = 0^\circ$ plane are higher at the higher frequencies. This trend is qualitatively consistent with the theoretical predictions of Balsa⁽³⁵⁾. The emission angles from 40° to 60° to the jet axis are the most significant contributors to overall acoustic power and it is significant that the shielding predictions provide the proper qualitative results. These results also indicate that neither of the supposed mechanisms acts in isolation. Thus, the source alteration effects are judged to be dominant at large angles to the jet axis and the radiation pattern of these sources appears to be strongly modified at shallow angles to the jet axis by shielding effects on the mean flow.

The trend of ΔPWL_ψ increasing with frequency, evident in the power spectra of Figure 5-13, agrees well with shielding theory. Figure 5-14 shows that the differences (in terms of OASPL) are dependent on the angle to the jet axis. At angles close to the jet axis, there is a second reversal, with the OASPL measured in the $\psi = 0^\circ$ plane again being less than that measured in the $\psi = 90^\circ$ plane. This second reversal in $\Delta OASPL_\psi$ is due to dominance of the OASPL by the low frequency portion of the SPL spectrum at low angles, as can be seen in Figure 5-15. At the higher frequencies, acoustic shielding is still evident at the shallow angles. The high frequency ΔSPL_ψ at $\theta = 30^\circ$ is approximately the same as at $\theta = 90^\circ$ and maximum ΔSPL_ψ occurs near $\theta = 60^\circ$. More variations of ΔSPL_ψ with emission angle are shown on Figure 5-16, where data at three Strouhal numbers are compared to Balsa's theoretical predictions. The large negative values at ΔSPL_ψ for the very shallow angles are unexpected. It is expected that, for on-axis source, ΔSPL_ψ will tend towards zero at shallow angles as the rectangular jet degenerates to a more round-line plume, but it should not become negative.

The observed trend can be explained by considering that the sources are distributed across the jet and taking into account the propagation paths through the diffusing jet. Figure 5-17 illustrates the proposed mechanism. For sources in the region of high flow asymmetry, it is possible to have sources located much further away from the centerline at $\psi = 90^\circ$ compared to those at $\psi = 0^\circ$. The source at $\psi = 90^\circ$ would have a relatively unimpeded propagation path to the shallow angle microphone, while the source at $\psi = 0^\circ$ would have a high-impedance path. This explanation is speculative, but the data illustrates trends which follow this reasoning. A stronger effect is seen at the high frequencies (see Figure 5-16) where the sources are close to the nozzle.

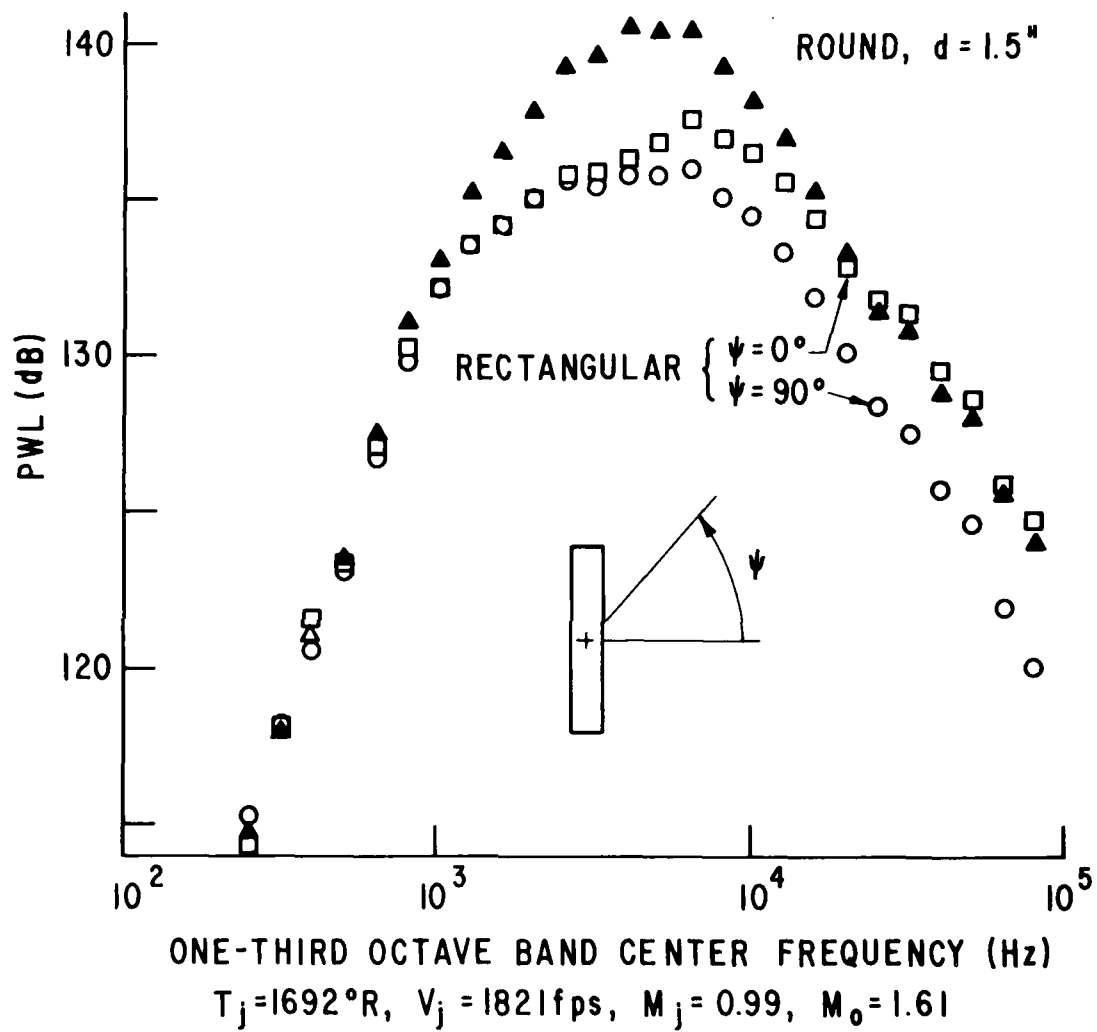


Figure 5-13. Power Spectra Comparison, Round Versus Rectangular.

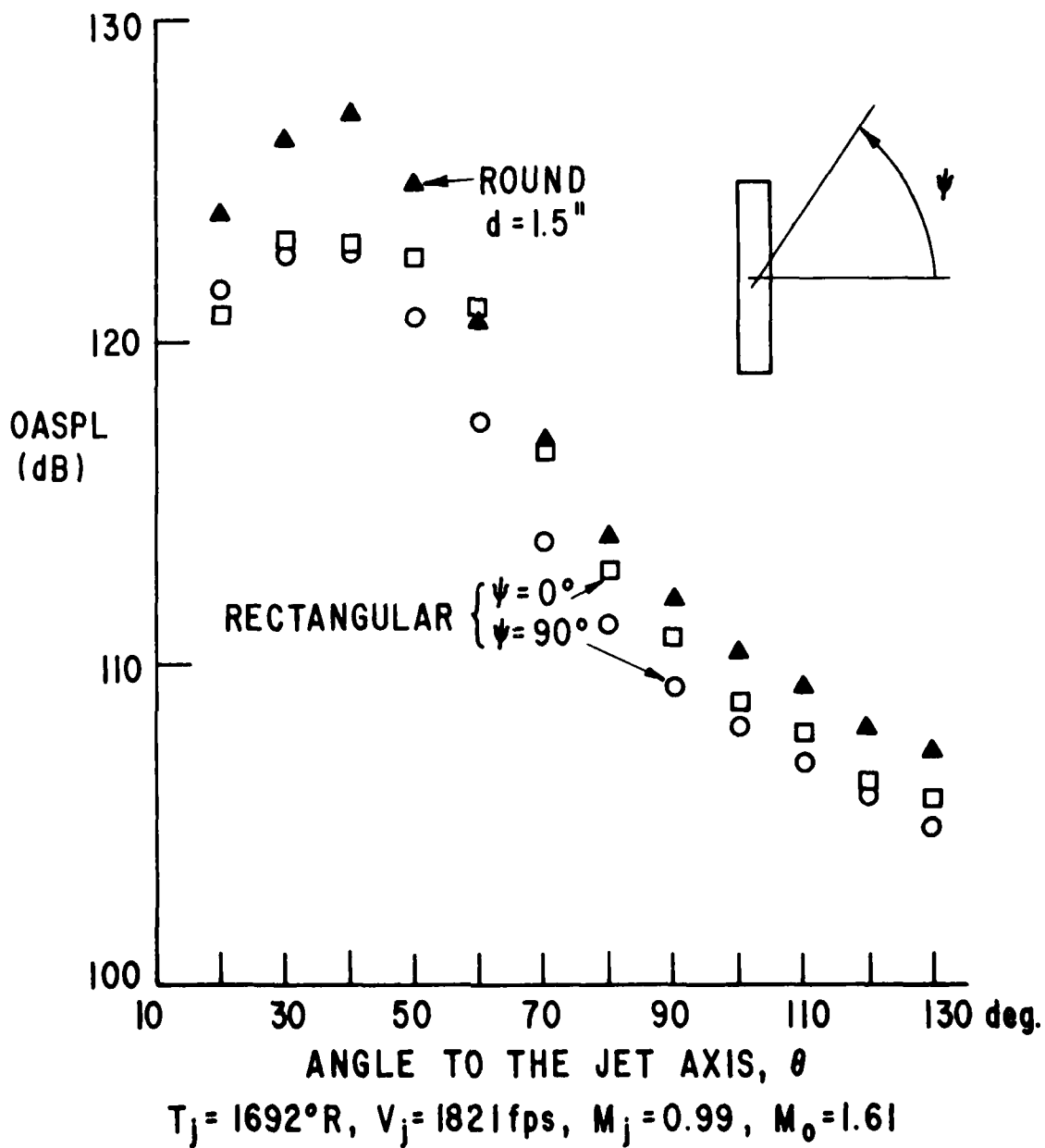


Figure 5-14. Directivity Comparison, Round Versus Rectangular.

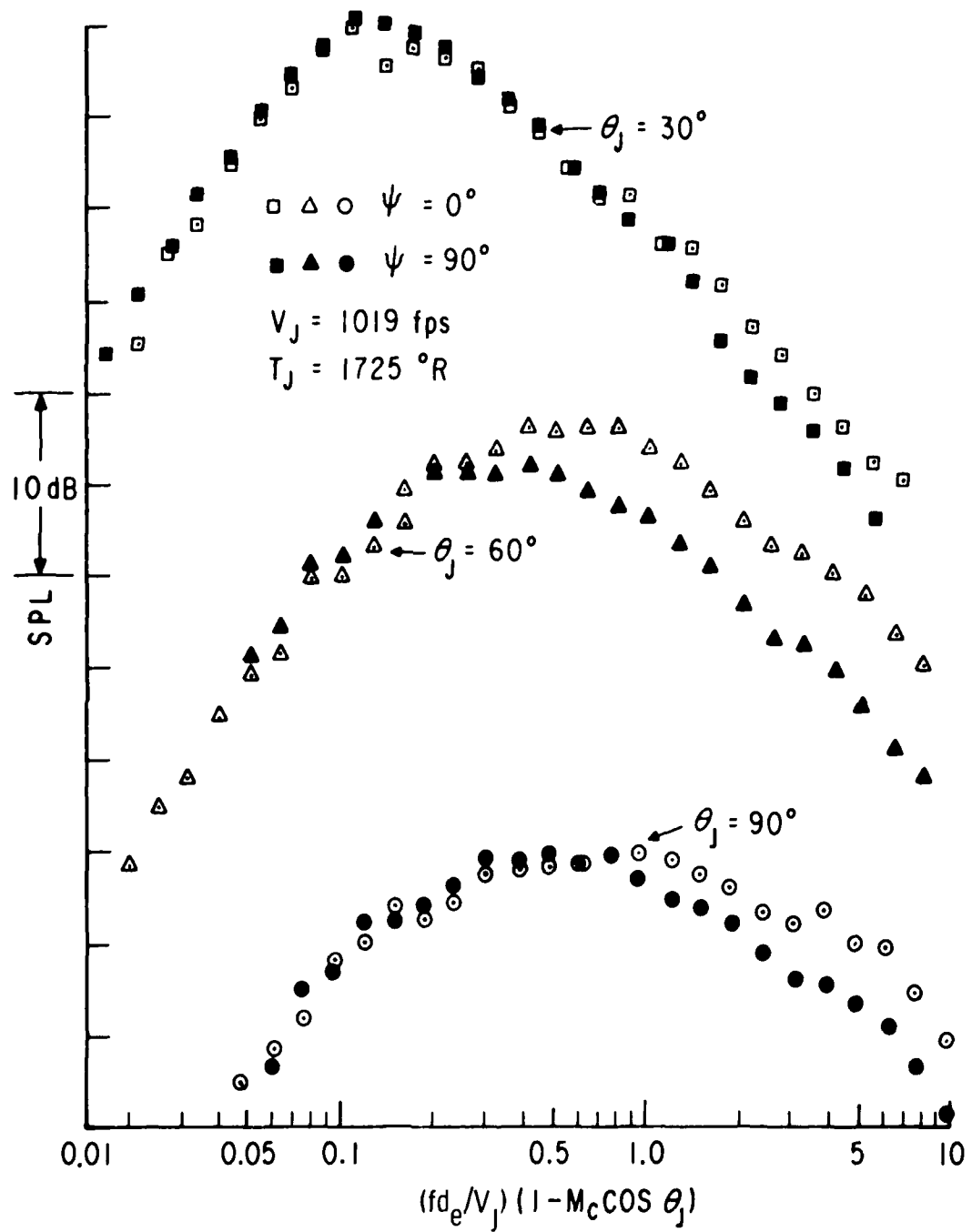


Figure 5-15. SPL Versus Convected Strouhal No., Rectangular.

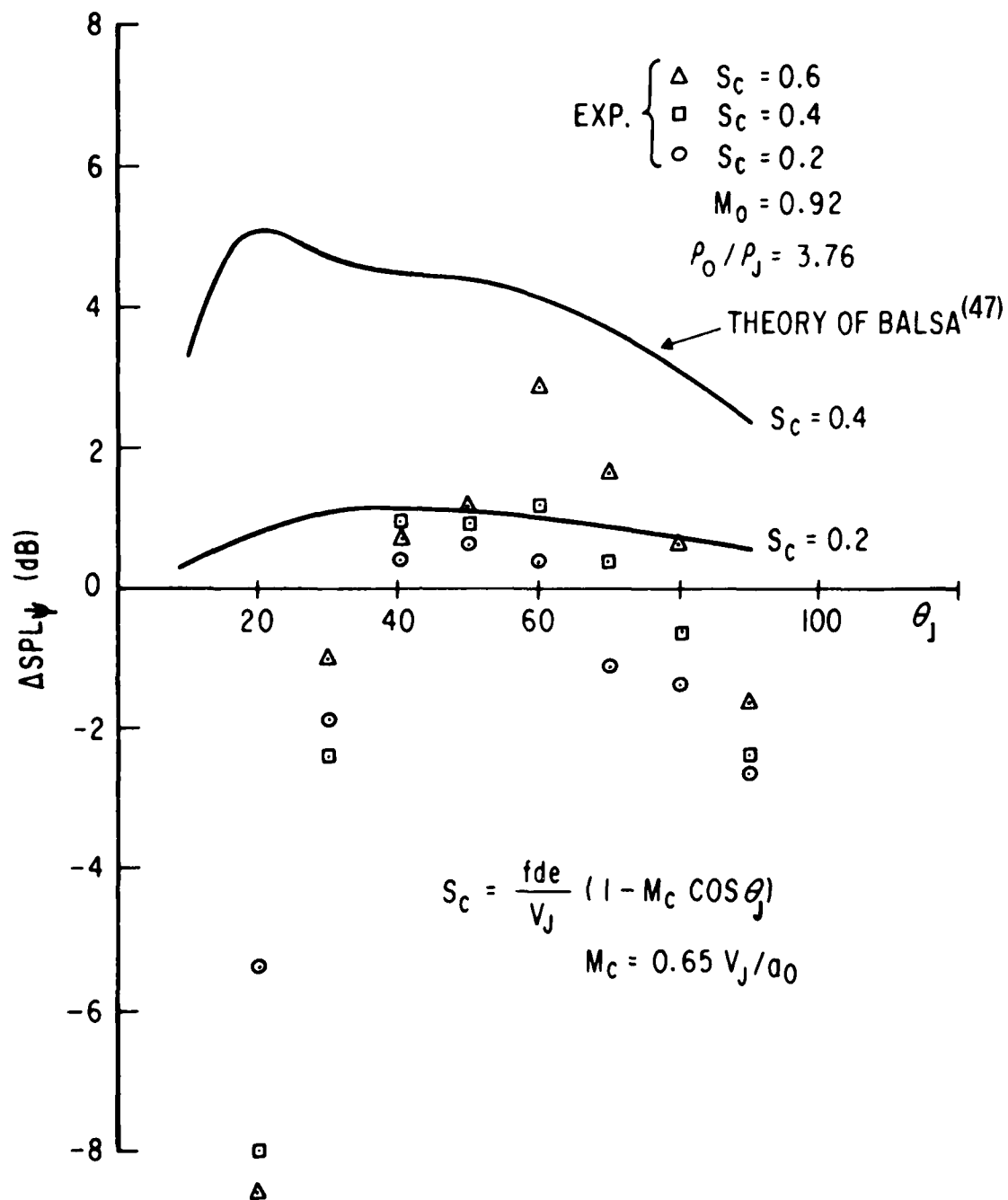


Figure 5-16. $\Delta S_{PL\psi}$ Versus θ . Theory and Experiments.

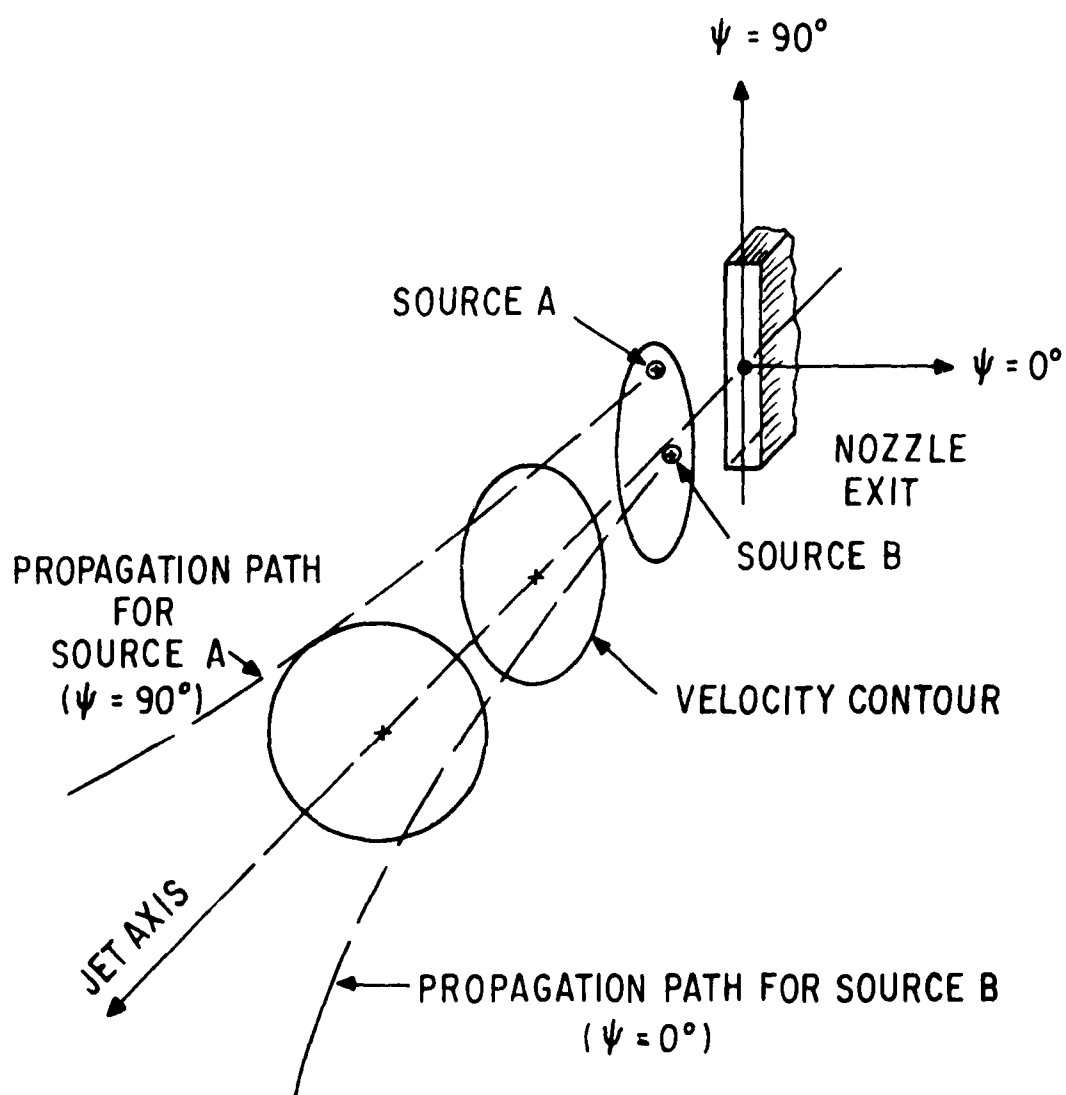


Figure 5-17. Propagation Paths at Shallow Angles.

The tendency of the ΔSPL_ψ to depart from shielding predictions at shallow angles is tentatively concluded to be due to off-axis distribution of the noise sources, and to the inability of present parallel flow shielding theory to account for jet diffusion effects. This conclusion points out the importance of shielding considerations and of the fact that current parallel flow acoustic shielding models are not completely adequate for noncircular jets.

5.2.2.3 Velocity and Temperature Effects

One of the most important conclusions to be drawn from the shielding theory (17,35) is the significant effect of jet velocity and temperature on the radiation properties. The asymmetry exhibited by the high frequency radiation patterns of a rectangular jet is amplified by increasing jet velocity, and is dependent on jet temperature. This is illustrated in Figures 5-18a, b, and c where the acoustic power spectra in the measurement planes ($\psi = 0^\circ$ and $\psi = 90^\circ$) for the rectangular jet are shown for a fixed velocity and several different temperatures, and are compared with round jet data. A different velocity is represented on each of the three figures. The temperature range is the greatest on Figure 5-18a and the ΔPWL_ψ increases monotonically with temperature. This supports the importance of acoustic shielding in asymmetric jet noise. At the low frequencies there is little difference between the loud and quiet planes of the rectangular jet and of the round jet. This is consistent with the shielding theory and it is not inconsistent with turbulent structure considerations.

Comparing the rectangular data to the round jet data, the round jet noise spectrum is more peaked than that of the rectangular jet. As the jet temperature increases at a constant jet velocity (Figure 5-18a), the round jet spectral peak dominance increases slightly, while the high frequency portion drops relative to the rectangular jet spectrum. This high frequency fall-off with jet temperature is observed to be more drastic at the lower jet velocities. The effect of jet temperature on overall power difference between the quiet and loud planes at a constant jet velocity is seen in Figure 5-19.

The sound pressure spectra (SPL) at $\theta = 30^\circ$ at several velocities, with temperature held constant, are shown in Figure 5-20. Similar comparisons for $\theta = 90^\circ$ are shown in Figure 5-21.

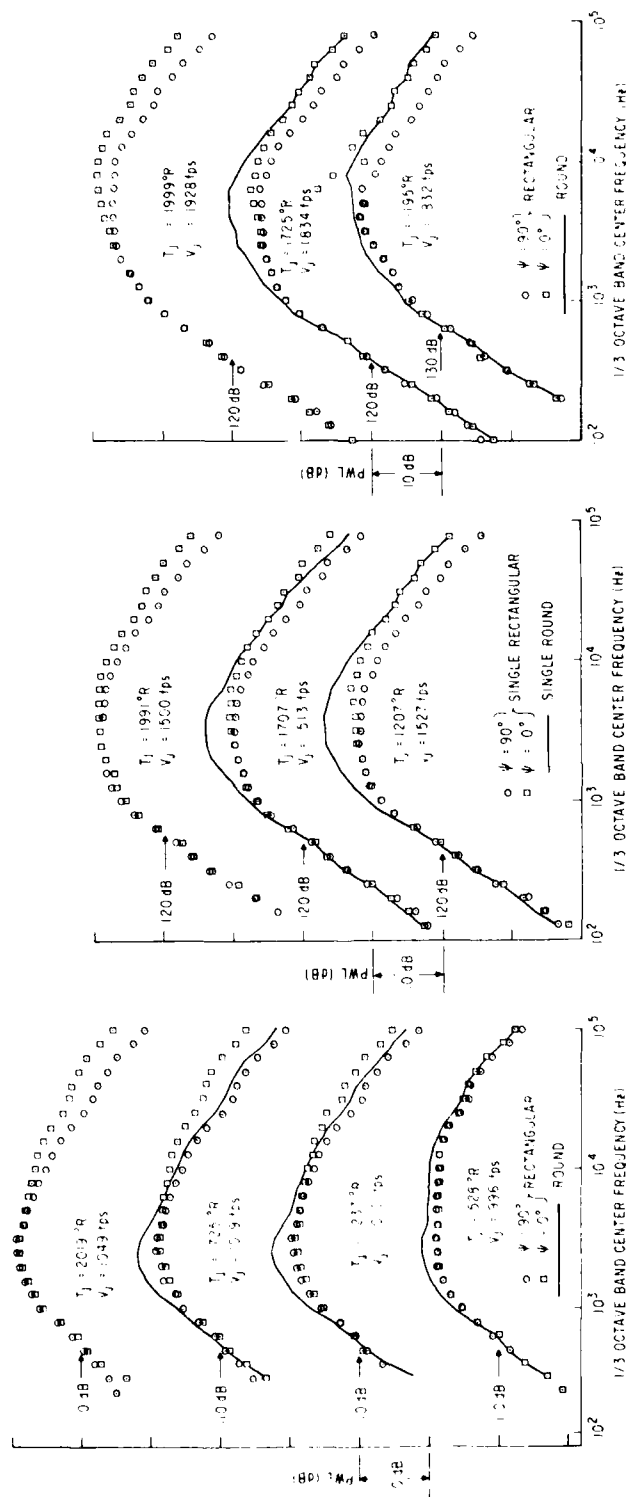


Figure 5-18. PWL Spectra, Effect of Temperature, $V_j \approx 1000$ fps.

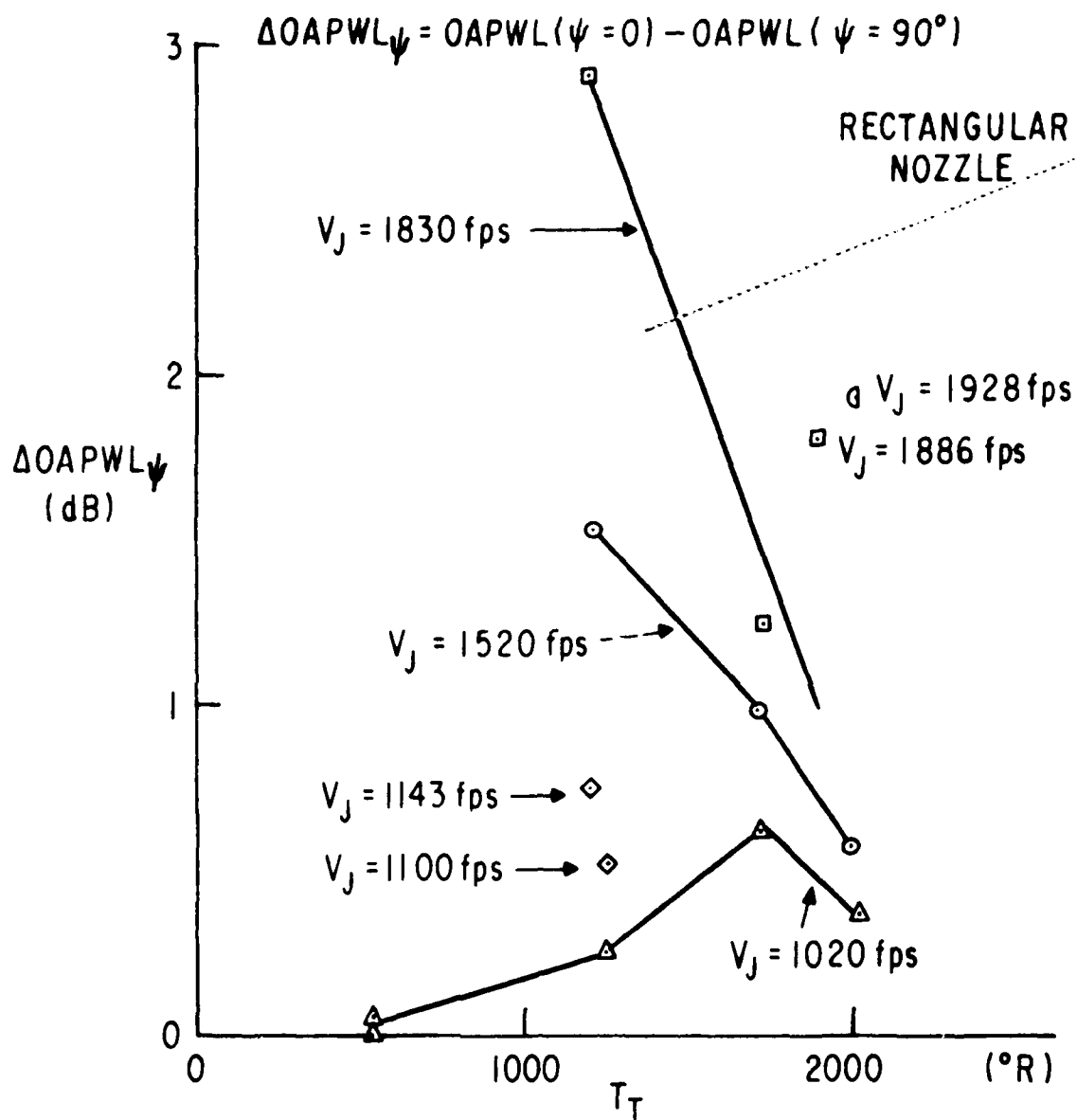


Figure 5-19. Effect of Temperature on $\Delta OAPWL_{\psi}$.

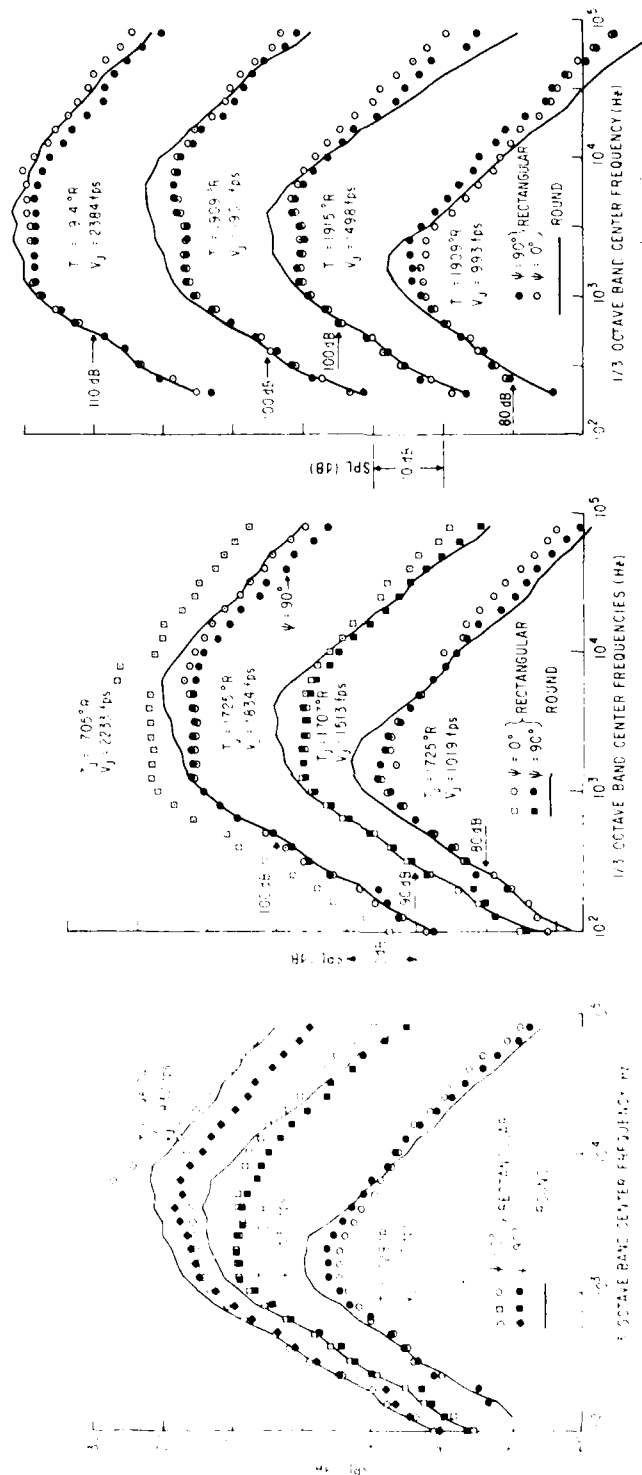


Figure 5-20. SPL Spectra, $\theta = 30$ Degrees.

Raising the jet temperature appears to enhance the reversal of the quiet and loud planes at shallow angles. This trend is illustrated in Figure 5-22. Figures 5-20 and 5-21 show that the differences in the SPL between a round and a rectangular jet are much like the PWL results discussed earlier (shown in Figure 5-20). From these two sets of data it can be concluded that the principal differences between the round jet noise and the rectangular jet noise occur at the frequency and emission angle of peak intensity.

Some shock-associated noise is also visible on Figures 5-20a and 5-21a in the highest velocity data. This shock noise appears in both the round and the rectangular SPL levels at $\theta = 90^\circ$ (Figure 5-21a).

The effects of velocity and temperature on the ΔSPL_ψ for fixed source Strouhal numbers are shown in Figures 5-23a, b, and c. These figures illustrate that ΔSPL_ψ increases with frequency and velocity and is dependent on jet temperature. The major changes with emission angle occur at the peak intensity (intermediate) Strouhal numbers. Very little change is noted at the low Strouhal numbers, where the source alteration effect is the only significant noise mechanism. Again, a maximizing of ΔSPL_ψ is seen to occur near $\theta = 60^\circ$. These results, however, do not take into account the variation of convection speed M_c with jet temperature and nozzle geometry.

5.2.3 Effect of Velocity on Peak Frequency

Lush⁽¹⁰⁾ found that at shallow angles to the jet axis the spectral peak frequency for unheated round subsonic jets was independent of velocity. An increase in spectral peak frequency (at $\theta = 30^\circ$) is clearly evident in Figures 5-20a, b, and c, however, as the velocity and temperature are raised above cold sonic conditions. The trend exhibited by the rectangular jet spectra follows that of the round jet data. The spectra become more rounded at the higher velocities, however, making identification of a spectral peak more difficult. A similar pattern can also be seen at $\theta = 90^\circ$ as shown in Figures 5-21a, b, and c. This upward shift of the peak frequency at high velocity is in agreement with the heated round jet data of Lush and Burrin⁽⁹⁹⁾ as shown on Figures 5-24a and b. Unheated subsonic data are also presented in Figure 5-24 and exhibit the stationary behavior of the peak frequency with velocity as found in the earlier work of Lush.⁽¹⁰⁾

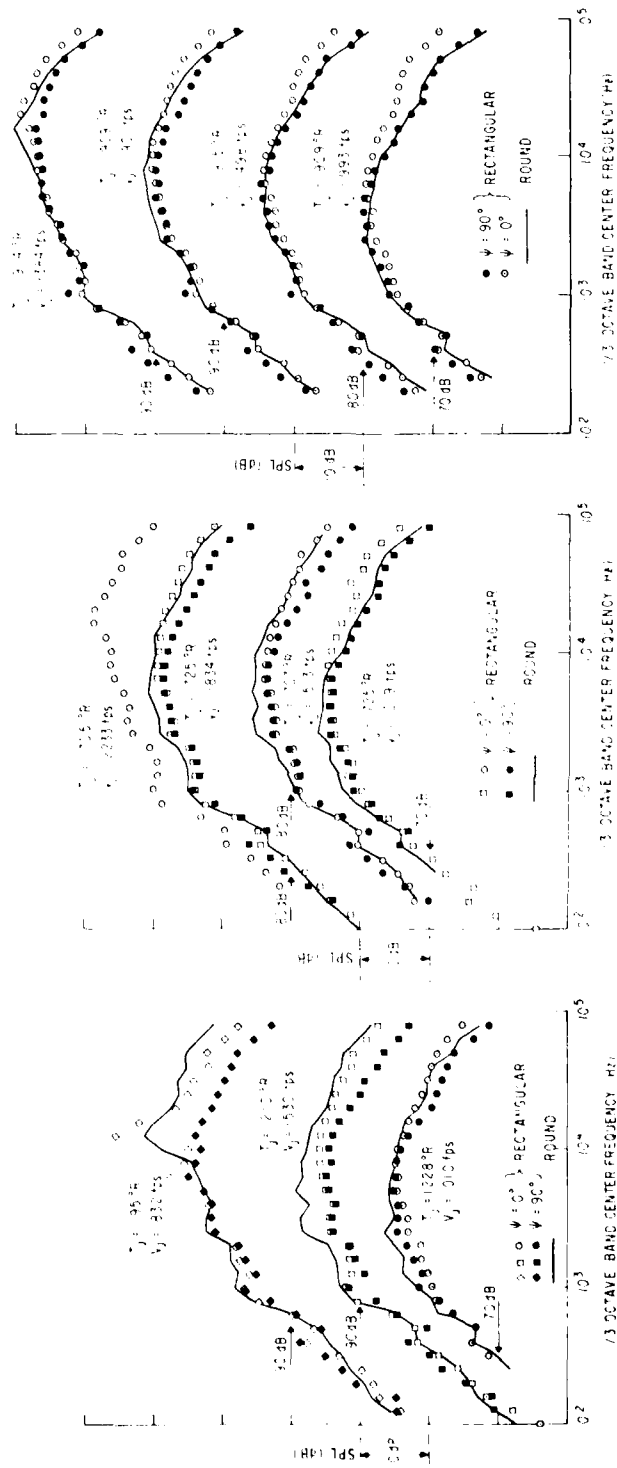


Figure 5-21. SPL Spectra, $\theta = 90$ Degrees.

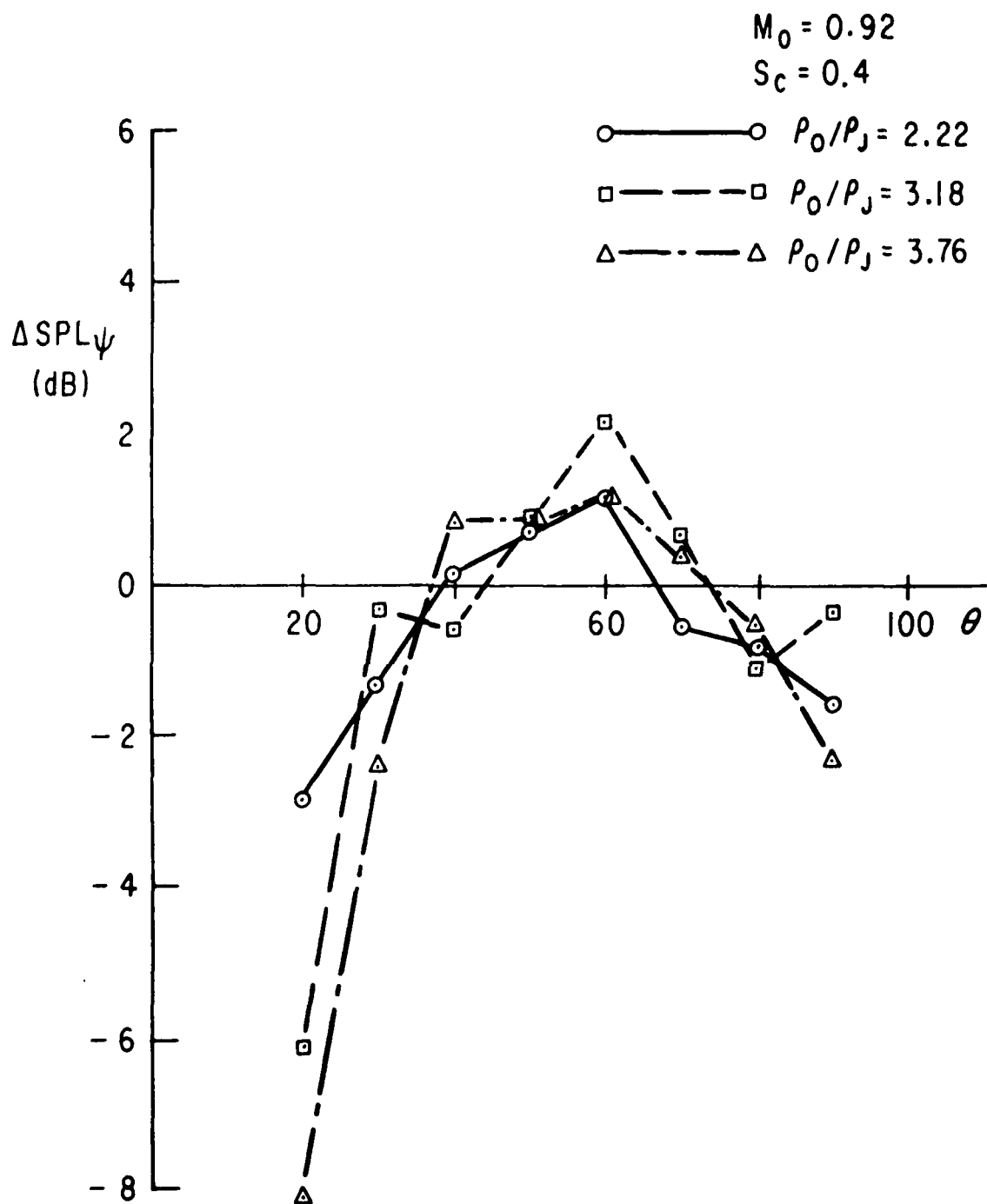


Figure 5-22. Effect of Density Ratio, ρ_0/ρ_j , on ΔSPL_ψ .

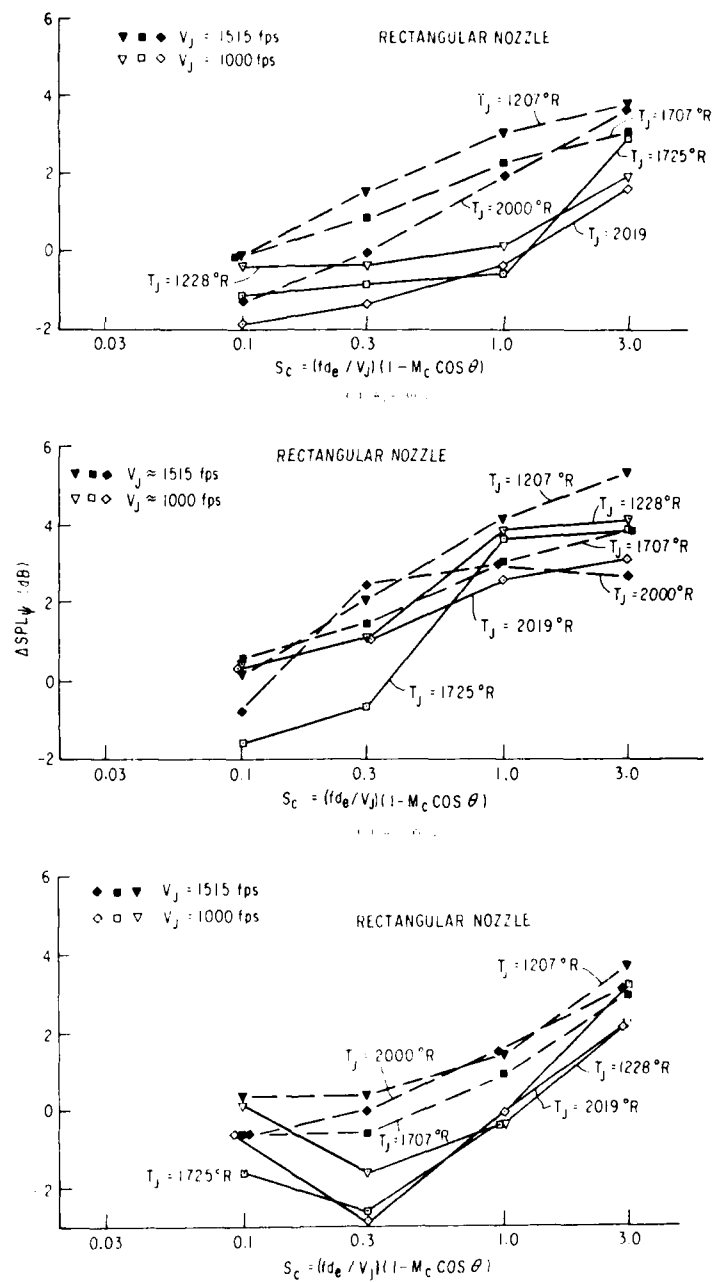


Figure 5-23. ΔSPL_{ψ} Versus Convected Strouhal No., S_c .

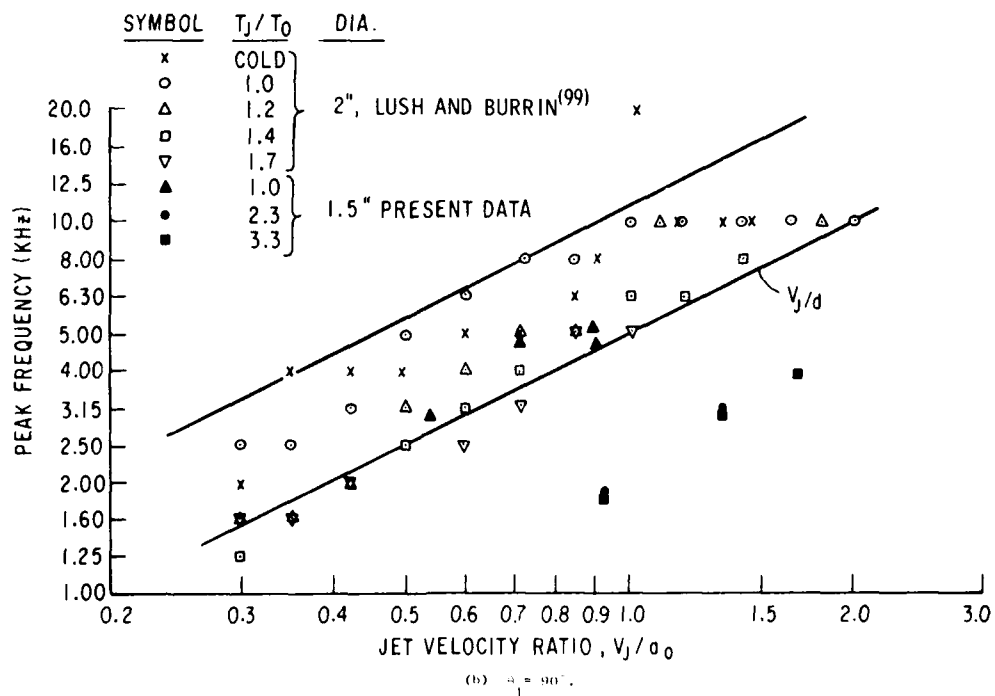
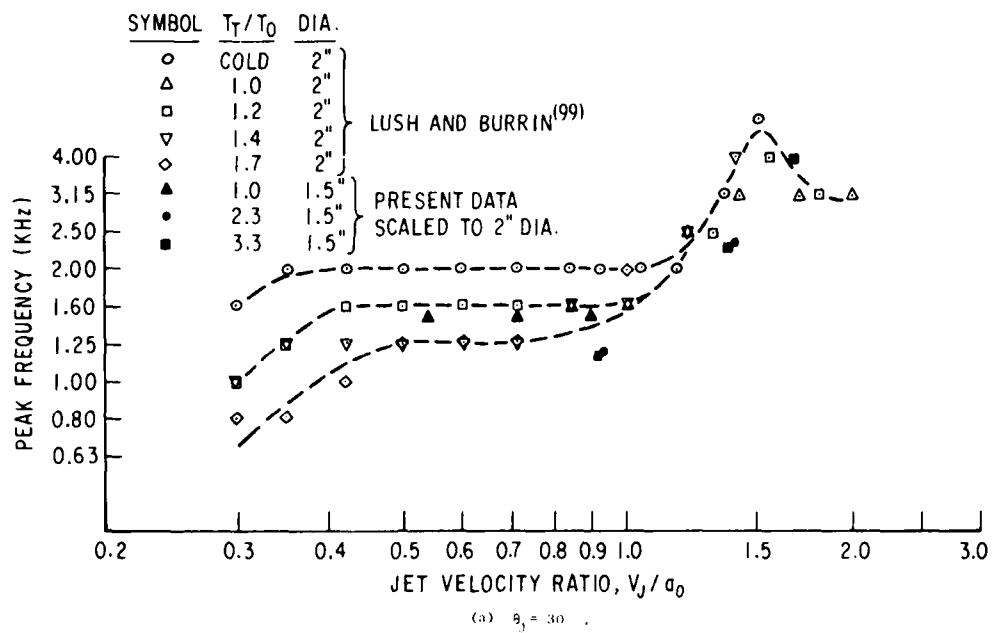


Figure 5-24. Peak Frequency Versus Jet Velocity.

5.2.4 Summary

The major conclusion of this section is that the reduction in overall acoustic power of a rectangular jet, when compared to an equivalent area round jet, is mainly due to shielding effects of the mean velocity and temperature field. This conclusion is based on the observations that the major differences between the round and rectangular jet noise occurred at emission angles of peak intensity, and that these differences increased with jet velocity. There are no observable differences in the power spectrum at low frequencies, and, in general, the SPL spectral shapes are more similar at right angles to the jet axis than at the shallow angles. These observations are in qualitative agreement with the predictions of acoustic shielding theory. Small differences between the round and rectangular SPL spectrum taken at a right angle to jet axis, for unheated flow, are also observed, indicating that some differences exist in the noise source distributions. When comparing the PWL and SPL data from round and rectangular jets, the largest differences are seen to occur near the frequencies of peak power and intensity, respectively. The effect of jet temperature on round and rectangular jet noise is apparently modified by the enhanced diffusion of the jet plume with heating, and the data displays a more complicated dependence on jet temperature than on jet velocity.

With regard to the noise as measured in the two planes of symmetry ($\psi = 0^\circ$ and $\psi = 90^\circ$) for the rectangular jet itself, the source location effects are dominant when the observer is nearly at a right angle to the jet axis. The radiation patterns of these distributed sources are strongly modified by the shielding effects of the jet plume as the observer approaches the jet axis. Shielding theory, in its present form, is valid in the vicinity of the peak intensity and is inadequate at shallow angles. The largest values of ΔSPL_ψ occurred from 40 to 60 degrees to the jet axis, coinciding with the locations of peak power contribution.

The difference power level, ΔPWL_ψ , showed a monotonic increase with frequency, a general increase with jet velocity, and was negligible at low frequencies. These observations generally support the acoustic shielding arguments. At shallow angles to the jet axis, however, the agreement breaks down and reversals of the roles of the quiet and loud planes take place. These reversals are more severe at high temperatures and low velocities. It appears that in order for shielding theory to properly predict the shallow angle noise of a noncircular jet it will be necessary to include the effects of jet spreading and diffusion, and the effects of off-axis source locations.

5.3 TWIN ROUND JET NOISE

Jet noise suppressors are usually constructed so that the exhaust plume of the engine is subdivided into many separate smaller jets. Noise data exists on a wide variety of complex suppressor configurations, but there is a lack of data on simpler elemental configurations. This section provides a thorough study of the simplest possible multielement suppressor, the twin-round jet configuration. This configuration has received minor attention in the published literature (Greatrex⁽¹⁰⁰⁾ and Goethert⁽¹⁰¹⁾ present some limited information).

Emphasis is placed on discerning between suppressed effects of the turbulent field (noise source aspects) and effects of the steady velocity and temperature fields (shielding aspects). These two noise suppression mechanisms can be clearly separated on the simple twin-jet experiments.

5.3.1 Experimental Methods

The experiments reported in this section were conducted at the General Electric Research and Development Center jet noise test facility (see Section 3.1). Convergent nozzles used for testing are shown in Figure 5-25. Each nozzle has an exit diameter of 1.5 inches. Test conditions were recorded as described in Section 5.2.1.

5.3.2 Experimental Results and Discussion

5.3.2.1 Overall Acoustic Power

The principal method of clarifying the role of turbulent mixing and acoustic shielding in the twin jet experiments is the use of variable nozzle spacing. At large spacings, turbulent mixing effects will be minimal and acoustic shielding effects will dominate. Conversely, at close spacings the turbulent mixing effects will be enhanced, and, as will be explained later, the acoustic shielding will be minimized. By measuring the acoustic radiation in different azimuthal planes, further clarification of the effects of these two different mechanisms is realized. In the measurement plane containing the nozzle centerlines ($\psi = 0^\circ$), the acoustic shielding will be the greatest; while in the plane perpendicular ($\psi = 90^\circ$) to the plane containing the nozzle centerlines, little or no acoustic shielding should be evident. This is indeed the case, as seen in Figures 5-26 and 5-27, where the quiet plane ($\psi = 0^\circ$) overall acoustic power, OAPWL, measurements are consistently less than the sum of two independent twin jets (single jet + 3 dB).

As the spacing, s , is increased, the measured OAPWL in the quiet plane, for the most part, decreases until the spacing to nozzle diameter ratio, exceeds 3. At spacing ratios above 3.0, the OAPWL in the quiet plane is rather insensitive to further increases in spacing. The loud plane ($\psi = 90^\circ$) OAPWL measurements are seen to vary from less than the single + 3 dB result (indicating mixing suppression) to greater than the single + 3 dB result

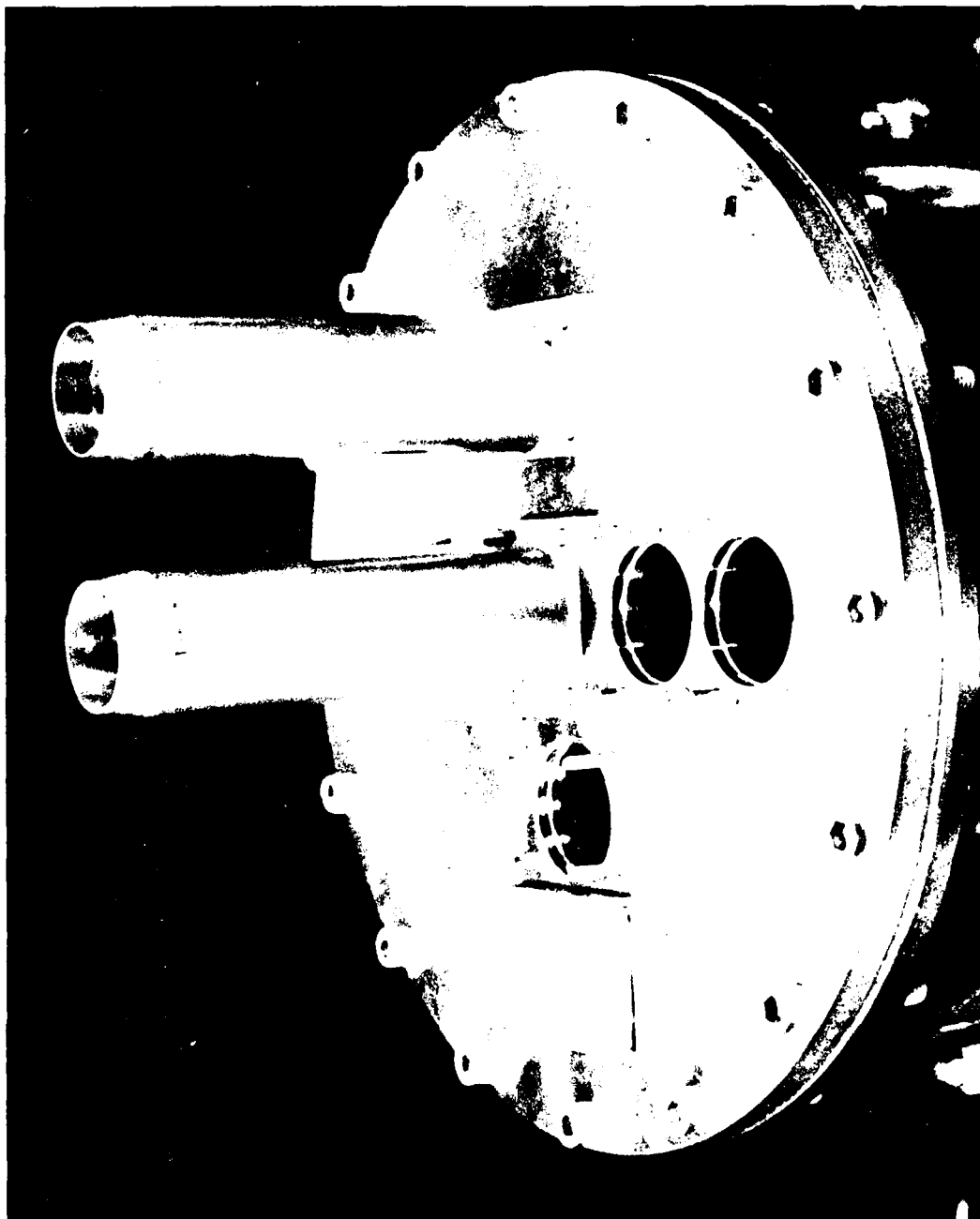


Figure 5-25. Twin Round Jet Nozzles.

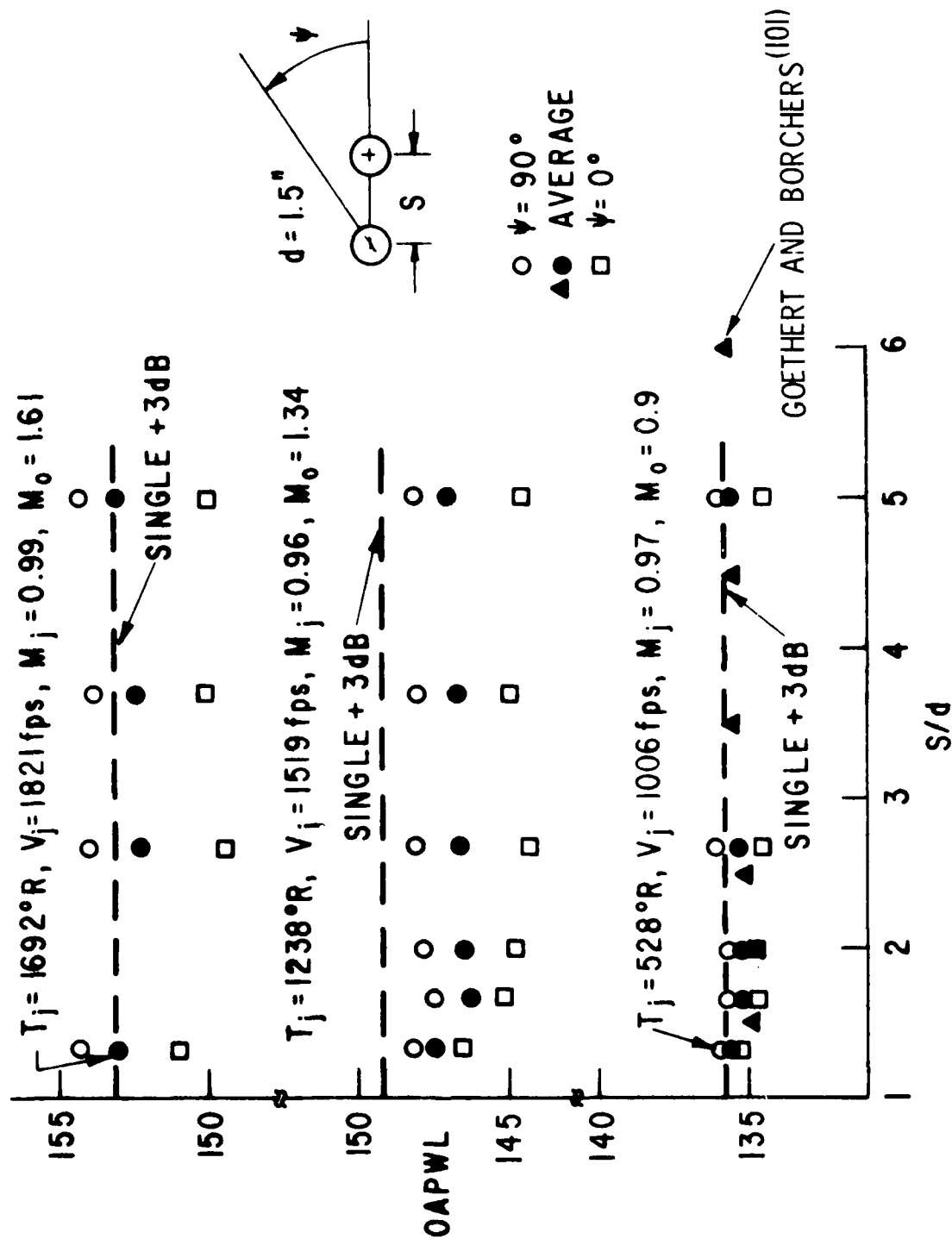


Figure 5-26. Effect of Nozzle Spacing on Acoustic Power of Twin Round Jets at $M_j \approx 1$.

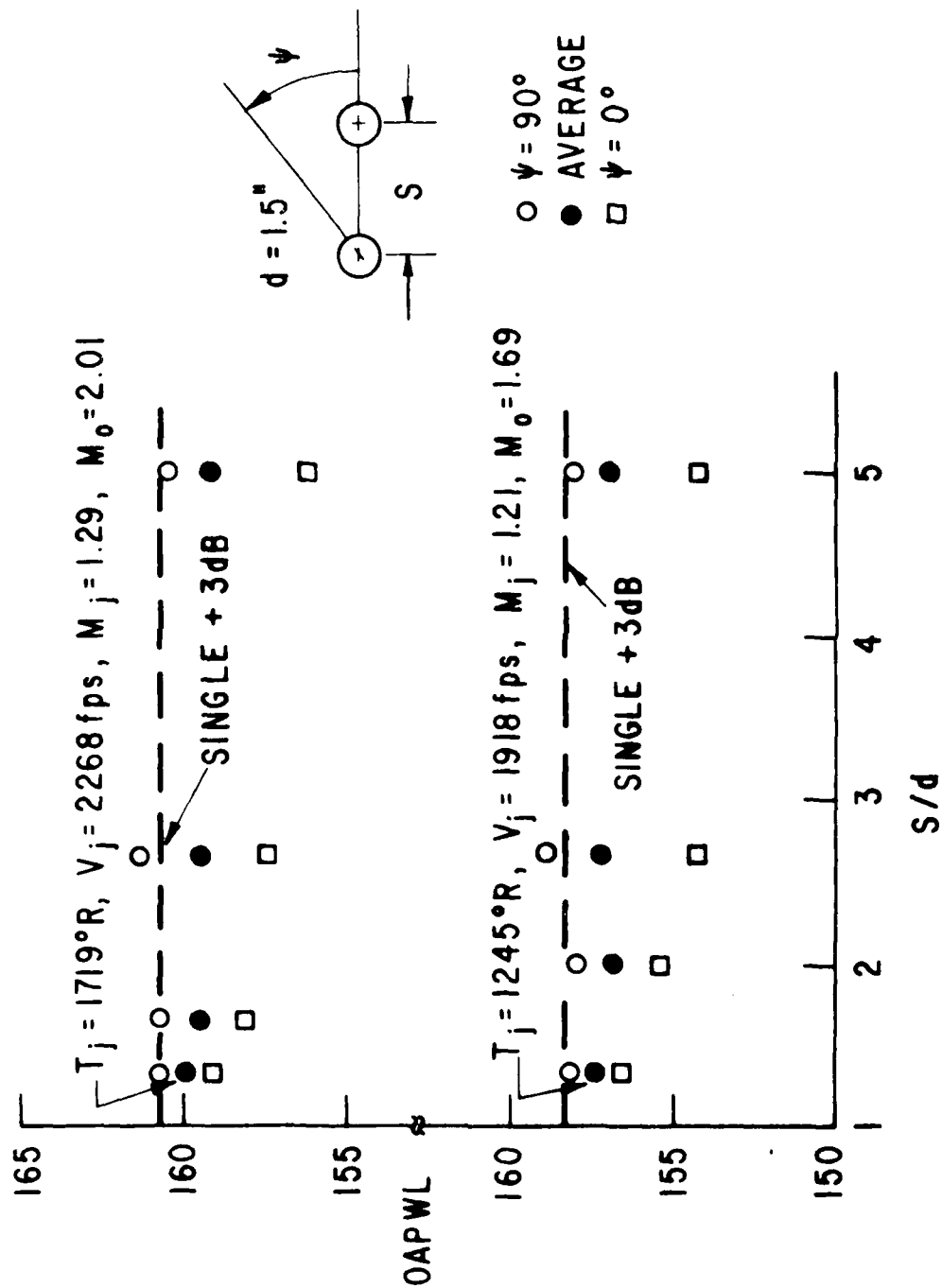


Figure 5-27. Effect of Nozzle Spacing on Acoustic Power of Twin Round Jets
 $M_j > 1$.

(indicating additional noise generation). The large differences between the quiet and loud planes were at first surprising since Goethert and Borchers⁽¹⁰¹⁾ had reported only small acoustic power changes at very close spacing. Goethert's experiments, conducted with cold subsonic flow, were confirmed in the cold flow tests under this program (see Figure 5-26).

Results of an earlier investigation of a twin-jet configuration by Greatrex and Brown⁽¹⁰⁰⁾ (although considered by the authors to be preliminary and of uncertain reliability) are compared with the results of the current study in Figure 5-28. The comparison is hampered by the lack of specified conditions for the earlier work, but a reasonable agreement exists except for spacings of less than two nozzle diameters. At these close spacings, it is expected that the nozzle exit profile would play an important part. In the current work convergent nozzles are used, but it is not known what type of nozzle was used for the earlier work. Comparisons are therefore probably not valid for very close spacings. Goethert and Borchers used unheated subsonic flow from constant diameter round tubes and found a slight reduction in total acoustic power at very close spacings in agreement with the results shown on Figure 5-26.

These small differences for unheated, low-velocity jets are increased by raising the temperature (and hence the velocity) at a constant jet Mach number (Figures 5-26 and 5-27) causing an increase in the asymmetry of the radiation patterns. This trend agrees with acoustic shielding arguments. The separate effects of velocity and temperature are discussed in more depth in Section 5.3.2.5.

5.3.2.2 Azimuthal Directivity

The effect of nozzle spacing on OAPWL as measured in different azimuthal planes is shown in Figure 5-29. The effect is visualized as the casting of an "acoustic shadow" by the near jet. At very close spacing, the shadow is broad and not very deep, but as the spacing is increased, the shadow deepens. Increasing spacing beyond a certain point causes a narrowing of the shadow, but at $\psi = 0^\circ$ the reduction in acoustic energy remains at the maximum value.

5.3.2.3 Polar Directivity

Shielding theory [as described by Mani⁽¹⁷⁾ and Balsa⁽³⁵⁾] predicts a reduction in the sound radiation of imbedded sources as the observer approaches the jet axis. Likewise it would be expected that radiation of nonimbedded sources, such as those from an adjacent jet, which traverse the near jet would suffer a similar reduction as the observer approached the jet axis. Figure 5-30 illustrates this effect very clearly with an increasing reduction of noise in the quiet ($\psi = 0^\circ$) plane as the jet axis is approached. This reduction is seen whether comparison is made to the twin-jet measurement in the loud ($\psi = 90^\circ$) plane or the sum of two independent jets (single + 3 dB). About 1.5 dB of the reduction can be attributed to mixing suppression (for angles greater than 20°), deduced from comparing

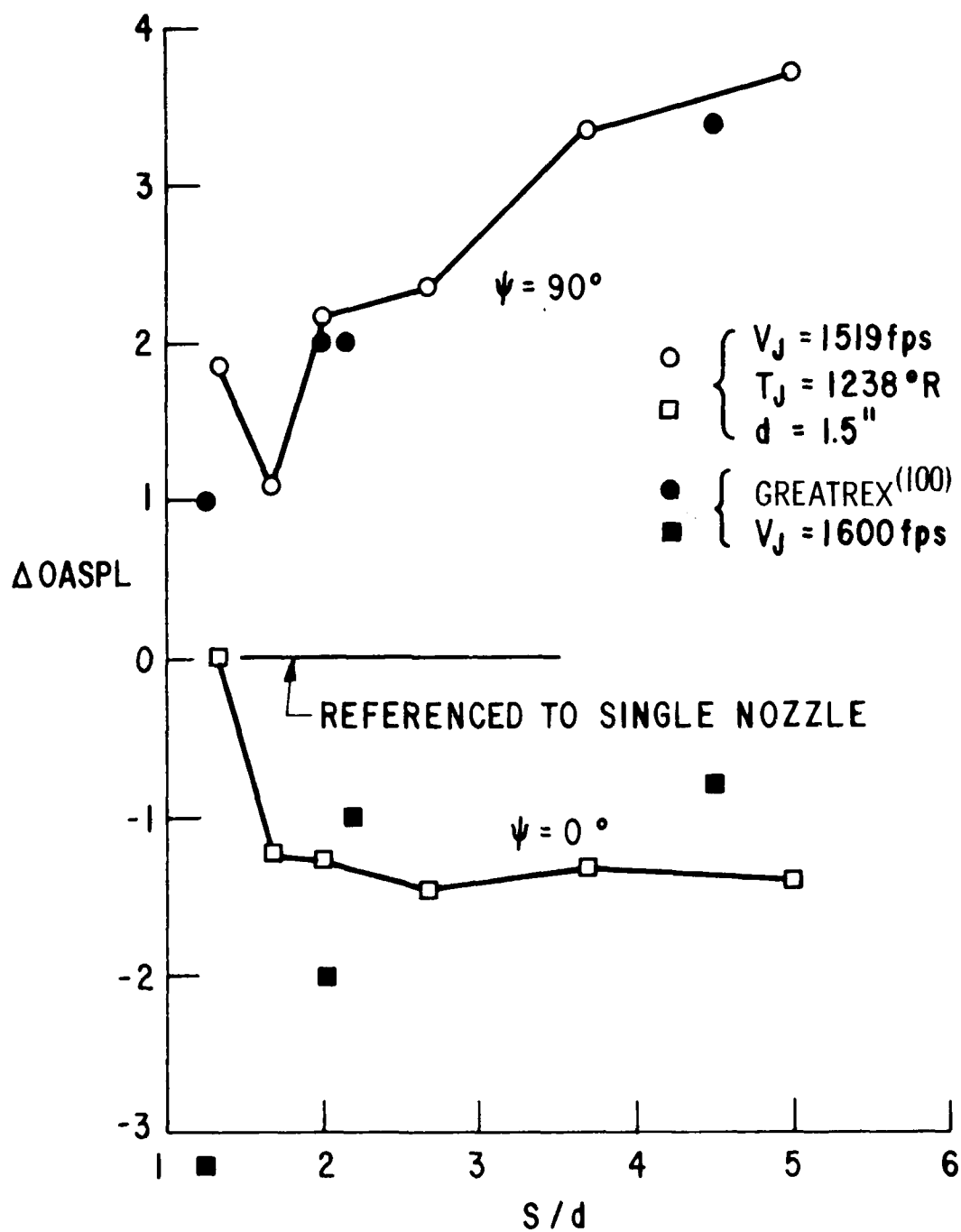


Figure 5-28. Peak Polar ΔOASPL with Twin Round Nozzle Spacing.

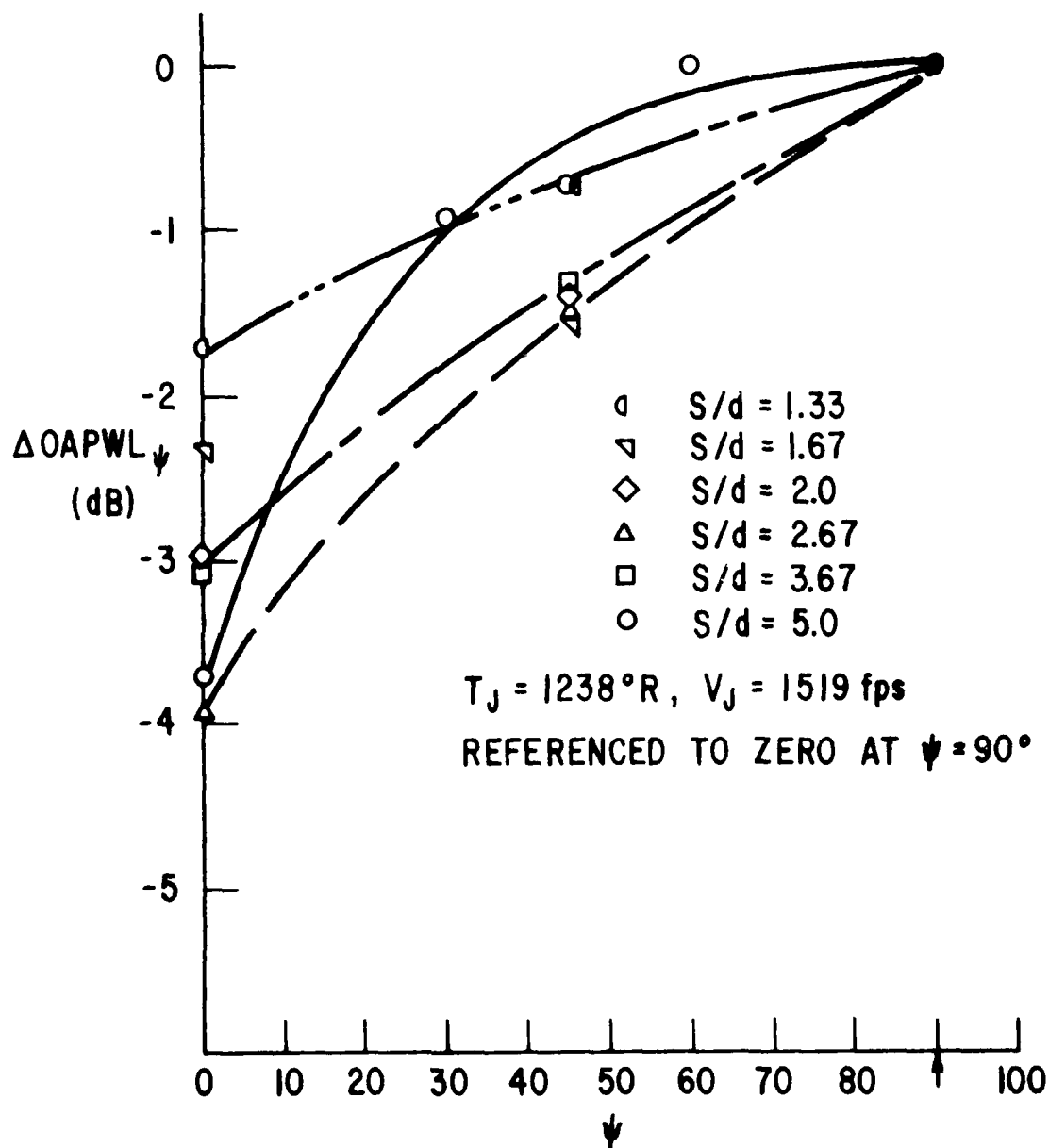


Figure 5-29. Change in Acoustic Power with Azimuthal Angle, Twin Round Jets.

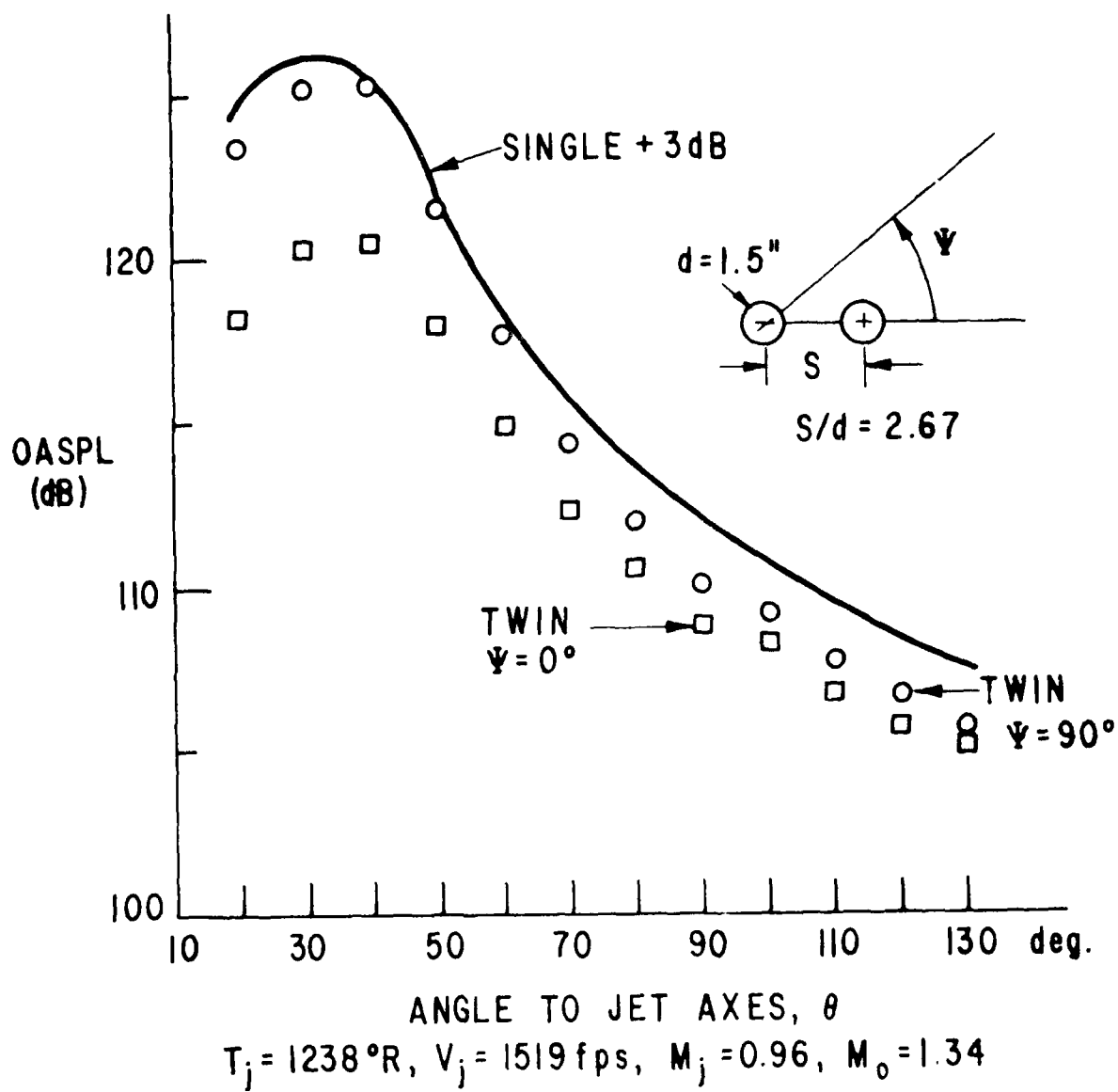


Figure 5-30. Directivity Comparison, Twin Round Vs. Single.

AD-A094 291

GENERAL ELECTRIC CO CINCINNATI OH AIRCRAFT ENGINE GROUP F/G 20/1
HIGH VELOCITY JET NOISE SOURCE LOCATION AND REDUCTION, TASK 2. --ETC(U)
MAY 78 T F Balsa, P R GLIEBE, R A KANTOLA DOT-05-30034
R78AE6323 FAA-RD-76-79-2 NL

UNCLASSIFIED

6 of 9
AD
R78AE6323



the twin-jet noise at $\psi = 90^\circ$ to the single jet + 3 dB level. This is because, in the $\psi = 90^\circ$ plane, there is no shielding by an adjacent jet. The additional reduction seen in the ($\psi = 0^\circ$) twin jet noise at $\theta = 90^\circ$ cannot be attributed solely to mixing suppression, because acoustic shielding is possible at $\theta = 90^\circ$ with heated flows.

5.3.2.4 Spectral Effects

The part of the jet noise spectrum most responsible for the asymmetries of the spectral-averaged measurements mentioned earlier has not been identified in the current literature. The frequency dependence of the shielding of the far jet by the near jet is shown in Figure 5-31. Low frequency mixing suppression can also be noted by comparing the single + 3 dB data to the twin data at $\psi = 90^\circ$.

The sound pressure spectra, SPL, at $\theta = 30^\circ$, 60° , and 90° are shown on Figures 5-32a, b, and c. The trends are similar to what would be expected from the OASPL and PWL results, with the shallow-angle, high frequency data showing the largest amounts of shielding. Low frequency mixing suppression for the twin-round nozzles, is evident at $\theta = 30^\circ$ (Figure 5-32a). At $\theta = 90^\circ$ (Figure 5-32c), mixing suppression appears over the majority of the frequency range.

5.3.2.5 Velocity and Temperature Effects

To define the separate effects of velocity and temperature on the acoustic properties, the differences in overall power, ΔOAPWL_ψ , are considered first. Figures 5-33a, b, and c illustrate the change in ΔOAPWL_ψ with jet velocity, for a range of spacings, with jet temperature as a parameter. The numbers adjacent to the data points indicate the jet exit total temperature in $^\circ\text{R}$. At the middle and largest spacings (Figures 5-33b and c), ΔOAPWL_ψ increases with velocity until the velocity becomes supersonic.

The effects of temperature on ΔOAPWL_ψ are less clear than the effects of velocity. For all spacings (Figures 5-33a, b, and c), the point of maximum ΔOAPWL_ψ occurs near the sonic point. This indicates that maximum noise reduction is obtained at the highest velocity and temperature, provided that the jet plume is shock free.

The power spectra of the twin-round jets exhibit interaction noise generation, mixing suppression, and acoustic shielding. At certain test conditions, all three are seen to occur simultaneously (in different parts of the spectrum). The discussion of this data first considers the low velocity (1000 fps) case, with jet spacing and jet temperature as parameters. A measure of the amount of interaction noise generation of the twin jets (with respect to the sum of two isolated single round jets) is found by comparing the twin-jet $\psi = 90^\circ$ data to the single + 3 dB data (solid line), as shown on Figures 5-34 through 5-39. If the twin-jet ($\psi = 90^\circ$) data are above the single + 3 dB data, then there must be additional noise generated by the

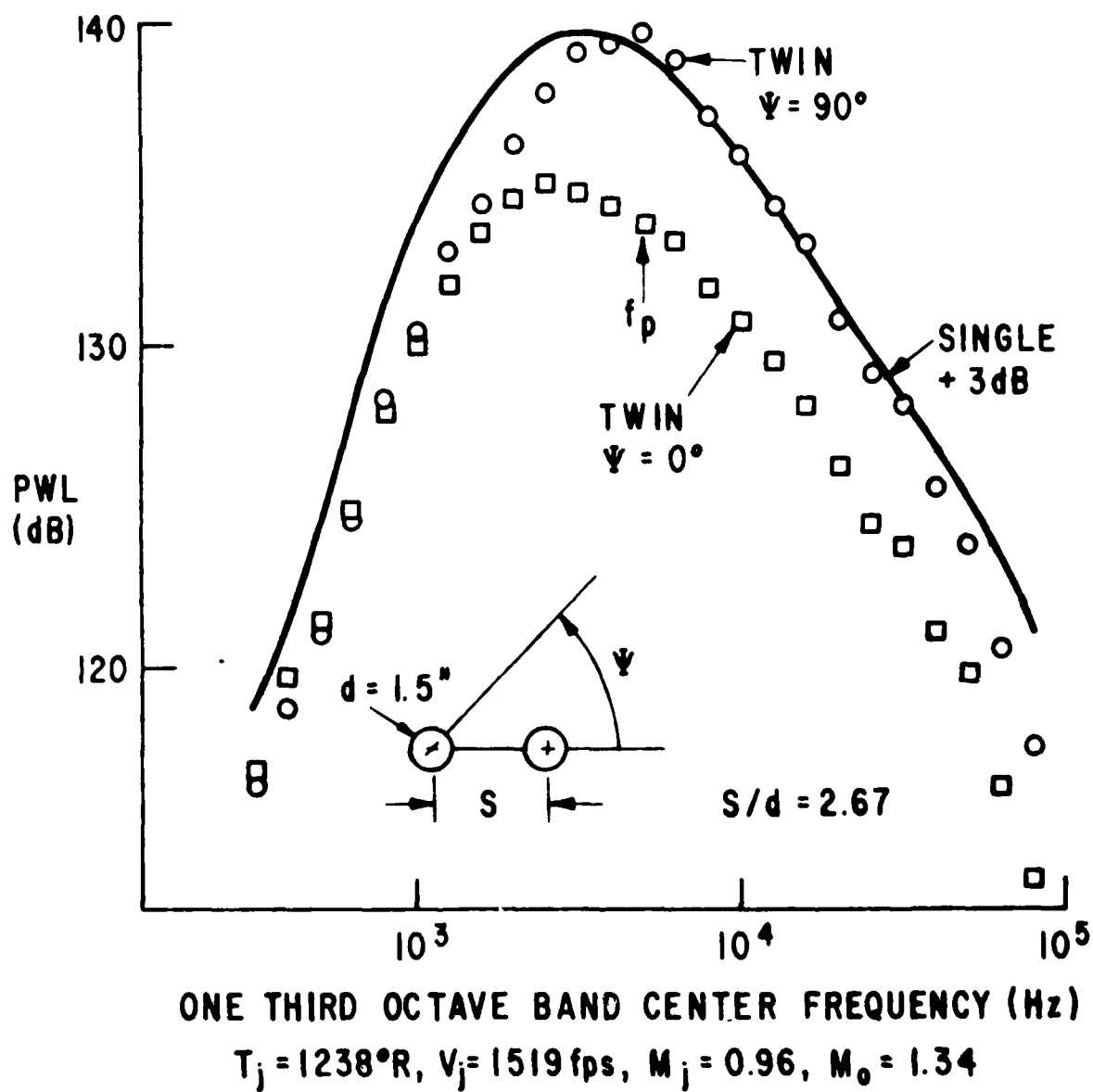


Figure 5-31. Power Spectra Comparison, Twin Round Vs. Single.

480

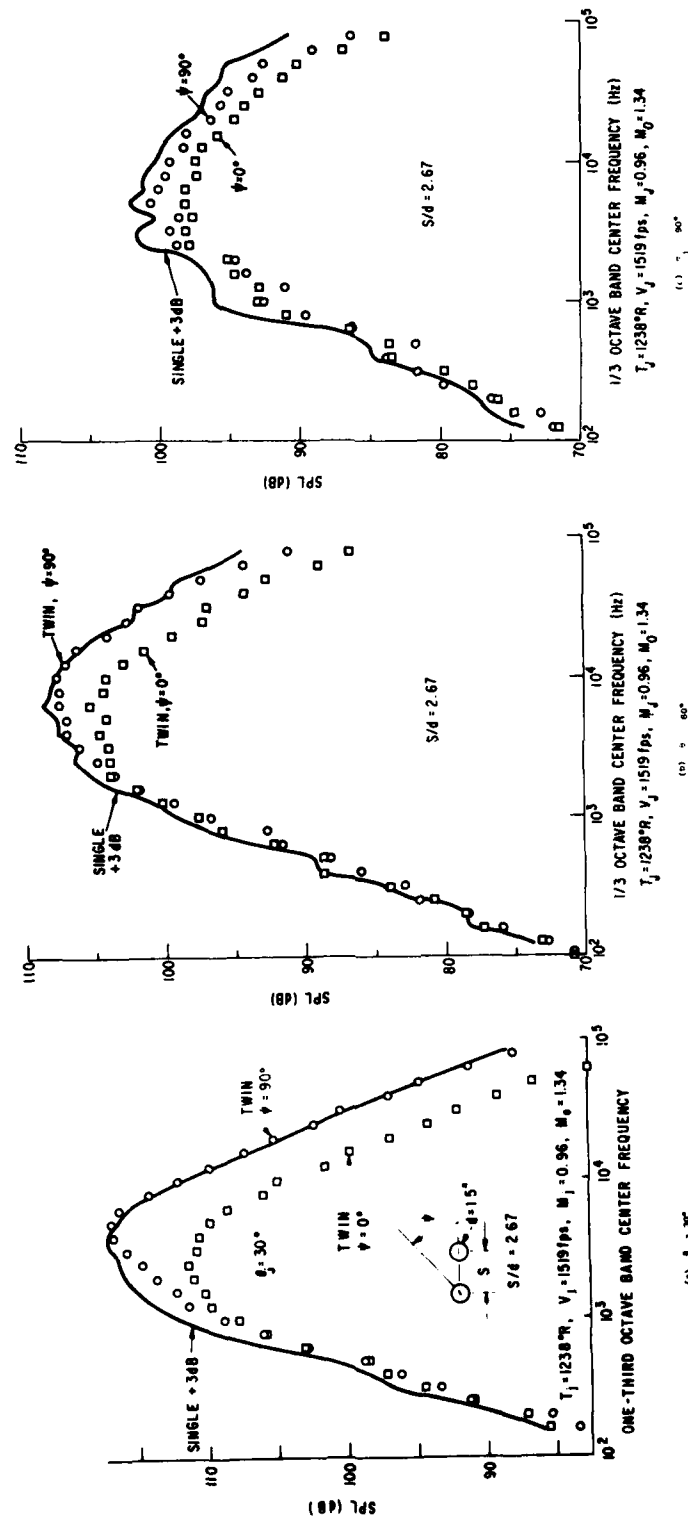


Figure 5-32. SPL Comparison, Twin Round Vs. Single.

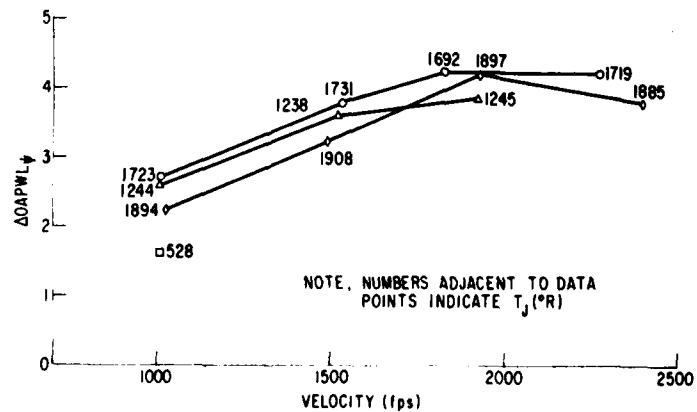
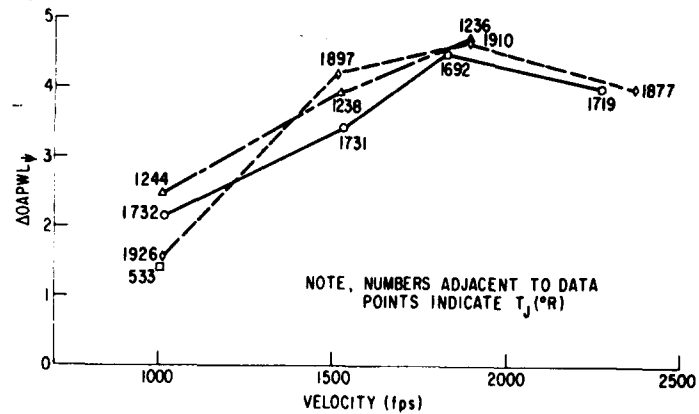
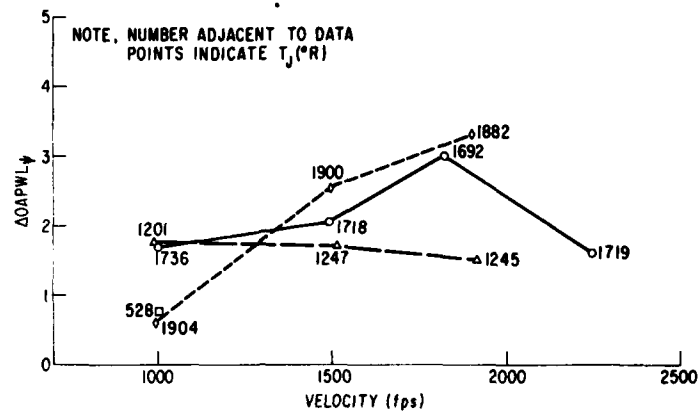


Figure 5-33. Azimuthal Difference Power Level, Twin Round.

(410)

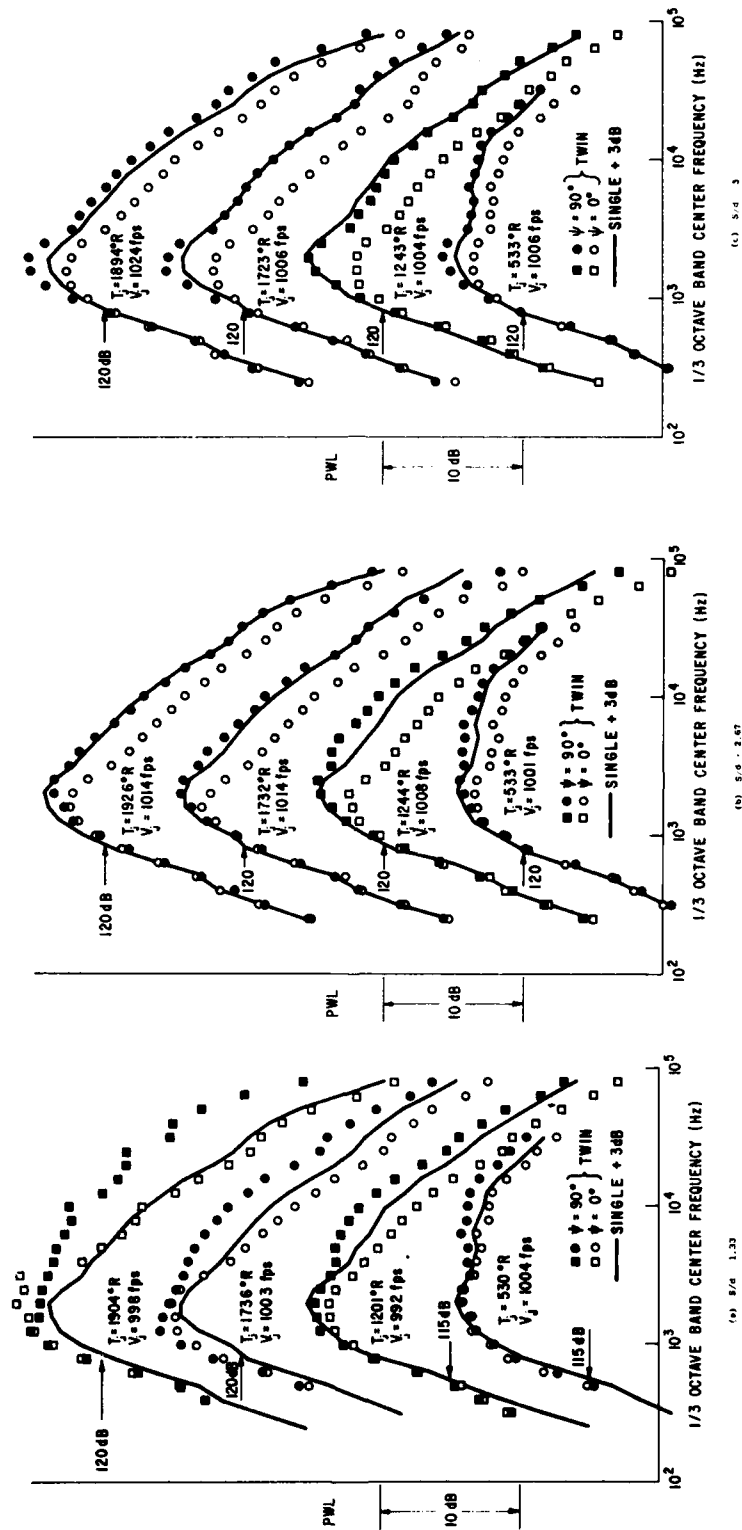
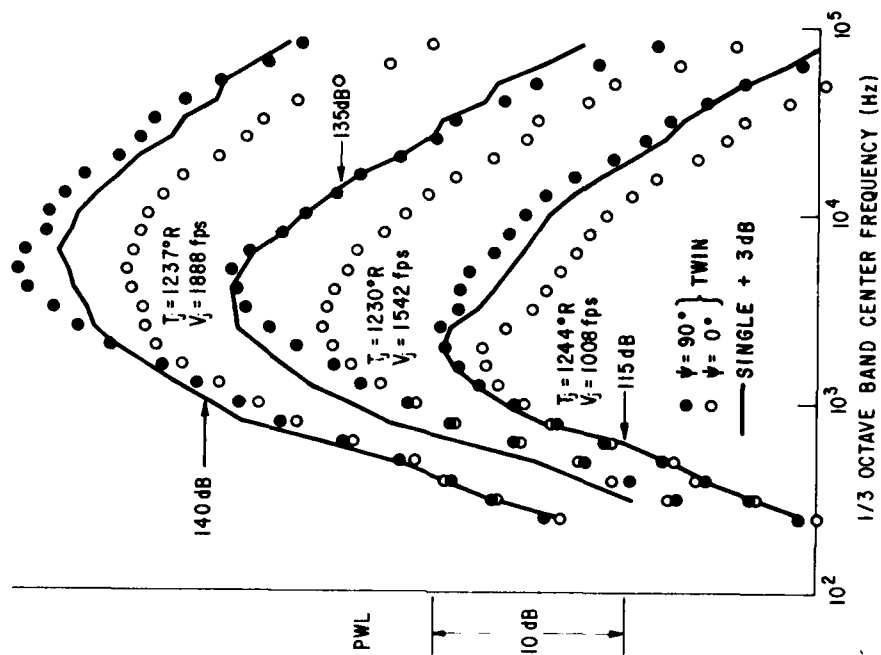
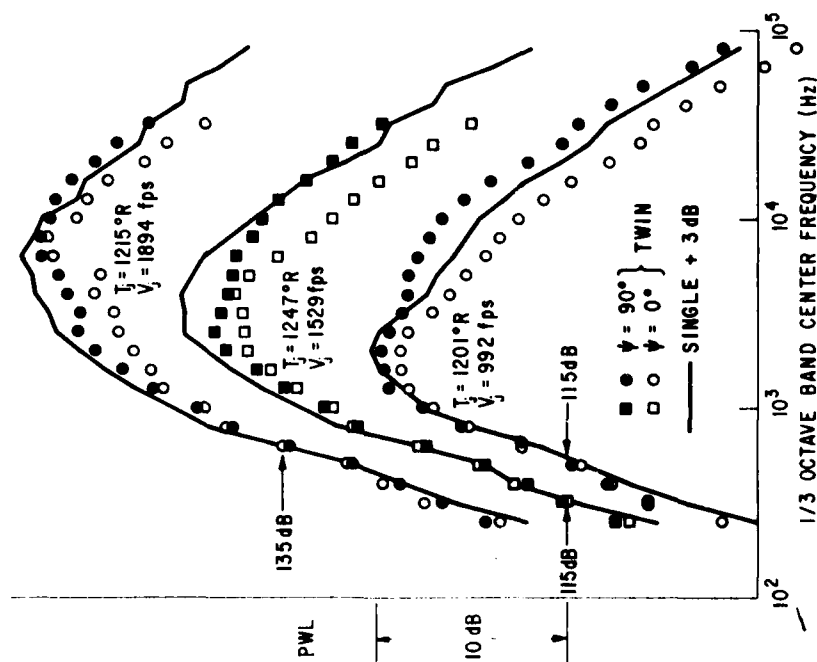


Figure 5-34. Twin Round Power Spectra.

(485)



(b) $T_j = 1200^\circ \text{ R}$, $S.d = 2.67$



(c) $T_j = 1200^\circ \text{ R}$, $S.d = 1.33$

Figure 5-35. Twin Round Power Spectra.

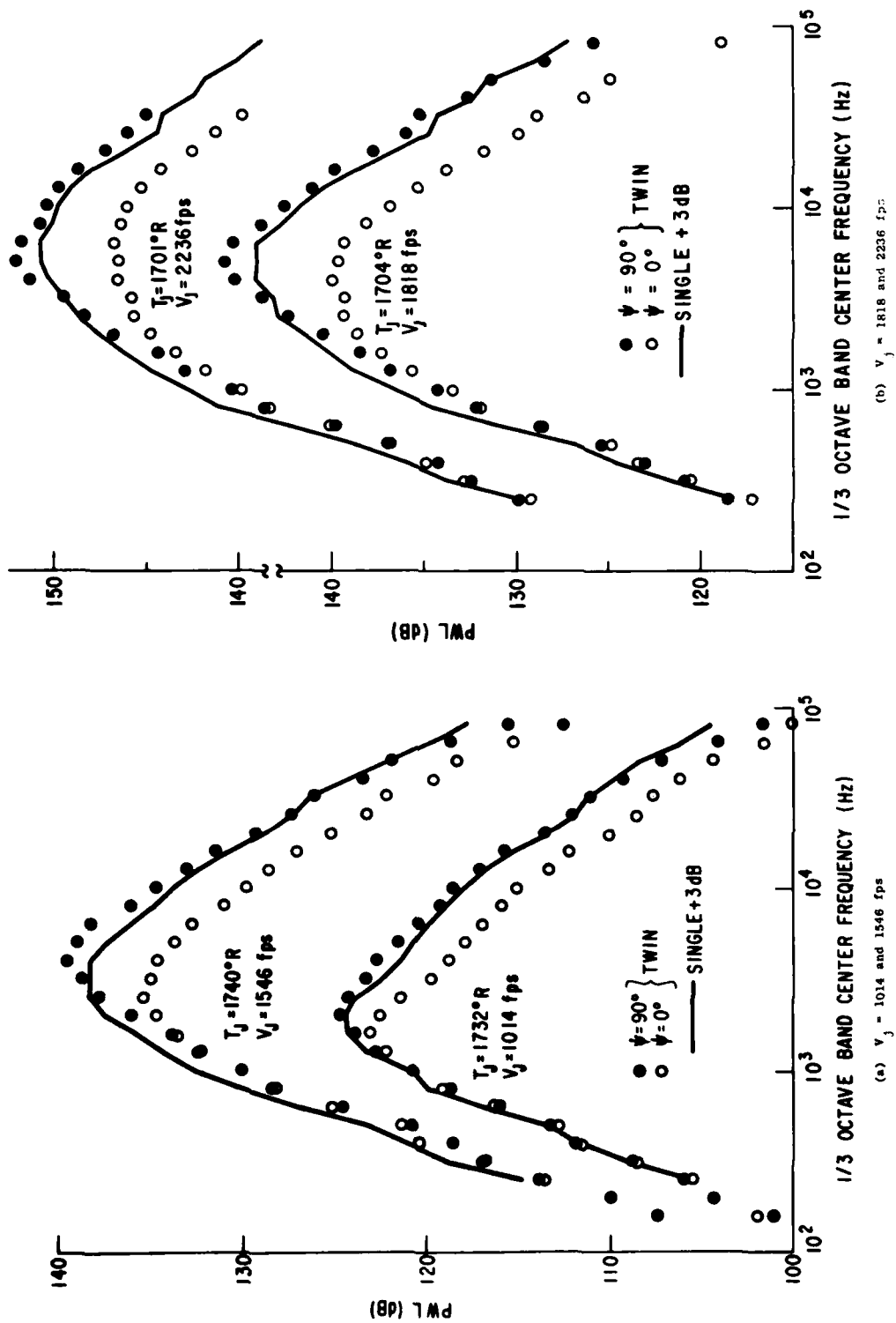


Figure 5-36. Twin Round Power Spectra, $T_j \approx 1700^\circ R$, $S/d = 1.33$.

5118

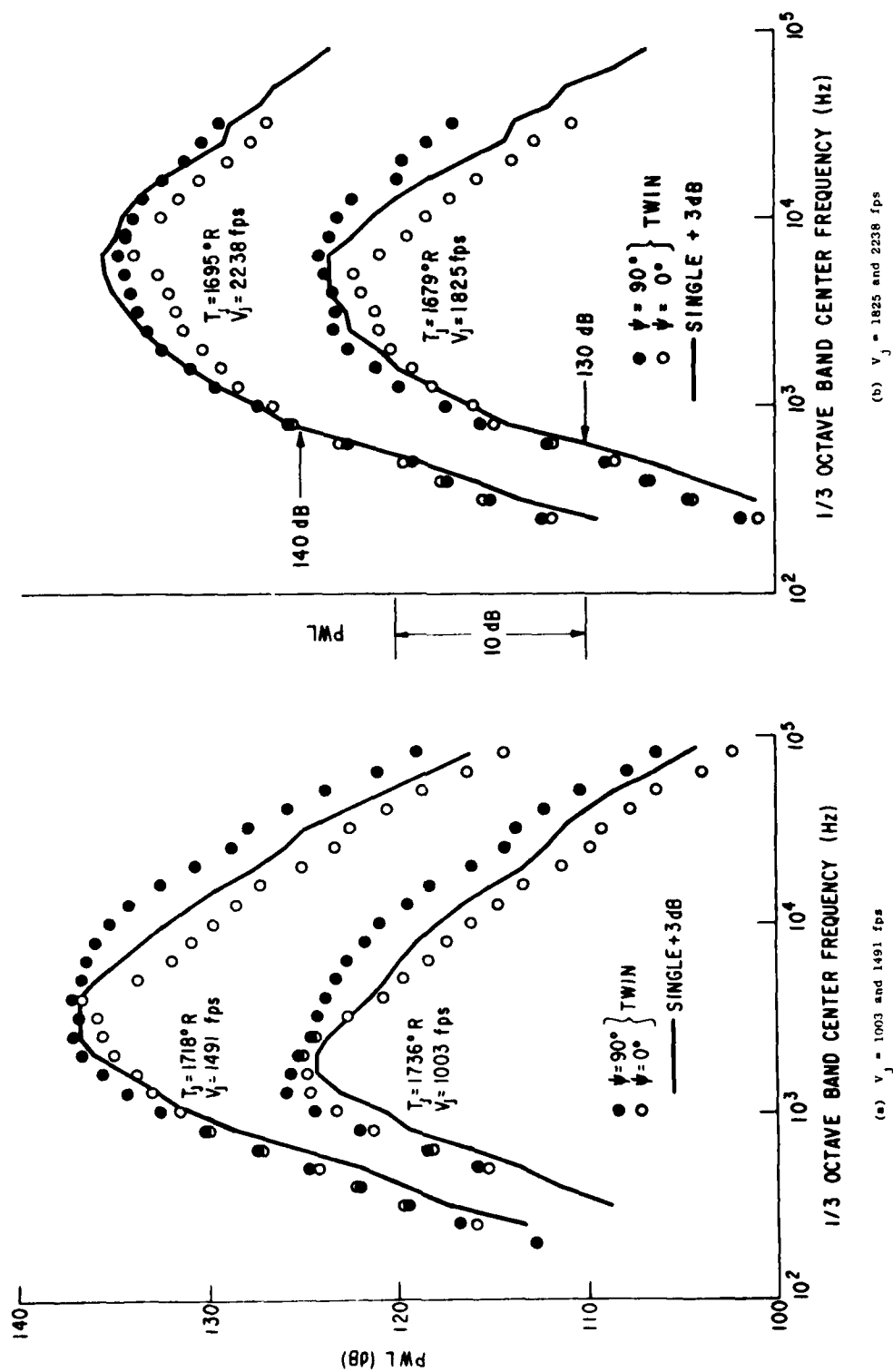


Figure 5-37. Twin Round Power Spectra, $T_j \approx 1700^\circ R$, $S/d = 2.67$.

(4/16)

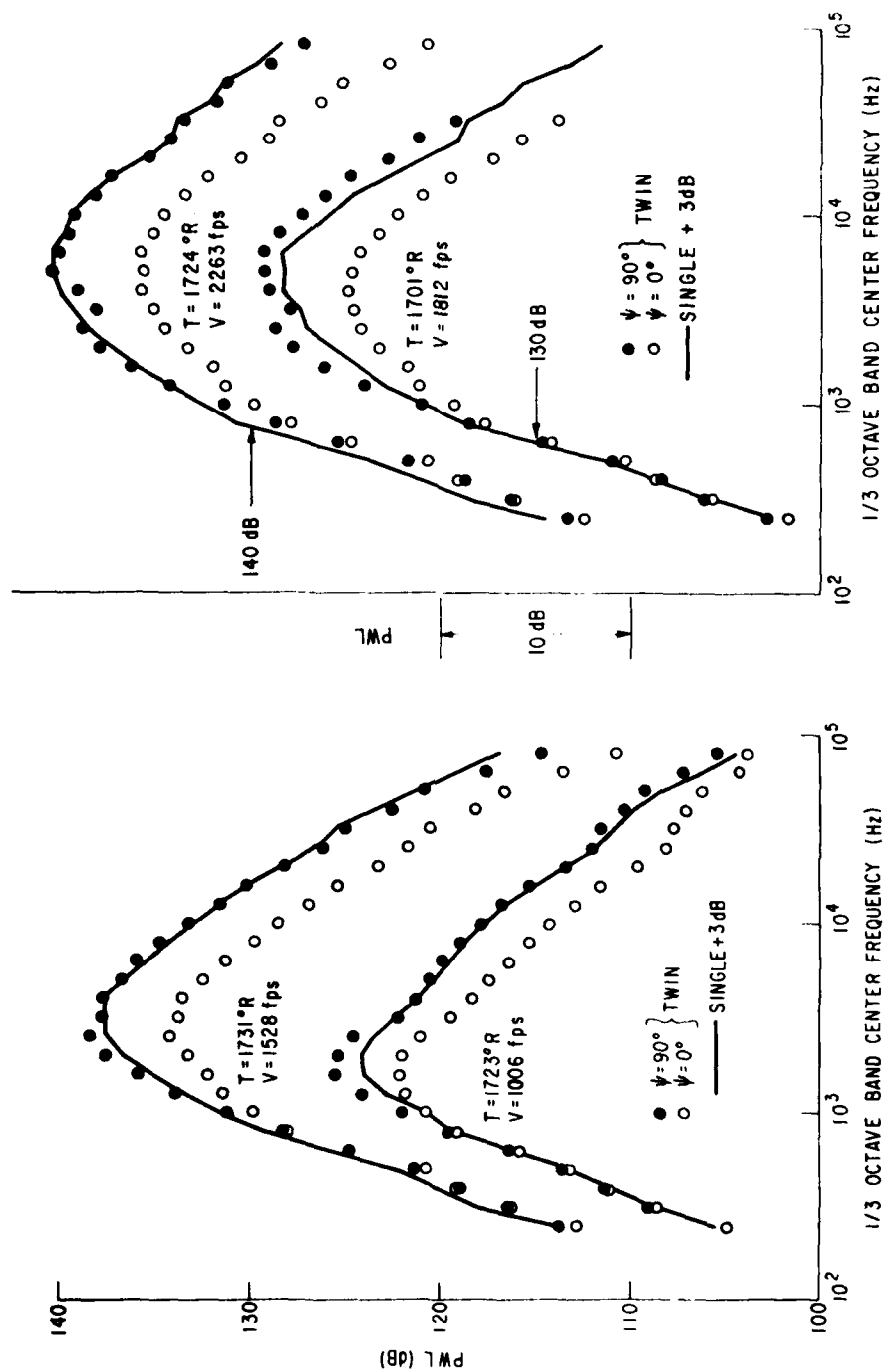
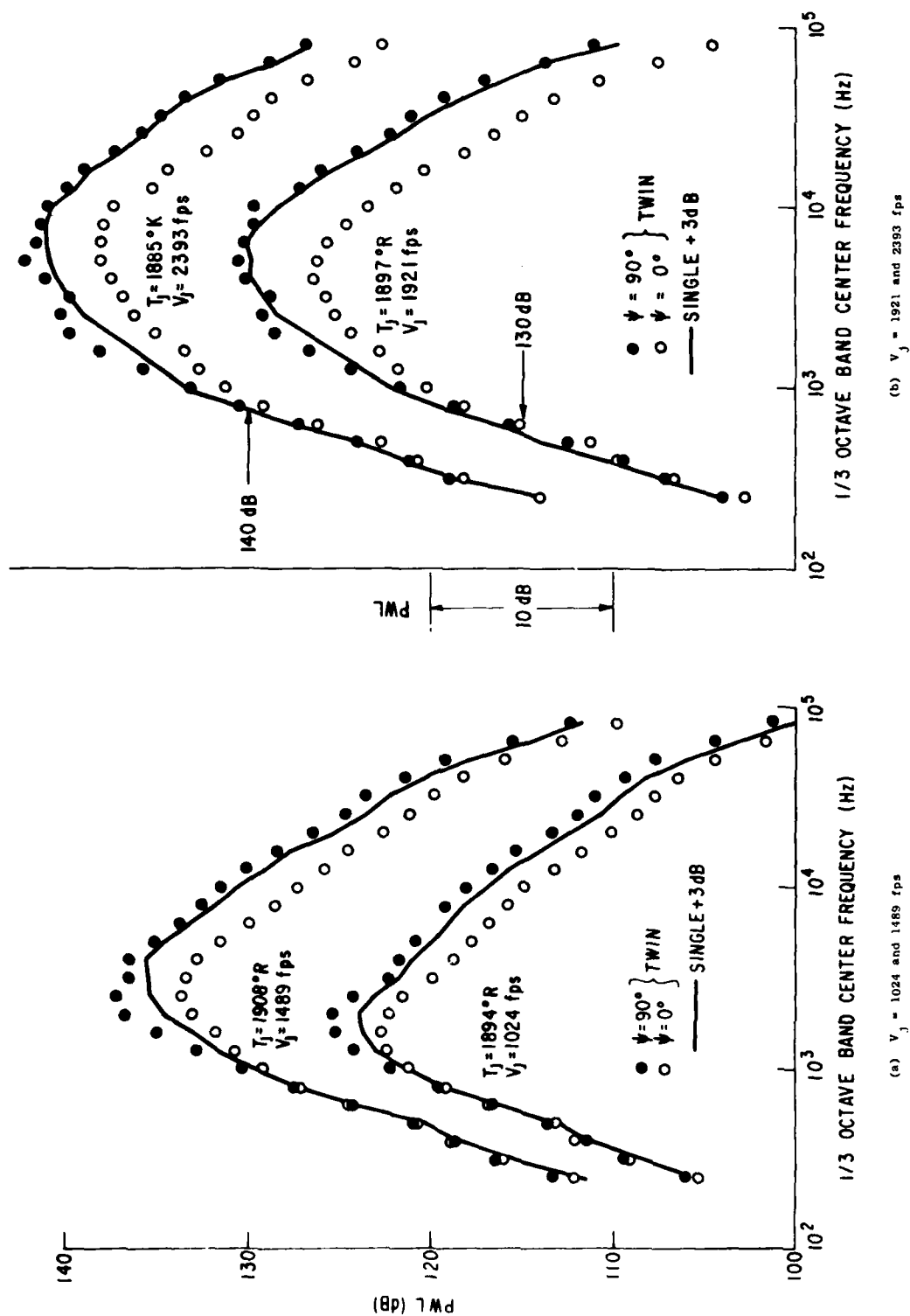


Figure 5-38. Twin Round Spectra, $T_j \approx 1700^\circ R$, $S/d = 5$.



(b) $V_j = 1921$ and 2393 fps

(a) $V_j = 1024$ and 1489 fps

Figure 5-39. Twin Round Power Spectra, $T_j \approx 1900^\circ R$, $S/d = 5$.

interaction of the two jets. If the twin data are below the single + 3 dB data, then there is a noise suppression caused by the interaction of the twin round jets. At the closest spacing ratio, $s/d = 1.33$ (Figure 5-34a), noise generation occurs only at high frequencies for jet temperatures of 1200° R and below. For higher temperatures noise generation occurs throughout the spectrum. As jet spacing is increased to $s/d = 5$, see Figures (5-34b and c), the noise generation is reduced until it exists only over a small frequency range near the peak frequency. Interaction noise generation is significant only at the close spacing, but acoustic shielding is shown at all conditions. Interpretation of what constitutes shielding is complicated by the presence of the interaction noise, which is clearly identified only in the $\psi = 90^\circ$ plane. Since interaction noise at $\psi = 0^\circ$ can be shielded by the adjacent jet, the level of acoustic shielding shall be defined as the difference between the twin round jet acoustic power spectra (ΔPWL_ψ) at $\psi = 90^\circ$ and at $\psi = 0^\circ$. The interaction noise generation in some cases also has a directivity such that more than a 3 dB difference between the twin round jet noise in the $\psi = 90^\circ$ and the $\psi = 0^\circ$ planes occurs. This is seen at a jet temperature of 1904° R on Figure 5-34a. Note that while the maximum value of ΔPWL_ψ is not a strong function of spacing, the frequency of the onset of shielding is. As the spacing increases, the frequency at which shielding starts decreases. This observation on the frequency of the onset of shielding is discussed in Section 5.3.2.6. There is no evidence of significant mixing suppression at any of the jet spacing ratios at the low 1000 fps velocity conditions (Figures 5-34a, b, and c).

When the temperature is held constant at $T_T = 1200^\circ$ R and the jet velocity is raised to 1500 fps and above (as shown on Figures 5-35a and 5-35b) the interaction noise (seen at $V_J = 1000$ fps) disappears. For these high velocity conditions, mixing suppression now becomes noticeable in the low to middle frequencies. The acoustic shielding exhibits the same frequency-spacing effect as seen on Figures 5-34a, b, and c, with the exception of the supercritical case with the closest spacing (Figure 5-35a). For these closely spaced twin jets, supercritical flow conditions result in two affects. The first is the appearance of shock-associated noise in the power spectra. Second, the expansion of the jets immediately downstream of the nozzle exit planes tends to cause the jet plumes to merge prematurely and inhibit the shielding.

At a higher temperature (1700° R), the $s/d = 1.33$ data (Figures 5-36a and 5-36b) exhibit the most complicated behavior, with interaction noise appearing at all velocities except at the supercritical conditions. This interaction noise decreases as the jet spacing is increased, as shown on Figures 5-37a, 5-37b, 5-38a, and 5-38b. At the intermediate spacing (Figure 5-37b), some slight noise generation at middle and high frequencies is evident, as well as suppression at the low frequencies. For the largest spacing, $s/d = 5$ (Figures 5-38a, 5-38b, 5-39a, and 5-39b), very little suppression is noted and the interaction noise is concentrated near the peak frequency. Also, for the $s/d = 5$ case, further heating of the jets to $T_T = 1900^\circ$ R (shown on Figures 5-39a and 5-39b) produces a slight reduction in the levels of ΔPWL_ψ , at the lower velocities, when compared to the 1700° R data. This was also seen in the $\Delta OAPWL_\psi$ comparisons on Figure 5-34c and discussed earlier.

In general, it seems that the very complicated interaction of temperature and velocity on the observed $\Delta OAPWL_\psi$ at $s/d = 1.33$ (Figure 5-33a) is due to the presence of interaction noise generation and acoustic shielding in roughly equal amounts, as evidenced by the ΔPWL_ψ results shown on Figures 5-34a, 5-35a, 5-36a, and 5-36b. As the spacing is increased, the trends are less obscure, and at $s/d = 2.67$ a large reduction in noise generation is seen, along with a relatively constant amount of acoustic shielding. At the largest spacing, $s/d = 5$, the acoustic shielding is the only dominant affect, with very little noise generation and no mixing suppression. This dominance of shielding effects provides a relatively simple variation of $\Delta OAPWL_\psi$ with velocity and temperature, in accordance with the predictions of acoustic shielding theory^(17,35).

5.3.2.6 Nozzle Separation and Shielded Frequency

To further clarify the effect of nozzle separation s/d on the far-field noise, the difference power spectra (ΔPWL_ψ) between the loud and the quiet plane of the twin round jets is shown on Figure 5-40. Two conclusions can be drawn from Figure 5-40. First, the onset of shielding begins at lower frequencies for the larger spacings. Second, the shielding quickly reaches a maximum value that is not strongly dependent on the nozzle spacing. This behavior is believed to be due to the layer of slow moving, cooler air that exists between the two jet plumes. In the quiet plane, the acoustic waves from the far jet have to traverse this layered flow and temperature field, causing reflection of the incident waves by the velocity and temperature mismatches. As the jet nozzle spacing is increased, the downstream extent of the layer increases. This downstream extension of the intermediate layer with nozzle spacing then reduces the frequency of onset of shielding shown in Figure 5-40. Another interesting aspect of this phenomenon is the effect of the angle to the jet axis on the difference in sound pressure spectra at any fixed nozzle spacing. Figure 5-41 shows that the ΔSPL_ψ is larger at the shallow angles to the jet axis and that the onset of shielding starts at lower frequencies at shallow angles. To quantify the variation of shielding with frequency and nozzle spacing, the identification of the lowest frequency f_m at which the ΔSPL_ψ equals 3 dB is defined. The variation of the shielding frequency f_m with separation distance, as determined from information such as that on Figure 5-41 shown on Figure 5-49. Note that the angle at which f_m occurs varies with s/d and with the operating conditions.

The rather good data collapse of Figure 5-42 confirms that the parameter f_m is largely dependent on the geometry of the flow field, and is seen to be only weakly effected by the jet temperature and velocity, for subsonic flows. The angle to the jet axis, θ_0 , at which ΔSPL_ψ equals 3 dB is not specified on Figure 5-42 but this shielding angle does increase with frequency, as can be seen on Figure 5-43. The results of Figure 5-43 show that the cone of shielding, defined by the half angle θ_0 , encompasses more of the radiation field at the higher frequencies. The effect of increased spacing is to extend the onset of this shielded region to lower frequencies.

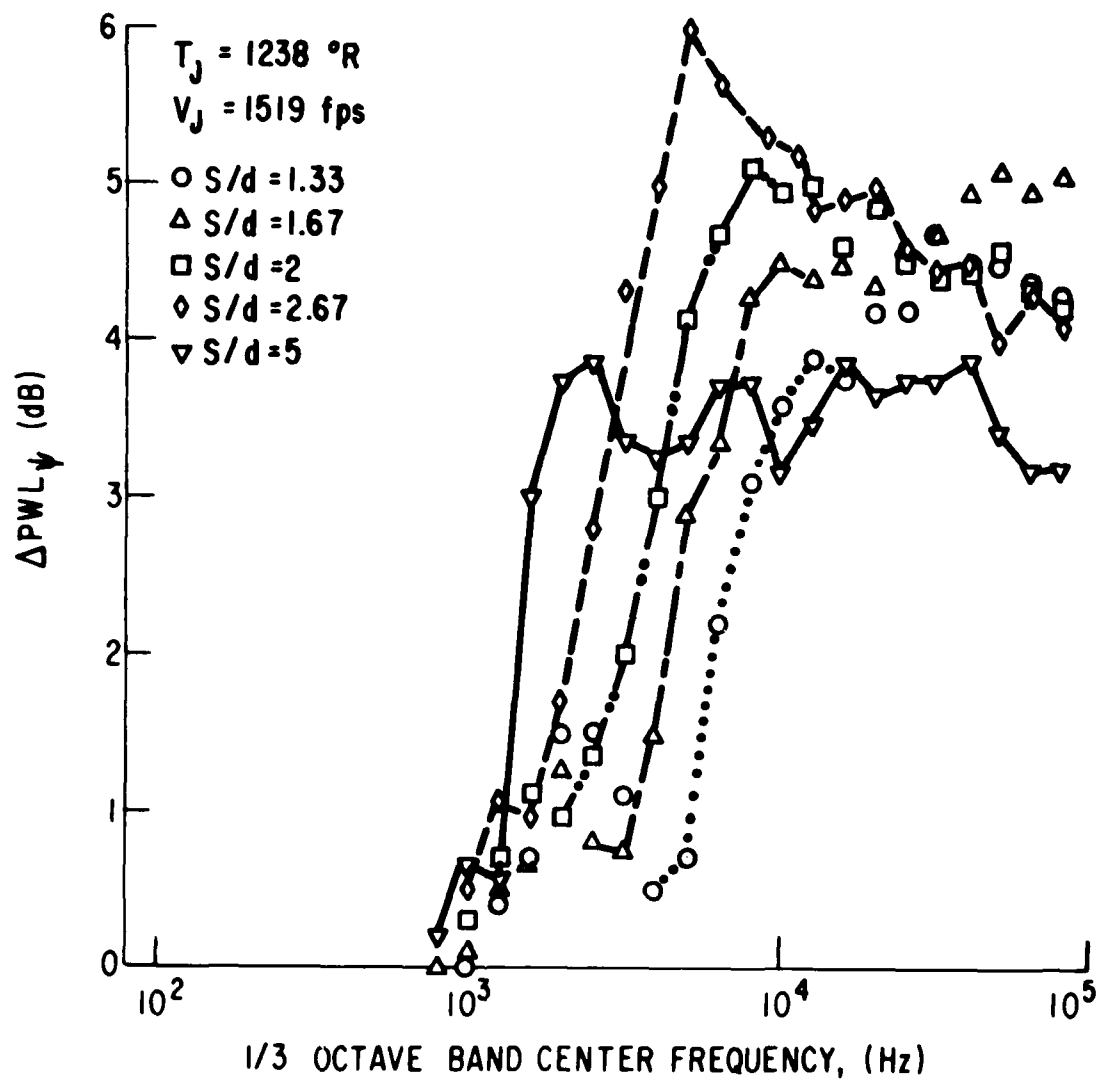


Figure 5-40. Azimuthal Difference Power Spectra, Twin Round for Various Spacings.

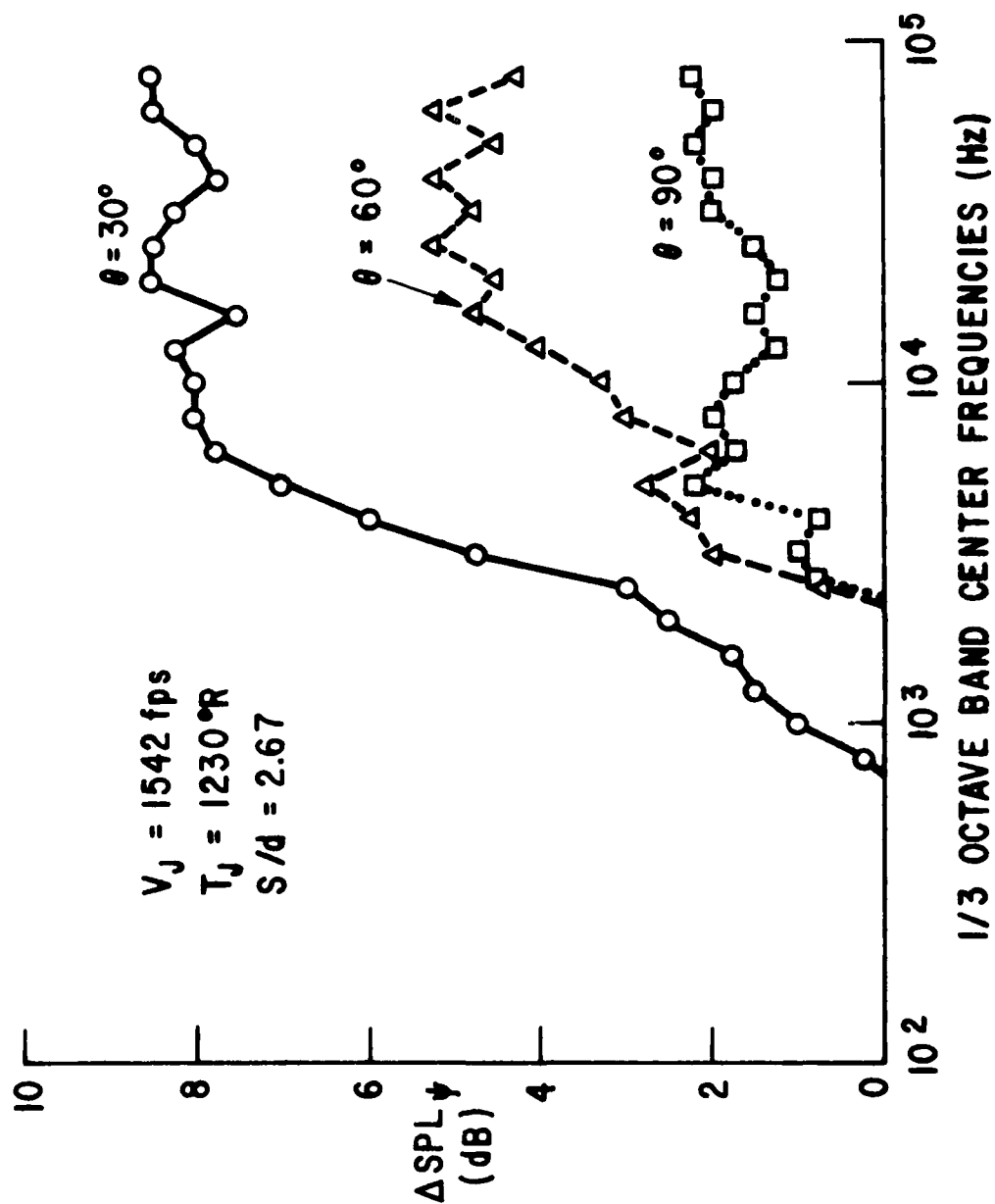


Figure 5-41. Azimuthal Difference Pressure Spectra, Twin-Round.

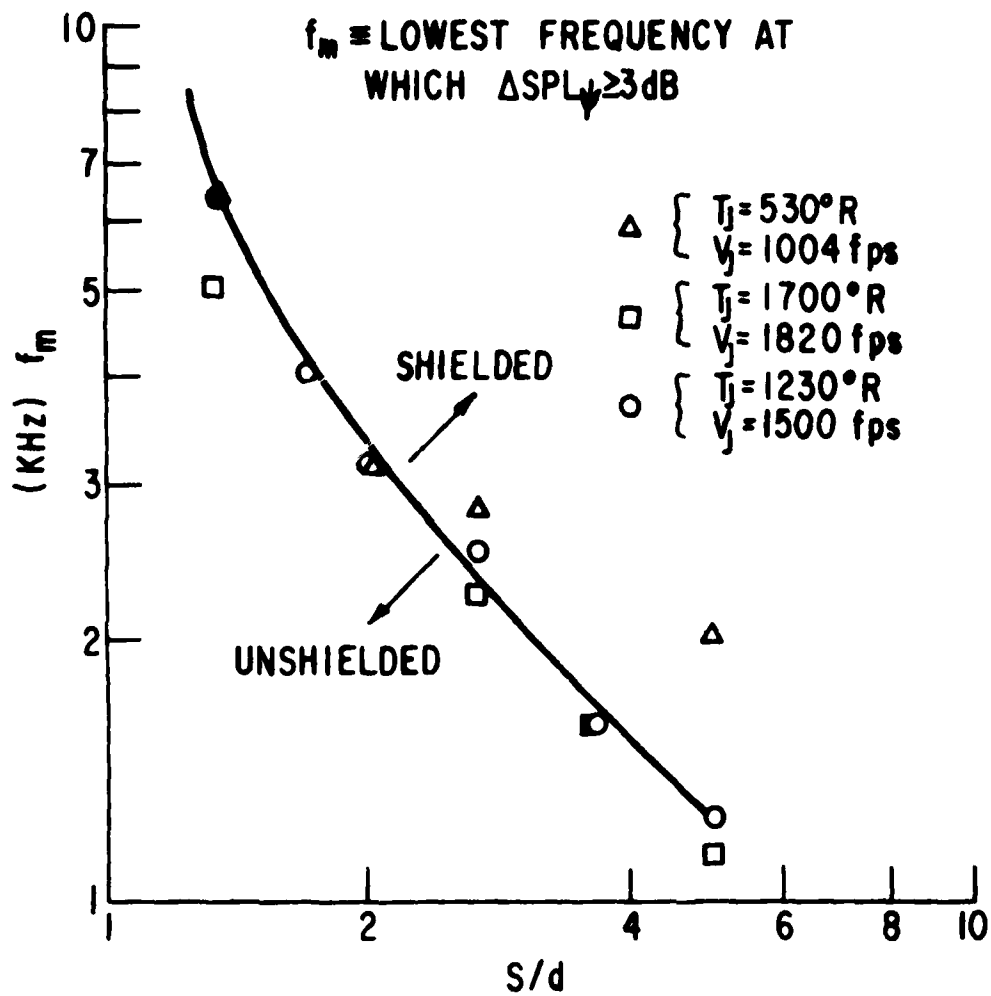


Figure 5-42. Frequency of Onset Shielding, f_m Versus Nozzle Spacing, Twin-Round.

(4-1)

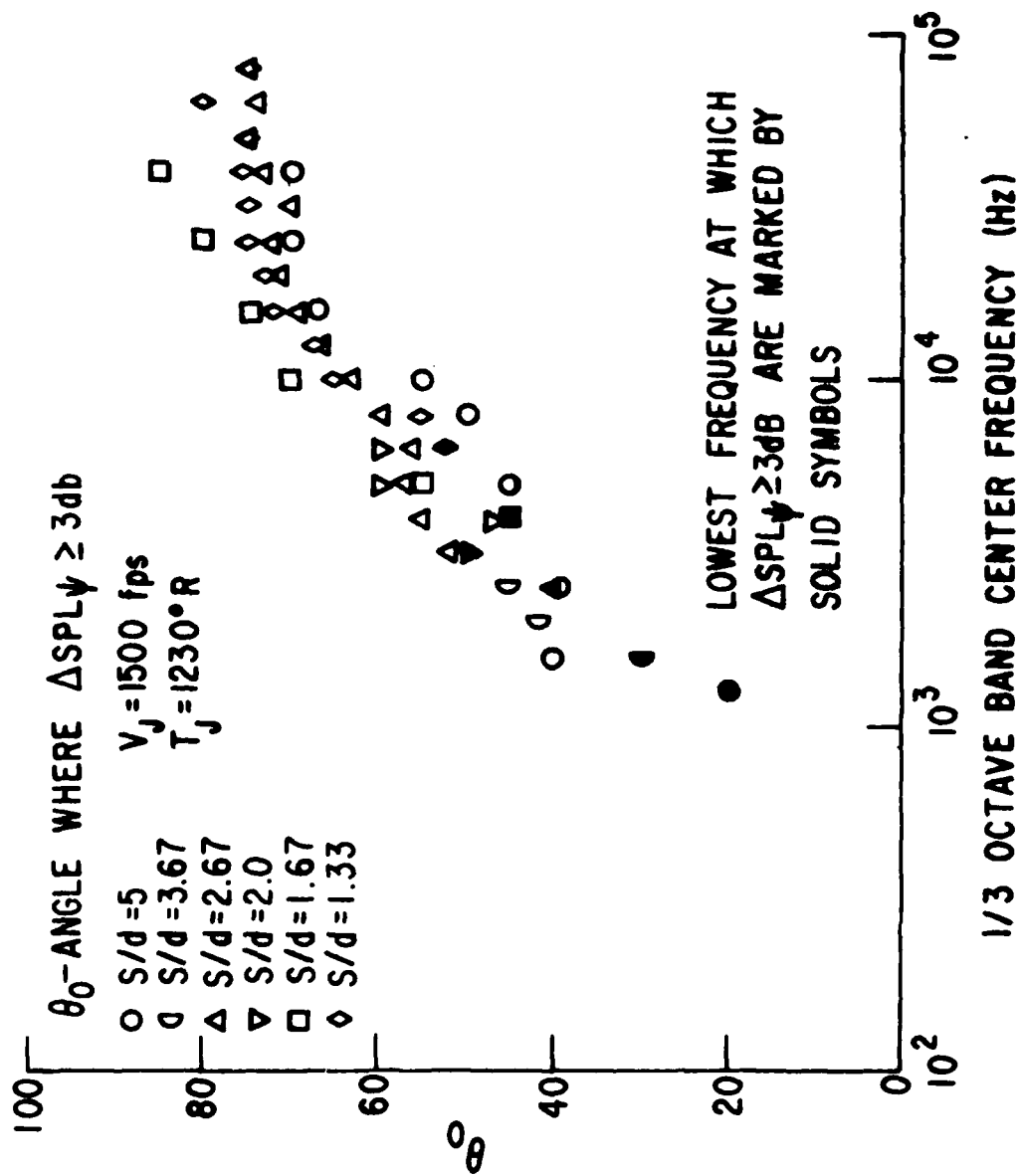


Figure 5-43. Shielded Angles Versus Frequency, Twin-Round.

494

To quantify this effect of spacing on the shielded frequency and angle, a simplified analytical model of the situation has been formulated. A diagram defining the terms and geometry is shown in Figure 5-44.

Several assumptions are necessary to carry out the analysis of this shielding effect. First, the far jet is assumed to be made up of stationary, discrete, single-frequency radiators arranged on the jet axis such that the radiation frequency decreases with distance from the nozzle exit plane. It is possible to use a more realistic model of the jet noise radiation wherein the amplitude of a given frequency is assumed to be a distributed function which is peaked at a given axial location. However, this distributed model would unduly complicate the problem, and for the present purpose is not considered warranted. Second, the near jet will be assumed to be locally parallel and to be of uniform temperature and velocity profile. The jet temperature and velocity will, however, change with axial distance. With these assumptions, an analysis by Yeh⁽¹⁰²⁾ of the acoustic transmission through a layered temperature and velocity field can be applied. Consider the acoustic ray which has been emitted from the far jet and is impinging on the near jet. Figure 5-45 illustrates the problem.

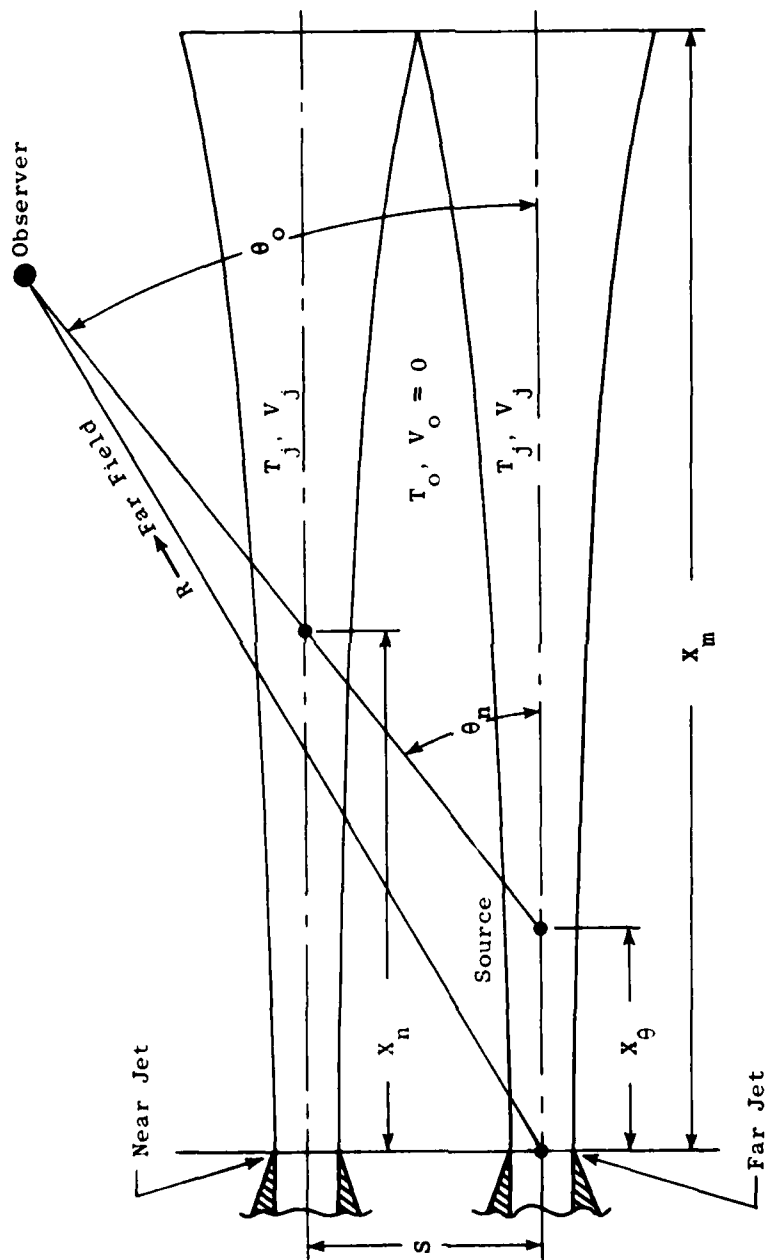


Figure 5-44. Twin-Jet Shielding Definition.

79E

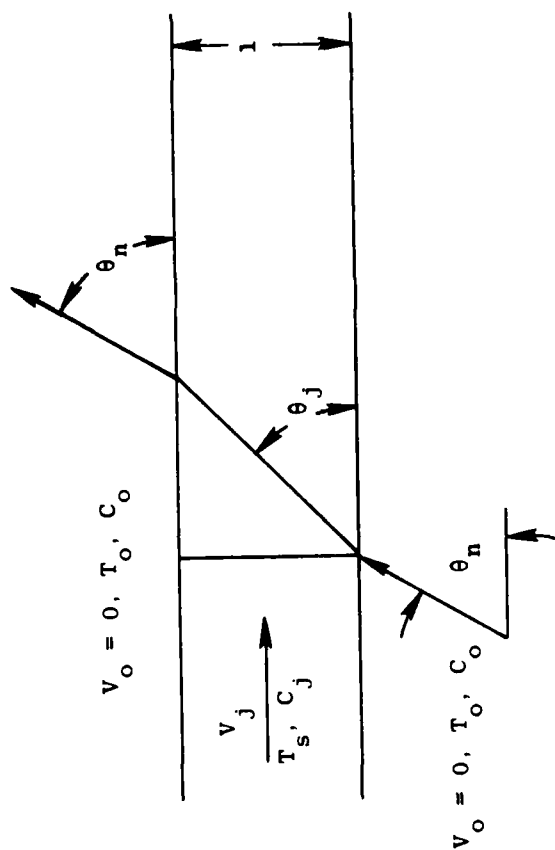


Figure 5-45. Sound Transmission Through a Layered Medium.

447

Yeh's result considered a more complicated case, but for the situation here the amplitude of the transmitted wave $|T|$ can be reduced to;

$$|T| = \cos^2 \psi_1 + \frac{\Gamma_1 + \Gamma_2}{2} \sin^2 \psi_1^{-1/2} \quad (365)$$

where

$$\psi_1 = \frac{2\pi f \ell}{C_J} \sin \theta_J, \quad (366)$$

$$\theta_J = \cos^{-1} \frac{C_J \cos \theta_n}{C_0 - V_J \cos \theta_n} \quad (367)$$

and

$$\Gamma_1 = \Gamma_2^{-1} = \sin^2 \theta_J / \sin^2 \theta_n. \quad (368)$$

This result is identical to an earlier result by Rayleigh(103) with the exception of the V_J term in the expression for θ_J [equation (367)]. Rayleigh solved the problem of acoustic transmission through a thermal discontinuity in a still medium. A more convenient form of relation 1 is,

$$|T| = 1 + \frac{\Gamma_1 + \Gamma_2}{2}^2 - 1 \sin^2 \psi_1^{-1/2}. \quad (369)$$

The inner bracketed term is independent of frequency, and its parameter dependence is

$$\frac{\Gamma_1 + \Gamma_2}{2}^2 - 1 = g(C_J, C_0, V_J \text{ and } \theta_n).$$

The extremes of the variation of $\sin^2 \psi_1$ with ψ_1 are between 0 and 1 with nodal points at $\psi_1 = n\pi$. When $\psi_1 = (n + 1/2)\pi$, $\sin^2 \psi_1 = 1$ and the frequency is such that minimum transmission occurs and $|T|$ is given by,

$$|T| \bigg|_{\psi_1 = \frac{n+1}{2} \pi} = \frac{2}{\Gamma_1 + \Gamma_2}. \quad (370)$$

The value of $|T|$ at maximum transmission is unity so the frequency dependence has the effect of changing the value of $|T|$ from $2/\Gamma_1 + \Gamma_2$ to unity

498

every time the frequency causes ψ_1 to go from $(n+1/2)\pi$ to $n\pi$. Figure 5-46 illustrates the nature of the change in $|T|$ at $\psi_1 = (n + 1/2)\pi$ with incidence angle θ_n . There is practically complete transmission up to the critical angle, θ_c , occurs when the angle θ_J becomes parallel to the jet direction, $\theta_J = 0$. Then

$$C_J \cos \theta_c = C_0 - V_J \cos \theta_c \quad (371)$$

or

$$\cos \theta_c = \frac{C_0}{C_J + V_J} \quad (372)$$

Yeh's results indicate that the transmission properties of the moving nonturbulent layer can be approximated quite well by a step function from unity to zero at the critical angle θ_c . The layer thickness l determines the frequency difference between the nodes and antinodes, and, having only a small effect, can be neglected. The near jet can now be considered as a shield that only allows passage of acoustic rays with an incidence angle θ_n greater than the critical angle, θ_c . The critical angle depends on the local velocity V_J and speed of sound C_J , which are varying with axial distance. Since the transmission properties did not greatly depend on the layer thickness, the values of the centerline velocity and temperature were used to predict the variation of θ_c [equation (372)] with axial distance X_f , as shown on Figure 5-47. The velocities used here were measured by Wang⁽⁹⁸⁾ in a companion investigation, and the centerline temperature difference from ambient was assumed to scale as the square of the centerline velocity.

To demonstrate the utility of this analysis, two features that were exhibited by the data on Figures 5-40 and 5-41 are examined. The first feature, shown on Figure 5-40, is that shielding exhibits a rather sharp "cut-on" with frequency, and this "cut-on" frequency increases as the nozzle spacing decreases. The second feature, shown on Figure 5-41, is that, for a given nozzle spacing, the shielded zone becomes wider as frequency increases. An additional aspect seen in Figure 5-40 is the relative independence from frequency effects exhibited by ΔPWL_ψ above the "cut-on" frequency. This particular effect is expected, but the presence of interaction noise in the $\psi = 90^\circ$ plane is apparently causing ΔPWL_ψ to reach values above 3 dB. The first two observations can be explained if one accepts the premise that the higher frequency sources reside closer to the nozzle exit and, therefore, are subject to more effective shielding by the near jet. To further bring out this latter observation, the observed angle of shielding θ_0 versus frequency shown in Figure 5-43 can be used to calculate the far jet angle of shielding, θ_n , and the intersection point X_n , by assuming an axial location of source frequencies, f . Referring to Figure 5-44, the necessary relations are:

$$\tan \theta_n = \frac{R \sin \theta_0}{R \cos \theta_0 - X_f} \quad (373)$$

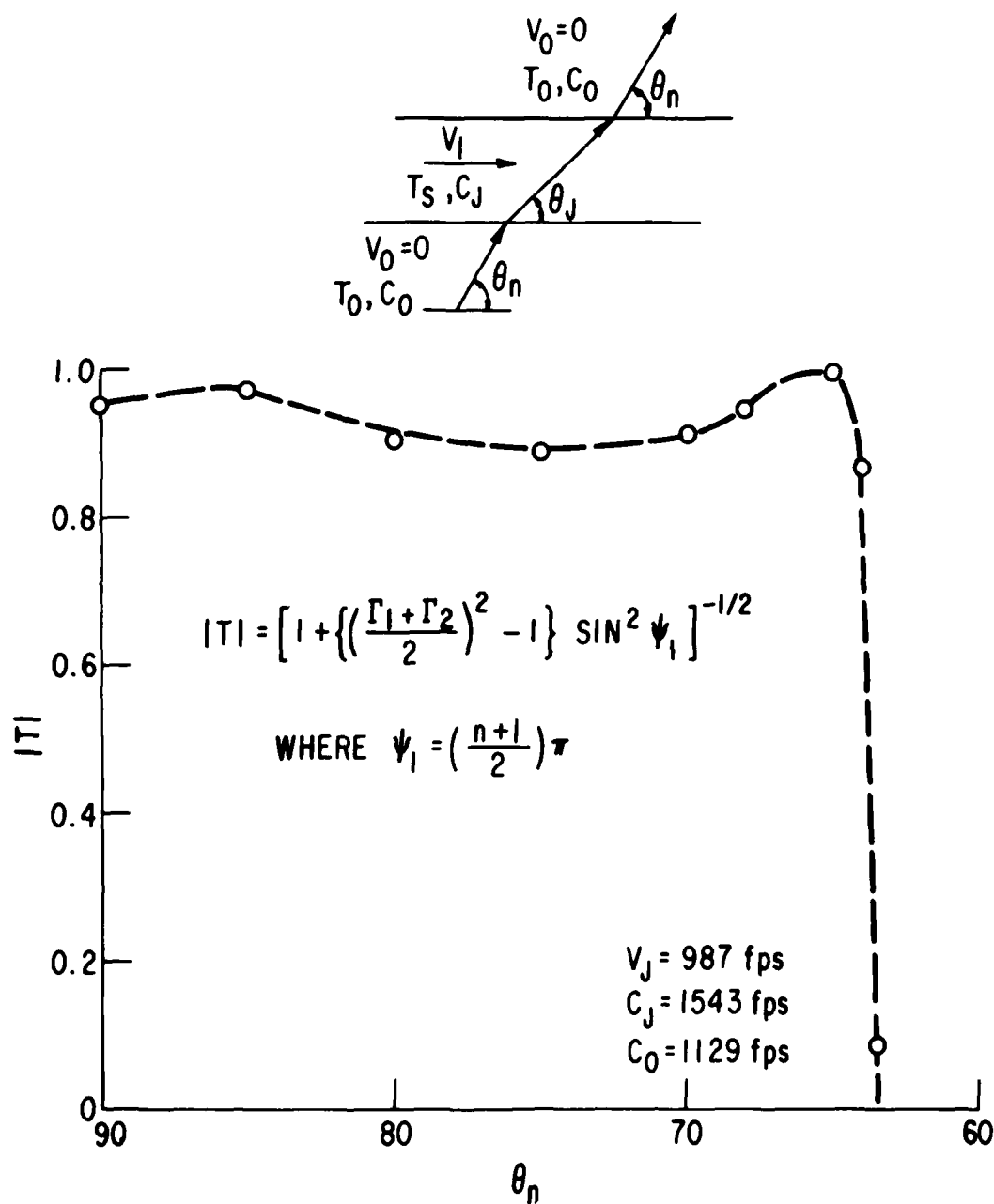


Figure 5-46. Transmission Properties of a Heated High Velocity Layer at Frequencies of Minimum Transmission.

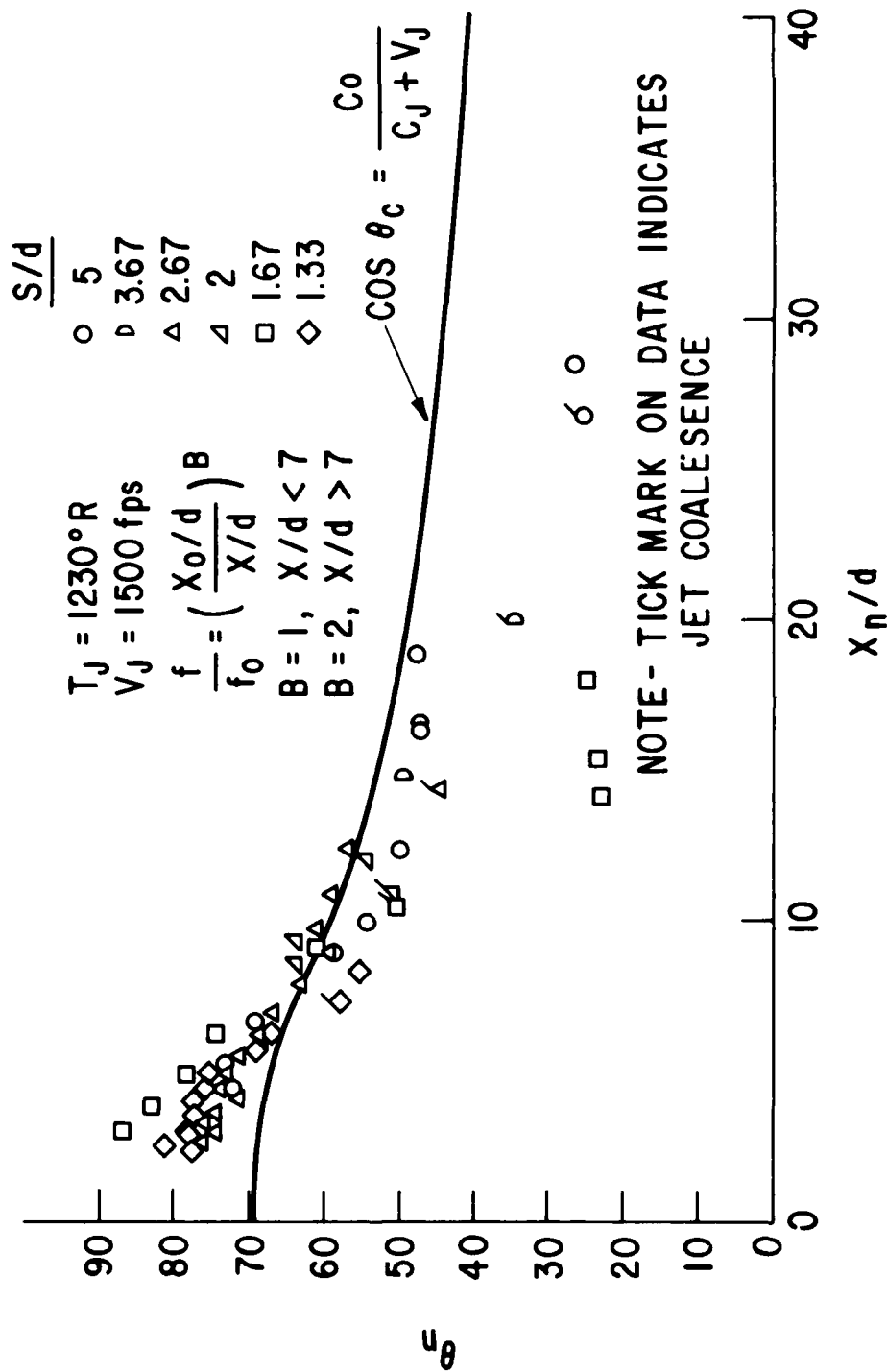


Figure 5-47. Far Jet Shielded Angle, θ_n , Versus Shielding Distance of Near Jet, X_n , Twin-Round.

and

$$\theta_n = \tan^{-1} \frac{s}{X_n - X_f} \quad (374)$$

The source frequencies, f , were assumed to be distributed as,

$$f = f_0 (X_0/X)^\beta$$

with $\beta = 1$ for $x/d < 7$ and $\beta = 2$ for $x/d \geq 7$.

If the location of source frequencies is reasonably accurate, then it would be expected that the data should collapse on a θ_n versus X_n plot, provided that the two jets have not coalesced. Negative departure of the data from the aggregate can be used as an indicator of jet coalescence. As seen on Figure 5-47, the data indeed does collapse rather well and is in reasonable agreement with the critical shielding angle, θ_c , as predicted by equation (372). Complete agreement is not expected, as this analysis did not consider the effects of turbulence on the critical angle. The effect of the turbulence is to cause a statistical variation of the incidence angle between the acoustic wave and the local turbulent eddy. Norum⁽⁹⁷⁾ found that this turbulence effect caused a smoothing of the sharp drop of $|T|$ with incidence angle (as seen on Figure 5-46) such that $|T|$ does not reach unity above θ_c . This explains why the far-field data points on Figure 5-47 are showing shielding effects at angles above those corresponding to the critical incidence angle. Perhaps the most important result of this analysis and comparison is the confirmation of the proposed shielding mechanism from the observation that the points of negative departure from the collapsed data are occurring further downstream with increased separation distance. This trend is exhibited on Figure 5-48 and can be reasonably represented by a linear increase with nozzle separation distance.

5.3.3 Summary

At the beginning of this section, it is stated that the reasons for investigating the noise properties of twin-jets was the capability for separately defining the effects of acoustic shielding and turbulent mixing. In this regard, these experiments have been very successful. It has been found by using a wide range of nozzle spacings that the turbulent mixing effect (both interaction noise generation and mixing suppression) occur for the closely spaced nozzles. While acoustic shielding occurs at all nozzle spacings, it is more significant at the wide nozzle spacings. An important result of this investigation is the establishment of the level of suppression that is possible when an adjacent jet is used as an acoustic shield. These suppression levels are sufficient to cause a nearly complete masking of the jet noise by an adjacent jet interposed between the source and the receiver. The properties of the observed acoustic shielding were also found to follow the trends of the theories of Mani⁽¹⁷⁾ and Balsa⁽³⁵⁾. In particular, for a given spacing, the shielding increased as the observer approached the jet axis, increased with frequency, and was dependent on jet velocity and temperature.

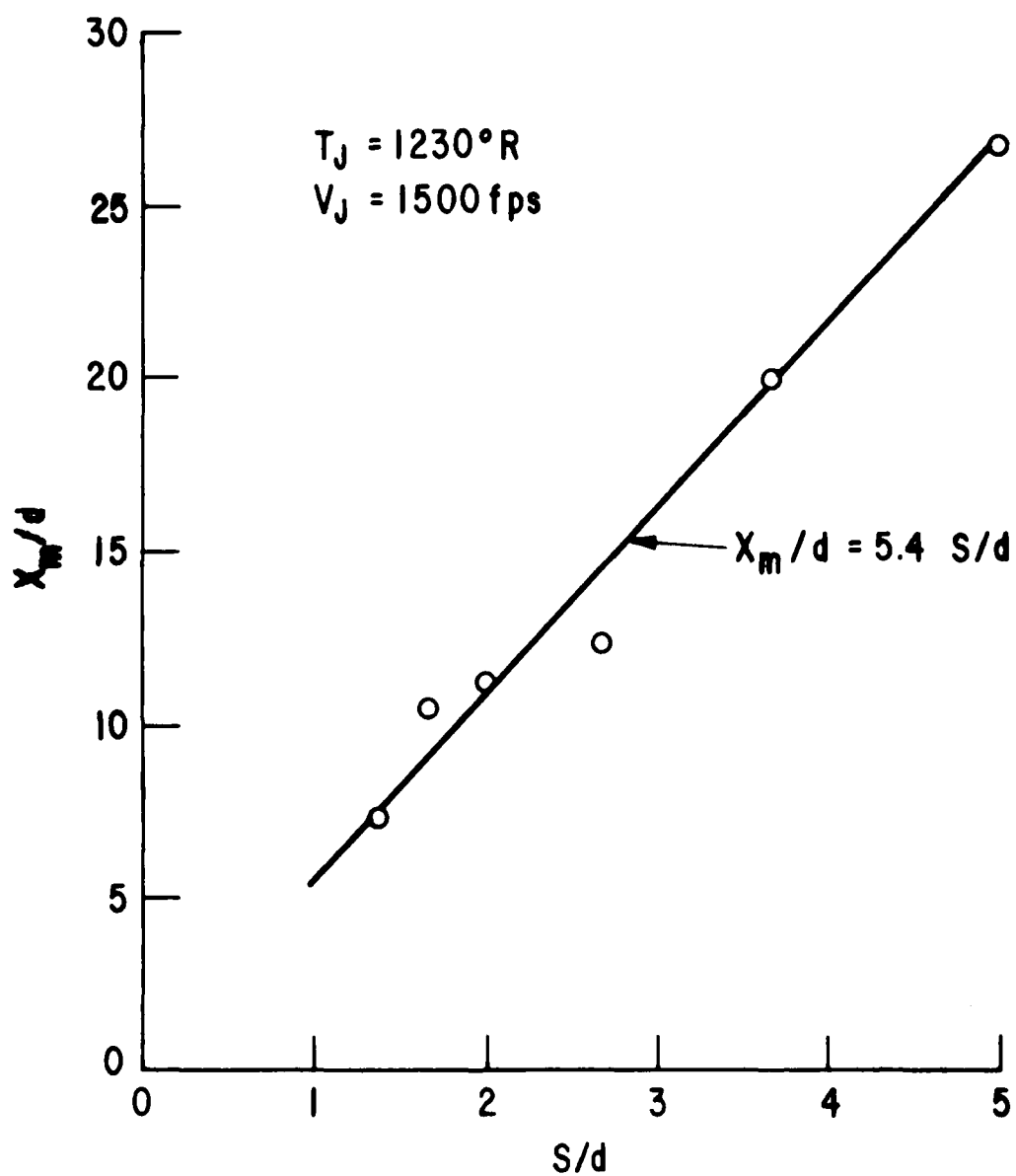


Figure 5-48. Acoustically Merged Distance Versus Twin-Round Nozzle Spacing.

A rather unexpected effect was the strong dependence of the acoustic shielding on the nozzle spacing. Data available at the start of the program gave indications that only small variations of overall power (on the order of 1 to 2 dB) would occur, and these would be concentrated at very low nozzle spacings. While this conclusion is valid at low velocities with unheated flow, it was found, as a result of this program, that very significant differences occur in different azimuthal planes; and additionally, at high temperatures and velocities, the overall power shows significant variations. In a quantitative sense, the measured difference in the total acoustic power, as measured in two orthogonal azimuthal planes, at high velocity and temperature is found to be as high as 4.5 dB. These large azimuthal differences have been found to be due to the layer of cooler, slower moving air that exists between the two jet plumes. Acoustic waves propagating in the plane of the nozzles are forced to traverse velocity and temperature profiles that cause refraction and reflection of the acoustic energy. For close nozzle spacing, this inter-nozzle layer extends only a short distance and therefore only a small shielding effect is seen. As the nozzle spacing is increased, the inter-nozzle layer extends downstream, and the shielding effect increases. This observation is confirmed by estimating the frequency at which the shielding becomes significant, and comparing that frequency to the nozzle spacing. The result shows a definite lowering of the frequency of the onset of shielding with increased nozzle spacing. This would be expected from the proposed mechanism; that is, as the nozzle spacing increases, the inter-nozzle shielding layer extends further downstream and shields the lower-frequency jet noise sources that exist in the downstream portion of the plume.

Two observed aspects of this proposed acoustic shielding mechanism have been confirmed with the aid of a simplified theoretical model. The first feature is that once shielding is achieved it is rather independent of frequency; and second, the angle of the onset of shielding widens for the higher frequencies.

Increasing the jet velocity, at all nozzle spacings except the closest, was found to increase the acoustic shielding for subsonic conditions. However, increases in jet velocity above the critical value cause a slight decrease in shielding, apparently because of the jet supersonic expansion downstream of the nozzle exit plane. Variations in the jet temperature do not produce as significant acoustic effects as do variations in jet velocity.

5.4 TWIN RECTANGULAR JET NOISE

Twin rectangular jet noise experiments were conducted concurrently with the twin round tests described in Section 5.3. Rectangular nozzles with a 6 to 1 aspect ratio and with a flow area equal to that of the round nozzles were used. The hardware, shown in Figure 5-49, allowed both variable spacing and angular orientation. Lip thickness of the nozzles, as seen in Figure 5-49, was reduced to a knife edge part way through the tests with no observable effect on the data. The test methods, range of conditions, and test apparatus were the same as described in Section 5.2.1.

5.4.1 Experimental Results and Discussion

5.4.1.1 Overall Acoustic Power

As in the twin round jet tests discussed in Section 5.3, the principal method of clarifying the roles of turbulent mixing and acoustic shielding in twin rectangular jets is to use variable nozzle spacing in the experiments. At large spacings, the turbulent mixing effects are minimal, and the acoustic shielding effects dominate. Conversely, at close spacings, the turbulent mixing effects are enhanced and, as is explained later, the acoustic shielding is minimized. The twin rectangular jet data is somewhat more complicated to analyze due to the azimuthal asymmetry of the single rectangular nozzle, as described in Section 5.2. In the measurement plane containing the nozzle centerlines ($\psi = 0^\circ$), the acoustic shielding by the adjacent jet will be the greatest, while in the plane perpendicular to the plane containing the nozzle centerlines ($\psi = 90^\circ$), only the self-shielding of the individual nozzles should be evident.

The shielding by the adjacent jet is shown in Figures 5-50 and 5-51, where the quiet plane ($\psi = 0^\circ$) overall acoustic power level, OAPWL, is consistently less (except for very close spacings) than the sum of two independent jets (single jet + 3dB) at $\psi = 0^\circ$.

As the spacing s is increased, the measured OAPWL in the quiet plane decreases until s/t exceeds eight. Above this value, the OAPWL in the quiet plane is rather insensitive to further spacing increases. Some exceptions to this general behavior do occur at the closest spacing where an entrainment-induced flapping mode and/or vortex-shedding mechanism creates a large tone in the quiet plane. This added noise raises the "quiet" plane ($\psi = 0^\circ$) level well above the loud plane, as shown in Figures 5-50 and 5-51.

There are only slight azimuthal differences (seen in Figures 5-50 and 5-51) in the unheated, low-velocity points. By raising the temperature, and hence the velocity, at a constant jet Mach number, these differences become larger, as does the asymmetry of the radiation patterns. This trend supports the acoustic shielding arguments.

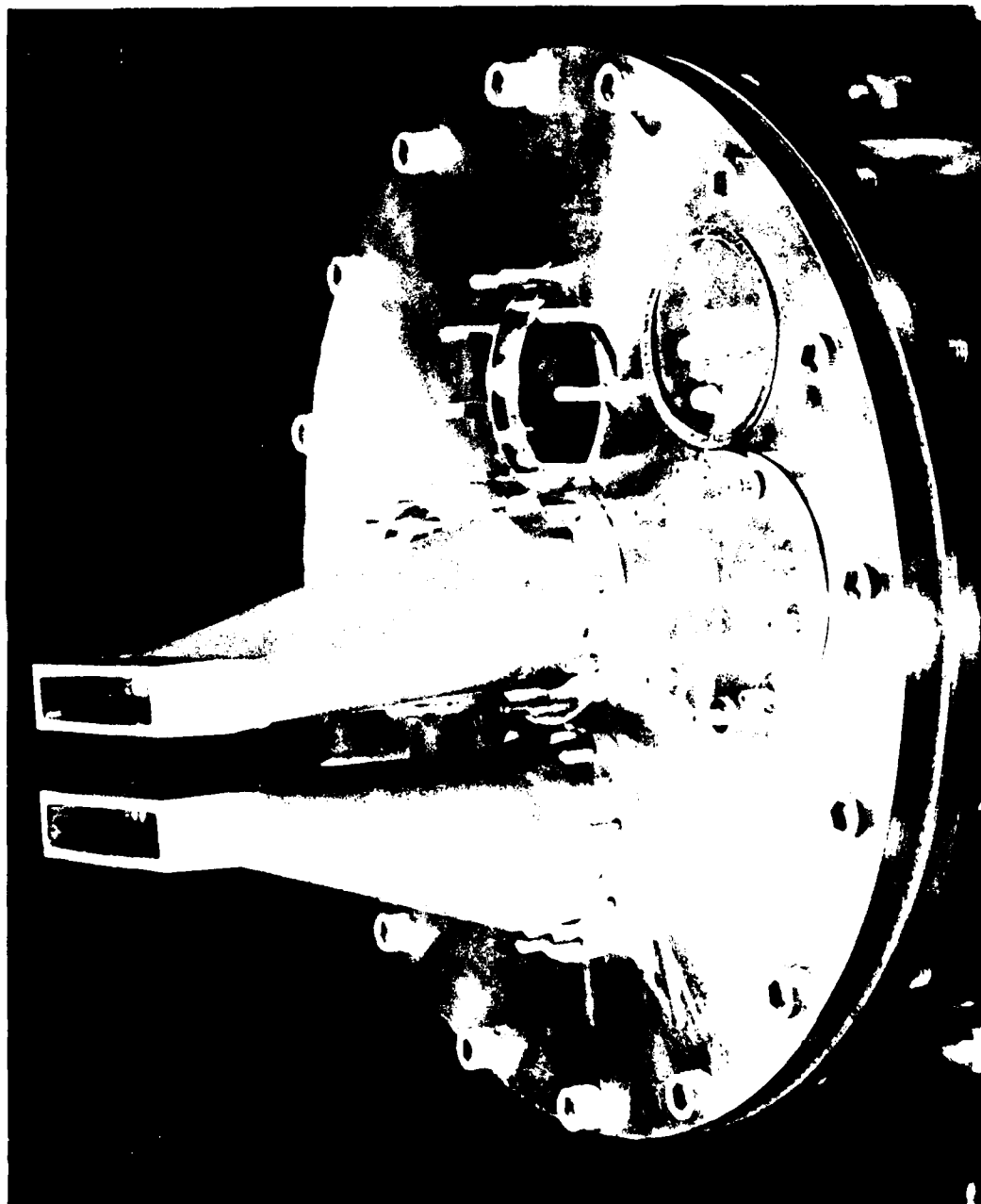


Figure 5-49. Twin Rectangular Jets.

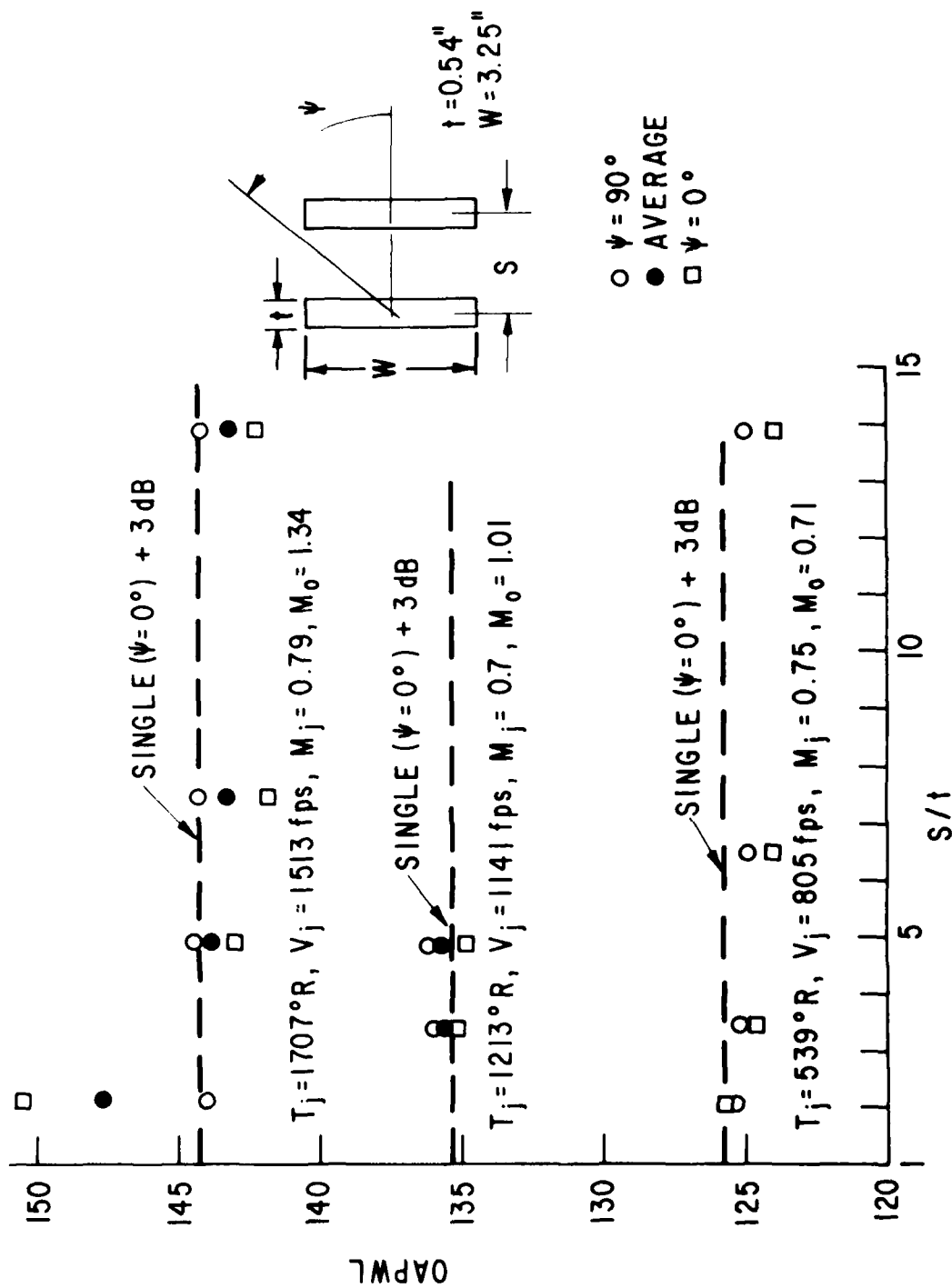


Figure 5-50. Effect of Nozzle Spacing on Acoustic Power of Twin-Rectangular Jets at $M_j < 1$.

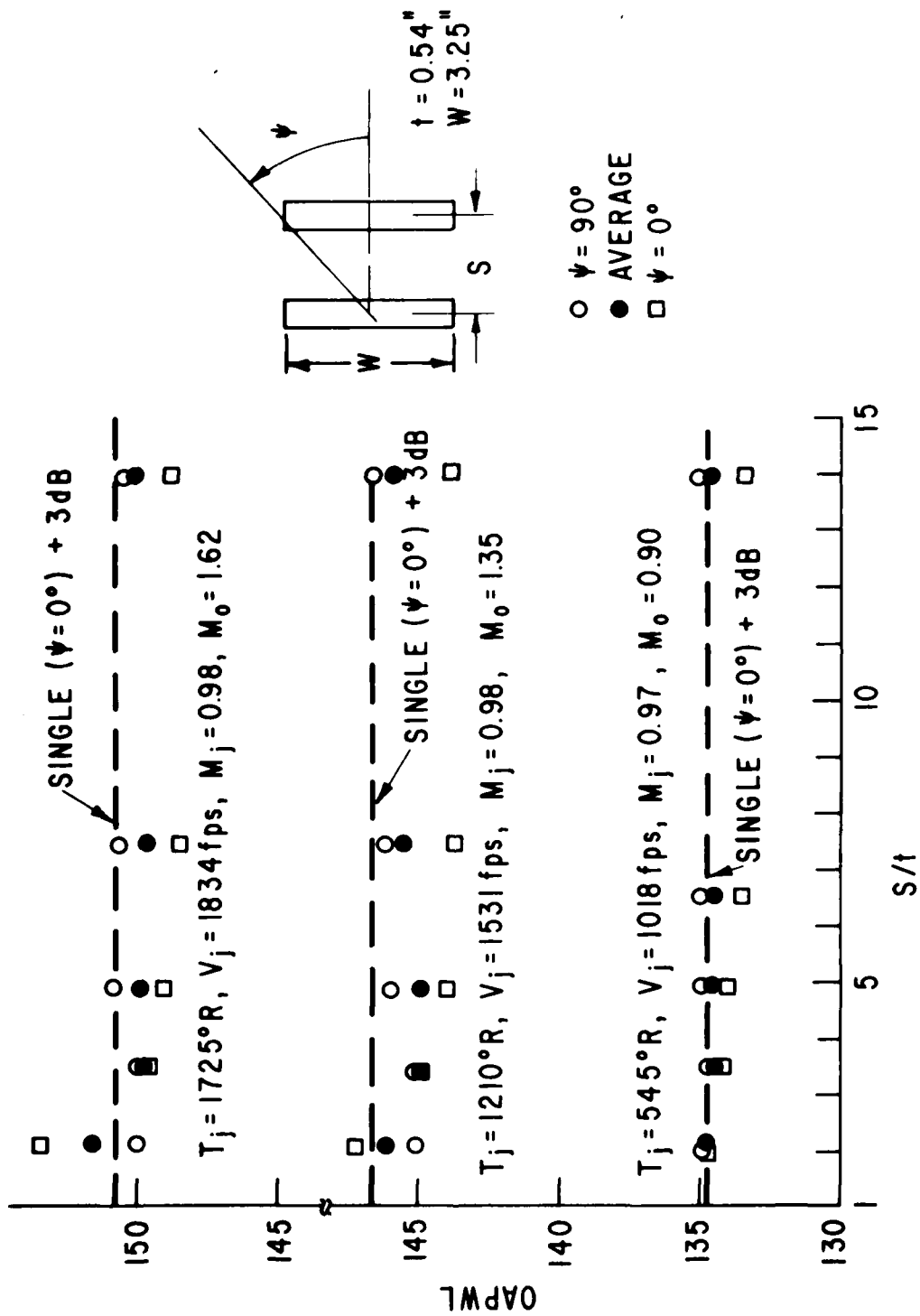


Figure 5-51. Effect of Nozzle Spacing on Acoustic Power of Twin-Rectangular Jets at $M_j \approx 1$.

5.4.1.2 Azimuthal Directivity

The effect of nozzle spacing on the change in OAPWL ψ as measured in different azimuthal planes is shown in Figure 5-52. The effect can be visualized as the near jet casting an "acoustic shadow." At close spacing ($s/t = 4.9$), the shadow is broad; as the spacing is increased, the shadow becomes smaller. Increases in spacing beyond a certain point cause a narrowing of the shadow without any further increase in the OAPWL difference.

5.4.1.3 Polar Directivity

Shielding theory, as described by Mani⁽¹⁷⁾ and Balsa⁽³⁵⁾, predicts an increasing reduction in the sound radiation of embedded sources as the observer approaches the jet axis; this is due to the long propagation path through the jet flow at shallow angles. Likewise, it would be expected that the radiation of nonembedded sources, such as those from an adjacent jet which traverse an adjacent jet, would suffer a similar reduction as the observer approaches the jet axis. Figure 5-53 illustrates this effect clearly, showing an increasing reduction in the twin jet "quiet" plane ($\psi = 0^\circ$) noise relative to the noise of two isolated jets (at $\psi = 0^\circ$), as the jet axis is approached.

The comparison (Figure 5-53) of the single + 3 dB results in the $\psi = 90^\circ$ plane to the twin jet data results in the 90° plane shows that the interaction of the twin jets produces additional noise over most of the emission angles. The asymmetry of the single rectangular jet noise field is also evident in Figure 5-53, as discussed in Section 5.2.

5.4.1.4 Spectral Effects

It is of interest to evaluate which part of the jet noise spectrum is primarily responsible for the asymmetries of the overall measurements just examined. The shielding theories of Mani and Balsa indicate that the shielding effects become pronounced at high frequency. The shielding of the far jet by the near jet can be seen in Figure 5-54. The presence of mixing suppression can be determined by comparing twin jet data with the single + 3 dB data in the $\psi = 90^\circ$ plane. At low frequencies (Figure 5-54), a small amount of mixing suppression can be noted. For nearly identical flow conditions and the same nozzle spacing ($s = 4$ in.), the twin round jet configuration exhibits a larger shielding effect at $\psi = 0^\circ$ (Figure 5-31). Part of this is due to the self-shielding of the rectangular jets which at high frequency counterbalances the adjacent jet shielding effect.

The sound pressure spectra, SPL, for the twin rectangular nozzles at $\theta = 30^\circ$, 60° , and 90° are shown in Figures 5-55a, 5-55b, and 5-55c. The trends are consistent with OASPL and PWL results, with the shallow-angle, high frequency data showing the largest amounts of shielding. This high frequency acoustic shielding is measured by the difference between the single

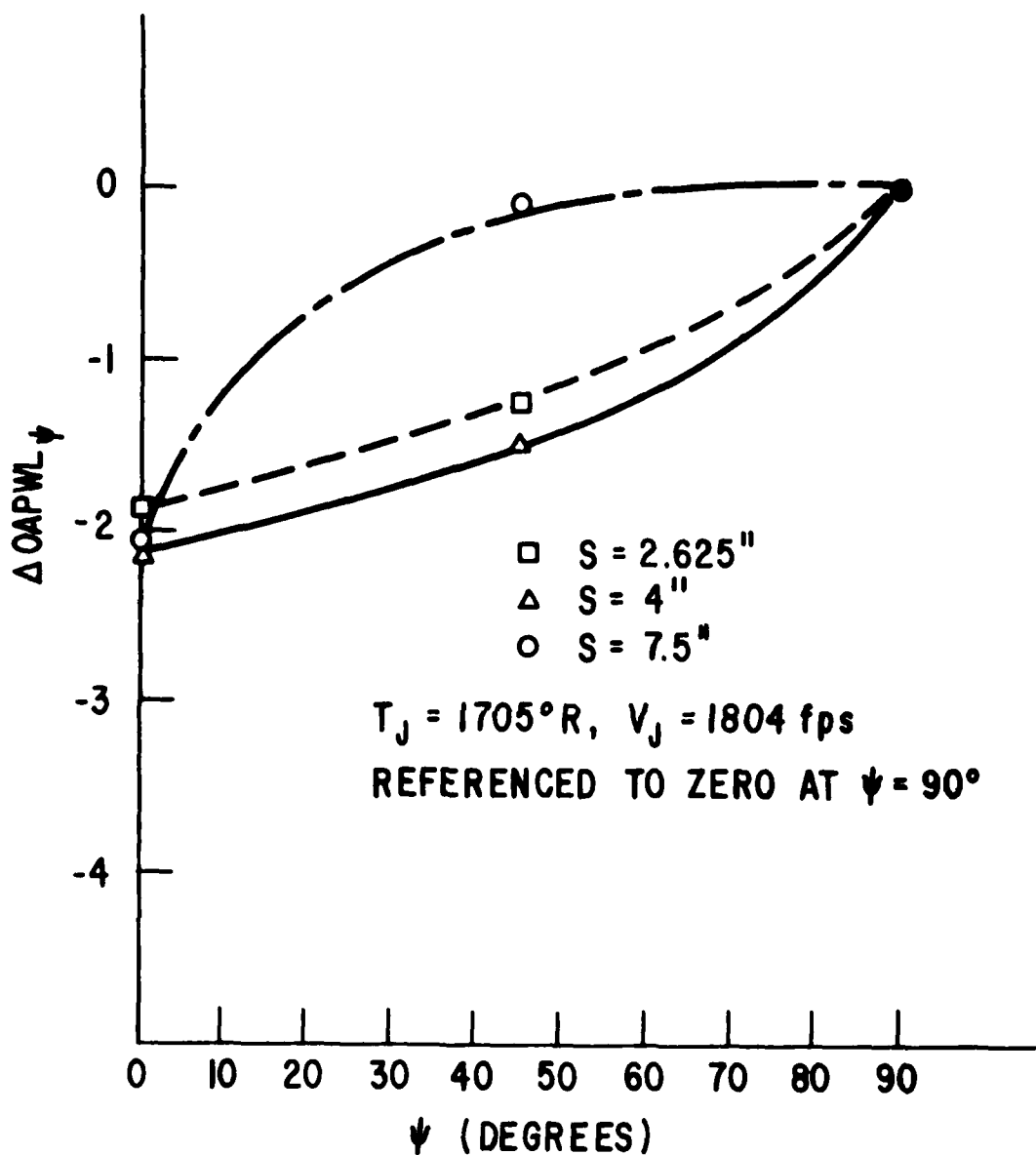


Figure 5-52. Change in Acoustic Power with Azimuthal Angle, Twin-Rectangular Jets.

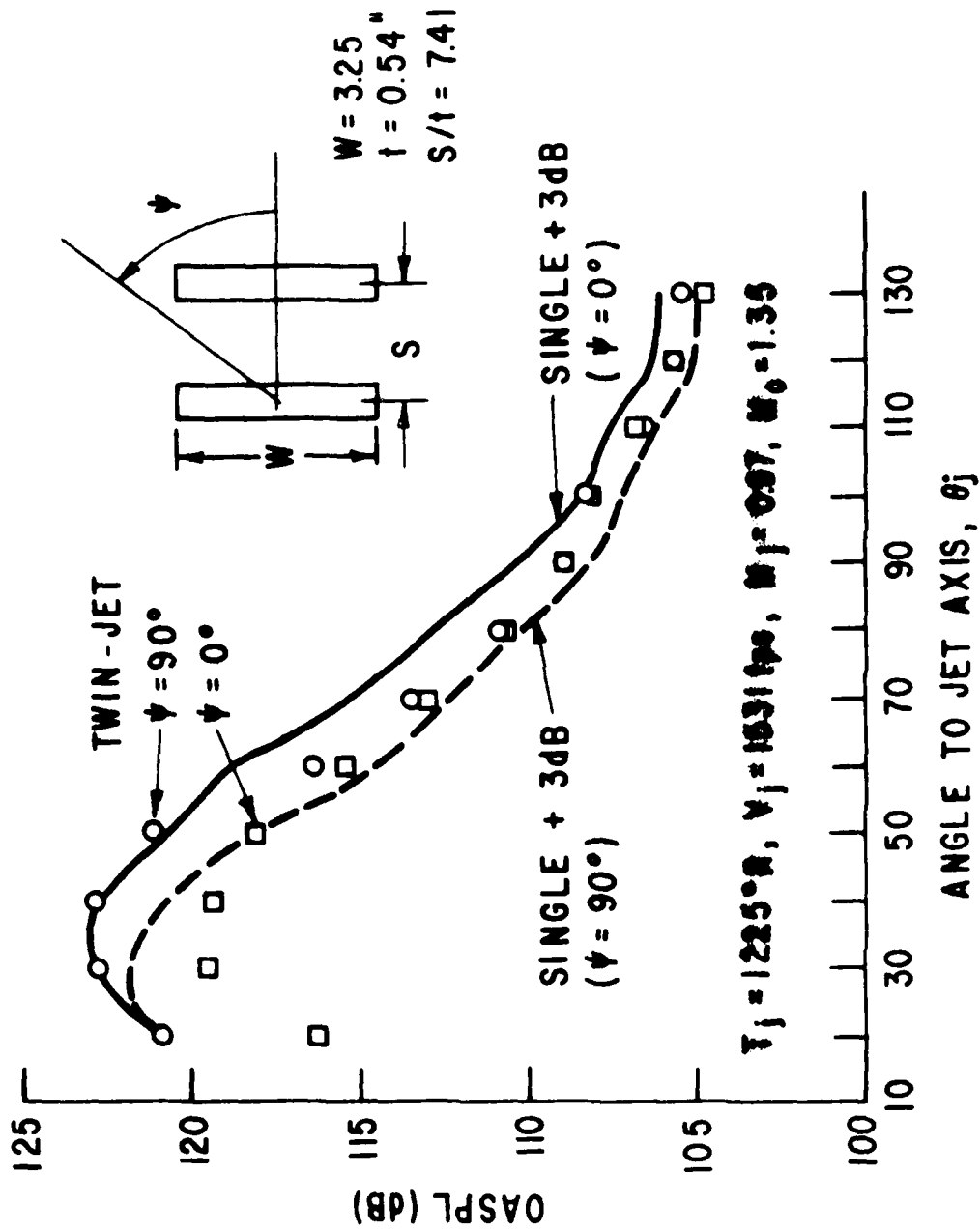


Figure 5-53. Directivity Comparison, Twin-Rectangular Versus Single.

(511)

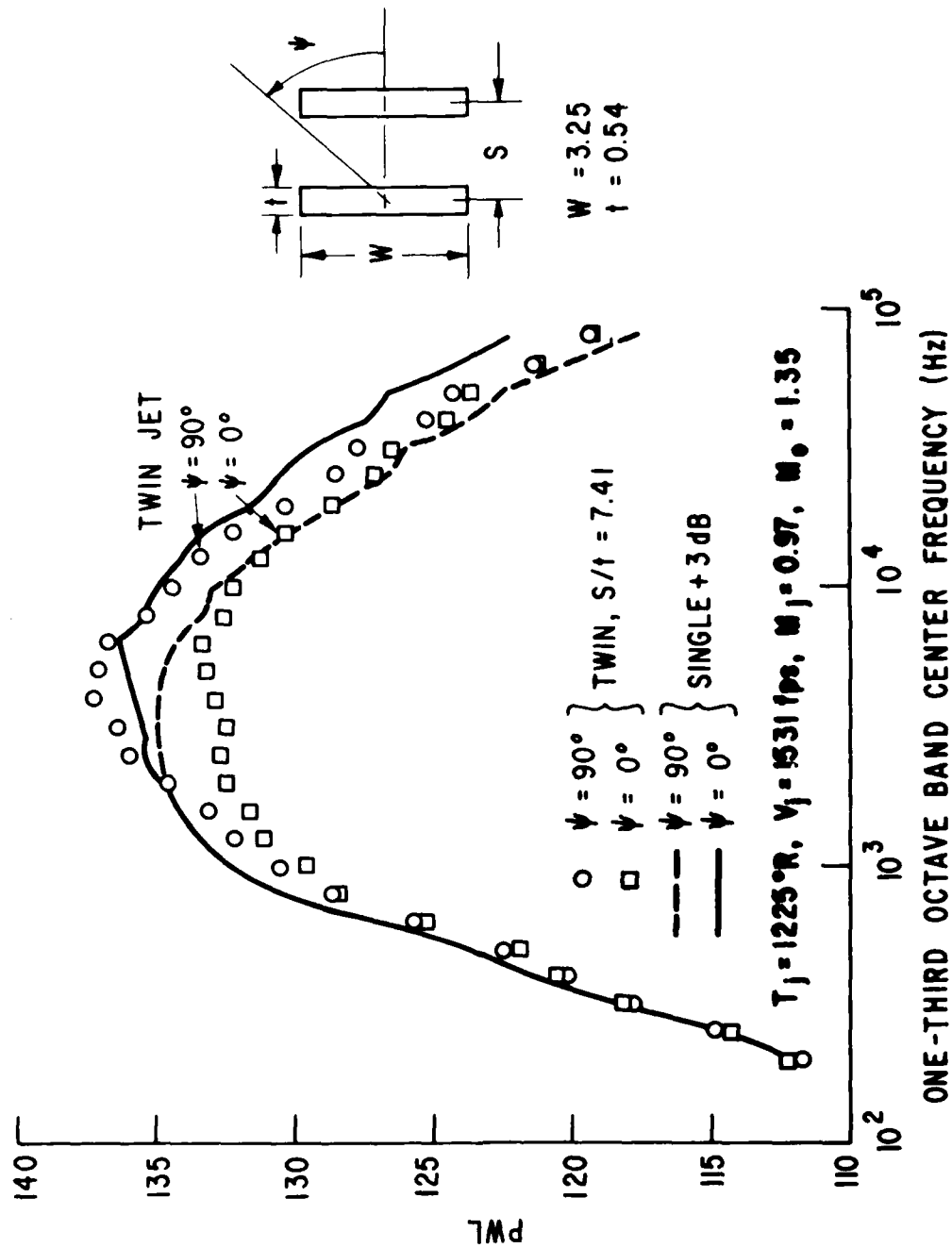


Figure 5-54. Power Spectra Comparison, Twin-Rectangular Versus Single.

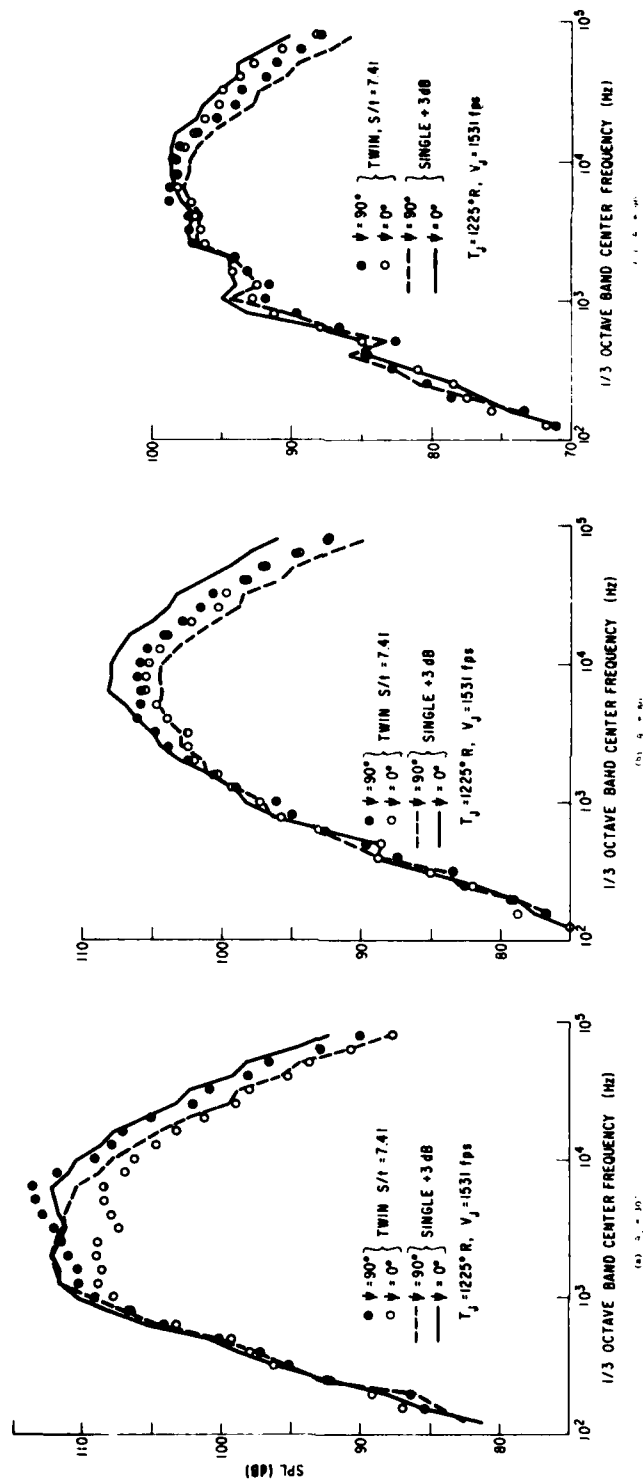


Figure 5-55. SPL Comparison, Twin-Rectangular Versus Single.

(573)

+ 3 dB and twin-jet data at $\psi = 0^\circ$, and is seen to increase as the angle to the jet axis decreases. Both mixing suppression and interaction noise generation appear at $\theta = 30^\circ$, while interaction noise only shows up at $\theta = 60^\circ$ and 90° . Interaction noise occurs when the twin-jet noise level is higher than the single + 3 dB level in the $\psi = 90^\circ$ plane.

5.4.1.5 Velocity and Temperature Effects

5.4.1.5.1 Overall Power

The variation of $\Delta OAPWL_\psi$ for the twin rectangular jets, as seen in Figure 5-56, correlates well with jet nozzle Mach number, M_j , for a variety of jet temperatures. This is unlike the twin round case, where jet velocity provides a better data collapse. For both nozzle spacings, the general trend of the $\Delta OAPWL_\psi$ data (within experimental error) shows a moderate increase with Mach number until M_j exceeds unity, and then shows a rather sharp decrease. This decrease is more pronounced at the closer spacing ($s/t = 4.86$). In general, the level of $\Delta OAPWL_\psi$ for the large spacing ($s/t = 13.89$) is about 0.5 dB higher than the closely spaced jets. Again (as with the twin round jets) the decrease in $\Delta OAPWL_\psi$ above $M_j = 1$ is apparently due to the presence of the underexpanded shock structure immediately downstream of the jet exit planes. The effect of jet temperature is small, and seems to have a significant effect only above the sonic point. This holds only for heated jets, since the unheated data show very little azimuthal effects.

The twin rectangular jet noise data interpretation is complicated by the asymmetry of the single rectangular jet noise (described in Section 5.2). Due to this azimuthal asymmetry, it is necessary to evaluate the difference between the sum of two isolated single rectangular jets at $\psi = 0^\circ$ and the twin rectangular jet at $\psi = 0^\circ$ ($\Delta OAPWL_0$) rather than to find the difference between the loud ($\psi = 90^\circ$) and quiet ($\psi = 0^\circ$) planes of the twin jet, as was done in Figures 5-56a and 5-56b. The parameter $\Delta OAPWL_0$ was determined from data which were taken weeks apart in time, and therefore contain somewhat larger experimental variance than the $\Delta OAPWL_\psi$ data. Due to this unavoidable variance, only limited data are shown in Figure 5-57, (data sets that were not closely matched in temperature and velocity were eliminated). As in the $\Delta OAPWL_\psi$ comparisons, the most consistent feature of this data is the decrease in $\Delta OAPWL_0$ with Mach number when the flow is supercritical ($M_j > 1$). This is also observed on some of the twin round jet data (Section 5.3), particularly at the higher temperatures.

5.4.1.5.2 Power Spectra

An example of the complications resulting from the asymmetry of the single rectangular jet noise field can be seen in Figure 5-54, where twin-rectangular jet noise and the single + 3 dB noise are compared at both $\psi = 0^\circ$ and $\psi = 90^\circ$. At $\psi = 0^\circ$, acoustic shielding is seen to occur over the middle to high frequencies. In order to draw conclusions about the $\psi = 90^\circ$ plane,

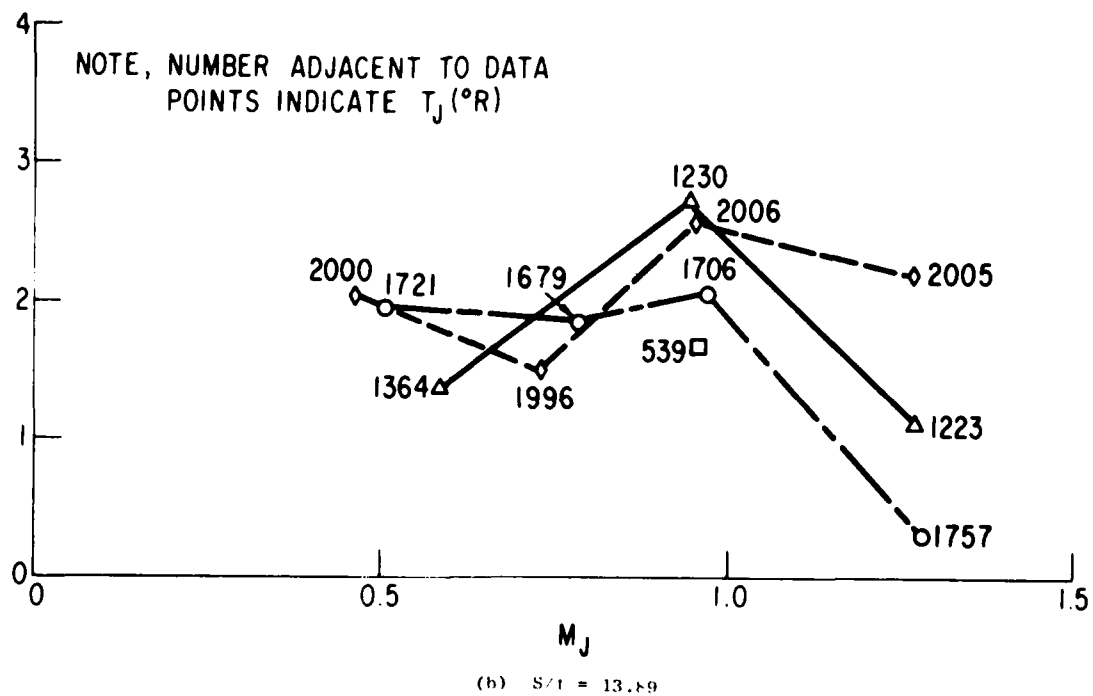
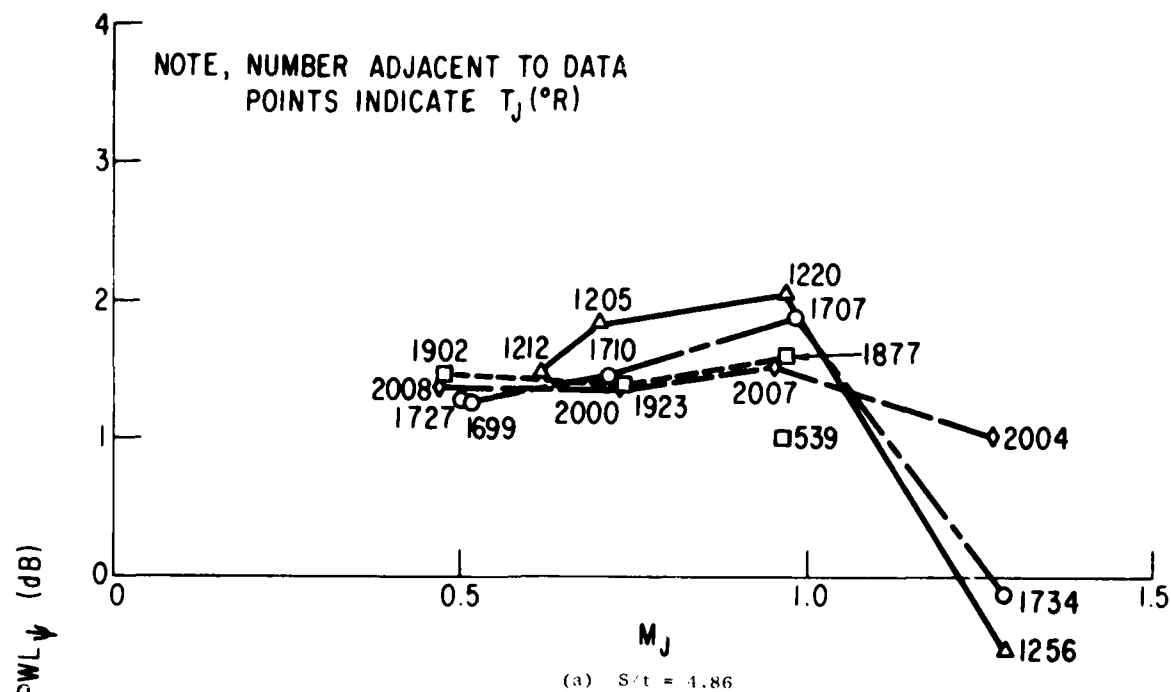
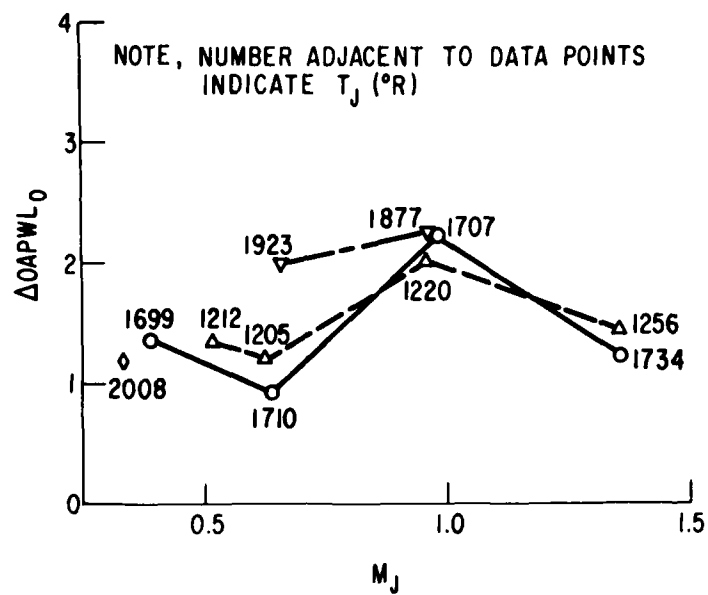
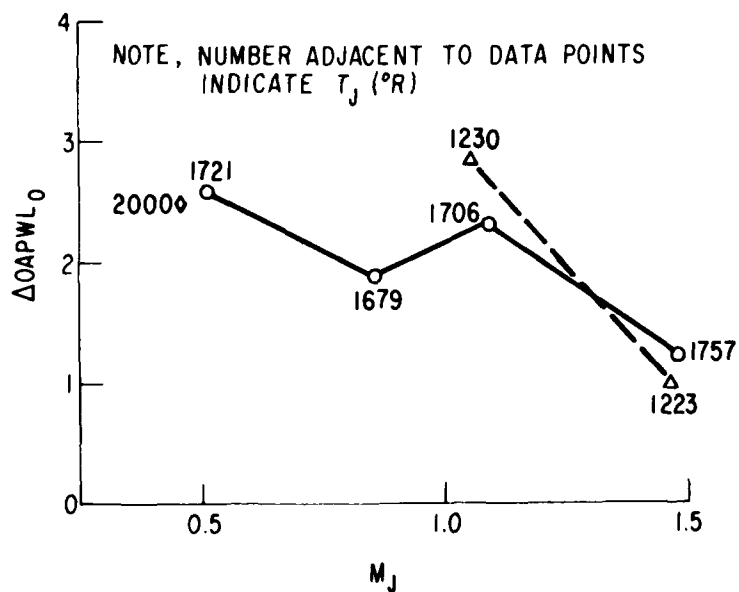


Figure 5-56. Azimuthal Difference Power Level, Twin-Rectangular.



(a) $S/t = 1.86$



(b) $S/t = 13.89$

Figure 5-57. Power Difference at $\Psi = 0^{\circ}$, Single Plus
3 dB Less Twin Rectangular.

the twin rectangular data must be compared to the single rectangular data as measured in the $\psi = 90^\circ$ plane. Since the twin data are below the single data at low frequencies and above at middle and high frequencies, it is concluded that a slight amount of suppression occurs at low frequencies, and a significant amount of interaction noise generation occurs at middle to high frequencies.

The reduction of noise emission in the $\psi = 90^\circ$ plane due to self-shielding causes the noise in the $\psi = 90^\circ$ plane to decrease faster with frequency than in the $\psi = 0^\circ$ plane. In some cases (at low velocity and high temperature) the $\psi = 90^\circ$ twin rectangular jet noise crosses over and is lower than the $\psi = 0^\circ$ data at high frequencies. This cross-over can be seen in Figure 5-58. The cross-over generally occurs at lower frequencies, at least at the larger spacing, as shown in Figures 5-59 through 5-61. A shift of the ΔPWL_ψ spectrum to lower frequencies with increased spacing is evident throughout the range of velocities and temperatures investigated; an example of which is shown in Figure 5-62.

At low frequencies (below the frequency of peak intensity) the azimuthal asymmetry of the single rectangular jet noise is sufficiently small that data taken in the $\psi = 0^\circ$ plane can be used to determine the mixing suppression of the twin rectangular jets seen in the $\psi = 90^\circ$ plane. Using this approximation, significant amounts of low frequency suppression are observed at the smaller spacing ($s/t = 4.86$) as velocity is increased (Figures 5-59, 5-60a, and 5-61a). This suppression is not found with the larger spacing ($s/t = 13.9$), as would be expected (see Figures 5-60b and 5-61b). For this large spacing, a low- to middle-frequency interaction noise peak appears at high temperatures and velocities. This emergence of the interaction noise peak then causes a double peak in the $\psi = 90^\circ$ data for the large spacing (Figures 5-60b and 5-61b). The higher frequency peak is coincident with peaks seen in the $\psi = 0^\circ$ measurements of both the twin and single rectangular jets. The lower frequency peak (dominant at the lower velocities), maintains its spectral location over a wide range of velocities and pressures (see Figures 5-58b, 5-60b, and 5-61b). This low frequency peak may be due to the coalescence of the two jets at lower velocity levels for the large spacing. This low-frequency peak also shows up at an intermediate spacing, $s/t = 7.4$ (Figure 5-55a), but only at shallow angles to the jet axis.

5.4.1.6 Nozzle Separation and Shielded Frequency

Due to the asymmetry of the single rectangular jet noise radiation patterns (Section 5.2), it is difficult to carry out the type of data analysis conducted for the twin round nozzle jet noise. The twin rectangular jet noise data does, however, exhibit similar trends, as shown in Figure 5-62. The difference power spectra again exhibits a trend toward lower frequency emergence with increasing separation distance. For this comparison to be exact, the twin-jet data in the quiet plane $\psi = 0^\circ$ must be compared to the single-jet data in the quiet plane. This difference spectrum, ΔPWL_0 , however, compares data taken days to weeks apart, and therefore has much more scatter than the ΔPWL_ψ data taken only minutes apart. This increased scatter can be

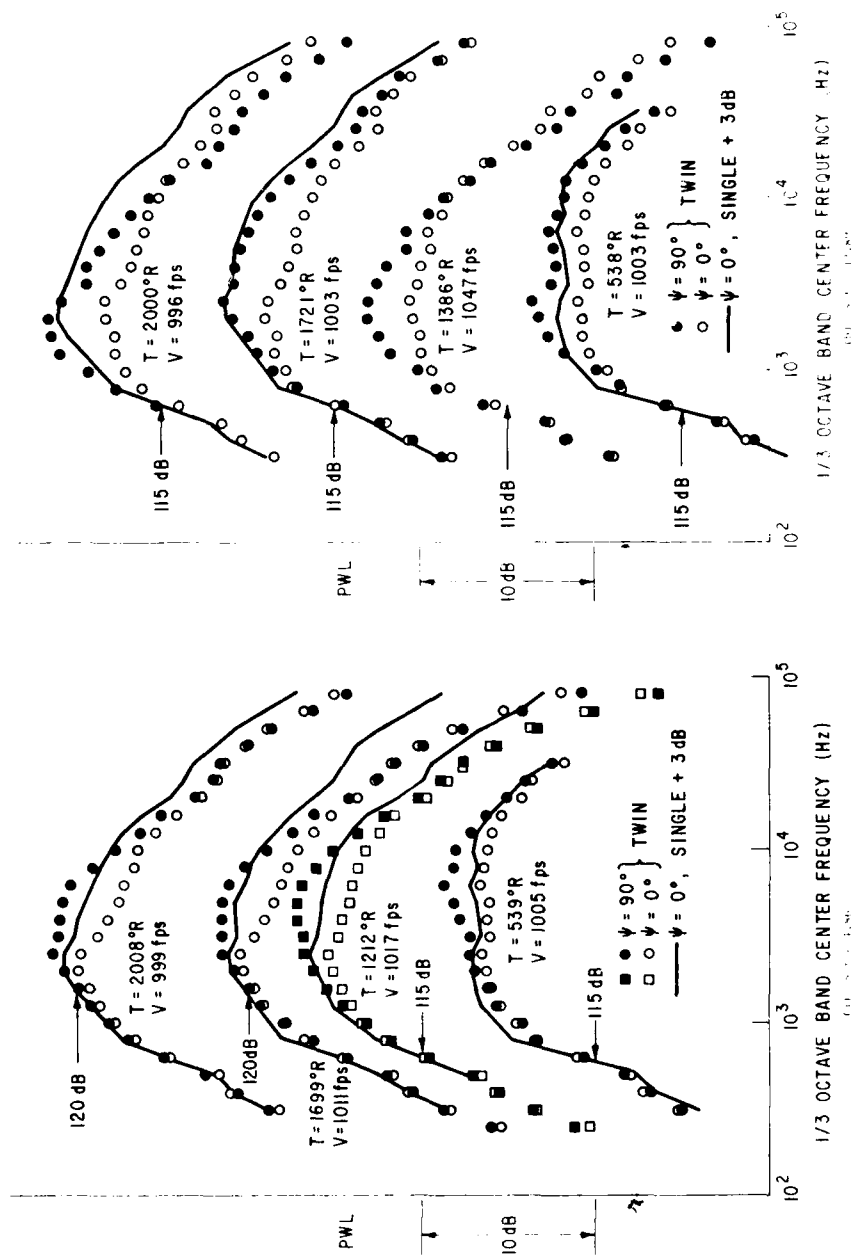


Figure 5-58. Twin Rectangular Power Spectra, $V_j \approx 1000$ fps.

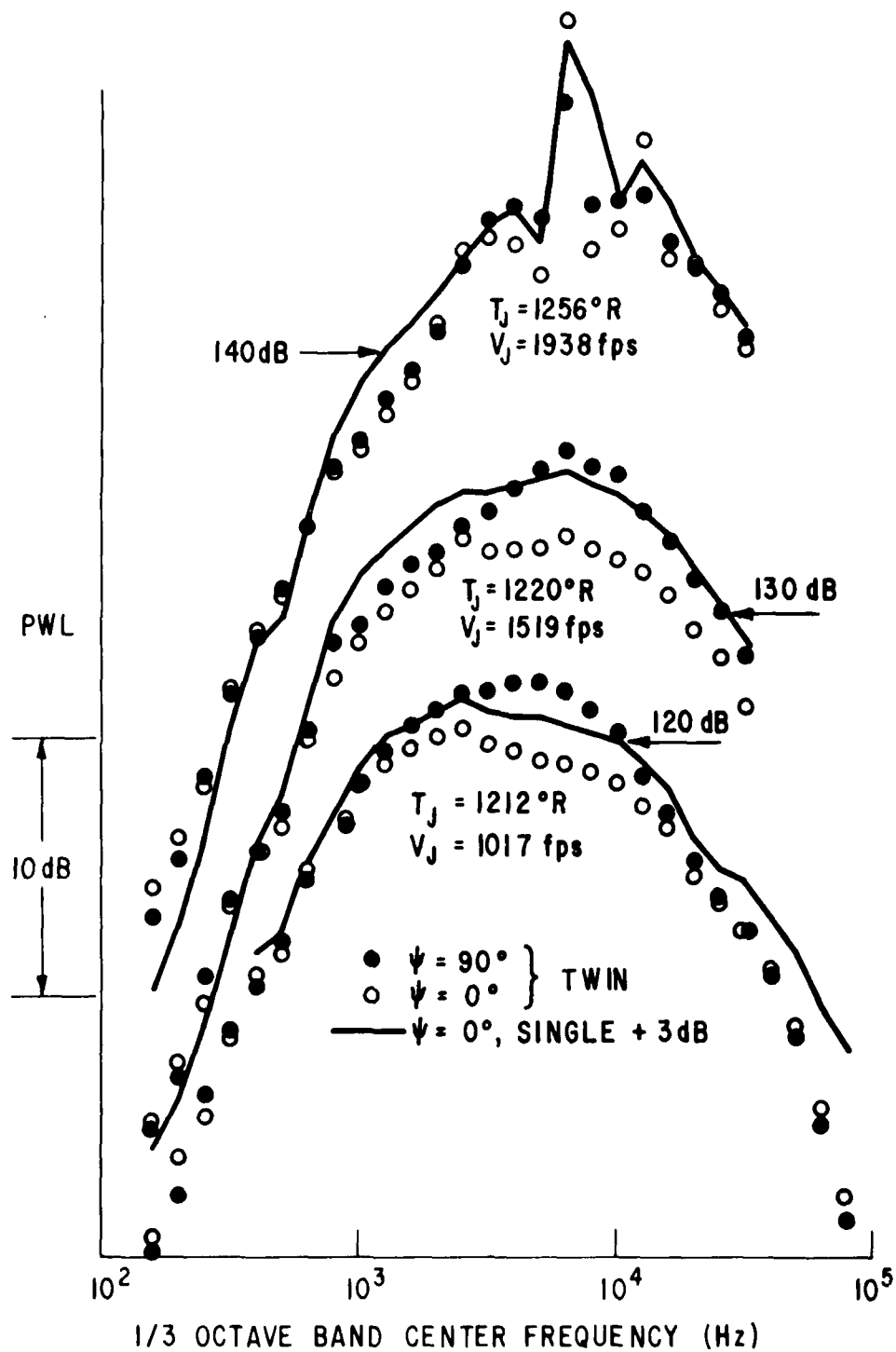


Figure 5-59. Twin Rectangular Power Spectra, $T_j \approx 1200^\circ R$, $S/t = 4.86$.

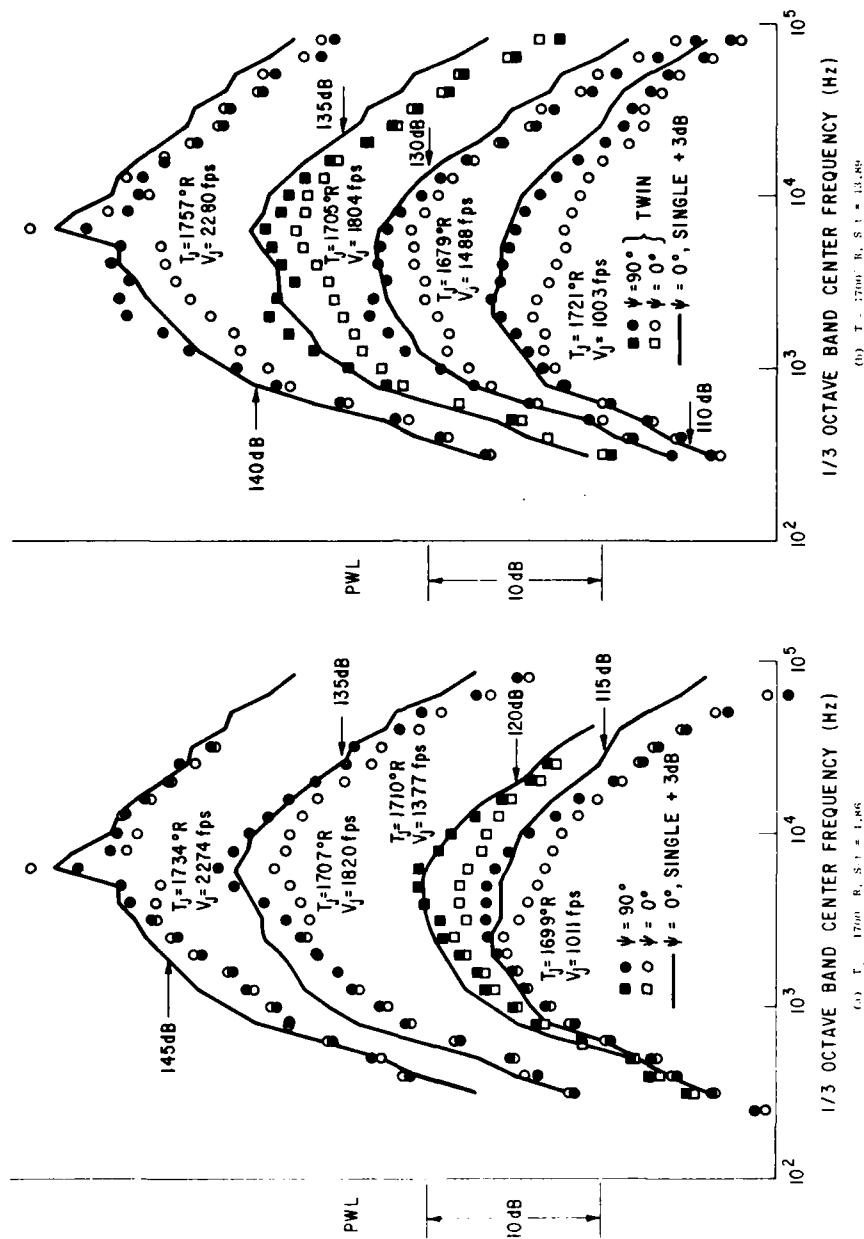


Figure 5-60. Twin Rectangular Power Spectra.

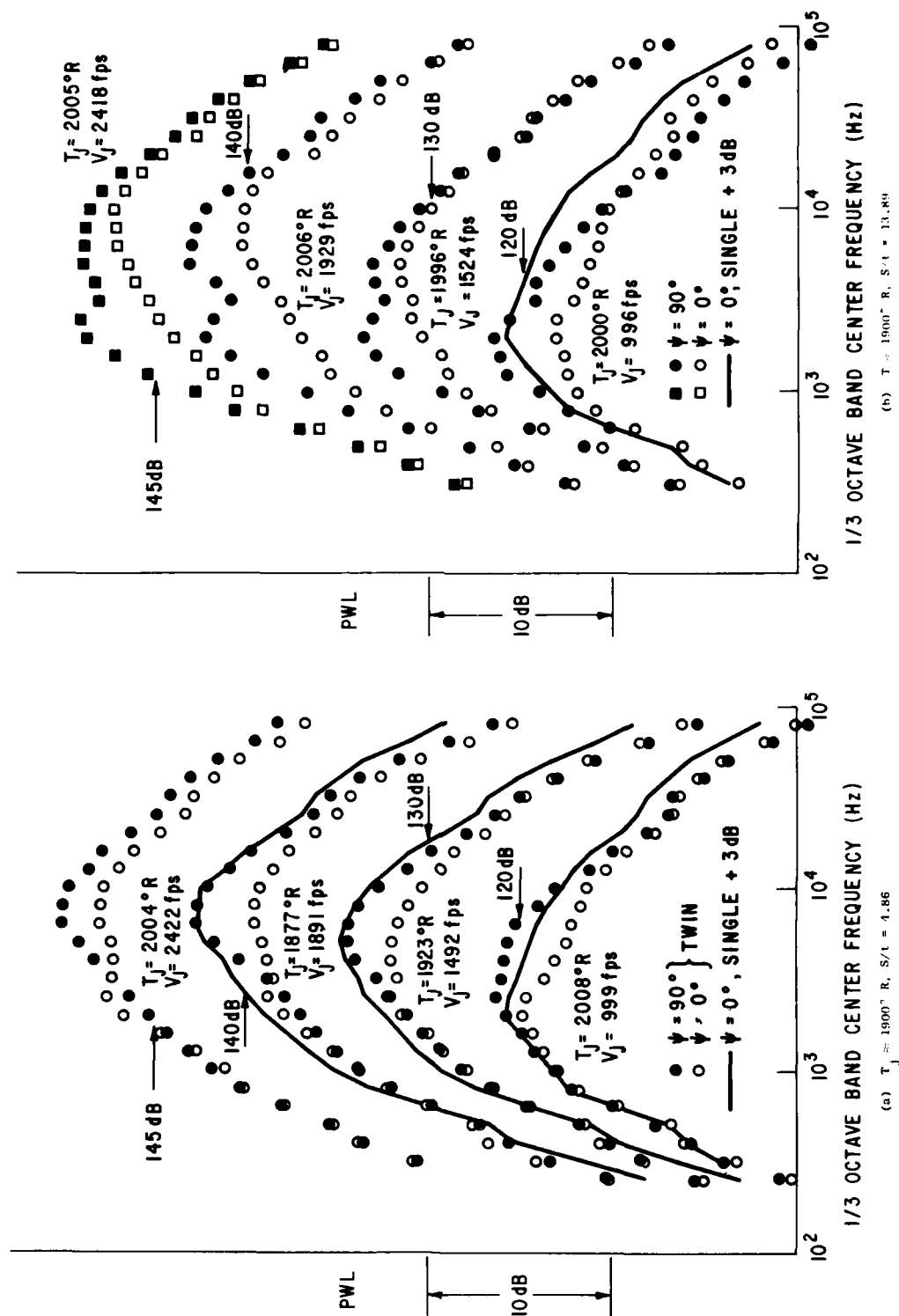


Figure 5-61. Twin-Rectangular Power Spectra.

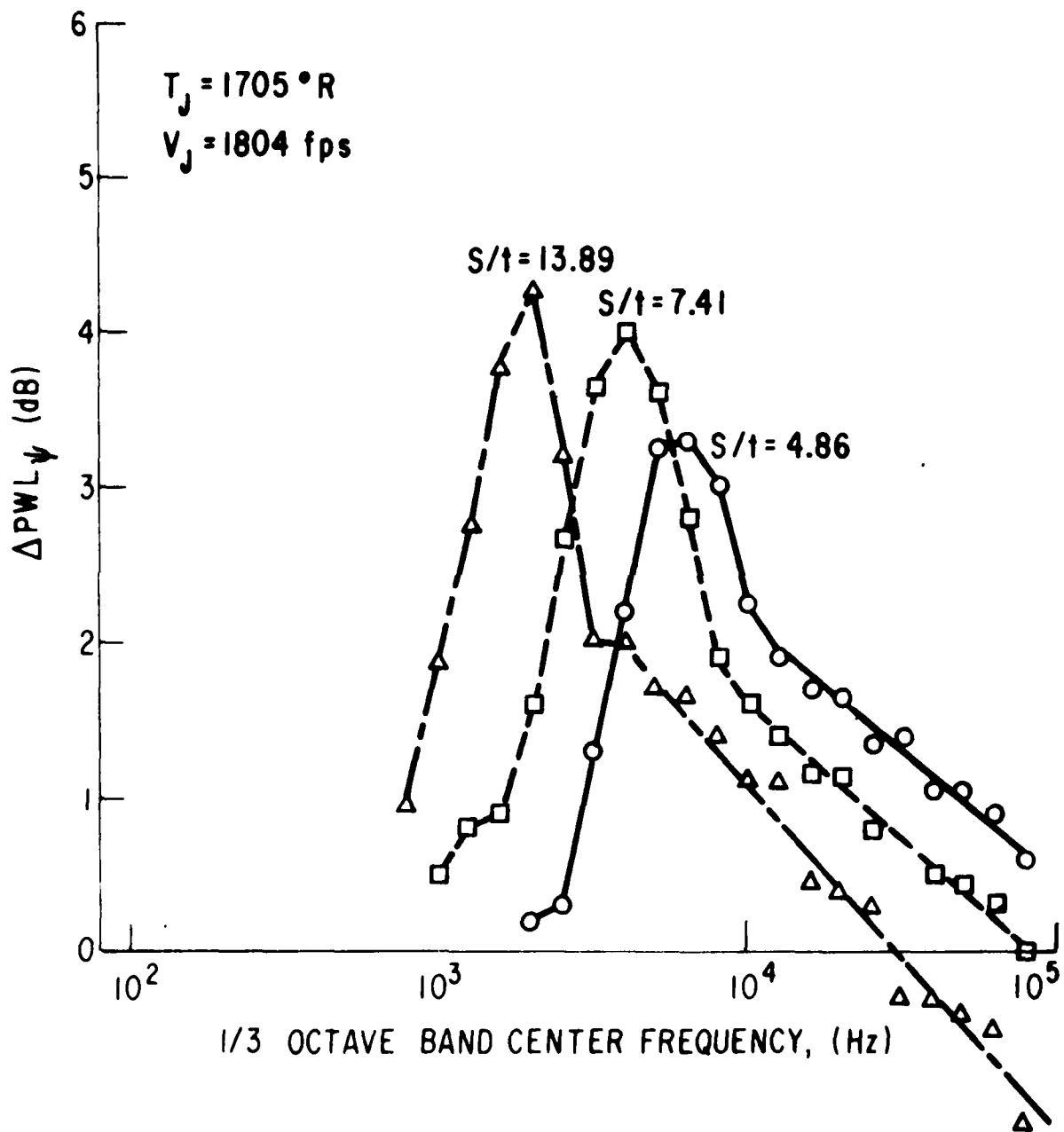


Figure 5-62. Azimuthal Difference Power Spectra, Twin Rectangular for Various Spacings.

(52)

seen on the ΔSPL_0 comparison shown in Figure 5-63. At high frequencies, the data trends exhibited by the twin rectangular jet in Figure 5-63 are in good agreement with those of the twin round jet data in Figure 5-41.

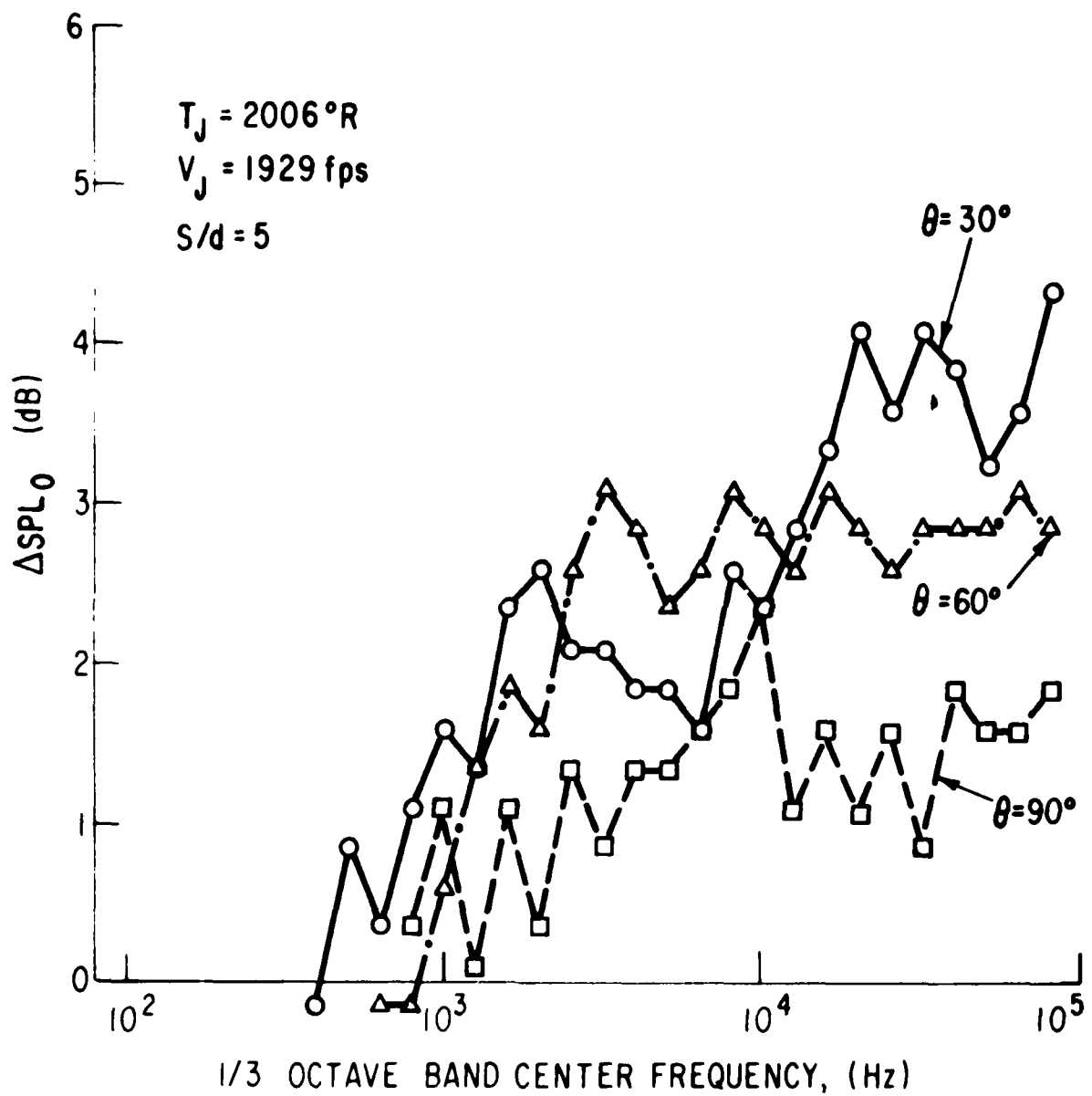


Figure 5-63. Azimuthal Difference Pressure Spectra, Twin Rectangular.

5.5 LINEAR ARRAY MULTITUBE JET NOISE

The acoustic characteristics of three 5-tube linear array nozzles were measured in the CR&DC jet noise facility using the facility measurement systems and data acquisition equipment described in Section 3.1. The purpose of these tests was to extend the twin-jet results of Section 5.3 to multitube configurations. A linear array of 5 round tubes ($d = 0.875$ inch diameter) was selected as the simplest configuration which would involve multielement interaction effects. This configuration also has application to multiengine aircraft installation systems. Tube spacing-to-diameter ratios of $s/d = 1.5$, 2.0, and 3.0 were selected for evaluation.

5.5.1 Overall Acoustic Power

The overall acoustic power of a five-jet linear array at various spacings is compared to an equivalent area single round jet in Figure 5-64. Hidden in this total power is the azimuthal variation of acoustic power. To illustrate the azimuthal dependence of the acoustic power, two azimuthal planes, one in line with the tube row ($\psi = 90^\circ$), and another perpendicular to it ($\psi = 0^\circ$), are examined. These measurement planes provide a means of assessing the relative contributions of acoustic shielding, mixing suppression, and interaction noise. The amount of acoustic shielding is evaluated from the reduction in the "quiet plane" ($\psi = 90^\circ$) noise level relative to an equivalent area round jet. Mixing suppression is measured by the amount of reduction in the "loud plane" ($\psi = 0^\circ$) relative to an equivalent area round jet. Interaction noise is determined from the increase in "loud plane" noise. Figure 5-65 shows little or no attenuation on an overall power basis. Acoustic shielding increases with tube spacing. Interaction noise appears in the loud plane ($\psi = 0^\circ$), but as seen in Figure 5-65, the azimuthal average is within ± 2 dB of the sum of five isolated round jets.

This excess noise increases with tube spacing, which, when combined with the shielding in the $\psi = 0^\circ$ plane, results in rather large differences in the overall power from $\psi = 0^\circ$ to $\psi = 90^\circ$. In some cases these differences (up to 10 dB) exceed the maximum difference possible based only on perfect shielding (7 dB). This is because excess noise appears in the $\psi = 0^\circ$ plane.

This power difference between $\psi = 0^\circ$ and $\psi = 90^\circ$, $\Delta OAPWL_\psi$, is shown on Figure 5-66. In this figure, the effect of jet velocity, V_j , and jet temperature, T_j , are shown for a fixed jet spacing. On Figure 5-66a, the variation with jet temperature at high velocity indicates that as the jet Mach number increases above the critical, the noise field becomes more axisymmetric. Figures 5-66b and 5-66c show that the $\Delta OAPWL_\psi$ is maximum near the sonic point; the only effect of temperature is to vary the jet sonic velocity. This maximum may be associated with the downstream supersonic expansion of the jets, which restricts the amount of ambient air separating them. The ambient air separating the individual jets provides an effective acoustic shield. The difference between the power ($\Delta OAPWL_0$) of an equivalent area round jet and that measured in the "quiet" ($\psi = 90^\circ$), plane of the linear array exhibits a slightly different trend, as seen on Figure 5-67. At

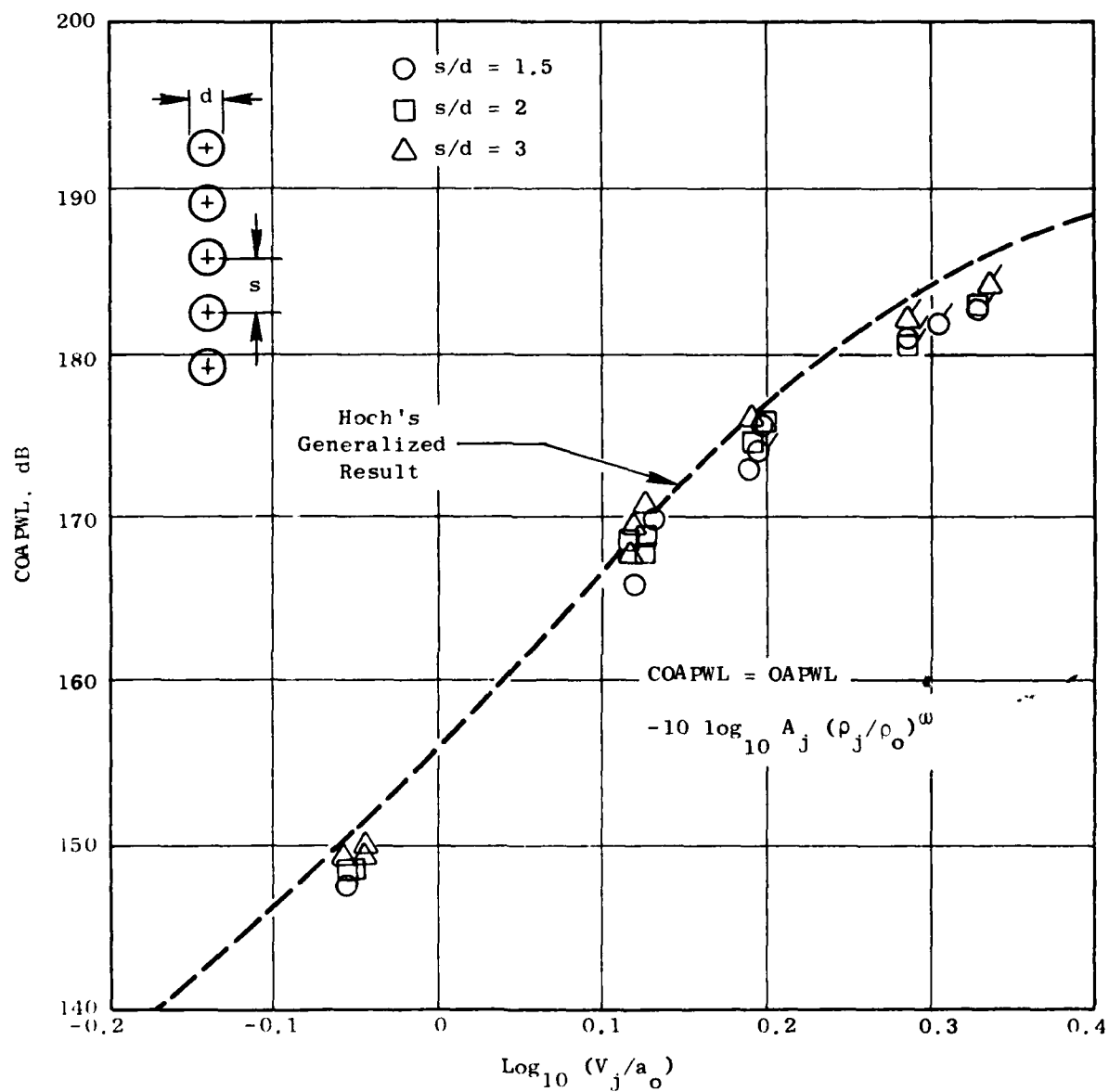


Figure 5-64. Five Jet Linear Array, Overall Power.

536

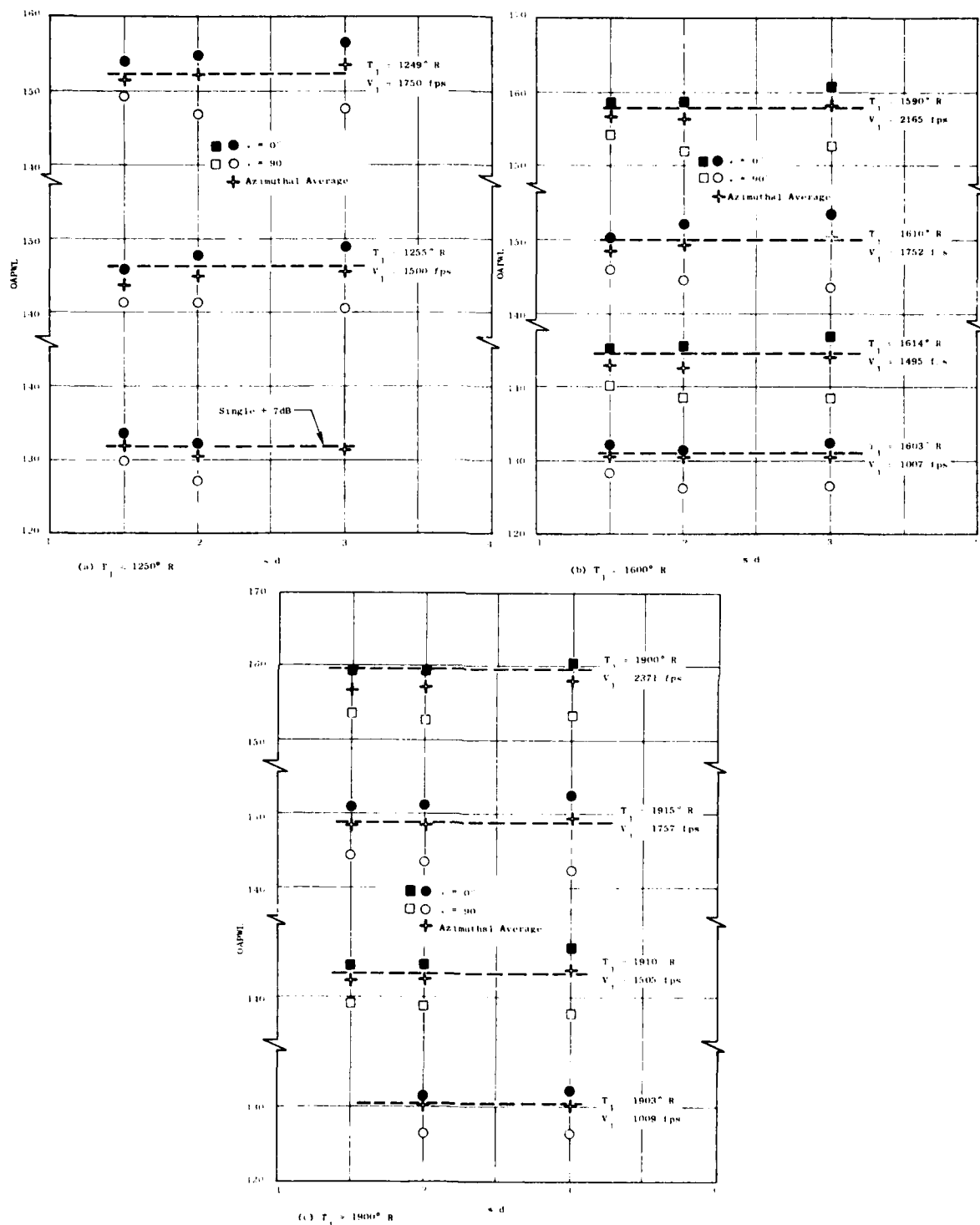


Figure 5-65. Effect of Nozzle Spacing on Acoustic Power.

527

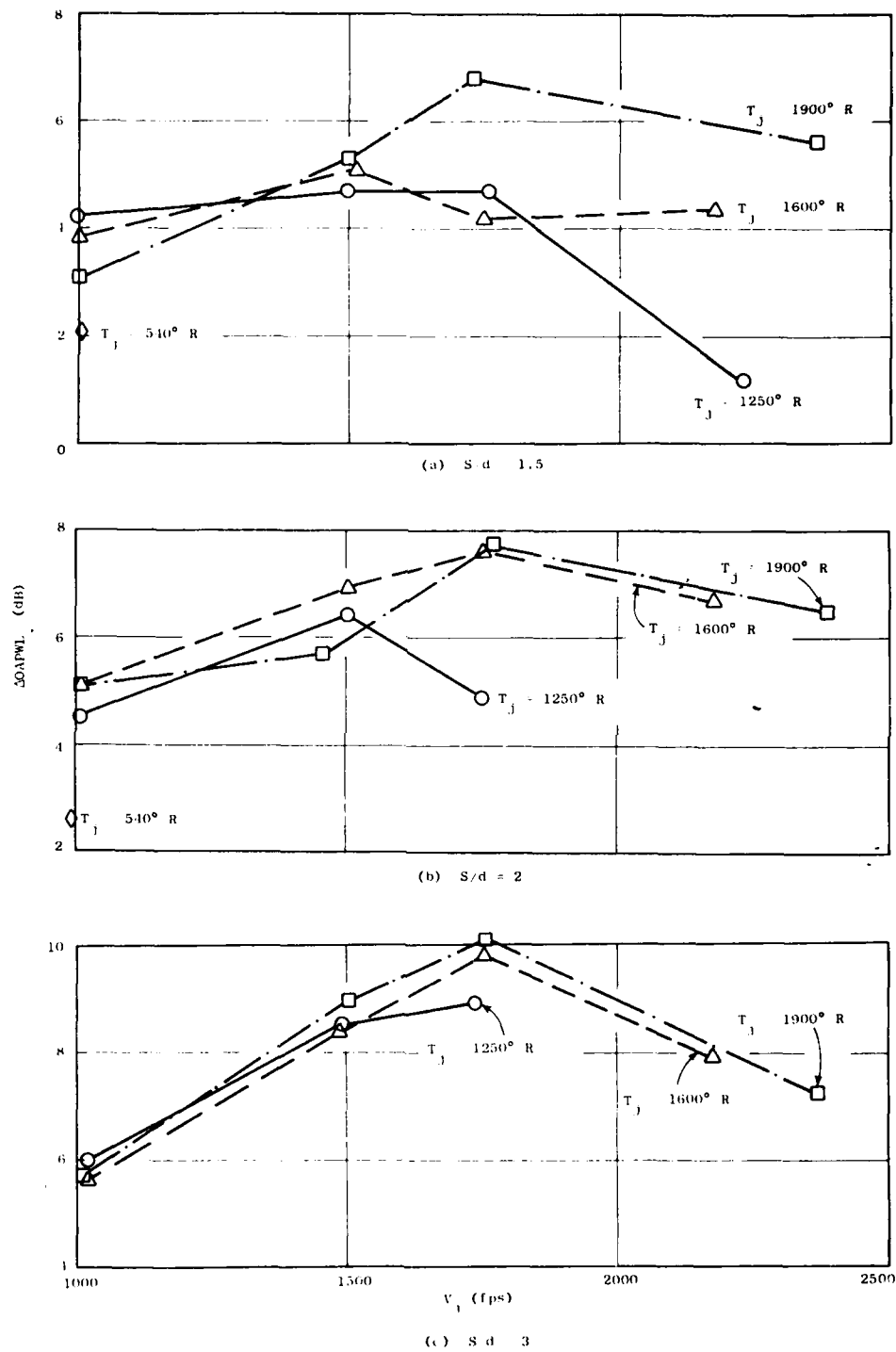


Figure 5-66. Effect of Velocity on Azimuthal Power Difference.

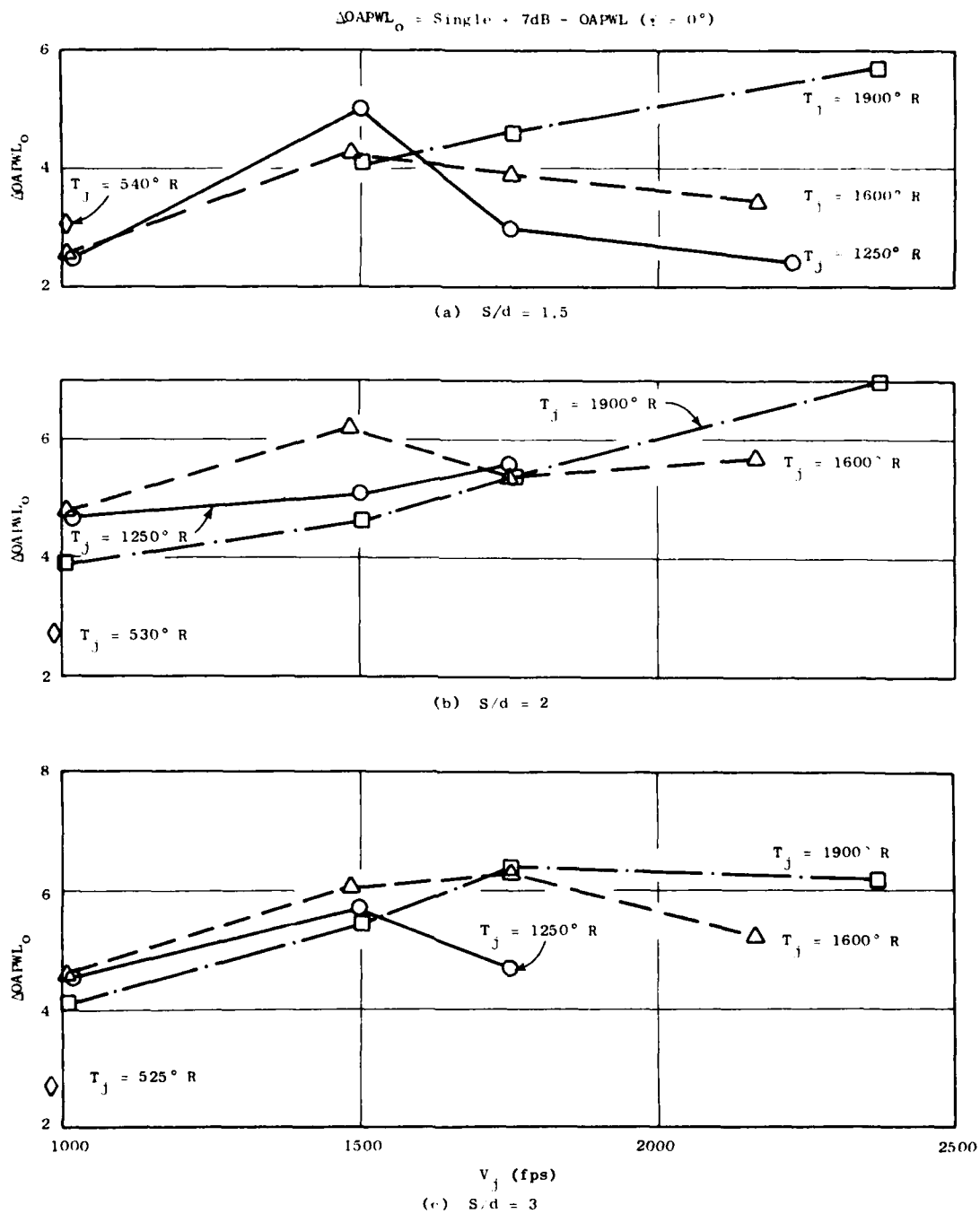


Figure 5-67. Effect of Velocity on Shielded Power Difference.

the lowest nozzle spacing, $s/d = 1.5$, the maximum near the sonic point does not occur for the highest temperature; and at $s/d = 2$, the general trend is a gradual increase in $\Delta OAPWL_0$ with jet velocity. Only at the largest spacing, $s/d = 3$, does the pattern seen for $\Delta OAPWL_\psi$ repeat for $\Delta OAPWL_0$. The principal difference between $\Delta OAPWL_\psi$ and $\Delta OAPWL_0$ is the excess noise that appears in the $\psi = 0^\circ$ plane. The major portion of this excess noise in the $\psi = 0^\circ$ plane is probably noise reflected out of the ($\psi = 90^\circ$) plane, which would be expected to peak at conditions of maximum interjet shielding. This is approximately what is observed in the difference between the $\Delta OAPWL_\psi$ and $\Delta OAPWL_0$ trends.

5.5.2 Azimuthal and Polar Directivity

The extent of the azimuthal asymmetry can be seen in Figure 5-68, where the SPL at the peak angle and frequency is seen to vary by as much as 13 dB with azimuthal angle, ψ ; it is also strongly dependent on spacing ratio, s/d . Since this level of asymmetry is greater than perfect shielding would predict, a portion of this asymmetry may be due to excess noise appearing in the $\psi = 0^\circ$ plane. Referring to Figure 5-65b, it can be seen (for the conditions of Figure 5-68) that there is a redistribution of acoustic energy such that the azimuthally averaged power is almost identical to that of five isolated single jets. Since, for most of these cases, the azimuthally averaged overall power rarely exceeds that of five isolated jets, it is conjectured that the excess noise seen in the $\psi = 0^\circ$ plane is energy re-directed by the jets originally propagating in the $\psi = 0^\circ$ plane. Due to the transmission through the jet flow, the incident energy is refracted or scattered to other azimuthal angles.

If shielding is the governing phenomenon, one expects to see a minimum value of asymmetry occur at $\theta_j = 90^\circ$ when the jet flow is unheated. The asymmetry should vanish at $\theta_j = 90^\circ$. Due to turbulence, however, the velocity vector can vary from the axial direction, causing some acoustic shielding to occur for unheated flows at $\theta_j = 90^\circ$. The observed azimuthal asymmetry in OASPL essentially vanishes at $\theta_j = 90^\circ$, as shown in Figure 5-69, indicating that these turbulence effects are negligible. The asymmetry is seen to peak in the shallow angles, as expected from the shielding theory. For a heated jet, however, acoustic shielding occurs at $\theta_j = 90^\circ$, as shown in Figure 5-70.

5.5.3 Power and Pressure Spectra

The power spectra results shown in Figure 5-70 indicate that the maximum reduction in noise in the $\psi = 90^\circ$ plane and the maximum excess noise in the $\psi = 0^\circ$ plane both occur at high frequency. This observation supports the conjecture that the excess energy found in the $\psi = 0^\circ$ plane is due primarily to refraction and scattering of the incident acoustic energy by the jets in the $\psi = 90^\circ$ plane. Examination of the sound pressure spectra shown in Figure 5-71 reveals that the noise in the $\psi = 0^\circ$ plane exceeds the (single +7 dB) results only at the shallow angles, while the noise reduction in the $\psi = 90^\circ$ plane occurs at all three angles.

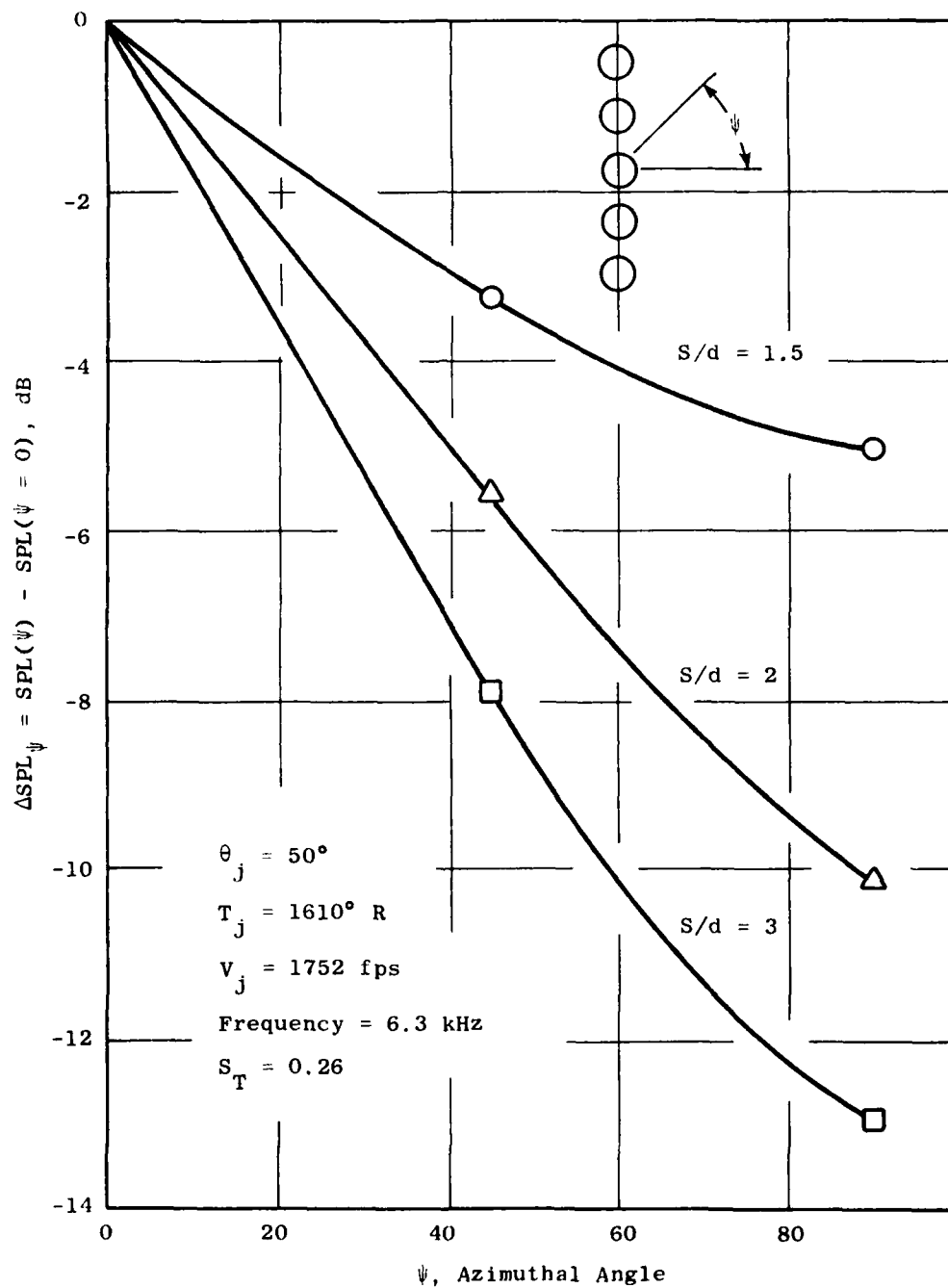


Figure 5-68. Five-Jet Linear Array, Azimuthal Directivity, re $\psi = 0^\circ$.

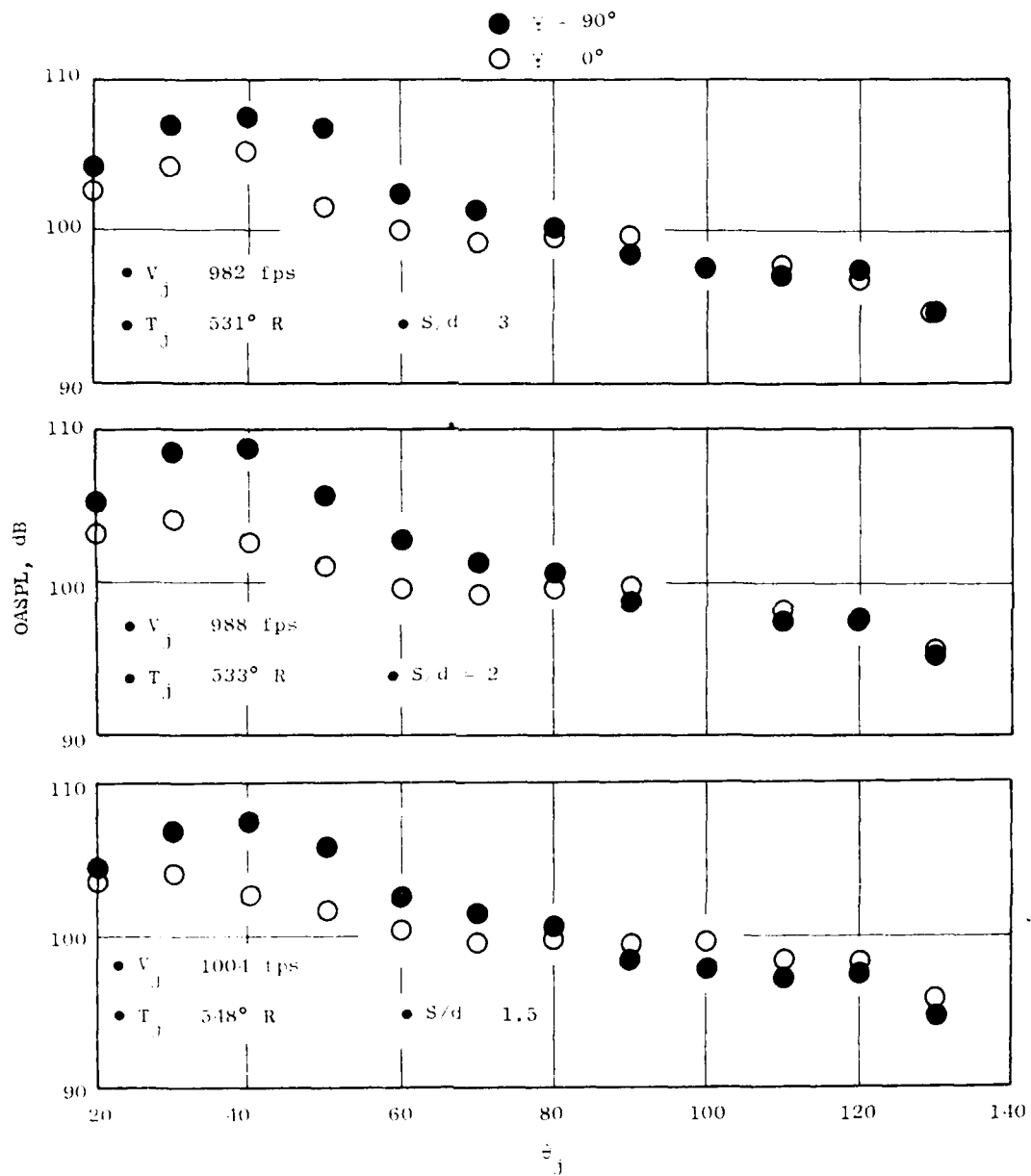


Figure 5-69. Five Jet Linear Array, Polar Directivity.

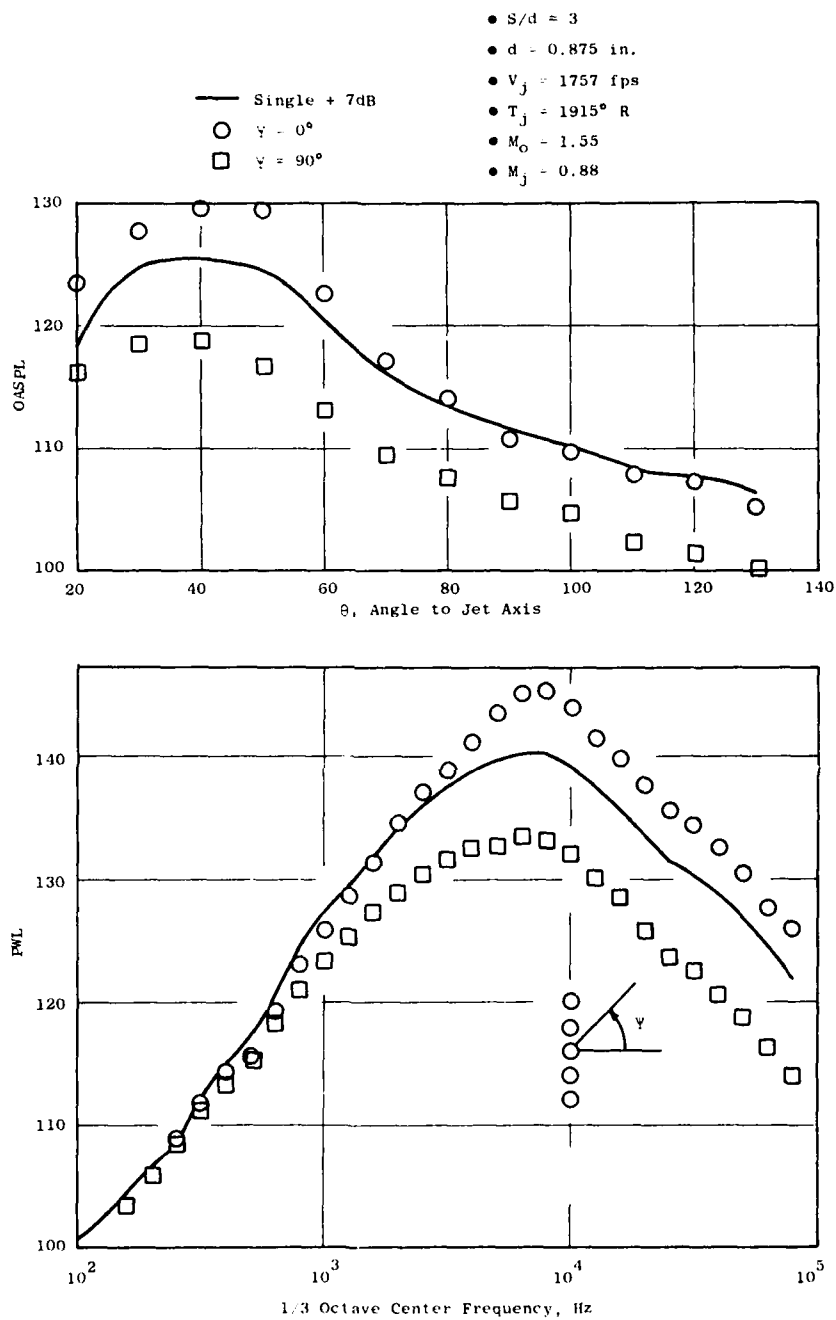


Figure 5-70. Linear Array, Power Spectra and Directivity.

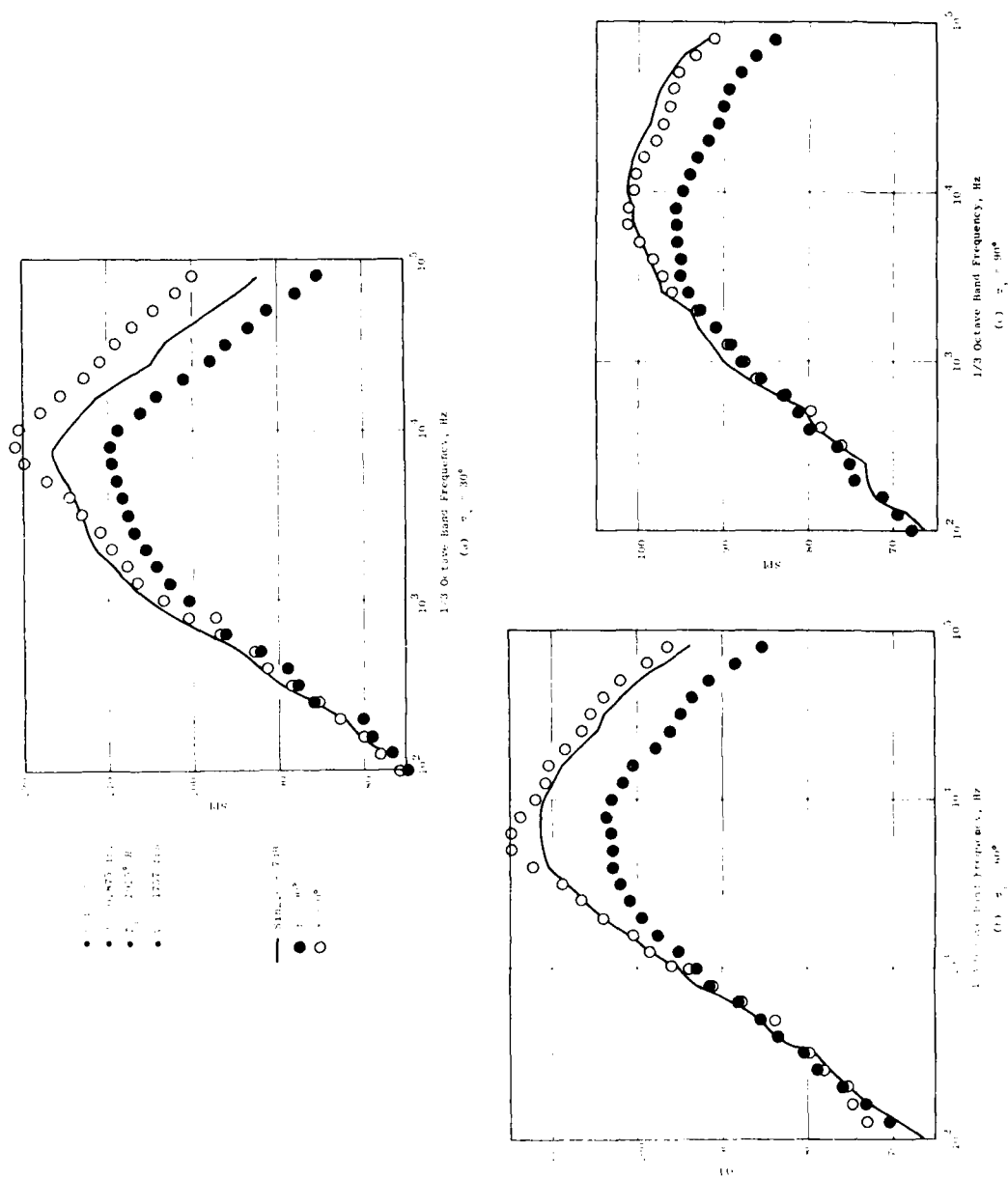


Figure 5-71. Linear Array, SPL Spectra.

For the smallest jet spacing, $s/d = 1.5$, low frequency excess noise is observed (which may be due to a mixing phenomenon), as shown in Figure 5-72a. This does not occur at the larger spacings (Figures 5-72b and 5-72c). Additional power spectra are shown in Figure 5-73, which show the effects of spacing at two jet velocities. Comparisons of the SPL spectra at $\psi = 0^\circ$ and $\psi = 90^\circ$ for $\theta_j = 30^\circ$, 60° , and 90° (as shown in Figure 5-74) indicate that this low frequency excess noise is asymmetric.

5.5.4 Summary

The principal feature of multijet linear arrays is the very large azimuthal directivity. Acoustic shieldings of the quiet plane ($\psi = 90^\circ$), and excess noise appearing in the loud plane ($\psi = 0^\circ$) are responsible for this feature. Some interchange of energy between the two planes takes place, since, for most of the data, the azimuthally averaged results are nearly identical to the single +7dB results, indicating a rough conservation of acoustic energy. A low frequency excess energy is also observed at shallow angles to the jet axis, with the closest nozzle spacing. This excess noise is thought to be due to a mixing phenomenon.

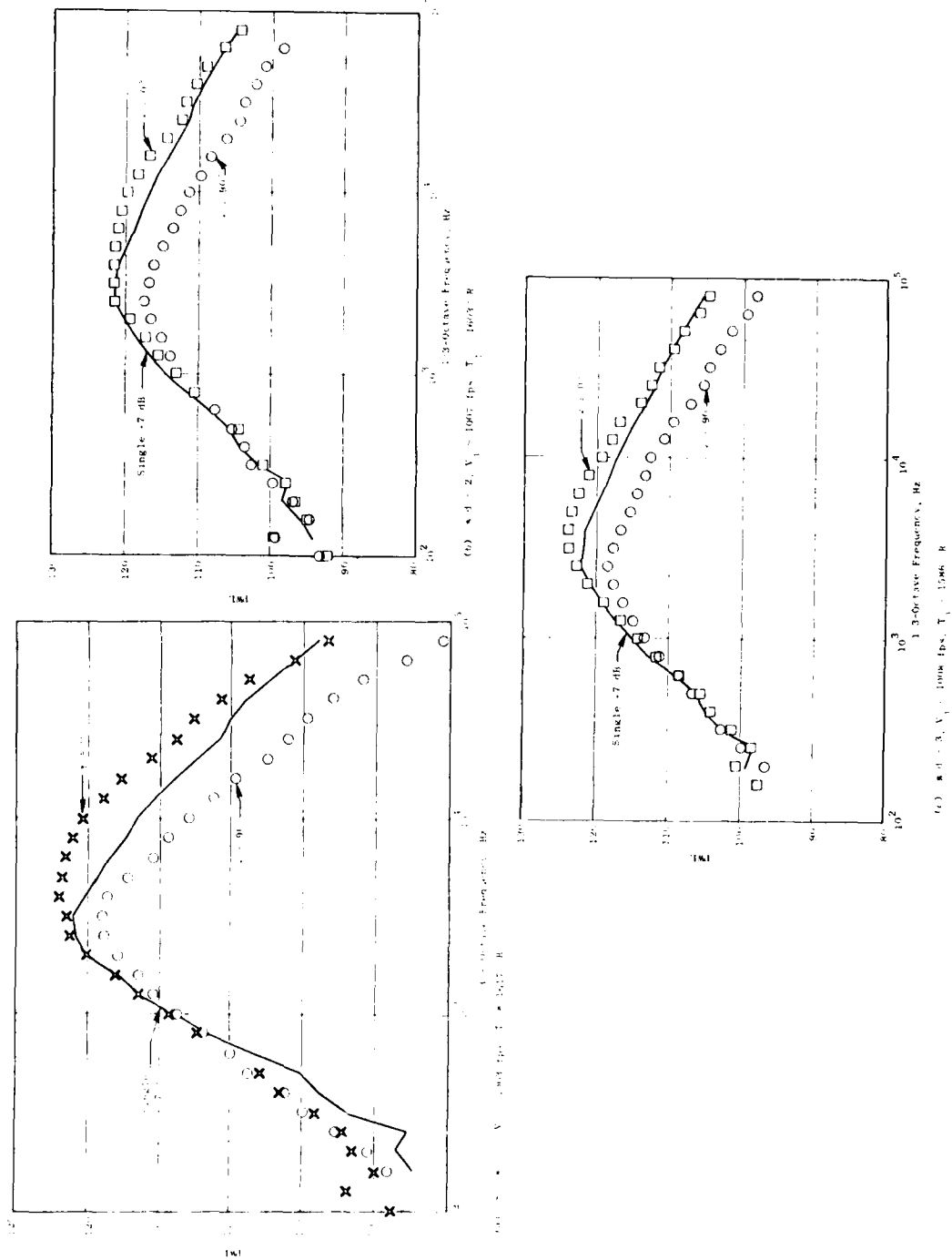


Figure 5-72. Power Spectra.

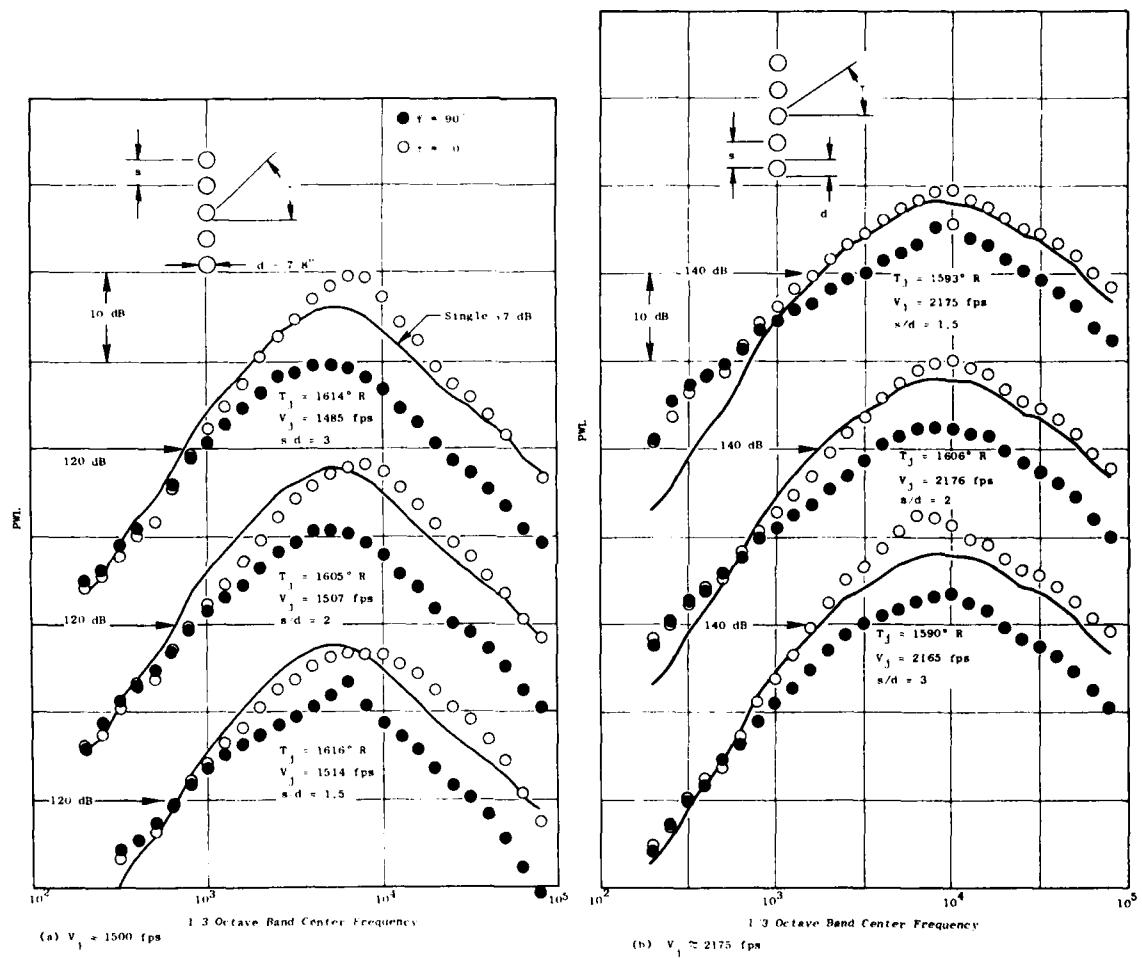


Figure 5-73. Power Spectra, Effect of Spacing.

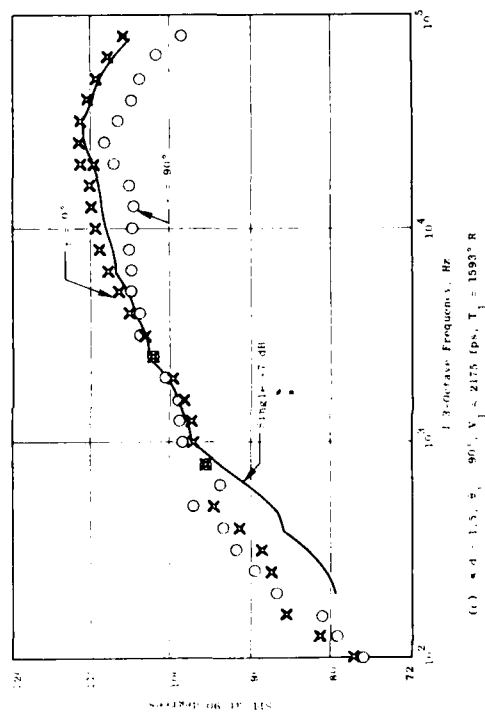
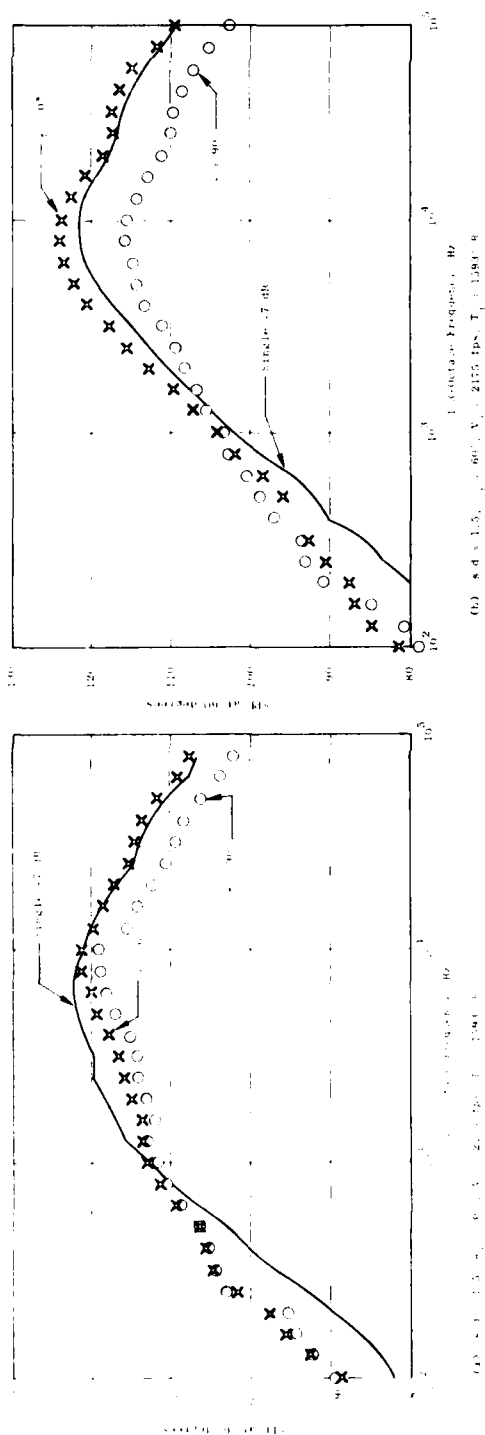


Figure 5-74. Power Spectra.

5.6 CIRCULAR ARRAY MULTITUBE JET NOISE

The acoustic characteristics of several six- and seven-tube cluster, circular-array nozzles were measured in the CR&DC jet noise facility. The purpose of these tests was to experimentally study the mixing/interference and acoustic shielding mechanisms and their effect on multielement nozzle jet noise. A hexagonal ring of six round tubes ($d = 0.875$ inch diameter), with and without a center tube, was selected for study. Denoting D as the diameter of the circle intersecting the centerlines of each of the tubes in the ring, spacing ratios D/d of 3.0, 4.0, and 6.0 were investigated. The following paragraphs summarize the important experimental results obtained from this investigation.

5.6.1 Overall Acoustic Power

When either six-tube or seven-tube clusters are compared to a single jet on an equal area basis, a net reduction in overall acoustic power level (OAPWL) is observed. The amount of this reduction depends on the area ratio (tube spacing), and increases with jet velocity as shown in Figures 5-75, 5-76, and 5-77. The total power level approaches the sum of the isolated jets as tube spacing increases, and the maximum suppression (at high velocity) is reduced from about 4 dB for the smallest cluster to about 2 dB for the largest cluster.

The effect of heating (density ratio) is normalized out in Figures 5-75 through 5-77 through the use of the method of Hoch, et al.⁽¹¹⁾ as developed for single round jets. The density exponent, ω , was also found directly (similar to Hoch, et al.) by plotting overall power versus density ratio at a fixed velocity ratio, V_j/a_0 . This result is shown on Figure 5-78, where the results of this study are compared to Hoch's result. As the cluster spacing becomes smaller, the density exponent ω exhibits a less rapid rise with velocity ratio. This indicates that the smaller clusters produce more noise at high temperatures and low velocities than do the large clusters. Therefore at a moderately high fixed velocity, the noise reduction afforded by reducing jet density, through heating for instance, is less with a highly packed cluster than with an open one.

At a fixed jet temperature, the velocity exponent can be determined in a similar manner to the density exponent, and the results (Figure 5-79) show that the large spacing cluster behaves much like the elemental single jet. Again, the small spacing cluster shows the lowest velocity exponent. These trends of velocity exponent are also reflected by the dependence on D/d shown on Figures 5-80, 5-81, and 5-82 where the power levels increase with D/d for all but the lowest jet velocities.

5.6.2 Directivity

Azimuthal directivity effects for all the clusters are quite small, particularly at the large spacing, where a nearly axisymmetric noise field is observed for both the six- and seven-tube clusters (Figures 5-83 and 5-84).

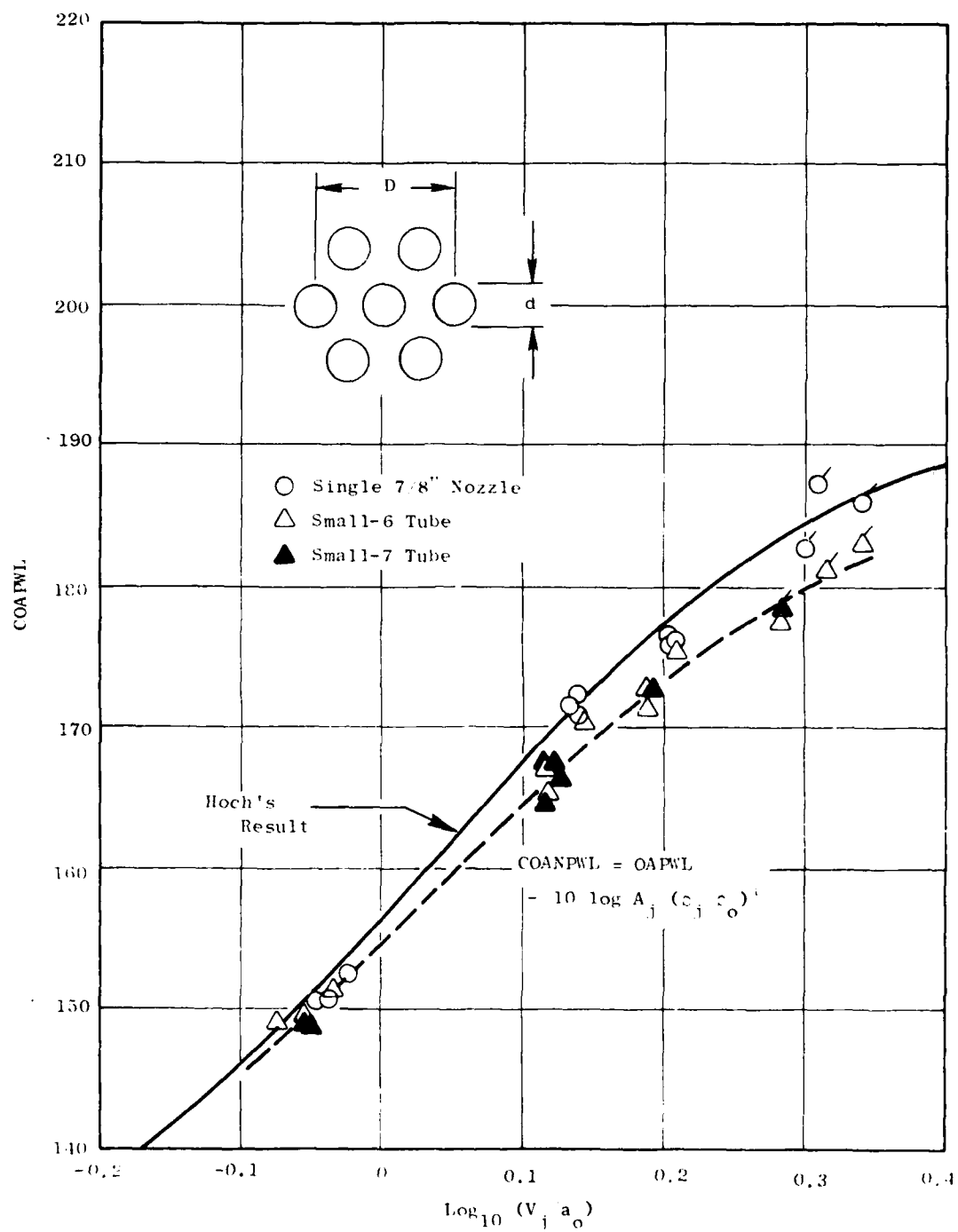


Figure 5-75. Overall Power Versus Velocity, $D/d = 3$.

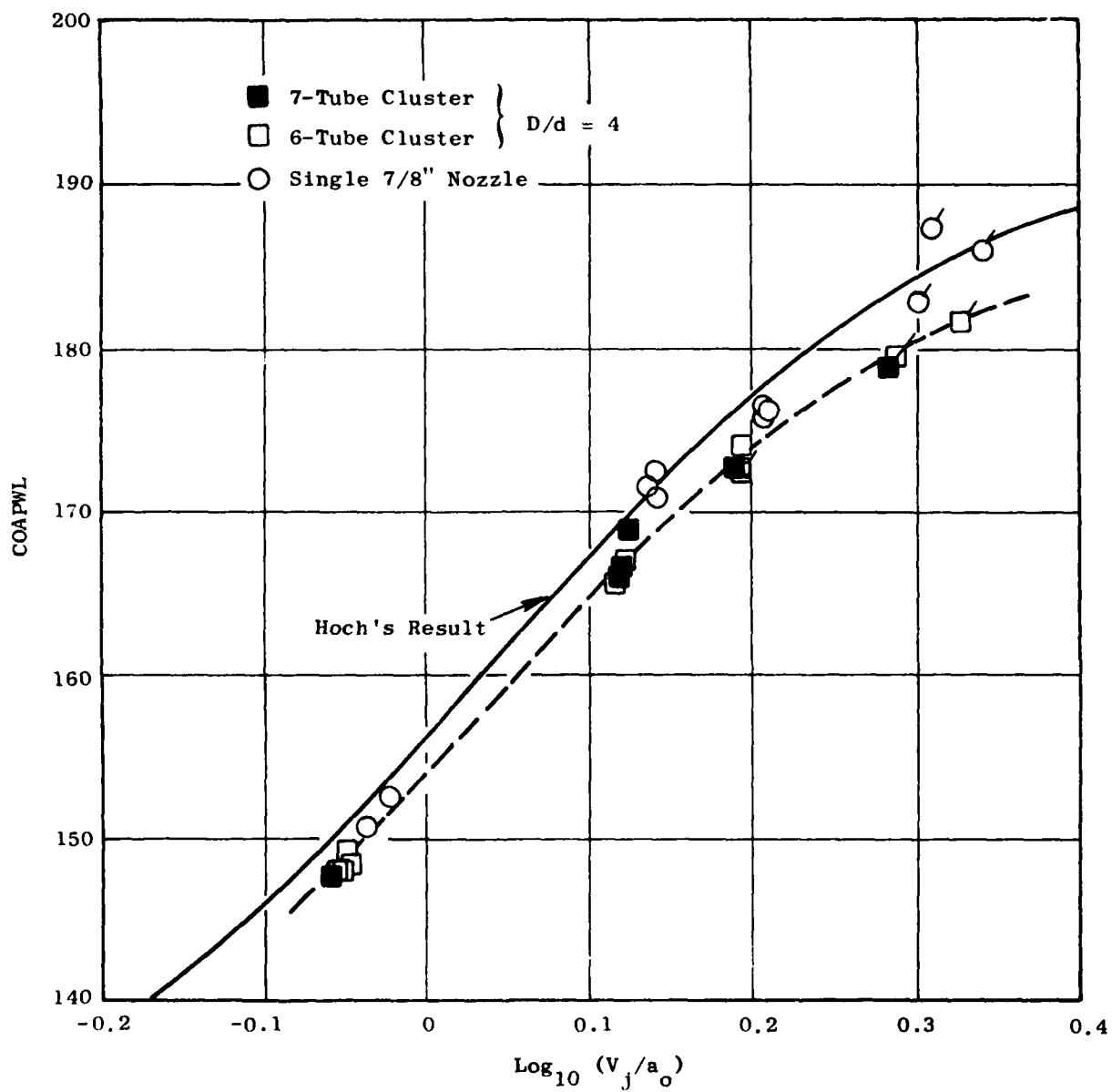


Figure 5-76. Overall Power versus Velocity, $D/d = 4$.

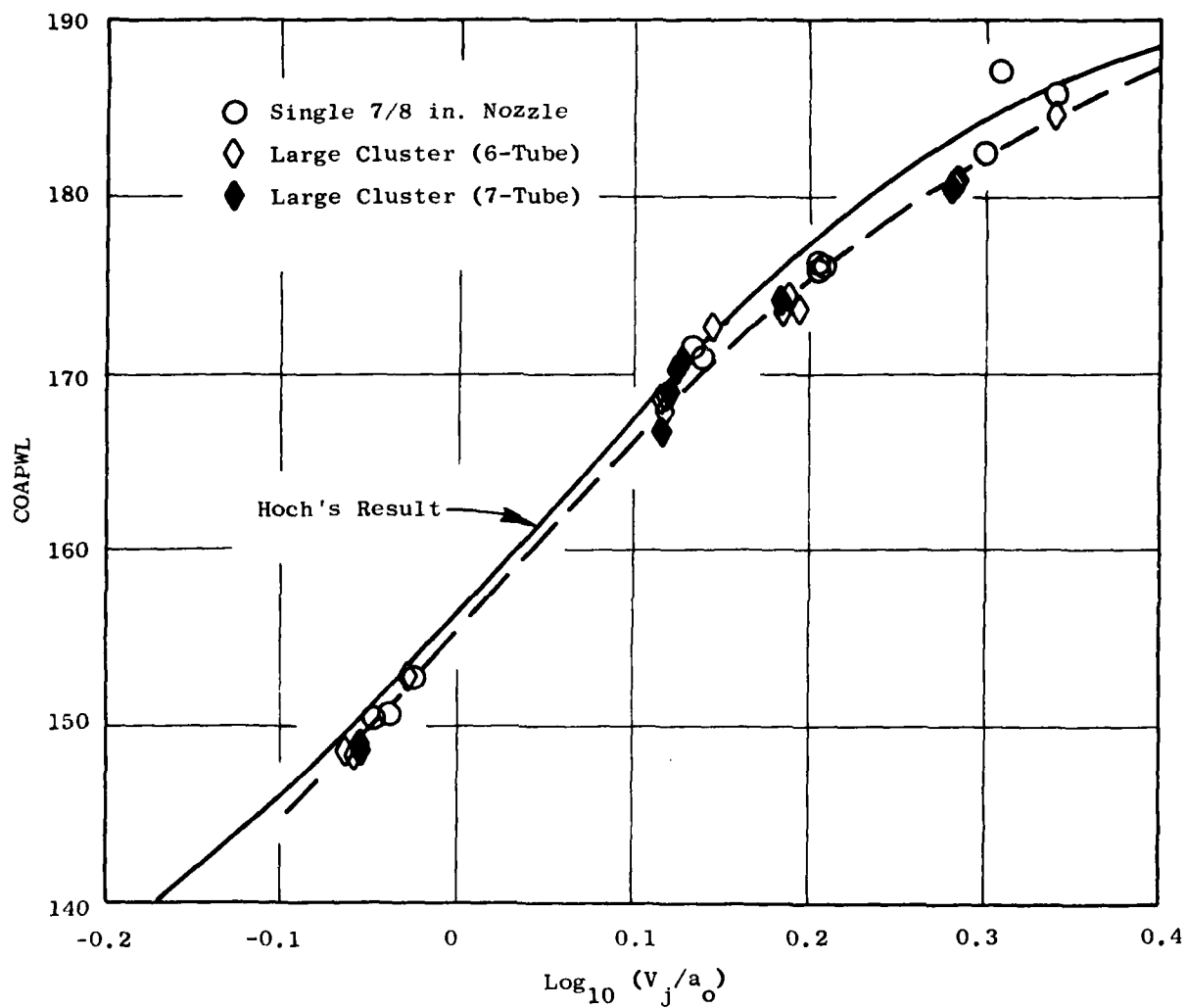


Figure 5-77. Overall Power Vs. Velocity, $D/d = 6$.

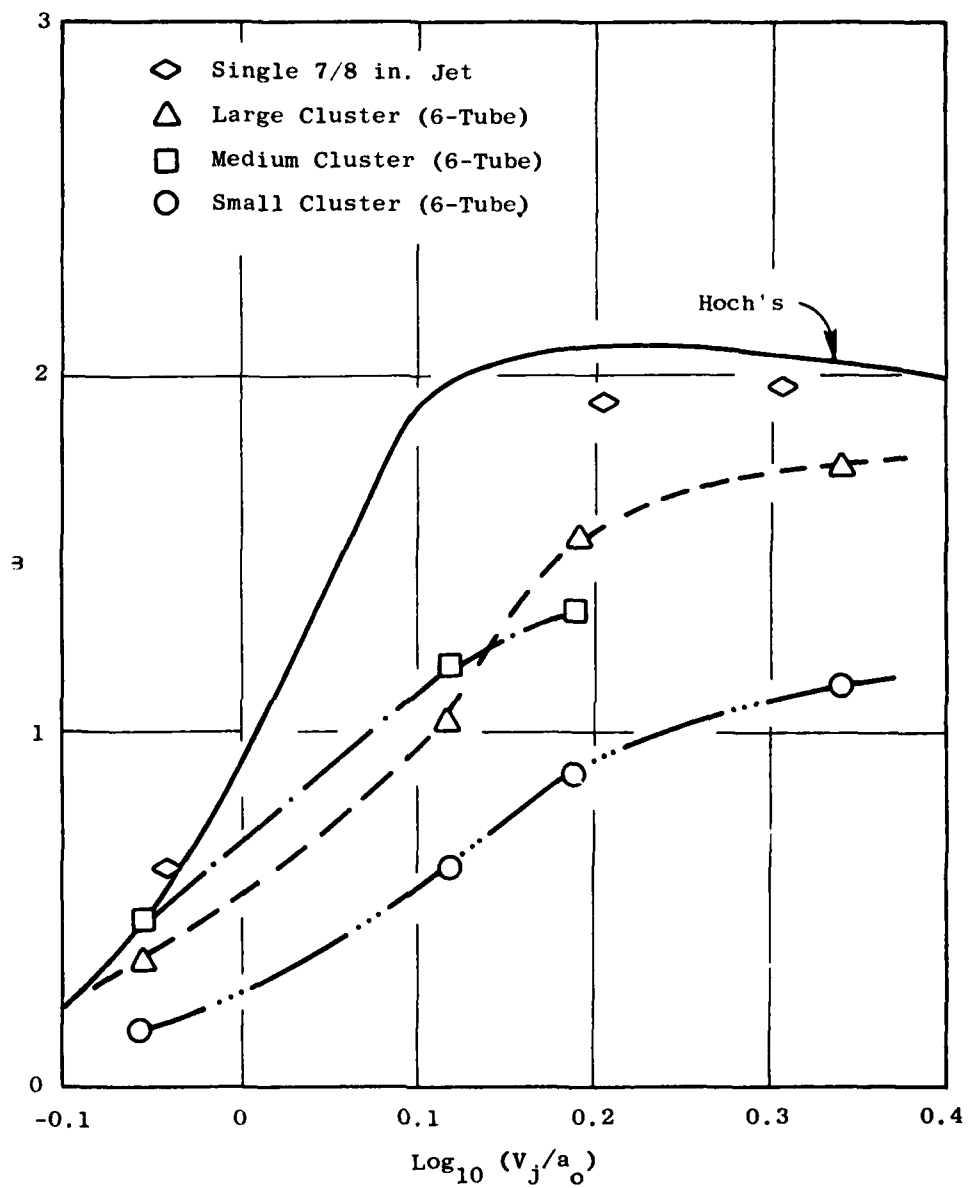


Figure 5-78. Density Exponent for OAPWL Vs. Velocity.

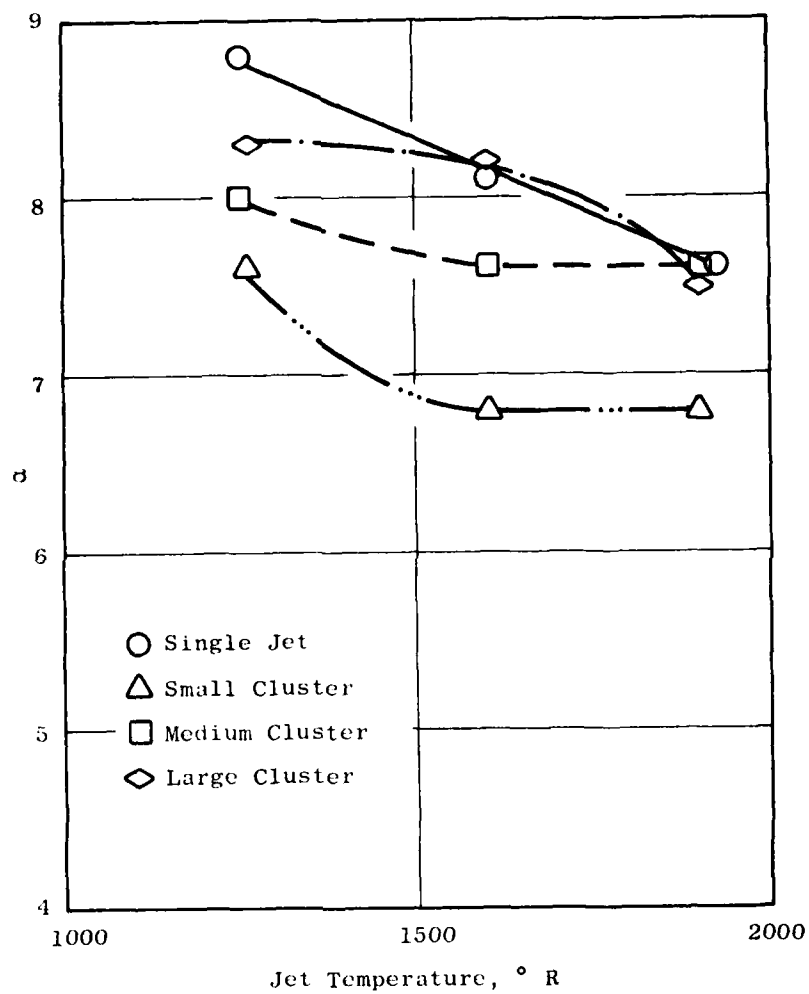


Figure 5-79. Velocity Exponent for OAPWL Versus Temperature.

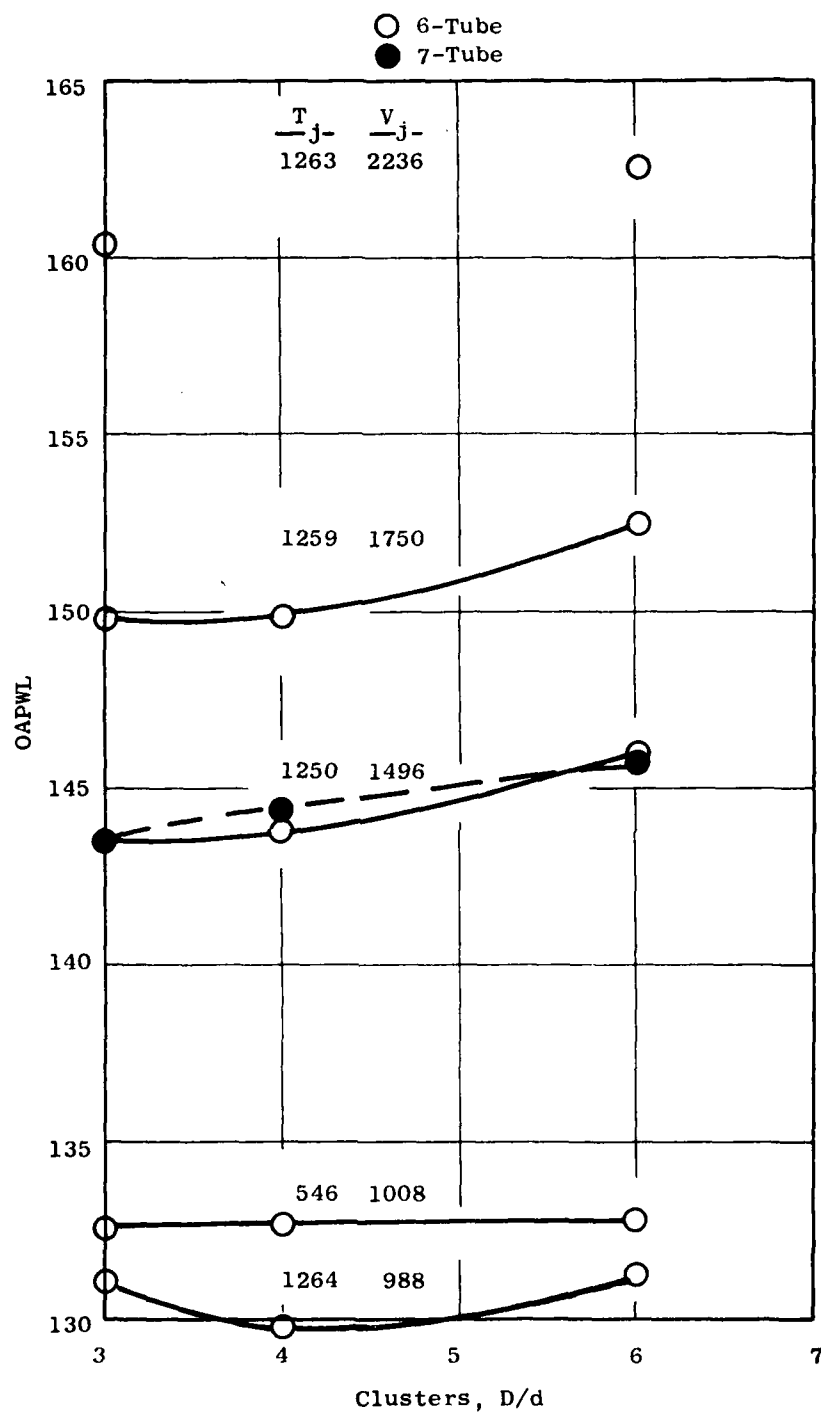


Figure 5-80. Effect of Spacing on Overall Power,
 $T_j \approx 1250^\circ \text{ R.}$

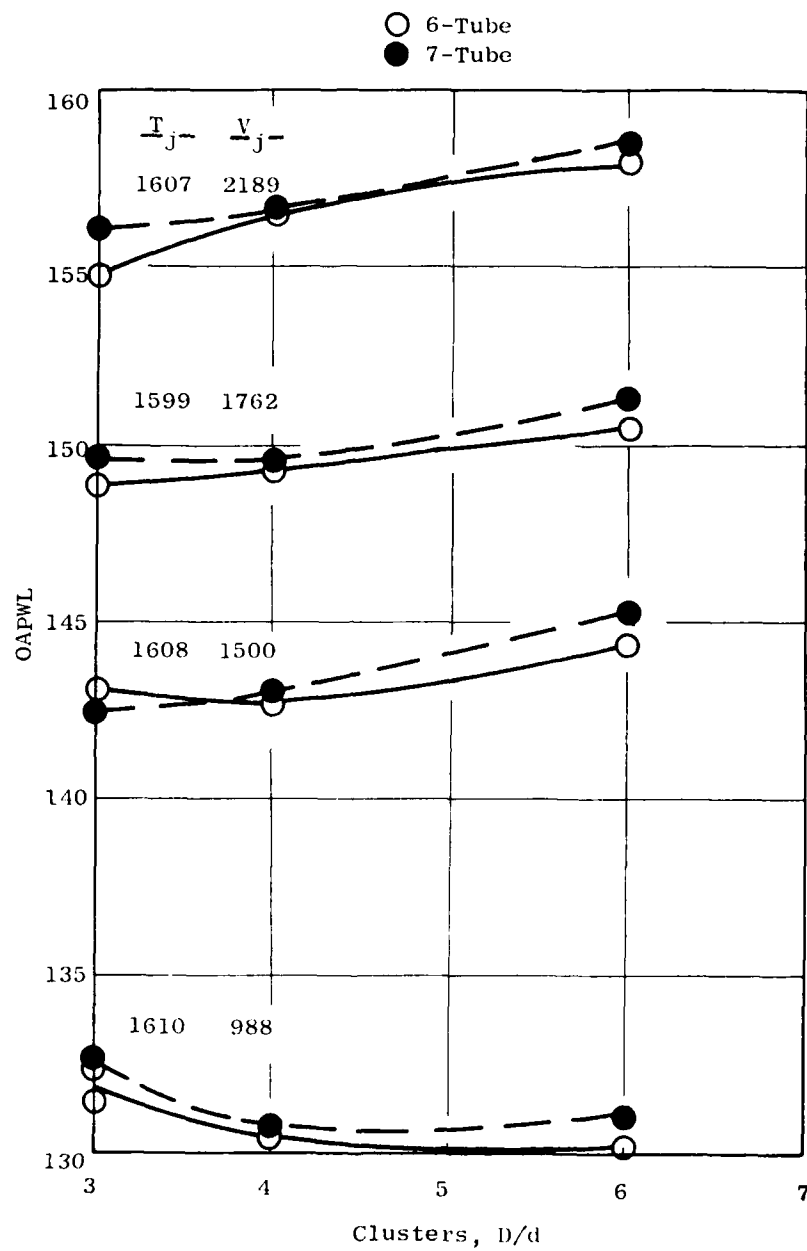


Figure 5-81. Effect of Spacing on Overall Power,
 $T_j \approx 1600^\circ \text{ R.}$

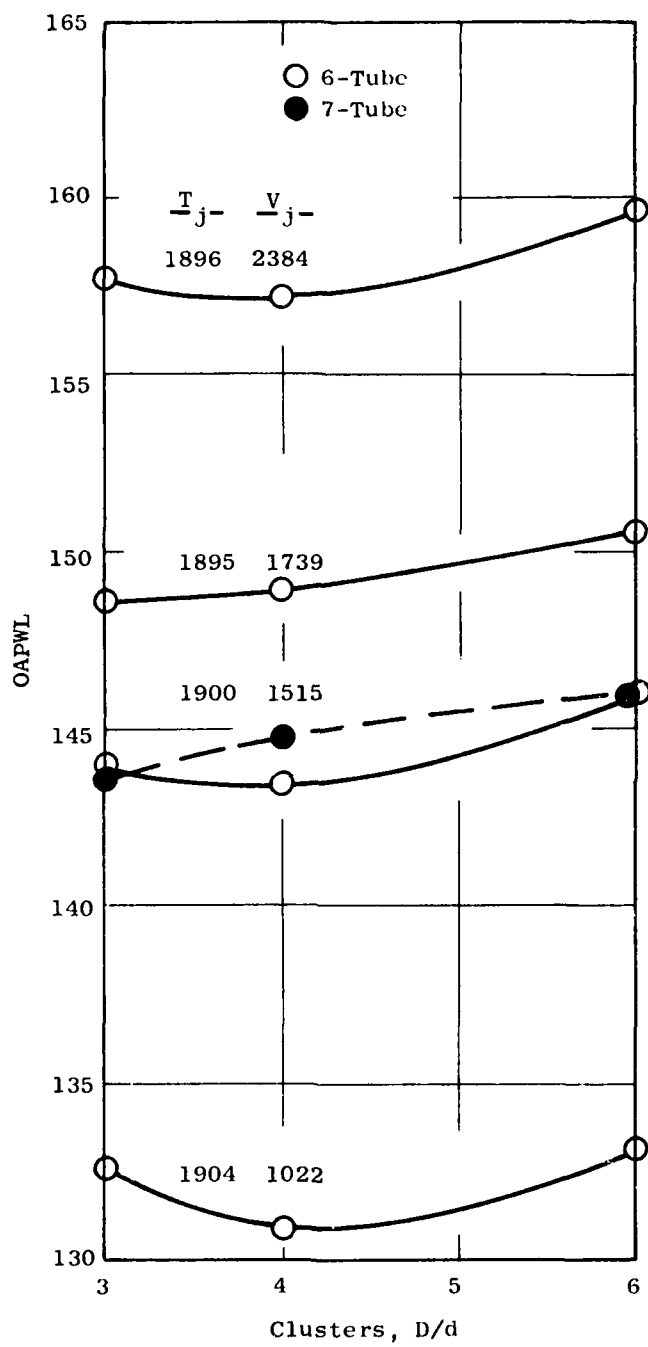


Figure 5-82. Effect of Spacing on Overall Power, $T_j \approx 1900^\circ \text{ R.}$

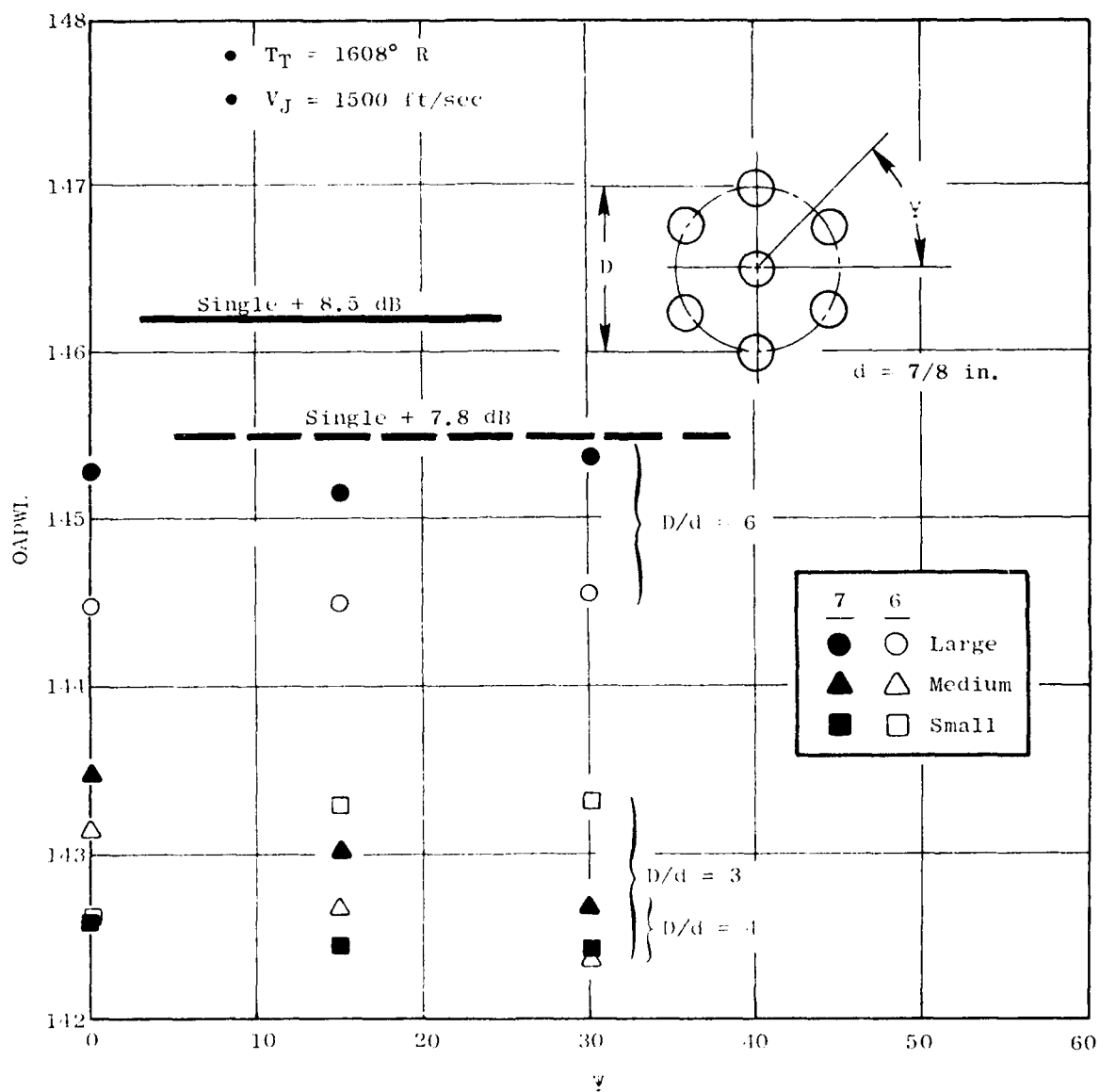


Figure 5-83. Azimuthal Variation of Overall Power, Subsonic.

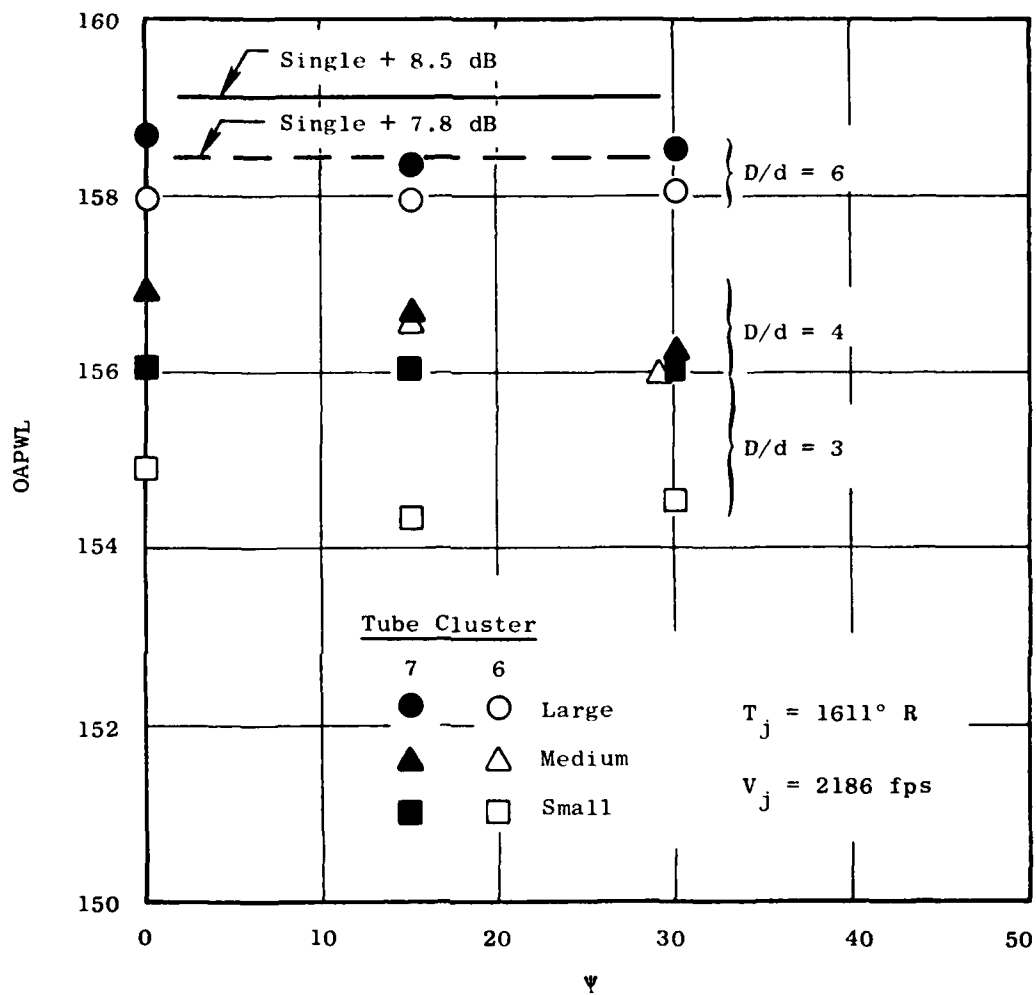


Figure 5-84. Azimuthal Variation of Overall Power, Supersonic.

The medium cluster shows a decreasing power level as the observer's line of sight approaches a direction defined by diametrically opposite tube center-lines. This dip occurs for both six- and seven-tube clusters at both subsonic and supersonic conditions, with the effect weakening at the supersonic conditions. For the smallest spacing, only the six-tube cluster shows any significant azimuthal dependence, and then only at subsonic conditions. There is a middle range of tube spacing conditions. There is a middle range of tube spacing where a small azimuthal dependence is observed but the spacing is effectively reduced when the flow is underexpanded and the azimuthal effect weakens. Both of these trends are seen clearly on Figure 5-85 where a definite peaking of the $\Delta OAPWL$ is seen at $D/d = 4$, at high subsonic velocity.

The polar OASPL directivities of the two azimuthal angles are compared on Figure 5-86 using the tube spacing and flow conditions of maximum $\Delta OAPWL_\psi$. The individual directivities peak near $\theta_j = 40^\circ$, and the difference is a maximum near $\theta = 60^\circ$. This difference in OASPL at $\theta_j = 60^\circ$, seen in Figure 5-86, shows up in the SPL spectra near the frequency of peak intensity, as seen in Figure 5-87, with very little difference at the low frequencies.

5.6.3 Power and Pressure Spectra

The primary variations in power and pressure spectra occur at frequencies less than the peak intensity frequency. Figures 5-88 through 5-91 show this by comparing the power spectra of the three clusters (for both six- and seven-tube versions) to that of the elemental single jet. When compared to the sum of isolated jets, only the closest tube spacing shows any high frequency reduction, and only at supersonic conditions (Figures 5-90 and 5-91). Attenuation does however, occur, at frequencies just below the peak intensity, and this attenuation increases as the tube spacing becomes smaller. At lower frequencies (4 to 5 octaves lower than the peak), excess noise generation occurs, and it increases as the tube spacing decreases. This excess noise is enhanced with seven tubes and with underexpanded (supersonic) flow. These characteristics point to an interaction of the individual tube flows that increases as the cluster becomes more closely packed and as the individual jet plumes swell due to an underexpanded flow condition. The frequency of the excess noise is very low, indicating that the excess noise source location is quite far downstream. As the cluster becomes more closely packed, the merging of the individual tube flows occurs earlier, and the frequency of the excess noise increases, as can be seen in Figures 5-88 through 5-91. Both the mid frequency attenuation and the low frequency excess noise peak are greatest at shallow angles to the jet axis (shown in Figure 5-92 for the six-tube clusters and Figure 5-93 for the seven-tube clusters). The strongest excess noise generation occurs when attenuation is greatest.

High frequency reduction is evident only with the six- and seven-tube small cluster at high subsonic and supersonic conditions. An example of this high frequency suppression is seen at an angle to the jet axes of $\theta_j = 60^\circ$ on Figures 5-92b and 5-93b.

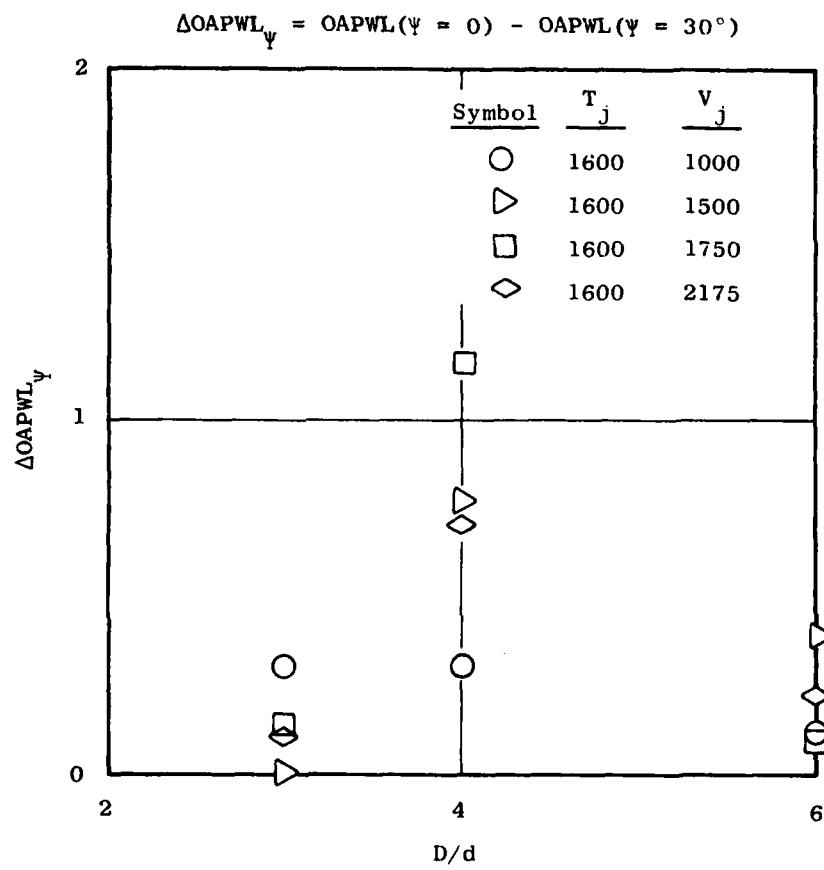


Figure 5-85. Effect of Spacing on Azimuthal Power Difference.

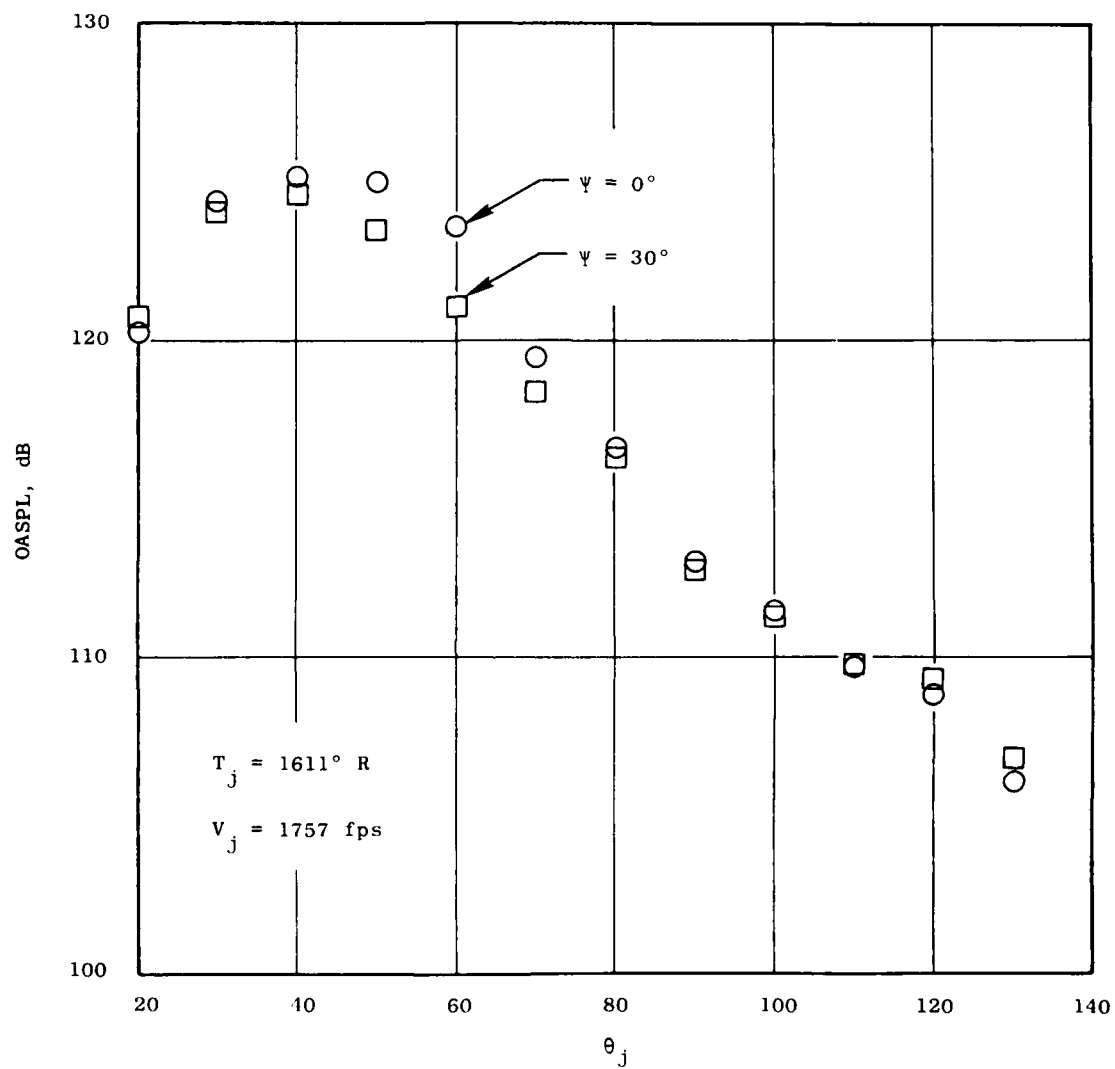


Figure 5-86. Polar Directivity, $D/d = 4$, 7-Tube Cluster.

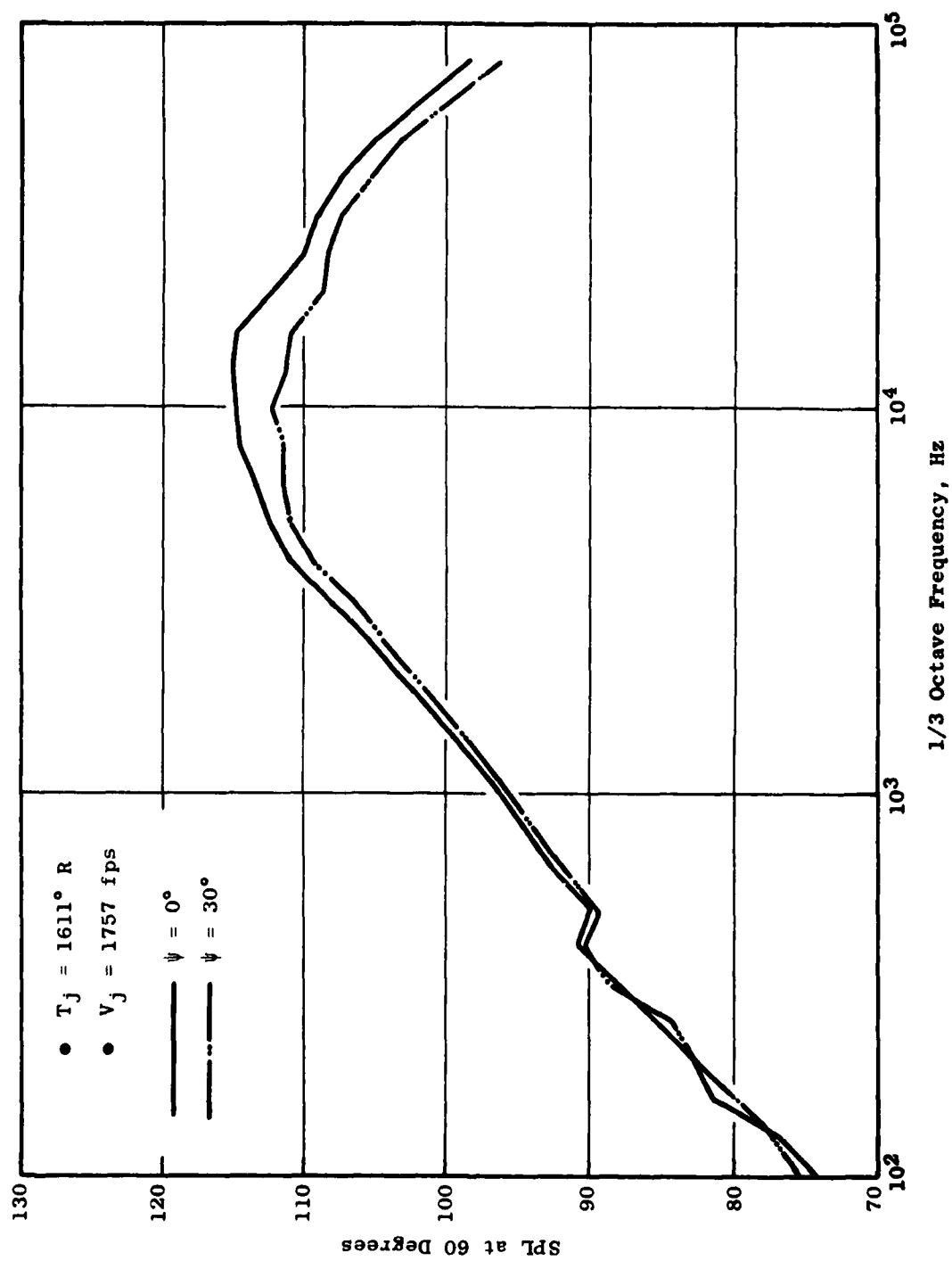


Figure 5-87. SPL Spectra, 7-Tube Cluster, $D/d = 4$.

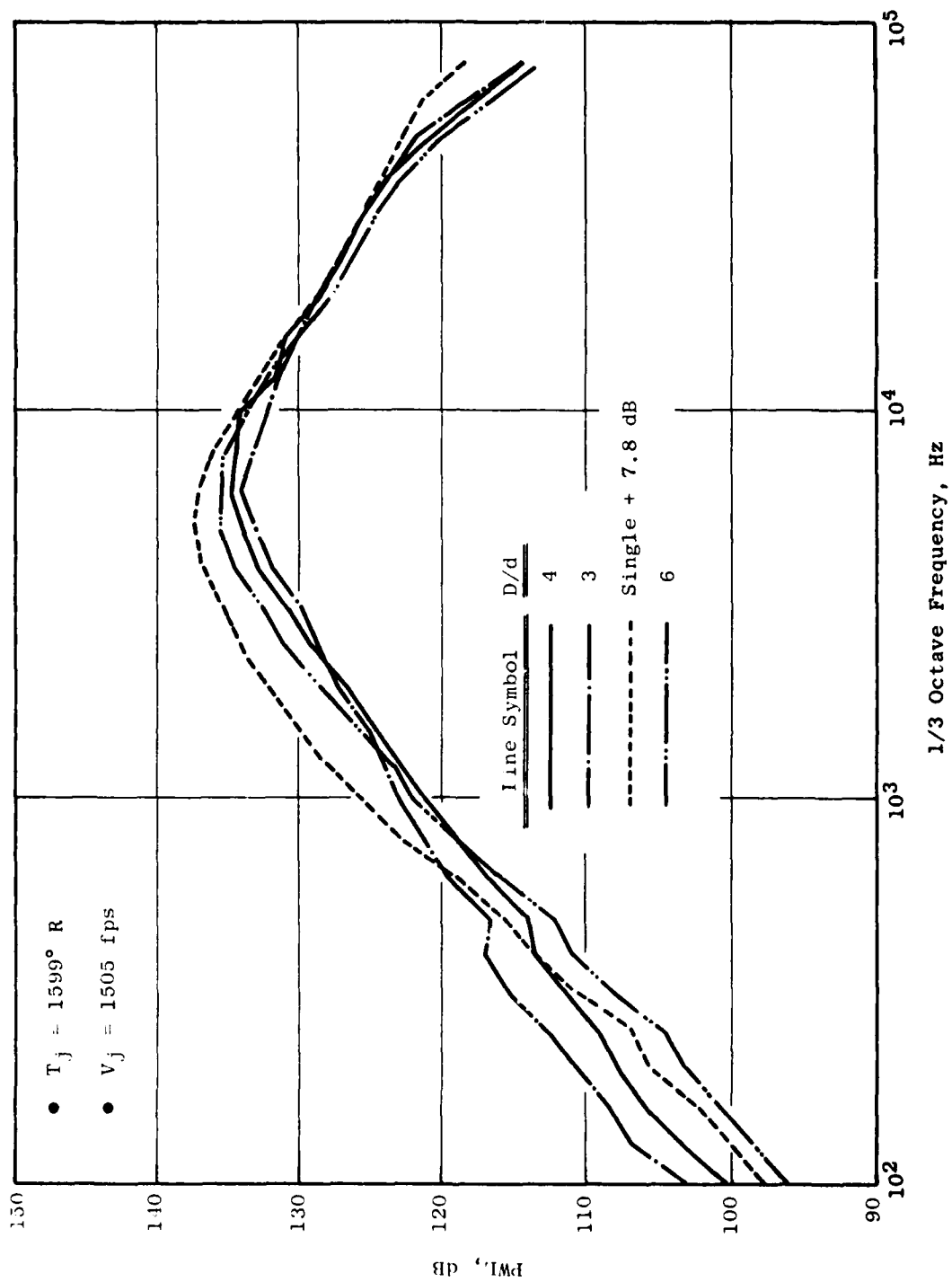


Figure 5-88. PWL Spectra, Effect of Spacing, 6-Tube, Subsonic.

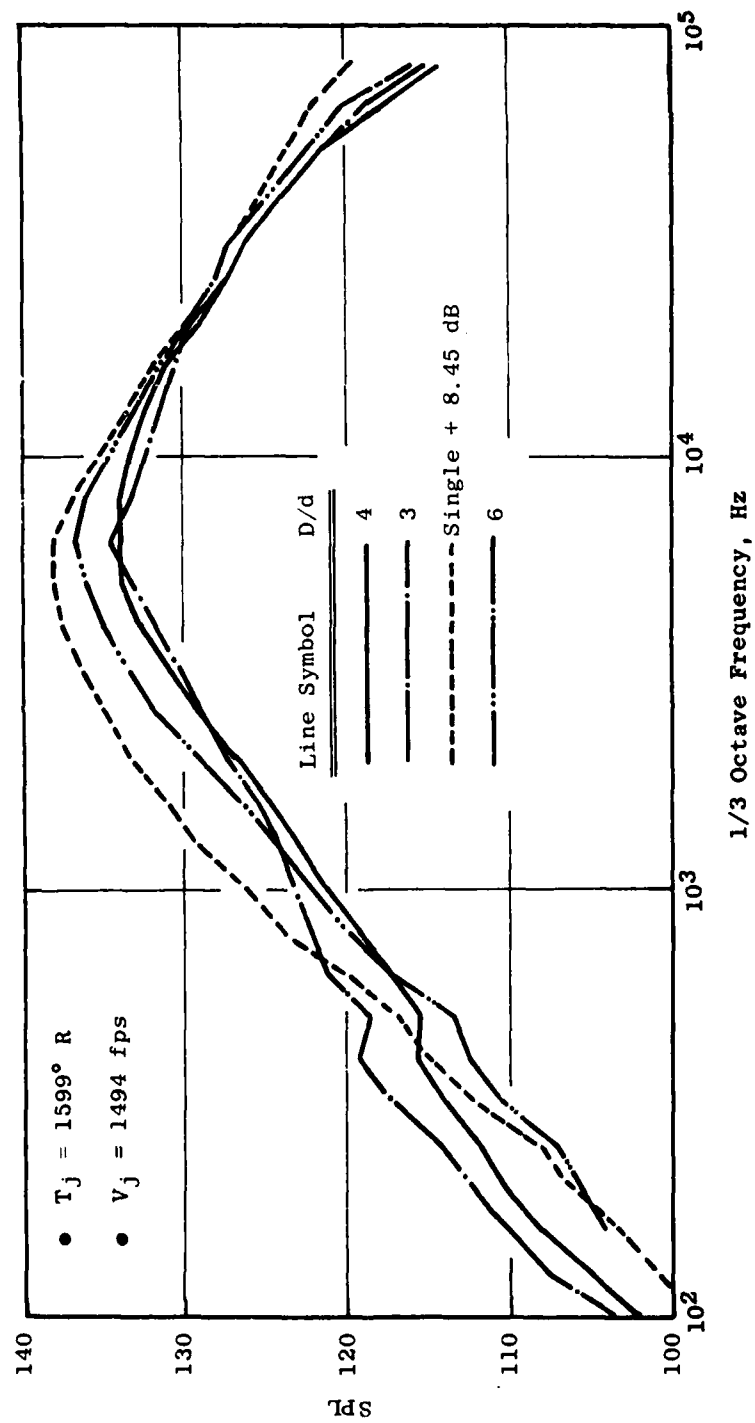


Figure 5-89. PWL Spectra, Effect of Spacing, 7-Tube Subsonic.

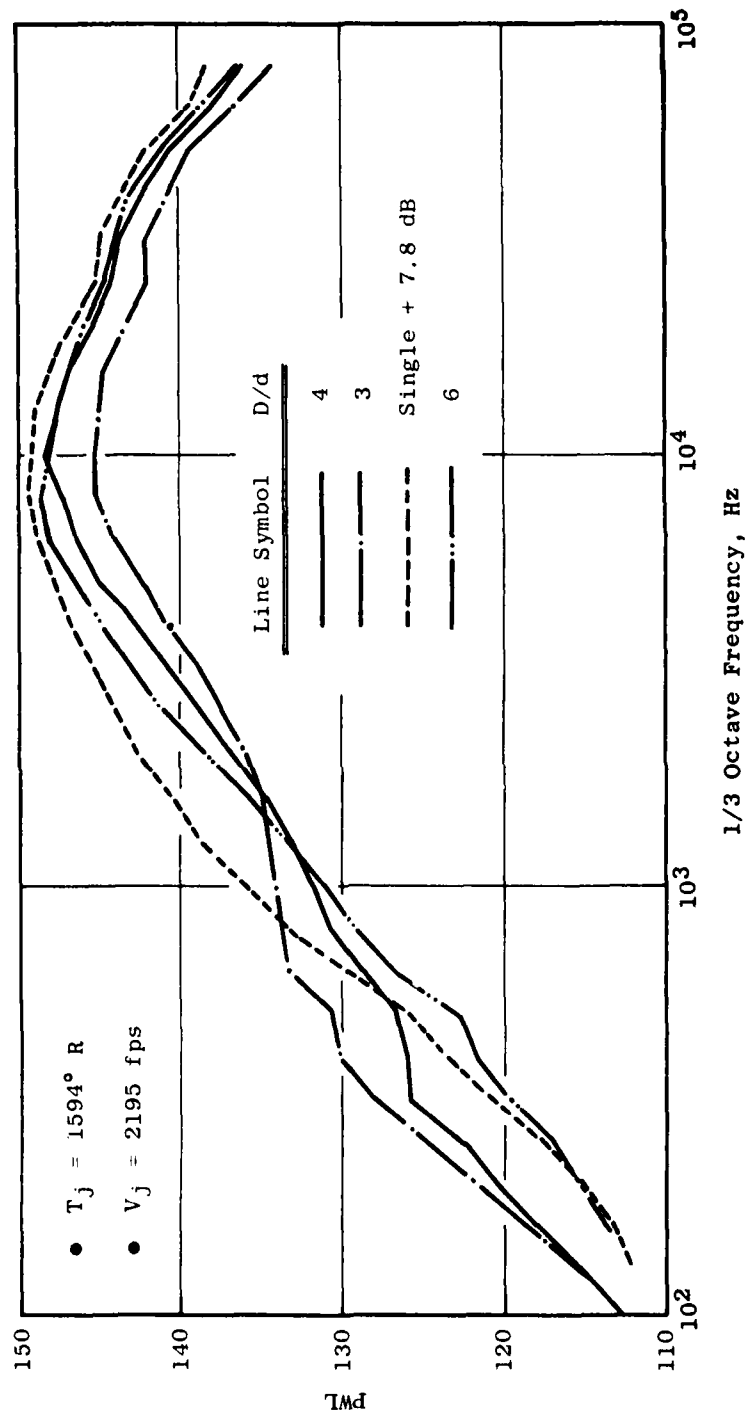


Figure 5-90. PWL Spectra, Effect of Spacing, 6-Tube Supersonic.

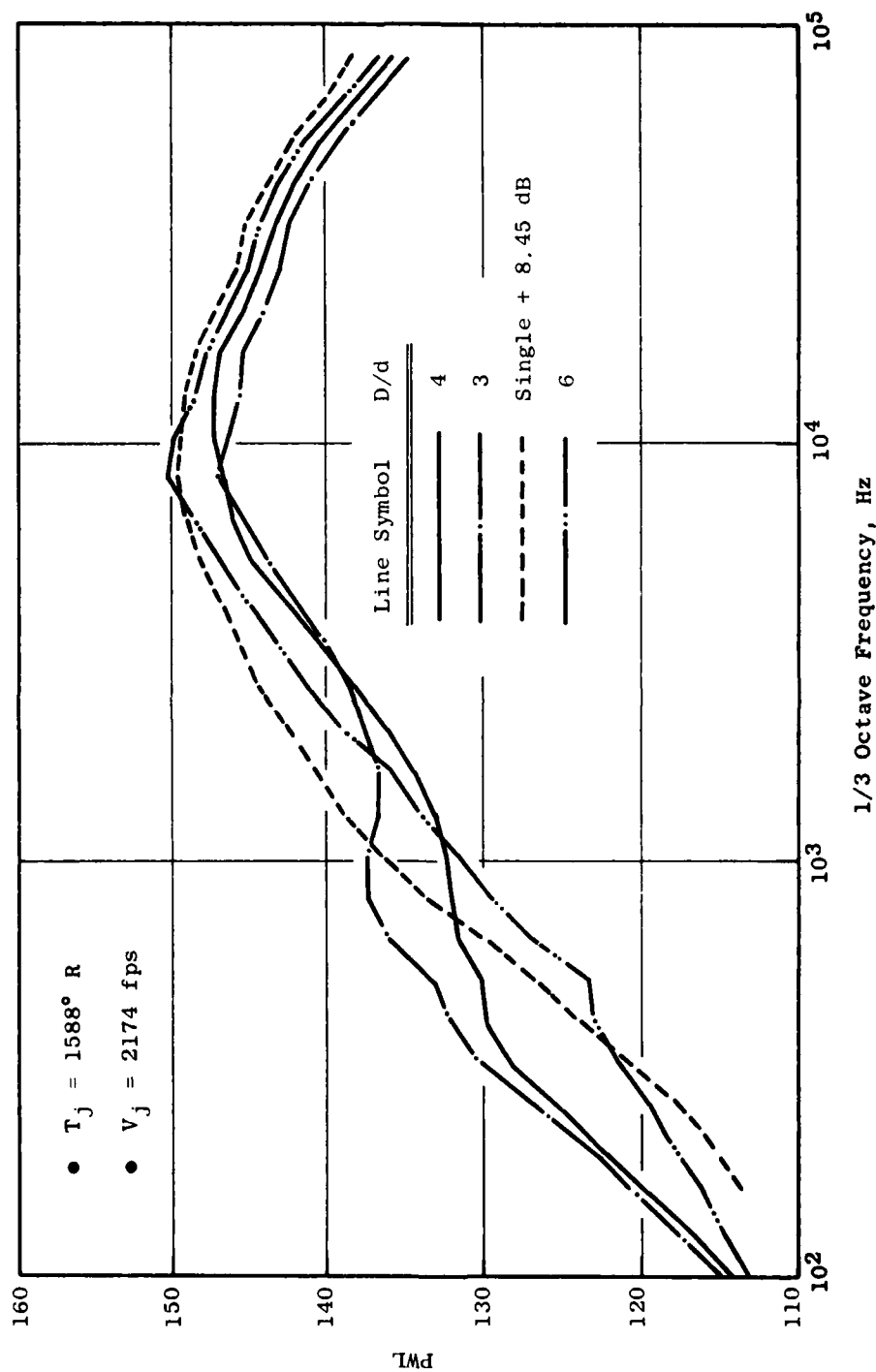


Figure 5-91. PWL Spectra, Effect of Spacing, 7-Tube Supersonic.

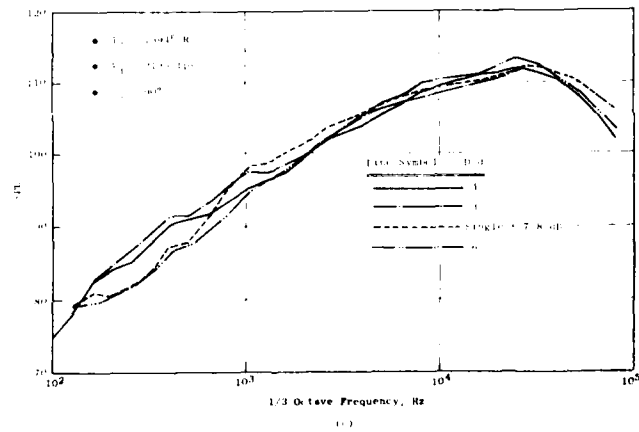
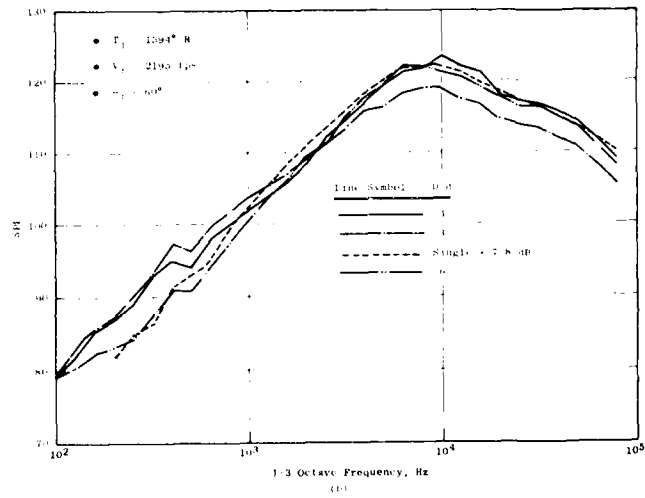
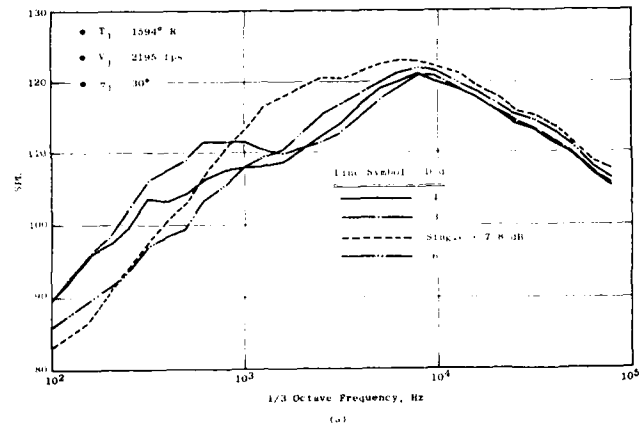


Figure 5-92. SPL Spectra, Effect of Spacing, 6-Tube.

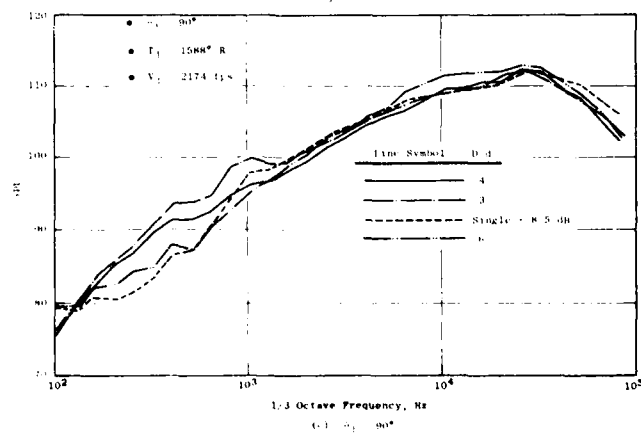
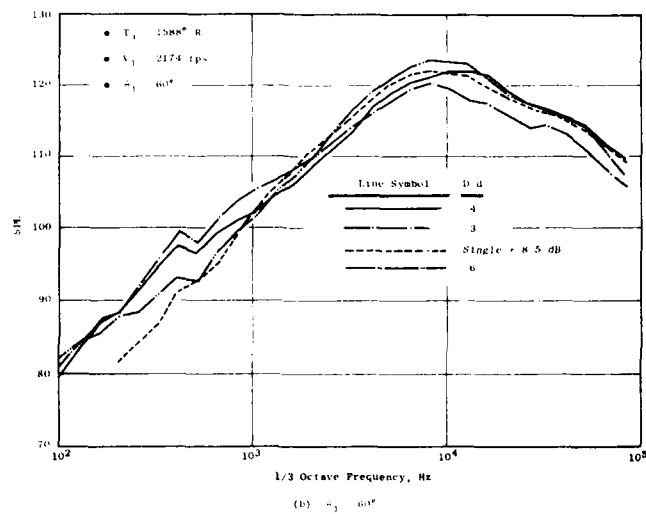
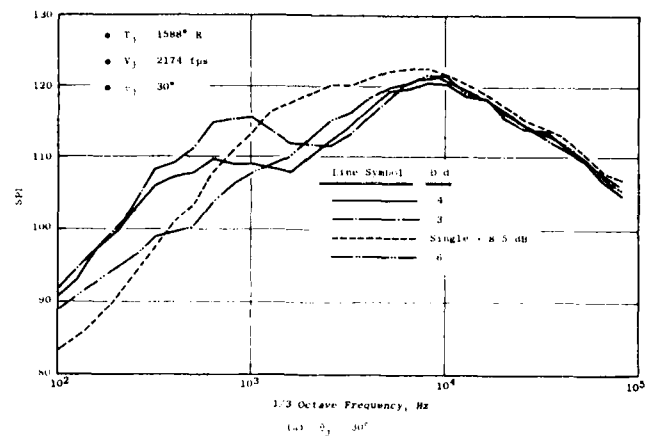


Figure 5-93. SPL Spectra, Effect of Spacing, 7-Tube.

To determine the effect of jet temperature on low frequency noise, the SPL spectra at $\theta_j = 30^\circ$ for the small cluster is compared to that of an equivalent area single round jet. This has been done at several velocities and jet temperatures on Figures 5-94 and 5-95. In general, the jet temperature has very little effect. For the case of $V_j = 1000$ fps (Figures 5-94, 5-95a, and 5-96a), raising the jet temperature from ambient to 1600° R had remarkably little effect on the low frequency excess noise. The velocity is clearly the dominant influence (a steady increase in the amount of excess low frequency noise occurs with increasing velocity on Figures 5-95 and Figure 5-96d).

5.6.4 Summary

The results of this investigation show that the noise reduction attained by heating a high velocity flow is reduced as the cluster becomes more compact.

Azimuthal directivity effects were found to be quite small, with the largest measured difference in OASPL only ≈ 2.5 dB. Acoustic shielding does not appear to produce very significant effects with six- and seven-tube circular clusters.

The most dramatic changes occur at frequencies below the peak intensity, and exhibited a very consistent trend with frequency and with tube spacing. At low frequencies, the tightly packed clusters produce large amounts of excess noise. At higher frequencies (still below the peak) significant attenuation occurred for the most tightly packed clusters. The low frequency excess noise is also relatively independent of jet temperature, and increases with jet velocity.

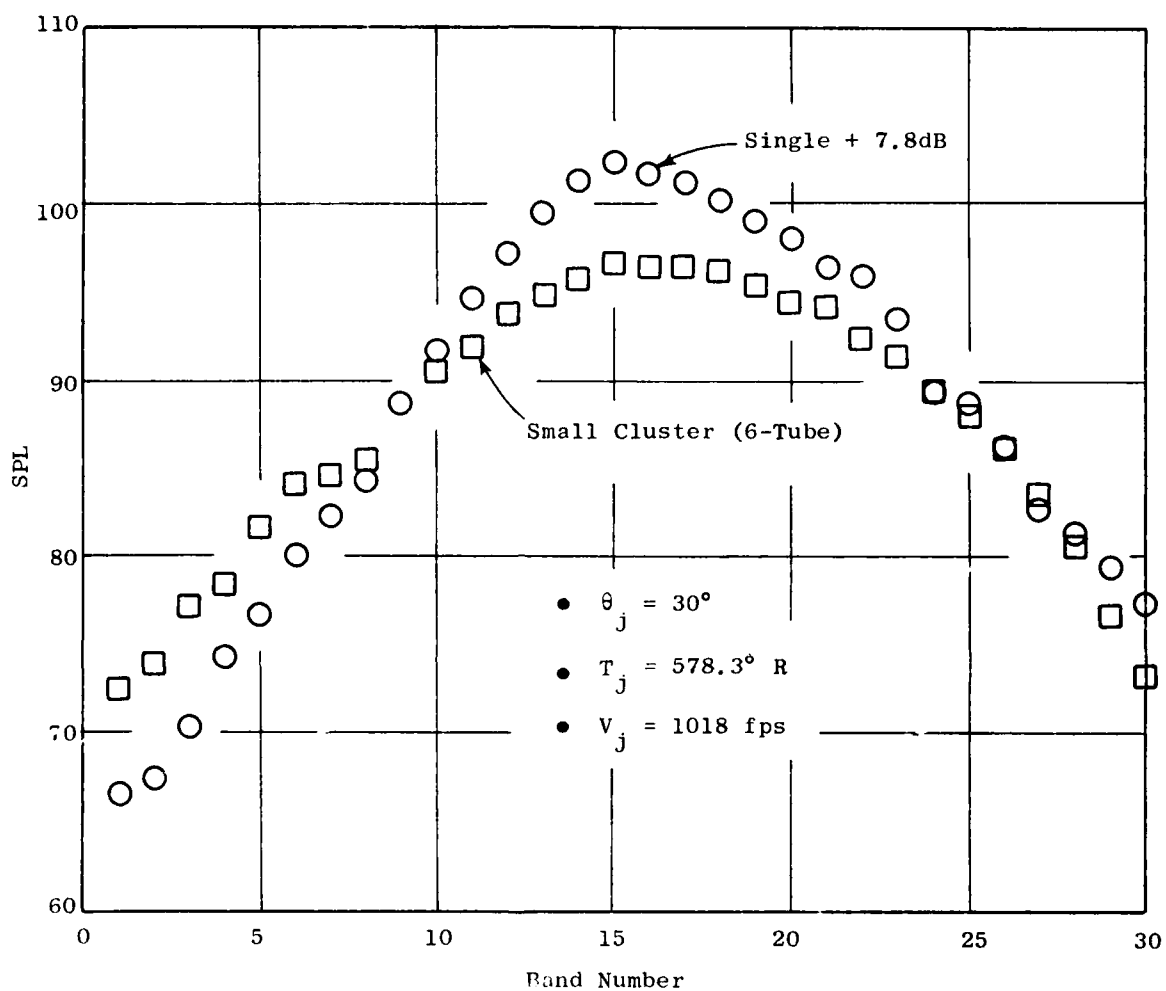


Figure 5-94. SPL Spectra, 6-Tube, $D/d = 3$, Cold, Subsonic.

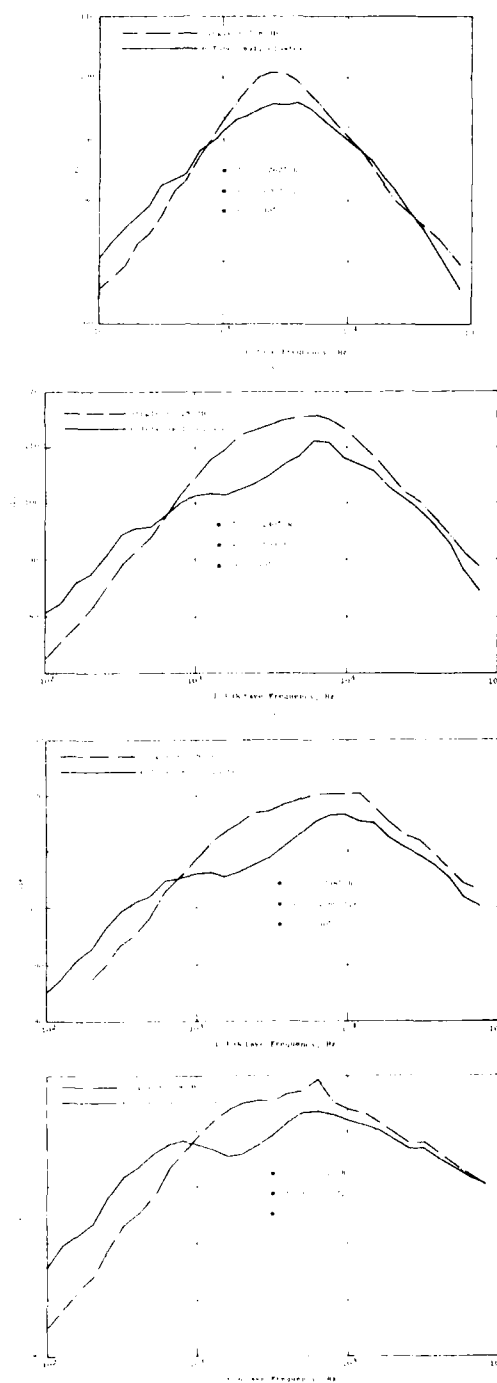
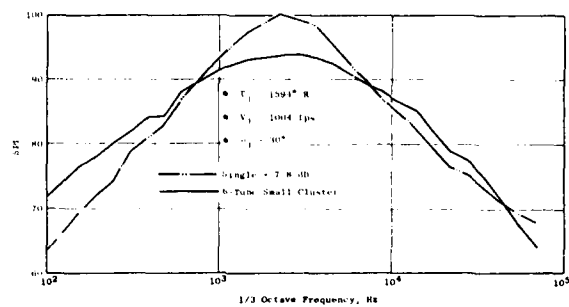
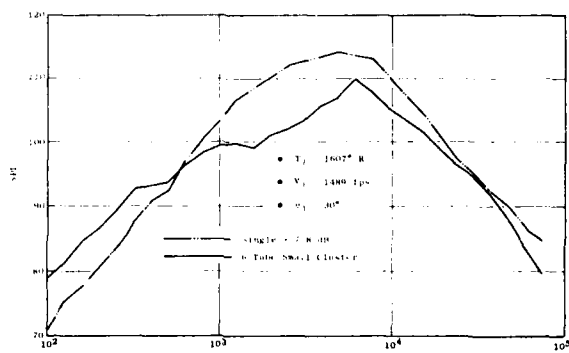


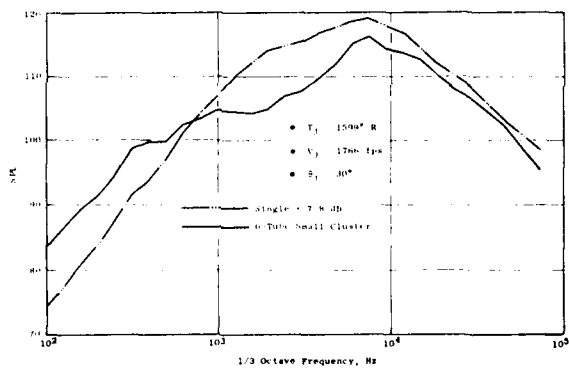
Figure 5-95. SPL Spectra, 6-Tube, $D/d = 3$.



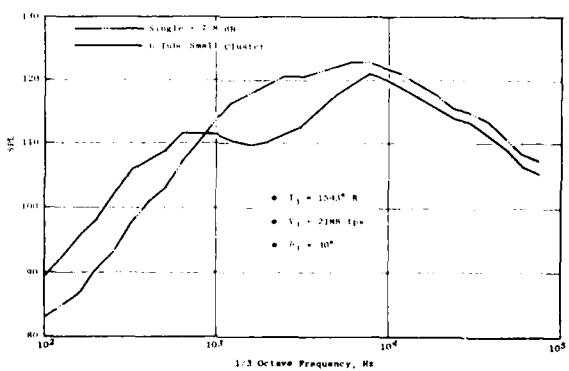
(a) $T_1 = 1594^\circ \text{ R}$, $V_1 = 1004 \text{ ips}$



(b) $T_1 = 1607^\circ \text{ R}$, $V_1 = 1480 \text{ ips}$



(c) $T_1 = 1590^\circ \text{ R}$, $V_1 = 1700 \text{ ips}$



(d) $T_1 = 1543^\circ \text{ R}$, $V_1 = 2188 \text{ ips}$

Figure 5-96. SPL Spectra, 6-Tube, $D/d = 3$.

5.7 LASER VELOCIMETER MEASUREMENTS

5.7.1 Calibration of the LV System

The laser velocimeter (LV) system described in Section 3.4 was checked against well-documented, hot-wire measurements obtained in a Mach 0.3 subsonic jet exhaust. The calibration flow used was a 19.05 mm diameter room temperature air jet. LV measurements of mean velocity and turbulence intensity in both radial and axial directions were obtained and are shown in Figures 5-97 and 5-98, respectively. The hot-wire measurements obtained in a similar Mach 0.3 jet by Lawrence⁽¹⁰⁴⁾ and Woolridge, et al.⁽¹⁰⁵⁾ are included in these figures for comparison. Very good agreement was obtained between the LV measurements and the hot-wire data. This calibration test demonstrated the capability and accuracy of the LV system for jet flow velocity and turbulence intensity measurement.

5.7.2 Experimental Results on Single Jets

Experimental results were obtained on the mean velocity and longitudinal turbulence intensity profiles of jet plumes from single round and single rectangular nozzles. Two temperature conditions of the jet flow were tested (294 and 644 K) on each nozzle. A fixed pressure ratio of approximately 1.8 was employed on all tests to obtain a fixed Mach number flow condition for the comparison of test results. The effects of temperature and nozzle geometry on jet noise source modification are deduced from the test results.

Due to limitations in the LV system capability at the time of the experiments reported in Section 5.7, no time dependent turbulence measurements were made during this effort. Nor was two component capability available at the time of the experiments. Hence longitudinal spectra, scale length and transverse turbulence measurements were not made.

5.7.2.1 Round Jets

Axial mean velocity and turbulence intensity distributions along the jet centerline are shown in Figure 5-99. The reference velocities \bar{U}_0 used in the figure were 303 and 448 m/sec for stagnation jet temperatures of 294 and 644 K, respectively. The mean velocity profiles from the jets at the two temperature conditions appear to be similar (the mean velocity profile shown in Figure 5-98 from a 19.05 mm diameter nozzle (Mach 0.3 flow) can be shown to be similar to the profiles in Figure 5-99. The effect of temperature on mean velocity decay along the jet axis appears insignificant. Similar profiles hold for a wide range of subsonic Mach number jet flows. Very similar profiles were obtained also independent of the temperature of the jets for the turbulence intensity distributions. A maximum turbulence intensity of approximately 16% was obtained 10 nozzle exit diameters downstream. Similar observations have been reported by other investigators [Lawrence⁽¹⁰⁴⁾]. The potential core was found to extend about six nozzle diameters downstream on the jet axis (this also agrees with Lawrence).

Radial velocity profiles of the single round jet are shown in Figures 5-100 through 5-106 at various downstream stations from the nozzle exit. Similar velocity profiles were obtained for flows at 294 and 644 K temperature conditions. Maximum turbulence intensity occurs at the lip location (0.5 nozzle diameters radially outward) at two and six nozzle diameters

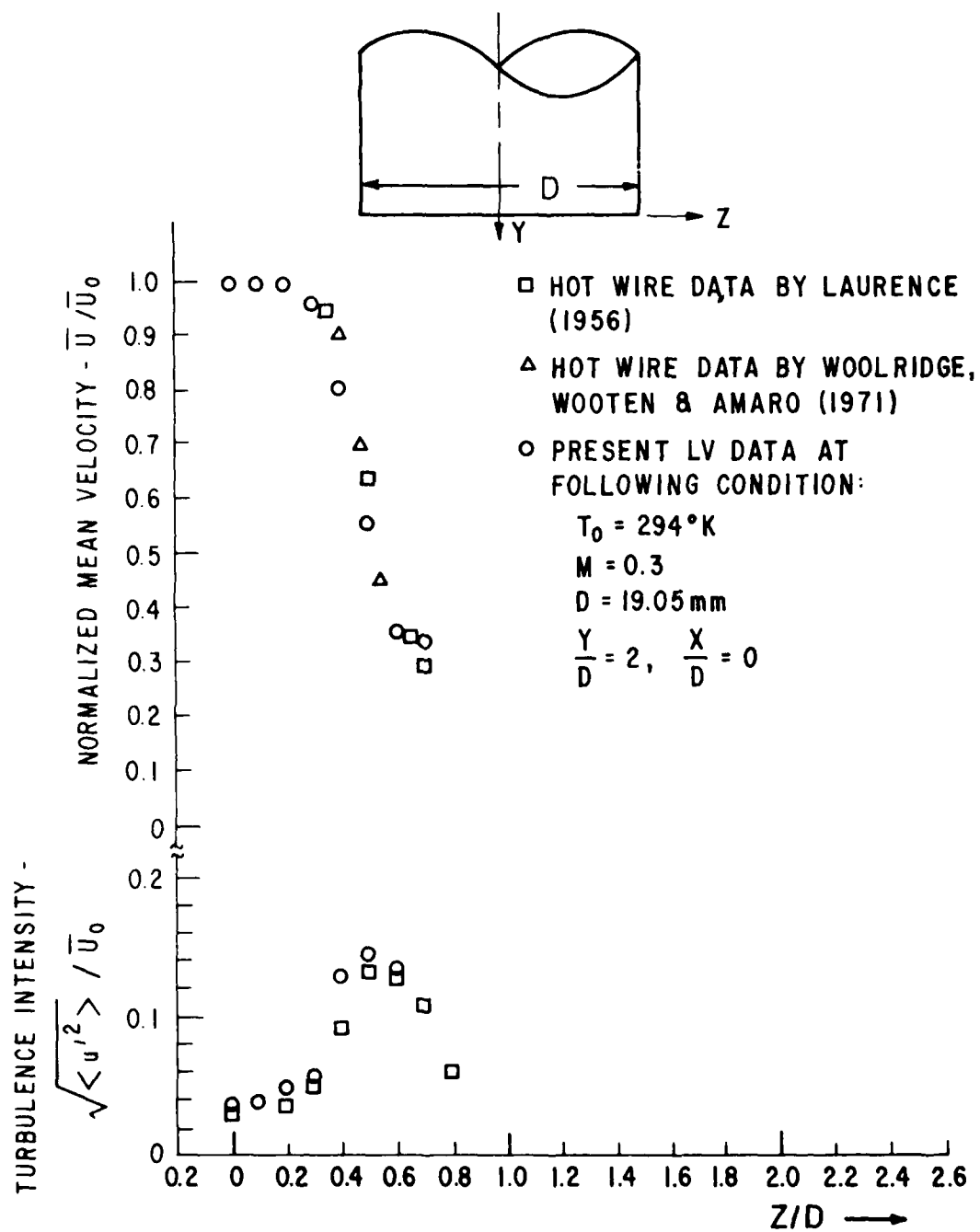


Figure 5-97. Radial Velocity and Turbulence Profiles of LV Calibration Jet Test Results ($D = 19.05$ mm).

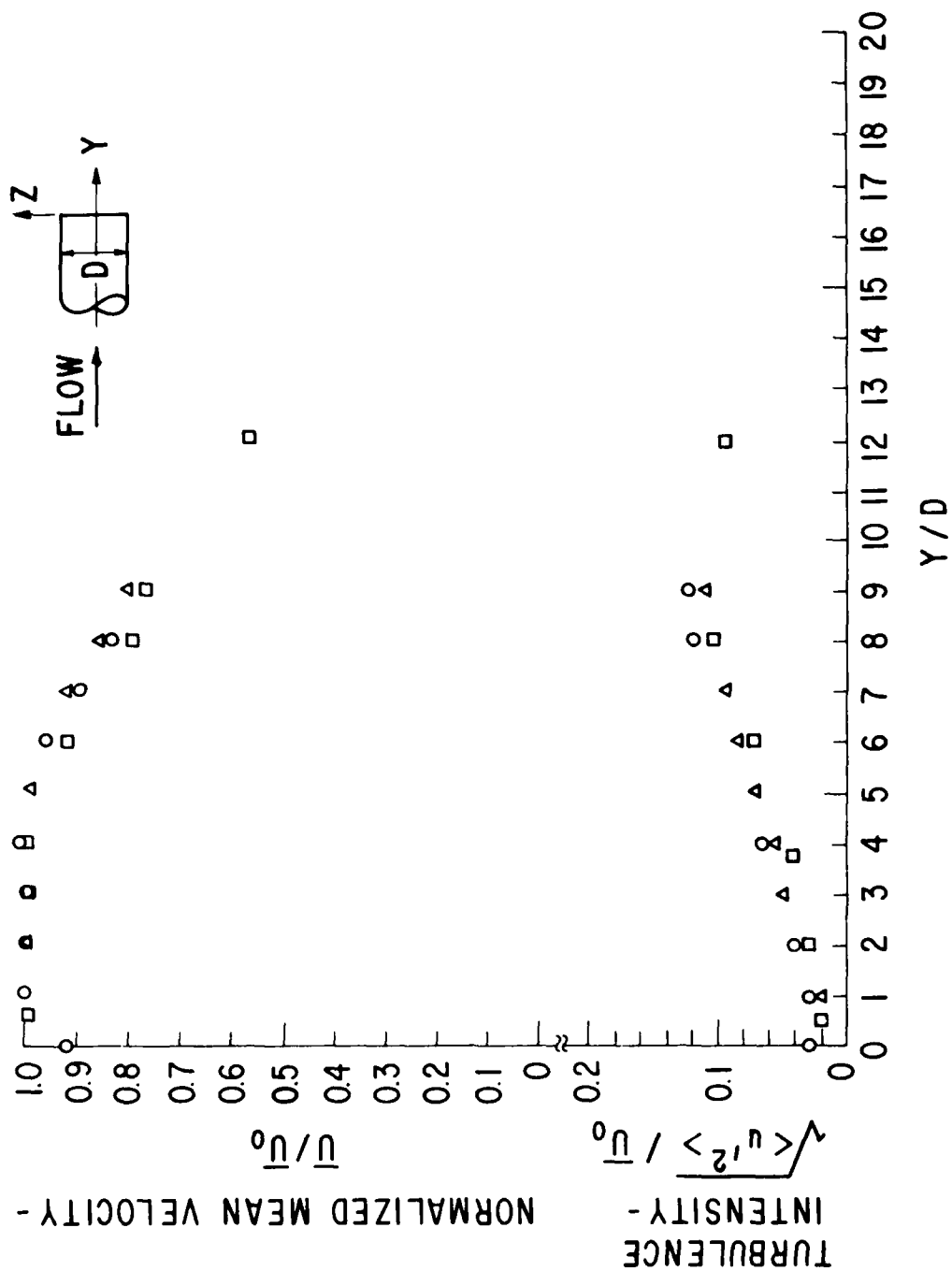


Figure 5-98. Axial Velocity and Turbulence Profiles of LV Calibration Jet Results ($D = 19.05$ mm).

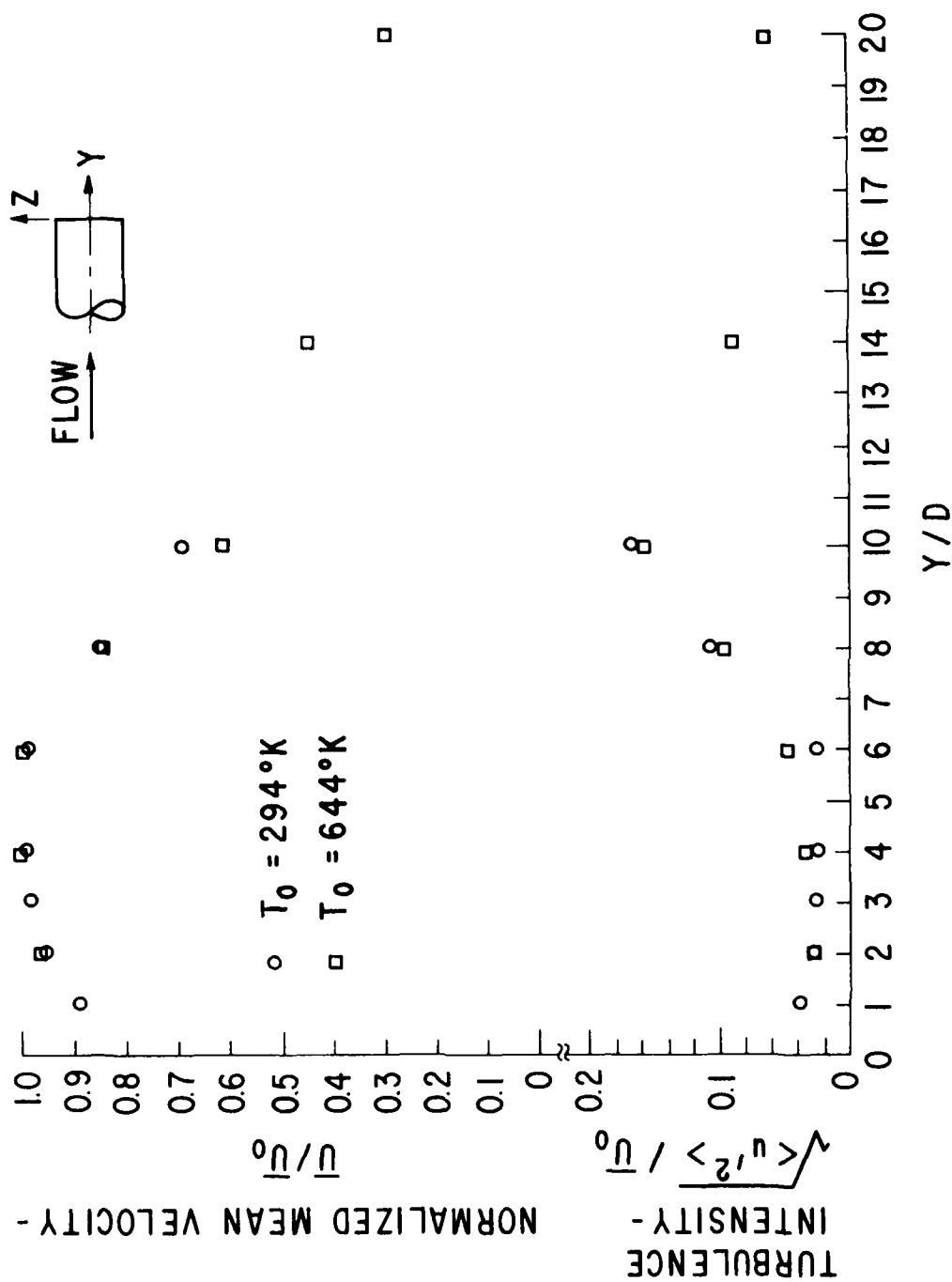


Figure 5-99. Axial Velocity Profiles of a Round Jet ($M = 0.967$, $D = 38.1 \text{ mm}$).

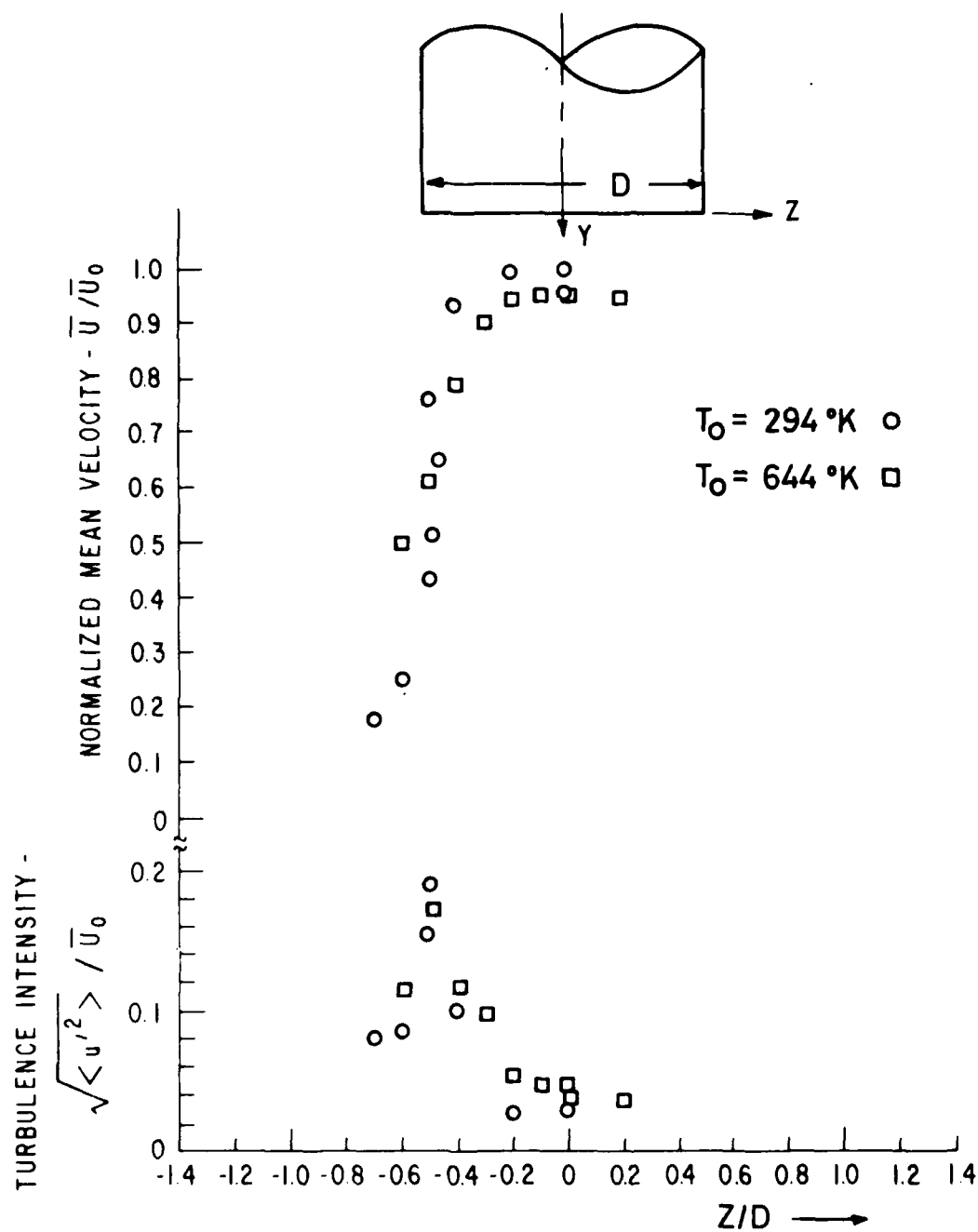


Figure 5-100. Radial Velocity Profiles of a Round Jet at $Y/D = 2$ ($M = 0.967$, $D = 38.1$ mm).

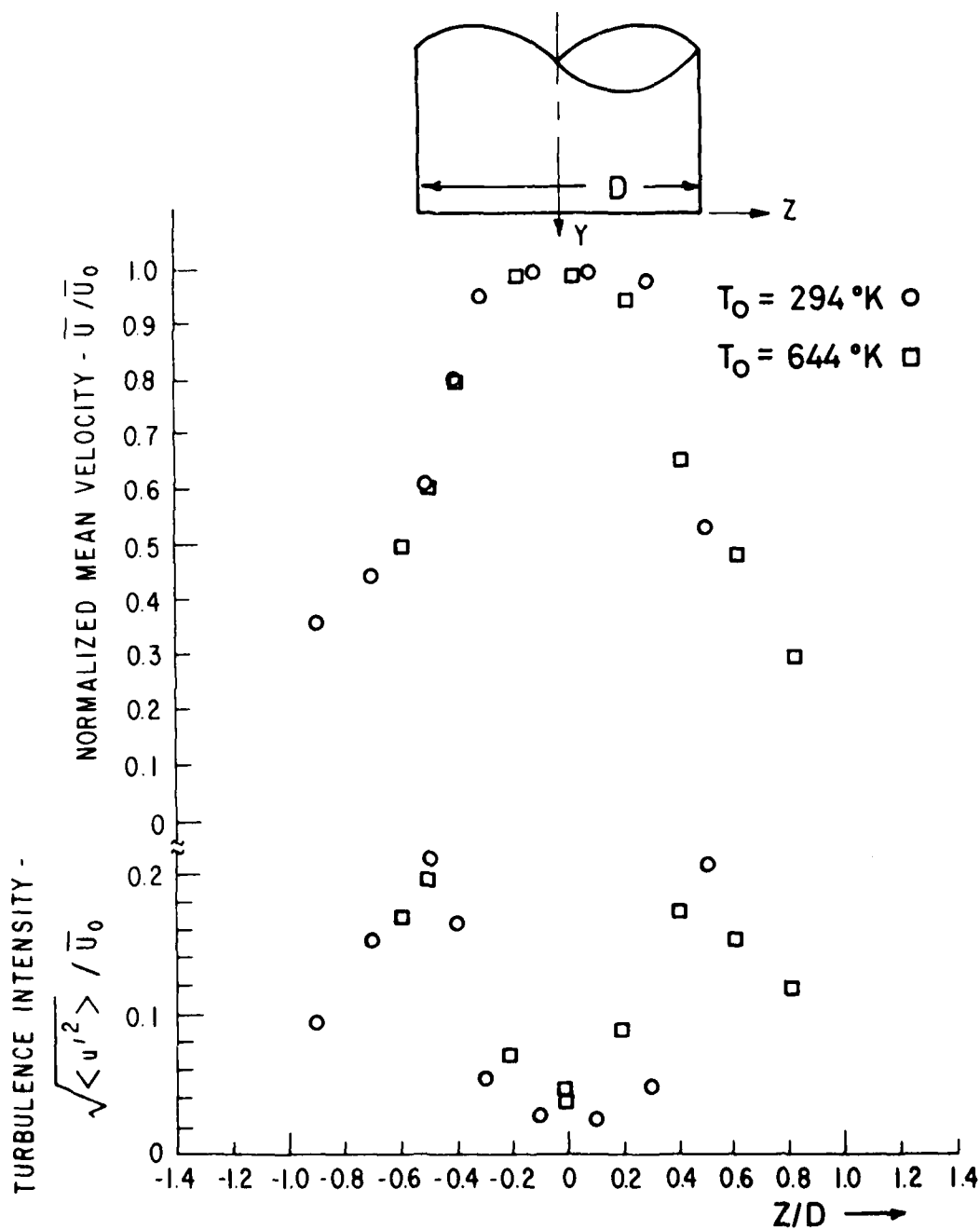


Figure 5-101. Radial Velocity Profiles of a Round Jet at $Y/D = 6$ ($M = 0.967$, $D = 38.1$ mm).

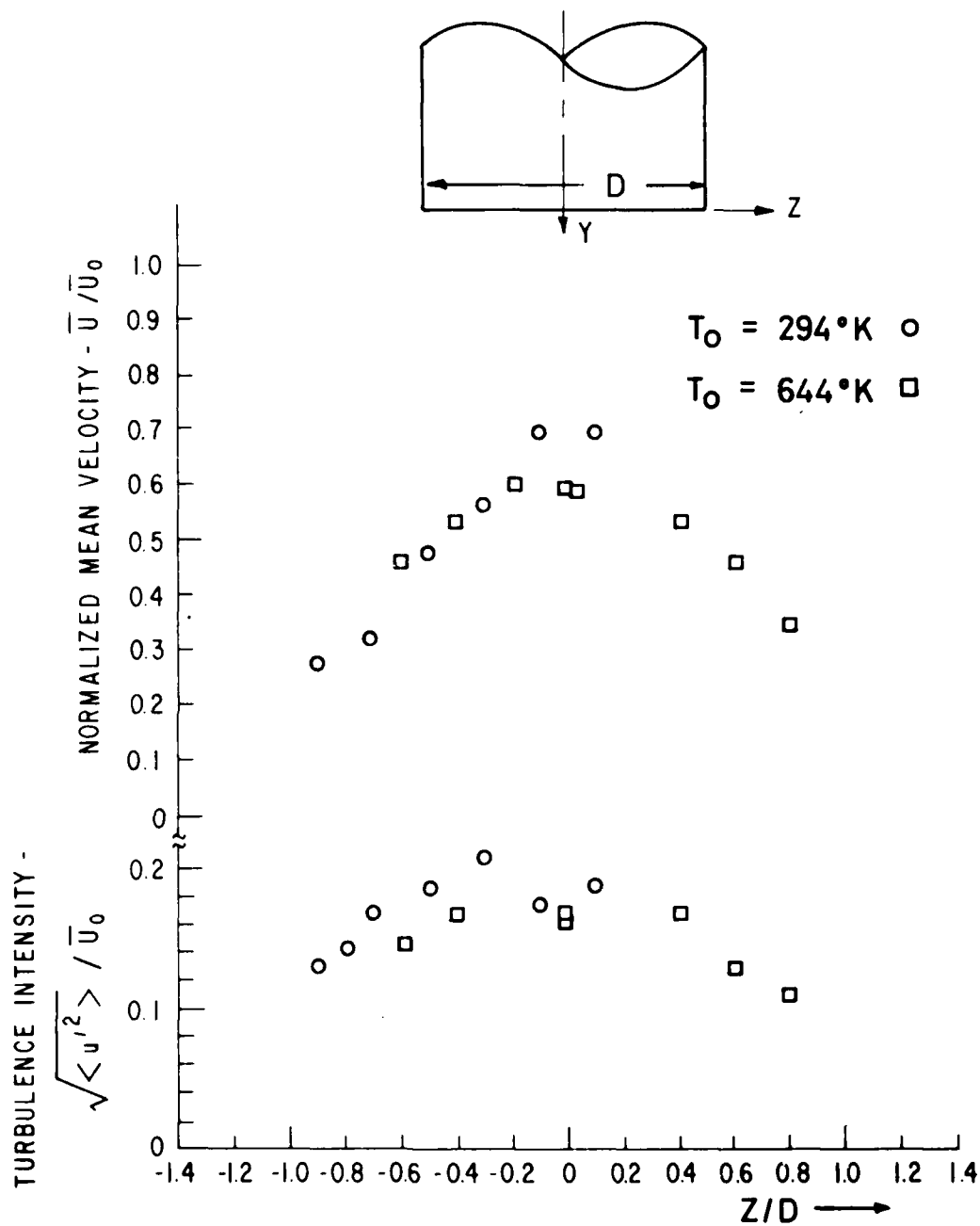


Figure 5-102. Radial Velocity Profiles of a Round Jet at $Y/D = 10$
($M = 0.967$, $D = 38.1$ mm).

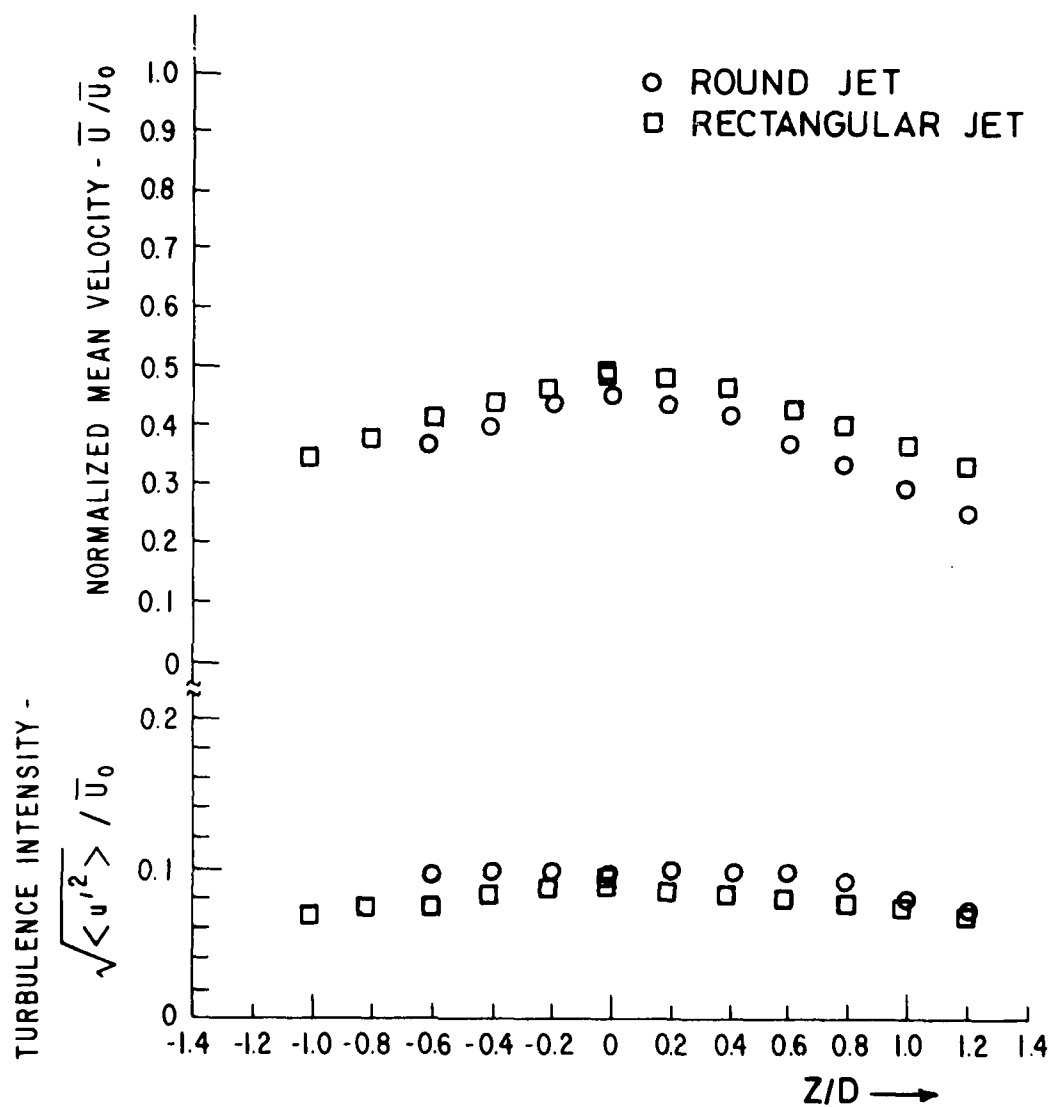


Figure 5-103. Radial Velocity Profiles of a Round and a Rectangular Jet at $Y/D = 14$ ($M = 0.967$, $D = 38.1$ mm).



Figure 5-104. Single Rectangular Jet Configuration.

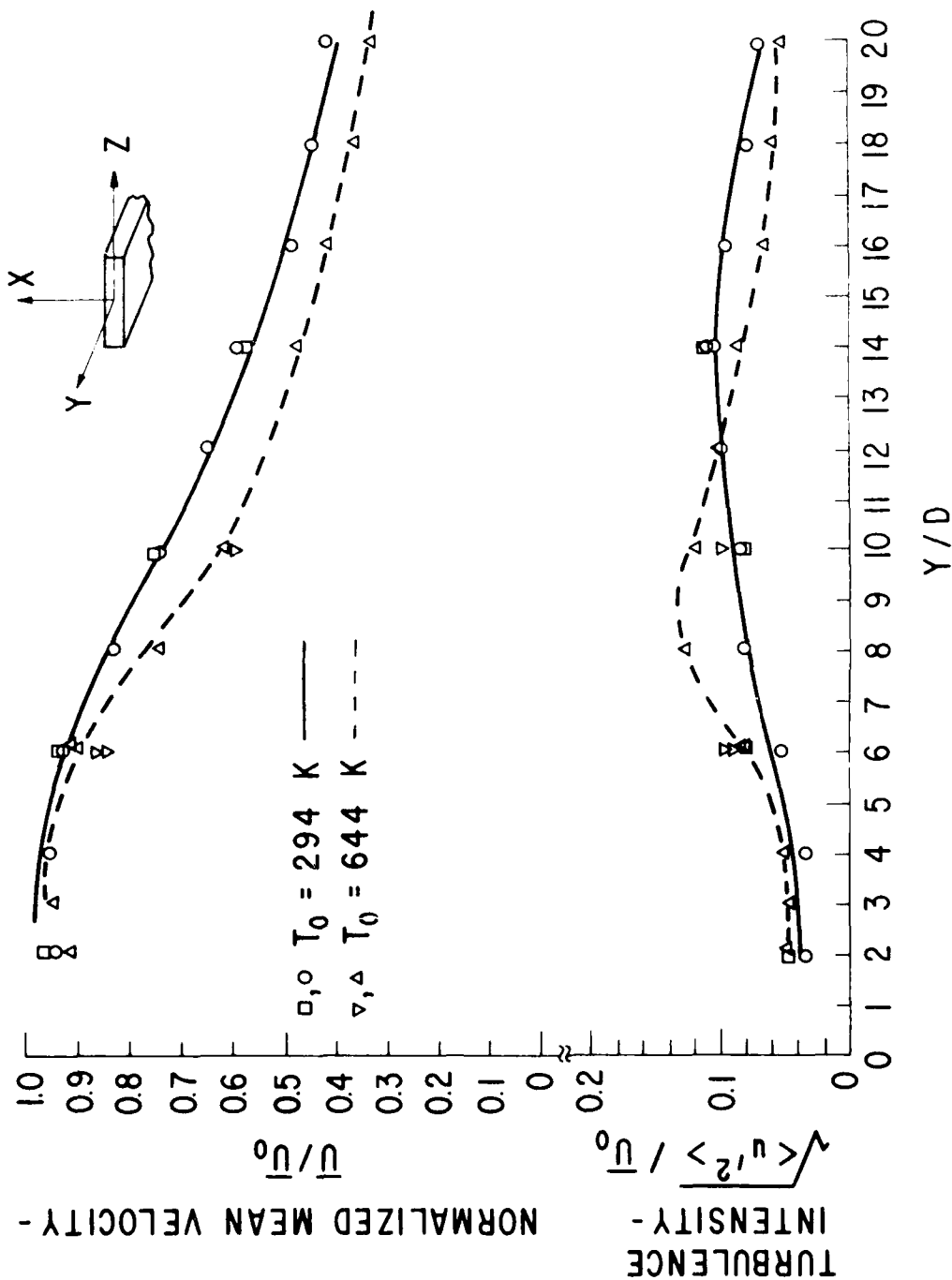


Figure 5-105. Axial Velocity Profile of a Rectangular Jet ($M = 0.967$, $D = 38.1 \text{ mm}$).

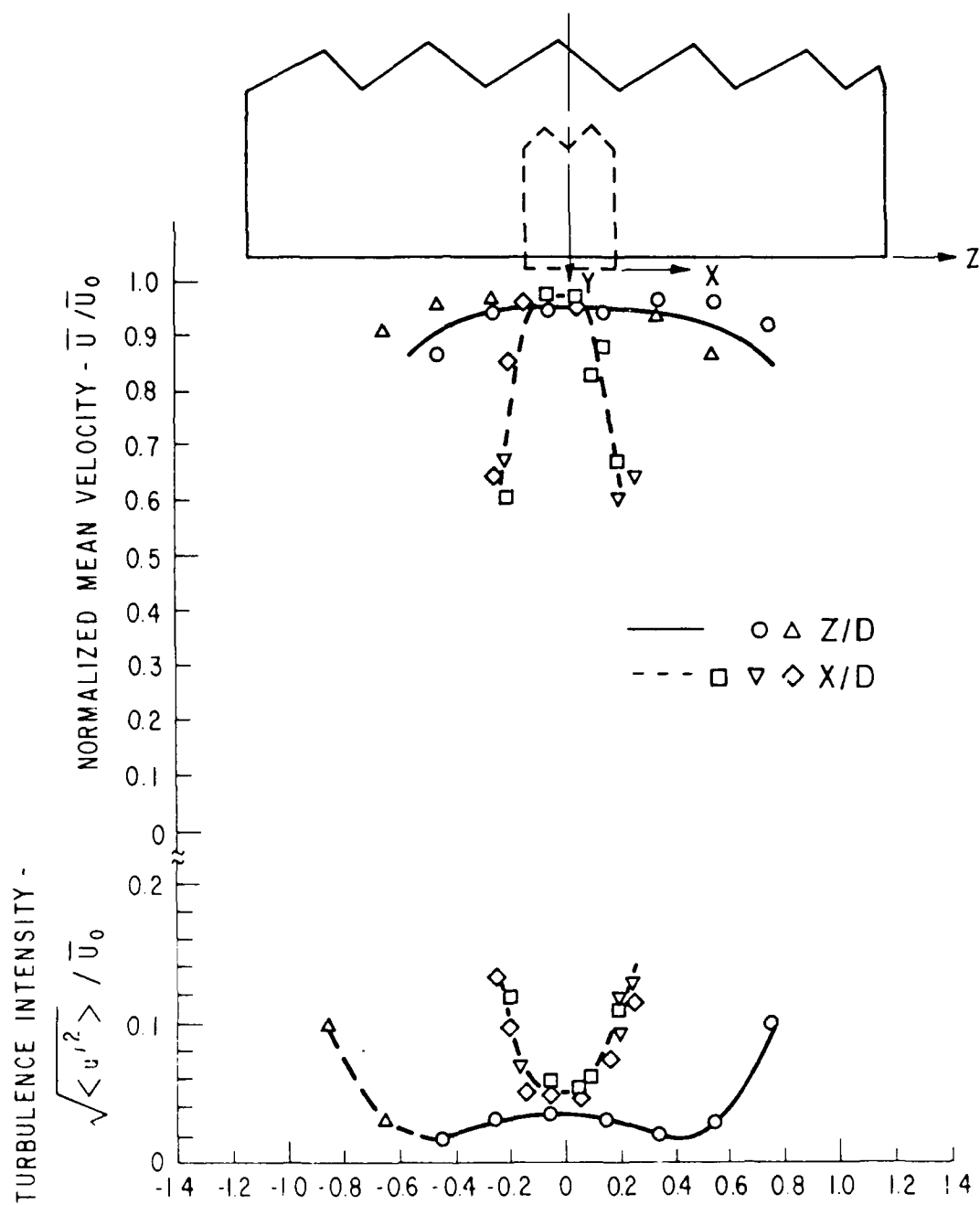


Figure 5-106. Transverse Velocity Profiles of a Rectangular Jet at $Y/D = 2$ ($T_0 = 294$ K, $\bar{U}_0 = 303$ m/s, $D = 38.1$ mm).

AD-A094 291

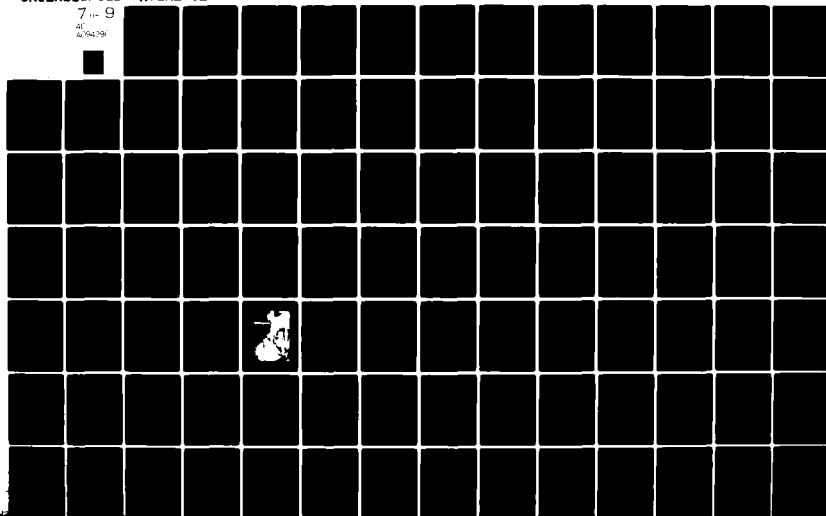
GENERAL ELECTRIC CO CINCINNATI OH AIRCRAFT ENGINE GROUP F/B 20/1
HIGH VELOCITY JET NOISE SOURCE LOCATION AND REDUCTION. TASK 2. --ETC(U)
MAY 78 T F Balsa, P R GLIEBE, R A KANTOLA DOT-05-30034
R78AE9323 FAA-RD-76-79-2 NL

UNCLASSIFIED

7-9

AL

62-794-79



downstream. At 10 diameters downstream, the radial location of the maximum turbulence intensity is shifted toward the center of the jet. The turbulence intensity is a maximum on the jet axis at 14 diameters downstream where a fully turbulent flow is developed (as shown in Figure 5-103). The maximum turbulence intensity at 2, 6, and 10 diameters downstream appears to be higher in the LV measurements than in the conventional hot-wire measurements. This may be attributed to the "noise" contained in the LV velocity histogram. This "noise" was found generally far away from the bulk of the histogram data on the velocity scale and is believed due to the imperfection of the validation test in the LV processor. No special data treatment or smoothing technique was performed on the histograms in the data analysis procedure.

5.7.2.2 Rectangular Jets

The single rectangular jet configuration is shown in Figure 5-104. Axial velocity distributions along the jet centerline are shown in Figure 5-105*. The reference diameter, D , used in this figure and in other data on the following figures is the equivalent diameter based on the exit area of the nozzle, i.e., 38.1 mm.** The mean velocity profile of the hot jet (644 K) appears to decay faster than that of the room temperature jet (294 K). The length of the potential core of the hot jet is shorter than that of the room temperature jet based on mean velocity and turbulence intensity profiles. A peak turbulence intensity of approximately 14% exists eight equivalent diameters downstream for the hot jet. A more gradual increase in turbulence intensity with axial distance downstream from the nozzle exit is observed for the room temperature jet. A peak value of turbulence intensity of 12% exists along the jet centerline 14 diameters downstream for the room temperature jet. These observations agree with those from transverse velocity profiles (to be described next), suggesting that the hot rectangular jet plume spreads out faster than does the room temperature jet plume.

Transverse velocity profiles of the rectangular jets are shown in Figures 5-109 through 5-114. The mean velocity and turbulence intensity data recorded along both the major (Z) axis and the minor (X) axis at a fixed downstream location from the jet exit are presented on each figure. The physical dimensions of the rectangular nozzle with respect to the abscissa scale are sketched on top of each figure. The velocity profiles of the hot jet are more diffused than those of the room temperature jet, at the same axial locations (Figures 5-110, 5-111, 5-113, and 5-114). This is most apparent from the velocity profiles along the minor axis (Z) of the jets.

As discussed above, unlike the round jet, jet temperature affects the shape of the rectangular jet plume. Thus, the distribution of noise sources which are related to the turbulence in the jet flow change as the temperature of the jet changes. Preliminary data from the acoustic measurements on the rectangular jets at the two temperature conditions (Section 5.2) show some difference in the noise directivity pattern. Noise source modifications due to temperature may be one of the major causes of this difference.

* The solid and the dashed lines in Figures 5-105 through 5-111 are faired through the corresponding data groupings.

**The aspect ratio of the rectangular jet is 6:1.

575

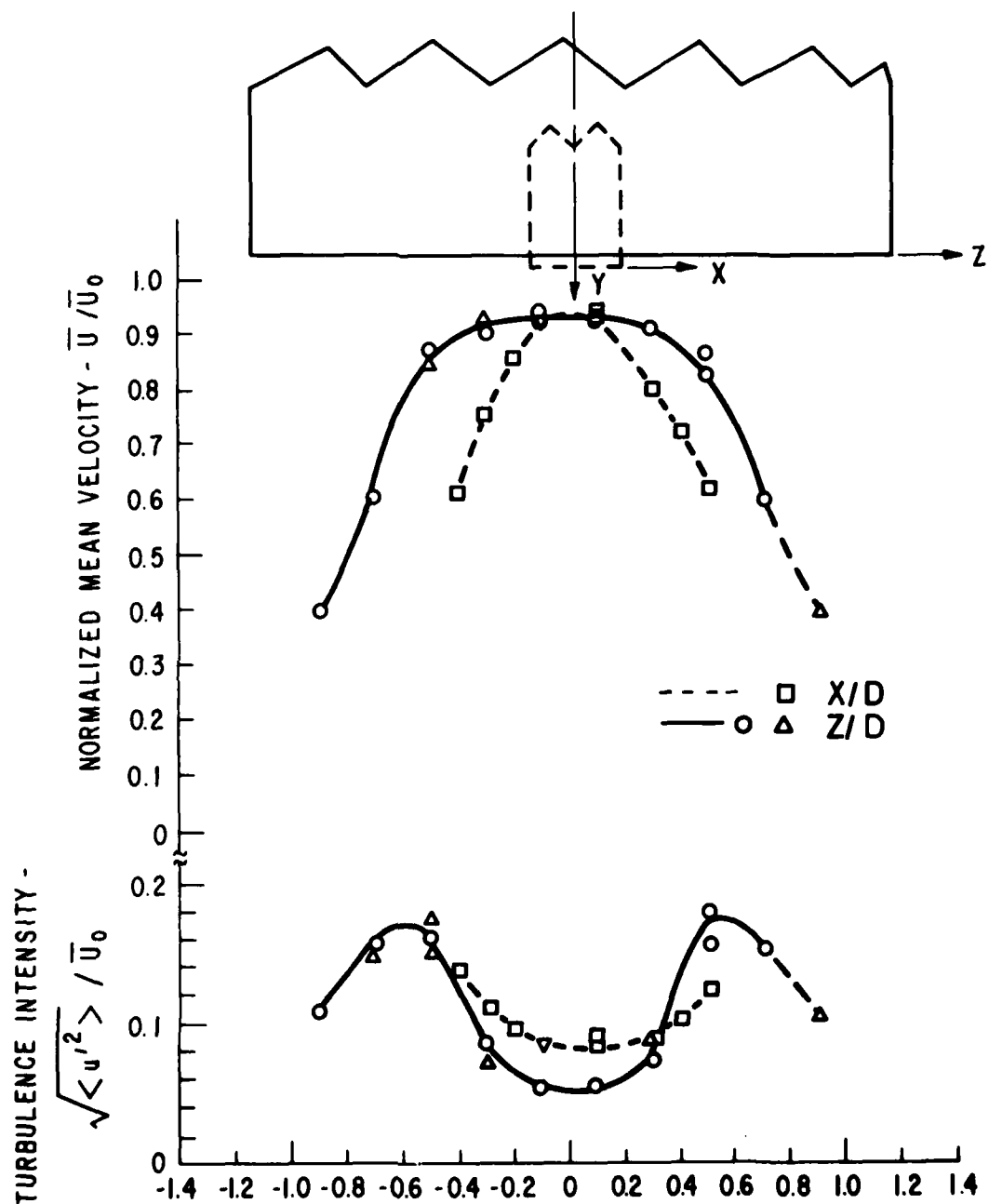


Figure 5-107. Transverse Velocity Profiles of a Rectangular Jet at $Y/D = 6$ ($T_0 = 294$ K, $\bar{U}_0 = 303$ m/s, $D = 38.1$ mm).

(57-

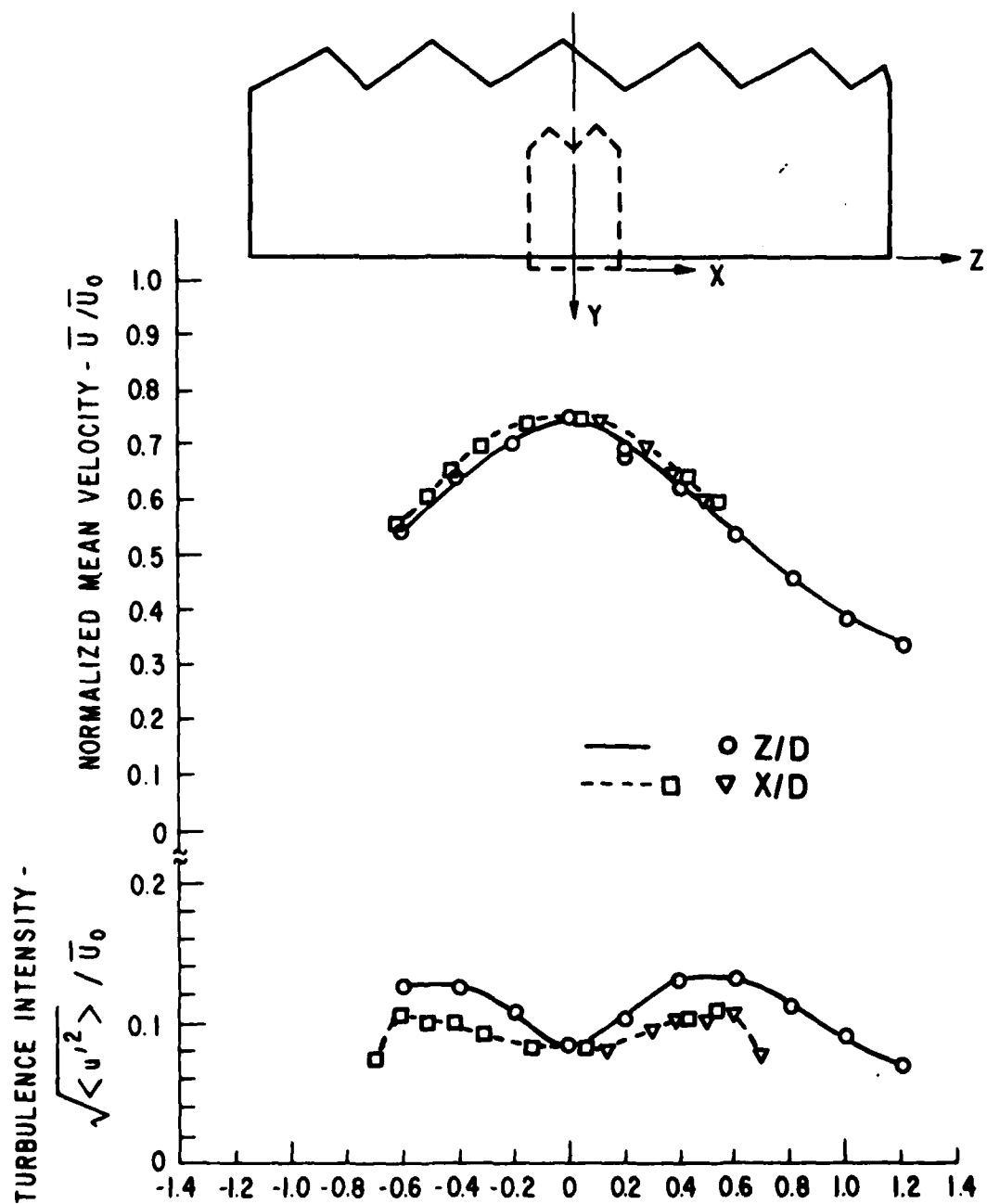


Figure 5-108. Transverse Velocity Profiles of a Rectangular Jet at $Y/D = 10$ ($T_0 = 294$ K, $\bar{U}_0 = 303$ m/s, $D = 38.1$ mm).

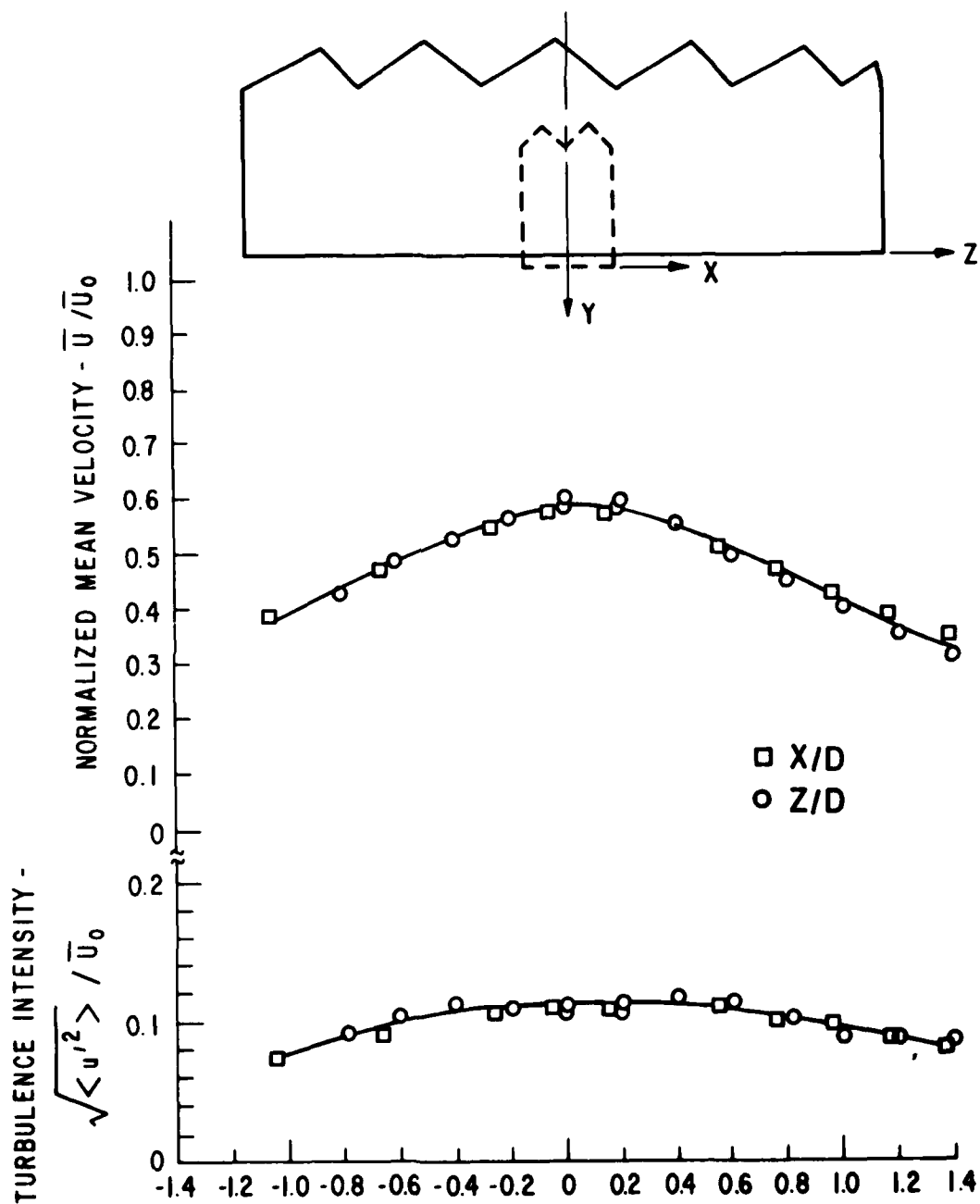


Figure 5-109. Transverse Velocity Profiles of a Rectangular Jet at $Y/D = 14$ ($T_0 = 294$ K, $\bar{U}_0 = 303$ m/s, $D = 38.1$ mm).

572

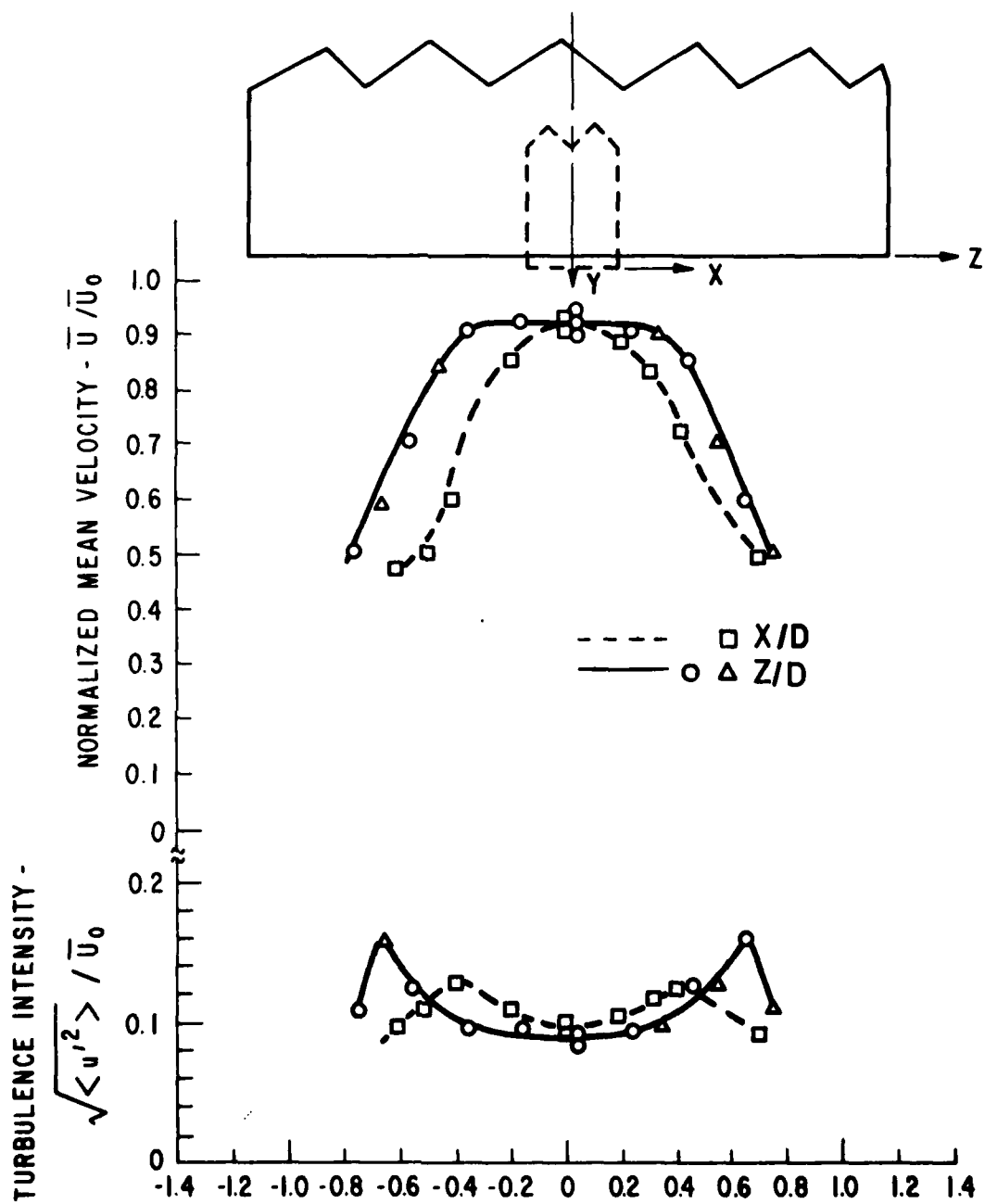


Figure 5-110. Transverse Velocity Profiles of a Hot Rectangular Jet at $Y/D = 6$ ($T_0 = 644$ K, $U_0 = 448$ m/sec, $D = 38.1$ mm).

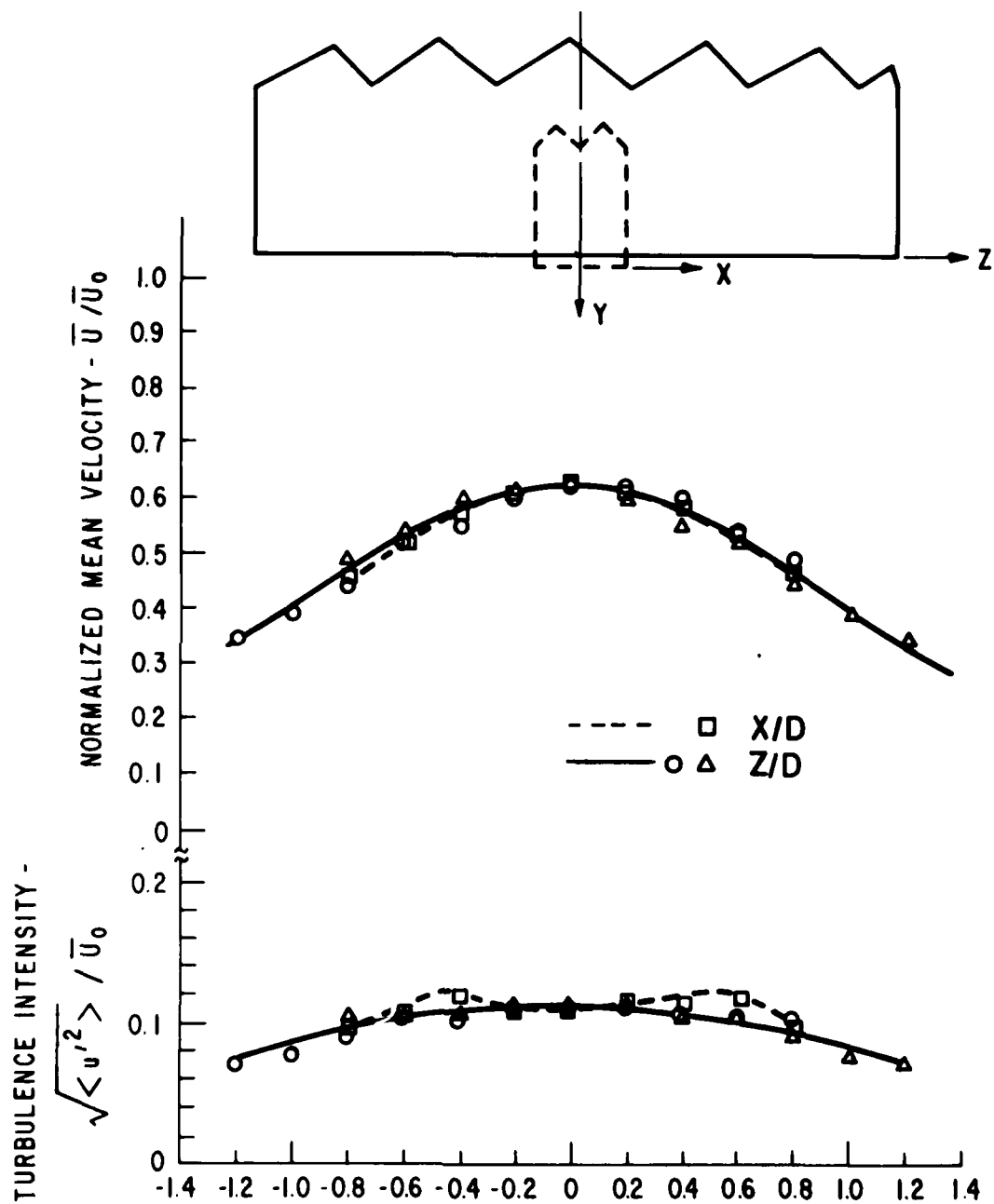
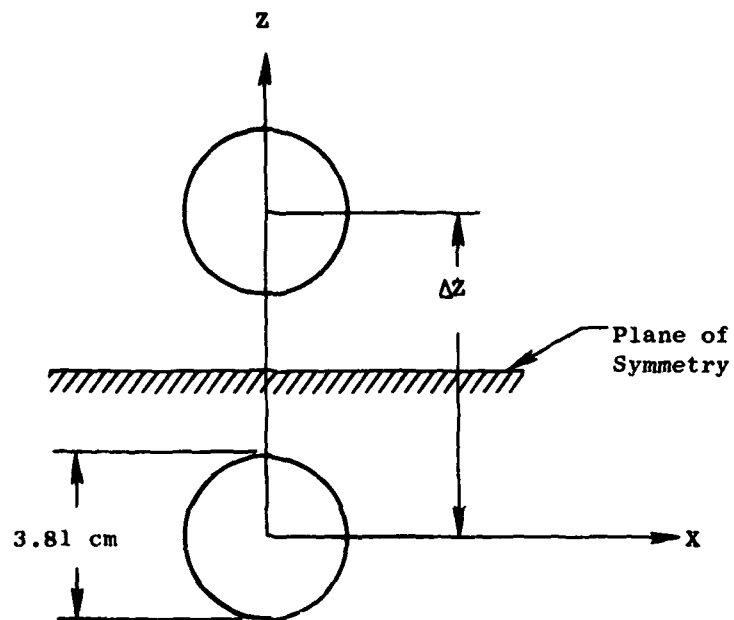
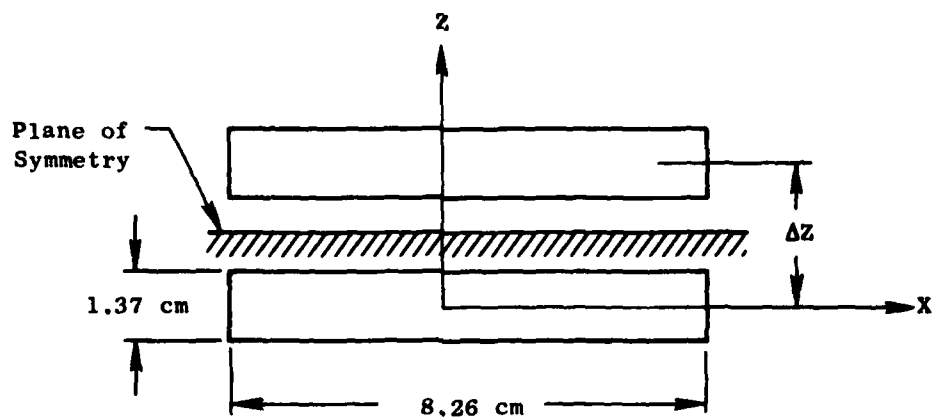


Figure 5-111. Transverse Velocity Profiles of a Hot Rectangular Jet at $Y/D = 10$ ($T_0 = 644$ K, $\bar{U}_0 = 448$ m/s, $D = 38.1$ mm).



(a) Twin-Round Jet Configuration



(b) Twin-Rectangular Jet Configuration

Figure 5-112. Twin-Jet Configurations and Coordinates.

581

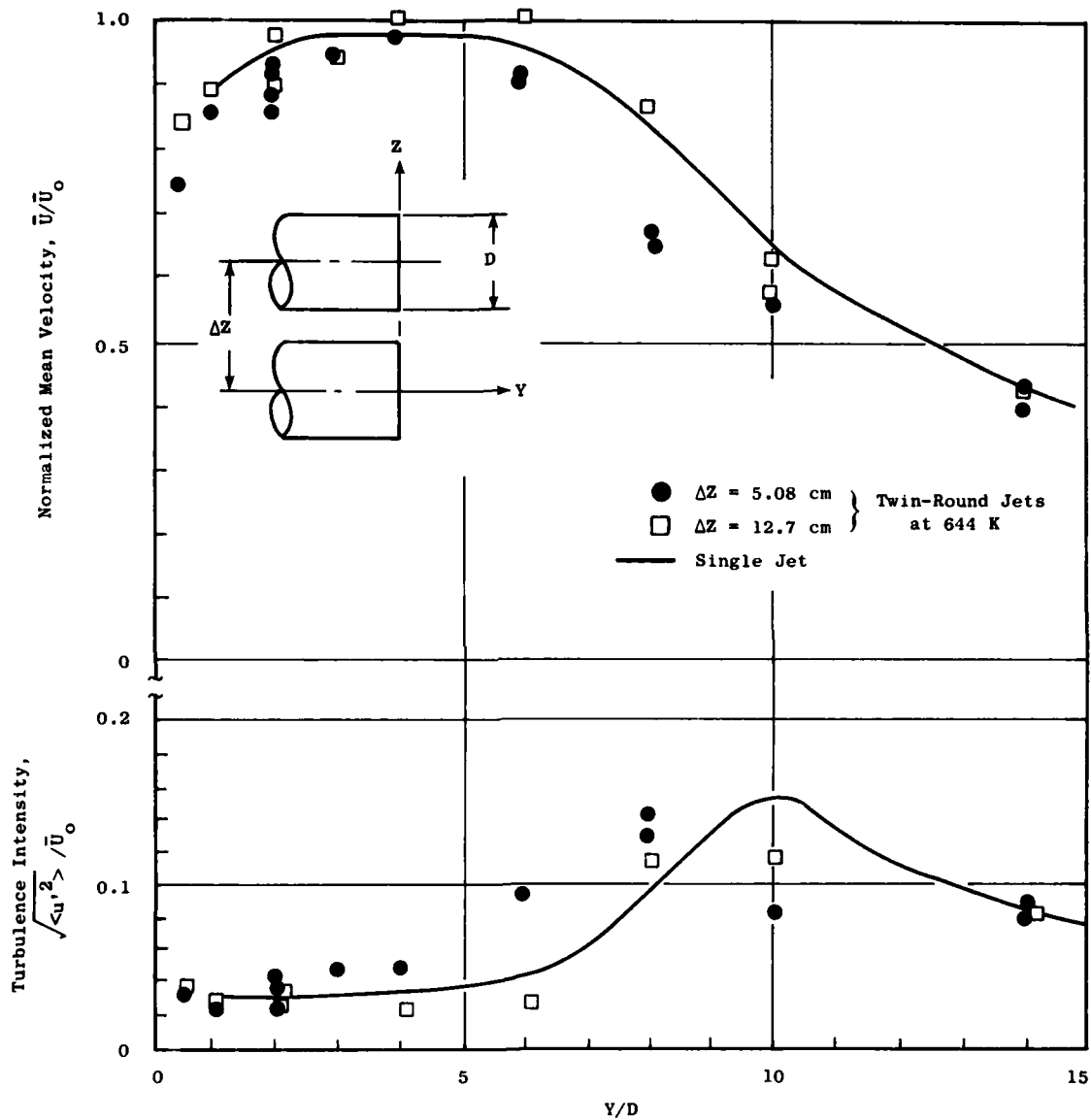


Figure 5-113. Axial Velocity Profiles Along the Centerline of one of the Twin-Round Jets ($T_o = 644$ K, $\bar{U}_o = 448$ m/s, $D = 38.1$ mm).

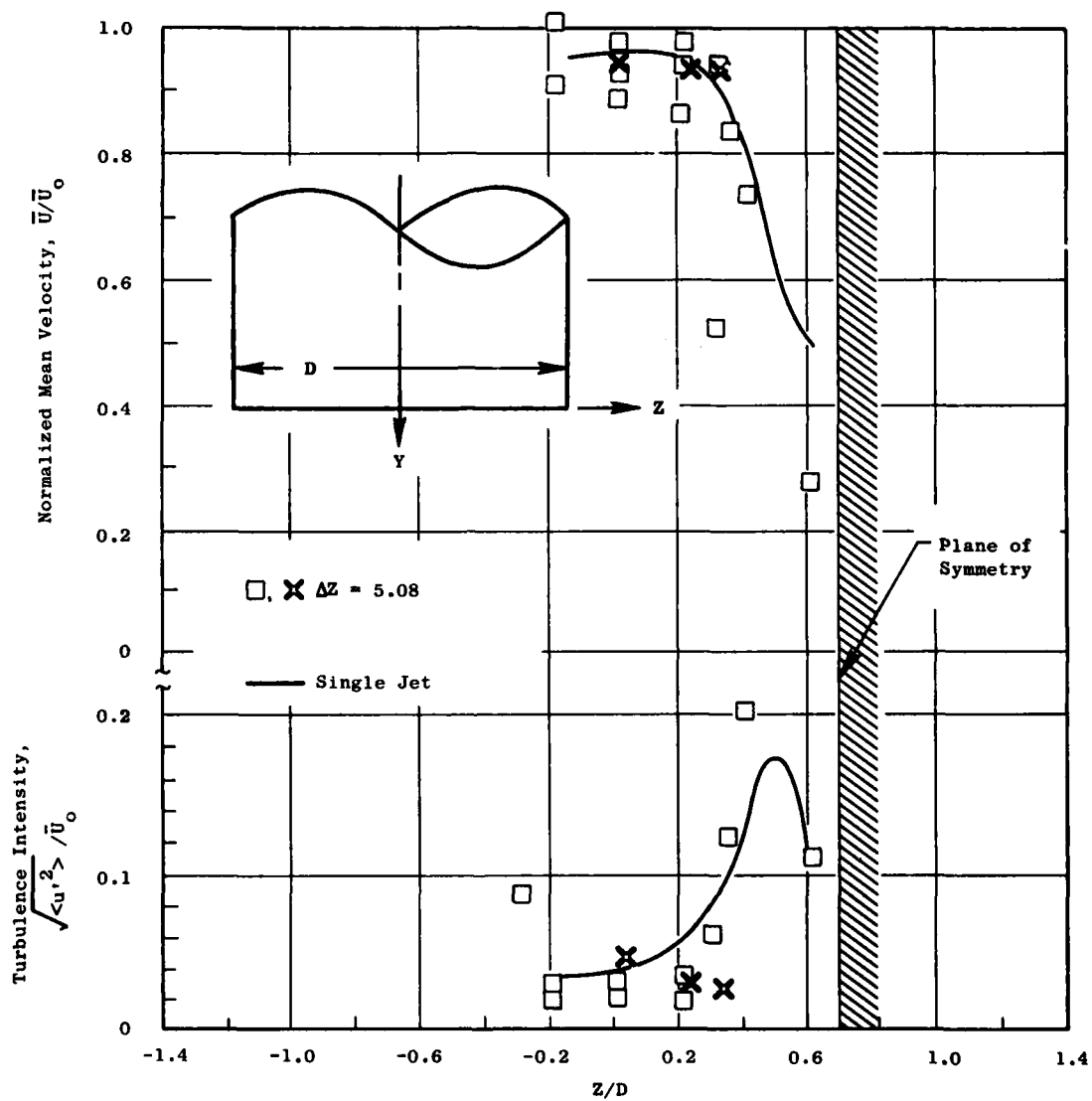


Figure 5-114. Radial Velocity Profiles of the Twin-Round Jets at $Y/D = 2$ ($T_0 = 644$ K, $\bar{U}_0 = 448$ m/s, $D = 38.1$ mm).

Transverse mean velocity and turbulence intensity profiles along the major and the minor axes for the rectangular jets were found to become similar far downstream of the nozzle exit, e.g., $Y/D = 10$ and 14 (Figures 5-108 and 5-109). At $Y/D = 14$, the velocity profiles from the rectangular jet were also very similar to those from the round jet at a temperature of 644 K (Figure 5-103). Therefore, the rectangular jet profile degenerates to that of a round jet around 10 equivalent diameters downstream of the nozzle.

The distribution of turbulence intensity in the rectangular jet (in the transverse directions) peaks near the edge of the jet plume, as in the round jet measurements. The size of the jet can be deduced from the location of the peak turbulence intensity in the transverse direction. From Figures 5-106 through 5-111, the physical size of the jet is generally smaller in the minor-axis direction than in the major axis direction, between the nozzle exit and 10 diameters downstream.

5.7.3 Experimental Results on Twin Jets

Profiles of the mean velocity and turbulence intensity of twin round and twin rectangular jet flows measured with the LV system are reported in this section. For the twin round jet configuration, two separation distances between jets were tested, i.e., $\Delta Z = 5\text{ cm}$ and 12.7 cm , as shown in Figure 5-112. Most data were taken with flows at 644 K , and a limited number of profiles were obtained with room temperature jets. For the twin rectangular jets, the distances between jets were 3.81 cm and 10.48 cm with wide sides parallel to each other (Figure 5-112). The temperature of the twin rectangular jet tests was also 644 K . A fixed pressure ratio of 1.8 was used for all twin round and twin rectangular jet tests. The characteristic length used for twin round jets was the diameter of the jet, and for the twin rectangular jets was the equivalent diameter based on the jet cross sectional area. Profiles of the single round and single rectangular jets described in Section 5.7.2 are included in the twin jet presentation for comparison.

5.7.3.1 Twin Round Jets

Figure 5-113 shows the axial mean velocity and turbulence intensity profiles along one of the twin jet centerlines at 644 K . The profiles of the twin jets at 12.7 cm separation appear to be very similar to those of a single round jet. However, both mean velocity and turbulence intensity of the twin jet at smaller separation distance, i.e., $\Delta Z = 5\text{ cm}$ deviate from those of a single round jet after six jet diameters downstream from the jet exit. It is logical that less interference occurs if two jets are separated by a larger distance. Referring to the profiles shown in Figure 5-113, two jets at 5 cm separation begin to merge at 6 to 8 jet diameters downstream of the nozzle exit. The twin round jet at 12.7 cm separation still behaves as two independent round jets, even at 14 jet diameters downstream.

Radial profiles of mean velocity and turbulence intensity along the vertical axis passing through both jet centerlines are shown in Figures 5-114 through 5-117. The plane of symmetry shown in these figures indicates the

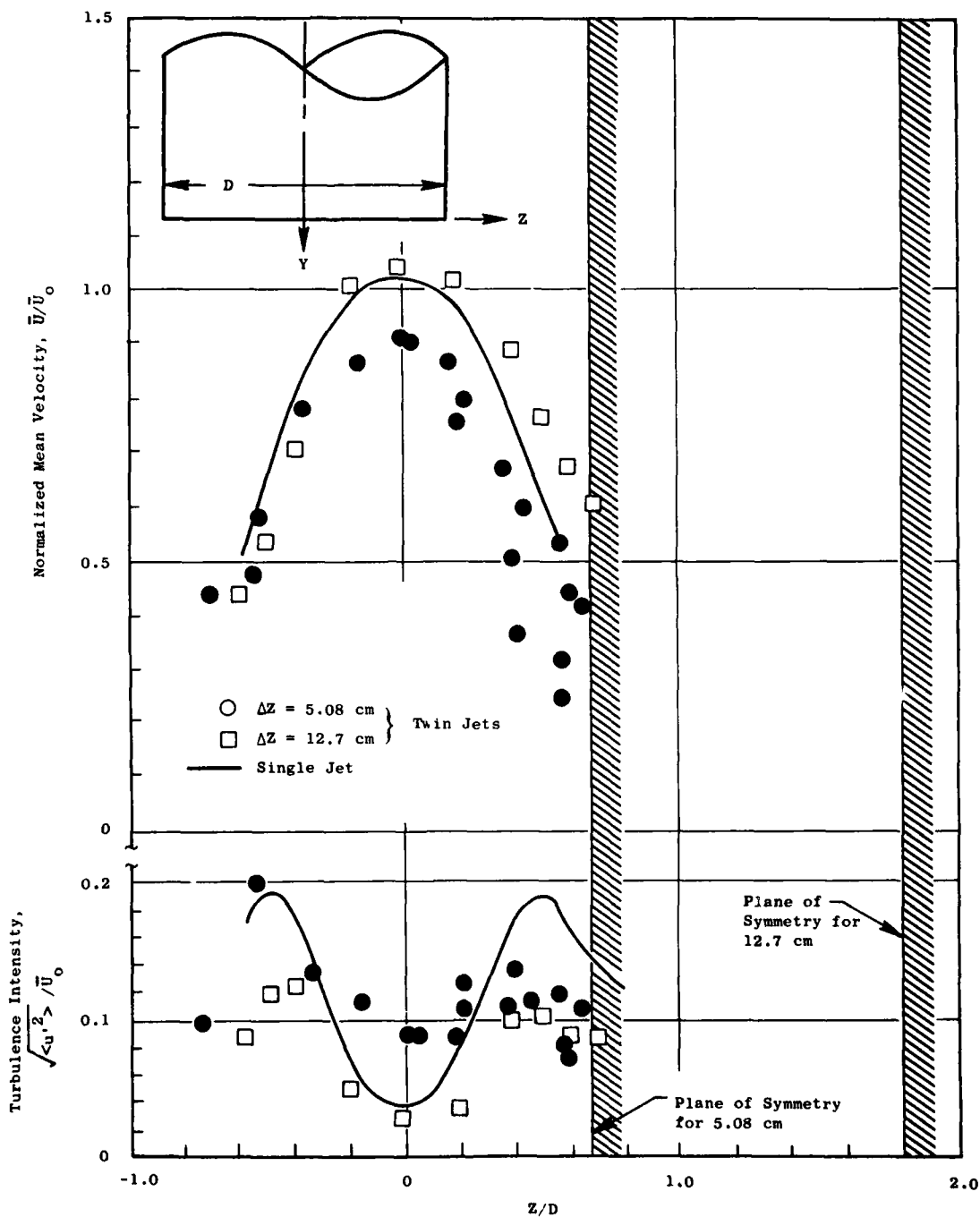


Figure 5-115. Radial Velocity Profiles of the Twin-Round Jets at $Y/D = 6$ ($T_0 = 644$ K, $\bar{U}_0 = 448$ m/s, $D = 38.1$ mm).

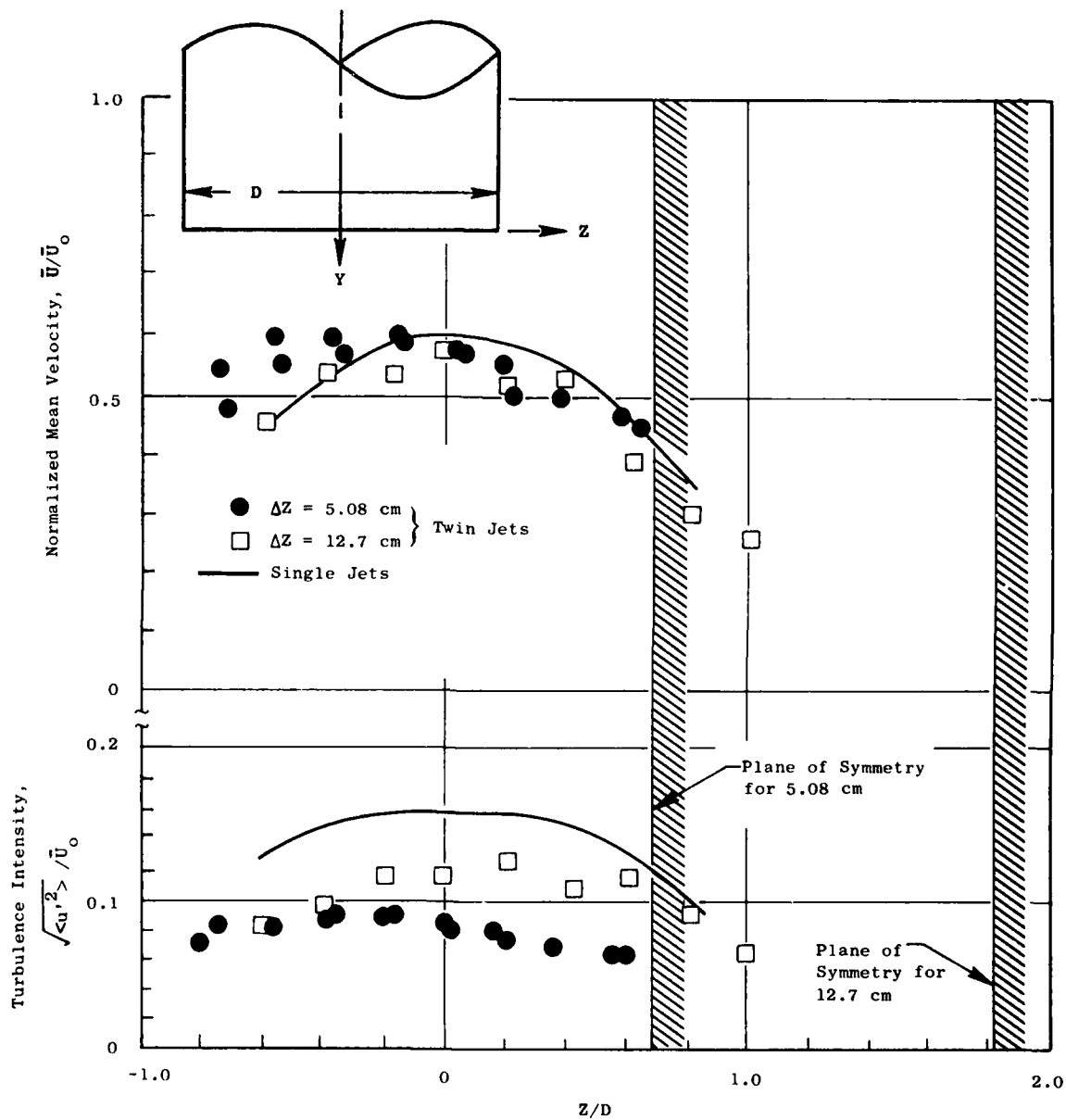


Figure 5-116. Radial Velocity Profiles of the Twin-Round Jets at $Y/D = 10$ ($T_o = 644$ K, $\bar{u}_o = 448$ m/s, $D = 38.1$ mm).

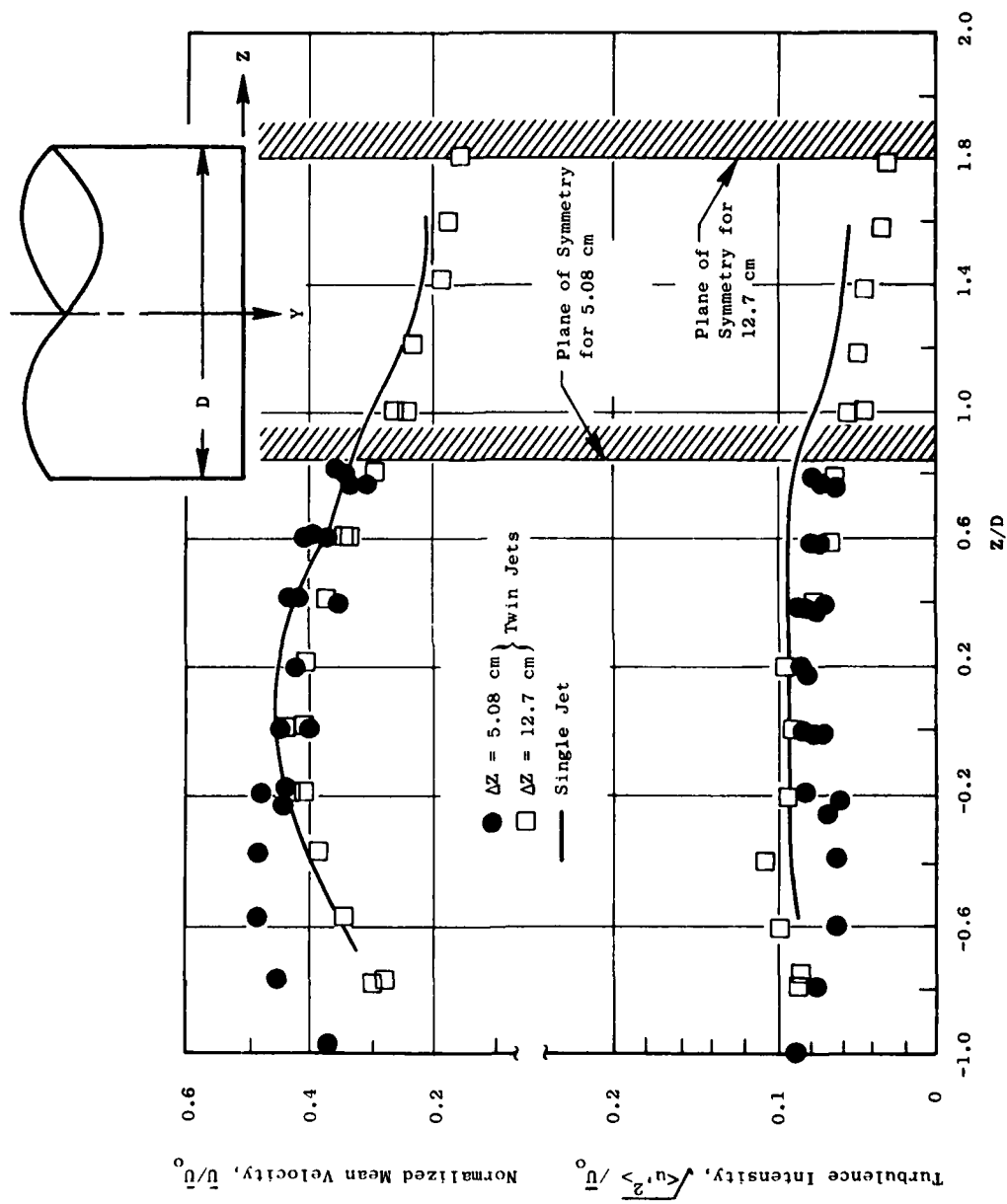


Figure 5-117. Radial Velocity Profiles of the Twin-Round Jets at $Y/D = 14$ ($T_0 = 644$ K, $\bar{u}_0 = 448$ m/s, $D = 38.1$ mm).

halfway point between the two jets. Measurements in both jet flows were overlaid with respect to the plane of symmetry in those figures. Based on the mean velocity profiles shown at 2, 6, 10, and 14 jet diameters downstream, the twin jets at 12.7 cm separation closely resemble the behavior of a single round jet. The twin jet at 5 cm separation deviates from the single round jet velocity profile at (and after) six jet diameters downstream. The centerlines of the two jets are shifted outward from each other at both 10 and 14 jet diameters downstream. This is a clear indication of the merging process between the two jets. No such centerline shift was observed for the twin jets at 12.7 cm separation.

The turbulence intensity profiles at 2, 6, 10, and 14 jet diameters downstream for the twin jets are shown as the lower data plot in Figures 5-114 through 5-117. Again, the profiles for the 12.7 cm separation twin jet appear to be symmetric about the jet centerlines and resemble the shape of those from a single round jet. The turbulence intensity profiles for the 5 cm separation twin jet were found skewed, with lower turbulence near the interface between two jets (plane of symmetry). The turbulence intensities on the opposite side of the jet centerline (i.e., free jet boundary) are similar to those of a single round jet. The lower turbulence intensity near the jet interface region is an evidence of jet noise source reduction. This skewed turbulence intensity profile observation is further confirmed from measurements in a room temperature twin jet at 5 cm separation, shown in Figure 5-118.

5.7.3.2 Twin Rectangular Jets

The axial mean velocity and turbulence intensity distributions along one of the twin jet centerlines are shown in Figure 5-119. Profiles of the twin rectangular jet at both 3.81 cm and 10.48 cm separations agree closely with those of a single rectangular jet, and no jet interference is therefore observed along the jet centerline. Close agreement in the velocity profiles between the twin jets and a single rectangular jet is also observed along the major axis of the rectangular jet for both jet separation distances (Figures 5-120 through 5-123). Mean velocity profiles shown in Figures 5-124 through 5-127 were measured along the minor axis of the rectangular jet, through the plane of symmetry. Again, very similar profiles result for the twin rectangular jets at both separations and for a single rectangular jet. The turbulence intensity profiles shown in Figures 5-120 through 5-123 suggest that the difference between those of the twin jet and a single rectangular jet are also minimal. Thus, the conclusion on the twin rectangular jets tested at both 3.81 cm and 10.48 cm separations is that each of the twin jets behaves as an independent free jet. The interaction between jets on the mean velocity and turbulence intensity appears to be minimal, even at 14 jet equivalent diameters downstream of the jet exit.

5.7.4 Experimental Results on Seven-Jet Cluster Flows

The mean velocity and turbulence intensity of flows from two 7-jet cluster arrangements were measured using the LV system. Seven converging

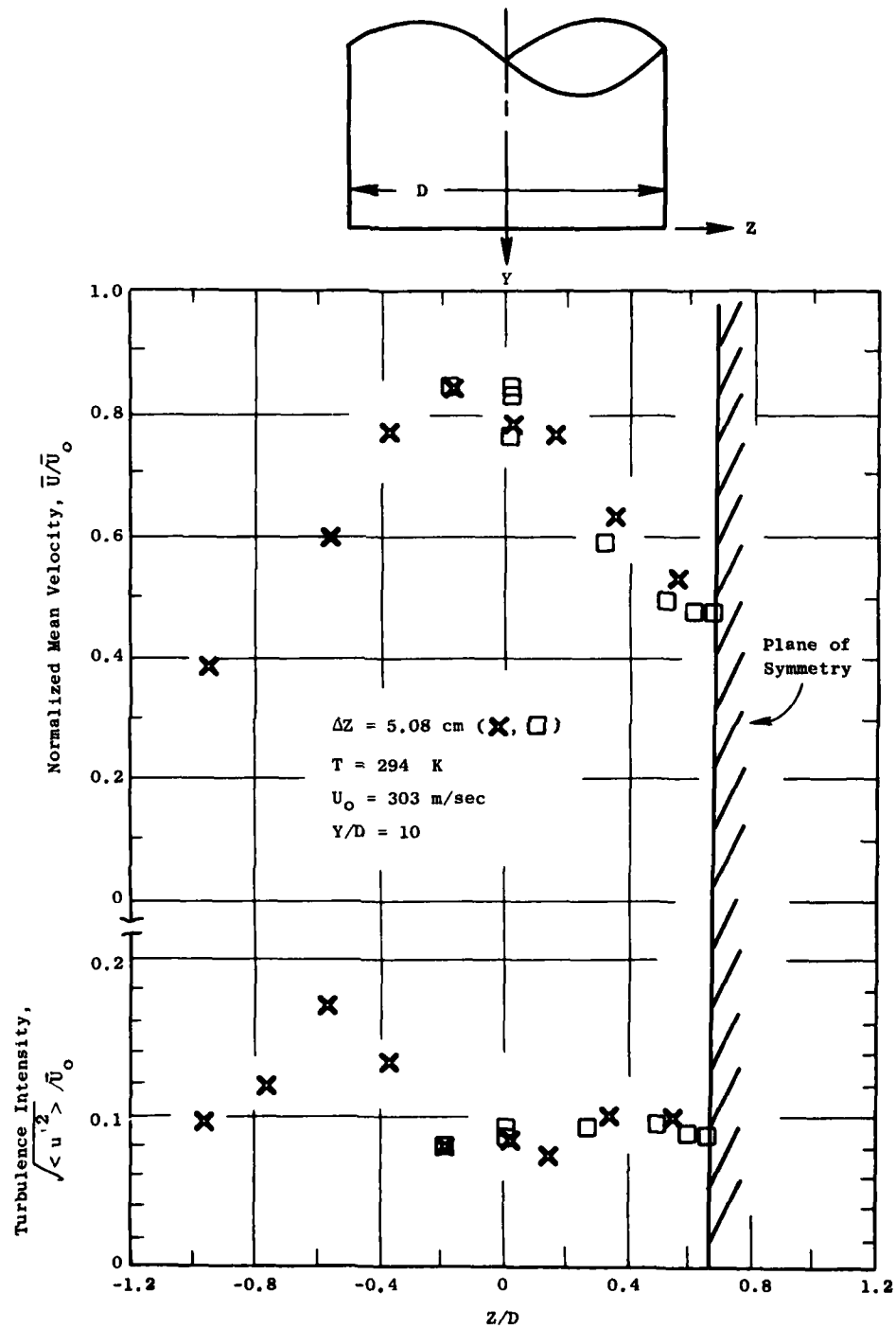


Figure 5-118. Radial Velocity Profiles of the Twin Round Jets at $Y/D = 2$ ($T_0 = 294 \text{ K}$, $\bar{U}_0 = 303 \text{ m/s}$, $D = 38.1 \text{ mm}$).

587

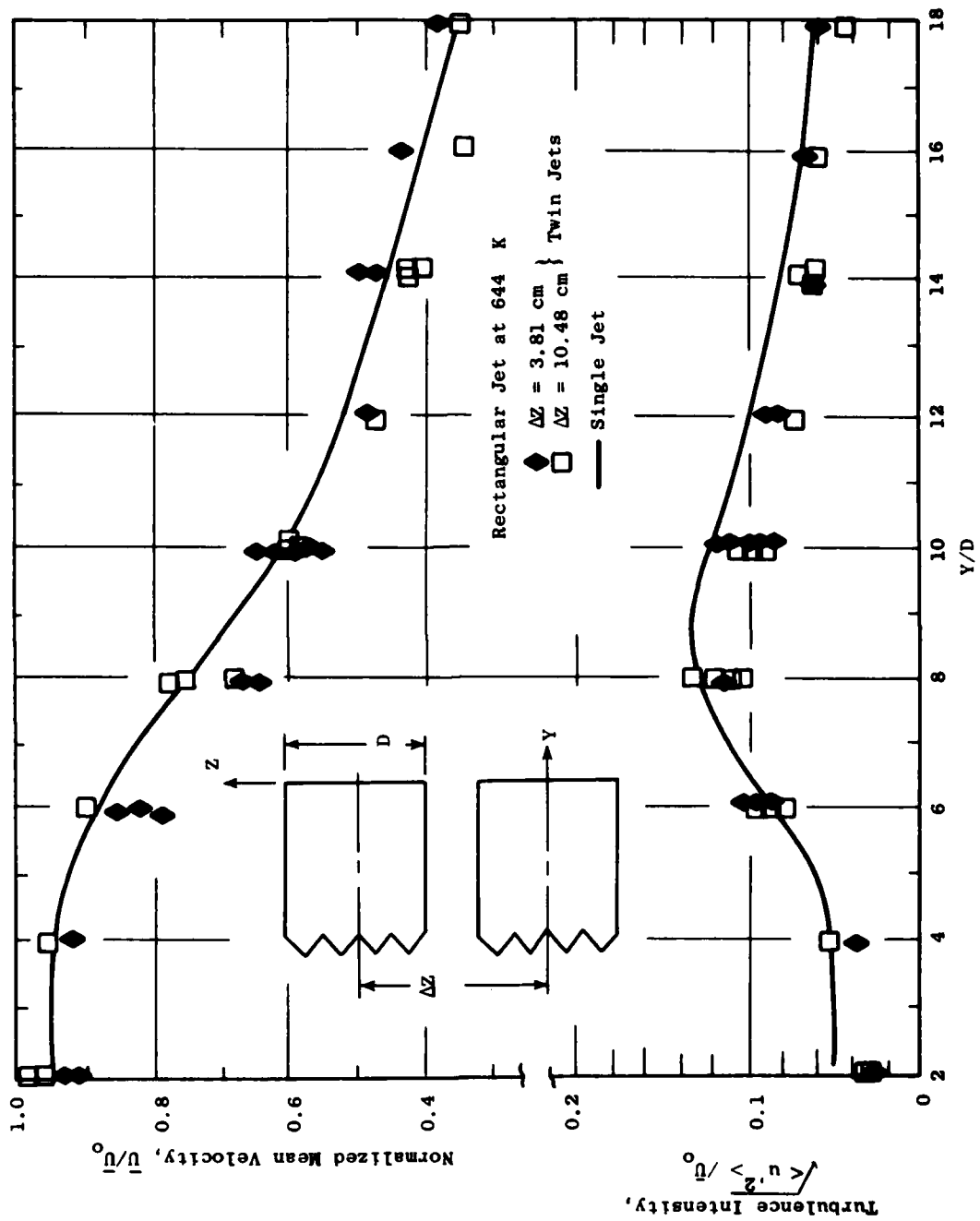


Figure 5-119. Axial Velocity Profiles Along the Centerline of One of the Twin Rectangular Jets ($T_0 = 644$ K, $\bar{u}_0 = 448$ m/s).

590

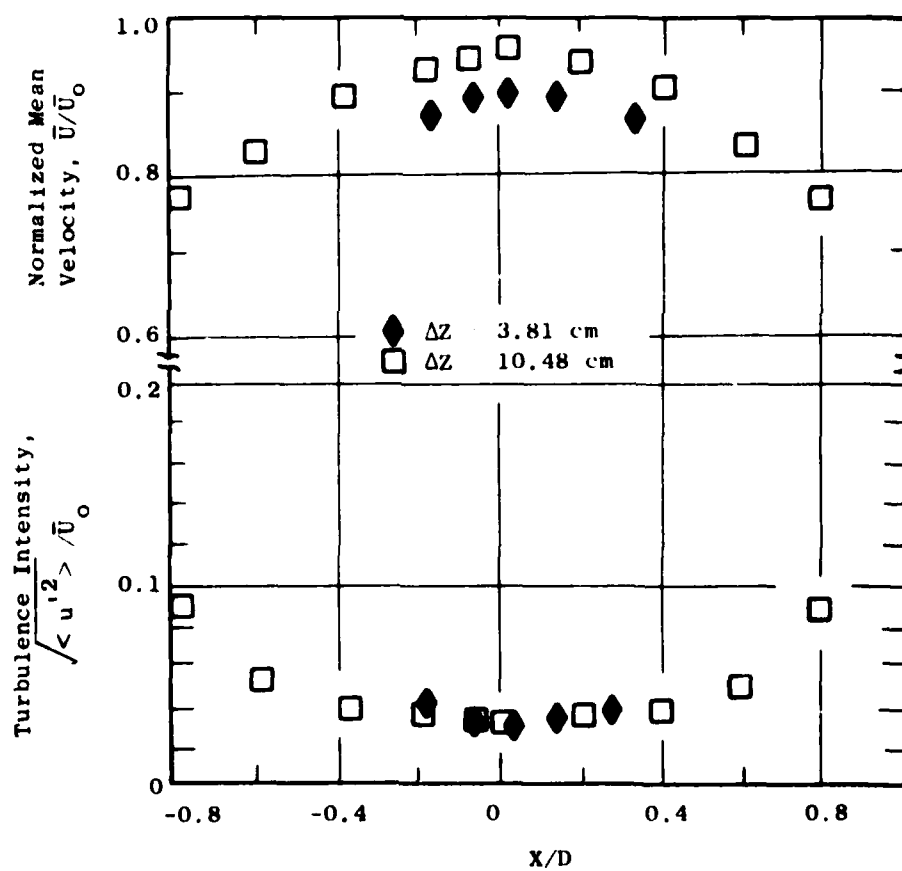
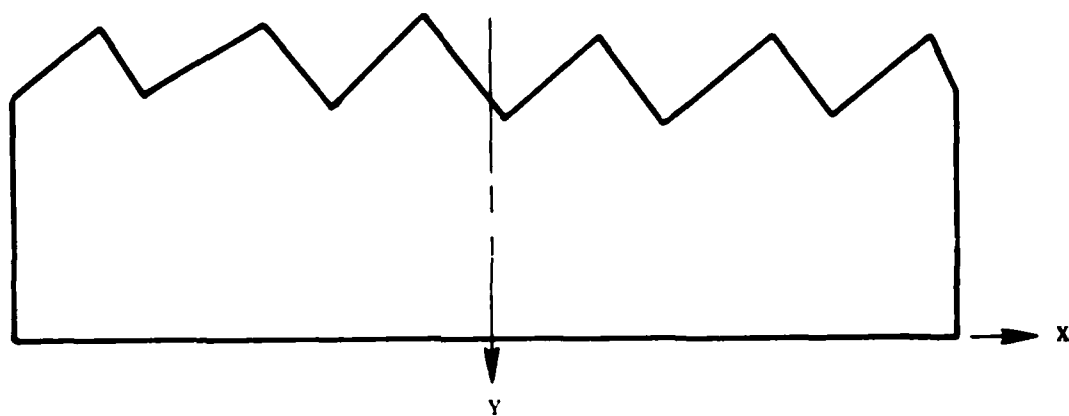


Figure 5-120. X-Transverse Velocity Profiles of the Twin-Rectangular Jets at $Y/D = 2$ ($T_0 = 644$ K, $\bar{U}_0 = 448$ m/s).

(541)

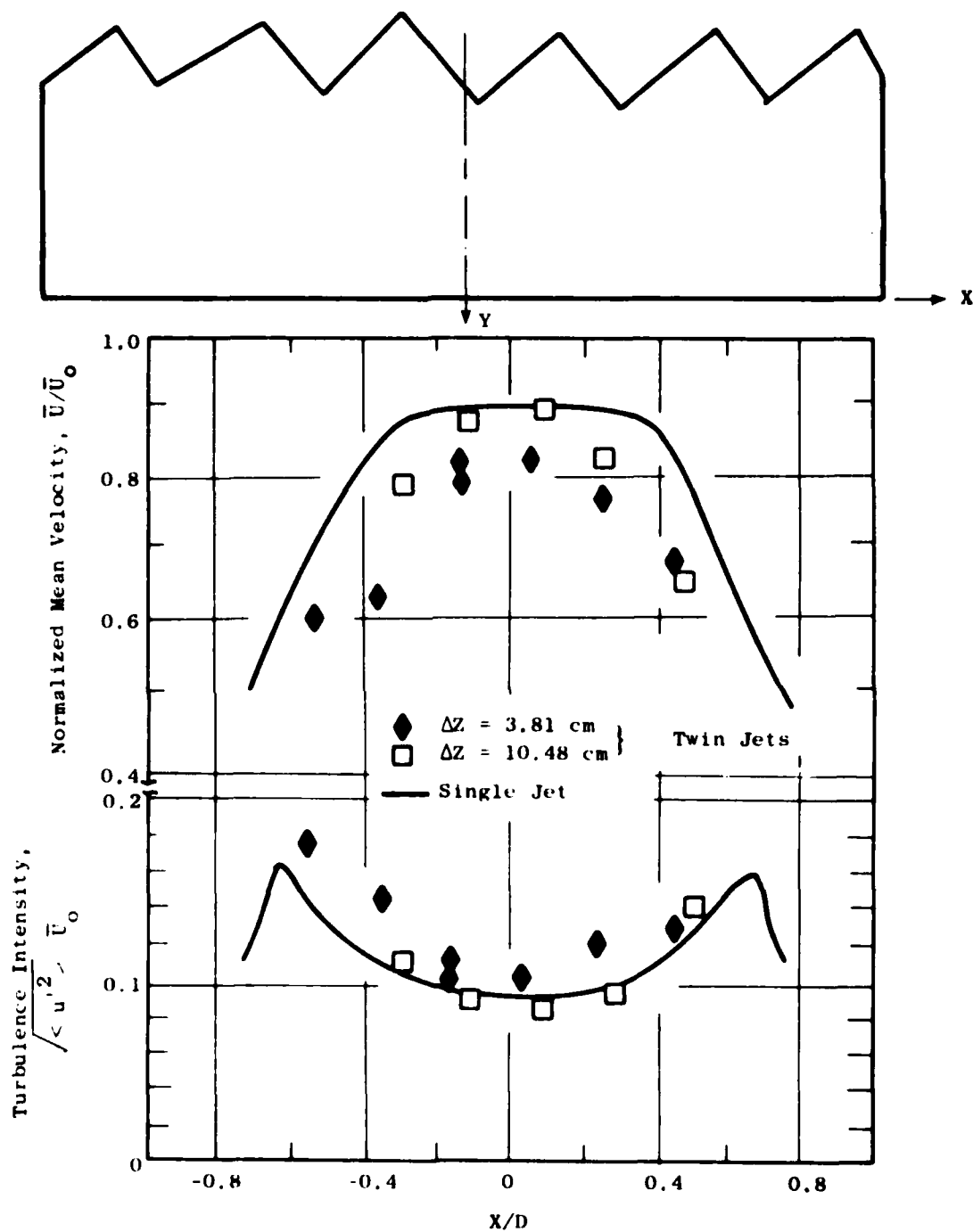


Figure 5-121. X-Transverse Velocity Profiles of the Twin Rectangular Jets at $Y/D = 6$ ($T_o = 644$ K, $\bar{U}_o = 448$ m/s).

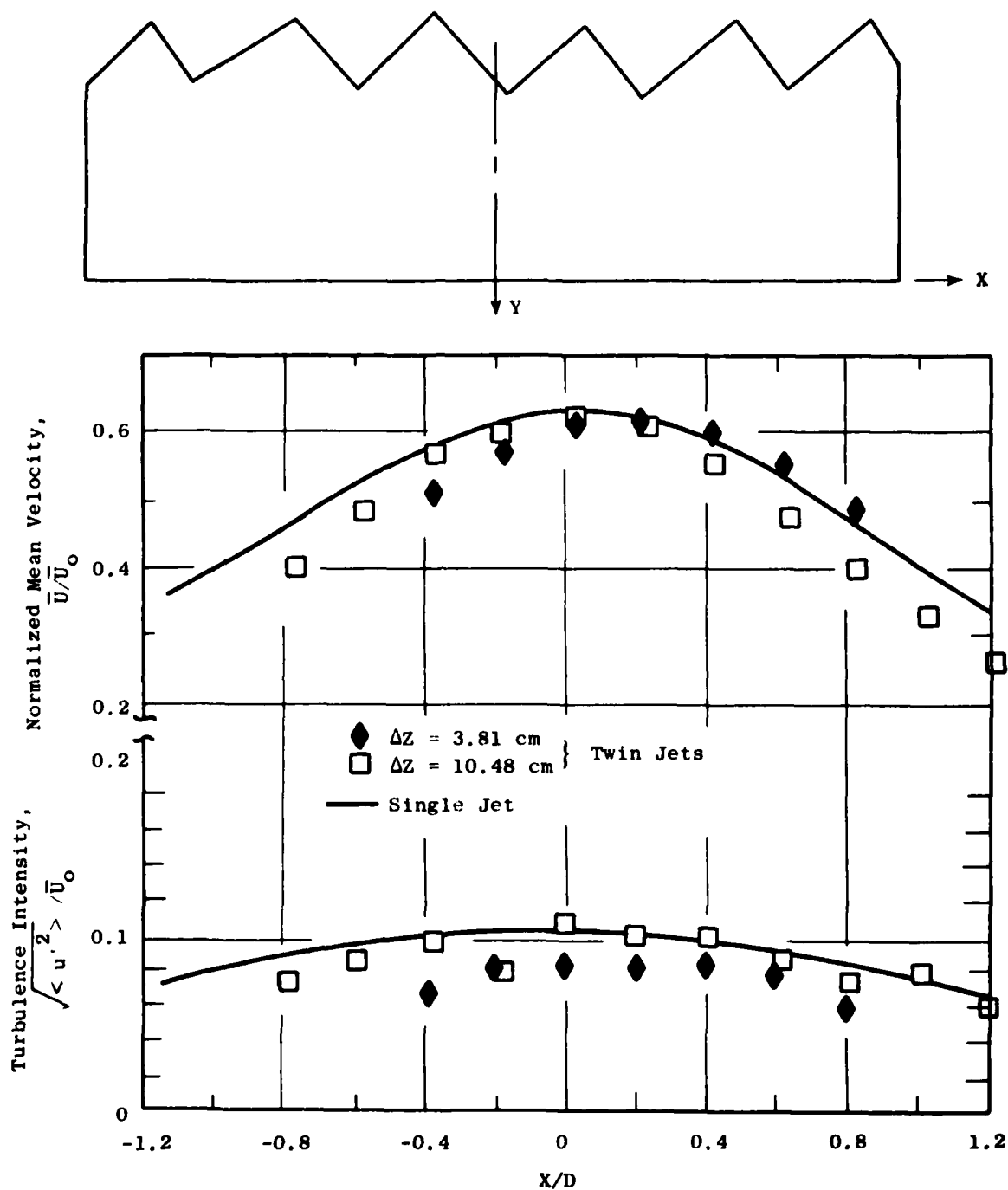


Figure 5-122. X-Transverse Velocity Profiles of the Twin Rectangular Jets at $Y/D = 10$ ($T_0 = 644$ K, $\bar{U}_0 = 448$ m/s).

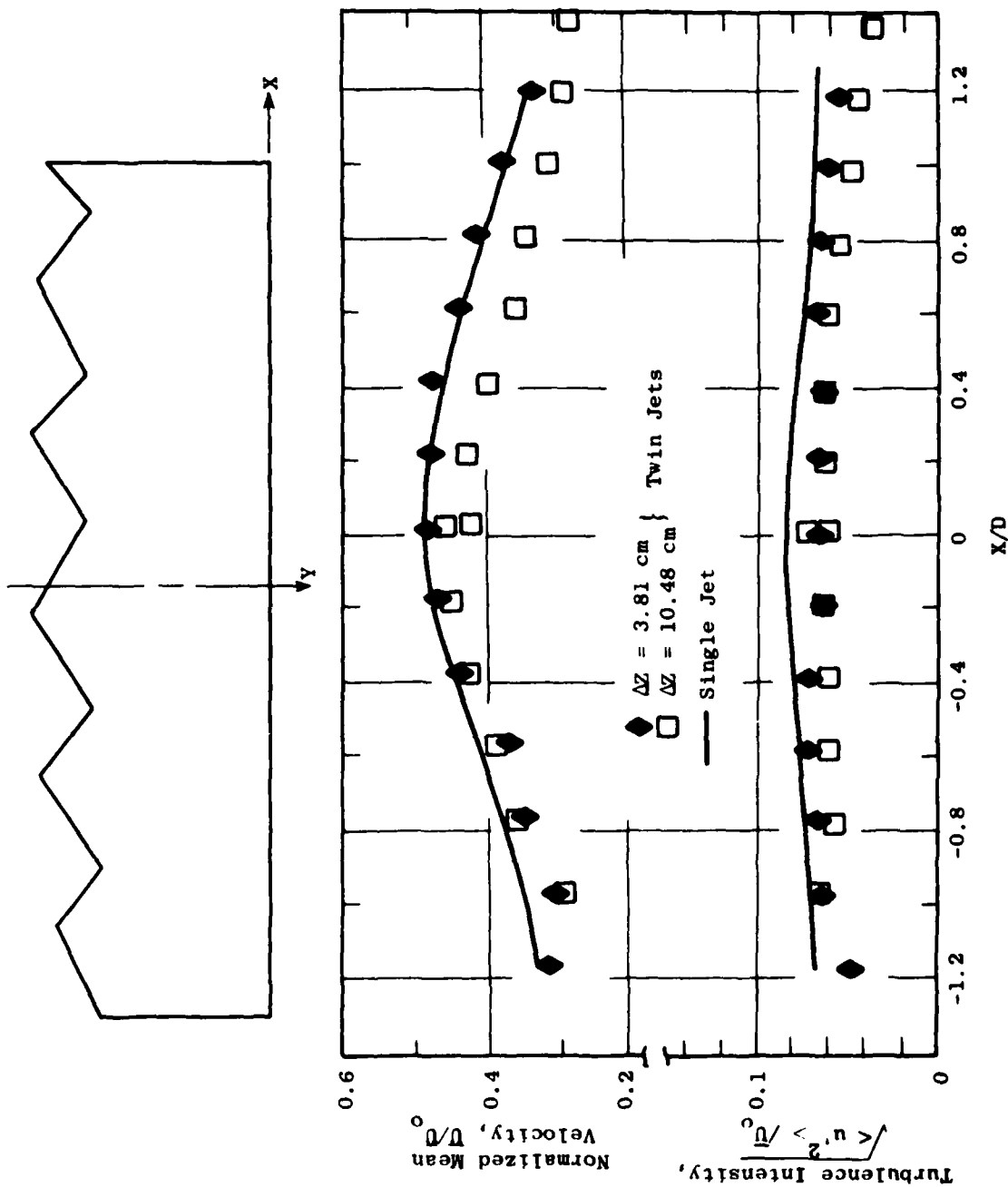


Figure 5-123. X-Transverse Velocity Profiles of the Twin Rectangular Jets at $Y/D = 14$ ($T_0 = 644$ K, $\bar{U}_0 = 448$ m/s).

511

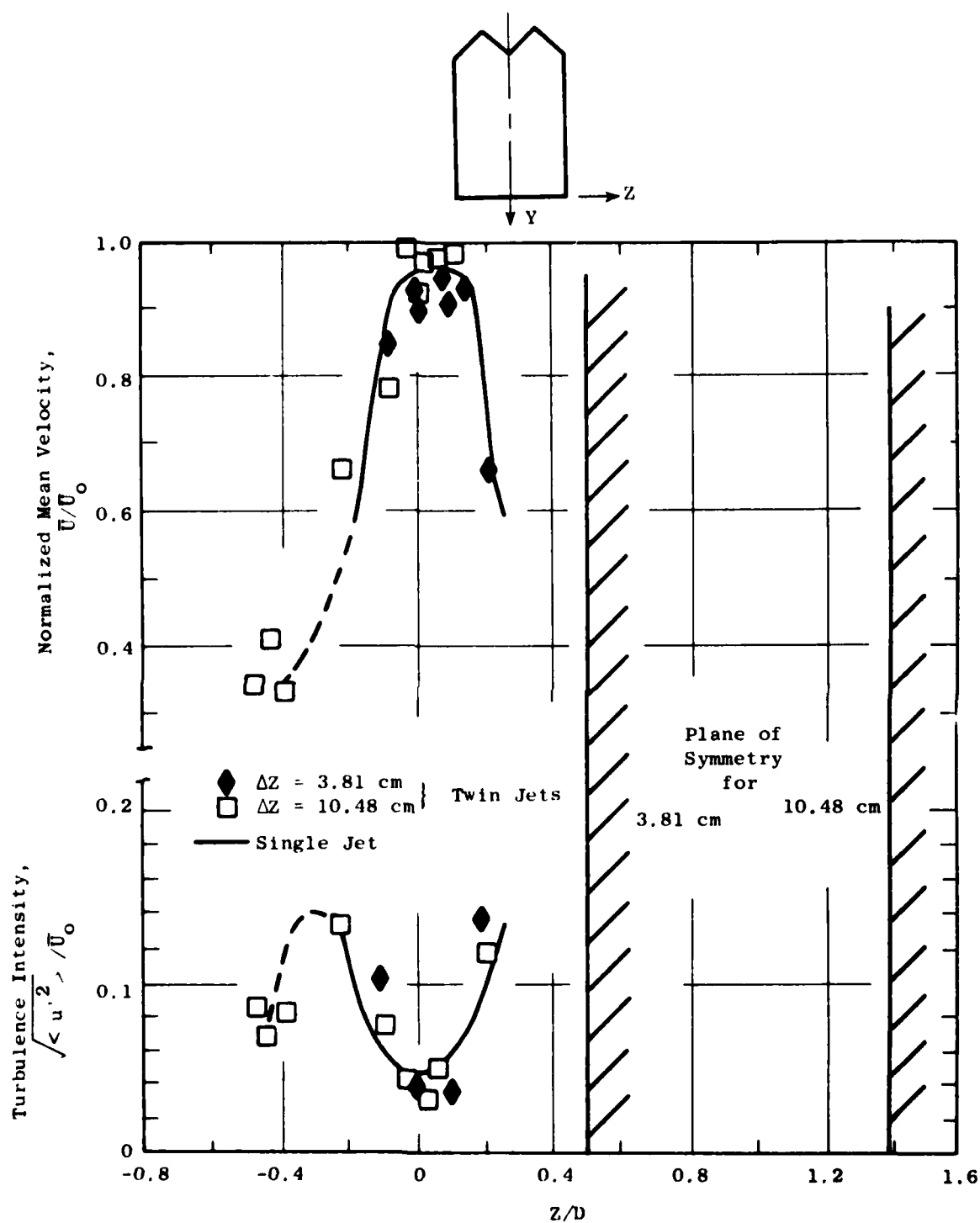


Figure 5-124. Z-Transverse Velocity Profiles of the Twin Rectangular Jets at $Y/D = 2$ ($T_0 = 644$ K, $\bar{U}_0 = 448$ m/s).

95

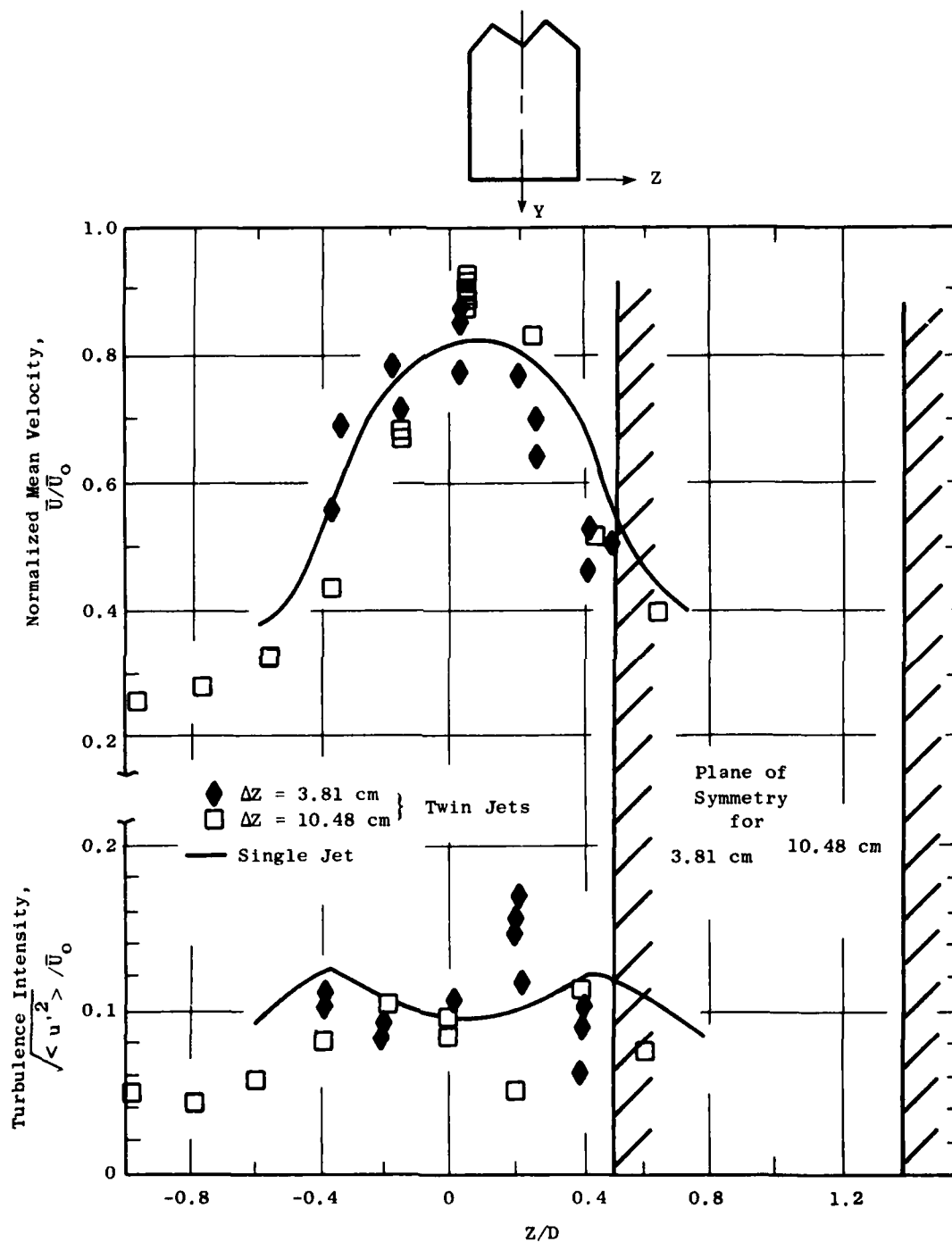


Figure 5-125. Z-Transverse Velocity Profiles of the Twin-Rectangular Jets at $Y/D = 6$ ($T_0 \approx 664$ K, $U_0 = 448$ mps).

(516)

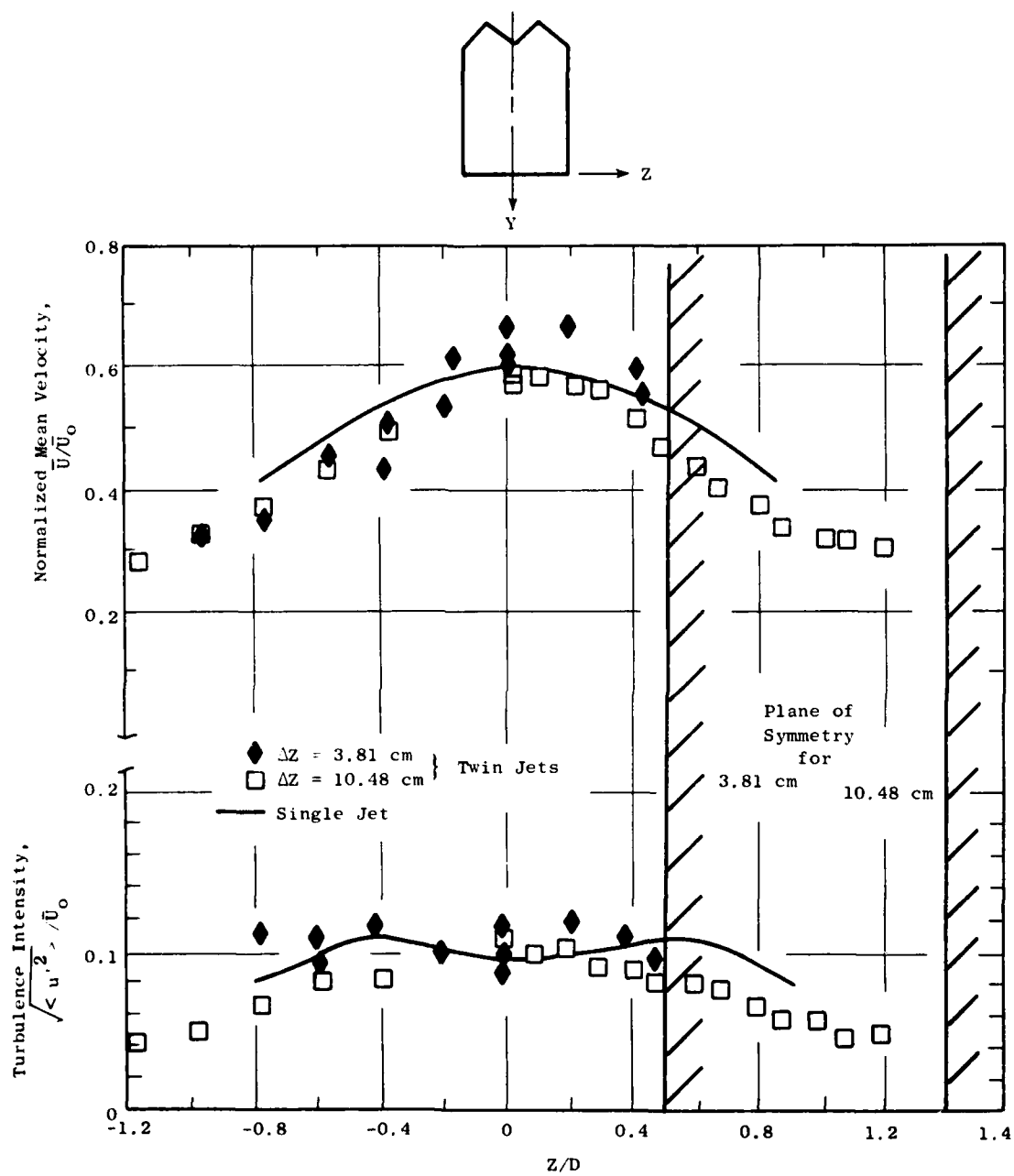


Figure 5-126. Z-Transverse Velocity Profiles of the Twin-Rectangular Jets at $Y/D = 10$ ($T_0 = 664$ K, $\bar{U}_0 = 448$ mps).

597

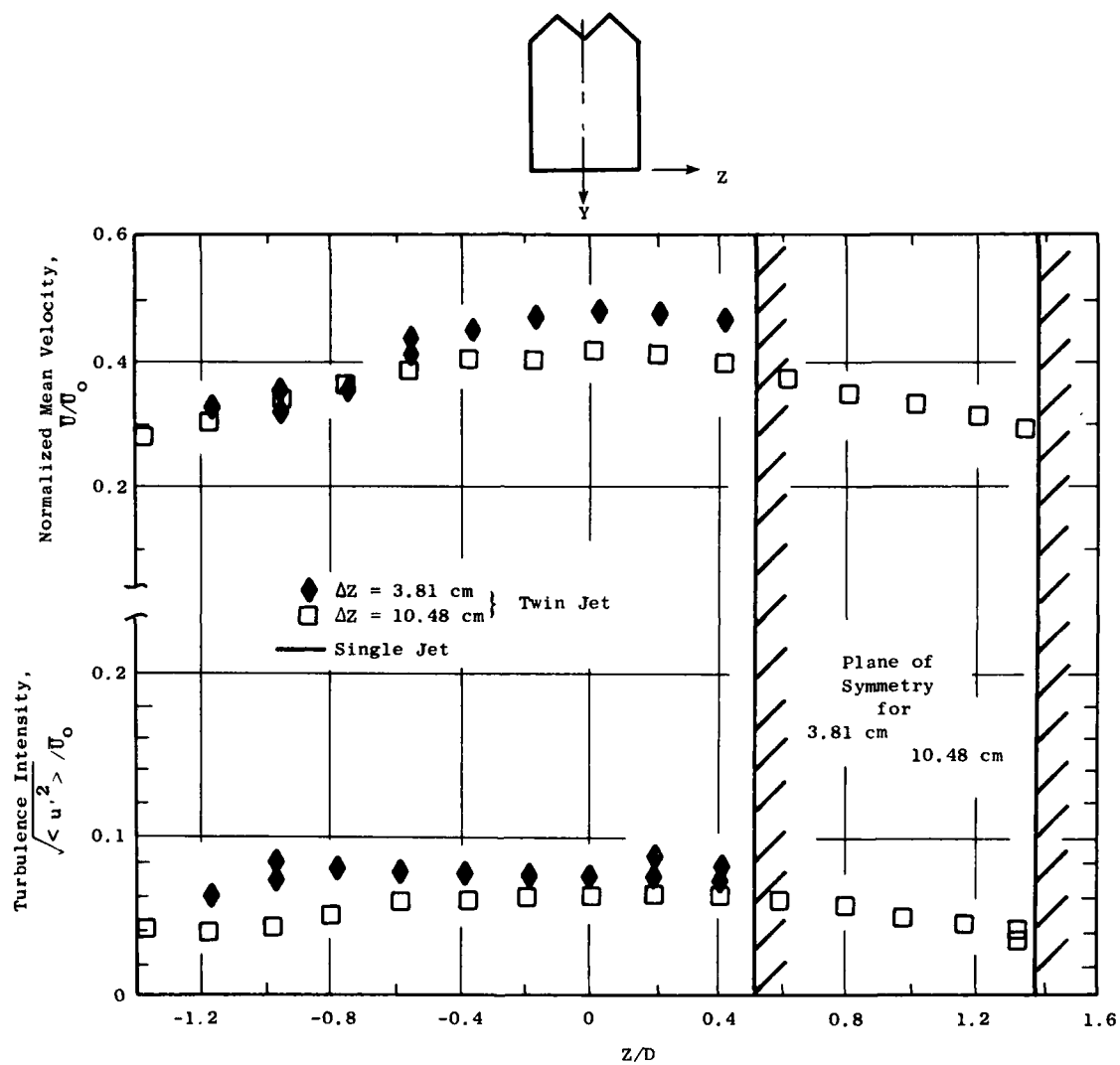


Figure 5-127. Z-Transverse Velocity Profiles of the Twin-Rectangular Jets at $Y/D = 14$ ($T_0 = 664$ K, $\bar{U}_0 = 448$ mps).

598

nozzles of 2.22 cm diameter were mounted on the hot-jet test facility as shown in Figure 5-128. Six of the seven nozzles were distributed evenly on a circle of 3.81 cm and 6.67 cm radius around the centerline of the center jet nozzle. The cluster flows were at 890 K and 600 m/s (Mach 1.12) for both configurations, i.e., $\Delta Z = 3.81$ and 6.67 cm. For the cluster configuration at $\Delta Z = 3.81$ cm, flows at 890 K and 506 m/s (Mach 0.86) were also tested. The velocity and turbulence of the cluster flows were measured along the centerline of the center jet and the transverse direction connecting the centerlines of the center jet and one outer jet. The coordinates on the data presented in the following subsections are shown in Figure 5-128.

5.7.4.1 Large Cluster Jets ($\Delta Z = 6.67$ cm)

The axial velocity and turbulence intensity profiles of the large cluster flow, along the centerline of the center jet is shown in Figure 5-129. These profiles are similar to those from a single round jet (shown in Figures 5-98 and 5-99). However, the turbulence intensity at six nozzle diameters downstream ($Y/D = 6$) appears to be much higher than that of a single jet flow. This may be explained by the existence of the shock pockets in a supersonic jet exhaust. Figure 5-130 shows the radial velocity profiles around one of the outer jets at $Y/D = 4$ and is similar to that of a single round jet flow at the same downstream location. Radial velocity profiles of the large cluster jet flows at $Y/D = 10, 14, 20$, and 26 are shown in Figures 5-131 through 5-134. Peaks are observed around the centerline of each nozzle in the mean velocity profiles. Each jet flow behaves as a single free jet in this large cluster configuration. Some indications of the jet interaction are observed at the $Y/D = 14$ station in the interface region between the jets. The turbulence in the interface region is approximately 12% of the nozzle exit velocity and is slightly higher than the values at the corresponding location for a single free jet, shown in Figure 5-105. However, the effect of the observed jet interaction was minimal. Even at 20 nozzle diameters downstream, the mean velocity peaks around each jet centerline are still discernible. At $Y/D = 26$, the jets are so spread out that flat velocity and turbulence intensity profiles are obtained, as expected.

5.7.4.2 Small Cluster Jets ($\Delta Z = 3.81$ cm)

Two jet exit velocities were tested on this cluster configuration, i.e., $\bar{U}_0 = 506$ and 600 m/s. The axial velocity and turbulence intensity profiles along the axis of the center jet are shown in Figure 5-135. At subsonic jet exit velocity, $\bar{U}_0 = 506$ m/s, the mean velocity decay along the jet centerline is faster than at supersonic speed. The mean velocity axial profiles at $\bar{U}_0 = 600$ m/s are similar to results from the large cluster configurations. However, the turbulence intensity at $Y/D = 8$ is lower for the small cluster configuration. This is an indication of the jet interference effect as the distance between jets becomes smaller. For the case where jet exit velocity is 506 m/s, the maximum turbulence intensity occurs at $Y/D = 6$ (instead of 8 as in the case of 600 m/sec). The maximum turbulence intensity along the center jet axis is approximately 12% of the exit jet speed for both velocity conditions for this small cluster configuration. The value of the maximum

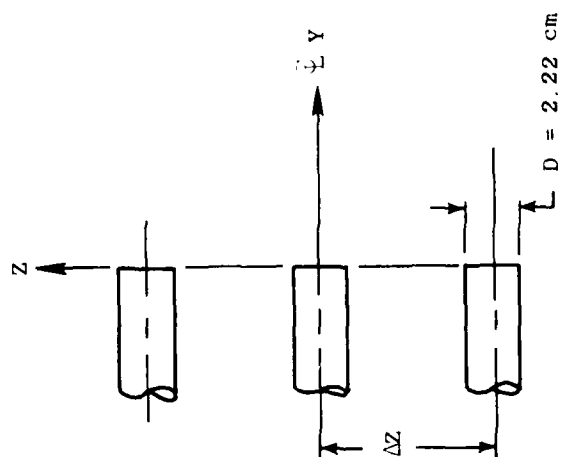
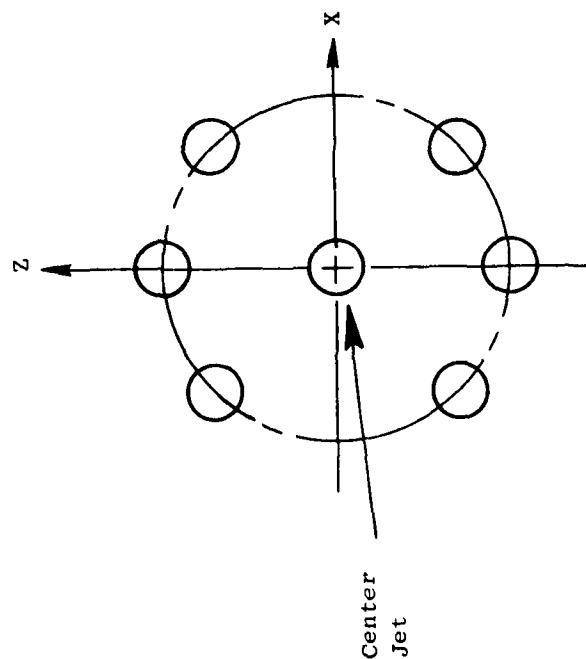


Figure 5-128. Schematic of the 7-Jet Duster Configuration and Coordinates.

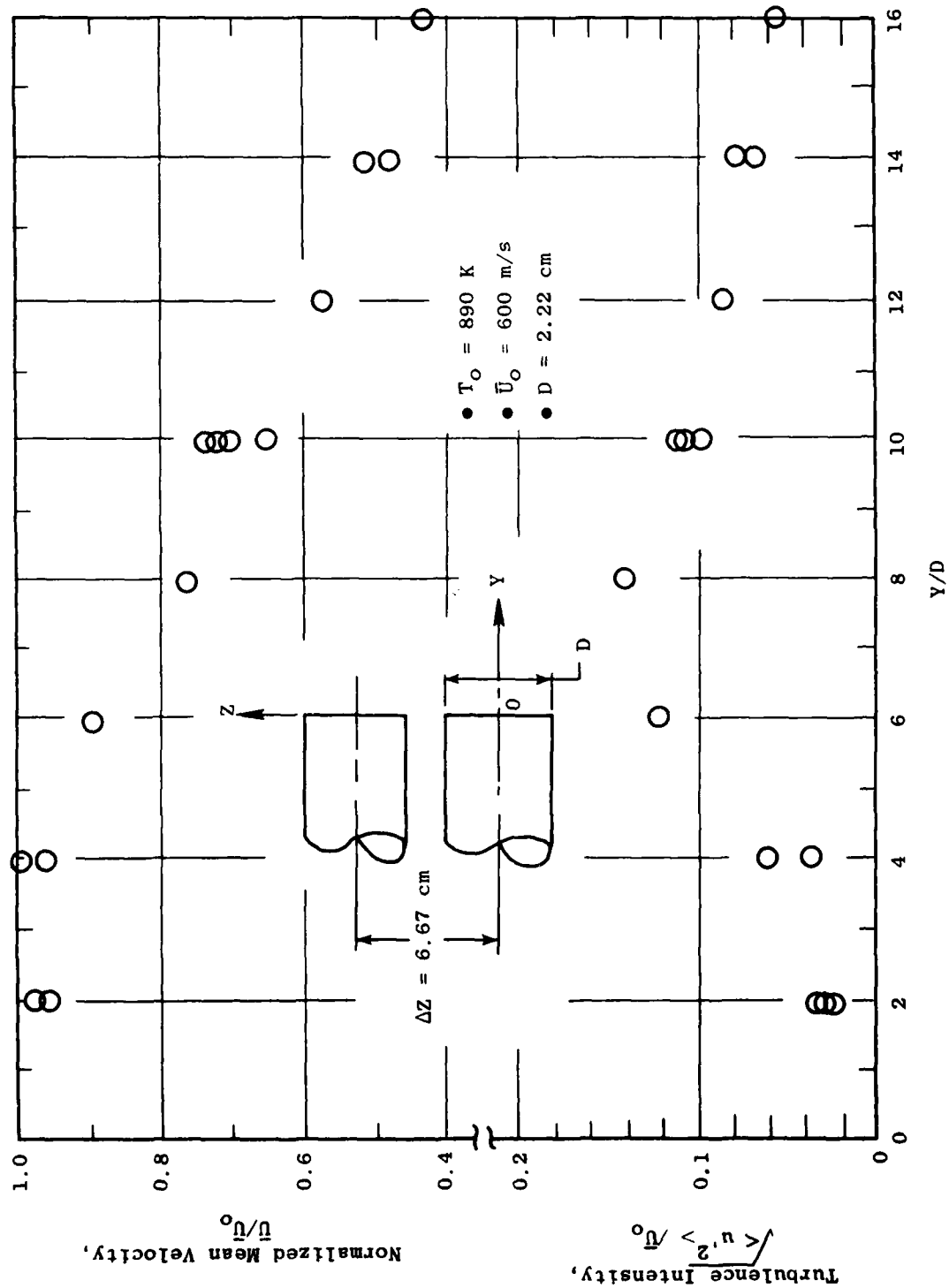


Figure 5-129. Axial Velocity Profile of the 7-Jet Cluster Flow Along One Jet Centerline ($\Delta Z = 6.67$ cm).

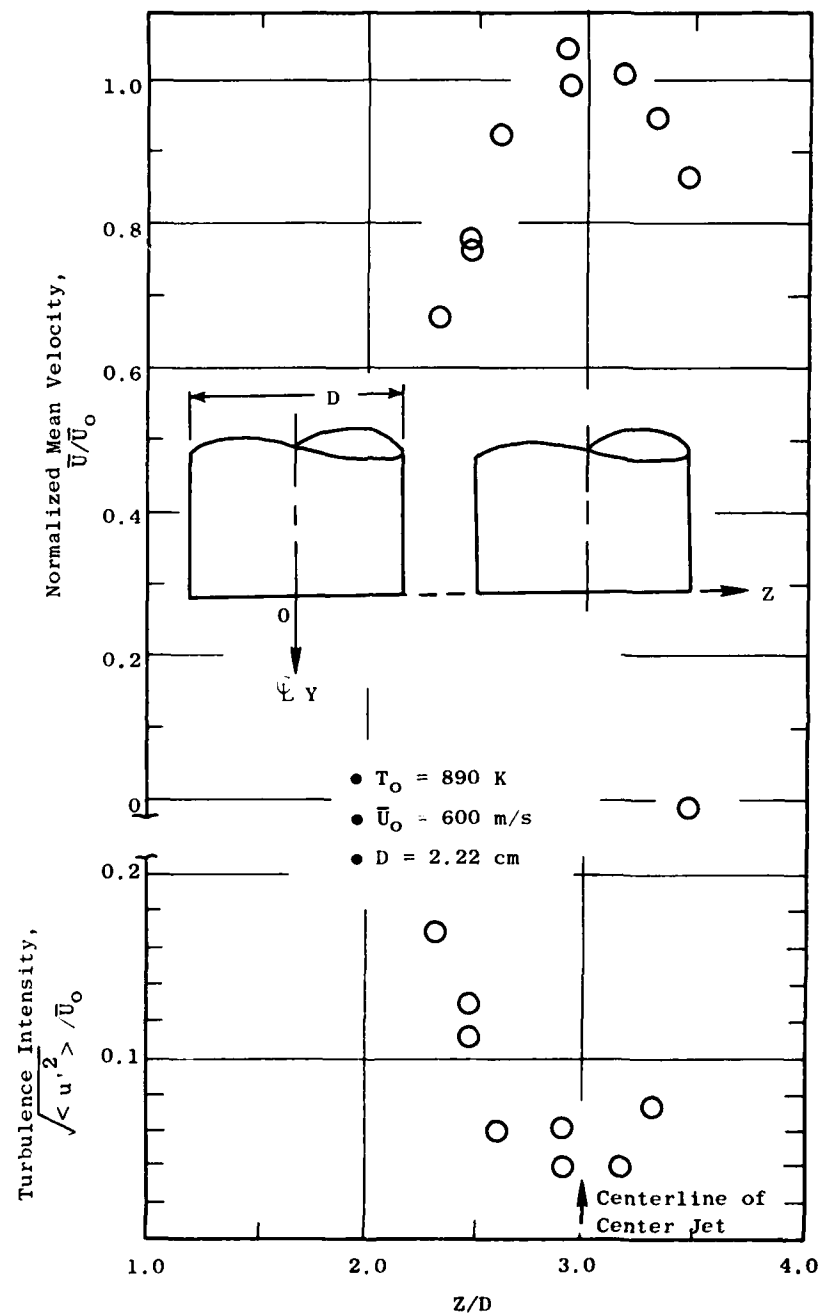


Figure 5-130. Radial Velocity Profile of the 7-Jet Cluster Flow Around the Center Jet at $Y/D = 4$ ($\Delta Z = 6.67$ cm).

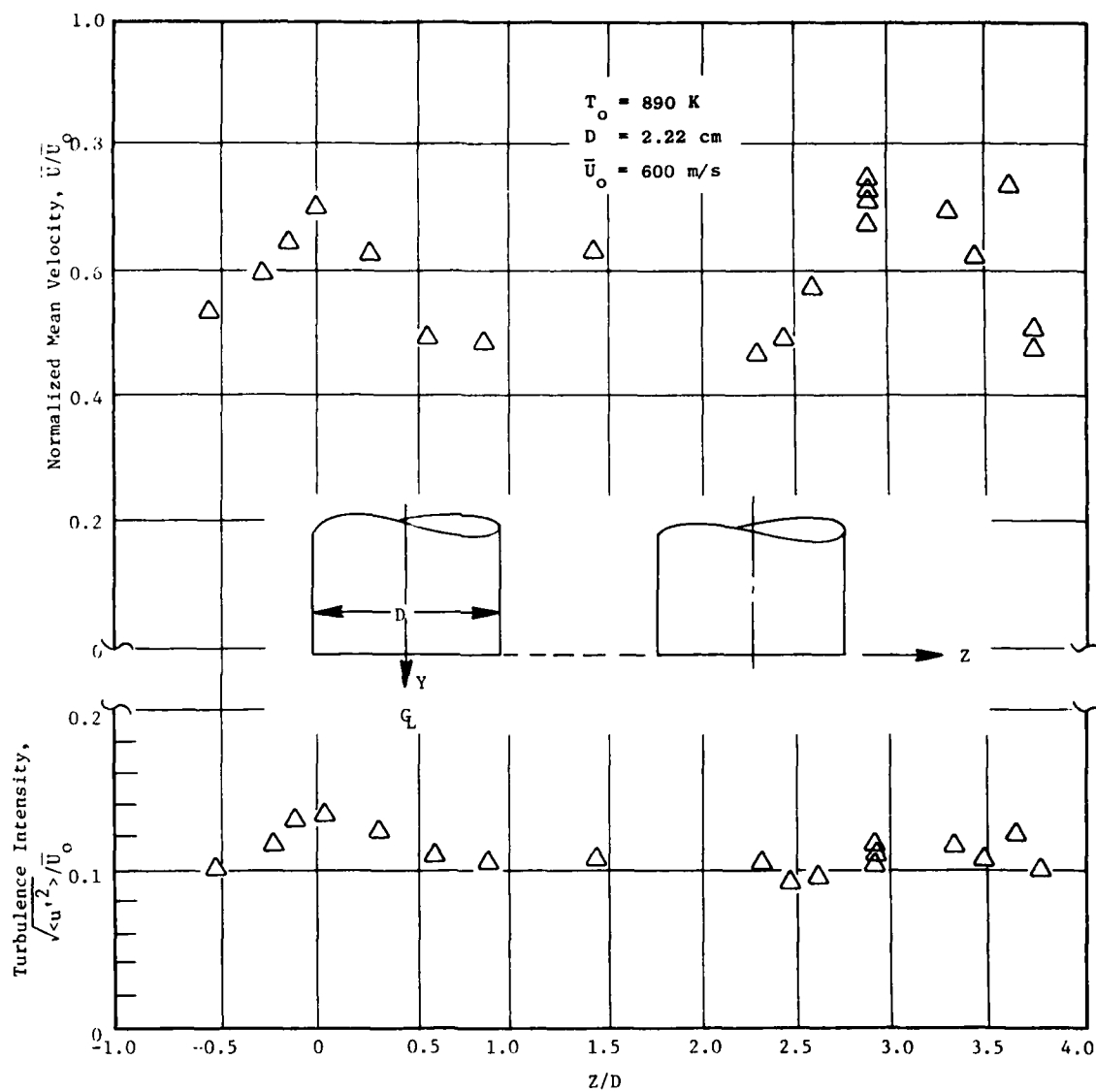


Figure 5-131. Radial Velocity Profile of the 7-Jet Cluster Flow at $Y/D = 10$ ($\Delta Z \approx 6.67 \text{ cm}$).

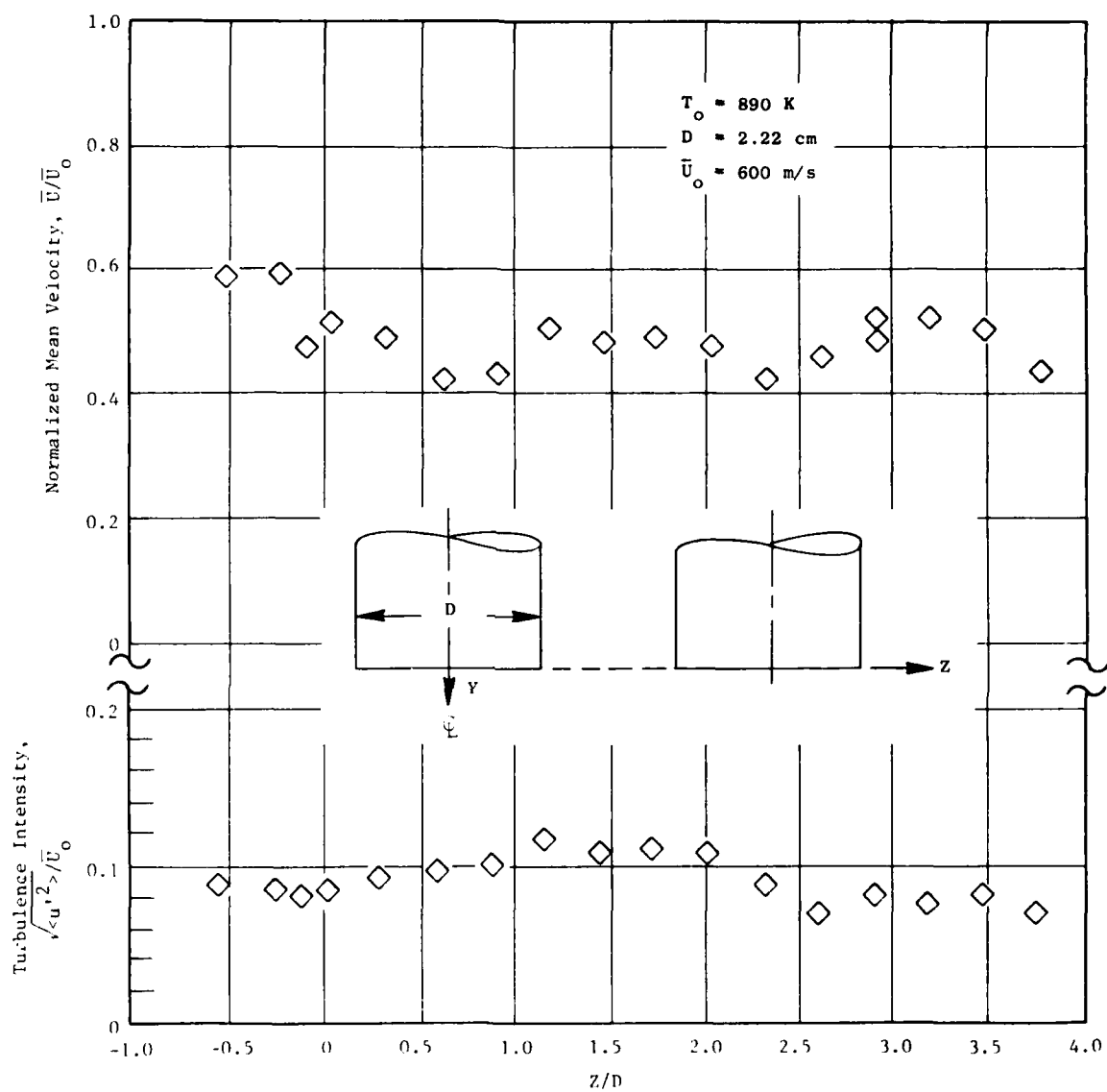


Figure 5-132. Radial Velocity Profile of the 7-Jet Cluster Flow at $Y/D = 14$ ($\Delta Z = 6.67 \text{ cm}$).

601

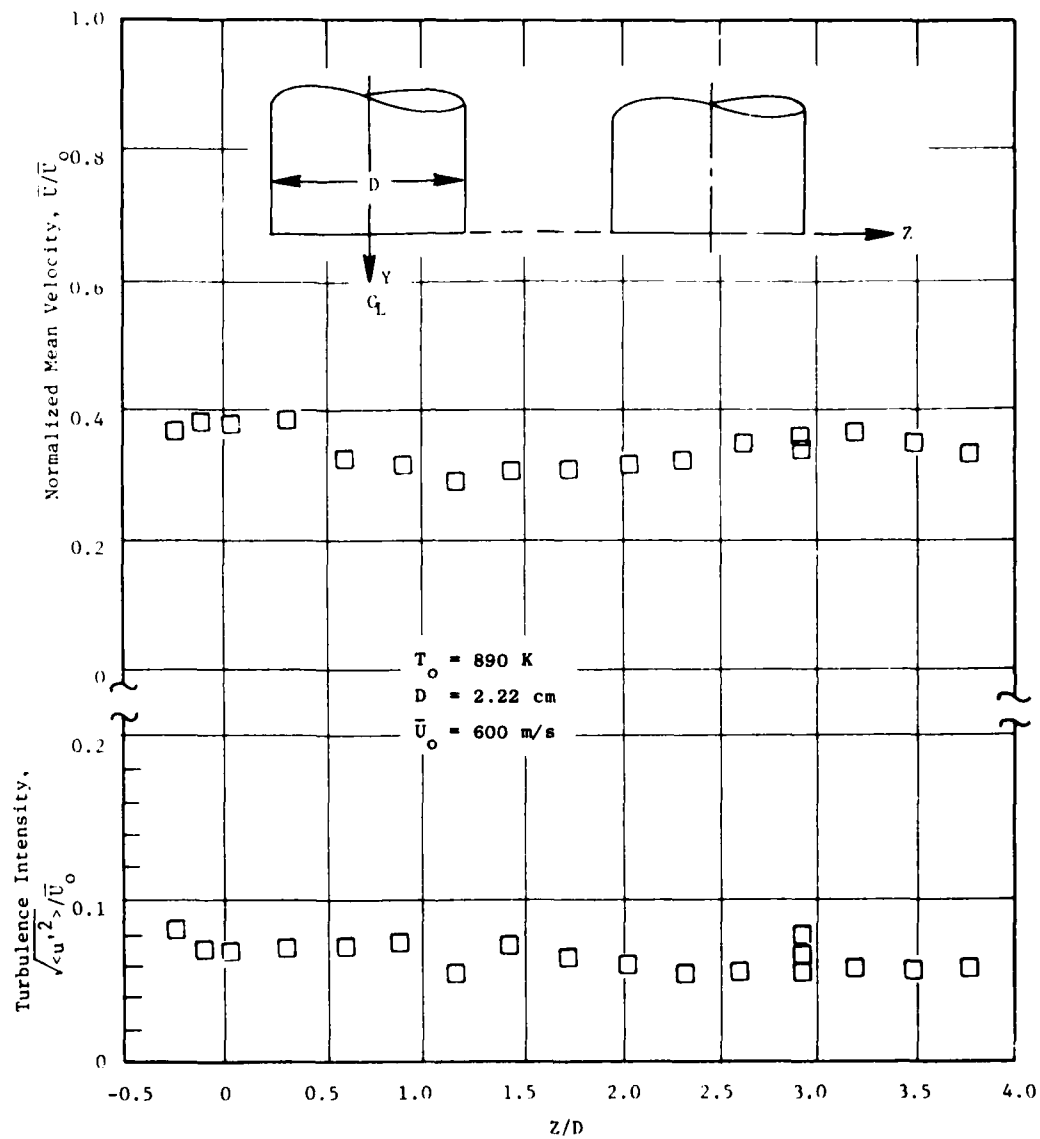


Figure 5-133. Radial Velocity Profile of the 7-Jet Cluster Flow at $Y/D = 20$ ($\Delta Z = 6.67 \text{ cm}$).

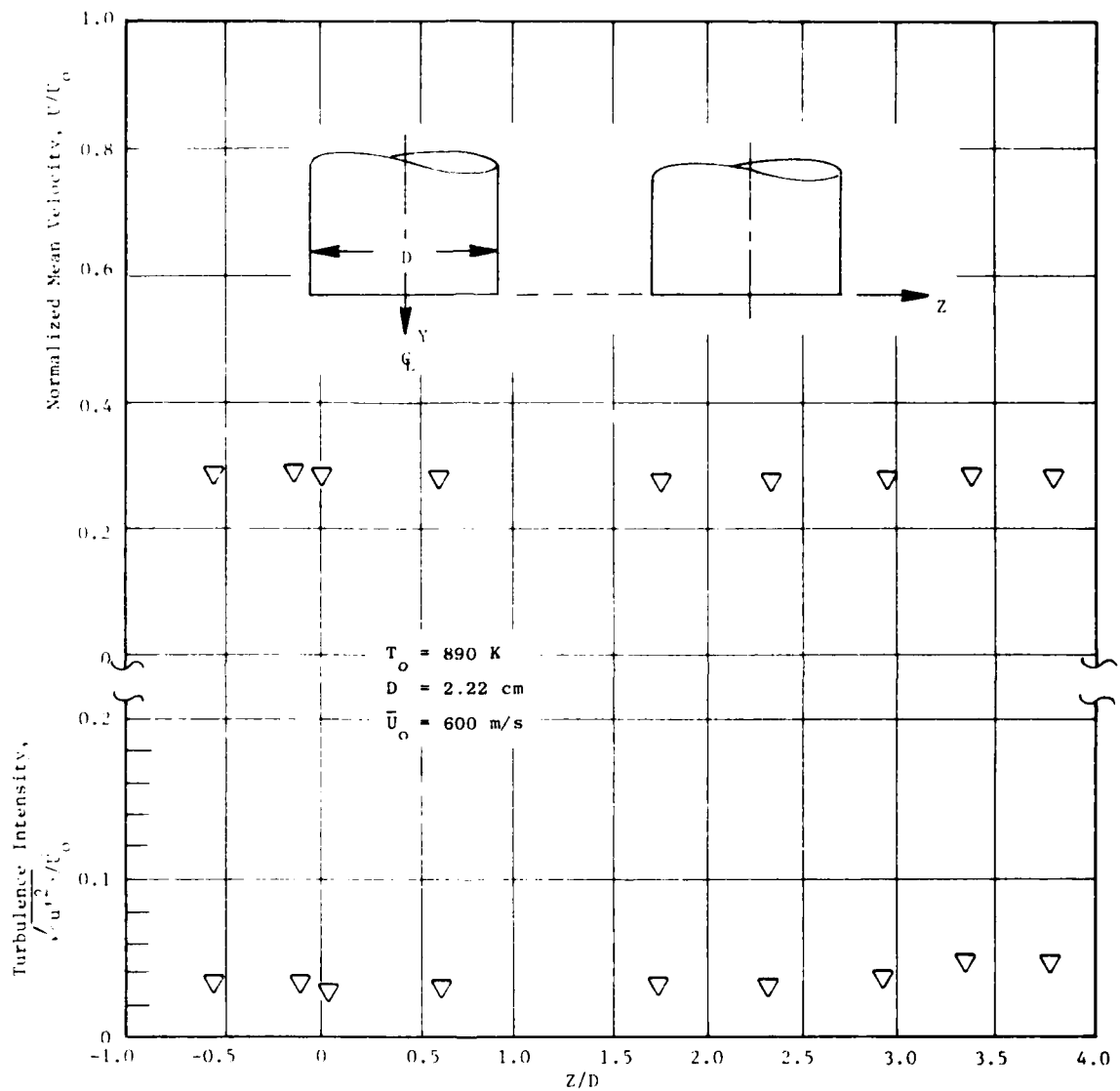


Figure 5-134. Radial Velocity Profile of the 7-Jet Cluster Flow at $Y/D = 26$ ($\Delta Z = 6.67 \text{ cm}$).

(606)

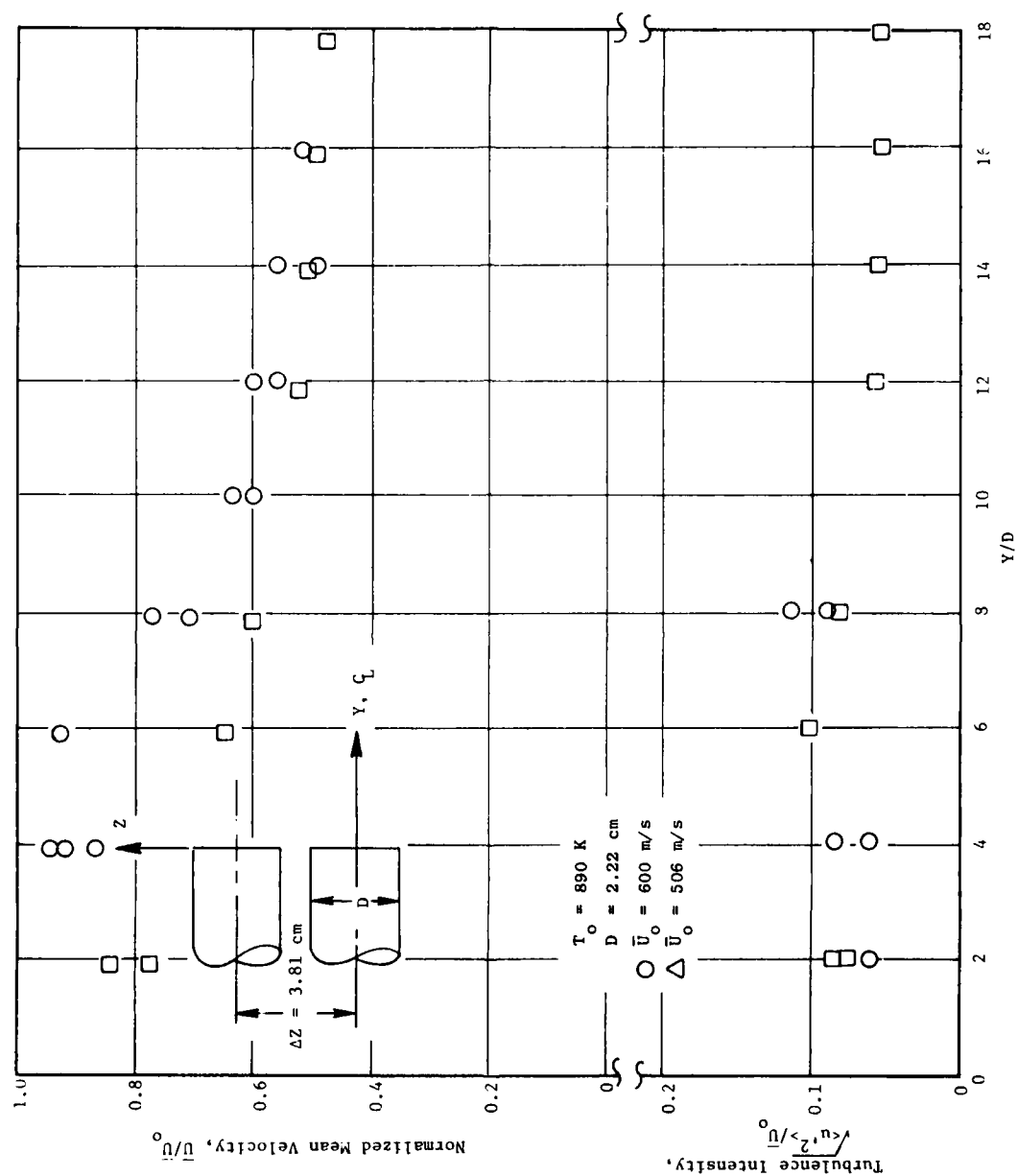


Figure 5-135. Axial Velocity Profile of the 7-Jet Cluster Flow Along the Centerline of the Center Jet ($\Delta Z = 3.81 \text{ cm}$, $Z/D = 1.7$).

turbulence intensity is approximately 14% in a large cluster arrangement (shown in Figure 5-129).

Radial velocity and turbulence intensity profiles of the small cluster are shown in Figures 5-136 through 5-140. Based on the profiles shown in Figure 5-136, interaction between the center jet and the outer jet begins at the $Y/D = 4$ station. The turbulence intensity on the edge of the center jet appears suppressed to 12% from the free jet value of 15%, while the corresponding intensity on the edge of the outer jet increases to 17%. The mean velocity peaks are distinct and symmetric about each jet axis. As the cluster flow moves downstream to $Y/D = 10$ and 14, the outer jet appears to migrate outward. The mean velocity value at the outer jet peak decays faster than that of the center jet. An important observation on this small cluster arrangement, different from the large one, is that a strong interaction occurs between the center and the outer jet and the interaction starts as early as four nozzle diameters downstream from the jet exit.

The faster decay in mean velocity and turbulence intensity at the subsonic speed can be clearly observed in Figure 5-137 at $Y/D = 10$. At $Y/D = 14$, the outer jet velocity peak disappears, in contrast to the case of flows at the supersonic speed. These observations suggest that a stronger interaction occurs between jets of the small cluster arrangement at subsonic speed. The cluster jet flow becomes a large simple jet at (or even before) 14 nozzle diameters downstream, for flows at subsonic speed. For supersonic jet speed, the cluster flow becomes a large simple jet at about 20 nozzle diameters downstream, where the outer jet velocity peaks disappear.

5.7.2.3 Concluding Remarks

A successful application of the LV technique to high temperature and high speed subsonic jet flows has been demonstrated in the experiments reported in this section. Use of the LV technique with high temperature and high speed subsonic jet flows has yielded detailed velocity and turbulence intensity mappings of several combinations of a round and a rectangular jet. Observations from these LV Measurements are summarized as follows:

1. A minimal temperature effect is found on the velocity profiles of a round jet.
2. Strong similarity in mean velocity and turbulence intensity profiles along the jet axis is obtained over large Mach number and temperature ranges (e.g., $M = 0.3$ to 0.965 , $T_0 = 294$ to 644 K for a round jet).
3. The jet plume decays faster and spreads wider at high temperature compared to room temperature for a round jet.
4. A rectangular jet exhaust degenerates to that of a circular jet approximately 10 equivalent diameters downstream of the nozzle exit.

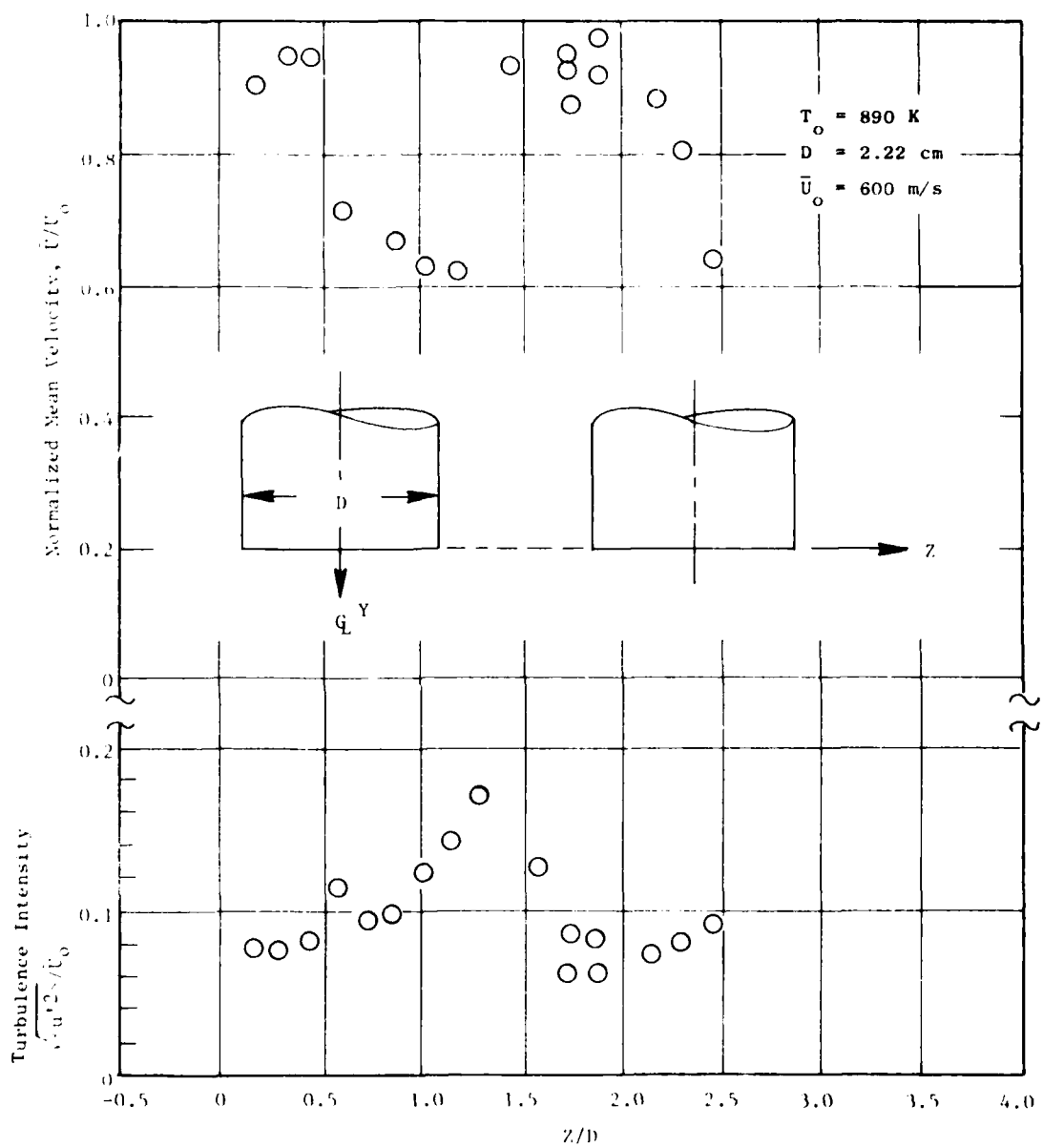


Figure 5-136. Radial Velocity Profile of the 7-Jet Cluster Flows at $Y/D = 4$ ($\Delta Z = 3.81 \text{ cm}$, $X/D = 0$).

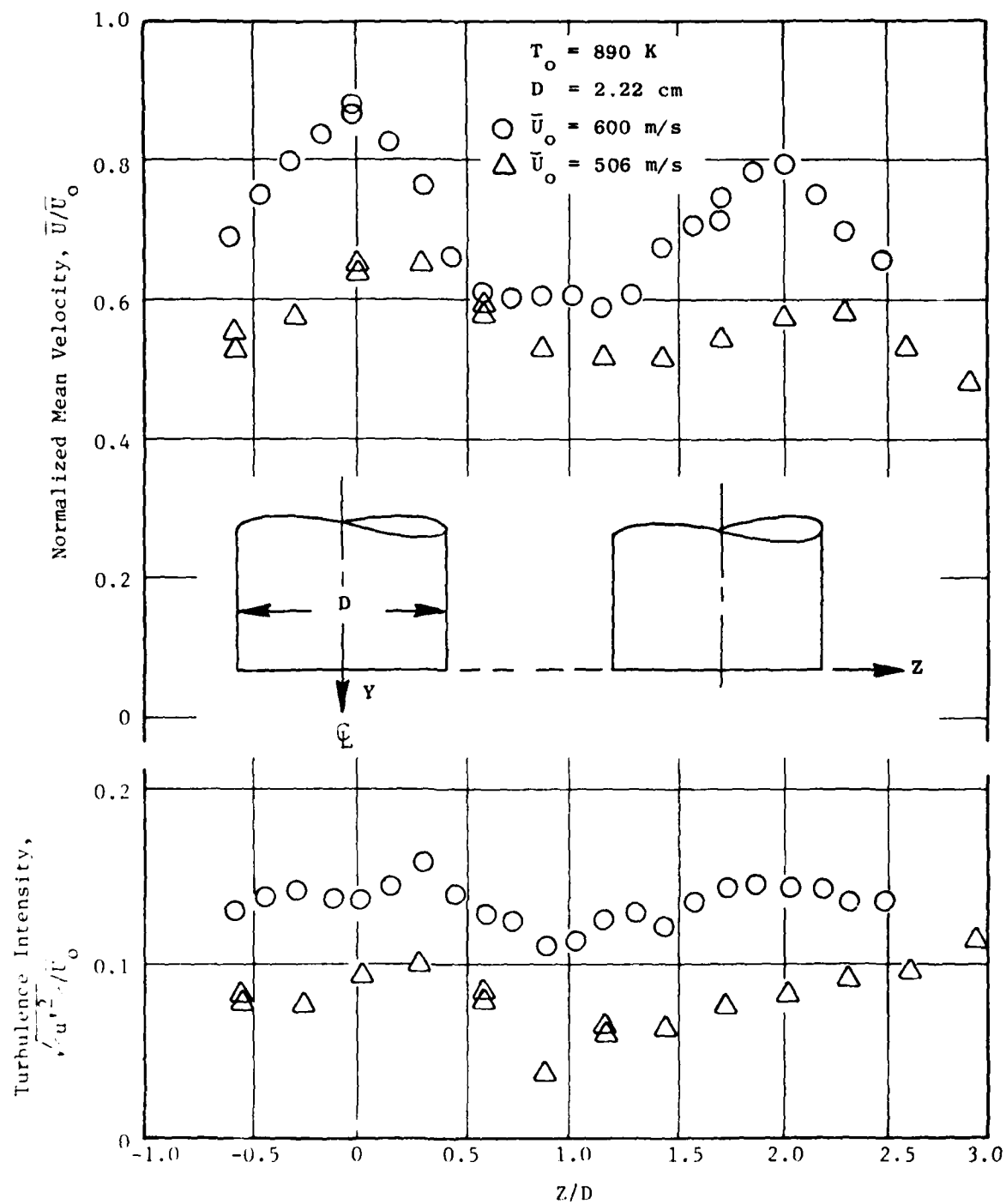


Figure 5-137. Radial Velocity Profiles of the 7-Jet Cluster Flows at $Y/D = 10$ ($\Delta Z = 3.81 \text{ cm}$, $X/D = 0$).

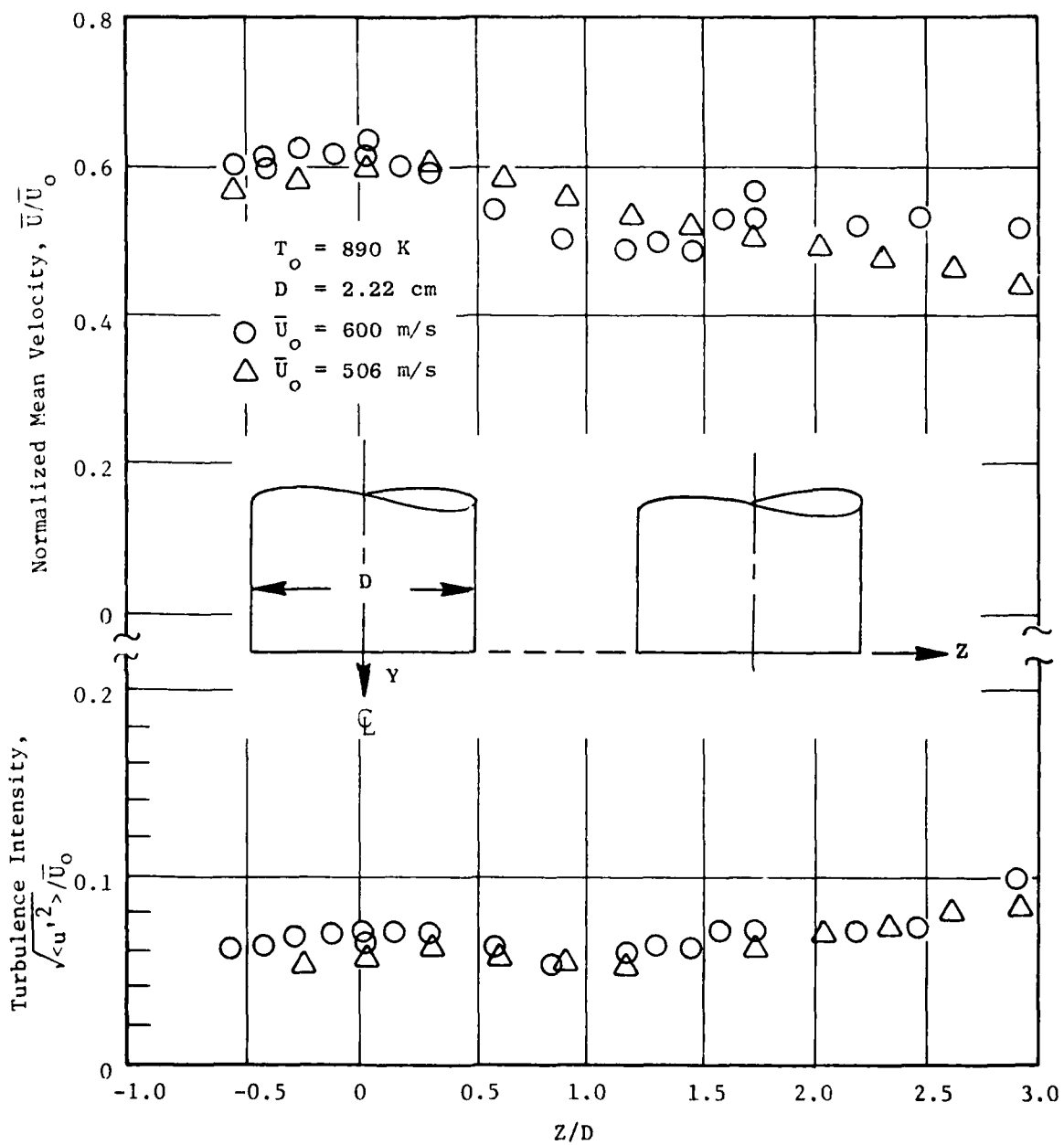


Figure 5-138. Radial Velocity Profile of the 7-Jet Cluster Flows at $Y/D = 14$ ($\Delta Z = 3.81 \text{ cm}$, $X/D = 0$).

(611)

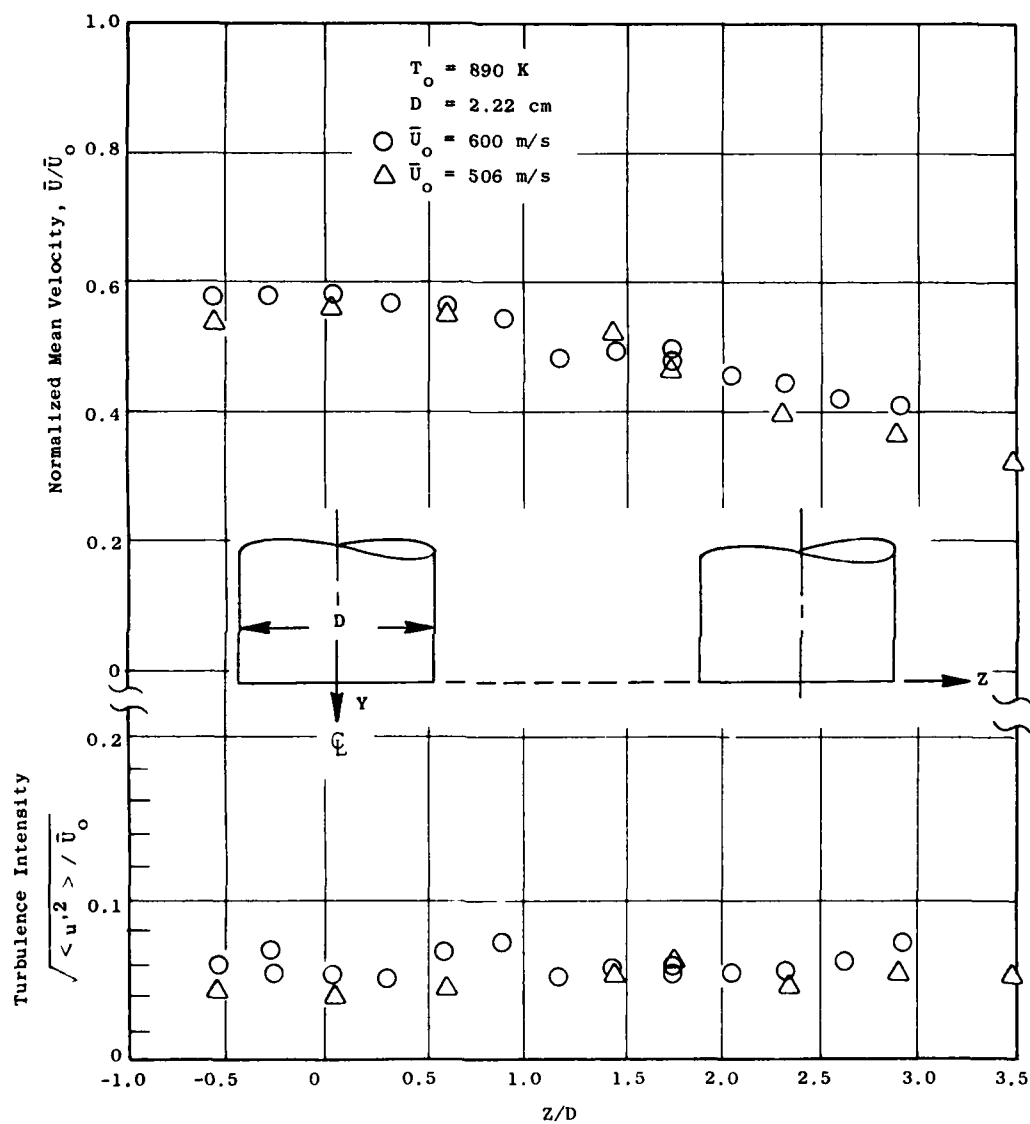


Figure 5-139. Radial Velocity Profiles of the 7-Jet Cluster Flows at $Y/D = 20$ ($\Delta Z = 3.81 \text{ cm}$, $X/D = 0$).

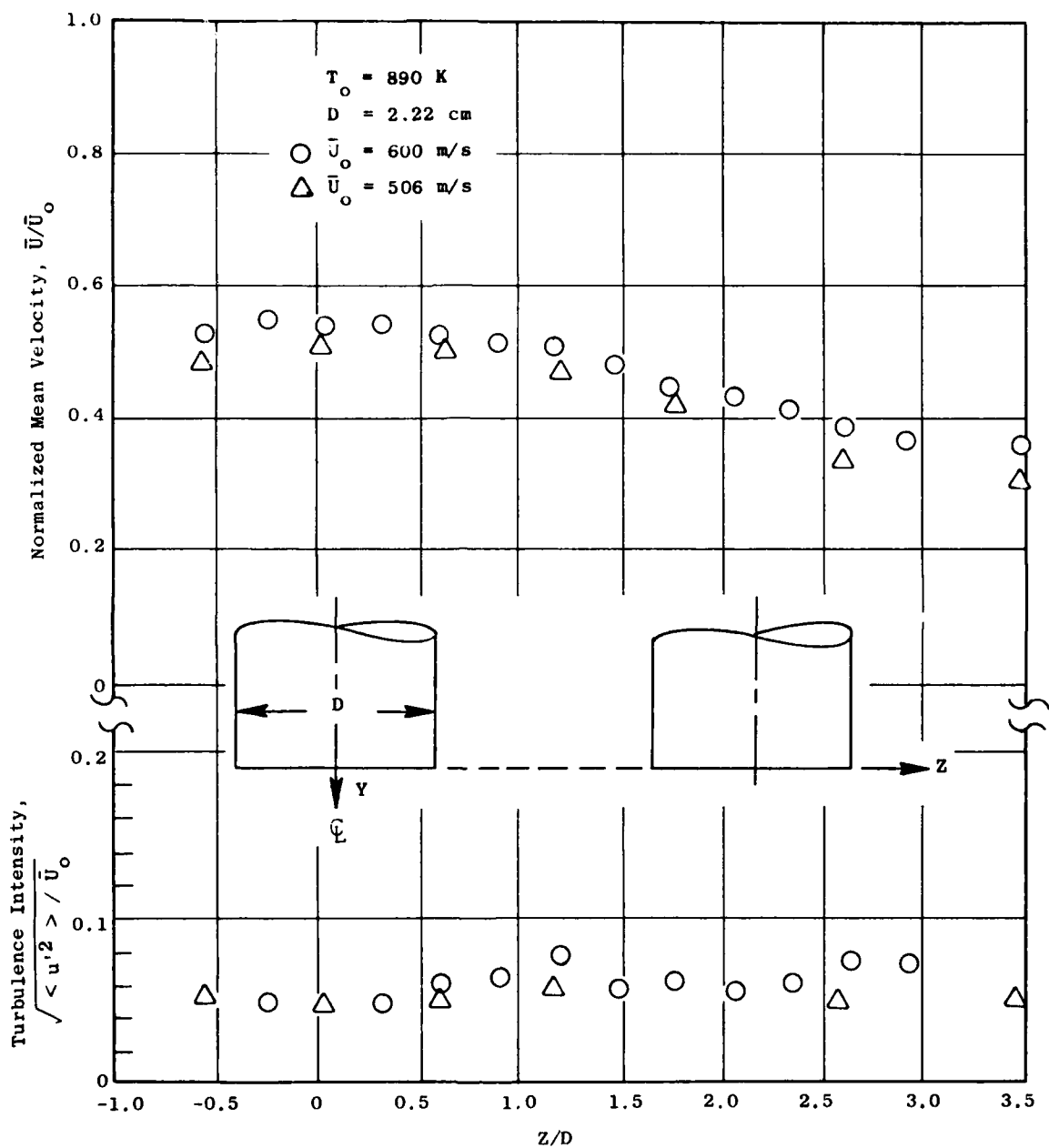


Figure 5-140. Radial Velocity Profiles of the 7-Jet Cluster Flows at $Y/D = 26$ ($\Delta Z = 3.81 \text{ cm}$, $X/D = 0$).

5. The values of maximum turbulence intensity along both axes of the rectangular jet are similar (only the thickness of the jet is different along the minor and the major axes).
6. At small jet separation distance, i.e., 5 cm, twin round jet flows begin to merge six nozzle diameters downstream. The jet centerlines begin to shift outward from each other at 10 and 14 nozzle diameters downstream. The turbulence intensity profiles are not symmetrical to the jet centerline, with lower intensity near the interface between jets. This is evidence of the reduction in jet noise source strength due to the jet mixing process.
7. For the twin round jet at large separation, i.e., 12.7 cm, mean velocity and turbulence intensity profiles agree closely with those of a single round jet. Each jet behaves as an independent jet up to 14 nozzle diameters downstream.
8. The twin rectangular jets at two separation distances (i.e., 3.81 and 10.48 cm) resemble the flow field of a single rectangular jet. No jet mixing interference is observed for either jet separation distance, from the nozzle exit to 14 equivalent jet diameters downstream. Both jets become round cross-sectional jets between six and eight equivalent jet diameters, similar to a single rectangular jet.
9. For the 7-jet cluster flows, at large cluster separation ($\Delta Z = 6.67$ cm), each jet in the cluster behaves as a single free jet. Some jet interaction is observed at 14 nozzle diameters downstream. However, the turbulence intensity peaks at about eight nozzle diameters downstream. The effect of jet interaction at $Y/D = 14$ and further downstream is minimal.
10. At small cluster separation ($\Delta Z = 3.81$ cm), strong interaction occurs between the center jet and the outer jets. Evidence of the interaction is observed as early as four nozzle diameters downstream from the jet exit. Flows at subsonic speeds appear to have stronger interaction between jets than those at supersonic speeds.
11. The small cluster flows ($\Delta Z = 3.81$ cm) degenerate to a large single jet at about 14 nozzle diameters downstream for the subsonic case and 20 nozzle diameters for the supersonic case, based on the data obtained in the hot jet test experiments.

5.8 HOLE-IN-THE-WALL SOURCE LOCATION MEASUREMENTS

Axial noise source location measurements of the twin rectangular and twin round jet configurations were conducted using the hole-in-the-wall source location method. The test apparatus is described in Section 3.2 of this report. To provide the aperture for these configurations, a system of four plates was used to form a rectangular opening sized so as to accommodate a 14° flare angle from the outer points of the jet periphery. Several axial positions of each aperture were used to minimize the buffeting of the jet flow against the aperture and yet achieve good isolation of the noise upstream of the aperture. Three azimuthal microphone measurement planes (0° , 45° and 90°) were used to capture the total acoustic power. Eight inches of acoustic foam were used as ground covering to reduce the effects of ground reflections.

5.8.1 Twin Round Jets

5.8.1.1 Overall Power and Power Spectra

Axial surveys were taken up to 15 jet diameters downstream on three different nozzle spacings, and at two different flow conditions, as shown in Figure 5-141(a). The experimental measurement procedure is illustrated in Figure 5-141(b). The principal utility of the hole-in-the-wall technique is in measuring the axial acoustic power distribution, since the presence of the isolation chamber and aperture tends to alter the SPL directivity patterns. As discussed in Section 3.3, acoustic energy escapes from the upstream side of the aperture and contaminates the downstream measurement. This effect is seen in Figure 5-142, where the azimuthally averaged overall power level (OAPWL) is plotted versus aperture location, x , for several nozzle spacings. The leakage increases so rapidly at the large axial distances that there is hardly any drop-off of OAPWL observed with distance. In the high frequency portion of the spectrum, the drop-off of the azimuthally averaged power level (PWL) is more rapid than the OAPWL, as shown in Figure 5-143. This is because the high frequency sources are close to the nozzle, and because there is a lack of any buffeting noise in this part of the spectrum. Increased spacing shows lower drop-off of both PWL and OAPWL with x (and hence more acoustic leakage from upstream to downstream). Higher jet temperature and velocity causes a slight increase in the rate of the drop-off of OAPWL or PWL with axial distance, as seen on Figure 5-144.

The power spectra (shown in Figure 5-145 and 5-146) illustrate the low-frequency noise caused by buffeting of the jet plume on the aperture. This interaction noise is present in all the data, but increases with downstream axial distance because of both this interaction noise and the excessive acoustic leakage through the aperture, the data have not been converted into source strength distributions.

5.8.1.2 Shielding Distributions

The concept of the hole-in-the-wall technique should (theoretically), allow determination of the axial distribution of acoustic shielding effects.

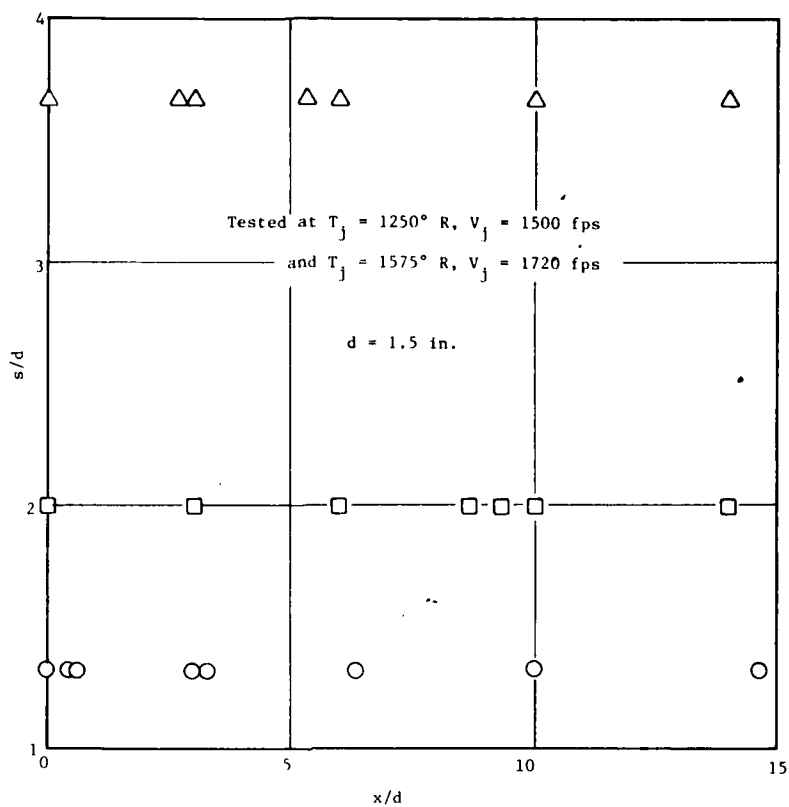


Figure 5-141 (a). "Hole-In-The-Wall" Test Matrix, Twin-Round.

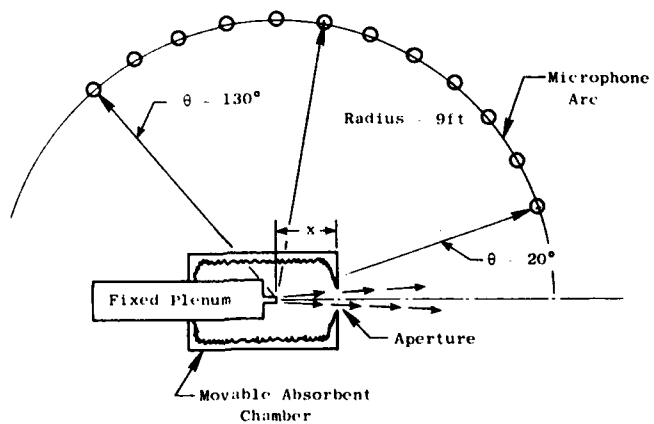


Figure 5-141 (b). "Hole-In-The-Wall" Experiment.

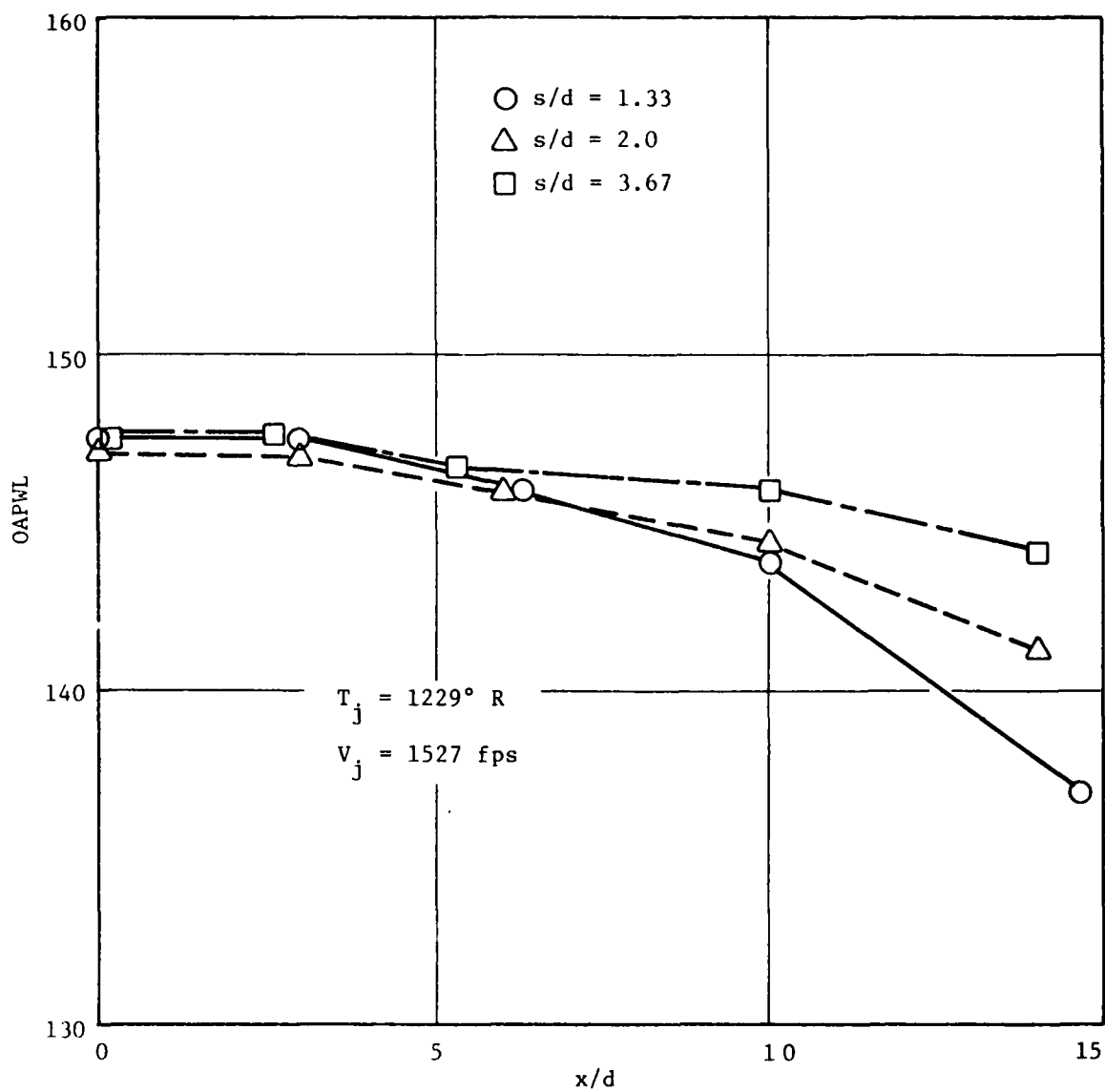


Figure 5-142. Twin Round, Overall Power Decay.

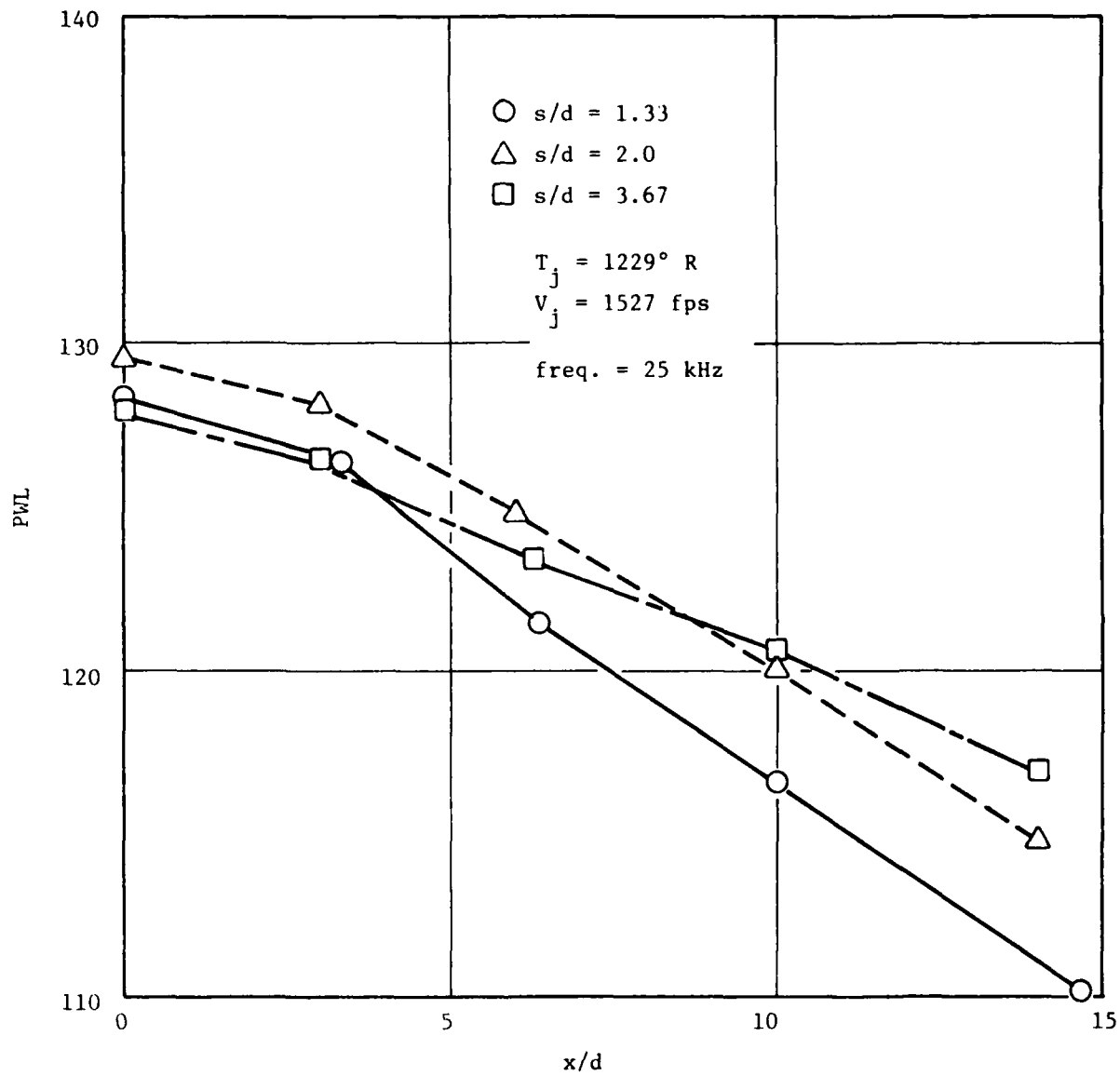


Figure 5-143. Twin Round, High Frequency Decay.

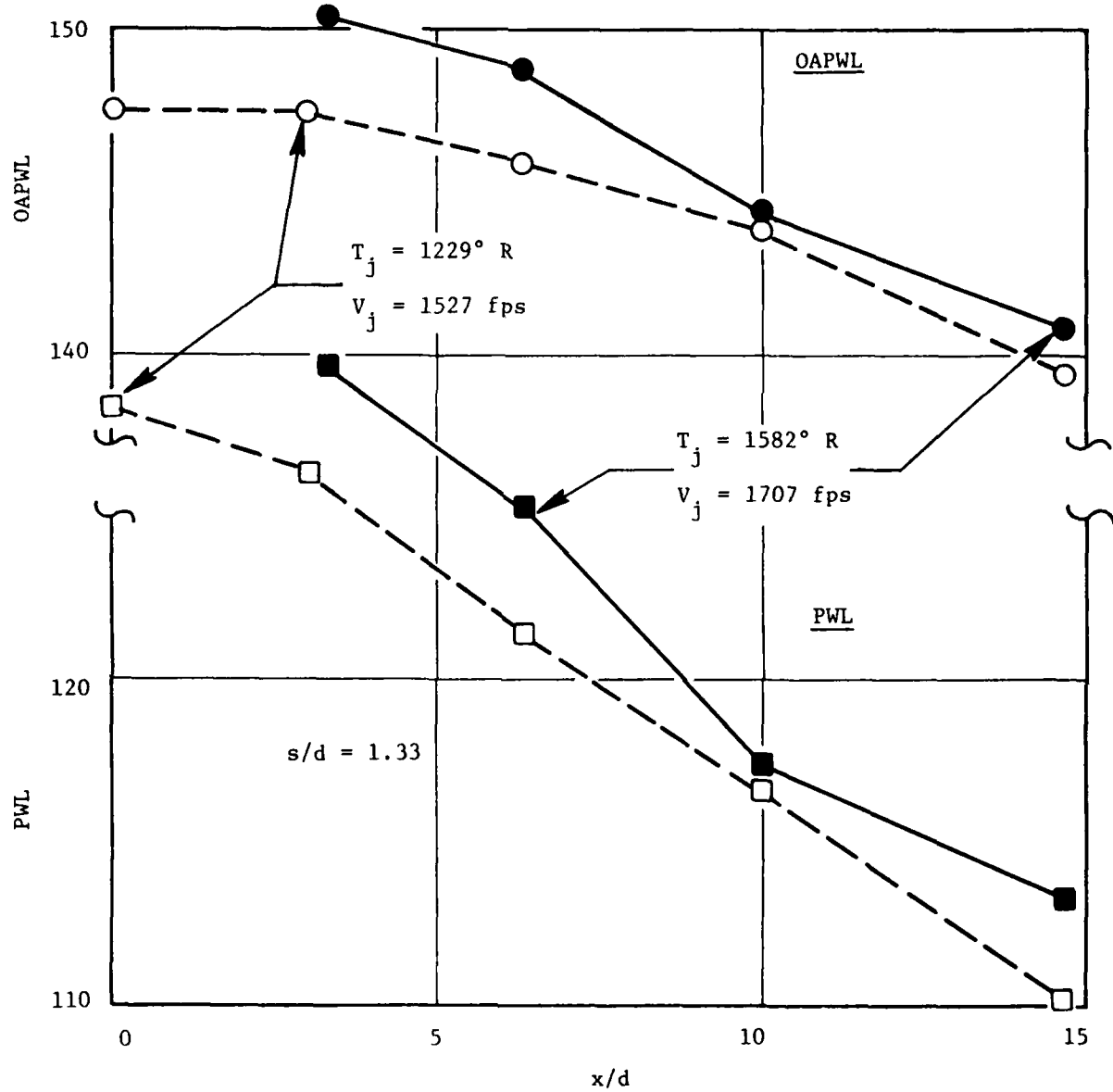


Figure 5-144. Twin Round, Effect of Velocity and Temperature.

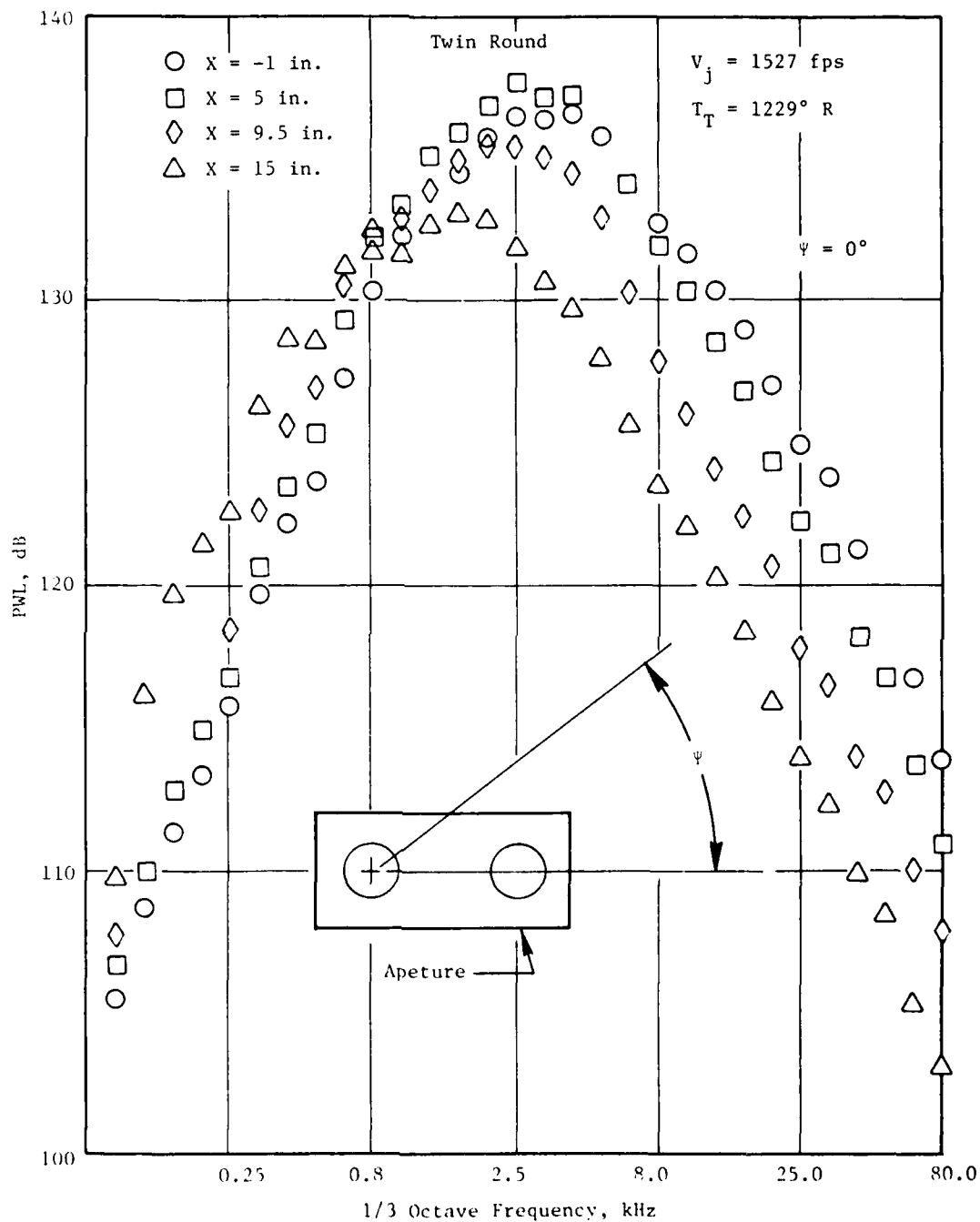


Figure 5-145. Twin-Round, Power Spectra ($s/d = 1.33$).

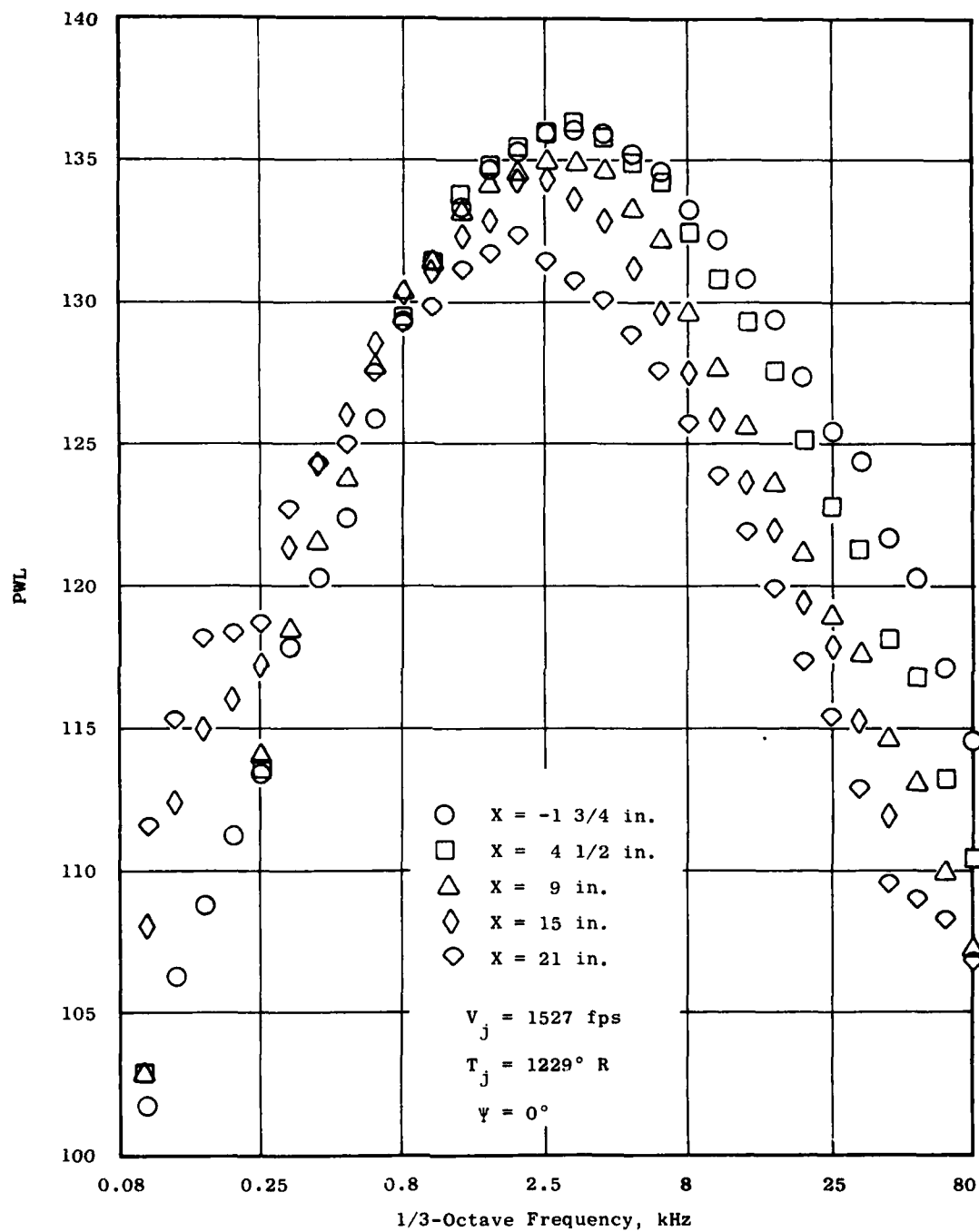


Figure 5-146. Twin Round, Power Spectra, $S/d = 1.33$.

The contribution to the total shielding by any axial section can be determined by comparing the differences in overall power and power spectra as measured in the "loud" $\psi = 90^\circ$ plane and in the "quiet" $\psi = 0^\circ$ plane. The realities of this technique however, force the acceptance of only qualitative indications of shielding effects. The difference in overall power level, as shown on Figure 5-147, is found to be a decreasing function of distance, as expected. This is due to the merging of the two streams at some downstream location, and the gradual subsidence of acoustic shielding as the two jets merge. For high frequencies, the responsible sources (and hence the shielding) are located close to the nozzle exit plane $X = 0$. Figure 5-148 supports this (the drop-off of Δ PWL with distance is more rapid than for the Δ OAPWL results).

5.8.2 Twin Rectangular Jets

5.8.2.1 Overall Power and Power Spectra

A series of tests was conducted on twin rectangular jets similar to the above twin round nozzle tests. The twin rectangular jet plume, however, allows much better isolation of the upstream noise from the acoustic arena and the results are therefore more useful. Three different nozzle spacings were employed, at one heated high subsonic flow condition.

Figure 5-149 shows the spacing and the axial position of the isolation aperture, x . Axial surveys of the azimuthally averaged overall sound power level are shown on Figure 5-150. Flattening of the curves with increased spacing (observed in the twin round tests) is *not* observed here, although buffeting noise is present and contributes to a larger extent as axial distance increases.

The 25 kHz band levels (Figure 5-151) drop much more rapidly with axial distance, but there still appears to be some acoustic leakage (increased PWL as s/t increases at any given axial position x/t). The buffeting or "interaction" noise which contributes to the OAPWL can be seen in Figures 5-152 and 5-153, in the low frequency portions of the spectra. An intense tone appears in Figure 5-154 in the $\psi = 0^\circ$ plane, when the axial location of the isolation aperture x is less than 20 nozzle widths. This is thought to be due to an entrainment-induced flapping of the two jet flows when they are very close together as discussed in Section 5.4.

5.8.2.2 Shielding and Azimuthal Effects

The most interesting result of the hole-in-the-wall source location work is shown on Figure 5-154. Three mechanisms are present: (1) the self-shielding of the rectangular jets by themselves, which reduces the levels of the $\psi = 90^\circ$ plane; (2) the shielding by the adjacent jet which reduces the levels in the $\psi = 0^\circ$ plane; and (3) the induced tone in the $\psi = 0^\circ$ plane for the smallest spacing. For the smallest spacing, $s/t = 2.08$, the tone in the $\psi = 0^\circ$ plane dominates at $x = 0$, resulting in negative values of Δ OAPWL. However, as x increases, this source is gradually isolated until, at about 20

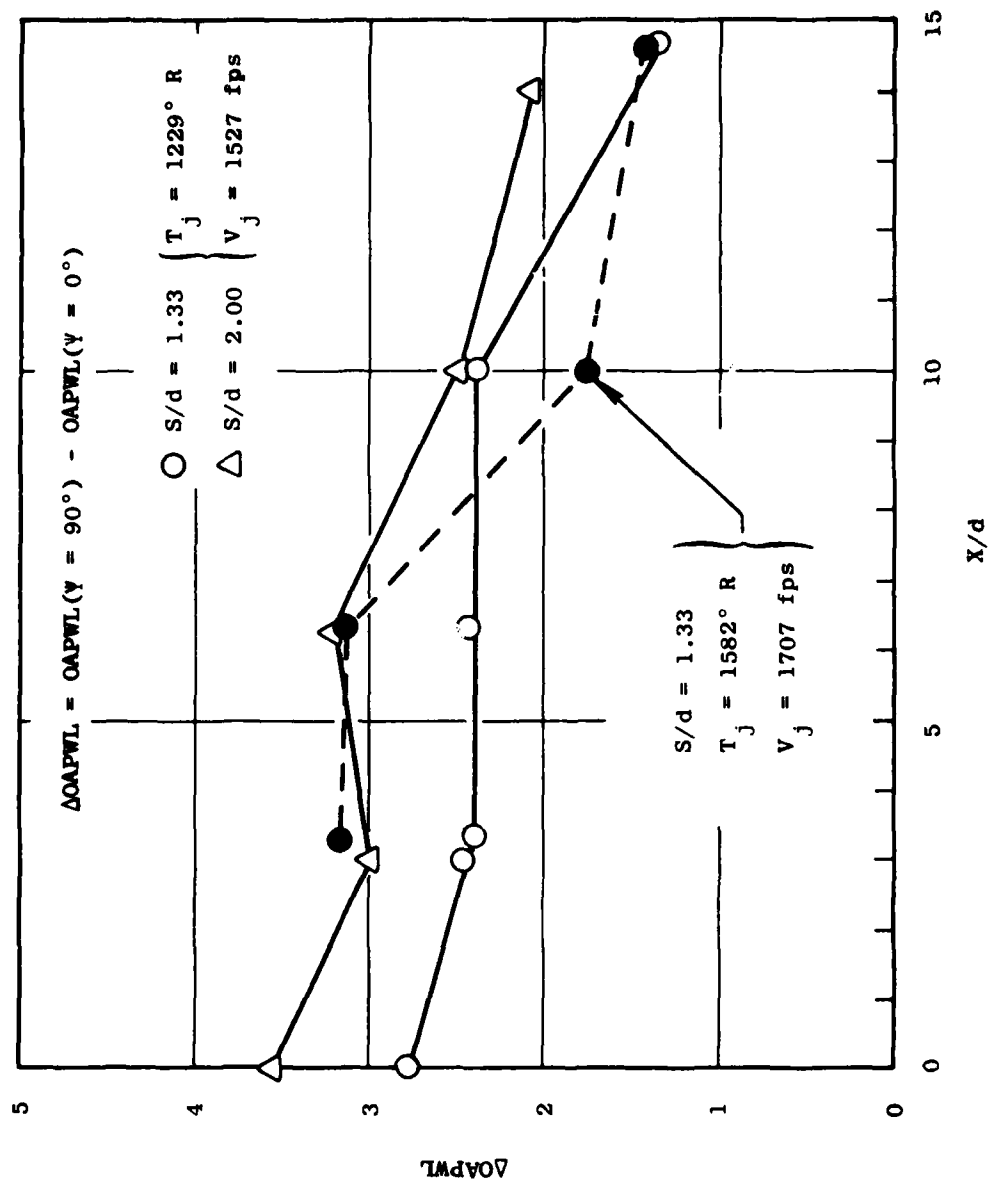


Figure 5-147. Twin Round, $\Delta OAPWL$ Versus Axial Location.

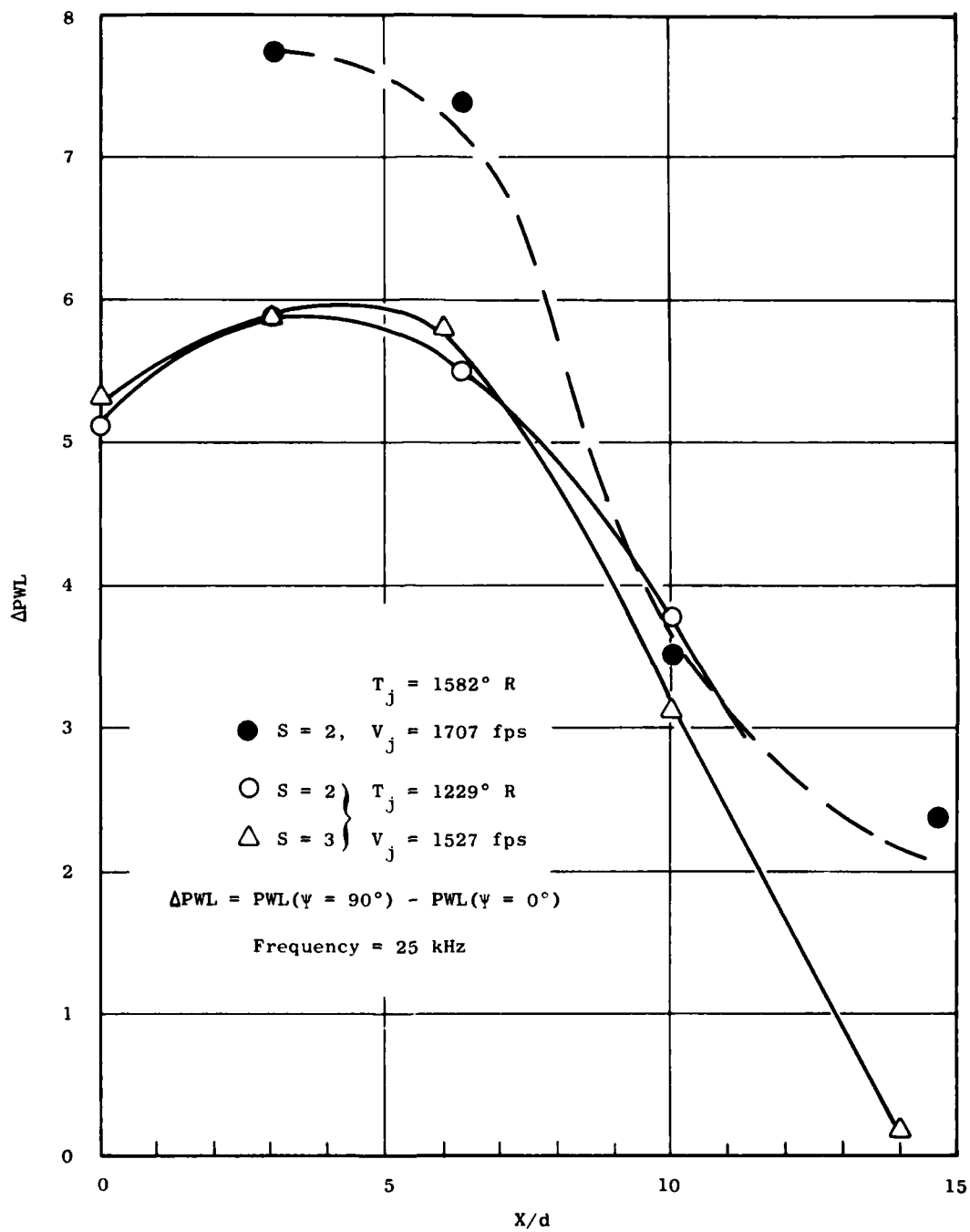


Figure 5-148 Twin Round, ΔPWL Versus Axial Location.

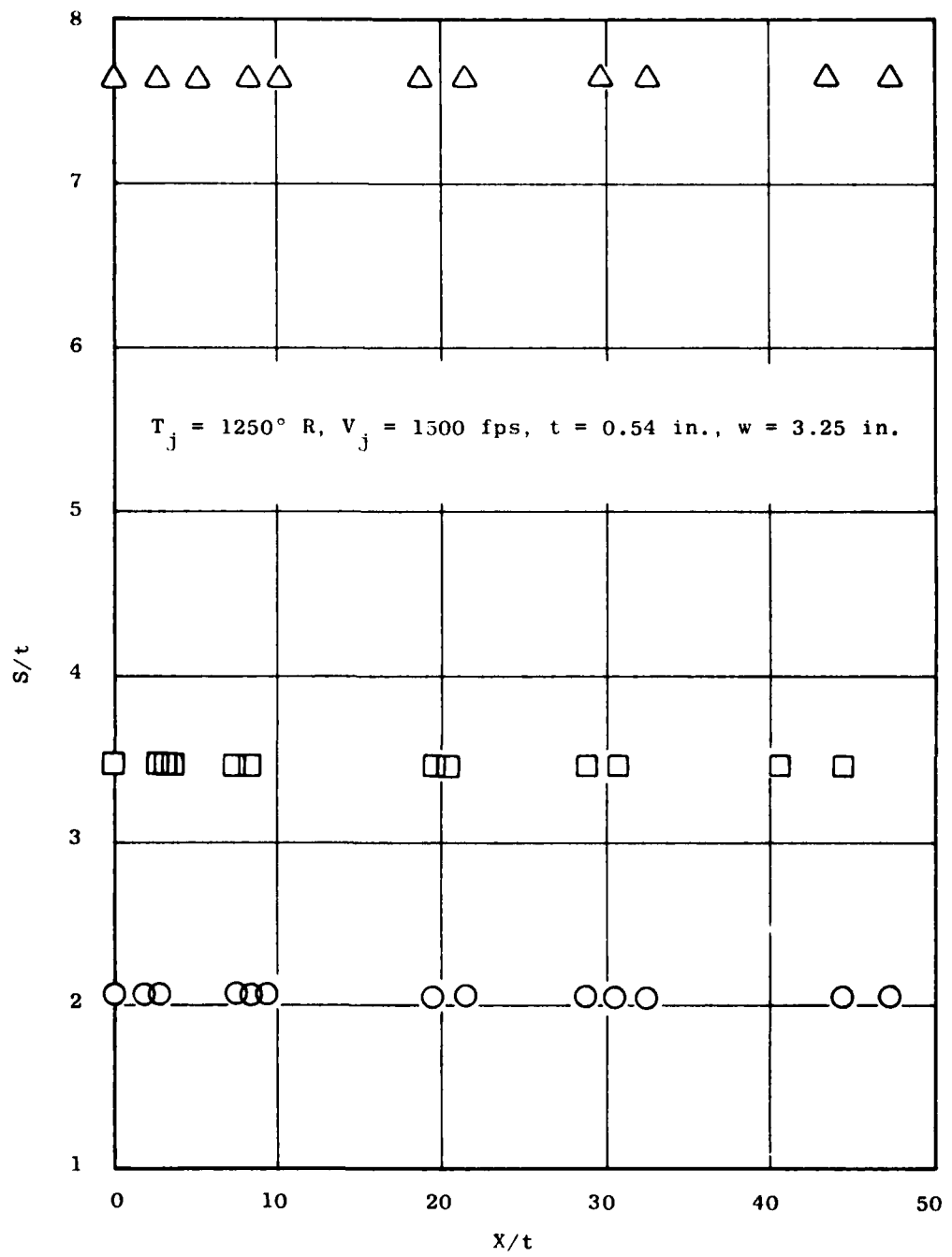


Figure 5-149. Hole-in-the-Wall Test Matrix, Twin Rectangular.

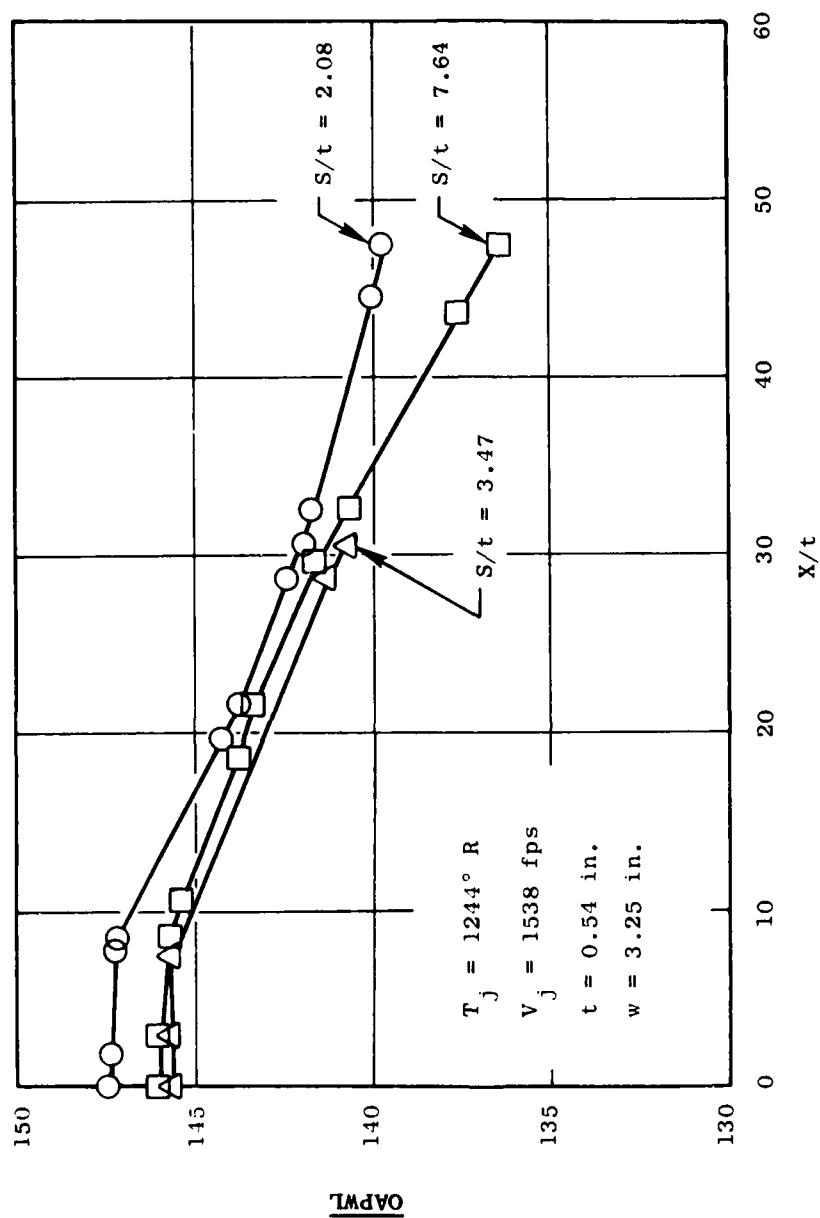


Figure 5-150. Twin Rectangular Overall Power Decay.

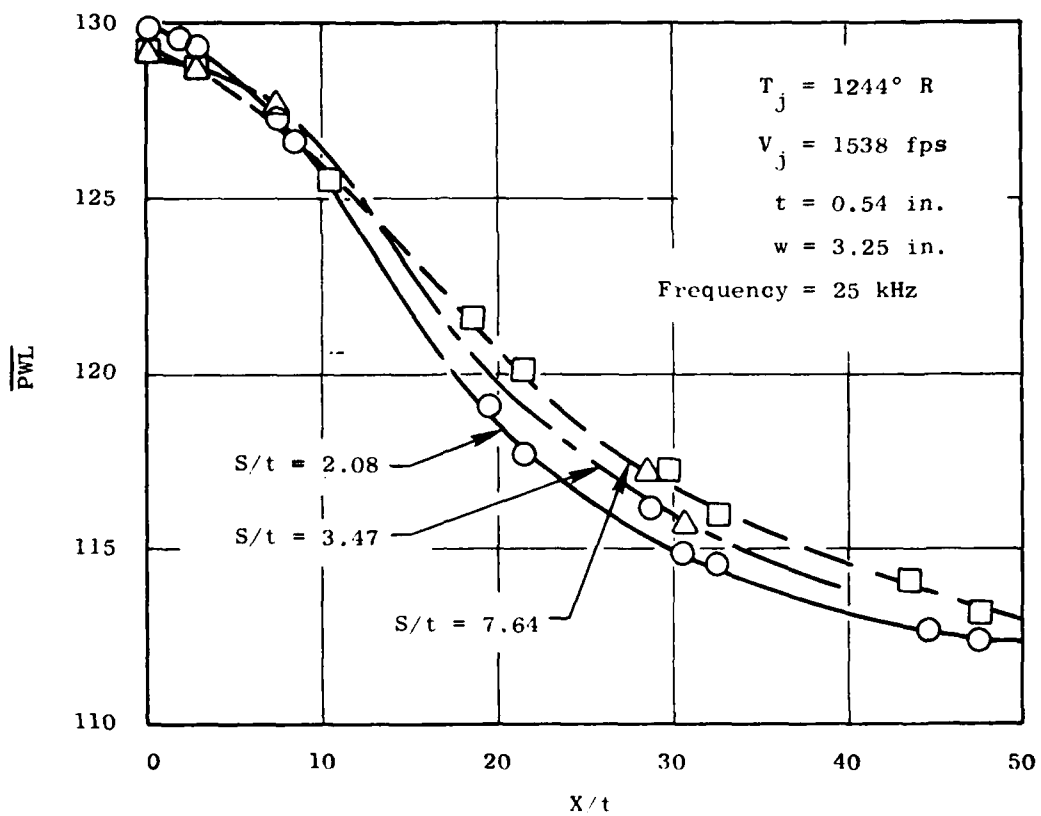


Figure 5-151. Twin Rectangular High Frequency Power Decay.

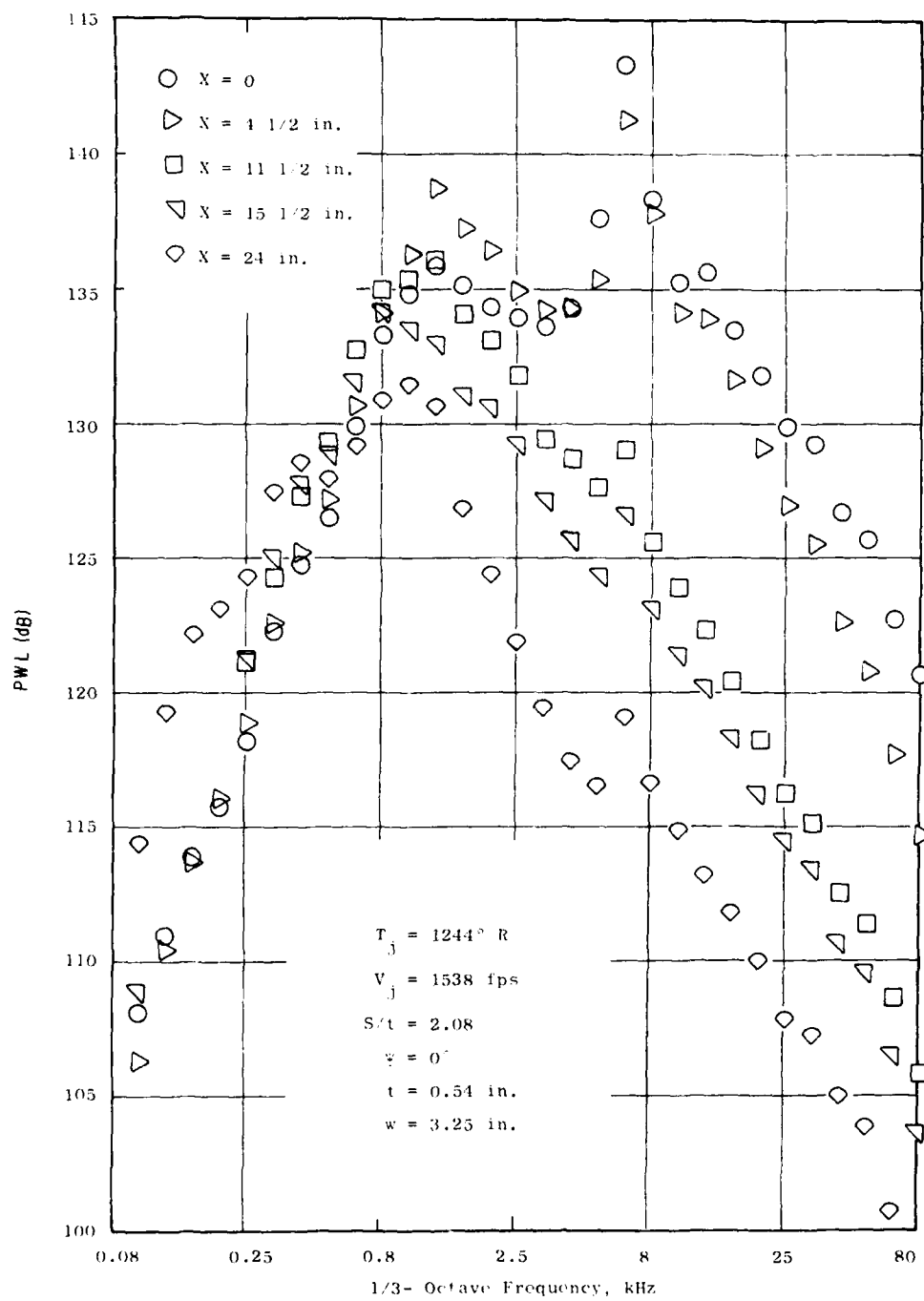


Figure 5-152. Twin Rectangular, Power Spectra, $S/t = 2.08$.

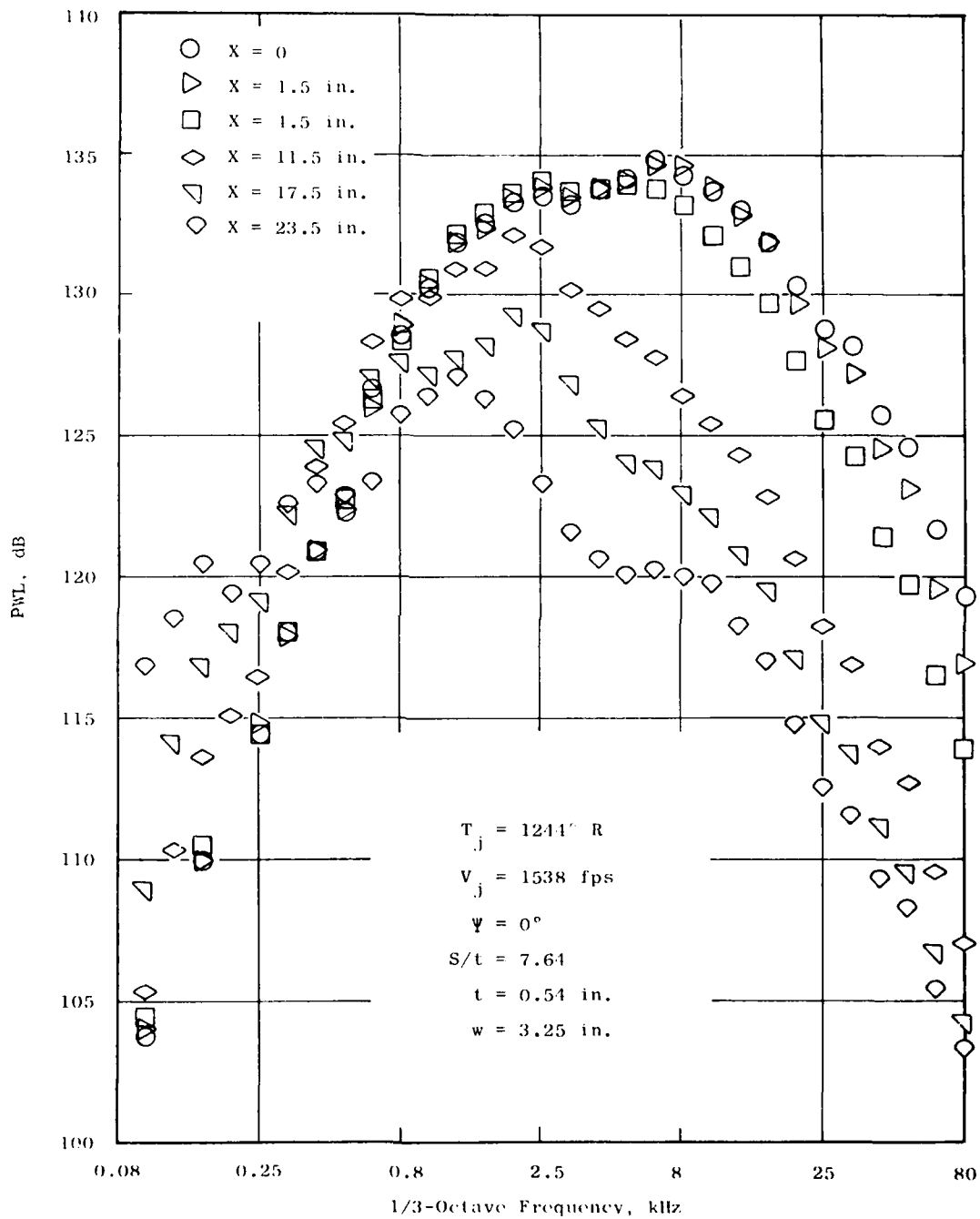


Figure 5-153. Twin Rectangular, Power Spectra, $S/t = 7.64$.

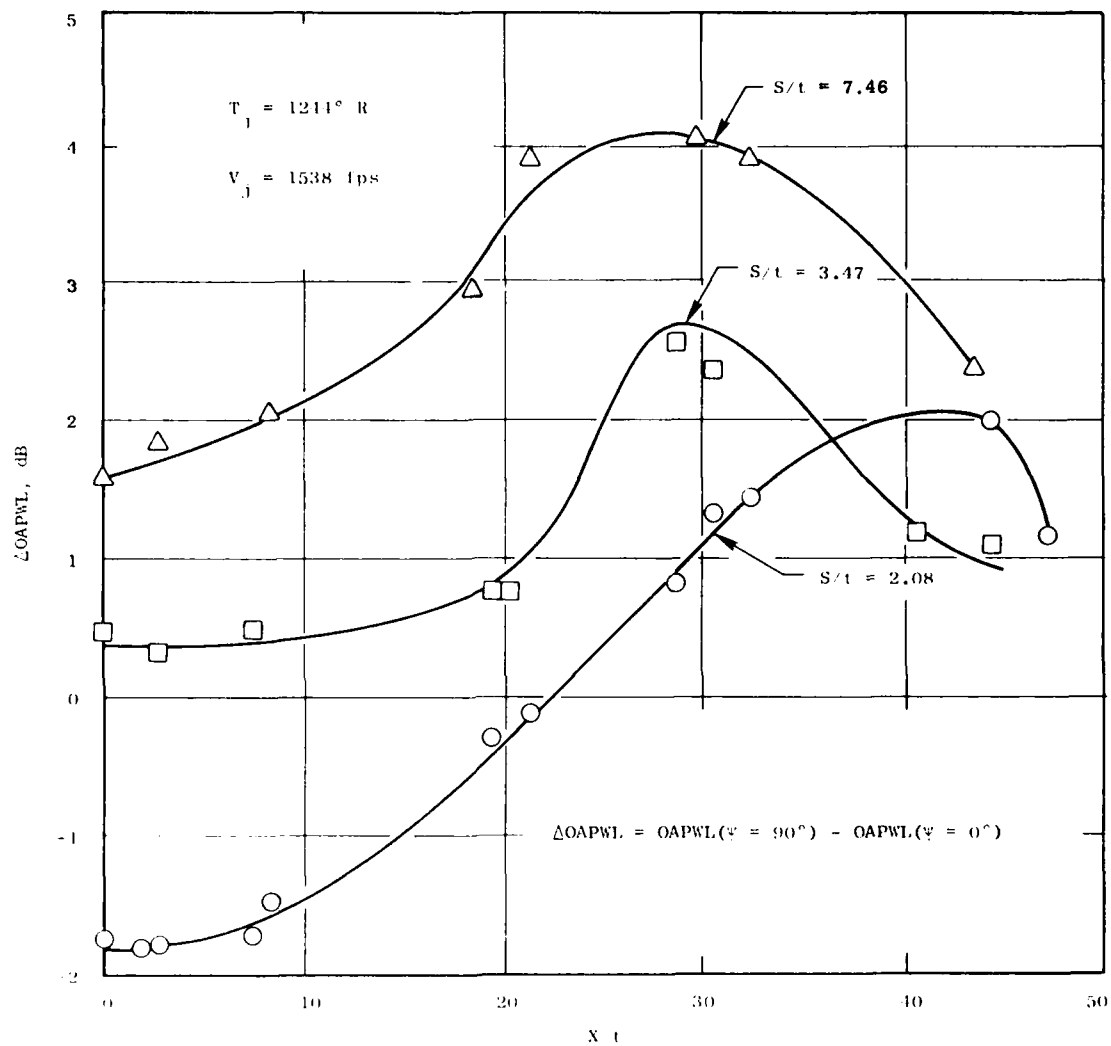


Figure 5-151. Twin Rectangular, ΔOAPWL Versus Axial Location.

diameters, the shielding by the adjacent jet has started to produce a net positive $\Delta OAPWL$. Further increases in x leave only the diffused downstream portions of the jets exposed and $\Delta OAPWL$ tends towards zero. At the two larger spacings ($s/t = 3.47$ and $s/t = 7.46$), the combination of self-shielding and adjacent shielding produces a net positive $\Delta OAPWL$ with full exposure of the plumes ($x = 0$). As the plume is progressively isolated however (x becomes larger), the effect of the self-shielding (apparently predominant near the jet exit plane) diminishes, the adjacent-jet shielding becomes predominant, and $\Delta OAPWL$ increases. This explanation is reasonable because the self-shielding depends on a high aspect ratio jet flow, which exists near the exit planes, whereas the adjacent shielding only requires a separation of the two streams. The larger nozzle separation ($s/t = 7.46$) shows the adjacent shielding to be more dominant than in the case of the medium spacing ($s/t = 3.47$).

5.8.3 Concluding Remarks

In order to produce reasonable results from the hole-in-the-wall technique, the nozzle must have a plume that allows a tight "acoustic" seal by the isolation aperture. Lack of such isolation hampered the work carried out with the twin round nozzles. The technique is very time consuming, requiring roughly 10 to 20 times as long to survey a jet plume as to record normal far-field measurements. The method only produces quantitatively adequate results at high frequencies due to contamination by the plume aperture buffeting noise. The technique is, however, capable of producing some useful qualitative results. The relative location of dominance of adjacent-jet shielding and self-shielding were identified, for example, for twin rectangular nozzles.

6.0 ACOUSTIC SHIELDING EXPERIMENTS

6.1 DESCRIPTION OF TEST PROGRAM AND RESULTS

The basic objective of the acoustic shielding test program was to investigate the purely acoustic aspects of the shielding of noise sources by a surrounding jet. An annular jet flow at Mach number M , with inner and outer radii of a and b , respectively, was tested in the outdoor hot jet facility shown in Figures 6-1 and 6-2. Two types of noise sources were tested: (1) a stationary source from a whistle and (2) a moving noise source from a small high speed jet placed along the annular jet centerline. Data were obtained on the acoustic power output radiated by the source and on the changes in the source directivity pattern.

6.1.1 Test Results with a Stationary Source (Whistle)

Figure 6-3 shows a typical spectrum of the whistle noise source at 30° from the jet axis and 10 feet away from the jet exit, with no annular jet. The central pure tone frequency is between 4 and 5 kHz. Some higher order harmonics also exist. When the coannular shielding jet is imposed, the whistle noise is reduced. Figure 6-4 shows frequency spectra of the whistle at 30° and 90° from the jet axis with shielding jet flow at a Mach number of 0.6 and at room temperature. The noise spectra from the shielding jet alone are also shown in the same figures. The amplitude reduction of the whistle's central frequency is more at 30° (5 kHz) than at 90° . At a shielding jet flow Mach number of 0.8, the whistle noise is further reduced at both 30° and 90° (Figure 6-5). The stationary sound source from the whistle is therefore suppressed in the far field due to the presence of shielding jet flow. The reduction in amplitude of this stationary source at a fixed angle from the jet centerline increases as the velocity of the shielding jet flow increases.

The angular difference in the acoustic shielding of a stationary sound source is observed in the directivity measurements shown in Figure 6-6. The noise generated only from the shielding jet flows at Mach 0.6 and 0.8 is small relative to that from the whistle, and can be neglected. By comparing the directivity pattern of the whistle alone (Figure 6-7) with that of the whistle with shielding jet flows (Figure 6-6), the amount of shielding on a stationary sound source as a function of direction is obtained as shown in Figure 6-8. Figure 6-8 shows that the shielding effect appears to be significant at shallow angles ($\theta < 50^\circ$) and increases as the angle decreases toward the jet centerline.

6.1.2 Test Results with a Moving Source (A Small Jet Inside the Shielding Jet)

A base-purge arrangement was employed in the region near the exit of the annular shielding jet; however, the ventilation was apparently insufficient. The annular shielding jet is pulled in toward the jet centerline. Typical



Figure 6-1. Acoustic Shielding Experimental Test Facility.

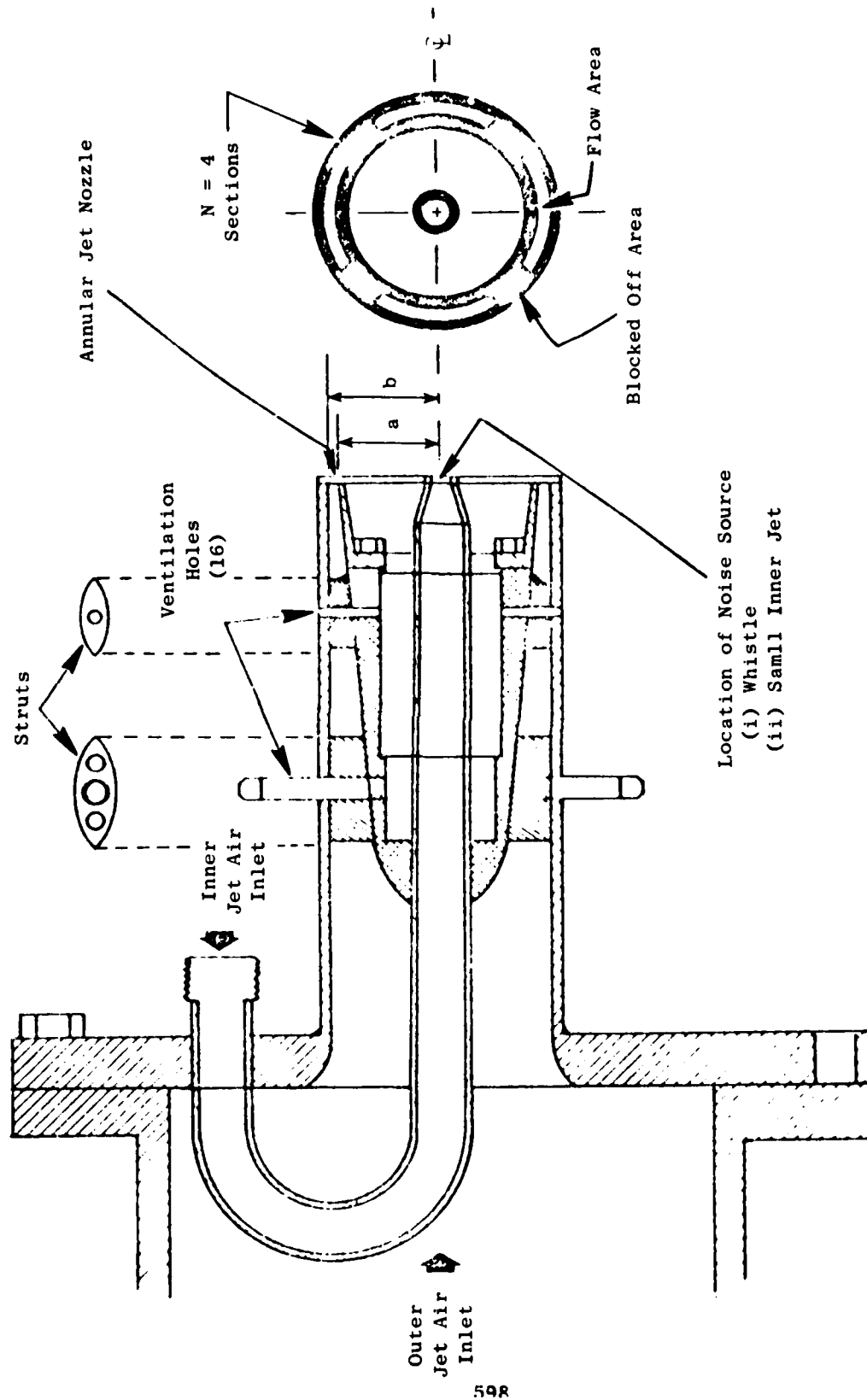


Figure 6-2. Schematic of the Coannular Jet Experiment Setup.

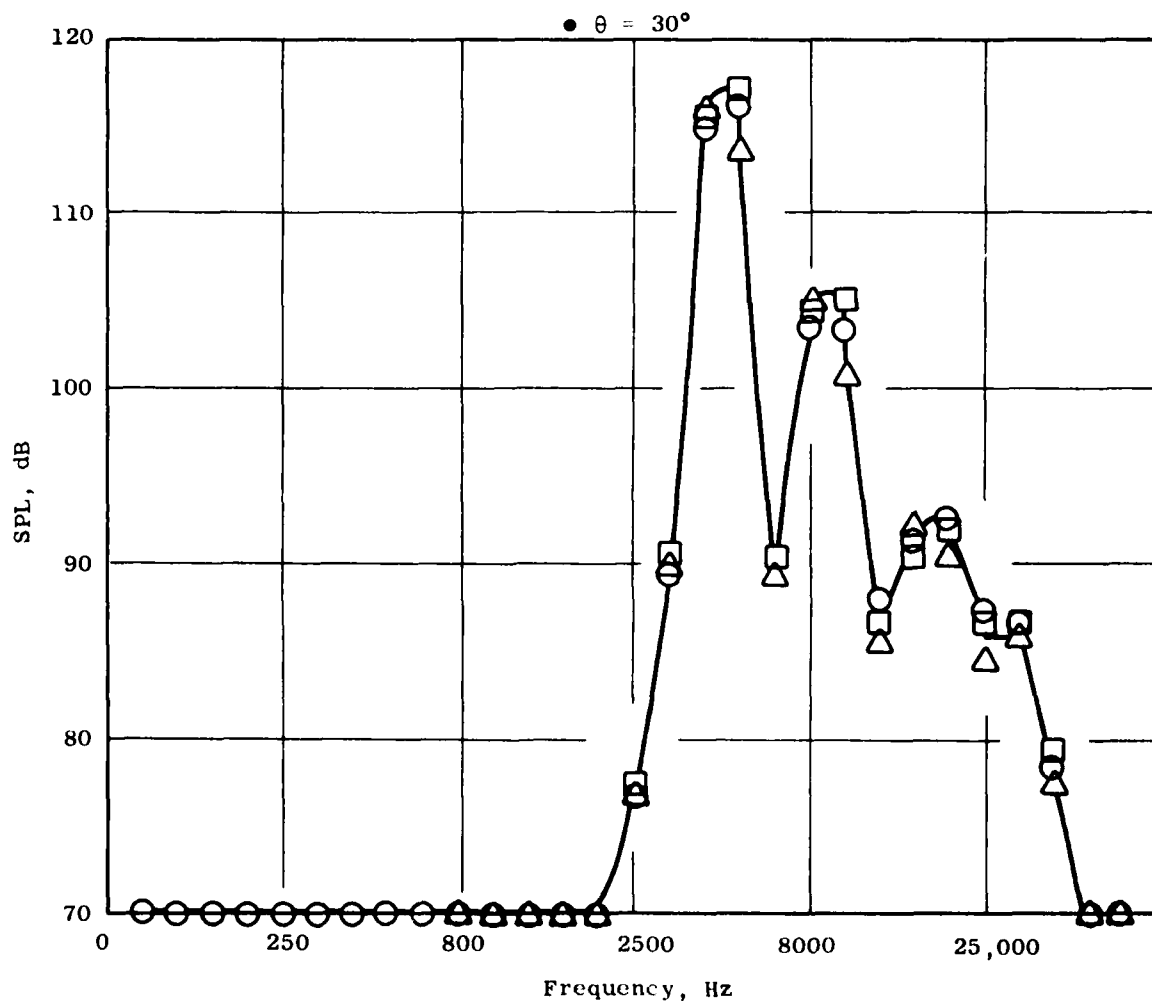


Figure 6-3. SPL Spectrum of Whistle Alone.

Δ Whistle and Shielding Jet
 \circ Shielding Jet Alone
 $\gamma_b = 0.85$

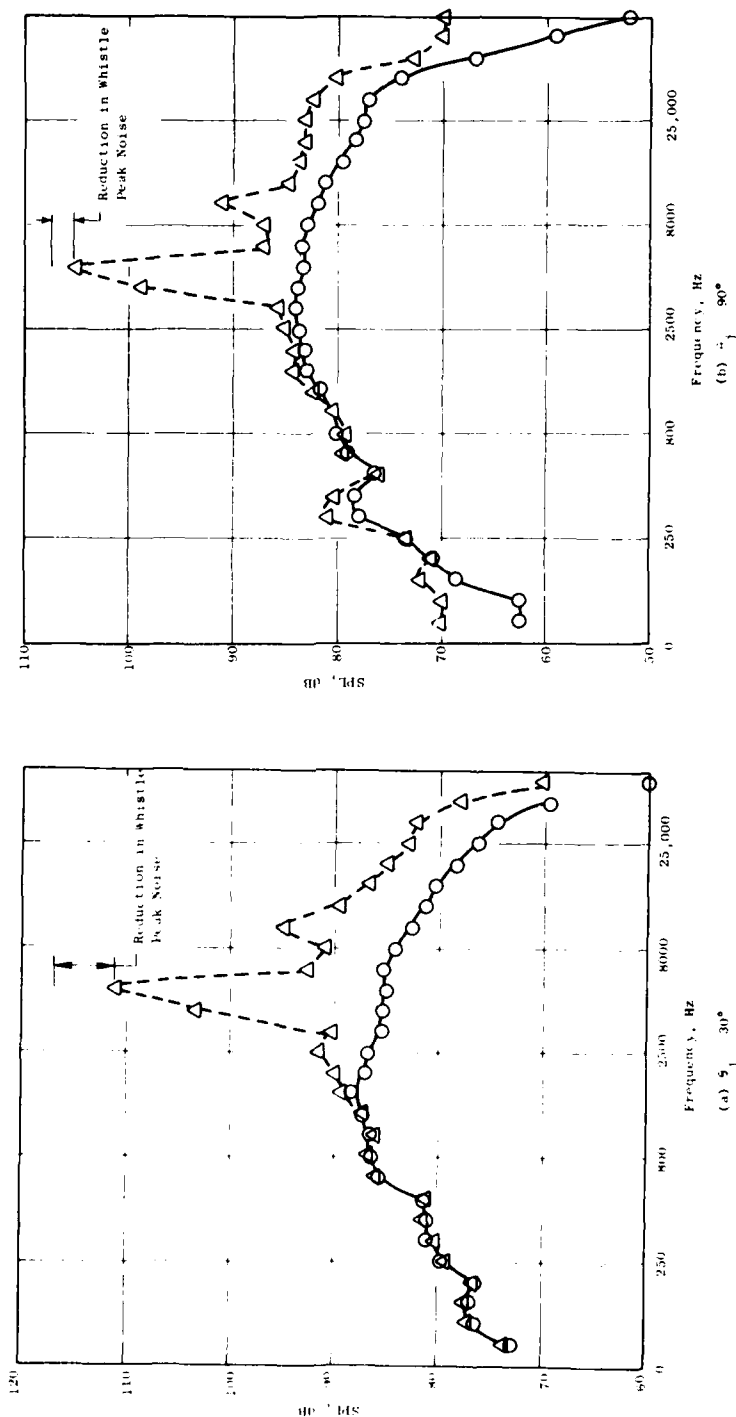


Figure 6-4. SPL Spectrum of Whistle with a Mach 0.6 Annular Shielding Jet Flow.

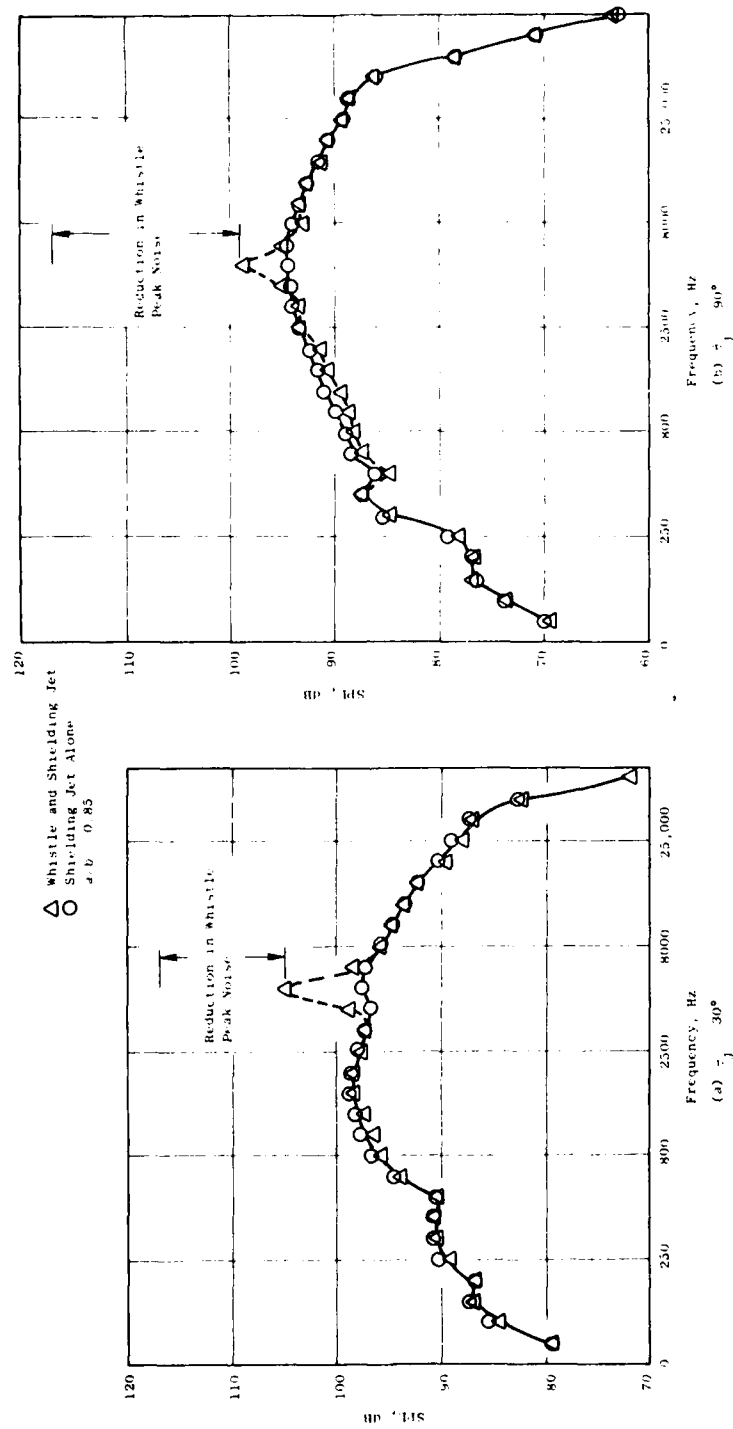


Figure 6-5. SPL Spectra of Whistle with a Mach 0.8 Shielding Jet Flow.

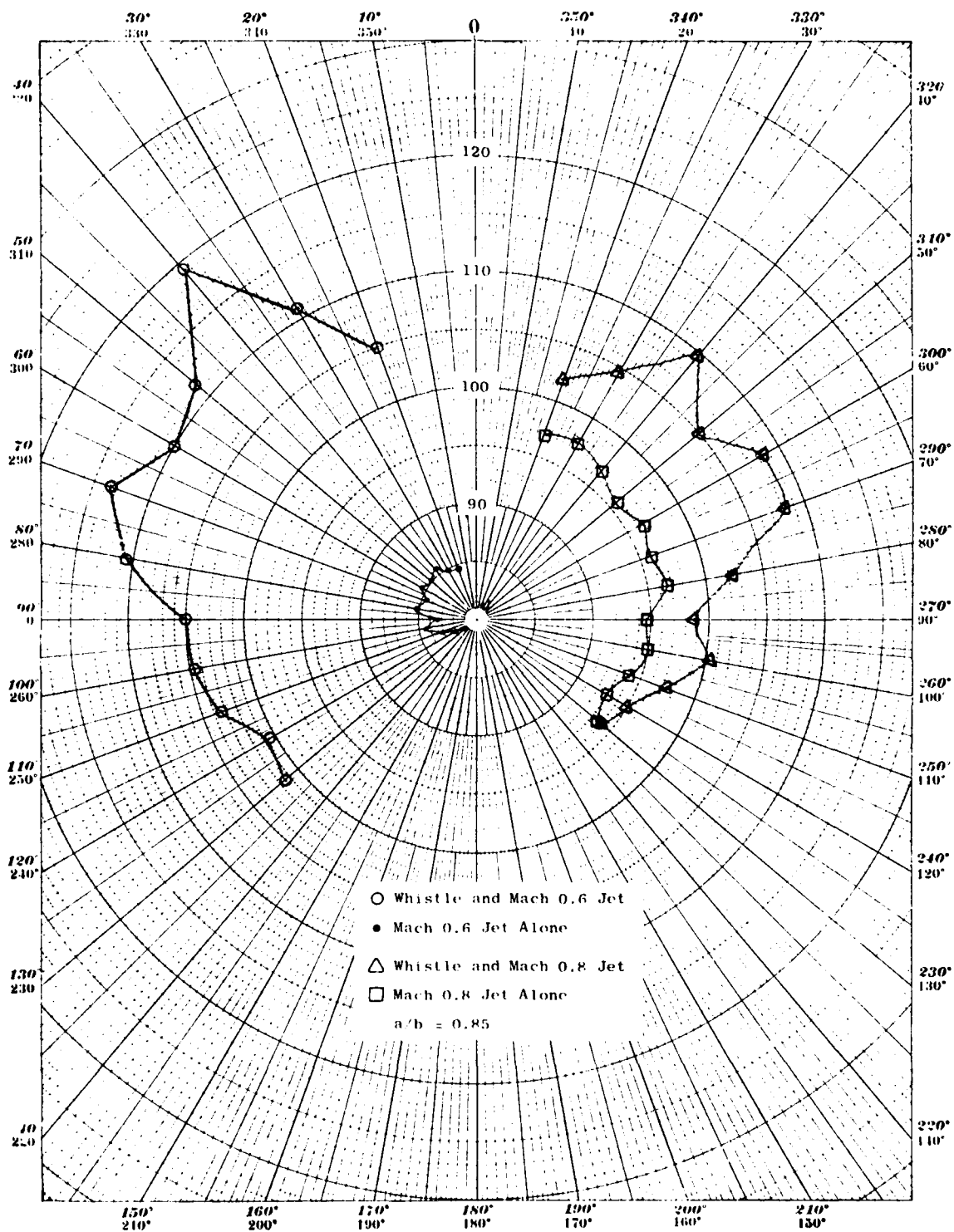


Figure 6-6. Directivity Patterns of Whistle with Shieldings Jet Flows at Mach 0.6 and 0.8 ($f_c = 5\text{kHz}$).

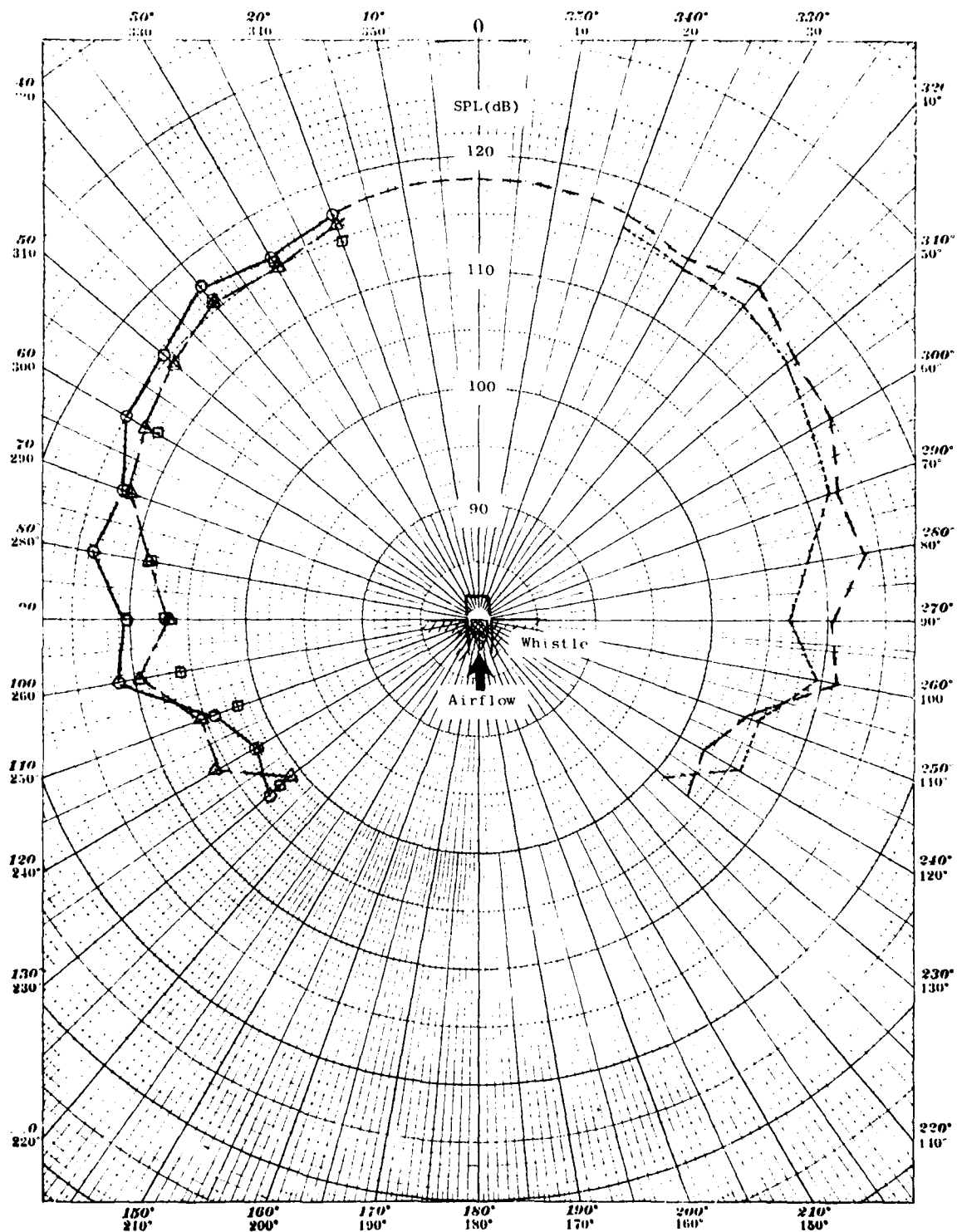


Figure 6-7. Directivity Patterns of Whistle Alone ($f_c = 5\text{kHz}$).

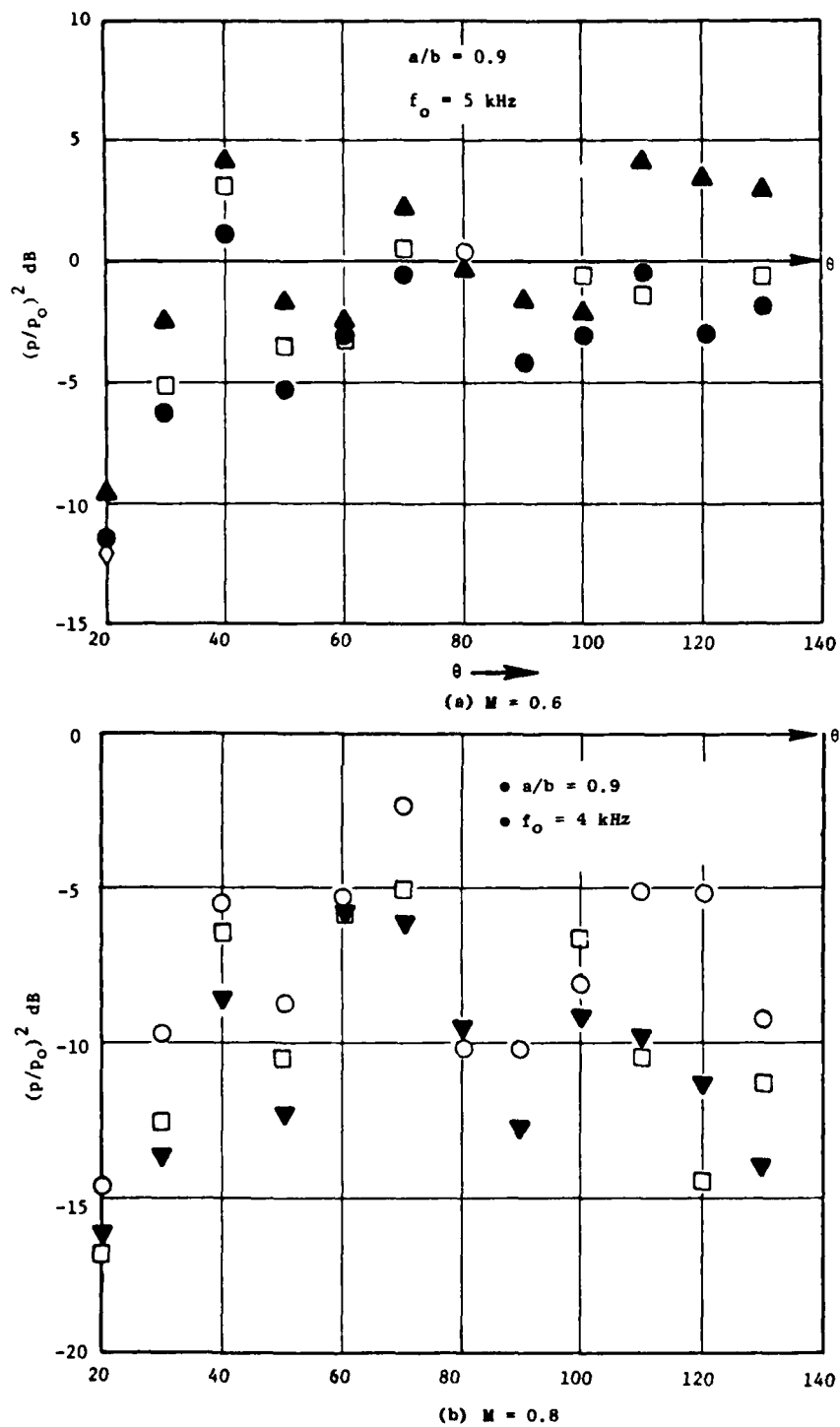


Figure 6-8. Reduction in SPL Due to Shielding Jet Flow on a Stationary Source.

velocity profiles are shown in Figure 6-9 (indicated as the case without segments). The annular jet collapses into a single round jet after some distance downstream from the jet exit. There is a region near the base of the jet centerline where reverse flow is observed due to insufficient ventilation. After additional ventilation was provided to the base region via segmentation of the shielding jet (Figure 6-2), the shielding jet behaved as an ideal annular jet. The velocity profile is shown in Figure 6-9.

Flow reversal was not observed near the jet base region with the segmented arrangement. In order to provide a fair comparison between the experimental results and the theoretical slug flow model, the flow arrangement with segments was selected as the standard test configuration in order to duplicate the effects of an ideal annular jet. Table 6-1 shows a list of various jet configurations tested and the test conditions of the shielding jet flows. The inner sound source jet flow was fixed at Mach 2 and ambient temperature.

Figure 6-10 shows the OASPL directivity patterns from the source (inner) jet, the shielding jet, and both jets together. The acoustic shielding of the source jet noise is again obtained by direct comparison of the directivity patterns for the source jet alone and for the combined source and shielding jets (provided that the noise from the shielding jet alone is insignificant, as is generally the case).

Two shielding jet thickness configurations at similar operating conditions are shown in Figure 6-10, which represents typical test results. A few important observations from these directivity measurements are summarized as follows: (1) the noise from shielding jet flow alone was at least 10 dB lower than that from either the source jet or from both source and shielding jets. The contamination from the shielding jet noise in the both-jet measurements, was therefore, minimal. (2) The amplitude of the moving noise source jet is reduced at shallow angles ($\theta < 50^\circ$). (3) The magnitude of the source noise reduction increases as the observer angle decreases. (4) The angular extent of this shielding phenomenon (noise reduction) increases with the thickness of the shielding jet. (5) Shielding effect appears to be minimal at 90° direction, particularly when the shielding jet flow was at room temperature. This last observation is further substantiated by the SPL spectral measurements shown in Figure 6-11 with the room temperature shielding jet flow. At 90° , the SPL spectra of the source jet noise are almost identical with and without the shielding jet flow. However, at 40° from the jet centerline (where shielding exists) the source noise shows an amplitude reduction between 2 to 20 kHz.

Figure 6-12 shows the power spectra at two shielding jet flow temperatures. The abscissa is nondimensional source frequency, $A = (2\pi a/c)f_0$, where f_0 is the source frequency. In terms of the observed frequency, f , f_0 is given by

$$f_0 = f \sqrt{(1 - M_c \cos \theta)^2 + (0.3 M_c)^2}$$

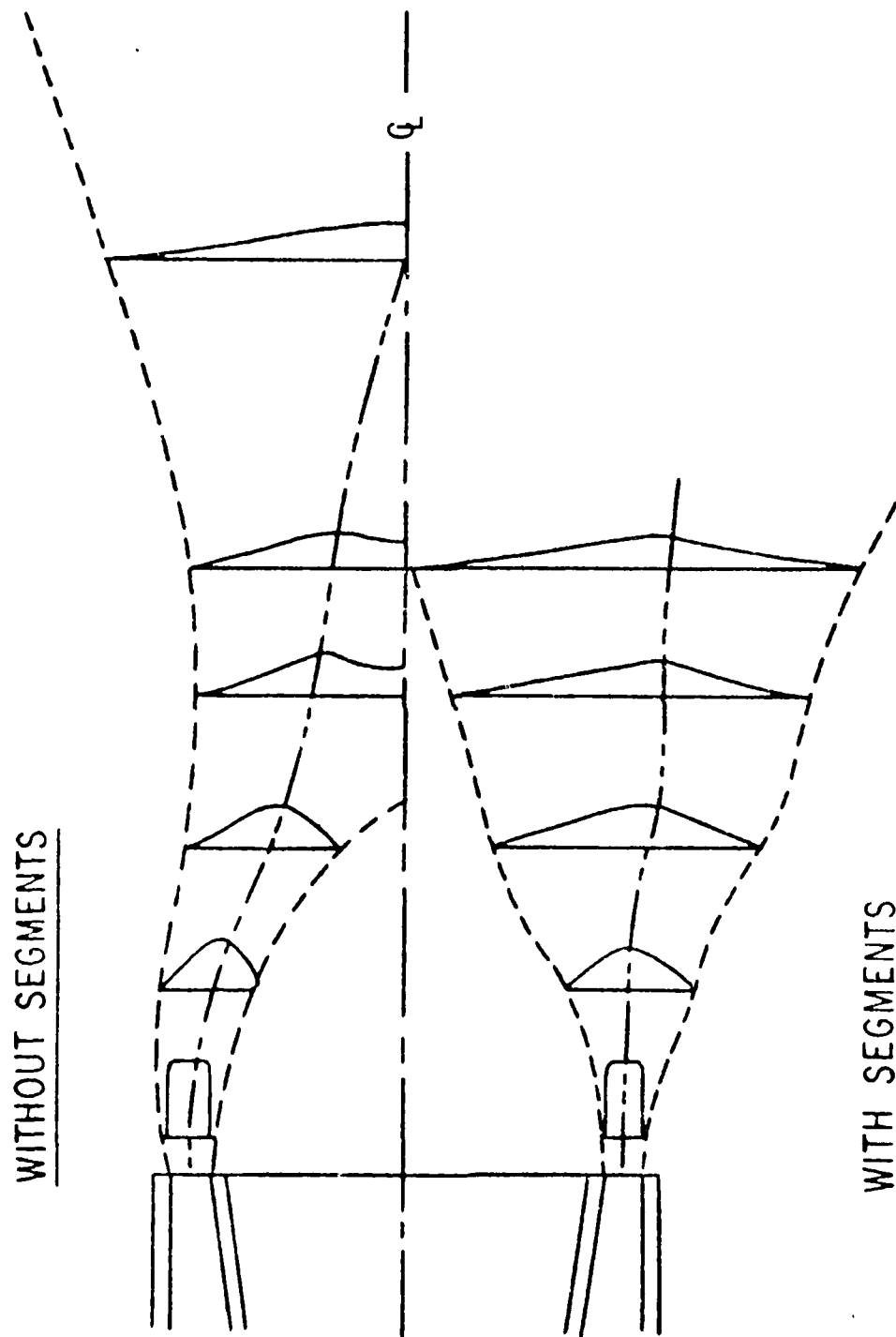


Figure 6-9. Velocity Profile of the Annular Shielding Jet.

Table 6.1. Experimental Configurations and Test Conditions.

- Model Configurations

Jet Radius Ratio (a/b)	Segments(N)	% Area Blocked
0.85	0	0
0.85	4	18
0.85	4	36
0.85	8	36
0.95	0	0
0.95	4	18
0.95	4	36
0.95	8	36

- Shielding jet temperature: 500° R, 850° R and 1500° R
- Shielding jet velocity: 650 ft/sec to 1100 ft/sec
- Convective noise source jet at 500° R and 2200 ft/sec

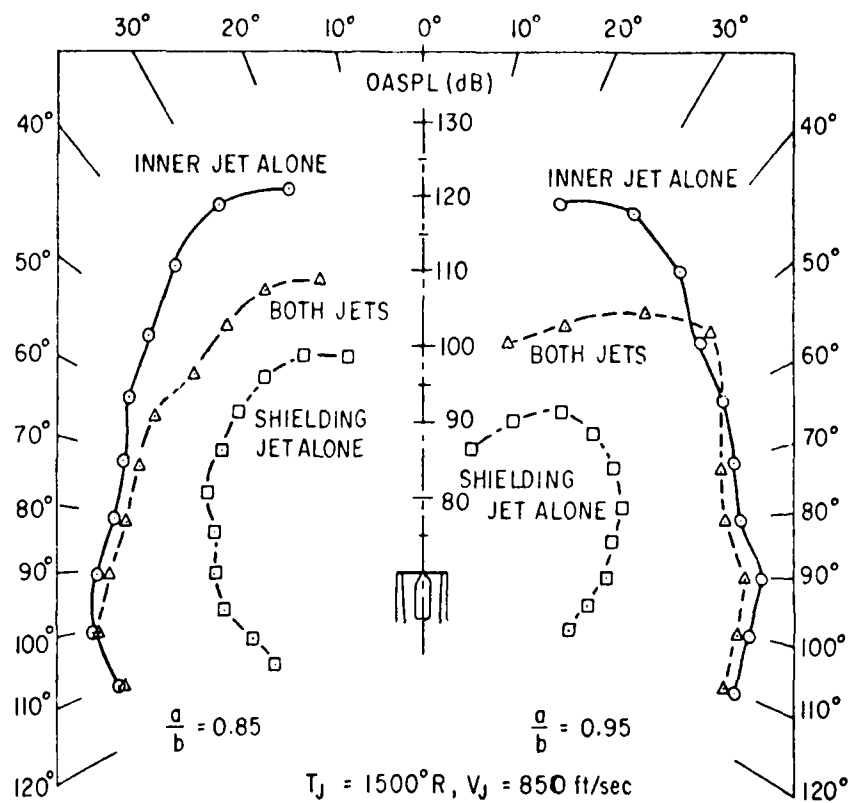


Figure 6-10. Typical OASPL Directivity Patterns from Jet Shielding Experiments.

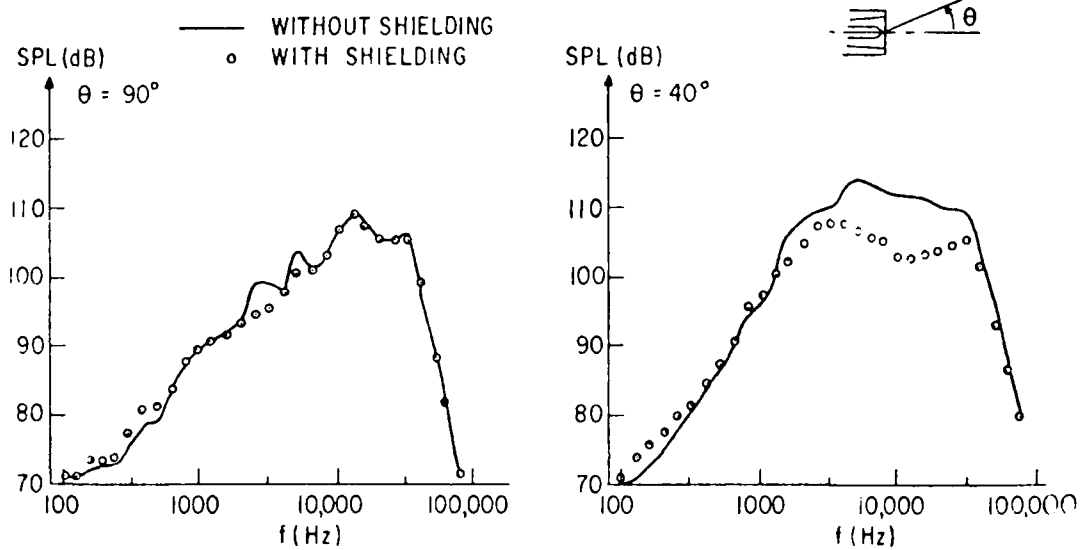


Figure 6-11. Typical SPL Spectra at $T_j = 480^\circ \text{R}$ $V_j = 850 \text{ fps}$.

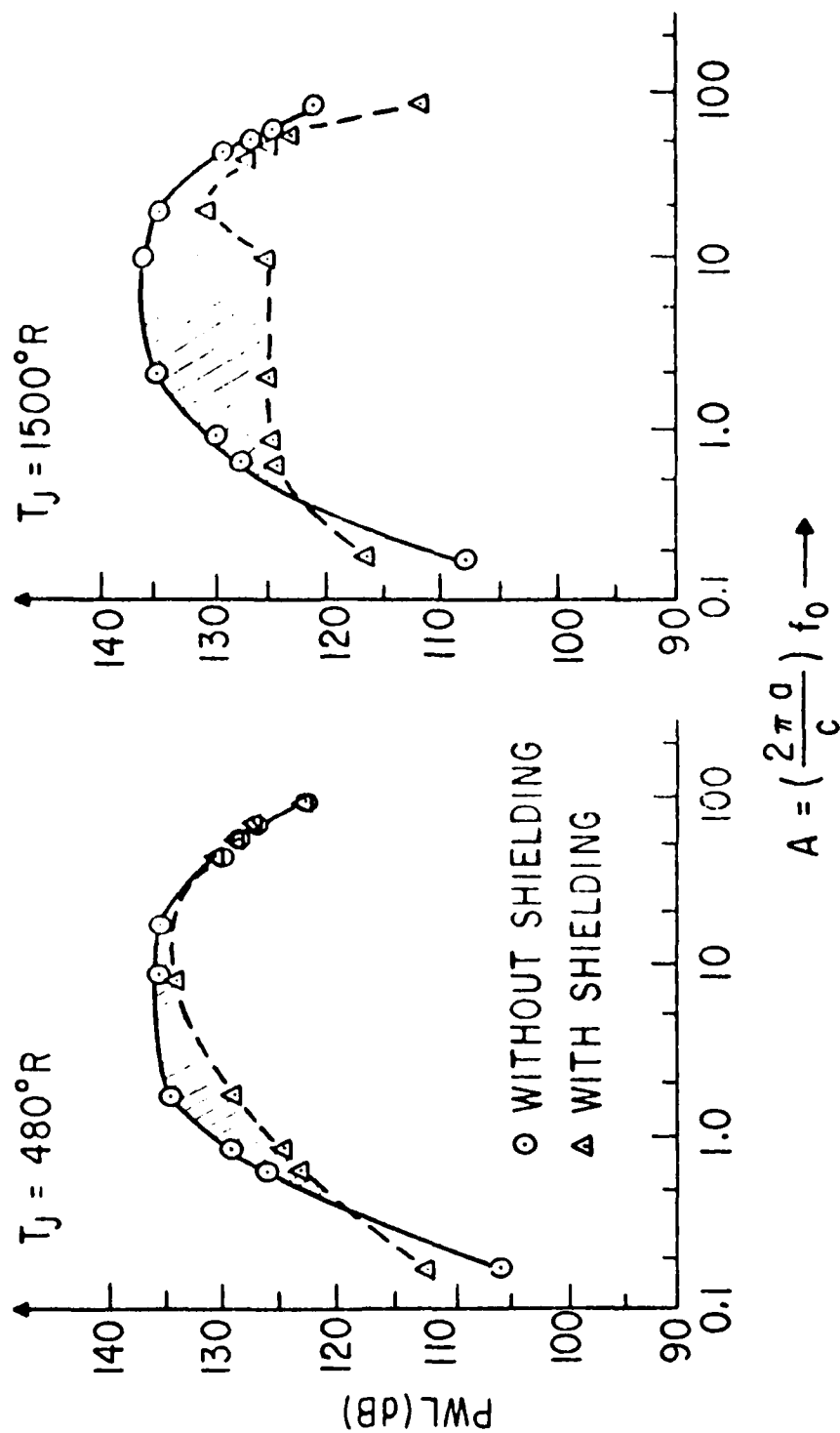


Figure 6-12. Sound Power Level Spectrum at $a/b = 0.85$, $V_j = 850$ fps.

where M_c is the source convective Mach number and θ is angular position measured from the forward jet centerline. By integrating the sound pressure level at a fixed frequency over the entire hemisphere, it is found that the sound power of the inner jet is reduced due to the presence of the shielding jet. This demonstrates that there is a reduction in the sound power with the acoustic flow shielding arrangement, and not simply a redirection of sound.

Figure 6-13 shows typical directivity plots of the source sound pressure level reduction due to acoustic shielding for two shielding jet flow segmentation configurations. The difference in sound level reduction among the various shielding jet flow segmentation arrangements is minimal. The effects of temperature and velocity of the shielding jet flow on acoustic shielding are observed in Figures 6-14 and 6-15. The shielding jet flow segmentation dependence is again minimal. The amount of shielding for the moving sound source increases as the temperature and velocity of the shielding jet flow increase. The correlation of the source sound power reduction in dB and temperature or velocity of the shielding jet appears to be linear in the temperature and velocity ranges tested.

6.2 THEORY-DATA COMPARISONS

The theoretical far field radiation pattern for a convecting source placed on the centerline of an annular jet is derived in subsection 4.2.2.2. For the purpose of the theory/data comparisons shown in Figures 6-13 through 6-15, the magnitude of the square of the pressure [the acoustic pressure is given by equation (89)] is normalized by that of a freely convecting source. The coefficient D' of equation (89) is given by equation (77b), where in the evaluation of the latter quantity the Correspondence Principle (section 4.2.2.3) is observed. For a freely convecting source, $D' = 1/2$. Thus $(\Delta SPL)_{theory} = 10 \log_{10} |p/p_0|^2$ where p_0 is the acoustic pressure of the freely convecting source. The experimental value of ΔSPL is the difference in SPL between the unshielded and shielded source.

The results in Figure 6-13 show that the difference in the acoustic pressure of a shielded and unshielded source is negligible at relatively large angles to the jet axis. At shallow angles, the difference becomes larger and larger as the angle decreases. There is a slight overestimation of the shielding at 20° to the jet axis; this minor discrepancy can be attributed to the overidealization of the effects of a real jet by a slug flow profile. In general, there is good qualitative agreement between theory and experiment.

In Figure 6-14 the difference in sound pressure level (ΔSPL) is shown as a function of shielding jet temperature for a fixed jet velocity ($V_j = 850$ fps) and at a fixed source Strouhal number ($A = 8.4$). In general, acoustic shielding increases with annular jet temperature. Note that, because the slug flow theory overestimates shielding at shallow angles to the jet axis, only the slope of the theoretical curve is correct. The absolute level has been adjusted to pass through the first set of experimental points. Of course, the most important quantity is the slope, because it leads to the so-called density exponent for hot jets.

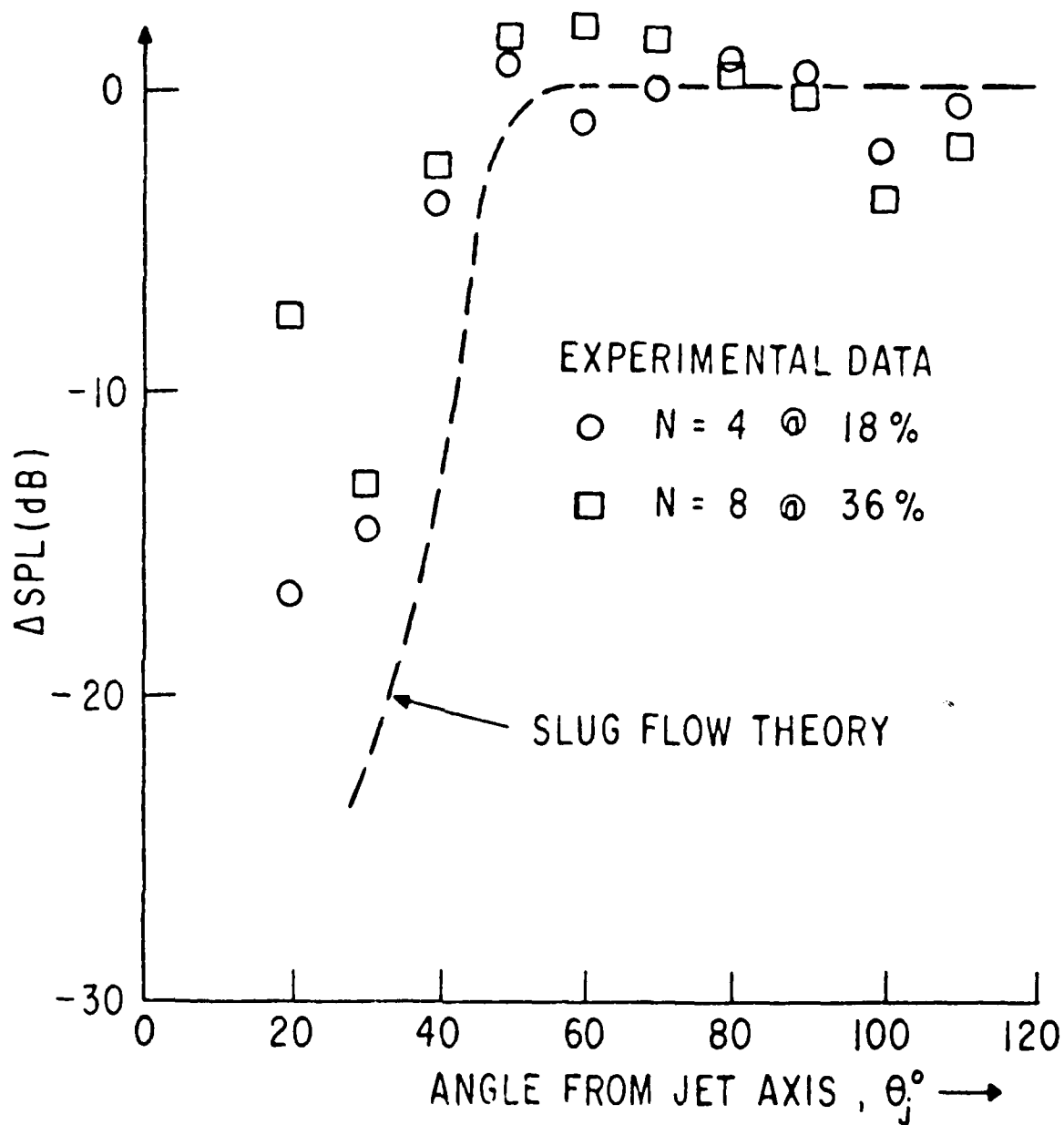


Figure 6-13. SPL Shielding at $a/b = 0.85$, $T_j = 480^\circ \text{ R}$, $V_j = 840 \text{ fps}$ and $A = 8.4$.

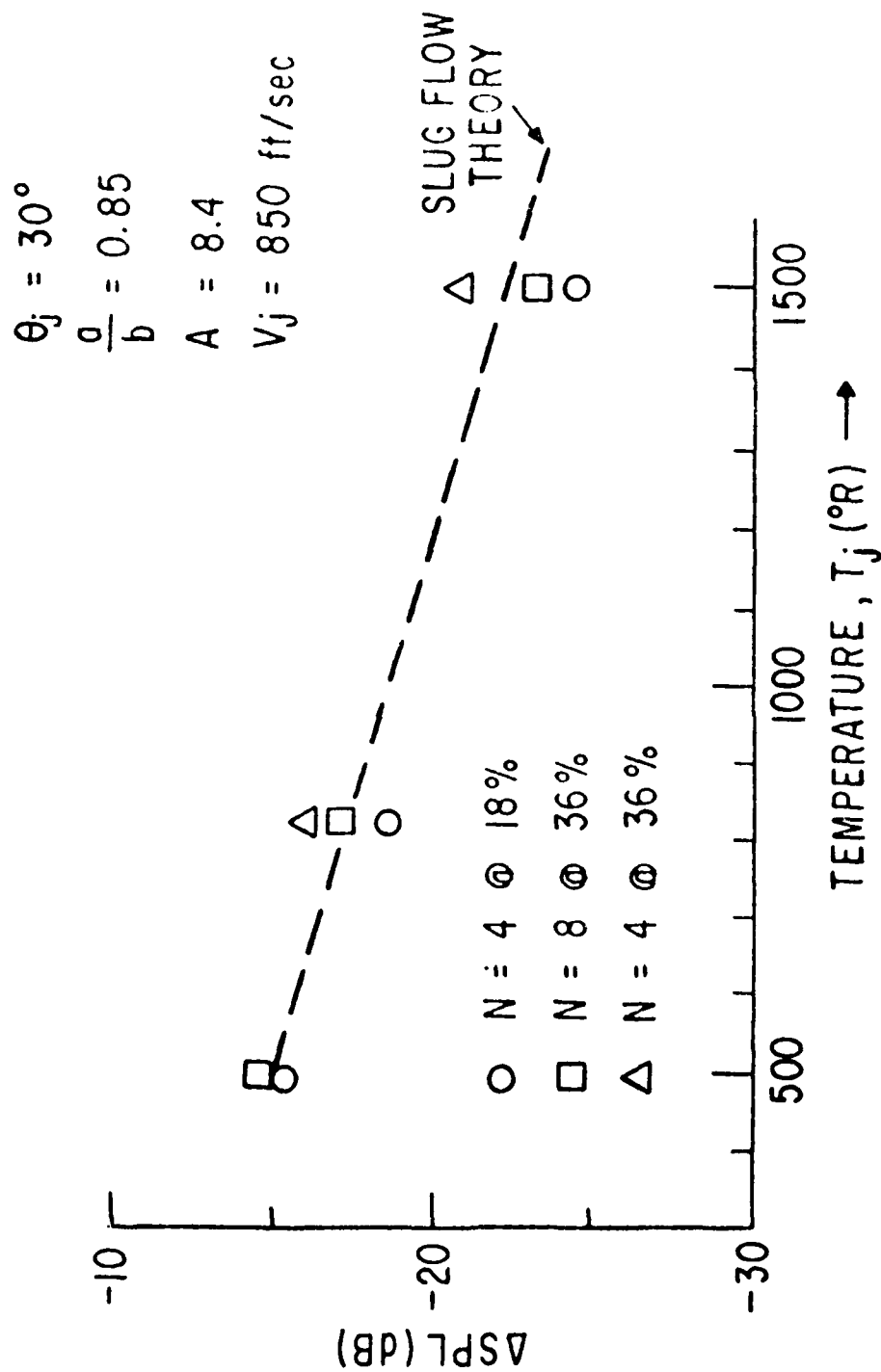


Figure 6-14. Reduction in SPL Due to Shielding Vs. the Temperature of the Shielding Jet Flow.

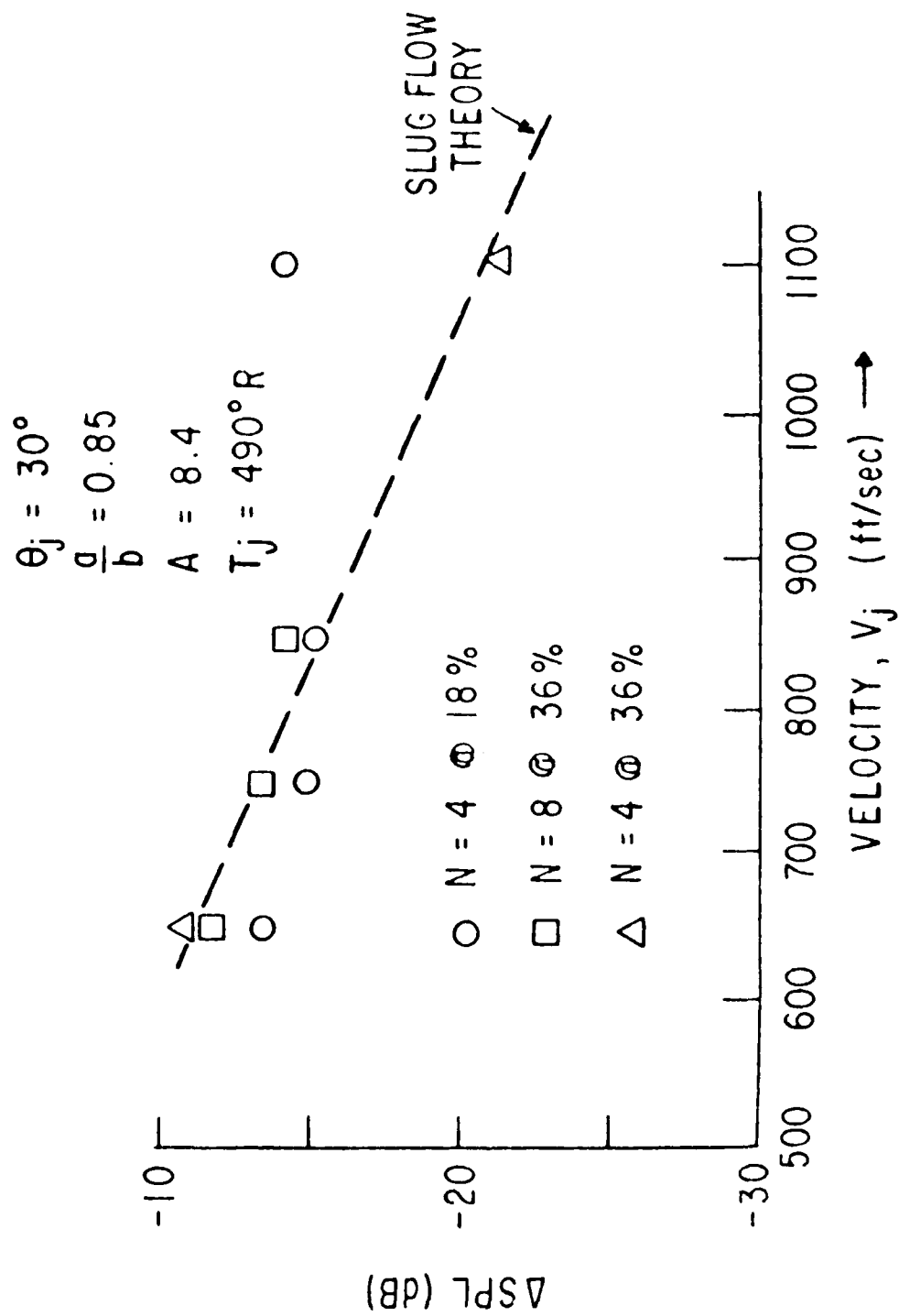


Figure 6-15. Reduction in SPL Due to Shielding Vs. the Velocity of the Jet Flows.

The results shown in Figure 6-15 are similar, except the annular jet velocity is varied at a fixed jet temperature. The slope of the theoretical curve is again predicted; its absolute level is adjusted to obtain a best fit to the data. There is good agreement again; acoustic shielding generally increases with jet velocity.

A number of qualitative remarks can also be made for the radiated power given by equation (79) of a convecting source on the axis of an annular jet as stated earlier in subsection (4.22.1.5).

With reference to Figure 4-15, the radiated power of a shielded source decreases with frequency; it decreases with increasing jet Mach number and increasing jet thickness. The power also decreases with increasing temperature. The experimental verification of some of these remarks can be seen in Figure 6-12.

6.3 CONCLUSIONS

Based on the experimental results and theory/data comparisons described in Section 6.2, the conclusions from the acoustic shielding experiments can be summarized as follows:

1. Trends of the experimental results from both a stationary and a moving source agree reasonably with the predictions from slug flow theory (described in Section 4.2.2).
2. Acoustic shielding provides a genuine reduction in the sound power instead of merely a redirection of sound.
3. Shielding occurs mostly at shallow angles ($\theta < 50^\circ$) and increases as the angle decreases.
4. Shielding increases with temperature, velocity, and thickness of the annular shielding jet flow.
5. The angular extent of shielding increases with the thickness of the shielding jet.
6. Minimal effect of shielding on the moving sound source at 90° from the jet forward centerline is observed, especially with a room temperature shielding jet flow.
7. The type and degree of segmentation of the shielding jet flow appears to have minimal effect on shielding.

7.0 PHYSICAL SHIELDING EXPERIMENTS

7.1 DESCRIPTION OF TEST PROGRAM AND RESULTS

The acoustic suppression potential of a simple flat plate shield was evaluated using a six tube circular cluster to represent a typical multi-element suppressor. This portion of the effort was not meant to be a comprehensive study of physical shielding, but rather to highlight the more important parameters involved in shielding a circular cluster of jets by a flat plate. These tests were carried out at the General Electric CRD Hot Jet Noise Facility. The shield width was held fixed while the length and offset from the cluster centerline were adjustable. Three shield lengths and three offsets were used at five different combinations of velocity and temperature. Rather than carry out a full factorial experiment, it was decided to investigate only the most interesting features. It was felt that except for supercritical flow conditions, the changes in the axial source distribution of the cluster caused by jet velocity and temperature would be of less interest than the geometrical parameters of the shield and its location. Therefore, in selecting the test matrix, only one configuration was examined to determine the effect of velocity (including supercritical flows) at a given temperature, and the effect of temperature at a subsonic velocity. Then at a given thermodynamic condition, the shield length and offset were varied. Figure 7-1(a) illustrates the test matrix. The shield length L , is measured from the nozzle base plate, located six inches upstream of the nozzle tube exit plane. Figure 7-1(b) illustrates the geometry of the experiment.

7.1.1 Results

For any given jet velocity and temperature, the reduction in the noise of a small ($D/d = 3$) six tube cluster jet plume observed in the shielded plane depends on the frequency, angle to the jet axis, and the shield length and offset. For a fixed shield length, the effect of emission angle and frequency is shown in Figures 7-2, 7-3, and 7-4. Generally, only the high frequency sources close to the nozzle exit plane are effectively shielded. This shielding increases as the observer moves away from the jet axis, and approaches 15 to 16 dB at high frequencies, at right angles to the jet centerline. The difference sound pressure level, $\Delta SPL = SPL(\psi = 180^\circ) - SPL(\psi = 0^\circ)$, is also very sensitive to shield length, as shown in Figure 7-5. The interdependence of emission angle and shield length shown on Figure 7-5 is in general agreement with a ray acoustics viewpoint. There is very little difference between the measurements taken at $\psi = 90^\circ$ and $\psi = 180^\circ$, as seen in Figures 7-2, 7-3, and 7-4.

On a difference power level basis, ΔPWL , the effect of shield length is not quite as dramatic as for the ΔSPL results, as seen in Figure 7-6. Shield offset also plays an important role (increasing the offset from $s = 6$ inches to $s = 9$ inches reduces the shielding from $\Delta PWL = 8.3$ dB to 3.7 dB in Figure 7-6).

Jet velocity and temperature effects are not significant except in the case of supercritical flow, as shown on Figure 7-7, where a 2 dB decrease in

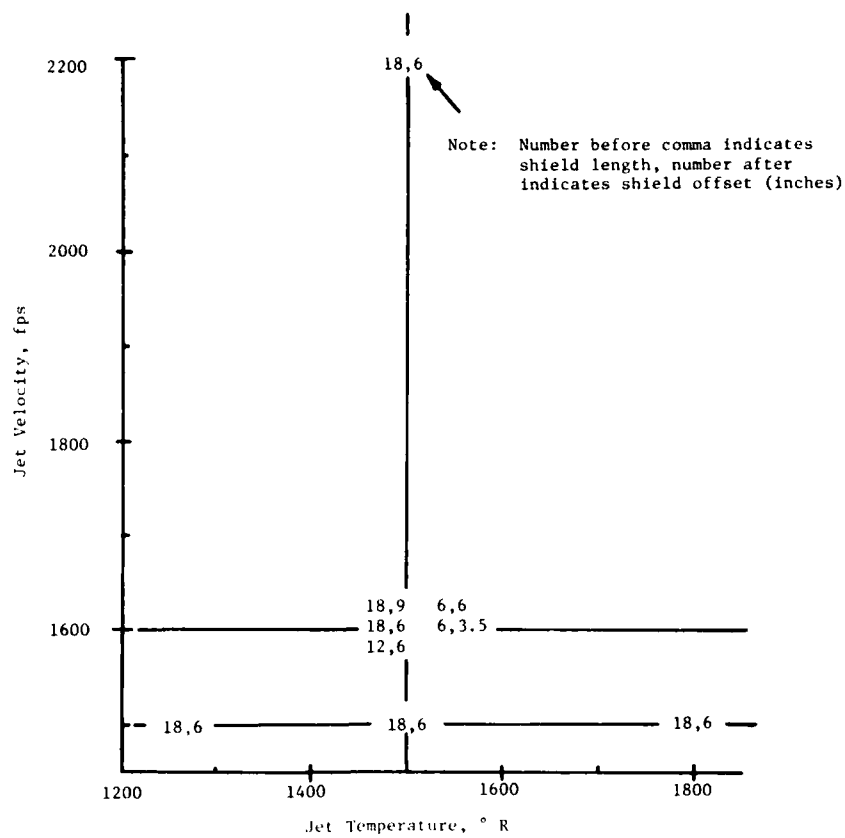


Figure 7-1 (a). Test Matrix.

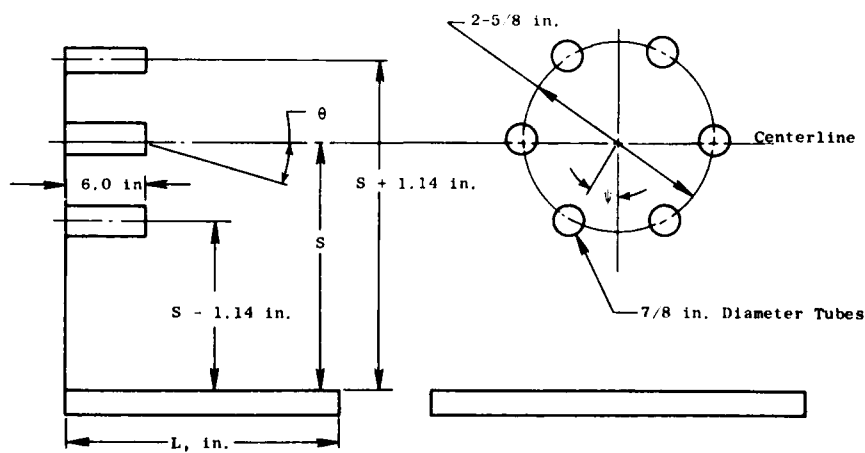


Figure 7-1 (b). Geometry of Experiment.

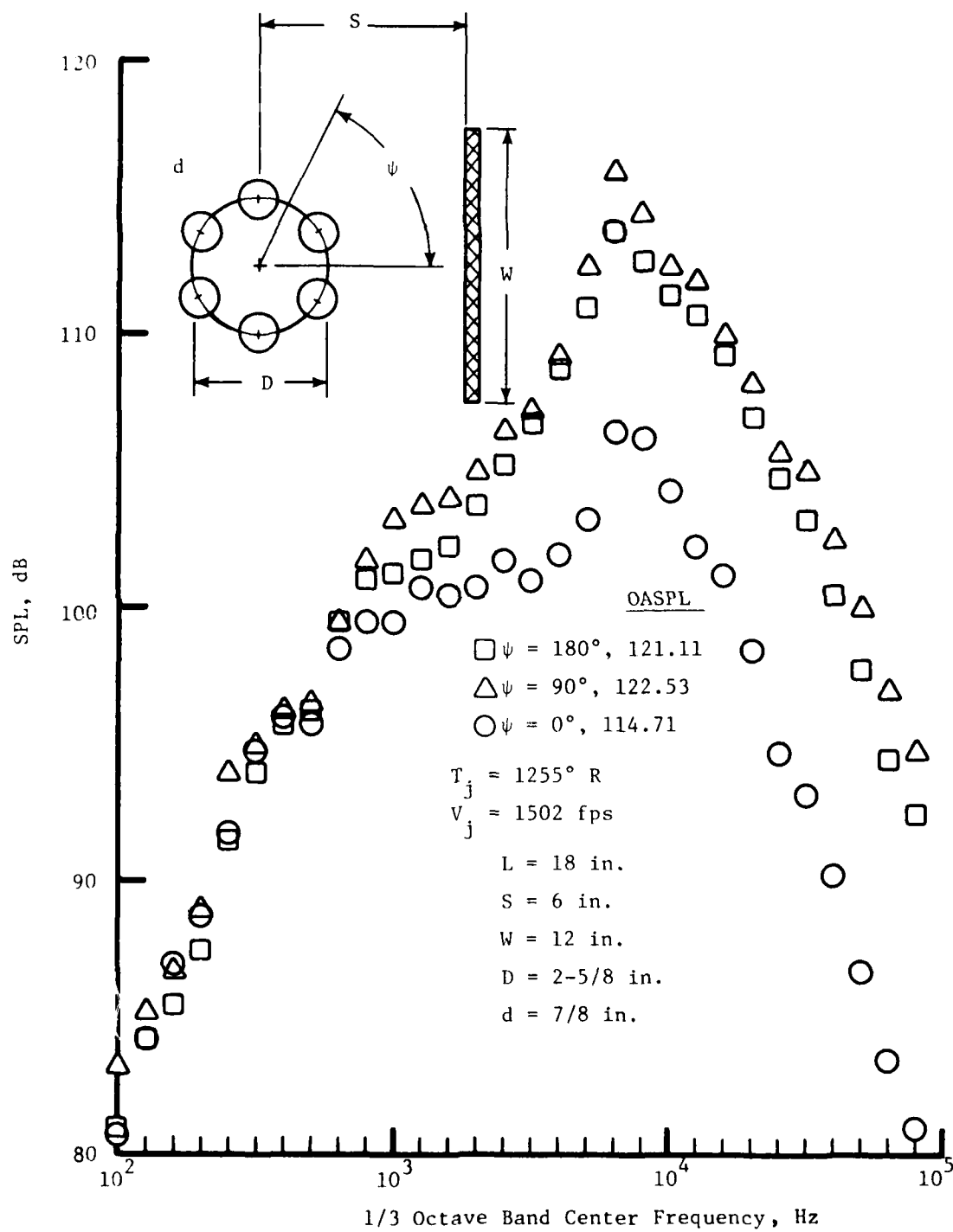


Figure 7-2. Shielding at $\theta_j = 30^\circ$.
618

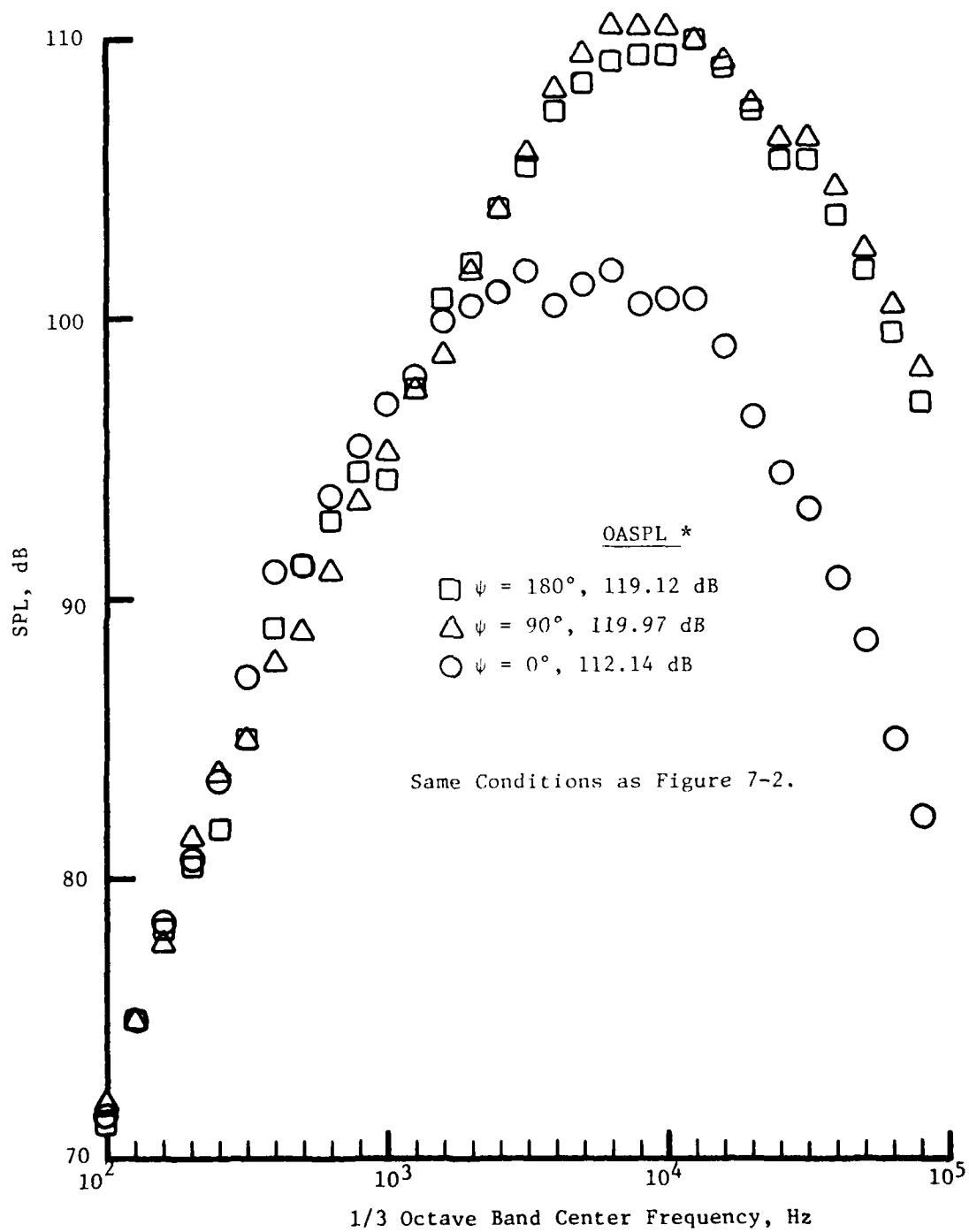


Figure 7-3. Shielding at $\theta_j = 60^\circ$.

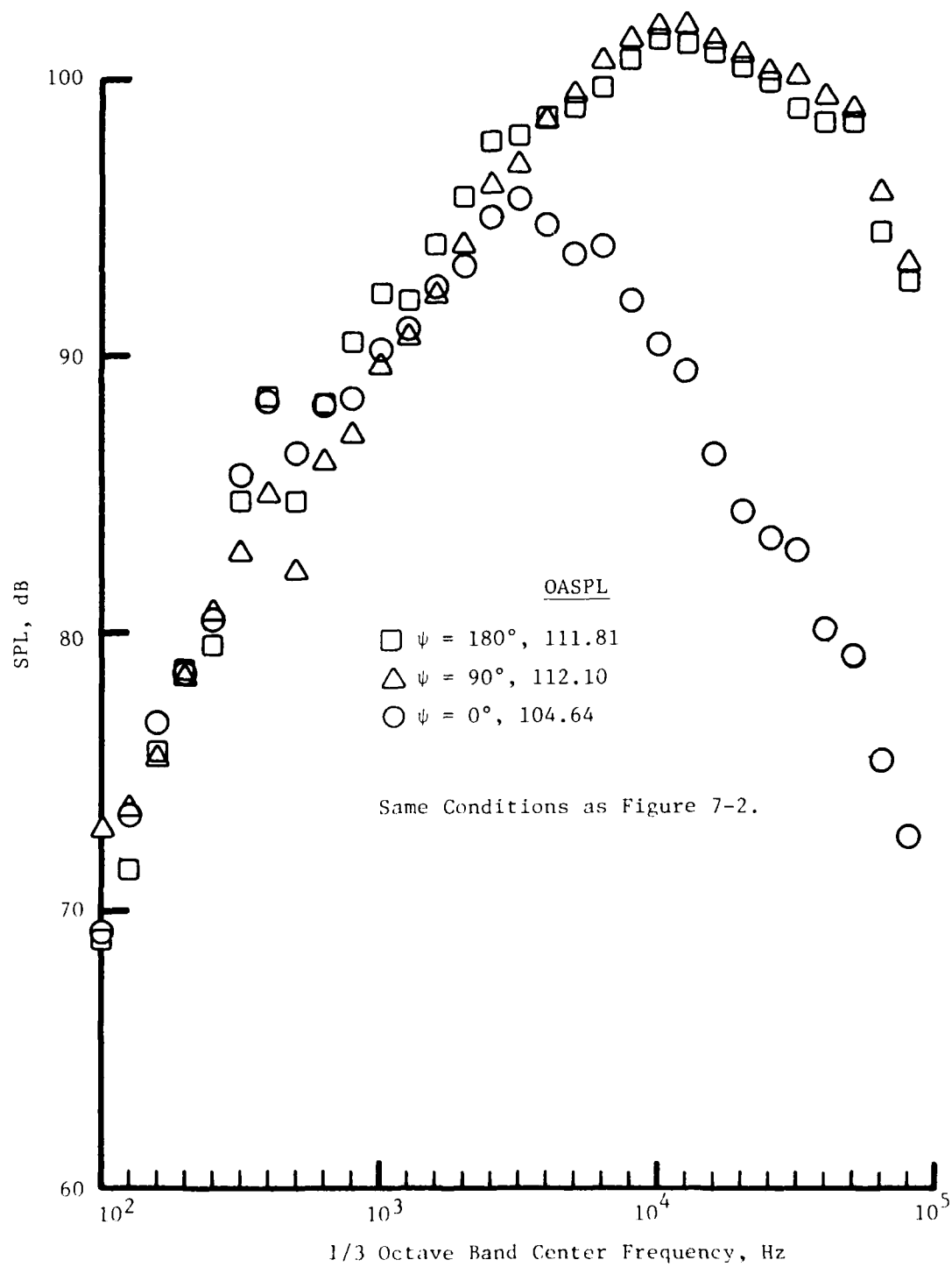


Figure 7-4. Shielding at $\theta_j = 90^\circ$.

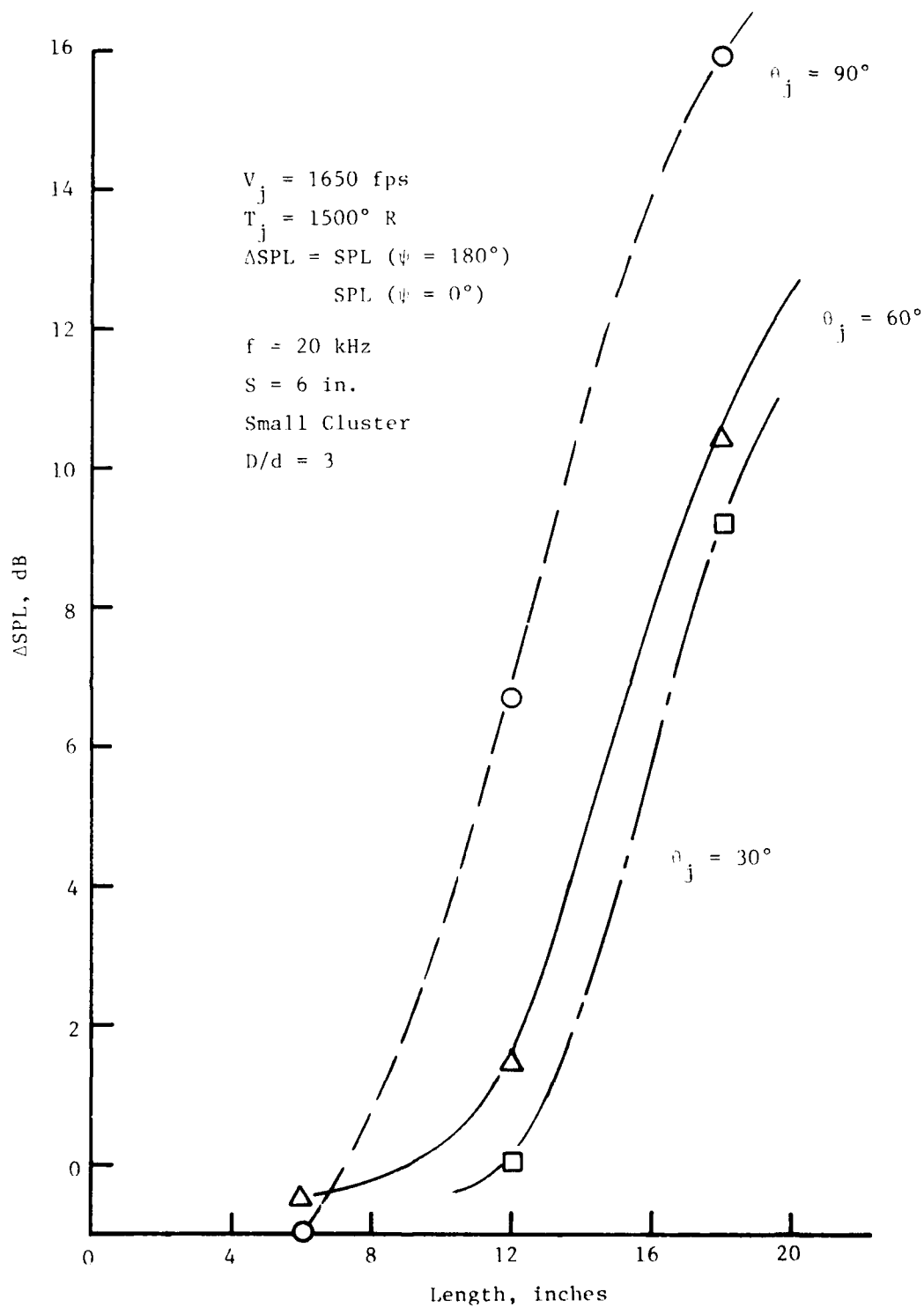


Figure 7-5. Effect of Shield Length and Emission Angle.

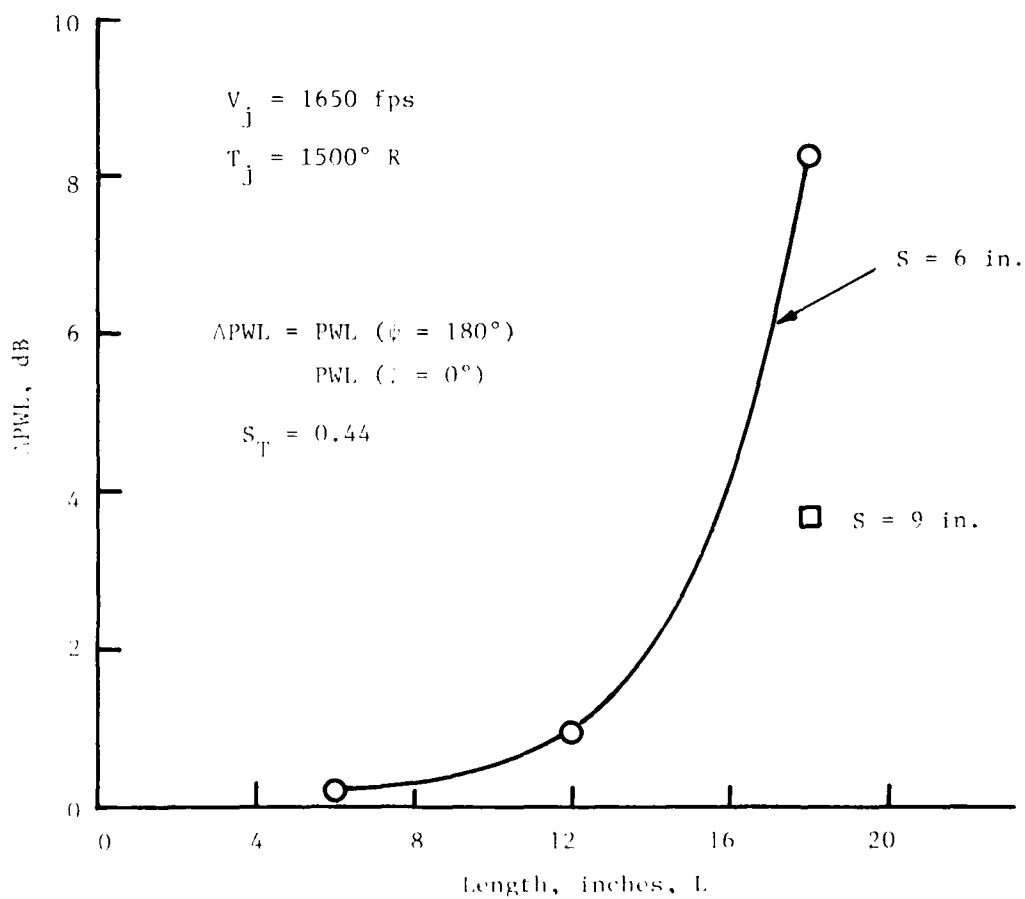
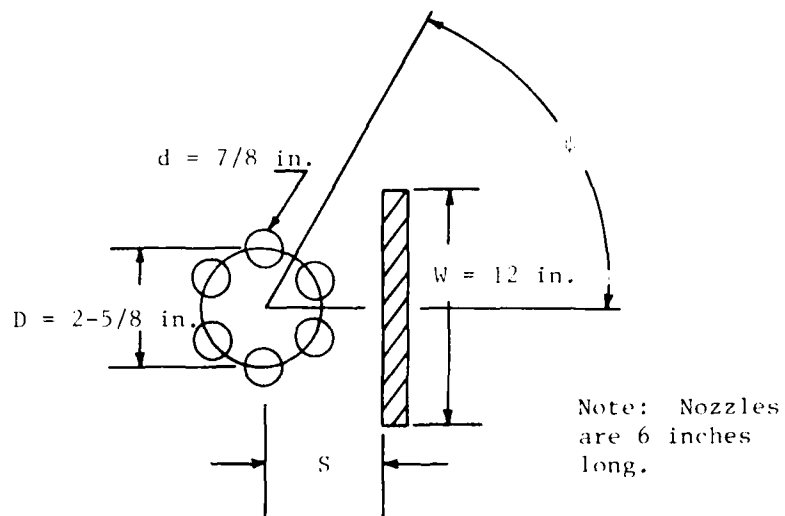


Figure 7-6. Effect of Length, L, on Shielded Power.

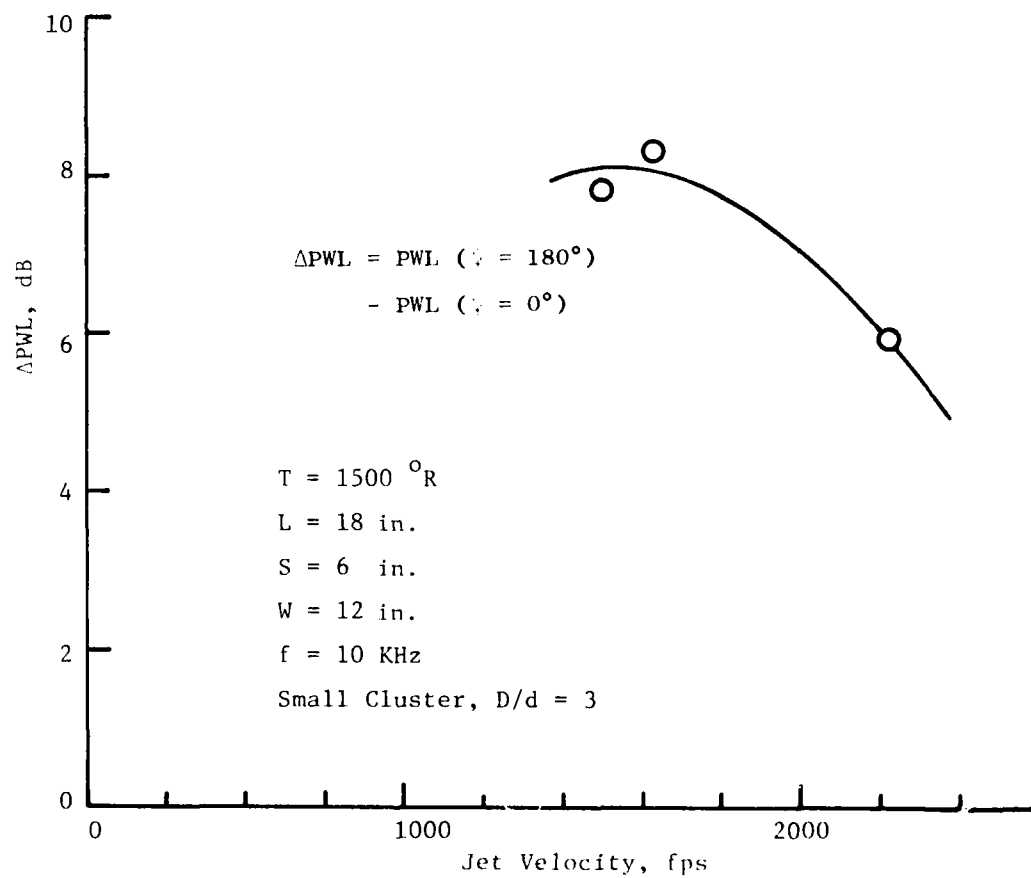


Figure 7-7. Effect of Jet Velocity on Shielding.

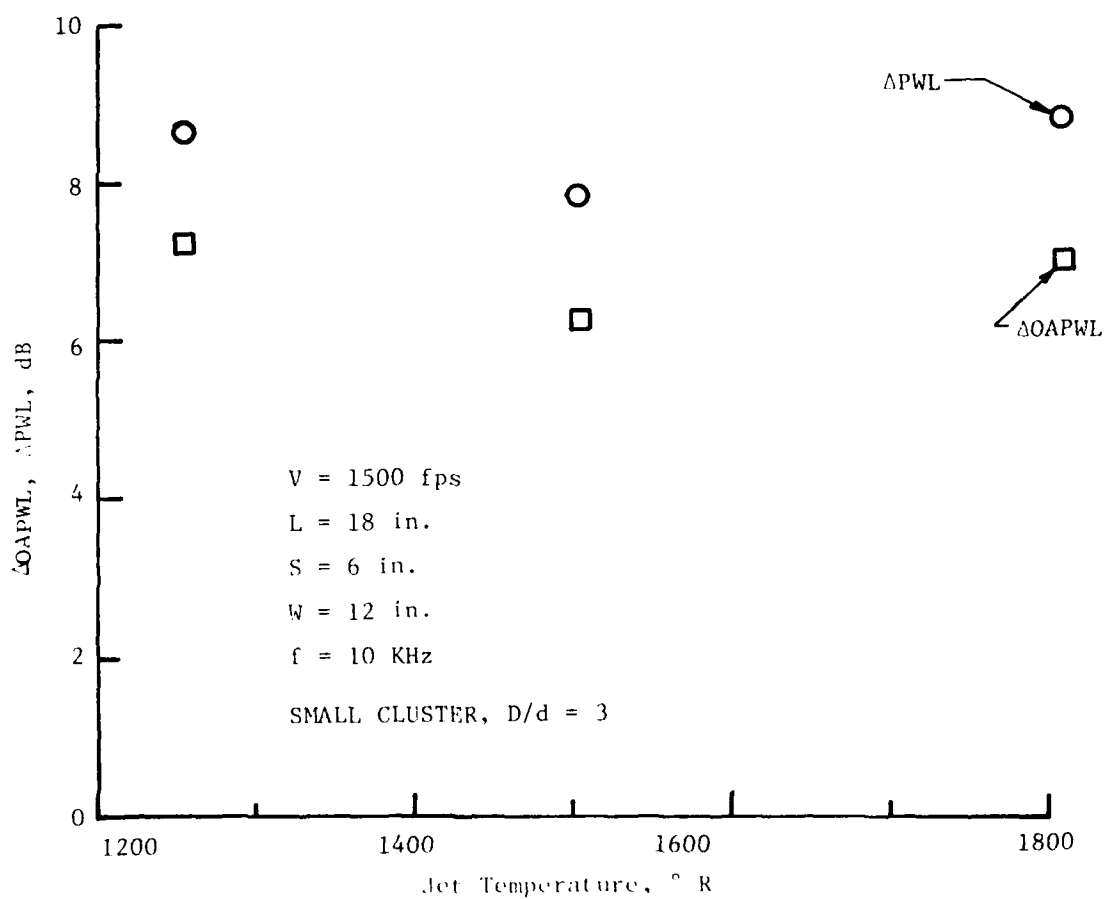


Figure 7-8. Effect of Jet Temperature on Shielding.

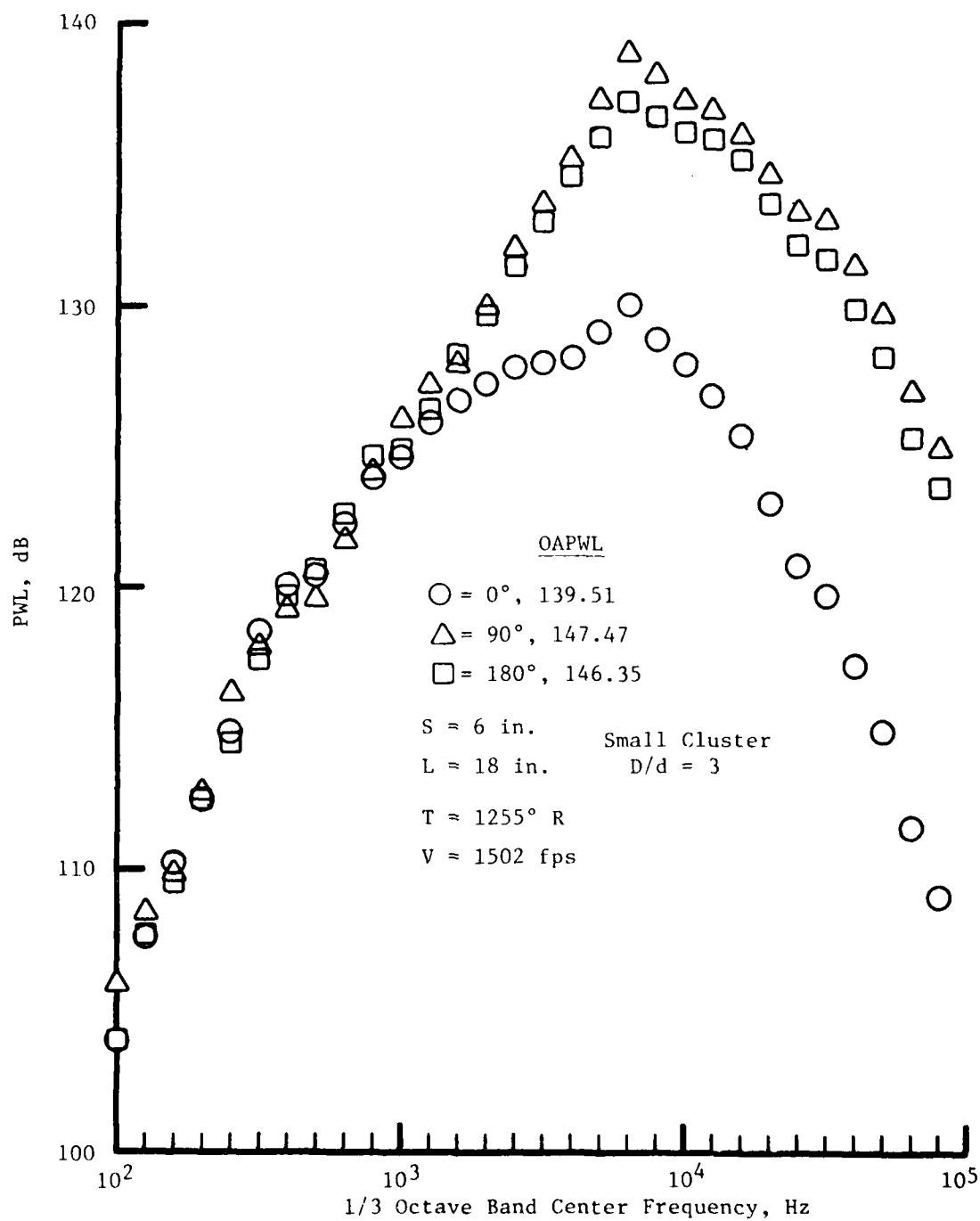


Figure 7-9. Power Spectra, Medium Offset High Subsonic.

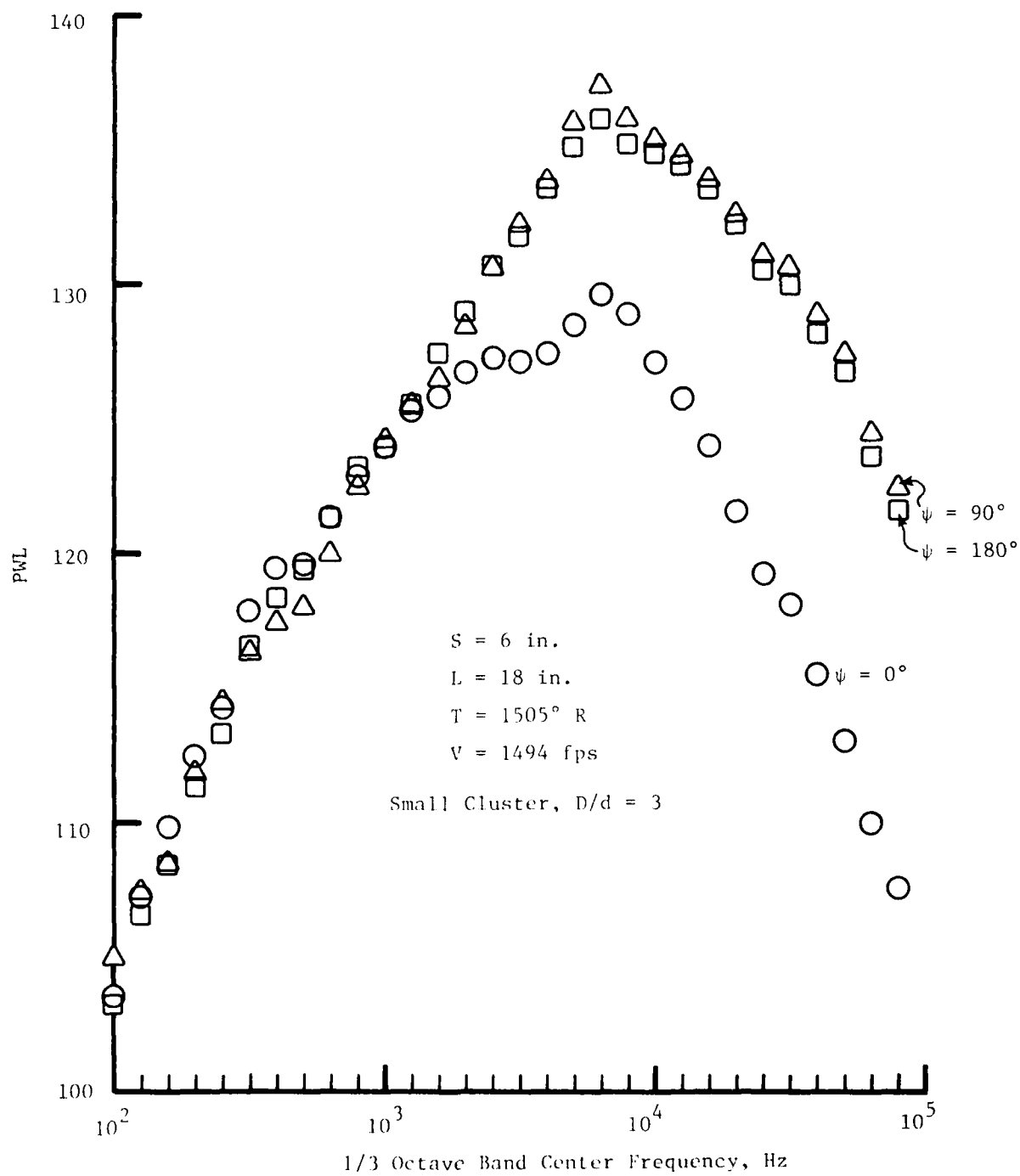


Figure 7-10. Power Spectra, Medium Offset Subsonic.

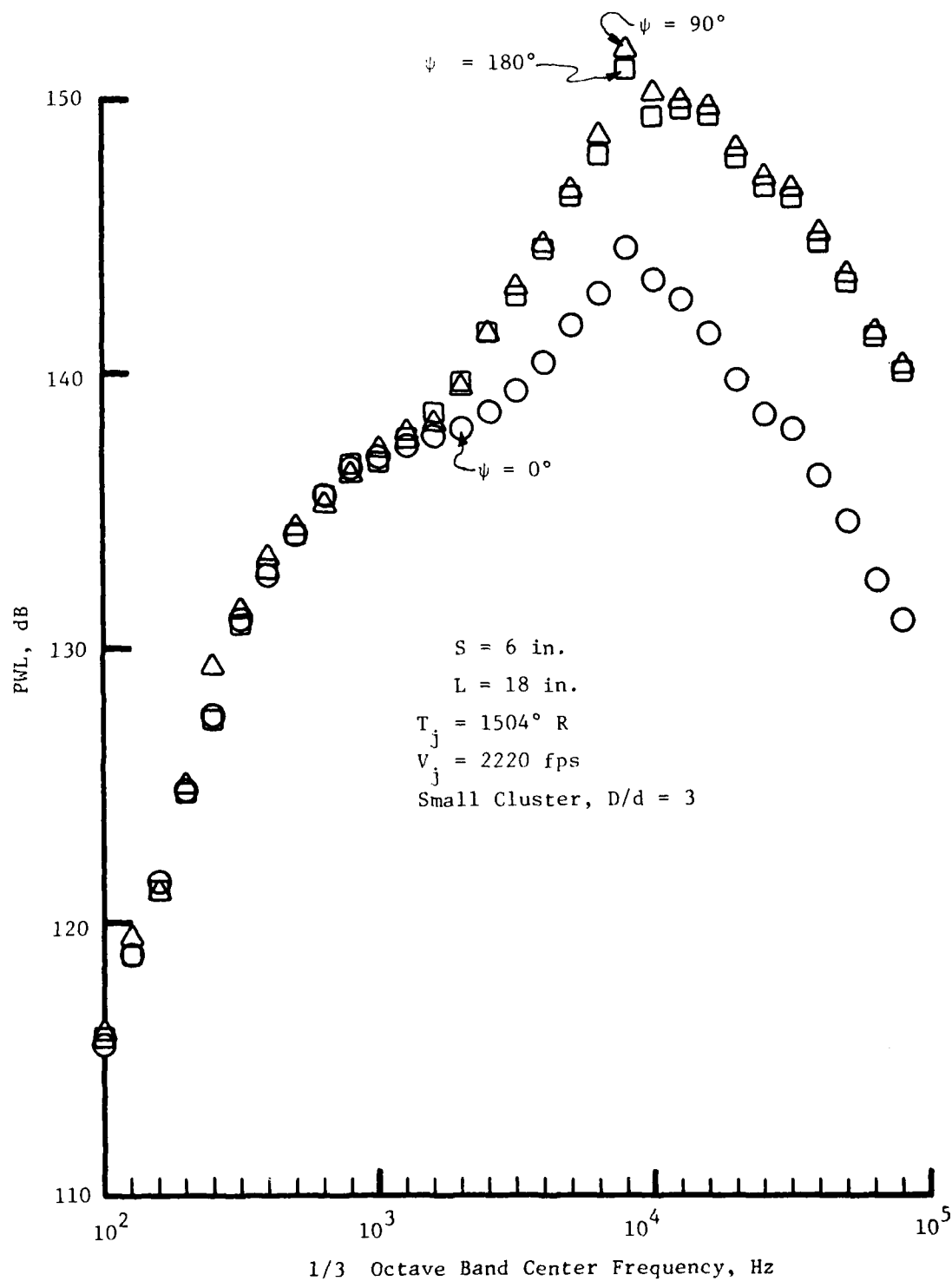


Figure 7-11. Power Spectra, Medium Offset Supersonic.

shielding occurs from subsonic to supersonic flow. This decrease is thought to be due to the lengthening of the noise source distribution which causes an unmasking of the noise sources.

At subsonic velocities, the effect of jet temperature is very slight as can be seen on Figure 7-8. The effect of jet temperature and velocity on the power spectrum can be seen on Figures 7-9, 7-10, and 7-11. A reduction in shielding in the midrange of frequencies is observed for the supersonic velocity (Figure 7-11), in line with the earlier conjecture on the noise source lengthening with supersonic flow. When the shield offset is increased, as in Figure 7-12, the principal effect is a uniform increase in noise throughout the shielded portion of the power spectrum.

7.2 THEORY-DATA COMPARISONS

7.2.1 Multitube Suppressor and Flat Plate Shield Experiments

This section attempts to apply the results of the theory of Section 4.8.1 to the data obtained in Section 7.1.1. A simple analytical model is adopted for describing the axial noise source distributions. It can be assumed that the six jet cluster employed in Section 7.1.1 has a noise signature which is essentially six times the noise emitted by any one jet (except possibly at very shallow angles to the jet axis and at low frequencies where physical shielding effects are not very important).

For subsonic jets, an approximate relationship giving the peak-noise frequency f generated by an axial station located a distance x from the nozzle exit plane is given by Howes, et al.⁽¹⁰⁶⁾ as

$$\frac{fD}{V} = (1.25 \frac{x}{D})^{-1.22} \quad (375)$$

It is well known that Noise generation occurs further and further downstream of the nozzle exit plane as the jet Mach number increases. Motsinger and Sieckman⁽³⁶⁾ show that equation (375) must be modified to:

$$\frac{fD}{V} = \left\{ \left(\frac{x - x_0}{D} \right) (1.25) \right\}^{-1.22} \quad (376)$$

where $x_0/D = 4M^{1.153}$ where M is the jet Mach number. In the present application (barely sonic jets), both equations (375) and (374) are used, with $x_0/D = 4$ in the latter.

The six jets are modeled as shown in Figure 7-13 as linear radiators. Motsinger and Sieckman⁽³⁶⁾ show that, for a given frequency band f , the actual distribution of the noise-per-unit length at f is a unique function of (x/x_p) , where x_p is the axial location at which the noise level per unit length is maximum at frequency. Motsinger and Sieckman sketch the unique function, but a rough approximation is to assume that the distribution varies as $(x/x_p)^{0.8}$ for $x < x_p$, and as $(x/x_p)^{-2}$ for $x > x_p$. These relations determine, for a given frequency, the axial distribution of noise sources radiated from each of the six jets in Figure 7-13. Equation (323) can be directly applied to predict the Δ SPL due to the shield as a function of frequency and θ_j . Note however, that if the source-observer geometry is such that the observer is not in the shadow of the source, equation (323) does not apply, and

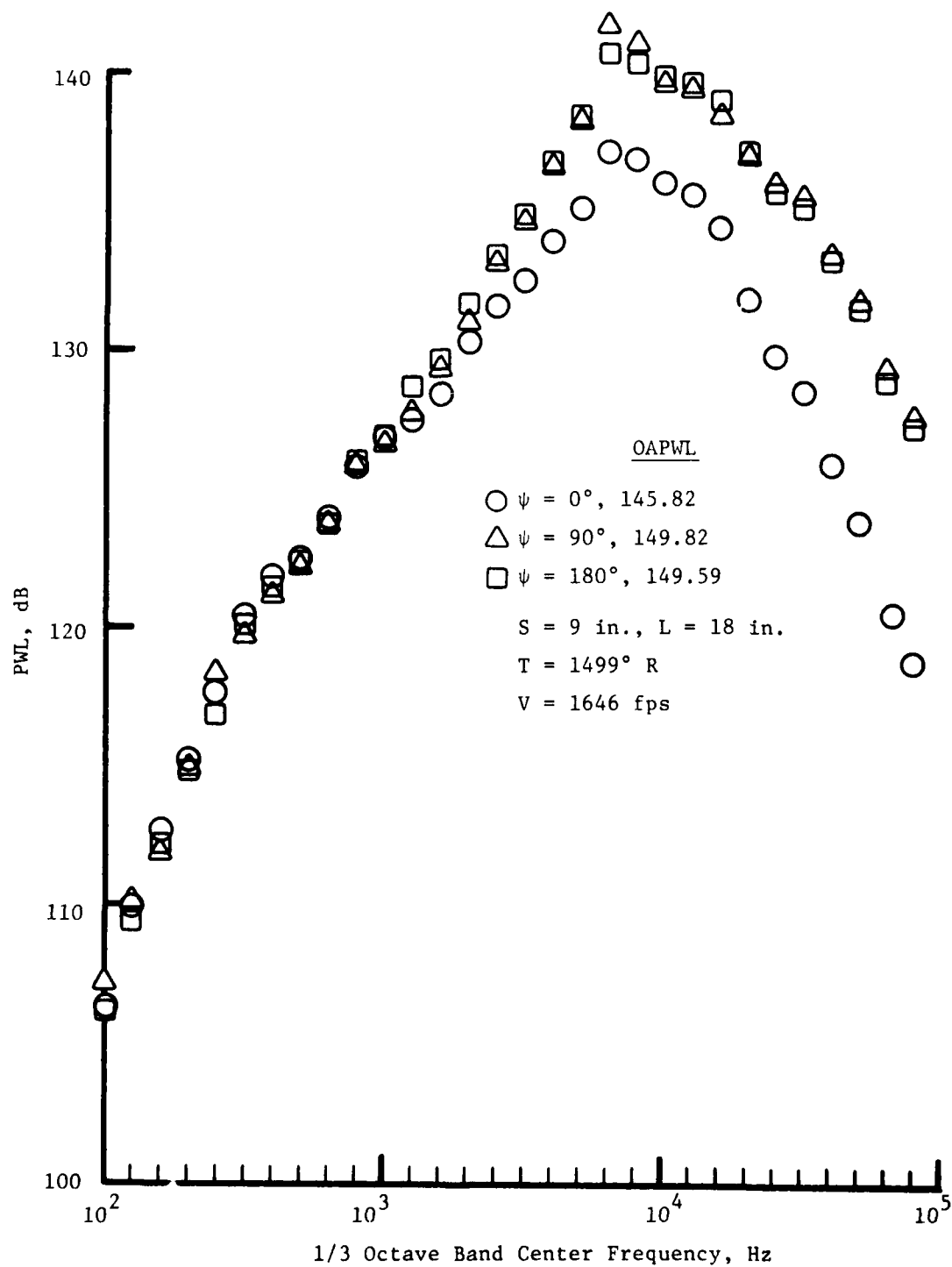


Figure 7-12. Power Spectra, Large Offset.
 629

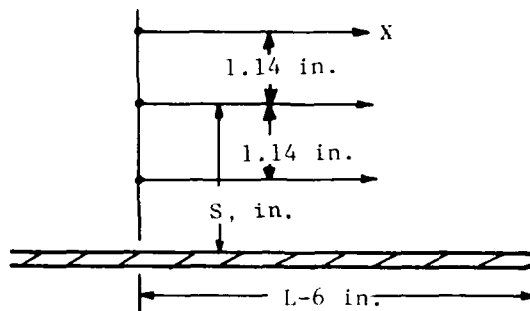


Figure 7-13. Linear Radiator Model of Shielded Cluster.

physical shielding is assumed to be zero. Also, equation (323) is not uniformly valid as ϕ tends to $(\pi + \phi_0)$ (i.e., observer approaching the edge of the shadow). This situation is handled by assuming that, the attenuation is at least 6 dB. For $\phi > (\pi + \phi_0)$, i.e., the observer is truly within the shadow of the source. The jet is treated as an assemblage of independent radiators at each axial slice. The jets are broken up for numerical purposes, into axial slices which are one diameter thick, and the integration is carried out for 40 diameters along the jet axis. Each of the six jets is treated as an independent radiator.

A Boeing study, D.G. Dunn, et al.(107), examines physical shielding of engine turbomachinery noise sources by wings with considerable analysis devoted to edge interaction noise due to jet flows in close proximity to the shield. Their method of approach to estimate the physical shielding of jet noise was to examine the applicability of the empirical expression for the shielding derived by VonGlahn, et al.(108), based on studies with a cold flow jet placed near a shielding surface. This correlation method is shown to be able to predict the measured shielding to within ± 2.5 dB. The method proposed in the Boeing study is not comparable to that proposed herein since the present method proceeds more or less directly from first principles,

while the Boeing study examines the applicability of a correlation method based on test data from one study, VonGlahn, et al.(108) to their own results.

In what follows, theory-data comparisons are carried out both with the General Electric method (developed in this report and explained earlier) and with the Boeing-VonGlahn correlation. Both of these comparisons are shown in Figures 7-14 and 7-15. However, the discussion of how these comparisons fared will be carried out separately. The next six paragraphs discuss the GE method, and the last paragraph discusses the Boeing-VonGlahn method. Since the Boeing-VonGlahn recommendation is to estimate the shielding with a mean line with an estimated ± 2.5 dB confidence limit, the results of applying this method are shown as a predicted band in Figures 7-14 and 7-15.

In the results shown in Figures 7-14 and 7-15, the data points depicting the shielding effect are interpreted by looking at the Δ SPL between $\psi = 180^\circ$ and $\psi = 0^\circ$ in Figures 7-2 through 7-5. For the GE theory, both the assumptions $x_0/D = 0$ and $x_0/D = 4$ were tested. As shown on Figures 7-14(b), 7-14(c), 7-15(b) and 7-15(c), the agreement at $\theta_j = 60^\circ$ and 90° with the theoretical predictions is remarkable, considering the rather straightforward (simplistic) modeling of the axial source distributions in the six jets.

As shown in Figures 7-14(a) and 7-15(a), at $\theta_j = 30^\circ$, the measured shielding at this shallow angle is considerably greater than that predicted by the theory, even with $x_0/D = 0$. An additional calculation, assuming that radiation at $\psi = 180^\circ$ is enhanced by 3 dB due to a "reflection" effect of the barrier, is also presented. This improves the theory-data comparison below 10 kHz, but the general shapes, etc., in both Figures 7-14(a) and 7-15(a) still appear to be at variance with the data. One explanation for the discrepancy is that a pressure deficit develops due to the greater impediment to the jet entrainment on the side where the flat plate shield is located, causing the jet flow to attach to the plate. Such an asymmetric velocity and temperature profile would produce greater fluid shielding in the plane $\psi = 0^\circ$ as opposed to the plane $\psi = 180^\circ$. This speculation requires both experimental and theoretical verification.

Figure 7-6 shows the reduction in PWL attenuation at 10 kHz for $V = 1650$ fps, $T_j = 1500^\circ$ R, and $L = 18$ ", in going from $s = 6$ " to $s = 9$ ". The measured reduction in PWL attenuation is 4.5 dB. The predicted reduction in SPL attenuation for θ_j from 30° to 90° due to this reduction is tabulated below:

θ_j , degrees	Predicted Reduction in SPL Attenuation at 10 kHz
30	0.1 dB
40	2.1 dB
50	3.5 dB
60	2.0 dB
90	0.1 dB

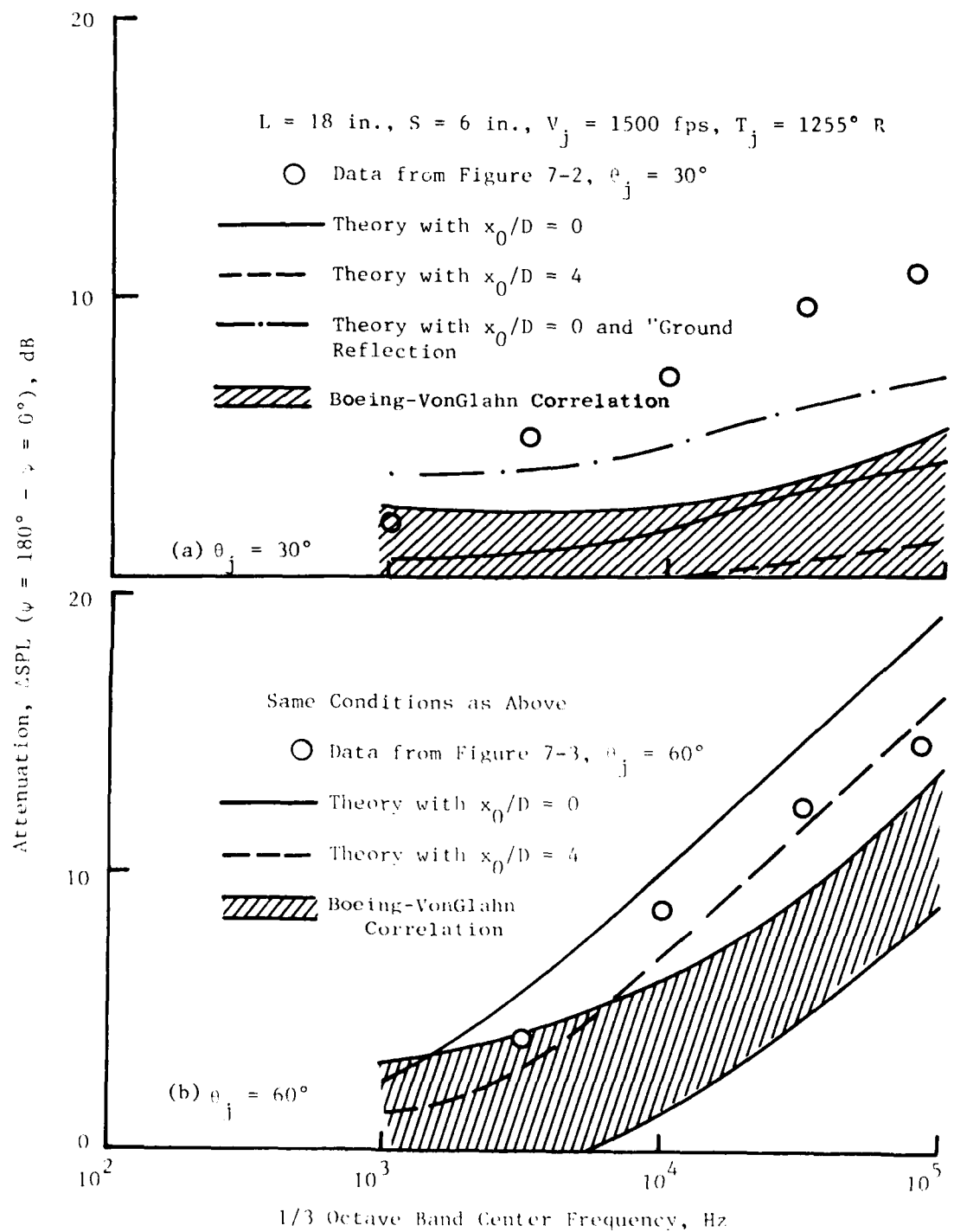


Figure 7-14. Comparison of Predicted and Measured Shielding Attenuation for 6-Tube Cluster, $V_j = 1500 \text{ fps}$.

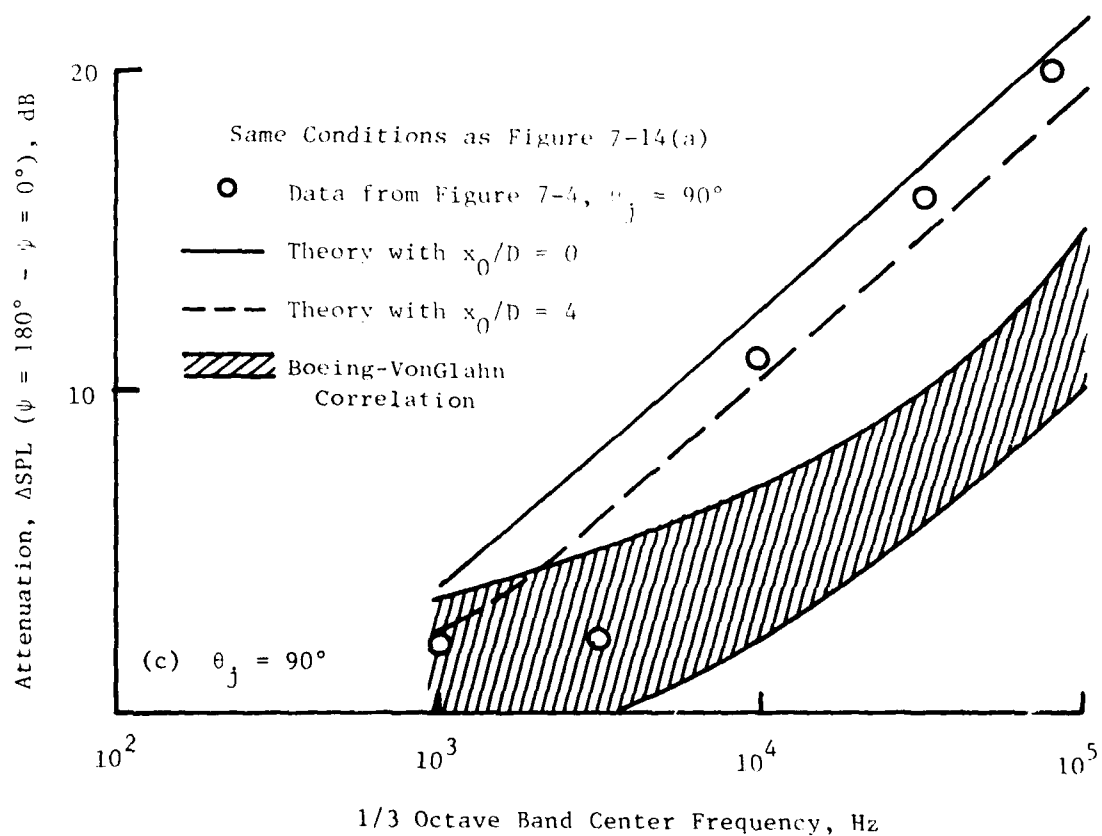


Figure 7-14. Comparison of Predicted and Measured Shielding Attenuation for 6-Tube Cluster, $V_j = 1500$ fps (Concluded).

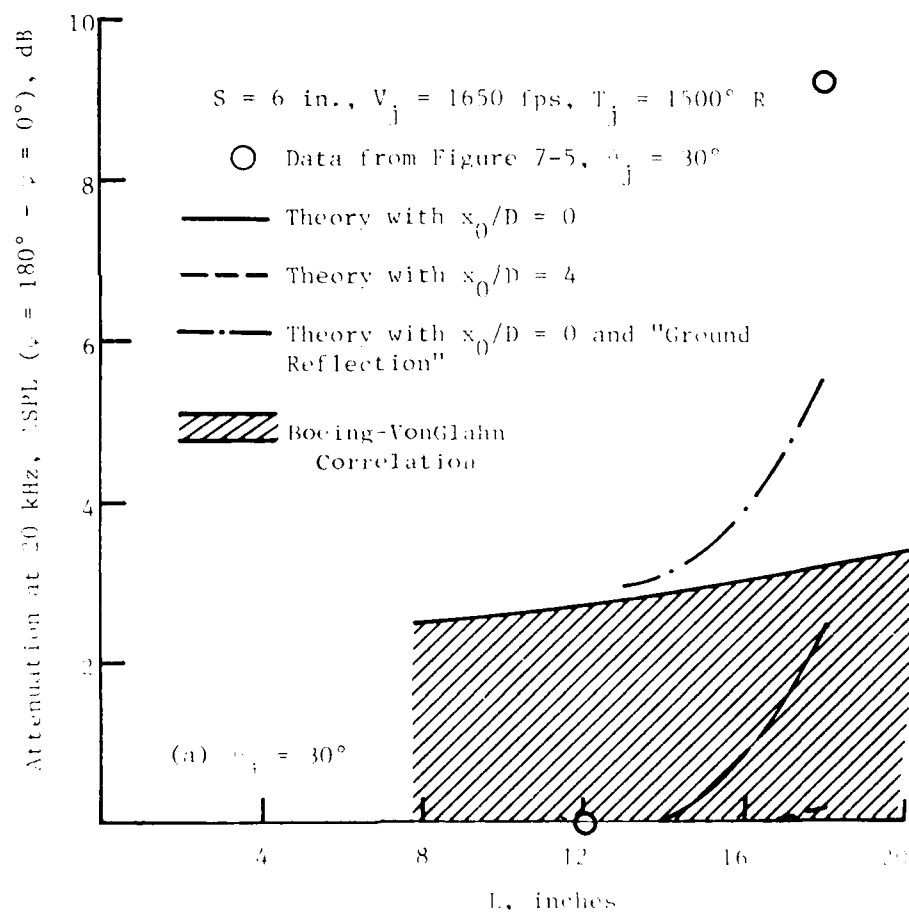


Figure 7-15. Comparison of Predicted and Measured Δ SPL Attenuation for 6-Tube Cluster, $V_j = 1650$ fps.

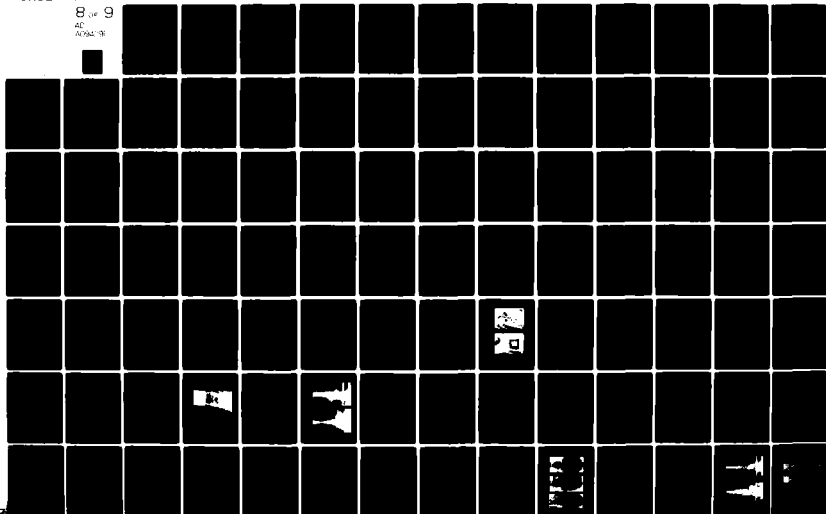
AD-A094 291

GENERAL ELECTRIC CO CINCINNATI OH AIRCRAFT ENGINE GROUP F/G 20/1
HIGH VELOCITY JET NOISE SOURCE LOCATION AND REDUCTION. TASK 2. --ETC(U)
MAY 78 T F BALSA, P R GLIEBE, R A KANTOLA DOT-05-30034
R78AE6323 FAA-RD-76-79-2 NL

UNCLASSIFIED

8 of 9

AD
A094 291



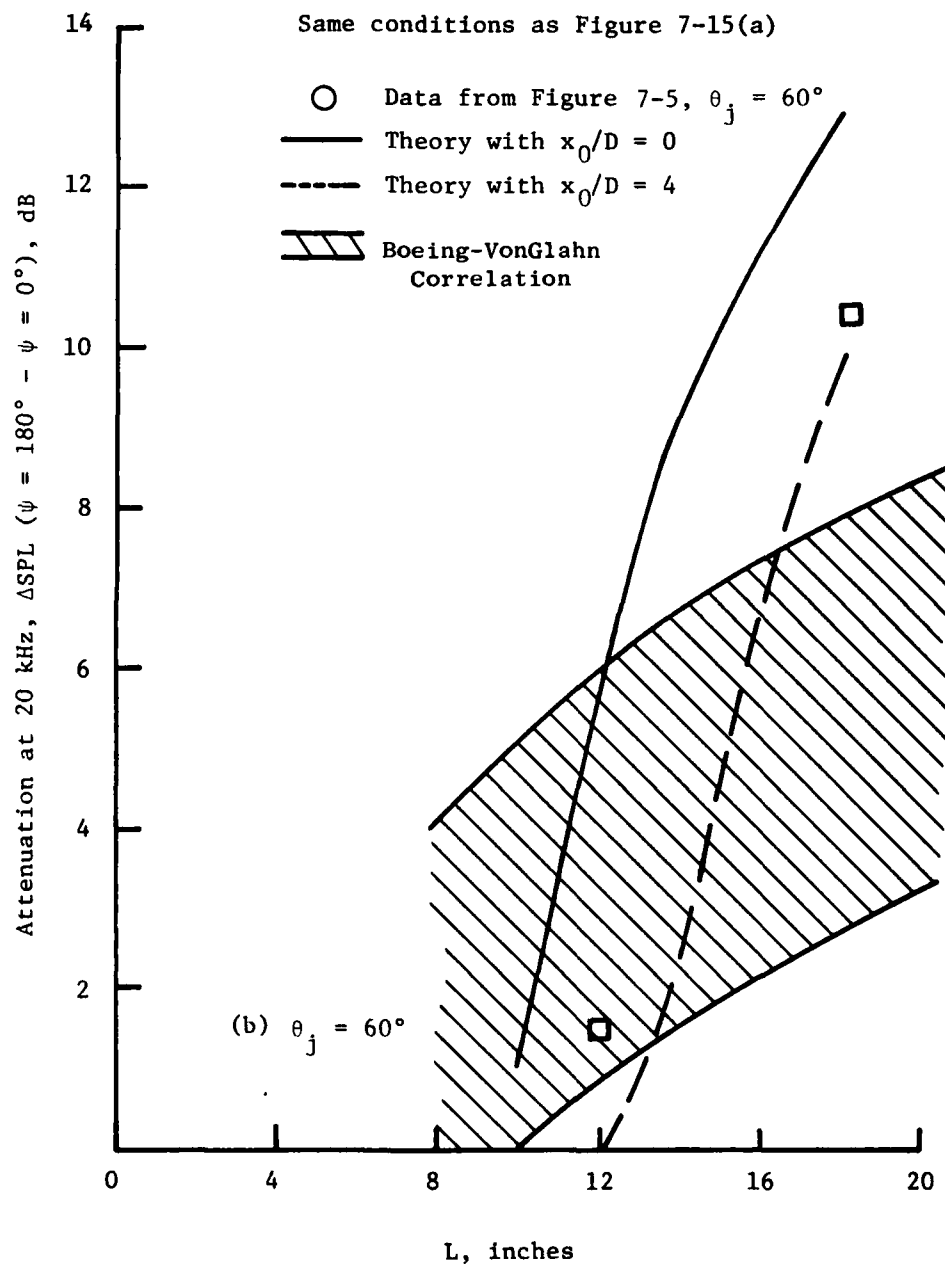


Figure 7-15. Comparison of Predicted and Measured Shielding Attenuation of 6-Tube Cluster, $V_j = 1650$ fps (Continued). 635

671

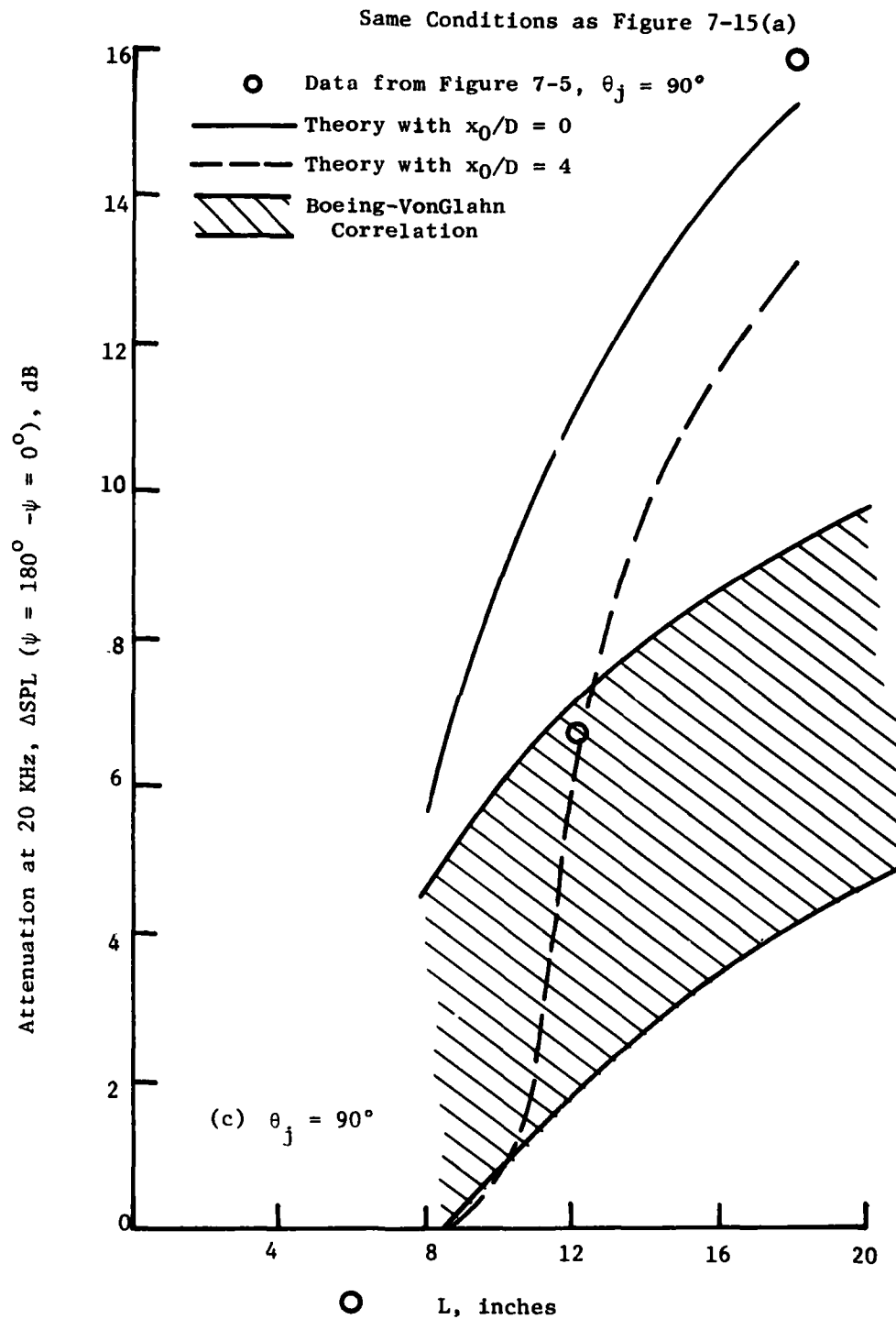


Figure 7-15. Comparison of Predicted and Measured Shielding Attenuation for 6-Tube Cluster, $V_j = 1650$ fps (Concluded). 636

(672)

The directivity of the noise at 10 kHz shows the SPL peaking between $\theta_j = 40^\circ$ and $\theta_j = 60^\circ$ (it is flat to ± 1 dB over this angular range), and on this basis one would roughly expect a reduction in PWL attenuation of 2.5 dB as compared to the measured value of 4.5 dB.

Figure 7-7 shows that the measured reduction in PWL attenuation is about 2 dB at 10 kHz when jet velocity is raised from 1500 to 2200 fps at T_j of 1500° R, $L = 18"$, and $s = 6"$. The predicted reduction in attenuation due to this velocity increase is 0.1, 2.7, and 2.3 dB at $\theta_j = 30^\circ$, 60° , and 90° , respectively.

Except for underestimation of the attenuation at $\theta_j = 30^\circ$, the physical shielding theory of Section 4.8.1, used in conjunction with the axial source distribution correlations of Motsinger and Sieckman⁽³⁶⁾, appears to predict reasonably well the measured shielding effects. The agreement holds for variations with θ_j , f , L , s , and jet velocity.

Since the aeroacoustic prediction method of chapter 4 proceeds from the noise contribution of each elemental volume of the jet, it should be an easy matter to additively integrate the results of Section 4.8.1 to produce a prediction procedure which includes the effects of a wing-like shield.

Finally, this chapter is concluded by discussing the theory-data comparison using the Boeing-von Glahn correlation. As can be seen in Figures 7-14 and 7-15, this method generally under-estimates the measured shielding, even after allowing for the ± 2.5 dB estimated confidence limit. The chief reason for this under-estimation is believed to be the lack of accounting of the parameter s/D (see Figure 7-13) in this method. In Reference 107, a better theory-data agreement than evident here was demonstrated for tests with a 21 tube nozzle configuration, but for $s/D = 13.7$, whereas in Figures 7-14, 7-15, s/D is approximately 7. Since decreasing s/D does increase shielding benefits, there is no contradiction between the results of Reference 107 and those shown in Figures 7-14 and 7-15. The comparison does, however, point out the need to account for the s/D parameter -- a deficiency of the Boeing-von Glahn method acknowledged in Reference 107. Even the slopes of variation of shielding with frequency and shield length are not very well predicted by the Boeing-von Glahn method. This deficiency is apparently due to a failure to account for the virtual source distribution of jets, i.e., the need to recognize that high frequency sources are located closer to the nozzle exit plane than low frequency sources. This feature is fully allowed for in the GE method. The conclusion from the comparative evaluation of the two methods is that if good estimates can be made of the source distributions in the jet plume, a first principles based diffraction model approach is the best approach to estimate physical shielding benefits.

8.0 OTHER TOPICS

This section contains a survey of several items whose relevance to jet noise has not been totally clear. These items include lip noise, orderly structure, jet noise suppression by the use of particle or fluid additives, etc. The studies were probing in nature, rather than comprehensive. The fluid injection and physical obstruction noise efforts were primarily literature surveys. Static lip noise was studied extensively. A wind-on lip noise investigation was contaminated by unexpected valve noise. Experiments were carried out to a sufficient extent, however, to substantiate that there is no significant lip noise at jet velocities above 1000 fps. Orderly structure experiments failed to establish any direct relevance to far-field jet noise. No novel jet noise suppression concept is evident from these studies. A planned analytical ejector aero-acoustic effort failed because a suitable analysis to predict ejector aerodynamics at takeoff conditions does not exist. The Task 3 report contains details of an empirical ejector noise prediction which must be used until the theoretical aerodynamics can be modeled.

8.1 LIP NOISE

The objective of this study was to determine the relative contribution to far-field noise of incident turbulence, separated flow, and vortex shedding from nozzle surfaces. All the activities were conducted under the direction of Dr. T.E. Siddon of the University of British Columbia. A causality technique was used to correlate nozzle surface pressures with far-field sound pressures. Important parameters include (1) shape of the convergent section of the nozzle, (2) nature and thickness of the boundary layer at the nozzle exit plane (laminar or turbulent), (3) lip thickness, and (4) level of incident turbulence. The effects of external flow on the radiated lip noise were also studied.

8.1.1 Fundamental Lip Noise Mechanisms

8.1.1.1 Background

One-third octave jet noise data often appear to display a rise to a maximum plateau in the high frequencies, particularly near 90° to the jet axis (see References 109, 110, 111, and 112). When jet noise model data are recorded at values of $\log fD/V_j$ greater than 0.4 (frequencies above 40 kHz), a distinct second maximum is apparent (attributed to lip noise) as shown in Figure 8-1. Since these higher model scale frequencies translate into the 3,000 to 12,000 Hz frequency range when converted to full scale, the noise levels could be significant for certain subjective noise assessments.

A set of hypothetical spectral pairs has been postulated for each of the three spectra shown in Figure 8-1 in order to roughly separate the high frequency "hump" from legitimate jet noise. The total SPL inherent jet noise and the excess noise are deduced separately by summing the energy in each band (plotted on Figure 8-4). The excess noise begins to become important at the lower Mach numbers, even though the data are for basically clean jet

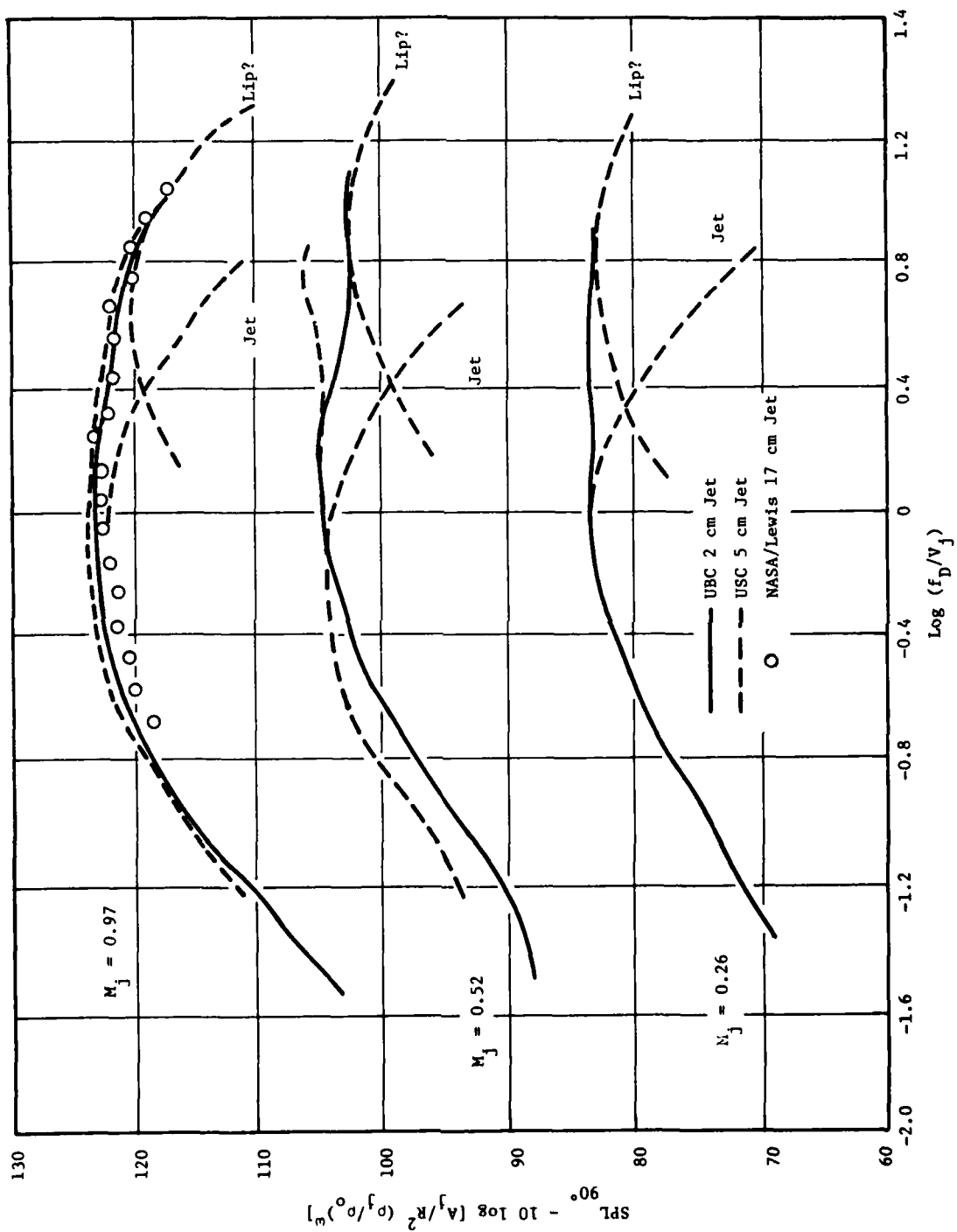


Figure 8-1. Normalized 90° Spectra as a Function of M_j .

flows. Whether or not such a spectral separation is realistic, and whether the excess noise fraction radiates from the vicinity of the nozzle lips remains to be determined.

If one adopts the hypothesis that the double-humped spectral signature is a consequence of induced unsteady pressure fluctuations at the trailing edges of the nozzle lips, arising from unsteady fluctuations of the shear layer boundary, then dipole-like radiation should result, and its effect should become increasingly prominent with reduction in jet velocity, due to its tendency to vary roughly as V_0^6 . The curves in Figure 8-2 show an increase in the relative importance of the nozzle noise at lower velocities. Further enhancement of this nozzle noise should occur if the internal nozzle flow is made to be unsteady (i.e., turbulent boundary layer or flow separation). Experiments reported herein tend to support this reasoning.

Very clean nozzle jets also show incidence of a high-frequency hump, yet correlation experiments reported later indicate almost no contribution from the lips. The alternative hypothesis also seems reasonable that the process of transition to a turbulent shear layer may result in legitimate quadrupole radiation. In the current clean jet tests, the process of transition seems to occur outside the nozzle, at a point a few shear layer thicknesses downstream of the exit plane.

8.1.1.2 Theory

The main diagnostic tool used in this investigation is the "causality" correlation technique. Various source fluctuations are measured and correlated in real time against the overall sound pressure at a specified far field point. The use of this technique, as well as several experimental precedents have been reported in the literature(113,114,115,116).

In this case, one correlates the time-delayed pressure fluctuations sensed over the nozzle lips with the far-field sound. From these correlations it is possible to predict the portion of the far-field radiation associated with the nozzle surface pressure fluctuations.

Analytical Frame Work

According to Curle's generalized solution of Lighthill's aerodynamic noise equation, the total far field pressure radiated from a fluid noise source field can be approximated by:

$$p(r,t) \approx \frac{1}{4\pi r} \int_S [\rho \dot{u}_n] dS + \frac{r_1}{4\pi r^2 a_o} \int_S \left[\frac{\partial}{\partial t} (f_1 + \rho u_1 u_n) \right] dS + \frac{r_1 r_j}{4\pi r^3 a_o^2} \int_v \left[\frac{\partial^2 T_{1j}}{\partial t^2} \right] dv \quad (377)$$

676

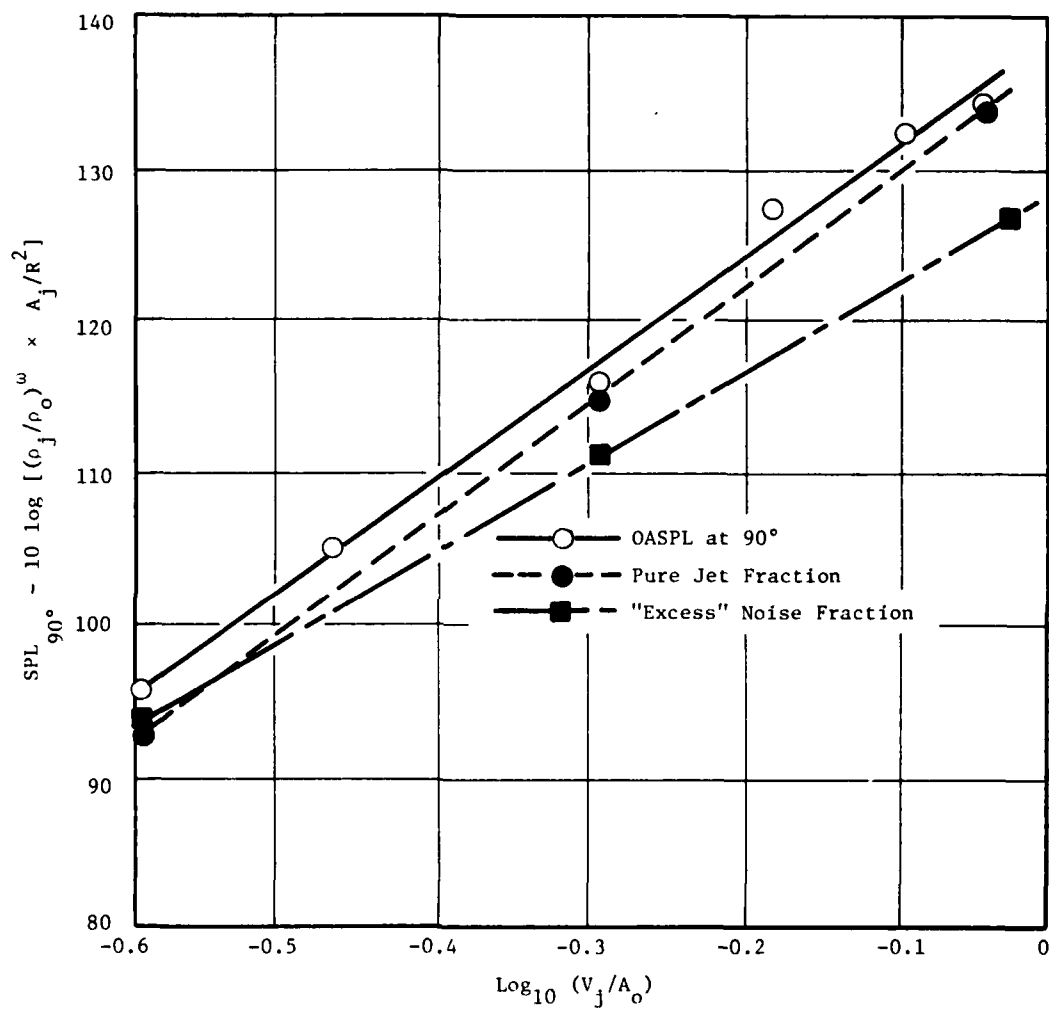


Figure 8-2. Postulated Contributions of Pure Jet Noise and Excess Jet Noise to OASPL_{90°}.

where:

square brackets denote evaluation at retarded time,

\underline{r} is the vector pointing from the source region to the far-field point.

The surface integrals are associated with noise generation by interaction between the fluid and the control surface S (real or imaginary) which may deform with arbitrary surface velocity u_n and may experience local stress fluctuations f_i . This surface generated noise is sometimes referred to as excess noise, since it adds to the turbulence generated jet noise, and is referred to herein as nozzle lip noise.

To ensure that the control surface S contains the region of primary lip noise generation, a surface is chosen as shown in Figure 8-3(a).

If the nozzle surfaces are rigid ($u_n = 0$), then the excess acoustic pressure sensed in the far field can be written:

$$p_{lip}(\underline{r}, t) \approx \frac{1}{4\pi r a_0} \int_S \cos \phi \left[\frac{\partial p_s}{\partial t} \right] dS \quad (378)$$

Where p_s is the local surface pressure and approximates f_i , the local resultant stress;* ϕ is the angle between the surface normal \underline{n} and the direction of far-field emission [see Figure 8-3(b)]. Individual elements of the above integral represent discrete dipole radiators.

It is likely that lip noise sources are concentrated very close to the exit plane. This means that the surface source strength should fall to insignificant values within a wavelength or so of the exit plane. If, in this region, the nozzle contour is relatively parallel to the z -axis, then one can make the approximations:

$$\cos \phi \approx \cos \epsilon \sin \theta; \text{ and at } \theta \approx 90^\circ, \cos \phi \approx \cos \epsilon.$$

In causality formalism (after Reference 114) both sides of the solution integral are multiplied by the far-field pressure $p(\underline{r}, t')$ evaluated at a different time t' . After time averaging, one can obtain:

$$\overline{p(t)p(t')} \approx \frac{1}{4\pi r a_0} \int_S \cos \phi p(t') \left[\frac{\partial p_s}{\partial t} \right]_{t-r/a_0} dS \quad (379)$$

When statistical stationarity is assumed (see Reference 113):

$$\overline{pp'}_s(\tau) \approx \frac{-1}{4\pi r a_0} \int_S \cos \phi \left[\frac{\partial}{\partial t} \overline{p_s p}(\tau) \right] dS, \text{ where } \tau = t' - t. \quad (380)$$

*Shear stress fluctuations can safely be neglected, relative to normal stress fluctuations (pressure), for most cases of flow at relatively high Reynolds number (see Reference 112).

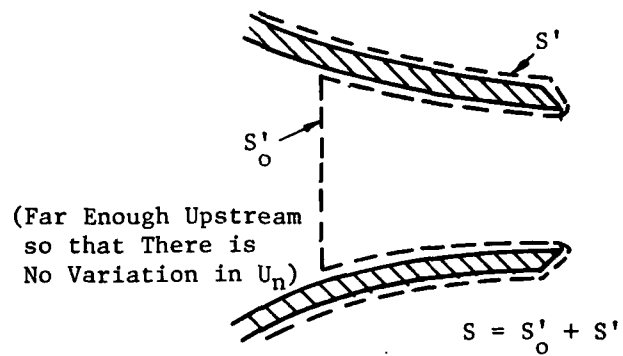


Figure 8-3(a). Control Surface Selected.

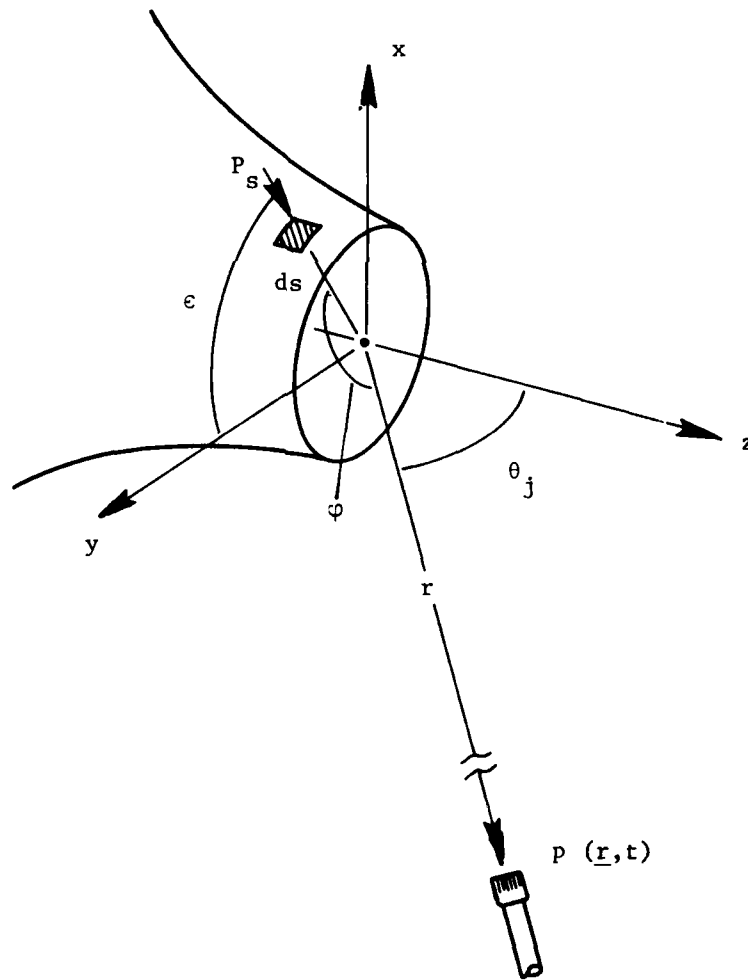


Figure 8-3(b). Coordinate System Used.

Thus, the autocorrelation of the excess far-field sound depends upon the integral distribution of the surface pressure far-field causality functions.

The autocorrelation of a local source contribution is given by the differential form of equation (380). If τ is set equal to zero, the acoustic contribution from each unit of nozzle surface area is:

$$\frac{d\overline{p^2}}{dS} \approx - \frac{\cos \phi}{4\pi r a_0} \left[\frac{\partial}{\partial \tau} \overline{p_s p}(\tau) \right]_{\tau = r/a_0} \quad (381)$$

It is expected that only those elements of surface which undergo substantial pressure fluctuations in the direction of \underline{r} will contribute to the total noise. This fact is emphasized by the multiplicative factor $\cos \phi$, which means that those surface elements which lie more-or-less normal to the direction of radiation \underline{r} will be the dominant radiators.

In Reference 113, it is shown that the spectrum of $p(\underline{r}, t)$ may be found by taking the Fourier cosine transform of equation (380):

$$\phi_p(\omega) \approx - \frac{1}{4\pi r a_0} \int_S \frac{\cos \phi}{2\pi} \int_{-\infty}^{\infty} \left[\frac{\partial}{\partial \tau} \overline{p_s p} \right] \cos \omega \left(\tau - \frac{r}{a_0} \right) d\tau dS \quad (382)$$

Thus if one defines:

$$\psi_{p_s p}(\omega) \approx - \frac{\cos \phi}{2\pi} \int_{-\infty}^{\infty} \left[\frac{\partial}{\partial \tau} \overline{p_s p} \right] \cos \omega \left(\tau - \frac{r}{a_0} \right) d\tau \quad (383)$$

then;

$$\frac{d\phi_p}{dS} \approx \frac{1}{4\pi r a_0} \left[\psi_{p_s p}(\omega) \right] \quad (384)$$

This gives the local source spectrum, or the fraction of $\phi_p(\omega)$ associated with unit surface area at the point where p_s was measured. Thus the complete spectrum is built up by superposition of elementary spectra from all points on the surface.

8.1.1.3 Possible Nozzle Noise Mechanisms

In the absence of any significant experimental conclusions about lip noise operating mechanisms, it is useful to hypothesize a variety of flow conditions which could result in noise emission from the trailing extremities of the nozzle. Several possible lip noise mechanisms are discussed below.

Condition: Smooth Approach Flow/Laminar Boundary Layer

Boundary layer transition occurs outside the nozzle (Figure 8-4) for this hypothesized correlation. The initial shear layer is laminar. The transition distance in a laminar shear layer is unknown, but will generally depend on the Reynold's number, boundary layer state, and nozzle geometry. Limited experimental data, supported by shear layer stability analysis (e.g., see Reference 112), suggest that

$$x_t \approx 50 \delta_\theta$$

where δ_θ is the momentum thickness of the initial shear layer at the exit plane ($x = 0$). Unlike the case of transition in a laminar boundary layer, the shear layer transition does not appear to occur at a unique Reynolds number.

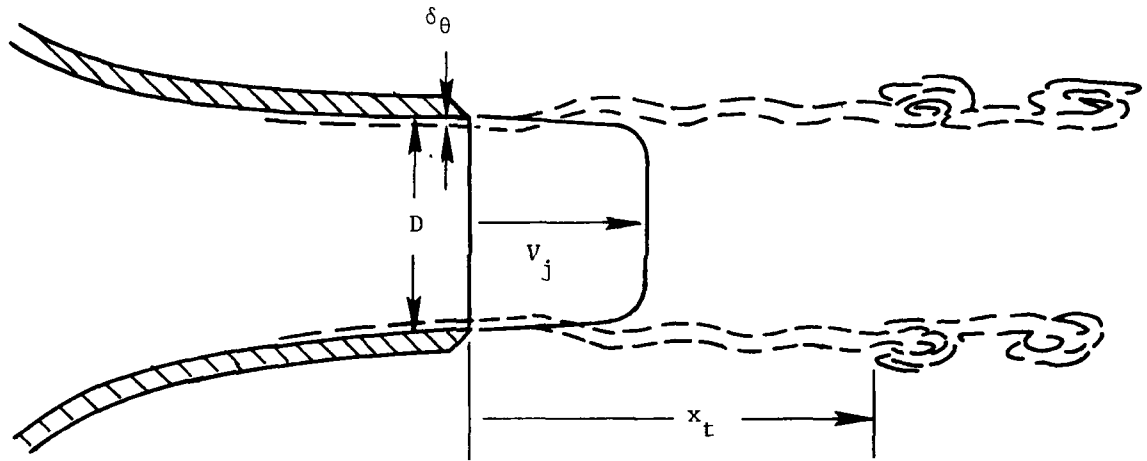


Figure 8-4. Transition Outside Nozzle.

Reference 112 also suggests that the frequency of the periodic transitional waves (which begin to occur within a distance x_t from the exit plane) can be predicted from the formula:

$$f \approx \frac{0.1V_{jet}}{2\pi\delta_\theta} \quad (385)$$

where

$$\delta_\theta \approx \frac{0.7x}{\sqrt{Re_x}} \quad (386)$$

Grosche⁽¹¹⁷⁾ shows a shadowgraph of a 2-cm jet of air operating at $M_j = 0.7$ wavelets of about 1 to 2 mm wavelength appear to develop, in circumferential bands, at a distance 1 to 2 mm downstream of the exit plane. An increase of noise emanating from the exit plane region of the jet is believed by Grosche to be caused by ring vortices or similar disturbances in the laminar/turbulent transition region, or its vicinity.

The process of turbulent evolution through transition follows from the birth of the unstable waves; these quickly distort into discrete vortices by nonlinear amplification (see Reference 118). The entire process occurs within approximately the first jet diameter and may constitute a spatially compact and highly efficient source of aerodynamic noise. The radiation efficiency is especially good if the evolving structures have a high degree of circumferential symmetry.

If the unstable wavelets develop very close to the nozzle, there is also the potential for inducing substantial levels of fluctuating pressure on the extremities of the nozzle surface (Figure 8-5). The initial laminar shear layer distorts and oscillates as a compliant boundary would.

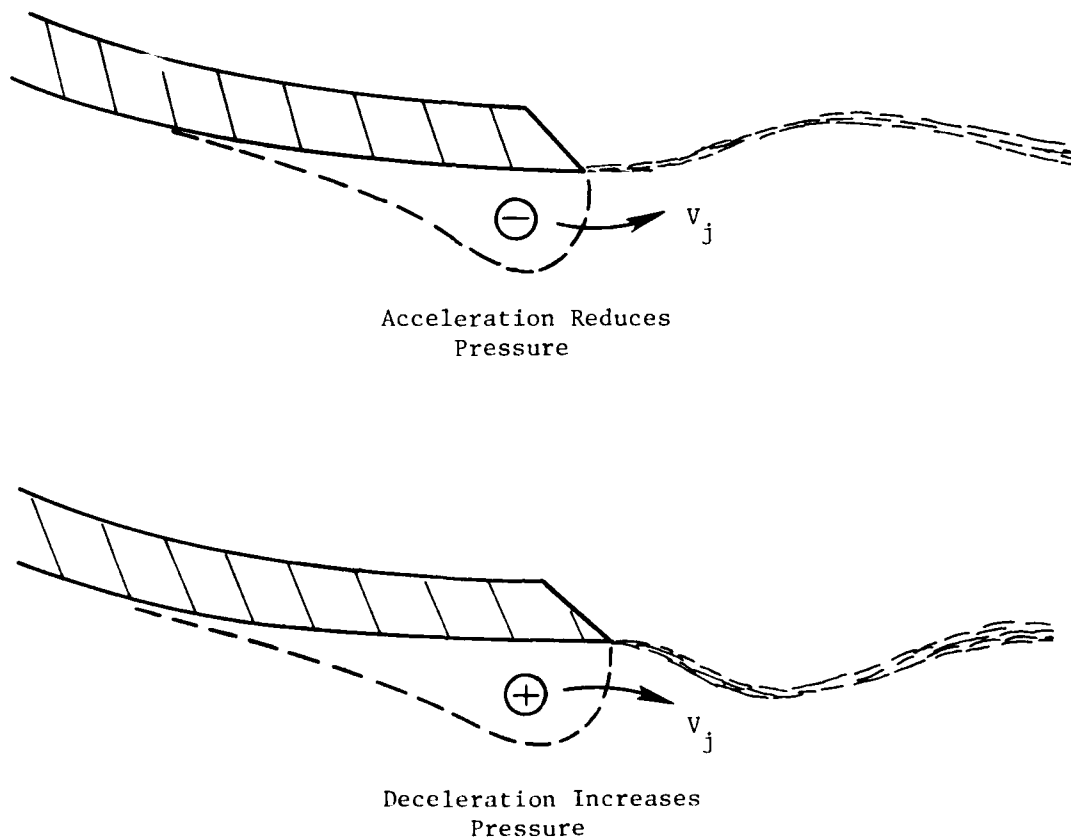


Figure 8-5. Exit Plane Instability.

A "hinge" effect occurs at the rigid lip of the nozzle; alternate accelerations and decelerations are imposed by the time-varying boundary condition. These are accompanied by a fluctuating, inertially induced pressure disturbance acting on the internal nozzle surface. The radiation power of this mechanism is unknown at this time. However, Grosche⁽¹¹⁷⁾ notes that, upon inserting a "turbulence ring" in the nozzle, some distance upstream of the exit plane, the excess "lip noise" appeared to be reduced substantially, presumably because it helped to destroy the strong circumferential coherence in the wavelet pattern.

By combining equations (385) and (386) with the assumption that $x \approx 1+2D$ in equation (386) the frequency of the shear layer instability can be predicted approximately from:

$$f \approx \frac{V_j^{3/2}}{50\sqrt{VD}} \quad (387)$$

If this instability contributes to the acoustic spectrum, the contribution should be of fairly narrow bandwidth, and centered on the following frequencies, for a room temperature free air jet:

M_j	0.2	0.4	0.6	0.8	1.0
$f_{D=2 \text{ cm}}$	20 kHz	60 kHz	112 kHz	170 kHz	240 kHz
$f_{D=50 \text{ cm}}$	4 kHz	12 kHz	22 kHz	34 kHz	48 kHz

These frequency predictions above are only nominal estimates; the actual values may be higher or lower by 50% or more, depending on the actual momentum thickness at the exit plane. For a full-size jet ($D=50 \text{ cm}$) exhausting near $M_j = 1$, the shear layer instability would be well into the ultrasonic range, and probably of little consequence to the subjective noise. Furthermore, there is little likelihood of a laminar boundary layer and smooth core flow in a real engine exhaust.

Condition: Smooth Approach Flow/Transition Near Exit Plane

If one assumes that the nozzle cone affords an optimum inlet contour and sufficiently smooth surface for the initiation of a laminar boundary layer, the boundary layer transition distance may be deduced from the well known transition Reynolds number:

$$Re_{\delta^*} \approx \frac{V_j \delta^*}{\nu} \approx 400 \rightarrow 600 \quad (388)$$

This range is based on the flat plate transition experiments of Schubauer and Skramsted, and the theory of C.C. Lin. To apply in the jet nozzle, the boundary layer thickness δ^* must be small compared to the nozzle diameter D. The displacement thickness δ^* is given by:

$$\delta^* \approx \frac{1.75 x}{\sqrt{Re_x}} \approx 2.5 \delta_\theta \quad (389)$$

Combining equations (388) and (389) yields:

$$Re_{x_t} \approx \frac{V_j x_t}{\nu} \approx 50,000 \rightarrow 120,000 \quad (390)$$

Thus, for free air jets of 2 cm diameter, or 50 cm diameter, operating at room temperature, the transition distances (in numbers of jet diameters) will be:

M_j	0.2	0.6	1.0
$(x_t/D)_{2 \text{ cm}}$	0.5 \rightarrow 1.2	0.17 \rightarrow 0.4	0.10 \rightarrow 0.24
$(x_t/D)_{50 \text{ cm}}$	0.02 \rightarrow 0.05	0.007 \rightarrow 0.016	0.004 \rightarrow 0.01

Since most jet nozzles would have an "effective" boundary layer origin on the order of one diameter upstream of the exit plane, it is evident that the boundary layer in small model jets will generally undergo transition very near the exit plane, at low values of M_j . Transition may occur upstream of the lip as M_j approaches unity. But for a 50 cm nozzle more typical of a full-scale jet, the boundary layer should always become turbulent well upstream of the exit plane.

In the event that Tollmein-Schlichting (T-S) waves do begin to form immediately upstream of the nozzle lip (possible for a 2 cm nozzle as $M_j \rightarrow 1$), there is a likelihood of vortex generation right at the exit plane (Figure 8-6).

This occurrence could lead to strong periodic pulses of negative pressure being induced at the lip, as a consequence of rapid accelerations associated with the "rolling up" process. This provides a mechanism for efficient radiation of surface dipole noise, especially if there is a substantial degree of lateral coherence in the approaching T-S wave patterns.

The frequencies of the earliest forming T-S waves can be deduced from Lin's stability analysis (Reference 119) which gives:

$$f \approx 48 \frac{V_j^2}{\nu} \times 10^{-6} \text{ Hz} \quad (391)$$

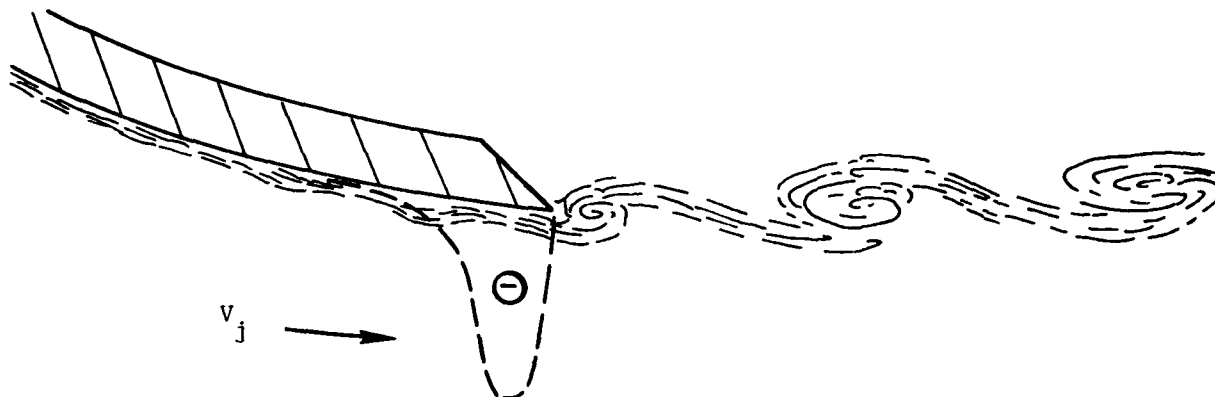


Figure 8-6. Transition at Exit Plane.

Hence, for a room temperature air jet:

M_j	0.2	0.6	1.0
f	16 kHz	140 kHz	400 kHz

Thus the transition/lip interaction process may be a source of ultra-sonic noise for small diameter (model) jets, but it is not likely to be present with larger nozzles.

Condition: Smooth Approach Flow/Turbulent Boundary Layer

In a full-scale jet nozzle ($D \approx 50$ cm) the boundary layer will undoubtedly be turbulent well upstream of the exit plane, for reasons offered in the previous discussion. It is known that the largest eddies in a turbulent boundary layer have a longitudinal wavelength of about one boundary layer thickness δ (roughly four times the integral length scale)*. The lateral scales will be roughly 1/3 to 1/2 of this magnitude. The turbulent structures will pass the nozzle lip at a velocity of approximately 60% of the core jet velocity, and in the process may induce intensified, but circumferentially localized pressure fluctuations at the exit plane. These pressure fluctuations result from the random redirection of fluid as it passes the nozzle lip, with possible "birth" of the initial shear layer eddies (Figure 8-7).

* δ is the total boundary layer thickness. Assuming a 1/7 power velocity profile $\delta^* \approx \delta/8$ and $\delta_0 \approx \delta/10$

685



Figure 8-7. Turbulent Boundary Layer at Sharp Edge.

The lip pressure spectrum will be broadband, but with a peak corresponding to the frequency of passage of the dominant energy-bearing structures:

$$f_{\text{eddies}} \approx \frac{V_c}{\lambda_{\text{eddy}}} \approx 0.6 \frac{V_j}{\delta} \quad (392)$$

Assuming the turbulent boundary layer has a 1/7 power velocity profile, and that it initiates roughly one diameter upstream of the exit plane, its effective thickness is given by:

$$\delta \approx 0.37 D \frac{V_j D}{\nu}^{-1/5} \quad (393)$$

On the basis of the above assumption, the following quantities may be calculated for an unheated air jet:

M_j		0.2	0.6	1.0
$D = 2 \text{ cm}$	δ	0.74 mm	0.60 mm	0.54 mm
	f_{peak}	56 kHz	206 kHz	380 kHz
$D = 50 \text{ cm}$	δ	9.8 mm	7.8 mm	7.1 mm
	f_{peak}	4.2 kHz	16 kHz	29 kHz

Apparently, the frequencies of natural boundary layer surface pressures are generally in the ultrasonic range, even for a large jet nozzle. Furthermore, because of the limited lateral coherence of boundary layer "eddies" (the tangential wavelength is on the order of 1/20 to 1/50 of the jet diameter), they probably represent a very inefficient source of lip noise. It is possible in fact that a thin turbulent boundary layer ensures the quietest operating condition for a jet nozzle. This is consistent with Grosche's⁽¹¹⁷⁾ observation.

Condition: Smooth Approach Flow/Internal Separation

Poor nozzle contour or upstream obstructions can lead to an artificial thickening of the boundary layer, whether it be laminar or turbulent. The resulting internal pressure fluctuations may have substantial lateral coherence, and the separated region (Figure 8-8) may be thick enough at the exit plane to induce significant lip noise, by the process described in the previous discussion. The nominal thickness of the separation bubble, and whether or not it reattaches within the nozzle, will strongly influence the nature of the noise. These properties have a complex dependence on the "shape" of the nozzle or obstruction, on the properties of the approaching

6.7

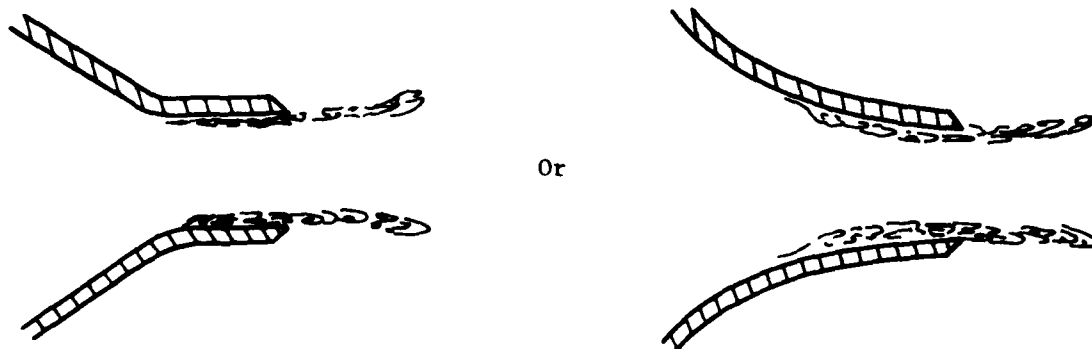


Figure 8-8. Internal Separation.

boundary layer, and on Mach number. However, one can estimate that the "length" scale of the resulting pressure field will be on the order of two to four times the obstruction height, and that the pressure field will convect with a velocity of 50% to 60% of the free stream velocity. Thus, the spectral peak for lip pressures may be predicted by a modified version of equation (392):

$$f_{\text{separation}} \approx \frac{0.6V_j}{3d} \approx 0.2 \frac{V_j}{d} \quad (394)$$

where d is the effective height of an obstruction, either real or virtual.*

Thus, for an obstruction height of 0.5 mm the following frequencies can be predicted:

M_j	0.2	0.6	1.0
f_{peak}	27 kHz	82 kHz	140 kHz

Whether this mechanism is capable of radiating significant noise depends on the details of the separation bubble, particularly its lateral coherence and reattachment point.

Condition: Smooth Approach Flow/Internal Separation with Coherent "Screech"

Under severe conditions of internal separation (especially where there is an axisymmetric character to the separation "bubble"), it is possible to generate a powerful nozzle screech. This arises from a resonant feedback loop involving the point of initial separation and the nozzle lip. Assuming that the obstruction is in the form of a circular trip ring (Figure 8-9), an axisymmetric ring vortex, "born" earlier at the obstruction edge, is suddenly relieved as it passes the exit plane. At this instant, its vorticity distribution is altered abruptly in a manner which sends a strong pulse of acoustic pressure back upstream. On interacting with the shear layer at the obstruction edge, the pressure pulse "triggers" the birth of a new ring vortex. The fundamental frequency of lip interaction is given by the inverse of the sum of the upstream and downstream propagation times:

$$f_{\text{screech}} \approx \frac{1}{\frac{\ell}{0.6V_j} + \frac{\ell}{a_j - V_j}} = \frac{0.6M_j a_j / \ell}{1 + \left(\frac{0.6M_j}{1 - M_j} \right)} \quad (395)$$

Here, a_j is the speed of sound in the nozzle throat.

* i.e., an obstruction capable of generating the same fully developed separation bubble as a "poor" nozzle contour.

(687)

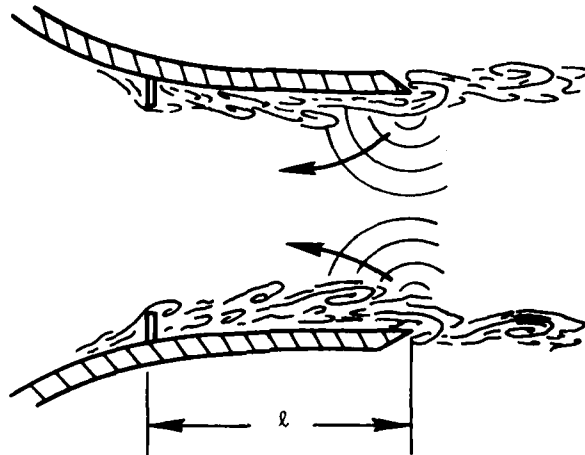


Figure 8-9. Nozzle Screech Mechanism.

Thus, for a path length $l \approx 2$ cm in a free air jet, the fundamental screech frequencies will be:

M_j	0.2	0.6	1.0
f_{screech}	1790 Hz	3250 Hz	0

Note that the screech frequency approaches zero at both limits $M_1 \rightarrow 0$ and $M_j \rightarrow 1$. At a particular Mach number, several harmonics of f_{screech} are possible, because the feedback cycle is pulsatile, rather than sinusoidal; i.e., the vortices may be much smaller than their core-to-core spacing.

The phenomenon described above has been observed to occur in nozzles when trip rings of heights greater than 1/2 mm are inserted. The acoustic emission from the lip rises to levels which are substantially larger than the pure jet noise, apparently due to the axisymmetric nature of the induced pressure field.

Condition: Large Scale Turbulent Approach Flow

If large scale turbulence is present throughout the internal approach flow it may have a variety of effects, depending on the shape of the eddies

670

and the relative scale size compared with jet diameter. If the unsteadiness has a scale larger than the nozzle diameter it will produce the effect of an acoustic monopole (mass flux pulsation) at the exit plane.

However, if the length scale is somewhat smaller than the nozzle diameter, an unsteady edge fluctuation will result, as the pressure field is suddenly "relieved" at the exit plane. The process will be similar to the turbulent boundary layer-edge interaction illustrated in Figure 8-7. However, due to the much larger circumferential extent of the turbulent structures, acoustic radiation should be much more efficient and at substantially lower frequencies than for the turbulent boundary layer. The actual level of excess noise generated will depend on the turbulence intensity and ratio of scale length to nozzle diameter. For fully developed turbulent pipe flow, maximum axial scale lengths on the order of one nozzle diameter, and maximum turbulence intensities of 6% to 10% in the near-wall region of the flow are expected. The resulting spectra of "lip" pressures should have a broad peak at frequencies where $f \approx V_j/D$. Thus, for fully developed pipe flow turbulence at the nozzle exit:

M_j	0.2	0.6	1.0
$f_{\text{peak}2 \text{ cm}}$	3.4 kHz	10 kHz	17 kHz
$f_{\text{peak}50 \text{ cm}}$	140 Hz	400 Hz	700 Hz

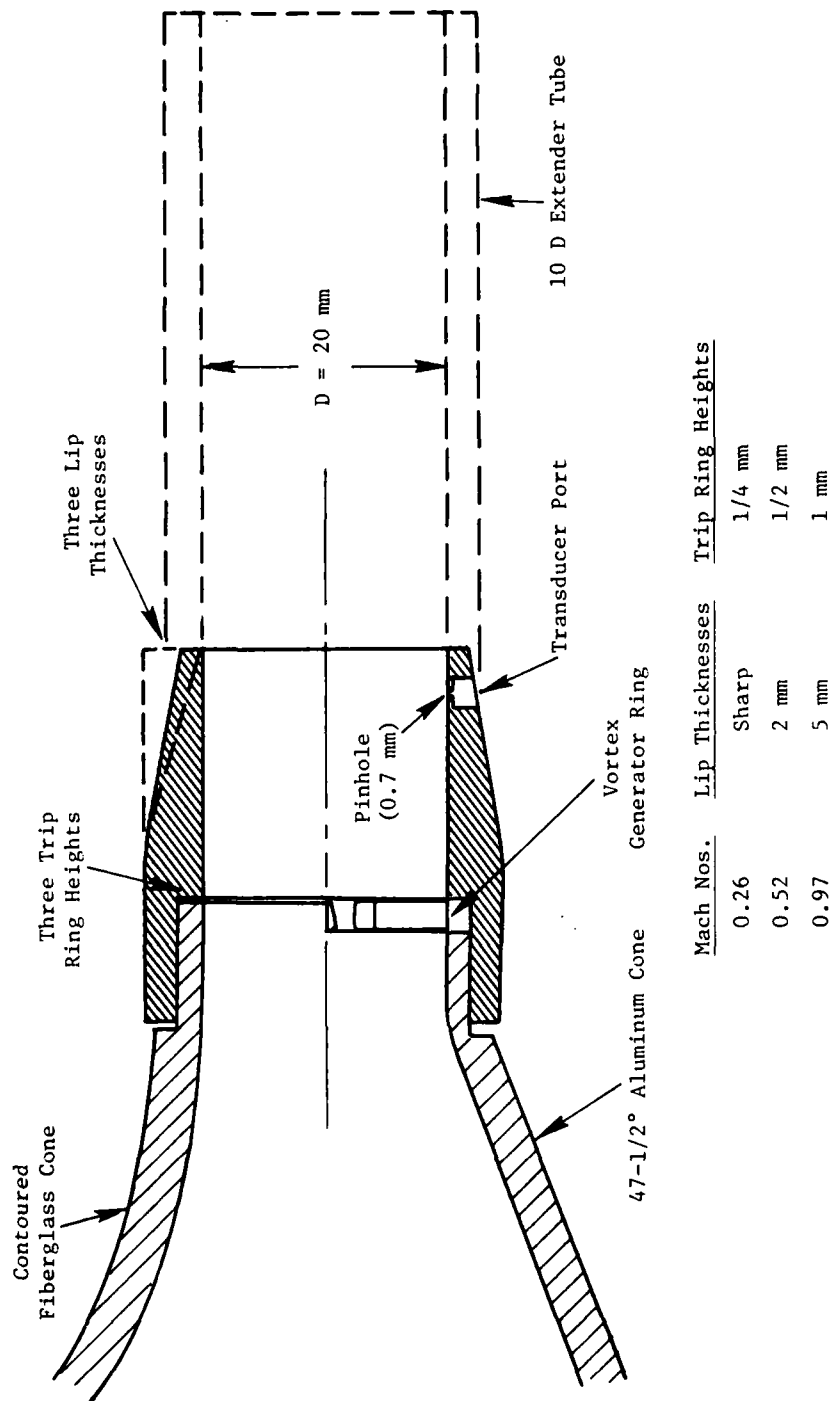
8.1.1.4 Experimental Technique

The experimental lip noise work consisted of measuring far-field spectra for various nozzle configurations and making correlation measurements between the fluctuating pressures on the nozzle walls and the far-field sound. All the experimental work was conducted in the University of British Columbia Anechoic Room(109,123).

Measurements of Far-Field Spectra

The far-field spectra were measured for a conical nozzle and a smoothly contoured nozzle (see Figure 8-10) under the following conditions:

- Clean, as shown in Figure 8-4.
- Various nozzle tips with lip thickness ranging from 2 mm to 5 mm.
- Internal tip rings placed 1 diameter upstream of the exit plane. The height of the rings varied from 1/4 mm to 1 mm.
- Internal turbulence generators of two types:
 - vortex generator placed upstream of the exit plane.
 - 10-diameter nozzle extender attached at the nozzle exit plane.



Mach Nos.	Lip Thicknesses	Trip Ring Heights
0.26	Sharp	1/4 mm
0.52	2 mm	1/2 mm
0.97	5 mm	1 mm

Figure 8-10. Nozzle Configurations Tested.

Correlation Measurements

The difficulty of making an accurate and reliable measurement of pressure fluctuations on the nozzle surface was only partially resolved. A number of difficulties were encountered in devising a tiny flush-mounted pressure transducer capable of accurate response to nozzle pressure fields, at frequencies up to 100 kHz. (Because of limited air supply capacity, the jet nozzle was designed with a 2 cm exit diameter. As discussed in Section 8.1.3, this suggests that the frequency range of interest for lip noise would lie between 20 kHz and 160 kHz.) The effective sensing dimension of the pressure transducer should be less than 1/4 of the wavelength of the convecting disturbance at the upper frequency limit to ensure adequate spatial resolution. For a disturbance convecting "hydrodynamically" at 300 fps, the required diameter is 0.010 inch or less for 100 kHz response. Many transducers and configurations were tried. The most satisfactory transducer was made from metallized mylar foil stretched over a roughened backplate. The active diaphragm diameter is approximately 0.050 inch. With only a clearance of 0.005 inch between pinhole and diaphragm, and a pinhole diameter of 0.030 inch, the Helmholtz resonant frequency is approximately 120 kHz. The pressure response is considered reliable to about 100 kHz.

The tip nozzle with 2 mm lip thickness was used for extensive cross-correlation measurements. The nozzle was machined of aluminum and contains a number of flat-bottomed holes drilled along its axial length. When the transducer was plugged in at a specific axial position, the other holes were plugged with Teflon.

The tip nozzle element is scribed at 15° intervals. The far-field microphone was located at selected angles θ_j relative to the jet axis, in the horizontal plane. The transducer port was rotated through 15° increments of ϕ in the x - y (exit) plane. In this way it is possible, in principle, to build up a complete surface distribution map of dp^2/dS for each jet operating condition, given enough separate data points. (In practice, it was not feasible to obtain data for points closer than 2 mm to the exit plane.)

8.1.1.5 Results/Measurement of Far-Field Spectra

Spectra for Basic Nozzles

Figure 8-11 shows 1/3-octave spectra for the basic fiberglass and aluminum contraction cones. The characteristic high frequency "humping" is evident for frequencies above 20 kHz (the secondary ripples at around 35 kHz and 80 kHz are relatively independent of velocity; it is believed that these arise from slight irregularities in the microphone frequency response). The spectra for the aluminum cone rise increasingly above those for the fiberglass cone at the high frequency and as Mach number is reduced. This is thought to be a consequence of internal separation, caused by the rather tight curvature just upstream of the exit plane, for the aluminum cone. By installing an aluminum shield around the nozzle exit, lined with 1/4-inch-thick fiberglass wool (see Figure 8-12), this high frequency excess noise of the aluminum cone was reduced to the level of the unshielded fiberglass cone. The shield caused a noticeable, but somewhat smaller reduction of the high frequency

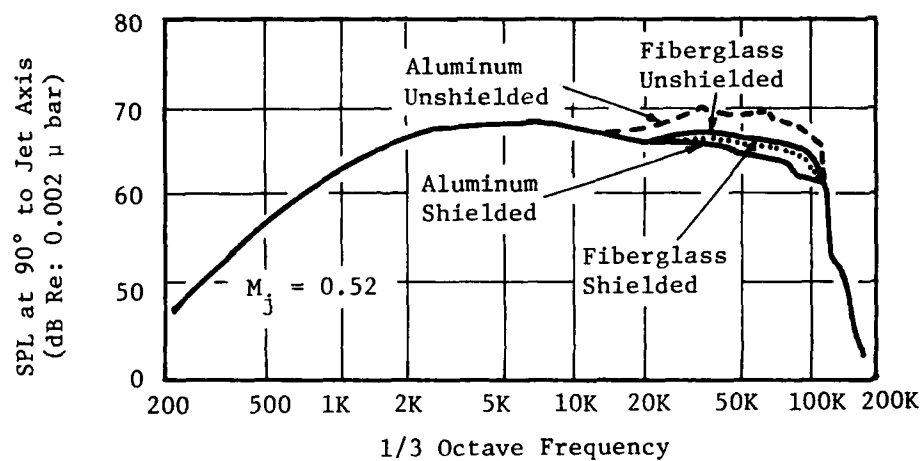


Figure 8-11. Basic Shielded and Unshielded Nozzle Spectra.

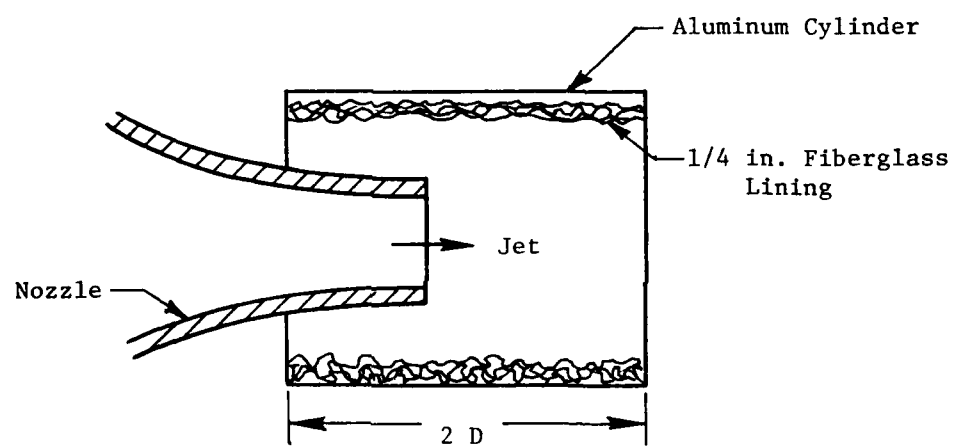


Figure 8-12. Schematic of Nozzle Tip Shroud.

levels for the fiberglass cone. The lesser influence of shielding on the fiberglass nozzle spectra, and correlation data reported later, jointly lend support to the notion that the excess noise for the baseline (smooth flow) nozzle emanates from the region of transition/turbulence generation in the free shear layer. By contrast, the aluminum cone seems to generate genuine lip noise.

Addition of Tip Nozzles with Different Lip Thickness

Figure 8-13 shows the consequences of adding different tip nozzles of various lip thicknesses to the fiberglass cone. The thicknesses range from very sharp to 5 mm thick. Only slight spectral irregularities are evident, with no consistent trend. The overall levels are virtually unaffected.

When any of the tip nozzles are added to the aluminum cone, however, there is a pronounced reduction of the high frequency excess noise (Figure 8-14). The longer channel length at constant diameter presumably induces the flow to reattach, or perhaps the more favorable pressure gradient prevents the flow from separating at all. The degree of suppression appears to be slightly dependent on lip thickness (the thin lip gives the quietest operation at $M_j = 0.52$).

Spectra with Internal Trip Rings

Figure 8-15 shows the very powerful effect of inserting a thin trip ring at a point one diameter upstream of the exit plane. It was anticipated that the trip rings, by producing a turbulent boundary layer on the inside of the nozzle, would increase the lip-generated noise. This was generally the case for the 1/2 mm trip ring, but for the least intrusive ring (1/4 mm height), the high frequency noise levels were actually reduced from those for the "clean" throat; the reduction is as large as 1.5 dB on overall level, for the case with the aluminum contraction cone. This may be explained by a reduction of tangential coherence, as discussed in Section 8.1.1.2. The 1/2 mm aluminum trip ring height increased the noise substantially, especially over the mid-frequency range. Intense nozzle screech is evident for the largest obstruction height. The characteristic screech frequencies agree well with predictions based on the vortex feedback model discussed in Section 8.1.1.3 (Figure 8-9).

Production of Internal Turbulence

In order to examine the role of upstream large-scale turbulence on the nozzle excess noise, two methods of turbulence generation were attempted:

1. A series of inward-protruding thin airfoils distributed around a ring one diameter upstream of the exit plane, and placed at 10° to 12° angle of attack (i.e., a vortex generator). Adjacent blades were pitched at opposite angles.

Figure 8-13. Various Tip Nozzles On Fiberglass Cone.

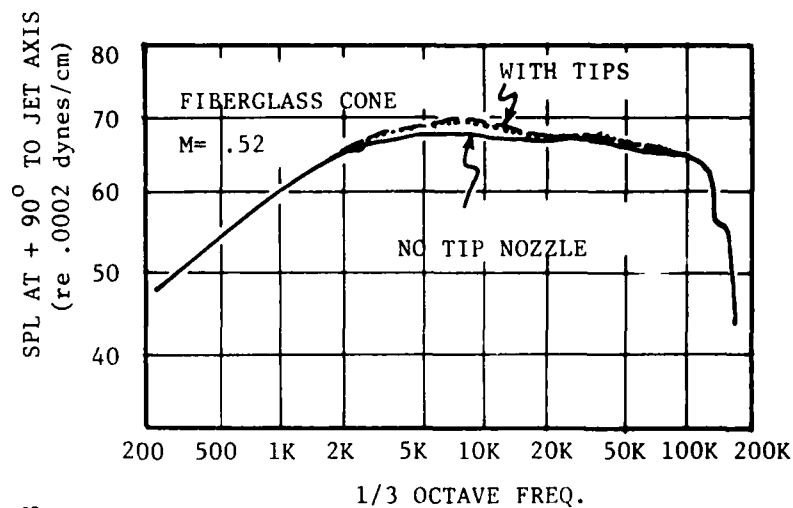


Figure 8-14. Various Tip Nozzles On Aluminum Cone.

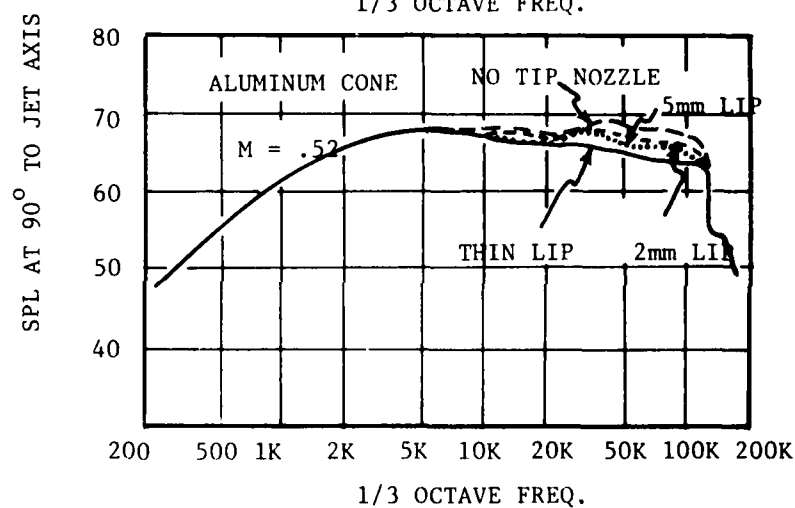
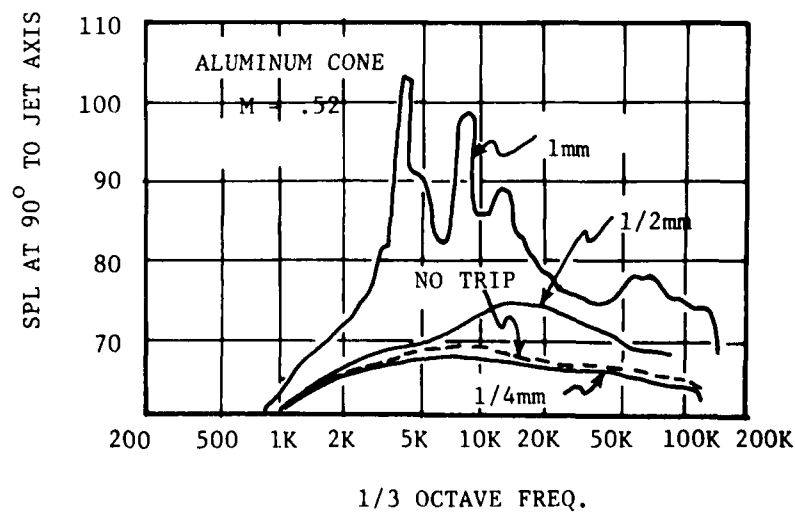


Figure 8-15. Effect of Trip Rings of Various Heights.



2. A 10-diameter long extension section was installed between the contraction cone and the tip nozzle.

Figure 8-16 shows the effect of introducing the multivaned vortex generator into the nozzle. At low jet speeds, the device increases the excess noise quite significantly, over the frequency range from 10 to 100 kHz. However, at intermediate speeds (Mach No. = 0.68), the low frequency jet noise is actually reduced somewhat*. Perhaps the vortex generator, by introducing random turbulence into the flow, destroys the coherence of some fundamental jet noise producing mechanism (e.g. collapse of ring vortices at $x/D \approx 4-6$). On the other hand, the high frequency noise is increased, probably because of enhanced dipole mechanisms associated with the vortex generator blades.

Spectra obtained with the 10-diameter tube extender (Figure 8-17) show that, compared with the baseline nozzle data, the tube extender appears to reduce the high frequency noise above 20 kHz quite significantly (by as much as 6 to 7 dB at 80 kHz). Below 20 kHz, the shapes of the two types of spectra are quite similar with the extender nozzle still being 1 to 2 dB quieter (the exit plane stagnation pressure was again held equal to that of the standard nozzle).

Apparently, the thick turbulent boundary layer produced by the tube extender reduces the initial shear of the developing jet, and thereby achieves some significant suppression of the high frequency jet noise. This factor must strongly override any tendency for an increase in lip noise due to the internal turbulence.

8.1.1.6 Results/Causality Correlation Measurements-Lip Source Strength in Axial Direction

Figure 8-18 shows typical correlation plots for the 1/2 mm trip ring installed. Positions 1, 2, and 3 refer to transducer locations at $z \approx -2.6$ mm, -4.9 mm, and -6.55 mm (upstream of the nozzle lip). At position No. 1, the normalized causality coefficient R_{psp} reaches values of about 0.17, indicating that a substantial fraction of the total 90° jet noise is coming from that region of the lip. As the transducer point is moved further upstream, the correlation "blip" shifts to later time delay and weakens. At position No. 2, the source strength goes slightly negative. At position No. 3, the slope of $\overline{p_{sp}}$ is essentially zero, indicating negligible sound radiation from this point.

The axial source information for separated internal flow is illustrated in Figure 8-19.

* To make sure that the head loss of the vortex generator did not reduce the effective jet speed, the centerline total head at exit plane was maintained at the same values as for unobstructed flow cases.

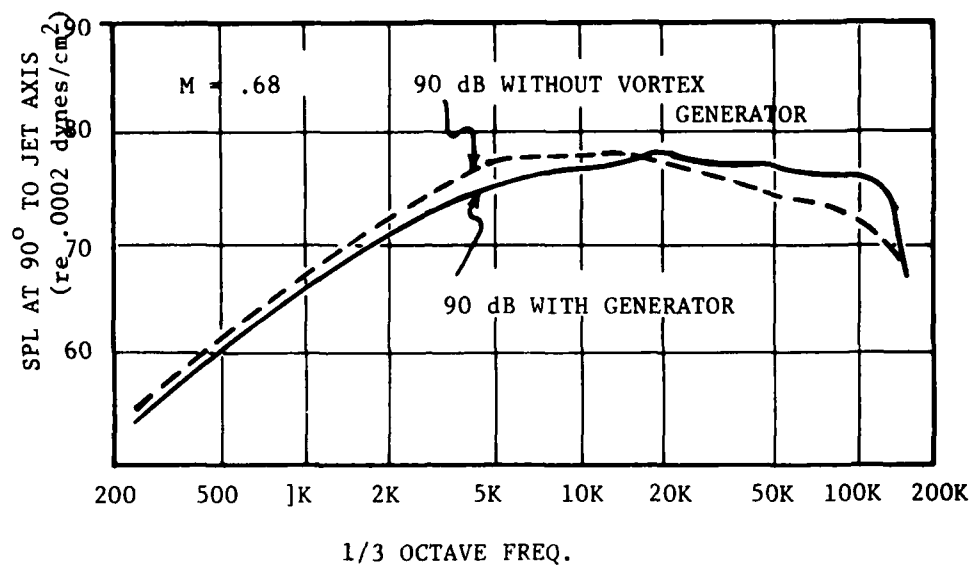


Figure 8-16. Multivane Vortex Generator Effect.

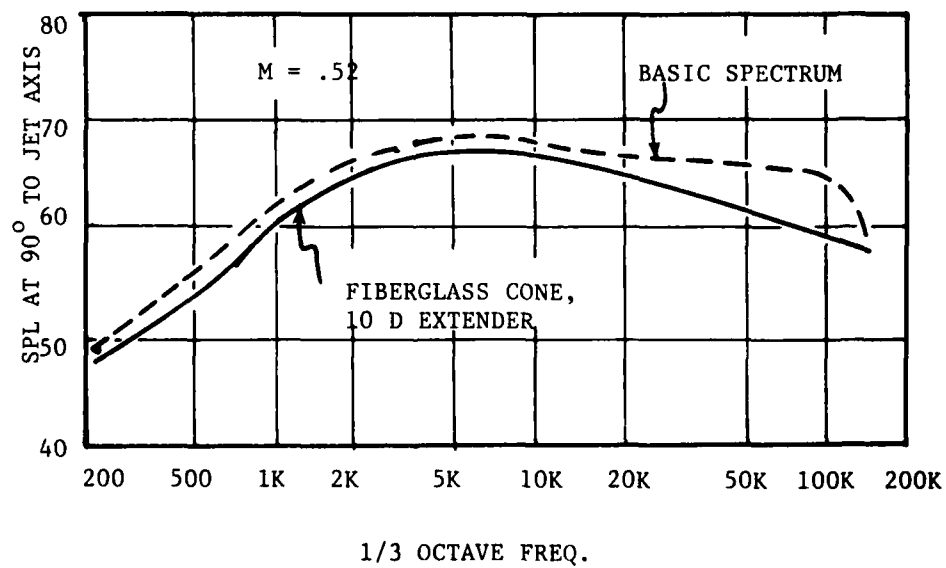


Figure 8-17. Contraction Cone Tip Nozzle Extender Tube Effect.

$$C(\tau) = \overline{P_S P(\tau)} / P'_S P'$$

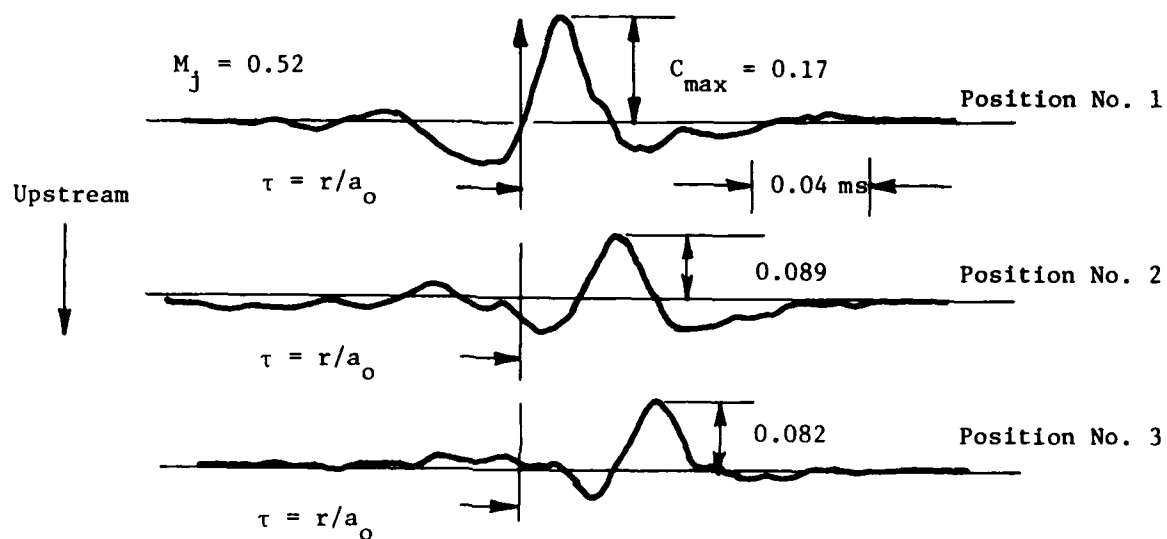


Figure 8-18. Causality Correlations, $\phi = 0^\circ$, $\theta_j = 90^\circ$, $r = 1$ m.

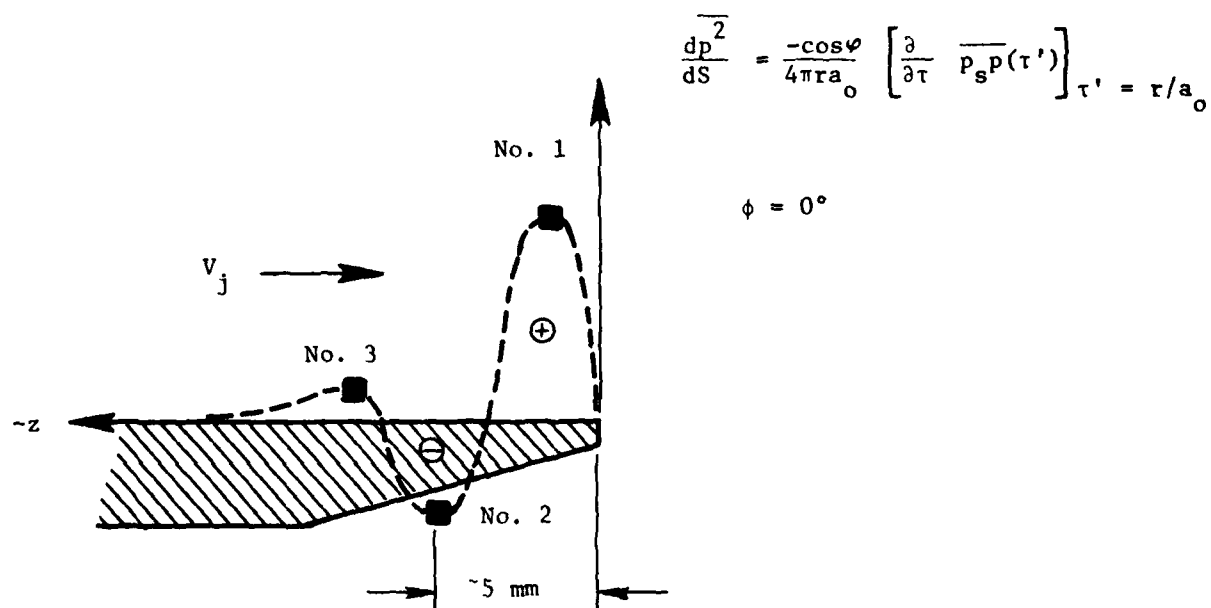


Figure 8-19. z-Wise Variation of Lip Source Strength.

M = 0.52, Position No. 1, Test Point 3, Variation of $\overline{p_s p}$ with ϕ

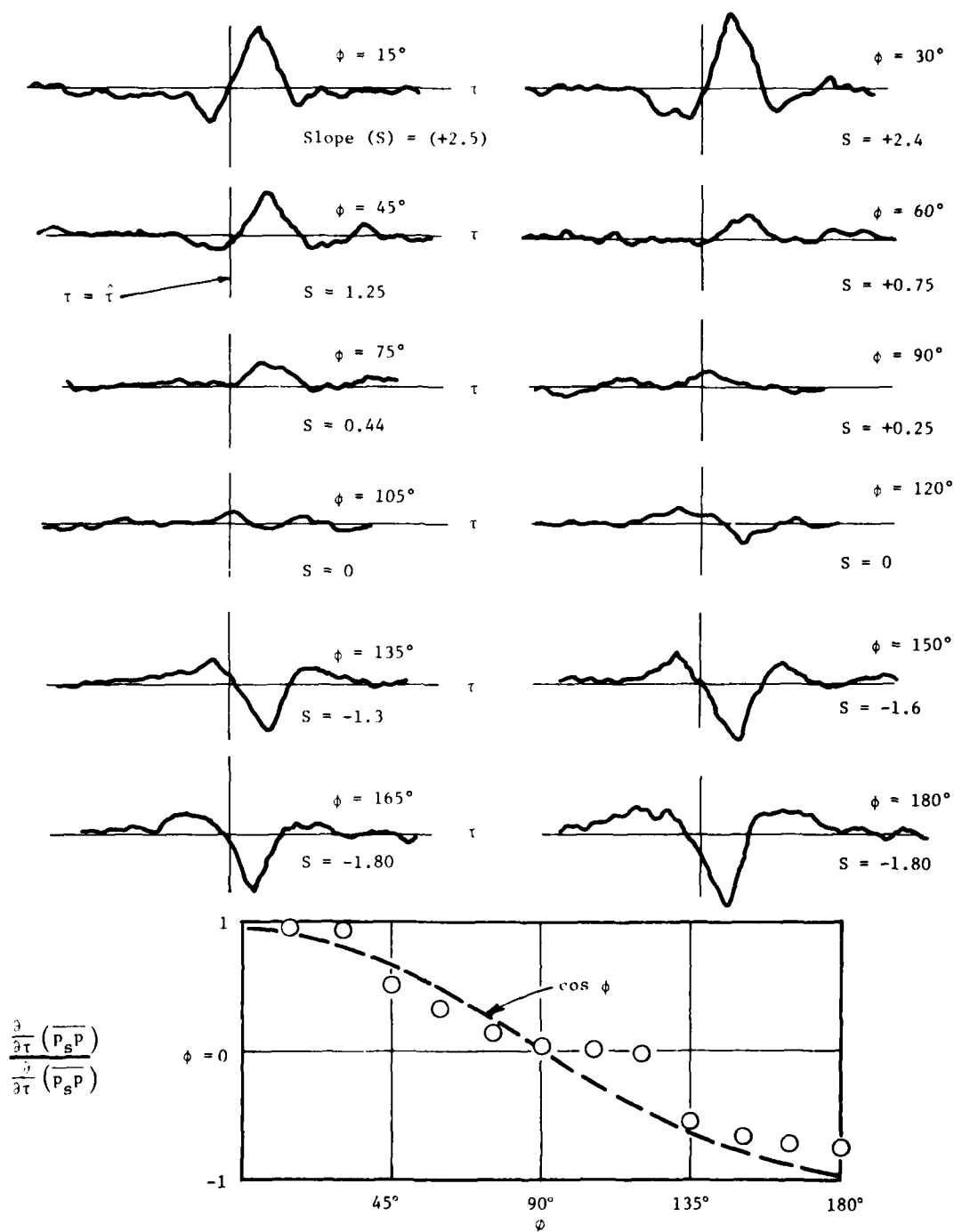


Figure 8-20. Variation of $\overline{p_s p}(\tau)$ with ϕ .

Correlation Strength in Tangential Direction

The data for the far side of the nozzle ($\phi \approx 180^\circ$) and axial position 1 shows a large negative slope at the required offset time (see Figure 8-20). Since $\cos \phi$ is positive for $90^\circ < |\phi| < 180^\circ$ this region is also one of positive source strength, in accordance with equation (381). Taking slope data from the correlation plots and multiplying by $\cos \phi$, yields a tangential source distribution function of the appearance shown in Figure 8-21.

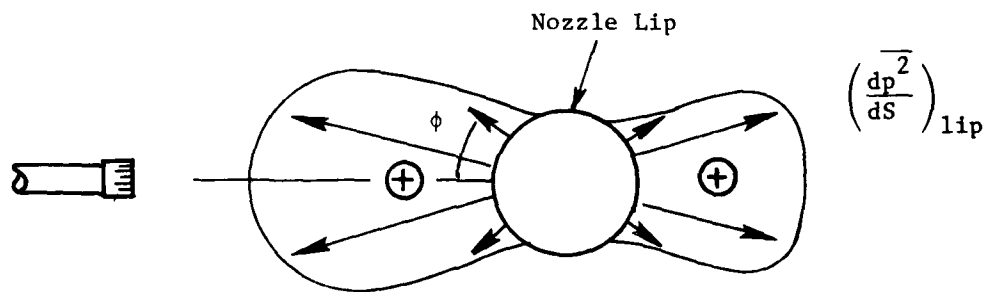


Figure 8-21. Source Strength Variation with ϕ .

The source strength is evidently concentrated in the region between $\pm 45^\circ$ on the near side, and between $\pm 135^\circ$ on the back side of the nozzle. The back-side source strength is about 60% of that for the near side. The correlation coefficient drops approximately 0.13 on the back side (from 0.17 for the near side). These observations suggest that convection, shielding, and/or refraction must somehow reduce the radiation efficiency of lip noise generated on the far side of the nozzle.

Source Strength Data for "Clean" Nozzles

Correlations were taken for the three axial positions nearest the exit plane and for $\phi = 0^\circ$, using the basic fiberglass cone and aluminum tip nozzle at $M = 0.52$. In order to detect any significant cross-correlation, the integrating time had to be tripled, relative to that for the autocorrelation functions. The maximum value of R_{psp} is about 0.008 on the near side of the nozzle. There is evidence of a slight source strength (slope) for position 1, but nothing significant is noted for positions further upstream. A periodic ripple occurs on the cross-correlation function with a dominant period of about 70 μs (frequency of 14 kHz). There is nothing particularly prominent on the acoustic spectrum however, at this frequency.

Tangential data were also taken for the "clean" nozzle case with ϕ varying from between 15° and 180° for axial location 1. The maximum correlation coefficient is somewhat higher on the back side (contrary to what one would expect), reaching a value of about 0.02 at $\phi = 180^\circ$. Here also, a noticeable negative slope at $\hat{\tau}$ indicated a definite source strength. In this case the characteristic period is about $150 \mu \text{ sec}$, for an indicated frequency of 6700 Hz.

The values of overall $\overline{p_s^2}$ within the nozzle are somewhat dependent on angular orientation of the tip nozzle (ϕ). This dependence is spatially repeatable, suggesting that a degree of nonaxisymmetric separation occurs inside the nozzle due to slight imperfections at the junction between the tip nozzle and contraction cone. If such separation occurs, the low frequency ripples in the cross-correlation functions are explainable (however, their acoustic radiation potential would have to be very weak). On the basis of the very small correlation coefficients detected with the unobstructed (optimum) nozzle, it is concluded that very little noise appears to come from the nozzle lips in this case, and that the transitional lip noise mechanisms discussed in Section 8.1.3 (Figures 8-4 and 8-5) are probably not operative (unless they are occurring above 100 kHz).

Estimates of Lip Noise Fractions

The overall intensity due to lip noise can be deduced by carrying out the surface integral in equation (380) evaluated at $\tau = 0$:

$$\overline{p_{lip}^2} = \frac{-1}{4\pi r_{a0}} \int_S \cos \phi \left[\frac{\partial}{\partial \tau} \overline{p_s p}(\tau) \right]_{\hat{\tau}} dS = \int_S \frac{d\overline{p^2}}{dS} dS \quad (396)$$

(Note that $\cos \phi = \cos \epsilon \sin \theta_j$, and also that $\partial/\partial \tau \overline{p_s p}(\tau)$ also varies approximately as $\cos \phi$ (see Figure 8-22).

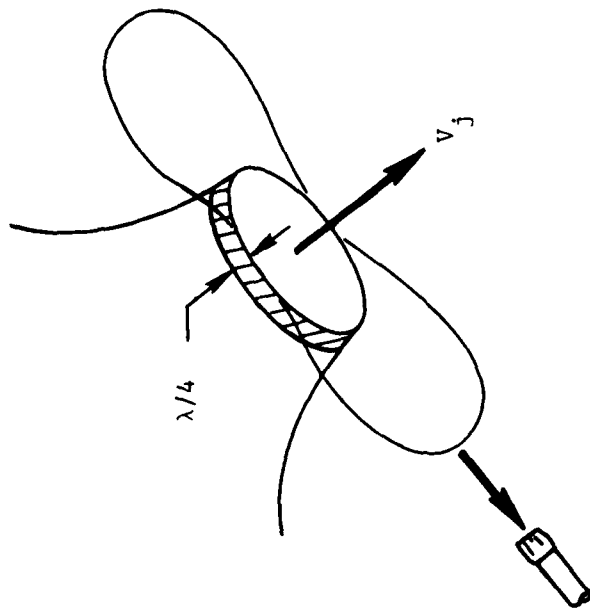
Thus,

$$\overline{p_{lip}^2} \approx \frac{-\sin \theta_j}{4\pi r_{a0}} \left[\frac{\partial}{\partial \tau} \overline{p_s p}(\tau) \right]_{\substack{\text{max} \\ \text{at } \phi=0}} \int_S \cos^2 \phi dS \quad (397)$$

$$\int_S \cos^2 \phi dS \approx \frac{D\lambda}{4} \times \frac{\pi}{2} \approx \frac{\pi D\lambda}{8}$$

Evaluation of equation (397) is expected to give an upper bound estimate of the lip noise intensity in any direction θ_j .

- These estimates are conservative upper limits.



669

$$\frac{\overline{p_{lip}^2}}{\overline{p_{total}^2}} \approx \frac{\left(\frac{dp^2}{ds} \right)_{\max} (\lambda/4) \int_0^{2\pi} \cos^2 \phi (D/2) d\phi}{\overline{p_{total}^2}}$$

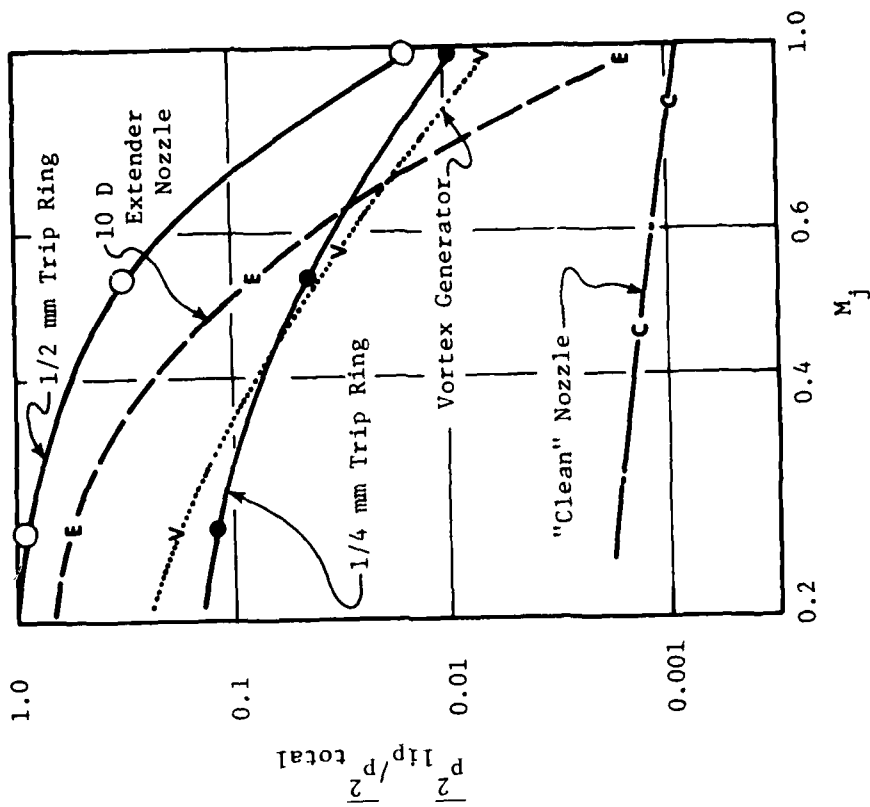


Figure 8-22. Estimates of Lip Noise Fractions.

$$\left. \frac{\overline{p_{lip}^2}}{\overline{p_{total}^2}} \right|_{\theta_j} = \frac{-\sin \theta_j}{4\pi r a_o \overline{p_{total}^2}} \left[\frac{\partial}{\partial \tau} C(\tau) \right]_{\max} p_s' p' \frac{\pi D \lambda}{8} \quad (398)$$

but $SPL \equiv 20 \log p/p_{ref}$

$$\therefore \left. \frac{\overline{p_{lip}^2}}{\overline{p_{total}^2}} \right|_{\theta_j} = \frac{-\lambda D \sin \theta_j}{32 r a_o} \times \text{Antilog} \left[\frac{SPL_{lip} - SPL_{total}}{20} \right] \times \left[\frac{\partial C}{\partial \tau} \right]_{\max} \quad (399)$$

If $\lambda = a_o T$ where T is a typical period of the causality correlation function then:

$$\left. \frac{\overline{p_{lip}^2}}{\overline{p_{total}^2}} \right|_{\theta_j} = \frac{-\sin \theta_j}{32} \left(\frac{D}{r} \right) \text{Antilog} \left[\frac{SPL_{lip} - SPL_{total}}{20} \right] \times T \left[\frac{\partial C}{\partial \tau} \right]_{\max} \quad (400)$$

If the lip noise fractions for various nozzle operating conditions are plotted, Figure 8-22 results.

At very low Mach numbers, $\overline{p_{total}^2}$ is almost entirely due to lip noise for cases of disturbed nozzle flow (i.e., the lip noise fraction tends to unity).

8.1.1.7 Conclusions

On the basis of the correlation experiments, it is suspected that the excess noise for an ideally contoured nozzle with laminar boundary layer is likely to be generated outside the nozzle, as a consequence of turbulence evolution from a laminar shear layer. The estimate for the "clean" nozzle case (Figure 8-22), predicts no more than 0.2% lip noise, as an upper limit.

However, in the presence of internal separation, or a turbulent boundary layer, genuine lip noise is indicated by the experiments, and may approach a substantial percentage of the total jet noise, especially for jet Mach number less than 0.5.

8.1.2 The Effect of External Flow

8.1.2.1 Background

The degree of jet noise contamination due to nozzle "lip" noise measured for an optimum contoured round model jet nozzle is presented in Section 8.1.1 as a function of Mach number for various conditions of nozzle flow. This section examines the possible effects of a slower shrouding stream on the radiated lip noise. If the shear layer instabilities are altered, the pressure fluctuations at the nozzle lip will be affected, and, therefore, the resultant acoustic radiation. If the effect of secondary flow is important, the following items are of interest:

- The forward-flight effect on the lip noise of a single round nozzle, and how it varies with flight speed.
- Changes in the mechanisms of lip noise and in their distribution plus the relative importance of each.
- The importance as a baseline mechanism of nozzle lip noise as the edge-length of a multielement nozzle is progressively increased.

8.1.2.2 Possible Noise Mechanisms with External Flow

In the case where flow velocities on either side of the surface are relatively equal (Figure 8-23), a row of countercirculating vortices develops from the narrow wake behind the lip (classical vortex street):

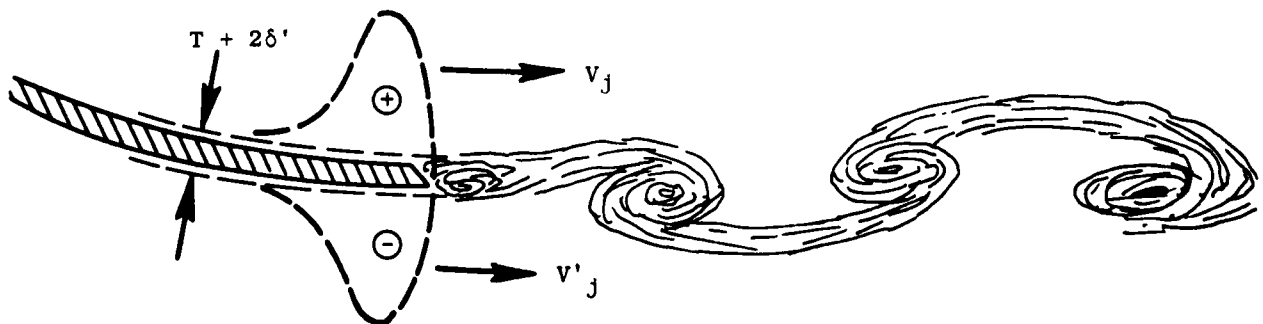


Figure 8-23. Vortex Shedding from Trailing Edge.

The abrupt change of boundary condition at the trailing edge provides a "hinge point". Here, the wake oscillates sinusoidally to form new vortices under the influence of their downstream predecessors. The Kutta condition is

not maintained at every instant, leading to a concentrated unsteady force fluctuation at the trailing edge of the nozzle.

At low Reynolds numbers (but > 40), the oscillation is very discrete and the accompanying force fluctuation is quite sinusoidal, at a frequency of:

$$f \approx 0.2 \frac{V_j}{t + 2\delta'} \quad (401)$$

Here, t is the lip thickness at the trailing edge and δ' is the displacement thickness of the approaching boundary layers. The spacing between the vortex cores is about $2.5(t + 2\delta')$. As the Reynolds number is increased, the shedding frequency becomes less discrete; the spectrum of the resulting force field is broadened and weakened substantially. This is because the parent shear layers become turbulent more quickly, so that the regularity of vortex birth is reduced. Nevertheless, the vortex-induced force field remains quasi-regular at the Strouhal frequency for Reynolds numbers as large as 100,000.

When the fluid streams on opposite sides of the lip are of dissimilar velocities, the vortex street is unbalanced; i.e., vortices induced by the rolling up of the shear layer on one side of the surface will be stronger than their counterparts from the opposite shear layers. There is not much information available on the consequences this may have on the regularity of shedding, nor on the magnitude of the force fluctuation at the lip. The imbalance of circulation may cause the wake to deflect laterally in its early stages, or perhaps to degenerate into a turbulent mixing layer quicker than usual. This should reduce the coherence and intensity of the lip pressure field and any consequent noise. However, there is little experimental information on this point. A better understanding of this problem would be extremely useful in assisting interpretation of the effects of forward flight, internozzle ventilation, and bypass flow on the performance of multi-element suppressor nozzles.

8.1.2.3 Experimental Technique

The causality correlation technique is used, where nozzle surface pressures are correlated with far-field sound pressures. In this test series, a two inch diameter primary nozzle with a standard STA contour was instrumented with 12 miniature Kulite transducers, located as shown in Figure 8-24. The placement of the far-field microphone array is also shown in this figure.

The test series was conducted at the General Electric Jet Engine Noise Test Site (JENOTS) where the 2-inch primary nozzle was mounted coaxially in the existing 12-inch diameter freejet nozzle (Reference 72).

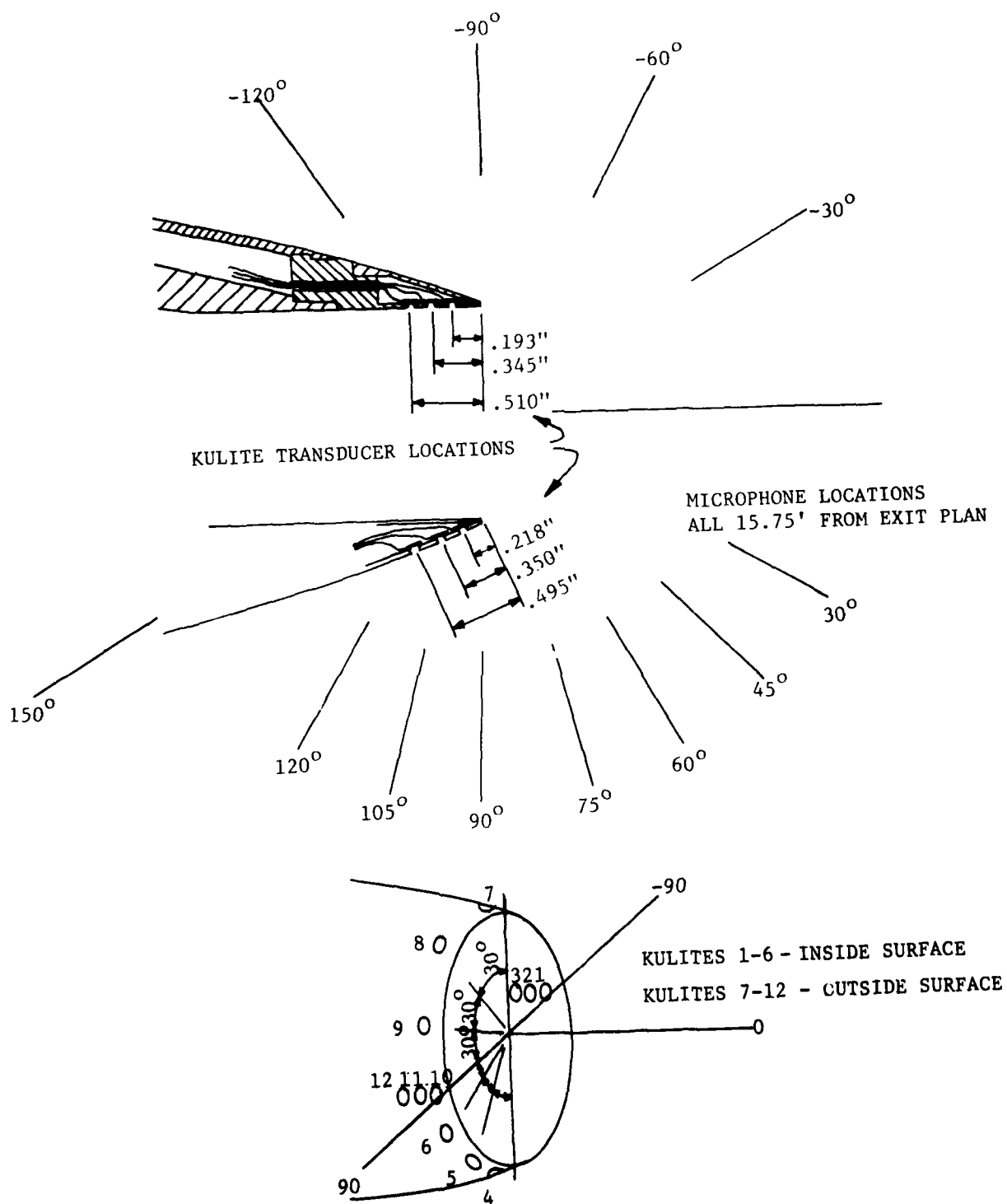


Figure 8-24. Nozzle Transducer and Far-Field Microphone Locations.

Both the primary and the external air streams were unheated. The following flow combinations were investigated:

Test Point	Primary Air Velocity, ft/sec	External Air Velocity, ft/sec
1	607	0
2	583	98
3	589	180
4	589	261
5	816	0
6	806	90
7	805	193
8	811	276
9	1019	0
10	1008	124
11	1012	183
12	1015	297
13	374	307

Each data set was recorded simultaneously on a 28-channel FM Honeywell tape recorder with frequency response conforming to IRIG standards for Wide Band Type I (0 to 40 kHz at 60 ips). Data tapes were substantially played back using a compatible Honeywell tape recorder to signal processing instrumentation.

8.1.2.4 Results/Far-Field Spectra

The radiated noise spectra for each test point at the +90° field microphone have been superimposed in Figure 8-25 to show differences more clearly. At test points which do not include external airflow (test points 1, 5, and 9) the resulting spectrum shape is relatively smooth, and typical for "clean" jet noise. The "ripples" at low frequencies result from ground plane reflections for most of the remaining test conditions, however, the spectra show a strong peaking tendency near 150 Hz and 2000 Hz. This excess noise is thought to be due to an extremely noisy, choked valve in the external air supply system. Since this noise rises above the legitimate jet noise, particularly at low primary velocities (i.e., 500 and 808 ft/sec) the valve noise dominates the overall RMS sound pressures at the field microphones. Thus, the normalized correlation coefficients between nozzle surface pressures and the sound pressure fluctuations at the field microphones could be affected, significantly and adversely. If there is coherent valve noise propagating through the system with frequency content in the vicinity of 2000 Hz, it could mask any legitimate lip noise correlation.

The degree of "valve noise" contamination can be appreciated if the OASPL at 90° is plotted as a function of velocity ratio and compared with a similar uncontaminated case. This has been done in Figure 8-26, for each of

SOUND PRESSURE LEVEL AT +90° FIELD MICROPHONE
(DB RE .0002 DYNES/CM²)

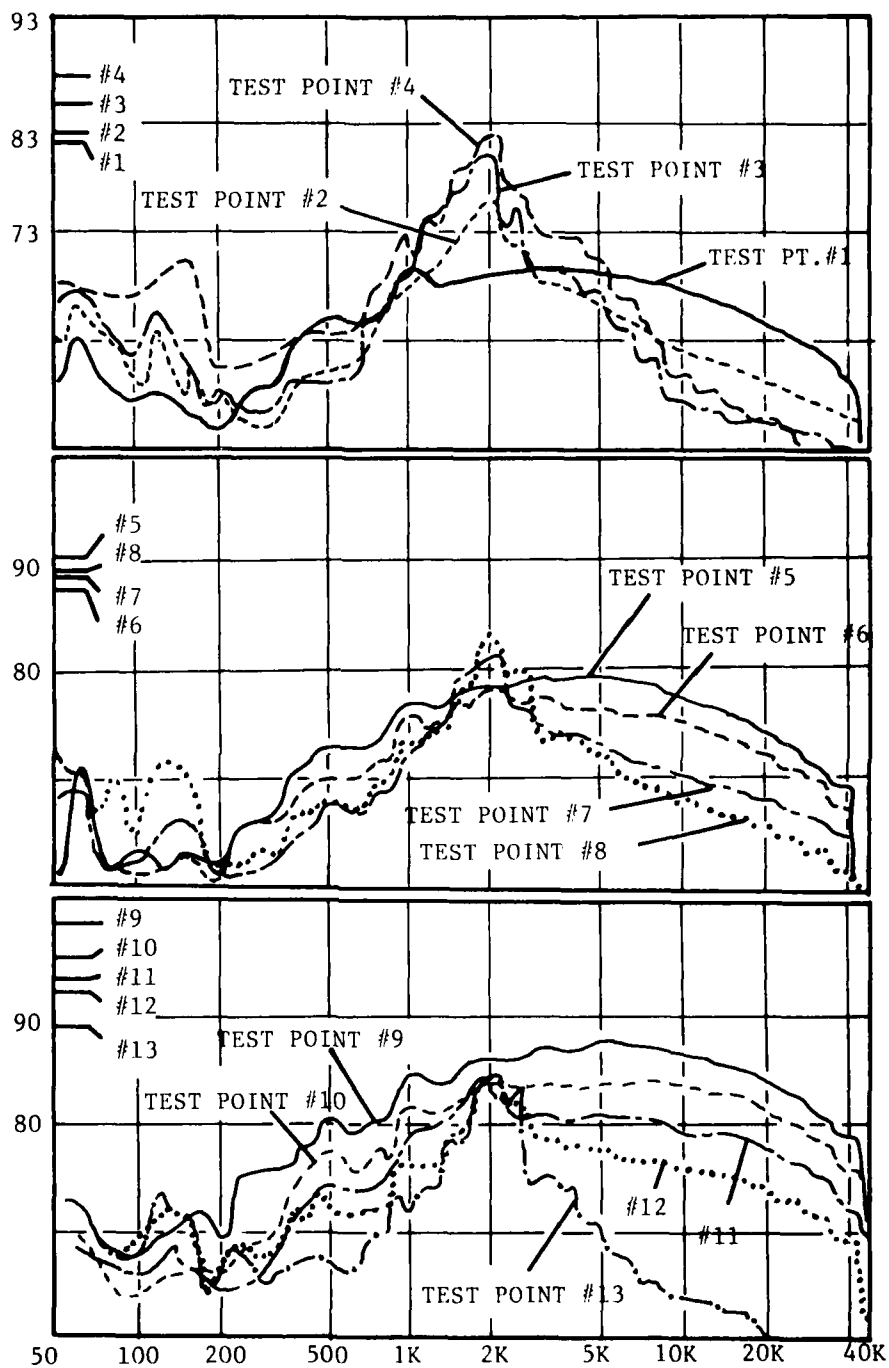


Figure 8-25. Far-Field 1/3 Octave Spectra at each Test Point.

OASPL AT +90° FIELD MICROPHONE (..RE .0002 DYNES/CM²)

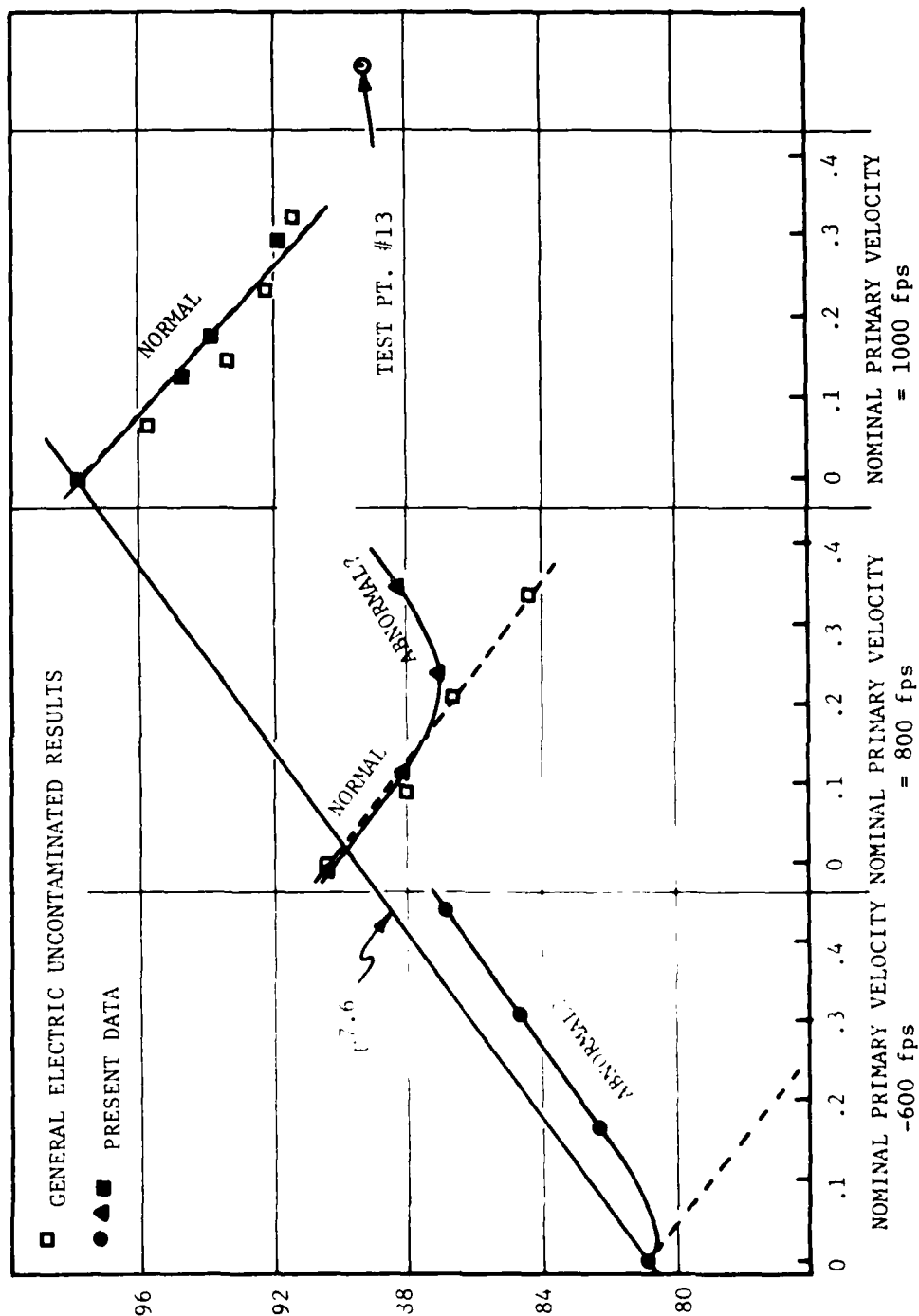


Figure 8-26. OASPL at 90° Field Microphone Versus Velocity Ratio.

the three primary velocities tested. The present data are compared to results for identically sized primary and secondary nozzles recorded at JENOTS and which are apparently free of valve noise. As the velocity ratio is increased, the shear is reduced and the OASPL is reduced. The valve noise effect however, boosts the OASPL as secondary flow increases, thereby causing errors as large as 10 to 15 dB. This appears to be especially severe at the lower primary velocities.

At test point 13, the primary and secondary velocities are almost equal. As the shrouding velocity approaches the primary velocity, the effectiveness of the shrouding flow in reducing shear generated noise is gradually overshadowed by the basic noise of the larger (12-inch diameter) shrouding jet. A 12-inch diameter jet produces a sound pressure level at least 15 dB higher than a 2-inch diameter jet, for the same nozzle velocity. Nevertheless for test point 13 the combined level should be about 73 dB, not 89 dB as indicated on Figure 8-26.

One might speculate that the 2000 Hz energy is being produced due to regular vortex shedding at the nozzle lip. For test point 13, however, the Strouhal frequency could not be much less than 40 kHz. Furthermore, the frequency of vortex shedding noise should be highly dependent on the primary jet velocity. The data of Figure 8-25 show no evidence of such behavior.

8.1.2.5 Results - Nozzle Surface Correlation Measurements

Axial Direction - Figure 8-27 shows cross correlations between two Kulite transducers on the outside surface of the nozzle for three different external flow velocities. At the lowest external flow, the 2 kHz valve noise gives a definite ripple to the correlation function. At higher flows, a shifted correlation peak is observed which is equivalent to a convection speed of about $0.8 V_j$. Typical time scales can be estimated from the autocorrelation functions at the bottom of Figure 8-27. In turn, length scales can be estimated from the product of convection speed and typical time scale. Results for the external flow velocity of 261 ft/sec indicate an axial length scale of about 0.13 inch (surprisingly, the length scale appears to get smaller as the external velocity diminishes).

The pressure field on the inside surface of the nozzle is correlated over very small axial lengths in Figure 8-28. The dominant time scale taken from autocorrelations is governed by extremely high frequency energy resulting in time scales of about 10 μ s. Typical convection speeds tend to be slower than in the external flow, ranging between $0.5U$ and $0.8U_1$. Length scales are less than 0.050 inch. The peculiar double-humped shape of the correlation at highest primary velocity is probably also present for the other flow cases at negative time delay. It suggests that the boundary layer inside the nozzle is so quiet that acoustic disturbances traveling upstream in the shear layer can produce an additional, superimposed correlation which is as significant as the correlation due to downstream-traveling disturbances in the boundary layer.

* Kulite No. 10 and 11 are separated only by 0.132 inch (see Figure 8-24).

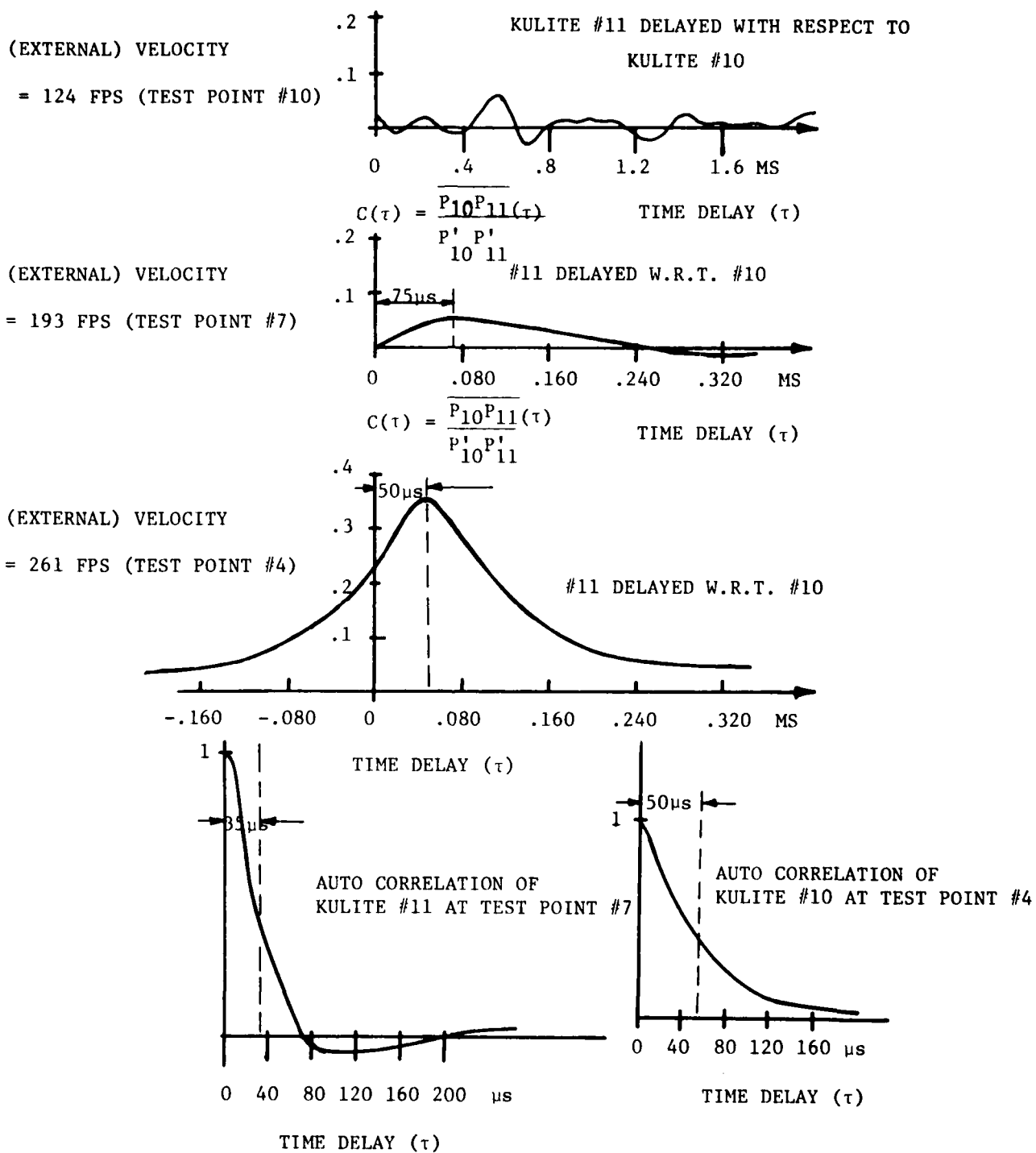
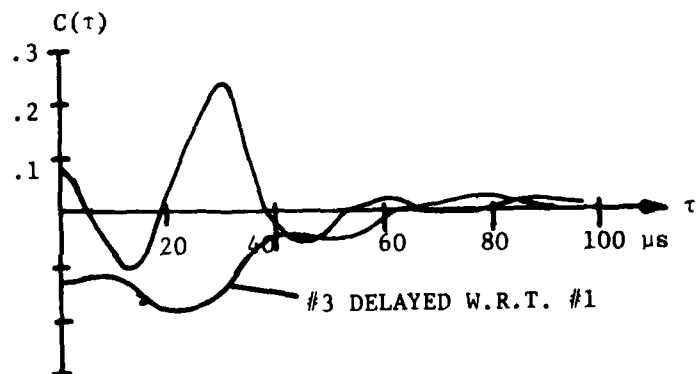
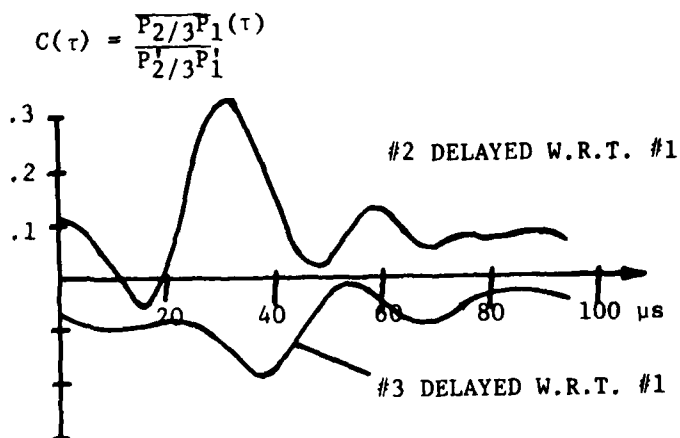


Figure 8-27. Nozzle Correlation Functions on Outside Surface.

PRIMARY VELOCITY =
589 FPS (TEST POINT #4)



PRIMARY VELOCITY = 1008 FPS
(TEST POINT #10)

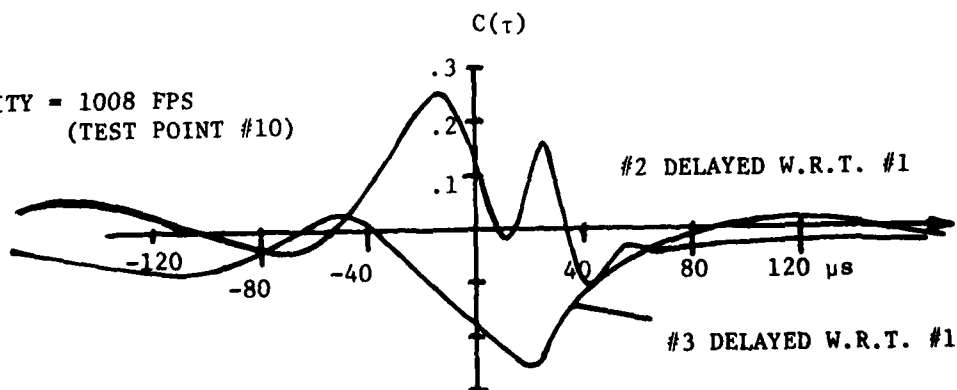


Figure 8-28. Nozzle Correlation Functions, Inside Surface.

Tangential Direction - Figure 8-29 shows the degree of tangential coherence on the inside surface of the nozzle. The correlations are slightly larger for faster flow, but the effective tangential correlation scales are still less than 10° in tangential extent.

The tangential correlations are stronger on the outside surface of the nozzle, with an integral tangential scale extending about 15° (see Figure 8-30).

8.1.2.6 Results - Causality Correlations

The attempted correlations of Kulite (source) signals with microphone (far-field) signals, with appropriate time delay, show no significant correlation between suspected genuine sources of lip noise and the far-field microphone for all cases tested. For cases with external flow, correlations between the outside surface transducers and far-field microphones appeared to be dominated by valve noise at 150 Hz and 2200 Hz, as Figure 8-31 indicates. Upstream disturbances, such as valve noise, appear to propagate down the air supply piping and are sensed by the Kulite transducers as they pass by. At the acoustic time delay between the Kulites and the far-field microphones, correlation occurs. The valve noise (a legitimate excess noise source) appears to be emanating from the exit plane region.

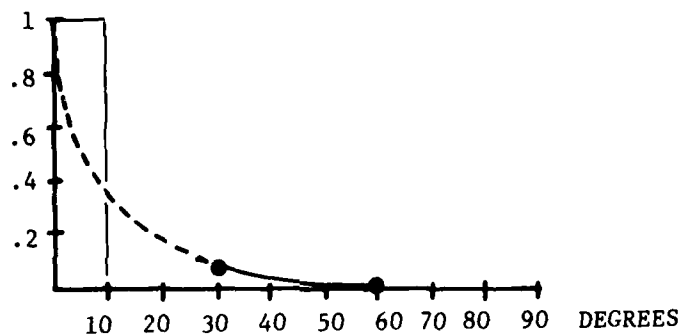
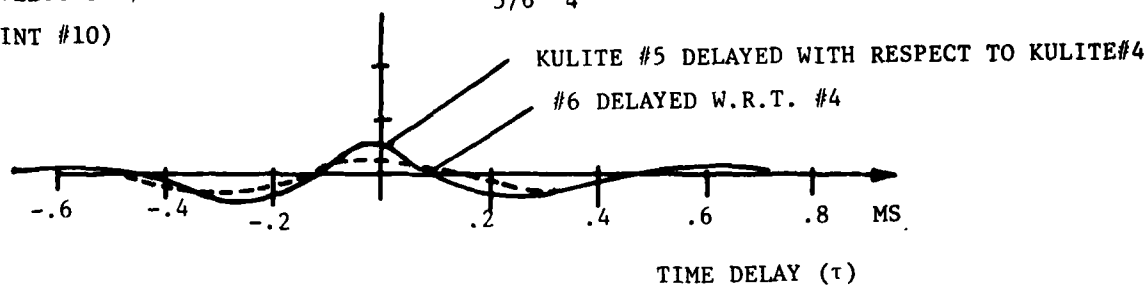
8.1.2.7 Conclusions

The precise effect of external flow on generation of lip noise is not clear due to the valve noise contamination, but the following can be stated:

- The turbulent pressure field on the exterior nozzle surface near the exit plane is much less affected by the external flow. This may be because the axial length scales are smaller inside the nozzle, so that the pressure taps do not record significant disturbance events arising from external flow effects.
- It appears unlikely that sources on the nozzle surface of a smoothly contoured jet constitute an important noise source. This is especially true on the interior of a properly contoured nozzle, where the boundary layer exhibits very low levels of pressure fluctuation ($<0.3\%$ of the jet dynamic pressure).

PRIMARY VELOCITY = 1008 FPS
(TEST POINT #10)

$$C(\tau) = \frac{\overline{P_{5/6} P_4}(\tau)}{\overline{P_{5/6}'} \overline{P_4}'}$$



PRIMARY VELOCITY = 589 FPS
(TEST POINT #4)

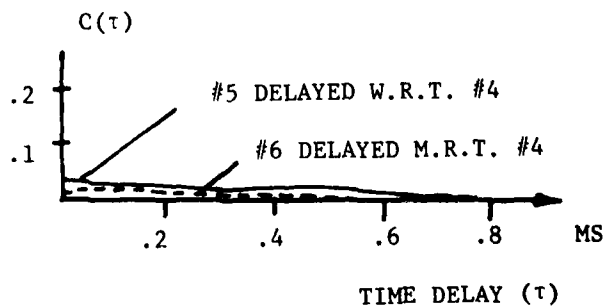


Figure 8-29. Tangential Correlation - Inside Surface.

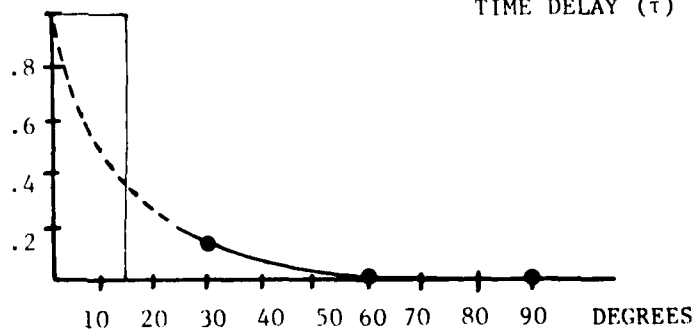
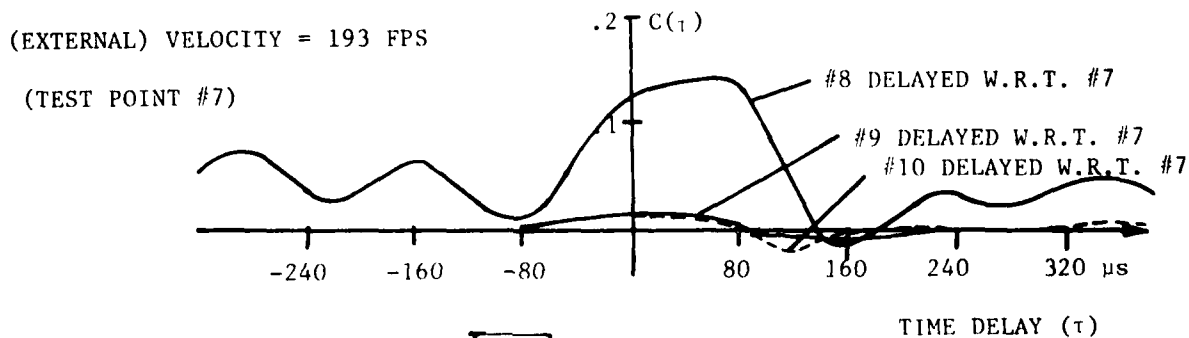
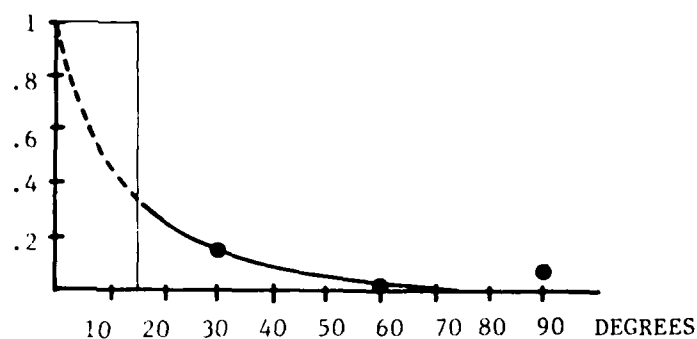
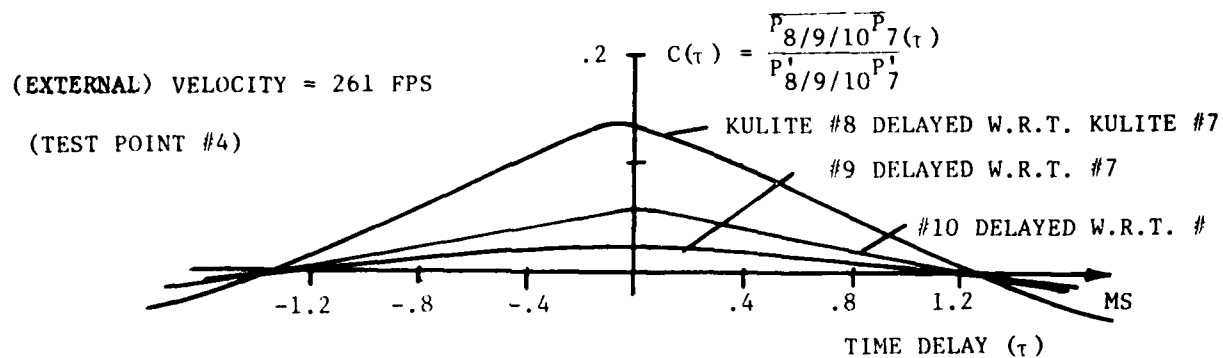
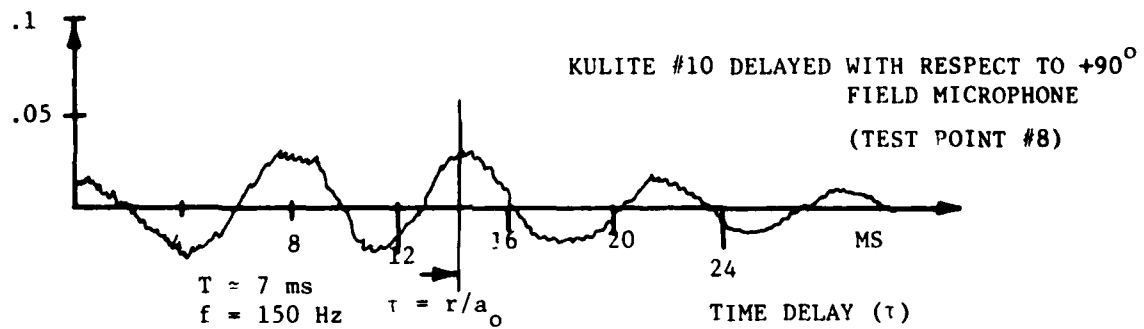
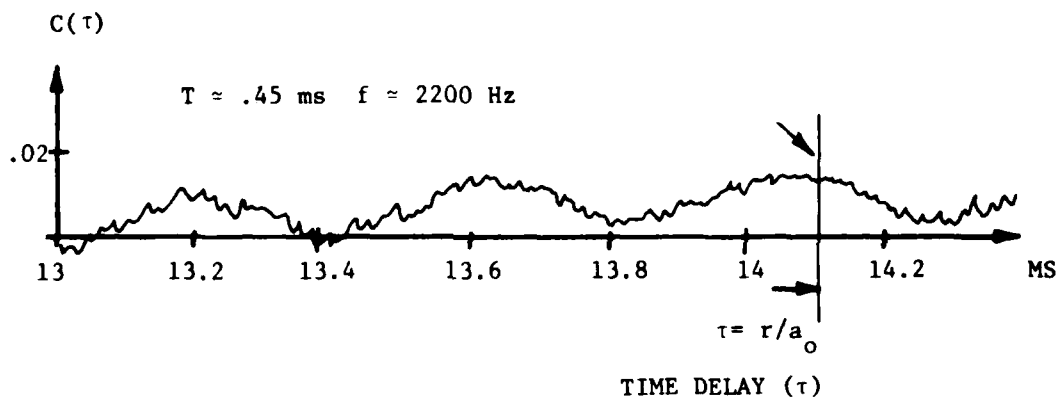


Figure 8-30. Tangential Correlation - Outside Surface.

$$C(\tau) = \frac{\overline{P_{\#10} P_{90^\circ}(\tau)}}{\overline{P_{\#10} P_{90^\circ}}}$$



VALVE NOISE!



$$C(\tau) = \frac{\overline{P_{\#1} P_{90^\circ}(\tau)}}{\overline{P_{\#1} P_{90^\circ}}}$$

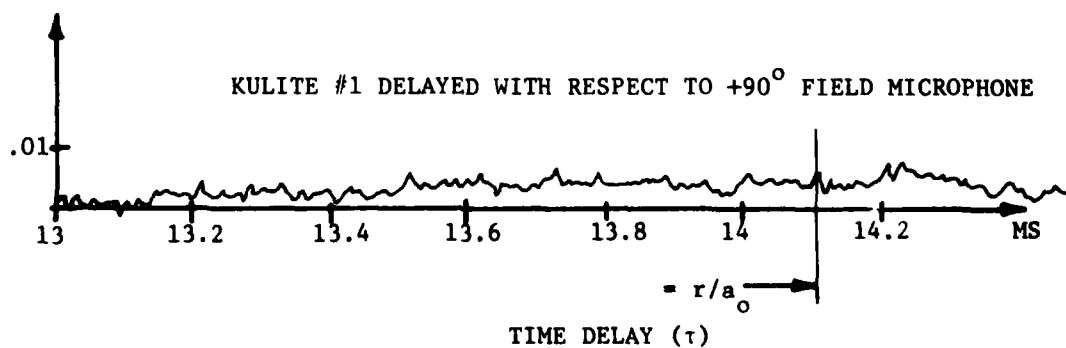


Figure 8-31. Typical Causality Correlations.

8.2 PARTICLE/FLUID INJECTION

A comprehensive literature survey of the physical mechanisms and practical implications of the possibilities of suppressing jet noise by the addition of solid particles, liquid droplets, and foam was carried out. The three most pertinent literature sources are references 120, 121, and 122.

8.2.1 Physical Mechanisms of Damping

Attenuation of sound occurs for a solid particle additive because the velocity of the solid particle "lags" behind the gas velocity (leading to an effective drag force exerted by the particles on the gas) and because the temperature of the particle lags behind the gas temperature.

An attenuation per unit wavelength is obtained due to these two mechanisms which peaks at a frequency of $f_V = 3\sigma \mu/m$ for the velocity lag mechanism and at a frequency $f_T = 2\sigma k/m c_s$ for the temperature lag mechanism; where σ = particle radius, μ = coefficient of viscosity of gas, m = mass of individual solid particle, k = coefficient of thermal conductivity of gas, and c_s = specific heat of solid particle. The peak value of attenuation/unit wavelength for the velocity mechanism is $(\pi/2)\kappa$, and the peak value for the temperature lag mechanism is $(\pi/2)(\gamma - 1)\kappa c_s/c_p$; where κ = ratio of density of particulate phase/gas phase, γ = specific heat ratio of gas phase, and c_p = specific heat at constant pressure of gas phase. The variation with frequency of the attenuation/unit wavelength is given by $2(f/f_V)[1 + (f/f_V)^2]^{-1}$ and $2(f/f_V)[1 + (f/f_T)^2]^{-1}$ times the peak values, respectively, for the two mechanisms. The above results assume the validity of Stokes law for the drag exerted by the particles on the gas and associated Nusselt's numbers of unity for the heat transfer between the gas and particulate phase (which should be quite reasonable for small particle sizes and the acoustic damping problem). For the acoustic damping problem, the relevant velocity on which to calculate a relevant Reynolds number is the acoustic particle velocity, the relevant length scale is the particle radius, and hence the relevant Reynolds number is small enough to justify the use of Stokes drag law and Nusselt's numbers of unity.

The above two mechanisms are operative for liquid droplets capable of phase change, but in addition, a low frequency attenuation peaked at a frequency $k_l f_T$ appears, where k_l = liquid mass fraction. It is essential for the liquid droplets to be able to retain their integrity as liquid droplets in order for this mechanism to be operative.

Attenuation by foams was studied and reported in Reference 122. Foams are basically an agglomeration of gas bubbles separated from each other by thin liquid films. They can provide high frequency (on the order of 5 to 6 kHz) absorption at the resonant frequency of oscillation of the gas bubble, but again, require a gas temperature low enough to avoid evaporation of the liquid films to be effective.

8.2.2 Practical Implications

There do not appear to be any promising, practically useful techniques for reducing heated jet noise by the use of foam or particle additives (either by solid particles or by liquid droplets). Solid particles or foam yield some attenuation in the kHz range which is not of interest for jet noise. Foam will not retain its integrity in a hot flow, being basically a collection of gas bubbles separated by thin liquid films. A promising technique for low frequency (i.e., audio frequencies) noise suppression in cold gas flows, such as occur in jet engine inlets or in the fan, is the use of liquid droplet addition. The storage requirements of liquid appear prohibitively large, however. For example, the authors calculate that to suppress fan noise from a three-engine DC-10 to achieve 5 dB/m suppression (roughly what acoustic treatment yields currently) during a two minute takeoff maneuver, something like 3000 kg of water would have to be carried aboard. Of course with a hot jet flow, the droplets would vaporize instantly, negating all three mechanisms of attenuation cited previously.

8.3 ORDERLY STRUCTURE

Certain studies have suggested that in jet flows, the unsteadiness, which is normally termed "turbulence" and hence considered a random, disorganized process, may be characterized by a hitherto unsuspected degree of coherence and order. Generally, experimental evidence of such order has been confined to rather low Reynolds number cold jets. The basic nature of this jet noise program dictated an effort, primarily experimental in nature, which was formulated and conducted under the direction of Dr. J. Laufer at the University of Southern California (USC).

The present investigation examines two aspects that may permit the jet noise suppressor designer to attain lower noise levels, (1) mixing enhancement, and (2) redirection of the radiation pattern. The first item can be obtained by choice of an appropriate nozzle configuration (e.g. mechanical suppressor) or by introducing certain types of perturbations into the flow that will change the turbulence level and/or mean velocity distribution at the nozzle end. The main idea motivating the second item is an attempt to minimize the noise radiated in certain azimuthal directions by using asymmetric nozzle shapes. In formulating the experimental program, it is of great advantage to make observations of both the jet flow itself and its noise field. The choice of visual technique (flow field study) and microphone setup (far-field noise) proved to be a fortunate one, since a number of conclusions could not have been arrived at without this procedure.

In particular, one is interested to know whether or not the vortex pairing process, clearly in evidence from visual studies, has an important bearing on the radiation process. The results contained herein cannot give a conclusive answer, although one can make certain conjectures on the basis of the near and far field observations that indicate such a connection is possible.

8.3.1 Facilities and Equipment

8.3.1.1 Anechoic Chamber

A detailed description of the USC Anechoic Facility can be found in the Task 1 Final Report (Reference 123). Figure 8-32 shows a schematic drawing of the layout of the facility. Figure 8-33 is a schematic of the stilling (plenum) section and nozzle.

8.3.1.2 Water Jet Apparatus

The water jet consisted of a stilling chamber and detachable nozzle (Figure 8-34). The axisymmetric nozzle has a contraction ratio of 16:1 and an exit diameter of 1.5 inches. Jet exit velocities ranged from about 5 inch/sec to 15 inch/sec; the corresponding jet Reynolds numbers were 5,000-15,000. The thickness of the laminar shear layer, δ , at about 1 cm downstream from the nozzle exit was,

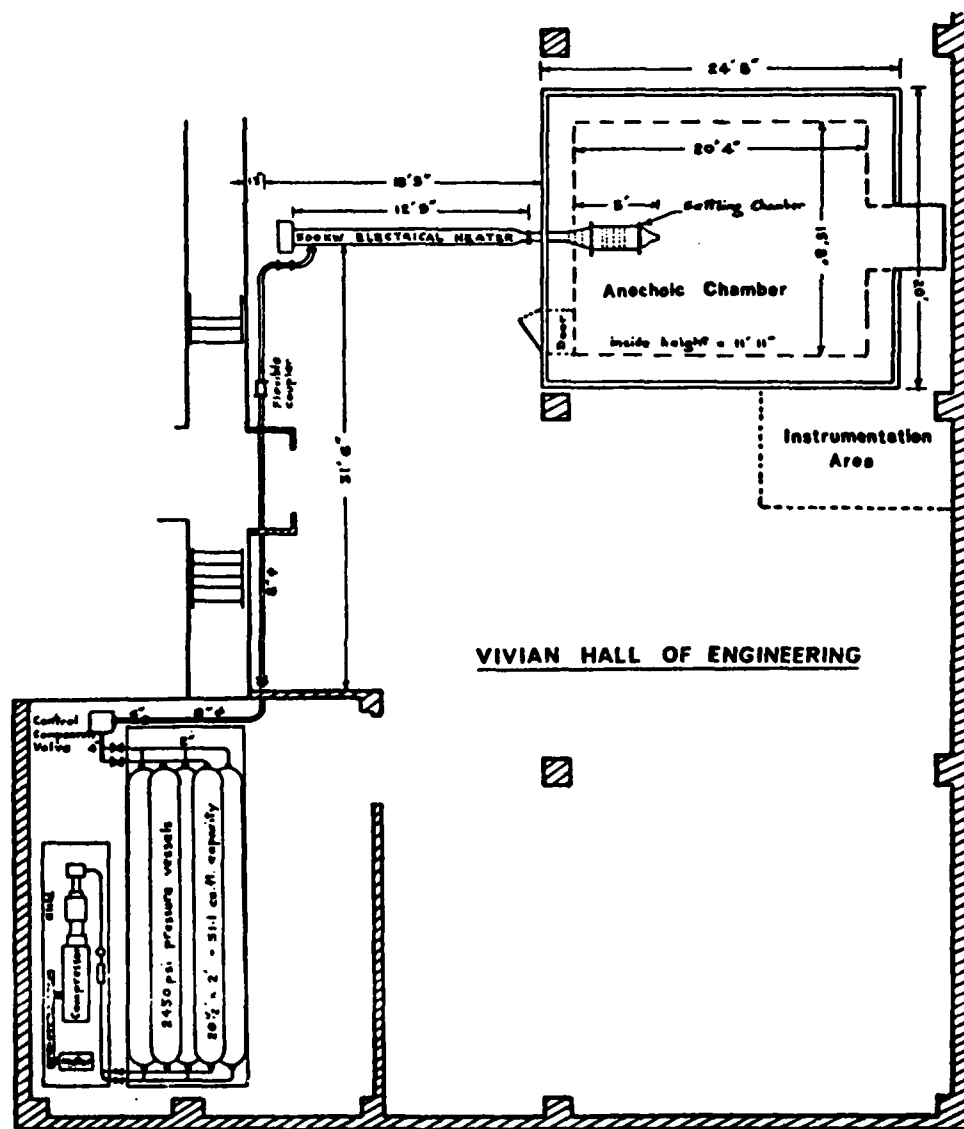


Figure 8-32. Jet Noise Research Facility at USC.

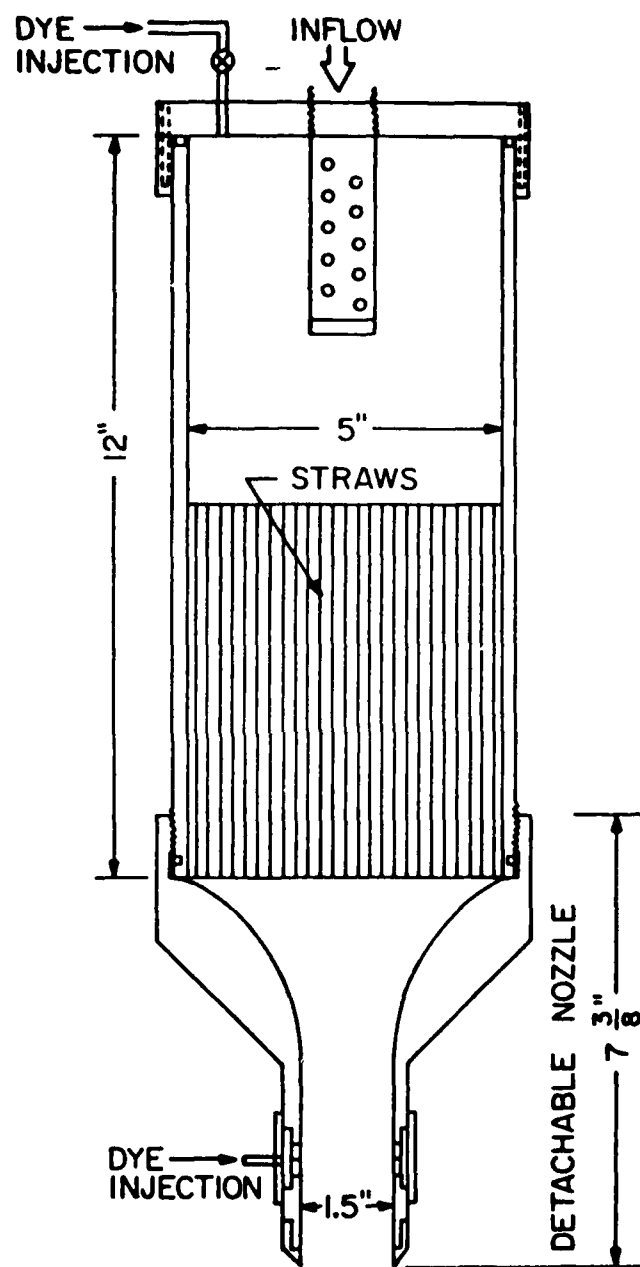


Figure 8-34. Water Jet Stilling Chamber and Nozzle.

$$\delta/D \approx 4\sqrt{Re}$$

The coefficient 4 was determined by measuring the frequency of the initial unstable wave, and utilizing the theory of Michalke(124) to determine the shear layer thickness. This value agrees with direct visual observations (hydrogen bubble traces), and is consistent with the value found by Crow and Champagne(125). The turbulence level was measured on the jet centerline just upstream of the nozzle exit with a hot-film anemometer. The rms longitudinal fluctuation was about $0.005 U_j$, at a jet speed of 5 inch/sec, and was somewhat lower at higher jet speeds. A schematic of the entire jet apparatus is shown in Figure 8-35. In operation, the jet is immersed vertically in a large tank. Flow rate through the jet is monitored by a Fischer-Porter flow meter. The jet is supplied by gravity feed from a second tank overhead. The supply tank is fitted with an overflow tube and a pumped return from a lower sump to maintain constant supply head. When desired, artificial disturbances could be introduced by periodically constricting the jet supply tube. This was done in a controlled manner to produce rms fluctuations in velocity of between 2.5 and 3.5 percent of the mean jet exit velocity over a wide range of forcing frequencies.

8.3.1.3 Nozzle Configurations

In addition to a single axisymmetric nozzle, a number of other configurations were used in both the air and water facilities.

An elliptic nozzle with a 5 to 1 aspect ratio is shown in Figure 8-36. It was fabricated with molding plastic and could be attached to the settling chamber of the air as well as the water facility. It was designed to have, essentially, a constant cross-sectional area along the downstream half of its length and equal to a 1.0-inch diameter circular jet.

The contours of the 1/2-inch diameter nozzle and the 1/2-inch diameter, 2-foot long pipe nozzle are shown in Figures 8-37 and 8-38. They were used in the air jet facility. In order to generate a rough pipe flow, the first half of the pipe nozzle inner wall was lined with coarse sandpaper.

In addition to the elliptic nozzle, the water jet facility utilized the following configurations: a 1.5-inch diameter axisymmetric nozzle into which a trip ring could be inserted to thicken the initial mixing layer, a single axisymmetric jet with exit plane inclined 45° to the jet axis and a 7-tube, hexagonally packed array of jets with 2 diameter spacing between jet axes (Figure 8-39).

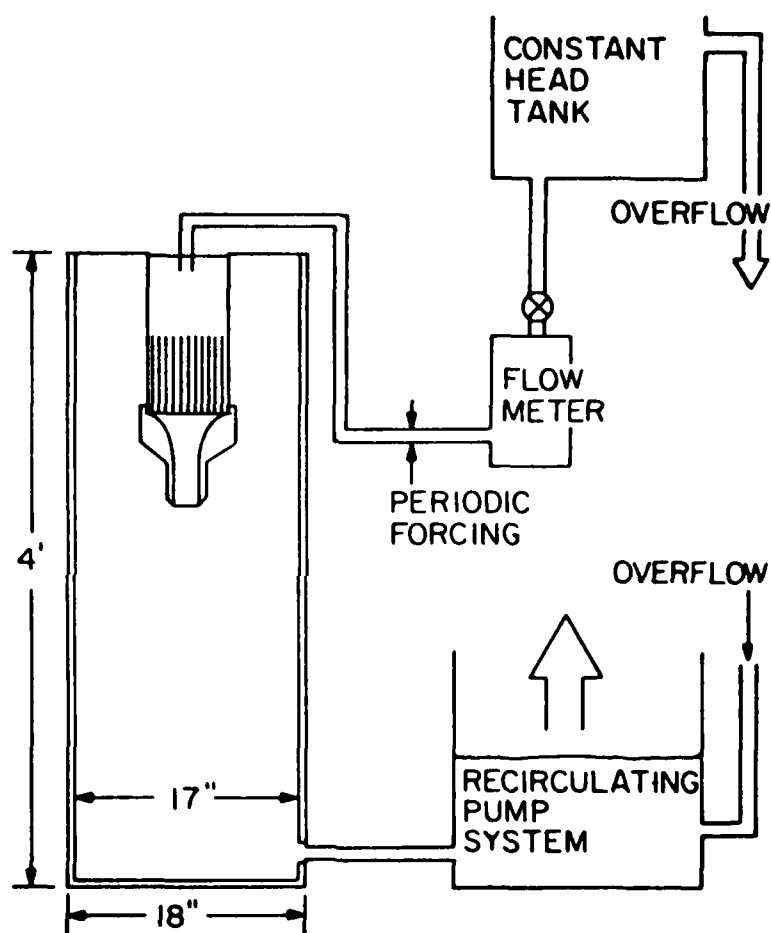


Figure 8-35. Schematic of Water Jet Apparatus.

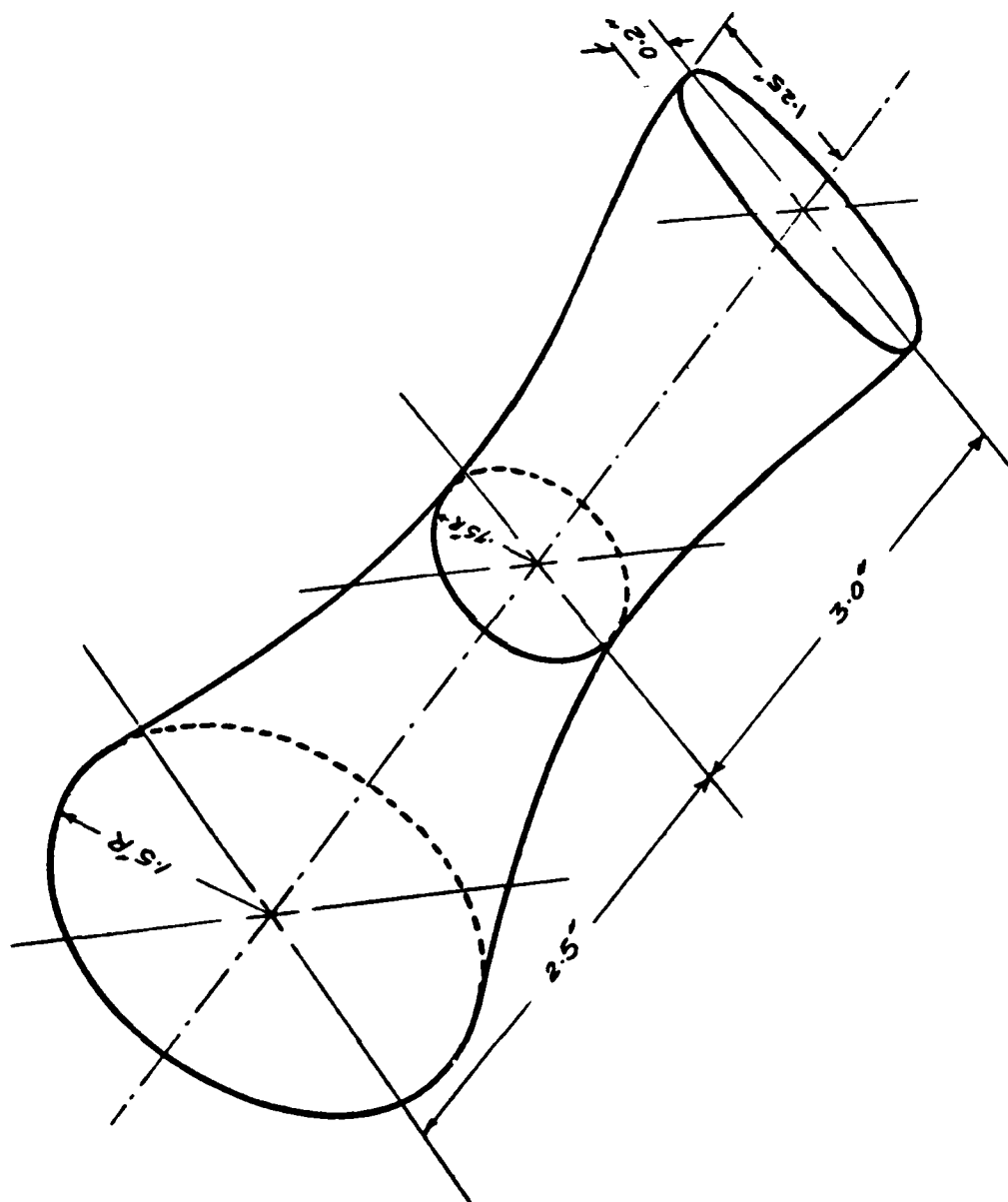


Figure 8-36. Schematic Drawing of Elliptical Nozzle.

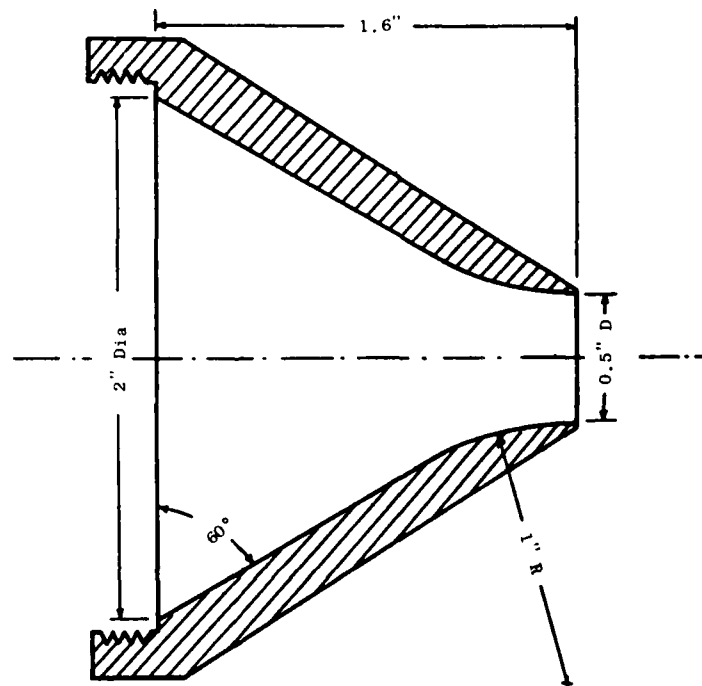
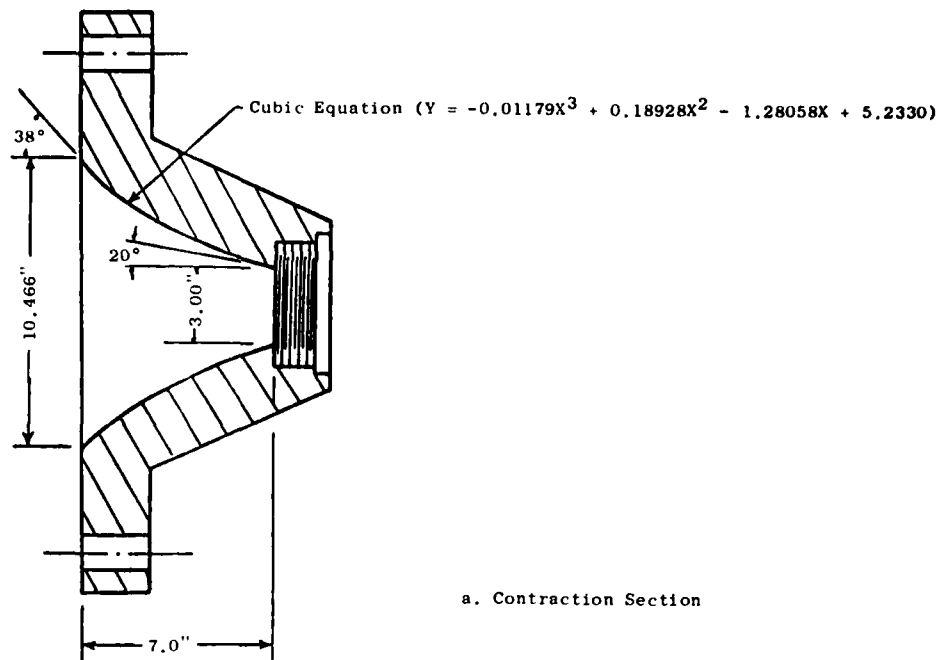


Figure 8-37. Schematic Diagram Showing Contraction Section and Contour of 1/2 inch Diameter Nozzle.

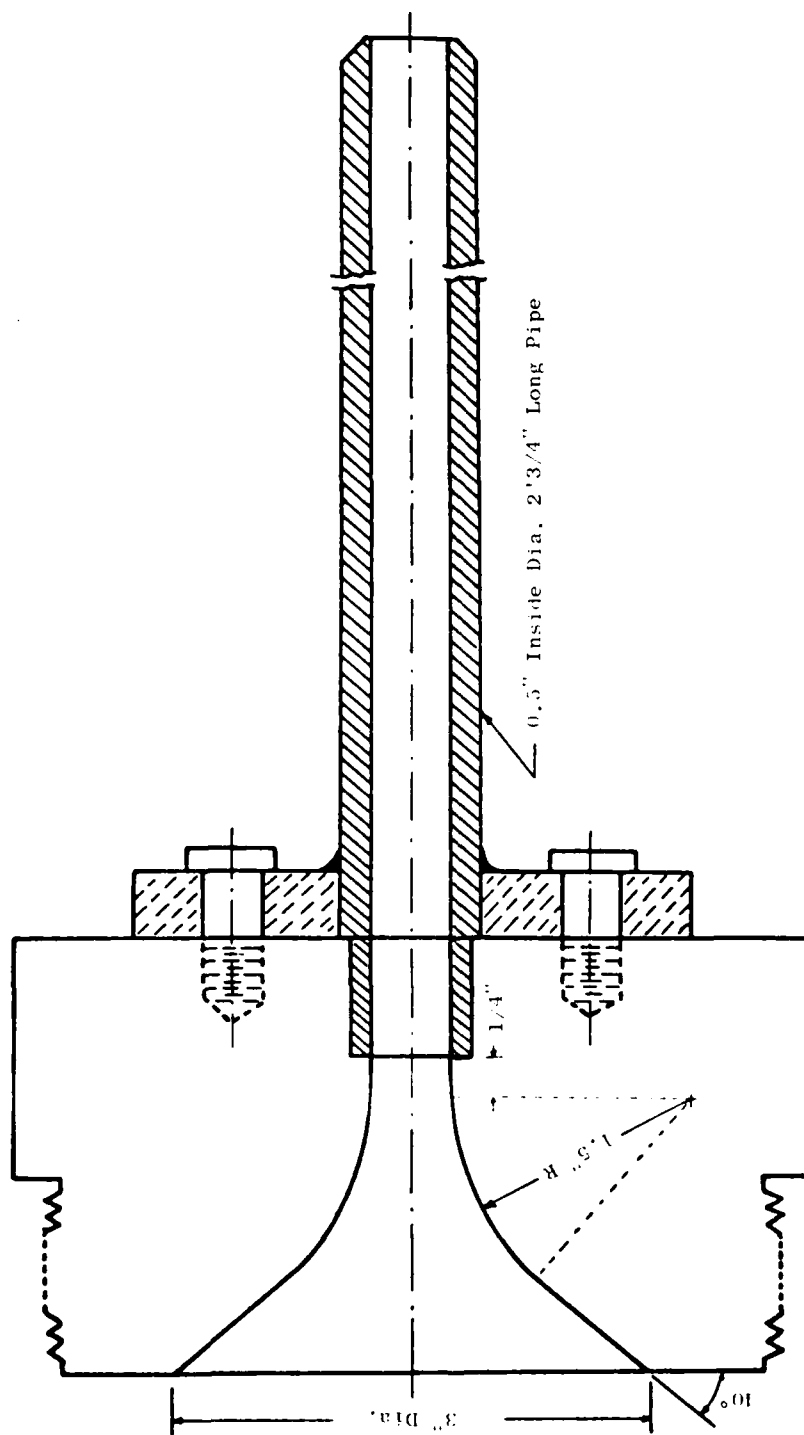


Figure 8-38. Schematic Diagram of 1/2 inch Diameter 2 foot Long Pipe Arrangement.

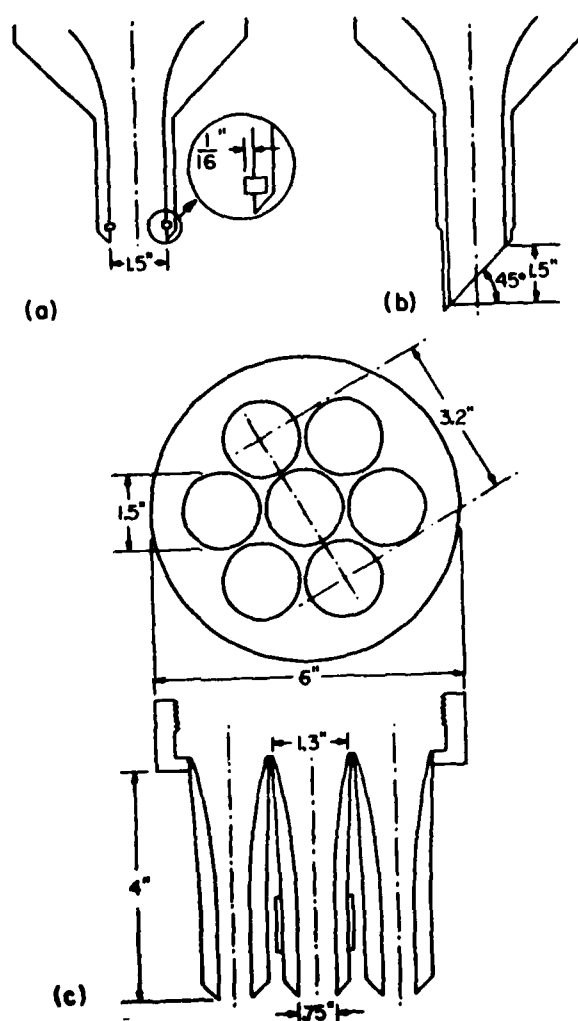


Figure 8-39. Various Nozzle Configurations Used in the Water Jet.

- (a) Axisymmetric Nozzle with Trip Ring
- (b) Axisymmetric Nozzle with Inclined Exit Plane
- (c) Seven-Nozzle Hexagonally Packed Array

8.3.2 Experimental Procedure

8.3.2.1 Far-Field Intensity Measurements

Acoustic far-field measurements were performed in the USC anechoic chamber. Ten B & K microphones were mounted at a distance of 90-inches from the nozzle exit on a curved pipe forming an arc centered at the nozzle exit, as shown in Figure 8-40. These microphones were arranged at different angles from the inlet axis (θ_I) as depicted in Figure 8-41. A mixture of 1/2, 1/4, and 1/8-inch microphones were used depending on the noise intensities at different angles. These were carefully noted so that proper free field corrections for the different microphones used could be incorporated in the data analysis.

During each run, the room temperature, pressure, and humidity were recorded to give detailed information of the environment under which the data was taken. In addition, the settling chamber pressure and temperature were recorded on the strip-chart recorder for jet exit condition calculations. For the long pipe flow cases, the jet exit conditions were calculated from pitot tube measurements at the center of the pipe exit. The settling chamber pressure was maintained to within $\pm 3\%$ of the operating pressure. The microphone signals were recorded on the 14-track Hewlett-Packard tape recorder. Before the measurements were made, sinusoidal signals at a number of selected frequencies were recorded on tape first for obtaining the frequency response of the recorder. After each run, the microphones were calibrated with the B & K 4220 piston phone, and the background noise (both acoustic and electronic) was also recorded on tape with the jet turned off, with the same gain setting of all instruments to ensure that for each case the data obtained for jet noise are not influenced by the background noise.

The far-field noise data reduction was carried out using a General Radio 1921 Real-Time Analyzer to give 1/3-octave spectra. By means of a tape speed reduction of 4, the frequency range covered was from 160 Hz to 80 kHz.

8.3.2.2 Directional Microphone Measurements

Axial source strength distributions along the jet axis have been taken for the 1/2-inch nozzle, the 2-foot long smooth pipe and the 2-foot long rough pipe cases using the reflector type directional microphone system described in Reference 125 and schematically illustrated on Figure 8-42. The reflector was located at the nozzle or pipe exit plane at a distance of 81-1/2-inches from the jet axis. The reflector was rotated by an automatic controller to scan along the jet axis. There were 64 scanning points along the jet axis starting from about 10 diameters upstream of the jet exit plane to some 40 diameters downstream. At each aiming point, about 6 seconds of data were recorded on magnetic tape. In addition a voltage from the automatic controller, which is proportional to the tangent of the complementary angle between the jet axis and the reflector axis, was also recorded for subsequent determination of the aiming position. Using this voltage, it was found that the aiming position could be determined to within 1/8 inch.



Figure 8-40. Interior of USC Anechoic Chamber.

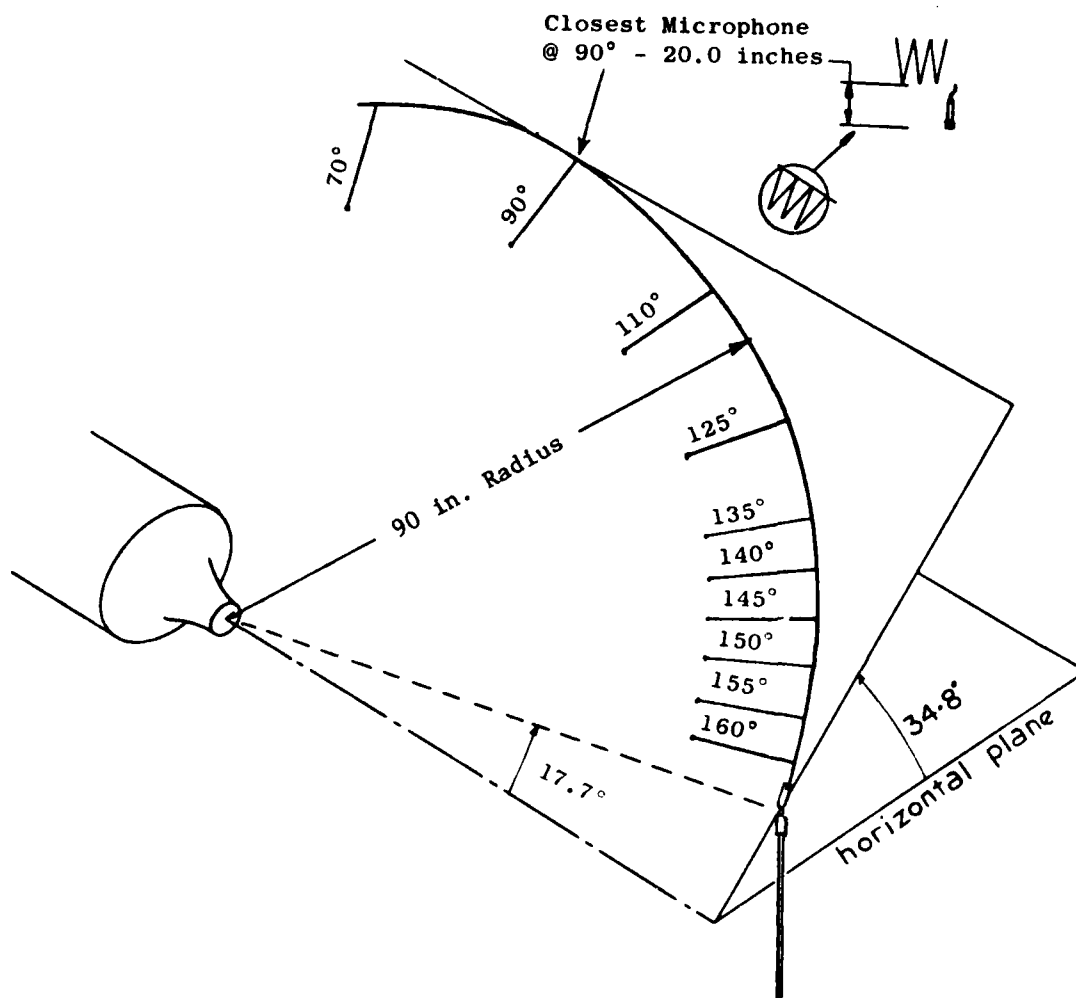


Figure 8-41. Schematic Diagram Showing Arrangement of Microphones for Far-Field Measurements at USC.

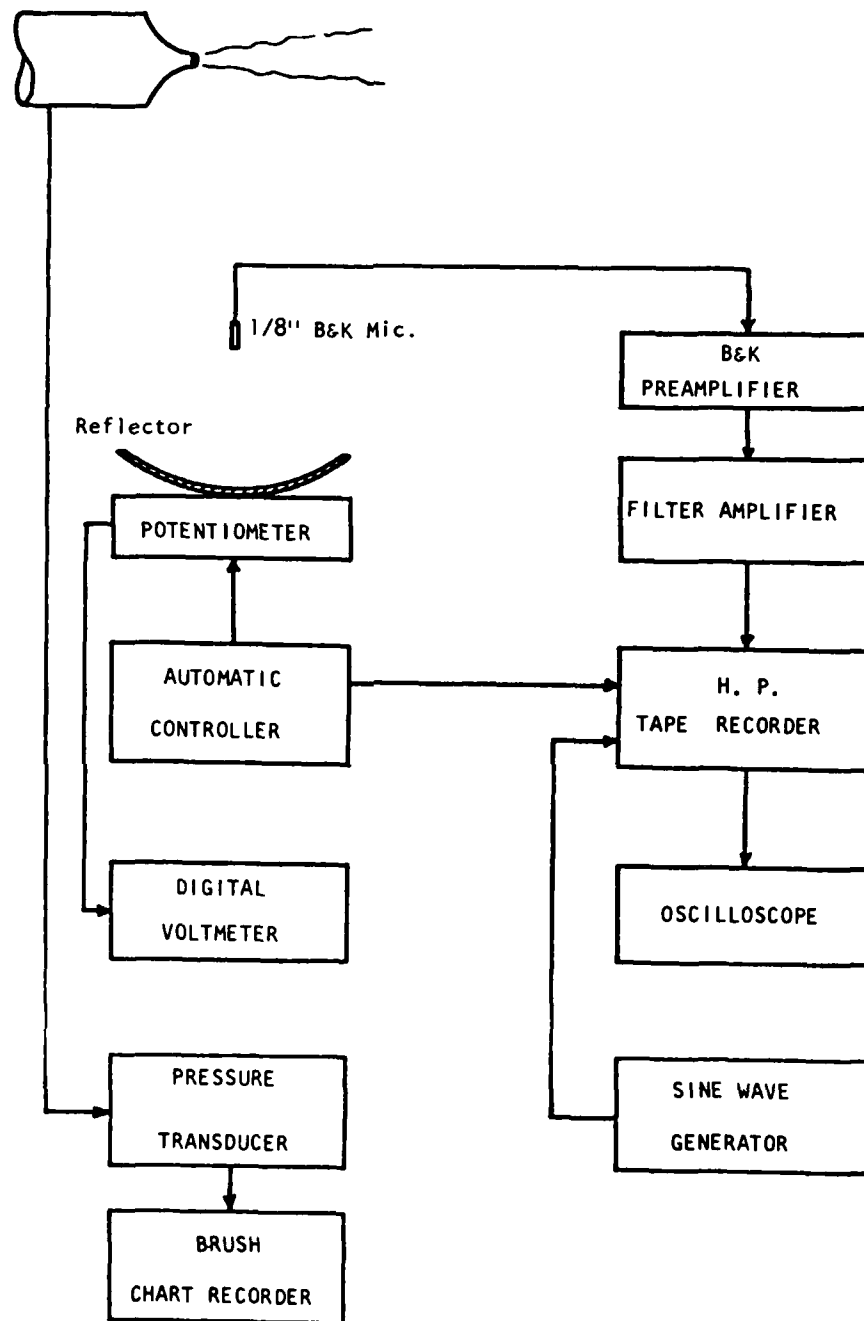


Figure 8-42. Block Diagram of Experimental Setup for Axial Source Strength Measurement.

The stagnation pressure was monitored by a Validyne DP15TL pressure transducer and recorded on a Gould Brush 220 strip chart recorder. After each run, the microphone was calibrated by means of a B & K 4220 piston phone, and the aiming points were determined by sighting targets placed at several known distances from the jet exit.

As discussed in Reference 126, for a semiquantitative analysis of the data (and without using the elaborate mathematical inversion to obtain the axial source strength distribution) a filter amplifier can be incorporated to counteract the frequency discrimination of the gain of the reflector, and analyze the data in 1/3-octave (or percentage frequency) bands. A schematic diagram of the instrumentation set-up for data acquisition is shown in Figure 8-42. The frequency response of the filter amplifier is shown in Figure 8-43. The filtered signal was recorded at a tape speed of 30 ips. This adequately covered the frequency range of 150 Hz to 100 kHz dictated by the low frequency cutoff of the anechoic chamber and the upper frequency limit of the 1/8-inch B & K microphone used.

To determine accurately the frequency response of the recording and data reduction instrumentation, a set of equal-amplitude sine waves at different frequencies was recorded in the beginning of each reel of magnetic tape. After the data were recorded, the microphone was calibrated by means of the B & K 4220 piston phone and the output signal was recorded on tape so that a conversion from electrical signal to acoustic pressure could be made directly.

During the scanning process, a pulse was available from the automatic controller at the start of each step. This pulse train was recorded on a separate FM channel for identification purposes in the data reduction procedure.

For the set of experimental results reported here, the recorded data were processed by analogue. A 1/3-octave spectrum was obtained of the acoustic signal for each aiming position of the reflector using a General Radio 1921 Real-Time Analyzer. By means of a tape speed reduction of four, the frequency range covered was from 150 Hz to 80 kHz. Since the reflector microphone has poor focusing ability below 1 kHz, the useful frequency range of the reduced data is from 1 kHz to 80 kHz. An 8-second integration time was used which corresponds to 2 seconds in real time. From these spectra, cross plots of intensity in frequency bands as a function of aiming point could be generated.

8.3.2.3 Flow Visualization

For the water jet experiments, the flow was visualized by using a dye or hydrogen bubbles.

Dye could be introduced at the top of the stilling chamber, to color the entire jet column. Information on jet spreading rates in the region 0-10 diameters downstream was determined from photographs of the dyed jet. The

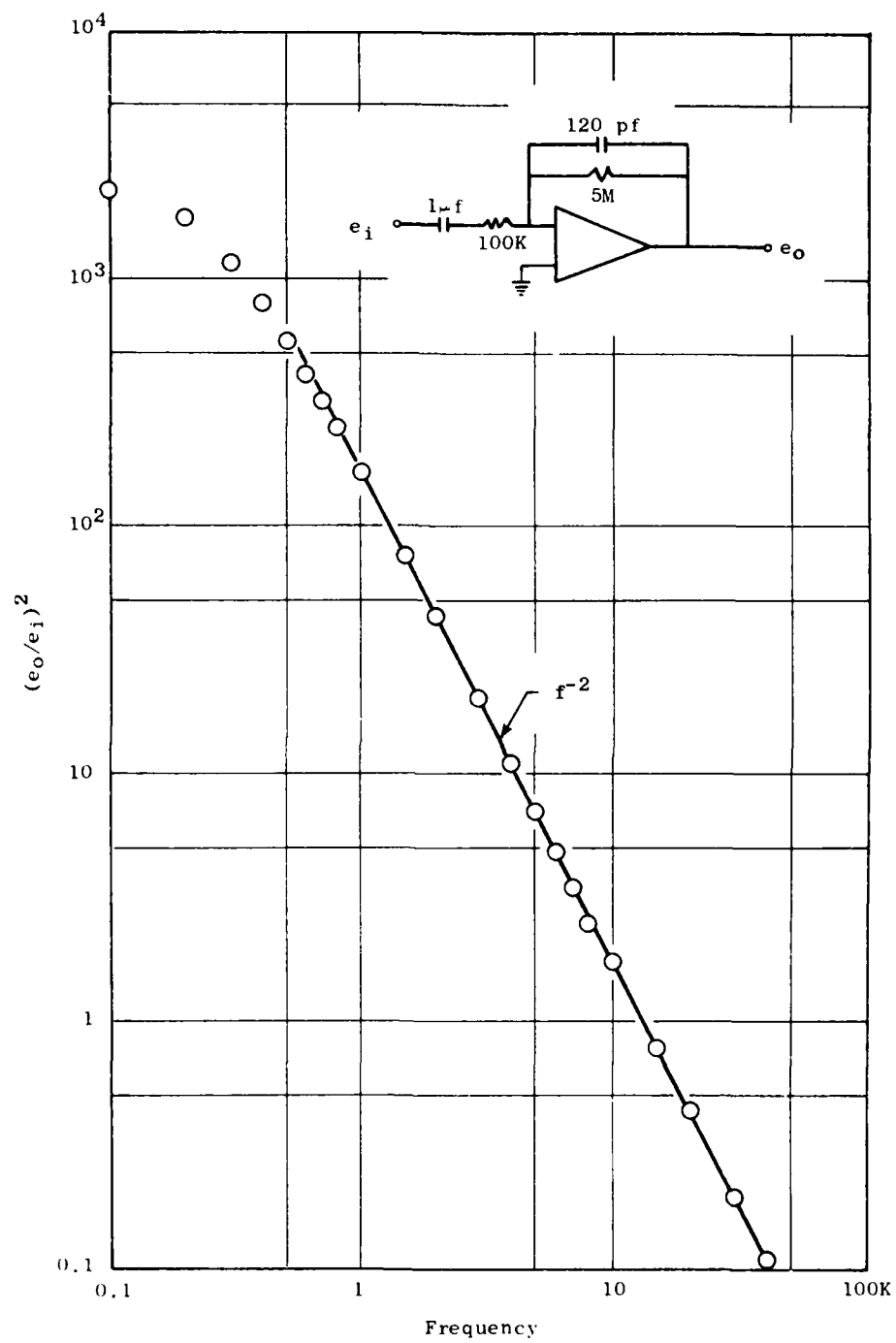


Figure 8-43. Frequency Response of Filter Amplifier.

dye used was common red food coloring. It is a convenient coloring agent because it can be removed with ordinary household laundry bleach. After each injection of dye the tank could be cleared of color in a few moments, thus, eliminating the costly and time-consuming task of draining and replacing the water.

Hydrogen bubbles were also used. A thin platinum wire was placed across the exit plane and pulsed periodically to produce a sequence of lines. By trial and error it was determined that 0.002-inch diameter platinum wire at voltages of about 100V produced the best results. This wire is small enough to give the desired quantity of microscopic bubbles, and yet strong enough to withstand normal use. An axial slice of the jet was illuminated using a commercial spot lamp and a vertical slit; the arrangement is sketched in Figure 8-44. The room must be completely darkened to provide good contrast between bubbles and background. Even so, obtaining enough light is a problem. Shutter speeds were normally 1/250, using a Nikon F camera with f 1.4 lens. The Tri-X film was pushed to approximately ASA 3000 by a special developing technique. Photographs of the bubble traces give a good qualitative picture of the jet flow field in the region of 0 to 4 diameters. In certain regions of the flow field, instantaneous velocities were obtained by measuring the spacing between lines.

8.3.2.4 Variation of the Initial Flow Conditions by Artificial Means

Since a very limited amount of information is available on the effect of initial flow conditions on the development of a turbulent jet and on the radiation field, a number of different ideas have been explored using the two facilities.

Change of the Initial Shear Layer Thickness

In the air facility, this was accomplished by the use of a 48-diameter pipe nozzle. It is estimated that the boundary layers developing along the pipe wall are merged at the nozzle exit and the velocity distribution at the exit corresponds to that of a fully developed pipe flow. The measured center velocity at the exit is 867 ft/sec.

In the water jet facility, limited space prevented the use of a pipe nozzle and, instead, a corrugated trip ring was placed 1/4-inch upstream of the nozzle exit. The square corrugations protruded from the wall approximately one boundary layer thickness (1/16-inch), and were separated around the perimeter of the ring by 1/16-inch spaces. At the low jet Reynolds numbers used for the visualization experiments, the trip ring did not produce a fully turbulent boundary layer at the nozzle exit. It did, however, increase the initial shear layer thickness by about a factor of 1.5 as estimated from photographs (and also produced noticeable turbulent fluctuations in the developing shear layer).

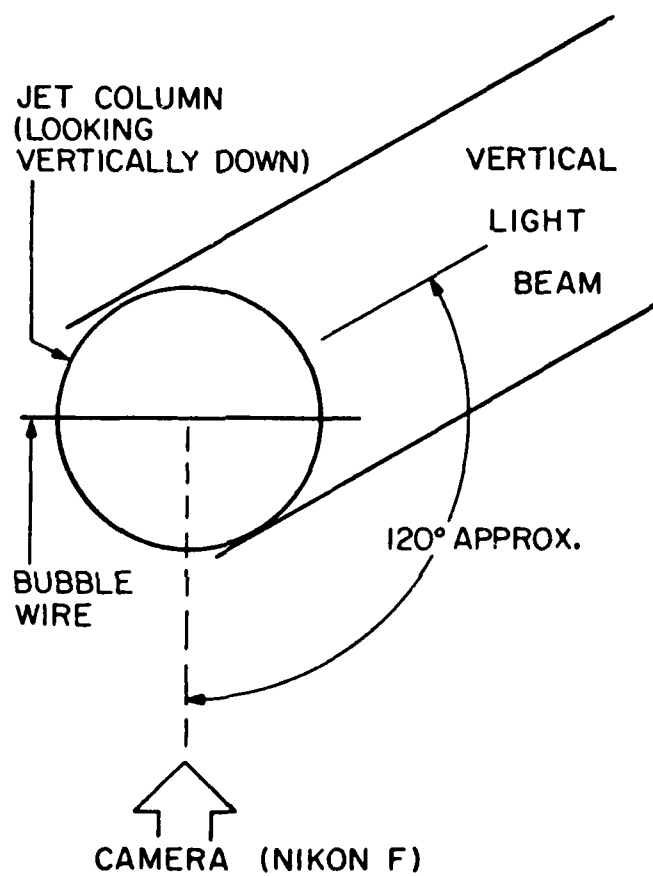


Figure 8-44. Sketch of Arrangement for Hydrogen Bubble Photography.

Change of the Initial Fluctuation Level (Introduction of Periodic Disturbances)

In the air jet facility, the turbulence level at the nozzle exit was increased by the use of a "fully rough" pipe nozzle as described in Section 8.3.1. It is estimated that the turbulence level at the nozzle exit was increased by approximately 75% over that corresponding to the smooth pipe nozzle.

In the water facility, the fluctuations were introduced in the form of periodic disturbances having an rms amplitude between 2.5% and 3.5% of the jet exit velocity. This was done by periodically constricting the jet supply tube at a known frequency and amplitude. Such periodic constrictions caused the flow in the jet nozzle to exhibit a small, unsteady component which was in phase over the jet cross section. To maintain constant velocity fluctuation amplitude at the jet exit plane required a different amplitude of forcing for each frequency. The response of the jet apparatus to a periodic forcing of fixed amplitude is shown in Figure 8-45 for three Reynolds numbers (flow rates). (These amplitude measurements were made with a hot-film probe placed approximately 1 inch upstream from the nozzle exit plane.) The velocity induced by a displacement of fixed amplitude might be expected to increase linearly with frequency as indicated by the line of unit slope. This is seen to be only approximately true, since the apparatus has a resonance at about 3.5 Hz. These measured response curves were used to determine the required amplitude of forcing at each frequency to keep the velocity fluctuation amplitudes within the specified range.

8.3.3 Results and Discussion

It is important to emphasize that the results presented here should be considered preliminary. The primary purpose of the investigation was to look at several different cases to obtain an overview of the effect of nozzle shapes and entrance conditions, and to discover certain trends. Emphasis is placed upon qualitative features rather than absolute measurements.

8.3.3.1 Elliptic Jet

Before discussing the characteristics of the noise radiation in the far field, it is useful to describe the observations of the jet flow itself.

Transition to turbulence in the elliptic jet occurs in a particularly violent manner that is best visualized by dyeing only the thin boundary layer on the nozzle wall, as in Figure 8-46. (This was done by introducing dye through a series of fine, (0.010-inch) slots cut through the nozzle wall just upstream of the jet exit plane.) The vortices which form initially are nearly two dimensional and are parallel to the major axis. At about 3 minor diameters downstream, the corner regions literally explode and spread vorticity rapidly into the core along the plane containing the major axis. The overall width of the jet spreads only slowly in the plane of the major

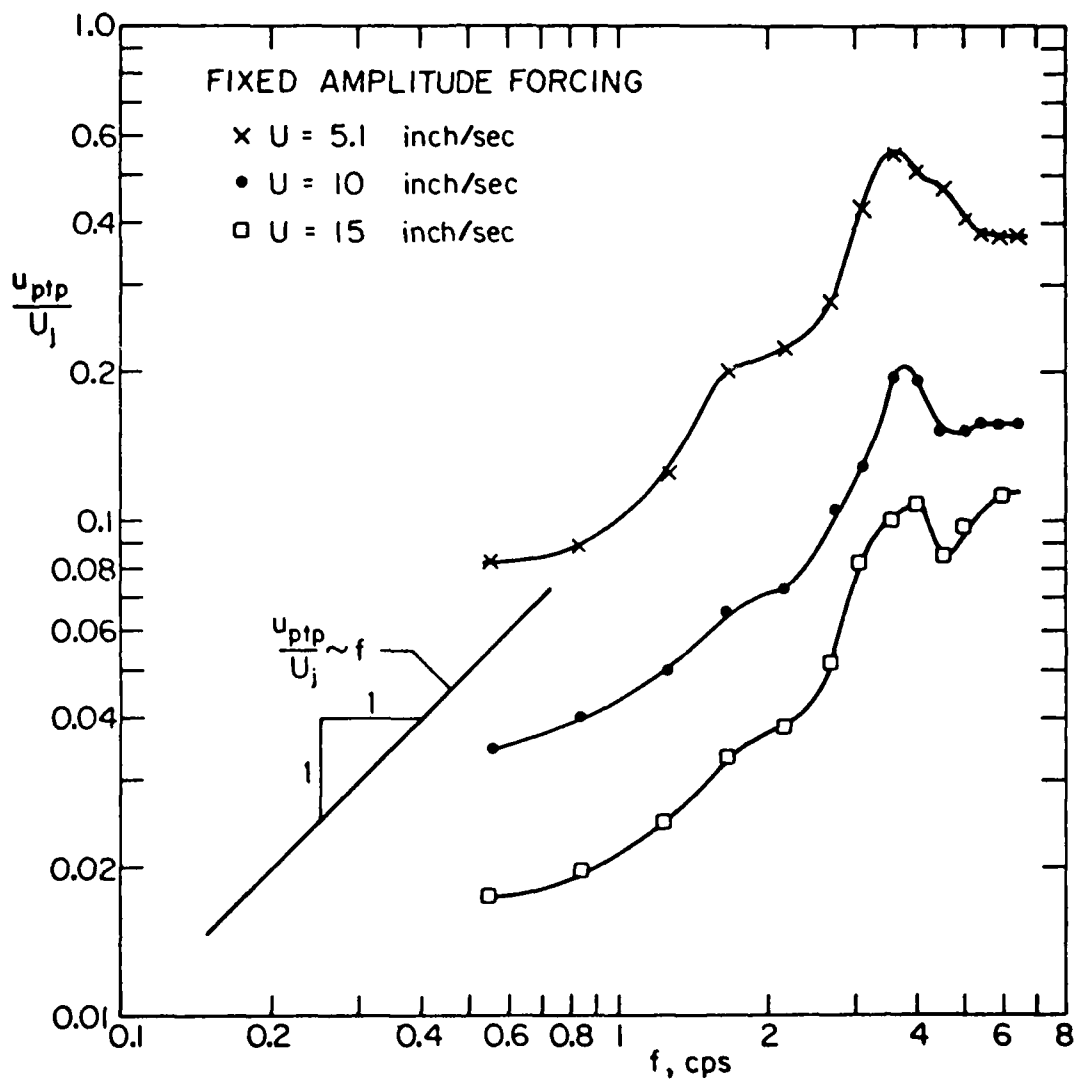


Figure 8-45. Peak-to-Peak Velocity Fluctuations Produced Near the Jet Exit Plane as a Result of a Periodic, Fixed-Amplitude Forcing.



Figure 8-46. Dye Visualization of 5:1 Elliptic Nozzle (The Major Axis is in View). Dye is Introduced into the Nozzle Boundary Layer at a Jet Reynolds Number of 1325 (Based Upon Minor Diameter).

axis; but viewed in the plane of the minor axis, the growth is much more rapid, Figure 8-47. The jet actually attains, at 10 diameters downstream, its greater width in the plane of the minor axis. (Forcing does not affect this growth rate much, although it does increase the spreading rate in the plane of the major axis.)

Particular significance should be attached to the following three points: (1) the jet attains a nearly symmetric character within 10 diameters from the nozzle, (2) the interaction between neighboring vortices shows a very different process from the circular case suggesting that the quadrupole character of the acoustic sources is different, and (3) the large spreading rate in the plane of the minor axis is accomplished by a strong vorticity flux into the core along the major axis and outward in the plane of the minor axis.

The far-field noise intensities measured at 10 different directions from the jet axis and at two azimuthal angles are shown in Figure 8-48. Plotted on the same figure is the OASPL directivity of a 1-inch circular nozzle operated at approximately the same exit velocity. The 1-inch nozzle, incidentally, has exactly the same cross-sectional area as that of the elliptic one and, therefore, the intensity measurements are directly comparable. The result is that there is no significant difference between the three sets of data. This is particularly true for the large ($\theta_1 > 140^\circ$) and small ($\theta_1 < 110^\circ$) radiation angles. Nevertheless, closer examination of the results, especially the noise spectral density distributions (Figures 8-49 through 8-51) does point to a number of differences. The radiation intensity of the elliptic jet is larger than that of the circular jet in the range $140^\circ > \theta_1 > 110^\circ$; this is true even in the azimuthal direction $\phi = 0^\circ$ where a different trend might be expected. The higher energy radiation is occurring primarily in the low frequency region (for all values of θ_1) and only at large radiation angles at high frequency do the measurements show less intensity emanating in the direction perpendicular to the plane of the minor axis ($\phi = 0^\circ$). These results are consistent with the conjecture that the low frequency radiation is associated with the pairing process of the large scale vortices which is observed to be more "violent" than seen in a round jet; the high frequency radiation, on the other hand, is related to the smaller scale vorticity fluctuations that seem to have considerably larger amplitude in the direction $\phi = 90^\circ$ than for $\phi = 0^\circ$ (Tables 8-1 and 8-2).

It is interesting to note that the above observations might also give a possible explanation of the observed fact that at supersonic speeds an elliptic nozzle is more effective in redirecting the radiated energy than at subsonic Mach numbers. In a recent work⁽¹²⁷⁾ it has been shown that a large part of the radiated energy is generated by Mach waves around the potential core region of a supersonic jet; furthermore, it is conjectured that the waves are produced by the supersonically convected "turbulent bumps". It might be speculated, therefore, that on the basis of visual observations the formation of the bumps are more numerous (and of larger amplitude) in the plane of the major axis of an elliptic jet compared to that of the minor axis. Thus, the fact that less energy is radiated in the direction normal to the minor axis might be explained by a lower intensity Mach wave radiation in that direction.



(a) Major Axis in View



(b) Minor Axis in View

Figure 8-47. Dye Visualization of 5:1 Elliptic Jet at Reynolds Number 5300.

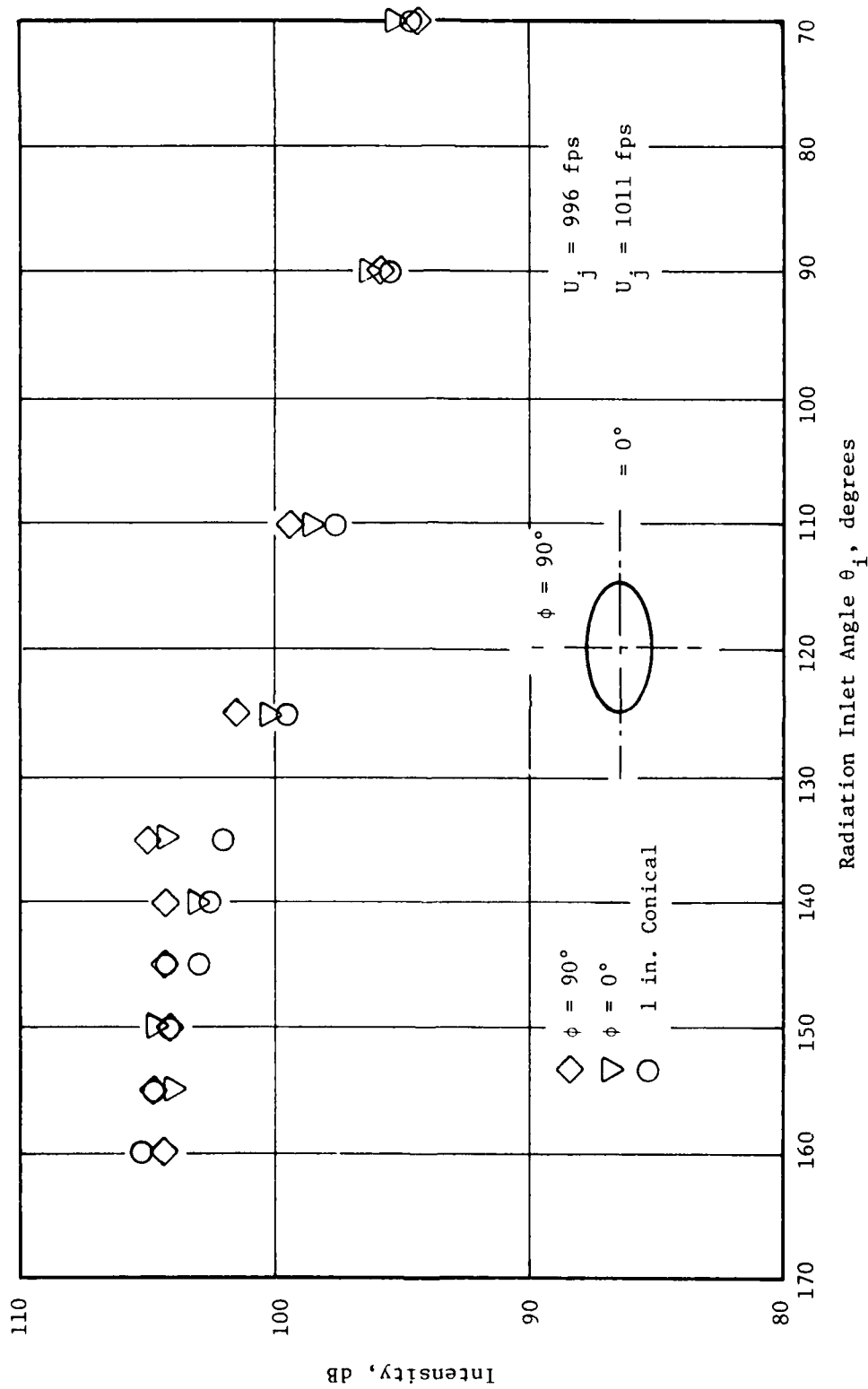


Figure 8-48. Comparison of Directivities of Jet Noise Between Elliptical Nozzle and Conical Nozzle.

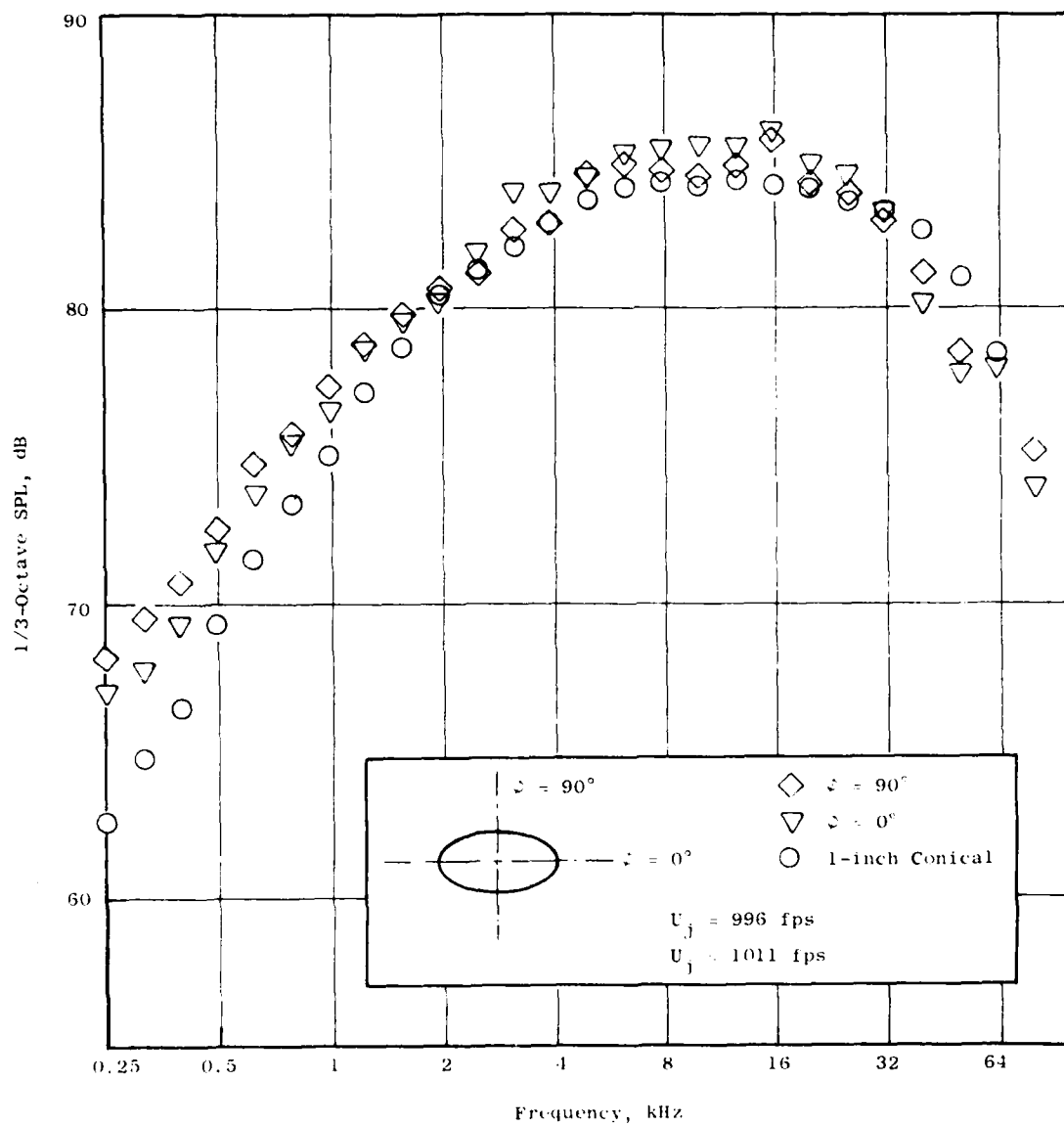


Figure 8-49. Comparison of 1/3-Octave Sound Pressure Levels at $\theta_I = 90^\circ$.

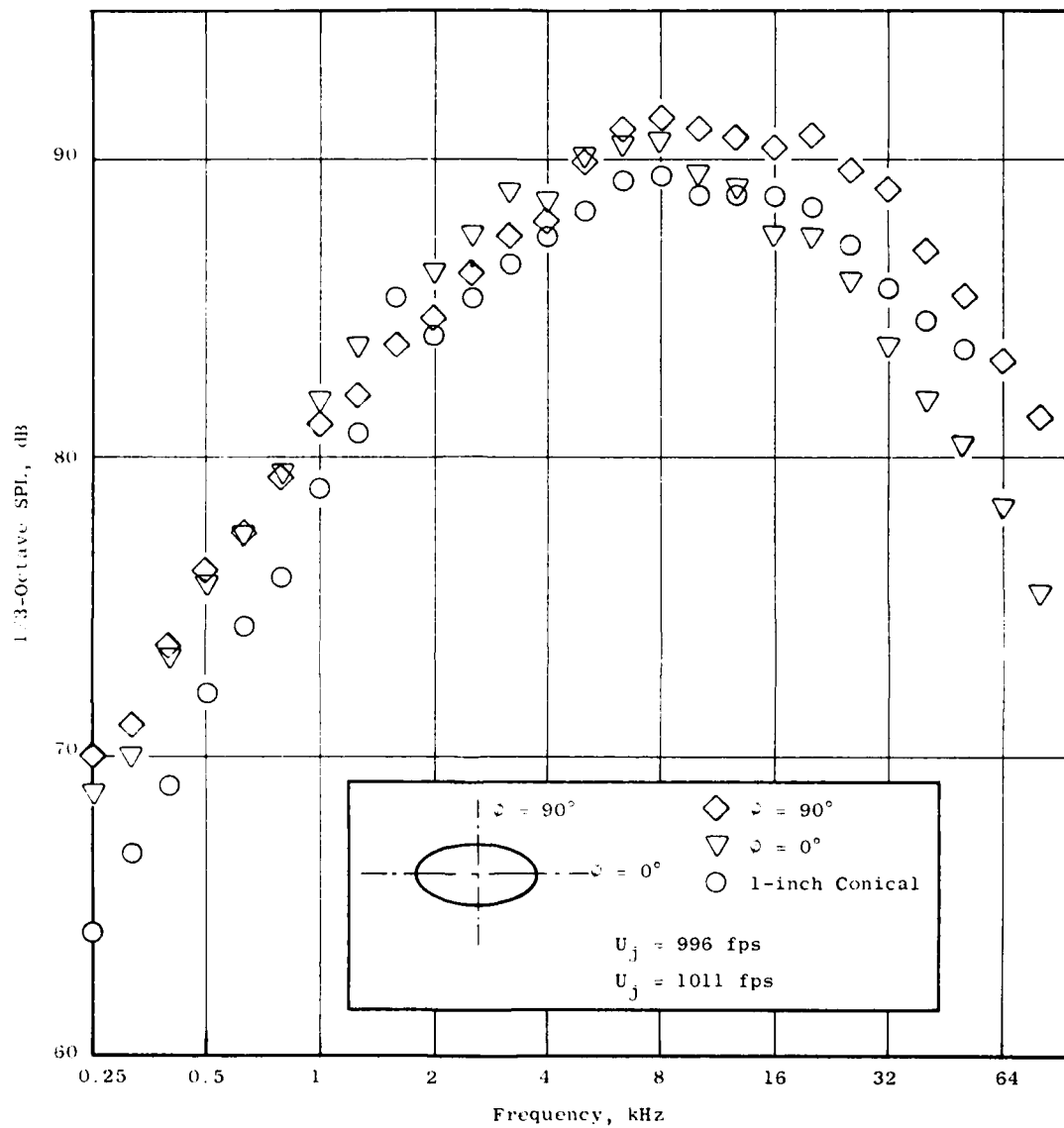


Figure 8-50. Comparison of 1/3-Octave Sound Pressure Levels at $\theta_I = 125^\circ$.

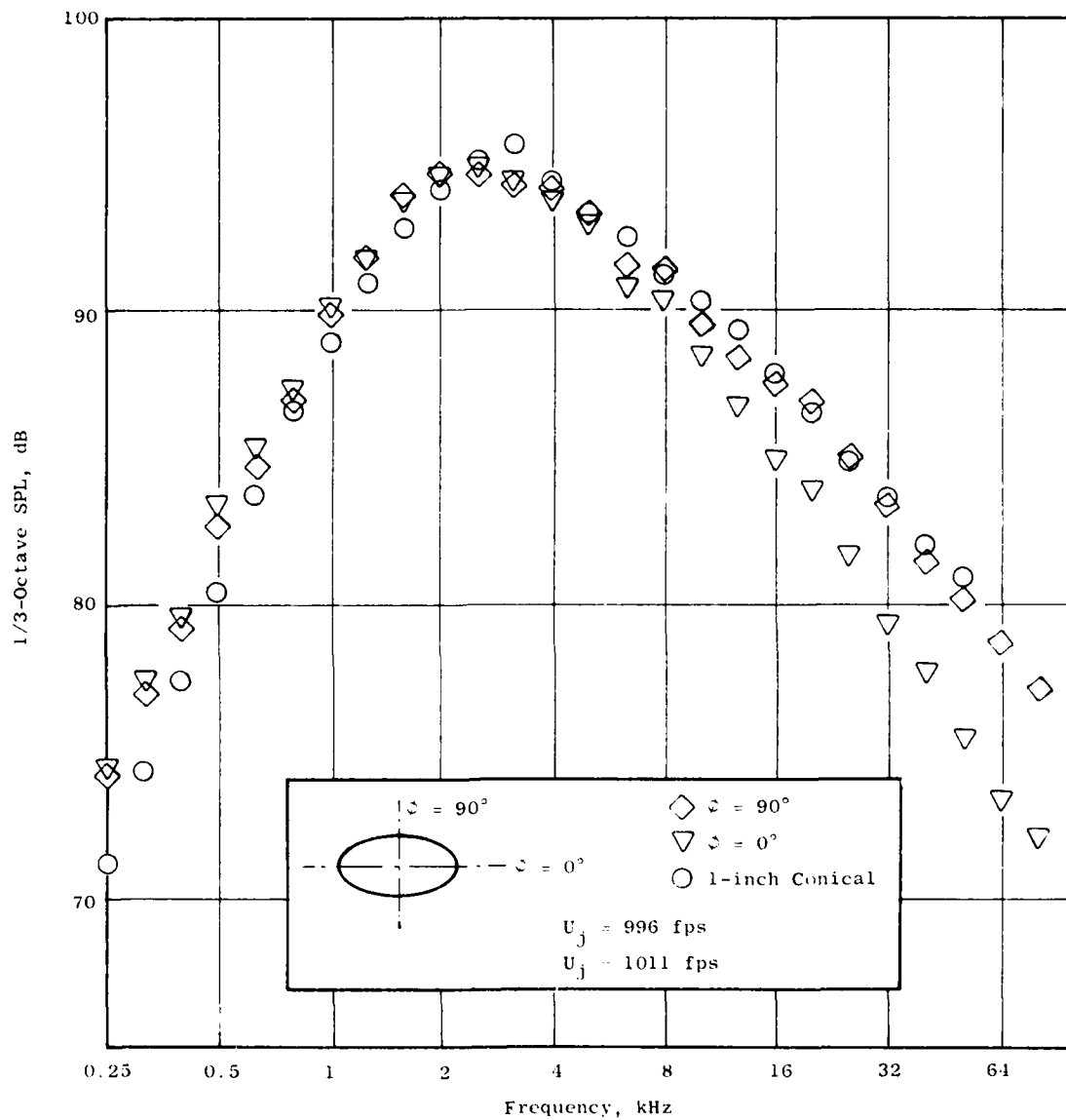


Figure 8-51. Comparison of 1/3-Octave Sound Pressure Levels at $\theta_I = 150^\circ$.

Table 8-1. Far-Field Noise Intensity, $\phi = 0^\circ$ Direction.

Elliptical Nozzle : 2.5" x 0.4"
 Speed : 996fps
 ϕ : 0°
 Temperature : 530° R
 Distance : 90"

f/θ	70°	90°	110°	125°	135°	140°	145°	150°	155°
160Hz	58.75dB	61.00dB	64.75dB	66.25dB	68.00dB	69.25dB	69.00dB	68.25dB	71.50dB
200	61.50	63.75	67.75	68.25	69.00	71.75	71.75	71.50	73.50
250	65.50	67.00	70.00	68.75	73.25	73.25	74.25	74.50	76.50
315	64.00	67.75	69.50	70.00	73.50	74.00	77.00	77.50	79.00
400	65.75	69.25	71.50	73.25	75.50	77.50	78.75	79.75	81.75
500	68.00	71.75	74.25	75.75	78.25	81.50	82.75	83.50	84.75
630	70.25	73.75	76.25	77.50	81.25	82.75	85.50	85.50	88.50
800	71.50	75.50	77.75	79.50	82.75	84.50	86.25	87.75	89.25
1K	74.25	76.65	79.15	81.90	85.15	87.65	89.90	90.40	88.90
1.25K	75.75	78.60	80.60	83.85	89.10	89.10	91.10	92.10	93.60
1.6K	77.75	79.55	82.55	85.05	94.30	90.55	93.05	93.80	95.30
2K	78.75	80.25	84.75	86.25	100.25	91.50	94.25	94.75	95.25
2.5K	79.50	81.98	87.48	87.73	91.23	92.48	94.98	94.98	95.73
3.15K	81.25	83.95	85.95	88.95	91.20	92.95	94.70	94.45	94.45
4K	82.25	83.93	86.68	88.68	91.93	92.68	94.18	93.68	93.43
5K	83.00	84.66	87.41	90.16	91.66	93.66	93.91	93.00	92.41
6.3K	84.15	85.35	87.85	90.60	91.85	93.10	93.35	90.85	91.10
8K	85.40	85.45	87.95	90.70	90.20	92.70	92.45	90.45	89.20
10K	84.65	85.65	88.15	89.65	90.65	90.60	90.15	88.40	87.60
12.5K	84.30	85.60	87.85	89.10	90.05	89.05	89.40	86.85	85.80
16K	84.05	86.05	87.80	87.55	88.75	88.25	88.75	85.00	84.50
20K	83.00	85.00	86.25	87.50	87.35	87.45	86.20	83.95	82.65
25K	85.00	84.50	85.50	86.00	86.10	85.60	84.20	81.70	80.65
31.5K	84.60	83.45	82.85	83.85	84.40	83.10	82.20	79.45	78.50
40K	83.60	80.20	81.75	82.00	81.80	81.10	80.20	77.70	76.90
50K	79.25	77.80	79.30	80.55	79.80	79.40	78.25	75.50	73.55
63.5K	74.55	78.00	76.95	78.30	78.05	77.25	76.90	73.40	72.95
80K	74.00	74.00	75.45	75.65	75.60	75.60	73.45	72.20	70.55
Overall	95.31dB	96.29dB	98.75dB	100.31dB	104.42dB	103.13dB	104.3dB	104.83dB	104.19dB

Table 8-2. Far-Field Noise Intensity, $\phi = 90^\circ$ Direction.

Elliptical Nozzle : 2.5" x 0.4"
 Speed : 996 fps
 ϕ : 90°
 Temperature : 530° R
 Distance : 90"

f/ \bar{u}_1	70°	90°	110°	125°	135°	140°	145°	150°	155°	160°
160Hz	59.25dB	62.00dB	66.00dB	66.50dB	67.75dB	68.75dB	67.50dB	68.25dB	71.75dB	72.50dB
200	62.00	64.25	68.75	68.75	68.75	71.00	70.25	71.25	73.25	75.50
250	66.25	68.25	71.25	70.00	73.75	72.75	73.75	74.25	76.25	78.25
315	65.00	69.50	71.00	71.00	73.00	73.75	76.00	77.00	78.75	80.25
400	66.50	70.75	73.50	73.75	74.50	76.75	77.50	79.25	81.75	82.75
500	68.50	72.50	76.00	76.25	77.25	79.50	80.75	82.75	84.50	85.50
630	71.00	74.75	78.25	77.50	80.25	81.50	83.00	84.75	89.50	88.50
800	72.50	75.75	79.00	79.25	81.25	83.25	84.50	87.00	93.00	91.25
1K	74.50	77.40	80.65	81.15	84.15	86.40	88.40	89.90	94.15	93.15
1.25K	76.25	78.85	81.30	82.10	88.35	88.10	89.60	91.85	96.10	94.60
1.6K	78.00	79.80	82.30	83.80	94.55	90.30	91.80	94.05	95.55	95.80
2K	79.00	80.75	84.25	84.75	99.75	91.75	93.75	94.75	96.25	95.50
2.5K	79.50	81.23	86.98	86.23	90.98	92.98	94.23	94.73	94.48	94.98
3.15K	80.75	82.70	85.45	87.45	90.95	93.20	94.45	94.45	93.45	94.45
4K	81.00	82.92	85.93	88.18	92.18	93.68	93.93	94.18	92.93	92.80
5K	82.00	84.66	87.41	89.91	93.16	94.16	93.91	93.41	90.90	91.40
6.3K	82.65	84.85	88.10	91.10	93.10	93.85	93.60	91.60	91.10	89.85
8K	83.15	84.70	88.45	91.45	92.45	94.20	93.20	91.70	88.90	88.75
10K	82.65	84.65	88.65	91.15	93.40	93.35	91.90	89.65	87.60	87.10
12.5K	82.80	84.85	88.60	90.85	92.55	91.80	91.10	88.35	86.55	86.10
16K	83.05	85.80	89.05	90.55	92.25	90.75	90.50	87.50	85.50	84.35
20K	82.25	84.25	88.25	91.00	91.10	90.95	88.45	86.95	84.90	83.20
25K	84.75	84.00	87.25	89.75	89.85	89.60	87.70	85.20	83.60	83.05
31.5K	84.35	82.95	86.35	89.10	88.40	87.35	86.45	83.40	82.50	81.60
40K	83.10	81.20	85.25	87.00	86.55	86.10	84.20	81.40	81.15	77.85
50K	79.50	78.55	83.05	85.55	85.30	84.40	82.75	80.25	77.55	74.85
63.5K	75.30	78.50	81.45	83.30	83.05	82.75	81.15	78.75	75.20	73.40
80K		75.25	79.95	81.40	79.80	80.45	78.20	77.20		
Overall	94.4dB	95.88dB	99.41dB	101.54dB	105.23dB	104.28dB	104.36dB	104.20dB	104.85dB	104.46dB

8.3.3.2 Smooth- and Rough-Pipe Cases

Far-field noise - Far-field noise spectra and intensities at 10 different directions from the jet axis have also been obtained for these two cases. Results of the 1/3-octave spectra are tabulated in Tables 8-3 and 8-4. As it has been demonstrated in the other part of this program that jet noise scales with diameter, the present results will be compared with an "equivalent" 1/2-inch nozzle results scaled from the 2-inch nozzle data. Figure 8-52 shows the OASPL directivities of the smooth pipe, rough pipe, and the equivalent 1/2-inch nozzle.

Since the momentum flux through the three nozzles is not the same, a direct comparison of the intensities as shown in the figure is not possible. Estimating the average discharge velocities in the three cases and assuming that the intensity varies with the eighth power of the velocity (an assumption that overestimates the intensity for $\theta_I > 135^\circ$), the intensities have been recalculated and compared in Figure 8-53. The following interesting observations can be made on the basis of this comparison:

1. The difference in OASPL directivities of the nozzle and smooth pipe flow is small, it is within the accuracy of the correction described above. This is further born out when the normalized spectral densities are compared at $\theta_I = 160^\circ$ (Figure 8-54) and a lesser extent at $\theta_I = 90^\circ$ (Figure 8-55). In the latter case, the smooth-pipe spectrum exhibits more low frequency energy; this could possibly be explained by the fact that the initial shear layer thickness near the jet exit is considerably larger for the pipe case and, consequently, the corresponding time scales are also larger. An even more sensitive basis for comparison is the spectral density of the source strength distribution per unit length. Contours of equal spectral density are shown in Figures 8-56 and 8-57. It is seen that the two cases exhibit great similarity with the possible exception of the low frequency range. In both distributions, the maximum energy occurs at a Strouhal number of about 0.2 and at approximately 7 to 8 diameters downstream of the nozzle exit.
2. Considerable differences exist, however, between the rough pipe and nozzle data (excepting perhaps the radiation field near the nozzle axis). The most remarkable feature of the noise field produced by the rough pipe flow is the high frequency radiation emanating from regions near the exit plane. Figure 8-58 shows that the most intense radiation occurs at Strouhal number of 0.6 within the first diameter of the jet. The directivity pattern of the radiation is also different, as seen in Figure 8-53.

On the basis of these preliminary measurements it would be unwise to make general conclusions. Indications are, however, that provided the initial mean velocity distribution is not too different from a top hat profile, and provided the initial turbulence fluctuation levels are not higher than those found in a smooth turbulent pipe flow, the intensity and directivity of the far-field radiation is not altered considerably. However, for turbulence levels of higher magnitude at the exit plane, important changes in the character of the radiation should be expected. A monopole source

Table 8-3. 1/3 Octave Far-Field Noise Spectra for Smooth Pipe.

2' Long Smooth Pipe : 1/2" diameter
 Speed : 867 fps
 Temperature : 530° R
 Distance : 79"

f/v ₁	70°	90°	110°	125°	135°	140°	145°	150°	155°	160°
160Hz	36.25dB	43.50dB	48.75dB	47.50dB	51.50dB	55.25dB	49.50	47.75dB	49.75dB	50.50dB
200	42.00	44.25	48.75	47.50	52.50	57.00	51.25	49.50	51.75	52.50
250	47.50	47.50	53.25	53.25	58.50	58.50	57.00	55.00	56.75	56.50
315	44.00	46.00	48.00	48.75	51.25	53.75	53.25	53.75	55.50	56.75
400	46.00	49.25	50.25	49.50	52.50	54.25	55.25	57.00	58.50	59.50
500	49.00	50.75	52.75	53.00	55.25	57.00	58.25	59.25	60.00	61.00
630	51.00	53.75	55.25	55.00	57.25	58.75	60.00	60.00	63.00	64.25
800	53.50	58.00	57.25	57.75	61.50	62.75	64.00	65.00	64.75	66.25
1K	55.50	58.00	59.05	59.90	63.65	65.65	67.25	68.25	68.50	69.00
1.25K	57.75	60.25	61.80	63.05	65.10	66.60	68.50	70.75	71.75	72.50
1.6K	59.95	61.45	63.20	64.45	67.80	70.05	71.25	72.25	74.75	76.50
2K	61.15	63.65	64.75	66.00	69.75	71.75	74.25	76.00	76.50	77.50
2.5K	62.45	64.70	69.20	68.20	71.48	73.48	76.25	77.50	78.00	78.50
3.15K	65.00	67.25	68.60	70.35	73.90	75.65	77.75	79.75	81.00	81.75
4K	65.50	68.00	70.35	72.35	75.30	76.55	79.50	81.25	81.50	82.00
5K	67.50	70.00	71.70	74.45	77.15	77.90	80.75	81.50	82.50	82.75
6.3K	68.20	70.70	73.00	75.75	77.60	79.35	81.15	81.40	82.15	81.65
8K	69.40	71.40	73.45	76.45	77.25	80.25	81.40	82.15	80.75	80.00
10K	68.90	70.65	73.95	76.70	78.60	79.10	80.65	80.15	79.00	78.25
12.5K	69.10	71.85	74.35	76.85	78.60	78.85	80.05	78.55	77.40	75.90
16K	69.50	71.75	73.95	75.45	77.85	77.60	79.05	76.80	75.85	74.35
20K	67.50	70.25	72.45	74.95	75.95	76.45	77.25	76.00	74.00	72.50
25K	67.00	69.25	71.00	73.25	76.05	75.30	76.00	73.50	73.00	71.25
31.5K	66.75	67.50	70.25	72.50	73.85	72.35	75.35	72.35	71.25	69.25
40K	66.50	65.25			69.85	69.10	74.35	71.10	68.40	66.15
50K					66.10	64.85	70.25	67.50	62.15	60.65
63.5K					64.40	63.15	64.05	61.30	57.05	54.55
Overall	78.91dB	81.02dB	83.22dB	85.52dB	87.69dB	88.58dB	90.37dB	90.53dB	90.55dB	90.52dB

Table 8-4. 1/3 Octave Far-Field Noise Spectra for Rough Pipe.

2' Long Rough Pipe : 1 1/2" diameter
 Speed : 878 fps
 Temperature : 530° R
 Distance : 79"

f/Hz	70°	90°	110°	125°	135°	140°	145°	150°	155°	160°
160Hz	37.00dB	40.50dB	47.00dB	48.00dB	50.25dB	53.75dB	46.00dB	43.75dB	48.25dB	47.25dB
200	39.50	41.25	48.25	48.25	53.00	56.00	48.25	45.50	47.75	54.25
250	46.00	46.50	55.00	55.25	60.25	57.50	53.75	50.50	52.75	54.50
315	40.00	42.75	45.50	47.00	49.50	52.75	49.75	50.25	51.75	53.75
400	42.75	45.50	48.25	48.25	50.50	52.00	52.50	52.75	54.50	55.50
500	46.00	47.25	51.50	52.00	54.00	54.50	55.75	55.75	53.25	57.25
630	47.75	50.25	53.25	53.50	56.25	56.25	57.50	56.50	57.00	60.50
800	49.50	53.00	55.75	56.25	59.75	59.50	60.75	60.75	60.50	62.50
1K	51.50	54.75	57.65	58.90	61.40	62.40	64.75	62.50	65.00	64.00
1.25K	54.50	56.50	59.80	62.05	63.10	63.35	65.25	65.00	67.75	67.75
1.6K	56.50	58.95	61.70	63.70	66.05	66.55	67.75	66.75	70.75	71.50
2K	58.15	60.65	63.25	65.00	67.50	68.00	70.75	69.75	71.75	73.00
2.5K	59.70	61.70	67.70	67.20	69.48	69.73	72.25	70.75	73.00	73.50
3.15K	62.00	65.00	67.60	70.10	71.65	72.15	74.00	72.50	75.75	76.25
4K	63.50	66.75	69.10	71.60	74.30	73.05	75.25	73.75	75.75	75.75
5K	65.50	68.25	71.95	73.95	75.65	75.15	76.75	75.25	76.75	76.50
6.3K	67.20	69.70	74.00	75.75	77.35	76.85	77.90	74.90	77.65	75.90
8K	68.15	70.65	73.70	76.70	76.50	77.50	78.90	75.90	77.00	75.25
10K	67.40	70.15	75.20	77.45	78.10	76.60	77.90	74.65	75.00	73.50
12.5K	67.35	71.10	75.35	77.85	78.60	76.60	77.05	73.30	73.65	71.90
16K	69.25	73.25	74.20	76.45	77.85	76.10	77.30	72.55	73.10	71.35
20K	68.00	72.00	75.20	77.70	77.45	74.95	75.50	72.00	71.75	69.25
25K	68.75	72.75	75.25	77.50	78.30	74.55	75.25	71.00	71.75	70.00
31.5K	68.75	73.50	76.25	79.50	77.35	73.10	75.85	70.85	72.25	70.25
40K					75.35	71.60	76.10	71.60	70.40	68.40
50K					72.60	68.35	73.50	69.25	65.90	64.15
63.5K					70.90	66.90	68.30	63.80	60.55	58.80
Overall	78.33dB	81.92dB	84.67dB	87.10dB	88.08dB	86.43dB	88.01dB	84.93dB	86.31dB	85.53dB

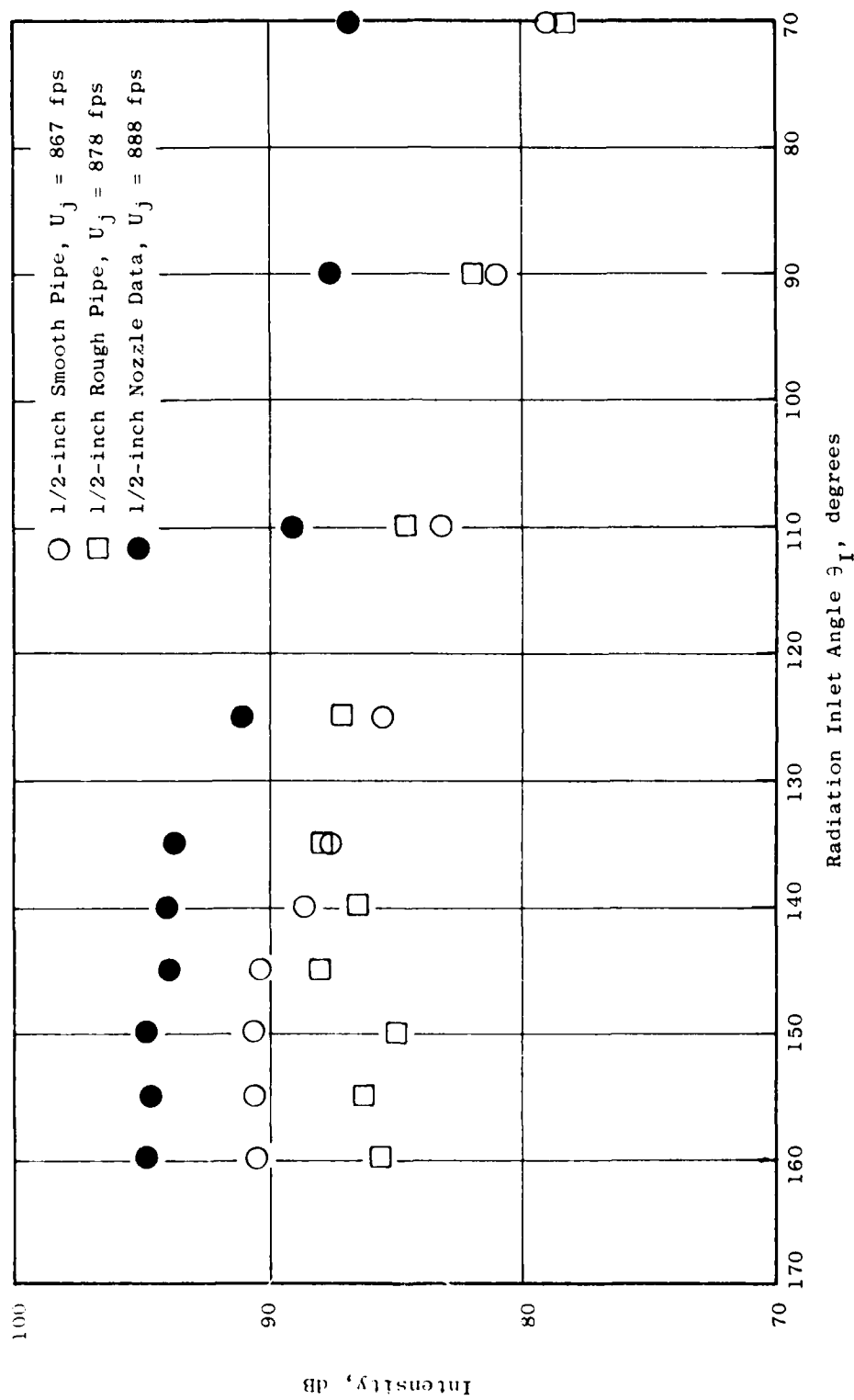


Figure 8-52. Comparison of Directivities of Jet Noise Between Nozzle, Smooth Pipe and Rough Pipe.

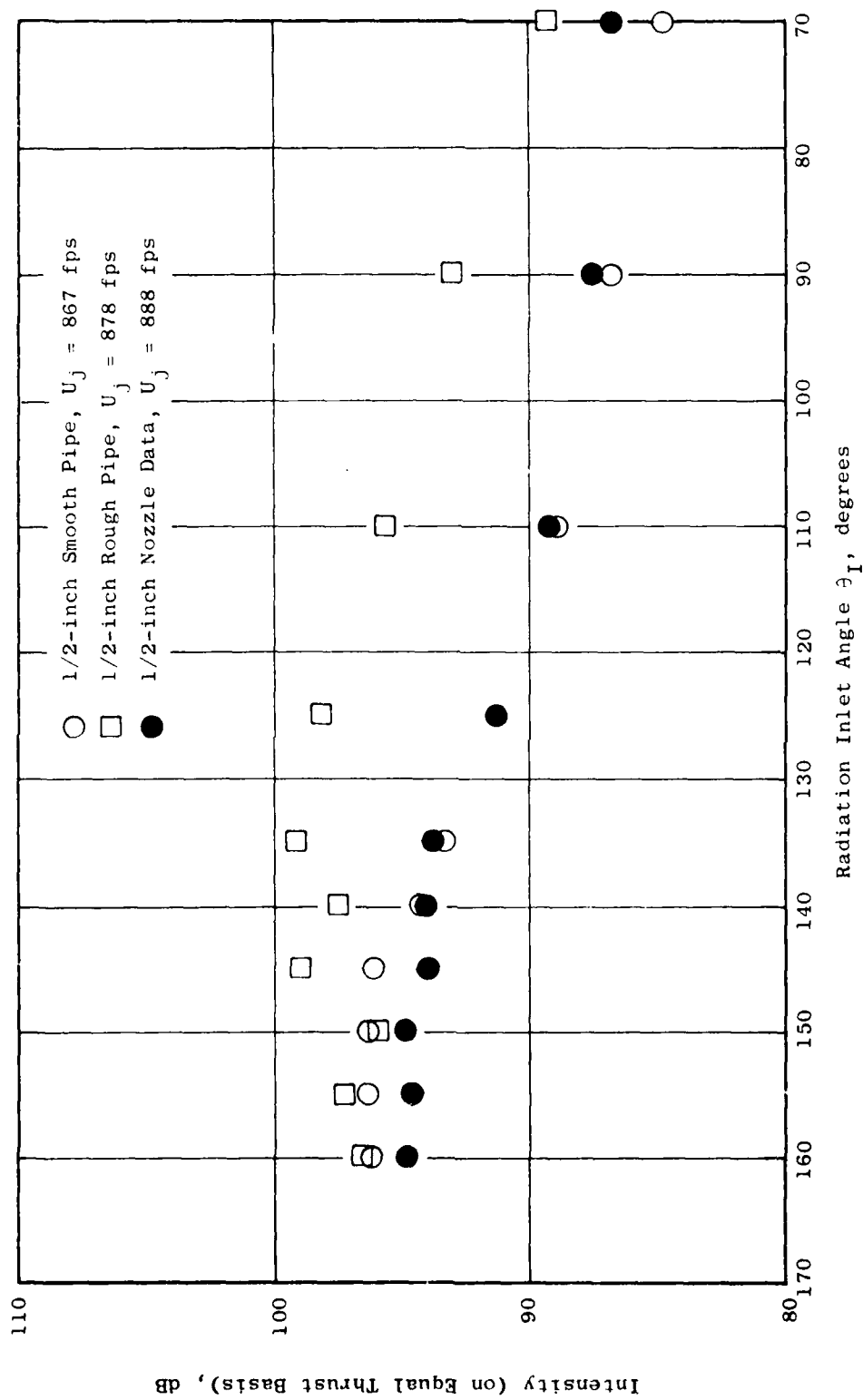


Figure 8-53. Comparison of Directivities of Jet Noise Between Nozzle, Smooth Pipe, and Rough Pipe: Data Have Been Corrected for Equal Thrust.

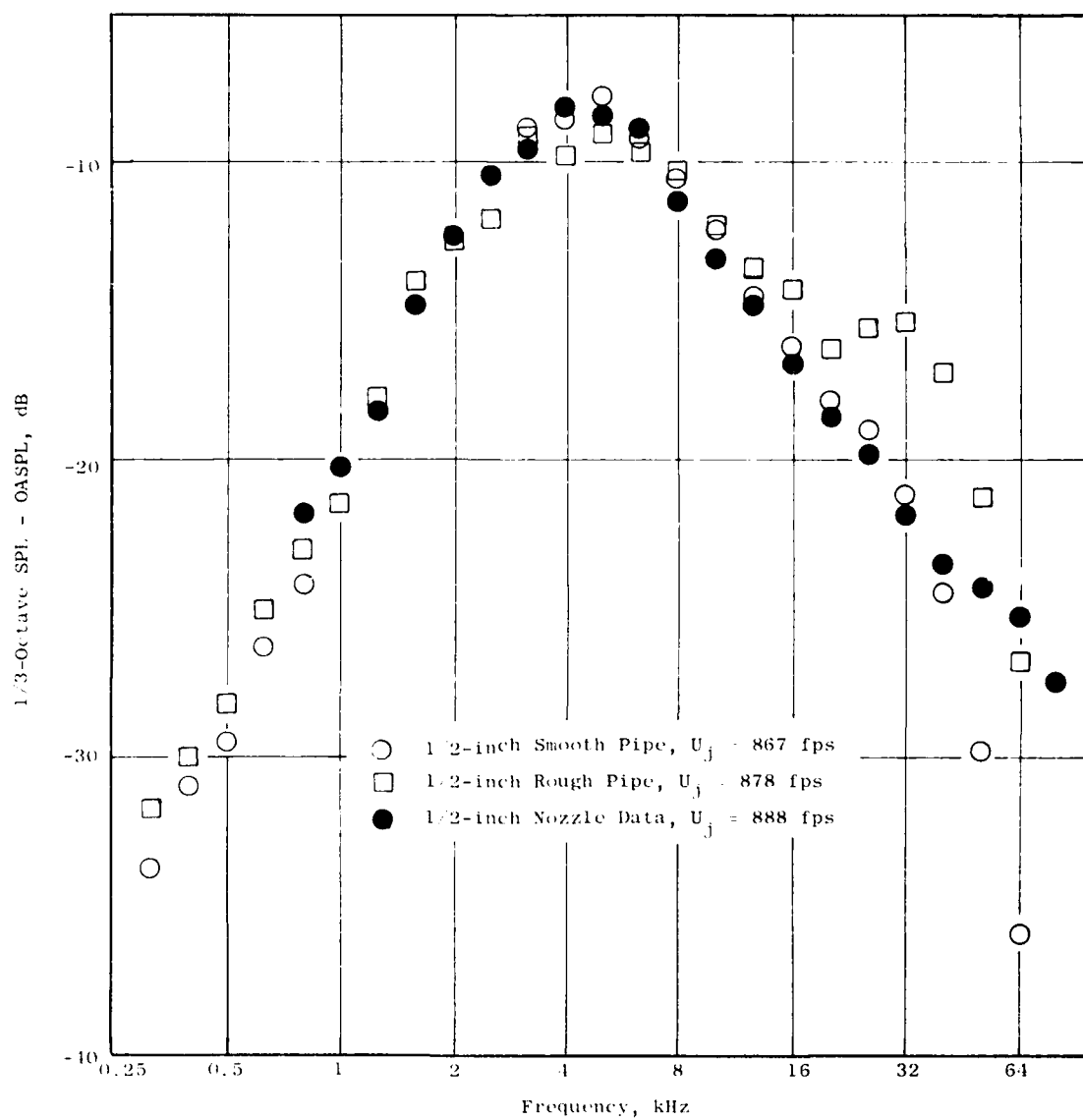


Figure 8-54. Comparison of Normalized 1/3-Octave Sound Pressure Levels at $\theta_I = 160^\circ$ Between Nozzle, Smooth Pipe, and Rough Pipe.

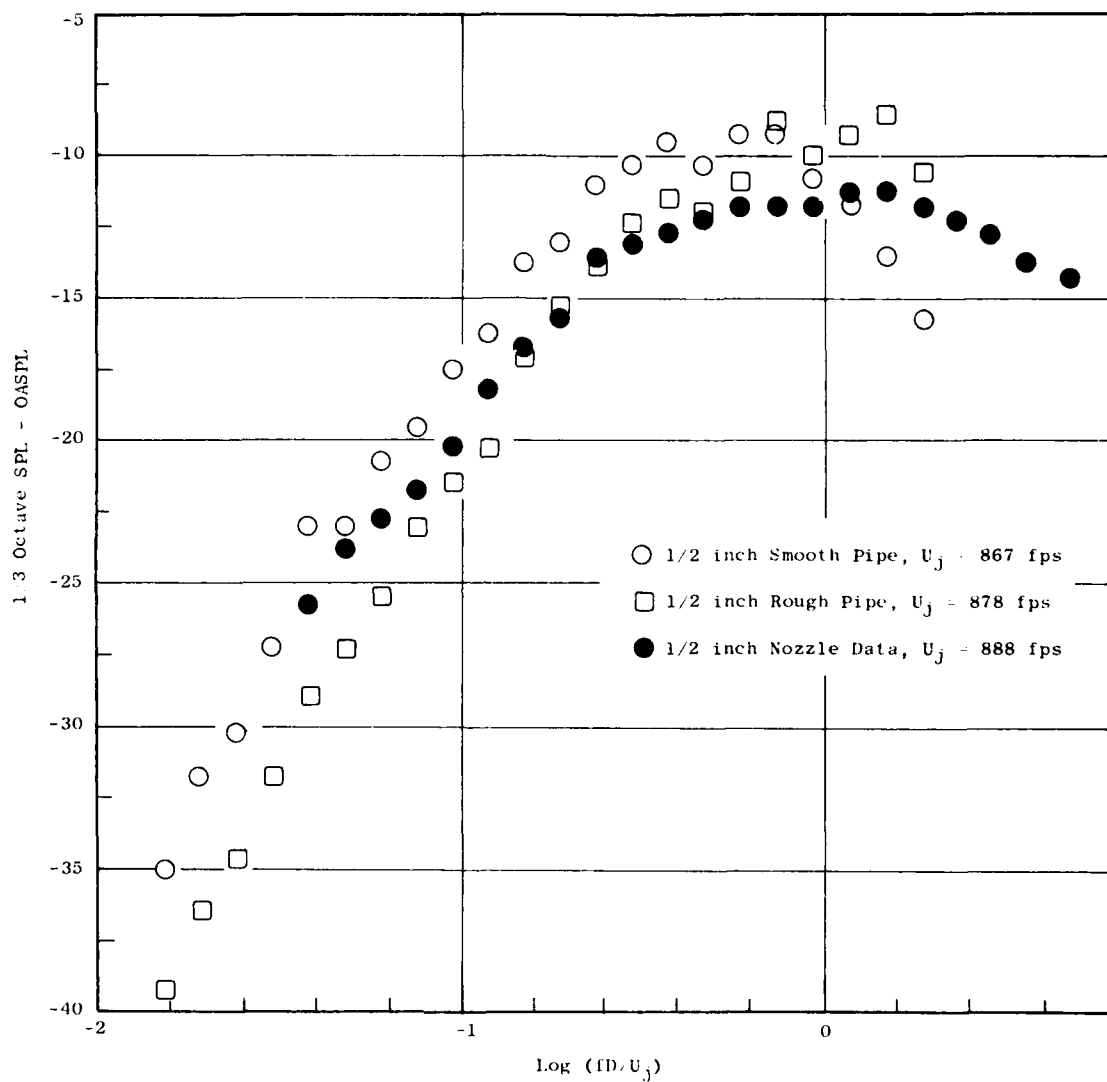


Figure 8-55. Comparison of Normalized 1/3-Octave Sound Pressure Levels at $\theta_I = 90^\circ$ Between Nozzle, Smooth Pipe, and Rough Pipe.

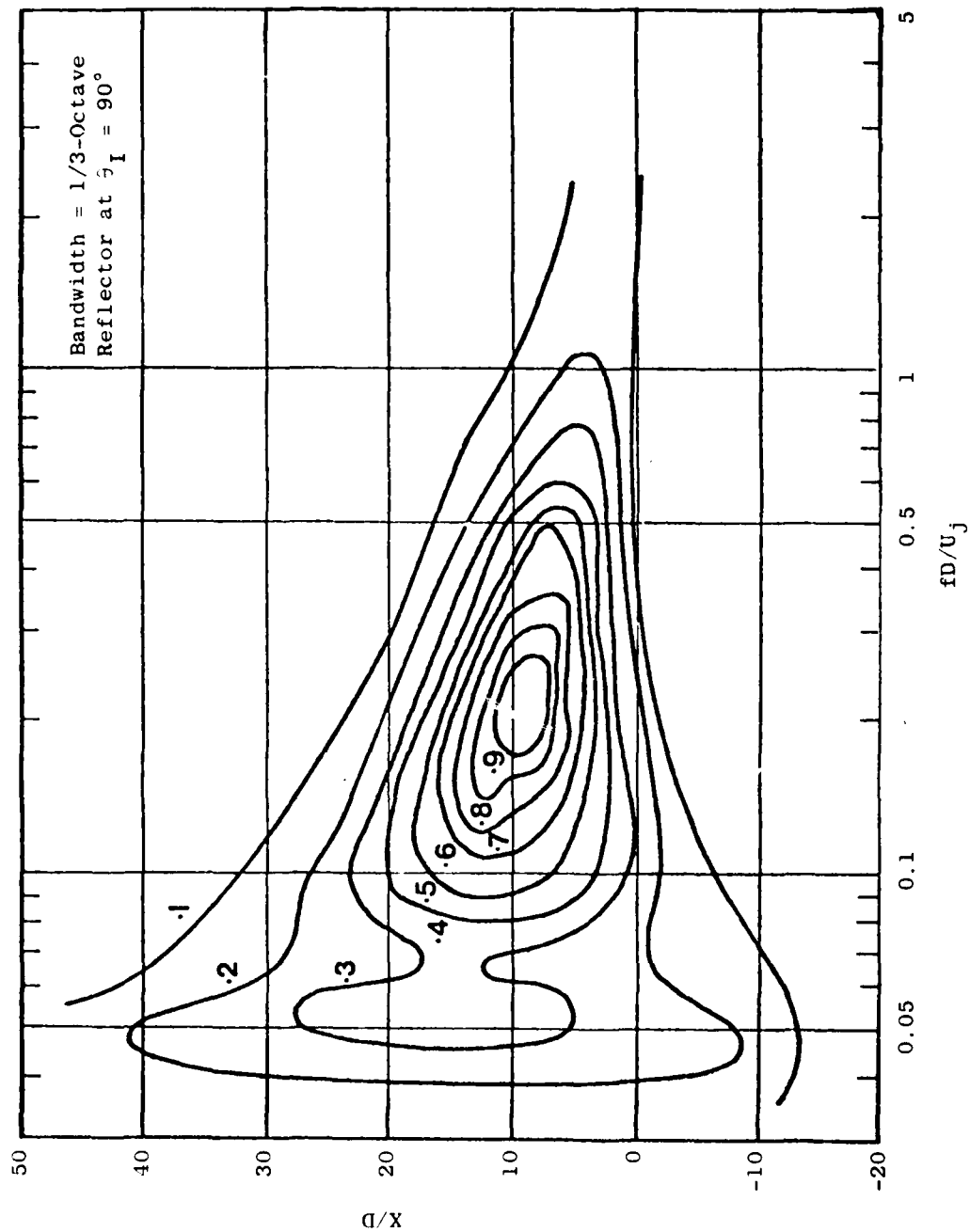


Figure 8-56. Contour Plot of Source Strength Distribution; 1/2-in. Nozzle, $U_j = 888$ fps.

757

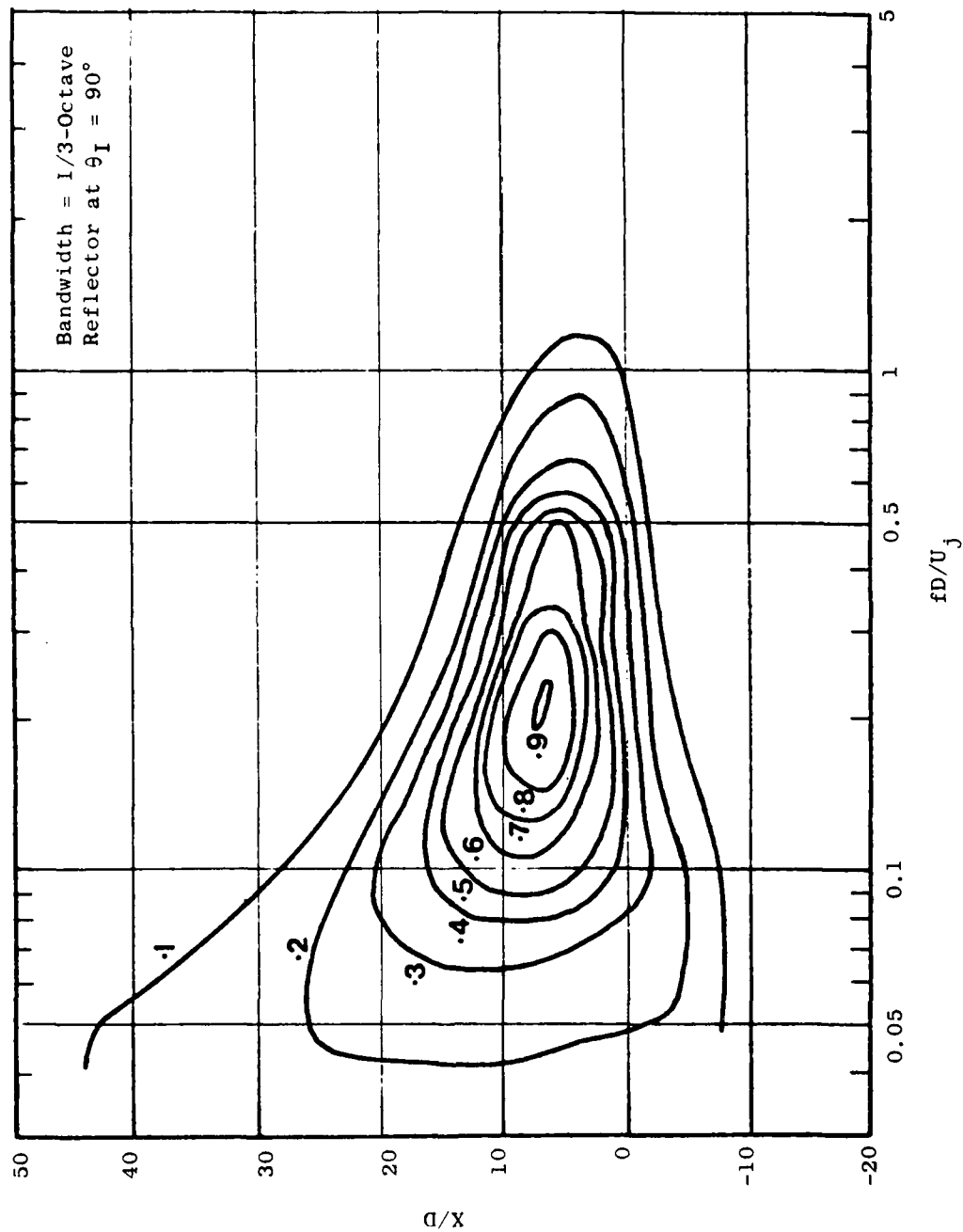


Figure 8-57. Contour Plot of Source Strength Distribution; 1/2-in. Diameter, 2-ft Long Smooth Pipe, $U_j = 867$ fps.

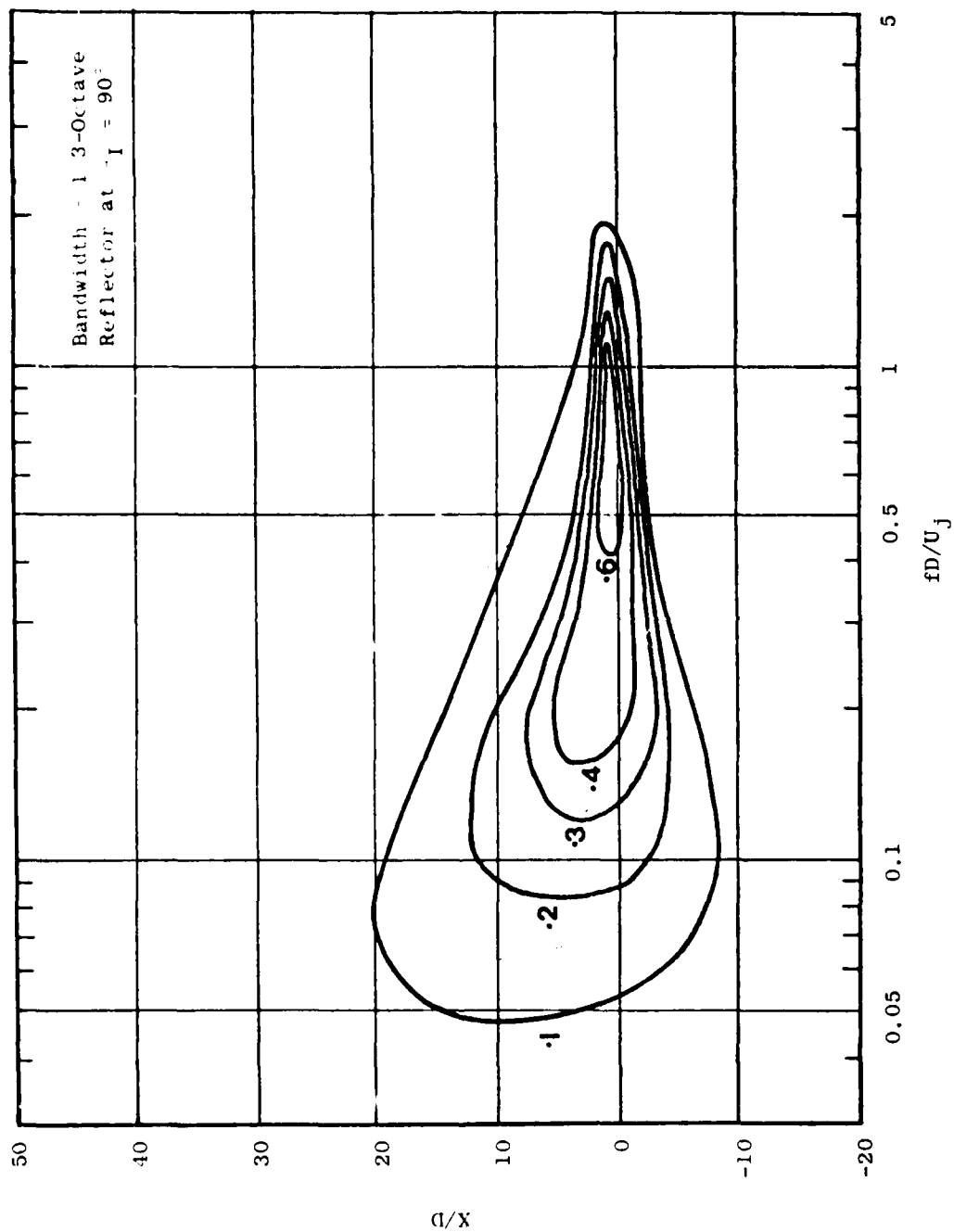


Figure 8-58. Contour Plot of Source Strength Distribution; 1/2-in. Diameter, 2-ft Long Rough Pipe, $U_j = 878$ fps.

located at the nozzle exit is one possibility that is consistent with the measurements: it produces considerably higher intensities for $\theta_1 < 135^\circ$ but its effect diminishes compared to the convectively amplified quadrupole source intensities at larger angles.

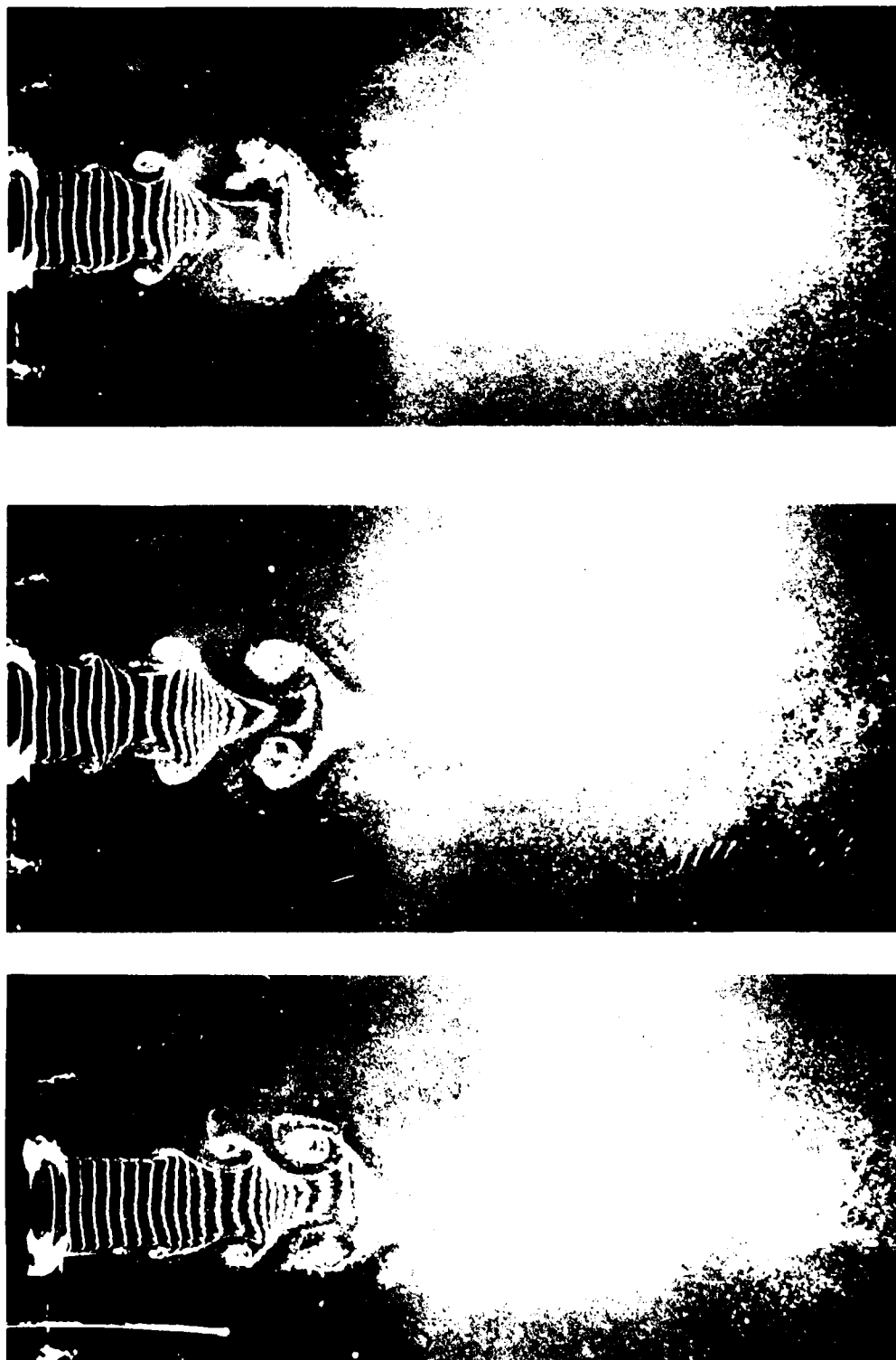
8.3.3.3 Effect of Artificial Periodic Disturbances

The introduction of a controlled, fixed-frequency forcing has a complicated effect on the jet which depends upon the Strouhal number of the forcing and the jet geometry (Strouhal number of forcing is defined as $St_f = fD/U_j$; where f is the frequency in Hz). From observations of jet spreading rates, it appears possible to affect the structure of the jet by periodic forcing, at least in the first ten diameters of the jet. The various jets respond most dramatically to Strouhal numbers of forcing which lie in the range between (1) an upper bound comparable to (or slightly larger than) the Strouhal numbers characteristic of the initial jet instability (in this case about $St_f = 1.25$ at $Re = 5000$) and (2) a lower bound of about $St_f = 0.15$ - 0.20 . Forcing below $St_f = 0.2$ seems to have little effect in the region $x < 10$ diameters downstream. In the range of greatest response, the effect of forcing is to increase the spatial coherence of the flow. For example, fluctuations in the spatial positions of vortex interactions are much reduced. The spatial region along the jet column which is most strongly influenced by the forcing occurs farther downstream with decreasing Strouhal number. That is, forcing the jet at a frequency comparable to the initial instability has a strong organizing influence on the flow near the nozzle exit, while forcing at a lower frequency organizes the flow farther downstream - after an appropriate number of pairings has reduced the characteristic frequency to a value commensurate with the forcing. It also follows that certain lower frequencies - those which are approximate subharmonic multiples, $f_i/2^n$, of the initially unstable frequency, f_i , will elicit **greater response** in the jet.

Figure 8-59 shows (1) the unforced jet contrasted with two examples of forcing (2) $St_f = .88$ and (3) $St_f = 1.12$. The same structure is present in all three cases - in fact the interaction of vortices is even more violent in (2) and (3). Compare, for example, the magnitude of velocities induced along the jet axis (in the potential core) for the forced and unforced cases.

Another observation which can be made from Figure 8-59 is that, at least in the single axisymmetric jet, the vortices seem to lose their organized core structure in the region 4 to 5 diameters downstream. Visualization of the flow, in which a thin layer of dye is introduced into the nozzle boundary layer, thus marking the fluid which initially has vorticity, shows the same result. At about 4 to 5 diameters, the vortices undergo a transformation (possibly as a result of instability), and become much more diffuse regions of vorticity. They remain as individual entities (Crow and Champagne used the term "puffs"), but their interaction must certainly be different after having lost the strongly rotating cores.

The gross influence of forcing for the various jet geometries was studied by comparing the jet spreading rates using dye introduced into the jet plenum



(a) No Forcing

(b) Forcing at $St_f = 0.88$

(c) Forcing at $St_f = 1.12$

Figure 8-59. Hydrogen Bubble Visualization of Axisymmetric Jet Flow at $Re = 5000$, Jet Diameter 1.5 inch, Time Interval Between Lines = 35 m sec.

section. The boundary between jet (dyed) fluid and ambient fluid is easily distinguished. All other details of the flow are lost, but the variations in spreading rates are related to the location and strength of the vortex interactions. The width of the jet at any point is taken to be the maximum extent of dyed fluid. The points are then plotted and smoothed by eye. This is roughly equivalent to fitting an envelope near the points of maximum excursion and ignoring any "holes" of undyed fluid along the irregular jet boundary. Data on spreading rates for the five geometries studied are described below (again it is emphasized that trends rather than numbers are important).

Axisymmetric Jet

The single axisymmetric jet was operated with a smooth-walled nozzle and also with a corrugated ring inserted 1/4-inch upstream from the nozzle exit as described earlier. The data for the jet with corrugated ring showed less scatter and will be presented; results for the smooth-walled jet show the same trends, but have growth rates roughly 15% larger. Figure 8-60 shows the growth of the jet (with corrugated ring) as a function of downstream distance for a Reynolds number of 15,000. In the absence of forcing, the growth of the jet in the first 10 diameters is well fitted by the straight line,

$$W/D = 0.32 \left(\frac{x - x_0}{D} \right), \quad \frac{x_0}{D} = -3.1,$$

independent of Reynolds number (for Re from 5,000 to 15,000). Several data points from photographs presented in the literature are given as a comparison. The effect of forcing is first to increase the growth rate substantially, and later to retard growth. At 10 diameters downstream, the jet may be either wider or narrower than the unforced jet, depending upon the frequency of forcing. The strength of the forced interaction, measured by the departure from the unforced growth rate, is largest for $St_f = 0.45$.

Axisymmetric Jet, Inclined Exit Plane

Surprisingly, the inclination of the exit plane has practically no effect on jet spreading in the absence of forcing. With forcing present, the jet grows more rapidly on the lee side (the side nearest the acute angle of the nozzle cross section). This is illustrated by photographs of the dyed jet in Figure 8-61. Again, the largest interaction occurs for a Strouhal number of about $St_f = 0.45$. The reason for enhanced growth on the lee side is apparently related to the complicated manner in which the vortex pairing interaction takes place. A hydrogen bubble photograph of the flow is shown in Figure 8-62 for a Reynolds number of 5000.

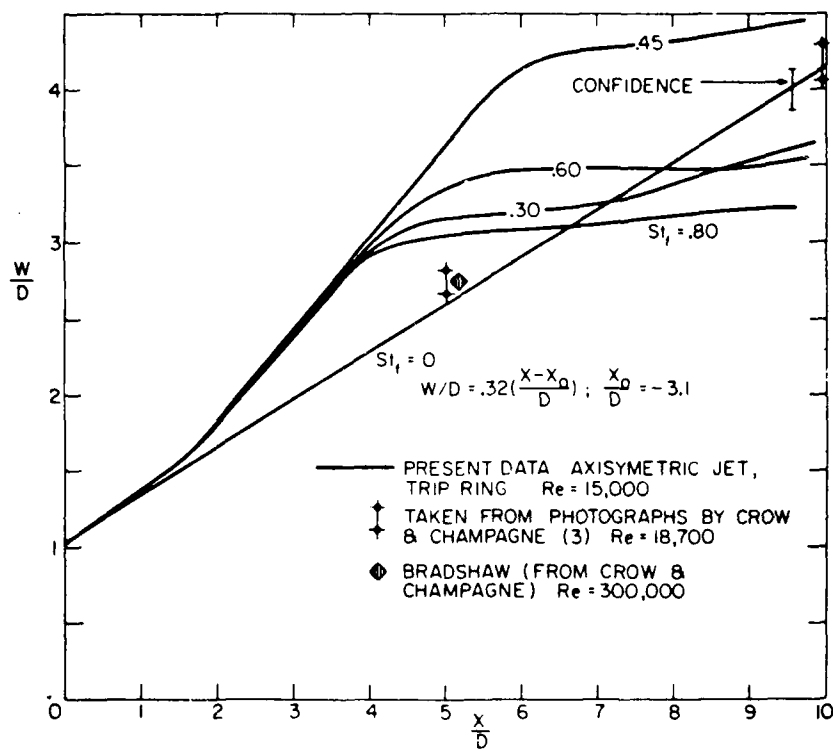


Figure 8-60. Visually Determined Axisymmetric Jet Spreading Rate with Periodic Forcing.



(a) No Forcing



(b) Forcing at $St_f = 0.45$

Figure 8-61. Spreading of Jet with Inclined Exit Plane, $Re = 15,000$.

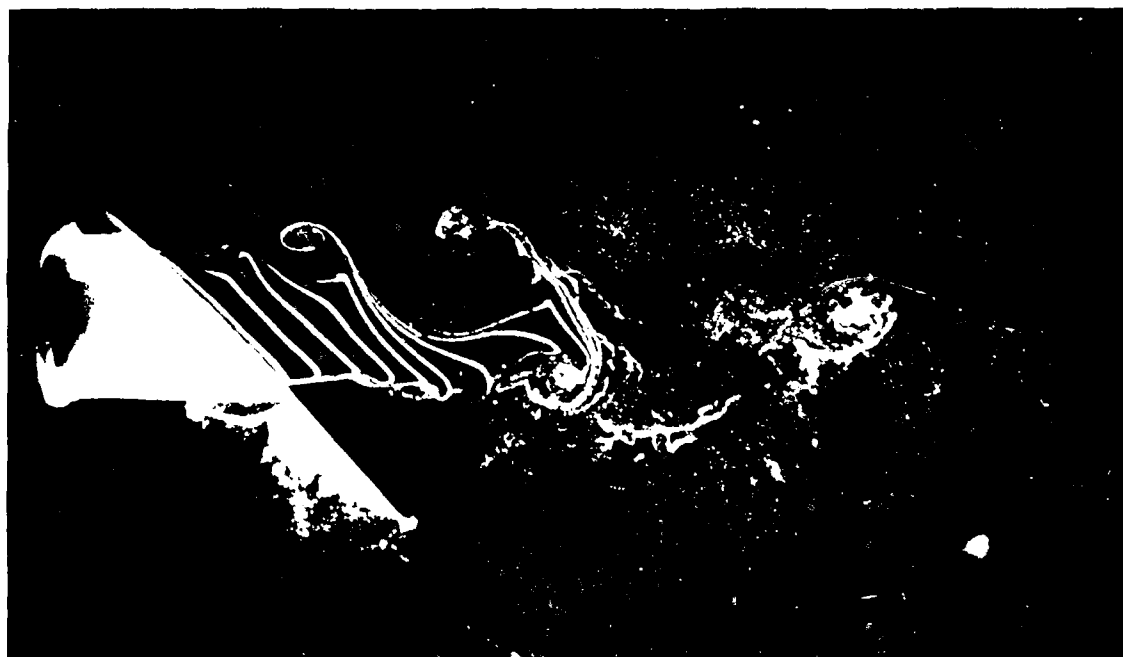


Figure 8-32 Hydrogen Bubble Visualization of Jet with Inclined Exit Plane,
 $Re = 5,000$, $\beta_1 = 0.15$.

AD-A094 291

GENERAL ELECTRIC CO CINCINNATI OH AIRCRAFT ENGINE GROUP F/G 20/1
HIGH VELOCITY JET NOISE SOURCE LOCATION AND REDUCTION, TASK 2. --ETC(U)
MAY 78 T F Balsa, P R GLIEBE, R A KANTOLA DOT-05-30034
R78AE6323 FAA-RD-76-79-2 NL

UNCLASSIFIED

9 9

201

201

201

201

201

201

201

201

201

201

201

201

201

201

201

201

201

201

201

201

201

201

201

201

201

201

201

201

201

201

201

201

201

201

201

201

201

201

201

201

201

201

201

201

201

201

201

201

201

201

201

201

201

201

201

201

201

201

201

201

201

201

201

201

201

201

201

END

DATE

FILED

2 81

DTIC

7 Tube, Hexagonal Array

It is interesting to compare the spreading rate of the tube array with that of the single jet. For this purpose, the width of the turbulent jet and the downstream distance are normalized by the maximum width of the array at the exit plane (equal to 5 times the diameter of the individual tubes). The results are shown plotted in Figure 8-63. With no forcing, the multiple jet width grows at a slightly faster rate than the single jet - at least in the first 5 diameters downstream. The effects of forcing are somewhat different from those of the single jet, however. At the higher Strouhal numbers, the multiple jet initially grows more slowly than in the unforced case. Here the Strouhal numbers are based on the diameter of the individual tubes. Strouhal numbers based upon the maximum width of the array would be 5 times larger.

8.3.4 Conclusions

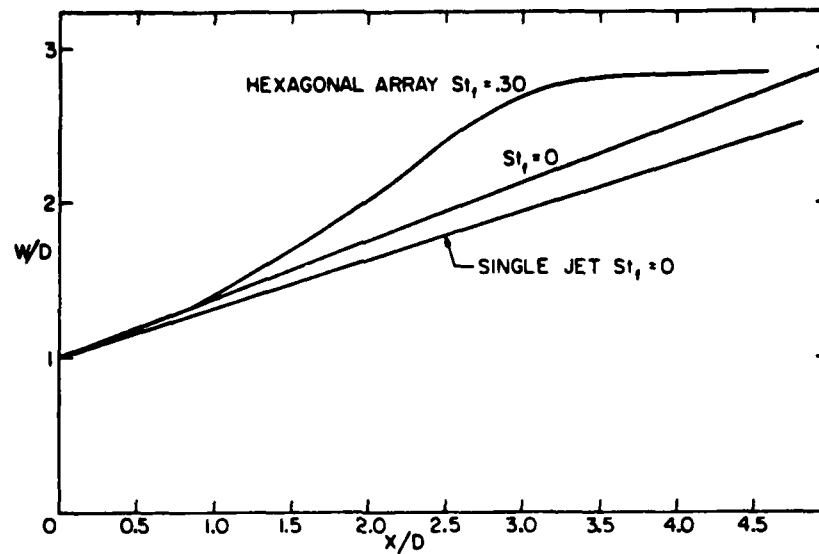
The exploratory experiments described in this report were designed primarily to provide qualitative, basic information concerning two possible techniques that have been suggested for altering the noise characteristics of turbulent jets: (1) redirecting the radiation pattern by the use of elliptic nozzle shapes, and (2) disturbing the exit flow conditions and thereby affecting the mixing process.

The experiments with a 5 to 1 aspect ratio elliptic nozzle produced the following results:

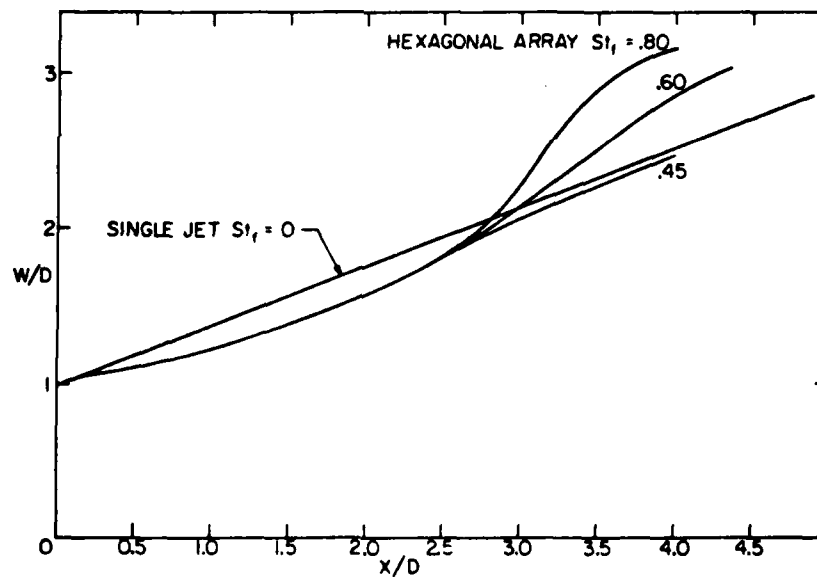
1. No significant differences were found in the directivity characteristics of the noise intensities for subsonic jets;
2. The small but observable increase in radiation intensity around $\theta \approx 135^\circ$ (for both of the measured azimuthal angles) is believed to be caused by a different entrainment process visually observed along the first ten diameters of the jet.
3. It is conjectured that this difference could produce a noticeable decrease in the Mach wave radiation for supersonic jets.

Several experiments have been carried out to study the effect of flow disturbances at the exit plane.

1. If the disturbances at the exit correspond to those of a fully developed turbulent pipe flow having an amplitude on the centerline of about 2% of the mean velocity, only small changes in character of the radiation field are found. Apparently, whatever changes occur in the mixing process due to the disturbed exit conditions must occur only over a few diameters from the exit plane and do not affect appreciably the radiation field. This, however, is not the case for an exit flow corresponding to a rough pipe flow. (The mean discharge velocity is 75% of the center velocity and the centerline fluctuations are about 4% of the mean velocity). In



(a) $St_f = 0, 0.30$



(b) $St_f = 0.45, 0.60, \text{ and } 0.60$

Figure 8-63. Visually Determined Spreading Rate for Hexagonal Array of Jets with Periodic Forcing at $Re_D = 15,000$

this case a strong, high frequency acoustic source was found to exist close to the nozzle exit. It is conjectured that this is produced by mass flow fluctuations across the exit plane.

2. Artificial periodic disturbances (with amplitudes of approximately 3% of the jet velocity) introduced upstream of the nozzle produced measurable changes in the spreading rates of the various jet configurations under investigation. The changes and the axial location of the changes strongly depended on the Strouhal number of the disturbances. It was possible to enhance or to inhibit the local mixing rates of the jet. It is still to be shown whether or not such a method could serve as a practical means to reduce the intensity of jet noise radiation.

8.4 EJECTOR AEROACOUSTICS

Since the mid-1950's, the concept of adding an ejector to the exhaust nozzle of a gas turbine aircraft engine has been under investigation as a means of suppressing jet noise. The results to date have been mixed, i.e., some investigators have reported 10 to 12 dB suppression with the addition of an ejector, while others have found little or no noise reduction. A need therefore, exists to undertake a systematic study of ejector nozzles and understand the principal mechanisms involved in ejector nozzle operation and associated noise emission.

A plan was formulated in the present program to examine the aeroacoustic characteristics of ejector nozzles. An experimental investigation was planned which would consist of a parametric study of the influence of ejector geometric variables (ejector length, axial position and diameter) on the acoustic characteristics for a round, convergent nozzle. Concurrently, an analytical study was formulated which consisted of developing an existing NASA ejector flow analysis for integration into the Task 2 aeroacoustic modeling program. The basic plan was to utilize the NASA ejector flow analysis computer program for predicting the ejector nozzle exit flow conditions, and then use these exit flow conditions as initial conditions to a jet plume mixing calculation, from which the noise could then be calculated. Subsequent comparisons of predicted and measured ejector nozzle jet noise characteristics could then be made to evaluate the relevance of turbulent mixing, convective amplification, and fluid shielding mechanisms in explaining these characteristics.

A survey of the experimental results on ejector nozzle acoustics available in the open literature showed that, for a round, convergent nozzle, the addition of an ejector shroud does not provide significant acoustic suppression unless the ejector length exceeds 10 to 12 primary nozzle diameters. The results of Middleton⁽¹²⁸⁾, for example, show that the peak noise suppression is less than 3 dB for $L/d \leq 12$, where L = ejector length and d = primary nozzle diameter. A maximum suppression of 7 to 8 dB was demonstrated for $L/d = 32$. These results are shown in Figure 8-64. Practical exhaust nozzle systems cannot tolerate ejector lengths much greater than $L/d \sim 1.5$ to 2.0, due to the severe weight penalty incurred.

Based on the previous results obtained by other investigators [Middleton⁽¹²⁸⁾ summarizes the early NACA work], it was concluded that additional parametric experiments on conical nozzle/ejector systems are of little practical value. It was found, however, from the survey of previous work, that ejectors, when combined with suppressor nozzles (e.g., lobe nozzles, multi-tube nozzles, etc.) can provide additional modest noise reductions (2 to 4 dB) over the bare primary nozzle levels without excessive ejector lengths. Experimental evaluation of several suppressor nozzles with ejectors has been carried out in Task 3 of the present program.

A computer program for predicting the internal flow field of ejector nozzle systems was developed by Anderson⁽¹²⁹⁾ of NASA. This program was provided to General Electric Company by NASA-Lewis and was subsequently modified for use on the GE computer facilities. A computer users manual for

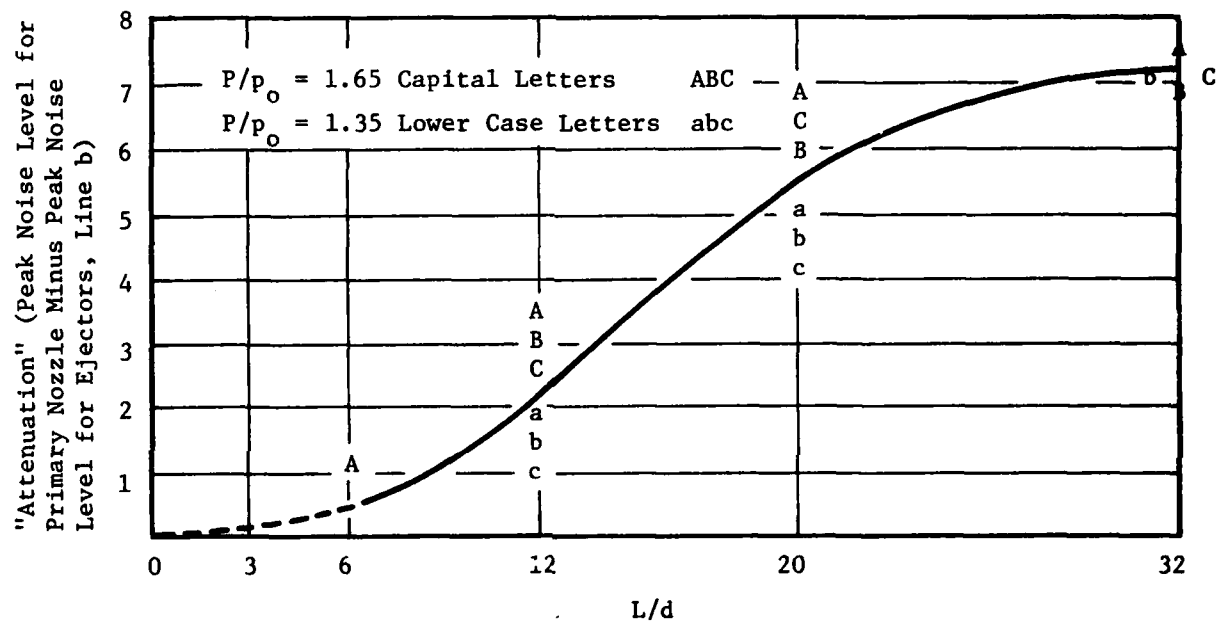


Figure 8-64. Attenuation Versus Nondimensionalized Ejector Length, Conical Primary Nozzle (Middleton, Ref. 128).

the GE version was written [Bridges⁽¹³⁰⁾], and the capability for automatic computer-plotting of nozzle flow field characteristics was incorporated (an example of which is shown in Figure 8-65).

After exercising the ejector nozzle program for several nozzle configurations and operating conditions, it was found that it had certain limitations which prevented it from being a useful tool in predicting ejector noise. Specifically, it is only applicable to primary nozzles operating at supercritical pressure ratios which are sufficiently high so as to preclude the occurrence of subsonic flow regions inside the ejector nozzle. No provision is made for computing subsonic flow in the primary stream. It was not possible to obtain ejector exit plane solutions at pressure ratios corresponding to engine takeoff power settings. Additionally, it is limited to axisymmetric nozzles, so that suppressor configurations cannot be handled with this procedure. Because of these limitations, further development of the NASA ejector nozzle flow analysis program was not warranted, and an entirely new ejector nozzle flow prediction procedure is not practical.

A discussion of the acoustic properties of ejectors in terms of physical shielding mechanisms is given in Section 4.8 of this report.

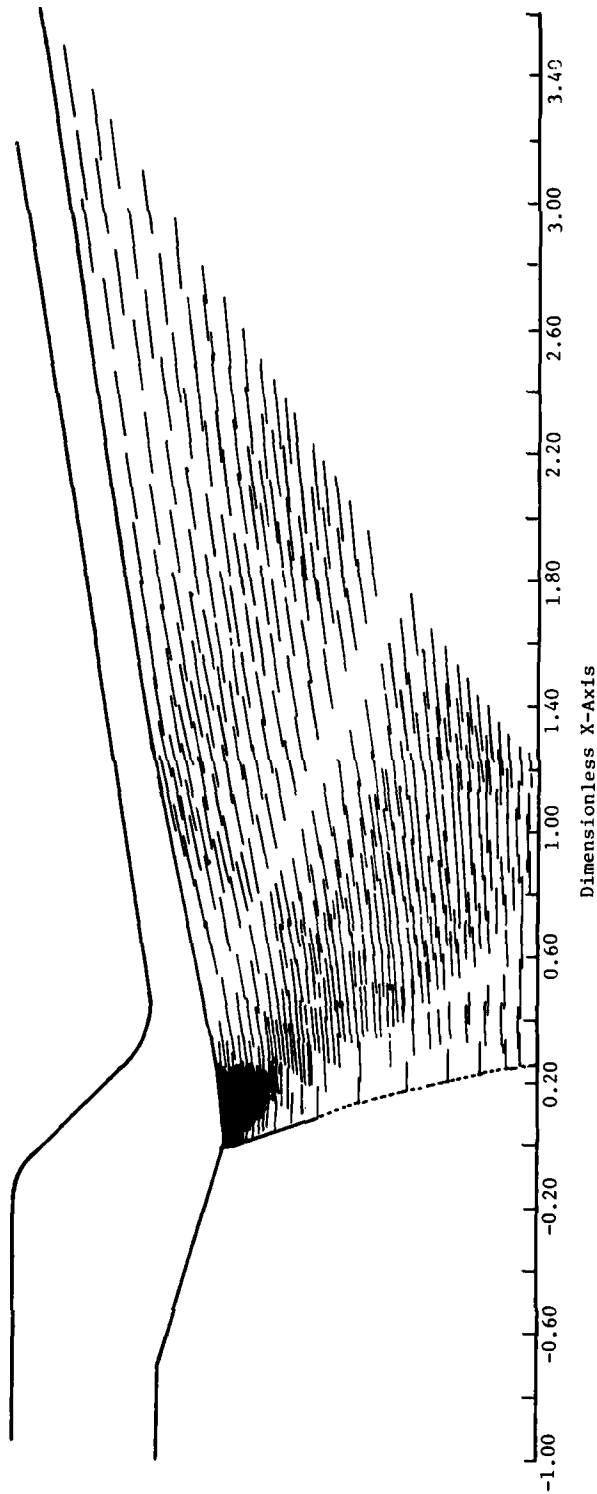


Figure 8-65. Example Ejector Nozzle Flow Field (Program Generated).

8.5 PHYSICAL OBSTRUCTION NOISE

This section addresses the issue of excess noise that may be generated by the placement of suppressor elements normal to the flow path, such as spokes or chutes.

Two pertinent literature sources in this area are Gordon⁽¹³¹⁾ and Yudin⁽¹³²⁾ which studied experimentally the noise generated by the insertion of obstructions in pipes carrying flow. The most important conclusion reached is that the total noise radiated by such obstructions can be successfully correlated by the total pressure drop induced by such elements, in other words, by a formula of the type:

$$P = k (\Delta p)^3 D^2 / \rho_a c_a^3 \quad (402)$$

where P is the total noise power radiated due to insertion of the obstruction, Δp the total pressure drop induced by the insertion of the element, D the diameter of the pipe carrying the flow, ρ_a the density of the ambient medium and c_a the speed of sound of the ambient. k is a nondimensional constant (discussed later).

The remarkable feature of equation (402) is that, independent of the type of "spoiler" or obstruction element, the total pressure drop induced by the element suffices to characterize its noise generating potential. There is no dependence in equation (402) on the Reynolds number, although the total pressure drop itself is a function of Reynolds number through its dependence on obstruction drag coefficient C_D . Neither study reports any dependence on the flow Mach number but this may be related to the fact that the tests were primarily for low Mach numbers flows, i.e., $M < 0.3$.

Both references (131 and 132) point out that a dependence of type (402) can be expected if a free field dipole type mechanism is postulated and if some additional assumptions are made regarding the strength and frequency of the free field dipole. The argument is as follows. The total power radiated by a point dipole oscillating in a free field at frequency f and strength F_u can be shown to be

$$P \sim F_u^2 f^2 / \rho_a c_a^3 \quad (403)$$

assuming first that the unsteady force exerted by such an obstruction is proportional to the steady drag force F exerted by such an obstruction element. In the above, $F \sim (\Delta p) D t$ where (Δp) is the total pressure drop produced by the steady flow past the obstruction D , the pipe diameter and t the thickness of the obstruction (" t " is identified in reference 131 more with the thickness of the wake created by the obstruction). The velocities U created by the constricting effect of the obstruction will be of order $\sqrt{(\Delta p) / \rho_a}$ and the frequency f of the dipole excitation mechanism is assumed to vary as U/t . Substituting the above into equation (403) leads to (402). Gordon credits Yudin with this rather simple but effective scheme of basing the power prediction on (Δp) . Gordon⁽¹³¹⁾ demonstrates that for a wide range of obstruction types, except for

classical eighth power law (i.e., power $\sim (\Delta p)^4$) jet noise contamination at high (Δp) , an equation of type (402) succeeds in collapsing the data. With regard to "k", Gordon finds that for obstructions deeply embedded in semi-infinite pipes, "k" has a value of about $(2.5) \cdot 10^{-4}$. For jet noise applications, however, one is more interested in obstructions located at the pipe exit plane. For these obstruction types, Gordon finds a much lower value of "k" of $(3) \cdot 10^{-5}$. Except for some limited test data by Gordon, there is very little information on the case of obstructions located at the nozzle exit plane in either reference 131 and 132.

The collapse of the power spectrum achieved by Gordon is not as satisfactory as that for the total power, but he does show the following: Defining a constricted velocity U_ℓ by $\sqrt{2\Delta p/\rho_a}$, the power spectrum on a percent bandwidth basis (i.e., one-third octave, etc.) peaks at $[(0.4) U_\ell/t]$ and varies as $f^{3/2}$ from low frequencies up to this peak value, and as $f^{-0.8}$ thereafter. Finally (at least for low Mach number flows), the relative directivity of this noise source is essentially very similar to that of classical jet noise at the same frequency.

Summarizing the above discussion for prediction purposes, note the following: The total pressure drop (Δp) induced by the obstruction element is of crucial significance and must be determined either experimentally or deduced from prior experience. The total power can then be estimated from equation (402) with $k = (3)(10^{-5})$ for obstruction elements located at the nozzle exit plane and $k = (2.5)(10^{-4})$ for obstruction elements located well upstream (within the pipe) of the nozzle exit plane. The power spectrum on a percent bandwidth basis peaks at a frequency $[(0.4) U_\ell/t]$ where $U_\ell = \sqrt{2\Delta p/\rho_a}$ and t = transverse thickness of the obstruction (i.e., maximum width of a chute or spoke element, etc.). Up to the peak frequency, the variation with frequency of the percent bandwidth power spectrum is as $f^{3/2}$ and subsequently as $f^{-0.8}$. The directivity of this obstruction noise mechanism appears to be the same as that of jet noise at the same frequency.

As noted in Section 10.0, it would be desirable to conduct further experimental studies of physical obstruction noise with high velocity, high temperature flows, with obstructions located at the exit of the nozzle. A problem may arise, however, with this high-velocity/high-temperature regime, in separating out the contribution of physical obstruction noise from that of jet mixing noise. A much more comprehensive discussion of obstruction noise appears in reference 137.

9.0 CONCLUDING REMARKS

The major thrust of Task 2 of this program has been to examine, explore, and quantify various mechanisms thought to play an important role in the generation and/or emission of jet noise. The approach has been to conduct parallel theoretical and experimental studies of these mechanisms, with the experiments specifically designed to compliment and/or verify the theoretical results. Emphasis has also been placed on mechanisms responsible for the suppression and reduction of jet noise.

It has been concluded that jet noise is primarily a result of turbulent mixing processes occurring in the jet plume itself. The turbulent momentum fluctuations produced in the shear layers of the jet are the primary source of noise generation. The turbulent fluctuations behave as multipole sources of sound which convect downstream with the flow. Their emission is altered through convective amplification due to source motion, and through acoustic shielding by the surrounding jet flow itself. For underexpanded jets operating at supercritical pressure ratios, an additional mechanism, shock-cell broadband noise, contributes significantly to the total jet noise spectrum, particularly in the forward quadrant. The many experimental and theoretical studies conducted during the course of Task 2 have pointed to the above mechanisms as primarily responsible for the observed characteristics of jet noise.

The unified aeroacoustic jet noise prediction model which has been developed is considered to be a major product of the Task 2 effort. This model embodies the mechanisms discussed above, and synthesizes the jet plume as a collection of uncorrelated, convecting, turbulent-eddy sound sources embedded in a parallel shear flow. The model, based on analytic descriptions of both the aerodynamic and acoustic characteristics of the jet, is capable of predicting the observed jet noise for a wide variety of jet nozzles over a wide range of operating conditions.

Based on the data/theory comparisons made in this study for both static and in-flight cases, it is concluded that the turbulent-mixing noise generation/convection/shielding mechanisms, in combination with the shock-cell noise mechanism, sufficiently explain the observed characteristics of jet noise, at least for jet velocities higher than ~ 1400 fps. There does not appear to be any significant unexplained excess noise mechanism responsible for the observed noise changes due to flight, and in fact the above aero-acoustic model adequately predicts these changes.

Several areas have been identified where improvements in the aero-acoustic model would be desirable. These include (1) a better description of the time-dependent turbulent structure parameters relevant to jet noise (length-scale, convection speeds, correlation spectra, etc.), (2) modeling of the base pressure effects for multielement nozzles, (3) incorporation of initial turbulence level effects, and (4) extension of the shock-cell noise prediction to multielement/multiflow configurations. All of these improvements are possible within the present model framework.

10.0 RECOMMENDATIONS FOR FURTHER WORK

10.1 AEROACOUSTIC MODEL

Since shock noise is known to be quite important under certain conditions, a generalized procedure of shock noise prediction is desirable. The Harper-Bourne/Fisher⁽⁶⁹⁾ method is restricted to the round nozzle static case. The method has been generalized to some extent in the present report by extending it to cover rectangular nozzles and by extending it to the flight case for round nozzles by the use of the dynamic correction $(1 - M_F \cos \theta_I)^{-4}$, but much more remains to be done in terms of a general procedure applicable to dual flow systems, suppressor nozzles, etc. It is quite probable that to accomplish this, a simplified method to predict shock structure aft of arbitrary nozzles will have to be developed.

The "turbulent mixing" analysis employed currently only predicts time independence plume properties and deduces the relevant time-dependent properties needed to predict jet noise by locally applied similarity arguments. Some of the more recent mixing analyses such as those associated with Spalding and his co-workers are (in principle) capable of predicting quantities such as length scales, etc. Incorporation of such methods may be warranted if systematic failures are found with the present method in future applications. Such a step must be taken with great caution, however, since these newer methods would add considerable complexity and cost to the computer program used in the present version of the method (and thus decrease its utility as a preliminary design tool).

Much more data-theory calibration and "fine tuning" of the present method needs to be carried out for the case of flight jet noise. This can be done as more reliable clean flight data become available for exhaust systems other than the round, conical nozzles.

In this report, a logical extension of Reichardt's method to allow for nonconstant static pressure mixing has been presented. However, this extension required the specification a-priori of these base pressure variations, and for this reason, was not exercised in the present report to predict jet noise, even in circumstances such as small area ratio suppressor nozzles where these effects may be important. Further work to implement this extension is desirable.

The aeroacoustic model has been used in the present task primarily as a far-field SPL spectrum prediction tool. However, it is capable of much more in that a wide variety of diagnostic and parametric calculations can be performed with it. As an example, since it basically uses a "lump-of-jet" approach (discretizes the jet plume into a very large number of small volumes and computes the radiation from each), it is in fact an analytical source location tool. That is, it can predict which part of the jet contributed what to the far-field SPL spectrum. Similarly, by running the

program in three options, first in totality, second by suppressing the fluid shielding terms, and third by suppressing the fluid shielding and convective amplification terms, one can assess in a given situation how much of the suppression can be attributed to source reduction, how much to fluid shielding, and how much to reduced convective amplification. By virtue of this ability to inexpensively run large numbers of diagnostic and parametric calculations, significant optimum design procedures may emerge. One such example already achieved was the 54-element coplanar suppressor nozzle tested in Tasks 3 and 5, which was conceived by the Task 2 program.

The inapplicability of the NASA Lewis ejector aerodynamic program at takeoff conditions prevented the extension of the present aeroacoustic model to predict jet noise with ejector nozzles. (An engineering correlation method of predicting ejector acoustic performance, however, is outlined in Task 3.) Should the employment of treated ejectors become a serious option for jet noise suppression, the extension of the aeroacoustic method to predict ejector aeroacoustics from "first principles" is recommended.

10.2 EXPERIMENTAL WORK

In application, the primary interest in jet noise is in heated jet flows, and the bulk of the experiments reported here as well as in the literature are for hot, high velocity flows. This poses a problem because temperature and velocity effects are combined. More fundamentally, since there is at present no convenient nonintrusive instrument comparable to the LV capable of mapping the temperature field in high velocity, high temperature jet flows, it has not been possible to check the predictions of Reichardt's method for temperature prediction as has been possible for the velocity prediction. Several laser techniques for temperature measurement based on Rayleigh and Raman scattering are under development, and as such techniques reach the maturity of current LV capability, independent checks of plume temperature prediction ought to be carried out. Since fluid shielding is both temperature and velocity sensitive, there is a need to independently measure both these quantities. Lacking such capability, additional isothermal or cold flow tests could be included in future work (although they are limited in relevance and limited in the velocity to which testing can be carried out) without confusing effects due to intrusion by shock noise.

Flow obstruction noise, especially as related to multichute, multispoke nozzles needs further experimental investigation.

Finally, as LV systems develop the same low cost versatility for time-dependent turbulence measurements as they currently possess for time-independent measurements, it would be highly desirable to make such measurements to check the validity of the similarity arguments used currently in

the aeroacoustic prediction method to see if these relations are correct. Such a study may reveal that either the similarity methods are acceptable (perhaps with revision) or that more time-consuming mixing analyses with capability of predicting time-dependent quantities need to be developed.

743/724

771

APPENDIX A

JET FLOW FIELD CALCULATION

The purpose of this appendix is to document very briefly the ideas that were used in the turbulence mixing calculations and in the coupling of this to the acoustic theory in Section 4.2.3. This particular development, described by the term "slice of jet," was originally used in the unified aeroacoustic predictions; later, it was replaced by a more sophisticated and detailed procedure which is described in Sections 4.5 and 4.7. Because the latter version is the current (and final) version of the aeroacoustic prediction scheme, the slice-of-jet approach will be described without all the details. The use of this approach is not recommended because it becomes quite inaccurate at high jet velocities (~ 1500 fps).

JET PLUME AERODYNAMICS

An aerodynamic prediction of the jet plume is required to provide the strength of the noise sources. The method selected is an extension of Reichardt's theory [Schlichting⁽⁶⁸⁾], which basically synthesizes the complex flows from nozzles of arbitrary geometry by superposition of a suitable distribution of elemental round jet flows. This approach was first suggested by Alexander, et al.⁽¹³³⁾ and applied directly to suppressor nozzle configurations by Lee, et al.⁽⁷⁶⁾ and Grose and Kendall⁽⁷⁷⁾.

Reichardt's theory is a semiempirical one, based on extensive experimental observations that the axial momentum flux profiles were bell-shaped or Gaussian in the fully developed similarity region (suitably far downstream) of a jet. From this observation, a hypothesis for the relation between axial and transverse momentum flux was formulated which yields a governing equation for the axial momentum flux. For the far downstream similarity region of a round jet with nozzle area A_j and exit velocity U_j , the governing equation and solution are as follows:

$$\frac{\partial}{\partial x} \langle \rho u^2 \rangle = \frac{\lambda(x)}{r} \frac{\partial}{\partial r} \left(r \frac{\partial}{\partial r} \langle \rho u^2 \rangle \right) \quad (A-1)$$

$$\langle \rho u^2 \rangle = \rho_j U_j^2 \frac{A_j}{\pi b_m^2} e^{-(r/b_m)^2} \quad (A-2)$$

where

$$\lambda(x) = \frac{1}{2} b_m \left(\frac{d b_m}{dx} \right) \quad (A-3)$$

(171)

and $b_m(x)$ is the axial momentum mixing region width, taken to be proportional to the axial distance x from the nozzle exit plane,

$$b_m(x) = C_m x \quad (A-4)$$

The jet spreading rate C_m becomes a key parameter in the theory and is determined experimentally. The coordinate system is shown in Figure A-1.

Because equation (A-1) is linear, the summation of elemental solutions is also a solution. This unique feature of Reichardt's theory allows the construction of quite complex jet flows with relatively simple mathematics. Although more rigorous (but containing just as much empiricism, albeit in different forms) theories are available for simple round and plane jets, there is no other technique available which offers the capability for modeling jet flows typical of aircraft engine suppressor nozzles such as multitube, lobe, and chute nozzles, etc.

Consider a distribution of elemental jets issuing parallel to the x -axis, whose exit areas lie in the $x = 0$ plane. Each elemental jet has an exit area $A_j = \sigma d\sigma d\alpha$, located at $(\sigma, \alpha, 0)$, as shown in Figure A-1. The axial momentum flux at a downstream point (r, θ, x) due to the elemental jet exhausting at $(\sigma, \alpha, 0)$ is given by

$$d\langle \rho u^2 \rangle = \rho_j U_j^2 (\sigma d\sigma d\alpha / \pi b_m^2) e^{-(\xi/b_m)^2} \quad (A-5)$$

where $\xi^2 = r^2 + \sigma^2 - 2r\sigma \cos(\theta - \alpha)$

Integrating (A-5), the following solution is obtained:

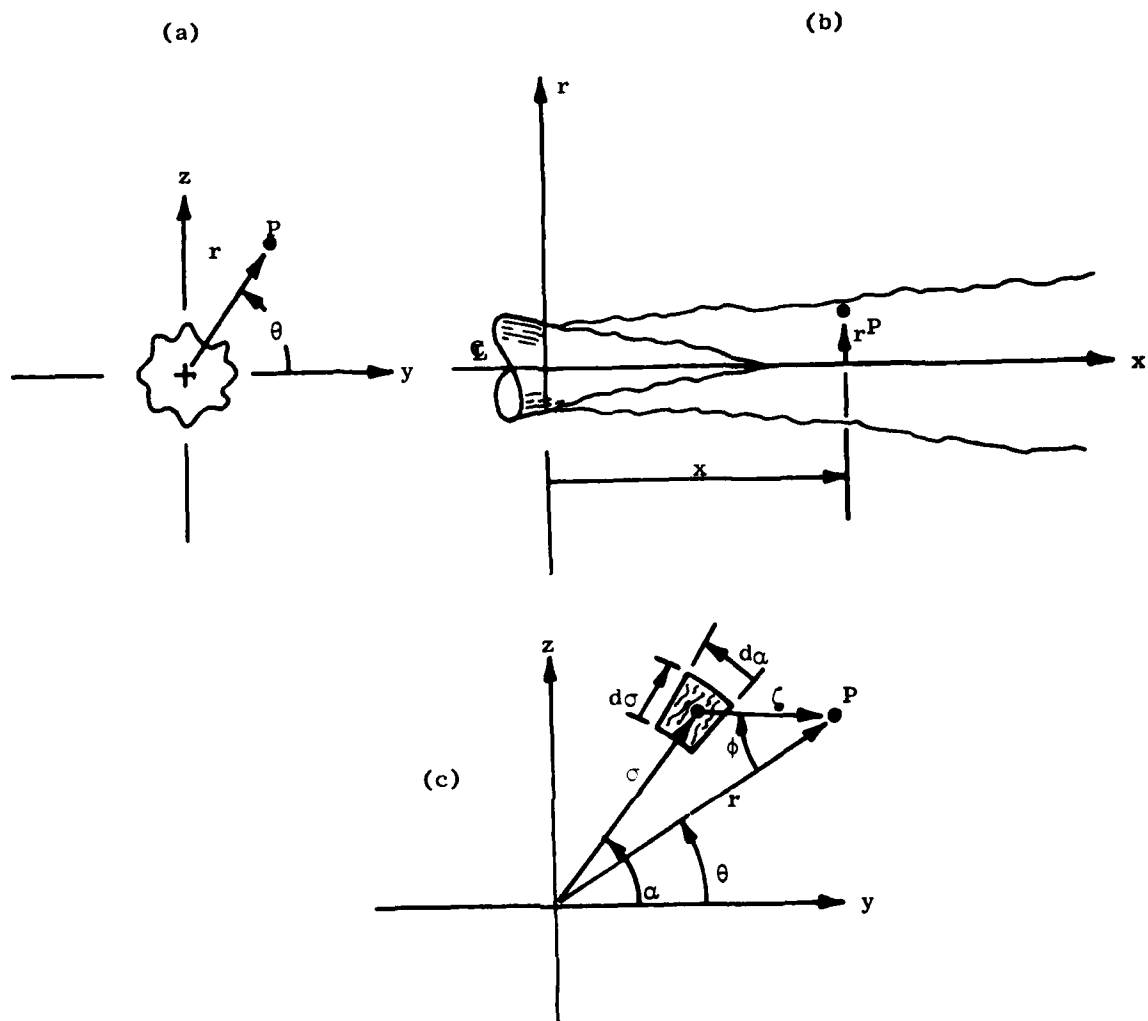
$$\langle \rho u^2 \rangle(r, \theta, x) = \frac{1}{\pi b_m^2} \iint (\rho_j U_j^2) e^{-(\xi/b_m)^2} \sigma d\sigma d\alpha \quad (A-6)$$

From the distribution of $(\rho_j U_j^2)$ in the exit plane, the local value of $\langle \rho u^2 \rangle$ at any point (r, θ, x) can be found from equation (A-6) by standard numerical integration. Assuming that the jet plume stagnation enthalpy flux H diffuses in the same manner as axial momentum, an analogous expression for stagnation enthalpy flux $\langle \rho u H \rangle$ can be derived,

$$\langle \rho u H \rangle(r, \theta, x) = \frac{1}{\pi b_h^2} \iint (\rho_j U_j H_j) e^{-(\xi/b_h)^2} \sigma d\sigma d\alpha \quad (A-7)$$

where b_h is the thermal shear layer width, taken to be proportional to x ,

$$b_h = C_h x, C_h = \text{constant} \quad (A-8)$$



- (a) Nozzle Exit Plane;
 (b) Plume in (r, x) -Plane;
 (c) Nomenclature for Elemental Jet at (σ, α, ϕ) and Field Point P.

Figure A-1. Jet Flow Coordinate System.

The stagnation enthalpy is defined as $H = c_p T + \frac{1}{2} u^2 - c_p T_0$, and the thermal layer spreading rate C_h must also be obtained experimentally. Assuming that the jet mixing occurs at constant static pressure equal to the ambient value, the solutions for $\langle \rho u^2 \rangle$ and $\langle \rho u H \rangle$ given by equations (A-6) and (A-7) are sufficient to determine the distributions of mean axial velocity \bar{u} and temperature \bar{T} throughout the jet plume.

In addition to the jet plume mean flow properties, the turbulent Reynolds stress, assumed to be proportional to the transverse momentum flux, can also be obtained. Reichardt's hypothesis [from which equation (A-1) evolved] states that the transverse momentum flux is proportional to the transverse gradient of the axial momentum flux, the proportionality factor being $\lambda(x)$. For a simple round jet, from equations (A-2) through (A-4), the Reynolds stress τ is given by

$$\tau = - \langle \rho u v \rangle \approx - \lambda \frac{\partial}{\partial r} \langle \rho u^2 \rangle = C_m \rho_j U_j^2 \frac{A_j}{\pi b_m^2} \frac{r}{b_m} e^{-(r/b_m)^2} \quad (A-9)$$

For an elemental jet exhausting at $(\sigma, \alpha, 0)$ the shear stress τ at (r, θ, x) lies along a line connecting $(\sigma, \alpha, 0)$ and the projection of (r, θ, x) onto the $x = 0$ plane. This vector is at an angle ϕ to the coordinate direction r (Figure A-1). The radial component of the shear stress $d\tau$ at point (r, θ, x) due to an elemental jet exhausting at $(\sigma, \alpha, 0)$ is then $d\tau_r = d\tau \cos \phi$. Similarly, the azimuthal component is $d\tau_\theta = d\tau \sin \phi$. Performing the same summation and limiting process over all elemental jets, the total shear stress at (r, θ, x) is then found to be

$$\tau = (\tau_r^2 + \tau_\theta^2)^{1/2} \quad (A-10)$$

where

$$\tau_r(r, \theta, x) = \frac{C_m}{\pi b_m^2} \iint \rho_j U_j^2 (\xi/b_m) e^{-(\xi/b_m)^2} \cos \phi \sigma d\sigma d\alpha \quad (A-11)$$

and $\tau_\theta(r, \theta, x)$ is given by a similar expression with $\cos \phi$ replaced by $\sin \phi$. The distance ξ is again given by the expression following equation (A-5), and the angle ϕ is given by

$$\xi \cos \phi = r - \sigma \cos(\theta - \alpha) \quad (A-12)$$

The above equations provide the basic expressions for computation of the jet plume flow parameters \bar{T} , \bar{u} and τ for a nozzle of arbitrary exit cross-section and exit distribution of velocity and temperature. It may be noted that, for axisymmetric nozzles, $\tau = \tau_r$ and $\tau_\theta = 0$. This will be the case for the

coaxial jet problem discussed in later sections, but the more general formulation is presented for completeness. The basic limiting assumptions made were: (1) the jet plume mixing occurs at constant static pressure equal to the ambient value, and (2) the flow is primarily axial with all nozzle exit elements in the same plane $x = 0$.

NOISE INTENSITY SPECTRUM AT 90°

The aerodynamic characteristics of the jet plume provide the information required to evaluate the acoustic intensity spectrum at 90° to the jet axis using the Lighthill-Ribner theory of jet noise. This basic spectrum provides a good* estimate of the far-field noise spectrum at 90° to the jet axis since sound/flow interaction effects are minimal there. Then the noise at any other point in the far field can be computed from this result and the directivity pattern derived in the main part of this section. The analysis presented below parallels the work of Ribner⁽¹³⁴⁾ and Powell⁽¹³⁵⁾; especially the work of the latter, as it relates to the use of various similarity arguments.

The far-field mean-square sound pressure, in absence of sound/flow interaction effects is given by [Ribner⁽¹³⁴⁾, Lighthill⁽⁴²⁾]

$$\langle p^2 \rangle (R, \theta, \theta) = \frac{x_1 x_j x_k x_l}{16 \pi^2 c_0^2 R^6} \iint \frac{\partial^2}{\partial t^2} (\rho v_i v_j) \frac{\partial^2}{\partial t^2} (\rho v_k v_l) > d^3 \vec{y}' d^3 \vec{y}''$$

where $(\rho v_i v_j)$ is the fluid momentum flux (i, j) component evaluated at vector position \vec{y}' and t' and $(\rho v_k v_l)$ is the (k, l) component evaluated at \vec{y}'' and t'' . The retarded times t' and t'' are given by $(t - R'/c_0)$ and $(t - R''/c_0)$, respectively. Note that v_i and x_i denote the i components of velocity and source-to-observer distance R , respectively. Defining separation vectors and time delay $\vec{\eta} = \vec{y}' - \vec{y}''$ and $T = t' - t''$, respectively, and an eddy coordinate $\vec{y} = \frac{1}{2}(\vec{y}' + \vec{y}'')$, the above expression may be written in the following form

$$\langle p^2 \rangle (R, \theta, \theta) = \frac{x_1 x_j x_k x_l}{16 \pi^2 c_0^4 R^6} \iint \frac{\partial^4}{\partial T^4} (\rho v_i v_j) (\rho v_k v_l) > d^3 \vec{\eta} d^3 \vec{y} \quad (A-13)$$

where

$$x_1 = R \cos \theta, x_2 = R \sin \theta \cos \theta, \text{ and } x_3 = R \sin \theta \sin \theta.$$

In order to evaluate equation (A-13), some assumptions about the turbulent structure must be made. Because of the lack of detailed experimental or theoretical information, approximations are made following the pioneering work of Ribner⁽¹³⁴⁾ and Powell⁽¹³⁵⁾.

*This statement is the most accurate for unheated jets.

The derivatives with respect to T are assumed to be equivalent to multiplying by a typical eddy fluctuation frequency ω relative to the moving eddy and the integral over the separation is equivalent to multiplication by ℓ^3 where ℓ is the eddy length scale. Thus

$$\langle p^2 \rangle (R, \theta, \theta) \sim \frac{x_i x_j x_k x_l}{16 \pi^2 c_0^4 R^6} \int \ell^3 \omega^4 \langle (\rho v_i v_j) (\rho v_k v_l) \rangle d^3 y \quad (A-14)$$

Since the aerodynamic model described in the previous section provides radial and azimuthal distributions of flow properties \bar{u} , \bar{T} , τ_θ , and τ_r at successive axial stations x , it is convenient to express the volume integration in (A-14) as $d^3 y = dS(x) dx$, where $S(x)$ is the cross-sectional area of the plume. The summation over all components (i, j) of the fluctuating momentum stress tensor in equation (A-14) yields one term that is omnidirectional (self-noise) and another term having a basic directivity of $(\cos^4 \theta + \cos^2 \theta)$. The latter is called shear noise; see, for example, the work of Ribner(39). The shear noise shall not be discussed for the reason given by Mani(37,38).

Confining attention to $\theta = 90^\circ$ for the moment, and referring to $\langle p^2 \rangle$ at $\theta = 90^\circ$ as the intrinsic or basic noise spectrum, it is now assumed that $\langle \rho v_i v_j \rangle$ in (A-14) is approximately represented by the turbulent shear stress τ . In addition, the typical frequency ω is assumed to be related to \bar{u} , ρ and τ by the equation

$$\omega \sim (\tau/\rho)^{1/2} / \ell \quad (A-15a)$$

and that

$$\ell \sim (x/\bar{u})(\tau/\rho)^{1/2} \quad (A-15b)$$

These assumed relationships, derived from similarity arguments by Lee, et al.(76), are consistent with the experimental measurements of Davies, et al.(16). The basic or intrinsic acoustic pressure level is then as follows, after combining (A-14 and A-15)

$$\langle p_0^2 \rangle \sim \frac{1}{16 \pi^2 c_0^4 R^2} \iint \rho^2 \bar{u} (\tau/\rho)^{7/2} dS(x) dx/x \quad (A-16)$$

Equation (A-15) implies that the typical eddy fluctuation frequency at any axial location x is given by

$$f = \frac{\omega}{2\pi} \sim \frac{\bar{u}}{x} \quad (A-17)$$

In practice, it was found that, through model calibrations with low velocity round jet data, (A-17) should be modified as follows:

$$f D/\bar{u}_M = 10(x/D)^{-4/3} \quad (A-18)$$

where \bar{u}_M is taken to be the maximum mean velocity at a given cross section. From equations (A-16) and (A-18), the source spectrum can be computed through the approximation, as suggested by Powell(135)

$$\frac{d}{df} \langle p_0^2 \rangle = \frac{dx}{df} \frac{d}{dx} \langle p_0^2 \rangle$$

Note that D is a characteristic length scale of the jet nozzle. For a round jet, D is simply the nozzle diameter. For a coaxial jet, D is defined in the main section. Substituting equations (A-16) and (A-18) into the above expression, the following equation for the far-field intrinsic spectrum at $\theta = 90^\circ$ results:

$$d\langle p_0^2 \rangle (f) \sim \frac{df/f}{16 \pi^2 c_0^4 R^2} \left[\frac{x}{\bar{u}_M} \frac{d\bar{u}_M}{dx} - \frac{4}{3} \right]^{-1} \int \rho^2 \bar{u}(\tau/\rho)^{7/2} dS(x) \quad (A-19)$$

To summarize the results of this Appendix, the intrinsic noise spectrum in the absence of convection and refraction effects at $\theta = 90^\circ$ is obtained from numerical evaluation of equation (A-19). This expression involves an integration, over the jet plume cross section, of a suitable source strength $[\rho^2 \bar{u}(\tau/\rho)^{7/2}]$, comprised of flow parameters, ρ , \bar{u} , and τ , which are evaluated from the extended Reichardt model discussed in this appendix.

APPENDIX B

RELATION BETWEEN C_m AND C_h

For an axisymmetric, round jet with uniform exit conditions, the momentum and heat transport is given by

$$f(x, r, \phi) = \frac{f_j}{\pi b_f^2} \int_0^{2\pi} \int_0^{d/2} e^{-R^2/b_f^2} v dv d\alpha \quad (B-1)$$

where $f = \overline{\rho u^2}$ for momentum transport and $f = \overline{\rho u h}$ for heat transport. The corresponding shear layer thicknesses are $b_m = C_m x$ for momentum and $b_h = C_h x$ for heat. The variable R is given by

$$R^2 = r^2 + v^2 - 2 r v \cos(\phi - \alpha) \quad (B-2)$$

After substituting (B-2) into (B-1) and performing some rather tedious algebraic manipulations, it can be shown that (B-1) can be rewritten in the following form [see, e.g., Gliebe (136)]:

$$f(x, r, \phi) = \frac{f_j}{\pi b_f^2} e^{-r^2/b_f^2} \int_0^{d/2} 2\pi I_0(2 r v/b_f^2) e^{-v^2/b_f^2} v dv \quad (B-3)$$

where I_0 is the hyperbolic Bessel function of zero order. This is an exact, closed-form solution of Reichardt's equation for a round jet. Consider the fully-developed region downstream of the potential core, $x/d \gg 1$. As $x/d \rightarrow \infty$, the argument of I_0 becomes small, and I_0 approaches unity. The integral in equation (B-3) can be evaluated directly, with the approximation $I_0 \sim 1$, to give

$$f(x, r, \phi) = \frac{f_j}{\pi b_f^2} e^{-r^2/b_f^2} \left[\pi b_f^2 (1 - e^{-d^2/4 b_f^2}) \right]$$

Again using the series expansion of $e^{-d^2/4 b_f^2}$ for large x/d , this expression simplifies to

$$f(x, r) = \frac{f_j A_j}{\pi b_f^2} e^{-r^2/b_f^2}, \quad x/d \ll 1 \quad (B-4)$$

where $A_j = \pi d^2/4$, the nozzle exit area. This is just Reichardt's⁽⁶⁰⁾ original formula for the similarity region of a round jet. Note that the subscript ϕ has been dropped because the flow is independent of ϕ , being axisymmetric. Thus, for momentum, equation (B-4) gives:

$$\overline{\rho u^2}(x,r) = \frac{\rho_j u_j^2 A_j}{\pi b_m^2} e^{-r^2/b_m^2}, \quad x/d \gg 1 \quad (B-5)$$

and for heat transport,

$$\overline{\rho u H}(x,r) = \frac{\rho_j u_j H_j A_j}{\pi b_h^2} e^{-r^2/b_h^2}, \quad x/d \gg 1 \quad (B-6)$$

It is now assumed that the jet is incompressible (or constant density everywhere), so that $\rho = \rho_j = \rho_0$. The solution for $\bar{u}(x,r)$ is then approximated by taking the square root of (B-5), after having factored the density:

$$\bar{u}(x,r) \approx u_j \sqrt{\frac{A_j}{\pi b_m^2}} e^{-r^2/2b_m^2} \quad (B-7)$$

The solution for $\bar{H}(x,r)$ is then approximated by dividing equation (B-6) by equation (B-7):

$$\bar{H}(x,r) = H_j \sqrt{\frac{A_j}{\pi}} \frac{b_m}{b_h^2} e^{-r^2/b_h^2} e^{r^2/2b_m^2} \quad (B-8)$$

The turbulent Prandtl number is defined as the ratio of the turbulent effective viscosity to thermal diffusivity,

$$Pr_t = \frac{\mu_t}{k_t C_p} \quad (B-9)$$

where μ_t and k_t are defined by

$$\mu_t = \frac{\overline{\rho u'v'}}{\partial \bar{u}/\partial r}, \quad k_t = C_p \frac{\overline{\rho v'H'}}{\partial \bar{H}/\partial r} \quad (B-10)$$

From Reichardt's hypothesis, equations (166) and (178), we have:

$$\overline{\rho u'v'} \approx \lambda_m \frac{\partial}{\partial r} (\overline{\rho u^2}), \quad \overline{\rho v'H'} \approx \lambda_h \frac{\partial}{\partial r} (\overline{\rho uH}) \quad (\text{B-11})$$

where $\lambda_m = C_m^2 x/2$ and $\lambda_h = C_h^2 x/2$. Combining equations (B-9), (B-10), and (B-11), the Prandtl number can be written as follows:

$$\text{Pr}_t = \frac{C_m^2}{C_h^2} \left(\frac{\left[\frac{\partial}{\partial r} (\overline{\rho u^2}) \right] \left[\frac{\partial \overline{H}}{\partial r} \right]}{\left[\frac{\partial}{\partial r} (\overline{\rho uH}) \right] \left[\frac{\partial \overline{u}}{\partial r} \right]} \right) \quad (\text{B-12})$$

By substituting expressions (B-5) - (B-8) into (B-12), after some lengthy algebra, it is found that:

$$\text{Pr}_t \approx \frac{C_m^2}{C_h^2} \left[2 - \frac{C_h^2}{C_m^2} \right] \quad (\text{B-13})$$

Since, in general, Pr_t does not vary appreciably throughout the flow, equation (B-12) provides a direct relation between C_m and C_h . Solving for C_h/C_m from equation (B-13), the final result is obtained:

$$\frac{C_h}{C_m} \approx \sqrt{\frac{2}{1 + \text{Pr}_t}} \quad (\text{B-14})$$

SYMBOLS AND ABBREVIATIONS

The material content of this report draws from various disciplines (aerodynamics, turbulence theory, shock wave theory, acoustic wave theory, experimental acoustics, etc.), and it is not practical to use a nomenclature which is consistent from section to section and still conform to accepted standard symbolism in each discipline (Section 4.2 uses the symbol b to denote the outer stream radius of coannular jet, for example, whereas Section 4.5 utilizes this same symbol to denote mixing layer thickness).

Different symbol conventions are therefore given for each major section of this report. Sections 4.2 and 4.3 deal with acoustic wave theory, which has its own specialized nomenclature. Section 4.5 deals with aerodynamics and turbulence modeling, so the nomenclature is again specialized. Similarly, Section 4.6 deals with shock cell structure and associated noise, again having a preferred symbol standard. Section 4.7, which is concerned with tying together the salient results of sections 4.3, 4.4, 4.5, and 4.6, has attempted to utilize a common symbolism where possible for purposes of clarity, and this convention may differ from that in any of the previous sections.

LIST OF SYMBOLS AND ABBREVIATIONS FOR SECTION 4.2 and 4.3

A_j	- jet nozzle cross-sectional area
a	- transverse dimension of jet (also inner stream exit radius)
a_{ij}	- circumferentially averaged amplitude of a ring of incoherent (i-j) quadrupoles
b	- transverse dimension of jet (also outer stream exit radius)
b_m	- mixing layer momentum thickness
b_h	- mixing layer enthalpy thickness
c	- speed of sound
c_o	- ambient speed of sound
c_p	- specific heat at constant pressure
C_m	- jet spreading rate parameter
C_h	- enthalpy spreading rate parameter
D	- jet nozzle effective diameter
f	- ($= (-g^2)^{1/2}$) shielding function (also observed frequency)
\mathcal{H}	- Lighthill noise source
g^2	- shielding function
G^2	- modified shielding function
g	- Green's function for Lilley's equation
H	- local stagnation enthalpy relative to ambient
$H_n^{(1)}$	- Hankel function of first kind of order n
i	- ($= \sqrt{-1}$) imaginary unit
I_n	- modified Bessel function of first kind of order n.
J_n	- Bessel function of first kind of order n.

k, k_0	- ratio of source radian frequency and speed of sound at infinity
K	- radial propagation constant
K_1^+, K_2^+	- radial propagation constants
K_n	- modified Bessel function of second kind of order n (K_1, K_2 and K_3 are also used to denote radial propagation constants)
ℓ	- typical turbulent correlation length scale
M	- ($=U/C_\infty$) jet acoustic Mach number relative to the nozzle
M_∞	- aircraft or wind tunnel Mach number
M_c	- ($=U_0/C_\infty$) source convective Mach number relative to the nozzle
N	- ($=(U-U_c)/C_\infty$) - relative acoustic Mach Number
p	- acoustic pressure
P	- acoustic power of source (also used to denote Fourier transform of acoustic pressure)
r	- radial variable
\tilde{r}	- ($=r/a$) inner variable
r_0 or r_{0V}	- turning points of shielding function
R	- distance from jet (also used for outer variable in Section 4.2.1, or to denote the ratio of inner to outer diameter for annular jets in Section 4.2.2)
S	- jet plume cross-sectional area at distance x
s	- axial Fourier transform variable
\mathcal{D}	- pressure source solution to Lilley's equation
St	- Strouhal Number $f(1-M_c \cos \theta)a/U_{1j}$
T	- jet temperature
T_0	- ambient temperature
t	- time
U_1, U_2	- velocity in inner and outer streams
u	- axial (x-component) of velocity

\underline{u}'	- fluctuating fluid velocity
U	- jet axial velocity component relative to the nozzle
U_c	- source convection velocity relative to the nozzle
v	- radial (r - component) of velocity
x	- coordinate along jet axis
x'	- coordinate along jet axis
y	- coordinate normal to jet axis
Y_n	- Bessel function of second kind of order n
z'	- coordinate normal to jet axis
α	- angular coordinate of elemental jet
δ	- delta function
Δ	- Laplacian in transverse variables
\hat{e}	- jump in the radial gradient of pressure across the source point
ϵ	- ratio of jet transverse dimension to wavelength
ϵ_n	- Neumann factor (= 1/2, 1 for n=0, ≥ 1 respectively)
η	- particle displacement (also used to denote radiation efficiency of the inner tubes of a multitube suppressor)
θ	- azimuthal angle
Θ	- angle with respect to the jet axis (also used to denote the azimuthal angle in Section 4.2.1)
ξ	- integral of shielding function
ρ	- fluid density
σ	- (=s/k or s/k ₀) nondimensional axial Fourier transform variable (also radial coordinate of elemental jet)
σ_*	- value of σ at point of stationary phase
ϕ	- velocity potential
Φ	- velocity potential; also angle between elemental shear stress vector and radial coordinate
τ	- turbulent Reynolds stress

χ	- integral of shielding function
ω	- radian frequency
ω_o	- source radian frequency
Ω	- Fourier time transform variable or frequency
VR	- nozzle exit velocity ratio $(U_2/U_1)_j$
AR	- nozzle exit area ratio $(b^2 - a^2)/a^2$
TR	- nozzle exit temperature ratio $(c_2/c_1)_j^2$
SPL	- 1/3-octave band sound pressure level, re: 2×10^{-4} dynes/cm ²
OASPL	- overall sound pressure level, re: 2×10^{-4} dynes/cm ²

Subscripts and Superscripts

$(\cdot)_{12}$	- $(\cdot)_1/(\cdot)_2$
$(\cdot)_o$	- variable defined at the location of a point source
$(\cdot)_B$	- value of a variable at infinity
$(\cdot)_1$	- value of a variable in various regions of a dual flow jet system
$(\cdot)_2$	
$(\cdot)_3$	
$(\cdot)_j$	- variable pertaining to the jet
$\langle \cdot \rangle$	- statistical time average

LIST OF SYMBOLS AND ABBREVIATIONS FOR SECTION 4.5

A	exhaust plane area
a	momentum transport parameter
b_m	momentum transport parameter
b_h	heat transfer parameter
C_m	momentum shear layer spreading rate
C_n	nozzle flow coefficient
C_h	heat (thermal) shear layer spreading rate
c_1, c_2	constants
c_p	specific heat at constant pressure
d, D	jet nozzle diameter
f	transport parameter
G	Green's function
H	stagnation enthalpy relative to ambient, $c_p (T_T - T_o)$
L_c	potential core length
$L(f)$	diffusion equation operator
M	Mach number
Pr_t	turbulent Prandtl number
p	static pressure
R	radial distance between field point P and source point Q in (r, ϕ)-plane
r	radial coordinate
Re_d	jet Reynolds number
S, dS	surface area, area increment
T	static temperature
T_T	stagnation (total) temperature
t	time
u, U	axial x-component of velocity
v	transverse y-component of velocity
w	transverse z-component of velocity
x, X	axial coordinate
y, z	transverse cartesian coordinates
α	variable of integration for ϕ -coordinate
γ	ratio of specific heats
$\delta(y)$	delta function

ζ	variable of integration for z - coordinate
η	variable of integration for y - coordinate
λ	transport coefficient
μ	viscosity
ν	variable of integration for r - coordinate
ξ	variable of integration for x - coordinate
ρ	density
τ	shear stress
ϕ	transverse angular coordinate
ψ	enthalpy function (also stream function)

Subscripts and Superscripts

e	external (ambient) condition or property
j	jet nozzle exit plane condition or property
m	pertaining to momentum transport
h	pertaining to heat transport
o	boundary contour
r	radial component
ϕ	azimuthal component
x	axial component
y	y-component
z	z-component
$(\bar{\quad})$	time-mean value
$(\quad)'$	fluctuating turbulent component

LIST OF SYMBOLS AND ABBREVIATIONS FOR SECTION 4.6

A	-	nozzle exit area
A _n	-	shock cell acoustic pressure amplitude, also area of individual nozzle element
a _o	-	ambient speed of sound
C _l	-	shock-cell cross-correlation coefficient spectrum
D _{eq}	-	diameter based on total equivalent area; $\sqrt{4A_j/\pi}$
D _{eq,n}	-	equivalent element area diameter $\sqrt{4A_n/\pi}$
D _h	-	hydraulic diameter, $4A_j/P_w$
f	-	frequency, Hz.
H _o	-	group source spectrum
L	-	shock cell spacing
M _c	-	eddy convection Mach number
M _j	-	nozzle exit ideally expanded flow Mach number
m	-	index of shock cell location
n	-	index of shock cell location
OASPL	-	overall sound pressure level, dB ref. 0.0002 μ -bar
P _n	-	acoustic pressure
P _{Tj}	-	nozzle exit stagnation pressure
P _w	-	wetted perimeter of nozzle
P _o	-	ambient static pressure
r _n	-	radial distance from nth cell to observer
r _o	-	radial distance from nozzle exit to observer
S _n	-	Strouhal number $\omega L_1/a_o$
SPL	-	1/3 - octave sound pressure level in 1/3-octave bands, dB (ref 0.0002 microbar)
T _{Tj}	-	nozzle exit stagnation temperature
t	-	time
U _c	-	eddy convection speed
V _j	-	ideally expended nozzle exit flow velocity
V _o	-	external flow or flight velocity
x _n	-	axial distance from nozzle exit to nth cell
α	-	high frequency spectrum slope, dB per octave (also exponent $\alpha=1^2$)

- β - shock strength parameter = $\sqrt{M_j^2 - 1}$
- γ - ratio of specific heats
- ϵ - shock cell spacing parameter $\Delta L/L_1$
- ΔL - shock cell spacing increment
- $\Delta f_{1/3}$ - 1/3 - octave bandwidth, Hz.
- θ_1 - observer angle, from inlet, degrees
- ν - frequency ratio, f/f_p
- ω - radian frequency, rad/sec.

Subscripts

- p - peak noise value
- avg - average over all cells
- j - nozzle jet exit value
- 1/3 - 1/3-octave value
- n - relating to n^{th} shock cell
- M - center - frequency of 1/3-octave band

(791)

LIST OF SYMBOLS AND ABBRECIATIONS FOR SECTION 4.7

A_{ann}	nozzle exit plane annulus area
A_j	nozzle exit plane flow area
AR	outer-to-inner stream area ratio
a_{xx}	(x-x) quadrupole directivity factor
a_{xy}	(x-y) quadrupole directivity factor
a_{yy}	(y-y) quadrupole directivity factor
a_{yz}	(y-z) quadrupole directivity factor
b_h	enthalpy mixing layer thickness
b_m	momentum mixing layer thickness
C	convective amplification factor
C_h	enthalpy mixing layer spreading parameter
C_m	momentum mixing layer spreading parameter
C_a	ambient speed of sound
C_p	specific heat at constant pressure
C_1	empirical constant in spreading parameter equation
C_2	empirical constant in spreading parameter equation
D_{eq}	equivalent area nozzle diameter $\sqrt{4A_j/\pi}$
D_h	nozzle hydraulic diameter
f	observed frequency
f_p	peak-noise observed frequency
$f(\xi)$	turbulence model spatial correlation function
$g(\tau)$	turbulence model time delay correlation function
$g^2(r)$	shielding function
H	stagnation enthalpy relative to ambient
$H(\Omega\tau_0)$	turbulence correlation spectrum function
I_{ijkl}	source intensity, (ijkl) - component
$I(\Omega)$	source intensity spectrum
k	source wave number Ω/c_a
L_{avg}	average shock cell spacing
L_x	axial turbulence correlation length scale
M	flow Mach number U/C_a

801

M_a	ambient (wind tunnel or flight) Mach number
M_c	eddy convection Mach number U_c/c_a
M_j	jet nozzle exit plane Mach number U_j/c_a (also U_j/c_j)
M_m	post-merged region potential core Mach number
M_o	Mach number at source location, $M(r_o)$
m	flight velocity exponent
N	number of shock cells
OASPL	overall sound pressure level, dB re 0.0002 μ -bar
PNL	perceived noise level, dB re 0.0002 μ -bar
PR	nozzle stagnation-to-ambient static pressure ratio
PWL	power watt level, dB re 10^{-13} watts
P_w	wetted perimeter of nozzle contour
p_a	ambient static pressure
$\overline{p^2}$	mean-square acoustic pressure
R	source-to-observer distance
R_i	component of R in i -direction ($i=1,2,3$)
R_{ij}	turbulence velocity spatial correlation tensor
R_o	flow field calculation transverse coordinate
R_g	gas constant (1716 $lb_f/slug \cdot ^\circ R$)
r	radial coordinate
$r_b(x)$	centerbody radius
r_o	radial source location
r_σ	radial turning point location
SPL	sound pressure level, dB re 0.0002 μ -bar
SPL_p	peak value of SPL 1/3-octave spectrum
S_{ij}	two-point velocity correlation tensor
S_{ijkl}	fourth-order two-point velocity correlation tensor
T	flow static temperature
T_a	ambient static temperature
T_T	flow stagnation temperature
T_{Tj}	nozzle exit jet stagnation temperature
TR	outer-to-inner stream temperature ratio
U	local mean flow velocity
U_a	ambient (wind tunnel or flight) velocity

U_c	eddy convection speed
U_j	jet exit plane velocity
U_m	post-merged potential core velocity
U_o	mean flow velocity at source location
u'	axial turbulence velocity (r.m.s. intensity)
V_j	ideally expanded jet velocity
VR	outer-to-inner stream velocity ratio
v_i	component of turbulence velocity in i-direction
x	axial coordinate
\bar{y}	vector location of eddy volume in jet
α	coefficient in acoustic calculation; also angular coordinate of nozzle boundary contour
α_t	turbulent decay parameter in convective amplification factor
β	shock strength parameter
β_{xx}	(x-x) quadrupole shielding factor
β_{xy}	(x-y) quadrupole shielding factor
β_{yy}	(y-y) quadrupole shielding factor
β_{yz}	(y-z) quadrupole shielding factor
β_{01}	shielding factor for case (c)
β_{02}	shielding factor for case (e)
β_{12}	shielding factor for case (f)
β_t	axial shear stress weighting factor
γ	ratio of specific heats
Δr	transformed radial coordinate
Δv	transformed boundary radius
δ_{ij}	kronecker delta; $\delta_{ij} = 1$ for $i = j$, $\delta_{ij} = 0$ for $i \neq j$
δ_t	azimuthal shear stress weighting factor
θ	observer angle relative to jet axis
θ_I	observer angle relative to inlet axis, $\theta_I = 180^\circ - \theta$
μ_t	characteristic time-delay azimuthal weighting factor
v_o	radial coordinate of nozzle boundary contour
\bar{r}	cross-correlation separation vector
ρ	flow mean density
ρ_a	ambient density

ρ_j	jet exit plane density
τ	time-delay of two-point cross-correlation
τ_o	characteristic time-delay
τ_x	axial shear stress
τ_r	radial shear stress
τ_ϕ	azimuthal shear stress
ϕ	flow field calculation azimuthal coordinate
ϕ	azimuthal angular coordinate
ψ	enthalpy function
Ω	source radian frequency
ω	observer radian frequency

Subscripts

a	ambient condition
ann	referring to annulus property
b	centerbody parameter
c	convection property
eq	equivalent condition
g	gas property
h	referring to enthalpy or heat transport
i	referring to component in i-direction
I	referenced to inlet axis
j	referring to jet exit plane condition
m	referring to momentum transport; also, post-merged condition
o	referring to source location condition
p	peak noise value
r	radial component
T	stagnation condition
t	referring to a turbulence parameter
x	axial component
xx	referring to (x-x) quadrupole property
xy	referring to (x-y) quadrupole property

803

yy	referring to (y-y) quadrupole property
yz	referring to (y-z) quadrupole property
σ	referring to turning point property
ϕ	azimuthal component

LIST OF SYMBOLS AND ABBREVIATIONS FOR SECTION 5

SPL	sound pressure level in 1/3 octave bands, dB (re. 0.0002 microbar)
OASPL	overall sound pressure level, dB (re. 0.0002 microbar)
PWL	sound power level in 1/3 octave bands, dB (re. 10^{-13} watts)
OAPWL	overall sound power level, dB (re. 10^{-13} watts)
ΔSPL_{ψ}	difference in SPL between measurements in the $\psi = 0^{\circ}$ plane and the $\psi = 90^{\circ}$ plane
ΔPWL_{ψ}	difference in PWL between measurements in the $\psi = 0^{\circ}$ plane and the $\psi = 90^{\circ}$ plane
$\Delta\text{OASPL}_{\psi}$	difference in OASPL between measurements in the $\psi = 0^{\circ}$ and the $\psi = 90^{\circ}$ plane
$\Delta\text{OAPWL}_{\psi}$	difference in OAPWL between measurements in the $\psi = 0^{\circ}$ and the $\psi = 90^{\circ}$ plane
ΔSPL_0	difference in SPL between single plus 3 dB and twin in the $\psi = 0^{\circ}$ plane
ΔOAPWL_0	difference in OAPWL between single plus 3 dB and twin in the $\psi = 0^{\circ}$ plane
ψ	azimuthal angle taken around the jet center-line
θ	angle to the jet axis
f	frequency (Hz)
f_m	lowest frequency at which $\Delta\text{SPL}_{\psi} \geq 3$ dB
θ_s	shielded angle where $\Delta\text{SPL}_{\psi} \geq 3$ dB
A	cross-sectional area of jet nozzle exit
d	diameter of round nozzle
D, d_e	equivalent diameter
U	jet mean velocity at measuring location
\bar{u}_o, v_j	jet velocity (fps)
u'	jet turbulent velocity
T_j	plenum temperature ($^{\circ}$ R)
M, M_j	jet Mach number
a_o	ambient speed of sound
C_o	ambient speed of sound

T_0	ambient temperature ($^{\circ}$ R), also jet stagnation temperature
M_0	V_J/a_0
M_c	convected Mach number
ρ_0	ambient air density
ρ_j	jet density at the exit plane
S_c	convected Strouhal number
s	center-to-center spacing between nozzles
w	length of rectangular nozzle
$ T $	absolute value of transmission coefficient
t	width of rectangular nozzle
x	transverse direction perpendicular to y and z
y	axial direction along jet centerline
z	transverse direction connecting the centerlines of twin or cluster jets
Δz	separation distance between jets
ω	density exponent
OAPWL*	$OAPWL - 10\log_{10}[(\rho_j/\rho_0)^{\omega}]$
COAPWL	$OAPWL - 10\log_{10}[A(\rho_j/\rho_0)^{\omega}]$
$C[]$	$[] - 10\log_{10}[A(\rho_j/\rho_0)^{\omega}]$

LIST OF SYMBOLS AND ABBREVIATIONS FOR SECTION 6

a	inner radius of the annular jet
b	outer radius of the annular jet
M	Mach number of the annular shielding jet
T	temperature of the annular shielding jet
ω	sound source radian frequency
C	speed of sound
θ	angle from the forward jet centerline
M_c	convective Mach number of the sound source
f_o	source frequency
f	frequency measured by the microphone
A	nondimensional source frequency $(\frac{2\pi a}{c}) f_o$
P	farfield sound pressure measured of the sound source with a shielding jet flow
P_o	farfield sound pressure of the sound source only

REFERENCES

1. Potter, R.C. and Jones, J.H., "An Experiment to Locate the Acoustic Sources in a High Speed Jet Exhaust System," Acoustic Society of America, 1967.
2. MacGregor, W.A. and Simcox, C.D., "The Location of Acoustic Sources in Jet Flows by Means of the Wall Isolation Technique," AIAA Paper 73-1041, 1973.
3. Asher, J.A., "Laser Velocimeter System Development and Testing," Instrumentation for Airbreathing Propulsion, Progress in Aeronautics, Vol. 34, MIT Press, 1974, pp. 141-166.
4. Lighthill, M.J., "On Sound Generated Aerodynamically. I. General Theory," Proc. Roy. Soc. of Lond., Vol. A211, 1952, pp. 564-587.
5. Lighthill, M.J., "On Sound Generated Aerodynamically. II. Turbulence as a Source of Sound," Proc. Roy. Soc. of Lond., Vol. A222, 1954, pp. 1-32.
6. Ffowcs-Williams, J.E., "The Noise from Turbulence Convected at High Speed," Phil. Trans. Roy. Soc. (Lond.), Vol. A255, 1963, pp. 469-503.
7. Ribner, H.S., "Aerodynamic Sound from Fluid Dilatations," U.T.I.A. Report No. 86, 1962.
8. Greatrix, F.B. and Brown, D.N., "Progress in Jet Engine Noise Reduction," Proc. First Internat. Congress Aero. Sci., Vol. 1, September 1958.
9. Ribner, H.S., "The Generation of Sound by Tubulent Jets," Advances in Applied Mechanics, Vol. 8, Academic Press, 1964.
10. Lush, P.A., "Measurements of Subsonic Jet Noise and Comparison with Theory," J. Fluid Mech. Vol. 46, 1971, pp. 477-500.
11. Hoch, R.G. et al, "Studies of the Influence of Density on Jet Noise," J. Sound Vib., Vol. 28(4), 1973, pp. 649-668.
12. Powell, A., "Concerning the Noise of Turbulent Jets," J. Acoust. Soc. Amer., Vol. 32(12), December 1960, pp. 1609-1612.
13. Phillips, O.M., "On the Generation of Sound by Supersonic Turbulent Shear Layers," J. Fluid Mech., Vol. 9, 1960, pp. 1-28.
14. Csanady, G.T., "The Effects of Mean Velocity Variations on Jet Noise," J. Fluid Mech. Vol. 26(1), 1966, pp. 183-197.
15. Lilley, G.M., Morris, P.J., and Tester, B.J., "On the Theory of Jet Noise and its Application," AIAA Paper No. 73-987, October 1973.

16. Davies, P.O.A.L., Fisher, M.J., and Barratt, M.J., "The Characteristics of the Turbulence in the Mixing Region of a Round Jet," J. Fluid Mech., Vol. 15, 1963, pp. 337-367.
17. Mani, R., "Moving Source Problem Relevant to Jet Noise," J. Sound and Vibration, 25, (2), 1972, p. 337.
18. Olsen, W.A., Gutierrez, O.A., and Dorsch, R.G., "The Effect of Nozzle Inlet Shape, Lip Thickness and Exit Shape and Size on Subsonic Jet Noise," NASA TMX-68182, 1973.
19. Crighton, D.G., "Instability of an Elliptic Jet," J. Fluid Mechanics, 59, pp. 665-672, 1973.
20. Germain, P., "Recent Evolution in Problems and Methods in Aerodynamics," J. Roy. Aero. Soc., 71, 1967, p. 677.
21. Miles, J.W., "On Radiation and Scattering from Small Cylinders," J.A.S.A., 25, 1953, p. 1087.
22. Landau, L.D. and Lifshitz, E.M., Fluid Mechanics, Addison-Wesley, 1959.
23. Van Dyke, M., Perturbation Methods in Fluid Mechanics, Academic, 1964.
24. Fraenkel, L.E., "On the Method of Matched Asymptotic Expansions," Proc. Camb. Phil. Soc., 65, 1969, p. 209.
25. Morse, P.M. and Ingard, K.U., Theoretical Acoustics, McGraw-Hill, 1968.
26. Miles, J.W., "On the Reflection of Sound at an Interface of Relative Motion," J.A.S.A., 29, 1957, p. 226.
27. Batchelor, G.K. and Gill, A.E., "Analysis of the Stability of Axisymmetric Jets," J.F.M., 14, 1962, p. 529.
28. Jones, D.S. and Morgan, J.D., "The Instability of a Vortex Sheet on a Subsonic Stream Under Acoustic Radiation," Proc. Camb. Phil. Soc., 72, 1972, p. 405.
29. Ffowcs-Williams, J.E., "Technical Evaluation Report," vii, AGARD - CPP - 131 (Noise Mechanisms), 1973.
30. Lush, P.A., "Measurements of Subsonic Jet Noise and Comparison with Theory," J.F.M., 46, 1971, p. 477.
31. Carrier, G.F., Krook, M., and Pearson, C.E., Functions of a Complex Variable, McGraw-Hill, 1966.
32. Gray, V.H., Gutierrez, O.A., Walker, D.Q., "Assessment of Jets as Acoustic Shields by Comparison of Single and Multitube Suppressor Nozzle Data," AIAA Paper 73-1001, 1973.

9

33. Cowan, S.J., Crouch, R.W., "Transmission of Sound Through a Two-Dimensional Shielding Jet," AIAA Paper 73-1002, 1973.
34. Abramowitz, M. and Stegun, I.A., Handbook of Mathematical Functions, Dover, 1965.
35. Balsa, T.F., "Fluid Shielding of Low Frequency Convected Sources by Arbitrary Jets," J. Fluid Mechanics, 70, 1975, p. 17.
36. Motsinger, R.E. and Sieckman, A.R., "Prediction of Supersonic Jet Noise Reduction Using Multitube Nozzle Suppressors," General Electric, R73AEG156, 1973.
37. Mani, R., "The Influence of Jet Flow on Jet Noise, Part I, The Noise of Unheated Jets," J. Fluid Mech., 76, 1976, p. 753.
38. Mani, R., "The Influence of Jet Flow on Jet Noise, Part II, The Noise of Heated Jets," J. Fluid Mech., 76, p. 779.
39. Ribner, H.S., "Quadrupole Correlations Governing the Pattern of Jet Noise," Journal of Fluid Mechanics, Vol. 38, 1969, p. 1.
40. Olsen, W. and Friedman, R., (1974), Jet Noise from Coaxial Nozzles Over a Wide Range of Geometric and Flow Parameters, AIAA Paper No. 74-43.
41. Kazin, S.B., et al., "Core Engine Noise Control Program," General Electric Company Contractor Final Report No. FAA-RD-74-125, 1974.
42. Lighthill, M.J., "On Sound Generated Aerodynamically: General Theory," Proceedings of the Royal Society of London, A211, 1952, p. 564.
43. Mani, R., The Jet Density Exponent Issue for the Noise of a Heated Subsonic Jet, JFM, 64, 1974, p. 611.
44. Schubert, L.K., "Numerical Study of Sound Refraction by a Jet Flow, I and II," J.A.S.A., 51, 439, 1972, p. 447.
45. Pao, S.P., (1973), Aerodynamic Noise Emission from Turbulent Shear Layers, JFM, 59, p. 451.
46. Gliebe, P.R. and Balsa, T.F., "The Aerodynamics and Acoustics of Coaxial Jet Noise," AIAA Paper 76-492, Third AIAA Aero-Acoustics Conference, Palo Alto, 1976.
47. Balsa, T.F., "The Far Field of High Frequency Convected Singularities in Sheared Flows, With an Application to Jet Noise Prediction," JFM, 74, 1976, p. 193.
48. Goldstein, M.E., "The Low Frequency Sound from Multipole Sources in Axisymmetric Shear Flows, With Application to Jet Noise," JFM, 70, 1975, p. 595.

49. Balsa, T.F., "The Acoustic Field of Sources in Shear Flow with Application to Jet Noise: Convective Amplification," JFM, 79, 1976, p. 33.
50. Goldstein, M.E., "The Low Frequency Sound from Multipole Sources in Axisymmetric Shear Flows - Part I," JFM, 75, 1976, p. 17.
51. Goldstein, M.E., Aeroacoustics, McGraw-Hill, 1976.
52. Tester, B.J. and Morfey, C.L., "Developments in Jet Noise Modeling -- Theoretical Predictions and Comparisons with Measured Data," JSV, 46(1), 1976, p. 79.
53. Magnus, W., Oberhettiger, F., Soni, R.P., Formulas and Theorems for the Special Functions of Mathematical Physics, Springer Verlag, 1966.
54. Balsa, T.F., "The Acoustic Field of Sources in Shear Flow With Application to Jet Noise: Convective Amplification," JFM, 79, 1977, p. 33.
55. Morse, P.M., Ingard, K.U., Theoretical Acoustics, McGraw-Hill, 1968.
56. Stringas, E.J., and Mani, R., "Aircraft/Engine Jet Noise Control - A Survey," AIAA Paper No. 74-947, August 1974.
57. Launder, B.E., and Spalding, D.B., "Lectures in Mathematical Models of Turbulence," Academic Press, London, 1972.
58. Kendall, R.M., and Grose, R.D., "Theoretical Predictions of the Sound Produced by Jets having an Arbitrary Cross Section," ASME Symposium on Fully Separated Flows, pp. 58-63, 1964.
59. Alexander, L.G., Baron, T., and Comings, W., "Transport of Momentum Mass, and Heat in Turbulent Jets," Univ. of Ill. Bulletin, Vol. 50, No. 66, May 1953.
60. Reichardt, H., "On a New Theory of Free Turbulence," Royal Aeronautical Society Journal, Vol. 47, 1943, pp. 167-176.
61. Hinze, J.O., Turbulence - An Introduction to its Mechanism and Theory, McGraw-Hill, Inc., New York, 1959.
62. Kantola, R.A., "Extension of Reichardt's Method to Include Base Pressure Effects on Jet Noise Suppressors," General Electric Tech. Info. Series Report No. 75CRD061, March 1975.
63. Greenberg, M.D., Application of Green's Functions in Science and Engineering, Prentice-Hall, Inc., Englewood Cliffs, New Jersey, 1971.
64. Forstall, W. Jr., and Shapiro, A.H., "Momentum and Mass Transfer in Coaxial Gas Jets," Journ. Appl. Mech., December 1950.

65. Bradbury, L.J.S., "Simple Expressions for the Spread of Turbulent Jets," Aero. Quart., May 1967.
66. Harsha, P.T., "Free Turbulent Mixing: A Critical Evaluation of Theory and Experiment," AEDC TR-71-36, February 1971.
67. VonGlahn, U., Groesbeck, D., and Goodykoontz, J. (1973, "Velocity Decay and Acoustic Characteristics of Various Nozzle Geometries with Forward Velocity," NASA TM X-68259, July 1973.
68. Schlichting, H., Boundary Layer Theory, 4th ed., McGraw-Hill, 1960.
69. Harper-Bourne, M. and Fisher, M.J., "The Noise from Shock Waves in Supersonic Jets," AGARD CPP-131, 1973. See also SAE A21 Committee letter dated 4/1/75, "Prediction of Single Stream Shock Cell Noise," by K.W. Bushell.
70. Ribner, H.S., "Shock-Turbulence Interaction and the Generation of Noise," NACA Report No. 1233, 1955.
71. SNECMA (1976) "Previous Simpliffee du Bruit d'ondes de Choc d'un Jet Supercritique de Tuyere Convergente," S.N.E.C.M.A. Report YKA No. 5982/76, October 11, 1976.
72. Clapper, W.S., et al., "High Velocity Jet Noise Source Location and Reduction: Task 4 - Development/Evaluation of Techniques for 'Inflight' Investigation," General Electric Company, Report No. FAA-RD-76-79, IV (R77AEG189), Final Report, February 22, 1977.
73. Cocking, B.J., "The Effect of Temperature on Subsonic Jet Noise," National Gas Turbine Establishment (U.K.) Report No. R.331, May 1974.
74. Kurn, A.G., "Observations of the Flow from a Rectangular Nozzle," Royal Aircraft Establishment, Tech. Rept. No. 74043, March 1974.
75. Drevet, P. et al (1976), "Effect of Flight on the Noise from a Convergent Nozzle as Observed on the Bertin Aerotraine," AIAA Paper No. 76-557, July 1976.
76. Lee, R., Kendall, R.M., et al., "Research Investigation of the Generation and Suppression of Jet Noise," General Electric Company, Report No. NOas 59-6160-C, January 1961.
77. Grose, R.D. and Kendall, R.M., "Theoretical Predictions of the Sound Produced by Jets Having an Arbitrary Cross Section," A.S.M.E. Symposium on Fully Separated Flows, May 1964, pp. 58-63.
78. Benzakein, M.J., Chen, C.Y., and Knott, P.R. (1971) "A Computational Technique for Jet Aerodynamic Noise," A.I.A.A. Paper No. 71-583, June 1971.

79. Jones, I.S.F., "Aerodynamic Noise Dependent on Mean Shear," J. Fluid Mech., Vol. 35, 1968, pp. 65-72.
80. Knott, P.R., and Benzakein, M.J. (1973), "Analytical and Experimental Supersonic Jet Noise Research," A.I.A.A. Paper No. 73-188, January 1973.
81. Moon, L.H., and Zelazny, S.W., "Jet Noise Modeling: Experimental Study and Models for the Noise and Turbulence Fields," A.I.A.A. Paper No. 74-3, 1974
82. Chen, C.Y. (1976), "A Model for Predicting Aero-Acoustic Characteristics of Coaxial Jets," A.I.A.A. Paper No. 76-4, January 1976.
83. Davis, P.O.A.L., "Turbulence Structure in Free Shear Layers," A.I.A.A. Journal, Vol. 4(11), November 1966, pp. 1971-1978.
84. Bass, H.E., Bauer, H.J., and Evans, L.B., "Atmospheric Absorption of Sound: Analytical Expressions," J. Acoust. Soc. Amer., Vol. 32(3), pp. 821-825.
85. Lin, C.C., Statistical Theories of Turbulence, Princeton Univ. Press, 1961.
86. Batchelor, G.K., The Theory of Homogeneous Turbulence, Cambridge Univ. Press, 1953.
87. Deneuville, P., "Prevision Simplifiee du Bruit d'Ondes de Choc d'un Jet Supercritique de Tuyere Convergente," SNECMA YKA No. 5982/76, October 11, 1976.
88. Gliebe, P.R. (1977), "A Simplified Prediction Method for Conical Nozzle Shock-Cell Noise," General Electric Company Tech. Memo. No. 76-673, March 1977.
89. Tanna, H.K., Dean, P.D., and Fisher, M.J., "The Influence of Temperature on Shock-Free Supersonic Noise," J. Sound and Vibration, Vol. 39, No. 4, 1975, pp 429-460.
90. Bushell, K.W., "Measurement and Prediction of Jet Noise in Flight," A.I.A.A. Paper No. 75-461, March 1975.
91. Bowman, J.J., et al., Electromagnetic and Acoustic Scattering by Simple Shapes, Amsterdam North Holland, 1969.
92. Butler, G.F., "A Note on Improving the Attenuation Given by a Noise Barrier," Journal of Sound and Vibration, 32(3), 1973, pp. 367-369.
93. Noble, B., The Wiener-Hopf Technique, London, Pergamon, 1958.
94. Kantola, R.A., "Outdoor Jet Noise Facility, A Unique Approach," AIAA Progress Series in Astronautics and Aeronautics, Vol. 46, 1976, pp. 223-245.
95. Maestrello, L. and McDaid, E., "Acoustic Characteristics of a High Subsonic Jet," AIAA Journal, Vol. 9, No. 6, June 1971, pp. 1058-1066.

96. Kouts, C. and Yu, J.C., "Far Noise Field of a Two-Dimensional Subsonic Jet," AIAA Paper No. 74-44, January 1974.
97. Norum, T.D., "Measured and Calculated Transmission Losses of Sound Waves Through a Helium Layer," NASA TN D-7230, May 1973.
98. Wang, J.C.F., "Velocity Measurement of High-temperature and High Speed Subsonic Jet Flows Using a Laser Velocimeter," Proceeding of ISL/AGARD Workshop on Laser Anemometry, pp. 325-374, St. Louis, France, May 1976.
99. Lush, P.A. and Burrin, R.H., "An Experimental Investigation of Jet Noise Variation with Velocity and Temperature," AFAPL-TR-72-53-Vol. V, July 1972.
100. Greatrex, F.B. and Brown, D.M., "Progress in Jet Engine Noise Reduction," presented at the First Congress International Council of the Aeronautical Sciences, Madrid, September 1959.
101. Goethert, B.H. and Borchers, I.U., "Noise and Thrust Characteristics of Shrouded Multi-Nozzles of Circular Cross Section," AIAA Paper 74-45, Washington, D.C., January 1974.
102. Yeh, C., "A Further Note on the Reflection and Transmission of Sound Waves by a Moving Fluid Layer," J. Acoust. Soc. Am., Vol. 43, No. 6, 1968, pp. 1454-1455.
103. Lord Rayleigh, Theory of Sound (Dover Publications, New York) 1945, Vol. 2, pp. 86-88.
104. Lawrence, J.C., (1956), "Intensity, Scale and Spectra of Turbulence in Mixing Region of Free Subsonic Jet," NACA Report No. 1292.
105. Wooldridge, C.E., Wooten, D.C., and Amaro, A.J., (1971), "The Structure of Jet Turbulence Producing Jet Noise," SRI Report, June, 1971.
106. Howes, W.L., Calahan, E.E., and Mull, H.R., "Near Noise Field of a Jet Engine Exhaust," NACA 1338, 1957.
107. Dunn, D.G. et al, "Aircraft Configuration Noise Reduction. Vol. 1 - Engineering Analysis," FAA-RD-76-76-1, June 1976.
108. von Glahn, V., et al., "Geometry Considerations for Jet Noise Shielding with CTOL Engine-Over-the-Wing Concept," AIAA Paper 76-568, June 1974.
109. Siddon, T.E., Hogland, L. and Davis, B., "Validation Report-UBC Anechoic Chamber and Jet Noise Facility, Submitted to General Electric Co. November 1974.
110. Chu, W.T., and Laufer, J., "Jet Noise Measurements in the University of Southern California Anechoic Chamber, report submitted to General Electric Co., 1974.

111. Olsen, W. and Friedman, R., - Jet Noise From Co-axial Nozzles Over a Wide Range of Geometric and Flow Parameters, AIAA Paper No. 74-43 presented at 12th Aerospace Sciences Meeting, Washington, D.C., January/February 1974.
112. Sato, H. - Experimental Investigation on the Transition of Laminar Separated Layer, Journal of Phys. Soc. of Japan, Vol. 11, No. 6, June 1956.
113. Siddon, T.E., "Surface Dipole Strength by Cross Correlation Method," JASA, Vol. 53, No. 2, pp 619-633, February 1973.
114. Siddon, T.E. - Development of a Miniature Condenser Microphone, Ling - Temco - Vought Research Center, Western Division, TR No. O-71200/6TR-106, September 1966.
115. Siddon, T.E. - Some Observations on Source Detection Methods with Application to Jet Noise, Paper B-3 at Second Inter-Agency Symposium on University Research in Transportation Noise, Raleigh, North Carolina, June 1947 (published in Proceedings - 16 pages).
116. Siddon, R.E. - Noise Source Diagnostics by Causality Correlations, Proc. of AGARD Specialist Conference on "Noise Mechanisms", September 1973, AGARD CPP - 131, pp. 7-1 to 7-12. See also contribution to Panel Discussion, pp A1-A4.
117. Grosche, F.R. - Distributions of Sound Source Intensities in Subsonic and Supersonic Jets, Paper No. 4 presented at AGARD Specialist Conference on Noise Mechanisms, September 1973. Published in AGARD CPP-131, pgs. 4.1-4.10.
118. Winant, C.D. and Browand, F.K. - Vortex Pairing: the Mechanism of Turbulent Mixing-Layer Growth at Moderate Reynolds Number. J. Fluid Mechanics (1974), Vol. 63, part 2, pg. 237-255.
119. Lin, C.C. - Hydrodynamic Stability, Quarterly of Applied Mathematics, Vol. 3, No. 3, 1945
120. Candel, S.M. and Marble, F.E., "Acoustic Attenuation in Fans and Ducts by Vaporization of Liquid Droplets," AIAA Journal, Vol. 13, No. 5, May 1975, pp. 634-639.
121. Marble, F.E., "Dynamics of Dusty Gases," Annual Review of Fluid Mechanics, Vol. 2, 1970.
122. Burge, H.L. and Manson, L., "Jet Noise Reduction Through Liquid-Base Foam Injection," Journal of Acoustical Society of America, Vol. 50, No. 4, Part 1, 1971.
123. Savell, C.T., Stringas, E.J., et al., "High Velocity Jet Noise Source Location and Reduction" - "Task 1, Activation of Facilities and Validation of Source Location Techniques," FAA-RD-76-79, I, February 1977.

124. Michalke, A., "Instabilität Eines Kompressiblen Runden Freistrahls Unter Berücksichtigung des Einflusses der Strahlgrenzschichtdicke," Z. Flugwiss, 19, (Heft 8/9), 1971.
125. Crow, S.C. and Champagne, F.H., "Orderly Structure in Jet Turbulence," JFM, Vol. 48, Part 3, 1971.
126. Chu, W.T., Kaplan, R.E., "A Diagnostic Tool for Jet Noise Strength Distribution Measurement," USCAE 128, March 1975.
127. Laufer, J., Schlinker, R. and Kaplan, R.E., "Experiments on Supersonic Jet Noise," AIAA Paper 75-478, March 1975.
128. Middleton, D., "The Noise of Ejectors," A.R.C., R&M. No. 3389, 1965.
129. Anderson, B.H., "Computer Program for Calculating the Flow Field of Supersonic Ejector Nozzles," NASA Tech. Note IND-7602, April 1974.
130. Bridges, E.H. (1975), "Users Guide for Ejector Nozzle Flow Analysis Program F10062," General Electric Company Technical Memorandum TM 75-607, September 1975.
131. Gordon, C.G., "Spoiler Generated Flow Noise II Results," Journal of the Acoustical Society of America, Vol. 45, No. 1, 1969, p. 214.
132. Yudin, Ya E., "The Acoustic Power of the Noise Created by Airduct Elements," Sov. Phys. - Acoust., 1, (1955) pp. 383-398.
133. Alexander, L.G., Baron, T. and Comings, W., (1953), "Transport of Momentum, Mass and Heat in Turbulent Jets," University of Illinois, Engineering Experiment Station Bulletin No. 413.
134. Ribner, H.S., "On the Strength Distribution of Noise Sources Along a Jet, University of Toronto," UTIAS Report No. 51, 1958.
135. Powell, A., (1959), Similarity and Turbulent Jet Noise, Journal of the Acoustic Society of America, 31, p. 812.
136. Gliebe, P.R., "Complex Jet Flow Simulation by Superposition," General Electric Tech. Memo No. 74-574, July 1974.
137. Bilwakesh K, et al.: Section 6, "Obstruction Noise", FAA Report FAA-RD-74-125, 11 (1974)

816 ALL

DATE
FILMED
— 8